SECOND EDITION

ELECTROCHEMICAL

METHODS

Fundamentals and

Applications

Allen J. Bard

Larry R. Faulkner

Department of Chemistry and Biochemistry
University of Texas at Austin

PREFACE

In the twenty years since the appearance of our first edition, the fields of electrochemistry and electroanalytical chemistry have evolved substantially. An improved understanding of phenomena, the further development of experimental tools already known in 1980, and the introduction of new methods have all been important to that evolution. In the preface to the 1980 edition, we indicated that the focus of electrochemical research seemed likely to shift from the development of methods toward their application in studies of chemical behavior. By and large, history has justified that view. There have also been important changes in practice, and our 1980 survey of methodology has become dated. In this new edition, we have sought to update the book in a way that will extend its value as a general introduction to electrochemical methods.

We have maintained the philosophy and approach of the original edition, which is to provide comprehensive coverage of fundamentals for electrochemical methods now in widespread use. This volume is intended as a textbook and includes numerous problems and chemical examples. Illustrations have been employed to clarify presentations, and the style is pedagogical throughout. The book can be used in formal courses at the senior undergraduate and beginning graduate levels, but we have also tried to write in a way that enables self-study by interested individuals. A knowledge of basic physical chemistry is assumed, but the discussions generally begin at an elementary level and develop upward. We have sought to make the volume self-contained by developing almost all ideas of any importance to our subject from very basic principles of chemistry and physics. Because we stress foundations and limits of application, the book continues to emphasize the mathematical theory underlying methodology; however the key ideas are discussed consistently apart from the mathematical basis. Specialized mathematical background is covered as needed. The problems following each chapter have been devised as teaching tools. They often extend concepts introduced in the text or show how experimental data are reduced to fundamental results. The cited literature is extensive, but mainly includes only seminal papers and reviews. It is impossible to cover the huge body of primary literature in this field, so we have made no attempt in that direction.

Our approach is first to give an overview of electrode processes (Chapter 1), showing the way in which the fundamental components of the subject come together in an electrochemical experiment. Then there are individual discussions of thermodynamics and potential, electron-transfer kinetics, and mass transfer (Chapters 2–4). Concepts from these basic areas are integrated together in treatments of the various methods (Chapters 5–11). The effects of homogeneous kinetics are treated separately in a way that provides a comparative view of the responses of different methods (Chapter 12). Next are discussions of interfacial structure, adsorption, and modified electrodes (Chapters 13 and 14); then there is a taste of electrochemical instrumentation (Chapter 15), which is followed by an extensive introduction to experiments in which electrochemistry is coupled with other tools (Chapters 16–18). Appendix A teaches the mathematical background; Appendix B provides an introduction to digital simulation; and Appendix C contains tables of useful data.

This structure is generally that of the 1980 edition, but important additions have been made to cover new topics or subjects that have evolved extensively. Among them are applications of ultramicroelectrodes, phenomena at well-defined surfaces, modified electrodes, modern electron-transfer theory, scanning probe methods, LCEC, impedance spectrometry, modern forms of pulse voltammetry, and various aspects of spectroelectrochemistry. Chapter 5 in the first edition ("Controlled Potential Microelectrode Techniques—Potential Step Methods") has been divided into the new Chapter 5 ("Basic Potential Step Methods") and the new Chapter 7 ("Polarography and Pulse Voltammetry"). Chapter 12 in the original edition ("Double Layer Structure and Adsorbed Intermediates in Electrode Processes") has become two chapters in the new edition: Chapter 12 ("Double-Layer Structure and Adsorption") and Chapter 13 ("Electroactive Layers and Modified Electrodes"). Whereas the original edition covered in a single chapter experiments in which other characterization methods are coupled to electrochemical systems (Chapter 14, "Spectrometric and Photochemical Experiments"), this edition features a wholly new chapter on "Scanning Probe Techniques" (Chapter 16), plus separate chapters on "Spectroelectrochemistry and Other Coupled Characterization Methods" (Chapter 17) and "Photoelectrochemistry and Electrogenerated Chemiluminescence" (Chapter 18). The remaining chapters and appendices of the new edition directly correspond with counterparts in the old, although in most there are quite significant revisions.

The mathematical notation is uniform throughout the book and there is minimal duplication of symbols. The List of Major Symbols and the List of Abbreviations offer definitions, units, and section references. Usually we have adhered to the recommendations of the IUPAC Commission on Electrochemistry [R. Parsons et al., *Pure Appl. Chem.*, **37**, 503 (1974)]. Exceptions have been made where customary usage or clarity of notation seemed compelling.

Of necessity, compromises have been made between depth, breadth of coverage, and reasonable size. "Classical" topics in electrochemistry, including many aspects of thermodynamics of cells, conductance, and potentiometry are not covered here. Similarly, we have not been able to accommodate discussions of many techniques that are useful but not widely practiced. The details of laboratory procedures, such as the design of cells, the construction of electrodes, and the purification of materials, are beyond our scope. In this edition, we have deleted some topics and have shortened the treatment of others. Often, we have achieved these changes by making reference to the corresponding passages in the first edition, so that interested readers can still gain access to a deleted or attenuated topic.

As with the first edition, we owe thanks to many others who have helped with this project. We are especially grateful to Rose McCord and Susan Faulkner for their conscientious assistance with myriad details of preparation and production. Valuable comments have been provided by S. Amemiya, F. C. Anson, D. A. Buttry, R. M. Crooks, P. He, W. R. Heineman, R. A. Marcus, A. C. Michael, R. W. Murray, A. J. Nozik, R. A. Osteryoung, J.-M. Savéant, W. Schmickler, M. P. Soriaga, M. J. Weaver, H. S. White, R. M. Wightman, and C. G. Zoski. We thank them and our many other colleagues throughout the electrochemical community, who have taught us patiently over the years. Yet again, we also thank our families for affording us the time and freedom required to undertake such a large project.

Allen J. Bard
Larry R. Faulkner

CONTENTS

MAJOR SYMBOLS

Listed below are symbols used in several chapters or in large portions of a chapter. Symbols similar to some of these may have different local meanings. In most cases, the usage follows the recommendations of the IUPAC Commission on Electrochemistry [R. Parsons et al., *Pure Appl. Chem.*, **37**, 503 (1974).]; however there are exceptions.

A bar over a concentration or a current [e.g., $\bar{C}_O(x, s)$] indicates the Laplace transform of the variable. The exception is when i indicates an average current in polarography.

▶ STANDARD SUBSCRIPTS

a	anodic	dl	double layer	O	pertaining to species O in O $+ ne \rightleftarrows$ R
c	(a) cathodic	eq	equilibrium	p	peak
	(b) charging	f	(a) forward	R	(a) pertaining to species R in O $+ ne \rightleftarrows$ R
D	disk		(b) faradaic		(b) ring
d	diffusion	l	limiting	r	reverse

▶ ROMAN SYMBOLS

Symbol	Meaning	Usual Units	Section References
A	(a) area	cm^2	1.3.2
	(b) cross-sectional area of a porous electrode	cm^2	11.6.2
	(c) frequency factor in a rate expression	depends on order	3.1.2
	(d) open-loop gain of an amplifier	none	15.1.1
$\mathscr{A}$	absorbance	none	17.1.1
a	(a) internal area of a porous electrode	cm^2	11.6.2
	(b) tip radius in SECM	μm	16.4.1
a_j^α	activity of substance j in a phase α	none	2.1.5
b	$\alpha F v / RT$	s^{-1}	6.3.1
b_j	$\beta_j \Gamma_{j,s}$	mol/cm^2	13.5.3
C	capacitance	F	1.2.2, 10.1.2
C_B	series equivalent capacitance of a cell	F	10.4
C_d	differential capacitance of the double layer	F, F/cm^2	1.2.2, 13.2.2
C_i	integral capacitance of the double layer	F, F/cm^2	13.2.2
C_j	concentration of species j	M, mol/cm^3	
C_j^*	bulk concentration of species j	M, mol/cm^3	1.4.2, 4.4.3
$C_j(x)$	concentration of species j at distance x	M, mol/cm^3	1.4

Symbol	Meaning	Usual Units	Section References
$C_j(x=0)$	concentration of species j at the electrode surface	M, mol/cm^3	1.4.2
$C_j(x, t)$	concentration of species j at distance x at time t	M, mol/cm^3	4.4
$C_j(0, t)$	concentration of species j at the electrode surface at time t	M, mol/cm^3	4.4.3
$C_j(y)$	concentration of species j at distance y away from rotating electrode	M, mol/cm^3	9.3.3
$C_j(y=0)$	surface concentration of species j at a rotating electrode	M, mol/cm^3	9.3.4
C_{SC}	space charge capacitance	F/cm^2	18.2.2
C_s	pseudocapacity	F	10.1.3
c	speed of light *in vacuo*	cm/s	17.1.2
D_E	diffusion coefficient for electrons within the film at a modified electrode	cm^2/s	14.4.2
D_j	diffusion coefficient of species j	cm^2/s	1.4.1, 4.4
$D_j(\lambda, \mathbf{E})$	concentration density of states for species j	cm^3 eV^{-1}	3.6.3
$\mathbf{D_M}$	model diffusion coefficient in simulation	none	B.1.3, B.1.8
D_S	diffusion coefficient for the primary reactant within the film at a modified electrode	cm^2/s	14.4.2
d	distance of the tip from the substrate in SECM	μm, nm	16.4.1
d_j	density of phase j	g/cm^3	
E	(a) potential of an electrode versus a reference	V	1.1, 2.1
	(b) emf of a reaction	V	2.1
	(c) amplitude of an ac voltage	V	10.1.2
ΔE	(a) pulse height in DPV	mV	7.3.4
	(b) step height in tast or staircase voltammetry	mV	7.3.1
	(c) amplitude (1/2 p-p) of ac excitation in ac voltammetry	mV	10.5.1
$\mathbf{E}$	electron energy	eV	2.2.5, 3.6.3
$\boldsymbol{\mathscr{E}}$	electric field strength vector	V/cm	2.2.1
$\mathscr{E}$	electric field strength	V/cm	2.2.1
$\dot{E}$	voltage or potential phasor	V	10.1.2
E^0	(a) standard potential of an electrode or a couple	V	2.1.4
	(b) standard emf of a half-reaction	V	2.1.4
ΔE^0	difference in standard potentials for two couples	V	6.6
$\mathbf{E}^0$	electron energy corresponding to the standard potential of a couple	eV	3.6.3
$E^{0\prime}$	formal potential of an electrode	V	2.1.6
E_A	activation energy of a reaction	kJ/mol	3.1.2
E_{ac}	ac component of potential	mV	10.1.1
E_b	base potential in NPV and RPV	V	7.3.2, 7.3.3
E_{dc}	dc component of potential	V	10.1.1

Symbol	Meaning	Usual Units	Section References
E_{eq}	equilibrium potential of an electrode	V	1.3.2, 3.4.1
$\mathbf{E}_F$	Fermi level	eV	2.2.5, 3.6.3
E_{fb}	flat-band potential	V	18.2.2
$\mathbf{E}_g$	bandgap of a semiconductor	eV	18.2.2
E_i	initial potential	V	6.2.1
E_j	junction potential	mV	2.3.4
E_m	membrane potential	mV	2.4
E_p	peak potential	V	6.2.2
ΔE_p	(a) $|E_{pa} - E_{pc}|$ in CV	V	6.5
	(b) pulse height in SWV	mV	7.3.5
$E_{p/2}$	potential where $i = i_p/2$ in LSV	V	6.2.2
E_{pa}	anodic peak potential	V	6.5
E_{pc}	cathodic peak potential	V	6.5
ΔE_s	staircase step height in SWV	mV	7.3.5
E_z	potential of zero charge	V	13.2.2
E_λ	switching potential for cyclic voltammetry	V	6.5
$E_{\tau/4}$	quarter-wave potential in chronopotentiometry	V	8.3.1
$E_{1/2}$	(a) measured or expected half-wave potential in voltammetry	V	1.4.2, 5.4, 5.5
	(b) in derivations, the "reversible" half-wave potential, $E^{0'} + (RT/nF) \ln(D_R/D_O)^{1/2}$	V	5.4
$E_{1/4}$	potential where $i/i_d = 1/4$	V	5.4.1
$E_{3/4}$	potential where $i/i_d = 3/4$	V	5.4.1
e	(a) electronic charge	C	
	(b) voltage in an electric circuit	V	10.1.1, 15.1
e_i	input voltage	V	15.2
e_o	output voltage	V	15.1.1
e_s	voltage across the input terminals of an amplifier	μV	15.1.1
erf(x)	error function of x	none	A.3
erfc(x)	error function complement of x	none	A.3
F	the Faraday constant; charge on one mole of electrons	C	
f	(a) F/RT	V^{-1}	
	(b) frequency of rotation	r/s	9.3
	(c) frequency of a sinusoidal oscillation	s^{-1}	10.1.2
	(d) SWV frequency	s^{-1}	7.3.5
	(e) fraction titrated	none	11.5.2
$f(\mathbf{E})$	Fermi function	none	3.6.3
$f_i(j, k)$	fractional concentration of species i in box j after iteration k in a simulation	none	B.1.3
G	Gibbs free energy	kJ, kJ/mol	2.2.4
ΔG	Gibbs free energy change in a chemical process	kJ, kJ/mol	2.1.2, 2.1.3
$\overline{G}$	electrochemical free energy	kJ, kJ/mol	2.2.4
G^0	standard Gibbs free energy	kJ, kJ/mol	3.1.2

Symbol	Meaning	Usual Units	Section References
ΔG^0	standard Gibbs free energy change in a chemical process	kJ, kJ/mol	2.1.2, 2.1.3
$\Delta G^{\ddagger}$	standard Gibbs free energy of activation	kJ/mol	3.1.2
$\Delta G_{transfer, j}^{0\alpha \rightarrow \beta}$	standard free energy of transfer for species j from phase α into phase β	kJ/mol	2.3.6
g	(a) gravitational acceleration	cm/s^2	
	(b) interaction parameter in adsorption isotherms	J-cm^2/mol^2	13.5.2
H	(a) enthalpy	kJ, kJ/mol	2.1.2
	(b) $k_f/D_O^{1/2} + k_b/D_R^{1/2}$	s$^{-1/2}$	5.5.1
ΔH	enthalpy change in a chemical process	kJ, kJ/mol	2.1.2
ΔH^0	standard enthalpy change in a chemical process	kJ, kJ/mol	2.1.2
$\Delta H^{\ddagger}$	standard enthalpy of activation	kJ/mol	3.1.2
h	Planck constant	J-s	
h_{corr}	corrected mercury column height at a DME	cm	7.1.4
I	amplitude of an ac current	A	10.1.2
$I(t)$	convolutive transform of current; semi-integral of current	C/s$^{1/2}$	6.7.1
$\dot{I}$	current phasor	A	10.1.2
$\bar{I}$	diffusion current constant for average current	μA-s$^{1/2}$/(mg$^{2/3}$-mM)	7.1.3
$(I)_{max}$	diffusion current constant for maximum current	μA-s$^{1/2}$/(mg$^{2/3}$-mM)	7.1.3
I_p	peak value of ac current amplitude	A	10.5.1
i	current	A	1.3.2
Δi	difference current in SWV $= i_f - i_r$	A	7.3.5
δi	difference current in DPV $= i(\tau) - i(\tau')$	A	7.3.4
$i(0)$	initial current in bulk electrolysis	A	11.3.1
i_A	characteristic current describing flux of the primary reactant to a modified RDE	A	14.4.2
i_a	anodic component current	A	3.2
i_c	(a) charging current	A	6.2.4
	(b) cathodic component current	A	3.2
i_d	(a) current due to diffusive flux	A	4.1
	(b) diffusion-limited current	A	5.2.1
$\bar{i}_d$	average diffusion-limited current flow over a drop lifetime at a DME	A	7.1.2
$(i_d)_{max}$	diffusion-limited current at t_{max} at a DME (maximum current)	A	7.1.2
i_E	characteristic current describing diffusion of electrons within the film at a modified electrode	A	14.4.2
i_f	(a) faradaic current	A	
	(b) forward current	A	5.7
i_K	kinetically limited current	A	9.3.4
i_k	characteristic current describing cross-reaction within the film at a modified electrode	A	14.4.2

Symbol	Meaning	Usual Units	Section References
i_l	limiting current	A	1.4.2
$i_{l,a}$	limiting anodic current	A	1.4.2
$i_{l,c}$	limiting cathodic current	A	1.4.2
i_m	migration current	A	4.1
i_P	characteristic current describing permeation of the primary reactant into the film at a modified electrode	A	14.4.2
i_p	peak current	A	6.2.2
i_{pa}	anodic peak current	A	6.5.1
i_{pc}	cathodic peak current	A	6.5.1
i_r	current during reversal step	A	5.7
i_S	(a) characteristic current describing diffusion of the primary reactant through the film at a modified electrode	A	14.4.2
	(b) substrate current in SECM	A	16.4.4
i_{ss}	steady-state current	A	5.3
i_T	tip current in SECM	A	16.4.2
$i_{T,\infty}$	tip current in SECM far from the substrate	A	16.4.1
i_0	exchange current	A	3.4.1, 3.5.4
$i_{0,t}$	true exchange current	A	13.7.1
$\text{Im}(w)$	imaginary part of complex function w		A.5
$J_j(x, t)$	flux of species j at location x at time t	$\text{mol cm}^{-2}\,\text{s}^{-1}$	1.4.1, 4.1
j	(a) current density	A/cm^2	1.3.2
	(b) box index in a simulation	none	B.1.2
	(c) $\sqrt{-1}$	none	A.5
j_0	exchange current density	A/cm^2	3.4.1, 3.5.4
K	equilibrium constant	none	
$K_{P,j}$	precursor equilibrium constant for reactant j	depends on case	3.6.1
k	(a) rate constant for a homogeneous reaction	depends on order	
	(b) iteration number in a simulation	none	B.1
	(c) extinction coefficient	none	17.1.2
k	Boltzmann constant	J/K	
k^0	standard heterogeneous rate constant	cm/s	3.3, 3.4
k_b	(a) heterogeneous rate constant for oxidation	cm/s	3.2
	(b) homogeneous rate constant for "backward" reaction	depends on order	3.1
k_f	(a) heterogeneous rate constant for reduction	cm/s	3.2
	(b) homogeneous rate constant for "forward" reaction	depends on order	3.1
$k_{i,j}^{\text{pot}}$	potentiometric selectivity coefficient of interferent j toward a measurement of species i	none	2.4
k_t^0	true standard heterogeneous rate constant	cm/s	13.7.1

Symbol	Meaning	Usual Units	Section References
L	length of a porous electrode	cm	11.6.2
$L\{f(t)\}$	Laplace transform of $f(t) = \bar{f}(s)$		A.1
$L^{-1}\{\bar{f}(s)\}$	inverse Laplace transform of $\bar{f}(s)$		A.1
l	thickness of solution in a thin-layer cell	cm	11.7.2
ℓ	number of iterations corresponding to t_k in a simulation	none	B.1.4
m	mercury flow rate at a DME	mg/s	7.1.2
$m(t)$	convolutive transform of current; semi-integral of current	$C/s^{1/2}$	6.7.1
m_j	mass-transfer coefficient of species j	cm/s	1.4.2
N	collection efficiency at an RRDE	none	9.4.2
N_A	(a) acceptor density	cm^{-3}	18.2.2
	(b) Avogadro's number	mol^{-1}	
N_D	donor density	cm^{-3}	18.2.2
N_j	total number of moles of species j in a system	mol	11.3.1
n	(a) stoichiometric number of electrons involved in an electrode reaction	none	1.3.2
	(b) electron density in a semiconductor	cm^{-3}	18.2.2
	(c) refractive index	none	17.1.2
$\hat{n}$	complex refractive index	none	17.1.2
n^0	number concentration of each ion in a $z:z$ electrolyte	cm^{-3}	13.3.2
n_i	electron density in an intrinsic semiconductor	cm^{-3}	18.2.2
n_j	(a) number of moles of species j in a phase	mol	2.2.4, 13.1.1
	(b) number concentration of ion j in an electrolyte	cm^{-3}	13.3.2
n_j^0	number concentration of ion j in the bulk electrolyte	cm^{-3}	13.3.2
O	oxidized form of the standard system $O + ne \rightleftarrows R$; often used as a subscript denoting quantities pertaining to species O		
P	pressure	Pa, atm	
p	(a) hole density in a semiconductor	cm^{-3}	18.2.2
	(b) $m_j A/V$	s^{-1}	11.3.1
p_i	hole density in an intrinsic semiconductor	cm^{-3}	18.3.2
Q	charge passed in electrolysis	C	1.3.2, 5.8.1, 11.3.1
Q^0	charge required for complete electrolysis of a component by Faraday's law	C	11.3.4
Q_d	chronocoulometric charge from a diffusing component	C	5.8.1
Q_{dl}	charge devoted to double-layer capacitance	C	5.8
q^j	excess charge on phase j	C, μC	1.2, 2.2
R	reduced form of the standard system, $O + ne \rightleftarrows R$; often used as a subscript denoting quantities pertaining to species R		

Symbol	Meaning	Usual Units	Section References
R	(a) gas constant	J mol^{-1} K^{-1}	
	(b) resistance	Ω	10.1.2
	(c) fraction of substance electrolyzed in a porous electrode	none	11.6.2
	(d) reflectance	none	17.1.2
R_B	series equivalent resistance of a cell	Ω	10.4
R_{ct}	charge-transfer resistance	Ω	1.3.3, 3.4.3
R_f	feedback resistance	Ω	15.2
R_{mt}	mass-transfer resistance	Ω	1.4.2, 3.4.6
R_s	(a) solution resistance	Ω	1.3.4
	(b) series resistance in an equivalent circuit	Ω	1.2.4, 10.1.3
R_u	uncompensated resistance	Ω	1.3.4, 15.6
R_{Ω}	ohmic solution resistance	Ω	10.1.3
r	radial distance from the center of an electrode	cm	5.2.2, 5.3, 9.3.1
r_c	radius of a capillary	cm	7.1.3
r_0	radius of an electrode	cm	5.2.2, 5.3
r_1	radius of the disk in an RDE or RRDE	cm	9.3.5
r_2	inner radius of a ring electrode	cm	9.4.1
r_3	outer radius of a ring electrode	cm	9.4.1
Re	Reynolds number	none	9.2.1
Re(w)	real part of complex function w		A.5
ΔS	entropy change in a chemical process	kJ/K, kJ mol^{-1} K^{-1}	2.1.2
ΔS^0	standard entropy change in a chemical process	kJ/K, kJ mol^{-1} K^{-1}	2.1.2
$\Delta S^{\ddagger}$	standard entropy of activation	kJ mol^{-1} K^{-1}	3.1.2
$S_{\tau}(t)$	unit step function rising at $t = \tau$	none	A.1.7
s	(a) Laplace plane variable, usually complementary to t		A.1
	(b) specific area of a porous electrode	cm^{-1}	11.6.2
T	absolute temperature	K	
t	time	s	
t_j	transference number of species j	none	2.3.3, 4.2
t_k	known characteristic time in a simulation	s	B.1.4
t_{max}	drop time at a DME	s	7.1.2
t_p	pulse width in SWV	s	7.3.5
u_j	mobility of ion (or charge carrier) j	cm^2 V^{-1} s^{-1}	2.3.3, 4.2
V	volume	cm^3	
v	(a) linear potential scan rate	V/s	6.1
	(b) homogeneous reaction rate	mol cm^{-3} s^{-1}	1.3.2, 3.1
	(c) heterogeneous reaction rate	mol cm^{-2} s^{-1}	1.3.2, 3.2
	(d) linear velocity of solution flow, usually a function of position	cm/s	1.4.1, 9.2
v_b	(a) "backward" homogeneous reaction rate	mol cm^{-3} s^{-1}	3.1
	(b) anodic heterogeneous reaction rate	mol cm^{-2} s^{-1}	3.2
v_f	(a) "forward" homogeneous reaction rate	mol cm^{-3} s^{-1}	3.1
	(b) cathodic heterogeneous reaction rate	mol cm^{-2} s^{-1}	3.2
v_j	component of velocity in the j direction	cm/s	9.2.1

Symbol	Meaning	Usual Units	Section References
v_{mt}	rate of mass transfer to a surface	mol cm^{-2} s^{-1}	1.4.1
$W_j(\lambda, \mathbf{E})$	probability density function for species j	eV^{-1}	3.6.3
w	width of a band electrode	cm	5.3
w_j	work term for reactant j in electron transfer	eV	3.6.2
X_C	capacitive reactance	Ω	10.1.2
X_j	mole fraction of species j	none	13.1.2
x	distance, often from a planar electrode	cm	
x_1	distance of the IHP from the electrode surface	cm	1.2.3, 13.3.3
x_2	distance of the OHP from the electrode surface	cm	1.2.3, 13.3.3
Y	admittance	Ω^{-1}	10.1.2
$\mathbf{Y}$	admittance vector	Ω^{-1}	10.1.2
y	distance from an RDE or RRDE	cm	9.3.1
Z	(a) impedance	Ω	10.1.2
	(b) dimensionless current parameter in simulation	none	B.1.6
$\mathbf{Z}$	impedance vector	Ω	10.1.2
Z_f	faradaic impedance	Ω	10.1.3
Z_{Im}	imaginary part of impedance	Ω	10.1.2
Z_{Re}	real part of impedance	Ω	10.1.2
Z_w	Warburg impedance	Ω	10.1.3
z	(a) distance normal to the surface of a disk electrode or along a cylindrical electrode	cm	5.3
	(b) charge magnitude of each ion in a $z:z$ electrolyte	none	13.3.2
z_j	charge on species j in signed units of electronic charge	none	2.3

▷ GREEK SYMBOLS

Symbol	Meaning	Usual Units	Section References
α	(a) transfer coefficient	none	3.3
	(b) absorption coefficient	cm^{-1}	17.1.2
β	(a) distance factor for extended charge transfer	Å^{-1}	3.6.4
	(b) geometric parameter for an RRDE	none	9.4.1
	(c) $1 - \alpha$	none	10.5.2
β_j	(a) $\partial E/\partial C_j(0, t)$	V-cm^3/mol	10.2.2
	(b) equilibrium parameter in an adsorption isotherm for species j	none	13.5.2
Γ_j	surface excess of species j at equilibrium	mol/cm^2	13.1.2
$\Gamma_{j(r)}$	relative surface excess of species j with respect to component r	mol/cm^2	13.1.2

Symbol	Meaning	Usual Units	Section References
$\Gamma_{j,s}$	surface excess of species j at saturation	mol/cm^2	13.5.2
γ	(a) surface tension	dyne/cm	
	(b) dimensionless parameter used to define frequency (time) regimes in step experiments at spherical electrodes	none	5.4.2, 5.5.2
γ_j	activity coefficient for species j	none	2.1.5
Δ	ellipsometric parameter	none	17.1.2
δ	$r_0(s/D_O)^{1/2}$, used to define diffusional regimes at a spherical electrode	none	5.5.2
δ_j	"diffusion" layer thickness for species j at an electrode fed by convective transfer	cm	1.4.2, 9.3.2
ε	(a) dielectric constant	none	13.3.1
	(b) optical-frequency dielectric constant	none	17.1.2
	(c) porosity	none	11.6.2
$\hat{\varepsilon}$	complex optical-frequency dielectric constant	none	17.1.2
ε_j	molar absorptivity of species j	M^{-1} cm^{-1}	17.1.1
ε_0	permittivity of free space	C^2 N^{-1} m^{-2}	13.3.1
ζ	zeta potential	mV	9.8.1
η	overpotential, $E - E_{eq}$	V	1.3.2, 3.4.2
η_{ct}	charge-transfer overpotential	V	1.3.3, 3.4.6
η_j	viscosity of fluid j	g cm^{-1} s^{-1} = poise	9.2.2
η_{mt}	mass-transfer overpotential	V	1.3.3, 3.4.6
θ	(a) $\exp[(nF/RT)(E - E^{0'})]$	none	5.4.1
	(b) $\tau^{1/2} + (t - \tau)^{1/2} - t^{1/2}$	s$^{1/2}$	5.8.2
θ_j	fractional coverage of an interface by species j	none	13.5.2
κ	(a) conductivity of a solution	S/cm = Ω^{-1} cm^{-1}	2.3.3, 4.2
	(b) transmission coefficient of a reaction	none	3.1.3
	(c) $r_0 k_f/D_O$, used to define kinetic regimes at a spherical electrode	none	5.5.2
	(d) double-layer thickness parameter	cm^{-1}	13.3.2
	(e) partition coefficient for the primary reactant in a modified electrode system	none	14.4.2
κ_{el}	electronic transmission coefficient	none	3.6
Λ	equivalent conductivity of a solution	cm^2 Ω^{-1} equiv^{-1}	2.3.3
λ	(a) reorganization energy for electron transfer	eV	3.6
	(b) $k_f \tau^{1/2}(1 + \xi\theta)/D_O^{1/2}$	none	5.5.1
	(c) dimensionless homogeneous kinetic parameter, specific to a method and mechanism	none	12.3
	(d) switching time in CV	s	6.5
	(e) wavelength of light *in vacuo*	nm	17.1.2
λ_i	inner component of the reorganization energy	eV	3.6.2
λ_j	equivalent ionic conductivity for ion j	cm^2 Ω^{-1} equiv^{-1}	2.3.3
λ_{0j}	equivalent ionic conductivity of ion j extrapolated to infinite dilution	cm^2 Ω^{-1} equiv^{-1}	2.3.3

Symbol	Meaning	Usual Units	Section References
λ_o	outer component of the reorganization energy	eV	3.6.2
μ	(a) reaction layer thickness	cm	1.5.2, 12.4.2
	(b) magnetic permeability	none	17.1.2
$\bar{\mu}_e^\alpha$	electrochemical potential of electrons in phase α	kJ/mol	2.2.4, 2.2.5
$\bar{\mu}_j^\alpha$	electrochemical potential of species j in phase α	kJ/mol	2.2.4
μ_j^α	chemical potential of species j in phase α	kJ/mol	2.2.4
$\mu_j^{0\alpha}$	standard chemical potential of species j in phase α	kJ/mol	2.2.4
ν	(a) kinematic viscosity	cm^2/s	9.2.2
	(b) frequency of light	s^{-1}	
ν_j	stoichiometric coefficient for species j in a chemical process	none	2.1.5
ν_n	nuclear frequency factor	s^{-1}	3.6
ξ	$(D_O/D_R)^{1/2}$	none	5.4.1
ρ	(a) resistivity	Ω-cm	4.2
	(b) roughness factor	none	5.2.3
$\rho(\mathbf{E})$	electronic density of states	cm^2 eV^{-1}	3.6.3
σ	(a) nFv/RT	s^{-1}	6.2.1
	(b) $(1/nFA\sqrt{2})[\beta_O/D_O^{1/2} - \beta_R/D_R^{1/2}]$	Ω-s$^{1/2}$	10.2.3
σ^j	excess charge density on phase j	C/cm^2	1.2, 2.2
σ_j	parameter describing potential dependence of adsorption energy	none	13.3.4
τ	(a) transition time in chronopotentiometry	s	8.2.2
	(b) sampling time in sampled-current voltammetry	s	5.1, 7.3
	(c) forward step duration in a double-step experiment	s	5.7.1
	(d) generally, a characteristic time defined by the properties of an experiment	s	
	(e) in treatments of UMEs, $4D_O t/r_0^2$	none	5.3
τ'	start of potential pulse in pulse voltammetry	s	7.3
τ_L	longitudinal relaxation time of a solvent	s	3.6.2
Φ	work function of a phase	eV	3.6.4
ϕ	(a) electrostatic potential	V	2.2.1
	(b) phase angle between two sinusoidal signals	degrees, radians	10.1.2
	(c) phase angle between $\dot{I}_{ac}$ and $\dot{E}_{ac}$	degrees, radians	10.1.2
	(d) film thickness in a modified electrode	cm	14.4.2
$\Delta\phi$	(a) electrostatic potential difference between two points or phases	V	2.2
	(b) potential drop in the space charge region of a semiconductor	V	18.2.2
ϕ^j	absolute electrostatic potential of phase j	V	2.2.1
$\Delta_\beta^\alpha\phi$	junction potential at a liquid-liquid interface	V	6.8

Symbol	Meaning	Usual Units	Section References
$\Delta_\beta^\alpha \phi_j^0$	standard Galvani potential of ion transfer for species j from phase α to phase β	V	6.8
ϕ_0	total potential drop across the solution side of the double layer	mV	13.3.2
ϕ_2	potential at the OHP with respect to bulk solution	V	1.2.3, 13.3.3
χ	$(12/7)^{1/2} k_f \tau^{1/2}/D_O^{1/2}$	none	7.2.2
$\chi(j)$	dimensionless distance of box j in a simulation	none	B.1.5
$\chi(bt)$	normalized current for a totally irreversible system in LSV and CV	none	6.3.1
$\chi(\sigma t)$	normalized current for a reversible system in LSV and CV	none	6.2.1
χ_f	rate constant for permeation of the primary reactant into the film at a modified electrode	cm/s	14.4.2
ψ	(a) ellipsometric parameter	none	17.1.2
	(b) dimensionless rate parameter in CV	none	6.5.2
ω	(a) angular frequency of rotation; $2\pi \times$ rotation rate	s^{-1}	9.3
	(b) angular frequency of a sinusoidal oscillation; $2\pi f$	s^{-1}	10.1.2

▶ STANDARD ABBREVIATIONS

Abbreviation	Meaning	Section Reference
ADC	analog-to-digital converter	15.8
AES	Auger electron spectrometry	17.3.3
AFM	atomic force microscopy	16.3
ASV	anodic stripping voltammetry	11.8
BV	Butler-Volmer	3.3
CB	conduction band	18.2.2
CE	homogeneous chemical process preceding heterogeneous electron transfer[1]	12.1.1
CV	cyclic voltammetry	6.1, 6.5
CZE	capillary zone electrophoresis	11.6.4
DAC	digital-to-analog converter	15.8
DME	(a) dropping mercury electrode	7.1.1
	(b) 1,2-dimethoxyethane	
DMF	N,N-dimethylformamide	
DMSO	Dimethylsulfoxide	
DPP	differential pulse polarography	7.3.4
DPV	differential pulse voltammetry	7.3.4

[1]Letters may be subscripted i, q, or r to indicate irreversible, quasi-reversible, or reversible reactions.

Abbreviation	Meaning	Section Reference
EC	heterogeneous electron transfer followed by homogeneous chemical reaction[1]	12.1.1
EC'	catalytic regeneration of the electroactive species in a following homogeneous reaction[1]	12.1.1
ECE	heterogeneous electron transfer, homogeneous chemical reaction, and heterogeneous electron transfer, in sequence[1]	12.1.1
ECL	electrogenerated chemiluminescence	18.1
ECM	electrocapillary maximum	13.2.2
EE	stepwise heterogeneous electron transfers to accomplish a 2-electron reduction or oxidation of a species[1]	12.1.1
EIS	electrochemical impedance spectroscopy	10.1.1
emf	electromotive force	2.1.3
EMIRS	electrochemically modulated infrared reflectance spectroscopy	17.2.1
ESR	electron spin resonance	17.4.1
ESTM	electrochemical scanning tunneling microscopy	16.2
EXAFS	extended X-ray absorption fine structure	17.6.1
FFT	fast Fourier transform	A.6
GCS	Gouy-Chapman-Stern	13.3.3
GDP	galvanostatic double pulse	8.6
HCP	hexagonal close-packed	13.4.2
HMDE	hanging mercury drop electrode	5.2.2
HOPG	highly oriented pyrolytic graphite	13.4.2
IHP	inner Helmholtz plane	1.2.3, 13.3.3
IPE	ideal polarized electrode	1.2.1
IRRAS	infrared reflection absorption spectroscopy	17.2.1
IR-SEC	infrared spectroelectrochemistry	17.2.1
ISE	ion-selective electrode	2.4
ITIES	interface between two immiscible electrolyte solutions	6.8
ITO	indium-tin oxide thin film	18.2.5
LB	Langmuir-Blodgett	14.2.1
LCEC	liquid chromatography with electrochemical detection	11.6.4
LEED	low-energy electron diffraction	17.3.3
LSV	linear sweep voltammetry	6.1
MFE	mercury film electrode	11.8
NHE	normal hydrogen electrode = SHE	1.1.1
NCE	normal calomel electrode, $Hg/Hg_2Cl_2/KCl$ (1.0 M)	
NPP	normal pulse polarography	7.3.2
NPV	normal pulse voltammetry	7.3.2
OHP	outer Helmholtz plane	1.2.3, 13.3.3
OTE	optically transparent electrode	17.1.1
OTTLE	optically transparent thin-layer electrode	17.1.1
PAD	pulsed amperometric detection	11.6.4
PC	propylene carbonate	
PDIRS	potential difference infrared spectroscopy	17.2.1
PZC	potential of zero charge	13.2.2
QCM	quartz crystal microbalance	17.5

[1]Letters may be subscripted i, q, or r to indicate irreversible, quasi-reversible, or reversible reactions.

Abbreviation	Meaning	Section Reference
QRE	quasi-reference electrode	2.1.7
RDE	rotating disk electrode	9.3
RDS	rate-determining step	3.5
RPP	reverse pulse polarography	7.3.4
RPV	reverse pulse voltammetry	7.3.4
RRDE	rotating ring-disk electrode	9.4.2
SAM	self-assembled monolayer	14.2.2
SCE	saturated calomel electrode	1.1.1
SECM	scanning electrochemical microscopy	16.4
SERS	surface enhanced Raman spectroscopy	17.2.2
SHE	standard hydrogen electrode = NHE	1.1.1
SHG	second harmonic generation	17.1.5
SMDE	static mercury drop electrode	7.1.1
SNIFTIRS	subtractively normalized interfacial Fourier transform infrared spectroscopy	17.2.1
SPE	solid polymer electrolyte	14.2.6
SPR	surface plasmon resonance	17.1.3
SSCE	sodium saturated calomel electrode, $Hg/Hg_2Cl_2/NaCl$ (sat'd)	
STM	scanning tunneling microscopy	16.2
SWV	square wave voltammetry	7.3.5
$TBABF_4$	tetra-n-butylammonium fluoborate	
TBAI	tetra-n-butylammonium iodide	
TBAP	tetra-n-butylammonium perchlorate	
TEAP	tetraethylammonium perchlorate	
THF	tetrahydrofuran	
UHV	ultrahigh vacuum	17.3
UME	ultramicroelectrode	5.3
UPD	underpotential deposition	11.2.1
XPS	X-ray photoelectron spectrometry	17.3.2
VB	valence band	18.2.2

C H A P T E R

1

INTRODUCTION
AND OVERVIEW
OF ELECTRODE
PROCESSES

1.1 INTRODUCTION

Electrochemistry is the branch of chemistry concerned with the interrelation of electrical and chemical effects. A large part of this field deals with the study of chemical changes caused by the passage of an electric current and the production of electrical energy by chemical reactions. In fact, the field of electrochemistry encompasses a huge array of different phenomena (e.g., electrophoresis and corrosion), devices (electrochromic displays, electroanalytical sensors, batteries, and fuel cells), and technologies (the electroplating of metals and the large-scale production of aluminum and chlorine). While the basic principles of electrochemistry discussed in this text apply to all of these, the main emphasis here is on the application of electrochemical methods to the study of chemical systems.

Scientists make electrochemical measurements on chemical systems for a variety of reasons. They may be interested in obtaining thermodynamic data about a reaction. They may want to generate an unstable intermediate such as a radical ion and study its rate of decay or its spectroscopic properties. They may seek to analyze a solution for trace amounts of metal ions or organic species. In these examples, electrochemical methods are employed as tools in the study of chemical systems in just the way that spectroscopic methods are frequently applied. There are also investigations in which the electrochemical properties of the systems themselves are of primary interest, for example, in the design of a new power source or for the electrosynthesis of some product. Many electrochemical methods have been devised. Their application requires an understanding of the fundamental principles of electrode reactions and the electrical properties of electrode–solution interfaces.

In this chapter, the terms and concepts employed in describing electrode reactions are introduced. In addition, before embarking on a detailed consideration of methods for studying electrode processes and the rigorous solutions of the mathematical equations that govern them, we will consider approximate treatments of several different types of electrode reactions to illustrate their main features. The concepts and treatments described here will be considered in a more complete and rigorous way in later chapters.

1

1.1.1 Electrochemical Cells and Reactions

In electrochemical systems, we are concerned with the processes and factors that affect the transport of charge across the interface between chemical phases, for example, between an electronic conductor (an *electrode*) and an ionic conductor (an *electrolyte*). Throughout this book, we will be concerned with the electrode/electrolyte interface and the events that occur there when an electric potential is applied and current passes. Charge is transported through the electrode by the movement of electrons (and holes). Typical electrode materials include solid metals (e.g., Pt, Au), liquid metals (Hg, amalgams), carbon (graphite), and semiconductors (indium–tin oxide, Si). In the electrolyte phase, charge is carried by the movement of ions. The most frequently used electrolytes are liquid solutions containing ionic species, such as, H^+, Na^+, Cl^-, in either water or a nonaqueous solvent. To be useful in an electrochemical cell, the solvent/electrolyte system must be of sufficiently low resistance (i.e., sufficiently conductive) for the electrochemical experiment envisioned. Less conventional electrolytes include fused salts (e.g., molten NaCl–KCl eutectic) and ionically conductive polymers (e.g., Nafion, polyethylene oxide–$LiClO_4$). Solid electrolytes also exist (e.g., sodium β-alumina, where charge is carried by mobile sodium ions that move between the aluminum oxide sheets).

It is natural to think about events at a single interface, but we will find that one cannot deal experimentally with such an isolated boundary. Instead, one must study the properties of collections of interfaces called *electrochemical cells*. These systems are defined most generally as two electrodes separated by at least one electrolyte phase.

In general, a difference in electric potential can be measured between the electrodes in an electrochemical cell. Typically this is done with a high impedance voltmeter. This *cell potential*, measured in volts (V), where 1 V = 1 joule/coulomb (J/C), is a measure of the energy available to drive charge externally between the electrodes. It is a manifestation of the collected differences in electric potential between all of the various phases in the cell. We will find in Chapter 2 that the transition in electric potential in crossing from one conducting phase to another usually occurs almost entirely at the interface. The sharpness of the transition implies that a very high electric field exists at the interface, and one can expect it to exert effects on the behavior of charge carriers (electrons or ions) in the interfacial region. Also, the magnitude of the potential difference at an interface affects the relative energies of the carriers in the two phases; hence it controls the direction and the rate of charge transfer. Thus, the measurement and control of cell potential is one of the most important aspects of experimental electrochemistry.

Before we consider how these operations are carried out, it is useful to set up a shorthand notation for expressing the structures of cells. For example, the cell pictured in Figure 1.1.1*a* is written compactly as

$$Zn/Zn^{2+}, Cl^-/AgCl/Ag \tag{1.1.1}$$

In this notation, a slash represents a phase boundary, and a comma separates two components in the same phase. A double slash, not yet used here, represents a phase boundary whose potential is regarded as a negligible component of the overall cell potential. When a gaseous phase is involved, it is written adjacent to its corresponding conducting element. For example, the cell in Figure 1.1.1*b* is written schematically as

$$Pt/H_2/H^+, Cl^-/AgCl/Ag \tag{1.1.2}$$

The overall chemical reaction taking place in a cell is made up of two independent *half-reactions*, which describe the real chemical changes at the two electrodes. Each half-reaction (and, consequently, the chemical composition of the system near the electrodes)
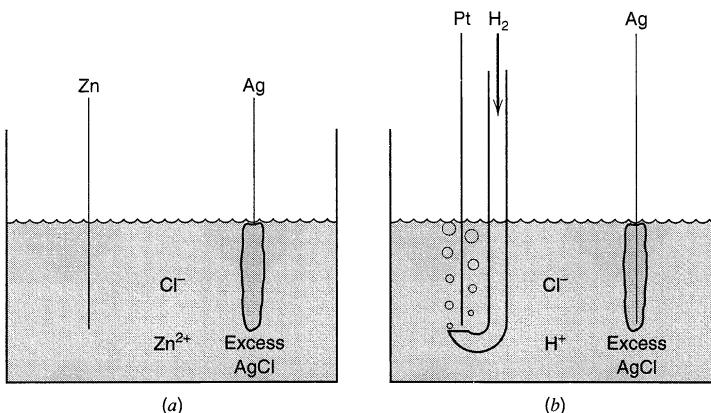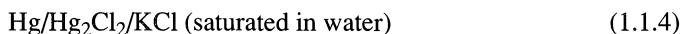
Figure 1.1.1 Typical electrochemical cells. (*a*) Zn metal and Ag wire covered with AgCl immersed in a ZnCl$_2$ solution. (*b*) Pt wire in a stream of H$_2$ and Ag wire covered with AgCl in HCl solution.

responds to the interfacial potential difference at the corresponding electrode. Most of the time, one is interested in only one of these reactions, and the electrode at which it occurs is called the *working* (or *indicator*) *electrode*. To focus on it, one standardizes the other half of the cell by using an electrode (called a *reference electrode*) made up of phases having essentially constant composition.

The internationally accepted primary reference is the *standard hydrogen electrode* (SHE), or *normal hydrogen electrode* (NHE), which has all components at unit activity:

$$\text{Pt/H}_2(a = 1)/\text{H}^+(a = 1, \text{aqueous}) \tag{1.1.3}$$

Potentials are often measured and quoted with respect to reference electrodes other than the NHE, which is not very convenient from an experimental standpoint. A common reference is the *saturated calomel electrode* (SCE), which is

$$\text{Hg/Hg}_2\text{Cl}_2/\text{KCl (saturated in water)} \tag{1.1.4}$$

Its potential is 0.242 V *vs*. NHE. Another is the *silver–silver chloride electrode*,

$$\text{Ag/AgCl/KCl (saturated in water)} \tag{1.1.5}$$

with a potential of 0.197 V *vs*. NHE. It is common to see potentials identified in the literature as "*vs*. Ag/AgCl" when this electrode is used.

Since the reference electrode has a constant makeup, its potential is fixed. Therefore, any changes in the cell are ascribable to the working electrode. We say that we observe or control the *potential* of the working electrode *with respect to* the reference, and that is equivalent to observing or controlling the energy of the electrons within the working electrode (1, 2). By driving the electrode to more negative potentials (e.g., by connecting a battery or power supply to the cell with its negative side attached to the working electrode), the energy of the electrons is raised. They can reach a level high enough to transfer into vacant electronic states on species in the electrolyte. In that case, a flow of electrons from electrode to solution (a *reduction current*) occurs (Figure 1.1.2*a*). Similarly, the energy of the electrons can be lowered by imposing a more positive potential, and at some point electrons on solutes in the electrolyte will find a more favorable energy on the electrode and will transfer there. Their flow, from solution to electrode, is an *oxidation current* (Figure 1.1.2*b*). The critical potentials at which these processes occur are related to the *standard potentials*, E^0, for the specific chemical substances in the system.
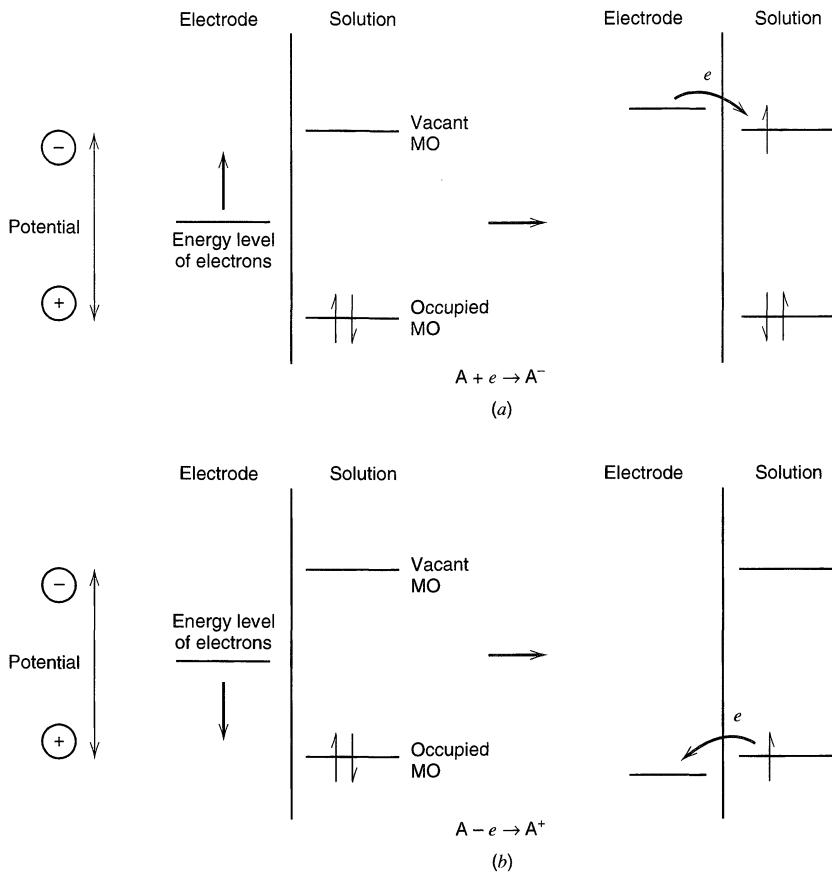
Figure 1.1.2 Representation of (a) reduction and (b) oxidation process of a species, A, in solution. The molecular orbitals (MO) of species A shown are the highest occupied MO and the lowest vacant MO. These correspond in an approximate way to the E^0s of the A/A$^-$ and A$^+$/A couples, respectively. The illustrated system could represent an aromatic hydrocarbon (e.g., 9,10-diphenylanthracene) in an aprotic solvent (e.g., acetonitrile) at a platinum electrode.

Consider a typical electrochemical experiment where a working electrode and a reference electrode are immersed in a solution, and the potential difference between the electrodes is varied by means of an external power supply (Figure 1.1.3). This variation in potential, E, can produce a current flow in the external circuit, because electrons cross the electrode/solution interfaces as reactions occur. Recall that the number of electrons that cross an interface is related stoichiometrically to the extent of the chemical reaction (i.e., to the amounts of reactant consumed and product generated). The number of electrons is measured in terms of the total charge, Q, passed in the circuit. Charge is expressed in units of coulombs (C), where 1 C is equivalent to 6.24×10^{18} electrons. The relationship between charge and amount of product formed is given by *Faraday's law*; that is, the passage of 96,485.4 C causes 1 equivalent of reaction (e.g., consumption of 1 mole of reactant or production of 1 mole of product in a one-electron reaction). The current, i, is the rate of flow of coulombs (or electrons), where a current of 1 ampere (A) is equivalent to 1 C/s. When one plots the current as a function of the potential, one obtains a *current-potential (i vs. E) curve*. Such curves can be quite informative about the nature of the solution and the electrodes and about the reactions that occur at the interfaces. Much of the remainder of this book deals with how one obtains and interprets such curves.
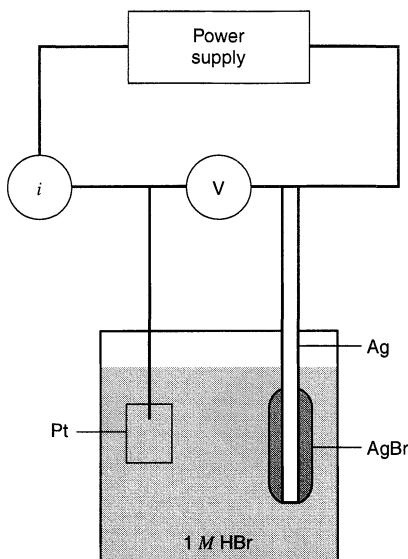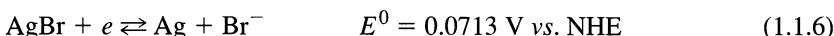
Figure 1.1.3 Schematic diagram of the electrochemical cell Pt/HBr(1 M)/AgBr/Ag attached to power supply and meters for obtaining a current-potential (i-E) curve.

Let us now consider the particular cell in Figure 1.1.3 and discuss in a qualitative way the current-potential curve that might be obtained with it. In Section 1.4 and in later chapters, we will be more quantitative. We first might consider simply the potential we would measure when a high impedance voltmeter (i.e., a voltmeter whose internal resistance is so high that no appreciable current flows through it during a measurement) is placed across the cell. This is called the *open-circuit potential* of the cell.[1]

For some electrochemical cells, like those in Figure 1.1.1, it is possible to calculate the open-circuit potential from thermodynamic data, that is, from the standard potentials of the half-reactions involved at both electrodes via the Nernst equation (see Chapter 2). The key point is that a true equilibrium is established, because a pair of redox forms linked by a given half-reaction (i.e., a *redox couple*) is present at each electrode. In Figure 1.1.1b, for example, we have H^+ and H_2 at one electrode and Ag and AgCl at the other.[2]

The cell in Figure 1.1.3 is different, because an overall equilibrium cannot be established. At the Ag/AgBr electrode, a couple is present and the half-reaction is

$$AgBr + e \rightleftarrows Ag + Br^- \qquad E^0 = 0.0713 \text{ V } vs. \text{ NHE} \qquad (1.1.6)$$

Since AgBr and Ag are both solids, their activities are unity. The activity of Br^- can be found from the concentration in solution; hence the potential of this electrode (with respect to NHE) could be calculated from the Nernst equation. This electrode is at equilibrium. However, we cannot calculate a thermodynamic potential for the $Pt/H^+,Br^-$ electrode, because we cannot identify a pair of chemical species coupled by a given half-reaction. The controlling pair clearly is not the H_2,H^+ couple, since no H_2 has been introduced into the cell. Similarly, it is not the O_2,H_2O couple, because by leaving O_2 out of the cell formulation we imply that the solutions in the cell have been deaerated. Thus, the Pt electrode and the cell as a whole are not at equilibrium, and an equilibrium potential

---

[1]In the electrochemical literature, the open-circuit potential is also called the *zero-current potential* or the *rest potential*.

[2]When a redox couple is present at each electrode and there are no contributions from liquid junctions (yet to be discussed), the open-circuit potential is also the *equilibrium potential*. This is the situation for each cell in Figure 1.1.1.

does not exist. Even though the open-circuit potential of the cell is not available from thermodynamic data, we can place it within a potential range, as shown below.

Let us now consider what occurs when a power supply (e.g., a battery) and a microammeter are connected across the cell, and the potential of the Pt electrode is made more negative with respect to the Ag/AgBr reference electrode. The first electrode reaction that occurs at the Pt is the reduction of protons,

$$2H^+ + 2e \rightarrow H_2 \tag{1.1.7}$$

The direction of electron flow is from the electrode to protons in solution, as in Figure 1.1.2a, so a reduction (*cathodic*) current flows. In the convention used in this book, cathodic currents are taken as positive, and negative potentials are plotted to the right.[3] As shown in Figure 1.1.4, the onset of current flow occurs when the potential of the Pt electrode is near E^0 for the H^+/H_2 reaction (0 V *vs.* NHE or -0.07 V *vs.* the Ag/AgBr electrode). While this is occurring, the reaction at the Ag/AgBr (which we consider the reference electrode) is the oxidation of Ag in the presence of Br^- in solution to form AgBr. The concentration of Br^- in the solution near the electrode surface is not changed appreciably with respect to the original concentration (1 M), therefore the potential of the Ag/AgBr electrode will be almost the same as at open circuit. The conservation of charge requires that the rate of oxidation at the Ag electrode be equal to the rate of reduction at the Pt electrode.

When the potential of the Pt electrode is made sufficiently positive with respect to the reference electrode, electrons cross from the solution phase into the electrode, and the ox-
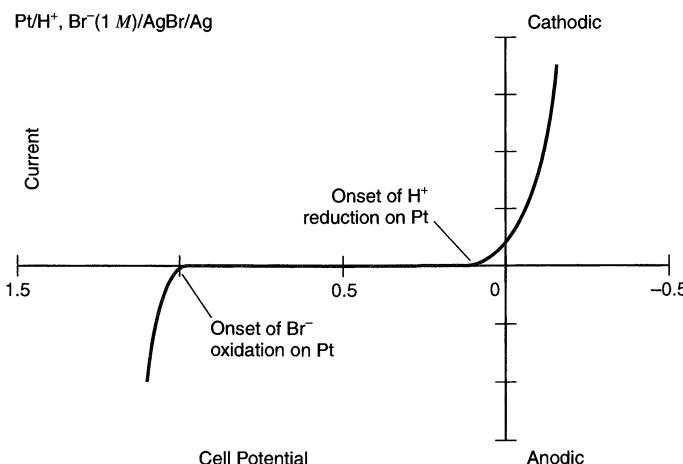
Figure 1.1.4 Schematic current-potential curve for the cell Pt/H^+, Br^-(1 M)/AgBr/Ag, showing the limiting proton reduction and bromide oxidation processes. The cell potential is given for the Pt electrode with respect to the Ag electrode, so it is equivalent to E_{Pt} (V *vs.* AgBr). Since $E_{Ag/AgBr} = 0.07$ V *vs.* NHE, the potential axis could be converted to E_{Pt} (V *vs.* NHE) by adding 0.07 V to each value of potential.

[3]The convention of taking i positive for a cathodic current stems from the early polarograhic studies, where reduction reactions were usually studied. This convention has continued among many analytical chemists and electrochemists, even though oxidation reactions are now studied with equal frequency. Other electrochemists prefer to take an anodic current as positive. When looking over a derivation in the literature or examining a published i-E curve, it is important to decide, first, which convention is being used (i.e., "Which way is up?").

idation of Br^- to Br_2 (and Br_3^-) occurs. An oxidation current, or *anodic* current, flows at potentials near the E^0 of the half-reaction,

$$Br_2 + 2e \rightleftarrows 2\,Br^- \tag{1.1.8}$$

which is +1.09 V *vs.* NHE or +1.02 V *vs.* Ag/AgBr. While this reaction occurs (right-to-left) at the Pt electrode, AgBr in the reference electrode is reduced to Ag and Br^- is liberated into solution. Again, because the composition of the Ag/AgBr/Br^- interface (i.e., the activities of AgBr, Ag, and Br^-) is almost unchanged with the passage of modest currents, the potential of the reference electrode is essentially constant. Indeed, the essential characteristic of a reference electrode is that its potential remains practically constant with the passage of small currents. When a potential is applied between Pt and Ag/AgBr, nearly all of the potential change occurs at the Pt/solution interface.

The *background limits* are the potentials where the cathodic and anodic currents start to flow at a working electrode when it is immersed in a solution containing only an electrolyte added to decrease the solution resistance (a *supporting electrolyte*). Moving the potential to more extreme values than the background limits (i.e., more negative than the limit for H_2 evolution or more positive than that for Br_2 generation in the example above) simply causes the current to increase sharply with no additional electrode reactions, because the reactants are present at high concentrations. This discussion implies that one can often estimate the background limits of a given electrode–solution interface by considering the thermodynamics of the system (i.e., the standard potentials of the appropriate half-reactions). This is frequently, but not always, true, as we shall see in the next example.

From Figure 1.1.4, one can see that the open-circuit potential is not well defined in the system under discussion. One can say only that the open-circuit potential lies somewhere between the background limits. The value found experimentally will depend upon trace impurities in the solution (e.g., oxygen) and the previous history of the Pt electrode.

Let us now consider the same cell, but with the Pt replaced with a mercury electrode:

$$Hg/H^+, Br^- (1\ M)/AgBr/Ag \tag{1.1.9}$$

We still cannot calculate an open-circuit potential for the cell, because we cannot define a redox couple for the Hg electrode. In examining the behavior of this cell with an applied external potential, we find that the electrode reactions and the observed current-potential behavior are very different from the earlier case. When the potential of the Hg is made negative, there is essentially no current flow in the region where thermodynamics predict that H_2 evolution should occur. Indeed, the potential must be brought to considerably more negative values, as shown in Figure 1.1.5, before this reaction takes place. The thermodynamics have not changed, since the equilibrium potential of half-reaction 1.1.7 is independent of the metal electrode (see Section 2.2.4). However, when mercury serves as the locale for the hydrogen evolution reaction, the rate (characterized by a *heterogeneous rate constant*) is much lower than at Pt. Under these circumstances, the reaction does not occur at values one would predict from thermodynamics. Instead considerably higher electron energies (more negative potentials) must be applied to make the reaction occur at a measurable rate. The rate constant for a heterogeneous electron-transfer reaction is a function of applied potential, unlike one for a homogeneous reaction, which is a constant at a given temperature. The additional potential (beyond the thermodynamic requirement) needed to drive a reaction at a certain rate is called the *overpotential*. Thus, it is said that mercury shows "a high overpotential for the hydrogen evolution reaction."

When the mercury is brought to more positive values, the anodic reaction and the potential for current flow also differ from those observed when Pt is used as the electrode.
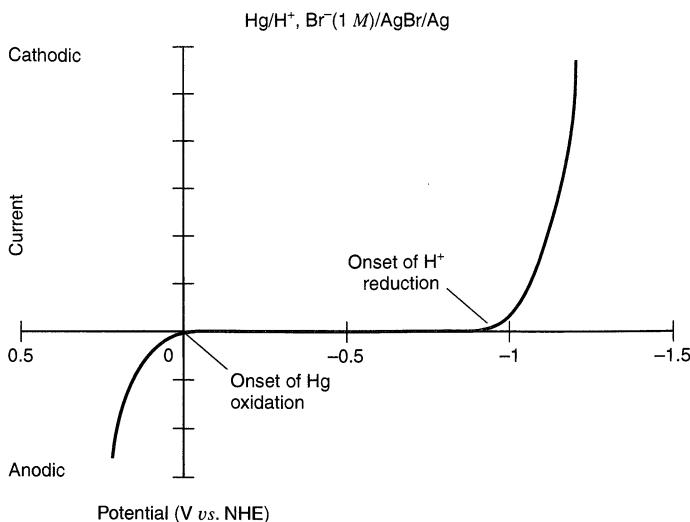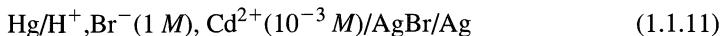
Figure 1.1.5 Schematic current-potential curve for the Hg electrode in the cell Hg/H^+, Br^-(1 M)/AgBr/Ag, showing the limiting processes: proton reduction with a large negative overpotential and mercury oxidation. The potential axis is defined through the process outlined in the caption to Figure 1.1.4.

With Hg, the anodic background limit occurs when Hg is oxidized to Hg_2Br_2 at a potential near 0.14 V $vs.$ NHE (0.07 V $vs.$ Ag/AgBr), characteristic of the half-reaction

$$Hg_2Br_2 + 2e \rightleftarrows 2Hg + 2Br^- \qquad (1.1.10)$$
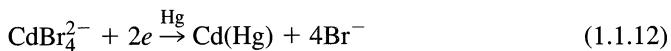
In general, the background limits depend upon both the electrode material and the solution employed in the electrochemical cell.

Finally let us consider the same cell with the addition of a small amount of Cd^{2+} to the solution,

$$Hg/H^+,Br^-(1\ M),\ Cd^{2+}(10^{-3}\ M)/AgBr/Ag \qquad (1.1.11)$$

The qualitative current-potential curve for this cell is shown in Figure 1.1.6. Note the appearance of the *reduction wave* at about -0.4 V $vs.$ NHE arising from the reduction reaction

$$CdBr_4^{2-} + 2e \xrightarrow{Hg} Cd(Hg) + 4Br^- \qquad (1.1.12)$$

where Cd(Hg) denotes cadmium amalgam. The shape and size of such waves will be covered in Section 1.4.2. If Cd^{2+} were added to the cell in Figure 1.1.3 and a current-potential curve taken, it would resemble that in Figure 1.1.4, found in the absence of Cd^{2+}. At a Pt electrode, proton reduction occurs at less positive potentials than are required for the reduction of Cd(II), so the cathodic background limit occurs in 1 M HBr before the cadmium reduction wave can be seen.

In general, when the potential of an electrode is moved from its open-circuit value toward more negative potentials, the substance that will be reduced first (assuming all possible electrode reactions are rapid) is the oxidant in the couple with the least negative (or most positive) E^0. For example, for a platinum electrode immersed in an aqueous solution containing 0.01 M each of Fe^{3+}, Sn^{4+}, and Ni^{2+} in 1 M HCl, the first substance reduced will be Fe^{3+}, since the E^0 of this couple is most positive (Figure 1.1.7a). When the poten-

Hg/H⁺, Br⁻(1 *M*), Cd²⁺(1m*M*)/AgBr/Ag
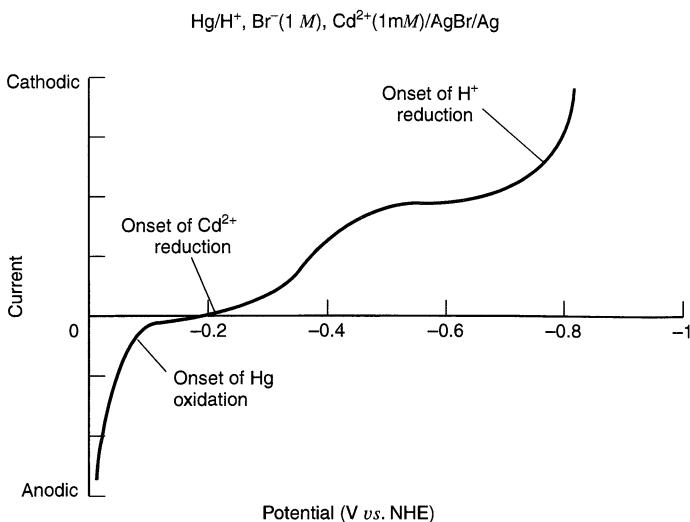
Figure 1.1.6 Schematic current-potential curve for the Hg electrode in the cell Hg/H⁺, Br⁻(1 *M*),Cd²⁺(10⁻³ M)/AgBr/Ag, showing reduction wave for Cd²⁺.

tial of the electrode is moved from its zero-current value toward more positive potentials, the substance that will be oxidized first is the reductant in the couple of least positive (or most negative) E^0. Thus, for a gold electrode in an aqueous solution containing 0.01 M each of Sn^{2+} and Fe^{2+} in 1 M HI, the Sn^{2+} will be first oxidized, since the E^0 of this couple is least positive (Figure 1.1.7*b*). On the other hand, one must remember that these predictions are based on thermodynamic considerations (i.e., reaction energetics), and slow kinetics might prevent a reaction from occurring at a significant rate in a potential region where the E^0 would suggest the reaction was possible. Thus, for a mercury electrode immersed in a solution of 0.01 M each of Cr^{3+} and Zn^{2+}, in 1 M HCl, the first reduction process predicted is the evolution of H_2 from H^+ (Figure 1.1.7*c*). As discussed earlier, this reaction is very slow on mercury, so the first process actually observed is the reduction of Cr^{3+}.

1.1.2 Faradaic and Nonfaradaic Processes

Two types of processes occur at electrodes. One kind comprises reactions like those just discussed, in which charges (e.g., electrons) are transferred across the metal–solution interface. Electron transfer causes oxidation or reduction to occur. Since such reactions are governed by Faraday's law (i.e., the amount of chemical reaction caused by the flow of current is proportional to the amount of electricity passed), they are called *faradaic processes*. Electrodes at which faradaic processes occur are sometimes called *charge-transfer electrodes*. Under some conditions, a given electrode–solution interface will show a range of potentials where no charge-transfer reactions occur because such reactions are thermodynamically or kinetically unfavorable (e.g., the region in Figure 1.1.5 between 0 and −0.8 V *vs.* NHE). However, processes such as adsorption and desorption can occur, and the structure of the electrode–solution interface can change with changing potential or solution composition. These processes are called *nonfaradaic* processes. Although charge does not cross the interface, external currents can flow (at least transiently) when the potential, electrode area, or solution composition changes. Both faradaic and
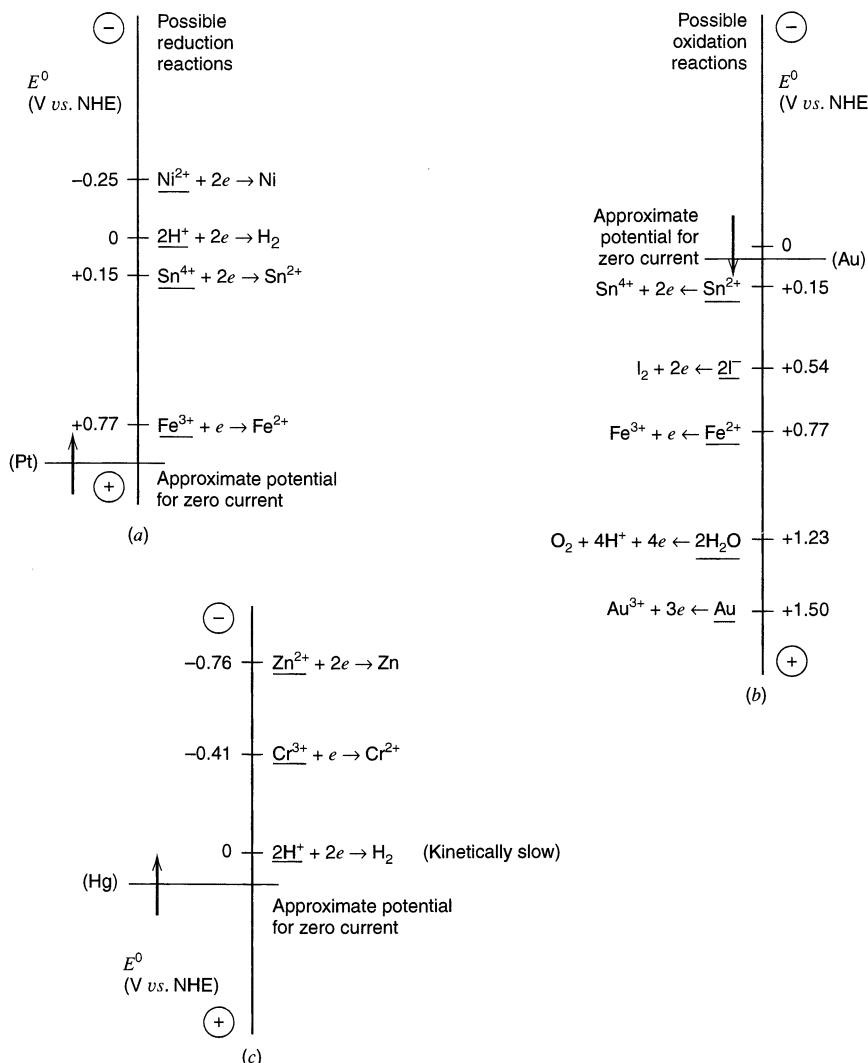
Figure 1.1.7 (*a*) Potentials for possible reductions at a platinum electrode, initially at ~1 V *vs.* NHE in a solution of 0.01 *M* each of Fe^{3+}, Sn^{4+}, and Ni^{2+} in 1 *M* HCl. (*b*) Potentials for possible oxidation reactions at a gold electrode, initially at ~0.1V *vs.* NHE in a solution of 0.01 *M* each of Sn^{2+} and Fe^{2+} in 1 *M* HI. (*c*) Potentials for possible reductions at a mercury electrode in 0.01 *M* Cr^{3+} and Zn^{2+} in 1 *M* HCl. The arrows indicate the directions of potential change discussed in the text.

nonfaradaic processes occur when electrode reactions take place. Although the faradaic processes are usually of primary interest in the investigation of an electrode reaction (except in studies of the nature of the electrode–solution interface itself), the effects of the nonfaradaic processes must be taken into account in using electrochemical data to obtain information about the charge transfer and associated reactions. Consequently, we next proceed by discussing the simpler case of a system where only nonfaradaic processes occur.
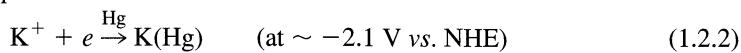
▷▷ 1.2 NONFARADAIC PROCESSES AND THE NATURE OF THE ELECTRODE–SOLUTION INTERFACE

1.2.1 The Ideal Polarized Electrode

An electrode at which no charge transfer can occur across the metal–solution interface, regardless of the potential imposed by an outside source of voltage, is called an *ideal polarized* (or *ideal polarizable*) *electrode* (IPE). While no real electrode can behave as an IPE over the whole potential range available in a solution, some electrode–solution systems can approach ideal polarizability over limited potential ranges,. For example, a mercury electrode in contact with a deaerated potassium chloride solution approaches the behavior of an IPE over a potential range about 2 V wide. At sufficiently positive potentials, the mercury can oxidize in a charge-transfer reaction:

$$\text{Hg} + \text{Cl}^- \to \tfrac{1}{2}\text{Hg}_2\text{Cl}_2 + e \qquad (\text{at} \sim +0.25 \text{ V } vs. \text{ NHE}) \qquad (1.2.1)$$

and at very negative potentials K^+ can be reduced:

$$\text{K}^+ + e \overset{\text{Hg}}{\to} \text{K(Hg)} \qquad (\text{at} \sim -2.1 \text{ V } vs. \text{ NHE}) \qquad (1.2.2)$$

In the potential range between these processes, charge-transfer reactions are not significant. The reduction of water:

$$\text{H}_2\text{O} + e \to \tfrac{1}{2}\text{H}_2 + \text{OH}^- \qquad (1.2.3)$$

is thermodynamically possible, but occurs at a very low rate at a mercury surface unless quite negative potentials are reached. Thus, the only faradaic current that flows in this region is due to charge-transfer reactions of trace impurities (e.g., metal ions, oxygen, and organic species), and this current is quite small in clean systems. Another electrode that behaves as an IPE is a gold surface hosting an adsorbed self-assembled monolayer of alkane thiol (see Section 14.5.2).

1.2.2 Capacitance and Charge of an Electrode

Since charge cannot cross the IPE interface when the potential across it is changed, the behavior of the electrode–solution interface is analogous to that of a capacitor. A capacitor is an electrical circuit element composed of two metal sheets separated by a dielectric material (Figure 1.2.1a). Its behavior is governed by the equation

$$\frac{q}{E} = C \qquad (1.2.4)$$

(a)　　　　　　　　　　*(b)*
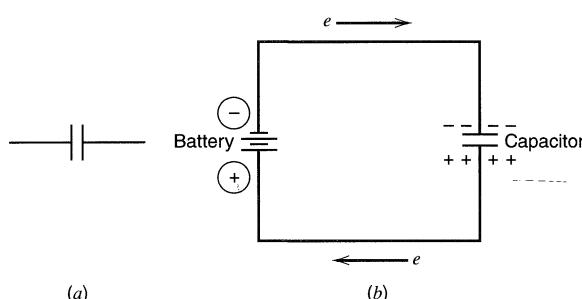
Figure 1.2.1 (*a*) A capacitor. (*b*) Charging a capacitor with a battery.

Figure 1.2.2 The metal–solution interface as a capacitor with a charge on the metal, q^M, (a) negative and (b) positive.

where q is the charge stored on the capacitor (in coulombs, C), E is the potential across the capacitor (in volts, V), and C is the capacitance (in farads, F). When a potential is applied across a capacitor, charge will accumulate on its metal plates until q satisfies equation 1.2.4. During this charging process, a current (called the *charging current*) will flow. The charge on the capacitor consists of an excess of electrons on one plate and a deficiency of electrons on the other (Figure 1.2.1*b*). For example, if a 2-V battery is placed across a 10-μF capacitor, current will flow until 20 μC has accumulated on the capacitor plates. The magnitude of the current depends on the resistance in the circuit (see also Section 1.2.4).

The electrode–solution interface has been shown experimentally to behave like a capacitor, and a model of the interfacial region somewhat resembling a capacitor can be given. At a given potential, there will exist a charge on the metal electrode, q^M, and a charge in the solution, q^S (Figure 1.2.2). Whether the charge on the metal is negative or positive with respect to the solution depends on the potential across the interface and the composition of the solution. At all times, however, $q^M = -q^S$. (In an actual experimental arrangement, two metal electrodes, and thus two interfaces, would have to be considered; we concentrate our attention here on one of these and ignore what happens at the other.) The charge on the metal, q^M, represents an excess or deficiency of electrons and resides in a very thin layer ($<$0.1 Å) on the metal surface. The charge in solution, q^S, is made up of an excess of either cations or anions in the vicinity of the electrode surface. The charges q^M and q^S are often divided by the electrode area and expressed as *charge densities*, such as, $\sigma^M = q^M/A$, usually given in μC/cm^2. The whole array of charged species and oriented dipoles existing at the metal–solution interface is called the *electrical double layer* (although its structure only very loosely resembles two charged layers, as we will see in Section 1.2.3). At a given potential, the electrode– solution interface is characterized by a double-layer capacitance, C_d, typically in the range of 10 to 40 μF/cm^2. However, unlike real capacitors, whose capacitances are independent of the voltage across them, C_d is often a function of potential.[4]

1.2.3 Brief Description of the Electrical Double Layer

The solution side of the double layer is thought to be made up of several "layers." That closest to the electrode, the *inner layer*, contains solvent molecules and sometimes other species (ions or molecules) that are said to be *specifically adsorbed* (Figure 1.2.3). This inner layer is also called the *compact, Helmholtz,* or *Stern layer.* The locus of the electri-

---

[4]In various equations in the literature and in this book, C_d may express the capacitance per unit area and be given in μF/cm^2, or it may express the capacitance of a whole interface and be given in μF. The usage for a given situation is always apparent from the context or from a dimensional analysis.
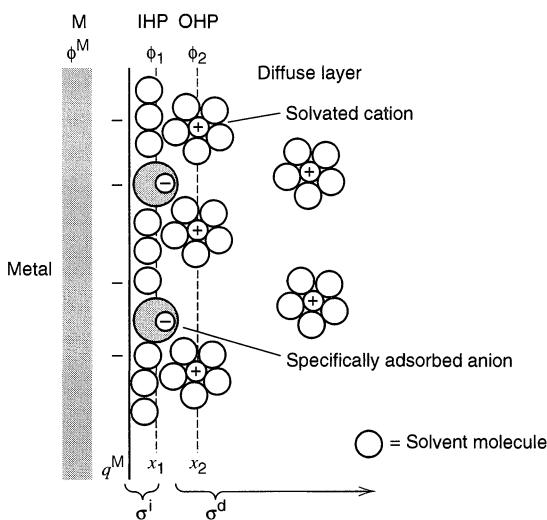
Figure 1.2.3 Proposed model of the double-layer region under conditions where anions are specifically adsorbed.

cal centers of the specifically adsorbed ions is called the *inner Helmholtz plane* (IHP), which is at a distance x_1. The total charge density from specifically adsorbed ions in this inner layer is σ^i (μC/cm^2). Solvated ions can approach the metal only to a distance x_2; the locus of centers of these nearest solvated ions is called the *outer Helmholtz plane* (OHP). The interaction of the solvated ions with the charged metal involves only long-range electrostatic forces, so that their interaction is essentially independent of the chemical properties of the ions. These ions are said to be *nonspecifically adsorbed*. Because of thermal agitation in the solution, the nonspecifically adsorbed ions are distributed in a three-dimensional region called the *diffuse layer*, which extends from the OHP into the bulk of the solution. The excess charge density in the diffuse layer is σ^d, hence the total excess charge density on the solution side of the double layer, σ^S, is given by

$$\sigma^S = \sigma^i + \sigma^d = -\sigma^M \qquad (1.2.5)$$

The thickness of the diffuse layer depends on the total ionic concentration in the solution; for concentrations greater than 10^{-2} M, the thickness is less than $\sim$100 Å. The potential profile across the double-layer region is shown in Figure 1.2.4.

The structure of the double layer can affect the rates of electrode processes. Consider an electroactive species that is not specifically adsorbed. This species can approach the electrode only to the OHP, and the total potential it experiences is less than the potential between the electrode and the solution by an amount $\phi_2 - \phi^S$, which is the potential drop across the diffuse layer. For example, in 0.1 M NaF, $\phi_2 - \phi^S$ is -0.021 V at $E = -0.55$ V vs. SCE, but it has somewhat larger magnitudes at more negative and more positive potentials. Sometimes one can neglect double-layer effects in considering electrode reaction kinetics. At other times they must be taken into account. The importance of adsorption and double-layer structure is considered in greater detail in Chapter 13.

One usually cannot neglect the existence of the double-layer capacitance or the presence of a charging current in electrochemical experiments. Indeed, during electrode reactions involving very low concentrations of electroactive species, the charging current can be much larger than the faradaic current for the reduction or oxidation reaction. For this reason, we will briefly examine the nature of the charging current at an IPE for several types of electrochemical experiments.
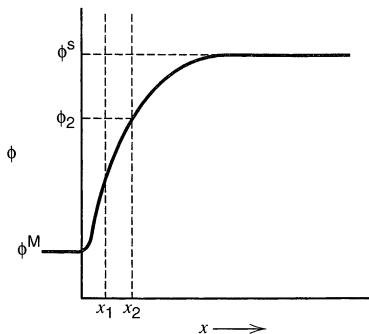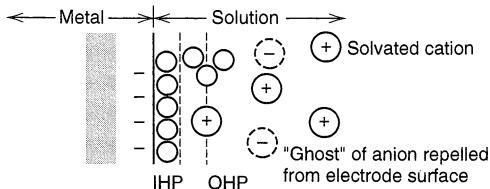
Figure 1.2.4 Potential profile across the double-layer region in the absence of specific adsorption of ions. The variable ϕ, called the *inner potential*, is discussed in detail in Section 2.2. A more quantitative representation of this profile is shown in Figure 12.3.6.

1.2.4 Double-Layer Capacitance and Charging Current in Electrochemical Measurements

Consider a cell consisting of an IPE and an ideal reversible electrode. We can approximate such a system with a mercury electrode in a potassium chloride solution that is also in contact with an SCE. This cell, represented by Hg/K^+, Cl^-/SCE, can be approximated by an electrical circuit with a resistor, R_s, representing the solution resistance and a capacitor, C_d, representing the double layer at the $Hg/K^+,Cl^-$ interface (Figure 1.2.5).[5] Since
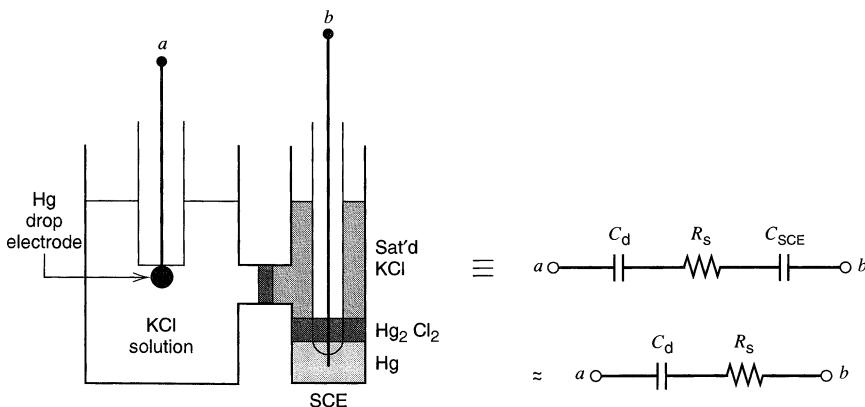
Figure 1.2.5 *Left*: Two-electrode cell with an ideal polarized mercury drop electrode and an SCE. *Right*: Representation of the cell in terms of linear circuit elements.

---

[5]Actually, the capacitance of the SCE, C_{SCE}, should also be included. However, the series capacitance of C_d and C_{SCE} is $C_T = C_d C_{SCE}/[C_d + C_{SCE}]$, and normally $C_{SCE} \gg C_d$, so that $C_T \approx C_d$. Thus, C_{SCE} can be neglected in the circuit.

C_d is generally a function of potential, the proposed model in terms of circuit elements is strictly accurate only for experiments where the overall cell potential does not change very much. Where it does, approximate results can be obtained using an "average" C_d over the potential range.

Information about an electrochemical system is often gained by applying an electrical perturbation to the system and observing the resulting changes in the characteristics of the system. In later sections of this chapter and later chapters of this book, we will encounter such experiments over and over. It is worthwhile now to consider the response of the IPE system, represented by the circuit elements R_s and C_d in series, to several common electrical perturbations.

(a) Voltage (or Potential) Step
The result of a potential step to the IPE is the familiar RC circuit problem (Figure 1.2.6). The behavior of the current, i, with time, t, when applying a potential step of magnitude E, is

$$i = \frac{E}{R_s} e^{-t/R_s C_d} \tag{1.2.6}$$

This equation is derived from the general equation for the charge, q, on a capacitor as a function of the voltage across it, E_C:

$$q = C_d E_C \tag{1.2.7}$$

At any time the sum of the voltages, E_R and E_C, across the resistor and the capacitor, respectively, must equal the applied voltage; hence

$$E = E_R + E_C = iR_s + \frac{q}{C_d} \tag{1.2.8}$$

Noting that $i = dq/dt$ and rearranging yields

$$\frac{dq}{dt} = \frac{-q}{R_s C_d} + \frac{E}{R_s} \tag{1.2.9}$$

If we assume that the capacitor is initially uncharged ($q = 0$ at $t = 0$), then the solution of (1.2.9) is

$$q = EC_d[1 - e^{-t/R_s C_d}] \tag{1.2.10}$$

By differentiating (1.2.10), one obtains (1.2.6). Hence, for a potential step input, there is an exponentially decaying current having a time constant, $\tau = R_s C_d$ (Figure 1.2.7). The current for charging the double-layer capacitance drops to 37% of its initial value at $t = \tau$, and to 5% of its initial value at $t = 3\tau$. For example, if $R_s = 1\ \Omega$ and $C_d = 20\ \mu F$, then $\tau = 20\ \mu s$ and double-layer charging is 95% complete in 60 μs.
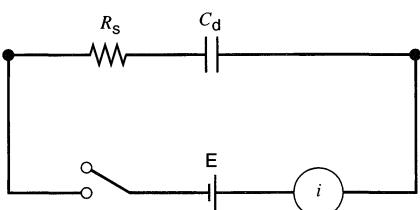
Figure 1.2.6 Potential step experiment for an RC circuit.
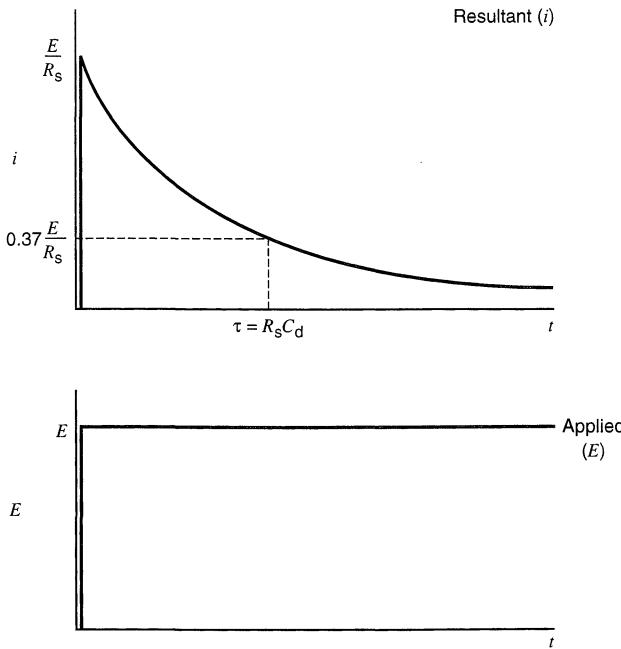
Figure 1.2.7 Current transient (i *vs.* t) resulting from a potential step experiment.

(b) Current Step

When the R_sC_d circuit is charged by a constant current (Figure 1.2.8), then equation 1.2.8 again applies. Since $q = \int i\,dt$, and i is a constant,

$$E = iR_s + \frac{i}{C_d}\int_0^t dt \tag{1.2.11}$$

or

$$\boxed{E = i(R_s + t/C_d)} \tag{1.2.12}$$

Hence, the potential increases linearly with time for a current step (Figure 1.2.9).

(c) Voltage Ramp (or Potential Sweep)

A *voltage ramp* or *linear potential sweep* is a potential that increases linearly with time starting at some initial value (here assumed to be zero) at a sweep rate v (in V s^{-1}) (see Figure 1.2.10a).

$$E = vt \tag{1.2.13}$$

Constant current source
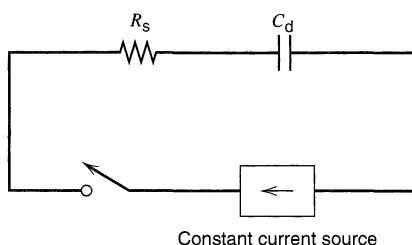
Figure 1.2.8 Current step experiment for an *RC* circuit.
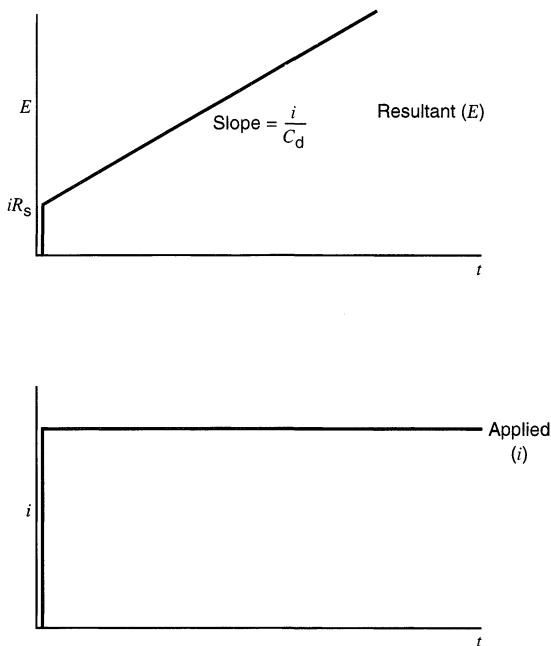
Figure 1.2.9 *E-t* behavior resulting from a current step experiment.

If such a ramp is applied to the R_sC_d circuit, equation 1.2.8 still applies; hence

$$vt = R_s(dq/dt) + q/C_d \tag{1.2.14}$$

If $q = 0$ at $t = 0$,

$$i = vC_d\,[1 - \exp(-t/R_sC_d)] \tag{1.2.15}$$

The current rises from zero as the scan starts and attains a steady-state value, vC_d (Figure 1.2.10b). This steady-state current can then be used to estimate C_d. If the time constant,

(a)

(b)
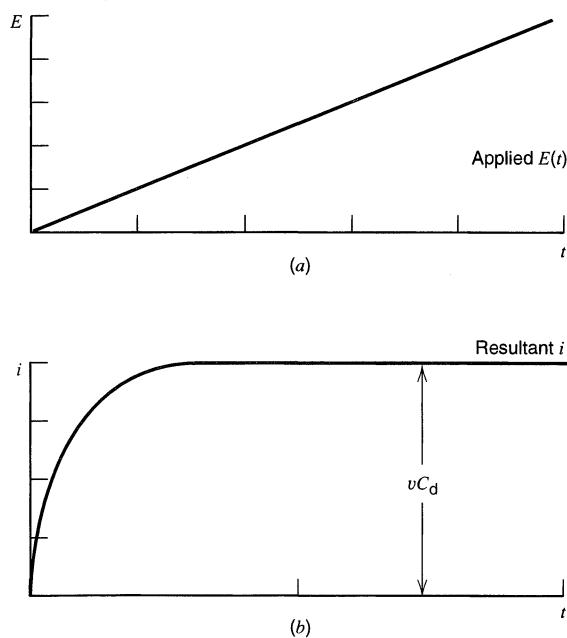
Figure 1.2.10 Current-time behavior resulting from a linear potential sweep applied to an *RC* circuit.
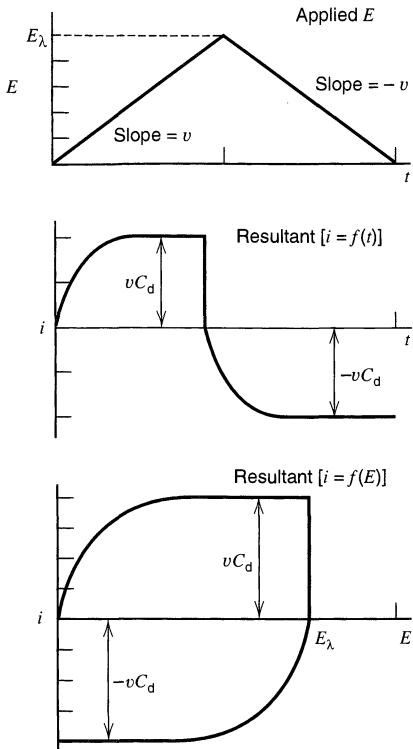
Figure 1.2.11 Current-time and current-potential plots resulting from a cyclic linear potential sweep (or triangular wave) applied to an RC circuit.

R_sC_d, is small compared to v, the instantaneous current can be used to measure C_d as a function of E.

If one instead applies a *triangular wave* (i.e., a ramp whose sweep rate switches from v to $-v$ at some potential, E_λ), then the steady-state current changes from vC_d during the forward (increasing E) scan to $-vC_d$ during the reverse (decreasing E) scan. The result for a system with constant C_d is shown in Figure 1.2.11.

⊁ 1.3 FARADAIC PROCESSES AND FACTORS AFFECTING RATES OF ELECTRODE REACTIONS

1.3.1 Electrochemical Cells—Types and Definitions

Electrochemical cells in which faradaic currents are flowing are classified as either *galvanic* or *electrolytic* cells. A *galvanic cell* is one in which reactions occur spontaneously at the electrodes when they are connected externally by a conductor (Figure 1.3.1*a*). These cells are often employed in converting chemical energy into electrical energy. Galvanic cells of commercial importance include *primary* (*nonrechargeable*) *cells* (e.g., the Leclanché Zn–MnO_2 cell), *secondary* (*rechargeable*) *cells* (e.g., a charged Pb–PbO_2 storage battery), and *fuel cells* (e.g., an H_2–O_2 cell). An *electrolytic cell* is one in which reactions are effected by the imposition of an external voltage greater than the open-circuit potential of the cell (Figure 1.3.1*b*). These cells are frequently employed to carry out desired chemical reactions by expending electrical energy. Commercial processes involving electrolytic cells include electrolytic syntheses (e.g., the production of chlorine and aluminum), electrorefining (e.g., copper), and electroplating (e.g., silver and gold). The lead–acid storage cell, when it is being "recharged," is an electrolytic cell.
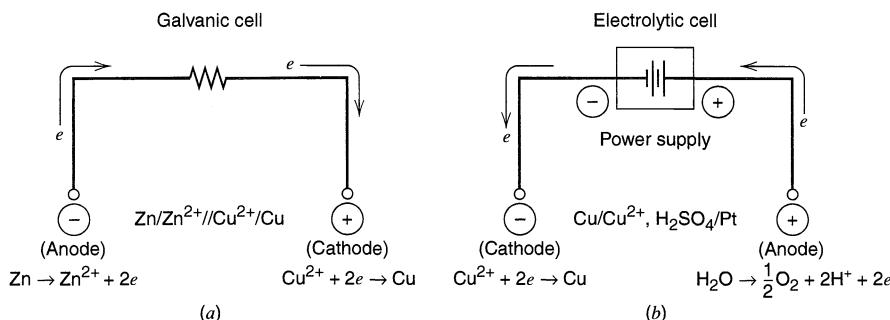
Figure 1.3.1 (a) Galvanic and (b) electrolytic cells.

Although it is often convenient to make a distinction between galvanic and electrolytic cells, we will most often be concerned with reactions occurring at only one of the electrodes. Treatment is simplified by concentrating our attention on only one-half of the cell at a time. If necessary, the behavior of a whole cell can be ascertained later by combining the characteristics of the individual half-cells. The behavior of a single electrode and the fundamental nature of its reactions are independent of whether the electrode is part of a galvanic or electrolytic cell. For example, consider the cells in Figure 1.3.1. The nature of the reaction $Cu^{2+} + 2e \rightarrow Cu$ is the same in both cells. If one desires to plate copper, one could accomplish this either in a galvanic cell (using a counter half-cell with a more negative potential than that of Cu/Cu^{2+}) or in an electrolytic cell (using any counter half-cell and supplying electrons to the copper electrode with an external power supply). Thus, *electrolysis* is a term that we define broadly to include chemical changes accompanying faradaic reactions at electrodes in contact with electrolytes. In discussing cells, one calls the electrode at which reductions occur the *cathode*, and the electrode at which oxidations occur the *anode*. A current in which electrons cross the interface from the electrode to a species in solution is a *cathodic current*, while electron flow from a solution species into the electrode is an *anodic current*. In an electrolytic cell, the cathode is negative with respect to the anode; but in a galvanic cell, the cathode is positive with respect to the anode.[6]

1.3.2 The Electrochemical Experiment and Variables in Electrochemical Cells

An investigation of electrochemical behavior consists of holding certain variables of an electrochemical cell constant and observing how other variables (usually current, potential, or concentration) vary with changes in the controlled variables. The parameters of importance in electrochemical cells are shown in Figure 1.3.2. For example, in *potentiometric* experiments, $i = 0$ and E is determined as a function of C. Since no current flows in this experiment, no net faradaic reaction occurs, and the potential is frequently (but not always) governed by the thermodynamic properties of the system. Many of the variables (electrode area, mass transfer, electrode geometry) do not affect the potential directly.

---

[6]Because a cathodic current and a cathodic reaction can occur at an electrode that is either positive or negative with respect to another electrode (e.g., an auxiliary or reference electrode, see Section 1.3.4), it is poor usage to associate the term "cathodic" or "anodic" with potentials of a particular sign. For example, one should not say, "The potential shifted in a cathodic direction," when what is meant is, "The potential shifted in a *negative* direction." The terms anodic and cathodic refer to electron flow or current direction, not to potential.
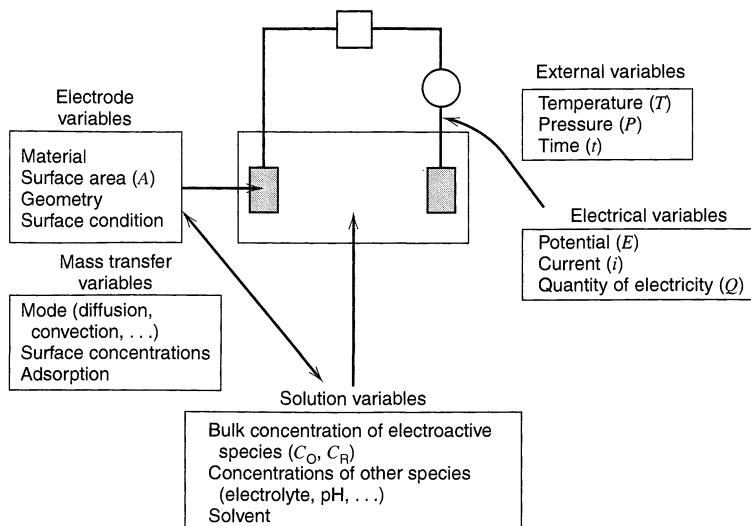
Figure 1.3.2 Variables affecting the rate of an electrode reaction.

Another way of visualizing an electrochemical experiment is in terms of the way in which the system responds to a perturbation. The electrochemical cell is considered as a "black box" to which a certain excitation function (e.g., a potential step) is applied, and a certain response function (e.g., the resulting variation of current with time) is measured, with all other system variables held constant (Figure 1.3.3). The aim of the experiment is to obtain information (thermodynamic, kinetic, analytical, etc.) from observation of the
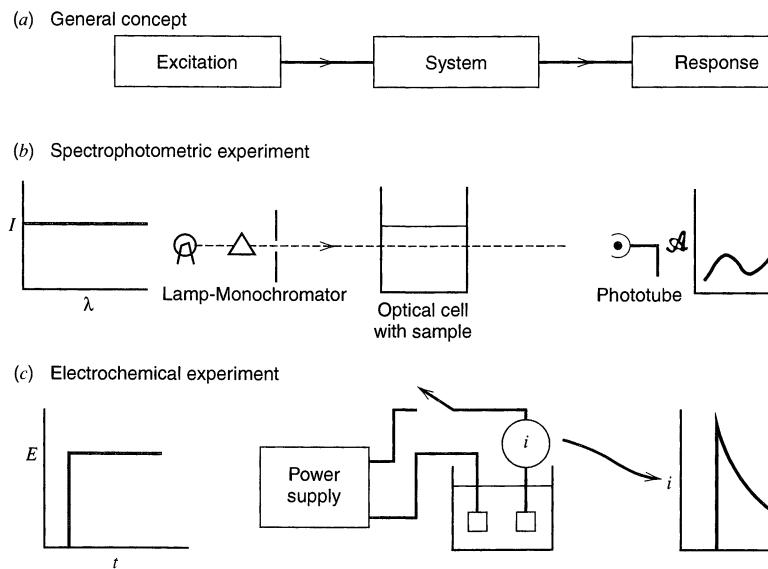
Figure 1.3.3 (*a*) General principle of studying a system by application of an excitation (or perturbation) and observation of response. (*b*) In a spectrophotometric experiment, the excitation is light of different wavelengths (λ), and the response is the absorbance ($\mathcal{A}$) curve. (*c*) In an electrochemical (potential step) experiment, the excitation is the application of a potential step, and the response is the observed *i-t* curve.
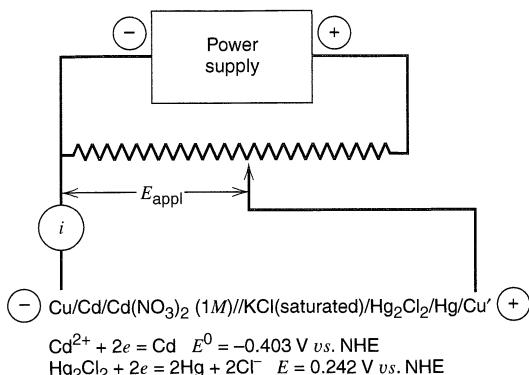
Figure 1.3.4 Schematic cell connected to an external power supply. The double slash indicates that the KCl solution contacts the $Cd(NO_3)_2$ solution in such a way that there is no appreciable potential difference across the junction between the two liquids. A "salt bridge" (Section 2.3.5) is often used to achieve that condition.

$Cu/Cd/Cd(NO_3)_2$ (1*M*)//KCl(saturated)/Hg_2Cl_2/Hg/Cu' $\,+\,$

$Cd^{2+} + 2e = Cd \quad E^0 = -0.403$ V *vs.* NHE
$Hg_2Cl_2 + 2e = 2Hg + 2Cl^- \quad E = 0.242$ V *vs.* NHE

excitation and response functions and a knowledge of appropriate models for the system. This same basic idea is used in many other types of investigation, such as circuit testing or spectrophotometric analysis. In spectrophotometry, the excitation function is light of different wavelengths; the response function is the fraction of light transmitted by the system at these wavelengths; the system model is Beer's law or a molecular model; and the information content includes the concentrations of absorbing species, their absorptivities, or their transition energies.

Before developing some simple models for electrochemical systems, let us consider more closely the nature of the current and potential in an electrochemical cell. Consider the cell in which a cadmium electrode immersed in 1 *M* $Cd(NO_3)_2$ is coupled to an SCE (Figure 1.3.4). The open-circuit potential of the cell is 0.64 V, with the copper wire attached to the cadmium electrode being negative with respect to that attached to the mercury electrode.[7] When the voltage applied by the external power supply, E_{appl}, is 0.64 V, $i = 0$. When E_{appl} is made larger (i.e., $E_{appl} > 0.64$ V, such that the cadmium electrode is made even more negative with respect to the SCE), the cell behaves as an electrolytic cell and a current flows. At the cadmium electrode, the reaction $Cd^{2+} + 2e \rightarrow Cd$ occurs, while at the SCE, mercury is oxidized to Hg_2Cl_2. A question of interest might be: "If $E_{appl} = 0.74$ V (i.e., if the potential of the cadmium electrode is made -0.74 V *vs.* the SCE), what current will flow?" Since *i* represents the number of electrons reacting with Cd^{2+} per second, or the number of coulombs of electric charge flowing per second, the question "What is *i*?" is essentially the same as "What is the rate of the reaction, $Cd^{2+} + 2e \rightarrow Cd$?" The following relations demonstrate the direct proportionality between faradaic current and electrolysis rate:

$$i \text{ (amperes)} = \frac{dQ}{dt} \text{ (coulombs/s)} \tag{1.3.1}$$

$$\frac{Q}{nF} \frac{\text{(coulombs)}}{\text{(coulombs/mol)}} = N \text{ (mol electrolyzed)} \tag{1.3.2}$$

where *n* is the stoichiometric number of electrons consumed in the electrode reaction (e.g., 2 for reduction of Cd^{2+}).

$$\boxed{\text{Rate (mol/s)} = \frac{dN}{dt} = \frac{i}{nF}} \tag{1.3.3}$$

---

[7]This value is calculated from the information in Figure 1.3.4. The experimental value would also include the effects of activity coefficients and the liquid junction potential, which are neglected here. See Chapter 2.

Interpreting the rate of an electrode reaction is often more complex than doing the same for a reaction occurring in solution or in the gas phase. The latter is called a *homogeneous reaction*, because it occurs everywhere within the medium at a uniform rate. In contrast, an electrode process is a *heterogeneous reaction* occurring only at the electrode–electrolyte interface. Its rate depends on mass transfer to the electrode and various surface effects, in addition to the usual kinetic variables. Since electrode reactions are heterogeneous, their reaction rates are usually described in units of mol/s per unit area; that is,

$$\text{Rate} \left(\text{mol s}^{-1} \text{ cm}^{-2} \right) = \frac{i}{nFA} = \frac{j}{nF}$$

(1.3.4)

where j is the *current density* (A/cm^2).

Information about an electrode reaction is often gained by determining current as a function of potential (by obtaining *i-E* curves). Certain terms are sometimes associated with features of the curves.[8] If a cell has a defined equilibrium potential (Section 1.1.1), that potential is an important reference point of the system. The departure of the electrode potential (or cell potential) from the equilibrium value upon passage of faradaic current is termed *polarization*. The extent of polarization is measured by the *overpotential*, η,

$$\eta = E - E_{eq}$$

(1.3.5)

Current-potential curves, particularly those obtained under steady-state conditions, are sometimes called *polarization curves*. We have seen that an ideal polarized electrode (Section 1.2.1) shows a very large change in potential upon the passage of an infinitesimal current; thus ideal polarizability is characterized by a horizontal region of an *i-E* curve (Figure 1.3.5a). A substance that tends to cause the potential of an electrode to be nearer to its equilibrium value by virtue of being oxidized or reduced is called a *depolarizer*.[9] An

(a) Ideal polarizable electrode   (b) Ideal nonpolarizable electrode
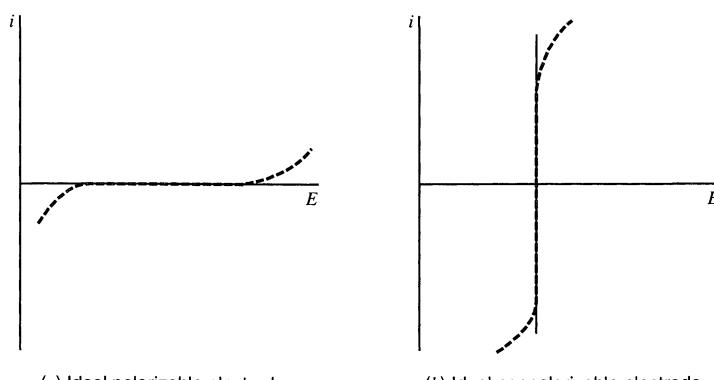
Figure 1.3.5 Current-potential curves for ideal (*a*) polarizable and (*b*) nonpolarizable electrodes. Dashed lines show behavior of actual electrodes that approach the ideal behavior over limited ranges of current or potential.

---

[8]These terms are carryovers from older electrochemical studies and models and, indeed, do not always represent the best possible terminology. However, their use is so ingrained in electrochemical jargon that it seems wisest to keep them and to define them as precisely as possible.

[9]The term *depolarizer* is also frequently used to denote a substance that is preferentially oxidized or reduced, to prevent an undesirable electrode reaction. Sometimes it is simply another name for an electroactive substance.

ideal nonpolarizable electrode (or *ideal depolarized electrode*) is thus an electrode whose potential does not change upon passage of current, that is, an electrode of fixed potential. Nonpolarizability is characterized by a vertical region on an *i-E* curve (Figure 1.3.5*b*). An SCE constructed with a large-area mercury pool would approach ideal nonpolarizability at small currents.

1.3.3 Factors Affecting Electrode Reaction Rate and Current

Consider an overall electrode reaction, $O + ne \rightleftarrows R$, composed of a series of steps that cause the conversion of the dissolved oxidized species, O, to a reduced form, R, also in solution (Figure 1.3.6). In general, the current (or electrode reaction rate) is governed by the rates of processes such as (1, 2):

1. Mass transfer (e.g., of O from the bulk solution to the electrode surface).

2. Electron transfer at the electrode surface.

3. Chemical reactions preceding or following the electron transfer. These might be homogeneous processes (e.g., protonation or dimerization) or heterogeneous ones (e.g., catalytic decomposition) on the electrode surface.

4. Other surface reactions, such as adsorption, desorption, or crystallization (electrodeposition).

The rate constants for some of these processes (e.g., electron transfer at the electrode surface or adsorption) depend upon the potential.

The simplest reactions involve only mass transfer of a reactant to the electrode, heterogeneous electron transfer involving nonadsorbed species, and mass transfer of the product to the bulk solution. A representative reaction of this sort is the reduction of the aromatic hydrocarbon 9,10-diphenylanthracene (DPA) to the radical anion (DPA$\overline{\cdot}$) in an aprotic solvent (e.g., *N,N*-dimethylformamide). More complex reaction sequences involving a series of electron transfers and protonations, branching mechanisms, parallel paths, or modifications of the electrode surface are quite common. When a steady-state current is obtained, the rates of all reaction steps in a series are the same. The magnitude of this current is often limited by the inherent sluggishness of one or more reactions called *rate-determining steps*. The more facile reactions are held back from their maximum rates by
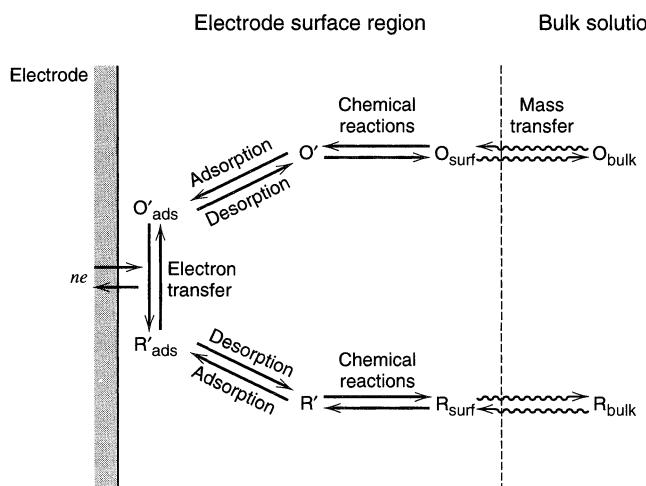
Figure 1.3.6 Pathway of a general electrode reaction.
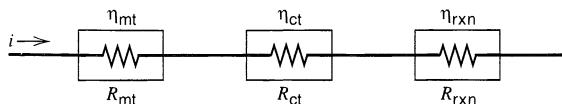
Figure 1.3.7 Processes in an electrode reaction represented as resistances.

the slowness with which a rate-determining step disposes of their products or creates their reactants.

Each value of current density, j, is driven by a certain overpotential, η. This overpotential can be considered as a sum of terms associated with the different reaction steps: η_{mt} (the *mass-transfer overpotential*), η_{ct} (the *charge-transfer overpotential*), η_{rxn} (the overpotential associated with a preceding reaction), etc. The electrode reaction can then be represented by a resistance, R, composed of a series of resistances (or more exactly, impedances) representing the various steps: R_{mt}, R_{ct}, etc. (Figure 1.3.7). A fast reaction step is characterized by a small resistance (or impedance), while a slow step is represented by a high resistance. However, except for very small current or potential perturbations, these impedances are functions of E (or i), unlike the analogous actual electrical elements.

1.3.4 Electrochemical Cells and Cell Resistance

Consider a cell composed of two ideal nonpolarizable electrodes, for example, two SCEs immersed in a potassium chloride solution: SCE/KCl/SCE. The i-E characteristic of this cell would look like that of a pure resistance (Figure 1.3.8), because the only limitation on current flow is imposed by the resistance of the solution. In fact, these conditions (i.e., paired, nonpolarizable electrodes) are exactly those sought in measurements of solution conductivity. For any real electrodes (e.g., actual SCEs), mass-transfer and charge-transfer overpotentials would also become important at high enough current densities.

When the potential of an electrode is measured against a nonpolarizable reference electrode during the passage of current, a voltage drop equal to iR_s is always included in the measured value. Here, R_s is the solution resistance between the electrodes, which, unlike the impedances describing the mass transfer and activation steps in the electrode reaction, actually behaves as a true resistance over a wide range of conditions. For example, consider once again the cell in Figure 1.3.4. At open circuit ($i = 0$), the potential of the cadmium electrode is the equilibrium value, $E_{eq,Cd}$ (about -0.64 V *vs.* SCE). We saw ear-
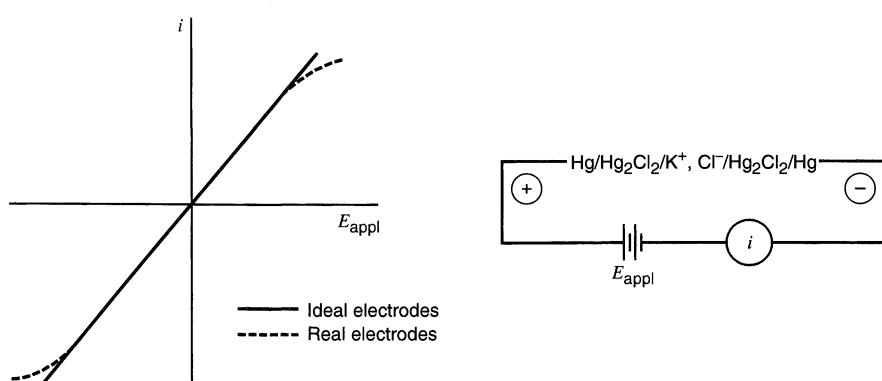
Figure 1.3.8 Current-potential curve for a cell composed of two electrodes approaching ideal nonpolarizability.

lier that with $E_{appl} = -0.64$ V (Cd *vs.* SCE), no current would flow through the ammeter. If E_{appl} is increased in magnitude to -0.80 V (Cd *vs.* SCE), current flows. The extra applied voltage is distributed in two parts. First, to deliver the current, the potential of the Cd electrode, E_{Cd}, must shift to a new value, perhaps -0.70 V *vs.* SCE. The remainder of the applied voltage (-0.10 V in this example) represents the ohmic drop caused by current flow in solution. We assume that the SCE is essentially nonpolarizable at the extant current level and does not change its potential. In general,

$$\boxed{E_{appl} \ (vs. \ \text{SCE}) = E_{Cd}(vs. \ \text{SCE}) - iR_s = E_{eq,Cd}(vs. \ \text{SCE}) + \eta - iR_s} \quad (1.3.6)$$

The last two terms of this equation are related to current flow. When there is a cathodic current at the cadmium electrode, both are negative. Conversely, both are positive for an anodic current. In the cathodic case, E_{appl} must manifest the (negative) overpotential ($E_{Cd} - E_{eq,Cd}$) needed to support the electrochemical reaction rate corresponding to the current. (In the example above, $\eta = -0.06$ V.) In addition E_{appl} must encompass the ohmic drop, iR_s, required to drive the ionic current in solution (which corresponds to the passage of negative charge from the cadmium electrode to the SCE).[10] The ohmic potential drop in the solution should not be regarded as a form of overpotential, because it is characteristic of the bulk solution and not of the electrode reaction. Its contribution to the measured electrode potential can be minimized by proper cell design and instrumentation.

Most of the time, one is interested in reactions that occur at only one electrode. An experimental cell could be composed of the electrode system of interest, called the *working* (or *indicator*) *electrode*, coupled with an electrode of known potential that approaches ideal nonpolarizability (such as an SCE with a large-area mercury pool), called the *reference electrode*. If the passage of current does not affect the potential of the reference electrode, the E of the working electrode is given by equation 1.3.6. Under conditions when iR_s is small (say less than 1–2 mV), this *two-electrode cell* (Figure 1.3.9) can be used to determine the *i-E* curve, with E either taken as equal to E_{appl} or corrected for the small iR_s drop. For example, in classic polarographic experiments in aqueous solutions, two-electrode cells were often used. In these systems, it is often true that $i < 10 \ \mu$A and $R_s < 100 \ \Omega$, so that $iR_s < (10^{-5} \ \text{A})(100 \ \Omega)$ or $iR_s < 1$ mV, which is negligible for most purposes. With more highly resistive solutions, such as those based on many nonaqueous solvents, a very small electrode (an *ultramicroelectrode*, Section 5.3) must be used if a two-electrode cell is to be employed without serious complica-
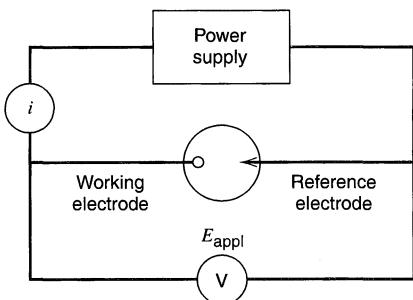
**Figure 1.3.9** Two-electrode cell.

---

[10]The sign preceding the ohmic drop in (1.3.6) is negative as a consequence of the sign convention adopted here for currents (cathodic currents taken as positive).
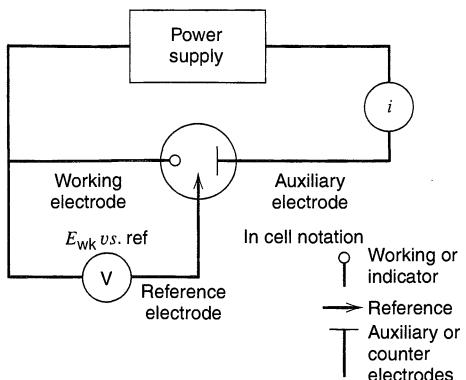
Figure 1.3.10 Three-electrode cell and notation for the different electrodes.

tions from the ohmic drop in solution. With such electrodes, currents of the order of 1 nA are typical; hence R_s values even in the MΩ range can be acceptable.

In experiments where iR_s may be high (e.g., in large-scale electrolytic or galvanic cells or in experiments involving nonaqueous solutions with low conductivities), a *three-electrode cell* (Figure 1.3.10) is preferable. In this arrangement, the current is passed between the working electrode and a *counter* (or *auxiliary*) *electrode*. The auxiliary electrode can be any convenient one, because its electrochemical properties do not
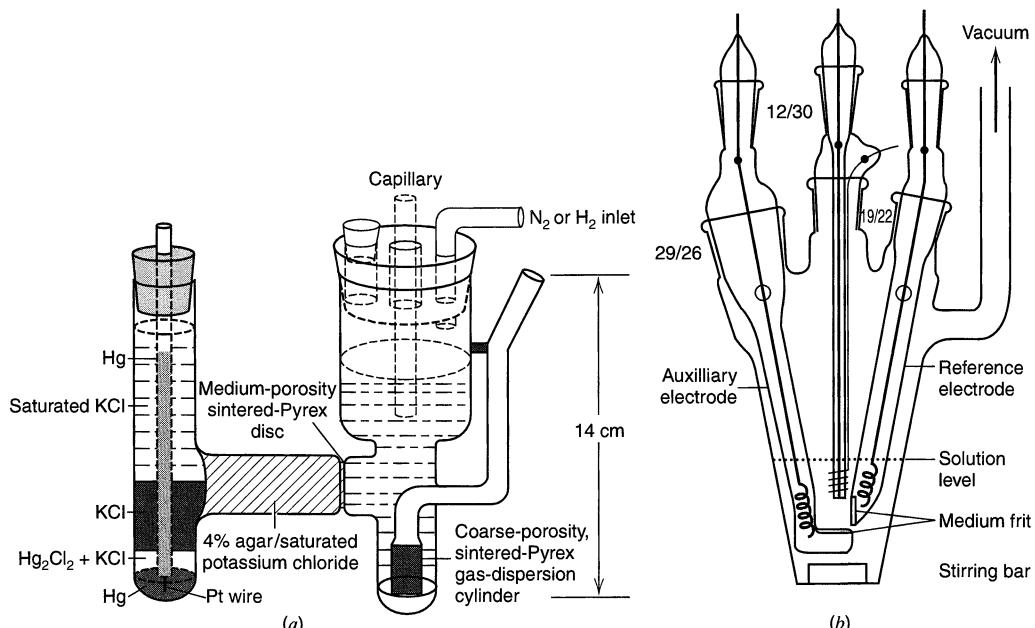
Figure 1.3.11 Typical two- and three-electrode cells used in electrochemical experiments. (*a*) Two-electrode cell for polarography. The working electrode is a dropping mercury electrode (capillary) and the N_2 inlet tube is for deaeration of the solution. [From L. Meites, *Polarographic Techniques,* 2nd ed., Wiley-Interscience, New York, 1965, with permission.] (*b*) Three-electrode cell designed for studies with nonaqueous solutions at a platinum-disk working electrode, with provision for attachment to a vacuum line. [Reprinted with permission from A. Demortier and A. J. Bard, *J. Am. Chem. Soc.*, **95**, 3495 (1973). Copyright 1973, American Chemical Society.] Three-electrode cells for bulk electrolysis are shown in Figure 11.2.2.

affect the behavior of the electrode of interest. It is usually chosen to be an electrode that does not produce substances by electrolysis that will reach the working electrode surface and cause interfering reactions there. Frequently, it is placed in a compartment separated from the working electrode by a sintered-glass disk or other separator. The potential of the working electrode is monitored relative to a separate reference electrode, positioned with its tip nearby. The device used to measure the potential difference between the working electrode and the reference electrode has a high input impedance, so that a negligible current is drawn through the reference electrode. Consequently, its potential will remain constant and equal to its open-circuit value. This three-electrode arrangement is used in most electrochemical experiments; several practical cells are shown in Figure 1.3.11.

Even in this arrangement, not all of the iR_s term is removed from the reading made by the potential-measuring device. Consider the potential profile in solution between the working and auxiliary electrodes, shown schematically in Figure 1.3.12. (The potential profile in an actual cell depends on the electrode shapes, geometry, solution conductance, etc.) The solution between the electrodes can be regarded as a potentiometer (but not necessarily a linear one). If the reference electrode is placed anywhere but exactly at the electrode surface, some fraction of iR_s, (called iR_u, where R_u is the *uncompensated resistance*) will be included in the measured potential. Even when the tip of the reference electrode is designed for very close placement to the working electrode by use of a fine tip called a *Luggin–Haber capillary*, some uncompensated resistance usually remains. This uncompensated potential drop can sometimes be removed later, for example, from steady-state measurements by measurement of R_u and point-by-point correction of each measured potential. Modern electrochemical instrumentation frequently includes circuitry for electronic compensation of the iR_u term (see Chapter 15).

If the reference capillary has a tip diameter d, it can be placed as close as $2d$ from the working electrode surface without causing appreciable shielding error. *Shielding* denotes a blockage of part of the solution current path at the working electrode surface, which causes nonuniform current densities to arise at the electrode surface. For a planar electrode with uniform current density across its surface,

$$R_u = x/\kappa A \qquad (1.3.7)$$
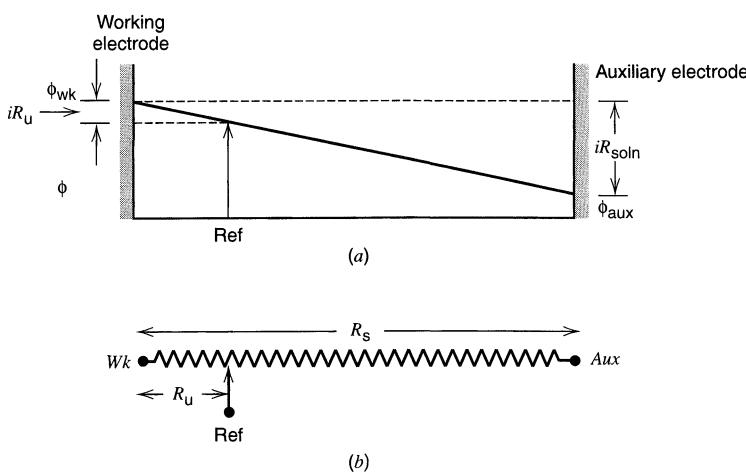
Figure 1.3.12 (*a*) Potential drop between working and auxiliary electrodes in solution and iR_u measured at the reference electrode. (*b*) Representation of the cell as a potentiometer.

where x is the distance of the capillary tip from the electrode, A is the electrode area, and κ is the solution conductivity. The effect of iR_u can be particularly serious for spherical microelectrodes, such as the hanging mercury drop electrode or the dropping mercury electrode (DME). For a spherical electrode of radius r_0,

$$R_u = \frac{1}{4\pi\kappa r_0}\left(\frac{x}{x + r_0}\right) \tag{1.3.8}$$

In this case, most of the resistive drop occurs close to the electrode. For a reference electrode tip placed just one electrode radius away ($x = r_0$), R_u is already half of the value for the tip placed infinitely far away. Any resistances in the working electrode itself (e.g., in thin wires used to make ultramicroelectrodes, in semiconductor electrodes, or in resistive films on the electrode surface) will also appear in R_u.

▶▶ 1.4 INTRODUCTION TO MASS-TRANSFER-CONTROLLED REACTIONS

1.4.1 Modes of Mass Transfer

Let us now be more quantitative about the size and shape of current-potential curves. As shown in equation 1.3.4, if we are to understand i, we must be able to describe the rate of the reaction, v, at the electrode surface. The simplest electrode reactions are those in which the rates of all associated chemical reactions are very rapid compared to those of the mass-transfer processes. Under these conditions, the chemical reactions can usually be treated in a particularly simple way. If, for example, an electrode process involves only fast heterogeneous charge-transfer kinetics and mobile, reversible homogeneous reactions, we will find below that (a) the homogeneous reactions can be regarded as being at equilibrium and (b) the *surface concentrations* of species involved in the faradaic process are related to the electrode potential by an equation of the Nernst form. The net rate of the electrode reaction, v_{rxn}, is then governed totally by the rate at which the electroactive species is brought to the surface by mass transfer, v_{mt}. Hence, from equation 1.3.4,

$$v_{rxn} = v_{mt} = i/nFA \tag{1.4.1}$$

Such electrode reactions are often called *reversible* or *nernstian*, because the principal species obey thermodynamic relationships at the electrode surface. Since mass transfer plays a big role in electrochemical dynamics, we review here its three modes and begin a consideration of mathematical methods for treating them.

Mass transfer, that is, the movement of material from one location in solution to another, arises either from differences in electrical or chemical potential at the two locations or from movement of a volume element of solution. The modes of mass transfer are:

1. *Migration.* Movement of a charged body under the influence of an electric field (a gradient of electrical potential).

2. *Diffusion.* Movement of a species under the influence of a gradient of chemical potential (i.e., a concentration gradient).

3. *Convection.* Stirring or hydrodynamic transport. Generally fluid flow occurs because of *natural convection* (convection caused by density gradients) and *forced convection*, and may be characterized by stagnant regions, laminar flow, and turbulent flow.

Mass transfer to an electrode is governed by the *Nernst–Planck equation*, written for one-dimensional mass transfer along the x-axis as

$$J_i(x) = -D_i \frac{\partial C_i(x)}{\partial x} - \frac{z_i F}{RT} D_i C_i \frac{\partial \phi(x)}{\partial x} + C_i v(x) \qquad (1.4.2)$$

where $J_i(x)$ is the flux of species i (mol s^{-1}cm^{-2}) at distance x from the surface, D_i is the diffusion coefficient (cm^2/s), $\partial C_i(x)/\partial x$ is the concentration gradient at distance x, $\partial \phi(x)/\partial x$ is the potential gradient, z_i and C_i are the charge (dimensionless) and concentration (mol cm^{-3}) of species i, respectively, and $v(x)$ is the velocity (cm/s) with which a volume element in solution moves along the axis. This equation is derived and discussed in more detail in Chapter 4. The three terms on the right-hand side represent the contributions of diffusion, migration, and convection, respectively, to the flux.

While we will be concerned with particular solutions of this equation in later chapters, a rigorous solution is generally not very easy when all three forms of mass transfer are in effect; hence electrochemical systems are frequently designed so that one or more of the contributions to mass transfer are negligible. For example, the migrational component can be reduced to negligible levels by addition of an inert electrolyte (a *supporting electrolyte*) at a concentration much larger than that of the electroactive species (see Section 4.3.2). Convection can be avoided by preventing stirring and vibrations in the electrochemical cell. In this chapter, we present an approximate treatment of steady-state mass transfer, which will provide a useful guide for these processes in later chapters and will give insight into electrochemical reactions without encumbrance by mathematical details.

1.4.2 Semiempirical Treatment of Steady-State Mass Transfer

Consider the reduction of a species O at a cathode: O + ne ⇌ R. In an actual case, the oxidized form, O, might be Fe(CN)$_6^{3-}$ and R might be Fe(CN)$_6^{4-}$, with only Fe(CN)$_6^{3-}$ initially present at the millimolar level in a solution of 0.1 M K$_2$SO$_4$. We envision a three-electrode cell having a platinum cathode, platinum anode, and SCE reference electrode. In addition, we furnish provision for agitation of the solution, such as by a stirrer. A particularly reproducible way to realize these conditions is to make the cathode in the form of a disk embedded in an insulator and to rotate the assembly at a known rate; this is called the *rotating disk electrode* (RDE) and is discussed in Section 9.3.

Once electrolysis of species O begins, its concentration at the electrode surface, $C_O(x = 0)$ becomes smaller than the value, C_O^*, in the *bulk solution* (far from the electrode). We assume here that stirring is ineffective at the electrode surface, so the solution velocity term need not be considered at $x = 0$. This simplified treatment is based on the idea that a stagnant layer of thickness δ_O exists at the electrode surface (*Nernst diffusion layer*), with stirring maintaining the concentration of O at C_O^* beyond $x = \delta_O$ (Figure 1.4.1). Since we also assume that there is an excess of supporting electrolyte, migration is not important, and the rate of mass transfer is proportional to the concentration gradient at the electrode surface, as given by the first (diffusive) term in equation 1.4.2:

$$v_{mt} \propto (dC_O/dx)_{x=0} = D_O(dC_O/dx)_{x=0} \qquad (1.4.3)$$

If one further assumes a linear concentration gradient within the diffusion layer, then, from equation 1.4.3

$$v_{mt} = D_O[C_O^* - C_O(x = 0)]/\delta_O \qquad (1.4.4)$$
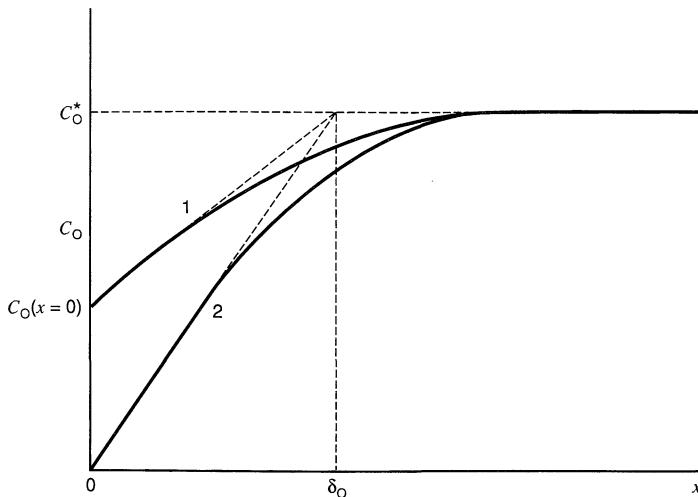
Figure 1.4.1 Concentration profiles (solid lines) and diffusion layer approximation (dashed lines). $x = 0$ corresponds to the electrode surface and δ_O is the diffusion layer thickness. Concentration profiles are shown at two different electrode potentials: (1) where $C_O(x = 0)$ is about $C_O^*/2$, (2) where $C_O(x = 0) \approx 0$ and $i = i_l$.

Since δ_O is often unknown, it is convenient to combine it with the diffusion coefficient to produce a single constant, $m_O = D_O/\delta_O$, and to write equation 1.4.4 as

$$v_{mt} = m_O[C_O^* - C_O(x = 0)] \tag{1.4.5}$$

The proportionality constant, m_O, called the *mass-transfer coefficient*, has units of cm/s (which are those of a rate constant of a first-order heterogeneous reaction; see Chapter 3). These units follow from those of v and C_O, but can also be thought of as volume flow/s per unit area (cm^3 s^{-1} cm^{-2}).[11] Thus, from equations 1.4.1 and 1.4.5 and taking a reduction current as positive [i.e., i is positive when $C_O^* > C_O(x = 0)$], we obtain

$$\boxed{\frac{i}{nFA} = m_O[C_O^* - C_O(x = 0)]} \tag{1.4.6}$$

Under the conditions of a net cathodic reaction, R is produced at the electrode surface, so that $C_R(x = 0) > C_R^*$ (where C_R^* is the bulk concentration of R). Therefore,

$$\boxed{\frac{i}{nFA} = m_R[C_R(x = 0) - C_R^*]} \tag{1.4.7}$$

[11]While m_O is treated here as a phenomenological parameter, in more exact treatments the value of m_O can sometimes be specified in terms of measurable quantities. For example, for the rotating disk electrode, $m_O = 0.62 D_O^{2/3} \omega^{1/2} \nu^{-1/6}$, where ω is the angular velocity of the disk (i.e., $2\pi f$, with f as the frequency in revolutions per second) and ν is the kinematic viscosity (i.e., viscosity/density, with units of cm^2/s) (see Section 9.3.2). Steady-state currents can also be obtained with a very small electrode (such as a Pt disk with a radius, r_0, in the μm range), called an ultramicroelectrode (UME, Section 5.3). At a disk UME, $m_O = 4D_O/\pi r_0$.

or for the particular case when $C_R^* = 0$ (no R in the bulk solution),

$$\frac{i}{nFA} = m_R C_R(x = 0)$$

(1.4.8)

The values of $C_O(x = 0)$ and $C_R(x = 0)$ are functions of electrode potential, E. The largest rate of mass transfer of O occurs when $C_O(x = 0) = 0$ (or more precisely, when $C_O(x = 0) << C_O^*$, so that $C_O^* - C_O(x = 0) \approx C_O^*$). The value of the current under these conditions is called the *limiting current*, i_l, where

$$i_l = nFAm_O C_O^*$$

(1.4.9)

When the limiting current flows, the electrode process is occurring at the maximum rate possible for a given set of mass-transfer conditions, because O is being reduced as fast as it can be brought to the electrode surface. Equations 1.4.6 and 1.4.9 can be used to obtain expressions for $C_O(x = 0)$:

$$\frac{C_O(x = 0)}{C_O^*} = 1 - \frac{i}{i_l}$$

(1.4.10)

$$C_O(x = 0) = \frac{i_l - i}{nFAm_O}$$

(1.4.11)

Thus, the concentration of species O at the electrode surface is linearly related to the current and varies from C_O^*, when $i = 0$, to a negligible value, when $i = i_l$.

If the kinetics of electron transfer are rapid, the concentrations of O and R at the electrode surface can be assumed to be at equilibrium with the electrode potential, as governed by the Nernst equation for the half-reaction[12]

$$E = E^{0'} + \frac{RT}{nF} \ln \frac{C_O(x = 0)}{C_R(x = 0)}$$

(1.4.12)

Such a process is called a *nernstian reaction*. We can derive the steady-state i-E curves for nernstian reactions under several different conditions.

(a) R Initially Absent

When $C_R^* = 0$, $C_R(x = 0)$ can be obtained from (1.4.8):

$$C_R(x = 0) = i/nFAm_R$$

(1.4.13)

Then, combining equations 1.4.11 to 1.4.13, we obtain

$$E = E^{0'} - \frac{RT}{nF} \ln \frac{m_O}{m_R} + \frac{RT}{nF} \ln \left(\frac{i_l - i}{i}\right)$$

(1.4.14)

An i-E plot is shown in Figure 1.4.2a. Note that when $i = i_l/2$,

$$E = E_{1/2} = E^{0'} - \frac{RT}{nF} \ln \frac{m_O}{m_R}$$

(1.4.15)

[12]Equation 1.4.12 is written in terms of $E^{0'}$, called the *formal potential*, rather than the standard potential E^0. The formal potential is an adjusted form of the standard potential, manifesting activity coefficients and some chemical effects of the medium. In Section 2.1.6, it will be introduced in more detail. For the present it is not necessary to distinguish between $E^{0'}$ and E^0.
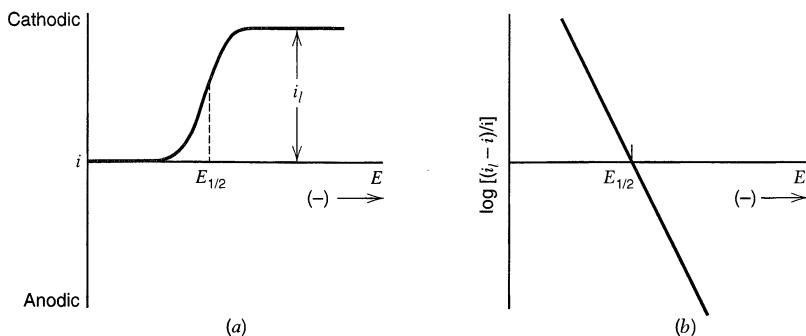
Figure 1.4.2 (*a*) Current-potential curve for a nernstian reaction involving two soluble species with only oxidant present initially. (*b*) $\log[(i_l - i)/i]$ *vs.* E for this system.

where $E_{1/2}$ is independent of the substrate concentration and is therefore characteristic of the O/R system. Thus,

$$E = E_{1/2} + \frac{RT}{nF} \ln\left(\frac{i_l - i}{i}\right) \tag{1.4.16}$$

When a system conforms to this equation, a plot of E *vs.* $\log[(i_l - i)/i]$ is a straight line with a slope of $2.3RT/nF$ (or $59.1/n$ mV at 25°C). Alternatively (Figure 1.4.2*b*), $\log[(i_l - i)/i]$ *vs.* E is linear with a slope of $nF/2.3RT$ (or $n/59.1$ mV^{-1} at 25°C) and has an E-intercept of $E_{1/2}$. When m_O and m_R have similar values, $E_{1/2} \approx E^{0'}$.

(b) Both O and R Initially Present

When both members of the redox couple exist in the bulk, we must distinguish between a *cathodic* limiting current, $i_{l,c}$, when $C_O(x = 0) \approx 0$, and an *anodic* limiting current, $i_{l,a}$, when $C_R(x = 0) \approx 0$. We still have $C_O(x = 0)$ given by (1.4.11), but with i_l now specified as $i_{l,c}$. The limiting anodic current naturally reflects the maximum rate at which R can be brought to the electrode surface for conversion to O. It is obtained from (1.4.7):

$$i_{l,a} = -nFAm_R C_R^* \tag{1.4.17}$$

(The negative sign arises because of our convention that cathodic currents are taken as positive and anodic ones as negative.) Thus $C_R(x = 0)$ is given by

$$C_R(x = 0) = \frac{i - i_{l,a}}{nFAm_R} \tag{1.4.18}$$

$$\frac{C_R(x = 0)}{C_R^*} = 1 - \frac{i}{i_{l,a}} \tag{1.4.19}$$

The *i-E* curve is then

$$E = E^{0'} - \frac{RT}{nF} \ln \frac{m_O}{m_R} + \frac{RT}{nF} \ln\left(\frac{i_{l,c} - i}{i - i_{l,a}}\right) \tag{1.4.20}$$

A plot of this equation is shown in Figure 1.4.3. When $i = 0$, $E = E_{eq}$ and the system is at equilibrium. Surface concentrations are then equal to the bulk values. When current flows,
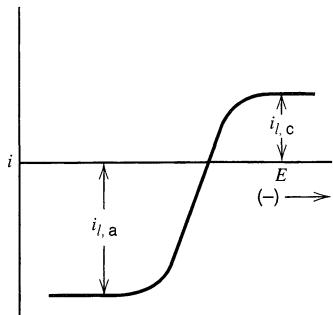
Figure 1.4.3 Current-potential curve for a nernstian system involving two soluble species with both forms initially present.

the potential deviates from E_{eq}, and the extent of this deviation is the concentration over-potential. (An equilibrium potential cannot be defined when $C_R^* = 0$, of course.)

(c) R Insoluble

Suppose species R is a metal and can be considered to be at essentially unit activity as the electrode reaction takes place on bulk R.[13] When $a_R = 1$, the Nernst equation is

$$E = E^{0'} + \frac{RT}{nF} \ln C_O(x = 0) \tag{1.4.21}$$

or, using the value of $C_O(x = 0)$ from equation 1.4.11,

$$E = E^{0'} + \frac{RT}{nF} \ln C_O^* + \frac{RT}{nF} \ln \left(\frac{i_l - i}{i_l} \right) \tag{1.4.22}$$

When $i = 0$, $E = E_{eq} = E^{0'} + (RT/nF) \ln C_O^*$ (Figure 1.4.4). If we define the *concentration overpotential*, η_{conc} (or the *mass-transfer overpotential*, η_{mt}), as

$$\eta_{conc} = E - E_{eq} \tag{1.4.23}$$

then

$$\eta_{conc} = \frac{RT}{nF} \ln \left(\frac{i_l - i}{i_l} \right) \tag{1.4.24}$$

When $i = i_l$, $\eta_{conc} \to \infty$. Since η is a measure of polarization, this condition is sometimes called *complete concentration polarization*.
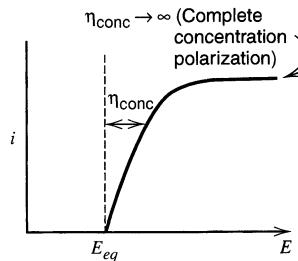
Figure 1.4.4 Current-potential curve for a nernstian system where the reduced form is insoluble.

---

[13]This will not be the case for R plated onto an inert substrate in amounts less than a monolayer (e.g., the substrate electrode being Pt and R being Cu). Under those conditions, a_R may be considerably less than unity (see Section 11.2.1).

Equation 1.4.24 can be written in exponential form:

$$1 - \frac{i}{i_l} = \exp\left(\frac{nF\eta_{\text{conc}}}{RT}\right) \tag{1.4.25}$$

The exponential can be expanded as a power series, and the higher-order terms can be dropped if the argument is kept small; that is,

$$e^x = 1 + x + \frac{x^2}{2} + \cdots \simeq 1 + x \text{ (when } x \text{ is small)} \tag{1.4.26}$$

Thus, under conditions of small deviations of potential from E_{eq}, the i-η_{conc} characteristic is linear:

$$\eta_{\text{conc}} = \frac{-RTi}{nFi_l} \tag{1.4.27}$$

Since $-\eta/i$ has dimensions of resistance (ohms), we can define a "small signal" mass-transfer resistance, R_{mt}, as

$$\boxed{R_{\text{mt}} = \frac{RT}{nF|i_l|}} \tag{1.4.28}$$

Here we see that the mass-transfer-limited electrode reaction resembles an actual resistance element only at small overpotentials.

1.4.3 Semiempirical Treatment of the Transient Response

The treatment in Section 1.4.2 can also be employed in an approximate way to time-dependent (transient) phenomena, for example, the buildup of the diffusion layer, either in a stirred solution (before steady state is attained) or in an unstirred solution where the diffusion layer continues to grow with time. Equation 1.4.4 still applies, but in this case we consider the diffusion layer thickness to be a time-dependent quantity, so that

$$i/nFA = v_{\text{mt}} = D_O[\,C_O^* - C_O(x = 0)]/\delta_O(t) \tag{1.4.29}$$

Consider what happens when a potential step of magnitude E is applied to an electrode immersed in a solution containing a species O. If the reaction is nernstian, the concentrations of O and R at $x = 0$ instantaneously adjust to the values governed by the Nernst equation, (1.4.12). The thickness of the approximately linear diffusion layer, $\delta_O(t)$, grows with time (Figure 1.4.5). At any time, the volume of the diffusion layer is
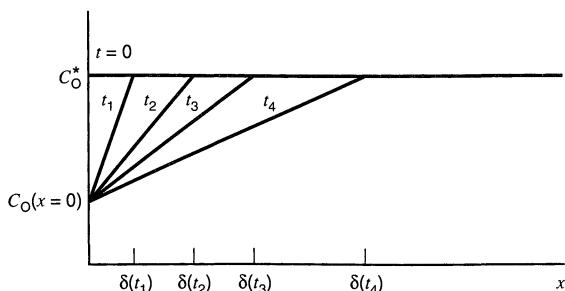
Figure 1.4.5 Growth of the diffusion-layer thickness with time.
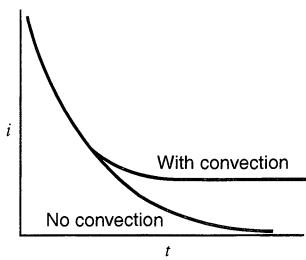
Figure 1.4.6 Current-time transient for a potential step to a stationary electrode (no convection) and to an electrode in stirred solution (with convection) where a steady-state current is attained.

$A\delta_O(t)$. The current flow causes a depletion of O, where the amount of O electrolyzed is given by

$$\text{Moles of O electrolyzed in diffusion layer} \cong [C_O^* - C_O(x = 0)] \frac{A\delta(t)}{2} = \int_0^t \frac{i\,dt}{nF} \qquad (1.4.30)$$

By differentiation of (1.4.30) and use of (1.4.29),

$$\frac{[C_O^* - C_O(x = 0)]}{2} \frac{A\,d\delta(t)}{dt} = \frac{i}{nF} = \frac{D_O A}{\delta(t)} [C_O^* - C_O(x = 0)] \qquad (1.4.31)$$

or

$$\frac{d\delta(t)}{dt} = \frac{2D_O}{\delta(t)} \qquad (1.4.32)$$

Since $\delta(t) = 0$ at $t = 0$, the solution of (1.4.32) is

$$\delta(t) = 2\sqrt{D_O t} \qquad (1.4.33)$$

and

$$\frac{i}{nFA} = \frac{D_O^{1/2}}{2t^{1/2}} [C_O^* - C_O(x = 0)] \qquad (1.4.34)$$

This approximate treatment predicts a diffusion layer that grows with $t^{1/2}$ and a current that decays with $t^{-1/2}$. In the absence of convection, the current continues to decay, but in a convective system, it ultimately approaches the steady-state value characterized by $\delta(t) = \delta_O$ (Figure 1.4.6). Even this simplified approach approximates reality quite closely; equation 1.4.34 differs only by a factor of $2/\pi^{1/2}$ from the rigorous description of current arising from a nernstian system during a potential step (see Section 5.2.1).

▶ 1.5 SEMIEMPIRICAL TREATMENT OF NERNSTIAN REACTIONS WITH COUPLED CHEMICAL REACTIONS

The current-potential curves discussed so far can be used to measure concentrations, mass-transfer coefficients, and standard potentials. Under conditions where the electron-transfer rate at the interface is rate-determining, they can be employed to measure heterogeneous kinetic parameters as well (see Chapters 3 and 9). Often, however, one is interested in using electrochemical methods to find equilibrium constants and rate constants of homogeneous reactions that are coupled to the electron-transfer step. This section provides a brief introduction to these applications.

1.5.1 Coupled Reversible Reactions

If a homogeneous process, fast enough to be considered always in thermodynamic equilibrium (a reversible process), is coupled to a nernstian electron-transfer reaction, then one can use a simple extension of the steady-state treatment to derive the *i-E* curve. Consider, for example, a species O involved in an equilibrium that precedes the electron-transfer reaction[14]

$$A \rightleftarrows O + qY \tag{1.5.1}$$

$$O + ne \rightleftarrows R \tag{1.5.2}$$

For example, A could be a metal complex, MY_q^{n+}; O could be the free metal ion, M^{n+}; and Y could be the free, neutral ligand (see Section 5.4.4). For reaction 1.5.2, the Nernst equation still applies at the electrode surface,

$$E = E^{0'} + \frac{RT}{nF} \ln \frac{C_O(x = 0)}{C_R(x = 0)} \tag{1.5.3}$$

and (1.5.1) is assumed to be at equilibrium everywhere:

$$\frac{C_O C_Y^q}{C_A} = K \text{ (all } x) \tag{1.5.4}$$

Hence

$$E = E^{0'} + \frac{RT}{nF} \ln \left[\frac{K C_A(x = 0)}{C_Y^q(x = 0) C_R(x = 0)} \right] \tag{1.5.5}$$

Assuming (1) that at $t = 0$, $C_A = C_A^*$, $C_Y = C_Y^*$, and $C_R = 0$ (for all x); (2) that C_Y^* is so large compared to C_A^* that $C_Y(x = 0) = C_Y^*$ at all times; and (3) that $K \ll 1$; then at steady state

$$\frac{i}{nFA} = m_A[C_A^* - C_A(x = 0)] \tag{1.5.6}$$

$$\frac{i_l}{nFA} = m_A C_A^* \tag{1.5.7}$$

$$\frac{i}{nFA} = m_R C_R(x = 0) \tag{1.5.8}$$

Then, as previously,

$$C_A(x = 0) = \frac{(i_l - i)}{nFAm_A} \qquad C_R(x = 0) = \frac{i}{nFAm_R} \tag{1.5.9}$$

$$\boxed{E = E^{0'} + \frac{RT}{nF} \ln K + \frac{RT}{nF} \ln \frac{m_R}{m_A} - \frac{RT}{nF} q \ln C_Y^* + \frac{RT}{nF} \ln \left(\frac{i_l - i}{i} \right)} \tag{1.5.10}$$

$$E = E_{1/2} + (0.059/n) \log \frac{i_l - i}{i} \qquad (T = 25°) \tag{1.5.11}$$

where

$$E_{1/2} = E^{0'} + \frac{0.059}{n} \log \frac{m_R}{m_A} + \frac{0.059}{n} \log K - \frac{0.059}{n} q \log C_Y^* \tag{1.5.12}$$

---

[14]To simplify notation, charges on all species are omitted.
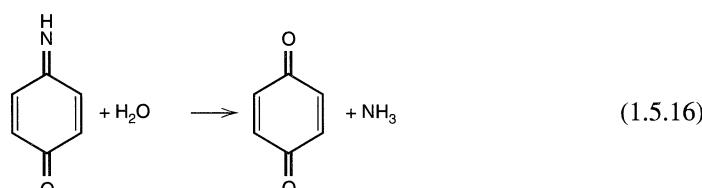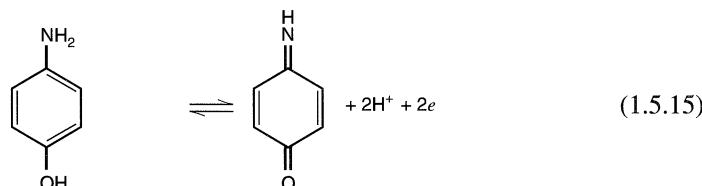
Thus, the *i-E* curve, (1.5.11), has the usual nernstian shape, but $E_{1/2}$ is shifted in a negative direction (since $K \ll 1$) from the position that would be found for process 1.5.2 unperturbed by the homogeneous equilibrium. From the shift of $E_{1/2}$ with log C_Y, both q [$= -(n/0.059)(dE_{1/2}/d \log C_Y^*)$] and K can be determined. Although these thermodynamic and stoichiometric quantities are available, no kinetic or mechanistic information can be obtained when both reactions are reversible.

1.5.2 Coupled Irreversible Chemical Reactions

When an irreversible chemical reaction is coupled to a nernstian electron transfer, the *i-E* curves can be used to provide kinetic information about the reaction in solution. Consider a nernstian charge-transfer reaction with a following first-order reaction:

$$O + ne \rightleftharpoons R \tag{1.5.13}$$

$$R \overset{k}{\rightarrow} T \tag{1.5.14}$$

where k is the rate constant (in s^{-1}) for the decomposition of R. (Note that k could be a pseudo-first-order constant, such as when R reacts with protons in a buffered solution and $k = k'C_{H^+}$.) As an example of this sequence, consider the oxidation of *p*-aminophenol in acid solution.

$$+ 2H^+ + 2e \tag{1.5.15}$$

$$+ H_2O \longrightarrow + NH_3 \tag{1.5.16}$$

Reaction 1.5.16 does not affect the mass transfer and reduction of O, so (1.4.6) and (1.4.9) still apply (assuming $C_O = C_O^*$ and $C_R = 0$ at all x at $t = 0$). However, the reaction causes R to disappear from the electrode surface at a higher rate, and this difference affects the *i-E* curve.

In the absence of the following reaction, we think of the concentration profile for R as decreasing linearly from a value $C_R(x = 0)$ at the surface to the point where $C_R = 0$ at δ, the outer boundary of the Nernst diffusion layer. The coupled reaction adds a channel for disappearance of R, so the R profile in the presence of the reaction does not extend as far into the solution as δ. Thus, the added reaction steepens the profile and augments mass transfer away from the electrode surface. For steady-state behavior, such as at a rotating disk, we assume the rate at which R disappears from the surface to be the rate of diffusion in the absence of the reaction [$(m_R C_R(x = 0)$; see (1.4.8)] plus an increment proportional to the rate of reaction [$\mu k C_R(x = 0)$]. Since the rate of formation of R, given by (1.4.6), equals its total rate of disappearance, we have

$$\frac{i}{nFA} = m_O[C_O^* - C_O(x = 0)] = m_R C_R(x = 0) + \mu k C_R(x = 0) \tag{1.5.17}$$

where μ is a proportionality constant having units of cm, so that the product μk has dimensions of cm/s as required. In the literature (3), μ is called the *reaction layer thickness*. For our purpose, it is best just to think of μ as an adjustable parameter. From (1.5.17),

$$C_O(x = 0) = \frac{i_l - i}{nFAm_O} \tag{1.5.18}$$

$$C_R(x = 0) = \frac{i}{nFA(m_R + \mu k)} \tag{1.5.19}$$

Substituting these values into the Nernst equation for (1.5.13) yields

$$E = E^{0'} + \frac{RT}{nF} \ln \frac{m_R + \mu k}{m_O} + \frac{RT}{nF} \ln \left(\frac{i_l - i}{i} \right) \tag{1.5.20}$$

or

$$E = E'_{1/2} + \frac{0.059}{n} \log \left(\frac{i_l - i}{i} \right) \qquad \text{(at 25° C)} \tag{1.5.21}$$

where

$$E'_{1/2} = E^{0'} + \frac{0.059}{n} \log \left(\frac{m_R + \mu k}{m_O} \right) \tag{1.5.22}$$

or

$$E'_{1/2} = E_{1/2} + \frac{0.059}{n} \log \left(1 + \frac{\mu k}{m_R} \right) \tag{1.5.23}$$

where $E_{1/2}$ is the half-wave potential for the kinetically unperturbed reaction.

Two limiting cases can be defined: (a) When $\mu k/m_R \ll 1$, that is $\mu k \ll m_R$, the effect of the following reaction, (1.5.14), is negligible, and the unperturbed *i-E* curve results. (b) When $\mu k/m_R \gg 1$, the following reaction dominates the behavior and

$$E'_{1/2} = E_{1/2} + \frac{0.059}{n} \log \frac{\mu k}{m_R} \tag{1.5.24}$$

The effect is to shift the reduction wave in a *positive* direction without a change in shape. For the rotating disk electrode, where $m_R = 0.62 D_R^{2/3} \omega^{1/2} \nu^{-1/6}$, (1.5.24) becomes [assuming $\mu \neq f(\omega)$]

$$E'_{1/2} = E_{1/2} + \frac{0.059}{n} \log \frac{\mu k}{0.62 D_R^{2/3} \nu^{-1/6}} - \frac{0.059}{2n} \log \omega \tag{1.5.25}$$

An increase of rotation rate, ω, will cause the wave to shift in a *negative* direction (toward the unperturbed wave; see Figure 1.5.1). A tenfold change in ω causes a shift of $0.03/n$ V.

A similar treatment can be given for other chemical reactions coupled to the charge-transfer reaction (4). This approach is often useful in formulating a qualitative or semi-quantitative interpretation of *i-E* curves. Notice, however, that unless explicit expressions for m_R and μ can be given in a particular case, the exact values of k cannot be determined. The rigorous treatment of electrode reactions with coupled homogeneous chemical reactions is discussed in Chapter 12.
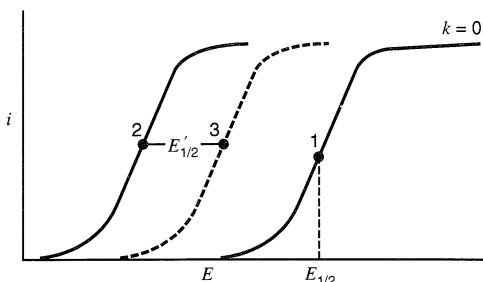
Figure 1.5.1 Effect of an irreversible following homogeneous chemical reaction on nernstian i-E curves at a rotating disk electrode. (*1*) Unperturbed curve. (*2*) and (*3*) Curves with following reaction at two rotation rates, where the rotation rate for (*3*) is greater than for (*2*).

1.6 THE LITERATURE OF ELECTROCHEMISTRY

We now embark on more detailed and rigorous considerations of the fundamental principles of electrode reactions and the methods used to study them. At the outset, we list the general monographs and review series in which many of these topics are treated in much greater depth. This listing is not at all comprehensive, but does represent the recent English-language sources on general electrochemical subjects. References to the older literature can be found in these and in the first edition. Monographs and reviews on particular subjects are listed in the appropriate chapter. We also list the journals in which papers relating to electrochemical methods are published regularly.

1.6.1 Books and Monographs

(a) General Electrochemistry

Albery, W. J., "Electrode Kinetics," Clarendon, Oxford, 1975.

Bockris, J. O'M., and A. K. N. Reddy, "Modern Electrochemistry," Plenum, New York, 1970 (2 volumes); 2nd ed., (Vol. 1) 1998.

Christensen, P. A., and A. Hamnett, "Techniques and Mechanisms in Electrochemistry," Blackie Academic and Professional, New York, 1994.

Conway, B. E., "Theory and Principles of Electrode Processes," Ronald, New York, 1965.

Gileadi, E., "Electrode Kinetics for Chemists, Chemical Engineers, and Materials Scientists," VCH, New York, 1993.

Goodisman, J., "Electrochemistry: Theoretical Foundations, Quantum and Statistical Mechanics, Thermodynamics, the Solid State," Wiley, New York, 1987.

Hamann, C. H., A. Hamnett, and W. Vielstich, "Electrochemistry," Wiley-VCH, Weinheim, Germany, 1997.

Koryta, J., J., Dvořák, and L. Kavan, "Principles of Electrochemistry," 2nd ed, Wiley, New York, 1993.

MacInnes, D. A., "The Principles of Electrochemistry," Dover, New York, 1961 (Corrected version of 1947 edition).

Newman, J. S., "Electrochemical Systems," 2nd ed., Prentice-Hall, Englewood Cliffs, NJ, 1991.

Oldham, K. B., and J. C. Myland, "Fundamentals of Electrochemical Science," Academic, New York, 1994.

Rieger, P. H., "Electrochemistry," 2nd ed., Chapman and Hall, New York, 1994.

Rubinstein, I., Ed., "Physical Electrochemistry: Principles, Methods, and Applications," Marcel Dekker, New York, 1995.

Schmickler, W., "Interfacial Electrochemistry," Oxford University Press, New York, 1996.

(b) Electrochemical Methodology

Adams, R. N., "Electrochemistry at Solid Electrodes," Marcel Dekker, New York, 1969.

Delahay, P., "New Instrumental Methods in Electrochemistry," Interscience, New York, 1954.

Galus, Z., "Fundamentals of Electrochemical Analysis," 2nd ed, Wiley, New York, 1994.

Gileadi, E., E. Kirowa-Eisner, and J. Penciner, "Interfacial Electrochemistry—An Experimental Approach," Addison-Wesley, Reading, MA, 1975.

Kissinger, P. T., and W. R. Heineman, Eds., "Laboratory Techniques in Electroanalytical Chemistry," 2nd ed., Marcel Dekker, New York, 1996.

Lingane, J. J., "Electroanalytical Chemistry," 2nd ed., Interscience, New York, 1958.

Macdonald, D. D., "Transient Techniques in Electrochemistry," Plenum, New York, 1977.

Sawyer, D. T., A. Sobkowiak, and J. L. Roberts, Jr., "Electrochemistry for Chemists," 2nd ed., Wiley, New York, 1995.

Southampton Electrochemistry Group, "Instrumental Methods in Electrochemistry," Ellis Horwood, Chichester, UK, 1985.

Vanýsek, P., Ed., "Modern Techniques in Electroanalysis," Wiley, New York, 1996.

(c) Descriptive Electrochemistry

Bard, A. J., and H. Lund, Eds., "Encyclopedia of the Electrochemistry of the Elements," Marcel Dekker, New York, 1973–1986, (16 volumes).

Lund, H., and M. M. Baizer, "Organic Electrochemistry: an Introduction and Guide," 3rd ed., Marcel Dekker, New York, 1991.

Mann, C. K., and K. K. Barnes, "Electrochemical Reactions in Nonaqueous Systems," Marcel Dekker, New York, 1970.

(d) Compilations of Electrochemical Data

Bard, A. J., R. Parsons, and J. Jordan, Eds., "Standard Potentials in Aqueous Solutions," Marcel Dekker, New York, 1985.

Conway, B. E., "Electrochemical Data," Elsevier, Amsterdam, 1952.

Horvath, A. L., "Handbook of Aqueous Electrolyte Solutions: Physical Properties, Estimation, and Correlation Methods," Ellis Horwood, Chichester, UK, 1985.

Janz, G. J., and R. P. T. Tomkins, "Nonaqueous Electrolytes Handbook," Academic, New York, 1972 (2 volumes).

Meites, L., and P. Zuman, "Electrochemical Data," Wiley, New York, 1974.

Meites, L., and P. Zuman et al., "CRC Handbook Series in Organic Electrochemistry," (6 volumes) CRC, Boca Raton, FL, 1977–1983.

Meites, L., and P. Zuman et al., "CRC Handbook Series in Inorganic Electrochemistry," (8 volumes), CRC, Boca Raton, FL, 1980–1988.

Parsons, R., "Handbook of Electrochemical Data," Butterworths, London, 1959.

Zemaitis, J. F., D. M. Clark, M. Rafal, and N. C. Scrivner, "Handbook of Aqueous Electrolyte Thermodynamics: Theory and Applications," Design Institute for Physical Property Data (for the American Institute of Chemical Engineers), New York, 1986.

1.6.2   Review Series

A number of review series dealing with electrochemistry and related areas exist. Volumes are published every year or few years and contain chapters written by authorities in particular subject areas.[15]

Bard, A. J., Ed., (from Vol. 19 with I. Rubinstein), "Electroanalytical Chemistry," Marcel Dekker, New York, 1966–1998, (20 volumes).

Bockris, J. O'M., and B. E. Conway, et al., Eds., "Modern Aspects of Electrochemistry," Plenum, New York, 1954–1997, (31 volumes).

Delahay, P., and C. W. Tobias (from Vol. 10, H. Gerischer and C. W. Tobias), Eds., "Advances in Electrochemistry and Electrochemical Engineering," Wiley, New York, 1961–1984, (13 volumes).

Gerischer, H., C.W. Tobias, et al., Eds., "Advances in Electrochemical Science and Engineering," Wiley-VCH, Weinheim, Germany, 1990–1997, (5 volumes).

Specialist Periodical Reports, "Electrochemistry," G. J. Hills (Vols. 1–3), H. R. Thirsk (Vols. 4–7), and D. Pletcher (Vols. 8–10) Senior Reporters, The Chemical Society, London, 1971–1985, (10 volumes).

Steckhan, E., Ed., "Electrochemistry (Topics in Current Chemistry)," Springer, New York, 1987–1997, (6 volumes).

Yeager, E., J. O'M. Bockris, B. E. Conway, et al., Eds., "Comprehensive Treatise of Electrochemistry," Plenum, New York, 1984, (10 volumes).

Yeager, E., and A. J. Salkind, Eds., "Techniques of Electrochemistry," Wiley-Interscience, New York, 1972–1978, (3 volumes).

Reviews on electrochemical topics also appear from time to time in the following:

Accounts of Chemical Research, The American Chemical Society, Washington.

Analytical Chemistry (Annual Reviews), The American Chemical Society, Washington.

Annual Reviews of Physical Chemistry, Annual Reviews, Inc., Palo Alto, CA, from 1950.

Chemical Reviews, The American Chemical Society, Washington.

1.6.3   Journals

The following journals are primarily devoted to electrochemistry:

Electroanalysis (1989–).

Electrochimica Acta (1959–).

Electrochemical and Solid State Letters (1998–)

Electrochemistry Communications (1999–)

Journal of Applied Electrochemistry (1971–).

Journal of Electroanalytical Chemistry (1959–).

Journal of the Electrochemical Society (1902–).

Journal of Solid State Electrochemistry (1997–).

[15]Articles in the first three series listed below are cited in this book, and often elsewhere in the literature, in journal reference format with the abbreviations *Electroanal. Chem., Mod. Asp. Electrochem., and Adv. Electrochem. Electrochem. Engr.*, repectively. Note that the first should not be confused with *J. Electroanal Chem.*

1.6.4 World Wide Web

A number of web pages contain bibliographies of books and chapters on electrochemical topics, simulation programs, information about societies, and meetings in the area of electrochemistry. Links to these pages, and other information of interest to readers of this book will be maintained at *http://www.wiley.com/college/bard.*

▷ 1.7 REFERENCES
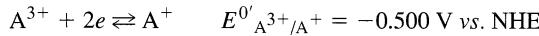
1. L. R. Faulkner, *J. Chem. Educ.*, **60**, 262 (1983).

2. L. R. Faulkner in "Physical Methods in Modern Chemical Analysis," Vol. 3, T. Kuwana, Ed., Academic, New York, 1983, pp. 137–248.

3. P. Delahay, "New Instrumental Methods in Electrochemistry," Wiley-Interscience, New York, 1954, p. 92 ff.

4. See, for example, G. J. Hoytink, J. Van Schooten, E. de Boer, and W. Aalbersberg, *Rec. Trav. Chim.*, **73**, 355 (1954), for an application of this type of method to the study of reactions coupled to the reduction of aromatic hydrocarbons.

▷ 1.8 PROBLEMS

1.1 Consider each of the following electrode–solution interfaces, and write the equation for the electrode reaction that occurs first when the potential is moved in (1) a negative direction and (2) a positive direction from the open-circuit potential. Next to each reaction write the approximate potential for the reaction in V *vs.* SCE (assuming the reaction is reversible).

    (a) $Pt/Cu^{2+}(0.01\ M)$, $Cd^{2+}(0.01\ M)$, $H_2SO_4(1\ M)$

    (b) $Pt/Sn^{2+}(0.01\ M)$, $Sn^{4+}(0.01\ M)$, $HCl(1\ M)$

    (c) $Hg/Cd^{2+}(0.01\ M)$, $Zn^{2+}(0.01\ M)$, $HCl(1\ M)$

1.2 For a rotating disk electrode, the treatment of steady-state, mass-transfer-controlled electrode reactions applies, where the mass-transfer coefficient is $m_O = 0.62 D_O^{2/3}\ \omega^{1/2}\ \nu^{-1/6}$. Here, D_O is the diffusion coefficient (cm^2/s), ω is the angular velocity of the disk (s^{-1}) ($\omega = 2\pi f$, where f is the frequency of rotation in revolutions per second), and ν is the kinematic viscosity ($\nu = \eta/d$, $\eta = $ viscosity, and $d = $ density; for aqueous solutions $\nu \sim 0.010\ cm^2/s$). A rotating disk electrode of area $0.30\ cm^2$ is used for the reduction of $0.010\ M\ Fe^{3+}$ to Fe^{2+} in $1\ M\ H_2SO_4$. Given D_O for Fe^{3+} at $5.2 \times 10^{-6}\ cm^2/s$, calculate the limiting current for the reduction for a disk rotation rate of 10 r/s. Include units on variables during calculation and give units of current in the answer.

1.3 A solution of volume $50\ cm^3$ contains $2.0 \times 10^{-3}\ M\ Fe^{3+}$ and $1.0 \times 10^{-3}\ M\ Sn^{4+}$ in $1\ M\ HCl$. This solution is examined by voltammetry at a rotating platinum disk electrode of area $0.30\ cm^2$. At the rotation rate employed, both Fe^{3+} and Sn^{4+} have mass-transfer coefficients, m, of 10^{-2} cm/s. (a) Calculate the limiting current for the reduction of Fe^{3+} under these conditions. (b) A current-potential scan is taken from +1.3 to −0.40 V *vs.* NHE. Make a labeled, quantitatively correct, sketch of the *i-E* curve that would be obtained. Assume that no changes in the bulk concentrations of Fe^{3+} and Sn^{4+} occur during this scan and that all electrode reactions are nernstian.

1.4 The conductivity of a $0.1\ M$ KCl solution is $0.013\ \Omega^{-1}cm^{-1}$ at 25°C. (a) Calculate the solution resistance between two parallel planar platinum electrodes of $0.1\ cm^2$ area placed 3 cm apart in this solution. (b) A reference electrode with a Luggin capillary is placed the following distances from a planar platinum working electrode ($A = 0.1\ cm^2$) in $0.1\ M$ KCl: 0.05, 0.1, 0.5, 1.0 cm. What is R_u in each case? (c) Repeat the calculations in part (b) for a spherical working electrode of the same area. [In parts (b) and (c) it is assumed that a large counter electrode is employed.]

1.5 A $0.1\ cm^2$ electrode with $C_d = 20\ \mu F/cm^2$ is subjected to a potential step under conditions where R_s is 1, 10, or 100 Ω. In each case, what is the time constant, and what is the time required for the double-layer charging to be 95% complete?
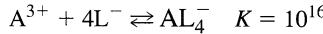
1.6 For the electrode in Problem 1.5, what nonfaradaic current will flow (neglecting any transients) when the electrode is subjected to linear sweeps at 0.02, 1, 20 V/s?

1.7 Consider the nernstian half-reaction:

$$A^{3+} + 2e \rightleftarrows A^+ \qquad E^{0'}{}_{A^{3+}/A^+} = -0.500 \text{ V } vs. \text{ NHE}$$

The i-E curve for a solution at 25°C containing 2.00 mM A^{3+} and 1.00 mM A^+ in excess electrolyte shows $i_{l,c} = 4.00 \ \mu A$ and $i_{l,a} = -2.40 \ \mu A$. (a) What is $E_{1/2}$ (V $vs.$ NHE)? (b) Sketch the expected i-E curve for this system. (c) Sketch the "log plot" (see Figure 1.4.2b) for the system.

1.8 Consider the system in Problem 1.7 under the conditions that a complexing agent, L^-, which reacts with A^{3+} according to the reaction

$$A^{3+} + 4L^- \rightleftarrows AL_4^- \quad K = 10^{16}$$

is added to the system. For a solution at 25°C containing only 2.0 mM A^{3+} and 0.1 M L^- in excess inert electrolyte, answer parts (a), (b), and (c) in Problem 1.7. (Assume m_O is the same for A^{3+} and AL_4^-.)

1.9 Derive the current-potential relationship under the conditions of Section 1.4.2 for a system where R is initially present at a concentration C_R^* and $C_O^* = 0$. Consider both O and R soluble. Sketch the expected i-E curve.

1.10 Suppose a mercury pool of 1 cm^2 area is immersed in a 0.1 M sodium perchlorate solution. How much charge (order of magnitude) would be required to change its potential by 1 mV? How would this be affected by a change in the electrolyte concentration to 10^{-2} M? Why?

1.11 Rearrangement of equation 1.4.16 yields the following expression for i as a function of E, which is convenient for calculating $i-E$ curves for nernstian reactions:

$$i/i_l = \{1 + \exp[(nF/RT)(E - E_{1/2})]\}^{-1}$$

(a) Derive this expression. (b) Consider the half-reaction $Ru(NH_3)_6^{3+} + e \rightleftarrows Ru(NH_3)_6^{2+}$. The E^0 for this reaction is given in Appendix C. A steady-state i-E curve is obtained with a solution containing 10 mM $Ru(NH_3)_6^{3+}$ and 1 M KCl (as supporting electrolyte). The working electrode is a Pt disk of area 0.10 cm^2 operating under conditions where $m = 10^{-3}$ cm/s for both Ru species. Use a spreadsheet program to calculate and plot the expected i-E curve.

1.12 (a) Derive an expression for i as a function of E, analogous to that in Problem 1.11, from equation 1.4.20, using (1.4.15) as the definition of $E_{1/2}$, for use in solutions that contain both components of a redox couple. (b) Consider the same system as in Problem 1.11, but for a solution containing 10 mM $Ru(NH_3)_6^{3+}$ and 5.0 mM $Ru(NH_3)_6^{2+}$ in 1M KCl. Use a spreadsheet program to calculate the i-E curve and plot the results. (c) What is η_{conc} at a cathodic current density of 0.48 mA/cm^2? (d) Estimate R_{mt}.

2

POTENTIALS
AND THERMODYNAMICS
OF CELLS

In Chapter 1, we sought to obtain a working feeling for potential as an electrochemical variable. Here we will explore the physical meaning of that variable in more detail. Our goal is to understand how potential differences are established and what kinds of chemical information can be obtained from them. At first, these questions will be approached through thermodynamics. We will find that potential differences are related to free energy changes in an electrochemical system, and this discovery will open the way to the experimental determination of all sorts of chemical information through electrochemical measurements. Later in this chapter, we will explore the mechanisms by which potential differences are established. Those considerations will provide insights that will prove especially useful when we start to examine experiments involving the active control of potential in an electrochemical system.

▶ ## 2.1 BASIC ELECTROCHEMICAL THERMODYNAMICS

2.1.1 Reversibility
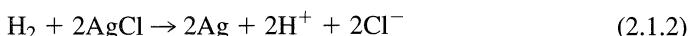
Since thermodynamics can strictly encompass only systems at equilibrium, the concept of *reversibility* is important in treating real processes thermodynamically. After all, the concept of equilibrium involves the idea that a process can move in either of two opposite directions from the equilibrium position. Thus, the adjective *reversible* is an essential one. Unfortunately, it takes on several different, but related, meanings in the electrochemical literature, and we need to distinguish three of them now.

(a) Chemical Reversibility
Consider the electrochemical cell shown in Figure 1.1.1b:

$$Pt/H_2/H^+, Cl^-/AgCl/Ag \qquad (2.1.1)$$

Experimentally, one finds that the difference in potential between the silver wire and the platinum wire is 0.222 V when all substances are in their standard states. Furthermore, the platinum wire is the negative electrode, and when the two electrodes are shorted together, the following reaction takes place:

$$H_2 + 2AgCl \rightarrow 2Ag + 2H^+ + 2Cl^- \qquad (2.1.2)$$

If one overcomes the cell voltage by opposing it with the output of a battery or other direct current (dc) source, the current flow through the cell will reverse, and the new cell reaction is

$$2Ag + 2H^+ + 2Cl^- \rightarrow H_2 + 2AgCl \qquad (2.1.3)$$

Reversing the cell current merely reverses the cell reaction. No new reactions appear, thus the cell is termed *chemically reversible*.

On the other hand, the system

$$Zn/H^+, SO_4^{2-}/Pt \qquad (2.1.4)$$
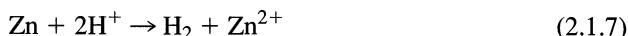
is not chemically reversible. The zinc electrode is negative with respect to platinum, and discharging the cell causes the reaction

$$Zn \rightarrow Zn^{2+} + 2e \qquad (2.1.5)$$
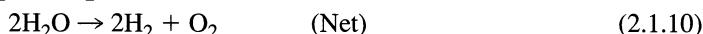
to occur there. At the platinum electrode, hydrogen evolves:

$$2H^+ + 2e \rightarrow H_2 \qquad (2.1.6)$$

Thus the net cell reaction is[1]

$$Zn + 2H^+ \rightarrow H_2 + Zn^{2+} \qquad (2.1.7)$$

By applying an opposing voltage larger than the cell voltage, the current flow reverses, but the reactions observed are

$$2H^+ + 2e \rightarrow H_2 \qquad \text{(Zn electrode)} \qquad (2.1.8)$$
$$2H_2O \rightarrow O_2 + 4H^+ + 4e \quad \text{(Pt electrode)} \qquad (2.1.9)$$
$$2H_2O \rightarrow 2H_2 + O_2 \qquad \text{(Net)} \qquad (2.1.10)$$

One has different electrode reactions as well as a different net process upon current reversal; hence this cell is said to be *chemically irreversible*.

One can similarly characterize half-reactions by their chemical reversibility. The reduction of nitrobenzene in oxygen-free, dry acetonitrile produces a stable radical anion in a chemically reversible, one-electron process:

$$PhNO_2 + e \rightleftarrows PhNO_2\overline{\cdot} \qquad (2.1.11)$$

The reduction of an aromatic halide, ArX, under similar conditions will often be chemically irreversible, since the radical anion product of the electron-transfer reaction rapidly decomposes:

$$ArX + e \rightarrow Ar\cdot + X^- \qquad (2.1.12)$$

Whether or not a half-reaction exhibits chemical reversibility depends upon solution conditions and the time scale of the experiment. For example, if the nitrobenzene reaction is carried out in an acidic acetonitrile solution, the reaction will become chemically irreversible, because $PhNO_2\overline{\cdot}$ reacts with protons under these conditions. Alternatively, if the reduction of ArX is studied by a technique that takes only a very short time, then the reaction can be chemically reversible in that time regime:

$$ArX + e \rightleftarrows ArX\overline{\cdot} \qquad (2.1.13)$$

---

[1]The net reaction will also occur without a flow of electrons in the external circuit, because H^+ in solution will attack the zinc. This "side reaction," which happens to be identical with the electrochemical process, is slow if dilute acid is involved.

(b) Thermodynamic Reversibility

A process is thermodynamically reversible when an infinitesimal reversal in a driving force causes it to reverse direction. Obviously this cannot happen unless the system feels only an infinitesimal driving force at any time; hence it must essentially be always at equilibrium. A reversible path between two states of the system is therefore one that connects a continuous series of equilibrium states. Traversing it would require an infinite length of time.

A cell that is chemically irreversible cannot behave reversibly in a thermodynamic sense. A chemically reversible cell may or may not operate in a manner approaching thermodynamic reversibility.

(c) Practical Reversibility

Since all actual processes occur at finite rates, they cannot proceed with strict thermodynamic reversibility. However, a process may in practice be carried out in such a manner that thermodynamic equations apply to a desired accuracy. Under these circumstances, one might term the process reversible. *Practical reversibility* is not an absolute term; it includes certain attitudes and expectations an observer has toward the process.

A useful analogy involves the removal of a large weight from a spring balance. Carrying out this process strictly reversibly requires continuous equilibrium; the "thermodynamic" equation that always applies is

$$kx = mg \tag{2.1.14}$$

where k is the force constant, x is the distance the spring is stretched when mass m is added, and g is the earth's gravitational acceleration. In the reversible process, the spring is never prone to contract more than an infinitesimal distance, because the large weight is removed progressively in infinitesimal portions.

Now if the same final state is reached by simply removing the weight all at once, equation 2.1.14 applies at no time during the process, which is characterized by severe disequilibrium and is grossly irreversible.

On the other hand, one could remove the weight as pieces, and if there were enough pieces, the thermodynamic relation, (2.1.14), would begin to apply a very large fraction of the time. In fact, one might not be able to distinguish the real (but slightly irreversible) process from the strictly reversible path. One could then legitimately label the real transformation as "practically reversible."

In electrochemistry, one frequently relies on the Nernst equation:

$$E = E^{0'} + \frac{RT}{nF} \ln \frac{C_O}{C_R} \tag{2.1.15}$$

to provide a linkage between electrode potential E and the concentrations of participants in the electrode process:

$$O + ne \rightleftarrows R \tag{2.1.16}$$

If a system follows the Nernst equation or an equation derived from it, the electrode reaction is often said to be thermodynamically or electrochemically reversible (or *nernstian*).
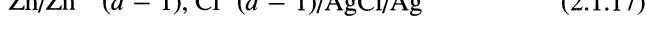
Whether a process appears reversible or not depends on one's ability to detect the signs of disequilibrium. In turn, that ability depends on the time domain of the possible measurements, the rate of change of the force driving the observed process, and the speed with which the system can reestablish equilibrium. If the perturbation applied to the system is small enough, or if the system can attain equilibrium rapidly enough compared to

the measuring time, thermodynamic relations will apply. A given system may behave reversibly in one experiment and irreversibly in another, even of the same genre, if the experimental conditions have a wide latitude. This theme will be met again and again throughout this book.

2.1.2 Reversibility and Gibbs Free Energy

Consider three different methods (1) of carrying out the reaction $Zn + 2AgCl \rightarrow Zn^{2+} + 2Ag + 2Cl^-$:

(a) Suppose zinc and silver chloride are mixed directly in a calorimeter at constant, atmospheric pressure and at 25°C. Assume also that the extent of reaction is so small that the activities of all species remain unchanged during the experiment. It is found that the amount of heat liberated when all substances are in their standard states is 233 kJ/mol of Zn reacted. Thus, $\Delta H^0 = -233$ kJ.[2]

(b) Suppose we now construct the cell of Figure 1.1.1*a*, that is,

$$Zn/Zn^{2+}(a = 1), Cl^-(a = 1)/AgCl/Ag \tag{2.1.17}$$

and discharge it through a resistance R. Again assume that the extent of reaction is small enough to keep the activities essentially unchanged. During the discharge, heat will evolve from the resistor and from the cell, and we could measure the total heat change by placing the entire apparatus inside a calorimeter. We would find that the heat evolved is 233 kJ/mol of Zn, independent of R. That is, $\Delta H^0 = -233$ kJ, regardless of the rate of cell discharge.

(c) Let us now repeat the experiment with the cell and the resistor in separate calorimeters. Assume that the wires connecting them have no resistance and do not conduct any heat between the calorimeters. If we take Q_C as the heat change in the cell and Q_R as that in the resistor, we find that $Q_C + Q_R = -233$ kJ/mol of Zn reacted, independent of R. However, the balance between these quantities does depend on the rate of discharge. As R increases, $|Q_C|$ decreases and $|Q_R|$ increases. In the limit of infinite R, Q_C approaches -43 kJ (per mole of zinc) and Q_R tends toward -190 kJ.

In this example, the energy Q_R was dissipated as heat, but it was obtained as electrical energy, and it might have been converted to light or mechanical work. In contrast, Q_C is an energy change that is inevitably thermal. Since discharge through $R \rightarrow \infty$ corresponds to a thermodynamically reversible process, the energy that must appear as heat in traversing a reversible path, Q_{rev}, is identified as $\lim_{R \to \infty} Q_C$. The entropy change, ΔS, is defined as Q_{rev}/T (2), therefore for our example, where all species are in their standard states,

$$T\Delta S^0 = \lim_{R \to \infty} Q_C = -43 \text{ kJ} \tag{2.1.18}$$

Because $\Delta G^0 = \Delta H^0 - T\Delta S^0$,

$$\Delta G^0 = -190 \text{ kJ} = \lim_{R \to \infty} Q_R \tag{2.1.19}$$

Note that we have now identified $-\Delta G$ with the maximum *net work* obtainable from the cell, where net work is defined as work other than PV work (2). For any finite R, $|Q_R|$

---

[2]We adopt the thermodynamic convention in which absorbed quantities are positive.

(and the net work) is *less* than the limiting value. Note also that the cell may absorb or evolve heat as it discharges. In the former case, $|\Delta G^0| > |\Delta H^0|$.

2.1.3 Free Energy and Cell emf
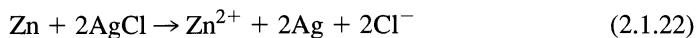
We found just above that if we discharged the electrochemical cell (2.1.17) through an infinite load resistance, the discharge would be reversible. The potential difference is therefore always the equilibrium (open-circuit) value. Since the extent of reaction is supposed to be small enough that all activities remain constant, the potential also remains constant. Then, the energy dissipated in R is given by

$$|\Delta G| = \text{charge passed} \times \text{reversible potential difference} \qquad (2.1.20)$$
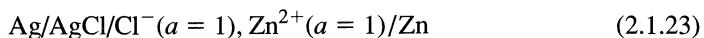
$$|\Delta G| = nF|E| \qquad (2.1.21)$$

where n is the number of electrons passed per atom of zinc reacted (or the number of moles of electrons per mole of Zn reacted), and F is the charge on a mole of electrons, which is about 96,500 C. However, we also recognize that the free energy change has a *sign* associated with the *direction* of the net cell reaction. We can reverse the sign by reversing the direction. On the other hand, only an infinitesimal change in the overall cell potential is required to reverse the direction of the reaction; hence E is essentially constant and independent of the direction of a (reversible) transformation. We have a quandary. We want to relate a direction-sensitive quantity (ΔG) to a direction-insensitive observable (E). This desire is the origin of almost all of the confusion that exists over electrochemical sign conventions. Moreover the actual meaning of the signs − and + is different for free energy and potential. For free energy, − and + signify energy lost or gained from the system, a convention that traces back to the early days of thermodynamics. For potential, − and + signify the excess or deficiency of electronic charge, an electrostatic convention proposed by Benjamin Franklin even before the discovery of the electron. In most scientific discussions, this difference in meaning is not important, since the context, thermodynamic *vs.* electrostatic, is clear. But when one considers electrochemical cells, where both thermodynamic and electrostatic concepts are needed, it is necessary to distinguish clearly between these two conventions.

When we are interested in thermodynamic aspects of electrochemical systems, we rationalize this difficulty by inventing a thermodynamic construct called the *emf of the cell reaction*. This quantity is assigned to the reaction (not to the physical cell); hence it has a directional aspect. In a formal way, we also associate a given chemical reaction with each cell schematic. For the one in (2.1.17), the reaction is

$$\text{Zn} + 2\text{AgCl} \rightarrow \text{Zn}^{2+} + 2\text{Ag} + 2\text{Cl}^- \qquad (2.1.22)$$

The right electrode corresponds to reduction in the implied cell reaction, and the left electrode is identified with oxidation. Thus, the reverse of (2.1.22) would be associated with the opposite schematic:

$$\text{Ag/AgCl/Cl}^-(a = 1), \text{Zn}^{2+}(a = 1)/\text{Zn} \qquad (2.1.23)$$

The cell reaction emf, E_{rxn}, is then defined as the electrostatic potential of the electrode written on the right in the cell schematic with respect to that on the left.

For example, in the cell of (2.1.17), the measured potential difference is 0.985 V and the zinc electrode is negative; thus the emf of reaction 2.1.22, the spontaneous direction, is +0.985 V. Likewise, the emf corresponding to (2.1.23) and the reverse of (2.1.22) is −0.985 V. By adopting this convention, we have managed to rationalize an (observable) *electrostatic* quantity (the cell potential difference), which is not sensitive to the direction

of the cell's operation, with a (defined) *thermodynamic* quantity (the Gibbs free energy), which is sensitive to that direction. One can avoid completely the common confusion about sign conventions of cell potentials if one understands this formal relationship between electrostatic measurements and thermodynamic concepts (3,4).

Because our convention implies a positive emf when a reaction is spontaneous,

$$\boxed{\Delta G = -nFE_{rxn}} \tag{2.1.24}$$

or as above, when all substances are at unit activity,

$$\boxed{\Delta G^0 = -nFE_{rxn}^0} \tag{2.1.25}$$

where E_{rxn}^0 is called the *standard emf of the cell reaction.*

Other thermodynamic quantities can be derived from electrochemical measurements now that we have linked the potential difference across the cell to the free energy. For example, the entropy change in the cell reaction is given by the temperature dependence of ΔG:

$$\Delta S = -\left(\frac{\partial \Delta G}{\partial T}\right)_P \tag{2.1.26}$$

hence

$$\Delta S = nF\left(\frac{\partial E_{rxn}}{\partial T}\right)_P \tag{2.1.27}$$

and

$$\boxed{\Delta H = \Delta G + T\Delta S = nF\left[T\left(\frac{\partial E_{rxn}}{\partial T}\right)_P - E_{rxn}\right]} \tag{2.1.28}$$

The equilibrium constant of the reaction is given by

$$\boxed{RT \ln K_{rxn} = -\Delta G^0 = nFE_{rxn}^0} \tag{2.1.29}$$

Note that these relations are also useful for predicting electrochemical properties from thermochemical data. Several problems following this chapter illustrate the usefulness of that approach. Large tabulations of thermodynamic quantities exist (5–8).

2.1.4 Half-Reactions and Reduction Potentials

Just as the overall cell reaction comprises two independent half-reactions, one might think it reasonable that the cell potential could be broken into two individual electrode potentials. This view has experimental support, in that a self-consistent set of half-reaction emfs and half-cell potentials has been devised.

To establish the absolute potential of any conducting phase according to definition, one must evaluate the work required to bring a unit positive charge, without associated matter, from the point at infinity to the interior of the phase. Although this quantity is not measurable by thermodynamically rigorous means, it can sometimes be estimated from a series of nonelectrochemical measurements and theoretical calculations, if the demand for thermodynamic rigor is relaxed. Even if we could determine these absolute phase potentials, they would have limited utility because they would

depend on magnitudes of the adventitious fields in which the phase is immersed (see Section 2.2). Much more meaningful is the *difference* in absolute phase potentials between an electrode and its electrolyte, for this difference is the chief factor determining the state of an electrochemical equilibrium. Unfortunately, we will find that it also is not rigorously measurable. Experimentally, we can find only the absolute potential difference between two electronic conductors. Still, a useful scale results when one refers electrode potentials and half-reaction emfs to a standard reference electrode featuring a standard half-reaction.

The primary reference, chosen by convention, is the *normal hydrogen electrode* (NHE), also called the *standard hydrogen electrode* (SHE):

$$Pt/H_2(a = 1)/H^+(a = 1) \tag{2.1.30}$$
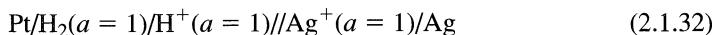
Its potential (the electrostatic standard) is taken as zero at all temperatures. Similarly, the standard emfs of the half-reactions:

$$2H^+ + 2e \rightleftarrows H_2 \tag{2.1.31}$$
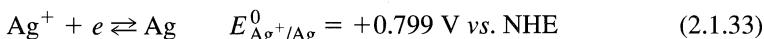
have also been assigned values of zero at all temperatures (the thermodynamic standard).

We can record half-cell potentials by measuring them in whole cells against the NHE.[3] For example, in the system

$$Pt/H_2(a = 1)/H^+(a = 1)//Ag^+(a = 1)/Ag \tag{2.1.32}$$

the cell potential is 0.799 V and silver is positive. Thus, we say that the *standard potential of the Ag$^+$/Ag couple* is +0.799 V *vs.* NHE. Moreover, the *standard emf of the Ag$^+$ reduction* is also +0.799 V *vs.* NHE, but that of the Ag oxidation is −0.799 V *vs.* NHE. Another valid expression is that the *standard electrode potential of Ag$^+$/Ag* is +0.799 V *vs.* NHE. To sum all of this up, we write:[4]

$$Ag^+ + e \rightleftarrows Ag \qquad E^0_{Ag^+/Ag} = +0.799 \text{ V } vs. \text{ NHE} \tag{2.1.33}$$

For the general system, (2.1.16), the electrostatic potential of the R/O electrode (with respect to NHE) and the emf for the *reduction* of O always coincide. Therefore, one can condense the electrostatic and thermodynamic information into one list by tabulating electrode potentials and writing the half-reactions as reductions. Appendix C provides some frequently encountered potentials. Reference (5) is an authoritative general source for aqueous systems.
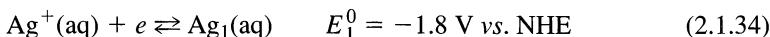
Tables of this sort are extremely useful, because they feature much chemical and electrical information condensed into quite a small space. A few electrode potentials can characterize quite a number of cells and reactions. Since the potentials are really indices of free energies, they are also ready means for evaluating equilibrium constants, complexation constants, and solubility products. Also, they can be taken in linear combinations to supply electrochemical information about additional half-reactions. One can tell from a glance at an ordered list of potentials whether or not a given redox process will proceed spontaneously.

---

[3]Note that an NHE is an ideal device and cannot be constructed. However, real hydrogen electrodes can approximate it, and its properties can be defined by extrapolation.
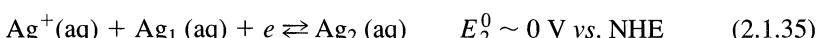
[4]In some of the older literature, the standard emfs of reduction and oxidation are, respectively, called the "reduction potential" and the "oxidation potential." These terms are intrinsically confusing and should be avoided altogether, because they conflate the chemical concept of reaction direction with the physical concept of electrical potential.

It is important to recognize that it is the electrostatic potential (not the emf) that is experimentally controlled and measured. When a half-reaction is chemically reversible, the potential of its electrode will usually have the same sign, whether the reaction proceeds as an oxidation or a reduction. [See also reference (9), and Sections 1.3.4, and 1.4.2(b).]

The standard potential of a cell or half-reaction is obtained under conditions where all species are in their standard states (10). For solids, like Ag in cell 2.1.32 or reaction 2.1.33, the standard state is the pure crystalline (bulk) metal. It is interesting to consider how many atoms or what particle size is needed to produce "bulk metal" and whether the standard potential is a function of particle size when one deals with metal clusters. These questions have been addressed (11–13); and for clusters containing n atoms (where $n < 20$), E_n^0 indeed turns out to be very different from the value for the bulk metal ($n >> 20$). Consider, for example, silver clusters, Ag_n. For a silver atom ($n = 1$), the value of E_1^0 can be related to E^0 for the bulk metal through a thermodynamic cycle involving the ionization potential of Ag and the hydration energy of Ag and Ag^+. This process yields

$$Ag^+(aq) + e \rightleftarrows Ag_1(aq) \qquad E_1^0 = -1.8 \text{ V } vs. \text{ NHE} \qquad (2.1.34)$$

which is 2.6 V more negative than for bulk Ag. This result implies that it is much easier energetically to remove an electron from a single isolated Ag atom than to remove an electron from Ag atoms within a lattice of other Ag atoms. Experimental work carried out with larger silver clusters shows that as the cluster size increases, E_n^0 moves toward the value for the bulk metal. For example, for $n = 2$

$$Ag^+(aq) + Ag_1(aq) + e \rightleftarrows Ag_2(aq) \qquad E_2^0 \sim 0 \text{ V } vs. \text{ NHE} \qquad (2.1.35)$$

These differences in standard potential can be explained by the greater *surface energy* of small clusters compared to bulk metal and is consistent with the tendency of small particles to grow into larger ones (e.g., the dimerization of $2Ag_1$ into Ag_2 or the Ostwald ripening of colloidal particles to form precipitates). Surface atoms are bonded to fewer neighbors than atoms within a crystal; thus an extra surface free energy is required to create additional surface area by subdivision of a metal. Conversely, the total energy of a system can be minimized by decreasing the surface area, such as by taking on a spherical shape or by fusing small particles into larger ones. If one adopts a microscopic viewpoint, one can see that the tendency for surfaces to reconstruct (see Section 13.4.2) and for different sites on surfaces to etch at different rates implies that even the standard potential for reduction to the "bulk metal" is actually an average of E^0 values for reduction at the different sites (14).

2.1.5 emf and Concentration

Consider a general cell in which the half-reaction at the right-hand electrode is

$$\nu_O O + ne \rightleftarrows \nu_R R \qquad (2.1.36)$$

where the ν's are stoichiometric coefficients. The cell reaction is then

$$\nu H_2 + \nu_O O \rightarrow \nu_R R + \nu H^+ \qquad (2.1.37)$$

and its free energy is given from basic thermodynamics (2) by

$$\Delta G = \Delta G^0 + RT \ln \frac{a_R^{\nu_R} a_{H^+}^{\nu}}{a_O^{\nu_O} a_{H_2}^{\nu}} \qquad (2.1.38)$$

where a_i is the activity of species i.[5] Since $\Delta G = -nFE$ and $\Delta G^0 = -nFE^0$,

$$E = E^0 - \frac{RT}{nF} \ln \frac{a_R^{\nu_R} a_{H^+}^{\nu_{H^+}}}{a_O^{\nu_O} a_{H_2}^{\nu_{H_2}}} \tag{2.1.39}$$

but since $a_{H^+} = a_{H_2} = 1$,

$$\boxed{E = E^0 + \frac{RT}{nF} \ln \frac{a_O^{\nu_O}}{a_R^{\nu_R}}} \tag{2.1.40}$$

This relation, the *Nernst equation*, furnishes the potential of the O/R electrode *vs.* NHE as a function of the activities of O and R. In addition, it defines the activity dependence of the emf for reaction 2.1.36.

It is now clear that the emf of any cell reaction, in terms of the electrode potentials of the two half-reactions, is

$$\boxed{E_{rxn} = E_{right} - E_{left}} \tag{2.1.41}$$

where E_{right} and E_{left} refer to the cell schematic and are given by the appropriate Nernst equation. The cell potential is the magnitude of this value.

2.1.6 Formal Potentials

It is usually inconvenient to deal with activities in evaluations of half-cell potentials, because activity coefficients are almost always unknown. A device for avoiding them is the *formal potential*, $E^{0'}$. This quantity is the *measured* potential of the half-cell (*vs.* NHE) when (a) the species O and R are present at concentrations such that the ratio $C_O^{\nu_O}/C_R^{\nu_R}$ is unity and (b) other specified substances, for example, miscellaneous components of the medium, are present at designated concentrations. At the least, the formal potential incorporates the standard potential and some activity coefficients, γ_i. For example, consider

$$Fe^{3+} + e \rightleftarrows Fe^{2+} \tag{2.1.42}$$

Its Nernst relation is simply

$$E = E^0 + \frac{RT}{nF} \ln \frac{a_{Fe^{3+}}}{a_{Fe^{2+}}} = E^0 + \frac{RT}{nF} \ln \frac{\gamma_{Fe^{3+}} [Fe^{3+}]}{\gamma_{Fe^{2+}} [Fe^{2+}]} \tag{2.1.43}$$

which is

$$E = E^{0'} + \frac{RT}{nF} \ln \frac{[Fe^{3+}]}{[Fe^{2+}]} \tag{2.1.44}$$

where

$$E^{0'} = E^0 + \frac{RT}{nF} \ln \frac{\gamma_{Fe^{3+}}}{\gamma_{Fe^{2+}}} \tag{2.1.45}$$

---

[5]For a solute i, the activity is $a_i = \gamma_i (C_i/C^0)$, where C_i is the concentration of the solute, C^0 is the standard concentration (usually 1 M), and γ_i is the activity coefficient, which is unitless. For a gas, $a_i = \gamma_i (P_i/P^0)$, where P_i is the partial pressure of i, P^0 is the standard pressure, and γ_i is the activity coefficient, which is again unitless. For most of the published literature, including all before the late 1980s, the standard pressure was 1 atm (101,325 Pa). The new standard pressure adopted by the International Union of Pure and Applied Chemistry is 10^5 Pa. A consequence of this change is that the potential of the NHE now differs from that used historically. The "new NHE" is +0.169 mV *vs.* the "old NHE" (based on a standard state of 1 atm). This difference is rarely significant, and is never so in this book. Most tabulated standard potentials, including those in Table C.1 are referred to the old NHE See reference 15.

Because the ionic strength affects the activity coefficients, $E^{0'}$ will vary from medium to medium. Table C.2 contains values for this couple in 1 M HCl, 10 M HCl, 1 M HClO$_4$, 1 M H$_2$SO$_4$, and 2 M H$_3$PO$_4$. The values of standard potentials for half-reactions and cells are actually determined by measuring formal potentials values at different ionic strengths and extrapolating to zero ionic strength, where the activity coefficients approach unity.

Often $E^{0'}$ also contains factors related to complexation and ion pairing; as it does in fact for the Fe(III)/Fe(II) couple in HCl, H$_2$SO$_4$, and H$_3$PO$_4$ solutions. Both iron species are complexed in these media; hence (2.1.42) does not accurately describe the half-cell reaction. However, one can sidestep a full description of the complex competitive equilibria by using the empirical formal potentials. In such cases, $E^{0'}$ contains terms involving equilibrium constants and concentrations of some species involved in the equilibria.
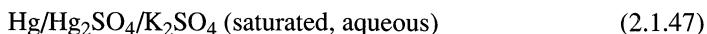
2.1.7 Reference Electrodes

Many reference electrodes other than the NHE and the SCE have been devised for electrochemical studies in aqueous and nonaqueous solvents. Several authors have provided discussions on the subject (16–18).
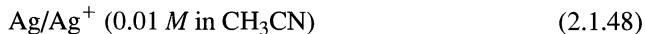
Usually there are experimental reasons for the choice of a reference electrode. For example, the system

$$\text{Ag/AgCl/KCl (saturated, aqueous)} \qquad (2.1.46)$$

has a smaller temperature coefficient of potential than an SCE and can be built more compactly. When chloride is not acceptable, the mercurous sulfate electrode may be used:

$$\text{Hg/Hg}_2\text{SO}_4\text{/K}_2\text{SO}_4 \text{ (saturated, aqueous)} \qquad (2.1.47)$$

With a nonaqueous solvent, one may be concerned with the leakage of water from an aqueous reference electrode; hence a system like

$$\text{Ag/Ag}^+ \text{ (0.01 } M \text{ in CH}_3\text{CN)} \qquad (2.1.48)$$

might be preferred.

Because of the difficulty in finding a reference electrode for a nonaqueous solvent that does not contaminate the test solution with undesirable species, a *quasireference electrode* (QRE)[6] is often employed. This is usually just a metal wire, Ag or Pt, used with the expectation that in experiments where there is essentially no change in the bulk solution, the potential of this wire, although unknown, will not change during a series of measurements. The actual potential of the quasireference electrode *vs.* a true reference electrode must be calibrated before reporting potentials with reference to the QRE. Typically the calibration is achieved simply by measuring (e.g., by voltammetry) the standard or formal potential *vs.* the QRE of a couple whose standard or formal potential is already known *vs.* a true reference under the same conditions. The ferrocene/ferrocenium (Fc/Fc$^+$) couple is recommended as a calibrating redox couple, since both forms are soluble and stable in many solvents, and since the couple usually shows nernstian behavior (19). Voltammograms for ferrocene oxidation might be recorded to establish the value of $E^{0'}_{\text{Fc/Fc}^+}$ *vs.* the QRE, so that the potentials of other reactions can be reported against $E^{0'}_{\text{Fc/Fc}^+}$. It is unacceptable to report potentials *vs.* an uncalibrated quasireference electrode. Moreover a QRE is not suitable in experiments, such as bulk electrolysis, where changes in the composition of the bulk solu-

---

[6]*Quasi* implies that it is "almost" or "essentially" a reference electrode. Sometimes such electrodes are also called *pseudoreference electrodes* (*pseudo*, meaning false); this terminology seems less appropriate.

	E vs. NHE (volts)	E vs. SCE (volts)	E vs. vacuum (volts)	E_F (Fermi energy) (eV)
$E^0(Zn^{2+}/Zn)$	−0.763	−1.00	3.7	−3.7
NHE	0	−0.242	4.5	−4.5
SCE	0.242	0	4.7	−4.7
$E^0(Fe^{3+}/Fe^{2+})$	0.77	0.53	5.3	−5.3

Figure 2.1.1 Relationship between potentials on the NHE, SCE, and "absolute" scales. The potential on the absolute scale is the electrical work required to bring a unit positive test charge into the conducting phase of the electrode from a point *in vacuo* just outside the system (see Section 2.2.5). At right is the Fermi energy corresponding to each of the indicated potentials. The Fermi energy is the electrochemical potential of electrons on the electrode (see Section 2.2.4).

tion can cause concomitant variations in the potential of the QRE. A proposed alternative approach (20) is to employ a reference electrode in which Fc and Fc$^+$ are immobilized at a known concentration ratio in a polymer layer on the electrode surface (see Chapter 14).

Since the potential of a reference electrode *vs.* NHE or SCE is typically specified in experimental papers, interconversion of scales can be accomplished easily. Figure 2.1.1 is a schematic representation of the relationship between the SCE and NHE scales. The inside back cover contains a tabulation of the potentials of the most common reference electrodes.

▷ 2.2 A MORE DETAILED VIEW OF INTERFACIAL POTENTIAL DIFFERENCES

2.2.1 The Physics of Phase Potentials

In the thermodynamic considerations of the previous section, we were not required to advance a mechanistic basis for the observable differences in potentials across certain phase boundaries. However, it is difficult to think chemically without a mechanistic model, and we now find it helpful to consider the kinds of interactions between phases that could create these interfacial differences. First, let us consider two prior questions: (1) Can we expect the potential within a phase to be uniform? (2) If so, what governs its value?

One certainly can speak of the potential at any particular point within a phase. That quantity, $\phi(x, y, z)$, is defined as the work required to bring a unit positive charge, without material interactions, from an infinite distance to point (x, y, z). From electrostatics, we have assurance that $\phi(x, y, z)$ is independent of the path of the test charge (21). The work is done against a coulombic field; hence we can express the potential generally as

$$\phi(x, y, x) = \int_{\infty}^{x,y,z} -\mathscr{E} \cdot d\mathbf{l} \tag{2.2.1}$$

where $\mathscr{E}$ is the electric field strength vector (i.e., the force exerted on a unit charge at any point), and $d\mathbf{l}$ is an infinitesimal tangent to the path in the direction of movement. The integral is carried out over any path to (x, y, z). The difference in potential between points (x', y', z') and (x, y, z) is then

$$\phi(x', y', z') - \phi(x, y, z) = \int_{x,y,z}^{x',y',z'} -\mathscr{E} \cdot d\mathbf{l} \qquad (2.2.2)$$

In general, the electric field strength is not zero everywhere between two points and the integral does not vanish; hence some potential difference usually exists.

Conducting phases have some special properties of great importance. Such a phase is one with mobile charge carriers, such as a metal, a semiconductor, or an electrolyte solution. When no current passes through a conducting phase, there is no net movement of charge carriers, so the electric field at all interior points must be zero. If it were not, the carriers would move in response to it to eliminate the field. From equation 2.2.2, one can see that the difference in potential between any two points in the interior of the phase must also be zero under these conditions; thus the entire phase is an *equipotential volume*. We designate its potential as ϕ, which is known as the *inner potential* (or *Galvani potential*) of the phase.

Why does the inner potential have the value that it does? A very important factor is any excess charge that might exist on the phase itself, because a test charge would have to work against the coulombic field arising from that charge. Other components of the potential can arise from miscellaneous fields resulting from charged bodies outside the sample. As long as the charge distribution throughout the system is constant, the phase potential will remain constant, but alterations in charge distributions inside or outside the phase will change the phase potential. Thus, we have our first indication that differences in potential arising from chemical interactions between phases have some sort of *charge separation* as their basis.

An interesting question concerns the location of any excess charge on a conducting phase. The Gauss law from elementary electrostatics is extremely helpful here (22). It states that if we enclose a volume with an imaginary surface (a *Gaussian surface*), we will find that the net charge q inside the surface is given by an integral of the electric field over the surface:

$$q = \varepsilon_0 \oint \mathscr{E} \cdot d\mathbf{S} \qquad (2.2.3)$$

where ε_0 is a proportionality constant,[7] and $d\mathbf{S}$ is an infinitesimal vector normal outward from the surface. Now consider a Gaussian surface located within a conductor that is uniform in its interior (i.e., without voids or interior phases). If no current flows, $\mathscr{E}$ is zero at all points on the Gaussian surface, hence the net charge within the boundary is zero. The situation is depicted in Figure 2.2.1. This conclusion applies to any Gaussian surface, even one situated just inside the phase boundary; thus we must infer that the excess charge actually resides on the surface of the conducting phase.[8]

---

[7]The parameter ε_0 is called the *permittivity of free space* or the *electric constant* and has the value 8.85419×10^{-12} $C^2\,N^{-1}\,m^{-1}$. See the footnote in Section 13.3.1 for a fuller explanation of electrostatic conventions followed in this book.

[8]There can be a finite thickness to this surface layer. The critical aspect is the size of the excess charge with respect to the bulk carrier concentration in the phase. If the charge is established by drawing carriers from a significant volume, thermal processes will impede the compact accumulation of the excess strictly on the surface. Then, the charged zone is called a *space charge region*, because it has three-dimensional character. Its thickness can range from a few angstroms to several thousand angstroms in electrolytes and semiconductiors. In metals, it is negligibly thick. See Chapters 13 and 18 for more detailed discussion along this line.
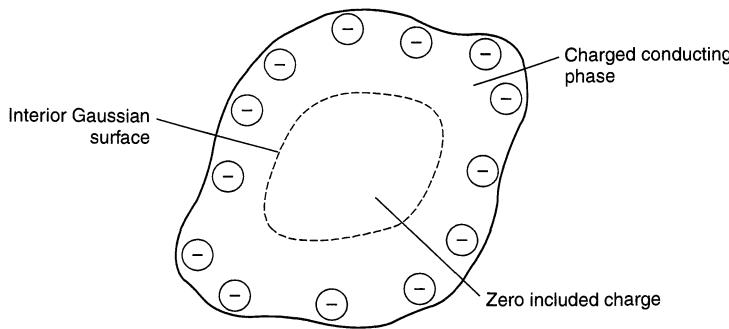
Figure 2.2.1 Cross-section of a three-dimensional conducting phase containing a Gaussian enclosure. Illustration that the excess charge resides on the surface of the phase.

A view of the way in which phase potentials are established is now beginning to emerge:

1. Changes in the potential of a conducting phase can be effected by altering the charge distributions on or around the phase.

2. If the phase undergoes a change in its excess charge, its charge carriers will adjust such that the excess becomes wholly distributed over an entire boundary of the phase.

3. The surface distribution is such that the electric field strength within the phase is zero under null-current conditions.

4. The interior of the phase features a constant potential, ϕ.

The excess charge needed to change the potential of a conductor by electrochemically significant amounts is often not very large. Consider, for example, a spherical mercury drop of 0.5 mm radius. Changing its potential requires only about 5×10^{-14} C/V (about 300,000 electrons/V), if it is suspended in air or in a vacuum (21).

2.2.2 Interactions Between Conducting Phases

When two conductors, for example, a metal and an electrolyte, are placed in contact, the situation becomes more complicated because of the coulombic interaction between the phases. Charging one phase to change its potential tends to alter the potential of the neighboring phase as well. This point is illustrated in the idealization of Figure 2.2.2, which portrays a situation where there is a charged metal sphere of macroscopic size, perhaps a mercury droplet 1 mm in diameter, surrounded by a layer of uncharged electrolyte a few millimeters in thickness. This assembly is suspended in a vacuum. We know that the
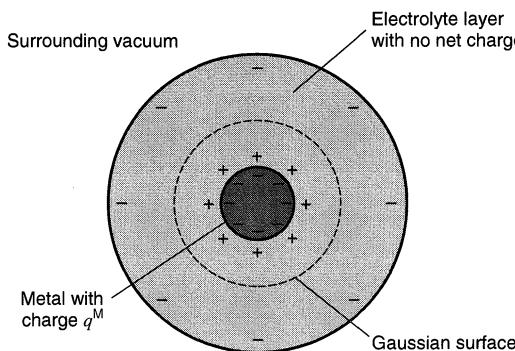
Figure 2.2.2 Cross-sectional view of the interacti56on between a metal sphere and a surrounding electrolyte layer. The Gaussian enclosure is a sphere containing the metal phase and part of the electrolyte.

charge on the metal, q^M, resides on its surface. This unbalanced charge (negative in the diagram) creates an excess cation concentration near the electrode in the solution. What can we say about the magnitudes and distributions of the obvious charge imbalances in solution?

Consider the integral of equation 2.2.3 over the Gaussian surface shown in Figure 2.2.2. Since this surface is in a conducting phase where current is not flowing, $\mathscr{E}$ at every point is zero and the net enclosed charge is also zero. We could place the Gaussian surface just outside the surface region bounding the metal and solution, and we would reach the same conclusion. Thus, we know now that the excess positive charge in the solution, q^S, resides at the metal–solution interface and exactly compensates the excess metal charge. That is,

$$q^S = -q^M \qquad (2.2.4)$$

This fact is very useful in the treatment of interfacial charge arrays, which we have already seen as *electrical double layers* (see Chapters 1 and 13).[9]

Alternatively, we might move the Gaussian surface to a location just inside the outer boundary of the electrolyte. The enclosed charge must still be zero, yet we know that the net charge on the whole system is q^M. A negative charge equal to q^M must therefore reside at the outer surface of the electrolyte.

Figure 2.2.3 is a display of potential *vs.* distance from the center of this assembly, that is, the work done to bring a unit positive test charge from infinitely far away to a given distance from the center. As the test charge is brought from the right side of the diagram, it is attracted by the charge on the outer surface of the electrolyte; thus negative work is required to traverse any distance toward the electrolyte surface in the surrounding vacuum, and the potential steadily drops in that direction. Within the electrolyte, $\mathscr{E}$ is zero everywhere, so there is no work in moving the test charge, and the potential is constant at ϕ^S. At the metal–solution interface, there is a strong field because of the double layer there, and it is oriented such that negative work is done in taking the positive test charge through the interface. Thus there is a sharp change in potential from ϕ^S to ϕ^M over the distance scale of the double layer.[10] Since the metal is a field-free volume, the
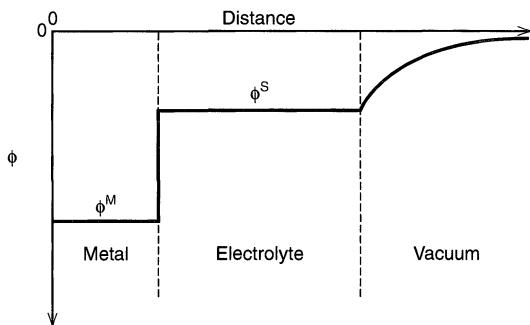
Figure 2.2.3 Potential profile through the system shown in Figure 2.2.2. Distance is measured radially from the center of the metallic sphere.

[9]Here we are considering the problem on a macroscopic distance scale, and it is accurate to think of q^S as residing strictly at the metal–solution interface. On a scale of 1 μm or finer, the picture is more detailed. One finds that q^S is still near the metal–solution interface, but is distributed in one or more zones that can be as thick as 1000 Å (Section 13.3).

[10]The diagram is drawn on a macroscopic scale, so the transition from ϕ^S to ϕ^M appears vertical. The theory of the double layer (Section 13.3) indicates that most of the change occurs over a distance equivalent to one to several solvent monolayers, with a smaller portion being manifested over the diffuse layer in solution.

potential is constant in its interior. If we were to increase the negative charge on the metal, we would naturally lower ϕ^M, but we would also lower ϕ^S, because the excess negative charge on the outer boundary of the solution would increase, and the test charge would be attracted more strongly to the electrolyte layer at every point on the path through the vacuum.

The difference $\phi^M - \phi^S$, called the *interfacial potential difference*, depends on the charge imbalance at the interface and the physical size of the interface. That is, it depends on the charge density (C/cm^2) at the interface. Making a change in this interfacial potential difference requires sizable alterations in charge density. For the spherical mercury drop considered above ($A = 0.03$ cm^2), now surrounded by 0.1 M strong electrolyte, one would need about 10^{-6} C (or 6×10^{12} electrons) for a 1-V change. These numbers are more than 10^7 larger than for the case where the electrolyte is absent. The difference appears because the coulombic field of any surface charge is counterbalanced to a very large degree by polarization in the adjacent electrolyte.

In practical electrochemistry, metallic electrodes are partially exposed to an electrolyte and partially insulated. For example, one might use a 0.1 cm^2 platinum disk electrode attached to a platinum lead that is almost fully sealed in glass. It is interesting to consider the location of excess charge used in altering the potential of such a phase. Of course, the charge must be distributed over the entire surface, including both the insulated and the electrochemically active area. However, we have seen that the coulombic interaction with the electrolyte is so strong that essentially all of the charge at any potential will lie adjacent to the solution, unless the percentage of the phase area in contact with electrolyte is really minuscule.[11]

What real mechanisms are there for charging a phase at all? An important one is simply to pump electrons into or out of a metal or semiconductor with a power supply of some sort. In fact, we will make great use of this approach as the basis for control over the kinetics of electrode processes. In addition, there are chemical mechanisms. For example, we know from experience that a platinum wire dipped into a solution containing ferricyanide and ferrocyanide will have its potential shift toward a predictable equilibrium value given by the Nernst equation. This process occurs because the electron affinities of the two phases initially differ; hence there is a transfer of electrons from the metal to the solution or vice versa. Ferricyanide is reduced or ferrocyanide is oxidized. The transfer of charge continues until the resulting change in potential reaches the equilibrium point, where the electron affinities of the solution and the metal are equal. Compared to the total charge that could be transferred to or from ferri- and ferrocyanide in a typical system, only a tiny charge is needed to establish the equilibrium at Pt; consequently, the net chemical effects on the solution are unnoticeable. By this mechanism, the metal adapts to the solution and reflects its composition.

Electrochemistry is full of situations like this one, in which charged species (electrons or ions) cross interfacial boundaries. These processes generally create a net transfer of charge that sets up the equilibrium or steady-state potential differences that we observe. Considering them in more detail must, however, await the development of additional concepts (see Section 2.3 and Chapter 3).

Actually, interfacial potential differences can develop without an excess charge on either phase. Consider an aqueous electrolyte in contact with an electrode. Since the electrolyte interacts with the metal surface (e.g., wetting it), the water dipoles in contact with the metal generally have some preferential orientation. From a coulombic standpoint, this situation is equivalent to charge separation across the interface, because the dipoles are

---

[11]As it can be with an ultramicroelectrode. See Section 5.3.
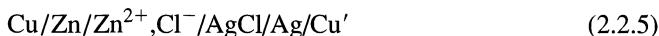
not randomized with time. Since moving a test charge through the interface requires work, the interfacial potential difference is not zero (23–26).[12]

2.2.3 Measurement of Potential Differences

We have already noted that the difference in the inner potentials, $\Delta\phi$, of two phases in contact is a factor of primary importance to electrochemical processes occurring at the interface between them. Part of its influence comes from the local electric fields reflecting the large changes in potential in the boundary region. These fields can reach values as high as 10^7 V/cm. They are large enough to distort electroreactants so as to alter reactivity, and they can affect the kinetics of charge transport across the interface. Another aspect of $\Delta\phi$ is its direct influence over the relative energies of charged species on either side of the interface. In this way, $\Delta\phi$ controls the relative electron affinities of the two phases; hence it controls the direction of reaction.

Unfortunately, $\Delta\phi$ cannot be measured for a single interface, because one cannot sample the electrical properties of the solution without introducing at least one more interface. It is characteristic of devices for measuring potential differences (e.g., potentiometers, voltmeters, or electrometers) that they can be calibrated only to register potential differences between two phases of the same composition, such as the two metal contacts available at most instruments. Consider $\Delta\phi$ at the interface Zn/Zn^{2+}, Cl^-. Shown in Figure 2.2.4*a* is the simplest approach one could make to $\Delta\phi$ using a potentiometric instrument with copper contacts. The measurable potential difference between the copper phases clearly includes interfacial potential differences at the Zn/Cu interface and the Cu/electrolyte interface in addition to $\Delta\phi$. We might simplify matters by constructing a voltmeter wholly from zinc but, as shown in Figure 2.2.4*b*, the measurable voltage would still contain contributions from two separate interfacial potential differences.

By now we realize that a measured cell potential is a sum of several interfacial differences, none of which we can evaluate independently. For example, one could sketch the potential profile through the cell

$$Cu/Zn/Zn^{2+},Cl^-/AgCl/Ag/Cu' \qquad (2.2.5)$$

according to Vetter's representation (24) in the manner of Figure 2.2.5.[13]

Even with these complications, it is still possible to focus on a single interfacial potential difference, such as that between zinc and the electrolyte in (2.2.5). If we can maintain constant interfacial potentials at all of the other junctions in the cell, then any *change* in E must be wholly attributed to a *change* in $\Delta\phi$ at the zinc/electrolyte boundary. Keeping the other junctions at a constant potential difference is not so difficult, for the metal-
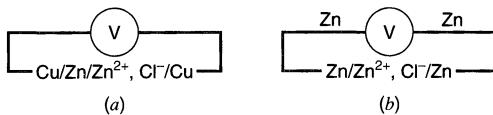
Figure 2.2.4 Two devices for measuring the potential of a cell containing the Zn/Zn^{2+} interface.

---

[12]Sometimes it is useful to break the inner potential into two components called the *outer* (or *Volta*) potential, ψ, and the *surface potential*, χ. Thus, $\phi = \psi + \chi$. There is a large, detailed literature on the establishment, the meaning, and the measurement of interfacial potential differences and their components. See references 23–26.

[13]Although silver chloride is a separate phase, it does not contribute to the cell potential, because it does not physically separate silver from the electrolyte. In fact, it need not even be present; one merely requires a solution saturated in silver chloride to measure the same cell potential.
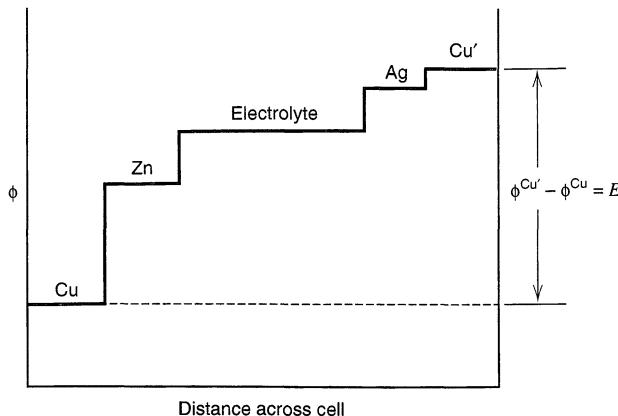
Figure 2.2.5 Potential profile across a whole cell at equilibrium.

metal junctions always remain constant (at constant temperature) without attention, and the silver/electrolyte junction can be fixed if the activities of the participants in its half-reaction remain fixed. When this idea is realized, the whole rationale behind half-cell potentials and the choice of reference electrodes becomes much clearer.

2.2.4 Electrochemical Potentials

Let us consider again the interface Zn/Zn^{2+}, Cl^- (aqueous) and focus on zinc ions in metallic zinc and in solution. In the metal, Zn^{2+} is fixed in a lattice of positive zinc ions, with free electrons permeating the structure. In solution, zinc ion is hydrated and may interact with Cl^-. The energy state of Zn^{2+} in any location clearly depends on the chemical environment, which manifests itself through short-range forces that are mostly electrical in nature. In addition, there is the energy required simply to bring the $+2$ charge, disregarding the chemical effects, to the location in question. This second energy is clearly proportional to the potential ϕ at the location; hence it depends on the electrical properties of an environment very much larger than the ion itself. Although one cannot experimentally separate these two components for a single species, the differences in the scales of the two environments responsible for them makes it plausible to separate them mathematically (23–26). Butler (27) and Guggenheim (28) developed the conceptual separation and introduced the *electrochemical potential*, $\bar{\mu}_i^\alpha$, for species i with charge z_i in phase α:

$$\boxed{\bar{\mu}_i^\alpha = \mu_i^\alpha + z_i F \phi^\alpha} \tag{2.2.6}$$

The term μ_i^α is the familiar *chemical potential*

$$\mu_i^\alpha = \left(\frac{\partial G}{\partial n_i}\right)_{T,P,n_{j\neq i}} \tag{2.2.7}$$

where n_i is the number of moles of i in phase α. Thus, the electrochemical potential would be

$$\bar{\mu}_i^\alpha = \left(\frac{\partial \bar{G}}{\partial n_i}\right)_{T,P,n_{j\neq i}} \tag{2.2.8}$$
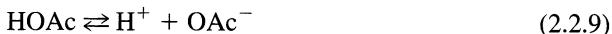
where the *electrochemical free energy*, $\bar{G}$, differs from the *chemical free energy*, G, by the inclusion of effects from the large-scale electrical environment.

(a) Properties of the Electrochemical Potential

1. For an uncharged species: $\overline{\mu}_i^\alpha = \mu_i^\alpha$.

2. For any substance: $\mu_i^\alpha = \mu_i^{0\alpha} + RT \ln a_i^\alpha$, where $\mu_i^{0\alpha}$ is the standard chemical potential, and a_i^α is the activity of species i in phase α.

3. For a pure phase at unit activity (e.g., solid Zn, AgCl, Ag, or H_2 at unit fugacity): $\overline{\mu}_i^\alpha = \mu_i^{0\alpha}$.

4. For electrons in a metal ($z = -1$): $\overline{\mu}_e^\alpha = \mu_e^{0\alpha} - F\phi^\alpha$. Activity effects can be disregarded because the electron concentration never changes appreciably.

5. For equilibrium of species i between phases α and β: $\overline{\mu}_i^\alpha = \overline{\mu}_i^\beta$.

(b) Reactions in a Single Phase

Within a single conducting phase, ϕ is constant everywhere and exerts no effect on a chemical equilibrium. The ϕ terms drop out of relations involving electrochemical potentials, and only chemical potentials will remain. Consider, for example, the acid–base equilibrium:

$$HOAc \rightleftarrows H^+ + OAc^- \tag{2.2.9}$$

This requires that
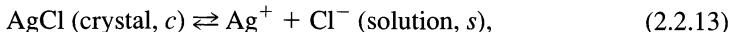
$$\overline{\mu}_{HOAc} = \overline{\mu}_{H^+} + \overline{\mu}_{OAc^-} \tag{2.2.10}$$

$$\mu_{HOAc} = \mu_{H^+} + F\phi + \mu_{OAc^-} - F\phi \tag{2.2.11}$$

$$\mu_{HOAc} = \mu_{H^+} + \mu_{OAc^-} \tag{2.2.12}$$

(c) Reactions Involving Two Phases Without Charge Transfer

Let us now examine the solubility equilibrium

$$AgCl \text{ (crystal, } c) \rightleftarrows Ag^+ + Cl^- \text{ (solution, } s), \tag{2.2.13}$$

which can be treated in two ways. First, one can consider separate equilibria involving Ag^+ and Cl^- in solution and in the solid. Thus

$$\overline{\mu}_{Ag^+}^{AgCl} = \overline{\mu}_{Ag^+}^s \tag{2.2.14}$$

$$\overline{\mu}_{Cl^-}^{AgCl} = \overline{\mu}_{Cl^-}^s \tag{2.2.15}$$

Recognizing that

$$\overline{\mu}_{AgCl}^{AgCl} = \overline{\mu}_{Ag^+}^{AgCl} + \overline{\mu}_{Cl^-}^{AgCl} \tag{2.2.16}$$

one has from the sum of (2.2.14) and (2.2.15),

$$\mu_{AgCl}^{0AgCl} = \overline{\mu}_{Ag^+}^s + \overline{\mu}_{Cl^-}^s \tag{2.2.17}$$

Expanding, we obtain

$$\mu_{AgCl}^{0AgCl} = \mu_{Ag^+}^{0s} + RT \ln a_{Ag^+}^s + F\phi^s + \mu_{Cl^-}^{0s} + RT \ln a_{Cl^-}^s - F\phi^s \tag{2.2.18}$$

and rearrangement gives

$$\mu_{AgCl}^{0AgCl} - \mu_{Ag^+}^{0s} - \mu_{Cl^-}^{0s} = RT \ln (a_{Ag^+}^s a_{Cl^-}^s) = RT \ln K_{sp} \tag{2.2.19}$$

where K_{sp} is the solubility product. A quicker route to this well-known result is to write down (2.2.17) directly from the chemical equation, (2.2.13).

Note that the ϕ^s terms canceled in (2.2.18), and that an implicit cancellation of ϕ^{AgCl} terms occurred in (2.2.16). Since the final result depends only on chemical potentials, the

equilibrium is unaffected by the potential difference across the interface. This is a general feature of interphase reactions without transfer of charge (either ionic or electronic). When charge transfer does occur, the ϕ terms will not cancel and the interfacial potential difference strongly affects the chemical process. We can use that potential difference either to probe or to alter the equilibrium position.

(d) Formulation of a Cell Potential

Consider now the cell (2.2.5), for which the cell reaction can be written

$$Zn + 2AgCl + 2e(Cu') \rightleftarrows Zn^{2+} + 2Ag + 2Cl^- + 2e(Cu) \qquad (2.2.20)$$

At equilibrium,

$$\overline{\mu}_{Zn}^{Zn} + 2\overline{\mu}_{AgCl}^{AgCl} + 2\overline{\mu}_e^{Cu'} = \overline{\mu}_{Zn^{2+}}^s + 2\overline{\mu}_{Ag}^{Ag} + 2\overline{\mu}_{Cl^-}^s + 2\overline{\mu}_e^{Cu} \qquad (2.2.21)$$

$$2(\overline{\mu}_e^{Cu'} - \overline{\mu}_e^{Cu}) = \overline{\mu}_{Zn^{2+}}^s + 2\overline{\mu}_{Ag}^{Ag} + 2\overline{\mu}_{Cl^-}^s - \overline{\mu}_{Zn}^{Zn} - 2\overline{\mu}_{AgCl}^{AgCl} \qquad (2.2.22)$$

But,

$$2(\overline{\mu}_e^{Cu'} - \overline{\mu}_e^{Cu}) = -2F(\phi^{Cu'} - \phi^{Cu}) = -2FE \qquad (2.2.23)$$

Expanding (2.2.22), we have

$$-2FE = \mu_{Zn^{2+}}^{0s} + RT \ln a_{Zn^{2+}}^s + 2F\phi^s + 2\mu_{Ag}^{0Ag} + 2\mu_{Cl^-}^{0s} \qquad (2.2.24)$$
$$+ 2RT \ln a_{Cl^-}^s - 2F\phi^s - \mu_{Zn}^{0Zn} - 2\mu_{AgCl}^{0AgCl}$$

$$-2FE = \Delta G^0 + RT \ln a_{Zn^{2+}}^s (a_{Cl^-}^s)^2 \qquad (2.2.25)$$
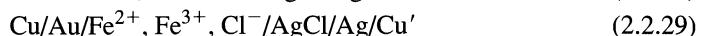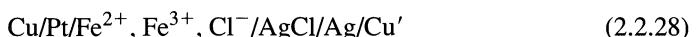
where

$$\Delta G^0 = \mu_{Zn^{2+}}^{0s} + 2\mu_{Cl^-}^{0s} + 2\mu_{Ag}^{0Ag} - \mu_{Zn}^{0Zn} - 2\mu_{AgCl}^{0AgCl} = -2FE^0 \qquad (2.2.26)$$

Thus, we arrive at

$$E = E^0 - \frac{RT}{2F} \ln(a_{Zn^{2+}}^s)(a_{Cl^-}^s)^2, \qquad (2.2.27)$$

which is the Nernst equation for the cell. This corroboration of an earlier result displays the general utility of electrochemical potentials for treating interfacial reactions with charge transfer. They are powerful tools. For example, they are easily used to consider whether the two cells

$$Cu/Pt/Fe^{2+}, Fe^{3+}, Cl^-/AgCl/Ag/Cu' \qquad (2.2.28)$$
$$Cu/Au/Fe^{2+}, Fe^{3+}, Cl^-/AgCl/Ag/Cu' \qquad (2.2.29)$$

would have the same cell potential. This point is left to the reader as Problem 2.8.

2.2.5 Fermi Level and Absolute Potential

The electrochemical potential of electrons in a phase α, $\overline{\mu}_e^\alpha$, is called the *Fermi level* or *Fermi energy* and corresponds to an electron energy (not an electrical potential) E_F^α. The Fermi level represents the average energy of available electrons in phase α and is related to the chemical potential of electrons in that phase, μ_e^α, and the inner potential of α.[14] The Fermi level of a metal or semiconductor depends on the work function of the material (see Section 18.2.2). For a solution phase, it is a function of the electrochemical potentials of

---

[14]More exactly, it is the energy where the occupation probability is 0.5 in the distribution of electrons among the various energy levels (the Fermi–Dirac distribution). See Sections 3.6.3 and 18.2.2 for more discussion of E_F.

the dissolved oxidized and reduced species. For example, for a solution containing Fe^{3+} and Fe^{2+}

$$\overline{\mu}_e^s = \overline{\mu}_{Fe^{2+}}^s - \overline{\mu}_{Fe^{3+}}^s \tag{2.2.30}$$

For an inert metal in contact with a solution, the condition for electrical (or electronic) equilibrium is that the Fermi levels of the two phases be equal, that is,

$$\mathbf{E}_F^s = \mathbf{E}_F^M \tag{2.2.31}$$

This condition is equivalent to saying that the electrochemical potentials of electrons in both phases are equal, or that the average energies of available (i.e., transferable) electrons are the same in both phases. When an initially uncharged metal is brought into contact with an initially uncharged solution, the Fermi levels will not usually be equal. As discussed in Section 2.2.2, equality is attained by the transfer of electrons between the phases, with electrons flowing from the phase with the higher Fermi level (higher $\overline{\mu}_e$ or more energetic electrons) to the phase with the lower Fermi level. This electron flow causes the potential difference between the phases (the electrode potential) to shift.

For most purposes in electrochemistry, it is sufficient to reference the potentials of electrodes (and half-cell emfs) arbitrarily to the NHE, but it is sometimes of interest to have an estimate of the *absolute* or *single electrode potential* (i.e., *vs.* the potential of a free electron in vacuum). This interest arises, for example, if one would like to estimate relative potentials of metals or semiconductors based on their work functions. The absolute potential of the NHE can be estimated as 4.5 ± 0.1 V, based on certain extrathermodynamic assumptions, such as about the energy involved in moving a proton from the gas phase into an aqueous solution (10, 29). Thus, the amount of energy needed to remove an electron from $Pt/H_2/H^+(a = 1)$ to vacuum is about 4.5 eV or 434 kJ.[15] With this value, the standard potentials of other couples and reference electrodes can be expressed on the absolute scale (Figure 2.1.1).

2.3 LIQUID JUNCTION POTENTIALS

2.3.1 Potential Differences at an Electrolyte–Electrolyte Boundary

To this point, we have examined only systems at equilibrium, and we have learned that the potential differences in equilibrium electrochemical systems can be treated exactly by thermodynamics. However, many real cells are never at equilibrium, because they feature different electrolytes around the two electrodes. There is somewhere an interface between the two solutions, and at that point, mass transport processes work to mix the solutes. Unless the solutions are the same initially, the *liquid junction* will not be at equilibrium, because net flows of mass occur continuously across it.

Such a cell is

$$Cu/Zn/Zn^{2+}/Cu^{2+}/Cu' \tag{2.3.1}$$
$$\alpha \quad \beta$$

for which we can depict the equilibrium processes as in Figure 2.3.1. The overall cell potential at null current is then

$$E = (\phi^{Cu'} - \phi^\beta) - (\phi^{Cu} - \phi^\alpha) + (\phi^\beta - \phi^\alpha) \tag{2.3.2}$$

---

[15]The potential and the Fermi energy of an electrode have different signs, because the potential is based on energy changes involving a positive test charge, while the Fermi energy refers to a negative electron.

Cu	Zn	α	β	Cu′
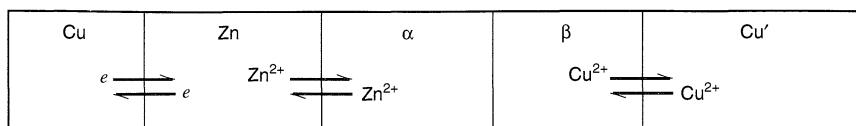
Figure 2.3.1 Schematic view of the phases in cell (2.3.1). Equilibrium is established for certain charge carriers as shown, but at the liquid junction between the two electrolyte phases α and β, equilibrium is not reached.

Obviously, the first two components of E are the expected interfacial potential differences at the copper and zinc electrodes. The third term shows that the measured cell potential depends also on the potential difference between the electrolytes, that is, on the *liquid junction potential*. This discovery is a real threat to our system of electrode potentials, because it is based on the idea that all contributions to E can be assigned unambiguously to one electrode or to the other. How could the junction potential possibly be assigned properly? We must evaluate the importance of these phenomena.

2.3.2 Types of Liquid Junctions

The reality of junction potentials is easily understood by considering the boundary shown in Figure 2.3.2a. At the junction, there is a steep concentration gradient in H^+ and Cl^-; hence both ions tend to diffuse from right to left. Since the hydrogen ion has a much larger mobility than Cl^-, it initially penetrates the dilute phase at a higher rate. This process gives a positive charge to the dilute phase and a negative charge to the concentrated one, with the result that a boundary potential difference develops. The corresponding electric field then retards the movement of H^+ and speeds up the passage of Cl^- until the two cross the boundary at equal rates. Thus, there is a detectable steady-state potential, which is not due to an equilibrium process (3, 24, 30, 31). From its origin, this interfacial potential is sometimes called a *diffusion potential*.

Lingane (3) classified liquid junctions into three types:

1. Two solutions of the same electrolyte at different concentrations, as in Figure 2.3.2a.

2. Two solutions at the same concentration with different electrolytes having an ion in common, as in Figure 2.3.2b.

3. Two solutions not satisfying conditions 1 or 2, as in Figure 2.3.2c.

We will find this classification useful in the treatments of junction potentials that follow.
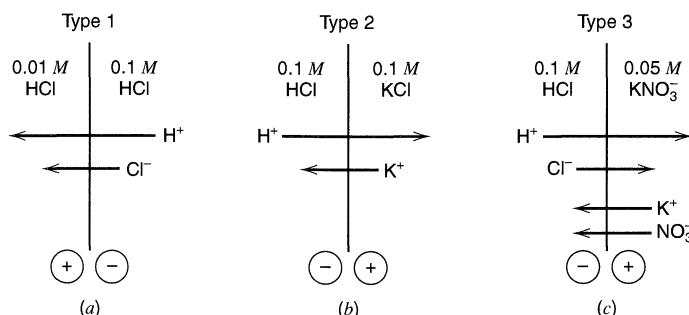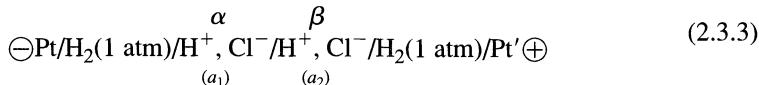
Figure 2.3.2 Types of liquid junctions. Arrows show the direction of net transfer for each ion, and their lengths indicate relative mobilities. The polarity of the junction potential is indicated in each case by the circled signs. [Adapted from J. J. Lingane, "Electroanalytical Chemistry," 2nd ed., Wiley-Interscience, New York, 1958, p. 60, with permission.]

Even though the boundary region cannot be at equilibrium, it has a composition that is effectively constant over long time periods, and the reversible transfer of electricity through the region can be considered.

Conductance, Transference Numbers, and Mobility

When an electric current flows in an electrochemical cell, the current is carried in solution by the movement of ions. For example, take the cell:

$$\alpha \qquad \beta$$
$$\ominus Pt/H_2(1 \text{ atm})/H^+, Cl^-/H^+, Cl^-/H_2(1 \text{ atm})/Pt' \oplus \qquad (2.3.3)$$
$$(a_1) \qquad (a_2)$$

where $a_2 > a_1$.[16] When the cell operates galvanically, an oxidation occurs at the left electrode,

$$H_2 \rightarrow 2H^+(\alpha) + 2e(Pt) \qquad (2.3.4)$$

and a reduction happens on the right,

$$2H^+(\beta) + 2e(Pt') \rightarrow H_2 \qquad (2.3.5)$$

Therefore, there is a tendency to build up a positive charge in the α phase and a negative charge in β. This tendency is overcome by the movement of ions: H^+ to the right and Cl^- to the left. For each mole of electrons passed, 1 mole of H^+ is produced in α, and 1 mole of H^+ is consumed in β. The total amount of H^+ and Cl^- migrating across the boundary between α and β must equal 1 mole.

The fractions of the current carried by H^+ and Cl^- are called their *transference numbers* (or *transport numbers*). If we let t_+ be the transference number for H^+ and t_- be that for Cl^-, then clearly,

$$t_+ + t_- = 1 \qquad (2.3.6)$$

In general, for an electrolyte containing many ions, i,

$$\boxed{\sum_i t_i = 1} \qquad (2.3.7)$$

Schematically, the process can be represented as shown in Figure 2.3.3. The cell initially features a higher activity of hydrochloric acid ($+$ as H^+, $-$ as Cl^-) on the right (Figure
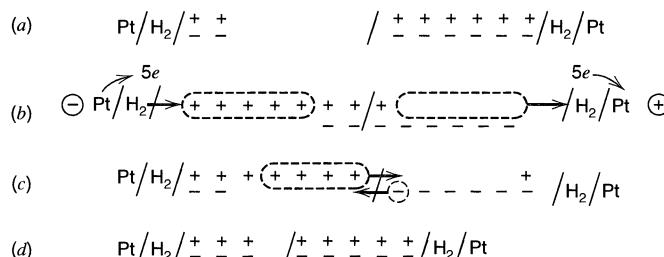
Figure 2.3.3 Schematic diagram showing the redistribution of charge during electrolysis of a system featuring a high concentration of HCl on the right and a low concentration on the left.

---

[16]A cell like (2.3.3), having electrodes of the same type on both sides, but with differing activities of one or both of the redox forms, is called a *concentration cell*.

2.3.3a); hence discharging it spontaneously produces H^+ on the left and consumes it on the right. Assume that five units of H^+ are reacted as shown in Figure 2.3.3b. For hydrochloric acid, $t_+ \approx 0.8$ and $t_- \approx 0.2$; therefore, four units of H^+ must migrate to the right and one unit of Cl^- to the left to maintain electroneutrality. This process is depicted in Figure 2.3.3c, and the final state of the solution is represented in Figure 2.3.3d.

A charge imbalance like that suggested in Figure 2.3.3b could not actually occur, because a very large electric field would be established, and it would work to erase the imbalance. On a macroscopic scale, electroneutrality is always maintained throughout the solution. The migration represented in Figure 2.3.3c occurs simultaneously with the electron-transfer reactions.

Transference numbers are determined by the details of ionic conduction, which are understood mainly through measurements of either the resistance to current flow in solution or its reciprocal, the conductance, L (31, 32). The value of L for a segment of solution immersed in an electric field is directly proportional to the cross-sectional area perpendicular to the field vector and is inversely proportional to the length of the segment along the field. The proportionality constant is the *conductivity*, κ, which is an intrinsic property of the solution:

$$L = \kappa A / l \tag{2.3.8}$$

The conductance, L, is given in units of siemens ($S = \Omega^{-1}$), and κ is expressed in S cm^{-1} or Ω^{-1} cm^{-1}.

Since the passage of current through the solution is accomplished by the independent movement of different species, κ is the sum of contributions from all ionic species, i. It is intuitive that each component of κ is proportional to the concentration of the ion, the magnitude of its charge $|z_i|$, and some index of its migration velocity.

That index is the *mobility*, u_i, which is the limiting velocity of the ion in an electric field of unit strength. Mobility usually carries dimensions of cm^2 V^{-1} s^{-1} (i.e., cm/s per V/cm). When a field of strength $\mathcal{E}$ is applied to an ion, it will accelerate under the force imposed by the field until the frictional drag exactly counterbalances the electric force. Then, the ion continues its motion at that terminal velocity. This balance is represented in Figure 2.3.4.

The magnitude of the force exerted by the field is $|z_i| e\mathcal{E}$, where e is the electronic charge. The frictional drag can be approximated from the Stokes law as $6\pi\eta r v$, where η is the viscosity of the medium, r is the radius of the ion, and v is the velocity. When the terminal velocity is reached, we have by equation and rearrangement,

$$u_i = \frac{v}{\mathcal{E}} = \frac{|z_i| e}{6\pi\eta r} \tag{2.3.9}$$

The proportionality factor relating an individual ionic conductivity to charge, mobility, and concentration turns out to be the Faraday constant; thus

$$\boxed{\kappa = F \sum_i |z_i| u_i C_i} \tag{2.3.10}$$

Direction of movement

Drag force — Electric force
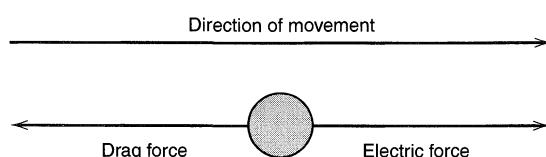
Figure 2.3.4 Forces on a charged particle moving in solution under the influence of an electric field. The forces balance at the terminal velocity.

The transference number for species i is merely the contribution to conductivity made by that species divided by the total conductivity:

$$t_i = \frac{|z_i| u_i C_i}{\sum\limits_{j} |z_j| u_j C_j} \qquad (2.3.11)$$

For solutions of simple, pure electrolytes (i.e., one positive and one negative ionic species), such as KCl, CaCl$_2$, and HNO$_3$, conductance is often quantified in terms of the *equivalent conductivity*, Λ, which is defined by

$$\Lambda = \frac{\kappa}{C_{eq}} \qquad (2.3.12)$$

where C_{eq} is the concentration of positive (or negative) charges. Thus, Λ expresses the conductivity per unit concentration of charge. Since $C|z| = C_{eq}$ for either ionic species in these systems, one finds from (2.3.10) and (2.3.12) that

$$\Lambda = F(u_+ + u_-) \qquad (2.3.13)$$

where u_+ refers to the cation and u_- to the anion. This relation suggests that Λ could be regarded as the sum of individual *equivalent ionic conductivities*,

$$\Lambda = \lambda_+ + \lambda_- \qquad (2.3.14)$$

hence we find

$$\lambda_i = F u_i \qquad (2.3.15)$$

In these simple solutions, then, the transference number t_i is given by

$$t_i = \frac{\lambda_i}{\Lambda} \qquad (2.3.16)$$

or, alternatively,

$$t_i = \frac{u_i}{u_+ + u_-} \qquad (2.3.17)$$

Transference numbers can be measured by several approaches (31, 32), and numerous data for pure solutions appear in the literature. Frequently, transference numbers are measured by noting concentration changes caused by electrolysis, as in the experiment shown in Figure 2.3.3 (see Problem 2.11). Table 2.3.1 displays a few values for aqueous solutions at 25°C. From results of this sort, one can evaluate the individual ionic conductivities, λ_i. Both λ_i and t_i depend on the concentration of the pure electrolyte, because interactions between ions tend to alter the mobilities (31–33). Lists of λ values, like Table 2.3.2, usually give figures for λ_{0i}, which are obtained by extrapolation to infinite dilution. In the absence of measured transference numbers, it is convenient to use these to estimate t_i for pure solutions by (2.3.16), or for mixed electrolytes by the following equivalent to (2.3.11),

$$t_i = \frac{|z_i| C_i \lambda_i}{\sum\limits_{j} |z_j| C_j \lambda_j} \qquad (2.3.18)$$

In addition to the liquid electrolytes that we have been considering, *solid electrolytes*, such as sodium β-alumina, the silver halides, and polymers like polyethylene

TABLE 2.3.1   Cation Transference Numbers for Aqueous Solutions at 25°C[a]

Electrolyte	Concentration, C_{eq}[b]			
	0.01	0.05	0.1	0.2
HCl	0.8251	0.8292	0.8314	0.8337
NaCl	0.3918	0.3876	0.3854	0.3821
KCl	0.4902	0.4899	0.4898	0.4894
NH_4Cl	0.4907	0.4905	0.4907	0.4911
KNO_3	0.5084	0.5093	0.5103	0.5120
Na_2SO_4	0.3848	0.3829	0.3828	0.3828
K_2SO_4	0.4829	0.4870	0.4890	0.4910

[a]From D. A. MacInnes, "The Principles of Electrochemistry," Dover, New York, 1961, p. 85 and references cited therein.

[b]Moles of positive (or negative) charge per liter.

oxide/$LiClO_4$ (34, 35), are sometimes used in electrochemical cells. In these materials, ions move under the influence of an electric field, even in the absence of solvent. For example, the conductivity of a single crystal of sodium β-alumina at room temperature is 0.035 S/cm, a value similar to that of aqueous solutions. Solid electrolytes are technologically important in the fabrication of batteries and electrochemical devices. In some of these materials (e.g., α-Ag_2S and AgBr), and unlike essentially all liquid electrolytes,

TABLE 2.3.2   Ionic Properties at Infinite Dilution in Aqueous Solutions at 25°C

Ion	λ_0, $cm^2\ \Omega^{-1}\ equiv^{-1}$[a]	u, $cm^2\ sec^{-1}\ V^{-1}$[b]
H^+	349.82	3.625×10^{-3}
K^+	73.52	7.619×10^{-4}
Na^+	50.11	5.193×10^{-4}
Li^+	38.69	4.010×10^{-4}
NH_4^+	73.4	7.61×10^{-4}
$\frac{1}{2}Ca^{2+}$	59.50	6.166×10^{-4}
OH^-	198	2.05×10^{-3}
Cl^-	76.34	7.912×10^{-4}
Br^-	78.4	8.13×10^{-4}
I^-	76.85	7.96×10^{-4}
NO_3^-	71.44	7.404×10^{-4}
OAc^-	40.9	4.24×10^{-4}
ClO_4^-	68.0	7.05×10^{-4}
$\frac{1}{2}SO_4^{2-}$	79.8	8.27×10^{-4}
HCO_3^-	44.48	4.610×10^{-4}
$\frac{1}{3}Fe(CN)_6^{3-}$	101.0	1.047×10^{-3}
$\frac{1}{4}Fe(CN)_6^{4-}$	110.5	1.145×10^{-3}

[a]From D. A. MacInnes, "The Principles of Electrochemistry," Dover, New York, 1961, p. 342

[b]Calculated from λ_0.
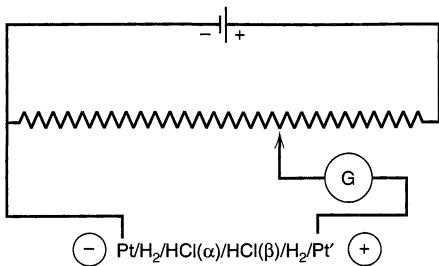
Figure 2.3.5 Experimental system for demonstrating reversible flow of charge through a cell with a liquid junction.

there is electronic conductivity as well as ionic conductivity. The relative contribution of electronic conduction through the solid electrolyte can be found by applying a potential to a cell that is too small to drive electrochemical reactions and noting the magnitude of the (nonfaradaic) current. Alternatively, an electrolysis can be carried out and the faradaic contribution determined separately (see Problem 2.12).
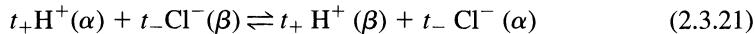
2.3.4 Calculation of Liquid Junction Potentials

Imagine the concentration cell (2.3.3) connected to a power supply as shown in Figure 2.3.5. The voltage from the supply opposes that from the cell, and one finds experimentally that it is possible to oppose the cell voltage exactly, so that no current flows through the galvanometer, G. If the magnitude of the opposing voltage is reduced very slightly, the cell operates spontaneously as described above, and electrons flow from Pt to Pt' in the external circuit. The process occurring at the liquid junction is the passage of an equivalent negative charge from right to left. If the opposing voltage is increased from the null point, the entire process reverses, including charge transfer through the interface between the electrolytes. The fact that an infinitesimal change in the driving force can reverse the direction of charge passage implies that the *electrochemical* free energy change for the whole process is zero.

These events can be divided into those involving the chemical transformations at the metal–solution interfaces:

$$\tfrac{1}{2}H_2 \rightleftharpoons H^+ (\alpha) + e(Pt) \tag{2.3.19}$$

$$H^+ (\beta) + e(Pt') \rightleftharpoons \tfrac{1}{2}H_2 \tag{2.3.20}$$

and that effecting charge transport at the liquid junction depicted in Figure 2.3.6:

$$t_+H^+(\alpha) + t_-Cl^-(\beta) \rightleftharpoons t_+ H^+ (\beta) + t_- Cl^- (\alpha) \tag{2.3.21}$$

Note that (2.3.19) and (2.3.20) are at strict equilibrium under the null-current condition; hence the electrochemical free energy change for each of them individually is zero. Of course, this is also true for their sum:

$$H^+ (\beta) + e(Pt') \rightleftharpoons H^+ (\alpha) + e(Pt), \tag{2.3.22}$$
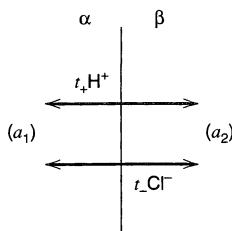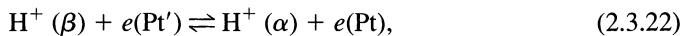
Figure 2.3.6 Reversible charge transfer through the liquid junction in Figure 2.3.5.

which describes the chemical change in the system. The sum of this equation and the charge transport relation, (2.3.21), describes the overall cell operation. However, since we have just learned that the electrochemical free energy changes for both the overall process and (2.3.22) are zero, we must conclude that the electrochemical free energy change for (2.3.21) is also zero. In other words, charge transport across the junction occurs in such a way that the electrochemical free energy change vanishes, even though it cannot be considered as a process at equilibrium. This important conclusion permits an approach to the calculation of junction potentials.

Let us focus first on the net chemical reaction, (2.3.22). Since the electrochemical free energy change is zero,

$$\bar{\mu}_{H+}^{\beta} + \bar{\mu}_{e}^{Pt'} = \bar{\mu}_{H+}^{\alpha} + \bar{\mu}_{e}^{Pt} \tag{2.3.23}$$

$$FE = F(\phi^{Pt'} - \phi^{Pt}) = \bar{\mu}_{H+}^{\beta} - \bar{\mu}_{H+}^{\alpha} \tag{2.3.24}$$

$$E = \frac{RT}{F} \ln \frac{a_2}{a_1} + (\phi^{\beta} - \phi^{\alpha}) \tag{2.3.25}$$

The first component of E in (2.3.25) is merely the Nernst relation for the reversible chemical change, and $\phi^{\beta} - \phi^{\alpha}$ is the liquid junction potential. In general, for a chemically reversible system under null current conditions,

$$E_{cell} = E_{Nernst} + E_j \tag{2.3.26}$$

hence the junction potential is always an additive perturbation onto the nernstian response.

To evaluate E_j, we consider (2.3.21), for which

$$t_+\bar{\mu}_{H+}^{\alpha} + t_-\bar{\mu}_{Cl-}^{\beta} = t_+\bar{\mu}_{H+}^{\beta} + t_-\bar{\mu}_{Cl-}^{\alpha} \tag{2.3.27}$$

Thus,

$$t_+(\bar{\mu}_{H+}^{\alpha} - \bar{\mu}_{H+}^{\beta}) + t_-(\bar{\mu}_{Cl-}^{\beta} - \bar{\mu}_{Cl-}^{\alpha}) = 0 \tag{2.3.28}$$

$$t_+\left[RT \ln \frac{a_{H+}^{\alpha}}{a_{H+}^{\beta}} + F(\phi^{\alpha} - \phi^{\beta})\right] + t_-\left[RT \ln \frac{a_{Cl-}^{\beta}}{a_{Cl-}^{\alpha}} - F(\phi^{\beta} - \phi^{\alpha})\right] = 0 \tag{2.3.29}$$

Activity coefficients for single ions cannot be measured with thermodynamic rigor (30, 36, 37–38); hence they are usually equated to a measurable *mean ionic activity coefficient*. Under this procedure, $a_{H+}^{\alpha} = a_{Cl-}^{\alpha} = a_1$ and $a_{H+}^{\beta} = a_{Cl-}^{\beta} = a_2$. Since $t_+ + t_- = 1$, we have

$$\boxed{E_j = (\phi^{\beta} - \phi^{\alpha}) = (t_+ - t_-) \frac{RT}{F} \ln \frac{a_1}{a_2}} \tag{2.3.30}$$

for a type 1 junction involving 1:1 electrolytes.

Consider, for example, HCl solutions with $a_1 = 0.01$ and $a_2 = 0.1$. We can see from Table 2.3.1 that $t_+ = 0.83$ and $t_- = 0.17$; hence at 25°C

$$E_j = (0.83 - 0.17)(59.1) \log\left(\frac{0.01}{0.1}\right) = -39.1 \text{ mV} \tag{2.3.31}$$

For the total cell,

$$E = 59.1 \log \frac{a_2}{a_1} + E_j = 59.1 - 39.1 = 20.0 \text{ mV} \tag{2.3.32}$$

thus, the junction potential is a substantial component of the measured cell potential.

In the derivation above, we made the implicit assumption that the transference numbers were constant throughout the system. This is a very good approximation for junctions

of type 1; hence (2.3.30) is not seriously compromised. For type 2 and type 3 systems, it clearly cannot be true. To consider these cases, one must imagine the junction region to be sectioned into an infinite number of volume elements having compositions that range smoothly from the pure α-phase composition to that of pure β. Transporting charge across one of these elements involves every ionic species in the element, and $t_i/|z_i|$ moles of species i must move for each mole of charge passed. Thus, the passage of positive charge from α toward β might be depicted as in Figure 2.3.7. One can see that the change in electrochemical free energy upon moving any species is $(t_i/z_i)d\overline{\mu}_i$ (recall that z_i is a signed quantity); therefore, the differential in free energy is

$$d\overline{G} = \sum_i \frac{t_i}{z_i} d\overline{\mu}_i \tag{2.3.33}$$

Integrating from the α phase to the β phase, we have

$$\int_\alpha^\beta d\overline{G} = 0 = \sum_i \int_\alpha^\beta \frac{t_i}{z_i} d\overline{\mu}_i \tag{2.3.34}$$

If μ_i^0 for the α phase is the same as that for the β phase (e.g., if both are aqueous solutions),

$$\sum_i \int_\alpha^\beta \frac{t_i}{z_i} RT\, d\ln a_i + \left(\sum_i t_i\right) F \int_\alpha^\beta d\phi = 0 \tag{2.3.35}$$

Since $\Sigma t_i = 1$,

$$\boxed{E_j = \phi^\beta - \phi^\alpha = \frac{-RT}{F} \sum_i \int_\alpha^\beta \frac{t_i}{z_i} d\ln a_i} \tag{2.3.36}$$

which is the general expression for the junction potential.

It is easy to see now that (2.3.30) is a special case for type 1 junctions between 1:1 electrolytes having constant t_i. Note that E_j is a strong function of t_+ and t_-, and that it actually vanishes if $t_+ = t_-$. The value of E_j as a function of t_+ for a 1:1 electrolyte with $a_1/a_2 = 10$ is

$$E_j = 59.1\,(2t_+ - 1)\,\text{mV} \tag{2.3.37}$$

at 25°C. For example, the cell

$$\text{Ag/AgCl/KCl (0.1 }M\text{)/KCl (0.01 }M\text{)/AgCl/Ag} \tag{2.3.38}$$

has $t_+ = 0.49$; hence $E_j = -1.2$ mV.

While type 1 junctions can be treated with some rigor and are independent of the method of forming the junction, type 2 and type 3 junctions have potentials that depend on the technique of junction formation (e.g., static or flowing) and can be treated only in an approximate manner. Different approaches to junction formation apparently lead to
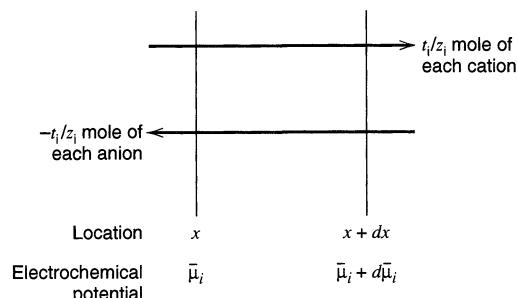
Figure 2.3.7 Transfer of net positive charge from left to right through an infinitesimal segment of a junction region. Each species must contribute t_i moles of charge per mole of overall charge transported; hence $t_i|z_i|$ moles of that species must migrate.
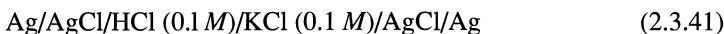
different profiles of t_i through the junction, which in turn lead to different integrals for (2.3.36). Approximate values for E_j can be obtained by assuming (a) that concentrations of ions everywhere in the junction are equivalent to activities and (b) that the concentration of each ion follows a linear transition between the two phases. Then, (2.3.36) can be integrated to give the *Henderson equation* (24, 30):

$$E_j = \frac{\sum_i \dfrac{|z_i| u_i}{z_i} [C_i(\beta) - C_i(\alpha)]}{\sum_i |z_i| u_i [C_i(\beta) - C_i(\alpha)]} \frac{RT}{F} \ln \frac{\sum_i |z_i| u_i C_i(\alpha)}{\sum_i |z_i| u_i C_i(\beta)} \tag{2.3.39}$$

where u_i is the mobility of species i, and C_i is its molar concentration. For type 2 junctions between 1:1 electrolytes, this equation collapses to the *Lewis–Sargent relation*:

$$E_j = \pm \frac{RT}{F} \ln \frac{\Lambda_\beta}{\Lambda_\alpha} \tag{2.3.40}$$

where the positive sign corresponds to a junction with a common cation in the two phases, and the negative sign applies to the case with a common anion. As an example, consider the cell

$$\text{Ag/AgCl/HCl } (0.1\,M)/\text{KCl } (0.1\,M)/\text{AgCl/Ag} \tag{2.3.41}$$

for which E_{cell} is essentially E_j. The measured value at 25°C is 28 ± 1 mV, depending on the technique of junction formation (30), while the estimated value from (2.3.40) and the data of Table 2.3.2 is 26.8 mV.

2.3.5 Minimizing Liquid Junction Potentials

In most electrochemical experiments, the junction potential is an additional troublesome factor, so attempts are often made to minimize it. Alternatively, one hopes that it is small or that it at least remains constant. A familiar method for minimizing E_j is to replace the junction, for example,

$$\text{HCl } (C_1)/\text{NaCl } (C_2) \tag{2.3.42}$$

with a system featuring a concentrated solution in an intermediate *salt bridge*, where the solution in the bridge has ions of nearly equal mobility. Such a system is

$$\text{HCl } (C_1)/\text{KCl } (C)/\text{NaCl } (C_2) \tag{2.3.43}$$
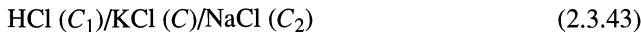
Table 2.3.3 lists some measured junction potentials for the cell,

$$\text{Hg/Hg}_2\text{Cl}_2/\text{HCl } (0.1\,M)/\text{KCl } (C)/\text{KCl } (0.1\,M)/\text{Hg}_2\text{Cl}_2/\text{Hg} \tag{2.3.44}$$

As C increases, E_j falls markedly, because ionic transport at the two junctions is dominated more and more extensively by the massive amounts of KCl. The series junctions become more similar in magnitude and have opposite polarities; hence they tend to cancel. Solutions used in aqueous salt bridges usually contain KCl ($t_+ = 0.49$, $t_- = 0.51$) or, where Cl^- is deleterious, KNO_3 ($t_+ = 0.51$, $t_- = 0.49$). Other concentrated solutions with equitransferent ions that have been suggested (39) for salt bridges include CsCl ($t_+ = 0.5025$), RbBr ($t_+ = 0.4958$), and NH_4I ($t_+ = 0.4906$). In many measurements, such as the determination of pH, it is sufficient if the junction potential remains constant between calibra-

TABLE 2.3.3 Effect of a Salt Bridge on Measured Junction Potentials[a]
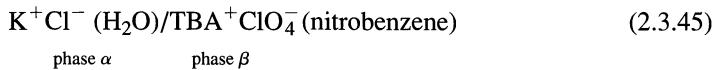
Concentration of KCl, $C(M)$	E_j, mV
0.1	27
0.2	20
0.5	13
1.0	8.4
2.5	3.4
3.5	1.1
4.2 (saturated)	<1

[a]See J. J. Lingane, "Electroanalytical Chemistry," Wiley-Interscience, New York, 1958, p. 65. Original data from H. A. Fales and W. C. Vosburgh, *J. Am. Chem. Soc..* **40**, 1291 (1918); E. A. Guggenheim, *ibid.*, **52**, 1315 (1930); and A. L. Ferguson, K. Van Lente, and R. Hitchens, *ibid.*, **54**, 1285 (1932).
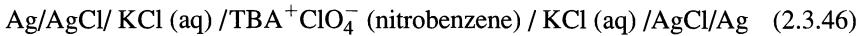
tion (e.g., with a standard buffer or solution) and measurement. However, variations in E_j of 1–2 mV can be expected, and should be considered in any interpretations made from potentiometric data.

2.3.6 Junctions of Two Immiscible Liquids

Another junction of interest is that between two immiscible electrolyte solutions (40–44). A typical junction of this type would be

$$K^+Cl^- \ (H_2O)/TBA^+ClO_4^- \ (\text{nitrobenzene}) \qquad (2.3.45)$$
$$\text{phase } \alpha \qquad \text{phase } \beta$$

where $TBA^+ClO_4^-$ is tetra-*n*-butylammonium perchlorate. Of interest in connection with ion-selective electrodes (Section 2.4.3) and as models for biological membranes are related cells with immiscible liquids between two aqueous phases, such as

$$Ag/AgCl/\ KCl\ (aq)\ /TBA^+ClO_4^-\ (\text{nitrobenzene})\ /\ KCl\ (aq)\ /AgCl/Ag \quad (2.3.46)$$

where the intermediate liquid layer behaves as a membrane. The treatment of the potentials across junctions like (2.3.45) is similar to that given earlier in this section, except that the standard free energies of a species i in the two phases, $\mu_i^{0\alpha}$ and $\mu_i^{0\beta}$, are now different. The junction potential then becomes (40, 41)

$$\phi^\beta - \phi^\alpha = -\frac{1}{z_i F}\left[\Delta G^{0\alpha\rightarrow\beta}_{\text{transfer},i} + RT \ln\left(\frac{a_i^\beta}{a_i^\alpha}\right)\right] \qquad (2.3.47)$$

where $\Delta G^{0\alpha\rightarrow\beta}_{\text{transfer},i}$ is the standard free energy required to transfer species i with charge z_i between the two phases and is defined as

$$\Delta G^{0\alpha\rightarrow\beta}_{\text{transfer},i} = \mu_i^{0\beta} - \mu_i^{0\alpha} \qquad (2.3.48)$$

This quantity can be estimated, for example, from solubility data, but only with an extrathermodynamic assumption of some kind. For example, for the salt tetraphenylarsonium tetraphenylborate ($TPAs^+TPB^-$), it is widely assumed that the free energy of solvation ($\Delta G^0_{\text{solvn}}$) of $TPAs^+$ is equal to that of TPB^-, since both are large ions with most of the charge buried deep inside the surrounding phenyl rings (45). Consequently, the in-

dividual ion solvation energies are taken as one-half of the solvation energy of the salt, which is measurable from the solubility product in a given solvent. That is,

$$\Delta G^0_{\text{solvn}} \, (\text{TPAs}^+) = \Delta G^0_{\text{solvn}}(\text{TPB}^-) = \tfrac{1}{2}\Delta G^0_{\text{solvn}} \, (\text{TPAs}^+\text{TPB}^-) \qquad (2.3.49)$$

$$\Delta G^{0\alpha\rightarrow\beta}_{\text{transfer, TPAs}+} = \Delta G^0_{\text{solvn}}(\text{TPAs}^+, \beta) - \Delta G^0_{\text{solvn}} \, (\text{TPAs}^+, \alpha) \qquad (2.3.50)$$

The free energy of transfer can also be obtained from the partitioning of the salt between the phases α and β. For each ion, the value determined in this way should be the same as that calculated in (2.3.50), if the intersolubility of α and β is very small.

The *rate* of transfer of ions across interfaces between immiscible liquids is also of interest and can be obtained from electrochemical measurements (Section 6.8).

▶ 2.4 SELECTIVE ELECTRODES (46–55)

2.4.1 Selective Interfaces

Suppose one could create an interface between two electrolyte phases across which only a single ion could penetrate. A selectively permeable membrane might be used as a separator to accomplish this end. Equation 2.3.34 would still apply; but it could be simplified by recognizing that the transference number for the permeating ion is unity, while that for every other ion is zero. If both electrolytes are in a common solvent, one obtains by integration

$$\frac{RT}{z_i} \ln \frac{a_i^\beta}{a_i^\alpha} + F(\phi^\beta - \phi^\alpha) = 0 \qquad (2.4.1)$$

where ion i is the permeating species. Rearrangement gives

$$E_m = -\frac{RT}{z_i F} \ln \frac{a_i^\beta}{a_i^\alpha} \qquad (2.4.2)$$

If the activity of species i is held constant in one phase, the potential difference between the two phases (often called the *membrane potential*, E_m) responds in a Nernst-like fashion to the ion's activity in the other phase.

This idea is the essence of ion-selective electrodes. Measurements with these devices are essentially determinations of membrane potentials, which themselves comprise junction potentials between electrolyte phases. The performance of any single system is determined largely by the degree to which the species of interest can be made to dominate charge transport in part of the membrane. We will see below that real devices are fairly complicated, and that selectivity in charge transport throughout the membrane is both rarely achieved and actually unnecessary.

Many ion-selective interfaces have been studied, and several different types of electrodes have been marketed commercially. We will examine the basic strategies for introducing selectivity by considering a few of them here. The glass membrane is our starting point because it offers a fairly complete view of the fundamentals as well as the usual complications found in practical devices.

2.4.2 Glass Electrodes

The ion-selective properties of glass/electrolyte interfaces were recognized early in the 20th century, and glass electrodes have been used since then for measurements of pH and the activities of alkali ions (24, 37, 46–55). Figure 2.4.1 depicts the construction of a typi-
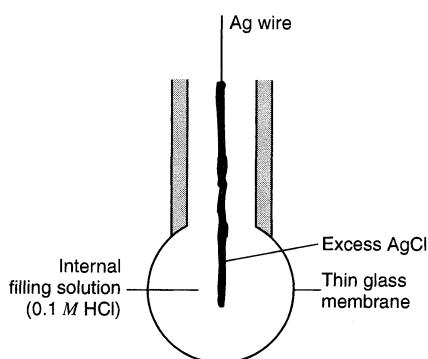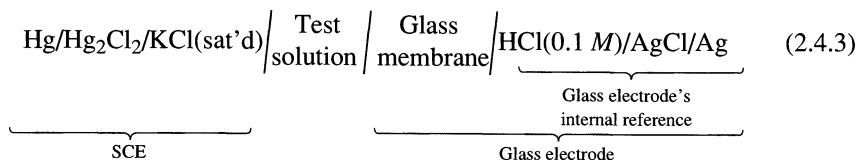
Figure 2.4.1 A typical glass electrode.

cal device. To make measurements, the thin membrane is fully immersed in the test solution, and the potential of the electrode is registered with respect to a reference electrode such as an SCE. Thus, the cell becomes,

$$\mathrm{Hg/Hg_2Cl_2/KCl(sat'd)} \left| \begin{array}{c} \mathrm{Test} \\ \mathrm{solution} \end{array} \right| \begin{array}{c} \mathrm{Glass} \\ \mathrm{membrane} \end{array} \left| \underbrace{\mathrm{HCl(0.1}\ M\mathrm{)/AgCl/Ag}}_{\substack{\mathrm{Glass\ electrode's} \\ \mathrm{internal\ reference}}} \right. \qquad (2.4.3)$$

$$\underbrace{\hphantom{\mathrm{Hg/Hg_2Cl_2/KCl(sat'd)}}}_{\mathrm{SCE}} \qquad\qquad \underbrace{\hphantom{\mathrm{Glass\ membrane\ HCl(0.1}\ M\mathrm{)/AgCl/Ag}}}_{\mathrm{Glass\ electrode}}$$

The properties of the test solution influence the overall potential difference of the cell at two points. One of them is the liquid junction between the SCE and the test solution. From the considerations of Section 2.3.5, we can hope that the potential difference there is small and constant. The remaining contribution from the test solution comes from its effect on the potential difference across the glass membrane. Since all of the other interfaces in the cell feature phases of constant composition, changes in the cell potential can be wholly ascribed to the junction between the glass membrane and the test solution. If that interface is selective toward a single species i, the cell potential is

$$E = \mathrm{constant} + \frac{RT}{z_i F} \ln a_i^{\mathrm{soln}} \qquad (2.4.4)$$

where the constant term is the sum of potential differences at all of the other interfaces.[17] The constant term is evaluated by "standardizing" the electrode, that is, by measuring E for a cell in which the test solution is replaced by a standard solution having a known activity for species i.[18]

Actually, the operation of the glass phase is rather complicated (24, 37, 46–48, 51). The bulk of the membrane, which might be about 50 μm thick, is dry glass through which charge transport occurs exclusively by the mobile cations present in the glass. Usually, these are alkali ions, such as Na^+ or Li^+. Hydrogen ion from solution does not contribute to conduction in this region. The faces of the membrane in contact with solution differ from the bulk, in that the silicate structure of the glass is hydrated. As shown in Figure 2.4.2, the hydrated layers are thin. Interactions between the glass and the adjacent solution, which occur exclusively in the hydrated zone, are facilitated kinetically by the swelling that accompanies the hydration.

---

[17]Equation 2.4.4 is derived from (2.4.2) by recognizing the test solution as phase α and the internal filling solution of the electrode as phase β. See also Figures 2.3.5 and 2.3.6.

[18]By the phrase "activity for species i" we mean the concentration of i multiplied by the mean ionic activity coefficient. See Section 2.3.4 for a commentary and references related to the concept of single-ion activities.
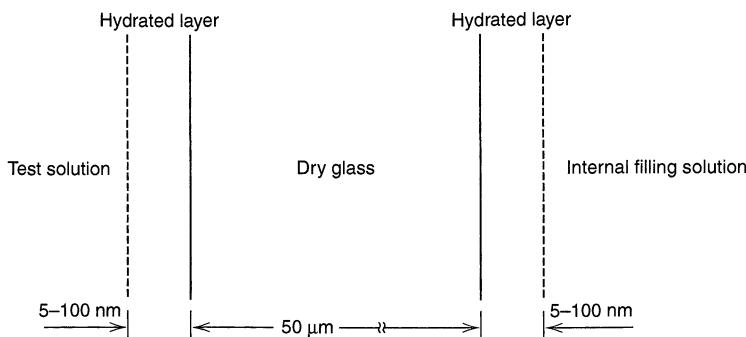
Figure 2.4.2 Schematic profile through a glass membrane.

The membrane potentials appear because the silicate network has an affinity for certain cations, which are adsorbed (probably at fixed anionic sites) within the structure. This action creates a charge separation that alters the interfacial potential difference. That potential difference, in turn, alters the rates of adsorption and desorption. Thus, the rates are gradually brought into balance by a mechanism resembling the one responsible for the establishment of junction potentials, as discussed above.

Obviously, the glass membrane does not adhere to the simplified idea of a selectively permeable membrane. In fact, it may not be at all permeable to some of the ions of greatest interest, such as H^+. Thus, the transference number of such an ion cannot be unity throughout the membrane, and it may actually be zero in certain zones. Can we still understand the observed selective response? The answer is yes, provided that the ion of interest dominates charge transport in the interfacial regions of the membrane.

Let us consider a model for the glass membrane like that shown in Figure 2.4.3. The glass will be considered as comprising three regions. In the interfacial zones, m' and m'', there is rapid attainment of equilibrium with constituents in solution, so that each adsorbing cation has an activity reflecting its corresponding activity in the adjacent solution. The bulk of the glass is denoted by m, and we presume that conduction there takes place by a single species, which is taken as Na^+ for the sake of this argument. The whole system therefore comprises five phases, and the overall difference in potential across the membrane is the sum of four contributions from the junctions between the various zones:

$$E_m = (\phi^\beta - \phi^{m''}) + (\phi^{m''} - \phi^m) + (\phi^m - \phi^{m'}) + (\phi^{m'} - \phi^\alpha) \tag{2.4.5}$$
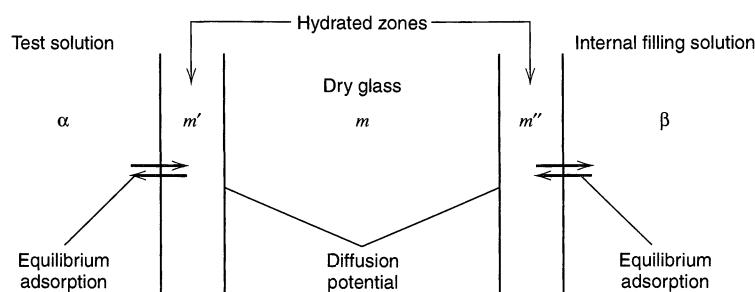
Figure 2.4.3 Model for treating the membrane potential across a glass barrier.

The first and last terms are interfacial potential differences arising from an *equilibrium balance* of selective charge exchange across an interface. This condition is known as *Donnan equilibrium* (24, 51). The magnitude of the resulting potential difference can be evaluated from electrochemical potentials. Suppose we have Na^+ and H^+ as interfacially active ions. Then at the α/m' interface,

$$\bar{\mu}_{H^+}^{\alpha} = \bar{\mu}_{H^+}^{m'} \tag{2.4.6}$$

$$\bar{\mu}_{Na^+}^{\alpha} = \bar{\mu}_{Na^+}^{m'} \tag{2.4.7}$$

Expanding (2.4.6), we have

$$\mu_{H^+}^{0\alpha} + RT \ln a_{H^+}^{\alpha} + F\phi^{\alpha} = \mu_{H^+}^{0m'} + RT \ln a_{H^+}^{m'} + F\phi^{m'} \tag{2.4.8}$$

and rearrangement gives

$$(\phi^{m'} - \phi^{\alpha}) = \frac{\mu_{H^+}^{0\alpha} - \mu_{H^+}^{0m'}}{F} + \frac{RT}{F} \ln \frac{a_{H^+}^{\alpha}}{a_{H^+}^{m'}} \tag{2.4.9}$$

An equivalent treatment of the interface between β and m'' gives

$$(\phi^{\beta} - \phi^{m''}) = \frac{\mu_{H^+}^{0m''} - \mu_{H^+}^{0\beta}}{F} + \frac{RT}{F} \ln \frac{a_{H^+}^{m''}}{a_{H^+}^{\beta}} \tag{2.4.10}$$

Note that $\mu_{H^+}^{0\alpha} = \mu_{H^+}^{0\beta}$, because both α and β are aqueous solutions. Similarly, $\mu_{H^+}^{0m'} = \mu_{H^+}^{0m''}$. When we add (2.4.9) and (2.4.10) later in this development, these equivalencies will cause the terms involving μ^0 to disappear.

The second and third components in (2.4.5) are junction potentials within the glass membrane. In the specialized literature, they are called *diffusion potentials*, because they arise from differential ionic diffusion in the manner discussed in Section 2.3.2. The systems correspond to type 3 junctions as defined there.

We can treat them through a variant of the Henderson equation, (2.3.39), which was introduced earlier in Section 2.3.4. The usual form of this equation is derived from (2.3.36) by neglecting activity effects and assuming linear concentration profiles through the junction. Here, we are interested only in univalent positive charge carriers; hence we can specialize (2.3.39) for the interface between m and m' as

$$(\phi^{m} - \phi^{m'}) = \frac{RT}{F} \ln \frac{u_{H^+} a_{H^+}^{m'} + u_{Na^+} a_{Na^+}^{m'}}{u_{Na^+} a_{Na^+}^{m}} \tag{2.4.11}$$

where the concentrations have been replaced by activities. Also, for the interface between m and m'',

$$(\phi^{m''} - \phi^{m}) = \frac{RT}{F} \ln \frac{u_{Na^+} a_{Na^+}^{m}}{u_{H^+} a_{H^+}^{m''} + u_{Na^+} a_{Na^+}^{m''}} \tag{2.4.12}$$

Now let us add the component potential differences, (2.4.9)–(2.4.12), as dictated by (2.4.5), to obtain the whole potential difference across the membrane:[19]

$$E_m = \frac{RT}{F} \ln \frac{a_{H^+}^{\alpha} + a_{H^+}^{m''}}{a_{H^+}^{\beta} + a_{H^+}^{m'}} \qquad \text{(Donnan Term)}$$

$$+ \frac{RT}{F} \ln \frac{(u_{Na^+}/u_{H^+}) a_{Na^+}^{m'} + a_{H^+}^{m'}}{(u_{Na^+}/u_{H^+}) a_{Na^+}^{m''} + a_{H^+}^{m''}} \qquad \text{(Diffusion term)} \tag{2.4.13}$$

[19]Note that the diffusion term here is the same as that which would be predicted by the Henderson equation from the compositions of m' and m'' without considering m as a separate phase. Many treatments of this problem follow such an approach. We have added the phase m because the three-phase model for the membrane is more realistic with regard to the assumptions underlying the Henderson equation.
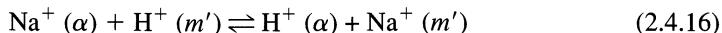
Some important simplifications can be made in this result. First, we combine the two terms in (2.4.13) and rearrange the parameters to give

$$E_m = \frac{RT}{F} \ln \frac{(u_{Na+}/u_{H+})(a_H^\alpha + a_{Na}^{m'}/a_{H+}^{m'}) + a_{H+}^\alpha}{(u_{Na+}/u_{H+})(a_H^\beta + a_{Na}^{m''}/a_{H+}^{m''}) + a_{H+}^\beta} \quad (2.4.14)$$

Now consider (2.4.6) and (2.4.7), which apply simultaneously. Their sum must also be true:

$$\overline{\mu}_{Na+}^\alpha + \overline{\mu}_{H+}^{m'} = \overline{\mu}_{H+}^\alpha + \overline{\mu}_{Na+}^{m'} \quad (2.4.15)$$

This equation is a free energy balance for the ion-exchange reaction:

$$Na^+ (\alpha) + H^+ (m') \rightleftharpoons H^+ (\alpha) + Na^+ (m') \quad (2.4.16)$$

Since it does not involve net charge transfer, it is not sensitive to the interfacial potential difference [see Section 2.2.4(c)], and it has an equilibrium constant given by

$$K_{H+,Na+} = \frac{a_{H+}^\alpha a_{Na+}^{m'}}{a_{H+}^{m'} a_{Na+}^\alpha} \quad (2.4.17)$$

An equivalent expression, involving the same numeric value of $K_{H+,Na+}$, would apply to the interface between phases β and m'. These relations can be substituted into (2.4.14) to give

$$E_m = \frac{RT}{F} \ln \frac{(u_{Na+}/u_{H+})K_{H+,Na+} a_{Na+}^\alpha + a_{H+}^\alpha}{(u_{Na+}/u_{H+})K_{H+,Na+} a_{Na+}^\beta + a_{H+}^\beta} \quad (2.4.18)$$

Since $K_{H+,Na+}$ and u_{Na+}/u_{H+} are constants of the experiment, it is convenient to define their product as the *potentiometric selectivity coefficient*, $k_{H+,Na+}^{pot}$:

$$E_m = \frac{RT}{F} \ln \frac{a_{H+}^\alpha + k_{H+,Na+}^{pot} a_{Na+}^\alpha}{a_{H+}^\beta + k_{H+,Na+}^{pot} a_{Na+}^\beta} \quad (2.3.19)$$

If the β phase is the internal filling solution (of constant composition) and the α phase is the test solution, then the overall potential of the cell is

$$\boxed{E = \text{constant} + \frac{RT}{F} \ln (a_{H+}^\alpha + k_{H+,Na+}^{pot} a_{Na+}^\alpha)} \quad (2.4.20)$$

This expression tells us that the cell potential is responsive to the activities of both Na^+ and H^+ in the test solution, and that the degree of selectivity between these species is defined $k_{H+,Na+}^{pot}$. If the product $k_{H+,Na+}^{pot} a_{Na+}^\alpha$ is much less than a_{H+}^α, then the membrane responds essentially exclusively to H^+. When that condition applies, charge exchange between the phases α and m' is dominated by H^+.

We have formulated this problem in a manner that considers only Na^+ and H^+ as active species. Glass membranes also respond to other ions, such as Li^+, K^+, Ag^+, and NH_4^+. The relative responses can be expressed through the corresponding potentiometric selectivity coefficients (see Problem 2.16 for some typical numbers), which are influenced to a great extent by the composition of the glass. Different types of electrodes, based on different types of glass, are marketed. They are broadly classified as (a) *pH electrodes* with a selectivity order $H^+ >>> Na^+ > K^+, Rb^+, Cs^+ >> Ca^{2+}$, (b) *sodium-sensitive electrodes* with the order $Ag^+ > H^+ > Na^+ >> K^+, Li^+ >> Ca^{2+}$, and (c) a more general *cation-sensitive electrode* with a narrower range of selectivities in the order $H^+ > K^+ > Na^+ > NH_4^+, Li^+ >> Ca^{2+}$.

There is a large literature on the design, performance, and theory of glass electrodes (37, 46–55). The interested reader is referred to it for more advanced discussions.

2.4.3 Other Ion-Selective Electrodes

The principles that we have just reviewed also apply to other types of selective membranes (48, 50–59). They fall generally into two categories.

(a) Solid-State Membranes

Like the glass membrane, which is a member of this group, the remaining common solid-state membranes are electrolytes having tendencies toward the preferential adsorption of certain ions on their surfaces.

Consider, for example, the single-crystal LaF_3 membrane, which is doped with EuF_2 to create fluoride vacancies that allow ionic conduction by fluoride. Its surface selectively accommodates F^- to the virtual exclusion of other species except OH^-.

Other devices are made from precipitates of insoluble salts, such as AgCl, AgBr, AgI, Ag_2S, CuS, CdS, and PbS. The precipitates are usually pressed into pellets or are suspended in polymer matrices. The silver salts conduct by mobile Ag^+ ions, but the heavy metal sulfides are usually mixed with Ag_2S, since they are not very conductive. The surfaces of these membranes are generally sensitive to the ions comprising the salts, as well as to other species that tend to form very insoluble precipitates with a constituent ion. For example, the Ag_2S membrane responds to Ag^+, S^{2-}, and Hg^{2+}. Likewise, the AgCl membrane is sensitive to Ag^+, Cl^-, Br^-, I^-, CN^-, and OH^-.

(b) Liquid and Polymer Membranes

An alternative structure utilizes a hydrophobic liquid membrane as the sensing element. The liquid is stabilized physically between an aqueous internal filling solution and an aqueous test solution by allowing it to permeate a porous, lipophilic diaphragm. A reservoir contacting the outer edges of the diaphragm contains this liquid. Chelating agents with selectivity toward ions of interest are dissolved in it, and they provide the mechanism for selective charge transport across the boundaries of the membrane.

A device based on these principles is a calcium-selective electrode. The hydrophobic solvent might be dioctylphenylphosphonate, and the chelating agent might be the sodium salt of an alkyl phosphate ester, $(RO)_2 PO_2^- Na^+$, where R is an aliphatic chain having 8–18 carbons. The membrane is sensitive to Ca^{2+}, Zn^{2+}, Fe^{2+}, Pb^{2+}, Cu^{2+}, tetra-alkylammonium ions, and still other species to lesser degrees. "Water hardness" electrodes are based on similar agents, but are designed to show virtually equal responses to Ca^{2+} and Mg^{2+}.

Other systems featuring liquid ion-exchangers are available for anions, such as NO_3^-, ClO_4^-, and Cl^-. Nitrate and perchlorate are sensed by membranes including alkylated 1,10-phenanthroline complexes of Ni^{2+} and Fe^{2+}, respectively. All three ions are active at other membranes based on quaternary ammonium salts.

In commercial electrodes, the liquid ion-exchanger is in a form in which the chelating agent is immobilized in a hydrophobic polymer membrane like poly(vinylchloride) (Figure 2.4.4). Electrodes based on this design (called *polymer* or *plastic membrane ISEs*) are more rugged and generally offer superior performance.

Liquid ion-exchangers all feature charged chelating agents, and various ion-exchange equilibria play a role in their operation. A related type of device, also featuring a stabilized liquid membrane, involves uncharged chelating agents that enable the transport of charge by selectively complexing certain ions. These agents are sometimes called *neutral carriers*. Systems based on them typically also involve the presence of some anionic sites in the membrane, either naturally occurring or added in the form of hydrophobic ions, and these anionic sites contribute to the ion-exchange process (56–58). It has also been proposed that electrodes based on neutral carriers operate by a phase-boundary (i.e., adsorption), rather than a carrier mechanism (59).
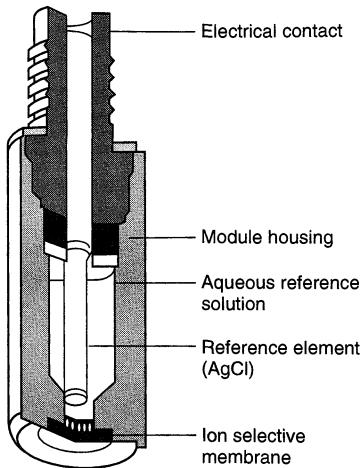
Figure 2.4.4 A typical plastic membrane ISE. [Courtesy of Orion Research, Inc.]

For example, potassium-selective electrodes can be constructed with the natural macrocycle valinomycin as a neutral carrier in diphenyl ether. This membrane has a much higher sensitivity to K^+ than to Na^+, Li^+, Mg^{2+}, Ca^{2+}, or H^+; but Rb^+ and Cs^+ are sensed to much the same degree as K^+. The selectivity seems to rest mostly on the molecular recognition of the target ion by the complexing site of the carrier.

(c) Commercial Devices

Table 2.4.1 is a listing of typical commercial ion-selective electrodes, the pH and concentration ranges over which they operate, and typical interferences. Selectivity coefficients for many of these electrodes are available (55, 57).

TABLE 2.4.1 Typical Commercially Available Ion-Selective Electrodes

Species	Type^a	Concentration Range(M)	pH Range	Interferences
Ammonium (NH_4^+)	L	10^{-1} to 10^{-6}	5–8	K^+, Na^+, Mg^{2+}
Barium (Ba^{2+})	L	10^{-1} to 10^{-5}	5–9	K^+, Na^+, Ca^{2+}
Bromide (Br^-)	S	1 to 10^{-5}	2–12	I^-, S^{2-}, CN^-
Cadmium (Cd^{2+})	S	10^{-1} to 10^{-7}	3–7	Ag^+, Hg^{2+}, Cu^{2+}, Pb^{2+}, Fe^{3+}
Calcium (Ca^{2+})	L	1 to 10^{-7}	4–9	Ba^{2+}, Mg^{2+}, Na^+, Pb^{2+}
Chloride (Cl^-)	S	1 to 5×10^{-5}	2–11	I^-, S^{2-}, CN^-, Br^-
Copper (Cu^{2+})	S	10^{-1} to 10^{-7}	0–7	Ag^+, Hg^{2+}, S^{2-}, Cl^-, Br^-
Cyanide (CN^-)	S	10^{-2} to 10^{-6}	10–14	S^{2-}
Fluoride (F^-)	S	1 to 10^{-7}	5–8	OH^-
Iodide (I^-)	S	1 to 10^{-7}	3–12	S^{2-}
Lead (Pb^{2+})	S	10^{-1} to 10^{-6}	0–9	Ag^+, Hg^{2+}, S^{2-}, Cd^{2+}, Cu^{2+}, Fe^{3+}
Nitrate (NO_3^-)	L	1 to 5×10^{-6}	3–10	Cl^-, Br^-, NO_2^-, F^-, SO_4^{2-}
Nitrite (NO_2^-)	L	1 to 10^{-6}	3–10	Cl^-, Br^-, NO_3^-, F^-, SO_4^{2-}
Potassium (K^+)	L	1 to 10^{-6}	4–9	Na^+, Ca^{2+}, Mg^{2+}
Silver (Ag^+)	S	1 to 10^{-7}	2–9	S^{2-}, Hg^{2+}
Sodium (Na^+)	G	Sat'd to 10^{-6}	9–12	Li^+, K^+, NH_4^+
Sulfide (S^{2-})	S	1 to 10^{-7}	12–14	Ag^+, Hg^{2+}

^{a}G = glass; L = liquid membrane; S = solid-state. Typical temperature ranges are 0–50°C for liquid-membrane and 0–80°C for solid-state electrodes.

(d) *Detection Limits*

As shown in Table 2.4.1, the lower limit for detection of an ion with an ISE is generally 10^{-6} to 10^{-7} M. This limit is largely governed by the leaching of ions from the internal electrolyte into the sample solution (60). The leakage can be prevented by using a lower concentration of the ion of interest in the internal electrolyte, so that the concentration gradient established in the membrane causes an ion flux from the sample to the inner electrolyte. This low concentration can be maintained with an *ion buffer*, that is, a mixture of the metal ion with an excess of a strong complexing agent. In addition, a high concentration of a second potential-determining ion is added to the internal solution. Under these conditions, the lower detection limit can be considerably improved. For example, for a conventional liquid-membrane Pb^{2+} electrode with an internal filling solution of 5×10^{-4} M Pb^{2+} and 5×10^{-2} M Mg^{2+}, the detection limit for Pb^{2+} was 4×10^{-6} M. When the internal solution was changed to 10^{-3} M Pb^{2+} and 5×10^{-2} M Na_2EDTA (yielding a free $[Pb^{2+}] = 10^{-12}$ M), the detection limit decreased to 5×10^{-12} M (61). In the internal solution, the dominant potential-determining ion is Na^+ at 0.1 M.

2.4.4 Gas-Sensing Electrodes

Figure 2.4.5 depicts the structure of a typical potentiometric gas-sensing electrode (62). In general, such a device involves a glass pH electrode that is protected from the test solution by a polymer diaphragm. Between the glass membrane and the diaphragm is a small volume of electrolyte. Small molecules, such as SO_2, NH_3, and CO_2, can penetrate the membrane and interact with the trapped electrolyte by reactions that produce changes in pH. The glass electrode responds to the alterations in acidity.

Electrochemical cells that use a solid electrolyte composed of zirconium dioxide containing Y_2O_3 (yttria-stabilized zirconia) are available to measure the oxygen content of gases at high temperature. In fact, sensors of this type are widely used to monitor the exhaust gas from the internal combustion engines of motor vehicles, so that the air-to-fuel mixture can be controlled to minimize the emission of pollutants such as CO and NO_x. This solid electrolyte shows good conductivity only at high temperatures (500–1,000°C), where the conduction process is the migration of oxide ions. A typical sensor is composed of a tube of zirconia with Pt electrodes deposited on the inside and outside of the tube. The outside electrode contacts air with a known partial pressure of
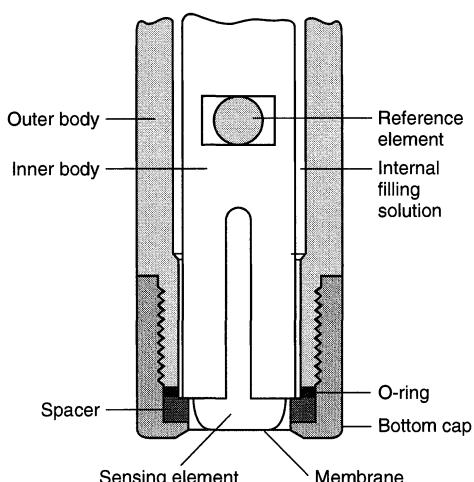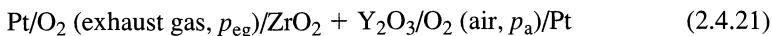
Figure 2.4.5 Structure of a gas-sensing electrode. [Courtesy of Orion Research, Inc.]

oxygen, p_a, and serves as the reference electrode. The inside of the tube is exposed to the hot exhaust gas with a lower oxygen partial pressure, p_{eg}. The cell configuration can thus be written

$$Pt/O_2 \text{ (exhaust gas, } p_{eg})/ZrO_2 + Y_2O_3/O_2 \text{ (air, } p_a)/Pt \qquad (2.4.21)$$
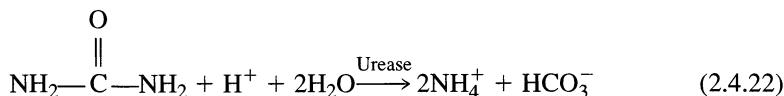
and the potential of this oxygen concentration cell can be used to measure p_{eg} (Problem 2.19).

We note here that the widely employed *Clark oxygen electrode* differs fundamentally from these devices (18, 63). The Clark device is similar in construction to the apparatus of Figure 2.4.5, in that a polymer membrane traps an electrolyte against a sensing surface. However, the sensor is a platinum electrode, and the analytical signal is the steady-state *current* flow due to the faradaic reduction of molecular oxygen.

2.4.5 Enzyme-Coupled Devices

The natural specificity of enzyme-catalyzed reactions can be used as the basis for selective detection of analytes (49, 64–68). One fruitful approach has featured potentiometric sensors with a structure similar to that of Figure 2.4.5, with the difference that the gap between the ion-selective electrode and the polymer diaphragm is filled with a matrix in which an enzyme is immobilized.

For example, urease, together with a buffered electrolyte, might be held in a cross-linked polyacrylamide gel. When the electrode is immersed in a test solution, there will be a selective response toward urea, which diffuses through the diaphragm into the gel. The response comes about because the urease catalyzes the process:

$$\underset{\displaystyle \text{NH}_2}{} \overset{\displaystyle \overset{\text{O}}{\overset{\|}{\text{C}}}}{} \text{—NH}_2 + \text{H}^+ + 2\text{H}_2\text{O} \xrightarrow{\text{Urease}} 2\text{NH}_4^+ + \text{HCO}_3^- \qquad (2.4.22)$$

The resulting ammonium ions can be detected with a cation-sensitive glass membrane. Alternatively, one could use a gas-sensing electrode for ammonia in place of the glass electrode, so that interferences from H^+, Na^+, and K^+ are reduced.

The research literature features many examples of this basic strategy. Different enzymes allow selective determinations of single species, such as glucose (with glucose oxidase), or groups of substances such as the L-amino acids (with L-amino acid oxidase). Recent reviews should be consulted for a more complete view of the field (66–68).

Amperometric enzyme electrodes are discussed in Sections 14.2.5 and 14.4.2(c).

▶ 2.5 REFERENCES

1. The arguments presented here follow those given earlier by D. A. MacInnes ("The Principles of Electrochemistry," Dover, New York, 1961, pp. 110–113) and by J. J. Lingane ("Electroanalytical Chemistry," 2nd ed., Wiley-Interscience, New York, 1958, pp. 40–45). Experiments like those described here were actually carried out by H. Jahn (*Z. Physik. Chem.*, **18**, 399 (1895).

2. I. M. Klotz and R. M. Rosenberg, "Chemical Thermodynamics," 4th ed., Benjamin/Cummings, Menlo Park, CA, 1986.

3. J. J. Lingane, "Electroanalytical Chemistry," 2nd ed., Wiley-Interscience, New York, 1958, Chap. 3.

4. F. C. Anson, *J. Chem. Educ.*, **36**, 394 (1959).

5. A. J. Bard, R. Parsons, and J. Jordan, Eds., "Standard Potentials in Aqueous Solutions," Marcel Dekker, New York, 1985.

6. *http://webbook.nist.gov/*, National Institute of Standards and Technology.

7. A. J. Bard and H. Lund, Eds., "Encyclopedia of Electrochemistry of the Elements," Marcel Dekker, New York, 1973–1980.

8. M. W. Chase, Jr., "NIST-JANAF Thermochemical Tables," 4th ed., American Chemical Society, Washington, and American Institute of Physics, New York, for the National Institute of Standards and Technology, 1998.

9. L. R. Faulkner, *J. Chem. Educ.*, **60**, 262 (1983).

10. R. Parsons in A. J. Bard, R. Parsons, and J. Jordan, Eds., *op.cit.*, Chap. 1.

11. A. Henglein, *Ber. Bunsenges. Phys. Chem.*, **94**, 600 (1990).

12. A. Henglein, *Top. Curr. Chem.*, **1988**, 113.

13. A. Henglein, *Accts. Chem. Res.*, **9**, 1861 (1989).

14. D. W. Suggs and A. J. Bard, *J. Am. Chem. Soc.*, **116**, 10725 (1994).

15. R. Parsons, *op. cit.*, p. 5.

16. D. J. G. Ives and G. J. Janz, Eds., "Reference Electrodes," Academic, New York, 1961.

17. J. N. Butler, *Adv. Electrochem. Electrochem. Engr.*, **7**, 77 (1970).

18. D. T. Sawyer, A. Sobkowiak, and J. L. Roberts, Jr., "Electrochemistry for Chemists," 2nd ed., Wiley, New York, 1995.

19. G. Gritzner and J. Kuta, *Pure Appl. Chem.*, **56**, 461 (1984).

20. (a) P. Peerce and A. J. Bard, *J. Electroanal. Chem.*, **108**, 121 (1980); (b) R. M. Kannuck, J. M. Bellama, E. A Blubaugh, and R. A. Durst, *Anal. Chem.*, **59**, 1473 (1987).

21. D. Halliday and R. Resnick, "Physics," 3rd ed., Wiley, New York, 1978, Chap. 29.

22. *Ibid.*, Chap. 28.

23. J. O'M. Bockris and A. K. N. Reddy, "Modern Electrochemistry," Vol. 2, Plenum, New York, 1970, Chap. 7.

24. K. J. Vetter, "Electrochemical Kinetics," Academic, New York, 1967.

25. B. E. Conway, "Theory and Principles of Electrode Processes," Ronald, New York, 1965, Chap. 13.

26. R. Parsons, *Mod. Asp. Electrochem.*, **1**, 103 (1954).

27. J. A. V. Butler, *Proc. Roy. Soc., London*, **112A**, 129 (1926).

28. E. A. Guggenheim, *J. Phys. Chem.*, **33**, 842 (1929); **34**, 1540 (1930).

29. S. Trasatti, *Pure Appl. Chem.*, **58**, 955 (1986).

30. D. A. MacInnes, "Principles of Electrochemistry," Dover, New York, 1961, Chap. 13.

31. J. O'M. Bockris and A. K. N. Reddy, *op. cit.*, Vol. 1, Chap. 4.

32. D. A. MacInnes, *op. cit.*, Chap. 4.

33. *Ibid.*, Chap. 18.

34. D. O. Raleigh, *Electroanal. Chem.*, **6**, 87 (1973).

35. G. Holzäpfel, "Solid State Electrochemistry" in *Encycl. Phys. Sci. Technol.*, R. A. Meyers, Ed., Academic, New York, 1992, Vol. 15, p. 471.

36. J. O'M. Bockris and A. K. N. Reddy, *op. cit.*, Chap. 3.

37. R. G. Bates, "Determination of pH," 2nd ed., Wiley-Interscience, New York, 1973.

38. R. M. Garrels in "Glass Electrodes for Hydrogen and Other Cations," G. Eisenman, Ed., Marcel Dekker, New York, 1967, Chap. 13.

39. P. R. Mussini, S. Rondinini, A. Cipolli, R. Manenti and M. Mauretti, *Ber. Bunsenges. Phys. Chem.*, **97**, 1034 (1993).

40. H. H. J. Girault and D. J. Schiffrin, *Electroanal. Chem.*, **15**, 1 (1989).

41. H. H. J. Girault, *Mod. Asp. Electrochem.*, **25**, 1 (1993).

42. P. Vanýsek, "Electrochemistry on Liquid/Liquid Interfaces," Springer, Berlin, 1985.

43. A. G. Volkov and D. W. Deamer, Eds., "Liquid-Liquid Interfaces," CRC, Boca Raton, FL, 1996.

44. A. G. Volkov, D. W. Deamer, D. L. Tanelian, and V. S Markin, "Liquid Interfaces in Chemistry and Biology," Wiley-Interscience, New York, 1997.

45. E. Grunwald, G. Baughman, and G. Kohnstam, *J. Am. Chem. Soc.*, **82**, 5801 (1960).

46. M. Dole, "The Glass Electrode," Wiley, New York, 1941.

47. G. Eisenman, Ed., "Glass Electrodes for Hydrogen and Other Cations," Marcel Dekker, New York, 1967.

48. R. A. Durst, Ed., "Ion Selective Electrodes," Nat. Bur. Stand. Spec. Pub. 314, U.S. Government Printing Office, Washington, 1969.

49. N. Lakshminarayanaiah in "Electrochemistry," (A Specialist Periodical Report), Vols. 2, 4, 5, and 7; G. J. Hills (Vol. 2); and H. R. Thirsk (Vols, 4, 5, and 7); Senior Reporters, Chemical Society, London, 1972, 1974, 1975, and 1980.

50. H. Freiser, "Ion-Selective Electrodes in Analytical Chemistry," Plenum, New York, Vol. 1, 1979; Vol. 2, 1980.

51. J. Koryta and K. Štulík, 'Ion-Selective Electrodes," 2nd ed., Cambridge University Press, Cambridge, 1983.

52. A. Evans, "Potentiometry and Ion Selective Electrodes," Wiley, New York, 1987.

53. D. Ammann, "Ion-Selective Microelectrodes: Principles, Design, and Application," Springer, Berlin, 1986.

54. E. Lindner, K. Toth, and E. Pungor, "Dynamic Characteristics of Ion-Sensitive Electrodes," CRC, Boca Raton, FL, 1988.

55. Y. Umezawa, Ed., "CRC Handbook of Ion-Selective Electrodes," CRC, Boca Raton, FL 1990.

56. E. Bakker, P. Bühlmann, and E. Pretsch, *Chem. Rev.*, **97**, 3083 (1997).

57. P. Bühlmann, E. Pretsch, and E. Bakker, *Chem. Rev.*, **98**, 1593 (1998).

58. R. P. Buck and E. Lindner, *Accts. Chem. Res.*, **31**, 257 (1998).

59. E. Pungor, *Pure Appl. Chem.*, **64**, 503 (1992).

60. S. Mathison and E. Bakker, *Anal. Chem.*, **70**, 303 (1998).

61. T. Sokalski, A. Ceresa, T. Zwicki, and E. Pretsch, *J. Am. Chem. Soc.*, **119**, 11347 (1997).

62. J. W. Ross, J. H. Riseman, and J. A. Krueger, *Pure Appl. Chem.*, **36**, 473 (1973).

63. L. C. Clark, Jr., *Trans. Am. Soc. Artif. Intern. Organs*, **2**, 41 (1956).

64. G. G. Guilbault, *Pure Appl. Chem.*, **25**, 727 (1971).

65. G. A. Rechnitz, *Chem. Engr. News*, **53** (4), 29 (1975).

66. E. A. H. Hall, "Biosensors," Prentice Hall, Englewood Cliffs, NJ, 1991, Chap. 9.

67. A. J. Cunningham, "Introduction to Bioanalytical Sensors," Wiley, New York, 1998, Chap. 4.

68. H. S. Yim, C. E. Kibbey, S. C. Ma, D. M. Kliza, D. Liu, S. B. Park, C. E. Torre, and M. E. Meyerhoff, *Biosens. Bioelectron.*, **8**, 1 (1993).

▶ 2.6 PROBLEMS

2.1 Devise electrochemical cells in which the following reactions could be made to occur. If liquid junctions are necessary, note them in the cell schematic appropriately, but neglect their effects.

(a) $H_2O \rightleftarrows H^+ + OH^-$

(b) $2H_2 + O_2 \rightleftarrows H_2O$

(c) $2PbSO_4 + 2H_2O \rightleftarrows PbO_2 + Pb + 4H^+ + 2SO_4^{2-}$

(d) $An^{\bar{\cdot}} + TMPD^{\bar{\cdot}+} \rightleftarrows An + TMPD$ (in acetonitrile, where An and $An^{\bar{\cdot}}$ are anthracene and its anion radical, and TMPD and $TMPD^{\bar{\cdot}+}$ are N,N,N',N'-tetramethyl-p-phenylenediamine and its cation radical. Use anthracene potentials for DMF solutions given in Appendix C.3).

(e) $2Ce^{3+} + 2H^+ + BQ \rightleftarrows 2Ce^{4+} + H_2Q$ (aqueous, where BQ is p-benzoquinone and H_2Q is p-hydroquinone)

(f) $Ag^+ + I^- \rightleftarrows AgI$ (aqueous)

(g) $Fe^{3+} + Fe(CN)_6^{4-} \rightleftarrows Fe^{2+} + Fe(CN)_6^{3-}$ (aqueous)

(h) $Cu^{2+} + Pb \rightleftarrows Pb^{2+} + Cu$ (aqueous)

(i) $An^{\bar{\cdot}} + BQ \rightleftarrows BO^{\bar{\cdot}}. + An$ (in N,N-dimethylformamide, where BQ, An, and $An^{\bar{\cdot}}$ are defined above and $BO^{\bar{\cdot}}$ is the anion radical of p-benzoquinone. Use BQ potentials in acetonitrile given in Appendix C.3).
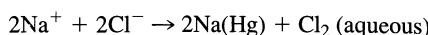
What half-reactions take place at the electrodes in each cell? What is the standard cell potential in each case? Which electrode is negative? Would the cell operate electrolytically or galvanically in carrying out a net reaction from left to right? Be sure your decisions accord with chemical intuition.

2.2 Several hydrocarbons and carbon monoxide have been studied as possible fuels for use in fuel cells. From thermodynamic data in references 5–8 and 16, derive E^0s for the following reactions at 25°C:

(a) $CO(g) + H_2O(l) \rightarrow CO_2(g) + 2H^+ + 2e$

(b) $CH_4(g) + 2H_2O(l) \rightarrow CO_2(g) + 8H^+ + 8e$

(c) $C_2H_6(g) + 4H_2O(l) \rightarrow 2CO_2(g) + 14H^+ + 14e$

(d) $C_2H_2(g) + 4H_2O(l) \rightarrow 2CO_2(g) + 10H^+ + 10e$

Even though a reversible emf could not be established (Why not?), which half-cell would ideally yield the highest cell voltage when coupled with the standard oxygen half-cell in acid solution? Which of the fuels above could yield the highest net work per mole of fuel oxidized? Which would give the most net work per gram?

2.3 Devise a cell in which the following reaction is the overall cell process ($T = 298$ K):

$$2Na^+ + 2Cl^- \rightarrow 2Na(Hg) + Cl_2 \text{ (aqueous)}$$

where Na(Hg) symbolizes the amalgam. Is the reaction spontaneous or not? What is the standard free energy change? Take the standard free energy of formation of Na(Hg) as -85 kJ/mol. From a thermodynamic standpoint, another reaction should occur more readily at the cathode of your cell. What is it? It is observed that the reaction written above takes place with good current efficiency. Why? Could your cell have a commercial value?

2.4 What are the cell reactions and their emfs in the following systems? Are the reactions spontaneous? Assume that all systems are aqueous.
   (a) Ag/AgCl/K$^+$, Cl$^-$ (1 M)/Hg$_2$Cl$_2$/Hg
   (b) Pt/Fe^{3+} (0.01 M), Fe^{2+} (0.1 M), HCl (1 M)//Cu^{2+} (0.1 M), HCl (1 M)/Cu
   (c) Pt/H$_2$ (1 atm)/H$^+$, Cl$^-$ (0.1 M)//H$^+$, Cl$^-$ (0.1 M)/O$_2$ (0.2 atm)/Pt
   (d) Pt/H$_2$ (1 atm)/Na$^+$, OH$^-$ (0.1 M)//Na$^+$, OH$^-$ (0.1 M)/O$_2$ (0.2 atm)/Pt
   (e) Ag/AgCl/K$^+$, Cl$^-$ (1 M)//K$^+$, Cl$^-$ (0.1 M)/AgCl/Ag
   (f) Pt/Ce^{3+} (0.01 M), Ce^{4+} (0.1 M), H$_2$SO$_4$ (1 M)//Fe^{2+} (0.01 M), Fe^{3+} (0.1 M), HCl (1 M)/Pt

2.5 Consider the cell in part (f) of Problem 2.4. What would the composition of the system be at the end of a galvanic discharge to an equilibrium condition? What would the cell potential be? What would the potential of each electrode be *vs.* NHE? *Vs.* SCE? Take equal volumes on both sides.

2.6 Devise a cell for evaluating the solubility product of PbSO$_4$. Calculate the solubility product from the appropriate E^0 values ($T = 298$ K).
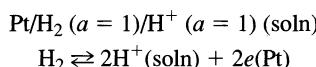
2.7 Obtain the dissociation constant of water from the parameters of the cell constructed for reaction (a) in Problem 2.1 ($T = 298$ K).

2.8 Consider the cell:

$$Cu/M/Fe^{2+}, Fe^{3+}, H^+//Cl^-/AgCl/Ag/Cu'$$

Would the cell potential be independent of the identity of M (e.g., graphite, gold, platinum) as long as M is chemically inert? Use electrochemical potentials to prove your point.

2.9 Given the half-cell of the standard hydrogen electrode,

$$Pt/H_2 \ (a = 1)/H^+ \ (a = 1) \text{ (soln)}$$
$$H_2 \rightleftarrows 2H^+(\text{soln}) + 2e(\text{Pt})$$

Show that although the emf of the cell half-reaction is taken as zero, the potential difference between the platinum and the solution, that is, $\phi^{Pt} - \phi^s$, is not zero.
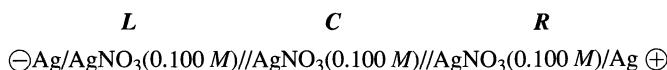
2.10 Devise a thermodynamically sound basis for obtaining the standard potentials for new half-reactions by taking linear combinations of other half-reactions ($T = 298$ K). As two examples, calculate E^0 values for
   (a) CuI + $e \rightleftarrows$ Cu + I$^-$
   (b) O$_2$ + 2H$^+$ + 2$e \rightleftarrows$ H$_2$O$_2$
   given the following half-reactions and values for E^0 (V *vs.* NHE):
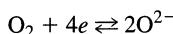
Cu^{2+} + 2$e \rightleftarrows$ Cu	0.340
Cu^{2+} + I$^-$ + $e \rightleftarrows$ CuI	0.86
O$_2$ + 4H$^+$ + 4$e \rightleftarrows$ 2H$_2$O	1.229
H$_2$O$_2$ + 2H$^+$ + 2$e \rightleftarrows$ 2H$_2$O	1.763

2.11 Transference numbers are often measured by the Hittorf method as illustrated in this problem. Consider the three-compartment cell:

L	*C*	*R*

$\ominus$Ag/AgNO$_3$(0.100 M)//AgNO$_3$(0.100 M)//AgNO$_3$(0.100 M)/Ag $\oplus$

where the double slashes (//) signify sintered glass disks that divide the compartments and prevent mixing, but not ionic movement. The volume of $AgNO_3$ solution in each compartment (L, C, R) is 25.00 mL. An external power supply is connected to the cell with the polarity shown, and current is applied until 96.5 C have passed, causing Ag to deposit on the left Ag electrode and Ag to dissolve from the right Ag electrode.

(a) How many grams of Ag have deposited on the left electrode? How many mmol of Ag have deposited?

(b) If the transference number for Ag^+ were 1.00 (i.e., $t_{Ag^+} = 1.00$, $t_{NO_3^-} = 0.00$), what would the concentrations of Ag^+ be in the three compartments after electrolysis?

(c) Suppose the transference number for Ag^+ were 0.00 (i.e., $t_{Ag^+} = 0.00$, $t_{NO_3^-} = 1.00$), what would the concentrations of Ag^+ be in the three compartments after electrolysis?

(d) In an actual experiment like this, it is found experimentally that the concentration of Ag^+ in the anode compartment R has increased to 0.121 M. Calculate t_{Ag^+} and $t_{NO_3^-}$.

2.12 Suppose one wants to determine the contribution of electronic (as opposed to ionic) conduction through doped AgBr, a solid electrolyte. A cell is prepared with a film of AgBr between two Ag electrodes, each of mass 1.00 g, that is, $\ominus Ag/AgBr/Ag \oplus$. After passage of 200 mA through the cell for 10.0 min, the cell was disassembled and the cathode was found to have a mass of 1.12 g. If Ag deposition is the only faradaic process that occurs at the cathode, what fraction of the current through the cell represents electronic conduction in AgBr?

2.13 Calculate the individual junction potentials at $T = 298$ K on either side of the salt bridge in (2.3.44) for the first two concentrations in Table 2.3.3. What is the sum of the two potentials in each case? How does it compare with the corresponding entry in the table?

2.14 Estimate the junction potentials for the following situations $(T = 298$ K):

(a) HCl (0.1 M)/NaCl (0.1 M)

(b) HCl (0.1 M)/NaCl (0.01 M)

(c) KNO_3 (0.01 M)/NaOH (0.1 M)

(d) $NaNO_3$ (0.1 M)/NaOH (0.1 M)

2.15 One often finds pH meters with direct readout to 0.001 pH unit. Comment on the accuracy of these readings in making comparisons of pH from test solution to test solution. Comment on their meaning in measurements of small changes in pH in a single solution (e.g., during a titration).

2.16 The following values of $k_{Na^+,i}^{pot}$ are typical for interferents i at a sodium-selective glass electrode: K^+, 0.001; NH_4^+, 10^{-5}; Ag^+, 300; H^+, 100. Calculate the activities of each interferent that would cause a 10% error when the activity of Na^+ is estimated to be 10^{-3} M from a potentiometric measurement.

2.17 Would Na_2H_2EDTA be a good ion-exchanger for a liquid membrane electrode? How about Na_2H_2EDTA-R, where R designates a C_{20} alkyl substituent? Why or why not?

2.18 Comment on the feasibility of developing selective electrodes for the direct potentiometric determination of uncharged substances.

2.19 Consider the exhaust gas analyzer based on the oxygen concentration cell, (2.4.21). The electrode reaction that occurs at high temperature at both of the $Pt/ZrO_2 + Y_2O_3$ interfaces is

$$O_2 + 4e \rightleftarrows 2O^{2-}$$

Write the equation that governs the potential of this cell as a function of the pressures, p_{eg} and p_a. What would the cell voltage be when the partial pressure of oxygen in the exhaust gas is 0.01 atm (1,013 Pa)?

3

KINETICS OF ELECTRODE REACTIONS
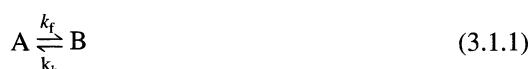
In Chapter 1, we established a proportionality between the current and the net rate of an electrode reaction, v. Specifically, $v = i/nFA$. We also know that for a given electrode process, current does not flow in some potential regions, yet it flows to a variable degree in others. The reaction rate is a strong function of potential; thus, we require potential-dependent rate constants for an accurate description of interfacial charge-transfer dynamics.

In this chapter, our goal is to devise a theory that can quantitatively rationalize the observed behavior of electrode kinetics with respect to potential and concentration. Once constructed, the theory will serve often as an aid for understanding kinetic effects in new situations. We begin with a brief review of certain aspects of homogeneous kinetics, because they provide both a familiar starting ground and a basis for the construction, through analogy, of an electrochemical kinetic theory.

▶ 3.1 REVIEW OF HOMOGENEOUS KINETICS

3.1.1 Dynamic Equilibrium

Consider two substances, A and B, that are linked by simple unimolecular elementary reactions.[1]

$$A \underset{k_b}{\overset{k_f}{\rightleftharpoons}} B \qquad (3.1.1)$$

Both elementary reactions are active at all times, and the rate of the forward process, v_f (M/s), is

$$v_f = k_f C_A \qquad (3.1.2)$$

whereas the rate of the reverse reaction is

$$v_b = k_b C_B \qquad (3.1.3)$$

The rate constants, k_f and k_b, have dimensions of s^{-1}, and one can easily show that they are the reciprocals of the mean lifetimes of A and B, respectively (Problem 3.8). The net conversion rate of A to B is

$$v_{net} = k_f C_A - k_b C_B \qquad (3.1.4)$$

---

[1]An *elementary reaction* describes an actual, discrete chemical event. Many chemical reactions, as written, are not elementary, because the transformation of products to reactants involves several distinct steps. These steps are the elementary reactions that comprise the *mechanism* for the overall process.

At equilibrium, the net conversion rate is zero; hence

$$\frac{k_f}{k_b} = K = \frac{C_B}{C_A} \tag{3.1.5}$$

The kinetic theory therefore predicts a constant concentration ratio at equilibrium, just as thermodynamics does.

Such agreement is required of *any* kinetic theory. In the limit of equilibrium, the kinetic equations must collapse to relations of the thermodynamic form; otherwise the kinetic picture cannot be accurate. Kinetics describe the evolution of mass flow throughout the system, including both the *approach* to equilibrium and the *dynamic maintenance* of that state. Thermodynamics describe only equilibrium. Understanding of a system is not even at a crude level unless the kinetic view and the thermodynamic one agree on the properties of the equilibrium state.

On the other hand, thermodynamics provide no information about the mechanism required to maintain equilibrium, whereas kinetics can be used to describe the intricate balance quantitatively. In the example above, equilibrium features nonzero rates of conversion of A to B (and vice versa), but those rates are equal. Sometimes they are called the *exchange velocity* of the reaction, v_0:

$$v_0 = k_f(C_A)_{eq} = k_b(C_B)_{eq} \tag{3.1.6}$$

We will see below that the idea of exchange velocity plays an important role in treatments of electrode kinetics.

3.1.2 The Arrhenius Equation and Potential Energy Surfaces (1, 2)

It is an experimental fact that most rate constants of solution-phase reactions vary with temperature in a common fashion: nearly always, ln k is linear with $1/T$. Arrhenius was first to recognize the generality of this behavior, and he proposed that rate constants be expressed in the form:

$$\boxed{k = Ae^{-E_A/RT}} \tag{3.1.7}$$

where E_A has units of energy. Since the exponential factor is reminiscent of the probability of using thermal energy to surmount an energy barrier of height E_A, that parameter has been known as the *activation energy*. If the exponential expresses the probability of surmounting the barrier, then A must be related to the frequency of attempts on it; thus A is known generally as the *frequency factor*. As usual, these ideas turn out to be oversimplifications, but they carry an essence of truth and are useful for casting a mental image of the ways in which reactions proceed.

The idea of activation energy has led to pictures of reaction paths in terms of potential energy along a *reaction coordinate*. An example is shown in Figure 3.1.1. In a simple unimolecular process, such as, the *cis-trans* isomerization of stilbene, the reaction coordinate might be an easily recognized molecular parameter, such as the twist angle about the central double bond in stilbene. In general, the reaction coordinate expresses progress along a favored path on the multidimensional surface describing potential energy as a function of all independent position coordinates in the system. One zone of this surface corresponds to the configuration we call "reactant," and another corresponds to the structure of the "product." Both must occupy minima on the energy surface, because they are the only arrangements possessing a significant lifetime. Even though other configurations are possible, they must lie at higher energies and lack the energy minimum required for
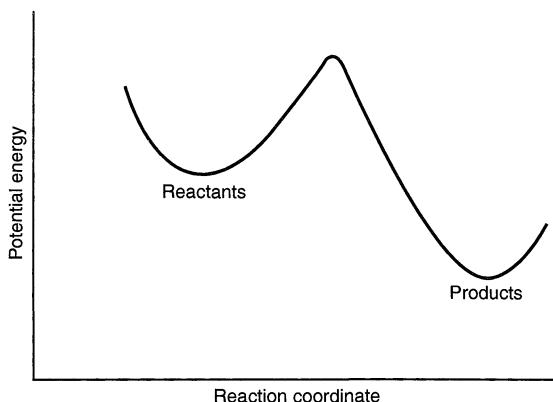
Figure 3.1.1 Simple representation of potential energy changes during a reaction.

stability. As the reaction takes place, the coordinates are changed from those of the reactant to those of the product. Since the path along the reaction coordinate connects two minima, it must rise, pass over a maximum, then fall into the product zone. Very often, the height of the maximum above a valley is identified with the activation energy, either $E_{A,f}$ or $E_{A,b}$, for the forward or backward reaction, respectively.

In another notation, we can understand E_A as the change in standard internal energy in going from one of the minima to the maximum, which is called the *transition state* or *activated complex*. We might designate it as the *standard internal energy of activation*, $\Delta E^{\ddagger}$. The *standard enthalpy of activation*, $\Delta H^{\ddagger}$, would then be $\Delta E^{\ddagger} + \Delta(PV)^{\ddagger}$, but $\Delta(PV)$ is usually negligible in a condensed-phase reaction, so that $\Delta H^{\ddagger} \approx \Delta E^{\ddagger}$. Thus, the Arrhenius equation could be recast as

$$k = A\, e^{-\Delta H^{\ddagger}/RT} \tag{3.1.8}$$

We are free also to factor the coefficient A into the product $A'\exp(\Delta S^{\ddagger}/R)$, because the exponential involving the *standard entropy of activation*, $\Delta S^{\ddagger}$, is a dimensionless constant. Then

$$k = A'e^{-(\Delta H^{\ddagger}-T\Delta S^{\ddagger})/RT} \tag{3.1.9}$$

or

$$\boxed{k = A'\, e^{-\Delta G^{\ddagger}/RT}} \tag{3.1.10}$$

where $\Delta G^{\ddagger}$ is the *standard free energy of activation*.[2] This relation, like (3.1.8), is really an equivalent statement of the Arrhenius equation, (3.1.7), which itself is an empirical generalization of reality. Equations 3.1.8 and 3.1.10 are derived from (3.1.7), but only by the *interpretation* we apply to the phenomenological constant E_A. Nothing we have written so far depends on a specific theory of kinetics.

[2]We are using *standard* thermodynamic quantities here, because the free energy and the entropy of a species are concentration-dependent. The rate constant is not concentration-dependent in dilute systems; thus the argument that leads to (3.1.10) needs to be developed in the context of a standard state of concentration. The choice of standard state is not critical to the discussion. It simply affects the way in which constants are apportioned in rate expressions. To simplify notation, we omit the superscript "0" from $\Delta E^{\ddagger}$, $\Delta H^{\ddagger}$, $\Delta S^{\ddagger}$, and $\Delta G^{\ddagger}$, but understand them throughout this book to be referred to the standard state of concentration.

3.1.3 Transition State Theory (1–4)

Many theories of kinetics have been constructed to illuminate the factors controlling reaction rates, and a prime goal of these theories is to predict the values of A and E_A for specific chemical systems in terms of quantitative molecular properties. An important general theory that has been adapted for electrode kinetics is the *transition state theory*, which is also known as the *absolute rate theory* or the *activated complex theory*.

Central to this approach is the idea that reactions proceed through a fairly well-defined transition state or activated complex, as shown in Figure 3.1.2. The standard free energy change in going from the reactants to the complex is $\Delta G_f^{\ddagger}$, whereas the complex is elevated above the products by $\Delta G_b^{\ddagger}$.

Let us consider the system of (3.1.1), in which two substances A and B are linked by unimolecular reactions. First we focus on the special condition in which the entire system—A, B, and all other configurations—is at thermal equilibrium. For this situation, the concentration of complexes can be calculated from the standard free energies of activation according to either of two equilibrium constants:

$$\frac{[\text{Complex}]}{[\text{A}]} = \frac{\gamma_A/C^0}{\gamma_{\ddagger}/C^0} K_f = \frac{\gamma_A}{\gamma_{\ddagger}} \exp\left(-\Delta G_f^{\ddagger}/RT\right) \tag{3.1.11}$$

$$\frac{[\text{Complex}]}{[\text{B}]} = \frac{\gamma_B}{\gamma_{\ddagger}} K_b = \frac{\gamma_B}{\gamma_{\ddagger}} \exp\left(-\Delta G_b^{\ddagger}/RT\right) \tag{3.1.12}$$

where C^0 is the concentration of the standard state (see Section 2.1.5), and γ_A, γ_B, and $\gamma_{\ddagger}$ are dimensionless activity coefficients. Normally, we assume that the system is ideal, so that the activity coefficients approach unity and divide out of (3.1.11) and (3.1.12).

The activated complexes decay into either A or B according to a combined rate constant, k', and they can be divided into four fractions: (a) those created from A and reverting back to A, f_{AA}, (b) those arising from A and decaying to B, f_{AB}, (c) those created from B and decaying to A, f_{BA}, and (d) those arising from B and reverting back to B, f_{BB}. Thus the rate of transforming A into B is

$$k_f [\text{A}] = f_{AB} k' [\text{Complex}] \tag{3.1.13}$$

and the rate of transforming B into A is

$$k_b [\text{B}] = f_{BA} k' [\text{Complex}] \tag{3.1.14}$$

Since we require $k_f[\text{A}] = k_b[\text{B}]$ at equilibrium, f_{AB} and f_{BA} must be the same. In the simplest version of the theory, both are taken as $1/2$. This assumption implies that
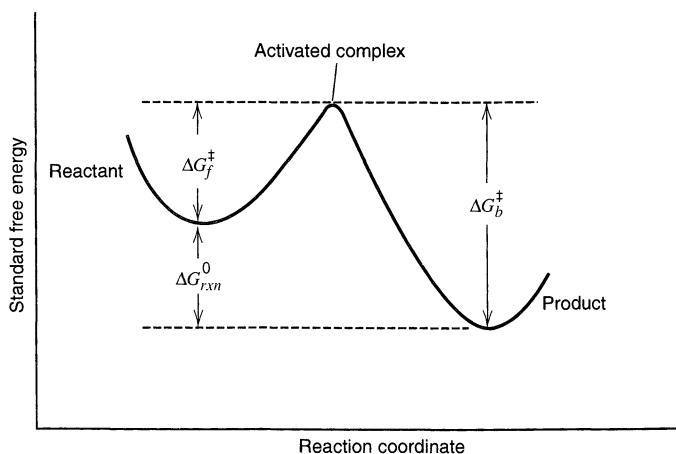
Figure 3.1.2 Free energy changes during a reaction. The activated complex (or transition state) is the configuration of maximum free energy.

$f_{AA} = f_{BB} \approx 0$; thus complexes are not considered as reverting to the source state. Instead, any system reaching the activated configuration is transmitted with unit efficiency into the product opposite the source. In a more flexible version, the fractions f_{AB} and f_{BA} are equated to $\kappa/2$, where κ, the *transmission coefficient*, can take a value from zero to unity.

Substitution for the concentration of the complex from (3.1.11) and (3.1.12) into (3.1.13) and (3.1.14), respectively, leads to the rate constants:

$$k_f = \frac{\kappa k'}{2} e^{-\Delta G_f^{\ddagger}/RT} \tag{3.1.15}$$

$$k_b = \frac{\kappa k'}{2} e^{-\Delta G_b^{\ddagger}/RT} \tag{3.1.16}$$

Statistical mechanics can be used to predict $\kappa k'/2$. In general, that quantity depends on the shape of the energy surface in the region of the complex, but for simple cases k' can be shown to be $2\mathit{k}T/h$, where, k and h are the Boltzmann and Planck constants. Thus the rate constants (equations 3.1.15 and 3.1.16) might both be expressed in the form:

$$\boxed{k = \kappa \frac{\mathit{k}T}{h} e^{-\Delta G^{\ddagger}/RT}} \tag{3.1.17}$$

which is the equation most frequently seen for calculating rate constants by the transition state theory.

To reach (3.1.17), we considered only a system at equilibrium. It is important to note now that the rate constant for an elementary process is fixed for a given temperature and pressure and does not depend on the reactant and product concentrations. Equation 3.1.17 is therefore a general expression. If it holds at equilibrium, it will hold away from equilibrium. The assumption of equilibrium, though useful in the derivation, does not constrain the equation's range of validity.[3]

► 3.2 ESSENTIALS OF ELECTRODE REACTIONS (6–14)

We noted above that an accurate kinetic picture of any dynamic process must yield an equation of the thermodynamic form in the limit of equilibrium. For an electrode reaction, equilibrium is characterized by the Nernst equation, which links the electrode potential to the bulk concentrations of the participants. In the general case:

$$O + ne \underset{k_b}{\overset{k_f}{\rightleftharpoons}} R \tag{3.2.1}$$

this equation is

$$\boxed{E = E^{0'} + \frac{RT}{nF} \ln \frac{C_O^*}{C_R^*}} \tag{3.2.2}$$

where C_O^* and C_R^* are the bulk concentrations, and $E^{0'}$ is the formal potential. Any valid theory of electrode kinetics must predict this result for corresponding conditions.

---

[3]Note that $\mathit{k}T/h$ has units of s^{-1} and that the exponential is dimensionless. Thus, the expression in (3.1.17) is dimensionally correct for a first-order rate constant. For a second-order reaction, the equilibrium corresponding to (3.1.11) would have the concentrations of two reactants in the denominator on the left side and the activity coefficient for each of those species divided by the standard-state concentration, C^0, in the numerator on the right. Thus, C^0 no longer divides out altogether and is carried to the first power into the denominator of the final expression. Since it normally has a unit value (usually 1 M^{-1}), its presence has no effect numerically, but it does dimensionally. The overall result is to create a prefactor having a numeric value equal to $\mathit{k}T/h$ but having units of $M^{-1} s^{-1}$, as required. This point is often omitted in applications of transition state theory to processes more complicated than unimolecular decay. See Section 2.1.5 and reference 5.

We also require that the theory explain the observed dependence of current on potential under various circumstances. In Chapter 1, we saw that current is often limited wholly or partially by the rate at which the electroreactants are transported to the electrode surface. This kind of limitation does not concern a theory of interfacial kinetics. More to the point is the case of low current and efficient stirring, in which mass transport is not a factor determining the current. Instead, it is controlled by interfacial dynamics. Early studies of such systems showed that the current is often related exponentially to the overpotential η. That is,

$$i = a' \, e^{\eta/b'} \tag{3.2.3}$$

or, as given by Tafel in 1905,

$$\boxed{\eta = a + b \log i} \tag{3.2.4}$$

A successful model of electrode kinetics must explain the frequent validity of (3.2.4), which is known as the *Tafel equation.*

Let us begin by considering that reaction (3.2.1) has forward and backward paths as shown. The forward component proceeds at a rate, v_f, that must be proportional to the surface concentration of O. We express the concentration at distance x from the surface and at time t as $C_O(x, t)$; hence the surface concentration is $C_O(0, t)$. The constant of proportionality linking the forward reaction rate to $C_O(0, t)$ is the rate constant k_f.

$$v_f = k_f C_O(0, t) = \frac{i_c}{nFA} \tag{3.2.5}$$

Since the forward reaction is a reduction, there is a cathodic current, i_c, proportional to v_f. Likewise, we have for the backward reaction

$$v_b = k_b C_R(0, t) = \frac{i_a}{nFA} \tag{3.2.6}$$

where i_a is the anodic component to the total current. Thus the net reaction rate is

$$v_{net} = v_f - v_b = k_f C_O(0, t) - k_b C_R(0, t) = \frac{i}{nFA} \tag{3.2.7}$$

and we have overall

$$i = i_c - i_a = nFA[k_f C_O(0, t) - k_b C_R(0, t)] \tag{3.2.8}$$

Note that heterogeneous reactions are described differently than homogeneous ones. For example, reaction velocities in heterogeneous systems refer to unit interfacial area; hence they have units of mol s^{-1} cm^{-2}. Thus heterogeneous rate constants must carry units of cm/s, if the concentrations on which they operate are expressed in mol/cm^3. Since the interface can respond only to its immediate surroundings, the concentrations entering rate expressions are always surface concentrations, which may differ from those of the bulk solution.

▷ 3.3 BUTLER-VOLMER MODEL OF ELECTRODE KINETICS (9, 11, 12, 15, 16)

Experience demonstrates that the potential of an electrode strongly affects the kinetics of reactions occurring on its surface. Hydrogen evolves rapidly at some potentials, but not at others. Copper dissolves from a metallic sample in a clearly defined potential range; yet the metal is stable outside that range. And so it is for all faradaic processes. Because the interfacial potential difference can be used to control reactivity, we want to be able to pre-

dict the precise way in which k_f and k_b depend on potential. In this section, we will develop a predictive model based purely on classical concepts. Even though it has significant limitations, it is very widely used in the electrochemical literature and must be understood by any student of the field. Section 3.6 will yield more modern models based on a microscopic view of electron transfer.

3.3.1 Effects of Potential on Energy Barriers

We saw in Section 3.1 that reactions can be visualized in terms of progress along a reaction coordinate connecting a reactant configuration to a product configuration on an energy surface. This idea applies to electrode reactions too, but the shape of the surface turns out to be a function of electrode potential.

One can see the effect easily by considering the reaction

$$Na^+ + e \overset{Hg}{\rightleftharpoons} Na(Hg) \qquad (3.3.1)$$

where Na^+ is dissolved in acetonitrile or dimethylformamide. We can take the reaction coordinate as the distance of the sodium nucleus from the interface; then the free energy profile along the reaction coordinate would resemble Figure 3.3.1a. To
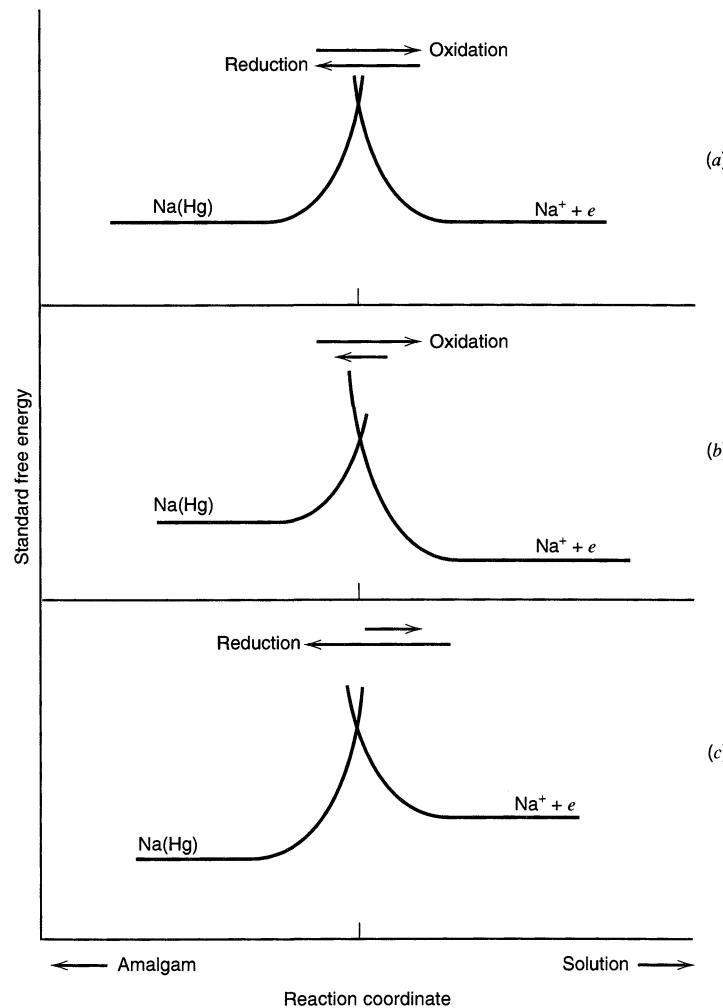
Figure 3.3.1 Simple representation of standard free energy changes during a faradaic process. (a) At a potential corresponding to equilibrium. (b) At a more positive potential than the equilibrium value. (c) At a more negative potential than the equilibrium value.

the right, we identify $Na^+ + e$. This configuration has an energy that depends little on the nuclear position in solution, unless the electrode is approached so closely that the ion must be partially or wholly desolvated. To the left, the configuration corresponds to a sodium atom dissolved in mercury. Within the mercury phase, the energy depends only slightly on position, but if the atom leaves the interior, its energy rises as the favorable mercury–sodium interaction is lost. The curves corresponding to these reactant and product configurations intersect at the transition state, and the heights of the barriers to oxidation and reduction determine their relative rates. When the rates are equal, as in Figure 3.3.1a, the system is at equilibrium, and the potential is E_{eq}.

Now suppose the potential is changed to a more positive value. The main effect is to lower the energy of the "reactant" electron; hence the curve corresponding to $Na^+ + e$ drops with respect to that corresponding to Na(Hg), and the situation resembles that of Figure 3.3.1b. Since the barrier for reduction is raised and that for oxidation is lowered, the net transformation is conversion of Na(Hg) to $Na^+ + e$. Setting the potential to a value more negative than E_{eq}, raises the energy of the electron and shifts the curve for $Na^+ + e$ to higher energies, as shown in Figure 3.3.1c. Since the reduction barrier drops and the oxidation barrier rises, relative to the condition at E_{eq}, a net cathodic current flows. These arguments show qualitatively the way in which the potential affects the net rates and directions of electrode reactions. By considering the model more closely, we can establish a quantitative relationship.

3.3.2 One-Step, One-Electron Process

Let us now consider the simplest possible electrode process, wherein species O and R engage in a one-electron transfer at the interface without being involved in any other chemical step,

$$O + e \underset{k_b}{\overset{k_f}{\rightleftarrows}} R \tag{3.3.2}$$

Suppose also that the standard free energy profiles along the reaction coordinate have the parabolic shapes shown in Figure 3.3.2. The upper frame of that figure depicts the full path from reactants to products, while the lower frame is an enlargement of the region near the transition state. It is not important for this discussion that we know the shapes of these profiles in detail.

In developing a theory of electrode kinetics, it is convenient to express potential against a point of significance to the chemistry of the system, rather than against an arbitrary external reference, such as an SCE. There are two natural reference points, *viz.* the equilibrium potential of the system and the standard (or formal) potential of the couple under consideration. We actually used the equilibrium potential as a reference point in the discussion of the preceding section, and we will use it again in this section. However, it is possible to do so only when both members of the couple are present, so that an equilibrium is defined. The more general reference point is $E^{0'}$. Suppose the upper curve on the $O + e$ side of Figure 3.3.2 applies when the electrode potential is equal to $E^{0'}$. The cathodic and anodic activation energies are then $\Delta G_{0c}^{\ddagger}$ and $\Delta G_{0a}^{\ddagger}$ respectively.

If the potential is changed by ΔE to a new value, E, the relative energy of the electron resident on the electrode changes by $-F\Delta E = -F(E - E^{0'})$; hence the $O + e$ curve moves up or down by that amount. The lower curve on the left side of Figure 3.3.2 shows this effect for a positive ΔE. It is readily apparent that the barrier for oxidation, $\Delta G_a^{\ddagger}$, has become less than $\Delta G_{0a}^{\ddagger}$ by a fraction of the total energy change. Let us call that fraction
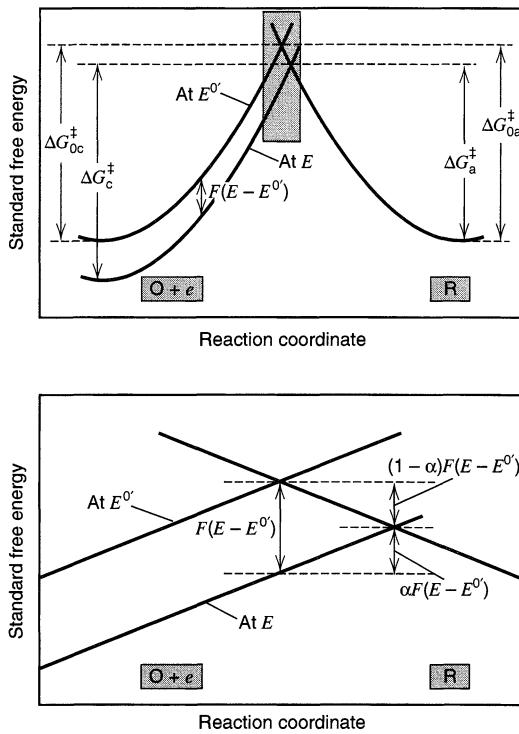
Figure 3.3.2 Effects of a potential change on the standard free energies of activation for oxidation and reduction. The lower frame is a magnified picture of the boxed area in the upper frame.

$1 - \alpha$, where α, the *transfer coefficient*, can range from zero to unity, depending on the shape of the intersection region. Thus,

$$\Delta G_a^{\ddagger} = \Delta G_{0a}^{\ddagger} - (1 - \alpha)F(E - E^{0'}) \tag{3.3.3}$$

A brief study of the figure also reveals that at potential E the cathodic barrier, $\Delta G_c^{\ddagger}$, is higher than $\Delta G_{0c}^{\ddagger}$ by $\alpha F(E - E^{0'})$; therefore,

$$\Delta G_c^{\ddagger} = \Delta G_{0c}^{\ddagger} + \alpha F(E - E^{0'}) \tag{3.3.4}$$

Now let us assume that the rate constants k_f and k_b have an Arrhenius form that can be expressed as

$$k_f = A_f \exp\left(-\Delta G_c^{\ddagger}/RT\right) \tag{3.3.5}$$

$$k_b = A_b \exp\left(-\Delta G_a^{\ddagger}/RT\right) \tag{3.3.6}$$

Inserting the activation energies, (3.3.3) and (3.3.4), gives

$$k_f = A_f \exp\left(-\Delta G_{0c}^{\ddagger}/RT\right)\exp[-\alpha f(E - E^{0'})] \tag{3.3.7}$$

$$k_b = A_b \exp\left(-\Delta G_{0a}^{\ddagger}/RT\right)\exp[(1 - \alpha)f(E - E^{0'})] \tag{3.3.8}$$

where $f = F/RT$. The first two factors in each of these expressions form a product that is independent of potential and equal to the rate constant at $E = E^{0'}$.[4]

Now consider the special case in which the interface is at equilibrium with a solution in which $C_O^* = C_R^*$. In this situation, $E = E^{0'}$ and $k_f C_O^* = k_b C_R^*$, so that $k_f = k_b$. Thus, $E^{0'}$ is the potential where the forward and reverse rate constants have the same value. That

---

[4]In other electrochemical literature, k_f and k_b are designated as k_c and k_a or as k_{ox} and k_{red}. Sometimes kinetic equations are written in terms of a complementary transfer coefficient, $\beta = 1 - \alpha$.

value is called the *standard rate constant, k^0*.[5] The rate constants at other potentials can then be expressed simply in terms of k^0:

$$k_f = k^0 \exp\left[-\alpha f (E - E^{0'})\right] \tag{3.3.9}$$

$$k_b = k^0 \exp\left[(1 - \alpha)f (E - E^{0'})\right] \tag{3.3.10}$$

Insertion of these relations into (3.2.8) yields the complete *current-potential characteristic:*

$$i = FAk^0 \left[C_O(0, t)e^{-\alpha f (E - E^{0'})} - C_R(0, t)e^{(1-\alpha)f (E - E^{0'})} \right] \tag{3.3.11}$$

This relation is very important. It, or a variation derived from it, is used in the treatment of almost every problem requiring an account of heterogeneous kinetics. Section 3.4 will cover some of its ramifications. These results and the inferences derived from them are known broadly as the *Butler–Volmer* formulation of electrode kinetics, in honor of the pioneers in this area (17, 18).

One can derive the Butler–Volmer kinetic expressions by an alternative method based on electrochemical potentials (8, 10, 12, 19–21). Such an approach can be more convenient for more complicated cases, such as requiring the inclusion of double-layer effects or sequences of reactions in a mechanism. The first edition develops it in detail.[6]

3.3.3 The Standard Rate Constant

The physical interpretation of k^0 is straightforward. It simply is a measure of the kinetic facility of a redox couple. A system with a large k^0 will achieve equilibrium on a short time scale, but a system with small k^0 will be sluggish. The largest measured standard rate constants are in the range of 1 to 10 cm/s and are associated with particularly simple electron-transfer processes. For example, the standard rate constants for the reductions and oxidations of many aromatic hydrocarbons (such as substituted anthracenes, pyrene, and perylene) to the corresponding anion and cation radicals fall in this range (22–24). These processes involve only electron transfer and resolvation. There are no significant alterations in the molecular forms. Similarly, some electrode processes involving the formation of amalgams [e.g., the couples $Na^+/Na(Hg)$, $Cd^{2+}/Cd(Hg)$, and Hg_2^{2+}/Hg] are rather facile (25, 26). More complicated reactions involving significant molecular rearrangement upon electron transfer, such as the reduction of molecular oxygen to hydrogen peroxide or water, or the reduction of protons to molecular hydrogen, can be very sluggish (25–27). Many of these systems involve multistep mechanisms and are discussed more fully in Section 3.5. Values of k^0 significantly lower than 10^{-9} cm/s have been reported (28–31); therefore, electrochemistry deals with a range of more than 10 orders of magnitude in kinetic reactivity.

Note that k_f and k_b can be made quite large, even if k^0 is small, by using a sufficiently extreme potential relative to $E^{0'}$. In effect, one drives the reaction by supplying the activation energy electrically. This idea is explored more fully in Section 3.4.

---

[5]The standard rate constant is also designated by $k_{s,h}$ or k_s in the electrochemical literature. Sometimes it is also called the *intrinsic rate constant.*

[6]First edition, Section 3.4.
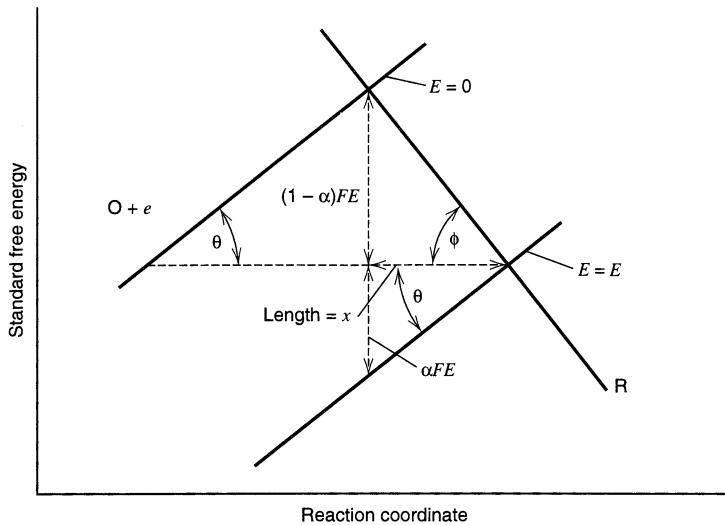
Figure 3.3.3 Relationship of the transfer coefficient to the angles of intersection of the free energy curves.

3.3.4 The Transfer Coefficient

The transfer coefficient, α, is a measure of the symmetry of the energy barrier. This idea can be amplified by considering α in terms of the geometry of the intersection region, as shown in Figure 3.3.3. If the curves are locally linear, then the angles θ and ϕ are defined by

$$\tan \theta = \alpha FE/x \qquad (3.3.12)$$

$$\tan \phi = (1 - \alpha)\, FE/x \qquad (3.3.13)$$

hence

$$\alpha = \frac{\tan \theta}{\tan \phi + \tan \theta} \qquad (3.3.14)$$

If the intersection is symmetrical, $\phi = \theta$, and $\alpha = \frac{1}{2}$. Otherwise $0 \le \alpha < \frac{1}{2}$ or $\frac{1}{2} < \alpha \le 1$, as shown in Figure 3.3.4. In most systems α turns out to lie between 0.3 and 0.7, and it can usually be approximated by 0.5 in the absence of actual measurements.

The free energy profiles are not likely to be linear over large ranges of the reaction coordinate; thus the angles θ and ϕ can be expected to change as the intersection between reactant and product curves shifts with potential. Consequently, α should generally be a
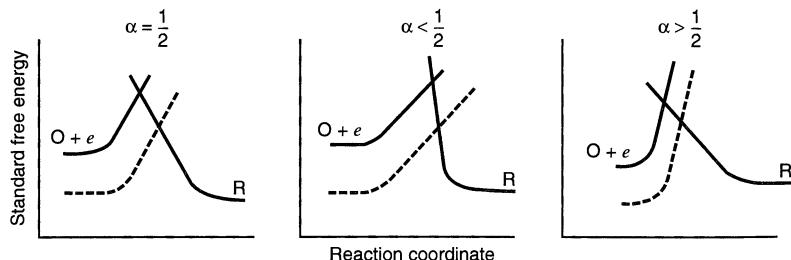
Figure 3.3.4 The transfer coefficient as an indicator of the symmetry of the barrier to reaction. The dashed lines show the shift in the curve for O + e as the potential is made more positive.

potential-dependent factor (see Section 6.7.3). However, in the great majority of experiments, α appears to be constant, if only because the potential range over which kinetic data can be collected is fairly narrow. In a typical chemical system, the free energies of activation are in the range of a few electron volts, but the full range of measurable kinetics usually corresponds to a *change* in activation energy of only 50–200 meV, or a few percent of the total. Thus, the intersection point varies only over a small domain, such as, the boxed region in Figure 3.3.2, where the curvature in the profiles can hardly be seen. The kinetically operable potential range is narrow in most systems, because the rate constant for electron transfer rises exponentially with potential. Not far beyond the potential where a process first produces a detectable current, mass transfer becomes rate-limiting and the electron-transfer kinetics no longer control the experiment. These points are discussed in much detail throughout the remainder of this book. In a few systems, mass transfer is not an issue and kinetics can be measured over very wide ranges of potential. Figure 14.5.8 provides an example showing large variations of α with potential in a case involving a surface-bound electroactive species.

▷ 3.4 IMPLICATIONS OF THE BUTLER-VOLMER MODEL FOR THE ONE-STEP, ONE-ELECTRON PROCESS

In this section, we will develop a number of operational relationships that will prove valuable in the interpretation of electrochemical experiments. Each is derived under the assumption that the electrode reaction is the one-step, one-electron process for which the primary relations were derived above. The validity of the conclusions for a multistep process will be considered separately in Section 3.5.

3.4.1 Equilibrium Conditions. The Exchange Current (8–14)

At equilibrium, the net current is zero, and the electrode is known to adopt a potential based on the bulk concentrations of O and R as dictated by the Nernst equation. Let us see now if the kinetic model yields that thermodynamic relation as a special case. From equation 3.3.11 we have, at zero current,

$$FAk^0C_O(0, t)e^{-\alpha f(E_{eq}-E^{0'})} = FAk^0C_R(0, t)e^{(1-\alpha)f(E_{eq}-E^{0'})} \tag{3.4.1}$$

Since equilibrium applies, the bulk concentrations of O and R are found also at the surface; hence

$$e^{f(E_{eq}-E^{0'})} = \frac{C_O^*}{C_R^*} \tag{3.4.2}$$

which is simply an exponential form of the Nernst relation:

$$\boxed{E_{eq} = E^{0'} + \frac{RT}{F} \ln \frac{C_O^*}{C_R^*}} \tag{3.4.3}$$

Thus, the theory has passed its first test of compatibility with reality.

Even though the net current is zero at equilibrium, we still envision balanced faradaic activity that can be expressed in terms of the *exchange current*, i_0, which is equal in magnitude to either component current, i_c or i_a. That is,

$$i_0 = FAk^0C_O^*e^{-\alpha f(E_{eq}-E^{0'})} \tag{3.4.4}$$

If both sides of (3.4.2) are raised to the $-\alpha$ power, we obtain

$$e^{-\alpha f(E_{eq}-E^{0'})} = \left(\frac{C_O^*}{C_R^*}\right)^{-\alpha}$$

(3.4.5)

Substitution of (3.4.5) into (3.4.4) gives[7]

$$i_0 = FAk^0 C_O^{*(1-\alpha)} C_R^{*\alpha}$$

(3.4.6)

The exchange current is therefore proportional to k^0 and can often be substituted for k^0 in kinetic equations. For the particular case where $C_O^* = C_R^* = C$,

$$i_0 = FAk^0 C$$

(3.4.7)

Often the exchange current is normalized to unit area to provide the *exchange current density*, $j_0 = i_0/A$.

3.4.2 The Current-Overpotential Equation

An advantage of working with i_0 rather than k^0 is that the current can be described in terms of the deviation from the equilibrium potential, that is, the overpotential, η, rather than the formal potential, $E^{0'}$. Dividing (3.3.11) by (3.4.6), we obtain

$$\frac{i}{i_0} = \frac{C_O(0, t)e^{-\alpha f(E-E^{0'})}}{C_O^{*(1-\alpha)}C_R^{*\alpha}} - \frac{C_R(0, t)e^{(1-\alpha)f(E-E^{0'})}}{C_O^{*(1-\alpha)}C_R^{*\alpha}}$$

(3.4.8)

or

$$\frac{i}{i_0} = \frac{C_O(0, t)}{C_O^*} e^{-\alpha f(E-E^{0'})}\left(\frac{C_O^*}{C_R^*}\right)^{\alpha} - \frac{C_R(0, t)}{C_R^*} e^{(1-\alpha)f(E-E^{0'})}\left(\frac{C_O^*}{C_R^*}\right)^{-(1-\alpha)}$$

(3.4.9)

The ratios $(C_O^*/C_R^*)^{\alpha}$ and $(C_O^*/C_R^*)^{-(1-\alpha)}$ are easily evaluated from equations 3.4.2 and 3.4.5, and by substitution we obtain

$$i = i_0\left[\frac{C_O(0, t)}{C_O^*} e^{-\alpha f\eta} - \frac{C_R(0, t)}{C_R^*} e^{(1-\alpha)f\eta}\right]$$

(3.4.10)

where $\eta = E - E_{eq}$. This equation, known as the *current-overpotential equation*, will be used frequently in later discussions. Note that the first term describes the cathodic component current at any potential, and the second gives the anodic contribution.[8]

The behavior predicted by (3.4.10) is depicted in Figure 3.4.1. The solid curve shows the actual total current, which is the sum of the components i_c and i_a, shown as dashed traces. For large negative overpotentials, the anodic component is negligible; hence the total current curve merges with that for i_c. At large positive overpotentials, the cathodic component is negligible, and the total current is essentially the same as i_a. In going either direction from E_{eq}, the magnitude of the current rises rapidly, because the exponential factors dominate behavior, but at extreme η, the current levels off. In these

---

[7]The same equation for the exchange current can be derived from the anodic component current i_a at $E = E_{eq}$.

[8]Since double-layer effects have not been included in this treatment, k^0 and i_0 are, in Delahay's nomenclature (8), *apparent* constants of the system. Both depend on double-layer structure to some extent and are functions of the potential at the outer Helmholtz plane, ϕ_2, relative to the solution bulk. This point will be discussed in more detail in Section 13.7.
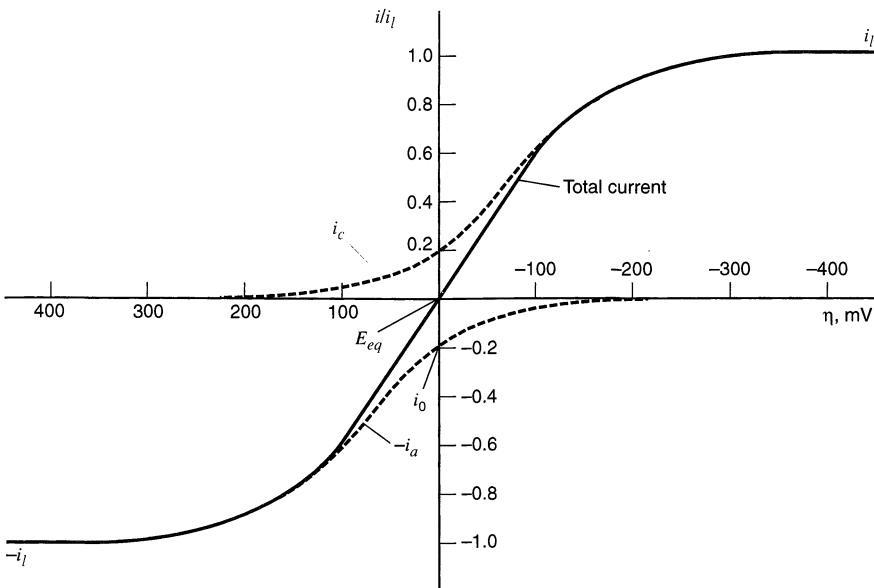
Figure 3.4.1 Current-overpotential curves for the system $O + e \rightleftarrows R$ with $\alpha = 0.5, T = 298$ K, $i_{l,c} = -i_{l,a} = i_l$ and $i_0/i_l = 0.2$. The dashed lines show the component currents i_c and i_a.

level regions, the current is limited by mass transfer rather than heterogeneous kinetics. The exponential factors in (3.4.10) are then moderated by the factors $C_O(0, t)/C_O*$ and $C_R(0, t)/C_R*$, which manifest the reactant supply.

3.4.3 Approximate Forms of the i-η Equation

(a) No Mass-Transfer Effects
If the solution is well stirred, or currents are kept so low that the surface concentrations do not differ appreciably from the bulk values, then (3.4.10) becomes

$$i = i_0\left[e^{-\alpha f\eta} - e^{(1-\alpha)f\eta}\right] \tag{3.4.11}$$

which is historically known as the *Butler–Volmer equation*. It is a good approximation of (3.4.10) when i is less than about 10% of the smaller limiting current, $i_{l,c}$ or $i_{l,a}$. Equations 1.4.10 and 1.4.19 show that $C_O(0, t)/C_O^*$ and $C_R(0, t)/C_R^*$ will then be between 0.9 and 1.1.

The curves in Figure 3.4.2 show the behavior of (3.4.11) for different exchange current densities. In each case $\alpha = 0.5$. Figure 3.4.3 shows the effect of α in a similar manner. There the exchange current density is 10^{-6} A/cm^2 for each curve. A notable feature of Figure 3.4.2 is the degree to which the inflection at E_{eq} depends on the exchange current density.

Since mass-transfer effects are not included here, the overpotential associated with any given current serves solely to provide the activation energy required to drive the heterogeneous process at the rate reflected by the current. The lower the exchange current, the more sluggish the kinetics; hence the larger this *activation overpotential* must be for any particular net current.
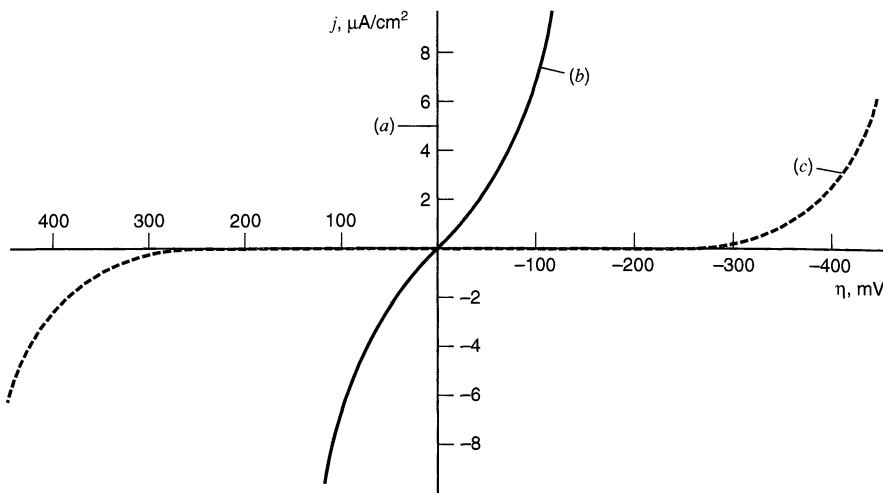
Figure 3.4.2 Effect of exchange current density on the activation overpotential required to deliver net current densities. (a) $j_0 = 10^{-3}$ A/cm^2 (curve is indistinguishable from the current axis), (b) $j_0 = 10^{-6}$ A/cm^2, (c) $j_0 = 10^{-9}$ A/cm^2. For all cases the reaction is O $+ e \rightleftarrows$ R with $\alpha = 0.5$ and $T = 298$ K.

If the exchange current is very large, as for case (a) in Figure 3.4.2, then the system can supply large currents, even the mass-transfer-limited current, with insignificant activation overpotential. In that case, any observed overpotential is associated with changing surface concentrations of species O and R. It is called a *concentration overpotential* and can be viewed as an activation energy required to drive mass transfer at the rate needed to support the current. If the concentrations of O and R are comparable, then E_{eq} will be near $E^{0'}$, and the limiting currents for both the anodic and cathodic segments will be reached within a few tens of millivolts of $E^{0'}$.

On the other hand, one might deal with a system with an exceedingly small exchange current because k^0 is very low, as for case (c) in Figure 3.4.2. In that circumstance, no sig-
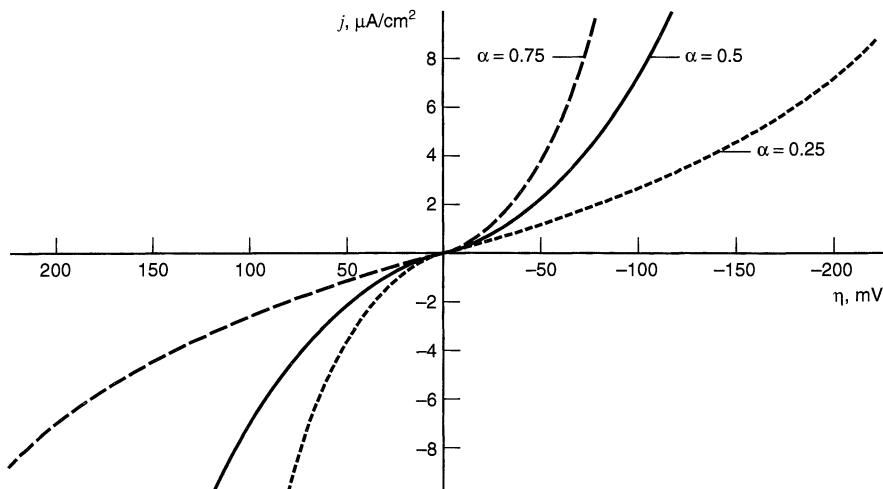
Figure 3.4.3 Effect of the transfer coefficient on the symmetry of the current-overpotential curves for O $+ e \rightleftarrows$ R with $T = 298$ K and $j_0 = 10^{-6}$ A/cm^2.

nificant current flows unless a large activation overpotential is applied. At a sufficiently extreme potential, the heterogeneous process can be driven fast enough that mass transfer controls the current, and a limiting plateau is reached. When mass-transfer effects start to manifest themselves, then a concentration overpotential will also contribute, but the bulk of the overpotential is for activation of charge transfer. In this kind of system, the reduction wave occurs at much more negative potentials than $E^{0'}$, and the oxidation wave lies at much more positive values.

The exchange current can be viewed as a kind of "idle current" for charge exchange across the interface. If we want to draw a net current that is only a small fraction of this bidirectional idle current, then only a tiny overpotential will be required to extract it. Even at equilibrium, the system is delivering charge across the interface at rates much greater than we require. The role of the slight overpotential is to unbalance the rates in the two directions to a small degree so that one of them predominates. On the other hand, if we ask for a net current that exceeds the exchange current, the job is much harder. We have to drive the system to deliver charge at the required rate, and we can only do that by applying a significant overpotential. From this perspective, we see that the exchange current is a measure of any system's ability to deliver a net current without a significant energy loss due to activation.

Exchange current densities in real systems reflect the wide range in k^0. They may exceed 10 A/cm^2 or be less than pA/cm^2 (8–14, 28–31).

(b) Linear Characteristic at Small η

For small values of x, the exponential e^x can be approximated as $1 + x$; hence for sufficiently small η, equation 3.4.11 can be reexpressed as

$$i = -i_0 f \eta \qquad (3.4.12)$$

which shows that the net current is linearly related to overpotential in a narrow potential range near E_{eq}. The ratio $-\eta/i$ has units of resistance and is often called the *charge-transfer resistance*, R_{ct}:

$$R_{ct} = \frac{RT}{F i_0} \qquad (3.4.13)$$

This parameter is the negative reciprocal slope of the i-η curve where that curve passes through the origin ($\eta = 0$, $i = 0$). It can be evaluated directly in some experiments, and it serves as a convenient index of kinetic facility. For very large k^0, it approaches zero (see Figure 3.4.2).

(c) Tafel Behavior at Large η

For large values of η (either negative or positive), one of the bracketed terms in (3.4.11) becomes negligible. For example, at large negative overpotentials, $\exp(-\alpha f \eta) \gg \exp[(1 - \alpha) f \eta]$ and (3.4.11) becomes

$$i = i_0 e^{-\alpha f \eta} \qquad (3.4.14)$$

or

$$\eta = \frac{RT}{\alpha F} \ln i_0 - \frac{RT}{\alpha F} \ln i \qquad (3.4.15)$$

Thus, we find that the kinetic treatment outlined above does yield a relation of the Tafel form, as required by observation, for the appropriate conditions. The empirical Tafel constants (see equation 3.2.4) can now be identified from theory as[9]

$$a = \frac{2.3RT}{\alpha F} \log i_0 \qquad b = \frac{-2.3RT}{\alpha F} \tag{3.4.16}$$

The Tafel form can be expected to hold whenever the back reaction (i.e., the anodic process, when a net reduction is considered, and vice versa) contributes less than 1% of the current, or

$$\frac{e^{(1-\alpha)f\eta}}{e^{-\alpha f\eta}} = e^{f\eta} \leq 0.01, \tag{3.4.17}$$

which implies that $|\eta| > 118$ mV at 25°C. If the electrode kinetics are fairly facile, the system will approach the mass-transfer-limited current by the time such an extreme overpotential is established. Tafel relationships cannot be observed for such cases, because they require the absence of mass-transfer effects on the current. When electrode kinetics are sluggish and significant activation overpotentials are required, good Tafel relationships can be seen. This point underscores the fact that Tafel behavior is an indicator of *totally irreversible* kinetics. Systems in that category allow no significant current flow except at high overpotentials, where the faradaic process is effectively unidirectional and, therefore, chemically irreversible.

(d) Tafel Plots (8–11, 32)

A plot of log i vs. η, known as a *Tafel plot*, is a useful device for evaluating kinetic parameters. In general, there is an anodic branch with slope $(1 - \alpha)F/2.3RT$ and a cathodic branch with slope $-\alpha F/2.3RT$. As shown in Figure 3.4.4, both linear segments extrapolate to an intercept of log i_0. The plots deviate sharply from linear behavior as η approaches zero, because the back reactions can no longer be regarded as negligible. The
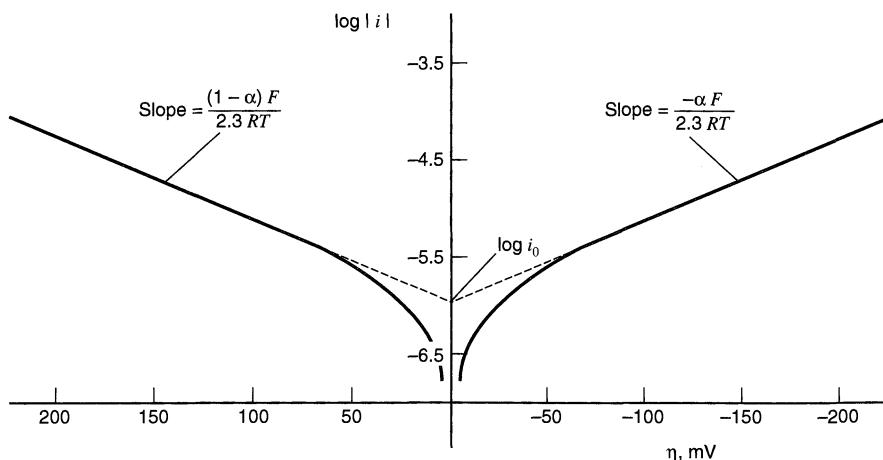
Figure 3.4.4 Tafel plots for anodic and cathodic branches of the current-overpotential curve for $O + e \rightleftarrows R$ with $\alpha = 0.5$, $T = 298$ K, and $j_0 = 10^{-6}$ A/cm^2.

[9]Note that for $\alpha = 0.5$, $b = 0.118$ V, a value that is sometimes quoted as a "typical" Tafel slope.
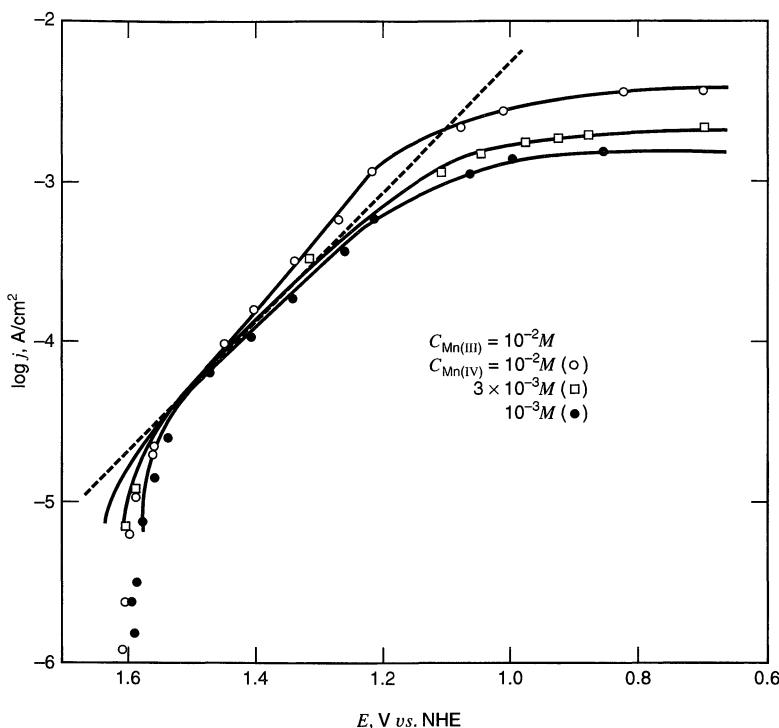
Figure 3.4.5 Tafel plots for the reduction of Mn(IV) to Mn(III) at Pt in 7.5 M H_2SO_4 at 298 K. The dashed line corresponds to $\alpha = 0.24$. [From K. J. Vetter and G. Manecke, *Z. Physik. Chem. (Leipzig)*, **195**, 337 (1950), with permission.]

transfer coefficient, α, and the exchange current, i_0, are obviously readily accessible from this kind of presentation, when it can be applied.

Some real Tafel plots are shown in Figure 3.4.5 for the Mn(IV)/Mn(III) system in concentrated acid (33). The negative deviations from linearity at very large overpotentials come from limitations imposed by mass transfer. The region of very low overpotentials shows sharp falloffs for the reasons outlined just above.

Allen and Hickling (34) suggested an alternative method allowing the use of data obtained at low overpotentials. Equation 3.4.11 can be rewritten as

$$i = i_0 e^{-\alpha f \eta} (1 - e^{f \eta}) \tag{3.4.18}$$

or

$$\log \frac{i}{1 - e^{f \eta}} = \log i_0 - \frac{\alpha F \eta}{2.3RT} \tag{3.4.19}$$

so that a plot of log $[i/(1 - e^{f \eta})]$ *vs.* η yields an intercept of log i_0 and a slope of $-\alpha F/2.3RT$. This approach has the advantage of being applicable to electrode reactions that are not totally irreversible, that is, those in which both anodic and cathodic processes contribute significantly to the currents measured in the overpotential range where mass-transfer effects are not important. Such systems are often termed *quasireversible,* because the opposing charge-transfer reactions must both be considered, yet a noticeable activation overpotential is required to drive a given net current through the interface.

3.4.4 Exchange Current Plots (8–14)

From equation 3.4.4, we recognize that the exchange current can be restated as

$$\log i_0 = \log FAk^0 + \log C_O^* + \frac{\alpha F}{2.3RT} E^{0'} - \frac{\alpha F}{2.3RT} E_{\text{eq}} \tag{3.4.20}$$

Therefore, a plot of $\log i_0$ vs. E_{eq} at constant C_O^* should be linear with a slope of $-\alpha F/2.3RT$. The equilibrium potential E_{eq} can be varied experimentally by changing the bulk concentration of species R, while that of species O is held constant. This kind of plot is useful for obtaining α from experiments in which i_0 is measured essentially directly (e.g., see Chapters 8 and 10).

Another means for determining α is suggested by rewriting (3.4.6) as

$$\log i_0 = \log FAk^0 + (1 - \alpha) \log C_O^* + \alpha \log C_R^* \tag{3.4.21}$$

Thus

$$\left(\frac{\partial \log i_0}{\partial \log C_O^*} \right)_{C_R^*} = 1 - \alpha \qquad \text{and} \qquad \left(\frac{\partial \log i_0}{\partial \log C_R^*} \right)_{C_O^*} = \alpha \tag{3.4.22}$$

An alternative equation, which does not require holding either C_O^* or C_R^* constant, is

$$\frac{d \log (i_0/C_O^*)}{d \log (C_R^*/C_O^*)} = \alpha \tag{3.4.23}$$

The last relation is easily derived from (3.4.6).

3.4.5 Very Facile Kinetics and Reversible Behavior

To this point, we have discussed in detail only those systems for which appreciable activation overpotential is observed. Another very important limit is the case in which the electrode kinetics require a negligible driving force. As we noted above, that case corresponds to a very large exchange current, which in turn reflects a big standard rate constant k^0. Let us rewrite the current-overpotential equation (3.4.10) as follows:

$$\frac{i}{i_0} = \frac{C_O(0, t)}{C_O^*} e^{-\alpha f \eta} - \frac{C_R(0, t)}{C_R^*} e^{(1 - \alpha) f \eta} \tag{3.4.24}$$

and consider its behavior when i_0 becomes very large compared to any current of interest. The ratio i/i_0 then approaches zero, and we can rearrange the limiting form of equation 3.4.24 to

$$\frac{C_O(0, t)}{C_R(0, t)} = \frac{C_O^*}{C_R^*} e^{f(E - E_{\text{eq}})} \tag{3.4.25}$$

and, by substitution from the Nernst equation in form (3.4.2), we obtain

$$\frac{C_O(0, t)}{C_R(0, t)} = e^{f(E_{\text{eq}} - E^{0'})} e^{f(E - E_{\text{eq}})} \tag{3.4.26}$$

or

$$\frac{C_O(0, t)}{C_R(0, t)} = e^{f(E - E^{0'})} \tag{3.4.27}$$

This equation can be rearranged to the very important result:

$$E = E^{0\prime} + \frac{RT}{F} \ln \frac{C_O(0, t)}{C_R(0, t)} \tag{3.4.28}$$

Thus we see that the electrode potential and the *surface* concentrations of O and R are linked by an equation of the Nernst form, regardless of the current flow.

No kinetic parameters are present because the kinetics are so facile that no experimental manifestations can be seen. In effect, the potential and the surface concentrations are always kept in equilibrium with each other by the fast charge-transfer processes, and the *thermodynamic* equation, (3.4.28), characteristic of equilibrium, always holds. Net current flows because the surface concentrations are not at equilibrium with the bulk, and mass transfer continuously moves material to the surface, where it must be reconciled to the potential by electrochemical change.

We have already seen that a system that is always at equilibrium is termed a *reversible* system; thus it is logical that an electrochemical system in which the charge-transfer interface is always at equilibrium be called a *reversible* (or, alternatively, a *nernstian*) *system*. These terms simply refer to cases in which the interfacial redox kinetics are so fast that activation effects cannot be seen. Many such systems exist in electrochemistry, and we will consider this case frequently under different sets of experimental circumstances. We will also see that any given system may appear reversible, quasireversible, or totally irreversible, depending on the demands we make on the charge-transfer kinetics.

3.4.6 Effects of Mass Transfer

A more complete i-η relation can be obtained from (3.4.10) by substituting for $C_O(0, t)/C_O^*$ and $C_R(0, t)/C_R^*$ according to (1.4.10) and (1.4.19):

$$\frac{i}{i_0} = \left(1 - \frac{i}{i_{l,c}}\right)e^{-\alpha f\eta} - \left(1 - \frac{i}{i_{l,a}}\right)e^{(1-\alpha)f\eta} \tag{3.4.29}$$

This equation can be rearranged easily to give i as an explicit function of η over the whole range of η. In Figure 3.4.6, one can see i-η curves for several ratios of i_0/i_l, where $i_l = i_{l,c} = -i_{l,a}$.

For small overpotentials, a linearized relation can be used. The complete Taylor expansion (Section A.2) of (3.4.24) gives, for $\alpha f\eta \ll 1$,

$$\frac{i}{i_0} = \frac{C_O(0, t)}{C_O^*} - \frac{C_R(0, t)}{C_R^*} - \frac{F\eta}{RT} \tag{3.4.30}$$

which can be substituted as above and rearranged to give

$$\eta = i\frac{RT}{F}\left(\frac{1}{i_0} + \frac{1}{i_{l,c}} - \frac{1}{i_{l,a}}\right) \tag{3.4.31}$$

In terms of the charge- and mass-transfer pseudoresistances defined in equations 1.4.28 and 3.4.13, this equation is

$$\eta = -i(R_{ct} + R_{mt,c} + R_{mt,a}) \tag{3.4.32}$$

Here we see very clearly that when i_0 is much greater than the limiting currents, $R_{ct} \ll R_{mt,c} + R_{mt,a}$ and the overpotential, even near E_{eq}, is a concentration over-
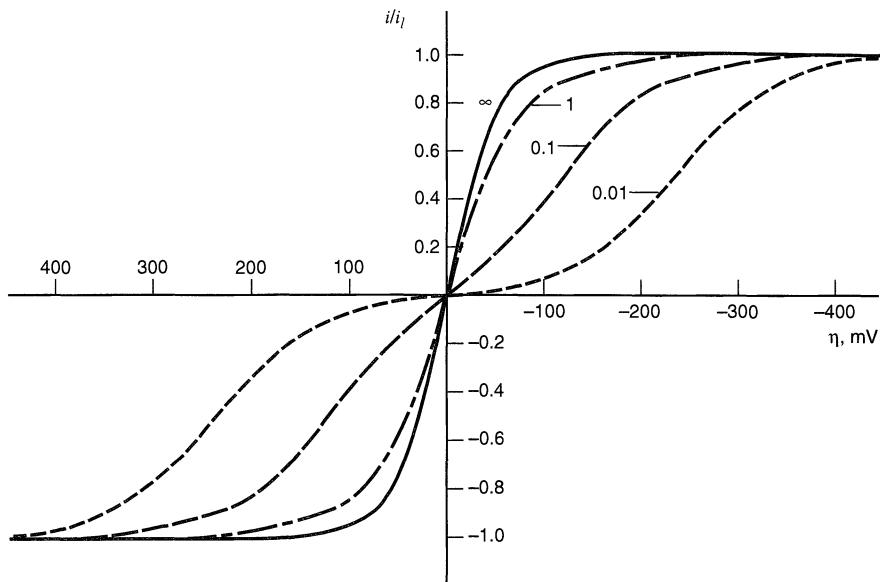
Figure 3.4.6 Relationship between the activation overpotential and net current demand relative to the exchange current. The reaction is $O + e \rightleftarrows R$ with $\alpha = 0.5$, $T = 298$ K, and $i_{l,c} = -i_{l,a} = i_l$. Numbers by curves show i_0/i_l.

potential. On the other hand, if i_0 is much less than the limiting currents, then $R_{mt,c} + R_{mt,a} \ll R_{ct}$, and the overpotential near E_{eq} is due to activation of charge transfer. This argument is simply another way of looking at the points made earlier in Section 3.4.3(a).

In the Tafel regions, other useful forms of (3.4.29) can be obtained. For the cathodic branch at high η values, the anodic contribution is insignificant, and (3.4.29) becomes

$$\frac{i}{i_0} = \left(1 - \frac{i}{i_{l,c}}\right)e^{-\alpha f \eta} \tag{3.4.33}$$
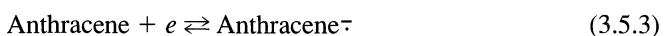
or

$$\eta = \frac{RT}{\alpha F}\ln\frac{i_0}{i_{l,c}} + \frac{RT}{\alpha F}\ln\frac{(i_{l,c} - i)}{i} \tag{3.4.34}$$
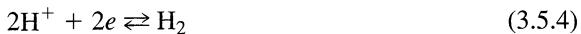
This equation can be useful for obtaining kinetic parameters for systems in which the normal Tafel plots are complicated by mass-transfer effects.

3.5 MULTISTEP MECHANISMS (11, 13, 14, 25, 26, 35)

The foregoing sections have concentrated on the potential dependences of the forward and reverse rate constants governing the simple one-step, one-electron electrode reaction. By restricting our view in this way, we have achieved a qualitative and quantitative understanding of the major features of electrode kinetics. Also, we have developed a set of relations that we can expect to fit a number of real chemical systems, for example,

$$Fe(CN)_6^{3-} + e \rightleftarrows Fe(CN)_6^{4-} \tag{3.5.1}$$

$$Tl^+ + e \overset{Hg}{\rightleftarrows} Tl(Hg) \tag{3.5.2}$$

$$\text{Anthracene} + e \rightleftarrows \text{Anthracene}^{\overline{\cdot}} \tag{3.5.3}$$

But we must now recognize that most electrode processes are mechanisms of several steps. For example, the important reaction

$$2H^+ + 2e \rightleftarrows H_2 \qquad (3.5.4)$$

clearly must involve several elementary reactions. The hydrogen nuclei are separated in the oxidized form, but are combined by reduction. Somehow, during reduction, there must be a pair of charge transfers and some chemical means for linking the two nuclei. Consider also the reduction

$$Sn^{4+} + 2e \rightleftarrows Sn^{2+} \qquad (3.5.5)$$

Is it realistic to regard two electrons as tunneling simultaneously through the interface? Or must we consider the reduction and oxidation sequences as two one-electron processes proceeding through the ephemeral intermediate Sn^{3+}? Another case that looks simple at first glance is the deposition of silver from aqueous potassium nitrate:

$$Ag^+ + e \rightleftarrows Ag \qquad (3.5.6)$$

However, there is evidence that this reduction involves at least a charge-transfer step, creating an adsorbed silver atom (*adatom*), and a crystallization step, in which the adatom migrates across the surface until it finds a vacant lattice site. Electrode processes may also involve adsorption and desorption kinetics of primary reactants, intermediates, and products.

Thus, electrode reactions generally can be expected to show complex behavior, and for each mechanistic sequence, one would obtain a distinct theoretical linkage between current and potential. That relation would have to take into account the potential dependences of all steps and the surface concentrations of all intermediates, in addition to the concentrations of the primary reactants and products.

A great deal of effort has been spent in studying the mechanisms of complex electrode reactions. One general approach is based on steady-state current-potential curves. Theoretical responses are derived on the basis of mechanistic alternatives, then one compares predicted behavior, such as the variation of exchange current with reactant concentration, with the behavior found experimentally. A number of excellent expositions of this approach are available in the literature (8–14, 25, 26, 35). We will not delve into specific cases in this chapter, except in Problems 3.7 and 3.10. More commonly, complex behavior is elucidated by studies of transient responses, such as cyclic voltammetry at different scan rates. The experimental study of multistep reactions by such techniques is covered in Chapter 12.

3.5.1 Rate-Determining Electron Transfer

In the study of chemical kinetics, one can often simplify the prediction and analysis of behavior by recognizing that a single step of a mechanism is much more sluggish than all the others, so that it controls the rate of the overall reaction. If the mechanism is an electrode process, this *rate-determining step* (RDS) can be a heterogeneous electron-transfer reaction.
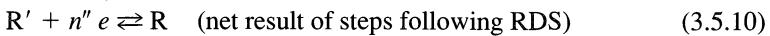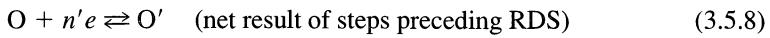
A widely held concept in electrochemistry is that truly elementary electron-transfer reactions always involve the exchange of one electron, so that an overall process involving a change of n electrons must involve n distinct electron-transfer steps. Of course, it may also involve other elementary reactions, such as adsorption, desorption, or various chemical reactions away from the interface. Within this view, a rate-determining electron-transfer is always a one-electron-process, and the results that we derived above for the

one-step, one-electron process can be used to describe the RDS, although the concentrations must often be understood as applying to intermediates, rather than to starting species or final products.

For example, consider an overall process in which O and R are coupled in an overall multielectron process

$$O + ne \rightleftarrows R \tag{3.5.7}$$

by a mechanism having the following general character:

$$O + n'e \rightleftarrows O' \quad \text{(net result of steps preceding RDS)} \tag{3.5.8}$$

$$O' + e \underset{k_b}{\overset{k_f}{\rightleftarrows}} R' \quad \text{(RDS)} \tag{3.5.9}$$

$$R' + n'' e \rightleftarrows R \quad \text{(net result of steps following RDS)} \tag{3.5.10}$$

Obviously $n' + n'' + 1 = n$.[10]

The current-potential characteristic can be written as

$$i = nFAk_{rds}^0 \, [C_{O'}(0, t)e^{-\alpha f(E - E_{rds}^{0'})} - C_{R'}(0, t)e^{(1-\alpha)f(E - E_{rds}^{0'})}] \tag{3.5.11}$$

where k_{rds}^0, α, and $E_{rds}^{0'}$ apply to the RDS. This relation is (3.3.11) written for the RDS and multiplied by n, because each net conversion of O' to R' results in the flow of n electrons, not just one electron, across the interface. The concentrations $C_{O'}(0, t)$ and $C_{R'}(0, t)$ are controlled not only by the interplay between mass transfer and the kinetics of heterogeneous electron transfer, as we found in Section 3.4, but also by the properties of the preceding and following reactions. The situation can become quite complicated, so we will make no attempt to discuss the general problem. However, a few important simple cases exist, and we will develop them briefly now.[11]

3.5.2 Multistep Processes at Equilibrium

If a true equilibrium exists for the overall process, all steps in the mechanism are individually at equilibrium. Thus, the surface concentrations of O' and R' are the values in equilibrium with the bulk concentrations of O and R, respectively. We designate them as $(C_{O'})_{eq}$ and $(C_{R'})_{eq}$. Recognizing that $i = 0$, we can proceed through the treatment leading to (3.4.2) to obtain the analogous relation

$$e^{f(E_{eq} - E_{rds}^{0'})} = \frac{(C_{O'})_{eq}}{(C_{R'})_{eq}} \tag{3.5.12}$$

For the mechanism in (3.5.8)–(3.5.10), nernstian relationships define the equilibria for the pre- and postreactions, and they can be written in the following forms:

$$e^{n'f(E_{eq} - E_{pre}^{0'})} = \frac{C_O^*}{(C_{O'})_{eq}} \qquad e^{n''f(E_{eq} - E_{post}^{0'})} = \frac{(C_{R'})_{eq}}{C_R^*} \tag{3.5.13}$$

---

[10]The discussions that follow hold if either or both of n' or n'' are zero.

[11]In the first edition and in much of the literature, one finds n_a used as the n value of the rate-determining step. As a consequence n_a appears in many kinetic expressions. Since n_a is probably always 1, it is a redundant symbol and has been dropped in this edition. The current-potential characteristic for a multistep process has often been expressed as

$$i = nFAk^0 \, [C_O(0, t)e^{-\alpha n_a f(E - E^{0'})} - C_R(0, t)e^{(1-\alpha)n_a f(E - E^{0'})}]$$

This is rarely, if ever, an accurate form of the i-E characteristic for multistep mechanisms.

where $E_{pre}^{0'}$ and $E_{post}^{0'}$ apply to (3.5.8) and (3.5.10), respectively. Substitution for the equilibrium concentrations of O' and R' in (3.5.12) gives

$$e^{f(E_{eq}-E_{rds}^{0'})}e^{n'f(E_{eq}-E_{pre}^{0'})}e^{n''f(E_{eq}-E_{post}^{0'})} = \frac{C_O^*}{C_R^*} \tag{3.5.14}$$

Recognizing that $n = n' + n'' + 1$ and that $E^{0'}$ for the overall process is (see Problem 2.10)

$$E^{0'} = \frac{E_{rds}^{0'} + n'E_{pre}^{0'} + n''E_{post}^{0'}}{n} \tag{3.5.15}$$

we can distill (3.5.14) into

$$e^{nf(E_{eq}-E^{0'})} = \frac{C_O^*}{C_R^*} \tag{3.5.16}$$

which is the exponential form of the Nernst equation for the overall reaction,

$$\boxed{E_{eq} = E^{0'} + \frac{RT}{nF}\ln\frac{C_O^*}{C_R^*}} \tag{3.5.17}$$

Of course, this is a required result if the kinetic model has any pretense to validity, and it is important that the BV model attains it for the limit of $i = 0$, not only for the simple one-step, one-electron process, but also in the context of an arbitrary multistep mechanism. The derivation here was carried out for a mechanism in which the prereactions and postreactions involve net charge transfer; however the same outcome can be obtained by a similar method for any reaction sequence, as long as it is chemically reversible and a true equilibrium can be established.

3.5.3 Nernstian Multistep Processes

If all steps in the mechanism are facile, so that the exchange velocities of all steps are large compared to the net reaction rate, the concentrations of all species participating in them are always essentially at equilibrium in a local context, even though a net current flows. The result for the RDS in this nernstian (reversible) limit has already been obtained as (3.4.27), which we now rewrite in exponential form:

$$\frac{C_{O'}(0, t)}{C_{R'}(0, t)} = e^{f(E-E_{rds}^{0'})} \tag{3.5.18}$$

Equilibrium expressions for the pre- and post-reactions link the surface concentrations of O' and R' to the surface concentrations of O and R. If these processes involve interfacial charge transfer, as in the mechanism of (3.5.8)–(3.5.10), the expressions are of the Nernst form:

$$e^{n'f(E-E_{pre}^{0'})} = \frac{C_O(0, t)}{C_{O'}(0, t)} \qquad e^{n''f(E-E_{post}^{0'})} = \frac{C_{R'}(0, t)}{C_R(0, t)} \tag{3.5.19}$$

By steps analogous to those leading from (3.5.12) to (3.5.16), one finds that for the reversible system
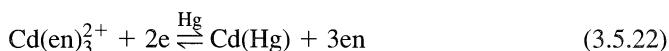
$$e^{nf(E_{eq}-E^{0'})} = \frac{C_O(0, t)}{C_R(0, t)} \tag{3.5.20}$$

which can be rearranged to

$$E = E^{0'} + \frac{RT}{nF} \ln \frac{C_O(0, t)}{C_R(0, t)} \tag{3.5.21}$$

This relationship is a very important general finding. It says that, for a kinetically facile system, the electrode potential and the surface concentrations of the initial reactant and the final product are in local nernstian balance at all times, regardless of the details of the mechanism linking these species and regardless of current flow. Like (3.5.17), (3.5.21) was derived for pre- and postreactions that involve net charge transfer, but one can easily generalize the derivation to include other patterns. The essential requirement is that all steps be chemically reversible and possess facile kinetics.[12]

A great many real systems satisfy these conditions, and electrochemical examination of them can yield a rich variety of chemical information (see Section 5.4.4). A good example is the reduction of the ethylenediamine (en) complex of Cd(II) at a mercury electrode:

$$Cd(en)_3^{2+} + 2e \overset{Hg}{\rightleftharpoons} Cd(Hg) + 3en \tag{3.5.22}$$

3.5.4 Quasireversible and Irreversible Multistep Processes

If a multistep process is neither nernstian nor at equilibrium, the details of the kinetics influence its behavior in electrochemical experiments, and one can use the results to diagnose the mechanism and to quantify kinetic parameters. As in the study of homogenous kinetics, one proceeds by devising a hypothesis about the mechanism, predicting experimental behavior on the basis of the hypothesis, and comparing the predictions against results. In the electrochemical sphere, an important part of predicting behavior is developing the current-potential characteristic in terms of controllable parameters, such as the concentrations of participating species.

If the RDS is a heterogeneous electron-transfer step, then the current-potential characteristic has the form of (3.5.11). For most mechanisms, this equation is of limited direct utility, because O' and R' are intermediates, whose concentration cannot be controlled directly. Still, (3.5.11) can serve as the basis for a more practical current-potential relationship, because one can use the presumed mechanism to reexpress $C_{O'}(0, t)$ and $C_{R'}(0, t)$ in terms of the concentrations of more controllable species, such as O and R (36).

Unfortunately, the results can easily become too complex for practical application. For example, consider the simple mechanism in (3.5.8)–(3.5.10), where the pre- and postreactions are assumed to be kinetically facile enough to remain in local equilibrium. The overall nernstian relationships, (3.5.19), connect the surface concentrations of O and R to those of O' and R'. Thus, the current-potential characteristic, (3.5.11), can be expressed in terms of the surface concentrations of the initial reactant, O, and the final product, R.

$$i = nFAk_{rds}^0 C_O(0, t)e^{-n'f(E-E_{pre}^{0'})}e^{-\alpha f(E-E_{rds}^{0'})} \tag{3.5.23}$$

$$- nFAk_{rds}^0 C_R(0, t)e^{n''f(E-E_{post}^{0'})}e^{(1-\alpha)f(E-E_{rds}^{0'})}$$

This relationship can be rewritten as

$$i = nFA[k_f C_O(0, t) - k_b C_R(0, t)] \tag{3.5.24}$$

---

[12]In the reversible limit, it is no longer appropriate to speak of an RDS, because the kinetics are not rate-controlling. We retain the nomenclature, because we are considering how a mechanism that does have an RDS begins to behave as the kinetics become more facile.

where

$$k_f = k_{rds}^0 e^{f[n'E_{pre}^{0'} + \alpha E_{rds}^{0'}]} e^{-(n'+\alpha)fE} \tag{3.5.25}$$
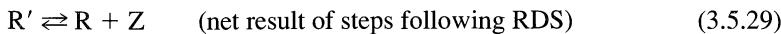
$$k_b = k_{rds}^0 e^{-f[n''E_{post}^{0'} + (1-\alpha)E_{rds}^{0'}]} e^{(n''+1-\alpha)fE} \tag{3.5.26}$$

The point of these results is to illustrate some of the difficulties in dealing with a multistep mechanism involving an embedded RDS. No longer is the potential dependence of the rate constant expressible in two parameters, one of which is interpretable as a measure of intrinsic kinetic facility. Instead, k^0 becomes obscured by the first exponential factors in (3.5.25) and (3.5.26), which express thermodynamic relationships in the mechanism. One must have ways to find out the individual values of n', n'', $E_{pre}^{0'}$, $E_{post}^{0'}$, and $E_{rds}^{0'}$ before one can evaluate the kinetics of the RDS in a fully quantitative way. This is normally a difficult requirement.

More readily usable results arise from some simpler situations:

(a) One-Electron Process Coupled Only to Chemical Equilibria

Many of the complications in the foregoing case arise from the fact that the pre- and postreactions involve heterogeneous electron transfer, so that their equilibria depend on E. Consider instead a mechanism that involves only chemical equilibria aside from the rate-determining interfacial electron transfer:

$$O + Y \rightleftarrows O' \qquad \text{(net result of steps preceding RDS)} \tag{3.5.27}$$

$$O' + e \underset{k_b}{\overset{k_f}{\rightleftarrows}} R' \qquad \text{(RDS)} \tag{3.5.28}$$

$$R' \rightleftarrows R + Z \qquad \text{(net result of steps following RDS)} \tag{3.5.29}$$

where Y and Z are other species (e.g., protons or ligands). If (3.5.27) and (3.5.29) are so facile that they are always at equilibrium, then $C_{O'}(0, t)$ and $C_{R'}(0, t)$ in (3.5.11) are calculable from the corresponding equilibrium constants, which may be available from separate experiments.

(b) Totally Irreversible Initial Step
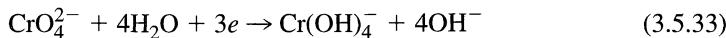
Suppose the RDS is the first step in the mechanism and is also a totally irreversible heterogeneous electron transfer:

$$O + e \overset{k_f}{\rightarrow} R' \qquad \text{(RDS)} \tag{3.5.30}$$

$$R' + n''e \rightarrow R \qquad \text{(net result of steps following RDS)} \tag{3.5.31}$$

The chemistry following (3.5.30) has no effect on the electrochemical response, except to add n'' electrons per molecule of O that reacts. Thus, the current is $n = 1 + n''$ times bigger than the current arising from step (3.5.30) alone. The overall result is given by the first term of (3.3.11) with $C_{O'}(0, t) = C_O(0, t)$,

$$i = nFAk^0 C_O(0, t)e^{-\alpha f(E - E_{rds}^{0'})} \tag{3.5.32}$$

Many examples of this kind of behavior exist in the literature; one is the polarographic reduction of chromate in 0.1 M NaOH:

$$CrO_4^{2-} + 4H_2O + 3e \rightarrow Cr(OH)_4^- + 4OH^- \tag{3.5.33}$$

Despite the obvious mechanistic complexity of this system, it behaves as though it has an irreversible electron transfer as the first step.

(c) Rate-Controlling Homogeneous Chemistry

A complete electrode reaction may involve homogeneous chemistry, one step of which could be the RDS. Although the rate constants of homogeneous reactions are not depen-

dent on potential, they affect the overall current-potential characteristic by their impact on the surface concentrations of species that are active at the interface. Some of the most interesting applications of electroanalytical techniques have been aimed at unraveling the homogeneous chemistry following the electrochemical production of reactive species, such as free radicals. Chapter 12 is devoted to these issues.

(d) Chemically Reversible Processes Near Equilibrium

A number of experimental methods, such as impedance spectroscopy (Chapter 10), are based on the application of small perturbations to a system otherwise at equilibrium. These methods often provide the exchange current in a relatively direct manner, as long as the system is chemically reversible. It is worthwhile for us to consider the exchange properties of a multistep process at equilibrium. The example that we will take is the overall process O + ne ⇌ R, effected by the general mechanism in (3.5.8)–(3.5.10) and having a standard potential $E^{0'}$.

At equilibrium, all of the steps in the mechanism are individually at equilibrium, and each has an exchange velocity. The electron-transfer reactions have exchange velocities that can be expressed as exchange currents in the manner that we have already seen. There is also an exchange velocity for the overall process that can be expressed as an exchange current. In a serial mechanism with a single RDS, such as we are now considering, the overall exchange velocity is limited by the exchange velocity through the RDS. From (3.4.4), we can write the exchange current for the RDS as

$$i_{0,\text{rds}} = FAk_{\text{rds}}^0 (C_{O'})_{\text{eq}} e^{-\alpha f(E_{\text{eq}} - E_{\text{rds}}^{0'})} \tag{3.5.34}$$

The overall exchange current is n-fold larger, because the pre- and postreactions contribute $n' + n''$ additional electrons per electron exchanged in the RDS. Thus,

$$i_0 = nFAk_{\text{rds}}^0 (C_{O'})_{\text{eq}} e^{-\alpha f(E_{\text{eq}} - E_{\text{rds}}^{0'})} \tag{3.5.35}$$

We can use the fact that the prereactions are at equilibrium to express $(C_{O'})_{\text{eq}}$ in terms of C_O^* By substitution from (3.5.13),

$$i_0 = nFAk_{\text{rds}}^0 \, C_O^* e^{-n'f(E_{\text{eq}} - E_{\text{pre}}^{0'})} e^{-\alpha f(E_{\text{eq}} - E_{\text{rds}}^{0'})} \tag{3.5.36}$$

Let us multiply by unity in the form $e^{(n' + \alpha)f(E^{0'} - E^{0'})}$ and rearrange to obtain

$$i_0 = nFAk_{\text{rds}}^0 \, e^{n'f(E_{\text{pre}}^{0'} - E^{0'})} e^{\alpha f(E_{\text{rds}}^{0'} - E^{0'})} C_O^* e^{-(n'+\alpha)f(E_{\text{eq}} - E^{0'})} \tag{3.5.37}$$

Because equilibrium is established, the Nernst equation for the overall process is applicable. Taking it in the form of (3.5.16) and raising both sides to the power $-(n' + \alpha)/n$, we have

$$i_0 = nFAk_{\text{rds}}^0 e^{n'f(E_{\text{pre}}^{0'} - E^{0'})} e^{\alpha f(E_{\text{rds}}^{0'} - E^{0'})} C_O^{*\ [1-(n'+\alpha)/n]} \, C_R^{*\ [(n'+\alpha)/n]} \tag{3.5.38}$$

Note that the two exponentials are constants of the system at a given temperature and pressure. It is convenient to combine them into an *apparent standard rate constant* for the overall process, k_{app}^0, by defining

$$k_{\text{app}}^0 = k_{\text{rds}}^0 e^{n'f(E_{\text{pre}}^{0'} - E^{0'})} e^{\alpha f(E_{\text{rds}}^{0'} - E^{0'})} \tag{3.5.39}$$

so that the final result is reached:

$$\boxed{i_0 = nFAk_{\text{app}}^0 C_O^{*\ [1-(n'+\alpha)/n]} C_R^{*[(n'+\alpha)/n]}} \tag{3.5.40}$$

This relationship applies generally to mechanisms fitting the pattern of (3.5.8)–(3.5.10), but not to others, such as those involving purely homogeneous pre- or

postreactions or those involving different rate-determining steps in the forward and reverse directions. Even so, the principles that we have used here can be employed to derive an expression like (3.5.40) for any other pattern, provided that the steps are chemically reversible and equilibrium applies. It will be generally possible to express the overall exchange current in terms of an apparent standard rate constant and the bulk concentrations of the various participants. If the exchange current can be measured validly for a given process, the derived relationship can provide insight into details of the mechanism.

For example, the variation of exchange current with the concentrations of O and R can provide $(n' + \alpha)/n$ for the sequential mechanism of (3.5.8)–(3.5.10). By an approach similar to that in Section 3.4.4, one obtains the following from (3.5.40):

$$\left(\frac{\partial \log i_0}{\partial \log C_O^*} \right)_{C_R^*} = 1 - \frac{n' + \alpha}{n} \tag{3.5.41}$$

$$\left(\frac{\partial \log i_0}{\partial \log C_R^*} \right)_{C_O^*} = \frac{n' + \alpha}{n} \tag{3.5.42}$$

Since n is often independently available from coulometry or from chemical knowledge of the reactants and products, one can frequently calculate $n' + \alpha$. From its magnitude, it may be possible to estimate separate values for n' and α, which in turn may afford chemical insight into the participants in the RDS. Practice in this direction is available in Problems 3.7 and 3.10.

As we have seen here, the apparent standard rate constant, k_{app}^0, is usually not a simple kinetic parameter for a multistep process. Interpreting it may require detailed understanding of the mechanism, including knowledge of standard potentials or equilibrium constants for various elementary steps.

We can usefully take this discussion a little further by developing a current-overpotential relationship for a quasireversible mechanism having the pattern of (3.5.8)–(3.5.10). Beginning with (3.5.24)–(3.5.26), we multiply the first term by unity in the form of $\exp[-(n' + \alpha)f(E_{eq} - E_{eq})]$ and the second by unity in the form of $\exp[(n'' + 1 - \alpha)f(E_{eq} - E_{eq})]$. The result is

$$i = nFAk_{rds}^0 C_O(0, t)e^{-(n'+\alpha)fE_{eq}}e^{f[n'E_{pre}^{0'}+\alpha E_{rds}^{0'}]}e^{-(n'+\alpha)f(E-E_{eq})} \tag{3.5.43}$$

$$- nFAk_{rds}^0 C_R(0, t)e^{(n''+1-\alpha)fE_{eq}}e^{f[n''E_{post}^{0'}+(1-\alpha)E_{rds}^{0'}]}e^{(n''+1-\alpha)f(E-E_{eq})}$$

Multiplication of the first term by unity in the form of $\exp[-(n' + \alpha)f(E^{0'} - E^{0'})]$ and the second by unity in the form of $\exp[(n'' + 1 - \alpha)f(E^{0'} - E^{0'})]$ gives

$$i = nFAk_{rds}^0 C_O(0, t)e^{-(n'+\alpha)f(E_{eq}-E^{0'})}e^{f[n'E_{pre}^{0'}+\alpha E_{rds}^{0'}-(n'+\alpha)E^{0'}]}e^{-(n'+\alpha)f\eta}$$

$$- nFAk_{rds}^0 C_R(0, t)e^{(n''+1-\alpha)f(E_{eq}-E^{0'})}e^{-f[n''E_{post}^{0'}+(1-\alpha)E_{rds}^{0'}-(n''+1-\alpha)E^{0'}]}e^{(n''+1-\alpha)f\eta}$$

$$\tag{3.5.44}$$

where $E - E_{eq}$ has been recognized as η. The first exponential in each of the two terms can be rewritten as a function of bulk concentrations by raising (3.5.16) to the appropriate power and substituting. The result is

$$i = nFAk_{rds}^0 C_O(0, t)C_O^{*[(n'+\alpha)/n]}C_R^{*[(n'+\alpha)/n]}e^{f[n'E_{pre}^{0'}+\alpha E_{rds}^{0'}-(n'+a)E^{0'}]}e^{-(n'+\alpha)f\eta}$$

$$- nFAk_{rds}^0 C_R(0, t)C_O^{*[(n''+1-\alpha)/n]}C_R^{*-[(n''+1-\alpha)/n]}e^{-f[n''E_{post}^{0'}+(1-\alpha)E_{rds}^{0'}-(n''+1-\alpha)E^{0'}]}e^{(n''+1-\alpha)f\eta}$$

$$\tag{3.5.45}$$

Division by the exchange current, as given by (3.5.40), and consolidation of the bulk concentrations provides

$$\frac{i}{i_0} = \frac{k_{\text{rds}}^0}{k_{\text{app}}^0} \frac{C_O(0, t)}{C_O^*} e^{f[n'E_{\text{pre}}^{0'} + \alpha E_{\text{rds}}^{0'} - (n'+\alpha)E^{0'}]} e^{-(n'+\alpha)f\eta}$$

$$- \frac{k_{\text{rds}}^0}{k_{\text{app}}^0} \frac{C_R(0, t)}{C_R^*} e^{-f[n''E_{\text{post}}^{0'} + (1-\alpha)E_{\text{rds}}^{0'} - (n''+1-\alpha)E^{0'}]} e^{(n''+1-\alpha)f\eta} \qquad (3.5.46)$$

where we have recognized that $n' + n'' + 1 = n$. Substitution for k_{app}^0 from (3.5.39) and consolidation of the exponentials leads to the final result,

$$\boxed{\frac{i}{i_0} = \frac{C_O(0, t)}{C_O^*} e^{-(n'+\alpha)f\eta} - \frac{C_R(0, t)}{C_R^*} e^{(n''+1-\alpha)f\eta}} \qquad (3.5.47)$$

which is directly analogous to (3.4.10).

When the current is small or mass transfer is efficient, the surface concentrations do not differ from those of the bulk, and one has

$$\boxed{i = i_0[e^{-(n'+\alpha)f\eta} - e^{(n''+1-\alpha)f\eta}]} \qquad (3.5.48)$$

which is analogous to (3.4.11). At small overpotentials, this relationship can be linearized via the approximation $e^x \approx 1 + x$ to give

$$\boxed{i = -i_0 n f \eta} \qquad (3.5.49)$$

which is the counterpart of (3.4.12). The charge-transfer resistance for this multistep system is then

$$\boxed{R_{\text{ct}} = \frac{RT}{nFi_0}} \qquad (3.5.50)$$

which is a generalization of (3.4.13).

The arguments leading to (3.5.47)–(3.5.50) are particular to the assumed mechanistic pattern of (3.5.8)–(3.5.10), but similar results can be obtained by the same techniques for any quasireversible mechanism. In fact, (3.4.49) and (3.4.50) are general for quasireversible multistep processes, and they underlie the experimental determination of i_0 via methods, such as impedance spectroscopy, based on small perturbations of systems at equilibrium.

▷ 3.6 MICROSCOPIC THEORIES OF CHARGE TRANSFER

The previous sections dealt with a generalized theory of heterogeneous electron-transfer kinetics based on macroscopic concepts, in which the rate of the reaction was expressed in terms of the phenomenological parameters, k^0 and α. While useful in helping to organize the results of experimental studies and in providing information about reaction mechanisms, such an approach cannot be employed to predict how the kinetics are affected by such factors as the nature and structure of the reacting species, the solvent, the electrode material, and adsorbed layers on the electrode. To obtain such information, one needs a microscopic theory that describes how molecular structure and environment affect the electron-transfer process.

A great deal of work has gone into the development of microscopic theories over the past 45 years. The goal is to make predictions that can be tested by experiments, so that
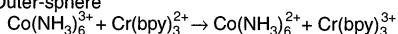
one can understand the fundamental structural and environmental factors causing reactions to be kinetically facile or sluggish. With that understanding, there would be a firmer basis for designing superior new systems for many scientific and technological applications. Major contributions in this area have been made by Marcus (37, 38), Hush (39, 40), Levich (41), Dogonadze (42), and many others. Comprehensive reviews are available (43–50), as are extensive treatments of the broader related field of electron-transfer reactions in homogeneous solution and in biological systems (51–53). The approach taken in this section is largely based on the Marcus model, which has been widely applied in electrochemical studies and has demonstrated the ability to make useful predictions about structural effects on kinetics with minimal computation. Marcus was recognized with the Nobel Prize in Chemistry for his contributions.

At the outset, it is useful to distinguish between *inner-sphere* and *outer-sphere* electron-transfer reactions at electrodes (Figure 3.6.1). This terminology was adopted from that used to describe electron-transfer reactions of coordination compounds (54). The term "outer-sphere" denotes a reaction between two species in which the original coordination spheres are maintained in the activated complex ["electron transfer from one primary bond system to another" (54)]. In contrast, "inner-sphere" reactions occur in an activated complex where the ions share a ligand ["electron transfer within a primary bond system" (54)].
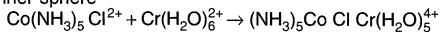
Likewise, in an *outer-sphere electrode reaction*, the reactant and product do not interact strongly with the electrode surface, and they are generally at a distance of at least a solvent layer from the electrode. A typical example is the heterogeneous reduction of $Ru(NH_3)_6^{3+}$, where the reactant at the electrode surface is essentially the same as in the bulk. In an *inner-sphere electrode reaction*, there is a strong interaction of the reactant, intermediates, or products with the electrode; that is, such reactions involve specific adsorption of species involved in the electrode reaction. The reduction of oxygen in water and the oxidation of hydrogen at Pt are inner-sphere reactions. Another type of inner-sphere reaction features a specifically adsorbed anion that serves as a *ligand bridge* to a metal ion (55). Obviously outer-sphere reactions are less dependent on electrode material than inner-sphere ones.[13]

Homogenous Electron Transfer

Outer-sphere
$$Co(NH_3)_6^{3+} + Cr(bpy)_3^{2+} \rightarrow Co(NH_3)_6^{2+} + Cr(bpy)_3^{3+}$$

Inner-sphere
$$Co(NH_3)_5 Cl^{2+} + Cr(H_2O)_6^{2+} \rightarrow (NH_3)_5Co\ Cl\ Cr(H_2O)_5^{4+}$$
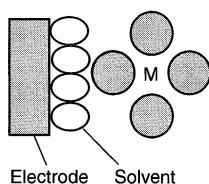
Homogenous Electron Transfer

Outer-sphere   Inner-sphere

Electrode   Solvent
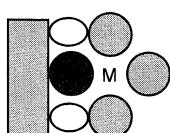
Figure 3.6.1 Outer-sphere and inner-sphere reactions. The inner sphere homogeneous reaction produces, with loss of H_2O, a ligand-bridged complex (shown above), which decomposes to $CrCl(H_2O)_5^{2+}$ and $Co(NH_3)_5(H_2O)^{2+}$. In the heterogeneous reactions, the diagram shows a metal ion (M) surrounded by ligands. In the inner sphere reaction, a ligand that adsorbs on the electrode and bridges to the metal is indicated in a darker color. An example of the latter is the oxidation of $Cr(H_2O)_5^{2+}$ at a mercury electrode in the presence of Cl^- or Br^-.

[13]Even if there is not a strong interaction with the electrode, an outer-sphere reaction can depend on the electrode material, because of (a) double-layer effects (Section 13.7), (b) the effect of the metal on the structure of the Helmholtz layer, or (c) the effect of the energy and distribution of electronic states in the electrode.

Outer-sphere electron transfers can be treated in a more general way than inner-sphere processes, where specific chemistry and interactions are important. For this reason, the theory of outer-sphere electron transfer is much more highly developed, and the discussion that follows pertains to these kinds of reactions. However, in practical applications, such as in fuel cells and batteries, the more complicated inner-sphere reactions are important. A theory of these requires consideration of specific adsorption effects, as described in Chapter 13, as well as many of the factors important in heterogeneous catalytic reactions (56).

3.6.1 The Marcus Microscopic Model

Consider an outer-sphere, single electron transfer from an electrode to species O, to form the product R. This heterogeneous process is closely related to the homogeneous reduction of O to R by reaction with a suitable reductant, R',

$$O + R' \rightarrow R + O' \tag{3.6.1}$$

We will find it convenient to consider the two situations in the same theoretical context. Electron-transfer reactions, whether homogeneous or heterogeneous, are radiationless electronic rearrangements of reacting species. Accordingly, there are many common elements between theories of electron transfer and treatments of radiationless deactivation in excited molecules (57). Since the transfer is radiationless, the electron must move from an initial state (on the electrode or in the reductant, R') to a receiving state (in species O or on the electrode) of the same energy. This demand for *isoenergetic electron transfer* is a fundamental aspect with extensive consequences.

A second important aspect of most microscopic theories of electron transfer is the assumption that the reactants and products do not change their configurations during the actual act of transfer. This idea is based essentially on the Franck–Condon principle, which says, in part, that nuclear momenta and positions do not change on the time scale of electronic transitions. Thus, the reactant and product, O and R, share a common nuclear configuration at the moment of transfer.

Let us consider again a plot of the standard free energy[14] of species O and R as a function of reaction coordinate (see Figure 3.3.2), but we now give more careful consideration to the nature of the reaction coordinate and the computation of the standard free energy. Our goal is to obtain an expression for the standard free energy of activation, $\Delta G^{\ddagger}$, as a function of structural parameters of the reactant, so that equation 3.1.17 (or a closely related form) can be used to calculate the rate constant. In earlier theoretical work, the pre-exponential factor for the rate constant was written in terms of a collision number (37, 38, 58, 59), but the formalism now used leads to expressions like:

$$k_f = K_{P,O}\nu_n\kappa_{el}\exp(-\Delta G_f^{\ddagger}/RT) \tag{3.6.2}$$

where $\Delta G_f^{\ddagger}$ is the activation energy for reduction of O; $K_{P,O}$ is a *precursor equilibrium constant*, representing the ratio of the reactant concentration in the reactive position at the electrode (the *precursor state*) to the concentration in bulk solution; ν_n is the *nuclear frequency factor* (s^{-1}), which represents the frequency of attempts on the energy barrier (generally associated with bond vibrations and solvent motion); and κ_{el} is the *electronic transmission coefficient* (related to the probability of electron tunneling; see Section 3.6.4). Often, κ_{el} is taken as unity for a reaction where the reactant is close to the electrode, so that there is strong coupling between the reactant and the electrode

---

[14]See the footnote relating to the use of standard thermodynamic quantities in Section 3.1.2.

(see Section 3.6.4).[15] Methods for estimating the various factors are available (48), but there is considerable uncertainty in their values.

Actually, equation 3.6.2 can be used for either a heterogeneous reduction at an electrode or a homogeneous electron transfer in which O is reduced to R by another reactant in solution. For a heterogeneous electron transfer, the precursor state can be considered to be a reactant molecule situated near the electrode at a distance where electron transfer is possible. Thus $K_{P,O} = C_{O,surf}/C_O^*$, where $C_{O,surf}$ is a surface concentration having units of mol/cm^2. Consequently $K_{P,O}$ has units of cm, and k_f has units of cm/s, as required. For a homogeneous electron transfer between O and R', one can think of the precursor state as a reactive unit, OR', where the two species are close enough to allow transfer of an electron. Then $K_{P,O} = [OR']/[O][R']$, which has units of M^{-1} if the concentrations are expressed conventionally. This result gives a rate constant, k_f, in units of $M^{-1}s^{-1}$, again as required.

In either case, we consider the reaction as occurring on a multidimensional surface defining the standard free energy of the system in terms of the nuclear coordinates (i.e., the relative positions of the atoms) of the reactant, product, and solvent. Changes in nuclear coordinates come about from vibrational and rotational motion in O and R, and from fluctuations in the position and orientation of the solvent molecules. As usual, we focus on the energetically favored path between reactants and products, and we measure progress in terms of a reaction coordinate, q. Two general assumptions are (a) that the reactant, O, is centered at some fixed position with respect to the electrode (or in a bimolecular homogeneous reaction, that the reactants are at a fixed distance from each other) and (b) that the standard free energies of O and R, G_O^0 and G_R^0, depend quadratically on the reaction coordinate, q (49):

$$G_O^0(q) = (k/2)(q - q_O)^2 \qquad (3.6.3)$$
$$G_R^0(q) = (k/2)(q - q_R)^2 + \Delta G^0 \qquad (3.6.4)$$

where q_O and q_R are the values of the coordinate for the equilibrium atomic configurations in O and R, and k is a proportionality constant (e.g., a force constant for a change in bond length). Depending on the case under consideration, ΔG^0 is either the free energy of reaction for a homogeneous electron transfer or $F(E - E^0)$ for an electrode reaction.

Let us consider a particularly simple case to give a physical picture of what is implied here. Suppose the reactant is A-B, a diatomic molecule, and the product is A-B$^-$. To a first approximation the nuclear coordinate could be the bond length in A-B (q_O) and A-B$^-$ (q_R), and the equations for the free energy could represent the energy for lengthening or contraction of the bond within the usual harmonic oscillator approximation. This picture is oversimplified in that the solvent molecules would also make a contribution to the free energy of activation (sometimes the dominant one). In the discussion that follows, they are assumed to contribute in a quadratic relationship involving coordinates of the solvent dipole.

Figure 3.6.2 shows a typical free energy plot based on (3.6.3) and (3.6.4). The molecules shown at the top of the figure are meant to represent the stable configurations of the reactants, for example, $Ru(NH_3)_6^{3+}$ and $Ru(NH_3)_6^{2+}$ as O and R, as well as to provide a view of the change in nuclear configuration upon reduction. The transition state is the position where O and R have the same configuration, denoted by the reaction coordinate

---

[15]The pre-exponential term sometimes also includes a nuclear tunneling factor, Γ_n. This arises from a quantum mechanical treatment that accounts for electron transfer for nuclear configurations with energies below the transition state (48, 60).
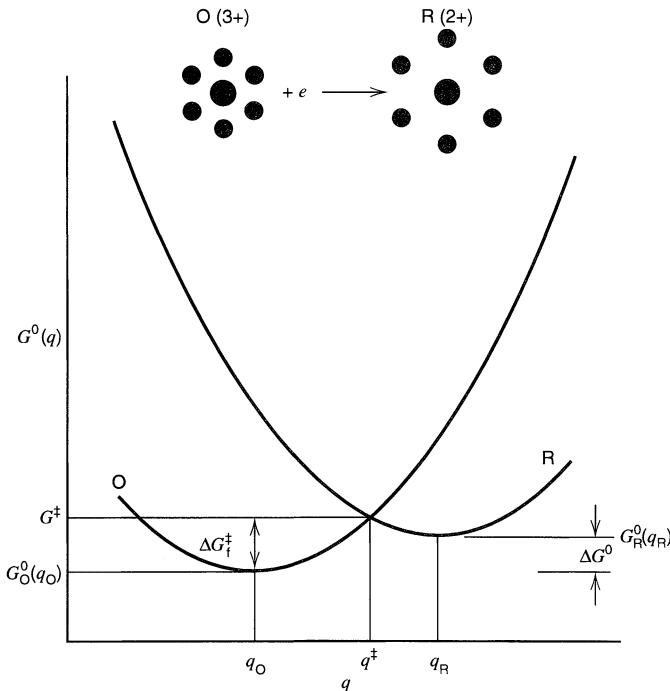
Figure 3.6.2 Standard free energy, G^0, as a function of reaction coordinate, q, for an electron transfer reaction, such as $Ru(NH_3)_6^{3+} + e \rightarrow Ru(NH_3)_6^{2+}$. This diagram applies either to a heterogeneous reaction in which O and R react at an electrode or a homogeneous reaction in which O and R react with members of another redox couple as shown in (3.6.1). For the heterogeneous case, the curve for O is actually the sum of energies for species O and for an electron on the electrode at the Fermi level corresponding to potential E. Then, $\Delta G^0 = F(E - E^0)$. For the homogeneous case, the curve for O is the sum of energies for O and its reactant partner, R', while the curve for R is a sum for R and O'. Then, ΔG^0 is the standard free energy change for the reaction. The picture at the top is a general representation of structural changes that might accompany electron transfer. The changes in spacing of the six surrounding dots could represent, for example, changes in bond lengths within the electroactive species or the restructuring of the surrounding solvent shell.

$q^{\ddagger}$. In keeping with the Franck–Condon principle, electron transfer only occurs at this position.

The free energies at the transition state are thus given by

$$G_O^0(q^{\ddagger}) = (k/2)(q^{\ddagger} - q_O)^2 \qquad (3.6.5)$$

$$G_R^0(q^{\ddagger}) = (k/2)(q^{\ddagger} - q_R)^2 + \Delta G^0 \qquad (3.6.6)$$

Since $G_O^0(q^{\ddagger}) = G_R^0(q^{\ddagger})$, (3.6.5) and (3.6.6) can be solved for $q^{\ddagger}$ with the result,

$$q^{\ddagger} = \frac{(q_R + q_O)}{2} + \frac{\Delta G^0}{k(q_R - q_O)} \qquad (3.6.7)$$

The free energy of activation for reduction of O is given by

$$\Delta G_f^{\ddagger} = G_O^0(q^{\ddagger}) - G_O^0(q_O) = G_O^0(q^{\ddagger}) \qquad (3.6.8)$$

where we have noted that $G_O^0(q_O) = 0$, as defined in (3.6.3). Substitution for $q^{\ddagger}$ from (3.6.7) into (3.6.5) then yields

$$\Delta G_f^{\ddagger} = \frac{k(q_R - q_O)^2}{8}\left[1 + \frac{2\Delta G^0}{k(q_R - q_O)^2}\right]^2 \tag{3.6.9}$$

Defining $\lambda = (k/2)(q_R - q_O)^2$, we have

$$\Delta G_f^{\ddagger} = \frac{\lambda}{4}\left(1 + \frac{\Delta G^0}{\lambda}\right)^2 \tag{3.6.10a}$$

or, for an electrode reaction

$$\Delta G_f^{\ddagger} = \frac{\lambda}{4}\left(1 + \frac{F(E - E^0)}{\lambda}\right)^2 \tag{3.6.10b}$$

There can be free energy contributions beyond those considered in the derivation just described. In general, they are energy changes involved in bringing the reactants and products from the average environment in the medium to the special environment where electron transfer occurs. Among them are the energy of ion pairing and the electrostatic work needed to reach the reactive position (e.g., to bring a positively charged reactant to a position near a positively charged electrode). Such effects are usually treated by the inclusion of *work terms*, w_O and w_R, which are adjustments to ΔG^0 or $F(E - E^0)$. For simplicity, they were omitted above. The complete equations, including the work terms, are[16]

$$\Delta G_f^{\ddagger} = \frac{\lambda}{4}\left(1 + \frac{\Delta G^0 - w_O + w_R}{\lambda}\right)^2 \tag{3.6.11a}$$

$$\Delta G_f^{\ddagger} = \frac{\lambda}{4}\left(1 + \frac{F(E - E^0) - w_O + w_R}{\lambda}\right)^2 \tag{3.6.11b}$$

The critical parameter is λ, the *reorganization energy*, which represents the energy necessary to transform the nuclear configurations in the reactant and the solvent to those of the product state. It is usually separated into inner, λ_i, and outer, λ_o, components:

$$\lambda = \lambda_i + \lambda_o \tag{3.6.12}$$

where λ_i represents the contribution from reorganization of species O, and λ_o that from reorganization of the solvent.[17]

---

[16]The convention is to define w_O and w_R as the work required to establish the reactive position from the average environment of reactants and products in the medium. The signs in (3.6.11a,b) follow from this. In many circumstances, the work terms are also the free energy changes for the precursor equilibria. When that is true, $w_O = -RT \ln K_{P,O}$ and $w_R = -RT \ln K_{P,R}$.

[17]One should not confuse the inner and outer components of λ with the concept of inner- and outer-sphere reaction. In the treatment under consideration, we are dealing with an outer-sphere reaction, and λ_i and λ_o simply apportion the energy to terms applying to changes in bond lengths (e.g., of a metal–ligand bond) and changes in solvation, respectively.

To the extent that the normal modes of the reactant remain harmonic over the range of distortion needed, one can, in principle, calculate λ_i by summing over the normal vibrational modes of the reactant, that is,

$$\lambda_i = \sum_j \frac{1}{2} k_j (q_{O,j} - q_{R,j})^2 \tag{3.6.13}$$

where the k's are force constants, and the q's are displacements in the normal mode coordinates.

Typically, λ_o is computed by assuming that the solvent is a dielectric continuum, and the reactant is a sphere of radius a_O. For an electrode reaction,

$$\lambda_o = \frac{e^2}{8\pi\varepsilon_0} \left(\frac{1}{a_O} - \frac{1}{R} \right) \left(\frac{1}{\varepsilon_{op}} - \frac{1}{\varepsilon_s} \right) \tag{3.6.14a}$$

where ε_{op} and ε_s are the optical and static dielectric constants, respectively, and R is taken as twice the distance from the center of the molecule to the electrode (i.e., $2x_0$, which is the distance between the reactant and its image charge in the electrode).[18] For a homogeneous electron-transfer reaction:

$$\lambda_o = \frac{e^2}{4\pi\varepsilon_0} \left(\frac{1}{2a_1} + \frac{1}{2a_2} - \frac{1}{d} \right) \left(\frac{1}{\varepsilon_{op}} - \frac{1}{\varepsilon_s} \right) \tag{3.6.14b}$$

where a_1 and a_2 are the radii of the reactants (O and R' in equation 3.6.1) and $d = a_1 + a_2$. Typical values of λ are in the range of 0.5 to 1 eV.

3.6.2 Predictions from Marcus Theory

While it is possible, in principle, to estimate the rate constant for an electrode reaction by computation of the pre-exponential terms and the λ values, this is rarely done in practice. The theory's greater value is the chemical and physical insight that it affords, which arises from its capacity for prediction and generalization about electron-transfer reactions.

For example, one can obtain the predicted α-value from (3.6.10b):

$$\alpha = \frac{1}{F} \frac{\partial G_f^{\ddagger}}{\partial E} = \frac{1}{2} + \frac{F(E - E^0)}{2\lambda} \tag{3.6.15a}$$

or with the inclusion of work terms:

$$\alpha = \frac{1}{2} + \frac{F(E - E^0) - (w_O - w_R)}{2\lambda} \tag{3.6.15b}$$

Thus, the theory predicts not only that $\alpha \approx 0.5$, but also that it depends on potential in a particular way. As mentioned in Section 3.3.4, the Butler–Volmer (BV) theory can accommodate a potential dependence of α, but in its classic version, the BV theory handles α as a constant. Moreover, there is no basis in the BV theory for predicting the form of the potential dependence. On the other hand, the potential-dependent term in (3.6.15a,b),

---

[18]In some treatments of electron transfer, the assumption is made that the reactant charge is largely shielded by counter ions in solution, so that an image charge does not form in the electrode. In this case, R is the distance between the center of the reactant molecule and the electrode (24, 39).

which depends on the size of λ, is usually not very large, so a clear potential dependency of α has been difficult to observe experimentally. The effect is more obvious in reactions involving electroactive centers bound to electrodes (see Section 14.5.2.).

The Marcus theory also makes predictions about the relation between the rate constants for homogeneous and heterogeneous reactions of the same reactant. Consider the rate constant for the self-exchange reaction,

$$O + R \overset{k_{ex}}{\rightarrow} R + O \tag{3.6.16}$$

in comparison with k^0 for the related electrode reaction, $O + e \rightarrow R$. One can determine k_{ex} by labeling O isotopically and measuring the rate at which the isotope appears in R, or sometimes by other methods like ESR or NMR. A comparison of (3.6.14a) and (3.6.14b), where $a_O = a_1 = a_2 = a$ and $R = d = 2a$, yields

$$\lambda_{el} = \lambda_{ex}/2 \tag{3.6.17}$$

where λ_{el} and λ_{ex} are the values of λ_o for the electrode reaction and the self-exchange reaction, respectively. For the self-exchange reaction, $\Delta G^0 = 0$, so (3.6.10a) gives $\Delta G_f^{\ddagger} = \lambda_{ex}/4$, as long as λ_o dominates λ_i in the reorganization energy. For the electrode reaction, k^0 corresponds to $E = E^0$, so (3.6.10b) gives $\Delta G_f^{\ddagger} = \lambda_{el}/4$, again with the condition that λ_i is negligible. From (3.6.17), one can express $\Delta G_f^{\ddagger}$ for the homogeneous and heterogeneous reactions in common terms, and one finds that k_{ex} is related to k^0 by the expression

$$(k_{ex}/A_{ex})^{1/2} = k^0/A_{el} \tag{3.6.18}$$

where A_{ex} and A_{el} are the pre-exponential factors for self-exchange and the electrode reaction. (Roughly, A_{el} is 10^4 to 10^5 cm/s and A_{ex} is 10^{11} to $10^{12}\ M^{-1}\ s^{-1}$.)[19]

The theory also leads to useful qualitative predictions about reaction kinetics. For example, equation 3.6.10b gives $\Delta G^{\ddagger} \approx \lambda/4$ at E^0, where $k_f = k_b = k^0$. Thus, k^0 will be larger when the internal reorganization is smaller, that is, in reactions where O and R have similar structures. Electron transfers involving large structural alterations (such as sizable changes in bond lengths or bond angles) tend to be slower. Solvation also has an impact through its contribution to λ. Large molecules (large a_O) tend to show lower solvation energies, and smaller changes in solvation upon reaction, by comparison with smaller species. On this basis, one would expect electron transfers to small molecules, such as, the reduction of O_2 to $O_2^{\div}$ in 2$^-$aprotic media, to be slower than the reduction of Ar to Ar$^{\div}$, where Ar is a large aromatic molecule like anthracene.

The effect of solvent in an electron transfer is larger than simply through its energetic contribution to λ_o. There is evidence that the dynamics of solvent reorganization, often represented in terms of a solvent longitudinal relaxation time, τ_L, contribute to the pre-exponential factor in (3.6.2) (47, 62–65), e.g., $\nu_n \propto \tau_L^{-1}$. Since τ_L is roughly proportional to the viscosity, an inverse proportionality of this kind implies that the heterogeneous rate constant would decrease as the solution viscosity increases (i.e., as the diffusion coefficient of the reactant decreases). This behavior is actually seen in the decrease of k^0 for electrode reactions in water upon adding sucrose to increase the viscosity (presumably without changing λ_o in a significant way) (66, 67). This effect was especially pronounced in other studies involving Co(III/II)tris(bipyridine) complexes modified by the addition of

---

[19]This equation also applies when the λ_i terms are included (but work terms are neglected). This is the case because the total contribution to λ_i is summed over two reactants in the homogeneous self-exchange reaction, but only over one in the electrode reaction (61).

long polyethylene or polypropylene oxide chains to the ligands, which cause large changes in diffusion coefficient in undiluted, highly viscous, ionic melts (68).

A particularly interesting prediction from this theory is the existence of an "inverted region" for homogeneous electron-transfer reactions. Figure 3.6.3 shows how equation 3.6.10a predicts $\Delta G_f^{\ddagger}$ to vary with the thermodynamic driving force for the electron transfer, ΔG^0. Curves are shown for several different values of λ, but the basic pattern of behavior is the same for all, in that there is a predicted minimum in the standard free energy of activation. On the right-hand side of the minimum, there is a *normal region*, where $\Delta G_f^{\ddagger}$ decreases, hence the rate constant increases, as ΔG^0 gets larger in magnitude (i.e., becomes more negative). When $\Delta G^0 = -\lambda$, $\Delta G_f^{\ddagger}$ is zero, and the rate constant is predicted to be at a maximum. At more negative ΔG^0 values, that is for very strongly driven reactions, the activation energy becomes larger, and the rate constant smaller. This is the *inverted region*, where an increase in the thermodynamic driving force leads to a decrease in the rate of electron transfer. There are two physical reasons for this effect. First, a large negative free energy of reaction implies that the products are required to accept the liberated energy very quickly in vibrational modes, and the probability for doing so declines as $-\Delta G^0$ exceeds λ (see Chapter 18). Second, one can develop a situation in the inverted region where the energy surfaces no longer allow for adiabatic electron transfer (see Section 3.6.4). The existence of the inverted region accounts for the phenomenon of electrogenerated chemiluminescence (Chapter 18) and has also been seen by other means for several electron-transfer reactions in solution.

Even though (3.6.10b) also has a minimum, an inverted-region effect should not occur for an electrode reaction at a metal electrode. The reason is that (3.6.10b) was derived with the implicit idea that electrons always react from a narrow range of states on the electrode corresponding to the Fermi energy (see the caption to Figure 3.6.2). Even though the reaction rate at this energy is predicted to show inversion at very negative overpotentials, there are always occupied states in the metal below the Fermi energy, and they can transfer an electron to O without inversion. Any low-level vacancy created in the metal by heterogeneous reaction is filled ultimately with an electron from the Fermi energy, with dissipation of the difference in energy as heat; thus the overall energy change is as expected from thermodynamics. A similar argument holds for oxidations at metals, where unoccupied states are always available. The ideas behind this discussion are developed much more fully in the next section.
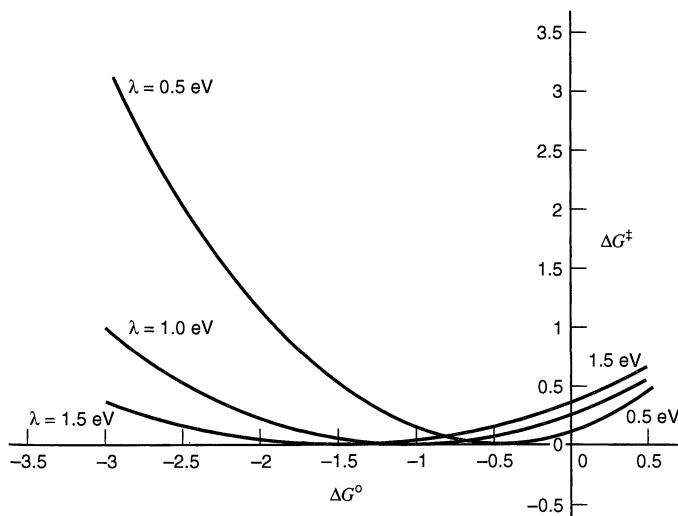
Figure 3.6.3 Effect of ΔG^0 for a homogeneous electron-transfer reaction on $\Delta G_{\ddagger}^{\ddagger}$ at several different values of λ.

An inverted region should be seen for interfacial electron transfer at the interface between immiscible electrolyte solutions, with an oxidant, O, in one phase, and a reductant, R', in the other (69). Experimental studies bearing on this issue have just been reported (70).

3.6.3 A Model Based on Distributions of Energy States

An alternative theoretical approach to heterogeneous kinetics is based on the overlap between electronic states of the electrode and those of the reactants in solution (41, 42, 46, 47, 71, 72). The concept is presented graphically in Figure 3.6.4, which will be discussed extensively in this section. This model is rooted in contributions from Gerischer (71, 72) and is particularly useful for treating electron transfer at semiconductor electrodes (Section 18.2.3), where the electronic structure of the electrode is important. The main idea is that an electron transfer can take place from any occupied energy state that is matched in energy, E, with an unoccupied receiving state. If the process is a reduction, the occupied state is on the electrode and the receiving state is on an electroreactant, O. For an oxidation, the occupied state is on species R in solution, and the receiving state is on the electrode. In general, the eligible states extend over a range of energies, and the total rate is an integral of the rates at each energy.
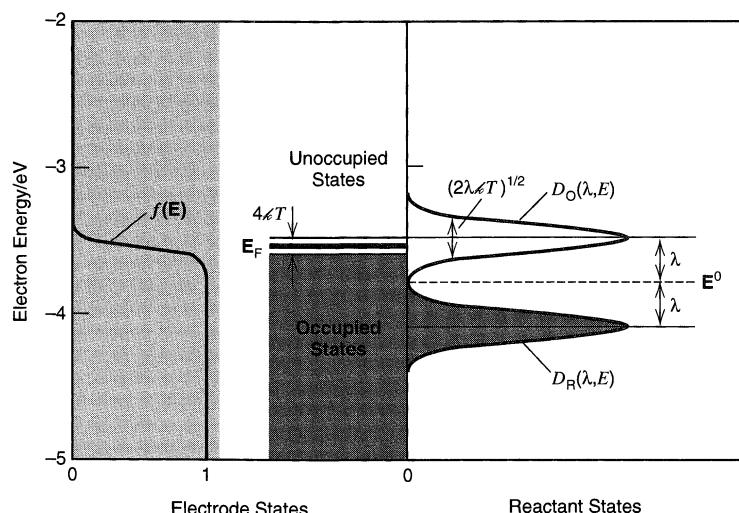
Figure 3.6.4 Relationships among electronic states at an interface between a metal electrode and a solution containing species O and R at equal concentrations. The vertical axis is electron energy, E, on the absolute scale. Indicated on the electrode side is a zone $4\ell T$ wide centered on the Fermi level, E_F, where $f(E)$ makes the transition from a value of nearly 1 below the zone to a value of virtually zero above. See the graph of $f(E)$ in the area of solid shading on the left. On the solution side, the state density distributions are shown for O and R. These are gaussians having the same shapes as the probability density functions, $W_O(\lambda, E)$ and $W_R(\lambda, E)$. The electron energy corresponding to the standard potential, E^0, is -3.8 eV, and $\lambda = 0.3$ eV. The Fermi energy corresponds here to an electrode potential of -250 mV vs. E^0. Filled states are denoted on both sides of the interface by dark shading. Since filled electrode states overlap with (empty) O states, reduction can proceed. Since the (filled) R states overlap only with filled electrode states, oxidation is blocked.

On the electrode, the number of electronic states in the energy range between E and $E + dE$ is given by $A\rho(E)dE$, where A is the area exposed to the solution, and $\rho(E)$ is the *density of states* [having units of (area-energy)$^{-1}$, such as $cm^{-2}eV^{-1}$]. The total number of states in a broad energy range is, of course, the integral of $A\rho(E)$ over the range. If the electrode is a metal, the density of states is large and continuous, but if it is a semiconductor, there is a sizable energy range, called the *band gap*, where the density of states is very small. (See Section 18.2 for a fuller discussion of the electronic properties of materials.)

Electrons fill states on the electrode from lower energies to higher ones until all electrons are accommodated. Any material has more states than are required for the electrons, so there are always empty states above the filled ones. If the material were at absolute zero in temperature, the highest filled state would correspond to the *Fermi level* (or the *Fermi energy*), E_F, and all states above the Fermi level would be empty. At any higher temperature, thermal energy elevates some of the electrons into states above E_F and creates vacancies below. The filling of the states at thermal equilibrium is described by the *Fermi function*, $f(E)$,

$$f(E) = \{1 + \exp[(E - E_F)/\mathscr{k}T]\}^{-1} \qquad (3.6.19)$$

which is the probability that a state of energy E is occupied by an electron. It is easy to see that for energies much lower than the Fermi level, the occupancy is virtually unity, and for energies much higher than the Fermi level, the occupancy is practically zero (see Figure 3.6.4). States within a few $\mathscr{k}T$ of E_F have intermediate occupancy, graded from unity to zero as the energy rises through E_F, where the occupancy is 0.5. This intermediate zone is shown in Figure 3.6.4 as a band $4\mathscr{k}T$ wide (about 100 meV at 25°C).

The number of electrons in the energy range between E and $E + dE$ is the number of occupied states, $AN_{occ}(E)dE$, where $N_{occ}(E)$ is the density function

$$N_{occ}(E) = f(E)\rho(E) \qquad (3.6.20)$$

Like $\rho(E)$, $N_{occ}(E)$ has units of (area-energy)$^{-1}$, typically $cm^{-2}\ eV^{-1}$, while $f(E)$ is dimensionless. In a similar manner, we can define the density of unoccupied states as

$$N_{unocc}(E) = [1 - f(E)]\rho(E) \qquad (3.6.21)$$

As the potential is changed, the Fermi level moves, with the change being toward higher energies at more negative potentials and vice versa. On a metal electrode, these changes occur not by the filling or emptying of many additional states, but mostly by charging the metal, so that all states are shifted by the effect of potential (Section 2.2). While charging does involve a change in the total electron population on the metal, the change is a tiny fraction of the total (Section 2.2.2). Consequently, the same set of states exists near the Fermi level at all potentials. For this reason, it is more appropriate to think of $\rho(E)$ as a consistent function of $E - E_F$, nearly independent of the value of E_F. Since $f(E)$ behaves in the same way, so do $N_{occ}(E)$ and $N_{unocc}(E)$. The picture is more complicated at a semiconductor, as discussed in Section 18.2.

States in solution are described by similar concepts, except that filled and empty states correspond to different chemical species, namely the two components of a redox couple, R and O, respectively. These states differ from those of the metal in being localized. The R and O species cannot communicate with the electrode without first approaching it closely. Since R and O can exist in the solution inhomogeneously and our concern is with the mix of states near the electrode surface, it is better to express the density of states

in terms of concentration, rather than total number. At any moment, the removable electrons on R species in solution in the vicinity of the electrode[20] are distributed over an energy range according to a concentration density function, $D_R(\lambda, \mathbf{E})$, having units of (volume-energy)$^{-1}$, such as cm^{-3} eV^{-1}. Thus, the *number concentration* of R species near the electrode in the range between $\mathbf{E}$ and $\mathbf{E} + d\mathbf{E}$ is $D_R(\lambda, \mathbf{E})d\mathbf{E}$. Because this small element of the R population should be proportional to the overall surface concentration of R, $C_R(0, t)$, we can factor $D_R(\lambda, \mathbf{E})$ in the following way:

$$D_R(\lambda, \mathbf{E}) = N_A C_R(0, t) W_R(\lambda, \mathbf{E}) \tag{3.6.22}$$

where N_A is Avogadro's number, and $W_R(\lambda, \mathbf{E})$ is a probability density function with units of (energy)$^{-1}$. Since the integral of $D_R(\lambda, \mathbf{E})$ over all energies must yield the total number concentration of all states, which is $N_A C_R(0, t)$, we see that $W_R(\lambda, \mathbf{E})$ is a normalized function

$$\int_{-\infty}^{\infty} W_R(\lambda, \mathbf{E})d\mathbf{E} = 1 \tag{3.6.23}$$

Similarly, the distribution of vacant states represented by O species is given by

$$D_O(\lambda, \mathbf{E}) = N_A C_O(0, t) W_O(\lambda, \mathbf{E}) \tag{3.6.24}$$

where $W_O(\lambda, \mathbf{E})$ is normalized, as indicated for its counterpart in (3.6.23). In Figure 3.6.4, the state distributions for O and R are depicted as gaussians for reasons that we will discover below.

Now let us consider the rate at which O is reduced from occupied states on the electrode in the energy range between $\mathbf{E}$ and $\mathbf{E} + d\mathbf{E}$. This is only a part of the total rate of reduction, so we call it a *local rate* for energy $\mathbf{E}$. In a time interval Δt, electrons from occupied states on the electrode can make the transition to states on species O in the same energy range, and the rate of reduction is the number that succeed divided by Δt. This rate is the instantaneous rate, if Δt is short enough (a) that the reduction does not appreciably alter the number of unoccupied states on the solution side and (b) that individual O molecules do not appreciably change the energy of their unoccupied levels by internal vibrational and rotational motion. Thus Δt is at or below the time scale of vibration. The local rate of reduction can be written as

$$\text{Local Rate}(\mathbf{E}) = \frac{P_{red}(\mathbf{E})AN_{occ}(\mathbf{E})d\mathbf{E}}{\Delta t} \tag{3.6.25}$$

where $AN_{occ}d\mathbf{E}$ is the number of electrons available for the transition and $P_{red}(\mathbf{E})$ is the probability of transition to an unoccupied state on O. It is intuitive that $P_{red}(\mathbf{E})$ is proportional to the density of states $D_O(\lambda, \mathbf{E})$. Defining $\varepsilon_{red}(\mathbf{E})$ as the proportionality function, we have

$$\text{Local Rate}(\mathbf{E}) = \frac{\varepsilon_{red}(\mathbf{E})D_O(\lambda, \mathbf{E})AN_{occ}(\mathbf{E})d\mathbf{E}}{\Delta t} \tag{3.6.26}$$

---

[20]In this discussion, the phrases "concentration in the vicinity of the electrode" and "concentration near the electrode" are used interchangeably to denote concentrations that are given by $C(0, t)$ in most mass-transfer and heterogeneous rate equations in this book. However, $C(0, t)$ is not the same as the concentration in the reactive position at an electrode (i.e., in the precursor state), but is the concentration just outside the diffuse layer. We are now considering events on a much finer distance scale than in most contexts in this book, and this distinction is needed. The same point is made in Section 13.7.

where $\varepsilon_{red}(E)$ has units of volume-energy (e.g., cm^3 eV). The total rate of reduction is the sum of the local rates in all infinitesimal energy ranges; thus it is given by the integral

$$\text{Rate} = \nu \int_{-\infty}^{\infty} \varepsilon_{red}(E)D_O(\lambda, E)AN_{occ}(E)dE \tag{3.6.27}$$

where, in accord with custom, we have expressed Δt in terms of a frequency, $\nu = 1/\Delta t$. The limits on the integral cover all energies, but the integrand has a significant value only where there is overlap between occupied states on the electrode and states of O in the solution. In Figure 3.6.4, the relevant range is roughly -4.0 to -3.5 eV.

Substitution from (3.6.20) and (3.6.24) gives

$$\text{Rate} = \nu AN_A C_O(0, t) \int_{-\infty}^{\infty} \varepsilon_{red}(E)W_O(\lambda, E)f(E)\rho(E)dE \tag{3.6.28}$$

This rate is expressed in molecules or electrons per second. Division by AN_A gives the rate more conventionally in mol cm^{-2} s^{-1}, and further division by $C_O(0, t)$ provides the rate constant,

$$\boxed{k_f = \nu \int_{-\infty}^{\infty} \varepsilon_{red}(E)W_O(\lambda, E)f(E)\rho(E)dE} \tag{3.6.29}$$

In an analogous way, one can easily derive the rate constant for the oxidation of R. On the electrode side, the empty states are candidates to receive an electron; hence $N_{unocc}(E)$ is the distribution of interest. The density of filled states on the solution side is $D_R(\lambda, E)$, and the probability for electron transfer in the time interval Δt is $P_{ox}(E) = \varepsilon_{ox}(E)D_R(\lambda, E)$. Proceeding exactly as in the derivation of (3.6.29), we arrive at

$$\boxed{k_b = \nu \int_{-\infty}^{\infty} \varepsilon_{ox}(E)W_R(\lambda, E)[1 - f(E)]\rho(E)dE} \tag{3.6.30}$$

In Figure 3.6.4, the distribution of states for species R does not overlap the zone of unoccupied states on the electrode, so the integrand in (3.6.30) is practically zero everywhere, and k_b is negligible compared to k_f. The electrode is in a reducing condition with respect to the O/R couple. By changing the electrode potential to a more positive value, we shift the position of the Fermi level downward, and we can reach a position where the R states begin to overlap unoccupied electrode states, so that the integral in (3.6.30) becomes significant, and k_b is enhanced.

The literature contains many versions of equations 3.6.29 and 3.6.30 manifesting different notation and involving wide variations in the interpretation applied to the integral prefactors and the proportionality functions $\varepsilon_{red}(E)$ and $\varepsilon_{ox}(E)$. For example, it is common to see a tunneling probability, κ_{el}, or a precursor equilibrium constant, $K_{P,O}$ or $K_{P,R}$, extracted from the ε-functions and placed in the integral prefactor. Often the frequency ν is identified with ν_n in (3.6.2). Sometimes the prefactor encompasses things other than the frequency parameter, but is still expressed as a single symbol. These variations in representation reflect the fact that basic ideas are still evolving. The treatment offered here is general and can be accommodated to any of the extant views about how the fundamental properties of the system determine ν, $\varepsilon_{red}(E)$, and $\varepsilon_{ox}(E)$.

With (3.6.29) and (3.6.30), it is apparently possible to account for kinetic effects of the electronic structure of the electrode by using an appropriate density of states, $\rho(E)$, for

the electrode material. Efforts in that direction have been reported. However, one must be on guard for the possibility that $\varepsilon_{red}(E)$ and $\varepsilon_{ox}(E)$ also depend on $\rho(E)$.[21]

The Marcus theory can be used to define the probability densities $W_O(\lambda, E)$ and $W_R(\lambda, E)$. The key is to recognize that the derivation leading to (3.6.10b) is based implicitly on the idea that electron transfer occurs entirely from the Fermi level. In the context that we are now considering, the rate constant corresponding to the activation energy in (3.6.10b) is therefore proportional to the *local rate* at the Fermi level, wherever it might be situated relative to the state distributions for O and R. We can rewrite (3.6.10b) in terms of electron energy as

$$\Delta G_f^{\ddagger} = \frac{\lambda}{4}\left(1 - \frac{E - E^0}{\lambda}\right)^2 \tag{3.6.31}$$

where E^0 is the energy corresponding to the standard potential of the O/R couple. One can easily show that $\Delta G_f^{\ddagger}$ reaches a minimum at $E = E^0 + \lambda$, where $\Delta G_f^{\ddagger} = 0$. Thus the maximum local rate of reduction at the Fermi level is found where $E_F = E^0 + \lambda$. When the Fermi level is at any other energy, E, the local rate of reduction at the Fermi level can be expressed, according to (3.6.2), (3.6.26), and (3.6.31), in terms of the following ratios

$$\frac{\text{Local Rate } (E_F = E)}{\text{Local Rate } (E_F = E^0 + \lambda)} = \frac{\nu_n \kappa_{el} \exp\left[-\frac{\lambda}{4\mathscr{k}T}\left(1 - \frac{E - E^0}{\lambda}\right)^2\right]}{\nu_n \kappa_{el}} \tag{3.6.32}$$

$$= \frac{\varepsilon_{red}(E) D_O(\lambda, E) f(E_F) \rho(E_F)}{\varepsilon_{red}(E^0 + \lambda) D_O(\lambda, E^0 + \lambda) f(E_F) \rho(E_F)}$$

Assuming that ε_{red} does not depend on the position of E_F, we can simplify this to

$$\frac{D_O(\lambda, E)}{D_O(\lambda, E^0 + \lambda)} = \exp\left[-\frac{(E - E^0 - \lambda)^2}{4\lambda\mathscr{k}T}\right] \tag{3.6.33}$$

This is a gaussian distribution having a mean at $E = E^0 + \lambda$ and a standard deviation of $(2\lambda\mathscr{k}T)^{1/2}$, as shown in Figure 3.6.4 (see also Section A.3). From (3.6.24), $D_O(\lambda, E)/D_O(\lambda, E^0 + \lambda) = W_O(\lambda, E)/W_O(\lambda, E^0 + \lambda)$. Also, since $W_O(\lambda, E)$ is normalized, the exponential prefactor, $W_O(\lambda, E^0 + \lambda)$, is quickly identified (Section A.3) as $(2\pi)^{-1/2}$ times the reciprocal of the standard deviation; therefore

$$W_O(\lambda, E) = (4\pi\lambda\mathscr{k}T)^{-1/2} \exp\left[-\frac{(E - E^0 - \lambda)^2}{4\lambda\mathscr{k}T}\right] \tag{3.6.34}$$

---

[21]Consider, for example, a simple model based on the idea that, in the time interval Δt, all of the electrons in the energy range between E and $E + dE$ redistribute themselves among all available states with equal probability. A refinement allows for the possibility that the states on species O participate with different weight from those on the electrode. If the states on the electrode are given unit weight and those in solution are given weight $\kappa_{red}(E)$, then

$$P_{red}(E) = \frac{\kappa_{red}(E) D_O(\lambda, E)\delta}{\rho(E) + \kappa_{red}(E) D_O(\lambda, E)\delta} = \varepsilon_{red}(E) D_O(\lambda, E)$$

where δ is the average distance across which electron transfer occurs, and $\kappa_{red}(E)$ is dimensionless and can be identified with the tunneling probability, κ_{el}, used in other representations of k_f. If the electrode is a metal, $\rho(E)$ is orders of magnitude greater than $\kappa_{red}(E) D_O(\lambda, E)\delta$; hence the rate constant becomes

$$k_f = \nu \int_{-\infty}^{\infty} \kappa_{red}(E)\delta W_O(\lambda, E) f(E) dE$$

which has no dependence on the electronic structure of the electrode.

In a similar manner, one can show that

$$W_R(\lambda, E) = (4\pi\lambda \text{\textit{k}}T)^{-1/2} \exp\left[\frac{-(E - E^0 + \lambda)^2}{4\lambda \text{\textit{k}}T}\right] \qquad (3.6.35)$$

thus the distribution for R has the same shape as that for O, but is centered on $E^0 - \lambda$, as depicted in Figure 3.6.4.

Any model of electrode kinetics is constrained by the requirement that

$$\frac{k_b}{k_f} = e^{f(E-E^0)} = e^{-(E-E^0)/\text{\textit{k}}T} \qquad (3.6.36)$$

which is easily derived from the need for convergence to the Nernst equation at equilibrium (Problem 3.16). The development of the Gerischer model up through equations 3.6.29 and 3.6.30 is general, and one can imagine that the various component functions in those two equations might come together in different ways to fulfill this requirement. By later including results from the Marcus theory without work terms, we were able to define the distribution functions, $W_O(\lambda, E)$ and $W_R(\lambda, E)$. Another feature of this simple *Gerischer–Marcus model* is that $\varepsilon_{ox}(E)$ and $\varepsilon_{red}(E)$ turn out to be identical functions and need no longer be distinguished. However, this will not necessarily be true for related models including work terms and a precursor equilibrium.

The reorganization energy, λ, has a large effect on the predicted current-potential response, as shown in Figure 3.6.5. The top frame illustrates the situation for $\lambda = 0.3$ eV, a value near the lower limit found experimentally. For this reorganization energy, an overpotential of -300 mV (case *a*) places the Fermi level opposite the peak of the state
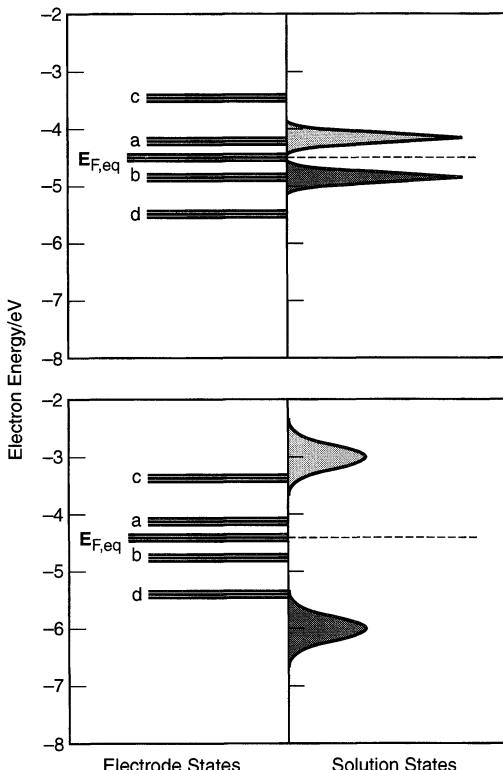
Figure 3.6.5 Effect of λ on kinetics in the Gerischer-Marcus representation. Top: $\lambda = 0.3$ eV. Bottom: $\lambda = 1.5$ eV. Both diagrams are for species O and R at equal concentrations, so that the Fermi level corresponding to the equilibrium potential, $E_{F,eq}$, is equal to the electron energy at the standard potential, E^0 (dashed line). For both frames, $E^0 = -4.5$ eV. Also shown in each frame is the way in which the Fermi level shifts with electrode potential. The different Fermi levels are for (*a*) $\eta = -300$ mV, (*b*) $\eta = +300$ mV, (*c*) $\eta = -1000$ mV, and (*d*) $\eta = +1000$ mV. On the solution side, $W_O(\lambda, E)$ and $W_R(\lambda, E)$ are shown with lighter and darker shading, respectively.

distribution for O; hence rapid reduction would be seen. Likewise, an overpotential of $+300$ mV (case *b*) brings the Fermi level down to match the peak in the state distribution for R and enables rapid oxidation. An overpotential of -1000 mV (case *c*) creates a situation in which $W_O(\lambda, \mathbf{E})$ overlaps entirely with filled states on the electrode, and for $\eta = +1000$ mV (case *d*), $W_R(\lambda, \mathbf{E})$ overlaps only empty states on the electrode. These latter two cases correspond to very strongly enabled reduction and oxidation, respectively.

The lower frame of Figure 3.6.5 shows the very different situation for the fairly large reorganization energy of 1.5 eV. In this case, an overpotential of -300 mV is not enough to elevate the Fermi level into a condition where filled states on the electrode overlap $W_O(\lambda, \mathbf{E})$, nor is an overpotential of $+300$ mV enough to lower the Fermi level into a condition where empty states on the electrode overlap $W_R(\lambda, \mathbf{E})$. It takes $\eta \approx -1000$ mV to enable reduction very effectively, and $\eta \approx +1000$ mV to do the same for oxidation. For this reorganization energy, the anodic and cathodic branches of the *i-E* curve would be widely separated, much as shown in Figure 3.4.2*c*.

Since this formulation of heterogeneous kinetics in terms of overlapping state distributions is linked directly to the basic Marcus theory, it is not surprising that many of its predictions are compatible with those of the previous two sections. The principal difference is that this formulation allows explicitly for contributions from states far from the Fermi level, which can be important in reactions at semiconductor electrodes (Section 18.2) or involving bound monolayers on metals (Section 14.5.2).

3.6.4 Tunneling and Extended Charge Transfer

In the treatments discussed above, the reactant was assumed to be held at a fixed, short distance, x_0, from the electrode. It is also of interest to consider whether a solution species can undergo electron transfer at different distances from the electrode and how the electron-transfer rate might depend on distance and on the nature of the intervening medium. The act of electron transfer is usually considered as tunneling of the electron between states in the electrode and those on the reactant. Electron tunneling typically follows an expression of the form:

$$\text{Probability of tunneling} \propto \exp(-\beta x) \tag{3.6.37}$$

where x is the distance over which tunneling occurs, and β is a factor that depends upon the height of the energy barrier and the nature of the medium between the states. For example, for tunneling between two pieces of metal through vacuum (73)

$$\beta \approx 4\pi(2m\Phi)^{1/2}/h \approx 1.02 \text{ Å}^{-1} \text{ eV}^{-1/2} \times \Phi^{1/2} \tag{3.6.38}$$

where m is the mass of the electron, 9.1×10^{-28} g, and Φ is the work function of the metal, typically given in eV. Thus for Pt, where $\Phi = 5.7$ eV, β is about 2.4 Å^{-1}. Within the electron-transfer theory, tunneling effects are usually incorporated by taking the transmission coefficient, κ_{el}, in (3.6.2) as

$$\kappa_{el}(x) = \kappa_{el}^0 \exp(-\beta x) \tag{3.6.39}$$

where $\kappa_{el}(x) \to 1$ when x is at the distance where the interaction of reactant with the electrode is sufficiently strong for the reaction to be *adiabatic* (48, 49).

In electron-transfer theory, the extent of interaction or electronic coupling between two reactants (or between a reactant and the electrode) is often described in terms of *adiabaticity*. If the interaction is strong, there is a splitting larger than kT in the energy curves at the point of intersection (e.g., Figure 3.6.6*a*). It leads to a lower curve (or surface) pro-
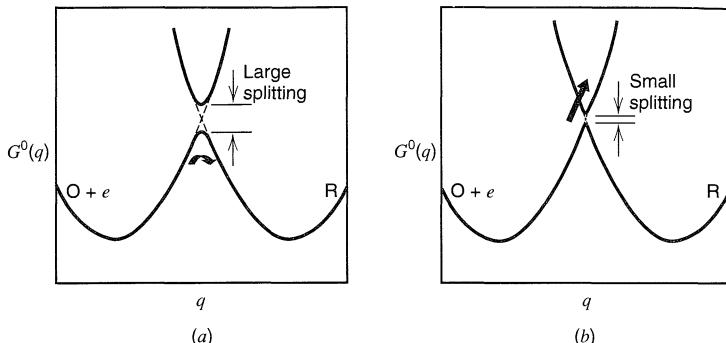
Figure 3.6.6 Splitting of energy curves (energy surfaces) in the intersection region. (*a*) A strong interaction between O and the electrode leads to a well-defined, continuous curve (surface) connecting O + *e* with R. If the reacting system reaches the transition state, the probability is high that it will proceed into the valley corresponding to R, as indicated by the curved arrow. (*b*) A weak interaction leads to a splitting less than kT. When the reacting system approaches the transition state from the left, it has a tendency to remain on the O + *e* curve, as indicated by the straight arrow. The probability of crossover to the R curve can be small. These curves are drawn for an electrode reaction, but the principle is the same for a homogeneous reaction, where the reactants and products might be O + R' and R + O', respectively.

ceeding continuously from O to R and an upper curve (or surface) representing an excited state. In this situation of strong coupling, a system will nearly always stay on the lower surface passing from O to R, and the reaction is said to be *adiabatic*. The probability of reaction per passage approaches unity for an adiabatic reaction.

If the interaction is small (e.g,. when the reactants are far apart), the splitting of the potential energy curves at the point of intersection is less than kT (Figure 3.6.6*b*). In this case, there is a smaller likelihood that the system will proceed from O to R. The reaction is said to be *nonadiabatic*, because the system tends to stay on the original "reactant" sur-face (or, actually, to cross from the ground-state surface to the excited-state surface). The probability of reaction per passage through the intersection region is taken into account by $\kappa_{el} < 1$ (47, 48). For example, κ_{el} could be 10^{-5}, meaning that the reactants would, on the average, pass through the intersection region (i.e., reach the transition state) 100,000 times for every successful reaction.

In considering dissolved reactants participating in a heterogeneous reaction, one can treat the reaction as occurring over a range of distances, where the rate constant falls off exponentially with distance. The result of such a treatment (48, 74) is that electron trans-fer occurs over a region near the electrode, rather than only at a single position, such as the outer Helmholtz plane. However, the effect for dissolved reactants should be observ-able experimentally only under rather restricted circumstances (e.g., $D < 10^{-10}$ cm^2/s), and is thus usually not important.

On the other hand, it is possible to study electron transfer to an electroactive species held at a fixed distance (10–30 Å) from the electrode surface by a suitable spacer, such as an adsorbed monolayer (Section 14.5.2) (75, 76). One approach is based on the use of a blocking monolayer, such as a self-assembled monolayer of an alkane thiol or an insulat-ing oxide film, to define the distance of closest approach of a dissolved reactant to the electrode. This strategy requires knowledge of the precise thickness of the blocking layer and assurance that the layer is free of pinholes and defects, through which solution species might penetrate (Section 14.5). Alternatively. the adsorbed monolayer may itself

Electroactive Centers

Alkylthiol
chains
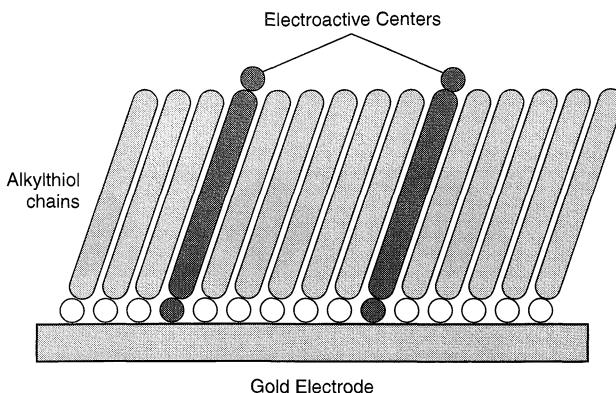
Gold Electrode

Figure 3.6.7 Schematic diagram of an adsorbed monolayer of alkane thiol containing similar molecules with attached electroactive groups held by the film at a fixed distance from the electrode surface.

contain electroactive groups. A typical layer of this kind (75) involves an alkane thiol (RSH) with a terminal ferrocene group (-Fc), that is, $HS(CH_2)_nOOCFc$ (often written as HSC_nOOCFc; typically $n = 8$ to 18) (Figure 3.6.7). These molecules are often diluted in the monolayer film with similar nonelectroactive molecules (e.g., HSC_nCH_3). The rate constant is measured as a function of the length of the alkyl chain, and the slope of the plot of $\ln(k)$ vs. n or x allows determination of β.

For saturated chains, β is typically in the range 1 to 1.2 Å^{-1}. The difference between this *through-bond* value and that for vacuum (*through-space*), $\sim 2 \text{ Å}^{-1}$, reflects the contribution of the molecular bonds to tunneling. Even smaller β values (0.4 to 0.6 Å^{-1}) have been seen with π-conjugated molecules [e.g., those with phenyleneethynyl (-Ph-C≡C-) units] as spacers (77, 78). Confidence in the β values found in these electrochemical studies is reinforced by the fact that they generally agree with those found for long-range intramolecular electron transfer, such as in proteins.

▶ 3.7 REFERENCES

1. W. C. Gardiner, Jr., "Rates and Mechanisms of Chemical Reactions," Benjamin, New York, 1969.

2. H. S. Johnston, "Gas Phase Reaction Rate Theory," Ronald, New York, 1966.

3. S. Glasstone, K. J. Laidler, and H. Eyring, "Theory of Rate Processes," McGraw-Hill, New York, 1941.

4. H. Eyring, S. H. Lin, and S. M. Lin, "Basic Chemical Kinetics," Wiley, New York, 1980, Chap. 4.

5. R. S. Berry, S. A. Rice, J. Ross, "Physical Chemistry," Wiley, New York, 1980, pp. 931–932.

6. J. Tafel, *Z. Physik. Chem.*, **50A**, 641 (1905).

7. P. Delahay, "New Instrumental Methods in Electrochemistry," Wiley-Interscience, New York, 1954, Chap. 2.

8. P. Delahay, "Double Layer and Electrode Kinetics," Wiley-Interscience, New York, 1965, Chap. 7.

9. B. E. Conway, "Theory and Principles of Electrode Processes," Ronald, New York, 1965, Chap. 6.

10. K. J. Vetter, "Electrochemical Kinetics," Academic, New York, 1967, Chap. 2.

11. J. O'M. Bockris and A. K. N. Reddy, "Modern Electrochemistry," Vol. 2, Plenum, New York, 1970, Chap. 8.

12. T. Erdey-Grúz, "Kinetics of Electrode Processes," Wiley-Interscience, New York, 1972, Chap. 1.

13. H. R. Thirsk, "A Guide to the Study of Electrode Kinetics," Academic, New York, 1972, Chap. 1.

14. W. J. Albery, "Electrode Kinetics," Clarendon, Oxford, 1975.

15. J. E. B. Randles, *Trans. Faraday Soc.*, **48**, 828 (1952).

16. C. N. Reilley in "Treatise on Analytical Chemistry," Part I, Vol. 4, I. M. Kolthoff and P. J. Elving, Eds., Wiley-Interscience, 1963, Chap. 42.

17. J. A. V. Butler, *Trans. Faraday Soc.*, **19**, 729, 734 (1924).

18. T. Erdey-Grúz and M. Volmer, *Z. Physik. Chem.*, **150A**, 203 (1930).

19. R. Parsons, *Trans. Faraday Soc.*, **47**, 1332 (1951).

20. J. O'M Bockris, *Mod. Asp. Electrochem.*, **1**, 180 (1954).

21. D. M. Mohilner and P. Delahay, *J. Phys. Chem.*, **67**, 588 (1963).

22. M. E. Peover, *Electroanal. Chem.*, **2**, 1 (1967).

23. N. Koizumi and S. Aoyagui, *J. Electroanal. Chem.*, **55**, 452 (1974).

24. H. Kojima and A. J. Bard, *J. Am. Chem. Soc.*, **97**, 6317 (1975).

25. K. J. Vetter, *op. cit.*, Chap. 4.

26. T. Erdey-Grúz, *op. cit.*, Chap. 4.

27. P. Delahay, "Double Layer and Electrode Kinetics," *op. cit.*, Chap. 10.

28. N. Tanaka and R. Tamamushi, *Electrochim. Acta*, **9**, 963 (1964).

29. B. E. Conway, "Electrochemical Data," Elsevier, Amsterdam, 1952.

30. R. Parsons, "Handbook of Electrochemical Data," Butterworths, London, 1959.

31. A. J. Bard and H. Lund, "Encyclopedia of the Electrochemistry of the Elements," Marcel Dekker, New York, 1973–1986.

32. E. Gileadi, E. Kirowa-Eisner, and J. Penciner, "Interfacial Electrochemistry," Addison-Wesley, Reading, MA, 1975, pp. 60–75.

33. K. J. Vetter and G. Manecke, *Z. Physik. Chem. (Leipzig).*, **195**, 337 (1950).

34. P. A. Allen and A. Hickling, *Trans. Faraday Soc.*, **53**, 1626 (1957).

35. P. Delahay, "Double Layer and Electrode Kinetics," *op. cit.*, Chaps. 8–10.

36. K. B. Oldham, *J. Am. Chem. Soc.*, **77**, 4697 (1955).

37. R. A. Marcus, *J. Chem Phys.*, **24**, 4966 (1956).

38. R. A. Marcus, *Electrochim. Acta*, **13**, 955 (1968).

39. N. S. Hush, *J. Chem. Phys.*, **28**, 962 (1958).

40. N. S. Hush, *Electrochim. Acta*, **13**, 1005 (1968).

41. V. G. Levich, *Adv. Electrochem. Electrochem. Engr.*, **4**, 249 (1966) and references cited therein.

42. R. R. Dogonadze in "Reactions of Molecules at Electrodes," N. S. Hush, Ed., Wiley-Interscience, New York, 1971, Chap. 3 and references cited therein.

43. J. O'M. Bockris, *Mod. Asp. Electrochem.*, **1**, 180 (1954).

44. P. P. Schmidt in "Electrochemistry," A Specialist Periodical Report, Vols. 5 and 6, H. R. Thirsk, Senior Reporter, The Chemical Society, London, 1977 and 1978.

45. A. M. Kuznetsov, *Mod. Asp. Electrochem.*, **20**, 95 (1989).

46. W. Schmickler, "Interfacial Electrochemistry," Oxford University Press, New York, 1996.

47. C. J. Miller in "Physical Electrochemistry. Principles, Methods, and Applications," I. Rubinstein, Ed., Marcel Dekker, New York, 1995, Chap. 2.

48. M. J. Weaver in "Comprehensive Chemical Kinetics,'" R. G. Compton, Ed., Elsevier, Amsterdam, Vol. 27, 1987. Chap. 1.

49. R. A. Marcus and P. Siddarth, "Photoprocesses in Transition Metal Complexes, Biosystems and Other Molecules," E. Kochanski, Ed., Kluwer, Amsterdam, 1992.

50. N. S. Hush, *J. Electroanal. Chem.*, **470**, 170 (1999).

51. L. Eberson, "Electron Transfer Reactions in Organic Chemistry," Springer-Verlag, Berlin, 1987.

52. N. Sutin, *Accts. Chem. Res.*, **15**, 275 (1982).

53. R. A. Marcus and N. Sutin, *Biochim. Biophys. Acta*, **811**, 265 (1985).

54. H. Taube, "Electron Transfer Reactions of Complex Ions in Solution," Academic, New York, 1970, p. 27.

55. J. J. Ulrich and F. C. Anson, *Inorg. Chem.*, **8**, 195 (1969).

56. G. A. Somorjai, "Introduction to Surface Chemistry and Catalysis," Wiley, New York, 1994.

57. S. F. Fischer and R. P. Van Duyne, *Chem. Phys.*, **26**, 9 (1977).

58. R. A. Marcus, *J. Chem. Phys.*, **43**, 679 (1965).

59. R. A. Marcus, *Annu. Rev. Phys. Chem.*, **15**, 155 (1964).

60. B. S. Brunschwig, J. Logan, M. D. Newton, and N. Sutin, *J. Am. Chem. Soc.*, **102**, 5798 (1980).

61. R. A. Marcus, *J. Phys. Chem.*, **67**, 853 (1963).

62. D. F. Calef and P. G. Wolynes. *J. Phys. Chem.*, **87**, 3387 (1983).

63. J. T. Hynes in "Theory of Chemical Reaction Dynamics," M. Baer, Editor, CRC, Boca Raton, FL, 1985, Chap. 4.

64. H. Sumi and R. A. Marcus, *J. Chem. Phys.*, **84**, 4894 (1986).

65. M. J. Weaver, *Chem. Rev.*, **92**, 463 (1992).

66. X. Zhang, J. Leddy, and A. J. Bard, *J. Am. Chem. Soc.*, **107**, 3719 (1985).

67. X. Zhang, H. Yang, and A. J. Bard, *J. Am. Chem. Soc.*, **109**, 1916 (1987).

68. M. E. Williams, J. C. Crooker, R. Pyati, L. J. Lyons, and R. W. Murray, *J. Am. Chem. Soc.*, **119**, 10249 (1997).

69. R. A. Marcus, *J. Phys. Chem.*, **94**, 1050 (1990); **95**, 2010 (1991).

70. M. Tsionsky, A. J. Bard, and M. V. Mirkin, *J. Am. Chem. Soc.*, **119**, 10785 (1997).

71. H. Gerischer, *Adv. Electrochem. Electrochem. Eng.*, **1**, 139 (1961).

72. H. Gerischer in "Physical Chemistry: An Advanced Treatise," Vol. 9A, H. Eyring, D. Henderson, and W. Jost, Eds., Academic, New York, 1970.

73. C. J. Chen, "Introduction to Scanning Tunneling Microscopy," Oxford University Press, New York, 1993, p. 5.

74. S. W. Feldberg, *J. Electroanal. Chem.*, **198**, 1 (1986).

75. H. O. Finklea, *Electroanal. Chem.*, **19**, 109 (1996).

76. J. F. Smalley, S. W. Feldberg, C. E. D. Chidsey, M. R. Linford, M. D. Newton, and Y.-P. Liu, *J. Phys. Chem.*, **99**, 13141 (1995).

77. S. B. Sachs, S. P. Dudek, R. P. Hsung, L. R. Sita, J. F. Smalley, M. D. Newton, S. W. Feldberg, and C. E. D. Chidsey, *J. Am. Chem. Soc.*, **119**, 10563 (1997).

78. S. Creager, S. J. Yu, D. Bamdad, S. O'Conner, T. MacLean, E. Lam, Y. Chong, G. T. Olsen, J Luo, M. Gozin, and J. F. Kayyem, *J. Am. Chem. Soc.*, **121**, 1059 (1999).
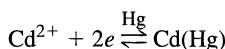
3.8 PROBLEMS

3.1 Consider the electrode reaction $O + ne \rightleftarrows R$. Under the conditions that $C_R^* = C_O^* = 1$ mM, $k^0 = 10^{-7}$ cm/s, $\alpha = 0.3$, and $n = 1$:

    (a) Calculate the exchange current density, $j_0 = i_0/A$, in μA/cm^2.

    (b) Draw a current density-overpotential curve for this reaction for currents up to 600 μA/cm^2 anodic and cathodic. Neglect mass-transfer effects.

    (c) Draw log $|j|$ *vs.* η curves (Tafel plots) for the current ranges in (b).

3.2 A general expression for the current as a function of overpotential, including mass-transfer effects, can be obtained from (3.4.29) and yields

$$i = \frac{\exp[-\alpha f\eta] - \exp[(1-\alpha)f\eta]}{\dfrac{1}{i_0} + \dfrac{\exp[-\alpha f\eta]}{i_{l,c}} - \dfrac{\exp[(1-\alpha)f\eta]}{i_{l,a}}}$$

    (a) Derive this expression.

    (b) Use a spreadsheet program to repeat the calculation of Problem 3.1, parts (b) and (c), including the effects of mass transfer. Assume $m_O = m_R = 10^{-3}$ cm/s.

3.3 Use a spreadsheet program to calculate and plot current *vs.* potential and ln(current) *vs.* potential for the general i-η equation given in Problem 3.2.

    (a) Show a table of results [potential, current, ln(current), overpotential] and graphs of i *vs.* η and ln$|i|$ *vs.* η for the following parameters: $A = 1$ cm^2; $C_O^* = 1.0 \times 10^{-3}$ mol/cm^3; $C_R^* = 1.0 \times 10^{-5}$ mol/cm^3; $n = 1$; $\alpha = 0.5$; $k^0 = 1.0 \times 10^{-4}$ cm/s; $m_O = 0.01$ cm/s; $m_R = 0.01$ cm/s; $E^0 = -0.5$ V *vs.* NHE.

    (b) Show the i *vs.* E curves for a range of k^0 values with the other parameters as in (a). At what values of k^0 are the curves indistinguishable from nernstian ones?

    (c) Show the i *vs.* E curves for a range of α values with the other parameters as in (a).

3.4 In most cases, the currents for individual processes are additive, that is, the total current, i_t, is given as the sum of the currents for different electrode reactions ($i_1, i_2, i_3, \ldots$). Consider a solution with a Pt working electrode immersed in a solution of 1.0 M HBr and 1 mM K$_3$Fe(CN)$_6$. Assume the following exchange current densities:

H$^+$/H$_2$	$j_0 = 10^{-3}$ A/cm^2
Br$_2$/Br$^-$	$j_0 = 10^{-2}$ A/cm^2
Fe(CN)$_6^{3-}$/Fe(CN)$_6^{4-}$	$j_0 = 4 \times 10^{-5}$ A/cm^2

Use a spreadsheet program to calculate and plot the current-potential curve for this system scanning from the anodic background limit to the cathodic background limit. Take the appropriate standard potentials from Table C.1 and values for other parameters $(m_O, \alpha, \ldots)$ from Problem 3.3.

3.5 Consider one-electron electrode reactions for which $\alpha = 0.50$ and $\alpha = 0.10$. Calculate the relative error in current resulting from the use in each case of:

(a) The linear i–η characteristic for overpotentials of 10, 20, and 50 mV.

(b) The Tafel (totally irreversible) relationship for overpotentials of 50, 100, and 200 mV.

3.6 According to G. Scherer and F. Willig [*J. Electroanal. Chem.*, **85**, 77 (1977)] the exchange current density, j_0, for $Pt/Fe(CN)_6^{3-}$ (2.0 mM), $Fe(CN)_6^{4-}$ (2.0 mM), NaCl (1.0 M) at 25°C is 2.0 mA/cm^2. The transfer coefficient, α, for this system is about 0.50. Calculate (a) the value of k^0; (b) j_0 for a solution 1 M each in the two complexes; (c) the charge-transfer resistance of a 0.1 cm^2 electrode in a solution 10^{-4} M each in ferricyanide and ferrocyanide.

3.7 Berzins and Delahay [*J. Am. Chem. Soc.*, **77**, 6448 (1955)] studied the reaction

$$Cd^{2+} + 2e \underset{}{\overset{Hg}{\rightleftharpoons}} Cd(Hg)$$

and obtained the following data with $C_{Cd(Hg)} = 0.40\ M$:
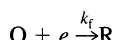
$C_{Cd^{2+}}$ (mM)	1.0	0.50	0.25	0.10
j_0 (mA/cm^2)	30.0	17.3	10.1	4.94

(a) Assume that the general mechanism in (3.5.8)–(3.5.10) applies. Calculate $n' + \alpha$, and suggest values for n', n'', and α individually. Write out a specific chemical mechanism for the process.

(b) Calculate k_{app}^0.

(c) Compare the outcome with the analysis provided by Berzins and Delahay in their original paper.

3.8 (a) Show that for a first-order homogeneous reaction,

$$A \overset{k_f}{\to} B$$

the average lifetime of A is $1/k_f$.

(b) Derive an expression for the average lifetime of the species O when it undergoes the heterogeneous reaction,

$$O + e \overset{k_f}{\to} R$$
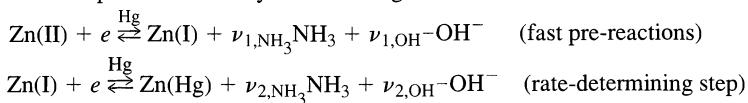
Note that only species within distance d of the surface can react. Consider a hypothetical system in which the solution phase extends only d (perhaps 10 Å) from the surface.

(c) What value of k_f would be needed for a lifetime of 1 ms? Are lifetimes as short as 1 ns possible?

3.9 Discuss the mechanism by which the potential of a platinum electrode becomes poised by immersion into a solution of Fe(II) and Fe(III) in 1 M HCl. Approximately how much charge is required to shift the electrode potential by 100 mV? Why does the potential become uncertain at low concentrations of Fe(II) and Fe(III), even if the ratio of their concentrations is held near unity? Does this experimental fact reflect thermodynamic considerations? How well do your answers to these issues apply to the establishment of potential at an ion-selective electrode?

3.10 In ammoniacal solutions ([NH$_3$] $\sim 0.05\ M$), Zn(II) is primarily in the form of the complex ion $Zn(NH_3)_3(OH)^+$ [hereafter referred to as Zn(II)]. In studying the electroreduction of this compound to zinc amalgam at a mercury cathode, Gerischer [*Z. Physik. Chem.*, **202**, 302 (1953)] found that

$$\frac{\partial \log i_0}{\partial \log [Zn(II)]} = 0.41 \pm 0.03 \qquad \frac{\partial \log i_0}{\partial \log [NH_3]} = 0.65 \pm 0.03$$

$$\frac{\partial \log i_0}{\partial \log [OH^-]} = -0.28 \pm 0.02 \qquad \frac{\partial \log i_0}{\partial \log [Zn]} = 0.57 \pm 0.03$$

where [Zn] refers to a concentration in the amalgam.

(a) Give the equation for the overall reaction.

(b) Assume that the process occurs by the following mechanism:

$$Zn(II) + e \overset{Hg}{\rightleftarrows} Zn(I) + \nu_{1,NH_3}NH_3 + \nu_{1,OH}^-OH^- \quad \text{(fast pre-reactions)}$$

$$Zn(I) + e \overset{Hg}{\rightleftarrows} Zn(Hg) + \nu_{2,NH_3}NH_3 + \nu_{2,OH}^-OH^- \quad \text{(rate-determining step)}$$

where Zn(I) stands for a zinc species of unknown composition in the $+1$ oxidation state, and the ν's are stoichiometric coefficients. Derive an expression for the exchange current analogous to (3.5.40), and find explicit relationships for the logarithmic derivatives given above.

(b) Calculate α and all stoichiometric coefficients.

(c) Identify Zn(I) and write chemical equations to give a mechanism consistent with the data.

(d) Consider an alternative mechanism having the pattern above, but with the first step being rate-determining. Is such a mechanism consistent with the observations?

3.11 The following data were obtained for the reduction of species R to R^- in a stirred solution at a 0.1 cm^2 electrode; the solution contained 0.01 M R and 0.01 M R^-.

$$\eta \text{ (mV):} \quad -100 \quad -120 \quad -150 \quad -500 \quad -600$$
$$i \text{ (μA):} \quad 45.9 \quad 62.6 \quad 100 \quad 965 \quad 965$$

Calculate: $i_0, k^0, \alpha, R_{ct}, i_l, m_O, R_{mt}$

3.12 From results in Figure 3.4.5 for 10^{-2} M Mn(III) and 10^{-2} M Mn(IV), estimate j_0 and k^0. What is the predicted j_0 for a solution 1 M in both Mn(III) and Mn(IV)?

3.13 The magnitude of the solvent term $(1/\varepsilon_{op} - 1/\varepsilon_s)$ is about 0.5 for most solvents. Calculate the value of λ_o and the free energy of activation (in eV) due only to solvation for a molecule of radius 4.0 Å spaced 7 Å from an electrode surface.

3.14 Derive (3.6.30).

3.15 Show from the equations for $D_O(E, \lambda)$ and $D_R(E, \lambda)$ that the equilibrium energy of a system, E_{eq}, is related to the bulk concentrations, C_O^* and C_R^* and E^0 by an expression resembling the Nernst equation. How does this expression differ from the Nernst equation written in terms of potentials, E_{eq} and E^0? How do you account for the difference?

3.16 Derive (3.6.36) by considering the reaction $O + e \rightleftarrows R$ at equilibrium in a system with bulk concentrations C_O^* and C_R^*.

4

MASS TRANSFER
BY MIGRATION
AND DIFFUSION

▷ 4.1 DERIVATION OF A GENERAL MASS TRANSFER EQUATION

In this section, we discuss the general partial differential equations governing mass transfer; these will be used frequently in subsequent chapters for the derivation of equations appropriate to different electrochemical techniques. As discussed in Section 1.4, mass transfer in solution occurs by diffusion, migration, and convection. Diffusion and migration result from a gradient in electrochemical potential, $\overline{\mu}$. Convection results from an imbalance of forces on the solution.

Consider an infinitesimal element of solution (Figure 4.1.1) connecting two points in the solution, r and s, where, for a certain species j, $\overline{\mu}_j(r) \neq \overline{\mu}_j(s)$. This difference of $\overline{\mu}_j$ over a distance (a gradient of electrochemical potential) can arise because there is a difference of concentration (or activity) of species j (a concentration gradient), or because there is a difference of ϕ (an electric field or potential gradient). In general, a flux of species j will occur to alleviate any difference of $\overline{\mu}_j$. The flux, $\mathbf{J}_j$ (mol s^{-1}cm^{-2}), is proportional to the gradient of $\overline{\mu}_j$:

$$\mathbf{J}_j \propto \mathbf{grad}\ \overline{\mu}_j \qquad \text{or} \qquad \mathbf{J}_j \propto \nabla\ \overline{\mu}_j \qquad (4.1.1)$$

where **grad** or ∇ is a vector operator. For linear (one-dimensional) mass transfer, $\nabla = \mathbf{i}(\partial/\partial x)$, where $\mathbf{i}$ is the unit vector along the axis and x is distance. For mass transfer in a three-dimensional Cartesian space,

$$\nabla = \mathbf{i}\frac{\partial}{\partial x} + \mathbf{j}\frac{\partial}{\partial y} + \mathbf{k}\frac{\partial}{\partial z} \qquad (4.1.2)$$

Point r

$\overline{\mu}_i(r) = \mu_i^0 + RT \ln a_i(r) + z_i F\phi(r)$

Point s

$\overline{\mu}_i(s) = \mu_i^0 + RT \ln a_i(s) + z_i F\phi(s)$

(a)

(b)
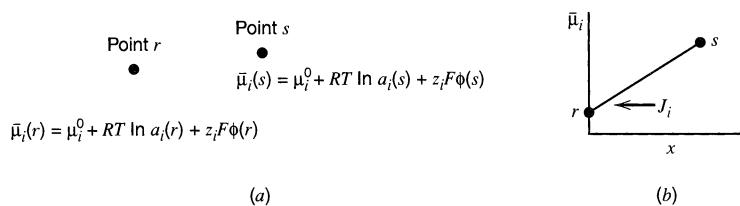
Figure 4.1.1 A gradient of electrochemical potential.

The constant of proportionality in (4.1.1) turns out to be $-C_j D_j / RT$; thus,

$$\mathbf{J}_j = -\left(\frac{C_j D_j}{RT}\right) \nabla \overline{\mu}_j \tag{4.1.3}$$

For linear mass transfer, this is

$$J_j(x) = -\left(\frac{C_j D_j}{RT}\right) \frac{\partial \overline{\mu}_j}{\partial x} \tag{4.1.4}$$

The minus sign arises in these equations because the direction of the flux opposes the direction of increasing $\overline{\mu}_j$.

If, in addition to this $\overline{\mu}$ gradient, the solution is moving, so that an element of solution [with a concentration $C_j(s)$] shifts from s with a velocity $\mathbf{v}$, then an additional term is added to the flux equation:

$$\mathbf{J}_j = -\left(\frac{C_j D_j}{RT}\right) \nabla \overline{\mu}_j + C_j \mathbf{v} \tag{4.1.5}$$

For linear mass transfer,

$$J_j(x) = -\left(\frac{C_j D_j}{RT}\right)\left(\frac{\partial \overline{\mu}_j}{\partial x}\right) + C_j v(x) \tag{4.1.6}$$

Taking $a_j \approx C_j$, we obtain the *Nernst–Planck equations*, which can be written as

$$J_j(x) = -\left(\frac{C_j D_j}{RT}\right)\left[\frac{\partial}{\partial x}(RT \ln C_j) + \frac{\partial}{\partial x}(z_j F \phi)\right] + C_j v(x) \tag{4.1.7}$$

$$\boxed{J_j(x) = -D_j \frac{\partial C_j(x)}{\partial x} - \frac{z_j F}{RT} D_j C_j \frac{\partial \phi(x)}{\partial x} + C_j v(x)} \tag{4.1.8}$$

or in general,

$$\boxed{\mathbf{J}_j = -D_j \nabla C_j - \frac{z_j F}{RT} D_j C_j \nabla \phi + C_j \mathbf{v}} \tag{4.1.9}$$

In this chapter, we are concerned with systems in which convection is absent. Convective mass transfer will be treated in Chapter 9. Under quiescent conditions, that is, in an unstirred or stagnant solution with no density gradients, the solution velocity, $\mathbf{v}$, is zero, and the general flux equation for species j, (4.1.9), becomes

$$\mathbf{J}_j = -D_j \nabla C_j - \frac{z_j F}{RT} D_j C_j \nabla \phi \tag{4.1.10}$$

For linear mass transfer, this is

$$J_j(x) = -D_j\left(\frac{\partial C_j(x)}{\partial x}\right) - \frac{z_j F}{RT} D_j C_j\left(\frac{\partial \phi(x)}{\partial x}\right) \tag{4.1.11}$$

where the terms on the right-hand side represent the contributions of diffusion and migration, respectively, to the total mass transfer.

If species j is charged, then the flux, J_j, is equivalent to a current density. Let us consider a linear system with a cross-sectional area, A, normal to the axis of mass flow. Then, J_j (mol s^{-1} cm^{-2}) is equal to $-i_j/z_j FA$ [C/s per (C mol^{-1} cm^2)], where i_j is the current

component at any value of x arising from a flow of species j. Equation 4.1.11 can then be written as

$$-J_j = \frac{i_j}{z_j FA} = \frac{i_{d,j}}{z_j FA} + \frac{i_{m,j}}{z_j FA} \tag{4.1.12}$$

with

$$\frac{i_{d,j}}{z_j FA} = D_j \frac{\partial C_j}{\partial x} \tag{4.1.13}$$

$$\frac{i_{m,j}}{z_j FA} = \frac{z_j F D_j}{RT} C_j \frac{\partial \phi}{\partial x} \tag{4.1.14}$$

where $i_{d,j}$ and $i_{m,j}$ are *diffusion* and *migration currents* of species j, respectively.

At any location in solution during electrolysis, the total current, i, is made up of contributions from all species; that is,

$$i = \sum_j i_j \tag{4.1.15}$$

or

$$i = \frac{F^2 A}{RT} \cdot \frac{\partial \phi}{\partial x} \sum_j z_j^2 D_j C_j + FA \sum_j z_j D_j \frac{\partial C_j}{\partial x} \tag{4.1.16}$$

where the current for each species at that location is made up of a migrational component (first term) and a diffusional component (second term).

We will now discuss migration and diffusion in electrochemical systems in more detail. The concepts and equations derived below date back to at least the work of Planck (1). Further details concerning the general problem of mass transfer in electrochemical systems can be found in a number of reviews (2–6).

▶▶ **4.2 MIGRATION**

In the bulk solution (away from the electrode), concentration gradients are generally small, and the total current is carried mainly by migration. All charged species contribute. For species j in the bulk region of a linear mass-transfer system having a cross-sectional area A, $i_j = i_{m,j}$ or

$$i_j = \frac{z_j^2 F^2 A D_j C_j}{RT} \cdot \frac{\partial \phi}{\partial x} \tag{4.2.1}$$

The mobility of species j, defined in Section 2.3.3, is linked to the diffusion coefficient by the *Einstein–Smoluchowski equation*:

$$\boxed{u_j = \frac{|z_j| F D_j}{RT}} \tag{4.2.2}$$

hence i_j can be reexpressed as

$$i_j = |z_j| FA u_j C_j \frac{\partial \phi}{\partial x} \tag{4.2.3}$$

For a linear electric field,

$$\frac{\partial \phi}{\partial x} = \frac{\Delta E}{l} \tag{4.2.4}$$

where $\Delta E/l$ is the gradient (V/cm) arising from the change in potential ΔE over distance l. Thus,

$$i_j = \frac{|z_j| FA u_j C_j \,\Delta E}{l} \tag{4.2.5}$$

and the total current in bulk solution is given by

$$i = \sum_j i_j = \frac{FA \,\Delta E}{l} \sum_j |z_j| u_j C_j \tag{4.2.6}$$

which is (4.1.16) expressed in particular for this situation. The conductance of the solution, L (Ω^{-1}), which is the reciprocal of the resistance, R (Ω), is given by Ohm's law,

$$L = \frac{1}{R} = \frac{i}{\Delta E} = \frac{FA}{l} \sum_j |z_j| u_j C_j = \frac{A}{l}\kappa \tag{4.2.7}$$

where κ, the *conductivity* ($\Omega^{-1}\,cm^{-1}$; Section 2.3.3) is given by

$$\kappa = F \sum_j |z_j| u_j C_j \tag{4.2.8}$$

Equally, one can write an equation for the solution resistance in terms of ρ, the *resistivity* (Ω-cm), where $\rho = 1/\kappa$:

$$R = \frac{\rho l}{A} \tag{4.2.9}$$

The fraction of the total current that a given ion j carries is t_j, the *transference number* of j, given by

$$t_j = \frac{i_j}{i} = \frac{|z_j| u_j C_j}{\sum\limits_k |z_k| u_k C_k} = \frac{|z_j| C_j \lambda_j}{\sum\limits_k |z_k| C_k \lambda_k} \tag{4.2.10}$$

See also equations 2.3.11 and 2.3.18.

▶ 4.3 MIXED MIGRATION AND DIFFUSION NEAR AN ACTIVE ELECTRODE

The relative contributions of diffusion and migration to the flux of a species (and of the flux of that species to the total current) differ at a given time for different locations in solution. Near the electrode, an electroactive substance is, in general, transported by both processes. The flux of an electroactive substance at the electrode surface controls the rate of reaction and, therefore, the faradaic current flowing in the external circuit (see Section 1.3.2). That current can be separated into diffusion and migration currents reflecting the diffusive and migrational components to the flux of the electroactive species at the surface:

$$i = i_d + i_m \tag{4.3.1}$$

Note that i_m and i_d may be in the same or opposite directions, depending on the direction of the electric field and the charge on the electroactive species. Examples of three reductions— of a positively charged, a negatively charged, and an uncharged substance—are shown in Figure 4.3.1. The migrational component is always in the same direction as i_d for cationic species reacting at cathodes and for anionic species reacting at anodes. It opposes i_d when anions are reduced at cathodes and when cations are oxidized at anodes.

$$Cu^{2+} + 2e \rightarrow Cu \qquad\qquad Cu(CN)_4^{2-} + 2e \rightarrow Cu + 4CN^- \qquad\qquad Cu(CN)_2 + 2e \rightarrow Cu + 2CN^-$$

(a) $i = i_d + |i_m|$ (b) $i = i_d - |i_m|$ (c) $i = i_d$
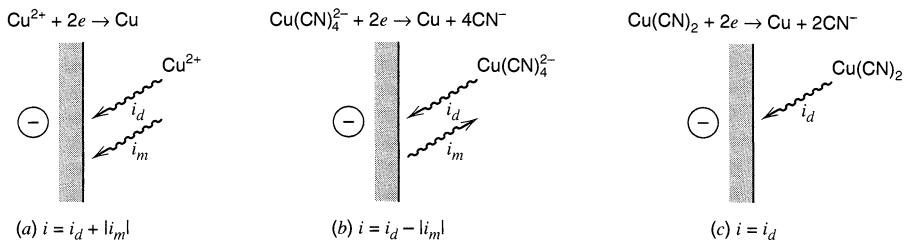
Figure 4.3.1 Examples of reduction processes with different contributions of the migration current: (a) positively charged reactant, (b) negatively charged reactant, (c) uncharged reactant.

For many electrochemical systems, the mathematical treatments are simplified if the migrational component to the flux of the electroactive substance is made negligible. We discuss in this section the conditions under which that approximation holds. The topic is discussed in greater depth in references 7–10.

4.3.1 Balance Sheets for Mass Transfer During Electrolysis

Although migration carries the current in the bulk solution during electrolysis, diffusional transport also occurs in the vicinity of the electrodes, because concentration gradients of the electroactive species arise there. Indeed, under some circumstances, the flux of electroactive species to the electrode is due almost completely to diffusion. To illustrate these effects, let us apply the "balance sheet" approach (11) to transport in several examples.

Example 4.1
Consider the electrolysis of a solution of hydrochloric acid at platinum electrodes (Figure 4.3.2a). Since the equivalent ionic conductance of H^+, λ_+, and of Cl^-, λ_-, relate as $\lambda_+ \approx 4\lambda_-$, then from (4.2.10), $t_+ = 0.8$ and $t_- = 0.2$. Assume that a total current equivalent to $10e$ per unit time is passed through the cell, producing five H_2 molecules
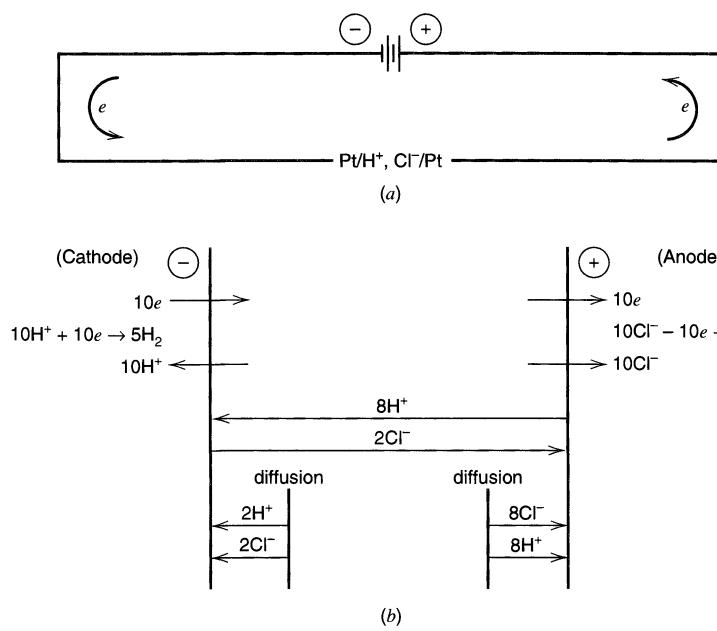
Figure 4.3.2 Balance sheet for electrolysis of hydrochloric acid solution. (a) Cell schematic. (b) Various contributions to the current when $10e$ are passed in the external circuit per unit time.

at the cathode and five Cl_2 molecules at the anode. (Actually, some O_2 could also be formed at the anode; for simplicity we neglect this reaction.) The total current is carried in the bulk solution by the movement of $8H^+$ toward the cathode and $2Cl^-$ toward the anode (Figure 4.3.2b). To maintain a steady current, 10 H^+ must be supplied to the cathode per unit time, so an additional $2H^+$ must diffuse to the electrode, bringing along $2Cl^-$ to maintain electroneutrality. Similarly at the anode, to supply 10 Cl^- per unit time, $8Cl^-$ must arrive by diffusion, along with $8H^+$. Thus, the different currents (in arbitrary e -units per unit time) are: for H^+, $i_d = 2$, $i_m = 8$; for Cl^-, $i_d = 8$, $i_m = 2$. The total current, i, is 10. Equation 4.3.1 holds, with migration in this case being in the same direction as diffusion.

For mixtures of charged species, the fraction of current carried by the jth species is t_j; and the amount of the total current, i, carried by the jth species is $t_j i$. The number of moles of the jth species migrating per second is $t_j i / z_j F$. If this species is undergoing electrolysis, the number of moles electrolyzed per second is $|t_j i| / nF$, while the number of moles arriving at the electrode per second by migration is $\pm i_m / nF$, where the positive sign applies to reduction of j, and the negative sign pertains to oxidation. Thus,

$$\pm \frac{i_m}{nF} = \frac{t_j i}{z_j F} \tag{4.3.2}$$

or

$$i_m = \pm \frac{n}{z_j} t_j i \tag{4.3.3}$$

From equation 4.3.1,

$$i_d = i - i_m \tag{4.3.4}$$

$$i_d = i\left(1 \mp \frac{nt_j}{z_j}\right) \tag{4.3.5}$$

where the minus sign is used for cathodic currents and the positive sign for anodic currents. Note that both i and z_j are signed.

In this simplified treatment, we assume that the transference numbers are essentially the same in the bulk solution and in the diffusion layer near an electrode. This will be true when the concentrations of ions in the solution are high, so that only small fractional changes in local concentration are caused by the electrolytic generation or removal of ions. This condition is met in most experiments. If the electrolysis significantly perturbs the ionic concentrations in the diffusion layer compared to those in the bulk solution, the t_j values clearly will differ, as shown by equation 4.2.10 (12).

Example 4.2
Consider the electrolysis of a solution of 10^{-3} M $Cu(NH_3)_4^{2+}$, 10^{-3} M $Cu(NH_3)_2^+$, and 3×10^{-3} M Cl^- in 0.1 M NH_3 at two Hg electrodes (Figure 4.3.3a). Assuming the limiting equivalent conductances of all ions are equal, that is,

$$\lambda_{Cu(II)} = \lambda_{Cu(I)} = \lambda_{Cl^-} = \lambda \tag{4.3.6}$$

we obtain the following transference numbers from (4.2.10): $t_{Cu(II)} = 1/3$, $t_{Cu(I)} = 1/6$ and $t_{Cl^-} = 1/2$. With an arbitrary current of $6e$ per unit time being passed, the migration current in bulk solution is carried by movement of one Cu(II) and one Cu(I) toward the cathode, and three Cl^- toward the anode. The total balance sheet for this system is shown in Figure 4.3.3b. At the cathode, one-sixth of the current for the electrolysis of Cu(II) is provided by migration and five-sixths by diffusion. The NH_3, being uncharged, does not con-
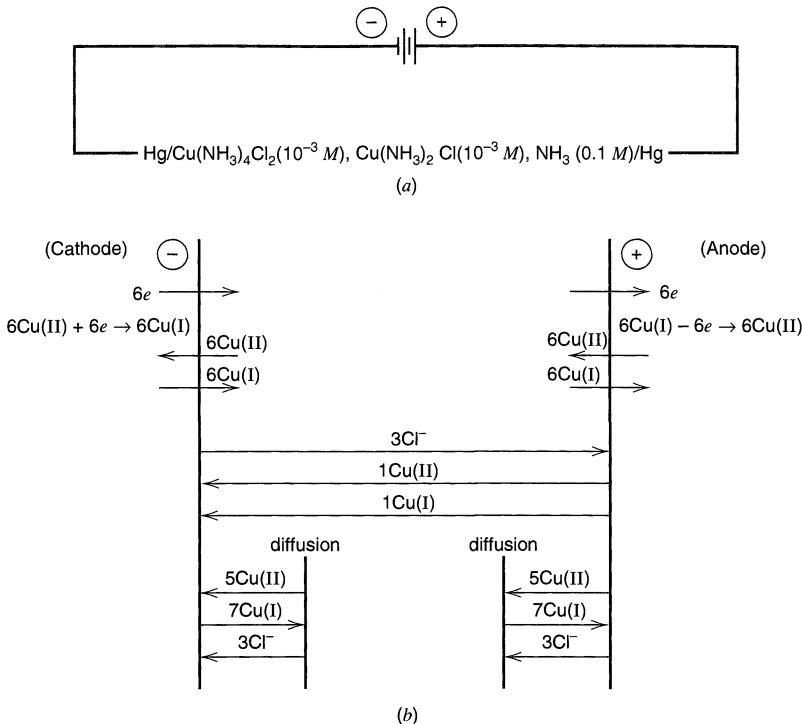
Figure 4.3.3 Balance sheet for electrolysis of the Cu(II), Cu(I), NH₃ system. (*a*) Cell schematic. (*b*) Various contributions to the current when 6*e* are passed in the external circuit per unit time; $i = 6$, $n = 1$. For Cu(II) at the cathode, $|i_m| = (1/2)(1/3)(6) = 1$ (equation 4.3.3), $i_d = 6 - 1 = 5$ (equation 4.3.4). For Cu(I) at the anode, $|i_m| = (1/1)(1/6)(6) = 1$, $i_d = 6 + 1 = 7$.

tribute to the carrying of the current, but serves only to stabilize the copper species in the +1 and +2 states. The resistance of this cell would be relatively large, since the total concentration of ions in the solution is small.

4.3.2 Effect of Adding Excess Electrolyte

Example 4.3

Let us consider the same cell as in Example 4.2, except with the solution containing 0.10 M $NaClO_4$ as an excess electrolyte (Figure 4.3.4*a*). Assuming that $\lambda_{Na^+} = \lambda_{ClO_4^-} = \lambda$, we obtain the following transference numbers: $t_{Na^+} = t_{ClO_4^-}, = 0.485$, $t_{Cu(II)} = 0.0097$, $t_{Cu(I)} = 0.00485$, $t_{Cl^-} = 0.0146$. The Na^+ and ClO_4^- do not participate in the electron-transfer reactions; but because their concentrations are high, they carry 97% of the current in the bulk solution. The balance sheet for this cell (Figure 4.3.4*b*) shows that most of the Cu(II) now reaches the cathode by diffusion, and only 0.5% of the total flux is by migration.

Thus, the addition of an excess of nonelectroactive ions (a *supporting electrolyte*) nearly eliminates the contribution of migration to the mass transfer of the electroactive species. In general, it simplifies the mathematical treatment of electrochemical systems by elimination of the $\nabla \phi$ or $\partial \phi / \partial x$ term in the mass transport equations (e.g., equations 4.1.10 and 4.1.11).

In addition to minimizing the contribution of migration, the supporting electrolyte serves other important functions. The presence of a high concentration of ions decreases
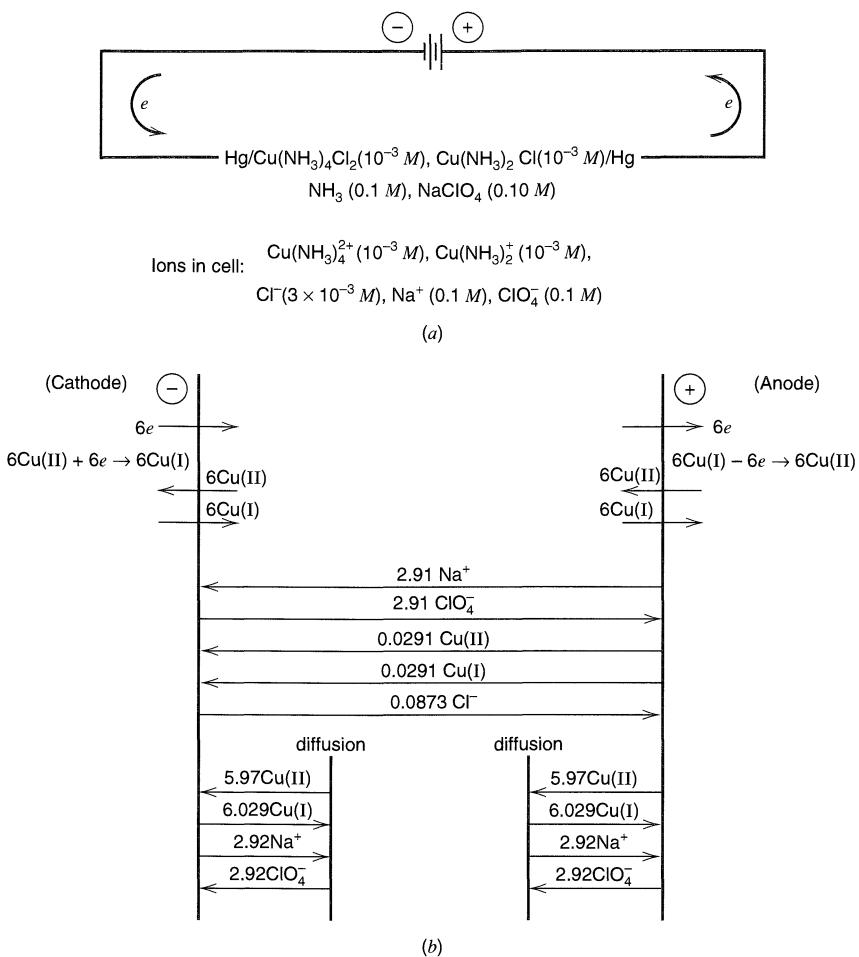
Figure 4.3.4 Balance sheet for the system in Figure 4.3.3, but with excess $NaClO_4$ as a supporting electrolyte. (*a*) Cell schematic. (*b*) Various contributions to the current when $6e$ are passed in the external circuit per unit time ($i = 6$, $n = 1$). $t_{Cu(II)} = [(2 \times 10^{-3})\lambda/(2 \times 10^{-3} + 10^{-3} + 3 \times 10^{-3} + 0.2)\lambda] = 0.0097$. For $Cu(II)$ at the cathode, $|i_m| = (1/2)(0.0097)(6) = 0.03$, $i_d = 6 - 0.03 = 5.97$.

the solution resistance, and hence the uncompensated resistance drop, between the working and reference electrodes (Section 1.3.4). Consequently, the supporting electrolyte allows an improvement in the accuracy with which the working electrode's potential is controlled or measured (Chapter 15). Improved conductivity in the bulk of the solution also reduces the electrical power dissipated in the cell and can lead to important simplifications in apparatus (Chapters 11 and 15). Beyond these physical benefits are chemical contributions by the supporting electrolyte, for it frequently establishes the solution composition (pH, ionic strength, ligand concentration) that controls the reaction conditions (Chapters 5, 7, 11, and 12). In analytical applications, the presence of a high concentration of electrolyte, which is often also a buffer, serves to decrease or eliminate sample matrix effects. Finally, the supporting electrolyte ensures that the double layer remains thin with respect to the diffusion layer (Chapter 13), and it establishes a uniform ionic strength throughout the solution, even when ions are produced or consumed at the electrodes.

Supporting electrolytes also bring some disadvantages. Because they are used in such large concentrations, their impurities can present serious interferences, for example,
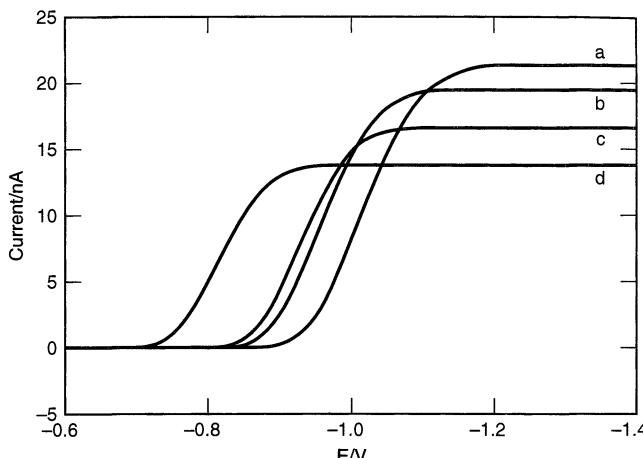
Figure 4.3.5 Voltammograms for reduction of 0.65 mM Tl$_2$SO$_4$ at a mercury film on a silver ultramicroelectrode (radius, 15 μm) in the presence of (a) 0, (b) 0.1, (c) 1, and (d) 100 mM LiClO$_4$. The potential was controlled vs. a Pt wire QRE whose potential was a function of solution composition. This variability is the basis for the shifts in wave position along the potential axis. [Reprinted with permission from M. Ciszkowska and J. G. Osteryoung, *Anal. Chem.*, **67**, 1125 (1995). Copyright 1995, American Chemical Society.]

by giving rise to faradaic responses of their own, by reacting with the intended product of an electrode process, or by adsorbing on the electrode surface and altering kinetics. Also, a supporting electrolyte significantly alters the medium in the cell, so that its properties differ from those of the pure solvent. The difference can complicate the comparison of results obtained in electrochemical experiments (e.g., thermodynamic data) with data from other kinds of experiments where pure solvents are typically employed.

Most electrochemical studies are carried out in the presence of a supporting electrolyte selected for the solvent and electrode process of interest. Many acids, bases, and salts are available for aqueous solutions. For organic solvents with high dielectric constants, like acetonitrile and N,N-dimethylformamide, normal practice is to employ tetra-*n*-alkylammonium salts, such as, Bu$_4$NBF$_4$ and Et$_4$NClO$_4$ (Bu = *n*-butyl, Et = ethyl). Studies in low-dielectric solvents like benzene inevitably involve solutions of high resistance, because most ionic salts do not dissolve in them to an appreciable extent. In solutions of salts that do dissolve in apolar media, such as Hx$_4$NClO$_4$ (where Hx = *n*-hexyl), ion pairing is extensive.

Studies in very resistive solutions require the use of UMEs, which usually pass low currents that do not give rise to appreciable resistive drops (see Section 5.9.2). The effect of supporting electrolyte concentration on the limiting steady-state current at UMEs has been treated (12–14). Typical results, shown in Figure 4.3.5, illustrate how the limiting current for reduction of Tl$^+$ to the amalgam at a mercury film decreases with an increase in LiClO$_4$ concentration (15). The current in the absence of LiClO$_4$, or at very low concentrations, is appreciably larger than at high concentrations, because migration of the positively charged Tl(I) species to the cathode enhances the current. At high LiClO$_4$ concentrations, Li$^+$ migration replaces that of Tl$^+$, and the observed current is essentially a pure diffusion current. A similar example involving the polarography of Pb(II) with KNO$_3$ supporting electrolyte was given in the first edition.[1]

---

[1] First edition, p. 127.

▶ 4.4 DIFFUSION

As we have just seen, it is possible to restrict mass transfer of an electroactive species near the electrode to the diffusive mode by using a supporting electrolyte and operating in a quiescent solution. Most electrochemical methods are built on the assumption that such conditions prevail; thus diffusion is a process of central importance. It is appropriate that we now take a closer look at the phenomenon of diffusion and the mathematical models describing it (16–19).

4.4.1 A Microscopic View—Discontinuous Source Model

Diffusion, which normally leads to the homogenization of a mixture, occurs by a "random walk" process. A simple picture can be obtained by considering a one-dimensional random walk. Consider a molecule constrained to a linear path and, buffeted by solvent molecules undergoing Brownian motion, moving in steps of length, l, with one step being made per unit time, τ. We can ask, "Where will the molecule be after a time, t?" We can answer only by giving the probability that the molecule will be found at different locations. Equivalently, we can envision a large number of molecules concentrated in a line at $t = 0$ and ask what the distribution of molecules will be at time t. This is sometimes called the "drunken sailor problem," where we envision a very drunk sailor emerging from a bar (Figure 4.4.1) and staggering randomly left and right (with a stagger-step size, l, one step every τ seconds). What is the probability that the sailor will get down the street a certain distance after a certain time t?

In a random walk, all paths that can be traversed in any elapsed period are equally likely; hence the probability that the molecule has arrived at any particular point is simply the number of paths leading to that point divided by the total of possible paths to all accessible points. This idea is developed in Figure 4.4.2. At time τ, it is equally likely that the molecule is at $+l$ and $-l$; and at time 2τ, the relative probabilities of being at $+2l$, 0, and $-2l$, are 1, 2, and 1, respectively.

The probability, $P(m, r)$, that the molecule is at a given location after m time units ($m = t/\tau$) is given by the binomial coefficient

$$P(m,r) = \frac{m!}{r!(m-r)!} \left(\frac{1}{2}\right)^m \qquad (4.4.1)$$

where the set of locations is defined by $x = (-m + 2r)l$, with $r = 0, 1, \ldots m$. The mean square displacement of the molecule, $\overline{\Delta^2}$, can be calculated by summing the squares of the displacements and dividing by the total number of possibilities (2^m). The squares of the displacements are used, just as when one obtains the standard deviation in statistics, because movement is possible in both the positive and negative directions, and the sum of the displacements is always zero. This procedure is shown in Table 4.4.1. In general, $\overline{\Delta^2}$ is given by

$$\overline{\Delta^2} = ml^2 = \frac{t}{\tau}l^2 = 2Dt \qquad (4.4.2)$$
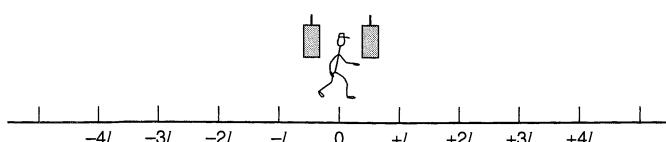
Figure 4.4.1 The one-dimensional random-walk or "drunken sailor problem."

-4l   -3l   -2l   -l   0   +l   +2l   +3l   +4l
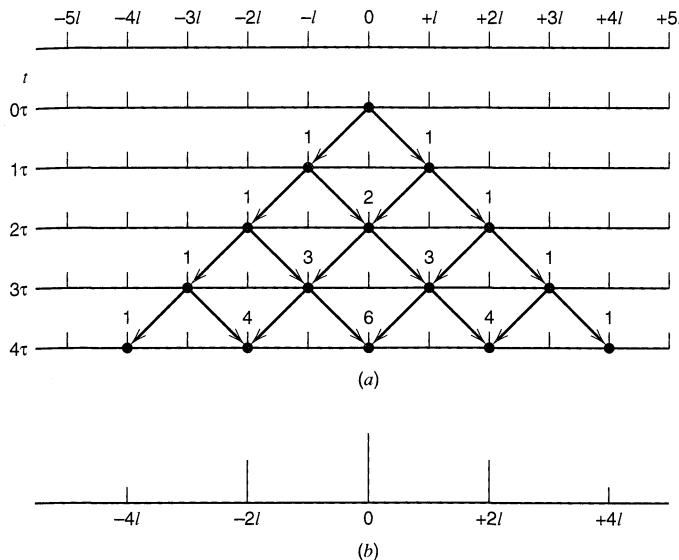
Figure 4.4.2 (*a*) Probability distribution for a one-dimensional random walk over zero to four time units. The number printed over each allowed arrival point is the number of paths to that point. (*b*) Bar graph showing distribution at $t = 4\tau$. At this time, probability of being at $x = 0$ is 6/16, at $x = \pm 2l$ is 4/16, and at $x = \pm 4l$ is 1/16.

where the diffusion coefficient, D, identified as $l^2/2\tau$, is a constant related to the step size and step frequency.[2] It has units of length^2/time, usually cm^2/s. The root-mean-square displacement at time t is thus

$$\overline{\Delta} = \sqrt{2Dt} \tag{4.4.3}$$

This equation provides a handy rule of thumb for estimating the thickness of a diffusion layer (e.g., how far product molecules have moved, on the average, from an electrode in a certain time). A typical value of D for aqueous solutions is 5×10^{-6} cm^2/s, so that a diffusion layer thickness of 10^{-4} cm is built up in 1 ms, 10^{-3} cm in 0.1 s, and 10^{-2} cm in 10 s. (See also Section 5.2.1.)

As m becomes large, a continuous form of equation 4.4.1 arises. For N_0 molecules located at the origin at $t = 0$, a Gaussian curve will describe the distribution at some later

TABLE 4.4.1 Distributions for a Random Walk Process[a]

t	n[b]	Δ[c]	$\Sigma \Delta^2$	$\overline{\Delta^2} = \frac{1}{n} \Sigma \Delta^2$
0τ	$1(= 2^0)$	0	0	0
1τ	$2(= 2^1)$	$\pm l(1)$	$2l^2$	l^2
2τ	$4(= 2^2)$	$0(2), \pm 2l(1)$	$8l^2$	$2l^2$
3τ	$8(= 2^3)$	$\pm l(3), \pm 3l(1)$	$24l^2$	$3l^2$
4τ	$16(= 2^4)$	$0(6), \pm 2l(4),$	$64l^2$	$4l^2$
		$\pm 4l(1)$		
$m\tau$	2^m		$mnl^2(= m2^m l^2)$	$m l^2$

[a]l = step size, $1/\tau$ = step frequency, $t = m\tau$ = time interval.

[b]n = total number of possibilities.

[c]Δ = possible positions; relative probabilities are parenthesized.

[2]This concept of D was derived by Einstein in another way in 1905. Sometimes D is given as $f l^2/2$, where f is the number of displacements per unit time ($= 1/\tau$).

time, t. The number of molecules, $N(x, t)$, in a segment Δx wide centered on position x is (20)

$$\frac{N(x, t)}{N_0} = \frac{\Delta x}{2\sqrt{\pi D t}} \exp\left(\frac{-x^2}{4Dt}\right) \tag{4.4.4}$$

A similar treatment can be applied to two- and three-dimensional random walks, where the root-mean-square displacements are $(4Dt)^{1/2}$ and $(6Dt)^{1/2}$, respectively (19, 21).

It may be instructive to develop a more molecular picture of diffusion in a liquid by considering the concepts of molecular and diffusional velocity (21). In a Maxwellian gas, a particle of mass m and average one-dimensional velocity, v_x, has an average kinetic energy of $\frac{1}{2}mv_x^2$. This energy can also be shown to be $\pounds T/2$, (22, 23); thus the average molecular velocity is $v_x = (\pounds T/m)^{1/2}$. For an O_2 molecule ($m = 5 \times 10^{-23}$ g) at 300 K, one finds that $v_x = 3 \times 10^4$ cm/s. In a liquid solution, a velocity distribution similar to that of a Maxwellian gas may apply; however, a dissolved O_2 molecule can make progress in a given direction at this high velocity only over a short distance before it collides with a molecule of solvent and changes direction. The net movement through the solution by the random walk produced by repeated collisions is much slower than v_x and is governed by the process described above. A "diffusional velocity," v_d, can be extracted from equation 4.4.3 as

$$v_d = \overline{\Delta}/t = (2D/t)^{1/2} \tag{4.4.5}$$

There is a time dependence in this velocity because a random walk greatly favors small displacements from a starting point *vs.* large ones.

The relative importance of migration and diffusion can be gauged by comparing v_d with the steady-state migrational velocity, v, for an ion of mobility u_i in an electric field (Section 2.3.3). By definition, $v = u_i \mathscr{E}$, where $\mathscr{E}$ is the electric field strength felt by the ion. From the Einstein-Smoluchowski equation, (4.2.2),

$$v = |z_i| FD_i\mathscr{E}/RT \tag{4.4.6}$$

When $v \ll v_d$, diffusion of a species dominates over migration at a given position and time. From (4.4.5) and (4.4.6), we find that this condition holds when

$$\frac{D_i\mathscr{E}}{RT/|z_i|F} \ll \left(\frac{2D_i}{t}\right)^{1/2}, \tag{4.4.7}$$

which can be rearranged to

$$(2D_i t)^{1/2}\mathscr{E} \ll 2\frac{RT}{|z_i|F} \tag{4.4.8}$$

where the left side is the diffusion length times the field strength, which is also the voltage drop in the solution over the length scale of diffusion. To ensure that migration is negligible compared to diffusion, this voltage drop must be smaller than about $2RT/|z_i|F$, which is $51.4/|z_i|$ mV at 25°C. This is the same as saying that the difference in electrical potential energy for the diffusing ion must be smaller than a few $\pounds T$ over the length scale of diffusion.

4.4.2 Fick's Laws of Diffusion

Fick's laws are differential equations describing the flux of a substance and its concentration as functions of time and position. Consider the case of linear (one-dimensional) diffusion. The flux of a substance O at a given location x at a time t, written as $J_O(x, t)$, is the

net mass-transfer rate of O, expressed as amount per unit time per unit area (e.g., mol s^{-1} cm^{-2}). Thus $J_O(x, t)$ represents the number of moles of O that pass a given location per second per cm^2 of area normal to the axis of diffusion.

Fick's first law states that the flux is proportional to the concentration gradient, $\partial C_O / \partial x$:

$$-J_O(x, t) = D_O \frac{\partial C_O(x, t)}{\partial x} \tag{4.4.9}$$

This equation can be derived from the microscopic model as follows. Consider location x, and assume $N_O(x)$ molecules are immediately to left of x, and $N_O(x + \Delta x)$ molecules are immediately to the right, at time t (Figure 4.4.3). All of the molecules are understood to be within one step-length, Δx, of location x. During the time increment, Δt, half of them move Δx in either direction by the random walk process, so that the net flux through an area A at x is given by the difference between the number of molecules moving from left to right and the number moving from right to left:

$$J_O(x, t) = \frac{1}{A} \frac{\frac{N_O(x)}{2} - \frac{N_O(x + \Delta x)}{2}}{\Delta t} \tag{4.4.10}$$

Multiplying by $\Delta x^2 / \Delta x^2$ and noting that the concentration of O is $C_O = N_O / A \Delta x$, we derive

$$-J_O(x, t) = \frac{\Delta x^2}{2 \Delta t} \frac{C_O(x + \Delta x) - C_O(x)}{\Delta x} \tag{4.4.11}$$

From the definition of the diffusion coefficient, (4.4.2), $D_O = \Delta x^2 / 2 \Delta t$, and allowing Δx and Δt to approach zero, we obtain (4.4.9).

Fick's second law pertains to the change in concentration of O with time:

$$\frac{\partial C_O(x, t)}{\partial t} = D_O \left(\frac{\partial^2 C_O(x, t)}{\partial x^2} \right) \tag{4.4.12}$$

This equation is derived from the first law as follows. The change in concentration at a location x is given by the difference in flux into and flux out of an element of width dx (Figure 4.4.4).

$$\frac{\partial C_O(x, t)}{\partial t} = \frac{J(x, t) - J(x + dx, t)}{dx} \tag{4.4.13}$$

Note that J/dx has units of (mol s^{-1} cm^{-2})/cm or change in concentration per unit time, as required. The flux at $x + dx$ can be given in terms of that at x by the general equation

$$J(x + dx, t) = J(x, t) + \frac{\partial J(x, t)}{\partial x} dx \tag{4.4.14}$$
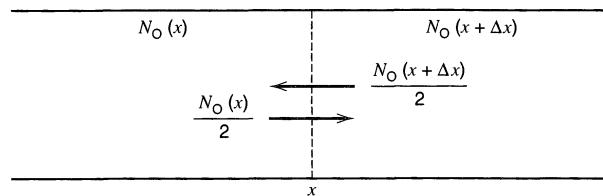
Figure 4.4.3 Fluxes at plane x in solution.
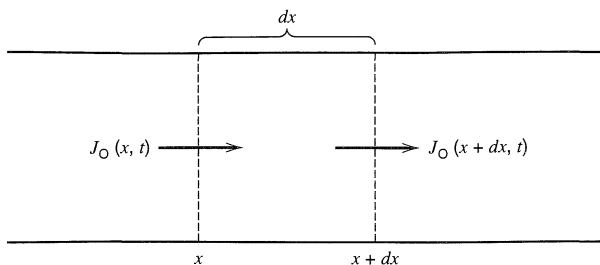
Figure 4.4.4 Fluxes into and out of an element at x.

and from equation 4.4.9 we obtain

$$-\frac{\partial J(x, t)}{\partial x} = \frac{\partial}{\partial x} D_O \frac{\partial C_O(x, t)}{\partial x} \tag{4.4.15}$$

Combination of equations 4.4.13 to 4.4.15 yields

$$\frac{\partial C_O(x, t)}{\partial t} = \left(\frac{\partial}{\partial x}\right)\left[D_O\left(\frac{\partial C_O(x, t)}{\partial x}\right)\right] \tag{4.4.16}$$

When D_O is not a function of x, (4.4.12) results.

In most electrochemical systems, the changes in solution composition caused by electrolysis are sufficiently small that variations in the diffusion coefficient with x can be neglected. However when the electroactive component is present at a high concentration, large changes in solution properties, such as the local viscosity, can occur during electrolysis. For such systems, (4.4.12) is no longer appropriate, and more complicated treatments are necessary (24, 25). Under these conditions, migrational effects can also become important.

We will have many occasions in future chapters to solve (4.4.12) under a variety of boundary conditions. Solutions of this equation yield *concentration profiles*, $C_O(x, t)$.

The general formulation of Fick's second law for any geometry is

$$\boxed{\frac{\partial C_O}{\partial t} = D_O \nabla^2 C_O} \tag{4.4.17}$$

where ∇^2 is the Laplacian operator. Forms of ∇^2 for different geometries are given in Table 4.4.2. Thus, for problems involving a planar electrode (Figure 4.4.5a), the linear diffusion equation, (4.4.12), is appropriate. For problems involving a spherical electrode

TABLE 4.4.2   Forms of the Laplacian Operator for Different Geometries[a]

Type	Variables	∇^2	Example
Linear	x	$\partial^2/\partial x^2$	Shielded disk electrode
Spherical	r	$\partial^2/\partial r^2 + (2/r)(\partial/\partial r)$	Hanging drop electrode
Cylindrical (axial)	r	$\partial^2/\partial r^2 + (1/r)(\partial/\partial r)$	Wire electrode
Disk	r, z	$\partial^2/\partial r^2 + (1/r)(\partial/\partial r) + \partial^2/\partial z^2$	Inlaid disk ultramicroelectrode[b]
Band	x, z	$\partial^2/\partial x^2 + \partial^2/\partial z^2$	Inlaid band electrode[c]

[a]See also J. Crank, "The Mathematics of Diffusion," Clarendon, Oxford, 1976.

[b]r = radial distance measured from the center of the disk; z = distance normal to the disk surface.

[c]x = distance in the plane of the band; z = distance normal to the band surface.
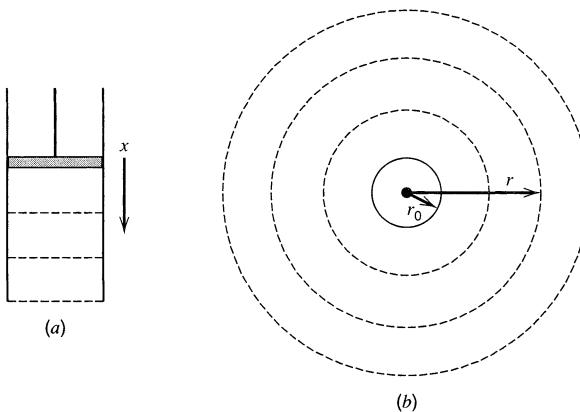
Figure 4.4.5 Types of diffusion occurring at different electrodes. (*a*) Linear diffusion to a planar electrode. (*b*) Spherical diffusion to a hanging drop electrode.

(Figure 4.4.5*b*), such as the hanging mercury drop electrode (HMDE), the spherical form of the diffusion equation must be employed:

$$\frac{\partial C_O(r, t)}{\partial t} = D_O \left(\frac{\partial^2 C_O(r, t)}{\partial r^2} + \frac{2}{r} \frac{\partial C_O(r, t)}{\partial r} \right)$$

(4.4.18)

The difference between the linear and spherical equations arises because spherical diffusion takes place through an increasing area as r increases.

Consider the situation where O is an electroactive species transported purely by diffusion to an electrode, where it undergoes the electrode reaction

$$O + ne \rightleftarrows R$$

(4.4.19)

If no other electrode reactions occur, then the current is related to the flux of O at the electrode surface ($x = 0$), $J_O(0, t)$, by the equation

$$-J_O(0, t) = \frac{i}{nFA} = D_O \left[\frac{\partial C_O(x, t)}{\partial x} \right]_{x=0}$$

(4.4.20)

because the total number of electrons transferred at the electrode in a unit time must be proportional to the quantity of O reaching the electrode in that time period. This is an extremely important relationship in electrochemistry, because it is the link between the evolving concentration profile near the electrode and the current flowing in an electrochemical experiment. We will draw upon it many times in subsequent chapters.

If several electroactive species exist in the solution, the current is related to the sum of their fluxes at the electrode surface. Thus, for q reducible species,

$$\frac{i}{FA} = - \sum_{k=1}^{q} n_k J_k(0, t) = \sum_{k=1}^{q} n_k D_k \left[\frac{\partial C_k(x, t)}{\partial x} \right]_{x=0}$$

(4.4.21)

4.4.3 Boundary Conditions in Electrochemical Problems

In solving the mass-transfer part of an electrochemical problem, a diffusion equation (or, in general, a mass-transfer equation) is written for each dissolved species (O, R, . . .). The solution of these equations, that is, the discovery of an equation expressing C_O, C_R, . . . as functions of x and t, requires that an initial condition (the concentration profile at

$t = 0$) and two boundary conditions (functions applicable at certain values of x) be given for each diffusing species. Typical initial and boundary conditions include the following.

(a) Initial Conditions
These are usually of the form

$$C_O(x, 0) = f(x) \tag{4.4.22}$$

For example, if O is uniformly distributed throughout the solution at a bulk concentration C_O^* at the start of the experiment, the initial condition is

$$C_O(x, 0) = C_O^* \qquad \text{(for all } x\text{)} \tag{4.4.23}$$

If R is initially absent from the solution, then

$$C_R(x, 0) = 0 \qquad \text{(for all } x\text{)} \tag{4.4.24}$$

(b) Semi-infinite Boundary Conditions
The electrolysis cell is usually large compared to the length of diffusion; hence the solution at the walls of the cell is not altered by the process at the electrode (see Section 5.2.1). One can normally assume that at large distances from the electrode ($x \to \infty$) the concentration reaches a constant value, typically the initial concentration, so that, for example,

$$\lim_{x \to \infty} C_O(x, t) = C_O^* \qquad \text{(at all } t\text{)} \tag{4.4.25}$$

$$\lim_{x \to \infty} C_R(x, t) = 0 \qquad \text{(at all } t\text{)} \tag{4.4.26}$$

For thin-layer electrochemical cells (Section 11.7), where the cell wall is at a distance, l, of the order of the diffusion length, one must use boundary conditions at $x = l$ instead of those for $x \to \infty$.

(c) Electrode Surface Boundary Conditions
Additional boundary conditions usually relate to concentrations or concentration gradients at the electrode surface. For example, if the potential is controlled in an experiment, one might have

$$C_O(0, t) = f(E) \tag{4.4.27}$$

$$\frac{C_O(0, t)}{C_R(0, t)} = f(E) \tag{4.4.28}$$

where $f(E)$ is some function of the electrode potential derived from the general current-potential characteristic or one of its special cases (e.g., the Nernst equation).

If the current is the controlled quantity, the boundary condition is expressed in terms of the flux at $x = 0$; for example,

$$-J_O(0, t) = \frac{i}{nFA} = D_O \left[\frac{\partial C_O(x, t)}{\partial x} \right]_{x=0} = f(t) \tag{4.4.29}$$

The conservation of matter in an electrode reaction is also important. For example, when O is converted to R at the electrode and both O and R are soluble in the solution phase, then for each O that undergoes electron transfer at the electrode, an R must be produced. Consequently, $J_O(0, t) = -J_R(0, t)$, and

$$D_O \left[\frac{\partial C_O(x, t)}{\partial x} \right]_{x=0} + D_R \left[\frac{\partial C_R(x, t)}{\partial x} \right]_{x=0} = 0 \tag{4.4.30}$$

4.4.4 Solution of Diffusion Equations

In the chapters that follow, we will examine the solution of the diffusion equations under a variety of conditions. The analytical mathematical methods for attacking these problems are discussed briefly in Appendix A. Numerical methods, including digital simulations (Appendix B), are also frequently employed.

Sometimes one is interested only in the steady-state solution (e.g., with rotating disk electrodes or ultramicroelectrodes). Since $\partial C_O/\partial t = 0$ in such a situation, the diffusion equation simply becomes

$$\nabla^2 C_O = 0 \tag{4.4.31}$$

Occasionally, solutions can be found by searching the literature concerning analogous problems. For example, the conduction of heat involves equations of the same form as the diffusion equation (26, 27);

$$\partial T/\partial t = \alpha_i \nabla^2 T \tag{4.4.32}$$

where T is the temperature, and $\alpha_i = \kappa/\rho s$ (κ = thermal conductivity, ρ = density, and s = specific heat). If one can find the solution of a problem of interest in terms of the temperature distribution, such as, $T(x, t)$, or heat flux, one can easily transpose the results to give concentration profiles and currents.

Electrical analogies also exist. For example, the steady-state diffusion equation, (4.4.31), is of the same form as that for the potential distribution in a region of space not occupied by electrically charged bodies (Laplace's equation),

$$\nabla^2 \phi = 0 \tag{4.4.33}$$

If one can solve an electrical problem in terms of the current density, j, where

$$-j = \kappa \nabla \phi \tag{4.4.34}$$

(where κ is the conductivity), one can write the solution to an analogous diffusion problem (as the function C_O) and find the flux from equation 4.4.20 or from the more general form,

$$-J = D_O \nabla C_O \tag{4.4.35}$$

This approach has been employed, for example, in determining the steady-state uncompensated resistance at an ultramicroelectrode (28) and the solution resistance between an ion-selective electrode tip and a surface in a scanning electrochemical microscope (29, 30). It also is sometimes possible to model the mass transport and kinetics in an electrochemical system by a network of electrical components (31, 32). Since there are a number of computer programs (e.g., SPICE) for the analysis of electric circuits, this approach can be convenient for certain electrochemical problems.
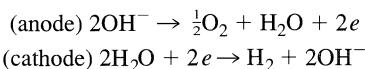
▶ 4.5 REFERENCES

1. M. Planck, *Ann. Physik*, **39**, 161; **40**, 561 (1890).

2. J. Newman, *Electroanal. Chem.*, **6**, 187 (1973).

3. J. Newman, *Adv. Electrochem. Electrochem. Engr.*, **5**, 87 (1967).

4. C. W. Tobias, M. Eisenberg, and C. R. Wilke, *J. Electrochem. Soc.*, **99**, 359C (1952).

5. W. Vielstich, *Z. Elektrochem.*, **57**, 646 (1953).

6. N. Ibl, *Chem. Ing. Tech.*, **35**, 353 (1963).

7. G. Charlot, J. Badoz-Lambling, and B. Tremillion, "Electrochemical Reactions," Elsevier, Amsterdam, 1962, pp. 18–21, 27–28.

8. I. M. Kolthoff and J. J. Lingane, "Polarography," 2nd ed., Interscience, New York, 1952, Vol. 1, Chap. 7.

9. K. Vetter, "Electrochemical Kinetics," Academic, New York, 1967.

10. J. Koryta, J. Dvořák, and V. Boháčková, "Electrochemistry," Methuen, London, 1970, pp. 88–112.

11. J. Coursier, as quoted in reference 7.

12. C. Amatore, B. Fosset, J. Bartelt, M. R. Deakin, and R. M. Wightman, *J. Electroanal. Chem.*, **256**, 255 (1988).

13. J. C. Myland and K. B. Oldham, *J. Electroanal. Chem.*, **347**, 49 (1993).

14. C. P. Smith and H. S. White, *Anal. Chem.*, **65**, 3343 (1993).

15. M. Ciszkowska and J. G. Osteryoung, *Anal. Chem.*, **67**, 1125 (1995).

16. W. Jost, *Angew. Chem., Intl. Ed. Engl.*, **3**, 713 (1964).

17. J. Crank, "The Mathematics of Diffusion," Clarendon, Oxford, 1979.

18. W. Jost, "Diffusion in Solids, Liquids, and Gases," Academic, New York, 1960.

19. S. Chandrasekhar, *Rev. Mod. Phys.*, **15**, 1 (1943).

20. L. B. Anderson and C. N. Reilley, *J. Chem. Educ.*, **44**, 9 (1967).

21. H. C. Berg, "Random Walks in Biology," Princeton University, Press, Princeton, NJ, 1983.

22. N. Davidson, "Statistical Mechanics," McGraw-Hill, New York, 1962, pp. 155–158.

23. R. S. Berry, S. A. Rice, and J. Ross, "Physical Chemistry," Wiley, New York, 1980, pp. 1056–1060.

24. R. B. Morris, K. F. Fischer, and H. S. White, *J. Phys. Chem.*, **92**, 5306 (1988).

25. S. C. Paulson, N. D. Okerlund, and H. S. White, *Anal. Chem.*, **68**, 581 (1996).

26. H. S. Carslaw and J. C. Jaeger, "Conduction of Heat in Solids," Clarendon, Oxford, 1959.

27. M. N. Ozisk, "Heat Conduction," Wiley, New York, 1980.

28. K. B. Oldham in "Microelectrodes, Theory and Applications," M. I. Montenegro, M. A. Queiros, and J. L. Daschbach, Eds., Kluwer, Amsterdam, 1991, p. 87.

29. B. R. Horrocks, D. Schmidtke, A. Heller, and A. J. Bard, *Anal. Chem.*, **65**, 3605 (1993).

30. C. Wei, A. J. Bard, G. Nagy, and K. Toth, *Anal. Chem.*, **67**, 1346 (1995).

31. J. Horno, M. T. García-Hernández, and C. F. González-Fernández, *J. Electroanal. Chem.*, **352**, 83 (1993).

32. A. A. Moya, J. Castilla, and J. Horno, *J. Phys. Chem.*, **99**, 1292 (1995).
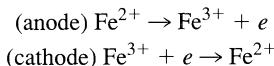
▶ 4.6 PROBLEMS

4.1 Consider the electrolysis of a 0.10 M NaOH solution at platinum electrodes, where the reactions are:

$$\text{(anode) } 2OH^- \rightarrow \tfrac{1}{2}O_2 + H_2O + 2e$$
$$\text{(cathode) } 2H_2O + 2e \rightarrow H_2 + 2OH^-$$

Show the balance sheet for the system operating at steady state. Assume $20e$ are passed in the external circuit per unit time, and use the λ_0 values in Table 2.3.2 to estimate transference numbers.

4.2 Consider the electrolysis of a solution containing 10^{-1} M Fe(ClO$_4$)$_3$ and 10^{-1} M Fe(ClO$_4$)$_2$ at platinum electrodes:

$$\text{(anode) } Fe^{2+} \rightarrow Fe^{3+} + e$$
$$\text{(cathode) } Fe^{3+} + e \rightarrow Fe^{2+}$$

Assume that both salts are completely dissociated, that the λ values for Fe^{3+}, Fe^{2+}, and ClO$_4^-$ are equal, and that $10e$ are passed in the external circuit per unit time. Show the balance sheet for the steady-state operation of this system.

4.3 For a given electrochemical system to be described by equations involving semi-infinite boundary conditions, the cell wall must be at least five "diffusion layer thicknesses" away from the electrode. For a substance with $D = 10^{-5}$ cm^2/s, what distance between the working electrode and the cell wall is required for a 100-s experiment?

4.4 The mobility, u_j, is related to the diffusion coefficient, D_j, by equation 4.2.2. (a) From the mobility data in Table 2.3.2, estimate the diffusion coefficients of H^+, I^-, and Li^+ at 25°C. (b) Write the equation for the estimation of D from the λ value.

4.5 Using the procedure of Section 4.4.2, derive Fick's second law for spherical diffusion (equation 4.4.18). [*Hint:* Because of the different areas through which diffusion occurs at r and at $r + dr$, it is more convenient to obtain the change of concentration in dr by considering the number of moles diffusing per second rather than the flux.]

5

BASIC POTENTIAL
STEP METHODS

The next three chapters are concerned with methods in which the electrode potential is forced to adhere to a known program. The potential may be held constant or may be varied with time in a predetermined manner as the current is measured as a function of time or potential. In this chapter, we will consider systems in which the mass transport of electroactive species occurs only by diffusion. Also, we will restrict our view to methods involving only step-functional changes in the working electrode potential. This family of techniques is the largest single group, and it contains some of the most powerful experimental approaches available to electrochemistry.

In the methods covered in this chapter, as well as in Chapters 6 and 7, the electrode area, A, is small enough, and the solution volume, V, is large enough, that the passage of current does not alter the bulk concentrations of electroactive species. Such circumstances are known as *small A/V conditions*. It is easy to show on the basis of results below that electrodes with dimensions of several millimeters operating in solutions of 10 mL or more do not consume a significant fraction of a dissolved electroactive species in experiments lasting a few seconds to a few minutes (Problem 5.2). Several decades ago, Laitinen and Kolthoff (1, 2) invented the term *microelectrode* to describe the electrode's role under small A/V conditions, which is to probe a system, rather than to effect compositional change.[1] In Chapter 11, we will explore *large A/V conditions*, where the electrode is intended to transform the bulk system.

▶ 5.1 OVERVIEW OF STEP EXPERIMENTS

5.1.1 Types of Techniques

Figure 5.1.1 is a picture of the basic experimental system. An instrument known as a *potentiostat* has control of the voltage across the working electrode–counter electrode pair, and it adjusts this voltage to maintain the potential difference between the working and reference electrodes (which it senses through a high-impedance feedback loop) in accord with the program defined by a function generator. One can view the potentiostat

---

[1] Recent years have seen the rapid development of extremely small working electrodes, of dimensions in the micrometer or nanometer range, which have a set of very useful properties. In much of the literature and in casual conversation, these are also called "microelectrodes," in reference to their dimensions. They always provide small A/V conditions, so they are indeed microelectrodes within the definition given above, but much larger electrodes also belong to the class. To preserve the usefulness of the earlier term, very small electrodes have been called *ultramicroelectrodes* (see Section 5.3). That distinction is respected consistently in the remainder of this book, although it now seems likely that the new usage of the term "microelectrode" will soon displace the historic one altogether.
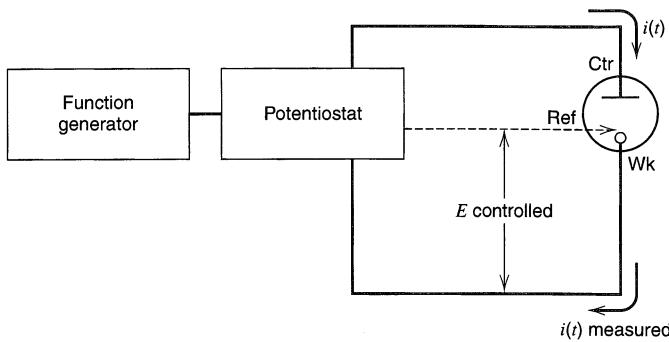
Figure 5.1.1
Experimental arrangement
for controlled-potential
experiments.

alternatively as an active element whose job is to force through the working electrode whatever current is required to achieve the desired potential at any time. Since the current and the potential are related functionally, that current is unique. Chemically, it is the flow of electrons needed to support the active electrochemical processes at rates consistent with the potential. Thus the response from the potentiostat (the current) actually is the experimental observable. For an introduction to the design of such apparatus, see Chapter 15.

Figure 5.1.2a is a diagram of the waveform applied in a basic potential step experiment. Let us consider its effect on the interface between a solid electrode and an unstirred solution containing an electroactive species. As an example, take anthracene in deoxygenated dimethylformamide (DMF). We know that there generally is a potential region where faradaic processes do not occur; let E_1 be in this region. On the other hand, we can also find a more negative potential at which the kinetics for reduction of anthracene become so rapid that no anthracene can coexist with the electrode, and its surface concentration goes nearly to zero. Consider E_2 to be in this "mass-transfer-limited" region. What is the response of the system to the step perturbation?

First, the electrode must reduce the nearby anthracene to the stable anion radical:

$$\text{An} + e \rightarrow \text{An}^{-} \qquad (5.1.1)$$

This event requires a very large current, because it occurs instantly. Current flows subsequently to maintain the fully reduced condition at the electrode surface. The initial reduction has created a concentration gradient that in turn produces a continuing flux of anthracene to the electrode surface. Since this arriving material cannot coexist with the electrode at E_2, it must be eliminated by reduction. The flux of anthracene, hence the cur-
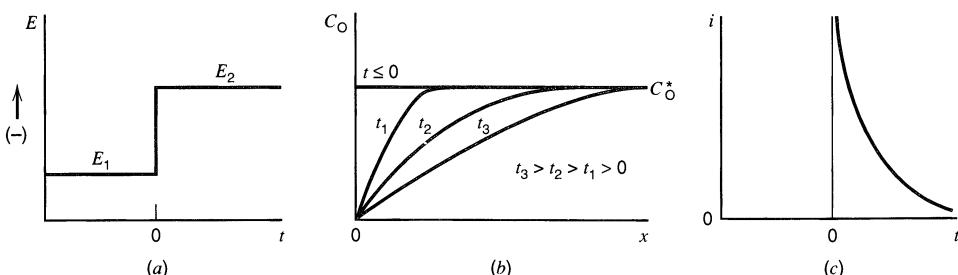
Figure 5.1.2 (a) Waveform for a step experiment in which species O is electroinactive at E_1, but is reduced at a diffusion-limited rate at E_2. (b) Concentration profiles for various times into the experiment. (c) Current flow *vs.* time.

rent as well, is proportional to the concentration gradient at the electrode surface. Note, however, that the continued anthracene flux causes the zone of anthracene depletion to thicken; thus the slope of the concentration profile at the surface declines with time, and so does the current. Both of these effects are depicted in Figures 5.1.2b and 5.1.2c. This kind of experiment is called *chronoamperometry*, because current is recorded as a function of time.

Suppose we now consider a series of step experiments in the anthracene solution discussed earlier. Between each experiment the solution is stirred, so that the initial conditions are always the same. Similarly, the initial potential (before the step) is chosen to be at a constant value where no faradaic processes occur. The change from experiment to experiment is in the step potential, as depicted in Figure 5.1.3a. Suppose, further, that experiment 1 involves a step to a potential at which anthracene is not yet electroactive; that experiments 2 and 3 involve potentials where anthracene is reduced, but not so effectively that its surface concentration is zero; and that experiments 4 and 5 have step potentials in the mass-transfer-limited region. Obviously experiment 1 yields no faradaic current, and experiments 4 and 5 yield the same current obtained in the chronoamperometric case above. In both 4 and 5, the surface concentration is zero; hence anthracene arrives as fast as diffusion can bring it, and the current is limited by this factor. Once the electrode potential becomes so extreme that this condition applies, the potential no longer influences the electrolytic current. In experiments 2 and 3 the story is different because the reduction process is not so dominant that some anthracene cannot coexist with the electrode. Still, its concentration is less than the bulk value, so anthracene does diffuse to the surface where it must be eliminated by reduction. Since the difference between the bulk and surface concentrations is smaller than in the mass-transfer-limited case, less material arrives at the surface per unit time, and the currents for corresponding times are smaller than in experiments 4 and 5. Nonetheless, the depletion effect still applies, which means that the current still decays with time.

Now suppose we sample the current at some fixed time τ into each of these step experiments; then we can plot the sampled current, $i(\tau)$, vs. the potential to which the step takes place. As shown in Figures 5.1.3b and 5.1.3c, the current-potential curve has a wave shape much like that encountered in earlier considerations of steady-state voltammetry under convective conditions (Section 1.4.2). This kind of experiment is called *sampled-current voltammetry*, several forms of which are in common practice. The simplest, usually operating exactly as described above, is called *normal pulse voltammetry*. In this chapter, we will consider sampled-current voltammetry in a general way, with the aim of establishing concepts that apply across a broad range of par-
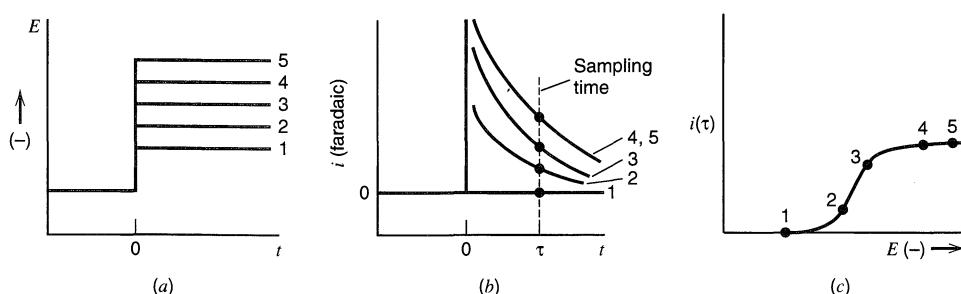
Figure 5.1.3 Sampled-current voltammetry. (a) Step waveforms applied in a series of experiments. (b) Current-time curves observed in response to the steps. (c) Sampled-current voltammogram.
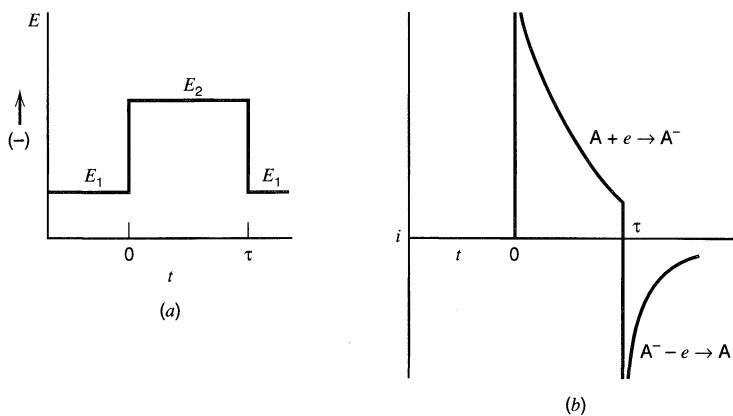
Figure 5.1.4
Double potential step
chronoamperometry.
(*a*) Typical waveform.
(*b*) Current response.

ticular methods. Chapter 7 covers the details of many forms of voltammetry based on step waveforms, including normal pulse voltammetry and its historical predecessors and successors.

Now consider the effect of the potential program displayed in Figure 5.1.4 *a*. The forward step, that is, the transition from E_1 to E_2 at $t = 0$, is exactly the chronoamperometric experiment that we discussed above. For a period τ, it causes a buildup of the reduction product (e.g., anthracene anion radical) in the region near the electrode. However, in the second phase of the experiment, after $t = \tau$, the potential returns to E_1, where only the oxidized form (e.g., anthracene) is stable at the electrode. The anion radical cannot coexist there; hence a large anodic current flows as it begins to reoxidize, then the current declines in magnitude (Figure 5.1.4*b*) as the depletion effect sets in.

This experiment, called *double potential step chronoamperometry*, is our first example of a *reversal technique*. Such methods comprise a large class of approaches, all featuring an initial generation of an electrolytic product, then a reversal of electrolysis so that the first product is examined electrolytically in a direct fashion. Reversal methods make up a powerful arsenal for studies of complex electrode reactions, and we will have much to say about them.

5.1.2 Detection

The usual observables in controlled-potential experiments are currents as functions of time or potential. In some experiments, it is useful to record the integral of the current versus time. Since the integral is the amount of charge passed, these methods are *coulometric* approaches. The most prominent examples are *chronocoulometry* and *double potential step chronocoulometry*, which are the integral analogs of the corresponding chronoamperometric approaches. Figure 5.1.5 is a display of the coulometric response to the double-step program of Figure 5.1.4*a*. One can easily see the linkage, through the integral, between Figures 5.1.4*b* and 5.1.5. Charge that is injected by reduction in the forward step is withdrawn by oxidation in the reversal.

Of course, one could also record the derivative of the current *vs.* time or potential, but *derivative techniques* are rarely used because they intrinsically enhance noise on the signal (Chapter 15).

Several more sophisticated detection modes involving convolution (or semi-integration), semidifferentiation, or other transformations of the current function also find useful applications. Since they tend to rest on fairly subtle mathematics, we defer discussions of them until Section 6.7.
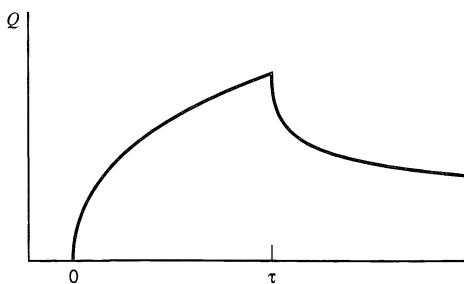
Figure 5.1.5 Response curve for double potential step chronocoulometry. Step waveform is similar to that in Figure 5.1.4*a*.

5.1.3 Applicable Current-Potential Characteristics

With only a qualitative understanding of the experiments described in Section 5.1.1, we saw that we could predict the general shapes of the responses. However, we are ultimately interested in obtaining quantitative information about electrode processes from these current-time or current-potential curves, and doing so requires the creation of a theory that can predict, quantitatively, the response functions in terms of the experimental parameters of time, potential, concentration, mass-transfer coefficients, kinetic parameters, and so on. In general, a controlled-potential experiment carried out for the electrode reaction

$$O + e \underset{k_b}{\overset{k_f}{\rightleftarrows}} R \tag{5.1.2}$$

can be treated by invoking the current-potential characteristic:

$$i = FAk^0 [C_O(0, t)e^{-\alpha f(E-E^{0'})} - C_R(0, t)e^{(1-\alpha)f(E-E^{0'})}] \tag{5.1.3}$$

in conjunction with Fick's laws, which can give the time-dependent surface concentrations $C_O(0, t)$ and $C_R(0, t)$. This approach is nearly always difficult, and it sometimes fails to yield closed-form solutions. The problem is even more difficult when a multistep mechanism applies (see Section 3.5). One is often forced to numerical solutions or approximations.

The usual alternative in science is to design experiments so that simpler theory can be used. Several special cases are easily identified:

(a) Large-Amplitude Potential Step

If the potential is stepped to the mass-transfer controlled region, the concentration of the electroactive species is nearly zero at the electrode surface, and the current is totally controlled by mass transfer and, perhaps, by the kinetics of reactions in solution away from the electrode. Electrode kinetics no longer influence the current, hence the general *i-E* characteristic is not needed at all. For this case, *i* is independent of *E*. In Sections 5.2 and 5.3, we will be concentrating on this situation.

(b) Small-Amplitude Potential Changes

If a perturbation in potential is small in size and both redox forms of a couple are present (so that an equilibrium potential exists), then current and potential are linked by a linearized *i-η* relation. For the one-step, one-electron reaction (5.1.2), it is (3.4.12),

$$i = -i_0 f\eta \tag{5.1.4}$$

(c) Reversible (Nernstian) Electrode Process

For very rapid electrode kinetics, we have seen that the *i-E* relation collapses generally to a relation of the Nernst form (Sections 3.4.5 and 3.5.3):

$$E = E^{0'} + \frac{RT}{nF} \ln \frac{C_O(0, t)}{C_R(0, t)} \tag{5.1.5}$$

Again the kinetic parameters k^0 and α are not involved, and mathematical treatments are nearly always greatly simplified.

(d) Totally Irreversible Electron Transfer

When the electrode kinetics are very sluggish (k^0 is very small), the anodic and cathodic terms of (5.1.3) are never simultaneously significant. That is, when an appreciable net cathodic current is flowing, the second term in (5.1.3) has a negligibly small effect, and vice versa. To observe the net current, the forward process must be so strongly activated (by application of an overpotential) that the back reaction is virtually totally inhibited. In such cases, observations are always made in the "Tafel region," hence one of the terms in (5.1.3) can be neglected (see also Sections 3.4.3 and 3.5.4).

(e) Quasireversible Systems

Unfortunately, electrode processes are not always facile or very sluggish, and we sometimes must consider the whole *i-E* characteristic. In such *quasireversible (or quasi-nernstian* cases), we recognize that the net current involves appreciable activated components from the forward and reverse charge transfers.

In delineating these special situations, we are mostly concentrating on electrode processes that are chemically reversible; however the mechanism of an electrode process often involves an irreversible chemical transformation, such as the decay of the electron-transfer product by a following homogeneous reaction. A good specific example features anthracene in DMF, which we have already considered previously. If a proton donor, such as water, is present in the solvent, the anthracene anion radical is protonated irreversibly and several other steps follow, eventually yielding 9,10-dihydroanthracene. Treating any case in which irreversible chemical steps are linked to heterogeneous electron transfer is much more complicated than dealing with the heterogeneous electron transfer alone. One of the simplified cases, given in (a)–(d) earlier might apply to the electron-transfer step, but the homogeneous kinetics must also be added into the picture. Even in the absence of coupled-solution chemistry, chemically reversible electrode processes can be complicated by multistep heterogeneous electron transfer to a single species. For example, the two-electron reduction of Sn^{4+} to Sn^{2+} can be treated and understood as a sequence of one-electron transfers. In Chapter 12, we will see how more complicated electrode reactions like these can be handled.

▶ 5.2 POTENTIAL STEP UNDER DIFFUSION CONTROL

5.2.1 A Planar Electrode

Previously, we considered an experiment involving an instantaneous change in potential from a value where no electrolysis occurs to a value in the mass-transfer-controlled region for reduction of anthracene, and we were able to grasp the current-time response qualitatively. Here we will develop a quantitative treatment of such an experiment. A planar electrode (e.g., a platinum disk) and an unstirred solution are presumed. In place of the

anthracene example, we can consider the general reaction $O + ne \rightarrow R$. Regardless of whether the kinetics of this process are basically facile or sluggish, they can be activated by a sufficiently negative potential (unless the solvent or supporting electrolyte is reduced first), so that the surface concentration of O becomes effectively zero. This condition will then hold at any more extreme potential. We will consider our instantaneous step to terminate in this region.

(a) Solution of the Diffusion Equation

The calculation of the diffusion-limited current, i_d, and the concentration profile, $C_O(x, t)$, involves the solution of the linear diffusion equation:

$$\frac{\partial C_O(x, t)}{\partial t} = D_O \frac{\partial^2 C_O(x, t)}{\partial x^2} \tag{5.2.1}$$

under the boundary conditions:

$$C_O(x, 0) = C_O^* \tag{5.2.2}$$

$$\lim_{x \to \infty} C_O(x, t) = C_O^* \tag{5.2.3}$$

$$C_O(0, t) = 0 \quad \text{(for } t > 0) \tag{5.2.4}$$

The *initial condition*, (5.2.2), merely expresses the homogeneity of the solution before the experiment starts at $t = 0$, and the *semi-infinite condition*, (5.2.3), is an assertion that regions distant from the electrode are unperturbed by the experiment. The third condition, (5.2.4), expresses the condition at the electrode surface after the potential transition, and it embodies the particular experiment we have at hand.

Section A.1.6 demonstrates that after Laplace transformation of (5.2.1), the application of conditions (5.2.2) and (5.2.3) yields

$$\overline{C}_O(x, s) = \frac{C_O^*}{s} + A(s) e^{-\sqrt{s/D_O}\, x} \tag{5.2.5}$$

By applying the third condition, (5.2.4), the function $A(s)$ can be evaluated, and then $\overline{C}_O(x, s)$ can be inverted to obtain the concentration profile for species O. Transforming (5.2.4) gives

$$\overline{C}_O(0, s) = 0 \tag{5.2.6}$$

which implies that

$$\overline{C}_O(x, s) = \frac{C_O^*}{s} - \frac{C_O^*}{s} e^{-\sqrt{s/D_O}\, x} \tag{5.2.7}$$

In Chapter 4, we saw that the flux at the electrode surface is proportional to the current; specifically,

$$-J_O(0, t) = \frac{i(t)}{nFA} = D_O \left[\frac{\partial C_O(x, t)}{\partial x} \right]_{x=0} \tag{5.2.8}$$

which is transformed to

$$\frac{\bar{i}(s)}{nFA} = D_O \left[\frac{\partial \overline{C}_O(x, s)}{\partial x} \right]_{x=0} \tag{5.2.9}$$

The derivative in (5.2.9) can be evaluated from (5.2.7). Substitution yields

$$\bar{i}(s) = \frac{nFAD_O^{1/2}C_O^*}{s^{1/2}} \tag{5.2.10}$$

and inversion produces the current-time response

$$i(t) = i_d(t) = \frac{nFAD_O^{1/2}C_O^*}{\pi^{1/2}t^{1/2}}$$

(5.2.11)

which is known as the *Cottrell equation* (3). Its validity was verified in detail by the classic experiments of Kolthoff and Laitinen, who measured or controlled all parameters (1, 2). Note that the effect of depleting the electroactive species near the surface leads to an inverse $t^{1/2}$ function. We will encounter this kind of time dependence frequently in other kinds of experiments. It is a mark of diffusive control over the rate of electrolysis.

In practical measurements of the *i-t* behavior under "Cottrell conditions" one must be aware of instrumental and experimental limitations:

1. *Potentiostatic limitations.* Equation 5.2.11 predicts very high currents at short times, but the actual maximum current may depend on the current and voltage output characteristics of the potentiostat (Chapter 15).

2. *Limitations in the recording device.* During the initial part of the current transient, the oscilloscope, transient recorder, or other recording device may be overdriven, and some time may be required for recovery, after which accurate readings can be displayed.

3. *Limitations imposed by R_u and C_d.* As shown in Section 1.2.4, a nonfaradaic current must also flow during a potential step. This current decays exponentially with a *cell time constant*, R_uC_d (where R_u is the uncompensated resistance and C_d is the double-layer capacitance). For a period of about five time constants, an appreciable contribution of charging current to the total measured current exists, and this superimposed signal can make it difficult to identify the faradaic current precisely. Actually, the charging of the double layer is the mechanism that establishes a change in potential; hence the cell time constant also defines the shortest time scale for carrying out a step experiment. The time during which data are collected after a step is applied must be much greater than R_uC_d if an experiment is to fulfill the assumption of a practically instantaneous change in surface concentration at $t = 0$ (see Sections 1.2.4 and 5.9.1).

4. *Limitations due to convection.* At longer times the buildup of density gradients and stray vibrations will cause convective disruption of the diffusion layer, and usually result in currents larger than those predicted by the Cottrell equation. The time for the onset of convective interference depends on the orientation of the electrode, the existence of a protective mantle around the electrode, and other factors (1, 2). In water and other fluid solvents, diffusion-based measurements for times longer than 300 s are difficult, and even measurements longer than 20 s may show some convective effects.

(b) Concentration Profile

Inversion of (5.2.7) yields

$$C_O(x, t) = C_O^*\left\{1 - \text{erfc}\left[\frac{x}{2(D_Ot)^{1/2}}\right]\right\}$$

(5.2.12)

or

$$C_O(x, t) = C_O^* \, \text{erf}\left[\frac{x}{2(D_Ot)^{1/2}}\right]$$

(5.2.13)
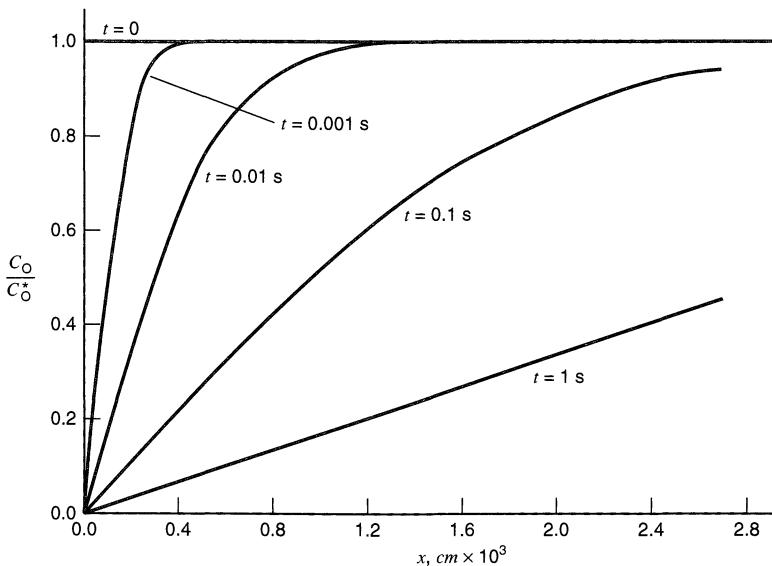
Figure 5.2.1 Concentration profiles for several times after the start of a Cottrell experiment. D_O = 1×10^{-5} cm^2/s.

Figure 5.2.1 comprises several plots from (5.2.13) for various values of time. The depletion of O near the electrode is easily seen, as is the time-dependent falloff in the concentration gradient at the electrode surface, which leads to the monotonically decreasing i_d function of (5.2.11).

One can also see from Figure 5.2.1 that the *diffusion layer*, that is the zone near the electrode where concentrations differ from those of the bulk, has no definite thickness. The concentration profiles asymptotically approach their bulk values. Still, it is useful to think about the thickness in terms of $(D_O t)^{1/2}$, which has units of length and characterizes the distance that species O can diffuse in time t. Note that the argument of the error function in (5.2.13) is the distance from the electrode expressed in units of $2(D_O t)^{1/2}$. The error function rises very rapidly toward its asymptote of 1 (see Section A.3). When its arguments are 1, 2, and 3 (i.e., when x is 2, 4, and 6 times $(D_O t)^{1/2}$), it has values, respectively, of 0.84, 0.995, and 0.99998; thus the diffusion layer is completely contained within a distance of $6(D_O t)^{1/2}$ from the electrode. For most purposes, one can think of it as being somewhat thinner. People often talk of a *diffusion layer thickness*, because there is a need to describe the reach of the electrode process into the solution. At distances much greater than the diffusion layer thickness, the electrode can have no appreciable effect on concentrations, and the reactant molecules there have no access to the electrode. At distances much smaller, the electrode process is powerfully dominant. Even though no consistent or accepted definition exists, people often define the thickness as 1, $2^{1/2}$, $\pi^{1/2}$, or 2 times $(D_O t)^{1/2}$. Any of these ideas suffices. We have already seen diffusion lengths defined in different ways in Sections 1.4.3 and 4.4.1.

Of course the thickness of the diffusion layer depends significantly on the time scale of the experiment, as one can see in Figure 5.2.1. For a species with a diffusion coefficient of 1×10^{-5} cm^2 s^{-1}, $(D_O t)^{1/2}$ is about 30 μm for an experimental time of 1 s, but only 1 μm at 1 ms, and just 30 nm at 1 μs.

5.2.2 Semi-Infinite Spherical Diffusion

If the electrode in the step experiment is spherical rather than planar (e.g., a hanging mercury drop), one must consider a spherical diffusion field, and Fick's second law becomes

$$\frac{\partial C_O(r, t)}{\partial t} = D_O\left[\frac{\partial^2 C_O(r, t)}{\partial r^2} + \frac{2}{r}\frac{\partial C_O(r, t)}{\partial r}\right] \qquad (5.2.14)$$

where r is the radial distance from the electrode center. The boundary conditions are then

$$C_O(r, 0) = C_O^* \quad (r > r_0) \qquad (5.2.15)$$

$$\lim_{r \to \infty} C_O(r, t) = C_O^* \qquad (5.2.16)$$

$$C_O(r_0, t) = 0 \qquad (t > 0) \qquad (5.2.17)$$

where r_0 is the radius of the electrode.

(a) Solution of the Diffusion Equation

The substitution, $v(r, t) = rC_O(r, t)$, converts (5.2.14) into an equation having the same form as the linear problem. The details are left to the reader (Problem 5.1). The resulting diffusion current is

$$i_d(t) = nFAD_OC_O^*\left[\frac{1}{(\pi D_O t)^{1/2}} + \frac{1}{r_0}\right] \qquad (5.2.18)$$

which can be written

$$i_d(\text{spherical}) = i_d(\text{linear}) + \frac{nFAD_OC_O^*}{r_0} \qquad (5.2.19)$$

Thus the diffusion current for the spherical case is just that for the linear situation plus a constant term. For a planar electrode,

$$\lim_{t \to \infty} i_d = 0 \qquad (5.2.20)$$

but in the spherical case,

$$\lim_{t \to \infty} i_d = \frac{nFAD_OC_O^*}{r_0} \qquad (5.2.21)$$

The reason for this curious nonzero limit is that one converges on a situation in which the growth of the depletion region fails to affect the concentration gradients at the surface because the diffusion field is able to draw material from a continually larger area at its outer limit. In actual experiments with working electrodes of millimeter diameters or larger, convection caused by density gradients or vibration becomes important at longer times and enhances the mass transfer, so that the diffusive steady state is rarely reached. On the other hand, it is easy to reach this condition with UMEs (radius of 25 μm or smaller), and the ability to exploit the steady state is one of their principal advantages (see Section 5.3).

(b) Concentration Profile

The distribution of the electroactive species near the electrode also can be obtained from the solution to the diffusion equation, and it turns out to be

$$C_O(r, t) = C_O^*\left[1 - \frac{r_0}{r}\text{erfc}\left(\frac{r - r_0}{2(D_O t)^{1/2}}\right)\right] \qquad (5.2.22)$$

Because $r - r_0$ is the distance from the electrode surface, this profile strongly resembles that for the linear case (equation 5.2.12). The difference is the factor r_0/r and, if the diffusion layer is thin compared to the electrode's radius, the linear and spherical cases are indistinguishable. The situation is directly analogous to our experience in living on a spherical planet. The zone of our activities above the earth's surface is small compared to its radius of curvature; hence we usually cannot distinguish the surface from a rough plane.

At the other extreme, when the diffusion layer grows much larger than r_0 (as at a UME), the concentration profile near the surface becomes independent of time and linear with $1/r$. One can see this effect in (5.2.22), where error function complement approaches unity for $(r - r_0) << 2(D_O t)^{1/2}$. In that case,

$$C_O(r, t) = C_O^*(1 - r_0/r) \tag{5.2.23}$$

The slope at the surface is C_O^*/r_0, which gives the steady-state current, (5.2.21), from the current-flux relationship for the spherical case,

$$\frac{i}{nFA} = D_O \left[\frac{\partial C_O(r, t)}{\partial r} \right]_{r=r_0} \tag{5.2.24}$$

(c) Applicability of the Linear Approximation

These ideas indicate that linear diffusion adequately describes mass transport to a sphere, provided the sphere's radius is large enough and the time domain of interest is small enough. More precisely, the linear treatment is adequate as long as the second (constant) term of (5.2.18) is small compared to the Cottrell term. For accuracy within $a\%$,

$$\frac{nFAD_O C_O^*}{r_0} \leq \frac{a}{100} \cdot \frac{nFAD_O^{1/2} C_O^*}{(\pi t)^{1/2}} \tag{5.2.25}$$

or

$$\frac{\pi^{1/2} D_O^{1/2} t^{1/2}}{r_0} \leq \frac{a}{100} \tag{5.2.26}$$

With $a = 10\%$ and $D_O = 10^{-5}$ cm^2/s, $t^{1/2}/r_0 \leq 18$ s$^{1/2}$/cm. A typical mercury drop might be 0.1 cm in radius; hence the linear treatment holds within 10% for about 3 s.

The numerator of (5.2.26) is the thickness of the diffusion layer; thus the importance of the steady-state term, which manifests spherical diffusion, depends mainly on the ratio of that thickness to the radius of the electrode. When the diffusion layer grows to a thickness that is an appreciable fraction of r_0, it is no longer appropriate to use equations for linear diffusion, and one can expect the steady-state term to contribute significantly to the measured current.

5.2.3 Microscopic and Geometric Areas

If the electrode surface is strictly a plane with a well-defined boundary, such as an atomically smooth metal disk mounted in a glass mantle, the area A in the Cottrell equation is easily understood. On the other hand, real electrode surfaces are not smooth planes, and the concept of area becomes much less clear. Figure 5.2.2 helps to define two different measures of area for a given electrode. First there is the *microscopic area*, which is computed by integrating the exposed surface over all of its undulations, crevices, and asperities, even down to the atomic level. An easier quantity to evaluate operationally, is the *geometric area* (sometimes called the *projected area*). Mathemati-
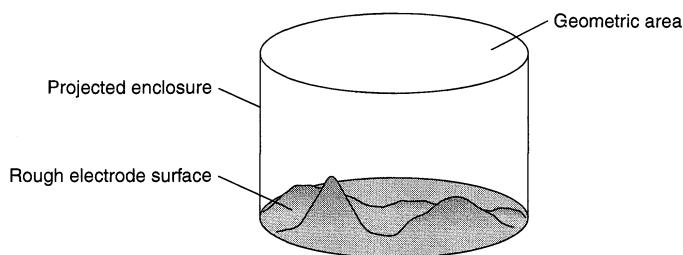
Figure 5.2.2 Electrode surface and the enclosure formed by projecting the boundary outward in parallel with the surface normal. The cross-section of the enclosure is the geometric area of the electrode.

cally, it is the cross-sectional area of the enclosure formed by projecting the boundary of the electrode outward in parallel with the mean surface normal. The microscopic area A_m is, of course, always larger than the geometric area A_g, and the *roughness factor ρ* is the ratio of the two:

$$\rho = A_m/A_g \tag{5.2.27}$$

Routinely polished metal electrodes typically have roughness factors of 2–3, but single crystal faces of high quality can have roughness factors below 1.5. Liquid–metal electrodes (e.g., mercury) are often assumed to be atomically smooth. One can estimate the microscopic area by measuring either the double-layer capacitance (Section 13.4) or the charge required to form or to strip a compact monolayer electrolytically from the surface. For example the true areas of platinum and gold electrodes are often evaluated from the charge passed in removal of adsorbed films under well-defined conditions. Thus, the true area of Pt can be estimated from the charge needed to desorb hydrogen ($210~\mu C/cm^2$) and that of Au from the reduction of a layer of adsorbed oxygen ($386~\mu C/cm^2$) (4). Uncertainty in this measurement arises because it can be difficult to subtract contributions from other faradaic processes and double-layer charging and because the charge for desorption depends upon the crystal face of the metal (see Figure 13.4.4).

The area to be used in the Cottrell equation, or in other similar equations describing current flow in electrochemical experiments, depends on the time scale of the measurements. In the derivation of the Cottrell equation (Section 5.2.1), the current is defined by the flux of species diffusing across the plane at $x = 0$. The total rate of reaction in moles per second, giving the total current in amperes, is the product of that flux and the *cross-sectional area of the diffusion field*, which is the area needed for the final result.

In most chronoamperometry, with measurement times of 1 ms to 10 s, the diffusion layer is several micrometers to even hundreds of micrometers thick. These distances are much larger than the scale of roughness on a reasonably polished electrode, which will have features no larger than a small fraction of a micrometer. Therefore, on the scale of the diffusion layer, the electrode appears flat; the surfaces connecting equal concentrations in the diffusion layer are planes parallel to the electrode surface; and the area of the diffusion field is the geometric area of the electrode. When these conditions apply, as in Figure 5.2.3a, the geometric area should be used in the Cottrell equation.

Let us now imagine a contrasting situation involving a much shorter time scale, perhaps 100 ns, where the diffusion layer thickness is only 10 nm. In this case, depicted in Figure 5.2.3b, much of the roughness is of a scale larger than the thickness of the diffusion layer; hence the surfaces of equal concentration in the diffusion layer tend to follow the features of the surface. They define the area of the diffusion field, which is generally larger than the geometric area. It approaches the microscopic area, but might not be quite as large, because features of roughness smaller in scale than the diffusion length tend to be averaged within the diffusion field.
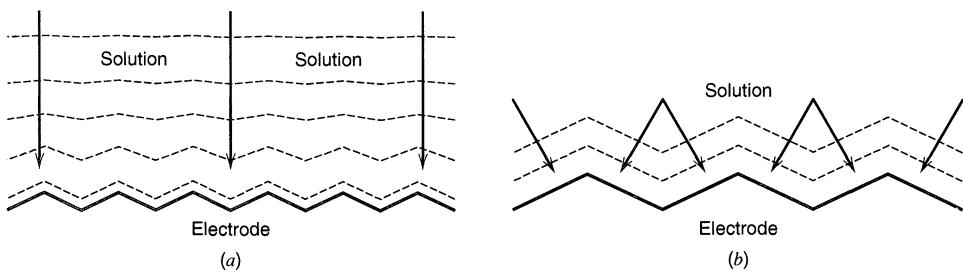
Figure 5.2.3 Diffusion fields at (*a*) long and (*b*) short times at a rough electrode. Depicted here is an idealized electrode where the roughness is caused by parallel triangular grooves cut on lines perpendicular to the page. Dotted lines show surfaces of equal concentration in the diffusion layer. Vectors show concentration gradients driving the flux toward the electrode surface.

Similar considerations are needed to understand chronoamperometry at an electrode that is active only over a portion of a larger area, as in Figure 5.2.4. Such a situation can arise when arrays of electrodes are fabricated by microelectronic methods, or when the electrode is a composite material based on conducting particles, such as graphite, in an insulating phase, such as a polymer. Another important case involves an electrode covered by a blocking layer with pinholes through which the electroactive species may access the electrode surface (Section 14.5.1). At short time scales, when the diffusion layer thickness is small compared to the size of the active spots, each spot generates its own diffusion field (Figure 5.2.4*a*), and the area of the overall diffusion field is the sum of the geometric areas of the individual active spots. At longer time scales, the individual diffusion fields begin to extend outside the projected boundaries of the spots, and linear diffusion is augmented by a radial component. (Figure 5.2.4*b*) At still longer time scales, when the diffusion layer is much thicker than the distances between the active zones, the separated diffusion fields merge into a single larger field, again exhibiting linear diffusion and having an area equal to the geometric area of the entire array, even including that of the insulating zones between the active sites (Figure 5.2.4*c*). Thus, the individual active areas are no longer distinguishable. Molecules diffusing to the electrode come, on the average, from so far away that the added distance (and time) required to reach an active place on the surface becomes negligible. This problem has been treated analytically for cases in which the active spots are uniform in size and situated in a regular array (5), but in the more general case digital simulation is required.

Since capacitive currents are generated by events occurring within very small distances at an electrode surface (Chapter 13), they always reflect the microscopic area. For an electrode made of a polished polycrystalline metal, the area giving rise to a nonfaradaic current may be significantly larger than that characterizing the diffusion field. On the other hand, the opposite can be true if one is using an array of small, widely spaced electrodes embedded in an inert matrix.

▶ 5.3 DIFFUSION-CONTROLLED CURRENTS AT ULTRAMICROELECTRODES

Early in this chapter we anticipated the unusual and advantageous properties of electrodes with very small sizes. Here we explore those properties more carefully, and we gain our first view of some of the experimental methods based on them. We will return

Solution phase

Inactive surface

Electronically
conducting phase

Insulating matrix

(a)

(b)

(c)
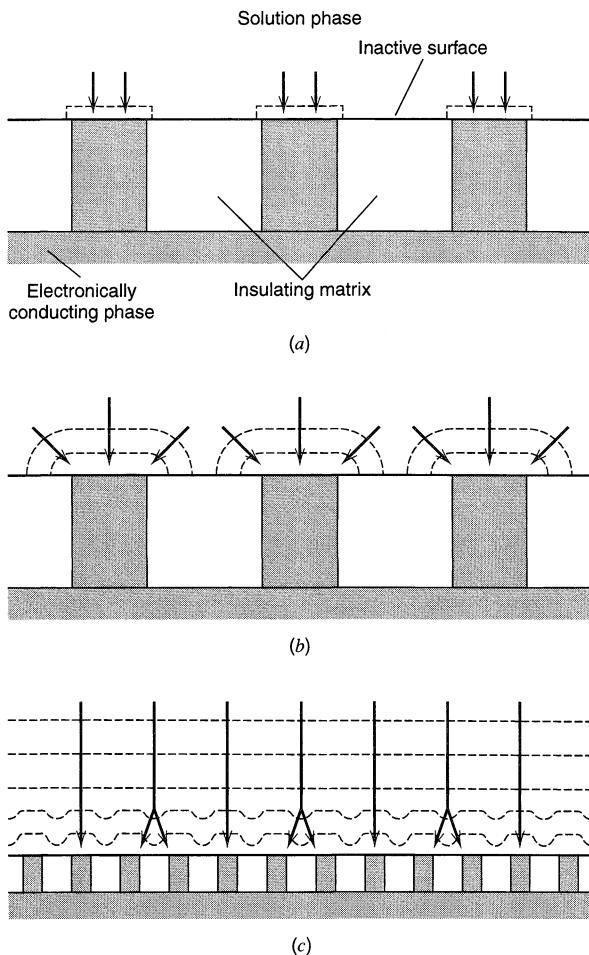
Figure 5.2.4 Evolution
of the diffusion field during
chronoamperometry at an electrode
with active and inactive areas on its
surface. In this case the electrode is
a regular array such that the active
areas are of equal size and spacing,
but the same principles apply for
irregular arrays. (a) Short
electrolysis times, (b) intermediate
times, (c) long times. Arrows
indicate flux lines to the electrode.

repeatedly to these UMEs and their applications. Since the first edition, no advance has changed electrochemical science to a greater degree than the advent of UMEs, which occurred principally through the independent work of Wightman and Fleischmann and their coworkers about 1980 (6, 7). These devices have extended electrochemical methodology into broad new domains of space, time, chemical medium, and methodology (6–13). In the remainder of this book, we will encounter many illustrations based on them.

It is obvious that UMEs are smaller than "normal" electrodes, which, depending on the application, might have dimensions of meters, centimeters, or millimeters. At present, there is no broadly accepted definition of a UME, although there is a general agreement on the essential concept, which is that the electrode is smaller than the scale of the diffusion layer developed in readily achievable experiments. Not all applications depend on the development of such a relationship between the diffusion layer and the electrode, but many do. To understand them, one must recognize the peculiar features of such systems and treat them theoretically. Other applications of UMEs rest on the small time constants or low ohmic drops that are characteristic of very small electrodes (Section 5.9).

In this book, we define a UME operationally as an electrode having at least one dimension (such as the radius of a disk or the width of a band) smaller than 25 μm. This

aspect is called the *critical dimension*. Electrodes with a critical dimension as small as 0.1 μm (= 100 nm = 1000 Å) can be made. Even smaller critical dimensions, down to a few nm, have been reported. When the electrode's critical dimension becomes comparable to the thickness of the double layer or to the size of molecules, one can expect to deal with new elements of theory and experimental behavior. These considerations place a lower limit of about 10 nm (100 Å) on the critical dimension of UMEs (12, 14, 15). Electrodes smaller than this limit have been called *nanodes* in some of the literature, but a definition of this term based on function is yet to be worked out.

5.3.1 Types of Ultramicroelectrodes

Since only one dimension of an electrode must be small to produce properties characteristic of a UME, there is a good deal of latitude in other physical dimensions and, consequently, a variety of useful shapes.

Most common is the *disk UME*, which can be fabricated by sealing a fine wire in an insulator, such as glass or a plastic resin, and then exposing and polishing a cross-section of the wire. The critical dimension is, of course, the radius, r_0, which must be smaller than ~25 μm. Electrodes made of Pt wire with a radius of 5 μm are commercially available. Disks with r_0 as small as 0.1 μm have been made from wire, and disk-like exposed areas with dimensions in the range of a few nm have been inferred for electrodes made by other means. The geometric area of a disk scales with the square of the critical radius and can be tiny. For $r_0 = 1$ μm, the area, A, is only 3×10^{-8} cm^2, six orders of magnitude smaller than the geometric area of a 1-mm diameter microelectrode. The very small scale of the electrode is the key to its special utility, but it also implies that the current flowing there is quite low, often in the range of nanoamperes or picoamperes, sometimes even in the range of femtoamperes. As we will see in Section 5.9 and Chapter 15, the small currents at UMEs offer experimental opportunities as well as difficulties.

Spherical UMEs can be made for gold (16), but are difficult to realize for other materials. *Hemispherical UMEs* can be achieved by plating mercury onto a microelectrode disk. In these two cases the critical dimension is the radius of curvature, normally symbolized by r_0. The geometry of these two types is simpler to treat than that of the disk, but in many respects behavior at a disk is similar to that at a spherical or hemispherical UME with the same r_0.

Quite different is the *band UME*, which has as its critical dimension a width, w, in the range below 25 μm. The length, l, can be much larger, even in the centimeter range. Band UMEs can be fabricated by sealing metallic foil or an evaporated film between glass plates or in a plastic resin, then exposing and polishing an edge. A band can also be produced as a microfabricated metallic line on an insulating substrate using normal methods of microelectronic manufacture. By these means, electrodes with widths ranging from 25 μm to about 0.1 μm can be obtained. The band differs from the disk in that the geometric area scales linearly with the critical dimension, rather than with the square. Thus electrodes with quite small values of w can possess appreciable geometric areas and can produce sizable currents. For example, a band of 1-μm width and 1-cm length has a geometric area of 10^{-4} cm^2, almost four orders of magnitude larger than that of a 1-μm disk.

A *cylindrical UME* can be fabricated simply by exposing a length l of fine wire with radius r_0. As in the case of the band, the length can be macroscopic, typically millimeters. The critical dimension is r_0. In general, the mass-transfer problem to a cylindrical UME is simpler than that to a band, but operationally, there are many similarities between a cylinder and a band.

5.3.2 Responses to a Large-Amplitude Potential Step

Let us consider an ultramicroelectrode in a solution of species O, but initially at a potential where O is not reduced. A step is applied at $t = 0$, so that O becomes reduced to R at the diffusion-controlled rate. What current flows under these Cottrell-like conditions?

(a) Spherical or Hemispherical UME

We already know the current-time relationship for the simplest case, the sphere, which was treated fully in Section 5.2.2. The result was given in (5.2.18) as

$$i = \frac{nFAD_O^{1/2}C_O^*}{\pi^{1/2}t^{1/2}} + \frac{nFAD_O C_O^*}{r_0} \tag{5.3.1}$$

where the first term dominates at short times, when the diffusion layer is thin compared to r_0, and the second dominates at long times, when the diffusion layer grows much larger than r_0. The first term is identically the Cottrell current that would be observed at a planar electrode of the same area, and the second describes the steady-state current flow achieved late in the experiment. The steady-state condition is readily realized at a UME, where the diffusion field need only grow to a thickness of 100 μm (or perhaps even much less). Many applications of UMEs are based on steady-state currents.

At the sphere, the steady-state current i_{ss} is,

$$\boxed{i_{ss}\; \frac{nFAD_O C_O^*}{r_0}} \tag{5.3.2a}$$

or

$$\boxed{i_{ss} = 4\pi nFD_O C_O^* r_0} \tag{5.3.2b}$$

A hemispherical UME bounded by a planar mantle has exactly half of the diffusion field of a spherical UME of the same r_0, so it has half of the current of the corresponding sphere. Equation 5.3.2a compensates for the difference through the proportionality with area, so it is accurate for the hemisphere as well as the sphere. Equation 5.3.2b applies only to the sphere.

(b) Disk UME

The disk is by far the most important practical case, but it is complicated theoretically by the fact that diffusion occurs in two dimensions (17, 18): radially with respect to the axis of symmetry and normal to the plane of the electrode (Figure 5.3.1). An important consequence of this geometry is that the current density is not uniform across the face of the disk, but is greater at the edge, which offers the nearest point of arrival to electroreactant drawn from a large surrounding volume. We can set up this problem in a manner similar to our approach to the one-dimensional cases of Section 5.2. The diffusion equation for species O is written as follows for this geometry (see Table 4.4.2):

$$\frac{\partial C_O(r, z, t)}{\partial t} = D\left[\frac{\partial^2 C_O(r, z, t)}{\partial r^2} + \frac{1}{r}\cdot\frac{\partial C_O(r, z, t)}{\partial r} + \frac{\partial^2 C_O(r, z, t)}{\partial z^2}\right] \tag{5.3.3}$$

where r describes radial position normal to the axis of symmetry at $r = 0$, and z describes linear displacement normal to the plane of the electrode at $z = 0$.

Five boundary conditions are needed for a solution. Three come from the initial condition and two semi-infinite conditions

$$C_O(r, z, 0) = C_O^* \tag{5.3.4}$$

$$\lim_{r\to\infty} C_O(r, z, t) = C_O^* \qquad \lim_{z\to\infty} C_O(r, z, t) = C_O^* \tag{5.3.5}$$
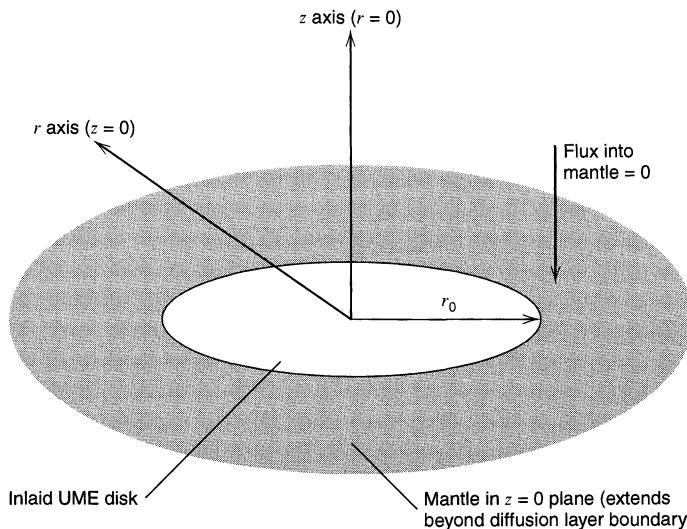
Figure 5.3.1 Geometry of diffusion at an ultramicroelectrode disk

A fourth condition comes from the recognition that there can be no flux of O into or out of the mantle, since O does not react there:

$$\left.\frac{\partial C_O(r, z, t)}{\partial z}\right|_{z=0} = 0 \qquad (r > r_0) \tag{5.3.6}$$

The conditions defined to this point apply for any situation in which the solution is uniform before the experiment begins and in which the electrolyte extends spatially beyond the limit of any diffusion layer. The final condition defines the experimental perturbation. In the present case, we are considering a large-amplitude potential step, which drives the surface concentration of O to zero at the electrode surface after $t = 0$.

$$C_O(r, 0, t) = 0 \qquad (r \le r_0, t > 0) \tag{5.3.7}$$

This problem can be simulated in the form given here (19, 20), but an analytical approach is best made by restating it in terms of other coordinates. In no form is it a simple problem. Aoki and Osteryoung (21) addressed it in terms of a dimensionless parameter, $\tau = 4D_O t/r_0^2$, representing the squared ratio of the diffusion length to the radius of the disk. Given any particular experimental system, τ becomes an index of t. The current-time curve is

$$i = \frac{4nFAD_O C_O^*}{\pi r_0} f(\tau) \tag{5.3.8}$$

where the function $f(\tau)$ was determined as two series applicable in different domains of τ (21–23). At short times, when $\tau < 1$,

$$f(\tau) = \frac{\pi^{1/2}}{2\tau^{1/2}} + \frac{\pi}{4} + 0.094\tau^{1/2} \tag{5.3.9a}$$

or, with the constants evaluated

$$f(\tau) = 0.88623\tau^{-1/2} + 0.78540 + 0.094\tau^{1/2} \tag{5.3.9b}$$

At long times, when $\tau > 1$,[2]

$$f(\tau) = 1 + 0.71835\tau^{-1/2} + 0.05626\tau^{-3/2} - 0.00646\tau^{-5/2} \cdots \tag{5.3.9c}$$

---

[2]Aoki and Osteryoung (23) show that the two versions of $f(\tau)$ overlap for $0.82 < \tau < 1.44$. The dividing point given in the text is convenient and appropriate.

Shoup and Szabo provided a single empirical relationship covering the entire range of τ, with an accuracy better than 0.6% at all points (22):

$$f(\tau) = 0.7854 + 0.8862\tau^{-1/2} + 0.2146e^{-0.7823\tau^{-1/2}} \tag{5.3.10}$$

The current-time relationship for a UME disk spans three regimes, as shown in Figure 5.3.2. If the experiment remains on a short time scale (Figure 5.3.2a), so that the diffusion layer remains thin compared to r_0, the radial diffusion does not manifest itself appreciably, and the diffusion has a semi-infinite linear character. The early current flowing in response to a large amplitude potential step is therefore the Cottrell current, (5.2.11). This intuitive conclusion is illustrated graphically in Figure 5.3.2a, where the two sets of symbols are superimposed. One can also see it mathematically as the limit of (5.3.8) and (5.3.9a) when τ approaches zero. For an electrode with $r_0 = 5$ μm and $D_O = 10^{-5}$ cm^2/s, the short-time region covered in Figure 5.3.2a is 60 ns to 60 μs. In this period, the diffusion layer thickness [taken as $2(D_O t)^{1/2}$] grows from 0.016 μm to 0.5 μm.

As the experiment continues into an intermediate regime where the diffusion layer thickness is comparable to r_0, radial diffusion becomes important. The current is larger than for a continuation of pure linear diffusion, that is, where this "edge effect" (17) could

τ

(a) Short time regime

τ

(b) Intermediate time regime

τ

(c) Long time regime
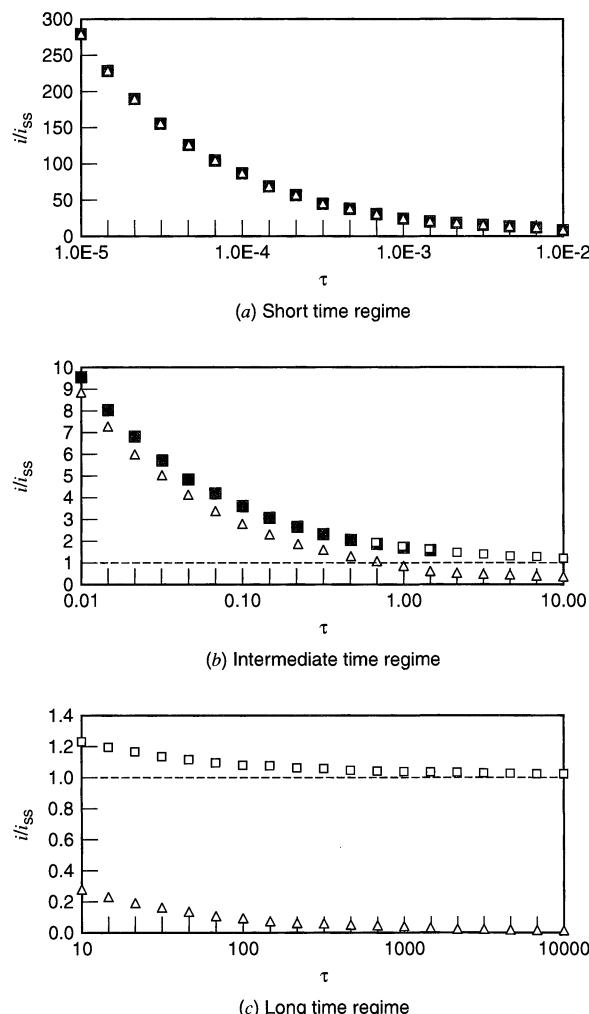
Figure 5.3.2 Current-time relationships at a disk UME. Current is expressed as i/i_{ss} and time is expressed as τ, which is proportional to t. Triangles, Cottrell current. Filled squares, (5.3.8) and (5.3.9b). Open squares, (5.3.8) and (5.3.9c). Dashed line at $i/i_{ss} = 1$ is steady-state.

be prevented. Figure 5.3.2b illustrates the result. For r_0 and D_O values of 5 μm and 10^{-5} cm^2/s, this frame corresponds to an experimental time between 60 μs and 60 ms. The diffusion layer thickness is in the range from 0.5 μm to 16 μm.

At still longer times, when the diffusion field grows to a size much larger than r_0, it resembles the hemispherical case and the current approaches a steady state (Figure 5.3.2c). For the specific values of r_0 and D_O used as examples above, Figure 5.3.2c describes the time period from 60 ms to 60 s, when the diffusion layer thickness enlarges from 16 μm to 500 μm.[3]

The experimental time ranges discussed here relate to practical values of electrode radius and diffusion coefficient and are all readily accessible with standard commercial electrochemical instrumentation. A distinguishing feature of a UME is the ability to operate in different mass-transfer regimes. Indeed, we used, in essence, the ability to approach or to achieve the steady-state as the basis for our operational definition of a UME in the opening paragraphs of this section.

The steady state for the disk can be seen easily as the limit of (5.3.8) and (5.3.9c) when τ becomes very large,

$$i_{ss} = \frac{4nFAD_O C_O^*}{\pi r_0} = 4nFD_O C_O^* r_0 \qquad (5.3.11)$$

It has the same functional form as for the sphere or hemisphere, however the i_{ss} at a disk is smaller (by a factor of $2/\pi$) than at a hemisphere with the same radius. This difference manifests the different shapes of the concentration profiles near the electrode surface.[4]

In the intermediate and late time regimes, the current density at a UME disk is intrinsically nonuniform because the edges of the electrode are more accessible geometrically to the diffusing electroreactant (17). This non-uniformity affects the interpretation of phenomena that depend on local current density, such as heterogeneous electron-transfer kinetics or the kinetics of second-order reactions involving electroactive species in the diffusion layer.

(c) Cylindrical UME

We return to a simpler geometry by considering a cylindrical electrode, which involves only a single dimension of diffusion. The corresponding expression of Fick's second law (see Table 4.4.2) is:

$$\frac{\partial C_O(r, t)}{\partial t} = D \left[\frac{\partial^2 C_O(r, t)}{\partial r^2} + \frac{1}{r} \cdot \frac{\partial C_O(r, t)}{\partial r} + \frac{\partial^2 C_O(r, t)}{\partial z^2} \right] \qquad (5.3.12)$$

where r describes radial position normal to the axis of symmetry, and z is the position along the length. Since we normally assume uniformity along the length of the cylinder, $\partial C/\partial z = \partial^2 C/\partial z^2 = 0$, and z drops out of the problem. The boundary conditions are exactly

---

[3]In practice, it would be difficult to achieve a diffusion layer as thick as 500 μm, because convection would normally begin to manifest itself before 60 s.

[4]By analogy to the rigorous result for the spherical system, one can estimate the current at the disk as the simple linear combination of the Cottrell and steady-state terms:

$$i = \frac{nFAD_O^{1/2} C_O^*}{\pi^{1/2} t^{1/2}} + 4nFD_O C_O^* r_0$$

This approximation is accurate at the short-time and long-time limits and deviates from the Aoki–Osteryoung result by only a few percent in the range of Figure 5.3.2b. The largest error ($\sim +7\%$) is near $\tau = 1$, as one would expect.

those used in solving the spherical case (see Section 5.2.2), and the result is available in the literature (10)

A practical approximation, reported by Szabo et al. (24) to be valid within 1.3%, is

$$i = \frac{nFAD_O C_O^*}{r_0} \left[\frac{2\exp(-0.05\pi^{1/2} \tau^{1/2})}{\pi^{1/2} \tau^{1/2}} + \frac{1}{\ln(5.2945 + 0.7493\tau^{1/2})} \right] \quad (5.3.13)$$

where $\tau = 4D_O t/r_0^2$. In the short-time limit, when τ is small, only the first term of (5.3.13) is important and the exponential approaches unity. Thus (5.3.13) reduces to the Cottrell equation, (5.2.11), as expected for the situation where the diffusion length is small compared to the curvature of the electrode. In fact, the deviation from the Cottrell current resulting from the cylindrical diffusion field does not become as great as 4% until τ reaches ~ 0.01, where the diffusion layer thickness has become about 10% of r_0.

In the long-time limit, when τ becomes very large, the first term in (5.3.13) dies away completely, and the logarithmic function in the denominator of the second term approaches $\ln \tau^{1/2}$. Thus the current becomes

$$i_{qss} = \frac{2nFAD_O C_O^*}{r_0 \ln \tau} \quad (5.3.14)$$

Because this relationship contains τ, the current depends on time; therefore it is not a steady-state limit such as we found for the sphere and the disk. Even so, time appears only as an inverse logarithmic function, so that the current declines rather slowly in the long-time limit. It can still be used experimentally in much the same way that steady-state currents are exploited at disks and spheres. In the literature, this case is sometimes called the *quasi-steady state*.

(d) Band UME

In the same way that a disk electrode is a two-dimensional diffusion system behaving very much like the simpler, one-dimensional, hemispherical case, a band electrode is a two-dimensional system behaving much like the simpler hemicylindrical system. The coordinate system used to treat diffusion at the band is shown in Figure 5.3.3. At short times, the current converges, as we now expect, to the Cottrell form, (5.2.11). At long times, the current-time relationship approaches the limiting form,

$$i_{qss} = \frac{2\pi nFAD_O C_O^*}{w \ln(64D_O t/w^2)} \quad (5.3.15)$$

Thus, the band UME also does not provide a true steady-state current at long times.
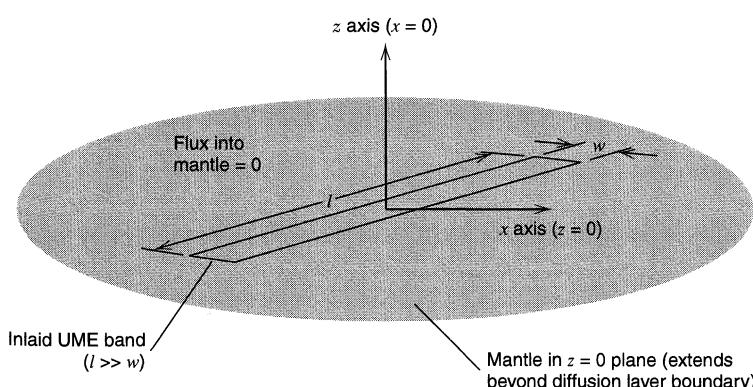
Figure 5.3.3 Diffusional geometry at a band electrode. Normally the length of the electrode is very much larger than the width, and the three-dimensional diffusion at the ends does not appreciably violate the assumption that diffusion occurs only along the x and z axes.

TABLE 5.3.1   Form of m_O for UMEs of Different Geometries

Band[a]	Cylinder[a]	Disk	Hemisphere	Sphere
$\dfrac{2\pi D_O}{w\ln(64D_O t/w^2)}$	$\dfrac{2D_O}{r_O\ln\tau}$	$\dfrac{4D_O}{\pi r_O}$	$\dfrac{D_O}{r_O}$	$\dfrac{D_O}{r_O}$

[a] Long-time limit is to a quasi-steady state.

5.3.3   Summary of Behavior at Ultramicroelectrodes

Although there are some important differences in the behavior of UMEs with different shapes, it is useful here to recollect some common features in the responses to a large-amplitude potential step:

First, at short times, where the diffusion-layer thickness is small compared to the critical dimension, the current at any UME follows the Cottrell equation, (5.2.11), and semi-infinite linear diffusion applies.

Second, at long times, where the diffusion-layer thickness is large compared to the critical dimension, the current at any UME approaches a steady state or a quasi-steady state. One can write the current in this limit in the manner developed empirically in Section 1.4.2,

$$i_{ss} = nFAm_O C_O^* \tag{5.3.16}$$

where m_O is a mass-transfer coefficient. The functional form of m_O depends on geometry as given in Table 5.3.1.

In practical experiments with UMEs, one normally tries to control the experimental conditions so that the electrode is operating either in the short-time regime (called the *early transient regime* or the *regime of semi-infinite linear diffusion* in the remainder of this book) or in the long-time limit (called the *steady-state regime*). The transition region between these two limiting regimes involves much more complicated theory and offers no advantage, so we will not be considering it in much detail.

▶ 5.4 SAMPLED-CURRENT VOLTAMMETRY FOR REVERSIBLE ELECTRODE REACTIONS

The basic experimental methodology for sampled-current voltammetry is described in Section 5.1.1, especially in the text surrounding Figure 5.1.3. After studying the diffusion-controlled responses to potential steps in Sections 5.2 and 5.3, we now understand that the result of a sampled-current experiment might depend on whether the sampling occurs in the time regime where a transient current flows or in the later period, when a steady-state could be reached. This idea leads us to consider the two modes separately for reversible chemistry in Sections 5.4.1 and 5.4.2 below. Applications of reversible voltammograms are then treated in Section 5.4.4.

5.4.1   Voltammetry Based on Linear Diffusion at a Planar Electrode

(a) A Step to an Arbitrary Potential

Consider again the reaction $O + ne \rightleftarrows R$ in a Cottrell-like experiment at an electrode where semi-infinite linear diffusion applies,[5] but this time let us treat potential steps of

---

[5]It is most natural to think of this experiment as taking place at a planar electrode, but as shown in Sections 5.2.2 and 5.3, the required condition is realized with any electrode shape as long as the diffusion layer thickness remains small compared to the radius of curvature of the electrode.

any magnitude. We begin each experiment at a potential at which no current flows; and at $t = 0$, we change E instantaneously to a value anywhere on the reduction wave. We assume here that charge-transfer kinetics are very rapid, so that

$$E = E^{0'} + \frac{RT}{nF} \ln \frac{C_O(0, t)}{C_R(0, t)} \tag{5.4.1}$$

always.

The equations governing this case are[6]

$$\frac{\partial C_O(x, t)}{\partial t} = D_O \frac{\partial^2 C_O(x, t)}{\partial x^2} \qquad \frac{\partial C_R(x, t)}{\partial t} = D_R \frac{\partial^2 C_R(x, t)}{\partial x^2} \tag{5.4.2}$$

$$C_O(x, 0) = C_O^* \qquad\qquad C_R(x, 0) = 0 \tag{5.4.3}$$

$$\lim_{x \to \infty} C_O(x, t) = C_O^* \qquad\qquad \lim_{x \to \infty} C_R(x, t) = 0 \tag{5.4.4}$$

and the flux balance is

$$D_O \left(\frac{\partial C_O(x, t)}{\partial x} \right)_{x=0} + D_R \left(\frac{\partial C_R(x, t)}{\partial x} \right)_{x=0} = 0 \tag{5.4.5}$$

It is convenient to rewrite (5.4.1) as

$$\theta = \frac{C_O(0, t)}{C_R(0, t)} = \exp\left[\frac{nF}{RT} (E - E^{0'}) \right] \tag{5.4.6}$$

In Section 5.2.1, we saw that application of the Laplace transform to (5.4.2) and consideration of conditions (5.4.3) and (5.4.4) would yield

$$\overline{C}_O(x, s) = \frac{C_O^*}{s} + A(s) e^{-\sqrt{s/D_O}\, x} \tag{5.4.7}$$

$$\overline{C}_R(x, s) = B(s) e^{-\sqrt{s/D_R}\, x} \tag{5.4.8}$$

Transformation of (5.4.5) gives

$$D_O \left(\frac{\partial \overline{C}_O(x, s)}{\partial x} \right)_{x=0} + D_R \left(\frac{\partial \overline{C}_R(x, s)}{\partial x} \right)_{x=0} = 0 \tag{5.4.9}$$

which can be simplified by evaluating the derivatives from (5.4.7) and (5.4.8):

$$-A(s) D_O^{1/2} s^{1/2} - B(s) D_R^{1/2} s^{1/2} = 0 \tag{5.4.10}$$

Thus, $B = -A(s)\xi$, where $\xi = (D_O/D_R)^{1/2}$. So far we have not invoked the Nernst relation, (5.4.1); hence our results:

$$\overline{C}_O(x, s) = \frac{C_O^*}{s} + A(s) e^{-(s/D_O)^{1/2}x} \tag{5.4.11}$$

$$\overline{C}_R(x, s) = -A(s)\xi\, e^{-(s/D_R)^{1/2}x} \tag{5.4.12}$$

hold for any i-E characteristic. We will make use of this fact in Section 5.5.

We introduce the assumption of reversibility to evaluate $A(s)$. Transformation of (5.4.6) shows that $\overline{C}_O(0, s) = \theta \overline{C}_R(0, s)$; thus

$$\frac{C_O^*}{s} + A(s) = -\xi\theta A(s) \tag{5.4.13}$$

---

[6]Clearly, (5.4.3) implies that R is initially absent. The case for $C_R(x, 0) = C_R^*$, follows analogously, and is left as Problem 5.10.

and $A(s) = -\bar{C}_O^* / s(1 + \xi\theta)$. The transformed profiles are then

$$\bar{C}_O(x, s) = \frac{C_O^*}{s} - \frac{C_O^* e^{-(s/D_O)^{1/2}x}}{s(1 + \xi\theta)} \tag{5.4.14}$$

$$\bar{C}_R(x, s) = \frac{\xi C_O^* e^{-(s/D_R)^{1/2}x}}{s(1 + \xi\theta)} \tag{5.4.15}$$

Equation 5.4.14 differs from (5.2.7) only by the factor $1/(1 + \xi\theta)$ in the second term. Since $(1 + \xi\theta)$ is independent of x and t, the current can be obtained exactly as in the treatment of the Cottrell experiment by evaluating $\bar{i}(s)$ and then inverting:

$$i(t) = \frac{nFAD_O^{1/2}C_O^*}{\pi^{1/2} t^{1/2} (1 + \xi\theta)} \tag{5.4.16}$$

This relation is the general response function for a step experiment in a reversible system. The Cottrell equation, (5.2.11), is a special case for the diffusion-limited region, which requires a very negative $E - E^{0'}$, so that $\theta \to 0$. It is convenient to represent the Cottrell current as $i_d(t)$ and to rewrite (5.4.16) as

$$i(t) = \frac{i_d(t)}{1 + \xi\theta} \tag{5.4.17}$$

Now we see that for a reversible couple, every current-time curve has the same shape; but its magnitude is scaled by $1/(1 + \xi\theta)$ according to the potential to which the step is made. For very positive potentials (relative to $E^{0'}$), this scale factor is zero; thus $i(t)$ has a value between zero and $i_d(t)$, depending on E, as sketched in Figure 5.1.3.

(b) Shape of the Current-Potential Curve

In sampled-current voltammetry, our goal is to obtain an $i(\tau)$-E curve by (a) performing several step experiments with different final potentials E, (b) sampling the current response at a fixed time τ after the step, and (c) plotting $i(\tau)$ vs. E. Here we consider the shape of this curve for a reversible couple and the kinds of information one can obtain from it.

Equation 5.4.17 really answers the question for us. For a fixed sampling time τ,

$$i(\tau) = \frac{i_d(\tau)}{1 + \xi\theta} \tag{5.4.18}$$

which can be rewritten as

$$\xi\theta = \frac{i_d(\tau) - i(\tau)}{i(\tau)} \tag{5.4.19}$$

and expanded:

$$E = E^{0'} + \frac{RT}{nF} \ln \frac{D_R^{1/2}}{D_O^{1/2}} + \frac{RT}{nF} \ln \frac{i_d(\tau) - i(\tau)}{i(\tau)} \tag{5.4.20}$$

When $i(\tau) = i_d(\tau)/2$, the current ratio becomes unity so that the third term vanishes. The potential for which this is so is $E_{1/2}$, the *half-wave potential*:

$$E_{1/2} = E^{0'} + \frac{RT}{nF} \ln \frac{D_R^{1/2}}{D_O^{1/2}} \tag{5.4.21}$$
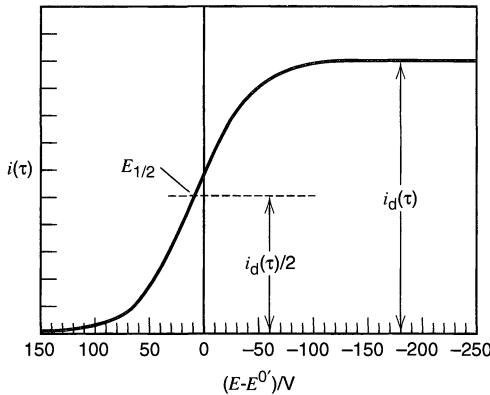
Figure 5.4.1 Characteristics of a reversible wave in sampled-current voltammetry. This curve is for $n = 1$, $T = 298$ K, and $D_O = D_R/2$. Because $D_O \neq D_R$, $E_{1/2}$ differs slightly from $E^{0'}$, in this case by about 9 mV. For $n > 1$, the wave rises more sharply to the plateau (see Figure 5.4.2).

and (5.4.20) is often written

$$E = E_{1/2} + \frac{RT}{nF} \ln \frac{i_d(\tau) - i(\tau)}{i(\tau)} \tag{5.4.22}$$

These equations describe the voltammogram for a reversible system in sampled-current voltammetry as long as semi-infinite linear diffusion holds. It is interesting to compare (5.4.20) and (5.4.22) with the wave shape equations derived in a naive way for steady-state voltammetry in Section 1.4.2(a). They are identical in form.

As shown in Figure 5.4.1, these relations predict a wave that rises from baseline to the diffusion-controlled limit over a fairly narrow potential region ($\sim$200 mV) centered on $E_{1/2}$. Since the ratio of diffusion coefficients in (5.4.21) is nearly unity in almost any case, $E_{1/2}$ is usually a very good approximation to $E^{0'}$ for a reversible couple.

Note also that E vs. log $[(i_d - i)/i]$ should be linear with a slope of $2.303RT/nF$ or $59.1/n$ mV at 25°C. This "wave slope" is often computed for experimental data to test for reversibility. A quicker test [the *Tomeš criterion* (25)] is that $|E_{3/4} - E_{1/4}| = 56.4/n$ mV at 25°C. The potentials $E_{3/4}$ and $E_{1/4}$ are those for which $i = 3i_d/4$ and $i = i_d/4$, respectively. If the wave slope or the Tomeš criterion significantly exceeds the expected values, the system is not reversible. (See also Section 5.5.4).

(c) Concentration Profiles

Taking the inverse transforms of (5.4.14) and (5.4.15) yields the concentration profiles:

$$C_O(x, t) = C_O^* - \frac{C_O^*}{1 + \xi\theta} \operatorname{erfc}\left[\frac{x}{2(D_O t)^{1/2}}\right] \tag{5.4.23}$$

$$C_R(x, t) = \frac{\xi C_O^*}{1 + \xi\theta} \operatorname{erfc}\left[\frac{x}{2(D_R t)^{1/2}}\right] \tag{5.4.24}$$

Some other convenient equations relating to concentrations can also be written. Let us solve for $A(s)$ and $B(s)$ in (5.4.7) and (5.4.8) in terms of the transformed surface concentrations $\overline{C}_O(0, s)$, and $\overline{C}_R(0, s)$, then substitute into (5.4.10):

$$D_O^{1/2}\left(\overline{C}_O(0, s) - \frac{C_O^*}{s}\right) + D_O^{1/2}\overline{C}_R(0, s) = 0 \tag{5.4.25}$$

or, using the inverse transform,

$$D_O^{1/2}C_O(0, t) + D_R^{1/2}C_R(0, t) = C_O^* D_O^{1/2} \tag{5.4.26}$$

The more general relation for R initially present is

$$D_O^{1/2} C_O(0, t) + D_R^{1/2} C_R(0, t) = C_O^* D_O^{1/2} + C_R^* D_R^{1/2} \tag{5.4.27}$$

For the special case when $D_O = D_R$,

$$C_O(0, t) + C_R(0, t) = C_O^* + C_R^* \tag{5.4.28}$$

Equations 5.4.26 to 5.4.28 were derived without reference to the sixth boundary condition in the diffusion problem; hence they do not depend on any particular electrochemical perturbation or $i\text{-}E$ function, and they hold for virtually any electrochemical method. The principal assumptions are that semi-infinite linear diffusion applies and that O and R are soluble, stable species.[7]

Returning now to the step experiments for which (5.4.23) and (5.4.24) apply, we see that the surface concentrations are

$$C_O(0, t) = C_O^* \left(1 - \frac{1}{1 + \xi\theta} \right) = C_O^* \left(\frac{\xi\theta}{1 + \xi\theta} \right) \tag{5.4.29}$$

$$C_R(0, t) = C_O^* \left(\frac{\xi}{1 + \xi\theta} \right) \tag{5.4.30}$$

Since (5.4.17) shows that $i(t)/i_d(t) = 1/(1 + \xi\theta)$,

$$\boxed{C_O(0, t) = C_O^* \left[1 - \frac{i(t)}{i_d(t)} \right]} \tag{5.4.31}$$

$$\boxed{C_R(0, t) = \xi C_O^* \frac{i(t)}{i_d(t)}} \tag{5.4.32}$$

We will use these relations in Section 5.4.3 to simplify the interpretation of reversible sampled-current voltammograms in various chemical situations. The reader interested in a quick view of applications can proceed directly to that point and beyond. However, a full view of reversible waves needs to include those recorded by sampling steady-state currents, so the next section is devoted to that topic.

5.4.2 Steady-State Voltammetry at a UME

(a) A Step to an Arbitrary Potential at a Spherical Electrode

Let us consider again the reaction $O + ne \rightleftarrows R$ in an experiment involving a step of any magnitude, but in contrast to the limitations of the previous section, let us allow the experiment to proceed beyond the regime where semi-infinite linear diffusion applies. For the moment let us also restrict the electrode geometry to a sphere or hemisphere of radius r_0. Species O is present in the bulk, but R is absent. We begin each experiment at a potential at which no current flows; and at $t = 0$, we change E instantaneously to a value anywhere on the reduction wave.

The governing equations are

$$\frac{\partial C_O(r, t)}{\partial t} = D_O \left(\frac{\partial^2 C_O(r, t)}{\partial r^2} + \frac{2}{r} \frac{\partial C_O(r, t)}{\partial r} \right) \tag{5.4.33}$$

---

[7]Note also that for the step experiments under discussion, (5.4.23) and (5.4.24) show that $C_O(x, t) + C_R(x, t) = C_O^*$ at any point along the profiles, when $D_O = D_R$.

$$\frac{\partial C_R(r, t)}{\partial t} = D_R\left(\frac{\partial^2 C_R(r, t)}{\partial r^2} + \frac{2}{r}\frac{\partial C_R(r, t)}{\partial r}\right) \tag{5.4.34}$$

$$C_O(r, 0) = C_O^* \qquad C_R(r, 0) = 0 \tag{5.4.35}$$

$$\lim_{r\to\infty} C_O(r, t) = C_O^* \qquad \lim_{r\to\infty} C_R(r, t) = 0 \tag{5.4.36}$$

$$D_O\left(\frac{\partial C_O(r, t)}{\partial r}\right)_{r=r_0} + D_R\left(\frac{\partial C_R(r, t)}{\partial r}\right)_{r=r_0} = 0 \tag{5.4.37}$$

$$\theta = \frac{C_O(r_0, t)}{C_R(r_0, t)} = \exp\left[\frac{nF}{RT}\left(E - E^{0'}\right)\right] \tag{5.4.38}$$

By the method addressed in Problem 5.1, one can show that (5.4.33)-(5.4.36) together yield the general solutions

$$\overline{C}_O(r, s) = \frac{C_O^*}{s} + \frac{A(s)}{r}e^{-(s/D_O)^{1/2}r} \tag{5.4.39}$$

$$\overline{C}_R(r, s) = \frac{B(s)}{r}e^{-(s/D_R)^{1/2}r} \tag{5.4.40}$$

Transformation and application of the flux balance, (5.4.37), in the same manner used in Section 5.4.1 give

$$\overline{C}_O(r, s) = \frac{C_O^*}{s} + \frac{A(s)}{r}e^{-(s/D_O)^{1/2}r} \tag{5.4.41}$$

$$\overline{C}_R(r, s) = -\frac{A(s)\xi^2\gamma}{r}e^{-(s/D_O)^{1/2}r_0}e^{-(s/D_R)^{1/2}(r-r_0)} \tag{5.4.42}$$

where $\xi = (D_O/D_R)^{1/2}$ and

$$\gamma = \frac{1 + r_0(s/D_O)^{1/2}}{1 + r_0(s/D_R)^{1/2}} \tag{5.4.43}$$

We have not yet called upon reversibility; hence (5.4.41) and (5.4.42) hold for any *i-E* characteristic.

By assuming reversibility and applying condition (5.4.38), we evaluate $A(s)$ essentially in the same way as in Section 5.4.1. The result is

$$A(s) = -\left(\frac{1}{1 + \xi^2\gamma\theta}\right)\frac{r_0 C_O^*}{s}e^{(s/D_O)^{1/2}r_0} \tag{5.4.44}$$

so that the transformed profiles are

$$\overline{C}_O(r, s) = \frac{C_O^*}{s} - \left(\frac{1}{1 + \xi^2\gamma\theta}\right)\frac{r_0 C_O^*}{rs}e^{-(s/D_O)^{1/2}(r-r_0)} \tag{5.4.45}$$

$$\overline{C}_R(r, s) = \left(\frac{\xi^2\gamma}{1 + \xi^2\gamma\theta}\right)\frac{r_0 C_O^*}{rs}e^{-(s/D_R)^{1/2}(r-r_0)} \tag{5.4.46}$$

The current is obtained from the slope of the concentration profiles at the electrode surface, for example,

$$i(t) = nFAD_O\left(\frac{\partial C_O(r, t)}{\partial r}\right)_{r=r_0} \tag{5.4.47}$$

which can be transformed on t to give

$$\bar{i}(s) = nFAD_O\left(\frac{\partial \bar{C}_O(r, s)}{\partial r}\right)_{r=r_0} \tag{5.4.48}$$

By allowing (5.4.48) to operate on (5.4.45), we obtain the transform of the current-time relationship,

$$\bar{i}(s) = \frac{nFAD_O C_O^*}{1 + \xi^2\gamma\theta}\left(\frac{1}{s^{1/2}D_O^{1/2}} + \frac{1}{r_0 s}\right) \tag{5.4.49}$$

which can be usefully reexpressed as

$$\bar{i}(s) = \frac{nFAD_O C_O^*}{1 + \xi^2\gamma\theta}\left(\frac{1 + r_0(s/D_O)^{1/2}}{r_0 s}\right) \tag{5.4.50}$$

Equation 5.4.50 describes current flow at the sphere in all time domains, including the early transient and steady-state regimes. Unfortunately, the complete current transform is not readily inverted to produce a closed-form result, because γ is a complex function of s. Still, one can develop useful results by considering limiting cases. Our main concern here is in distinguishing the early transient and steady-state limits, which can be done by recognizing the role of $r_0(s/D_O)^{1/2}$ in (5.4.43) and (5.4.50). The transform variable s has units of frequency [e.g., s^{-1}] and is, in fact, an alternate representation of time in the experiment. Thus $(D_O/s)^{1/2}$ has units of length, and $r_0(s/D_O)^{1/2}$ relates the radius of curvature of the electrode to the diffusion layer thickness.

When $r_0(s/D_O)^{1/2} \gg 1$, the diffusion layer is thin compared to r_0, and the system is in the early transient regime, where linear diffusion applies. Then the parenthesized factor in (5.4.50) collapses to $s^{-1/2}D_O^{-1/2}$ and $\gamma \to 1/\xi$, so that

$$\bar{i}(s) = \frac{nFAD_O^{1/2}C_O^*}{(1 + \xi\theta)s^{1/2}} \tag{5.4.51}$$

which is readily inverted to produce (5.4.16), as required. Section 5.4.1 fully covers the consequences of this case.

On the other hand, when $r_0(s/D_O)^{1/2} \ll 1$, the diffusion layer thickness greatly exceeds r_0 and the system is in the steady-state regime. By inspection, one sees that $\gamma \to 1$ and the parenthesized factor in (5.4.50) becomes $1/r_0 s$, so that

$$\bar{i}(s) = \frac{nFAD_O C_O^*}{(1 + \xi^2\theta)r_0 s} \tag{5.4.52}$$

which is easily inverted to the steady-state analogue of (5.4.16),

$$\boxed{i = \frac{nFAD_O C_O^*}{(1 + \xi^2\theta)r_0}} \tag{5.4.53}$$

This relation is the general response function for a step experiment in a reversible system when the sampling of current occurs in the steady-state regime. The steady-state limiting current, (5.2.21) or (5.3.2), is the special case for the diffusion-limited region, where $\theta \to 0$. Let us represent this limiting current as i_d and rewrite (5.4.53) as

$$\boxed{i = \frac{i_d}{1 + \xi^2\theta}} \tag{5.4.54}$$

This result is analogous to (5.4.17) and has essentially the same interpretation. The important difference in behavior at the steady state is that the key relations depend on the first power of diffusion coefficients, rather than on their square roots. This effect is seen in the numerator of (5.4.53) *vs.* that of (5.4.16) and also in the appearance of $\xi^2 = (D_O/D_R)$ in (5.4.53) and (5.4.54) *vs.* ξ in the analogous relations (5.4.16) and (5.4.17). The factor $1/(1 + \xi^2\theta)$ has a value between zero (for very positive potentials relative to $E^{0'}$) and unity (for very negative potentials); thus i has a value between zero and $i_d(t)$, much like the representation in Figure 5.1.3.

(b) Conditions for Recording Steady-State Voltammograms

In conception, sampled-current voltammetry involves the recording of an $i(\tau)$-E curve by the application of a series of steps to different final potentials E. The current is sampled at a fixed time τ after the step, then $i(\tau)$ is plotted *vs.* E. This defining protocol can be relaxed considerably when sampling occurs in the steady-state regime. Since the current is independent of time, it does not matter when sampling occurs or how precisely the sampling time is controlled. If the system is chemically reversible, it also does not matter how the steady-state was reached. One need not reinitialize the system after each step; thus the potential can be taken directly from step value to step value as long as the system has enough time to establish the new steady state before sampling occurs.

   Actually one need not even apply steps. It is satisfactory to change the potential linearly with time and to record the current continuously, as long as the rate of change is small compared to the rate of adjustment in the steady state. Section 6.2.3 contains a discussion of the required conditions in more quantitative terms. Virtually all "sampled current voltammetry" at UMEs is carried out experimentally in this linear-sweep form, but the results are the same as if a normal sampled-current voltammetric protocol were employed, except with respect to the charging-current background [see Sections 6.2.4 and 7.3.2(c)].

(c) Shape of the Wave

By rearranging (5.4.54), one derives the reversible steady-state voltammogram as

$$E = E^{0'} + \frac{RT}{nF}\ln\frac{D_R}{D_O} + \frac{RT}{nF}\ln\left(\frac{i_d - i}{i}\right) \tag{5.4.55}$$

This equation has the familiar form seen in (5.4.22), but the half-wave potential differs from that defined in (5.4.21), because the second term contains the first power of the diffusion coefficients, rather than the square root.

$$E_{1/2} = E^{0'} + \frac{RT}{nF}\ln\frac{D_R}{D_O} \tag{5.4.56}$$

   Thus, the shape of the reversible steady-state sampled-current voltammogram is identical to that of the reversible early-transient sampled-current voltammogram (Figure 5.4.1), and the comments made about wave shape in Section 5.4.1(b) also apply in the steady-state case. The only difference is that the steady-state wave is displaced at every point along the potential axis by $(RT/2nF)\ln(D_R/D_O)$ from the wave based on early transients. Unless the two diffusion coefficients differ markedly, this displacement is not experimentally significant.

(d) Concentration Profiles

Because the transformed concentration profiles, (5.4.45) and (5.4.46), contain γ, which is a function of s, they are not readily inverted to produce a equations covering all time regimes. However, we can obtain limiting cases for the early transient and steady-state regimes simply by recognizing limiting forms, just as we did earlier.

When $r_0(s/D)^{1/2} \gg 1$, so that the diffusion layer is thin compared to r_0, then $\gamma \to 1/\xi$ and $r/r_0 \approx 1$ throughout the diffusion layer. Thus the transformed profiles for the early transient regime are as given in (5.4.14) and (5.4.15), with x recognized as $r - r_0$. Inversion gives the concentration profiles in (5.4.23) and (5.4.24).

In the steady-state regime, $r_0(s/D)^{1/2} \ll 1$, and γ approaches unity. Thus the transformed profiles become

$$\overline{C}_O(r, s) = \frac{C_O^*}{s} - \left(\frac{1}{1 + \xi^2\theta}\right)\frac{r_0 C_O^*}{rs} e^{-(s/D_O)^{1/2}(r-r_0)} \tag{5.4.57}$$

$$\overline{C}_R(r, s) = \left(\frac{\xi^2\gamma}{1 + \xi^2\theta}\right)\frac{r_0 C_O^*}{rs} e^{-(s/D_R)^{1/2}(r-r_0)} \tag{5.4.58}$$

which can be inverted to give the desired results

$$C_O(r, t) = C_O^*\left[1 - \left(\frac{1}{1 + \xi^2\theta}\right)\frac{r_0}{r}\,\text{erfc}\left(\frac{r - r_0}{2(D_O t)^{1/2}}\right)\right] \tag{5.4.59}$$

$$C_R(r, t) = C_O^*\left(\frac{\xi^2}{1 + \xi^2\theta}\right)\frac{r_0}{r}\,\text{erfc}\left(\frac{r - r_0}{2(D_R t)^{1/2}}\right) \tag{5.4.60}$$

The surface concentrations are then

$$C_O(r_0, t) = C_O^*\left[1 - \frac{1}{1 + \xi^2\theta}\right] \tag{5.4.61}$$

$$C_R(r_0, t) = C_O^*\left[\frac{\xi^2}{1 + \xi^2\theta}\right] \tag{5.4.62}$$

Since (5.4.54) identifies $1/(1 + \xi^2\theta)$ as i/i_d,

$$\boxed{C_O(r_0, t) = C_O^*\left[1 - \frac{i}{i_d}\right]} \tag{5.4.63}$$

$$\boxed{C_R(r_0, t) = \xi^2 C_O^*\left[\frac{i}{i_d}\right]} \tag{5.4.64}$$

(e) Steady-State Voltammetry at a Disk UME

The results in this section have been derived for spherical geometry; thus they apply rigorously only for spherical and hemispherical electrodes. Because disk UMEs are important in practical applications, it is of interest to determine how well the results for spherical systems can be extended to them. As we noted in Section 5.3, the diffusion problem at the disk is considerably more complicated, because it is two-dimensional. We will not work through the details here. However, the literature contains solutions for steady state at the disk showing that the key equations, (5.4.55), (5.4.56), (5.4.63), and (5.4.64), apply for reversible systems (26, 27). The limiting current is given by (5.3.11).

5.4.3 Simplified Current-Concentration Relationships

Our treatments of sampling in both the early transient regime and the steady-state regime produced simple linkages between the surface concentrations and the current. For the early transient regime, the relationships (5.4.31) and (5.4.32) can be rearranged and re-expressed by recognizing i_d as the Cottrell relation:

$$i(t) = \frac{nFAD_O^{1/2}}{\pi^{1/2}t^{1/2}} [\, C_O^* - C_O(0, t)] \tag{5.4.65}$$

$$i(t) = \frac{nFAD_R^{1/2}}{\pi^{1/2}t^{1/2}} C_R(0, t) \tag{5.4.66}$$

Since these relations hold at any time along the current decay, for sampled voltammetry we can replace t by the sampling time τ. Likewise, for the steady-state regime at a sphere, equations (5.4.63) and (5.4.64) can be rearranged and reexpressed as

$$i = \frac{nFAD_O}{r_0} [\, C_O^* - C_O(0, t)] \tag{5.4.67}$$

$$i = \frac{nFAD_R}{r_0} C_R(0, t) \tag{5.4.68}$$

where the distance variable r has been converted to $r - r_0$ in the interest of comparability with (5.4.65) and (5.4.66) and related equations elsewhere in the book.

For either sampling regime, we arrive with rigor at a set of simple relations of precisely the same form as those *assumed* in the naive approach to mass transport used in Section 1.4. When early transients are sampled, one need only replace m_O with $D_O^{1/2}/\pi^{1/2}t^{1/2}$ and m_R with $D_R^{1/2}/\pi^{1/2}t^{1/2}$ to translate the relationships exactly. For sampled-current voltammetry under steady-state conditions at a sphere or hemisphere, one instead identifies m_O with D_O/r_0 and m_R with D_R/r_0. Similarly, m_O and m_R for steady state at a disk UME are $(4/\pi)D_O/r_0$ and $(4/\pi)D_R/r_0$, respectively (Table 5.3.1). The two approaches to deriving the *i-E* curve can be compared as follows:

Naive Approach

Nernstian behavior
and $i = nFAm_O[C_O^* - C_O(0, t)]$ Simple   *i-E*
$i = nFAm_R[C_R(0, t) - C_R^*]$ $\xrightarrow{\text{math}}$ curve
were assumed

Rigorous Approach

Nernstian behavior,   *i-E* curve
diffusion equations,   More complex   as before and
and boundary conditions $\xrightarrow{\text{math}}$ $i = nFAm_O[\, C_O^* - C_O(0, t)]$
were assumed $i = nFAm_R[C_R(0, t) - C_R^*]$ also
                              as before

The rigorous treatment has therefore justified the *i-C* linkages used before, and it increases confidence in the simpler approach as a means for treating other systems.

The essential reason for the general applicability of these equations is that, in reversible systems, the potential controls the surface concentrations directly and maintains uniformity in these concentrations everywhere on the face of the working electrode. Thus the geometry of the diffusion field, either at steady state or as long as semi-infinite linear diffusion holds, does not depend on potential, and the gradient of that field is simply proportional to the difference between the surface and bulk concentrations.

5.4.4 Applications of Reversible *i-E* Curves

(a) Information from the Wave Height

The plateau current of a simple reversible wave is controlled by mass transfer and can be used to determine any single system parameter that affects the limiting flux of electroreactant at the electrode surface. For waves based on either the sampling of early transients or steady-state currents, the accessible parameters are the *n*-value of the electrode reaction, the area of the electrode, and the diffusion coefficient and bulk concentration of the electroactive species. Certainly the most common application is to employ wave heights to determine concentrations, typically either by calibration or standard addition. The analytical application of sampled-current voltammetry is discussed more fully in Sections 7.1.3 and 7.3.6.

The plateau currents of steady-state voltammograms can also provide the critical dimension of the electrode (e.g., r_0 for a sphere or disk). When a new UME is constructed, its critical dimension is often not known; however, it can be easily determined from a single voltammogram recorded for a solution of a species with a known concentration and diffusion coefficient, such as $Ru(NH_3)_6^{3+}$ [$D = 5.3 \times 10^{-6}$ cm^2/s in 0.09 M phosphate buffer, pH 7.4 (8)].

(b) Information from the Wave Shape

With respect to the heterogeneous electron-transfer process, reversible (nernstian) systems are always at equilibrium. The kinetics are so facile that the interface is governed solely by thermodynamic aspects. Not surprisingly, then, the shapes and positions of reversible waves, which reflect the energy dependence of the electrode reaction, can be exploited to provide thermodynamic properties, such as standard potentials, free energies of reaction, and various equilibrium constants, just as potentiometric measurements can be. On the other hand, reversible systems can offer no kinetic information, because the kinetics are, in effect, transparent.

The wave shape is most easily analyzed in terms of the "wave slope," which is expected to be $2.303RT/nF$ (i.e., $59.1/n$ mV at 25°C) for a reversible system. Larger slopes are generally found for systems that do not have both nernstian heterogeneous kinetics and overall chemical reversibility [Section 5.5.4(b)]; thus the slope can be used to diagnose reversibility. If the system is known to be reversible, the wave slope can be used alternatively to suggest the value of *n*. Often one finds the idea that a wave slope near 60 mV can be taken as an indicator of *both* reversibility and an *n*-value of 1. If the electrode reaction is simple and does not implicate, for example, adsorbed species (Chapter 14), one can accurately draw both conclusions from the wave slope. However, electrode reactions are often subtly complex, and it is safer to determine reversibility by a technique that can view the reaction in both directions, such as cyclic voltammetry (Chapter 6). One can then test the conclusion against the observed wave slope in sampled-current voltammetry, which can also suggest the value of *n*.
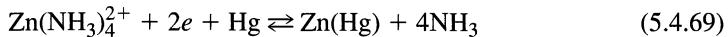
(c) Information from the Wave Position

Because the half-wave potential for a reversible wave is very close to $E^{0'}$, sampled-current voltammetry is readily employed to estimate the formal potentials for chemical systems that have not been previously characterized. It is essential to verify reversibility, because $E_{1/2}$ can otherwise be quite some distance from $E^{0'}$ (see Sections 1.5.2 and 5.5 and Chapter 12).
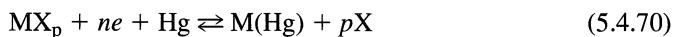
By definition, a formal potential describes the potential of a couple at equilibrium in a system where the oxidized and reduced forms are present at unit formal concentration, even though O and R may be distributed over multiple chemical forms (e.g., as both

members of a conjugate acid-base pair). Formal potentials always manifest activity coefficients. Frequently they also reflect chemical effects, such as complexation or participation in acid-base equilibria. Thus the formal potential can shift systematically as the medium changes. In sampled-current voltammetry the half-wave potential of a recorded wave would shift correspondingly. This phenomenon provides a highly profitable route to chemical information and has been exploited elaborately.

As a first example, let us consider the kinds of information that are contained in the sampled-current voltammogram for the reversible reduction of a complex ion, such as $Zn(NH_3)_4^{2+}$ in an aqueous ammonia buffer at a mercury drop electrode,[8]

$$Zn(NH_3)_4^{2+} + 2e + Hg \rightleftharpoons Zn(Hg) + 4NH_3 \tag{5.4.69}$$

To treat this problem, we derive the *i-E* curve using the simplified approach, as justified in the preceding sections. For generality, the process is represented as

$$MX_p + ne + Hg \rightleftharpoons M(Hg) + pX \tag{5.4.70}$$

where the charges on the metal, M, and the ligands, X, are omitted for simplicity. For $M + ne + Hg \rightleftharpoons M(Hg)$,

$$E = E_M^{0'} + \frac{RT}{nF} \ln \frac{C_M(0, t)}{C_{M(Hg)}(0, t)} \tag{5.4.71}$$

and for $M + pX \rightleftharpoons MX_p$

$$K_c = \frac{C_{MX_p}}{C_M C_X^p} \tag{5.4.72}$$

The presumption of reversibility implies that both of these processes are simultaneously at equilibrium. Substituting (5.4.72) into (5.4.71), we obtain

$$E = E_M^{0'} - \frac{RT}{nF} \ln K_c - \frac{pRT}{nF} \ln C_X(0, t) + \frac{RT}{nF} \ln \frac{C_{MX_p}(0, t)}{C_{M(Hg)}(0, t)} \tag{5.4.73}$$

Let us now add the assumptions (a) that initially $C_{M(Hg)} = 0$, $C_{MX_p} = C_{MX_p}^*$, and $C_X = C_X^*$ and (b) that $C_X^* >> C_{MX_p}^*$. For the specific example involving the zinc ammine complex, the latter condition would be assured by the strength of the buffer, in which ammonia would typically be present at 100 mM to 1 M, very much above the concentration of the complex, which would normally be at 1 mM or even lower. Even though reduction liberates ammonia and oxidation consumes it, the electrode process cannot have an appreciable effect on the value of C_X at the surface, and $C_X(0, t) \approx C_X^*$. Then the following relations apply:

$$i(t) = nFAm_C[C_{MX_p}^* - C_{MX_p}(0, t)] \tag{5.4.74}$$

$$i(t) = nFAm_A C_{M(Hg)}(0, t) \tag{5.4.75}$$

$$i_d(t) = nFAm_C C_{MX_p}^* \tag{5.4.76}$$

or,

$$C_{MX_p}(0, t) = \frac{i_d(t) - i(t)}{nFAm_C} \tag{5.4.77}$$

$$C_{M(Hg)}(0, t) = \frac{i(t)}{nFAm_A} \tag{5.4.78}$$

[8]Zinc deposits in the mercury during the potential steps; thus a question arises about how the initial conditions are restored after each cycle in a sampled-current voltammetric experiment. Because the system is reversible, one can rely on reversed electrolysis at the base potential imposed before each step to restore the initial conditions in each cycle. This point is discussed in Section 7.2.3.

Substituting (5.4.77) and (5.4.78) into (5.4.73), we obtain

$$E = E_{1/2}^C + \frac{RT}{nF} \ln\left[\frac{i_d(t) - i(t)}{i(t)}\right] \tag{5.4.79}$$

with

$$E_{1/2}^C = E_M^{0'} - \frac{RT}{nF} \ln K_c - \frac{pRT}{nF} \ln C_X^* + \frac{RT}{nF} \ln \frac{m_A}{m_C} \tag{5.4.80}$$

It is clear now that the wave *shape* is the same as that for the simple redox process O + $ne \rightleftarrows$ R, but the *location* of the wave on the potential axis depends on K_c and C_X^*, in addition to the formal potential of the metal/amalgam couple. For a given K_c, increased concentrations of the complexing agent shift the wave to more extreme potentials. In the specific chemical example that we have been discussing, the effect of complexation by ammonia is to stabilize Zn(II), that is, to lower the standard free energy of its predominant form. A consequence is that the change in free energy required for reduction of Zn(II) to Zn(Hg) is made larger. Since this added energy must be supplied electrically, the wave is displaced to more negative potentials (Figure 5.4.2). The stronger the binding in the complex (i.e., the larger K_c), the larger the shift from the free metal potential $E_M^{0'}$. Conveniently, K_c can be evaluated from this displacement:

$$E_{1/2}^C - E_M^{0'} = -\frac{RT}{nF} \ln K_c - \frac{RT}{nF} p \ln C_X^* + \frac{RT}{nF} \ln \frac{m_A}{m_C} \tag{5.4.81}$$

In a practice, $E_M^{0'}$ is usually identified with the voltammetric half-wave potential for the metal in a solution free of X, so that

$$E_{1/2}^C - E_{1/2}^M = -\frac{RT}{nF} \ln K_c - \frac{RT}{nF} p \ln C_X^* + \frac{RT}{nF} \ln \frac{m_M}{m_C} \tag{5.4.82}$$

From a plot of $E_{1/2}^C$ *vs.* $\ln C_X^*$ one can determine the stoichiometric number p. Equation 5.4.80 shows that such a plot should have a slope of $-pRT/nF$. Much that is known
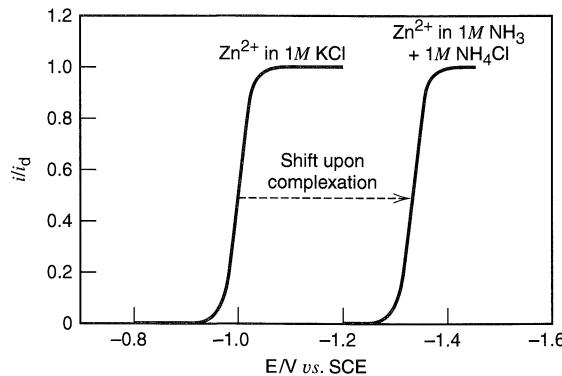
Figure 5.4.2 Shift of a reversible wave upon complexation of the reactant. Left curve is the reduction wave for Zn^{2+} in 1 M KCl at a Hg electrode ($E_{1/2} = -1.00$ V *vs.* SCE). Right curve is for Zn^{2+} in 1 M NH_3 + 1 M NH_4Cl ($E_{1/2} = -1.33$ V *vs.* SCE). Complexation by ammonia lowers the free energy of the oxidized form, so that it is no longer possible to reduce Zn(II) to the amalgam at the potentials of the wave recorded in the absence of ammonia. By applying a more negative potential, the combined free energy of Zn(II) plus the 2e on the electrode is elevated to match that of Zn(Hg) and interconversion between Zn(II) and Zn(Hg) becomes possible.
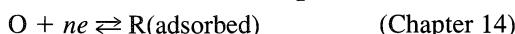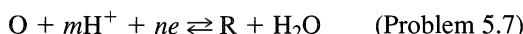
about the stoichiometry and stability constants of metal complexes has been determined from voltammetric measurements of the kind suggested here.

In the example just considered, the important feature was a shift in the wave position caused by selective chemical stabilization of one of the redox forms. In a reversible system the potential axis is a free energy axis, and the magnitude of the shift is a direct measure of the free energy involved in the stabilization. These concepts are quite general and can be used to understand many chemical effects on electrochemical responses. Any equilibrium in which either redox species participates will help to determine the wave position, and changes in concentrations of secondary participants in those equilibria (e.g., ammonia in the example above) will cause an additional shift in the half-wave potential. This state of affairs may seem confusing at first, but the principles are not complicated and are very valuable:
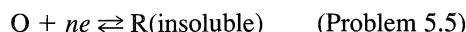
1. If the reduced form of a redox couple is chemically bound in an equilibrium process, then the reduced form has a lowered free energy relative to the situation where the binding is not present. Reduction of the oxidized form consequently becomes energetically easier, and oxidation of the reduced form becomes more difficult. Therefore, the voltammetric wave shifts in a positive direction by an amount reflecting the equilibrium constant (i.e., the change in standard free energy) for the binding process and the concentration of the binding agent.

2. If the oxidized form is chemically bound in an equilibrium process, then the oxidized form is stabilized. It becomes energetically easier to produce this species by oxidation of the reduced form, and it becomes harder to reduce the oxidized form. Accordingly, the voltammetric wave shifts in a negative direction by a degree that depends on the equilibrium constant for the binding process and the concentration of the binding agent. This is the situation that we encountered in the example involving $Zn(NH_3)_4^{2+}$ just above (Figure 5.4.2).

3. Increasing the concentration of the binding agent enlarges the equilibrium fraction of bound species, therefore the increase reinforces the basic effect and enhances the shift in the wave from its original position. We saw this feature in the example given above when we found that there is a progressive negative shift in the voltammetric wave for reduction of Zn(II) as the ammonia concentration is elevated.

4. Secondary equilibria can also affect the wave position in ways that can be interpreted within the framework of these first three principles. For example, the availability of ammonia in the buffer considered above is affected by the pH. If the pH were changed by adding HCl, the concentration of free ammonia would be lessened. Thus the added acid would tend to lower the fraction of complexation and would consequently cause a positive shift in the wave from its position before the change of pH, even though neither H^+ nor Cl^- is involved directly in the electrode process.

5. When both redox forms engage in binding equilibria, both are stabilized relative to the situation in which the binding processes are absent. The effects tend to offset each other. If the free energy of stabilization were exactly the same on both sides of the basic electron-transfer process, there would be no alteration of the free energy required for either oxidation or reduction, and the wave would not shift. If the stabilization of the oxidized form is greater, then the wave shifts in the negative direction, and vice versa.

A very wide variety of binding chemistry can be understood and analyzed within this framework. Obvious by the prior example is complexation of metals. Another case that we will soon encounter is the formation of metal amalgams, which produces useful positive shifts in waves for analytes of interest in polarography (Section 7.1.3). Generally important are acid-base equilibria, which affect many inorganic and organic redox species in protic media. The principles discussed here are also valid in systems involving such diverse phenomena as dimerization, ion pairing, adsorptive binding on a surface, coulombic binding to a polyelectrolyte, and binding to enzymes, antibodies, or DNA.

Detailed treatments like the one developed for the zinc–ammonia system are easily worked out for other types of electrode reactions, including

$$O + mH^+ + ne \rightleftarrows R + H_2O \qquad \text{(Problem 5.7)}$$
$$O + ne \rightleftarrows R(\text{adsorbed}) \qquad \text{(Chapter 14)}$$

Similar treatments can be developed for systems which do not involve the binding phenomena emphasized here, but which differ from the simple process $O + ne \rightleftarrows R$ and yet remain reversible. Such examples include

$$3O + ne \rightleftarrows R \qquad \text{(Problem 5.13)}$$
$$O + ne \rightleftarrows R(\text{insoluble}) \qquad \text{(Problem 5.5)}$$

Details are often available in references on polarography and voltammetry (28–30).

Reversible systems have the advantage of behaving as though all chemical participants are at equilibrium, thus they can be treated by any set of equilibrium relationships linking the species that define the oxidized and reduced states of the system. It is not important to treat the system according to an accurate mechanistic path, because the behavior is controlled entirely by free energy changes between initial and final states, and the mechanism is invisible to the experiment. In the case involving the zinc ammine complex discussed above, we formulated the chemistry as though the complex would become reduced by dissociating to produce Zn(II), which then would undergo conversion to the amalgam. This sequence probably does not describe the events in the real electrode process, but it offers a convenient thermodynamic cycle based on quantities that we can measure easily in other experiments, or perhaps even find in the literature.

In practical chemical analysis, one can obviously use half-wave potentials to identify the species giving rise to the observed waves; however the foregoing paragraphs illustrate the fact that the wave for a given species, such as Zn(II) can be found in different positions under different conditions. Thus it is important to control the analytical conditions, e.g. by employing a medium of controlled pH, buffer strength, and complexing characteristics. The analytical application of sampled current voltammetry is discussed more fully in Sections 7.1.3 and 7.3.6.

(d) Information from Change in Diffusion Current

For many processes D for MX_p is not very different from that of M, so that i_d, as given in (5.4.76) is about the same as that before complexation, as in the example in Figure 5.4.2. However if the ligand, X, is very large, as might occur when X is DNA, a protein, or a polymer, then the size of the species after complexation will be much larger than that of M, and there will be a significant decrease in D and in i_d. Under these conditions the change in i_d with addition of X can be used to obtain information about K_c and p. An investigation of this type was based on the interaction of $Co(\text{phen})_3^{3+}$ with double-strand DNA (31), where phen is 1,10-phenanthroline. The diffusion coefficient decreased from 3.7×10^{-6} cm^2/s for the free Co species to 2.6×10^{-7} cm^2/s upon binding to DNA.

▶ **5.5 SAMPLED-CURRENT VOLTAMMETRY FOR QUASIREVERSIBLE AND IRREVERSIBLE ELECTRODE REACTIONS**

In this section, we will treat the one-step, one-electron reaction O + $e \rightleftarrows$ R using the general (quasireversible) *i-E* characteristic. In contrast with the reversible cases just examined, the interfacial electron-transfer kinetics in the systems considered here are not so fast as to be transparent. Thus kinetic parameters such as k_f, k_b, k^0 and α influence the responses to potential steps and, as a consequence, can often be evaluated from those responses. The focus in this section is on ways to determine such kinetic information from step experiments, including sampled-current voltammetry. As in the treatment of reversible cases, the discussion will be developed first for early transients, then it will be redeveloped for the steady-state.

5.5.1 Responses Based on Linear Diffusion at a Planar Electrode

(a) Current-Time Behavior

The treatment of semi-infinite linear diffusion for the case where the current is governed by both mass transfer and charge-transfer kinetics begins according to the pattern used in Section 5.4.1. The diffusion equations for O and R are needed, as are the initial conditions, the semi-infinite conditions, and the flux balance. As we noted there, these lead to

$$\overline{C}_O(x, s) = \frac{C_O^*}{s} + A(s)e^{-(s/D_O)^{1/2}x} \tag{5.5.1}$$

$$\overline{C}_R(x, s) = -\xi A(s)e^{-(s/D_R)^{1/2}x} \tag{5.5.2}$$

where $\xi = (D_O/D_R)^{1/2}$.

For the quasireversible one-step, one-electron case, we can evaluate $A(s)$ by applying the condition:

$$\frac{i}{FA} = D_O\left(\frac{\partial C_O(x, t)}{\partial x}\right)_{x=0} = k_f C_O(0, t) - k_b C_R(0, t) \tag{5.5.3}$$

where

$$k_f = k^0 e^{-\alpha f(E-E^{0'})} \tag{5.5.4}$$

and

$$k_b = k^0 e^{(1-\alpha)f(E-E^{0'})} \tag{5.5.5}$$

with $f = F/RT$.

The transform of (5.5.3) is

$$D_O\left(\frac{\partial \overline{C}_O(x, s)}{\partial x}\right)_{x=0} = k_f \overline{C}_O(0, s) - k_b \overline{C}_R(0, s) \tag{5.5.6}$$

and, by substitution from (5.5.1) and (5.5.2),

$$A(s) = -\frac{k_f}{D_O^{1/2}} \frac{C_O^*}{s(H + s^{1/2})} \tag{5.5.7}$$

where

$$H = \frac{k_f}{D_O^{1/2}} + \frac{k_b}{D_R^{1/2}} \tag{5.5.8}$$

Then,

$$\overline{C}_O(x, s) = \frac{C_O^*}{s} - \frac{k_f C_O^* e^{-(s/D_O)^{1/2}x}}{D_O^{1/2} s(H + s^{1/2})} \tag{5.5.9}$$

From (5.5.3)

$$\bar{i}(s) = FAD_O \left[\frac{\partial \overline{C}_O(x, s)}{\partial x} \right]_{x=0} = \frac{FAk_f C_O^*}{s^{1/2}(H + s^{1/2})} \tag{5.5.10}$$

or, taking the inverse transform,

$$\boxed{i(t) = FAk_f C_O^* \exp(H^2 t)\, \mathrm{erfc}(Ht^{1/2})} \tag{5.5.11}$$

For the case when R is initially present at C_R^*, equation 5.5.11 becomes

$$\boxed{i(t) = FA(k_f C_O^* - k_b C_R^*) \exp(H^2 t)\, \mathrm{erfc}(Ht^{1/2})} \tag{5.5.12}$$

At a given step potential, k_f, k_b, and H are constants. The product $\exp(x^2)\mathrm{erfc}(x)$ is unity for $x = 0$, but falls monotonically toward zero as x becomes large; thus the current-time curve has the shape shown in Figure 5.5.1. Note that the kinetics limit the current at $t = 0$ to a finite value proportional to k_f (with R initially absent). In principle, k_f can be evaluated from the faradaic current at $t = 0$. Since a charging current also exists in the moments after the step is applied, the faradaic component at $t = 0$ typically would be determined by extrapolation from data taken after the charging current has decayed [see Sections 1.4.2 and 7.2.3(c)].

(b) Alternate Expression in Terms of η

If both O and R are present in the bulk, so that an equilibrium potential exists, one can describe the effect of potential on the current-time curve in terms of the overpotential, η. An alternate expression for (5.5.12) can be given by noting that

$$k_f C_O^* - k_b C_R^* = k^0 \left[C_O^* e^{-\alpha f(E-E^{0'})} - C_R^* e^{(1-\alpha)f(E-E^{0'})} \right] \tag{5.5.13}$$

or, by substituting for k^0 in terms of i_0 by (3.4.11),

$$k_f C_O^* - k_b C_R^* = \frac{i_0}{FA} \left[e^{-\alpha f\eta} - e^{(1-\alpha)f\eta} \right] \tag{5.5.14}$$
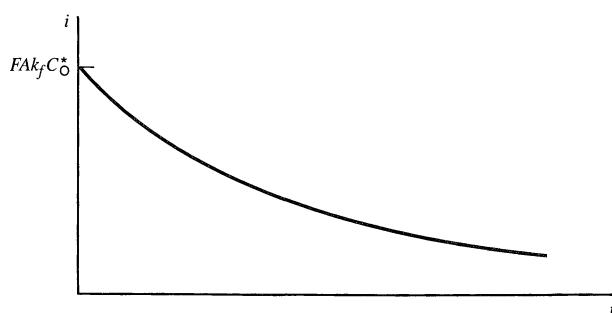
Figure 5.5.1 Current decay after the application of a step to a potential where species O is reduced with quasireversible kinetics.

Therefore, (5.5.12) may be written

$$i = i_0 \left[e^{-\alpha f \eta} - e^{(1-\alpha)f \eta} \right] \exp(H^2 t) \, \text{erfc}(Ht^{1/2}) \qquad (5.5.15)$$

By similar substitutions into the expression for H, one has

$$H = \frac{i_0}{FA} \left[\frac{e^{-\alpha f \eta}}{C_O^* D_O^{1/2}} - \frac{e^{(1-\alpha)f \eta}}{C_R^* D_R^{1/2}} \right] \qquad (5.5.16)$$

Note that the form of (5.5.12) and (5.5.15) is

$$i = [i \text{ in the absence of mass-transfer effects}] \times [f(H, t)]$$

where $f(H, t)$ accounts for the effects of mass transfer.

(c) Linearized Current-Time Curve

For small values of $Ht^{1/2}$, the factor $\exp(H^2 t)\text{erfc}(Ht^{1/2})$ can be linearized:

$$e^{x^2} \, \text{erfc}(x) \simeq 1 - \frac{2x}{\pi^{1/2}} \qquad (5.5.17)$$

Then, (5.5.11) becomes

$$i = FAk_f C_O^* \left(1 - \frac{2Ht^{1/2}}{\pi^{1/2}} \right) \qquad (5.5.18)$$

In a system for which R is initially absent, one can apply a step to the potential region at the foot of the wave (where k_f, hence H, is still small), then plot i vs. $t^{1/2}$ and extrapolate the linear plot to $t = 0$ to obtain k_f from the intercept.

Likewise, (5.5.15) can be written

$$i = i_0 \left[e^{-\alpha f \eta} - e^{(1-\alpha)f \eta} \right] \left(1 - \frac{2Ht^{1/2}}{\pi^{1/2}} \right) \qquad (5.5.19)$$

This relation applies only to a system containing both O and R initially, so that E_{eq} is defined. Stepping from E_{eq} to another potential involves a step of magnitude η; thus a plot of i vs. $t^{1/2}$ has as its intercept the kinetically controlled current free of mass-transfer effects. A plot of $i_{t=0}$ vs. η can then be used to obtain i_0.

For small values of η, the linearized i-η characteristic, (3.4.12), can be used, so that (5.5.15) becomes

$$i = -\frac{Fi_0 \eta}{RT} \exp(H^2 t) \, \text{erfc}(Ht^{1/2}) \qquad (5.5.20)$$

Then for small η and small $Ht^{1/2}$ one has a "completely linearized" form:

$$i = -\frac{Fi_0 \eta}{RT} \left(1 - \frac{2Ht^{1/2}}{\pi^{1/2}} \right) \qquad (5.5.21)$$

(d) Sampled-Current Voltammetry

In preparation for deriving the shape of a sampled-current voltammogram, let us return to (5.5.11), which is the full current-time expression for the case where only species O is present in the bulk. Recognizing that $k_b/k_f = \theta = \exp[f(E - E^{0'})]$, we find that

$$H = \frac{k_f}{D_O^{1/2}} (1 + \xi \theta) \qquad (5.5.22)$$

and that (5.5.11) can be rephrased as

$$i = \frac{FAD_O^{1/2}C_O^*}{\pi^{1/2}t^{1/2}(1 + \xi\theta)} [\pi^{1/2}Ht^{1/2} \exp(H^2t) \, \text{erfc} \, (Ht^{1/2})] \qquad (5.5.23)$$

Since semi-infinite linear diffusion applies, the diffusion-limited current is the Cottrell current, which is easily recognized in the factor preceding the brackets. Thus, we can simplify (5.5.23) to

$$\boxed{i = \frac{i_d}{(1 + \xi\theta)} F_1(\lambda)} \qquad (5.5.24)$$

where

$$F_1(\lambda) = \pi^{1/2} \lambda \exp(\lambda^2)\text{erfc}(\lambda) \qquad (5.5.25)$$

and

$$\lambda = Ht^{1/2} = \frac{k_f t^{1/2}}{D_O^{1/2}} (1 + \xi\theta) \qquad (5.5.26)$$

Equation 5.5.24 is a very compact representation of the way in which the current in a step experiment depends on potential and time, and it holds for all kinetic regimes: reversible, quasireversible, and totally irreversible. The function $F_1(\lambda)$ manifests the kinetic effects on the current in terms of the dimensionless parameter λ, which can be readily shown to compare the maximum current supportable by the reductive kinetic process at a given step potential ($FAk_f C_O^*$ vs. the maximum current supportable by diffusion at that potential [$i_d/(1+\xi\theta)$]. Thus a small value of λ implies a strong kinetic influence on the current, and a large value of λ corresponds to a situation where the kinetics are facile and the response is controlled by diffusion. The function $F_1(\lambda)$ rises monotonically from a value of zero at $\lambda = 0$ toward an asymptote of unity as λ becomes large (Figure 5.5.2).

Simpler forms of (5.5.24) are used for the reversible and totally irreversible limits. For example, consider (5.4.17), which we derived as a description of the current-time curve following an arbitrary step potential in a reversible system. That same relationship is available from (5.5.24) simply by recognizing that with reversible kinetics λ is very large, so that $F_1(\lambda)$ is always unity. The totally irreversible limit will be considered separately in Section 5.5.1(e).
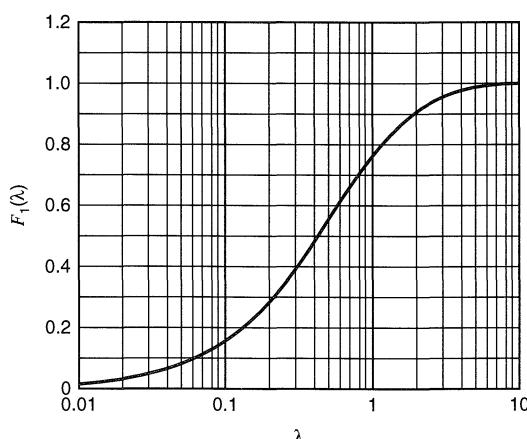
Figure 5.5.2 General kinetic function for chronoamperometry and sampled-current voltammetry.
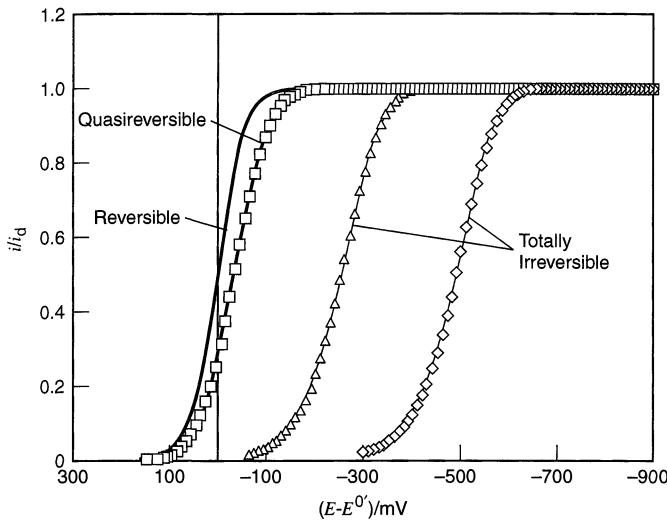
Figure 5.5.3 Sampled-current voltammograms for various kinetic regimes. Curves are calculated from (5.5.24) assuming Butler–Volmer kinetics with $\alpha = 0.5$ and $\tau = 1$ s, $D_O = D_R = 1 \times 10^{-5}$ cm^2/s. From left to right the values of k^0 are 10, 1×10^{-3}, 1×10^{-5}, and 1×10^{-7} cm/s.

So far, it has been most convenient to think of (5.2.24) as describing the current-time response following a potential step; however it also describes the current-potential curve in sampled-current voltammetry, just as we understood (5.4.17) to do for reversible systems. At a fixed sampling time τ, λ becomes $(k_f \tau^{1/2}/D_O^{1/2})(1 + \xi\theta)$, which is a function only of potential among the variables that change during a voltammetric run. At very positive potentials relative to $E^{0'}$, θ is very large, and $i = 0$. At very negative potentials, $\theta \rightarrow 0$ but k_f becomes very large; thus $F_1(\lambda)$ approaches unity, and $i \approx i_d$. From these simple considerations, we expect the sampled-current voltammogram to have a sigmoidal shape generally similar to that found in the reversible case. Figure 5.5.3, which contains several voltammograms corresponding to different kinetic regimes, bears out this expectation.

For very facile kinetics, corresponding to large k^0, the wave has the reversible shape, and the half-wave potential is near $E^{0'}$. (In Figure 5.5.3, where $D_O = D_R$, $E_{1/2} = E^{0'}$ exactly.) For smaller values of k^0, the kinetics must be driven, and the wave is displaced toward *more extreme* potentials (i.e., in the negative direction if the wave is for a reduction and in the positive direction for an oxidative wave). In addition, the wave is broadened by kinetic effects, as one can see clearly in Figure 5.5.3. The displacement is an overpotential and is proportional to the required kinetic activation. For small k^0, it can be hundreds of millivolts or even volts. Even so, k_f is activated exponentially with potential and can become large enough at sufficiently negative potentials to handle the diffusion-limited flux of electroactive species; thus the wave eventually shows a plateau at i_d, unless the background limit of the system is reached first.

(e) Totally Irreversible Reactions

The very displacement in potential that activates k_f also suppresses k_b; hence the backward component of the electrode reaction becomes progressively less important at potentials further to the negative side of $E^{0'}$. If k^0 is very small, a sizable activation of k_f is required for all points where appreciable current flows, and k_b is suppressed consistently to a negligible level. The irreversible regime is defined by the condition that $k_b/k_f \approx 0$ (i.e., $\theta \approx 0$) over the whole of the voltammetric wave. Then (5.5.11) becomes

$$i = FAk_f C_O^* \exp\left(\frac{k_f^2 t}{D_O}\right) \operatorname{erfc}\left(\frac{k_f t^{1/2}}{D_O^{1/2}}\right) \tag{5.5.27}$$

and (5.5.24) has the limiting form

$$\boxed{\frac{i}{i_d} = F_1(\lambda) = \pi^{1/2} \lambda \exp(\lambda^2) \, \mathrm{erfc}(\lambda)} \tag{5.5.28}$$

where λ has become $k_f t^{1/2}/D_O^{1/2}$.

The half-wave potential for an irreversible wave occurs where $F_1(\lambda) = 0.5$, which is where $\lambda = 0.433$. If k_f follows the usual exponential form and $t = \tau$, then

$$\frac{k^0 \tau^{1/2}}{D_O^{1/2}} \exp\left[-\alpha f(E_{1/2} - E^{0'})\right] = 0.433 \tag{5.5.29}$$

By taking logarithms and rearranging, one obtains

$$E_{1/2} = E^{0'} + \frac{RT}{\alpha F} \ln\left(\frac{2.31 k^0 \tau^{1/2}}{D_O^{1/2}}\right) \tag{5.5.30}$$

where the second term is the displacement required to activate the kinetics. Obviously (5.5.30) provides a simple way to evaluate k^0 if α is otherwise known.

(f) Kinetic Regimes

Conditions defining the three kinetic regimes can be distinguished in more precise terms by focusing on the particular value of λ at $E^{0'}$, which we will call λ^0. Since $k_f = k_b = k^0$ and $\theta = 1$ at $E^{0'}$, $\lambda^0 = (1 + \xi)k^0 \tau^{1/2}/D_O^{1/2}$, which can be taken for our purpose as $2k^0 \tau^{1/2}/D_O^{1/2}$. It is useful to understand λ^0 as a comparator of the intrinsic abilities of kinetics and diffusion to support a current. The greatest possible forward reaction rate at any potential is $k_f C_O^*$, corresponding to the absence of depletion at the electrode surface. At $E = E^{0'}$, this is $k^0 C_O^*$ and the resulting current is $FAk^0 C_O^*$. The greatest current supportable by diffusion at sampling time τ is, of course, the Cottrell current. The ratio of the two currents is $\pi^{1/2} k^0 \tau^{1/2}/D_O^{1/2}$, or $(\pi^{1/2}/2)\lambda^0$.

If a system is to appear reversible, λ^0 must be sufficiently large that $F_1(\lambda)$ is essentially unity at potentials neighboring $E^{0'}$. For $\lambda^0 > 2$ (or $k^0 \tau^{1/2}/D_O^{1/2} > 1$), $F_1(\lambda^0)$ exceeds 0.90, a value high enough to assure reversible behavior within practical experimental limits. Smaller values of λ^0 will produce measurable kinetic effects in the voltammetry. Thus we can set $\lambda^0 = 2$ as the boundary between the reversible and quasireversible regimes, although we also recognize that the delineation is not sharp and that it depends operationally on the precision of experimental measurements.

Total irreversibility requires that $k_b/k_f \approx 0$ ($\theta \approx 0$) at all potentials where the current is measurably above the baseline. Because θ is also $\exp[f(E - E^{0'})]$, this condition simply implies that the rising portion of the wave be significantly displaced from $E^{0'}$ in the negative direction. If $E_{1/2} - E^{0'}$ is at least as negative as $-4.6RT/F$, then k_b/k_f will be no more than 0.01 at $E_{1/2}$, and the condition for total irreversibility will be satisfied. The implication is that the second term on the right side of (5.5.30) is more negative than $-4.6RT/nF$, and by rearrangement one finds that $\log \lambda^0 < -2\alpha + \log(2/2.31)$. The final term can be neglected for our purpose here, so the condition for total irreversibility becomes $\log \lambda^0 < -2\alpha$. For $\alpha = 0.5$, λ^0 must be less than 0.1.

In the middle ground, where $10^{-2\alpha} \leq \lambda^0 \leq 2$, the system is quasireversible, and one cannot simplify (5.5.24) as a descriptor of either current decay or voltammetric wave shape.

It is important to recognize that the kinetic regime, determined by λ^0, depends not only on the intrinsic kinetic characteristics of the electrode reaction, but also on the experimental conditions. The time scale, expressed as the sampling time τ in voltammetry, is a particularly important experimental variable and can be used to change the kinetic regime for a given system. For example, suppose one has an electrode reaction with the following (not unusual) properties: $k^0 = 10^{-2}$ cm/s, $\alpha = 0.5$, and $D_O = D_R = 10^{-5}$ cm^2/s. For sam-

pling times longer than 1 s, $\lambda^0 > 2$ and the voltammetry would be reversible. Sampling times between 1 s and 250 μs correspond to $2 \geq \lambda^0 \geq 0.1$ and would produce quasireversible behavior. Values of τ smaller than 250 μs would produce total irreversibility.

5.5.2 General Current-Time Behavior at a Spherical Electrode

As a prelude to a treatment of steady-state voltammetry in quasireversible and totally irreversible systems, it is useful to develop a very general description of current flow in a step experiment at a spherical electrode. In Section 5.4.2(a) the basic diffusion problem was outlined, and the following relationships arose without invoking a particular kinetic condition.

$$\overline{C}_O(r, s) = \frac{C_O^*}{s} + \frac{A(s)}{r} e^{-(s/D_O)^{1/2}r} \tag{5.5.31}$$

$$\overline{C}_R(r, s) = -\frac{A(s)\xi^2 \gamma}{r} e^{-(s/D_O)^{1/2}r_0} e^{-(s/D_R)^{1/2}(r-r_0)} \tag{5.5.32}$$

where $\xi = (D_O/D_R)^{1/2}$ and

$$\gamma = \frac{1 + r_0(s/D_O)^{1/2}}{1 + r_0(s/D_R)^{1/2}} \tag{5.5.33}$$

Now we are interested in determining the function $A(s)$ for a step experiment to an arbitrary potential, but where the electron-transfer kinetics are described explicitly in terms of k_f and k_b. By so doing, we will be able to use the results to define current-time responses for any sort of kinetic regime, whether reversible, quasireversible, or irreversible. The problem is developed just as in the sequence from (5.5.3) to (5.5.9), but in this instance, the results are

$$\overline{C}_O(r, s) = \frac{C_O^*}{s} - \frac{C_O^* r_0}{rs} \left[\frac{\dfrac{k_f r_0}{D_O}}{r_0 \left(\dfrac{s}{D_O}\right)^{1/2} + 1 + \dfrac{k_f r_0}{D_O} + \dfrac{k_b r_0 \xi^2 \gamma}{D_O}} \right] e^{-(s/D_O)^{1/2}(r-r_0)} \tag{5.5.34}$$

$$\overline{C}_R(r, s) = \frac{C_O^* r_0 \xi^2 \gamma}{rs} \left[\frac{\dfrac{k_f r_0}{D_O}}{r_0 \left(\dfrac{s}{D_O}\right)^{1/2} + 1 + \dfrac{k_f r_0}{D_O} + \dfrac{k_b r_0 \xi^2 \gamma}{D_O}} \right] e^{-(s/D_R)^{1/2}(r-r_0)} \tag{5.5.35}$$

As always, the current is proportional to the difference between the rates of the forward and backward reactions. In transform space,

$$\frac{\overline{i}(s)}{FA} = k_f \overline{C}_O(r_0, s) - k_b \overline{C}_R(r_0, s) \tag{5.5.36}$$

By substitution from (5.5.34) and (5.5.35) and algebraic rearrangement, one obtains the following general expression for the current transform:

$$\overline{i}(s) = \frac{FAD_O C_O^*}{r_0 s} \left[\frac{\delta + 1}{\left(\dfrac{\delta + 1}{\kappa}\right) + (1 + \xi^2 \gamma \theta)} \right] \tag{5.5.37}$$

where δ and κ are two important dimensionless groups:

$$\delta = r_0 \left(\frac{s}{D_O}\right)^{1/2} \tag{5.5.38}$$

$$\kappa = \frac{r_0 k_f}{D_O} \tag{5.5.39}$$

Although the development of (5.5.37) from (5.5.34)–(5.5.36) is not obvious, it is straightforward. The steps are left to Problem 5.8(a). As one proceeds, it is useful to recognize that θ is not only $\exp[f(E-E^{0'})]$, but also k_b/k_f. Also, one can see by inspection of (5.5.33) that

$$\gamma = \frac{\delta + 1}{\xi\delta + 1} \tag{5.5.40}$$

Equation 5.5.37 is powerful because it compactly describes the current response *for all types of electrode kinetics* and *for all step potentials at any electrode* where *either linear diffusion or spherical diffusion* hold. The principal restriction is that it describes only situations where R is initially absent, but the following extension, covering the case where both O and R exist in the bulk, is readily derived by the same method [Problem 5.8(b)]:

$$\bar{i}(s) = \frac{nFAD_O(C_O^* - \theta C_R^*)}{r_0 s} \left[\frac{\delta + 1}{\left(\dfrac{\delta + 1}{\kappa}\right) + (1 + \xi^2\gamma\theta)}\right] \tag{5.5.41}$$

It is easy to see that (5.5.37) is the special case of (5.5.41) for the situation where $C_R^* = 0$.

In other words, all of the current-time relationships that we have so far considered in this chapter are special-case inverse transformations of (5.5.41). Because (5.5.37) and (5.5.41) contain the transform variable s not only explicitly, but also implicitly in δ and γ, a general analytical inversion is beyond our reach; however one can readily derive the special cases using either (5.5.37) or (5.5.41) as the starting point. The trick is to recognize δ, κ, and θ as manifesting comparisons that divide important experimental regimes.

In Section 5.4.2(a) we developed the idea that δ expresses the ratio of the electrode's radius of curvature to the diffusion-layer thickness. When $\delta \gg 1$, the diffusion layer is small compared to r_0, and the system is in the early transient regime where semi-infinite linear diffusion applies. When $\delta \ll 1$, the diffusion layer is much larger than r_0, and the system is in the steady-state regime.

We now recognize κ as the ratio of k_f to the steady-state mass-transfer coefficient $m_O = D_O/r_0$. When $\kappa \ll 1$, the interfacial rate constant for reduction is very small compared to the effective mass-transfer rate constant, so that diffusion imposes no limitation on the current. At the opposite limit, where $\kappa \gg 1$, the rate constant for interfacial electron transfer greatly exceeds the effective rate constant for mass transfer, but the interpretation of this fact depends on whether k_b is also large.[9]

---

[9]Note that κ is also the ratio of the largest current supportable by the kinetics divided by the largest current supportable by diffusion; thus it is analogous to the parameter λ used to characterize kinetic effects on systems based on semi-infinite linear diffusion.

As a first example of the way to develop special cases from (5.5.37), let us consider the limit of diffusion control. For this case, k_f is very large, so $\kappa \to \infty$ and $\theta = k_b/k_f \to 0$. Thus,

$$\bar{i}_d(s) = \frac{FAD_O C_O^*}{r_0 s}(\delta + 1) \tag{5.5.42}$$

For the early transient regime, $\delta \gg 1$ [see Section 5.4.2(a)], and (5.5.42) becomes (5.2.10), which is inverted to the Cottrell equation, (5.2.11). For the steady-state regime, $\delta \ll 1$ and (5.5.42) collapses to a form that is easily inverted to the relationship for the steady-state limiting current (5.3.2). Actually, (5.5.42) can be inverted directly to the full diffusion-controlled current-time relationship at a sphere, (5.2.18). All of these relationships also hold for a hemisphere of radius r_0, which has half of both the area and the current for the corresponding sphere.

It is similarly easy to derive other prior results from (5.5.41), including the early transient and steady-state responses for a reversible system [(5.4.17) and (5.4.54)] and the early transient responses for systems with quasireversible or irreversible kinetics [(5.5.11), (5.5.12), and (5.5.28)]. The details are left to Problem 5.8(c).

5.5.3 Steady-state Voltammetry at a UME

Our concern now is with steady-state responses in systems with quasireversible or irreversible electron-transfer kinetics. We can limit (5.5.37) to the steady state simply by imposing the condition that $\delta \ll 1$, which implies that $\gamma \to 1$ and

$$\bar{i}(s) = \frac{FAD_O C_O^*}{r_0 s}\left[\frac{1}{\left(\frac{1}{\kappa}\right) + (1 + \xi^2\theta)}\right] \tag{5.5.43}$$

Since nothing in the brackets depends on s, the current is readily obtained by inversion. With rearrangement the result is:

$$i = \frac{FAD_O C_O^*}{r_0}\left[\frac{\kappa}{1 + \kappa(1 + \xi^2\theta)}\right] \tag{5.5.44}$$

which describes the steady-state current for any kinetic regime at a sphere or hemisphere.

At very negative potentials relative to $E^{0'}$, θ approaches zero and κ becomes very large, so that the limiting current is given by

$$i_d = \frac{FAD_O C_O^*}{r_0} \tag{5.5.45}$$

as we have already seen. By dividing (5.5.44) with (5.5.45), one has

$$\frac{i}{i_d} = \frac{\kappa}{1 + \kappa(1 + \xi^2\theta)} \tag{5.5.46}$$

which compactly describes all steady-state voltammetric waves at spherical electrodes.

One can easily see that as the potential is changed from values far positive of $E^{0'}$ to values far negative, i/i_d goes from zero to unity. Thus a sigmoidal curve is found generally in steady-state voltammetry. Figure 5.5.4 is a display of voltammograms corresponding to the three kinetic regimes. For the reversible case, $\kappa \to \infty$ at all potentials, and (5.5.46)
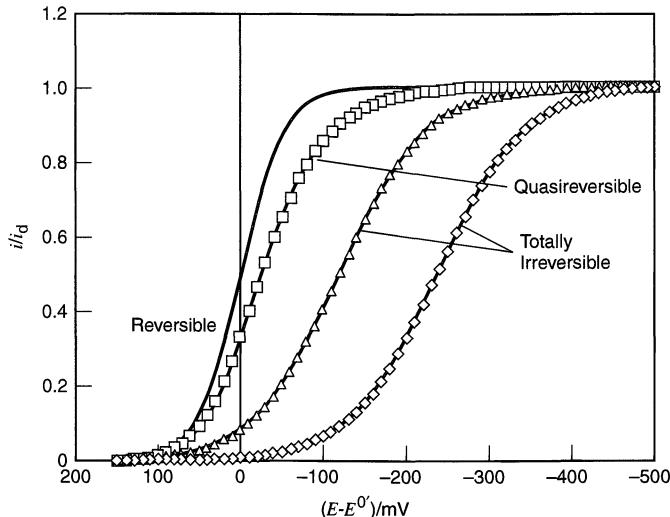
Figure 5.5.4 Steady-state voltammograms at a spherical or hemispherical electrode for various kinetic regimes. Curves are calculated from (5.5.46) assuming Butler–Volmer kinetics with $\alpha = 0.5$, and $r_0 = 5$ μm, $D_O = D_R = 1 \times 10^{-5}$ cm^2/s. From left to right the values of k^0 are 2, 2×10^{-2}, 2×10^{-3}, and 2×10^{-4} cm/s.

collapses to (5.4.54), represented as the leftmost curve in Figure 5.5.4. Smaller values of k^0 cause a broadening and a displacement of the wave toward more extreme potentials, just as for waves based on sampled transients.

(a) Total Irreversibility

In Section 5.5.1(e), we determined that the criterion for total irreversibility is that $\theta \approx 0$ over all points on the wave that are measurably above the baseline. Thus, the limiting form of (5.5.46) is

$$\frac{i}{i_d} = \frac{\kappa}{1 + \kappa} \tag{5.5.47}$$

One can substitute for k_f and rearrange (5.5.47) to the form

$$E = E^{0\prime} + \frac{RT}{\alpha F} \ln\left(\frac{r_0 k^0}{D_O}\right) + \frac{RT}{\alpha F} \ln\left(\frac{i_d - i}{i}\right) \tag{5.5.48}$$

which has a half-wave potential given by

$$E_{1/2} = E^{0\prime} + \frac{RT}{\alpha F} \ln\left(\frac{r_0 k^0}{D_O}\right) \tag{5.5.49}$$

so that a standard plot of E vs. $\log[(i_d - i)/i]$ is expected to be linear with a slope of $2.303RT/\alpha F$ (i.e., $59.1/\alpha$ mV at 25°C) and an intercept of $E_{1/2}$. From the slope and intercept, one can obtain α and k^0 straightforwardly.

(b) Kinetic Regimes

We can define the boundaries between the kinetic regimes in steady-state voltammetry in essentially the manner used in Section 5.5.1(f), but the focus now must be placed on the value of the parameter κ at $E^{0\prime}$, which is $r_0 k^0/D_O$. This quantity, designated as κ^0, has a significance for steady-state voltammetry essentially the same as that of λ^0 for voltammetry based on semi-infinite linear diffusion. Even though currents are small at UMEs, current densities can be extremely high because of the very high mass transfer rates that can apply at UMEs. This is the aspect of their nature that provides access to heterogeneous rate constants of the most facile known reactions.

If a system is to appear reversible, then κ at potentials in the neighborhood of $E^{0'}$ must be large enough that (5.5.46) converges to (5.4.54). This will be true within the limits of experimental precision if $\kappa^0 > 10$.

As argued in Section 5.5.1(f), total irreversibility applies when the wave is displaced negatively to such a degree that $\theta \approx 0$ across the whole wave. If $E_{1/2} - E^{0'}$ is at least as negative as $-4.6RT/F$, that condition will be satisfied. Thus the second term in (5.5.49) must be more negative than $-4.6RT/F$, implying that $\log \kappa^0 < -2\alpha$.

The quasireversible regime lies between these boundaries, in the range $10^{-2\alpha} \leq \kappa^0 \leq 10$.

(c) Other Electrode Shapes

The foregoing discussion is rigorous only for spherical and hemispherical electrodes, which are called *uniformly accessible* because there are no differences in mass transfer over the electrode surface. Steady-state voltammetry can be carried out readily at other UMEs, but for quasireversible and totally irreversible systems, the results are affected by the nonuniformity in the flux at different points on the electrode surface. At a disk UME, for example, mass transfer can support a flux to points near the edge that is much higher than to points near the center; thus the kinetics must be activated more strongly to support the diffusion-limited current at the edge than in the center. The recorded voltammogram would represent an average of behavior, with contributions from different points weighted by their diffusion-limited fluxes.

There is a significant contrast here with Section 5.4.2(e), where we found that the results for reversible systems observed at spherical electrodes could be extended generally to electrodes of other shapes. This is true for a reversible system because the potential controls the surface concentration of the electroactive species directly and keeps it uniform across the surface. Mass transfer to each point, and hence the current, is consequently driven in a uniform way over the electrode surface. For quasireversible and irreversible systems, the potential controls rate constants, rather than surface concentrations, uniformly across the surface. The concentrations become defined indirectly by the local balance of interfacial electron-transfer rates and mass-transfer rates. When the electrode surface is not uniformly accessible, this balance varies over the surface in a way that is idiosyncratic to the geometry. This is a complicated situation that can be handled in a general way (i.e., for an arbitrary shape) by simulation. For UME disks, however, the geometric problem can be simplified by symmetry, and results exist in the literature to facilitate the quantitative analysis of voltammograms (12).

5.5.4 Applications of Irreversible *i-E* Curves

(a) Information from the Wave Height

Exactly as in the reversible case, the plateau of an irreversible or quasireversible wave is controlled entirely by diffusion and can be used to determine any variable that contributes to i_d. The most important applications involve the evaluation of C^*, but it is sometimes useful to determine n, A, D, or r_0 from i_d. Section 5.4.4(a), which covers these ideas, is wholly applicable to irreversible and quasireversible systems.

(b) Information from the Wave Shape and Position
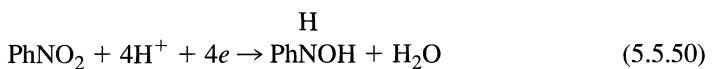
When the wave is not reversible, the half-wave potential is not a good estimate of the formal potential and cannot be used directly to determine thermodynamic quantities in the manner discussed in Section 5.4.4. In the case of a totally irreversible system, the wave shape and position can furnish only kinetic information, but quasireversible waves can

sometimes provide approximate values of $E^{0'}$ in addition to kinetic parameters. Because the interpretation and information content of a wave's shape and position depends on the kinetic regime, it is essential to be able to diagnose the regime confidently.

Wave shape is a useful indicator toward that end, especially if the n-value is known. One can characterize reversibility either by the slope of a plot of E vs. $\log[(i_d - i)/i]$ (the "wave slope") or by the difference $|E_{3/4} - E_{1/4}|$ (the Tomeš criterion). Table 5.5.1 provides a summary of expectations for sampled-current voltammetry based either on early transients or on the steady state in all three kinetic regimes. For reversible systems, these figures of merit are near $60/n$ mV at ambient temperatures. Significantly larger figures often signal a degree of irreversibility. For example, if the one-step, one-electron mechanism applies and α is between 0.3 and 0.7 (commonly true), then a totally irreversible system would show $|E_{3/4} - E_{1/4}|$ between 65 and 150 mV. Except when α is toward the upper end of the range, such behavior would represent a clear departure from reversibility. Similar effects are seen in wave slopes; however it is not always easy to analyze them precisely, because wave-slope plots are slightly nonlinear for quasireversible voltammograms and for totally irreversible voltammograms based on early transients. The advantage of the Tomeš criterion is that it is always applicable.

If the electrode process is more complex than the one-step, one-electron model (e.g., $n > 1$ with a rate-determining heterogeneous electron transfer), then the wave shape can become extremely difficult to analyze. An exception is the case where the initial step is the rate-determining electron transfer [Section 3.5.4(b)], in which case all that has been discussed for totally irreversible systems also applies, but with the current multiplied consistently by n.

Although a large wave slope is a clear indicator that a system is not showing clean reversible behavior, it does not necessarily imply that one has an electrode process controlled by the kinetics of electron transfer. Electrode reactions frequently include purely chemical processes away from the electrode surface. A system involving "chemical complications" of this kind can show a wave shape essentially identical with that expected for a simple electron transfer in the totally irreversible regime. For example, the reduction of nitrobenzene in aqueous solutions can lead, depending on the pH, to phenylhydroxylamine (32):

$$\text{H}$$
$$\text{PhNO}_2 + 4\text{H}^+ + 4e \rightarrow \text{PhNOH} + \text{H}_2\text{O} \tag{5.5.50}$$

However, the first electron-transfer step

$$\text{PhNO}_2 + e \rightarrow \text{PhNO}_2^{\cdot-} \tag{5.5.51}$$

is intrinsically quite rapid, as found from measurements in nonaqueous solvents, such as DMF (32). The irreversibility observed in aqueous solutions arises because of the series of protonations and electron transfers following the first electron addition. If one

TABLE 5.5.1 Wave Shape Characteristics at 25°C in Sampled-Current Voltammetry

Kinetic Regime	Linear Diffusion		Steady State	
	Wave Slope/mV	$\|E_{3/4} - E_{1/4}\|$/mV	Wave Slope/mV	$\|E_{3/4} - E_{1/4}\|$/mV
Reversible ($n \geq 1$)	Linear, $59.1/n$	$56.4/n$	Linear, $59.1/n$	$56.4/n$
Quasireversible ($n = 1$)	Nonlinear	Between 56.4 and $45.0/\alpha$	Nonlinear	Between 56.4 and $56.4/\alpha$
Irreversible ($n = 1$)	Nonlinear	$45.0/\alpha$	Linear, $59.1/\alpha$	$56.4/\alpha$

treated the observed voltammetric curve of nitrobenzene using the totally irreversible electron-transfer model, kinetic parameters for the electron transfer might be obtained, but they would be of no significance. Treatment of such complex systems requires a more complete elucidation of the electrode reaction mechanism as discussed in Chapter 12.

Before one uses wave shape parameters to diagnose the kinetic regime, one must be sure of the basic chemistry of the electrode process. It is easier to establish confidence on this point by investigating the system with a method, such as cyclic voltammetry, that can provide direct observations in the forward and reverse directions (Chapter 6).

If the system shows totally irreversible behavior based on the kinetics of interfacial electron transfer, then kinetic parameters can be obtained in any of several ways:

1. *Point-by-point evaluation of k_f.* From a recorded voltammogram, one can measure i/i_d at various potentials in the rising portion of the wave and find the corresponding values of k_f by a procedure that depends slightly on the voltammetric mode: (a) If the voltammetry is based on linear diffusion, then one uses a table or plot of $F_1(\lambda)$, such as Figure 5.5.2, to determine λ for each i/i_d. Given τ and D_O, a value of k_f can then be calculated from each value of λ. (b) In the case of steady-state voltammetry, one uses the array of i/i_d and (5.5.47) to obtain corresponding values of κ, which in turn will yield values of k_f if D_O/r_0 is known. This approach involves no assumption that the kinetics follow a particular model. If a model is subsequently assumed, then the set of k_f values can be analyzed to obtain other parameters. It is common to assume the Butler–Volmer model, which implies that a plot of log k_f vs. $E - E^{0'}$ will provide α from the slope and k^0 from the intercept. Of course, this procedure requires knowledge of $E^{0'}$ by some other means (e.g., potentiometry), because it cannot be determined from the wave position.

2. *Wave-slope plot.* Totally irreversible steady-state voltammograms give linear plots of E vs. log $[(i_d - i)/i]$ in accord with (5.5.48). The slope provides α and the intercept at $E^{0'}$ yields k^0 if D_O/r_0 is known. This approach involves the assumption that Butler–Volmer kinetics apply. For a totally irreversible wave based on early transients, the wave-slope plot is predicted to be slightly curved; consequently it does not have quantitative utility.

3. *Tomeš criterion and half-wave potential.* As one can see from Table 5.5.1, $|E_{3/4} - E_{1/4}|$ for a totally irreversible system provides α directly. That figure can then be used in conjunction with (5.5.30) [for early transients] or 5.5.49 [for steady-state voltammetry] to obtain k^0. Butler–Volmer kinetics are implicit and $E^{0'}$ must be known.

4. *Curve-fitting.* The most general approach to the evaluation of parameters is to employ a nonlinear least-squares algorithm to fit a whole digitized voltammogram to a theoretical function. For a totally irreversible wave, one could develop a fitting function from (5.5.28) [for early transients] or (5.5.47) [for steady-state currents] by using a specific kinetic model to describe the potential dependence of k_f in terms of adjustable parameters. If the Butler–Volmer model is assumed, the appropriate substitution is (5.5.4), and the adjustable parameters are α and k^0. (The latter might be carried in the fitting process as λ^0 or κ^0.) The algorithm then determines the values of the parameters that best describe the experimental results.

If the voltammetry is quasireversible, one cannot use simplified descriptions of the wave shape, but must analyze results according to the appropriate general expression, either (5.5.24) or (5.5.44). The most useful approaches are:

1. *Method of Mirkin and Bard (33).* If the voltammetry is based on steady-state currents, one can analyze a quasireversible wave very conveniently in terms of two differences, $|E_{1/4} - E_{1/2}|$ and $|E_{3/4} - E_{1/2}|$. Mirkin and Bard have published tables correlating these differences with corresponding sets of k^0 and α; hence one can evaluate the kinetic parameters by a look-up process. Reference 33 contains a table for uniformly accessible electrodes, which applies to a spherical or hemispherical UME. A second table is given for voltammetry at a disk UME, which is not a uniformly accessible electrode.

2. *Curve fitting.* This method applies to voltammetry based on either transient or steady-state currents and proceeds essentially exactly as described for totally irreversible systems, except that the fitting function must be developed from (5.5.24) or (5.5.44).

For a quasireversible wave, $E_{1/2}$ is not far removed from $E^{0'}$ and is sometimes used as a rough estimate of the formal potential. Better estimates can be made from fundamental equations after the kinetic parameters have been evaluated from the wave shape. The tables published by Mirkin and Bard for their method actually provide $n(E_{1/2} - E^{0'})$ with sets of k^0 and α (33).

Whenever one is concerned with the evaluation of kinetic parameters, it is important to remember that the kinetic regime is defined partly by experimental conditions and that it can change if those conditions are altered. The most important experimental variable affecting the kinetic regime in voltammetry based on linear diffusion is the sampling time τ. For steady-state voltammetry, it is the radius of the electrode r_0. See Sections 5.5.1(f) and 5.5.3(b) for more detailed discussion. In estimating kinetic parameters, the actual shape of the electrode can be important. For example in making small electrodes (sub-μm radius), the metal disk is sometimes recessed inside the insulating sheath and has access to the solution only through a small aperture (Problem 5.17). Such an electrode will show a limiting current characteristic of the aperture radius, but the heterogeneous kinetics will be governed by the radius of the recessed disk (34, 35).

▶ 5.6 MULTICOMPONENT SYSTEMS AND MULTISTEP CHARGE TRANSFERS

Consider the case in which two reducible substances, O and O', are present in the same solution, so that the consecutive electrode reactions O + ne → R and O' + $n'e$ → R' can occur. Suppose the first process takes place at less extreme potentials than the second and that the second does not commence until the mass-transfer-limited region has been reached for the first. The reduction of species O can then be studied without interference from O', but one must observe the current from O' superimposed on that caused by the mass-transfer-limited flux of O. An example is the successive reduction of Cd(II) and Zn(II) in aqueous KCl, where Cd(II) is reduced with an $E_{1/2}$ near -0.6 V *vs.* SCE, but the Zn(II) remains inactive until the potential becomes more negative than about -0.9 V.

In the potential region where both processes are limited by the rates of mass transfer [i.e., $C_O(0, t) = C_{O'}(0, t) = 0$], the total current is simply the sum of the individual diffu-

sion currents. For chronoamperometry or sampled-current voltammetry based on linear diffusion, one has

$$(i_d)_{total} = \frac{FA}{\pi^{1/2}t^{1/2}}(nD_O^{1/2}C_O^* + n'\,D_{O'}^{1/2}C_{O'}^*) \tag{5.6.1}$$

where t is either a sampling time or a variable time following the potential step. For sampled-current voltammetry based on the steady-state at an ultramicroelectrode

$$(i_d)_{total} = FA(nm_OC_O^* + n'm_{O'}\,C_{O'}^*) \tag{5.6.2}$$

where m_O and $m_{O'}$ are defined by Table 5.3.1 for the particular geometry of the UME.

In making measurements by sampled-current voltammetry, one would obtain traces like those in Figure 5.6.1. The diffusion current for the first wave can be subtracted from the total current of the composite wave to obtain the current attributable to O' alone. That is,

$$i_d' = (i_d)_{total} - i_d \tag{5.6.3}$$

where i_d and i_d' are the current components due to O and O', respectively.

This discussion assumes that the reactions of O and O' are independent and that the products of one electrode reaction do not interfere with the other. While this is frequently the situation, there are cases where reactions in solution can perturb the diffusion currents and invalidate (5.6.3) (36). The classic case is the reduction of cadmium ion and iodate at a mercury electrode in an unbuffered medium, where O is Cd^{2+} and O' is IO_3^-. The reduction of IO_3^- in the second wave occurs by the reaction $IO_3^- + 3H_2O + 6e \rightarrow I^- + 6OH^-$. The liberated hydroxide diffuses away from the electrode and reacts with Cd^{2+} diffusing toward the electrode, causing precipitation of $Cd(OH)_2$ and thus decreasing the contribution of the first wave (from reduction of Cd^{2+} to the amalgam) at potentials where the second wave occurs. The consequence is a second plateau that is much lower than that observed if the reactions were independent (or if the solution were buffered).

Similar considerations hold for a system in which a single species O is reduced in several steps, depending on potential, to more than one product. That is,

$$O + n_1e \rightarrow R_1 \tag{5.6.4}$$
$$R_1 + n_2e \rightarrow R_2 \tag{5.6.5}$$

where the second step occurs at more extreme potentials than the first. A simple example is molecular oxygen, which is reduced in two steps in neutral solution. Figure 5.6.2 shows the behavior of this system in the polarographic form of sampled-current voltammetry. (See Chapter 7 for more on polarography.) In the first reduction step, oxygen goes to hydrogen peroxide with a two-electron change manifested by a wave near -0.1 V *vs.* SCE.
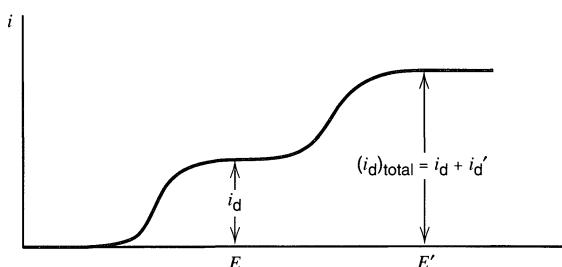
Figure 5.6.1 Sampled-current voltammogram for a two-component system.
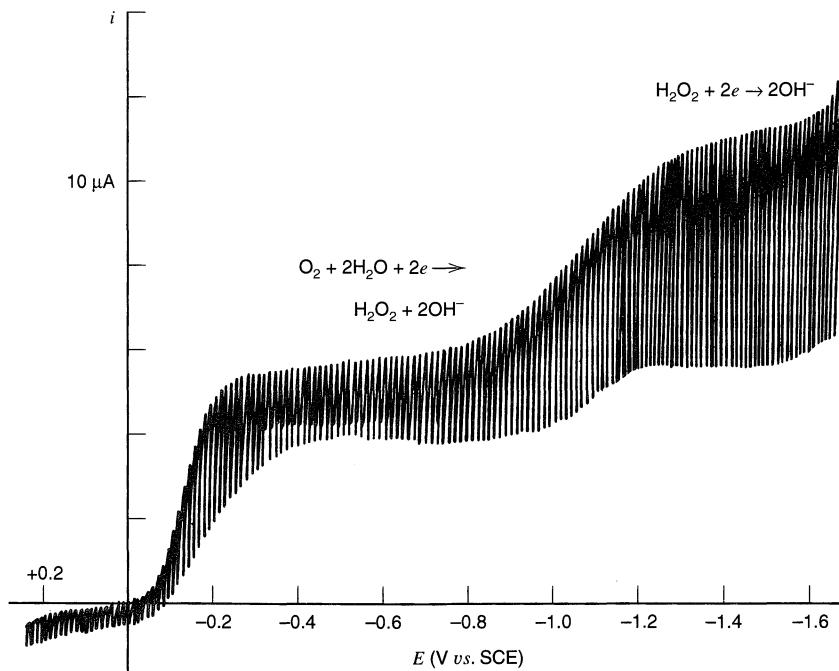
Figure 5.6.2 Polarographic form of sampled-current voltammetry for air-saturated 0.1 M KNO$_3$ with Triton X-100 added as a maximum suppressor. The working electrode is a dropping mercury electrode, which produces oscillations as individual drops grow and fall. This curve was recorded in the classical mode using a recorder that was fast enough to follow current changes near the end of drop life, but not at drop fall, when the current goes almost to zero. The top edge of the envelope can be regarded as a sampled-current voltammogram.

A second two-electron step takes hydrogen peroxide to water. At potentials less extreme than about -0.5 V, the second step does not occur to any appreciable extent; hence one sees only a single wave corresponding to a diffusion-limited, two-electron process. At still more negative potentials, the second step begins to occur, and beyond -1.2 V oxygen is reduced completely to water at the diffusion-limited rate.

For the entire process [(5.6.4) and (5.6.5)], it is clear that at potentials for which the reduction of O to R$_2$ is diffusion controlled, the early transient current following a potential step is simply

$$i_d = \frac{FAD_O^{1/2}C_O^*}{\pi^{1/2}t^{1/2}}(n_1 + n_2) \tag{5.6.6}$$

and the steady-state current at a UME is

$$i_d = FAm_O\, C_O^*(n_1 + n_2) \tag{5.6.7}$$

where m_O is given for the particular geometry in Table 5.3.1. Equations for currents measured in sampled-current voltammetric experiments can be written analogously. Our focus here is on the limiting current resulting from a multistep electron transfer involving a given chemical species. There are, in addition, many interesting kinetic and mechanistic aspects to processes involving sequential electron transfers, but we defer them for consideration in Chapter 12.

⫸ 5.7 CHRONOAMPEROMETRIC REVERSAL TECHNIQUES

After the application of an initial potential step, one might wish to apply an additional step, or even a complex sequence of steps. The most common arrangement is the double-step technique, in which the first step is used to generate a species of interest and the second is used to examine it. The latter step might be made to any potential within the working range, but it usually is employed to reverse the effects of the initial step. An example is shown in Figure 5.7.1. Suppose an electrode is immersed in a solution of species O that is reversibly reduced at $E^{0'}$. If the initial potential, E_i, is much more positive than $E^{0'}$, no electrolysis occurs until, at $t = 0$, the potential is changed abruptly to E_f, which is far more negative than $E^{0'}$. Species R is generated electrolytically for a period τ, then the second step shifts the electrode to the comparatively positive value E_r. Often E_r is equal to E_i. The reduced form R then can no longer coexist with the electrode, and it is reoxidized to O. This approach, like other reversal techniques, is designed to provide a direct observation of R after its electrogeneration. That feature is useful for evaluating R's participation in chemical reactions on a time scale comparable to τ.

This sort of experiment is not useful in the steady-state regime, because the current observed in the reversal step at steady state reflects the bulk concentration of R, rather than that generated in the forward step. Consequently, we treat the experiment described just above under the condition that semi-infinite linear diffusion applies.

5.7.1 Approaches to the Problem

To obtain a quantitative description of this experiment, one might consider first the result of the forward step, then use the concentration profiles applicable at τ as initial conditions for the diffusion equation describing events in the reversal step. In the case outlined above, the effects of the forward step are well known (see Section 5.4.1), and this direct approach can be followed straightforwardly. More generally, reversal experiments present very complex concentration profiles to the theoretician attempting to describe the second phase, and it is often simpler to resort to methods based on the *principle of superposition* (37, 38). We will introduce the technique here as a means for solving the present problem.

The applied potential can be represented as the superposition of two signals: a constant component E_f for all $t > 0$ and a step component $E_r - E_f$ superimposed on the con-
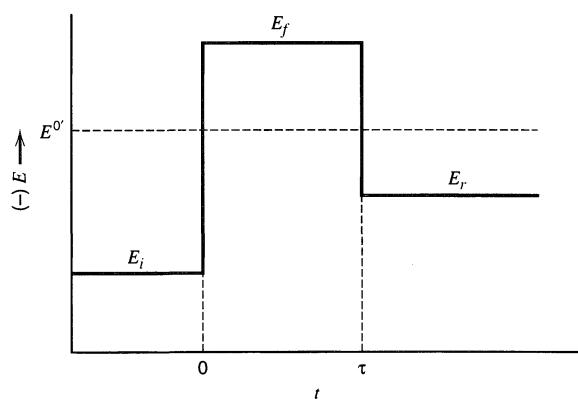
Figure 5.7.1 General waveform for a double potential step experiment.
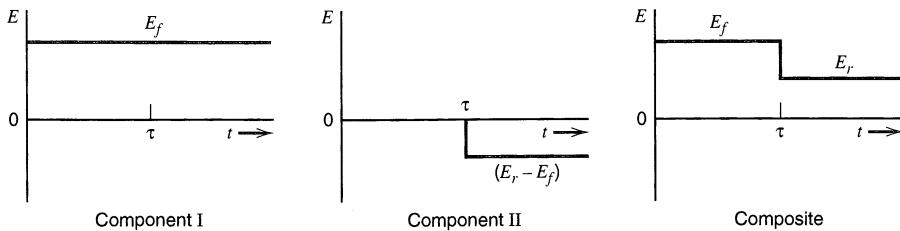
Figure 5.7.2 A double-step waveform as a superposition of two components.

stant perturbation for $t > \tau$. Figure 5.7.2 is an expression of this idea, which is embodied mathematically as

$$E(t) = E_f + S_\tau(t)(E_r - E_f) \qquad (t > 0) \tag{5.7.1}$$

where the step function $S_\tau(t)$ is zero for $t \le \tau$ and unity for $t > \tau$. Similarly, the concentrations of O and R can be expressed as a superposition of two concentrations that may be regarded as responsive to the separate potential components:

$$C_O(x, t) = C_O^I(x, t) + S_\tau(t)C_O^{II}(x, t - \tau) \tag{5.7.2}$$
$$C_R(x, t) = C_R^I(x, t) + S_\tau(t)C_R^{II}(x, t - \tau) \tag{5.7.3}$$

Of course, the boundary conditions and initial conditions for this problem are most easily formulated in terms of the actual concentrations $C_O(x, t)$ and $C_R(x, t)$, and we write the initial situation as

$$C_O(x, 0) = C_O^* \qquad C_R(x, 0) = 0 \tag{5.7.4}$$

During the forward step we have

$$C_O(0, t) = C_O' \qquad C_R(0, t) = C_R' \tag{5.7.5}$$

For reasons discussed below, we will treat only situations where the O/R couple is nernstian; thus

$$C_O' = \theta' C_R' \tag{5.7.6}$$

where

$$\theta' = \exp[nf(E_f - E^{0'})] \tag{5.7.7}$$

The reversal step is defined by

$$C_O(0, t) = C_O'' \qquad C_R(0, t) = C_R'' \tag{5.7.8}$$

and

$$C_O'' = \theta'' C_R'' \tag{5.7.9}$$

where

$$\theta'' = \exp[nf(E_r - E^{0'})] \tag{5.7.10}$$

By relying on (5.7.9) and (5.7.10), we have again confined our treatment to systems in which the electron transfer is nernstian. At all times, the semi-infinite conditions:

$$\lim_{x \to \infty} C_O(x, t) = C_O^* \qquad \lim_{x \to \infty} C_R(x, t) = 0 \tag{5.7.11}$$

and the flux balance:

$$J_O(0, t) = -J_R(0, t) \tag{5.7.12}$$

are applicable.

Note that all of these conditions, as well as the diffusion equations for O and R, are linear. An important mathematical consequence is that the component concentrations $C_O{}^I$, $C_O{}^{II}$, $C_R{}^I$, and $C_R{}^{II}$ can all be carried through the problem separately. Each makes a separable contribution to every condition. We can therefore solve individually for each component, then combine them through (5.7.2) and (5.7.3) to obtain the real concentration profiles, from which we derive the current-time relationship. These steps, which are detailed in the first edition,[10] are left for the reader now as Problem 5.12.

The method of superposition can succeed when linearity exists and separability of the component concentrations can be assured. Unfortunately, many electrochemical situations do not satisfy this requirement, and in such instances other predictive methods, such as simulation, must be applied.

Quasireversible electron transfer in a system with chemically stable O and R has been addressed, initially on the basis of a special case (39), and subsequently in a general way yielding a series solution (40) that allows the extraction of kinetic parameters from experimental data under a wide variety of conditions.

5.7.2 Current-Time Responses

Since the experiment for $0 < t \leq \tau$ is identical to that treated in Section 5.4.1, the current is given by (5.4.16), which is restated for the present context as

$$i_f(t) = \frac{nFAD_O^{1/2}C_O^*}{\pi^{1/2}t^{1/2}(1 + \xi\theta')} \tag{5.7.13}$$

From the treatment outlined in the previous section, the current during the reversal step turns out to be

$$-i_r(t) = \frac{nFAD_O^{1/2}C_O^*}{\pi^{1/2}} \left\{ \left(\frac{1}{1 + \xi\theta'} - \frac{1}{1 + \xi\theta''} \right) \left[\frac{1}{(t - \tau)^{1/2}} \right] - \frac{1}{(1 + \xi\theta')t^{1/2}} \right\} \tag{5.7.14}$$

A special case of interest involves stepping in the forward phase to a potential on the diffusion plateau of the reduction wave ($\theta' \approx 0$, $C_O' \approx 0$), then reversing to a potential on the diffusion plateau for reoxidation ($\theta'' \to \infty$, $C_R'' \approx 0$). In that instance, (5.7.14) simplifies to the result first obtained by Kambara (37):

$$-i_r(t) = \frac{nFAD_O^{1/2}C_O^*}{\pi^{1/2}} \left[\frac{1}{(t - \tau)^{1/2}} - \frac{1}{t^{1/2}} \right] \tag{5.7.15}$$

Note that this relation could also have been derived under the conditions $C_O'' = 0$ and $C_R'' = 0$ without requiring nernstian behavior. It therefore holds also for irreversible systems, provided large enough potential steps are employed.

Figure 5.7.3 shows the kind of current response predicted by (5.7.13) and (5.7.14). In comparing a real experiment to the prediction, it is inconvenient to deal with absolute currents because they are proportional to $AD_O^{1/2}$, which is often difficult to ascertain. To eliminate this factor, the reversal current, $-i_r$, is usually divided by some particular value of the forward current. If t_r and t_f are the times at which the current measurements are made, then for the purely diffusion-limited case described by (5.7.15),

$$\frac{-i_r}{i_f} = \left(\frac{t_f}{t_r - \tau} \right)^{1/2} - \left(\frac{t_f}{t_r} \right)^{1/2} \tag{5.7.16}$$

---

[10]First edition, pp. 178–180.
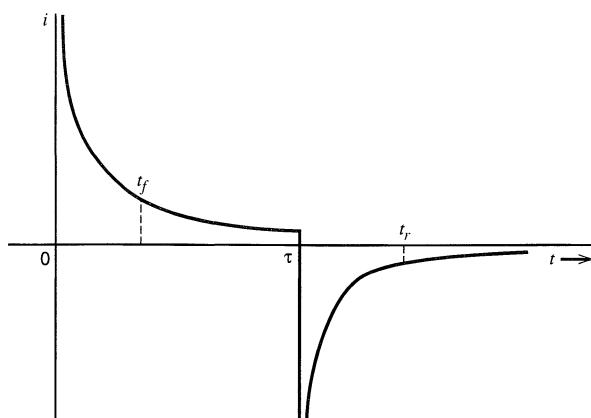
Figure 5.7.3 Current response in double-step chronoamperometry.
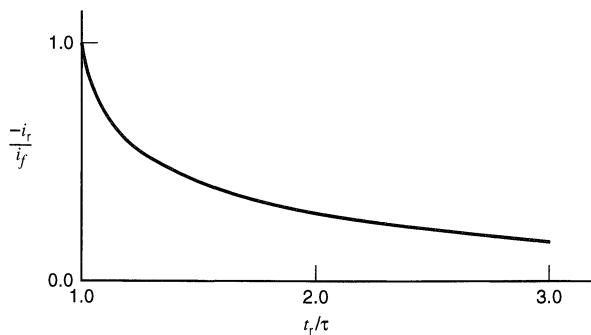
Figure 5.7.4 Working curve for $-i_r(t_r)/i_f(t_f)$ for $t_r = t_f + \tau$. The system is $O + ne \rightleftarrows R$, with both O and R being stable on the time scale of observation. Responses in both phases are diffusion-limited.

If t_r and t_f values are selected in pairs so that $t_r - \tau = t_f$ always, then

$$\frac{-i_r}{i_f} = 1 - \left(1 - \frac{\tau}{t_r}\right)^{1/2} \qquad (5.7.17)$$

When one calculates these ratios for several different values of t_r, they ought to fall on the working curve shown in Figure 5.7.4. A convenient quick reference for a stable system is that $-i_r(2\tau)/i_f(\tau) = 0.293$. Deviations from the working curve indicate kinetic complications in the electrode reaction. For example, if species R decays to an electroinactive species, then $|i_r|$ is smaller than predicted by (5.7.15) and the current ratio $-i_r/i_f$ deviates negatively from that given in Figure 5.7.4. Chapter 12 covers in more detail the ways in which these experiments can be used to diagnose and quantify complex electrode processes.

▷ 5.8 CHRONOCOULOMETRY

To this point, this chapter has concerned either current-time transients stimulated by potential steps or voltammograms constructed by sampling those curves. An alternative, and very useful, mode for recording the electrochemical response is to integrate the current, so that one obtains the charge passed as a function of time, $Q(t)$. This *chronocoulometric* mode was popularized by Anson (41) and co-workers and is widely employed in place of chronoamperometry because it offers important experimental advantages: (a) The measured signal often grows with time; hence the later parts of the transient, which are most accessible experimentally and are least distorted by nonideal potential rise, offer better sig-

nal-to-noise ratios than the early time results. The opposite is true for chronoamperometry. (b) The act of integration smooths random noise on the current transients; hence the chronocoulometric records are inherently cleaner. (c) Contributions to $Q(t)$ from double-layer charging and from electrode reactions of adsorbed species can be distinguished from those due to diffusing electroreactants. An analogous separation of the components of a current transient is not generally feasible. This latter advantage of chronocoulometry is especially valuable for the study of surface processes.

5.8.1 Large-Amplitude Potential Step

The simplest chronocoulometric experiment is the Cottrell case discussed in Section 5.2.1. One begins with a quiescent, homogeneous solution of species O, in which a planar working electrode is held at some potential, E_i, where insignificant electrolysis takes place. At $t = 0$, the potential is shifted to E_f, which is sufficiently negative to enforce a diffusion-limited current. The Cottrell equation, (5.2.11), describes the chronoamperometric response, and its integral from $t = 0$ gives the cumulative charge passed in reducing the diffusing reactant:

$$Q_d = \frac{2nFAD_O^{1/2}C_O^*t^{1/2}}{\pi^{1/2}} \tag{5.8.1}$$

As shown in Figure 5.8.1, Q_d rises with time, and a plot of its value *vs.* $t^{1/2}$ is linear. The slope of this plot is useful for evaluating any one of the variables n, A, D_O, or C_O^*, given knowledge of the others.

Equation 5.8.1 shows that the diffusional component to the charge is zero at $t = 0$, yet a plot of the total charge Q *vs.* $t^{1/2}$ generally does not pass through the origin, because additional components of Q arise from double-layer charging and from the electroreduction of any O molecules that might be adsorbed at E_i. The charges devoted to these processes are passed very quickly compared to the slow accumulation of the diffusional component; hence they may be included by adding two time-independent terms:

$$Q = \frac{2nFAD_O^{1/2}C_O^*t^{1/2}}{\pi^{1/2}} + Q_{dl} + nFA\Gamma_O \tag{5.8.2}$$
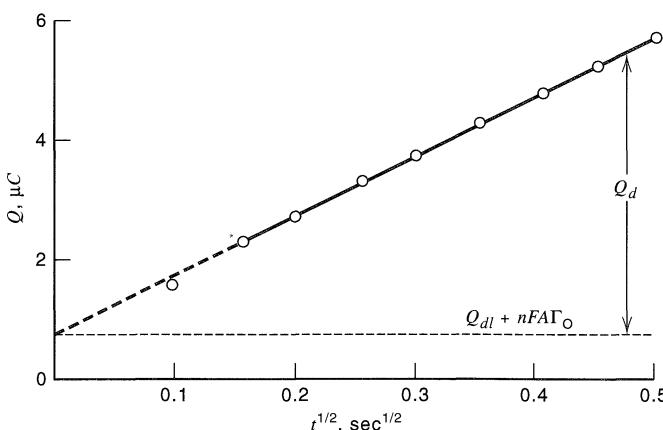
Figure 5.8.1 Linear plot of chronocoulometric response at a planar platinum disk. System is 0.95 m*M* 1,4-dicyanobenzene (DCB) in benzonitrile containing 0.1 *M* tetra-*n*-butylammonium fluoborate. Initial potential: 0.0 V *vs.* Pt QRE. Step potential: -1.892 V *vs.* Pt QRE. $T = 25°C$, $A = 0.018$ cm^2. $E^{0'}$ for DCB $+ e \rightleftarrows$ DCB$^{\cdot-}$ is -1.63 V *vs.* QRE. The actual chronocoulometric trace is the part of Figure 5.8.2 corresponding to $t < 250$ ms. [Data courtesy of R. S. Glass.]

where Q_{dl}, is the capacitive charge and $nFA\Gamma_O$ quantifies the faradaic component given to the reduction of the *surface excess*, Γ_O (mol/cm^2), of adsorbed O.

The intercept of Q vs. $t^{1/2}$ is therefore $Q_{dl} + nFA\Gamma_O$. A common application of chronocoulometry is to evaluate surface excesses of electroactive species; hence it is of interest to separate these two interfacial components. However, doing so reliably usually requires other experiments, such as those described in the next section. An approximate value of $nFA\Gamma_O$ can be had by comparing the intercept of the Q-$t^{1/2}$ plot obtained for a solution containing O, with the "instantaneous" charge passed in the same experiment performed with supporting electrolyte only. The latter quantity is Q_{dl} for the background solution, and it may approximate Q_{dl} for the complete system. Note, however, that these two capacitive components will not be identical if O is adsorbed, because adsorption influences the interfacial capacitance (see Chapter 13).

5.8.2 Reversal Experiments Under Diffusion Control

Chronocoulometric reversal experiments are nearly always designed with step magnitudes that are large enough to ensure that any electroreactant diffuses to the electrode at its maximum rate. A typical experiment begins exactly like the one described just above. At $t = 0$, the potential is shifted from E_i to E_f, where O is reduced under diffusion-limited conditions. That potential is enforced for a fixed period τ then the electrode is returned to E_i, where R is reconverted to O, again at the limiting rate. This sequence is a special case of the general reversal experiment considered in Section 5.7, and we have already found the chronoamperometric response for $t > \tau$ in (5.7.15), which is

$$i_r = \frac{-nFAD_O^{1/2}C_O^*}{\pi^{1/2}}\left[\frac{1}{(t-\tau)^{1/2}} - \frac{1}{t^{1/2}}\right] \tag{5.8.3}$$

Before τ, the experiment is clearly the same as that treated just above; hence the cumulative charge devoted to the diffusional component after τ is

$$Q_d(t > \tau) = \frac{2nFAD_O^{1/2}C_O^*\tau^{1/2}}{\pi^{1/2}} + \int_\tau^t i_r dt \tag{5.8.4}$$

or

$$Q_d(t > \tau) = \frac{2nFAD_O^{1/2}C_O^*}{\pi^{1/2}}\left[t^{1/2} - (t-\tau)^{1/2}\right] \tag{5.8.5}$$

This function declines with increasing t, because the second step actually withdraws charge injected in the forward step. The overall experimental record would resemble the curve of Figure 5.8.2, and one could expect a linear plot of $Q(t > \tau)$ vs. $[t^{1/2} - (t-\tau)^{1/2}]$. Note that there is no net capacitive component in the total charge after time τ, because the net potential change is zero. Although Q_{dl} was injected with the rise of the forward step, it was withdrawn upon reversal.

Now consider the quantity of charge removed in the reversal, $Q_r(t > \tau)$ which experimentally is the difference $Q(\tau) - Q(t > \tau)$, as depicted in Figure 5.8.2.

$$Q_r(t > \tau) = Q_{dl} + \frac{2nFAD_O^{1/2}C_O^*}{\pi^{1/2}}\left[\tau^{1/2} + (t-\tau)^{1/2} - t^{1/2}\right] \tag{5.8.6}$$

where the bracketed factor is frequently denoted as θ. For simplicity, we consider the case in which R is not adsorbed. A plot of Q_r vs. θ should be linear and possess the same slope magnitude seen in the other chronocoulometric plots. Its intercept is Q_{dl}.
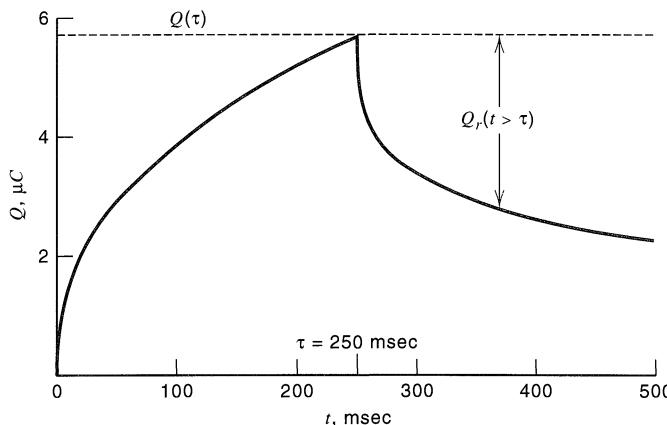
Figure 5.8.2 Chronocoulometric response for a double-step experiment performed on the system of Figure 5.8.1. The reversal step was made to 0.0 V *vs.* QRE. [Data courtesy of R. S. Glass.]

The pair of graphs depicting $Q(t < \tau)$ *vs.* $t^{1/2}$ and $Q_r(t > \tau)$ *vs.* θ in the manner of Figure 5.8.3 (often called an *Anson plot*) is extremely useful for quantifying electrode reactions of adsorbed species. In the case we have considered, where O is adsorbed and R is not, the difference between the intercepts is simply $nFA\Gamma_O$. This difference cancels Q_{dl} and leaves only a net faradaic charge devoted to adsorbate, which in general is $nFA(\Gamma_O - \Gamma_R)$. For details of interpretation concerning the various possible situations, the original literature should be consulted (41–43). (See also Section 14.3.6.)

Note that (5.8.3), (5.8.5), and (5.8.6) are all based on the assumption that the concentration profiles at the start of the second step are exactly those that would be produced by an uncomplicated Cottrell experiment. In other words, we have regarded those profiles as being unperturbed by the additions or subtractions of diffusing material that are implied by adsorption and desorption. This assumption obviously cannot hold strictly. Christie et al. avoided it in their rigorous treatments, and they showed how conventional chronocoulometric data can be corrected for such effects (42).
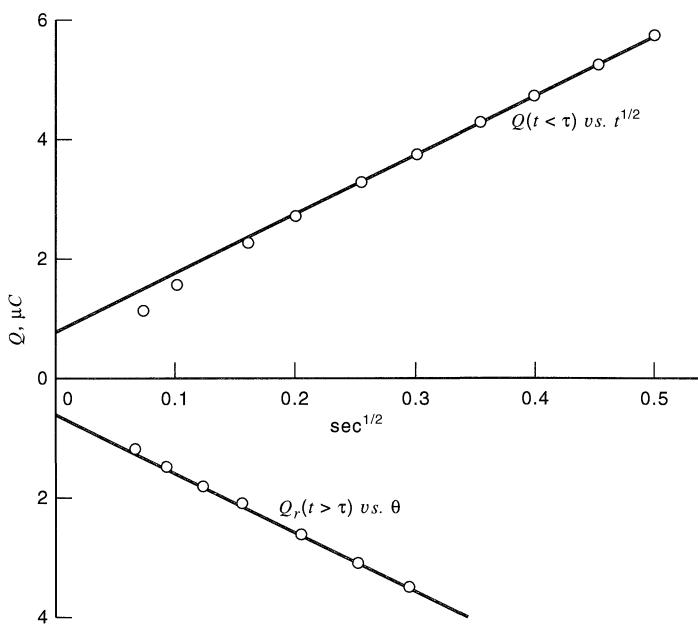
Figure 5.8.3 Linear chronocoulometric plots for data from the trace shown in Figure 5.8.2. For $Q(t < \tau)$ *vs.* $t^{1/2}$, the slope is 9.89 $\mu C/s^{1/2}$ and the intercept is 0.79 μC. For $Q_r(t > \tau)$ *vs.* θ, the slope is 9.45 $\mu C/s^{1/2}$ and the intercept is 0.66 μC. [Data courtesy of R. S. Glass.]

Reversal chronocoulometry is also useful for characterizing the homogeneous chemistry of O and R. The diffusive faradaic component $Q_d(t)$ is especially sensitive to solution-phase reactions (44, 43), and it can be conveniently separated from the overall charge $Q(t)$ as described above.

If both O and R are stable, and are not adsorbed, then $Q_d(t)$ is fully described by (5.8.1) and (5.8.5). Let us consider the result of dividing $Q_d(t)$ by the Cottrell charge passed in the forward step, that is, $Q_d(\tau)$. This charge ratio takes a particularly simple form:

$$\frac{Q_d(t \leq \tau)}{Q_d(\tau)} = \left(\frac{t}{\tau}\right)^{1/2} \tag{5.8.7}$$

$$\frac{Q_d(t > \tau)}{Q_d(\tau)} = \left(\frac{t}{\tau}\right)^{1/2} - \left[\left(\frac{t}{\tau}\right) - 1\right]^{1/2}, \tag{5.8.8}$$

which is independent of the specific experimental parameters n, C_O^*, D_O, and A. For a given value of t/τ, the charge ratio is even independent of τ. Equations 5.8.7 and 5.8.8 clearly describe the essential shape of the chronocoulometric response for a stable system. If the experimental results for any real system do not adhere to this shape function, then chemical complications are indicated. For a quick examination of chemical stability, one can conveniently evaluate the charge ratio $Q_d(2\tau)/Q_d(\tau)$ or, alternatively, the ratio $[Q_d(\tau) - Q_d(2\tau)]/Q_d(\tau)$. Equation 5.8.8 shows that these ratios for a stable system are 0.414 and 0.586, respectively.

In contrast, consider the nernstian O/R couple in which R rapidly decays in solution to electroinactive X. In the forward step O is reduced at the diffusion-controlled rate and (5.8.7) is obeyed. However, (5.8.8) is not followed, because species R cannot be fully reoxidized. The ratio $Q_d(t > \tau)/Q_d(\tau)$ falls less rapidly than for a stable system, and in the limit of completely effective conversion of R to X, no reoxidation is seen at all. Then $Q_d(t > \tau)/Q_d(\tau) = 1$ for all $t > \tau$.

Various other kinds of departure from (5.8.7) and (5.8.8) can be observed. See Chapter 12 for a discussion concerning the diagnosis of prominent homogeneous reaction mechanisms. The large body of chronoamperometric theory for systems with coupled chemistry can be used directly to describe chronocoulometric experiments, because there are no differences in fundamental assumptions. The only differences are that the response is integrated in chronocoulometry and that the chronocoulometric experiment manifests more visibly the contributions from double-layer capacitance and electrode processes of adsorbates.

5.8.3 Effects of Heterogeneous Kinetics

In the foregoing discussion, we have examined only situations in which electroreactants arrive at the electrode at the diffusion-limited rate. At the extreme potentials required to enforce that condition, the heterogeneous rate parameters are experimentally inaccessible. On the other hand, if one wished to evaluate those parameters, it would be useful to obtain a chronocoulometric response governed wholly or partially by the interfacial charge-transfer kinetics. That goal can be reached by using a step potential that is insufficiently extreme to enforce diffusion-controlled electrolysis throughout the experimental time domain. In other words, steps must be made to potentials in the rising portion of the sampled-current voltammogram corresponding to the time scale of interest, and that time scale must be sufficiently short that electrode kinetics govern current flow for a significant period.

The appropriate experiment involves a step at $t = 0$ from an initial potential where electrolysis does not occur, to potential E, where it does. Let us consider the special case (45, 46) in which species O is initially present at concentration C_O^* and species R is initially absent. In Section 5.5.1, we found that the current transient for quasireversible electrode kinetics was given by (5.5.11). Integration from $t = 0$ provides the chronocoulometric response:

$$Q(t) = \frac{nFAk_f C_O^*}{H^2}\left[\exp(H^2 t)\text{erfc}(Ht^{1/2}) + \frac{2Ht^{1/2}}{\pi^{1/2}} - 1 \right] \qquad (5.8.9)$$

where $H = (k_f/D_O^{1/2}) + (k_b/D_R^{1/2})$. For $Ht^{1/2} > 5$, the first term in the brackets is negligible compared to the others; hence (5.8.9) takes the limiting form:

$$Q(t) = nFAk_f C_O^*\left(\frac{2t^{1/2}}{H\pi^{1/2}} - \frac{1}{H^2} \right) \qquad (5.8.10)$$

A plot of the faradaic charge *vs.* $t^{1/2}$ should therefore be linear and display a negative intercept on the Q-axis and a positive intercept on the $t^{1/2}$ axis. The latter involves a shorter extrapolation, as shown in Figure 5.8.4, hence it can be evaluated more precisely. Designating it as $t_i^{1/2}$, we find H by the relation:

$$H = \frac{\pi^{1/2}}{2t_i^{1/2}} \qquad (5.8.11)$$

With H in hand, k_f is found from the linear slope, $2nFAk_f C_O^*/(H\pi^{1/2})$. Note that when E is very negative, H approaches $k_f/D_O^{1/2}$, and the slope approaches the Cottrell slope, $2nFAD_O^{1/2}C_O^*/\pi^{1/2}$. Moreover, H is large, so that the intercept approaches the origin. This limiting case is clearly that treated in Section 5.8.1.

Equations 5.8.9 and 5.8.10 do not include contributions from adsorbed species or double-layer charging. For accurate application of this treatment, one must correct for those terms or render them negligibly small compared to the diffusive component to the charge.

In practice, it is quite difficult to measure kinetic parameters in this way, so the method is not widely practiced. The principal value in considering the problem is in the
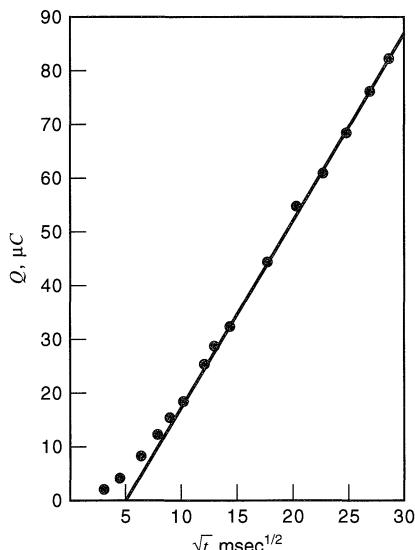
Figure 5.8.4 Chronocoulometric response for 10 mM Cd^{2+} in 1 M Na$_2$SO$_4$. The working electrode was a hanging mercury drop with $A = 2.30 \times 10^{-2}$ cm^2. The initial potential was -0.470 V *vs.* SCE, and the step potential was -0.620 V. The slope of the plot is 3.52 μC/ms$^{1/2}$ and $t_i^{1/2} = 5.1$ ms$^{1/2}$. [From J. H. Christie, G. Lauer, and R. A. Osteryoung, *J. Electroanal Chem.*, **7**, 60 (1964), with permission.]

insight that it provides to the origin of negative intercepts in chronocoulometry, which are rather common, especially with modified electrodes (Chapter 14). The lesson here is that a rate limitation on the delivery of charge to a diffusing species produces an intercept smaller than predicted in Sections 5.8.1 and 5.8.2. A negative intercept clearly indicates such a rate limitation. It may be due to sluggish interfacial kinetics, as treated here, but it may also be from other sources, including slow establishment of the potential because of uncompensated resistance. Using a more extreme step potential can ameliorate this behavior if it is not itself the object of study.

▶ 5.9 SPECIAL APPLICATIONS OF ULTRAMICROELECTRODES

The large impact of ultramicroelectrodes is rooted in their ability to support very useful extensions of electrochemical methodology into previously inaccessible domains of time, medium, and space. That is, UMEs allow one to investigate chemical systems on time scales that could not previously be reached, in media that could not previously be employed, or in microstructures where spatial relationships are important on a distance scale relevant to molecular events.

5.9.1 Cell Time Constants and Fast Electrochemistry

In Section 2.2 we learned that the establishment and control of a working electrode's potential is carried out operationally by adjusting the charge on the double layer. In Sections 1.2.4 and 5.2.1, we found that changing the double-layer charge, hence changing the potential, involves the *cell time constant*, $R_u C_d$, where R_u is the uncompensated resistance and C_d is the double-layer capacitance. It is not meaningful to try to impose a potential step on a time scale shorter than the cell time constant. In fact, the full establishment of a potential step requires $\sim 5 R_u C_d$, and the added time for taking data normally implies that the step must last at least $10 R_u C_d$, and often more than $100 R_u C_d$. To a large extent, the size of the electrode controls the cell time constant and, therefore, the lower limit of experimental time scale.

For example, let us consider a disk-shaped working electrode operating in an electrolyte solution such that the specific interfacial capacitance (capacitance per unit area, C_d^0) is in the typical range of 10–50 μF/cm^2. Obviously

$$C_d = \pi r_0^2 C_d^0 \tag{5.9.1}$$

With a radius of 1 mm, C_d is 0.3–1.5 μF, but for $r_0 = 1$ μm, C_d is six orders of magnitude smaller, only 0.3–1.5 pF.

The uncompensated resistance also depends on the electrode size, although in a less transparent way. As the current flows in solution between the working electrode and the counter electrode, one can think of it as passing along paths of roughly equal length, terminated by the faces of the two electrodes. These paths do not generally involve the whole of the electrolyte solution, but are largely contained in the portion bounded by the electrodes and the closed surface representing the locus of minimum-length connections between points on the perimeters of the electrodes (Figure 5.9.1). Usually the counter electrode is much larger than the working electrode; hence this solution volume is broadly based on the end connecting to the counter electrode, but narrowly based at the working electrode. The precise value of R_u depends on where the tip of the reference electrode intercepts the current path. Figure 5.9.1 shows the situation for a working electrode having a radius one tenth that of the counter electrode, but if the working electrode is a UME, its radius can easily be a thousandth or even a millionth of the counter electrode's radius. In

Electrolyte Solution

Working Electrode

Volume Containing Current Paths

Counter Electrode

Electrolyte Solution
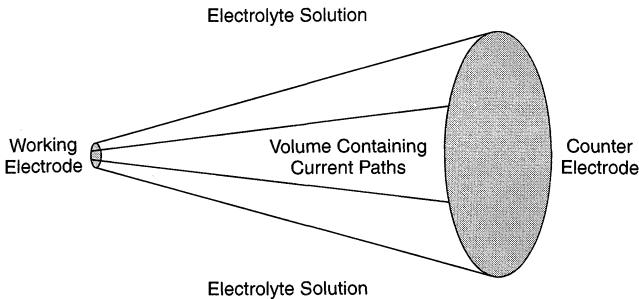
Figure 5.9.1 Schematic representation of the volume of solution containing current paths between disk-shaped working and counter electrodes situated on a common axis. Current paths are largely, but not strictly, confined to the volume defined by minimum-length connections between electrode perimeters.

such a case, all of the current must pass through a solution volume of extremely small cross-sectional area near the working electrode, and it turns out that this is the part of the current path that defines the value of R_u.

The resistance offered by any element of solution to uniform current flow is $l/(\kappa A)$, where l is the thickness of the element along the current path, A is the cross-sectional area, and κ is the conductivity. Thus the resistance of the disk-shaped volume of solution adjacent to the working electrode and extending out a distance $r_0/4$ is $1/(4\pi\kappa r_0)$. A similar relation applies for the counter electrode; but its radius is typically 10^3 to 10^6 bigger than r_0. One can readily see that the resistance contributed by a macroscopic portion of the current path extending out from the counter electrode is negligible compared to that developed in the tiny part of the solution less than $r_0/4$ from the working electrode.

In a system with spherical symmetry, which would apply approximately to any working electrode that is essentially a point with respect to the counter electrode, the uncompensated resistance is given by (47),

$$R_u = \frac{1}{4\pi\kappa r_0}\left(\frac{x}{x + r_0}\right) \tag{5.9.2}$$

where x is the distance from the working electrode to the tip of the reference. In a UME system, it is not generally practical to place a reference tip so that x is comparable to r_0; thus the parenthesized factor approaches unity, and R_u becomes $1/(4\pi\kappa r_0)$.

Note that R_u is inversely proportional to r_0, so that R_u rises as the electrode is made smaller. This behavior is rooted in the considerations given above, for as r_0 is reduced, the solution volume controlling R_u also becomes smaller, but with a length scale that shrinks proportionately with r_0 and a cross-sectional area that shrinks with the square. The effect of decreasing area overrides that of decreasing thickness.

From (5.9.1) and the limiting form of (5.9.2), one can express the cell time constant as

$$R_u C_d = \frac{r_0 C_d^0}{4\kappa} \tag{5.9.3}$$

Even though R_u rises inversely with r_0, C_d decreases with the square; hence $R_u C_d$ scales with r_0. This is an important result indicating that smaller electrodes can provide access to much shorter time domains. Consider, for example, the effect of electrode size in a system with $C_d^0 = 20\ \mu F/cm^2$ and $\kappa = 0.013\ \Omega^{-1}cm^{-1}$ (characteristic of 0.1 M aqueous KCl at ambient temperature). With $r_0 = 1$ mm, the cell time constant is about 30 μs and the lower limit of time scale in step experiments (defined as a minimum step width equal to $10R_u C_d$) is about 0.3 ms. This result is consistent with the general experience that experiments with electrodes of "normal" size need to be limited to the millisecond time domain

or longer. However, with $r_0 = 5$ μm the cell time constant becomes about 170 ns, so that the lower limit of time scale drops to about 1.7 μs. Before UMEs were understood and readily available, the microsecond regime was very difficult to reach in electrochemical studies. However, UMEs have opened it to relatively convenient investigation (10, 11), not only by potential step methods, but also by other experimental approaches covered later in this book.

UMEs even allow access to the nanosecond domain, although not yet with routine ease or convenience. To reach it, one must reduce the electrode size further and work with solutions having high conductivity. For example, by using a disk UME with $r_0 = 0.5$ μm and by working in 1 M H_2SO_4, one can, in principle, achieve a cell time constant below 1 ns, so that the lower limit of time scale could be smaller than 10 ns. However, experimental work in this range is complicated by serious instrumental problems and by fundamental issues related to the availability of molecules when the diffusion layer thickness becomes comparable to the molecular size (12, 14, 15, 48). For a step lasting 10 ns, $(Dt)^{1/2}$ is only about 3 nm; hence very few solute molecules are close enough to the electrode to react if they must reach it by diffusion. As this book is written, the fastest experiments conducted with diffusing species have been in the time scale range of 500 ns. Faster experiments, with step widths in the range of 100 ns, have been conducted with systems having the electroactive species attached to the electrode, so that they are present in large numbers and diffusion is not required (49, 50). Examples of such systems are discussed in Chapter 14.

5.9.2 Voltammetry in Media of Low Conductivity

The uncompensated resistance creates a control error in any potentiostatic experiment such that the true potential at the working electrode differs from the apparent (or applied) potential by iR_u (Sections 1.3.4 and 15.6). The true potential is more positive than the apparent value if a cathodic current is flowing, but more negative if the net current is anodic. As recorded with conventional instrumentation, voltammograms are plots of recorded current *vs.* apparent potential; thus the waves incorporate effects of iR_u, which generally mimic the effects of quasireversibility. That is, they cause a displacement of the voltammogram toward more extreme apparent potentials, and they cause a broadening of the voltammogram along the axis of apparent potential. Obviously, these effects can cause misinterpretation of data, so it is important to understand when they are significant and how to minimize or correct for them. The topic is discussed in various contexts in later chapters, especially in Section 15.6.

If one is using a diagnostic electrode of conventional size in a highly conductive medium, such as an aqueous electrolyte with a concentration of 0.1 M or more, R_u is typically only a few ohms, and iR_u is always smaller than a few mV unless currents exceed 1 mA, which they rarely do for voltammetry of the type discussed in this chapter.

On the other hand, if work is being carried out in a nonaqueous or viscous medium, especially in one of moderate or low polarity, R_u can be large enough to cause substantial errors. In a medium such as methylene chloride containing 0.1 M TBABF$_4$, it is not uncommon to have R_u in the range of several kΩ, so that iR_u exceeds a few mV for any current larger than 1 μA, which it normally does in voltammetry at a conventional electrode. For solvents of genuinely low polarity, such as toluene, R_u is very high even with added supporting electrolytes, because the electrolytes do not dissociate. The potential-control error is so large at a conventional electrode that the waves are broadened and shifted to the point of invisibility.

At UMEs, the picture is quite different, because the currents are extremely small; consequently, the error in potential control in a voltammetric experiment is often much smaller than in the same experiment with an electrode of conventional size. Consider, for example, a disk UME with radius r_0 at which we desire to carry out sampled-current voltammetry. What are the conditions that will allow the recording of a voltammogram in which the half-wave potential is shifted less than 5 mV by the effect of uncompensated resistance?

This condition implies that $iR_u < 5$ mV, where $i = i_l/2$ and R_u is given by the limiting form of (5.9.2). If the sampled-current voltammetry is based on semi-infinite linear diffusion (i.e., on early transients), then i is half of the Cottrell current for sampling time τ, and the condition becomes

$$\frac{nFD_O^{1/2}C_O^*r_0}{8\pi^{1/2}\kappa\tau^{1/2}} < 5 \times 10^{-3} \, V \tag{5.9.4}$$

Thus the error decreases with r_0, and one can improve the accuracy of the voltammogram by using a smaller electrode.

On the other hand, if the voltammetry is based on steady-state currents, i is half of the diffusion-limited steady-state current for a disk, which is $2nFD_OC_O^*r_0$, and the condition is

$$\frac{nFD_OC_O^*}{2\pi\kappa} < 5 \times 10^{-3} \, V \tag{5.9.5}$$

In this experimental mode, the error is independent of the size of the disk, but of course steady-state currents are generally achievable only at UMEs. With $n = 1$, $D_O = 10^{-5}$ cm^2/s, and $C_O^* = 1$ mM, the conductivity must exceed only 3×10^{-5} Ω^{-1}cm^{-1}. This minimum would characterize 10^{-4} M HCl and would be met by all aqueous electrolytes having concentrations above that of the electroactive species, as well as by most common solvent systems of lower polarity containing weakly dissociated electrolytes.

A fascinating empirical aspect of voltammetry at UMEs is that one can often record voltammograms in media that would not satisfy even the foregoing condition. Useful data have been gathered, for example, in solvents without any added supporting electrolyte or in polymers of very high viscosity. An example of the former is found in Figure 4.3.5. Systems of this kind typically do not adhere to the assumptions that we used to treat voltammetry in Sections 5.4 and 5.5, because migration becomes an important part of the mass transfer, and because the charged species produced or consumed at the electrode surface affect the local conductivity quite significantly (51). Equations 5.9.2 to 5.9.5 do not apply in that situation. Theory is available for nernstian systems (12, 15, 48, 52).

One can often simplify the instrumentation used with UMEs because iR_u is very frequently negligible and i is very small. Under these conditions, there is nothing to be gained by trying to position a separate reference electrode near the working electrode and there is no danger of polarizing the reference by passing the cell current through it. Thus two-electrode cells are often used, especially in high-speed experiments (Chapter 15).

5.9.3 Applications Based on Spatial Resolution

Because UMEs are physically small, they can be used to probe small spaces. Single electrodes have been employed frequently in physiological applications, such as the measurement of time-dependent concentrations of neurotransmitters near synapses of neurons (6).

Single electrodes also provide the basis for scanning electrochemical microscopy (SECM, Chapter 16). Groups of microelectrodes can be used in various interesting ways to provide a spatially sensitive characterization of a system.

Combinations and arrays of UMEs are often made by the microlithographic techniques common to microelectronics, and they frequently consist of parallel bands. If the bands are connected in parallel, they behave as a single segmented electrode and follow the principles outlined in Section 5.2.3. If they are independently addressable, they can be used as separate working electrodes to characterize different regions of a sample, such as a polymer overlayer (53).

One can also use the elements of an array to probe chemistry occurring at neighboring elements. The simplest example is a double-band system used in the *generator-collector mode* (Figure 5.9.2). The two bands are spaced closely enough together to allow the diffusion fields to overlap, so that events at each electrode can be affected by the other. One of the electrodes, called the *generator*, is used to drive the experiment, often by having its potential scanned slowly enough to produce a steady-state voltammogram. Suppose the double band assembly is immersed in a solution containing only species O in the bulk. Assume further that the reaction $O + ne \rightleftarrows R$ is reversible and that the product R is chemically stable. In the absence of any influence from the second electrode, one would record, at either of the electrodes, a quasi-steady-state voltammogram characteristic of a single band. However, in the generator-collector mode, the second electrode is set at a potential in the base region of the reduction wave for O, so that any R arriving there is immediately reconverted to O. A current will flow at this *collector* only when the generator is producing R, thus a plot of the current at the collector *vs.* the potential of the generator should have the same shape as that recorded at the generator, but with the opposite sign. Also, currents at the collector are smaller than corresponding values at the generator, because the collector does not collect all of the generated R. This is an example of a reversal experiment implemented in a spatial mode, and it has much in common with voltammetry at a rotating ring-disk assembly (Chapter 9) and with generation-collection experiments in scanning electrochemical microscopy (Chapter 16). Like other reversal experiments, generation-collection at the double band is sensitive to the chemical stability of species R. If it does not survive long enough to diffuse to the collector, no current will be recorded there, and if only a part survives, then only a part of the expected current will be seen. The kinetics of solution-phase reactions can be diagnosed and quantified in this sort of experiment.

An interesting phenomenon in a generation-collection experiment involving a UME array is that the current at the generator can be enhanced by the collector through a mechanism called *feedback*. Without active collection, all of the R produced at the generator
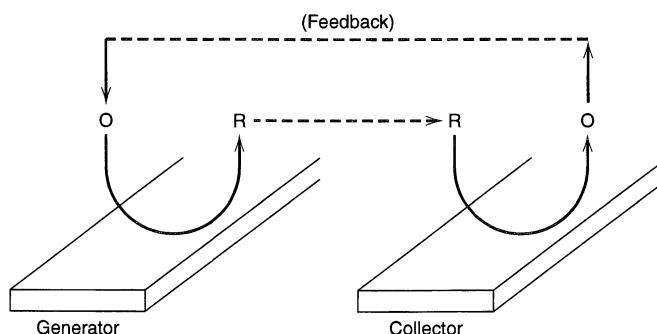
Figure 5.9.2 Schematic representation of two microband electrodes operating in the generator-collector mode.

would diffuse into solution and would have no further effect on the experiment at the generator electrode. However, if the collector reconverts a portion of the R to O, then some of the regenerated O will diffuse back ("feed back") to the generator where it adds to the flux arriving from the bulk. Thus the current at the generator becomes larger than it would be without activity at the collector. The feedback effect is also useful for diagnosis and quantification of chemical reactions involving O and R.

Generation-collection experiments can be carried out in UME arrays aside from the double band. An obvious extension is to use a *triple band* so that the middle electrode serves as a generator and the two flanking electrodes work in parallel as collectors. A more elaborate approach involves an *interdigitated array*, which is an extensive series of parallel bands, the alternate members of which are connected in parallel. One of the sets serves as the generator and the other as the collector.

For all of these systems, the dynamics are dependent on the widths of the bands and the gaps between them. Amatore provides a careful review of theory and application (12).

▶ 5.10 REFERENCES

1. H. A. Laitinen and I. M. Kolthoff, *J. Am. Chem. Soc.*, **61**, 3344 (1939).

2. H. A. Laitinen, *Trans. Electrochem. Soc.*, **82** 289 (1942).

3. F. G. Cottrell, *Z. Physik, Chem.*, **42**, 385 (1902).

4. R. Woods, *Electroanal. Chem.*, **9**, 1 (1976).

5. T. Gueshi, K. Tokuda, and H. Matsuda, *J. Electroanal. Chem.*, **89**, 247 (1978).

6. R. M. Wightman, *Anal. Chem.*, **53**, 1125A (1981).

7. M. Fleischmann, S. Pons, D. R. Rolison, and P. P. Schmidt, Eds., "Ultramicroelectrodes," Datatech Systems, Morganton, NC, 1987.

8. R. M. Wightman and D. O. Wipf, *Electroanal. Chem.*, **15**, 267 (1989).

9. M. I. Montenegro, M. A. Queirós, and J. L. Daschbach, Eds., "Microelectrodes: Theory and Applications," NATO ASI Series, Vol. 197, Kluwer, Dordrecht, 1991.

10. J. Heinze, *Angew. Chem. Int. Ed. Engl.*, **32**, 1268 (1993).

11. R. J. Forster, *Chem. Soc. Rev.*, **1994**, 289

12. C. Amatore in "Physical Electrochemistry," I. Rubinstein, Ed., Marcel Dekker, New York, 1995, Chap. 4.

13. C. G. Zoski in "Modern Techniques in Electroanalysis," P. Vanýsek. Ed., Wiley-Interscience, New York,. 1996, Chap. 6.

14. R. Morris, D. J. Franta, and H. S. White, *J. Phys. Chem.*, **91**, 3559 (1987).

15. J. D. Norton, H. S. White, and S. W. Feldberg, *J. Phys. Chem.*, **94**, 6772 (1990).

16. C. Demaille, M. Brust, M. Tsionsky, and A. J. Bard, *Anal. Chem.*, **69**, 2323 (1997).

17. Y. Saito, *Rev. Polarog. (Japan)*, **15**, 177 (1968).

18. K. B. Oldham, *J. Electroanal. Chem.*, **122**, 1 (1981).

19. M. Kakihana, H. Ikeuchi, G. P. Sato, and K. Tokuda, *J. Electroanal. Chem.*, **117**, 201 (1981).

20. J. Heinze, *J. Electroanal. Chem.*, **124**, 73 (1981).

21. K. Aoki and J. Osteryoung, *J. Electroanal. Chem.*, **122**, 19 (1981).

22. D. Shoup and A. Szabo, *J. Electroanal. Chem.*, **140**, 237 (1982).

23. K. Aoki and J. Osteryoung, *J. Electroanal. Chem.*, **160**, 335 (1984).

24. A. Szabo, D. K. Cope, D. E. Tallman. P. M. Kovach, and R. M. Wightman, *J. Electroanal. Chem.*, **217**, 417 (1987).

25. J. Tomeš, *Coll. Czech. Chem. Commun.*, **9**, 12, 81, 150, (1937).

26. A. M. Bond, K. B. Oldham, and C. G. Zoski, *J. Electroanal. Chem.*, **245**, 71 (1988).

27. K. B. Oldham and C. G. Zoski, *J. Electroanal. Chem.*, **256**, 11 (1988).

28. I. M. Kolthoff and J. J. Lingane, "Polarography," 2nd ed., Wiley-Interscience, New York, 1952.

29. L. Meites, "Polarographic Techniques," 2nd ed., Wiley-Interscience, New York, 1958.

30. A. Bond, "Modern Polarographic Methods in Analytical Chemistry," Marcel Dekker, New York, 1980.

31. M. T. Carter, M. Rodriguez, and A. J. Bard, *J. Am. Chem. Soc.*, **111**, 8901 (1989).

32. C. K. Mann and K. K. Barnes, "Electrochemical Reactions in Nonaqueous Solvents," Marcel Dekker, New York, 1970, Chap. 11.

33. M. V. Mirkin and A. J. Bard, *Anal. Chem.*, **64**, 2293 (1992).

34. S. Baranski, *J. Electroanal. Chem.*, **307**, 287 (1991).

35. K. B. Oldham, *Anal. Chem.*, **64**, 646 (1992).

36. I. M Kolthoff and J. J. Lingane, *op. cit.*, Chap. 6.

37. T. Kambara, *Bull. Chem. Soc. Jpn.*, **27**, 523 (1954).

38. D. D. Macdonald, "Transient Techniques in Electrochemistry," Plenum, New York, 1977.

39. W. M. Smit and M. D. Wijnen, *Rec. Trav. Chim.*, **79**, 5 (1960).

40. D. H. Evans and M. J. Kelly, *Anal. Chem.*, **54**, 1727 (1982).

41. F. C. Anson, *Anal. Chem.*, **38**, 54 (1966).

42. J. H. Christie, R. A. Osteryoung, and F. C. Anson, *J. Electroanal. Chem.*, **13**, 236 (1967).

43. J. H Christie, *J. Electroanal. Chem.*, **13**, 79 (1967).

44. M. K. Hanafey, R. L. Scott, T. H. Ridgway, and C. N. Reilley, *Anal. Chem.*, **50**, 116 (1978).

45. J. H. Christie, G. Lauer, R. A. Osteryoung, and F. C. Anson, *Anal. Chem.*, **35**, 1979 (1963).

46. J. H. Christie, G. Lauer, and R. A. Osteryoung, *J. Electroanal. Chem.*, **7**, 60 (1964).

47. L. Nemec, *J. Electroanal. Chem.*, **8**, 166 (1964).

48. C. P. Smith and H. S. White, *Anal. Chem.*, **65**, 3343 (1993).

49. C. Xu, Ph. D. Thesis, University of Illinois at Urbana-Champaign, 1992.

50. R. J. Foster and L. R. Faulkner, *J. Am. Chem. Soc.*, **116**, 5444, 5453 (1994).

51. K. B. Oldham, *J. Electroanal. Chem.*, **250**, 1 (1988).

52. C. Amatore, B. Fosset, J. Bartelt, M. R. Deakin, and R. M. Wightman, *J. Electroanal. Chem.*, **256**, 255 (1988).

52. I. Fritsch-Faules and L. R. Faulkner, *Anal. Chem.*, **64**, 1118, 1127 (1992).

5.11 PROBLEMS

5.1 Fick's law for diffusion to a spherical electrode of radius r_0 is written

$$\frac{\partial C(r, t)}{\partial t} = D\left[\frac{\partial^2 C(r, t)}{\partial r^2} + \frac{2}{r}\frac{\partial C(r, t)}{\partial r}\right]$$

Solve this expression for $C(r, t)$ with the conditions

$$C(r, 0) = C^*, \qquad C(r_0, t) = 0 \qquad (t > 0), \qquad \text{and} \qquad \lim_{r \to \infty} C(r, t) = C^*$$

Show that the current i follows the expression

$$i = nFADC^*\left[\frac{1}{r_0} + \frac{1}{(\pi Dt)^{1/2}}\right]$$

[Hint: By making the substitution $v(r,t) = rC(r, t)$ in Fick's equation and in the boundary conditions, the problem becomes essentially the same as that for linear diffusion.]
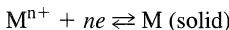
5.2 Given $n = 1$, $C^* = 1.00$ mM, $A = 0.02$ cm^2, and $D = 10^{-5}$ cm^2/s, calculate the current for diffusion-controlled electrolysis at (a) a planar electrode and (b) a spherical electrode (see Problem 5.1) at $t = 0.1, 0.5, 1, 2, 3, 5$, and 10 s, and as t → ∞. Plot both i *vs.* t curves on the same graph. How long can the electrolysis proceed before the current at the spherical electrode exceeds that at the planar electrode by 10%?

Integrate the Cottrell equation to obtain the total charge consumed in electrolysis at any time, then calculate the value for $t = 10$ s. Use Faraday's law to obtain the number of moles reacted by that time. If the total volume of the solution is 10 mL, what fraction of the sample has been altered by electrolysis?

5.3 Consider a diffusion-controlled electrolysis at a hemispherical mercury electrode protruding from a glass mantle. The radius of the mercury surface is 5 μm, and the diameter of the glass mantle is 5 mm. The electroactive species is 1 mM thianthrene in acetonitrile containing 0.1 M tetra-n-butylammonium fluoborate, and the electrolysis produces the cation radical. The diffusion coefficient is 2.7×10^{-5} cm^2/s. Calculate the current at $t = 0.1, 0.2, 0.5, 1, 2, 3, 5$, and 10 ms, and also at 0.1,

0.2, 0.5, 1, 2, 3, 5, and 10 s. Do the same for the system under the approximation that linear diffusion applies. Plot the pairs of curves for the short and long time regimes. How long is the linear approximation valid within 10%?

5.4 A disk UME gives a plateau current of 2.32 nA in the steady-state voltammogram for a species known to react with $n = 1$ and to have a concentration of 1 mM and a diffusion coefficient of 1.2×10^{-5} cm^2/s. What is the radius of the electrode?

5.5 Derive the sampled-current voltammogram for the reduction of a simple metal ion to a metal that plates out on the electrode. The electrode reaction is

$$\mathrm{M^{n+}} + ne \rightleftarrows \mathrm{M\ (solid)}$$
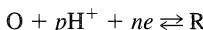
Assume that the reaction is reversible, and that the activity of solid M is constant and equal to 1. How does $E_{1/2}$ vary with i_d? With the concentration of $\mathrm{M^{n+}}$?

5.6 The following measurements were made at 25°C on the reversible sampled-current voltammogram for the reduction of a metallic complex ion to metal amalgam ($n = 2$):

Concentration of Ligand Salt, NaX (M)	$E_{1/2}$ (volts $vs.$ SCE)
0.10	−0.448
0.50	−0.531
1.00	−0.566

(a) Calculate the number of ligands $\mathrm{X^-}$ associated with the metal $\mathrm{M^{2+}}$ in the complex.

(b) Calculate the stability constant of the complex, if $E_{1/2}$ for the reversible reduction of the simple metal ion is +0.081 V $vs.$ SCE. Assume that the D values for the complex ion and the metal atom are equal, and that all activity coefficients are unity.

5.7 (a) Reductions of many organic substances involve the hydrogen ion. Derive the steady-state voltammogram for the reversible reaction

$$\mathrm{O} + p\mathrm{H^+} + ne \rightleftarrows \mathrm{R}$$

where both O and R are soluble substances, and only O is initially present in solution at a concentration C_O^*.

(b) What experimental procedure would be useful for determining p?

5.8 (a) Fill in the derivation of (5.5.37) from Fick's laws for spherical diffusion and the appropriate boundary conditions.

(b) Derive (5.5.41) by the method used to reach (5.5.37).

(c) Show that the following are special cases of (5.5.41):

(1) Equation 5.4.17 for early transients in a reversible system having only species O present in the bulk.

(2) Equation 5.4.54 for steady-state currents in a reversible system having only species O present in the bulk.

(3) Equation 5.5.11 for early transients in a quasireversible system having only species O present in the bulk.

(4) Equation 5.5.12 for early transients in a quasireversible system having both O and R present in the bulk.

(5) Equation 5.5.28 for early transients in a totally irreversible system having only species O present in the bulk.

5.9 From (5.5.41) derive the steady-state voltammogram at a hemispherical microelectrode for a reversible system containing both O and R in the bulk. How does it compare with the result for the analogous situation in Section 1.4.2(b)?

5.10 Consider the reversible system $\mathrm{O} + ne \rightleftarrows \mathrm{R}$ in which both O and R are present initially.

(a) From Fick's laws, derive the current-time curve for a step experiment in which the initial potential is the equilibrium potential and the final potential is any arbitrary value E. Assume that a

planar electrode is used and that semi-infinite linear diffusion applies. Derive the shape of the current-potential curve that would be recorded in a sampled-current experiment performed in the manner described here. What is the value of $E_{1/2}$? Does it depend on concentration?

(b) Show that the result of (a) is a special case of (5.5.41).

5.11 Derive the Tomeš criterion for (a) a reversible sampled-current voltammogram based on semi-infinite linear diffusion, (b) a totally irreversible sampled-current voltammogram based on semi-infinite linear diffusion, and (c) a totally irreversible steady-state voltammogram.

5.12 Derive (5.7.14) and (5.7.15) from (5.7.1)–(5.7.12).

5.13 Derive the shape of the sampled-current voltammogram that would be recorded at a stationary platinum microelectrode immersed in a solution containing only I^-. The couple:

$$I_3^- + 2e \rightleftarrows 3I^-$$

is reversible. What is the half-wave potential? Does it depend on the bulk concentration of I^-? Is this situation directly comparable to the case $O + ne \rightleftarrows R$?

5.14 Calculate k_f for the reduction of Cd^{2+} to the amalgam from the data in Figure 5.8.4.

5.15 Devise a chronocoulometric experiment for measuring the diffusion coefficient of Tl in mercury.

5.16 Consider the data in Figures 5.8.1 to 5.8.3. Calculate the diffusion coefficient of DCB. How well do the slopes of the two lines in Figure 5.8.3 bear out the expectations for a completely stable, reversible system? These data are typical for a solid planar electrode in nonaqueous media. Offer at least two possible explanations for the slight inequalities in the magnitudes of the slopes and intercepts in Figure 5.8.3.

5.17 An ultramicroelectrode has a "recessed disk" shape as shown in Figure 5.11.1. Assume the orifice diameter, d_0, is 1 μm and the Pt hemisphere diameter is 10 μm, with $\ell = 20$ μm. Assume the space within the recess fills with the bulk solution in which this tip is immersed (e.g., 0.01 M $Ru(NH_3)_6^{3+}$ in 0.1 M KCl).

(a) What magnitude of steady-state (long time) diffusion current, i_d, would be found?

(b) In using this electrode to study heterogeneous electron transfer kinetics from the steady state wave shape, what value is appropriate for r_0?
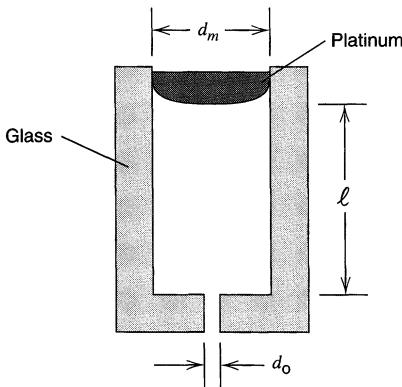
Figure 5.11.1 Recessed working electrode communicating with the solution through a small orifice.

5.18. The one-electron reduction of a species, O, is carried out at an ultramicroelectrode having a hemispherical shape with $r_0 = 5.0$ μm. The steady-state voltammogram in a solution containing 10 mM O and supporting electrolyte yields $\Delta E_{3/4} = E_{1/2} - E_{3/4} = 35.0$ mV, $\Delta E_{1/4} = E_{1/4} - E_{1/2} = 31.5$ mV, and $i_d = 15$ nA. Assume $D_O = D_R$ and $T = 298$ K.

(a) Find D_O.

(b) Using the method in reference 33, estimate k^0 and α.

5.19 G. Denault, M. Mirkin, and A. J. Bard [*J. Electroanal. Chem.*, **308**, 27 (1991)] suggested that by normalizing the diffusion-limited transient current, i, obtained at an ultramicroelectrode at short times, by the steady-state current, i_{ss}, one can determine the diffusion coefficient, D, without knowledge of the number electrons involved in the electrode reaction, n, or the bulk concentration of the reactant, C^*.

(a) Consider a disk ultramicroelectrode and derive the appropriate equation for i/i_{ss}.

(b) Why would this procedure not be suitable for a large electrode?

(c) A microdisk electrode of radius 13.1 μm is used to measure D for Ru(bpy)$_3^{2+}$ inside a polymer film. The slope of i/i_{ss} *vs.* $t^{-1/2}$ for the one-electron oxidation of Ru(bpy)$_3^{2+}$ is found to be 0.238 s$^{1/2}$ (with an intercept of 0.780). Calculate D.

(d) In the experiment in part (c), $i_{ss} = 16.0$ nA. What is the concentration of Ru(bpy)$_3^{2+}$ in the film?

CHAPTER

6

POTENTIAL SWEEP METHODS

6.1 INTRODUCTION

The complete electrochemical behavior of a system can be obtained through a series of steps to different potentials with recording of the current-time curves, as described in Sections 5.4 and 5.5, to yield a three-dimensional i-t-E surface (Figure 6.1.1a). However, the accumulation and analysis of these data can be tedious especially when a stationary electrode is used. Also, it is not easy to recognize the presence of different species (i.e., to observe waves) from the recorded i-t curves alone, and potential steps that are very closely spaced (e.g., 1 mV apart) are needed for the derivation of well-resolved i-E curves. More information can be gained in a single experiment by sweeping the potential with time and recording the i-E curve directly. This amounts, in a qualitative way, to traversing the three-dimensional i-t-E realm (Figure 6.1.1b). Usually the potential is varied linearly with time (i.e., the applied signal is a voltage ramp) with sweep rates v ranging from 10 mV/s (1 V traversed in 100 s) to about 1000 V/s with conventional electrodes and up to 10^6 V/s with UMEs. In this experiment, it is customary to record the current as a function of potential, which is obviously equivalent to recording current versus time. The formal name for the method is *linear potential sweep chronoamperometry*, but most workers refer to it as *linear sweep voltammetry* (LSV).[1]
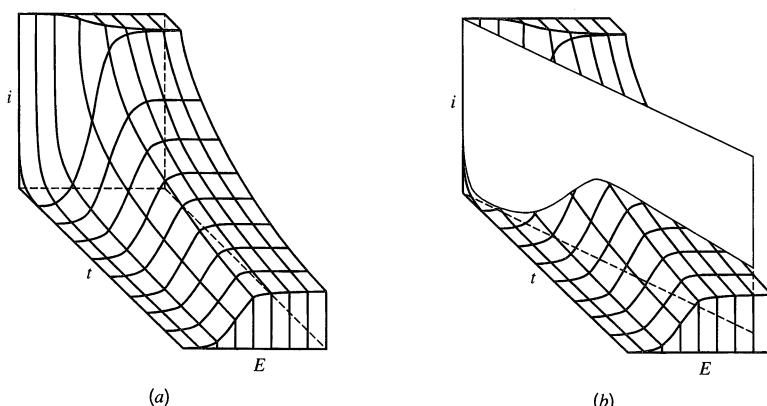
Figure 6.1.1 (a) A portion of the i-t-E surface for a nernstian reaction. Potential axis is in units of $60/n$ mV. (b) Linear potential sweep across this surface. [Reprinted with permission from W. H. Reinmuth, *Anal. Chem.*, **32**, 1509 (1960). Copyright 1960, American Chemical Society.]

---

[1]This method has also been called *stationary electrode polarography*; however, we will adhere to the recommended practice of reserving the term *polarography* for voltammetric measurements at the DME.
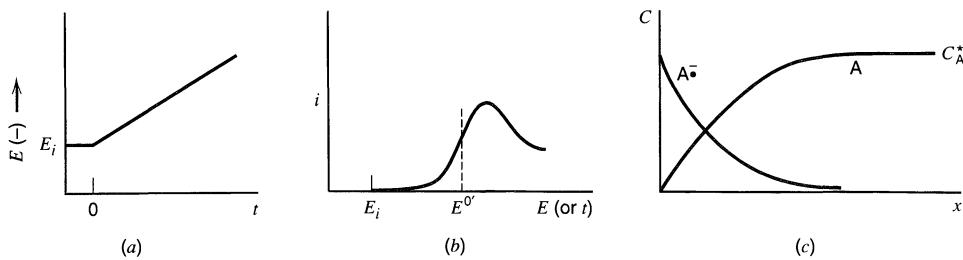
Figure 6.1.2 (*a*) Linear potential sweep or ramp starting at E_i. (*b*) Resulting *i-E* curve. (*c*) Concentration profiles of A and A^- for potentials beyond the peak.

A typical LSV response curve for the anthracene system considered in Section 5.1 is shown in Figure 6.1.2*b*. If the scan is begun at a potential well positive of $E^{0'}$ for the reduction, only nonfaradaic currents flow for a while. When the electrode potential reaches the vicinity of $E^{0'}$ the reduction begins and current starts to flow. As the potential continues to grow more negative, the surface concentration of anthracene must drop; hence the flux to the surface (and the current) increases. As the potential moves past $E^{0'}$, the surface concentration drops nearly to zero, mass transfer of anthracene to the surface reaches a maximum rate, and then it declines as the depletion effect sets in. The observation is therefore a peaked current-potential curve like that depicted.

At this point, the concentration profiles near the electrode are like those shown in Figure 6.1.2*c*. Let us consider what happens if we reverse the potential scan (see Figure 6.1.3). Suddenly the potential is sweeping in a positive direction, and in the electrode's vicinity there is a large concentration of the oxidizable anion radical of anthracene. As the potential approaches, then passes, $E^{0'}$, the electrochemical balance at the surface grows more and more favorable toward the neutral anthracene species. Thus the anion radical becomes reoxidized and an anodic current flows. This reversal current has a shape much like that of the forward peak for essentially the same reasons.

This experiment, which is called *cyclic voltammetry* (CV), is a reversal technique and is the potential-scan equivalent of double potential step chronoamperometry (Section 5.7). Cyclic voltammetry has become a very popular technique for initial electrochemical studies of new systems and has proven very useful in obtaining information about fairly complicated electrode reactions. These will be discussed in more detail in Chapter 12.

In the next sections, we describe the solution of the diffusion equations with the appropriate boundary conditions for electrode reactions with heterogeneous rate constants spanning a wide range, and we discuss the observed responses. An analytical approach based on an integral equation is used here, because it has been widely applied to these types of problems and shows directly how the current is affected by different experimen-
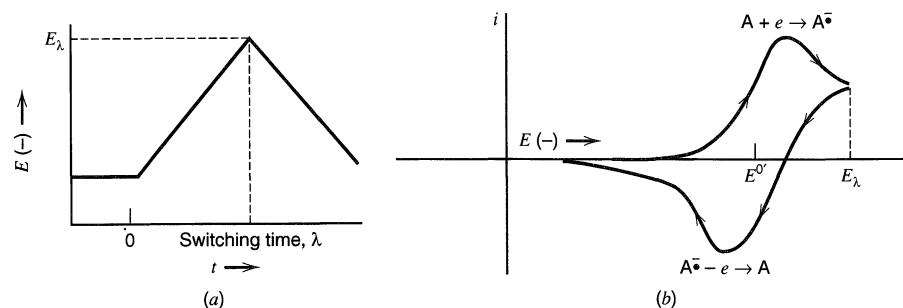
Figure 6.1.3 (*a*) Cyclic potential sweep. (*b*) Resulting cyclic voltammogram.

tal variables (e.g., scan rate and concentration). However, in most cases, particularly when the overall reactions are complicated by coupled homogeneous reactions (Chapter 12), digital simulation methods (Appendix B) are used to calculate voltammograms.

► 6.2 NERNSTIAN (REVERSIBLE) SYSTEMS

6.2.1 Solution of the Boundary Value Problem

We consider again the reaction $O + ne \rightleftarrows R$, assuming semi-infinite linear diffusion and a solution initially containing only species O, with the electrode held initially at a potential E_i, where no electrode reaction occurs. These initial conditions are identical to those in Section 5.4.1. The potential is swept linearly at v (V/s) so that the potential at any time is

$$E(t) = E_i - v t \tag{6.2.1}$$

If we can assume that the rate of electron transfer is rapid at the electrode surface, so that species O and R immediately adjust to the ratio dictated by the Nernst equation, then the equations of Section 5.4, that is, (5.4.2)–(5.4.6), still apply. However, (5.4.6) must be recognized as having a time-dependent form:

$$\frac{C_O(0, t)}{C_R(0, t)} = f(t) = \exp\left[\frac{nF}{RT}(E_i - v t - E^{0'})\right] \tag{6.2.2}$$

The time dependence is significant, because the Laplace transformation of (6.2.2) cannot be obtained as it could in deriving (5.4.13),[2] and the mathematics for sweep experiments are greatly complicated as a consequence. The problem was first considered by Randles (1) and Sevcik (2); the treatment and notation here follow the later work of Nicholson and Shain (3). The boundary condition (6.2.2) can be written

$$\frac{C_O(0, t)}{C_R(0, t)} = \theta\, e^{-\sigma t} = \theta S(t) \tag{6.2.3}$$

where $S(t) = e^{-\sigma t}$, $\theta = \exp[(nF/RT)(E_i - E^{0'})]$, and $\sigma = (nF/RT)v$. As before (see Section 5.4.1), Laplace transformation of the diffusion equations and application of the initial and semi-infinite conditions leads to [see (5.4.7)]

$$\bar{C}_O(x, s) = \frac{C_O^*}{s} + A(s) \exp\left[-\left(\frac{s}{D_O}\right)^{1/2} x\right] \tag{6.2.4}$$

The transform of the current is given by [see (5.2.9)]

$$\bar{i}(s) = nFAD_O\left[\frac{\partial \bar{C}_O(x, s)}{\partial x}\right]_{x=0} \tag{6.2.5}$$

Combining this with (6.2.4) and inverting, by making use of the convolution theorem (see Appendix A), we obtain[3]

$$\boxed{C_O(0, t) = C_O^* - [nFA(\pi D_O)^{1/2}]^{-1} \int_0^t i(\tau)(t - \tau)^{-1/2}\, d\tau} \tag{6.2.6}$$

---

[2]The Laplace transform of $C_O(0, t) = \theta C_R(0, t)$ is $\bar{C}_O(0, s) = \theta\, \bar{C}_R(0, s)$ only when θ is not a function of time; it is only under this condition that θ can be removed from the Laplace integral.

[3]This derivation is left as an exercise for the reader (see Problem 6.1). Equation 6.2.6 is often a useful starting point in other electrochemical treatments involving semi-infinite linear diffusion. τ in the integral is a dummy variable that is lost when the definite integral is evaluated.

By letting

$$f(\tau) = \frac{i(\tau)}{nFA} \tag{6.2.7}$$

(6.2.6) can be written

$$C_O(0, t) = C_O^* - (\pi D_O)^{-1/2} \int_0^t f(\tau)(t - \tau)^{-1/2} \, d\tau \tag{6.2.8}$$

Similarly from (5.4.12) an expression for $C_R(0, t)$ can be obtained (assuming R is initially absent):

$$C_R(0, t) = (\pi D_R)^{-1/2} \int_0^t f(\tau)(t - \tau)^{-1/2} \, d\tau \tag{6.2.9}$$

The derivation of (6.2.8) and (6.2.9) employed only the linear diffusion equations, initial conditions, semi-infinite conditions, and the flux balance. No assumption related to electrode kinetics or technique was made; hence (6.2.8) and (6.2.9) are general. From these equations and the boundary condition for LSV, (6.2.3), we obtain

$$\int_0^t f(\tau)(t - \tau)^{-1/2} \, d\tau = \frac{C_O^*}{[\theta S(t)(\pi D_R)^{-1/2} + (\pi D_O)^{-1/2}]} \tag{6.2.10}$$

$$\int_0^t i(\tau)(t - \tau)^{-1/2} \, d\tau = \frac{nFA\pi^{1/2}D_O^{1/2}C_O^*}{[\theta S(t)\xi + 1]} \tag{6.2.11}$$

where, as before, $\xi = (D_O/D_R)^{1/2}$. The solution of this last integral equation would be the function $i(t)$, embodying the desired current-time curve, or, since potential is linearly related to time, the current-potential equation. A closed-form solution of (6.2.11) cannot be obtained, and a numerical method must be employed.

Before solving (6.2.11) numerically, it is convenient (a) to change from $i(t)$ to $i(E)$, since that is the way in which the data are usually considered, and (b) to put the equation in a dimensionless form so that a single numerical solution will give results that will be useful under any experimental conditions. This is accomplished by using the following substitution:

$$\sigma t = \frac{nF}{RT} vt = \left(\frac{nF}{RT}\right)(E_i - E) \tag{6.2.12}$$

Let $f(\tau) = g(\sigma\tau)$. With $z = \sigma\tau$, so that $\tau = z/\sigma$, $d\tau = dz/\sigma$, $z = 0$ at $\tau = 0$, and $z = \sigma t$ at $\tau = t$, we obtain

$$\int_0^t f(\tau)\left(t - \tau\right)^{-1/2} \, d\tau = \int_0^{\sigma t} g(z)\left(t - \frac{z}{\sigma}\right)^{-1/2} \frac{dz}{\sigma} \tag{6.2.13}$$

so that (6.2.11) can be written

$$\int_0^{\sigma t} g(z)(\sigma t - z)^{-1/2} \sigma^{-1/2} \, dz = \frac{C_O^*(\pi D_O)^{1/2}}{1 + \xi\theta S(\sigma t)} \tag{6.2.14}$$

or finally, dividing by $C_O^*(\pi D_O)^{1/2}$, we obtain

$$\int_0^{\sigma t} \frac{\chi(z) \, dz}{(\sigma t - z)^{1/2}} = \frac{1}{1 + \xi\theta S(\sigma t)} \tag{6.2.15}$$

where

$$\chi(z) = \frac{g(z)}{C_O^*(\pi D_O \sigma)^{1/2}} = \frac{i(\sigma t)}{nFAC_O^*(\pi D_O \sigma)^{1/2}} \qquad (6.2.16)$$

Note that (6.2.15) is the desired equation in terms of the dimensionless variables $\chi(z)$, ξ, θ, $S(\sigma t)$ and σt. Thus at any value of $S(\sigma t)$, which is a function of E, $\chi(\sigma t)$ can be obtained by solution of (6.2.15) and, from it, the current can be obtained by rearrangement of (6.2.16):

$$\boxed{i = nFAC_O^*(\pi D_O \sigma)^{1/2} \chi(\sigma t)} \qquad (6.2.17)$$

At any given point, $\chi(\sigma t)$ is a pure number, so that (6.2.17) gives the functional relationship between the current at any point on the LSV curve and the variables. Specifically, i is proportional to C_O^* and $v^{1/2}$. The solution of (6.2.15) has been carried out numerically [Nicholson and Shain (3)], by a series solution [Sevcik (2), Reinmuth (4)], analytically in terms of an integral that must be evaluated numerically [Matsuda and Ayabe (5), Gokhshtein (6)], and by related methods (7, 8). The general result of solving (6.2.15) is a set of values of $\chi(\sigma t)$ (see Table 6.2.1 and Figure 6.2.1) as a function of σt or $n(E - E_{1/2})$.[4]

TABLE 6.2.1   Current Functions for Reversible Charge Transfer (3)[a,b]

$\dfrac{n(E - E_{1/2})}{RT/F}$	$n(E - E_{1/2})$ mV at 25°C	$\pi^{1/2}\chi(\sigma t)$	$\phi(\sigma t)$	$\dfrac{n(E - E_{1/2})}{RT/F}$	$n(E - E_{1/2})$ mV at 25°C	$\pi^{1/2}\chi(\sigma t)$	$\phi(\sigma t)$
4.67	120	0.009	0.008	−0.19	−5	0.400	0.548
3.89	100	0.020	0.019	−0.39	−10	0.418	0.596
3.11	80	0.042	0.041	−0.58	−15	0.432	0.641
2.34	60	0.084	0.087	−0.78	−20	0.441	0.685
1.95	50	0.117	0.124	−0.97	−25	0.445	0.725
1.75	45	0.138	0.146	−1.109	−28.50	0.4463	0.7516
1.56	40	0.160	0.173	−1.17	−30	0.446	0.763
1.36	35	0.185	0.208	−1.36	−35	0.443	0.796
1.17	30	0.211	0.236	−1.56	−40	0.438	0.826
0.97	25	0.240	0.273	−1.95	−50	0.421	0.875
0.78	20	0.269	0.314	−2.34	−60	0.399	0.912
0.58	15	0.298	0.357	−3.11	−80	0.353	0.957
0.39	10	0.328	0.403	−3.89	−100	0.312	0.980
0.19	5	0.355	0.451	−4.67	−120	0.280	0.991
0.00	0	0.380	0.499	−5.84	−150	0.245	0.997

[a]To calculate the current:

1. $i = i(\text{plane}) + i(\text{spherical correction})$.

2. $i = nFAD_O^{1/2}C_O^*\sigma^{1/2}\pi^{1/2}\chi(\sigma t) + nFAD_O C_O^*(1/r_0)\phi(\sigma t)$.

3. $i = 602n^{3/2}AD_O^{1/2}C_O^* v^{1/2}\{\pi^{1/2}\chi(\sigma t) + 0.160[D_O^{1/2}/(r_0 n^{1/2} v^{1/2})]\phi(\sigma t)\}$ at 25°C with quantities in the following units: i, amperes; A, cm^2; D_O, cm^2/s; v, V/s; C_O^*, M; r_0, cm.

[b]$E_{1/2} = E^{0'} + (RT/nF) \ln (D_R/D_O)^{1/2}$.

[4]Note that $\ln \xi\theta S(\sigma t) = nf(E - E_{1/2})$, where $E_{1/2} \equiv E^{0'} + (RT/nF) \ln (D_R/D_O)^{1/2}$.
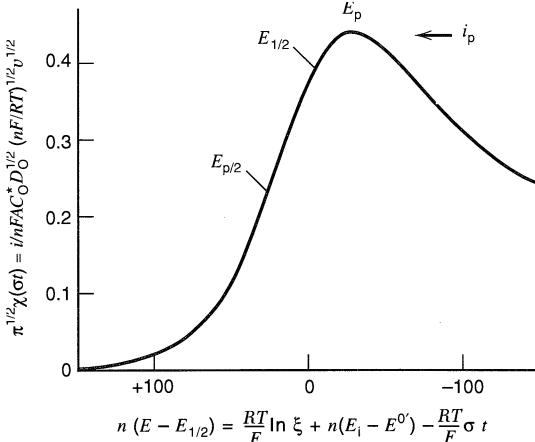
Figure 6.2.1 Linear potential sweep voltammogram in terms of dimensionless current function. Values on the potential axis are for 25°C

6.2.2 Peak Current and Potential

The function $\pi^{1/2}\chi(\sigma t)$, and hence the current, reaches a maximum where $\pi^{1/2}\chi(\sigma t) = 0.4463$. From (6.2.17) the *peak current*, i_p, is

$$i_p = 0.4463\left(\frac{F^3}{RT}\right)^{1/2} n^{3/2} AD_O^{1/2}C_O^* v^{1/2} \tag{6.2.18}$$

At 25°C, for A in cm^2, D_O in cm^2/s, C_O^* in mol/cm^3, and v in V/s, i_p in amperes is

$$i_p = (2.69 \times 10^5)n^{3/2} AD_O^{1/2}C_O^* v^{1/2} \tag{6.2.19}$$

The *peak potential*, E_p, is found from Table 6.2.1 to be

$$E_p = E_{1/2} - 1.109\frac{RT}{nF} = 28.5/n \text{ mV at 25°C} \tag{6.2.20}$$

Because the peak is somewhat broad, so that the peak potential may be difficult to determine, it is sometimes convenient to report the potential at $i_p/2$, called the *half-peak potential*, $E_{p/2}$, which is

$$E_{p/2} = E_{1/2} + 1.09\frac{RT}{nF} = E_{1/2} + 28.0/n \text{ mV at 25°C} \tag{6.2.21}$$

Note that $E_{1/2}$ is located just about midway between E_p and $E_{p/2}$, and that a convenient diagnostic for a nernstian wave is

$$|E_p - E_{p/2}| = 2.20\frac{RT}{nF} = 56.5/n \text{ mV at 25°C} \tag{6.2.22}$$

Thus for a reversible wave, E_p is independent of scan rate, and i_p (as well as the current at any point on the wave) is proportional to $v^{1/2}$. The latter property indicates diffusion control and is analogous to the variation of i_d with $t^{-1/2}$ in chronoamperometry. A convenient constant in LSV is $i_p/v^{1/2}C_O^*$ (sometimes called the *current function*), which depends on $n^{3/2}$ and $D_O^{1/2}$. This constant can be used to estimate n for an electrode

reaction, if a value of D_O can be estimated, for example, from the LSV of a compound of similar size or structure that undergoes an electrode reaction with a known n value.

6.2.3 Spherical Electrodes and UMEs

For LSV with a spherical electrode (e.g., a hanging mercury drop), a similar treatment can be presented (4); the resulting current is

$$i = i(\text{plane}) + \frac{nFAD_O C_O^* \phi(\sigma t)}{r_0} \qquad (6.2.23)$$

where r_0 is the radius of the electrode and $\phi(\sigma t)$ is a tabulated function (see Table 6.2.1). For large values of v and with electrodes of conventional size the i (plane) term is much larger than the spherical correction term, and the electrode can be considered planar under these conditions.

Basically, the same considerations apply to hemispherical and ultramicroelectrodes at fast scan rates. However, for a UME, where r_0 is small, the second term will dominate at sufficiently small scan rates. One can show from (6.2.23) that this is true when

$$v << RTD/nFr_0^2 \qquad (6.2.24)$$

so that the voltammogram will be a steady-state response independent of v.[5] For $r_0 = 5$ μm, $D = 10^{-5}$ cm^2/s, and $T = 298$ K, the right side of (6.2.24) has a value of 1000 mV/s; thus a scan made at ~100 mV/s or slower should permit the accurate recording of steady-state currents. The limit depends on the square of the radius, so it is generally impractical to record steady-state voltammograms with electrodes much larger than those normally considered to be UMEs. Conversely, with very small UMEs, one requires a high sweep rate to see any behavior other than the steady state. For example, at an electrode of 0.5-μm radius and with D and T as given above, steady-state behavior would hold up to 10 V/s.
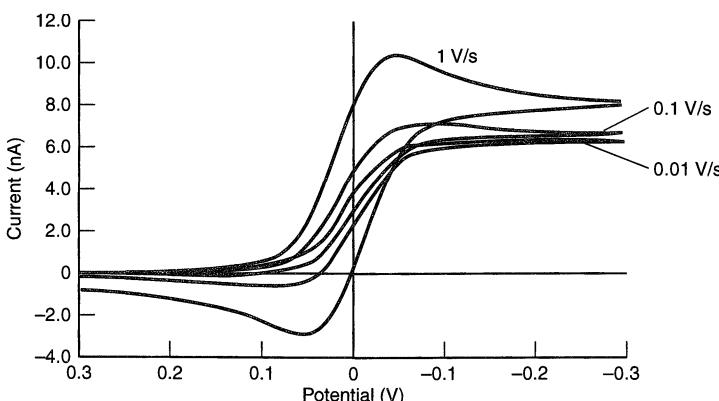
Figure 6.2.2 Effect of scan rate on cyclic voltammograms for an ultramicroelectrode (hemispherical diffusion) with 10 μm radius. Simulations for a nernstian reaction with $n = 1$, $E^{0'} = 0.0$ V, $D_O = D_R = 1 \times 10^{-5}$ cm^2/s, $C_O^* = 1.0$ mM, and $T = 25$°C. At 1 V/s, the response begins to show the peak expected for linear diffusion, but the height of the current at the switching potential and the small peak current ratio show that the steady-state component is still dominant.

---

[5]Relationship 6.2.24 involves a comparison of a diffusion length to the radius of the electrode in the manner discussed in Section 5.2.2. The diffusion length is $[D_O/(nfv)]^{1/2}$, which corresponds to the time $1/(nfv)$. This is the period required for the scan to cover an energy kT along the potential axis (25.7/n mV at 25°C). It is often regarded as the characteristic time of an LSV or CV experiment (Chapter 12).

The transition from typical peak-shaped voltammograms at fast sweep rates in the linear diffusion region to steady-state voltammograms at small v is shown for cyclic voltammetry in Figure 6.2.2. In the steady-state region, the voltammograms are S-shaped and follow the treatment in Sections 1.4.2 and 5.4.2. Ultramicroelectrodes are almost always employed in the limiting regions: the linear region when $v^{1/2}/r_0$ is large and the steady-state region when $v^{1/2}/r_0$ is small. There is nothing additional to be gained from working in the mathematically more complicated intermediate region.

6.2.4 Effect of Double-Layer Capacitance and Uncompensated Resistance

For a potential step experiment at a stationary, constant-area electrode, the charging current dies away after a time equivalent to a few time constants ($R_u C_d$) (see Section 1.2.4). Since the potential is continuously changing in a potential sweep experiment, a charging current, i_c, always flows (see equation 1.2.15):

$$|i_c| = AC_d v \qquad (6.2.25)$$

and the faradaic current must always be measured from a baseline of charging current (Figure 6.2.3). While i_p varies with $v^{1/2}$ for linear diffusion, i_c varies with v, so that i_c becomes relatively more important at faster scan rates. From (6.2.19) and (6.2.25)

$$\frac{|i_c|}{i_p} = \frac{C_d v^{1/2}(10^{-5})}{2.69 n^{3/2} D_O^{1/2} C_O^*} \qquad (6.2.26)$$

or for $D_O = 10^{-5} cm^2/s$ and $C_d = 20 \ \mu F/cm^2$,

$$\frac{|i_c|}{i_p} \approx \frac{(2.4 \times 10^{-8})v^{1/2}}{n^{3/2} C_O^*} \qquad (6.2.27)$$

Thus at high v and low C_O^* values, severe distortion of the LSV wave occurs. This effect often sets the limits of maximum useful scan rate and minimum useful concentration.

In general, a potentiostat controls $E + iR_u$, rather than the true potential of the working electrode (Sections 1.3.4 and 15.6.1). Since i varies with time as the peak is traversed, the error in potential varies correspondingly. If $i_p R_u$ is appreciable compared to the accuracy of measurement (e.g., a few mV), the sweep will not be truly linear and the condition given by (6.2.1) does not hold. Moreover, the time required for the current to rise to the level given in (6.2.25) depends upon the electrode time constant, $R_u C_d$, as shown in (1.2.15). The practical effect of R_u is to flatten the wave and to shift the reduction peak toward more negative potentials. Since the current increases with $v^{1/2}$, the larger the scan rate, the more E_p will be shifted, so that appreciable R_u causes E_p to be a function of v. It moves systematically in a negative direction with increasing v (for a reduction). Uncompensated resistance can thus have the insidious effect of mimicking the response found with heterogeneous kinetic limitations (as discussed in Sections 6.3 and 6.4).

By using a UME, one can extend the useful range of sweep rates to the 10^6 V/s region. Because the measured currents at the UME are small, the iR_u drop does not perturb the response or the applied excitation to the same extent as with larger electrodes. The much smaller $R_u C_d$ at the UME also leads to less distortion in the voltammogram. However, even with the UME (6.2.27) applies, so the faradaic wave lies on top of a large capacitive current. To extract the desired information from the voltammogram, the total response (capacitive plus faradaic) can be simulated (9) or perturbations caused by C_d and R_u can be subtracted (10). Alternatively, positive feedback circuitry with a fast response can be used to compensate for distortions otherwise caused by R_u (11).
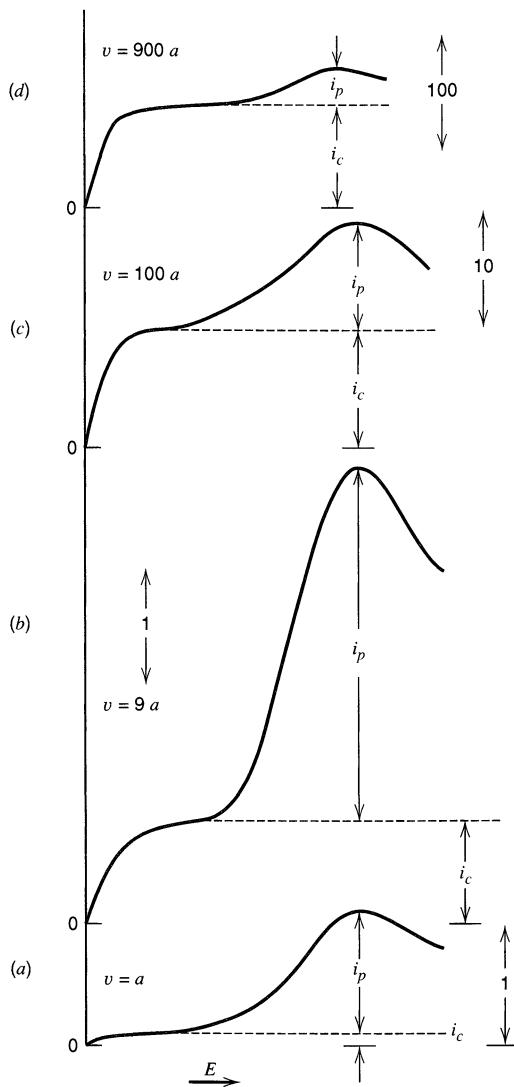
Figure 6.2.3 Effect of double-layer charging at different sweep rates on a linear potential sweep voltammogram. Curves are plotted with the assumption that C_d is independent of E. The magnitudes of the charging current, i_c, and the faradaic peak current, i_p, are shown. Note that the current scale in (c) is 10× and in (d) is 100× that in (a) and (b).

An important practical limitation of very fast voltammetry [other than instrumental and R_u and C_d considerations (11)], is the importance of adsorption of even small amounts of electroactive substance or faradaic changes involving the electrode surface (e.g., formation of an oxide layer). As shown in Section 14.3, for surface processes like double-layer charging, the current response varies directly with v. Therefore, surface effects of minor importance at small v can dominate at high scan rates.

▷ 6.3 TOTALLY IRREVERSIBLE SYSTEMS

6.3.1 The Boundary Value Problem

For a totally irreversible one-step, one-electron reaction ($O + e \xrightarrow{k_f} R$) the nernstian boundary condition, (6.2.2), is replaced by (see Section 5.5)

$$\frac{i}{FA} = D_O \left[\frac{\partial C_O(x, t)}{\partial x} \right]_{x=0} = k_f(t) C_O(0, t) \qquad (6.3.1)$$

where

$$k_f(t) = k^0 \exp\{-\alpha f[E(t) - E^{0'}]\}$$ (6.3.2)

Introducing $E(t)$ from (6.2.1) into (6.3.2) yields

$$k_f(t)C_O(0, t) = k_{fi}C_O(0, t)e^{bt}$$ (6.3.3)

where $b = \alpha f v$ and

$$k_{fi} = k^0 \exp[-\alpha f(E_i - E^{0'})]$$ (6.3.4)

The solution follows in an analogous manner to that described in Section 6.2.1 and again requires a numerical solution of an integral equation (3, 5). The current is given by

$$i = FAC_O^*(\pi D_O b)^{1/2} \chi(bt)$$ (6.3.5)

$$i = FAC_O^* D_O^{1/2} v^{1/2} \left(\frac{\alpha F}{RT}\right)^{1/2} \pi^{1/2}\chi(bt)$$ (6.3.6)

where $\chi(bt)$ is a function [different from $\chi(\sigma t)$] tabulated in Table 6.3.1. Again, i at any point on the wave varies with $v^{1/2}$ and C_O^*.

For spherical electrodes, a procedure analogous to that employed at planar electrodes has been proposed. Table 6.3.1 contains values of the spherical correction factor, $\phi(bt)$ employed in the equation

$$i = i(\text{plane}) + \frac{FAD_O C_O^* \phi(bt)}{r_0}$$ (6.3.7)

TABLE 6.3.1   Current Functions for Irreversible Charge Transfer (3)[a]

Dimensionless Potential[b]	Potential[c] mV at 25°C	$\pi^{1/2}\chi(bt)$	$\phi(bt)$	Dimensionless Potential[b]	Potential[c] mV at 25°C	$\pi^{1/2}\chi(bt)$	$\phi(bt)$
6.23	160	0.003		0.58	15	0.437	0.323
5.45	140	0.008		0.39	10	0.462	0.396
4.67	120	0.016		0.19	5	0.480	0.482
4.28	110	0.024		0.00	0	0.492	0.600
3.89	100	0.035		−0.19	−5	0.496	0.685
3.50	90	0.050		−0.21	−5.34	0.4958	0.694
3.11	80	0.073	0.004	−0.39	−10	0.493	0.755
2.72	70	0.104	0.010	−0.58	−15	0.485	0.823
2.34	60	0.145	0.021	−0.78	−20	0.472	0.895
1.95	50	0.199	0.042	−0.97	−25	0.457	0.952
1.56	40	0.264	0.083	−1.17	−30	0.441	0.992
1.36	35	0.300	0.115	−1.36	−35	0.423	1.000
1.17	30	0.337	0.154	−1.56	−40	0.406	
0.97	25	0.372	0.199	−1.95	−50	0.374	
0.78	20	0.406	0.253	−2.72	−70	0.323	

[a]To calculate the current:

1. $i = i(\text{plane}) + i(\text{spherical correction})$.
2. $i = FAD_O^{1/2}C_O^* b^{1/2}\pi^{1/2}\chi(bt) + FAD_O C_O^*(1/r_0)\phi(bt)$
3. $i = 602 AD_O^{1/2}C_O^*\alpha^{1/2}v^{1/2}\{\pi^{1/2}\chi(bt) + 0.160[D_O^{1/2}/(r_0\alpha^{1/2}v^{1/2})]\phi(bt)\}$. Units for step 3 are the same as in Table 6.2.1.

[b]Dimensionless potential is $(\alpha F/RT)(E - E^{0'}) + \ln[(\pi D_O b)^{1/2}/k^0]$.

[c]Potential scale in mV for 25°C is $\alpha(E - E^{0'}) + (59.1)\ln[(\pi D_O b)^{1/2}/k^0]$.

6.3.2 Peak Current and Potential

The function $\chi(bt)$ goes through a maximum at $\pi^{1/2}\chi(bt) = 0.4958$. Introduction of this value into (6.3.6) yields the following for the peak current:

$$i_p = (2.99 \times 10^5)\alpha^{1/2}AC_O^*D_O^{1/2}v^{1/2} \tag{6.3.8}$$

where the units are as for (6.2.19). From Table 6.3.1, the peak potential, E_p, is given by

$$\alpha(E_p - E^{0'}) + \frac{RT}{F}\ln\left[\frac{(\pi D_O b)^{1/2}}{k^0}\right] = -0.21\frac{RT}{F} = -5.34 \text{ mV at 25°C} \tag{6.3.9}$$

or

$$E_p = E^{0'} - \frac{RT}{\alpha F}\left[0.780 + \ln\left(\frac{D_O^{1/2}}{k^0}\right) + \ln\left(\frac{\alpha F v}{RT}\right)^{1/2}\right] \tag{6.3.10}$$

$$\left|E_p - E_{p/2}\right| = \frac{1.857RT}{\alpha F} = \frac{47.7}{\alpha} \text{ mV at 25°C} \tag{6.3.11}$$

where $E_{p/2}$ is the potential where the current is at half the peak value. For a totally irreversible wave, E_p is a function of scan rate, shifting (for a reduction) in a negative direction by an amount $1.15RT/\alpha F$ (or $30/\alpha$ mV at 25°C) for each tenfold increase in v. Also, E_p occurs *beyond* $E^{0'}$ (i.e., more negative for a reduction) by an activation overpotential related to k^0. An alternative expression for i_p in terms of E_p can be obtained by combining (6.3.10) with (6.3.6), so that the result contains the value of $\chi(bt)$ at the peak. After rearrangement and evaluation of the constants, the following equation is obtained (3, 6):

$$i_p = 0.227\, FAC_O^*k^0 \exp[-\alpha f(E_p - E^{0'})] \tag{6.3.12}$$

A plot of $\ln i_p$ *vs.* $E_p - E^{0'}$ (assuming $E^{0'}$ can be obtained) determined at different scan rates should have a slope of $-\alpha f$ and an intercept proportional to k^0.

For an irreversible process more complicated than the one-step, one-electron reaction, it is usually not feasible to derive equations describing the current-potential relationship. In the general case, the more practical approach is to compare experimental behavior with the predictions from simulations (see Appendix B and Chapter 12). Analytical equations may be achievable for a few of the simpler possibilities (see Section 3.5.4). The most important is an overall n-electron process having an irreversible heterogeneous one-electron transfer as the rate-controlling first step. In that case, all equations describing currents in this section [(6.3.5)–(6.3.8), (6.3.12), and in the notes to Table 6.3.1] apply, but with the right hand side multiplied by n. The equations describing potentials [(6.3.9)–(6.3.11)] apply without alteration.

▶ 6.4 QUASIREVERSIBLE SYSTEMS

Matsuda and Ayabe (5) coined the term *quasireversible* for reactions that show electron-transfer kinetic limitations where the reverse reaction has to be considered, and they provided the first treatment of such systems. For the one-step, one-electron case,

$$O + e \underset{k_b}{\overset{k_f}{\rightleftarrows}} R \tag{6.4.1}$$

the corresponding boundary condition is [from (5.5.3)]

$$D_O\left(\frac{\partial C_O(x, t)}{\partial x}\right)_{x=0} = k^0 e^{-\alpha f[E(t)-E^{0'}]}\{C_O(0, t) - C_R(0, t)e^{f[E(t)-E^{0'}]}\} \tag{6.4.2}$$

The shape of the peak and the various peak parameters were shown to be functions of α and a parameter Λ, defined as

$$\Lambda = \frac{k^0}{(D_O^{1-\alpha} D_R^\alpha fv)^{1/2}}$$

(6.4.3)

or, for $D_O = D_R = D$,

$$\Lambda = \frac{k^0}{(Dfv)^{1/2}}$$

(6.4.4)

The current is given by

$$i = FAD_O^{1/2} C_O^* f^{1/2} v^{1/2} \Psi(E)$$

(6.4.5)

where $\Psi(E)$ is shown in Figure 6.4.1. Note that when $\Lambda > 10$, the behavior approaches that of a reversible system.

The values of i_p, E_p, and $E_{p/2}$ depend on Λ and α. The peak current is given by

$$i_p = i_p(\text{rev})K(\Lambda, \alpha)$$

(6.4.6)

where $i_p(\text{rev})$ is the reversible i_p value (equation 6.2.18), and the function $K(\Lambda, \alpha)$ is shown in Figure 6.4.2. Note that for a quasireversible reaction, i_p is not proportional to $v^{1/2}$.

The peak potential is

$$E_p - E_{1/2} = -\Xi(\Lambda, \alpha)\left(\frac{RT}{F}\right) = -26\Xi(\Lambda, \alpha) \text{ mV at } 25°C$$

(6.4.7)
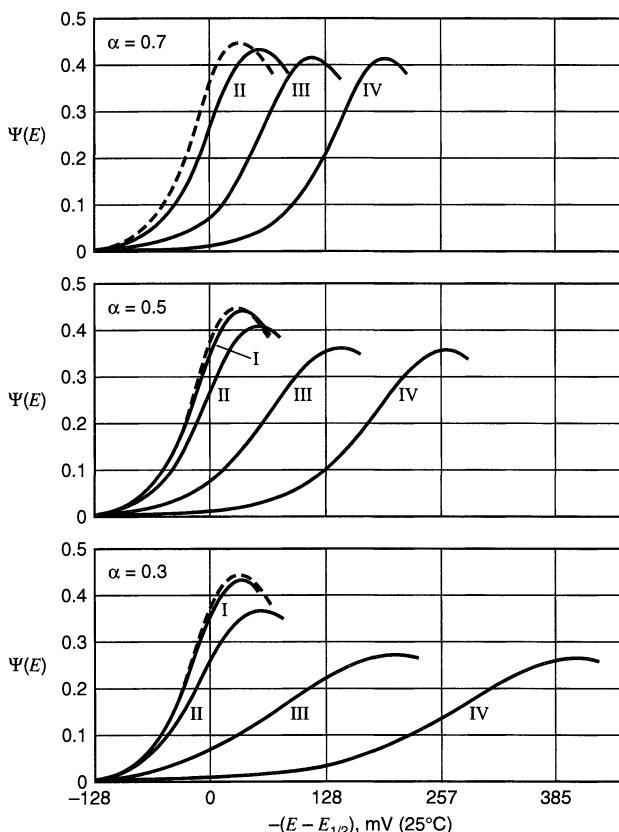
Figure 6.4.1 Variation of quasireversible current function, $\Psi(E)$, for different values of α (as indicated on each graph) and the following values of Λ: (I) $\Lambda = 10$; (II) $\Lambda = 1$; (III) $\Lambda = 0.1$; (IV) $\Lambda = 10^{-2}$. Dashed curve is for a reversible reaction. $\Psi(E) = i/FAC_O^* D_O^{1/2} (nF/RT)^{1/2} v^{1/2}$ and $\Lambda = k^0/[D^{1/2}(F/RT)^{1/2}v^{1/2}]$ (for $D_O = D_R = D$). [From H. Matsuda and Y. Ayabe, *Z. Elektrochem.*, **59**, 494 (1955), with permission. Abscissa label adapted for this text.]
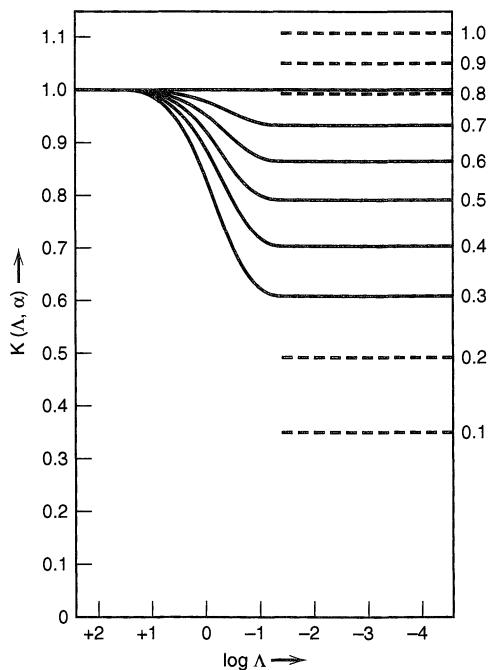
Figure 6.4.2 Variation of $K(\Lambda, \alpha)$ with Λ for different values of α. Dashed lines show functions for a totally irreversible reaction. $K(\Lambda, \alpha) = i_p/i_p(\text{rev})$. [From H. Matsuda and Y. Ayabe, *Z. Elektrochem.*, **59**, 494 (1955), with permission.]

where $\Xi(\Lambda, \alpha)$ is shown in Figure 6.4.3. For the half-peak potential, we have

$$E_{p/2} - E_p = \Delta(\Lambda, \alpha)\left(\frac{RT}{F}\right) = 26\Delta(\Lambda, \alpha) \text{ mV at } 25°C \qquad (6.4.8)$$

where $\Delta(\Lambda, \alpha)$ is given in Figure 6.4.4.

The parameters $K(\Lambda, \alpha)$, $\Xi(\Lambda, \alpha)$, and $\Delta(\Lambda, \alpha)$ attain limiting values characteristic of reversible or totally irreversible processes as Λ varies. For example, consider $\Delta(\Lambda, \alpha)$. For $\Lambda \geq 10$, $\Delta(\Lambda, \alpha) \approx 2.2$, yielding the $E_p - E_{p/2}$ value characteristic of a reversible wave, (6.2.22). For $\Lambda < 10^{-2}$ and $\alpha = 0.5$, $\Delta(\Lambda, \alpha) \approx 3.7$, yielding the totally irreversible charac-
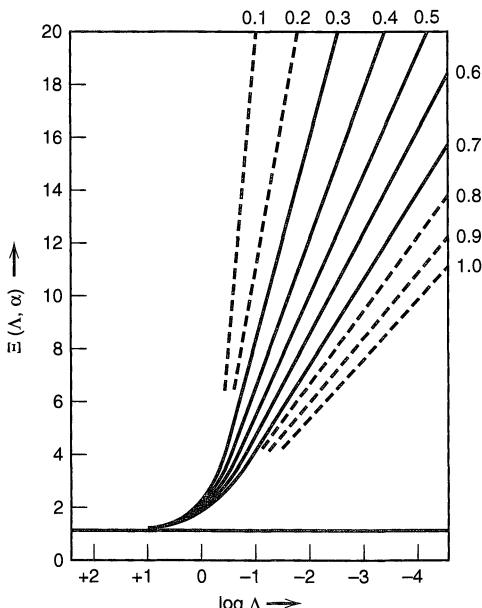
Figure 6.4.3 Variation of $\Xi(\Lambda, \alpha)$ with Λ for different values of α. Dashed lines show functions for a totally irreversible reaction. $\Xi(\Lambda, \alpha) = -(E_p - E_{1/2})F/RT$. [From H. Matsuda and Y. Ayabe, *Z. Elektrochem.*, **59**, 494 (1955), with permission.]
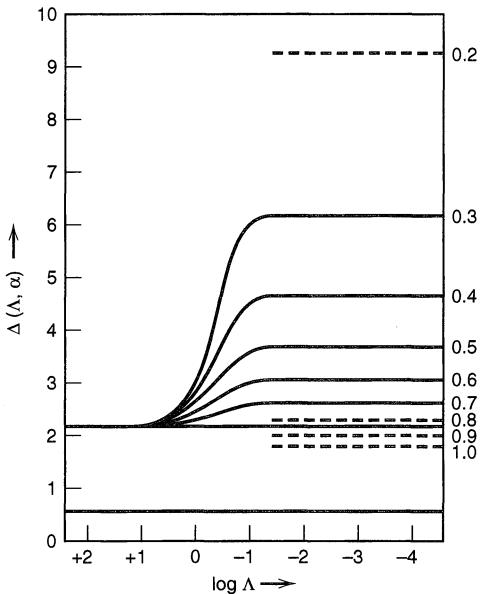
Figure 6.4.4 Variation of $\Delta(\Lambda, \alpha)$ with Λ and α. Dashed lines show functions for a totally irreversible reaction. $\Delta(\Lambda, \alpha) = (E_{p/2} - E_p)F/RT$. [From H. Matsuda and Y. Ayabe, *Z. Elektrochem.*, **59**, 494 (1955), with permission.]

teristic, (6.3.11). Thus a system may show nernstian, quasireversible, or totally irreversible behavior, depending on Λ, or experimentally, on the scan rate employed. The appearance of kinetic effects depends on the time window of the experiment, which is essentially the time needed to traverse the LSV wave (see Chapter 12). At small v (or long times), systems may yield reversible waves, while at large v (or short times), irreversible behavior is observed. In Section 5.5, we reached the same conclusions in the context of potential step experiments. Matsuda and Ayabe (5) suggested the following zone boundaries for LSV:[6]

Reversible (nernstian)	$\Lambda \geq 15;\ k^0 \geq 0.3v^{1/2}$ cm/s
Quasireversible	$15 \geq \Lambda \geq 10^{-2(1+\alpha)};\ 0.3v^{1/2} \geq k^0 \geq 2 \times 10^{-5}\,v^{1/2}$ cm/s
Totally irreversible	$\Lambda \leq 10^{-2(1+\alpha)};\ k^0 \leq 2 \times 10^{-5}\,v^{1/2}$ cm/s

▷▷ 6.5 CYCLIC VOLTAMMETRY

The reversal experiment in linear scan voltammetry is carried out by switching the direction of the scan at a certain time, $t = \lambda$ (or at the *switching potential, E_λ*). Thus the potential is given at any time by

$$(0 < t \leq \lambda) \quad E = E_i - vt \tag{6.5.1}$$

$$(t > \lambda) \quad E = E_i - 2v\lambda + vt \tag{6.5.2}$$

While it is possible to use a different scan rate (v') on reversal (12), this is rarely done, and only the case of a symmetrical triangular wave is considered here. The theoretical treatment follows that of Section 6.2, except that (6.5.2) is used in the concentration-potential equation, rather than (6.2.1), for $t > \lambda$. This sweep reversal method, called *cyclic voltammetry*, is extremely powerful and is among the most widely practiced of all electrochemical methods.

6.5.1 Nernstian Systems

Application of (6.5.2) in the equation for a nernstian system, (5.4.6), yields (6.2.3), where $S(t)$ is now given by

$$(t > \lambda) \quad S(t) = e^{\sigma t - 2\sigma\lambda} \tag{6.5.3}$$

---

[6]The k^0 values are based on $n = 1$, $\alpha = 0.5$, $T = 25°C$, and $D = 10^{-5}$ cm^2/s. With v in V/s, $\Lambda \approx k^0/(39Dv)^{1/2}$.

The derivation then proceeds as in Section 6.2. The shape of the curve on reversal depends on the switching potential, E_λ, or how far beyond the cathodic peak the scan is allowed to proceed before reversal. However, if E_λ is at least $35/n$ mV past the cathodic peak,[7] the reversal peaks all have the same general shape, basically consisting of a curve shaped like the forward i-E curve plotted in the opposite direction on the current axis, with the decaying current of the cathodic wave used as a baseline. Typical i-t curves for different switching potentials are shown in Figure 6.5.1. This type of presentation would result if the curves were recorded on a time base. The more usual i-E presentation is shown in Figure 6.5.2.

Two measured parameters of interest on these i-E curves (*cyclic voltammograms*) are the ratio of peak currents, i_{pa}/i_{pc}, and the separation of peak potentials, $E_{pa} - E_{pc}$. For a nernstian wave with stable product, $i_{pa}/i_{pc} = 1$ regardless of scan rate, E_λ (for $E_\lambda >$ $35/n$ mV past E_{pc}), and diffusion coefficients, when i_{pa} is measured from the decaying cathodic current as a baseline (see Figures 6.5.1 and 6.5.2). This baseline can be determined by the methods described in Section 6.6.

If the cathodic sweep is stopped and the current is allowed to decay to zero (Figure 6.5.2, curve 4), the resulting anodic i-E curve is identical in shape to the cathodic one, but is plotted in the opposite direction on both the i and E axes. This is so because allowing the cathodic current to decay to zero results in the diffusion layer being depleted of O and populated with R at a concentration near C_O^*, so that the anodic scan is virtually the same as that which would result from an initial anodic scan in a solution containing only R.

Deviation of the ratio i_{pa}/i_{pc} from unity is indicative of homogeneous kinetic or other complications in the electrode process (13), as discussed in more detail in Chapter 12.

Nicholson (14) suggested that if the actual baseline for measuring i_{pa} cannot be determined, the ratio can be calculated from (a) the uncorrected anodic peak current, $(i_{pa})_0$, with respect to the zero current baseline (see Figure 6.5.2, curve 3) and (b) the current at E_λ, $(i_{sp})_0$, by the expression:

$$\frac{i_{pa}}{i_{pc}} = \frac{(i_{pa})_0}{i_{pc}} + \frac{0.485(i_{sp})_0}{i_{pc}} + 0.086$$

(6.5.4)

In real cyclic voltammograms the faradaic response is superimposed on an approximately constant charging current. The situation for the forward scan was discussed in Section 6.2.4. Upon reversal, the magnitude of dE/dt remains constant but the sign changes; hence the charging current is also of the same size, but opposite in sign. It forms a baseline for the reversal response just as for the forward scan, and both i_{pc} and i_{pa} must be corrected correspondingly.

The measurement of peak currents in CV is imprecise because the correction for charging current is typically uncertain. For the reversal peak, the imprecision is increased further because one cannot readily define the folded faradaic response for the forward process (e.g., curve 1', 2', or 3' in Figure 6.5.2) to use as a reference for the measurement. Consequently, CV is not an ideal method for quantitative evaluation of system properties that must be derived from peak heights, such as the concentration of an electroactive species or the rate constant of a coupled homogeneous reaction. The method's power lies in its diagnostic strength, which is derived from the ease of interpreting qualitative and semi-quantitative behavior. Once a system is understood mechanistically, other methods are often better suited for the precise evaluation of parameters.

---

[7]This condition is based on the assumption that the potentiostat responds ideally and that the effects of R_u are negligible (see Section 1.2.4). A larger margin between the peak and the switching potential would be needed in less ideal circumstances.
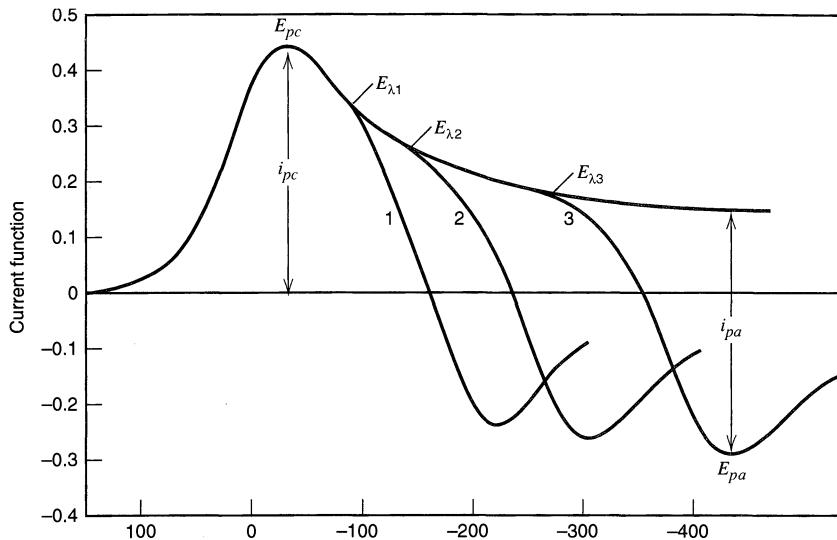
Figure 6.5.1 Cyclic voltammograms for reversal at different E_λ values, with presentation on a time base.

The difference between E_{pa} and E_{pc}, often symbolized by ΔE_p, is a useful diagnostic test of a nernstian reaction. Although ΔE_p is slightly a function of E_λ, it is always close to $2.3RT/nF$ (or $59/n$ mV at 25°C). Actual values as a function of E_λ are shown in Table 6.5.1. For repeated cycling the cathodic peak current decreases and the anodic one increases until a steady-state pattern is attained. At steady state $\Delta E_p = 58/n$ mV at 25°C (5).
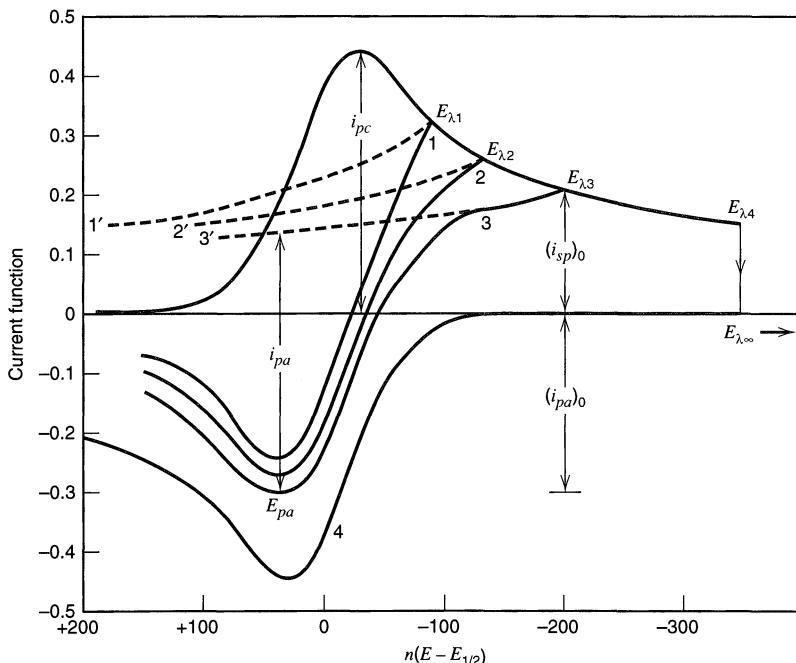
Figure 6.5.2 Cyclic voltammograms under the same conditions as in Figure 6.5.1, but in an i-E format. E_λ of (1) $E_{1/2} - 90/n$; (2) $E_{1/2} - 130/n$; (3) $E_{1/2} - 200/n$ mV; (4) for potential held at $E_{\lambda 4}$ until the cathodic current decays to zero. [Curve 4 results from reflection of the cathodic i-E curve through the E axis and then through the vertical line at $n(E - E_{1/2}) = 0$. Curves 1, 2, and 3 result by addition of this curve to the decaying current of the cathodic i-E curve ($1'$, $2'$, or $3'$).]

Table 6.5.1   Variation of ΔE_p with E_λ for a Nernstian System at 25°C (3)

$n(E_{pc} - E_\lambda)$ (mV)	$n(E_{pa} - E_{pc})$ (mV)
71.5	60.5
121.5	59.2
171.5	58.3
271.5	57.8
∞	57.0

6.5.2   Quasireversible Reactions

By using the potential program given by (6.5.1) and (6.5.2) in the equations for linear scan voltammetry in Section 6.4, the i-E curves for the quasireversible one-step, one-electron process can be derived. In this case the wave shape and ΔE_p are functions of v, k^0, α, and E_λ. As before, however, if E_λ is at least $90/n$ mV beyond the cathodic peak, the effect of E_λ is small. In this case the curves are functions of the dimensionless parameters α and either Λ (see equation 6.4.3) or an equivalent parameter, ψ defined by[8]

$$\psi = \Lambda \pi^{-1/2} = \frac{\left(\dfrac{D_O}{D_R}\right)^{\alpha/2} k^0}{(\pi D_O f v)^{1/2}} \tag{6.5.5}$$

Typical behavior is shown in Figure 6.5.3.

For $0.3 < \alpha < 0.7$ the ΔE_p values are nearly independent of α and depend only on ψ. Table 6.5.2, which provides data linking ψ to k^0 in this range (14), is the basis for a widely used method (often called the *method of Nicholson*) for estimating k^0 in quasireversible
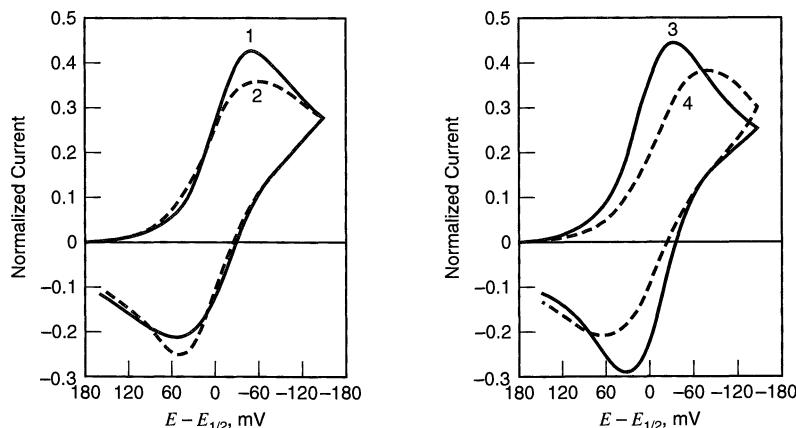
Figure 6.5.3   Theoretical cyclic voltammograms showing effect of ψ and α on curve shape for a one-step, one-electron reaction. Curve 1: $\psi = 0.5$, $\alpha = 0.7$. Curve 2: $\psi = 0.5$, $\alpha = 0.3$. Curve 3: $\psi = 7.0$, $\alpha = 0.5$. Curve 4: $\psi = 0.25$, $\alpha = 0.5$. [Reproduced with permission from R. S. Nicholson, *Anal. Chem.*, **37**, 1351 (1965). Copyright 1965, American Chemical Society. Abscissa label adapted for this text.]

---

[8]Note that ψ in (6.5.5) is not the same as $\Psi(E)$ in (6.4.5).

Table 6.5.2   Variation of
ΔE_p with ψ at 25°C (14)^a

ψ	$E_{pa} - E_{pc}$ mV
20	61
7	63
6	64
5	65
4	66
3	68
2	72
1	84
0.75	92
0.50	105
0.35	121
0.25	141
0.10	212

^{a}For a one-step, one-electron
process with $E_\lambda = E_p - 112.5/n$
mV and $\alpha = 0.5$.

systems. One determines the variation of ΔE_p with v, and from this variation, ψ. The approach is closely related to the determination of the electron-transfer kinetics by the shift of E_p with v as described in Section 6.4.

With both of these approaches one must be sure that the uncompensated resistance, R_u, is sufficiently small that the resulting voltage drops (of the order of i_pR_u) are negligible compared to the ΔE_p attributable to kinetic effects. In fact, Nicholson (14) has shown that resistive effects cannot be readily detected in the ΔE_p-v plot, because the effect of uncompensated resistance on the ΔE_p-v behavior is almost the same as that of ψ. The effect of R_u is most important when the currents are large and when k^0 approaches the reversible limit (so that) ΔE_p differs only slightly from the reversible value). It is especially difficult not to have a few ohms of uncompensated resistance in nonaqueous solvents (such as acetonitrile or tetrahydrofuran), even with positive-feedback circuitry (Chapter 15). Many reported studies made under these conditions have suffered from this problem.

6.6 MULTICOMPONENT SYSTEMS AND MULTISTEP CHARGE TRANSFERS

The consecutive reduction of two substances O and O′ in a potential scan experiment is more complicated than in the potential step (or sampled-current voltammetric) experiment treated in Section 5.6 (15, 16). As before, we consider that the reactions O + ne → R and O′ + $n'e$ → R′ occur. If the diffusion of O and O′ takes place independently, the fluxes are additive and the i-E curve for the mixture is the sum of the individual i-E curves of O and O′ (Figure 6.6.1). Note, however, that the measurement of i'_p must be made using the decaying current of the first wave as the baseline. Usually this baseline is obtained by assuming that the current past the peak potential follows that for the large-amplitude potential step and decays as $t^{-1/2}$. A better fit based on an equation with two adjustable parameters
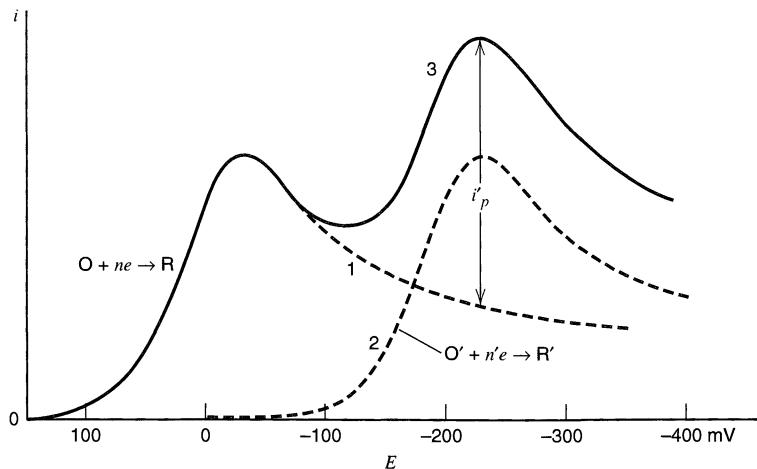
Figure 6.6.1
Voltammograms for
solutions of (*1*) O alone; (*2*)
O' alone and, (*3*) mixture of
O and O', with $n = n'$,
$C_O^* = C_{O'}^*$, and $D_O = D_{O'}$.

has been suggested by Polcyn and Shain (16); since this fitting procedure depends on the reversibility of the reactions and is a little messy, it is rarely used.

An experimental approach to obtaining the baseline was suggested by Reinmuth (unpublished). Since the concentration of O at the electrode falls essentially to zero at potentials just beyond E_p, the current beyond E_p is independent of potential. Thus if the voltammogram of a single-component system is recorded on a time base (rather than in an X-Y format) and the potential scan is held at about $60/n$ mV beyond E_p while the time base continues, the current-time curve that results will be the same as that obtained with the potential sweep continuing (until a new wave or background reduction occurs). For a two-component system this technique allows establishing the baseline for the second
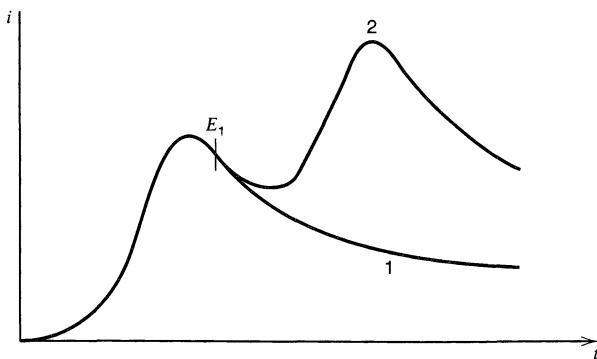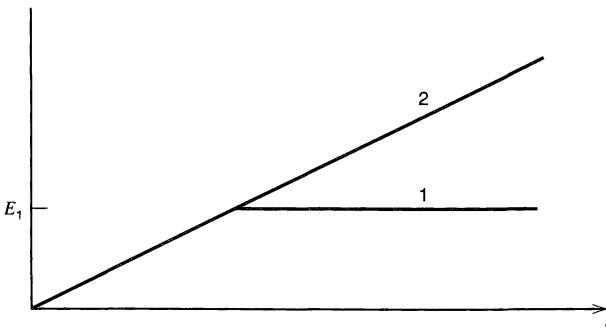
Figure 6.6.2 Method for
obtaining baseline for
measurement of i'_p of second
wave. *Upper curves:* potential
programs. *Lower curves:*
resulting voltammograms with
(curve 1) potential stopped at
E_1 and (curve 2) potential scan
continued. System as in Figure
6.6.1.

wave by halting the scan somewhere before the foot of the second wave and recording the *i-t* curve, and then repeating the experiment (after stirring the solution and allowing it to come to rest to reestablish the initial conditions). The second run is made at the same rate and continues beyond the second peak (Figure 6.6.2).

An alternative experimental approach involves stopping the sweep beyond E_p, as before, and allowing the current to decay to a small value (so that O is depleted in the vicinity of the electrode or the concentration gradient of O is essentially zero near the electrode). Then one continues the scan and measures i'_p from the potential axis as a baseline (Figure 6.6.3). The application of this method requires convection-free conditions (quiet, vibration-free solutions, and shielded electrodes oriented to prevent convection from density gradients; see Section 8.3.5), because the waiting time for the current decay must be 20 to 50 times the time needed to traverse a peak.

For the stepwise reduction of a single substance O, that is, $O + n_1 e \rightarrow R_1$ (E_1^0), $R_1 + n_2 e \rightarrow R_2$ (E_2^0), the situation is similar to the two-component case, but more complicated. If E_1^0 and E_2^0 are well separated, with $E_1^0 > E_2^0$ (i.e., O reduces before R_1), then two separate waves are observed. The first wave corresponds to reduction of O to R_1 in an n_1-electron reaction, with R_1 diffusing into the solution as the wave is traversed. At the second wave, O continues to be reduced, either directly at the electrode or by reaction with R_2 diffusing away from the electrode ($O_1 + R_2 \rightarrow 2R_1$), in an overall $(n_1 + n_2)$-electron reaction, and R_1 diffuses back toward the electrode to be reduced in an n_2-electron reaction. The voltammogram for this case resembles that of Figure 6.6.1.

In general the nature of the *i-E* curve depends on $\Delta E^0 (= E_2^0 - E_1^0)$, the reversibility of each step, and n_1 and n_2. Calculated cyclic voltammograms for different values of ΔE^0 in a system with two one-electron steps are shown in Figure 6.6.4. When ΔE^0 is between 0 and -100 mV, the individual waves are merged into a broad wave whose E_p is independent of scan rate. When $\Delta E^0 = 0$, a single peak with a peak current intermediate between those of single-step $1e$ and $2e$ reactions is found, and $E_p - E_{p/2} = 21$ mV. For $\Delta E^0 > 180$ mV (i.e., the second step is easier than the first), a single wave characteristic of a reversible $2e$ reduction ($O + 2e \rightleftarrows R_2$) is observed (i.e., $\Delta E_p = 2.3RT/2F$).
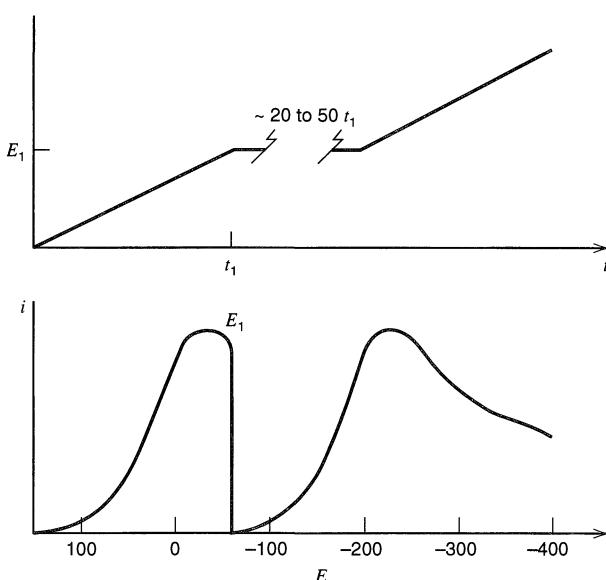
Figure 6.6.3 Method of allowing current of first wave to decay before scanning second wave. *Upper curve:* potential program. *Lower curve:* resulting voltammogram. System as in Figure 6.6.1.
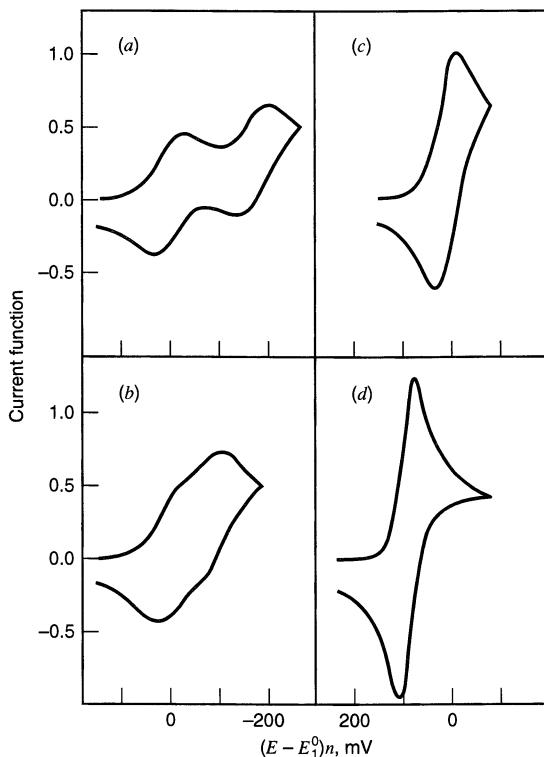
Figure 6.6.4 Cyclic voltammograms for a reversible two-step system at 25°C. Current function is analogous to $\chi(z)$ defined in (6.2.16). $n_2/n_1 = 1.0$. (*a*) $\Delta E^0 = -180$ mV. (*b*) $\Delta E^0 = -90$ mV. (*c*) $\Delta E^0 = 0$ mV. (*d*) $\Delta E^0 = 180$ mV. [Reprinted with permission from D. S. Polcyn and I. Shain, *Anal. Chem.*, **38**, 370 (1966). Copyright 1966, American Chemical Society.]

A case of particular interest occurs when $\Delta E^0 = -(2RT/F) \ln 2 = -35.6$ mV (25°C). This ΔE^0 occurs when there is no interaction between the reducible groups on O, and the additional difficulty in adding the second electron arises purely from statistical (entropic) factors (17). Under these conditions the observed wave has all of the shape characteristics of a one-electron transfer even though it is actually the result of two merged one-electron transfers. This same concept can be extended to the reduction of molecules containing k equivalent, noninteracting, reducible centers (e.g., reducible polymers). For this case the ΔE^0 between the first and kth electron transfers is given by

$$E_k^0 - E_1^0 = -\left(\frac{2RT}{F}\right) \ln k \qquad (6.6.1)$$

and again the reduction wave, now involving k merged waves, appears like a single one-electron wave with respect to shape, even though the height corresponds to a k-electron process (18). From these considerations it is clear that for two one-electron transfer reactions, ΔE^0 values more positive than $-(2RT/F) \ln 2$ represent positive interactions (i.e., the second electron transfer is assisted by the first), while ΔE^0 values more negative than $-(2RT/F) \ln 2$ represent negative interactions. Stepwise electron transfers (EE-reactions) are discussed in more detail in Sections 12.3.6 and 12.3.7; see also Polcyn and Shain (16).

Linear sweep and cyclic voltammetric methods have been employed for numerous basic studies of electrochemical systems and for analytical purposes. For example, the technique can be used for *in vivo* monitoring of substances in the kidney or brain (19); a typical example that employed a miniature carbon paste electrode to study ascorbic acid in a rat brain is illustrated in Figure 6.6.5. These techniques are especially powerful tools
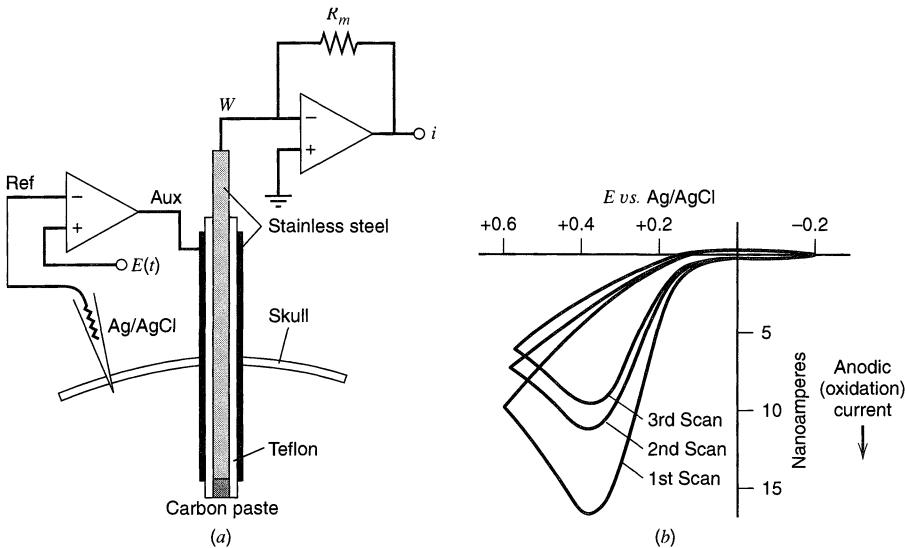
Figure 6.6.5 Application of cyclic voltammetry to *in vivo* analysis in brain tissue. (*a*) Carbon paste working electrode, stainless steel auxiliary electrode (18-gauge cannula), Ag/AgCl reference electrode, and other apparatus for voltammetric measurements. (*b*) Cyclic voltammogram for ascorbic acid oxidation at C-paste electrode positioned in the caudate nucleus of an anesthetized rat. [From P. T. Kissinger, J. B. Hart, and R. N. Adams, *Brain Res.*, **55**, 20 (1973), with permission.]

in the study of electrode reaction mechanisms (Chapter 12) and of adsorbed species (Chapter 14).

▶ 6.7 CONVOLUTIVE OR SEMI-INTEGRAL TECHNIQUES

6.7.1 Principles and Definitions

By proper treatment of the linear potential sweep data, the voltammetric *i-E* (or *i-t*) curves can be transformed into forms, closely resembling the steady-state voltammetric curves, which are frequently more convenient for further data processing. This transformation makes use of the convolution principle, (A.1.21), and has been facilitated by the availability of digital computers for the processing and acquisition of data. The solution of the diffusion equation for semi-infinite linear diffusion conditions and for species O initially present at a concentration C_O^* yields, for any electrochemical technique, the following expression (see equations 6.2.4 to 6.2.6):

$$C_O(0, t) = C_O^* - \frac{1}{nFAD_O^{1/2}} \left[\frac{1}{\pi^{1/2}} \int_0^t \frac{i(u)}{(t - u)^{1/2}} \, du \right] \tag{6.7.1}$$

If the term in brackets, which represents a particular (convolutive) transformation of the experimental *i(t)* data, is defined as *I(t)*, then equation 6.7.1 becomes (20)

$$C_O(0, t) = C_O^* - \frac{I(t)}{nFAD_O^{1/2}} \tag{6.7.2}$$

where

$$I(t) = \frac{1}{\pi^{1/2}} \int_0^t \frac{i(u)}{(t - u)^{1/2}} \, du \tag{6.7.3}$$

Following the generalized definition of the Riemann-Liouville operators, this integral can be considered as the *semi-integral* of $i(t)$, generated by the operator $d^{-1/2}/dt^{-1/2}$, so that (21, 22)

$$\frac{d^{-1/2}}{dt^{-1/2}} i(t) = m(t) = I(t) \tag{6.7.4}$$

Both $m(t)$ and $I(t)$, which represent the integral in equation 6.7.3, have been used in presentations of this transformation technique; clearly the convolutive (20) and semi-integral (21, 22) approaches are equivalent.

The transformed current data can be used directly, by (6.7.2), to obtain $C_O(0, t)$. Under conditions where $C_O(0, t) = 0$ (i.e., under purely diffusion-controlled conditions), $I(t)$ reaches its limiting or maximum value, I_l [or, in semi-integral notation, $m(t)_{max}$], where

$$I_l = nFAD_O^{1/2}C_O^* \tag{6.7.5}$$

or

$$C_O(0, t) = \frac{[I_l - I(t)]}{nFAD_O^{1/2}} \tag{6.7.6}$$

Note the similarity between this expression for the transformed current and that for the steady-state concentration in terms of the actual current, (1.4.11). Similarly for species R, assumed absent initially, the corresponding expression resulting from (6.2.9) is

$$C_R(0, t) = \frac{I(t)}{nFAD_R^{1/2}} \tag{6.7.7}$$

These equations hold for any form of signal excitation in any electrochemical technique applied under conditions in which semi-infinite diffusion is the only form of mass transfer controlling the current. No assumptions have been made concerning the reversibility of the charge-transfer reaction or even the form of the dependence of $C_O(0, t)$ and $C_R(0, t)$ on E. Thus, with the application of any excitation signal that eventually drives $C_O(0, t)$ to zero, the transformed current $I(t)$ will attain a limiting value, I_l, that can be used to determine C_O^* by equation 6.7.5 (22).

If the electron-transfer reaction is nernstian, the application of equations 6.7.6 and 6.7.7 yields

$$E = E_{1/2} + \frac{RT}{nF} \ln \frac{I_l - I(t)}{I(t)} \tag{6.7.8}$$

where $E_{1/2} = E^{0'} + (RT/nF) \ln (D_R/D_O)^{1/2}$, as usual. Note that this expression is identical in form with those for the steady-state or sampled-current *i-E* curves (equations 1.4.16 and 5.4.22). Transformation of a linear potential sweep *i-E* response thus converts the peaked *i-E* curve to an S-shaped one resembling a polarogram (Figure 6.7.1).

6.7.2 Transformation of the Current–Evaluation of $I(t)$

Although analog circuits that approximate $I(t)$ have been proposed (23), the function is usually evaluated by a numerical integration technique on a computer. Several different algorithms have been proposed for the evaluation (24, 25). The *i-t* data are usually divided into N equally spaced time intervals between $t = 0$ and $t = t_f$, indexed by j; then $I(t)$ becomes $I(k\Delta t)$, where $\Delta t = t_f/N$ and k varies between 0 and N, representing $t = 0$ and

(a)   (b)

(c)   (d)
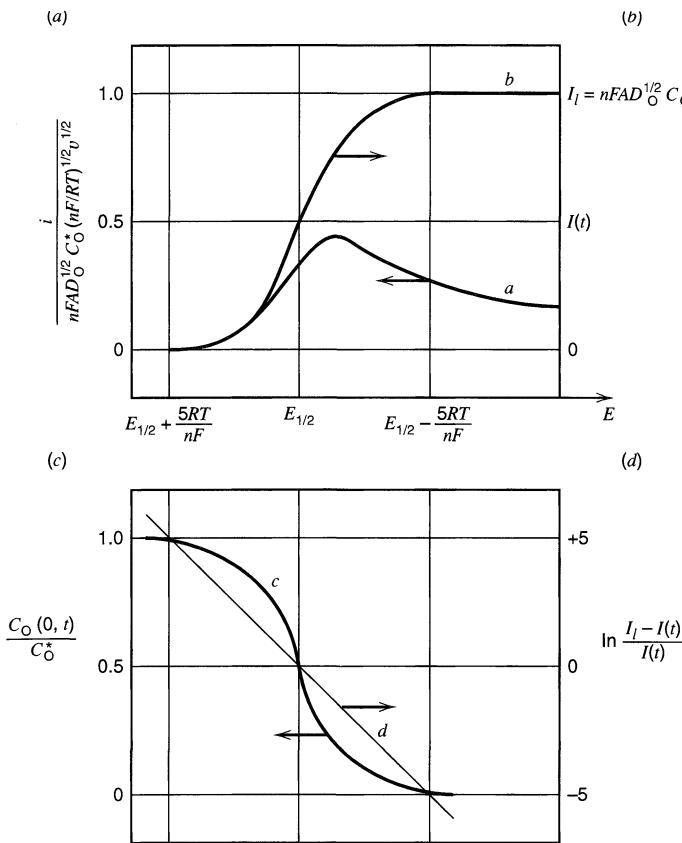
Figure 6.7.1 Variation of i, I, $C_O(0, t)/C_O^*$, and $\ln[(I_l - I)/I$ with E. [Adapted from J. C. Imbeaux and J.-M. Savéant, *J. Electroanal. Chem.*, **44**, 169 (1973), with permission.]

$t = t_f$ as in Figure 6.7.2). One convenient algorithm, which follows directly from the definition of $I(t)$, is (24)

$$I(t) = I(k\Delta t) = \frac{1}{\pi^{1/2}} \sum_{j=1}^{j=k} \frac{i(j\Delta t - \frac{1}{2}\Delta t)\, \Delta t}{\sqrt{k\Delta t - j\Delta t + \frac{1}{2}\Delta t}} \tag{6.7.9}$$

which is obtained from (6.7.3) by using $t = k\Delta t$ and $u = j\Delta t$, and measuring i at the midpoint of each interval. This can be simplified to

$$I(k\Delta t) = \frac{1}{\pi^{1/2}} \sum_{j=1}^{j=k} \frac{i(j\Delta t - \frac{1}{2}\Delta t)\, \Delta t^{1/2}}{\sqrt{k - j + \frac{1}{2}}} \tag{6.7.10}$$
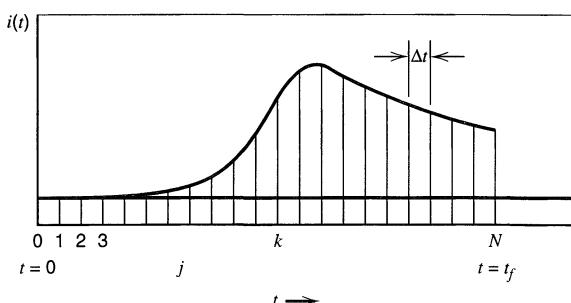
Figure 6.7.2 Division of experimental $i(t)$ *vs.* t [$i(t)$ or *vs.* $E(t)$] curve for digital evaluation of $I(t)$.

Another algorithm, which is especially convenient for digital processing, is

$$I(k\Delta t) = \frac{1}{\pi^{1/2}} \sum_{j=1}^{j=k} \frac{\Gamma(k-j+\frac{1}{2})}{(k-j)!} \Delta t^{1/2} i(j\Delta t) \tag{6.7.11}$$

where $\Gamma(x)$ is the Gamma function of x, where $\Gamma(1/2) = \pi^{1/2}$, $\Gamma(3/2) = \frac{1}{2}\pi^{1/2}$, $\Gamma(5/2) = (\frac{3}{2})(\frac{1}{2})\pi^{1/2}$, etc. Other algorithms based on standard methods of numerical evaluation of definite integrals also have been used (20–22, 25, 26).

6.7.3 Irreversible and Quasireversible Reactions

The convolutive form for a totally irreversible one-step, one-electron reaction follows directly from the *i-E* expression with no back reaction, equation 3.3.11:

$$i = FAk^0 C_O(0, t)e^{-\alpha f(E-E^{0'})} \tag{6.7.12}$$

and the expression for $C_O(0, t)$, equation 6.7.6. Thus (20),

$$i(t) = k^0 D_O^{-1/2}[I_l - I(t)]e^{-\alpha f(E-E^{0'})} \tag{6.7.13}$$

or

$$E = E^{0'} + \frac{RT}{\alpha F} \ln \frac{k^0}{D_O^{1/2}} + \frac{RT}{\alpha F} \ln \frac{I_l - I(t)}{i(t)} \tag{6.7.14}$$

For a quasireversible one-step, one-electron reaction, the full equation 3.3.11 is employed, along with equations 6.7.6 and 6.7.7, to yield

$$i(t) = k^0\{D_O^{-1/2}[I_l - I(t)]e^{-\alpha f(E-E^{0'})} - D_R^{-1/2}[I(t)]e^{(1-\alpha)f(E-E^{0'})}\} \tag{6.7.15}$$

$$i(t) = k^0 D_O^{-1/2}e^{-\alpha f(E-E^{0'})}\{I_l - I(t)[1 + \xi\theta]\} \tag{6.7.16}$$

$$E = E^{0'} + \frac{RT}{\alpha F} \ln \frac{k^0}{D_O^{1/2}} + \frac{RT}{\alpha F} \ln \frac{I_l - I(t)[1 + \xi\theta]}{i(t)} \tag{6.7.17}$$

where $\xi = (D_O/D_R)^{1/2}$ and $\theta = \exp[f(E - E^{0'})]$.

In deriving (6.7.14) and (6.7.17), we assumed that Butler–Volmer kinetics apply, as expressed in the *i-E* characteristic, (3.3.11). Indeed, this assumption (or the adoption of some other model) is necessary before equations can be derived for most electrochemical approaches. However, with the convolutive technique, this assumption is not essential, for the rate law can be written in the general form (27),

$$i(t) = FAk_f(E)[C_O(0, t) - \theta C_R(0, t)] \tag{6.7.18}$$

where $k_f(E)$ is the potential-dependent rate constant of the forward reaction and θ is also recognized as k_b/k_f. With (6.7.6) and (6.7.7),

$$\ln k_f(E) = \ln D_O^{1/2} - \ln\left\{\frac{I_l - I(t)[1 + \xi\theta]}{i(t)}\right\} \tag{6.7.19}$$

Analysis of experimental linear potential sweep experiments according to (6.7.19) or the equivalent expression for a totally irreversible one-step, one-electron reduction ($\xi\theta << 1$),
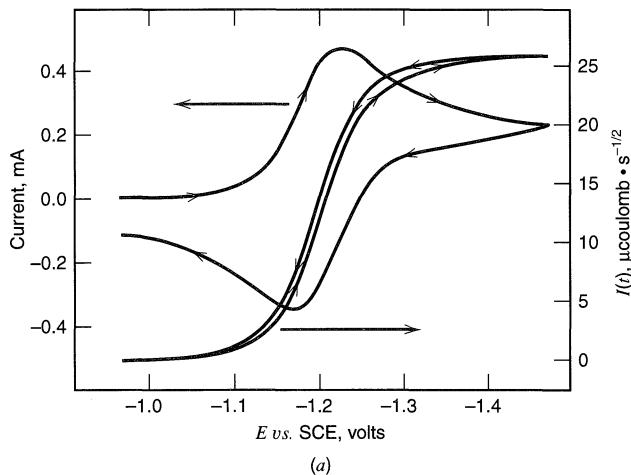
$$\ln k_f(E) = \ln D_O^{1/2} - \ln \frac{[I_l - I(t)]}{i(t)} \tag{6.7.20}$$

yields $\ln k_f(E)$ as a function of E at different v. If classic Butler–Volmer kinetics apply, then a plot of $\ln k_f(E)$ *vs.* E should be linear with a slope $-\alpha F/RT$. In an analysis of experimental data for the electroreduction of *tert*-nitrobutane in aprotic solvents, Savéant and Tessier (27) noted significant deviations from linearity (after necessary corrections for double-layer effects were carried out), demonstrating that the α value was potential dependent, as is indeed predicted by the microscopic theories of electron-transfer reactions (Section 3.6).
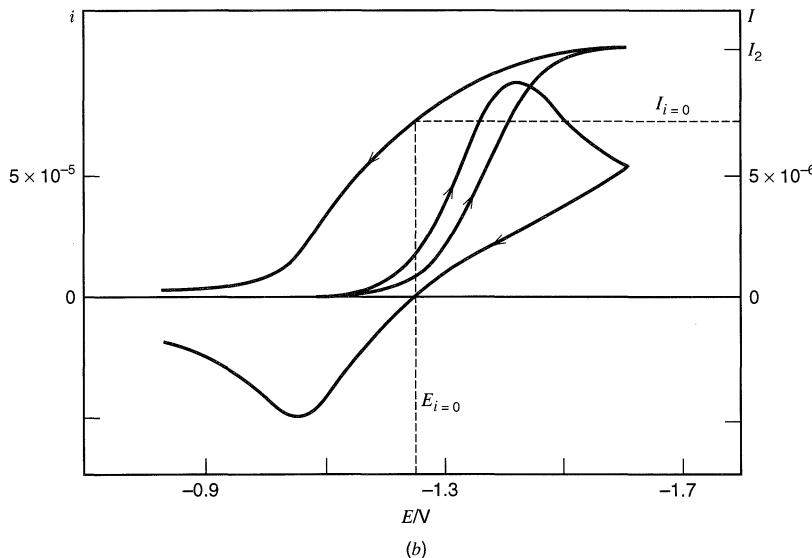
6.7.4 Applications

The convolution technique offers a number of advantages in the treatment of linear sweep data (and perhaps also in other electrochemical techniques). For a reversible reaction in a cyclic voltammetric experiment, the curves of $I(t)$ *vs.* E for the forward and backward scans superimpose, with $I(t)$ returning to zero at sufficiently positive potentials [where $C_R(0, t) = 0$]. This behavior has been verified experimentally (20, 25, 28) (Figure 6.7.3a).

For a quasireversible reaction, however, the forward and backward $I(t)$ curves do not coincide (Figure 6.7.3b). One can regard this effect as a consequence of the shifting of the E_{pc} and E_{pa} values from their reversible values. The procedure used to obtain the "reversible" $E_{1/2}$ value for such a system is shown in Figure 6.7.3b (27).

Figure 6.7.3 Experimental cyclic voltammogram and convolution of (*a*) 1.84 m*M* *p*-nitrotoluene in acetonitrile containing 0.2 *M* TEAP at HMDE, v = 50 V/s. [Reprinted with permission from P. E. Whitson, H. W. Vanden Born, and D. H. Evans, *Anal. Chem.*, **45**, 1298 (1973). Copyright 1975, American Chemical Society.] (*b*) 0.5 m*M* *tert*-nitrobutane in DMF containing 0.1 *M* TBAI, v = 17.9 V/s. $E_{1/2}$ determined for quasireversible system from $E_{1/2} = E(i = 0) - (RT/F) \ln [(I_l - I_{i\,=0})/I_{i\,=0}]$ [From J.-M. Savéant and D. Tessier, *J. Electroanal. Chem.*, **65**, 57 (1975), with permission.]

Correction for the uncompensated resistance, R_u, is also much more straightforward for $I(t)$-E curves than for the $i(t)$-E curve, since R_u affects the linearity of the potential sweep at the electrode (see Section 6.2.4). For the $I(t)$-E curves, correction is accomplished simply by replacing the applied potential E by $E' = E + iR_u$ (20, 25, 28).

A procedure for correcting the $I(t)$ curves for charging current has also been presented (10, 28). The charging current for a blank experiment in the absence of electroactive compound, i_c^b, is

$$i_c^b = \frac{-C_d \, dE'}{dt} \tag{6.7.21}$$

where C_d is the potential-dependent capacitance (μF) and E' is the potential corrected for R_u:

$$E' = E + i_c^b R_u = E_i - vt + i_c^b R_u \tag{6.7.22}$$

Thus, at any given value of E',

$$C_d = \frac{i_c^b}{v - R_u(di_c^b/dt)} \tag{6.7.23}$$

If R_u is known, the measured values of i_c^b, and di_c^b/dt allow the determination of C_d as a function of E'. When substance O is introduced into solution, the total current, i_t, is

$$i_t = i_f + i_c \tag{6.7.24}$$

where i_c may differ from i_c^b because of the presence of O. However, it is still true that

$$i_c = \frac{-C_d \, dE'}{dt} \tag{6.7.25}$$

$$E' = E - vt + i_t R_u \tag{6.7.26}$$

and finally

$$i_f = i_t - C_d v + C_d R_u \left(\frac{di_t}{dt}\right) \tag{6.7.27}$$

where C_d is assumed to be the same function of potential as determined in the blank experiment. Correction of i_t for C_d can be accomplished by (6.7.27) to give i_f before the convolution is performed.

Convolution methods simplify to some extent the treatment of data for electrode processes with coupled chemical reactions (20) and may be useful in analytical applications (22).

Although data acquisition is carried out digitally in modern electroanalytical instrumentation, and convolution can be readily applied in computer-based instruments, this approach has not been widely used. Most practitioners appear to prefer comparing conventional voltammograms to those obtained via digital simulation.

▷ 6.8 CYCLIC VOLTAMMETRY OF THE LIQUID–LIQUID INTERFACE

In Section 2.3.6 we considered ion transfer at the interface between two immiscible electrolyte solutions (ITIES), where we found that a potential difference can arise because of differential transfer of ions. Ion movement across the interface can also be driven by the application of an external potential, and the rate of ion transfer can be detected as a current flow. This response allows one to examine the ITIES via voltammetric methods in the same way that electron transfer can be monitored at electrode surfaces (29–32).

As shown in (2.3.47), the junction potential between phases α and β is given by

$$\phi^\beta - \phi^\alpha = \Delta_\alpha^\beta \phi = (-1/z_i F)[\Delta G_{transfer,i}^{0\alpha \rightarrow \beta} + RT \ln (a_i^\beta/a_i^\alpha)] \tag{6.8.1}$$

If one defines the standard free energy required to transfer species i, with charge z_i, between the two phases, $\Delta G_{transfer,i}^{0\alpha \rightarrow \beta}$, in terms of a standard potential difference, $\Delta_\alpha^\beta \phi_i^0$ (the *standard Galvani potential of ion transfer* of species i from α to β) that is,
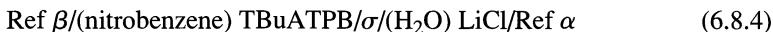
$$\Delta_\alpha^\beta \phi_i^0 = (-1/z_i F) \Delta G_{transfer,i}^{0\alpha \rightarrow \beta} \tag{6.8.2}$$

then (6.8.1) can be written in the form of a Nernst equation:

$$\boxed{\Delta_\alpha^\beta \phi = \Delta_\alpha^\beta \phi_i^0 + (RT/z_i F) \ln (a_i^\alpha/a_i^\beta)} \tag{6.8.3}$$

As shown in Section 2.3.6, $\Delta G_{transfer,i}^{0\alpha \rightarrow \beta}$, and hence $\Delta_\alpha^\beta \phi^0$, can be obtained from thermochemical, solubility, or potentiometric measurements (with an extrathermodynamic assumption). Thus by sweeping the potential drop across the ITIES, the activities of species in the two phases can be varied, with a resulting flow of current as ions cross the interface.

Consider the system shown in Figure 6.8.1, which can be represented as

$$\text{Ref } \beta/(\text{nitrobenzene}) \text{ TBuATPB}/\sigma/(\text{H}_2\text{O}) \text{ LiCl/Ref } \alpha \tag{6.8.4}$$

where TBuA$^+$ is tetra-n-butylammonium, TPB$^-$ is tetraphenylborate, Ref α and Ref β are reference electrodes, and σ represents the interface. The values of the ionic transfer free energies and the standard potential differences for the species in this system are given in Table 6.8.1 (29). The distributions of the four ions in this system, calculated from the data in this table and (6.8.3), are shown in Figure 6.8.2a. Note that the interface in this case is unpoised, since no common ion exists in both phases at open circuit. The salt LiCl is very hydrophilic and, with no potential applied across the interface, resides almost totally in the aqueous phase, while TBuATPB is hydrophobic and remains in the nitrobenzene. As shown in Figure 6.8.2, this remains true for -250 mV $< \Delta_\alpha^\beta \phi^0 < 150$ mV. The situation is equivalent to having a platinum electrode immersed in a solution that does not contain both halves of a redox couple.

If the potential across the interface is varied by applying a voltage between the working electrodes as shown in Figure 6.8.1, ions will tend to move across the interface. A positive potential applied to the electrode in the aqueous phase (a negative $\Delta_\alpha^\beta \phi$) will tend to transport Li$^+$ into the nitrobenzene and TPB$^-$ into the aqueous phase. A negative potential in the aqueous phase (producing a more positive $\Delta_\alpha^\beta \phi$) will drive Cl$^-$ into the nitrobenzene or TBuA$^+$ into the aqueous phase. At any potential across the interface (in-
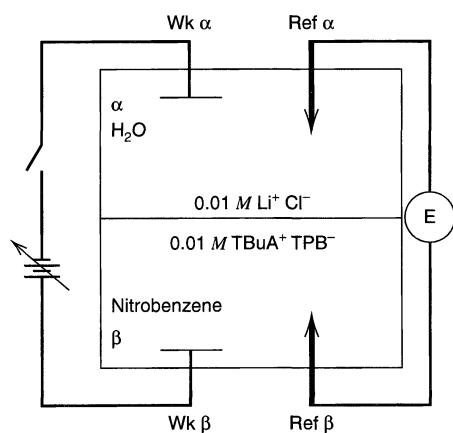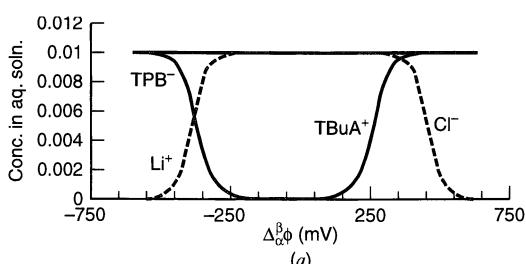
Figure 6.8.1   Schematic diagram for the apparatus for cyclic voltammetry at the ITIES between water and nitrobenzene. Ref α and Ref β are reference electrodes, Wk α and Wk β are metal working electrodes.

TABLE 6.8.1 Gibbs Energy of Transfer and Standard Interfacial Potential Differences for Ion Transfer Between Water and Nitrobenzene (29)[a]
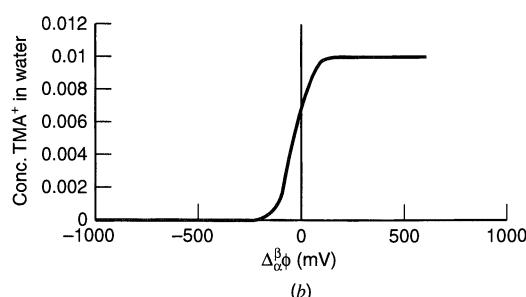
Species	$\Delta G^{0\alpha\to\beta}_{transfer,i}$/kJ mol^{-1}	$\Delta^{\beta}_{\alpha}\phi^0_i$/mV
Li$^+$	38.2	−396
Cl$^-$	43.9	455
TBuA$^+$	−24.7	256
TPB$^-$	−35.9	−372
TMA$^+$	4.0	−41

[a]Note that a positive Gibbs energy implies that work must be performed to move the species from the aqueous phase to the nitrobenzene. For cations, a negative $\Delta^{\beta}_{\alpha}\phi^0_i$ goes with a greater tendency to remain in the aqueous phase, while for anions a positive $\Delta^{\beta}_{\alpha}\phi^0_i$ shows greater tendency to remain in the aqueous phase.

dicated by that measured between the two reference electrodes), the relative activities of the ions at the interface can be calculated with (6.8.3), assuming equilibrium is attained (see Problem 6.11). Within the potential range of about −0.2 to 0.15 V no appreciable transfer occurs in this system, because the ratios (a^{α}_i/a^{β}_i) for the different ions are such that negligible amounts of Li$^+$ and Cl$^-$ are in the nitrobenzene and negligible amounts of TBuA$^+$ and TPB$^-$ are in the water. When the potential is swept beyond these limits, ion transfer can occur, with TBuA$^+$ moving into the aqueous phase and Cl$^-$ moving into the nitrobenzene at the positive extreme of $\Delta^{\beta}_{\alpha}\phi$, and TPB$^-$ moving into the water and Li$^+$ moving into the nitrobenzene at the negative extreme. Since these ionic movements represent passage of a net charge across the interface, they result in a current flow in the external circuit. A current-potential curve for this system is shown in Figure 6.8.3A. The limits shown are controlled by the commencement of movement of TBuA$^+$ into the water at a $\Delta^{\beta}_{\alpha}\phi$ of about 100 mV and the movement of TBP$^-$ into the water at $\Delta^{\beta}_{\alpha}\phi$ of about −200 mV. This curve resembles that seen as the faradaic background scan for metal–solution interfaces. In general, the available potential window in which the ITIES behaves as an ideal polarized interface depends upon the values of $\Delta^{\beta}_{\alpha}\phi^0_i$ for the ions present in the aque-

Figure 6.8.2
(a) Distribution of ions in the system in Figure 6.8.1 as a function of the interfacial Galvani potential difference, $\Delta^{\beta}_{\alpha}\phi$. In the middle range, LiCl is largely in the aqueous phase, and TBuATPB is in the nitrobenzene. (b) Distribution for 0.01 M TMA$^+$ in the same system.
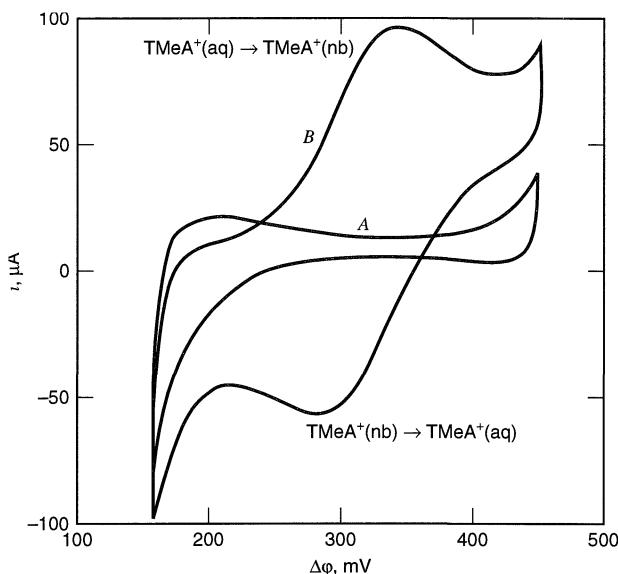
Figure 6.8.3 Voltammetry with the cell shown in (6.8.4). (*A*) Current-potential curve for 0.1 *M* LiCl in the aqueous phase and 0.1 *M* TBuATPB in the nitrobenzene; (*B*) with addition of 0.47 m*M* TMeA$^+$ to the aqueous phase. Scan rate, 20 mV/s. In this plot $\Delta\varphi$ is the potential of the reference electrode in the aqueous phase *vs.* that in the nitrobenzene and includes junction potentials at the liquid junctions of both reference electrodes, so that $\Delta\varphi \approx 300 - \Delta_\alpha^\beta\phi$ mV. Thus, the aqueous phase becomes more positive as the scan extends to the right, and a positive current represents transfer of TMeA$^+$ from aqueous phase to nitrobenzene. [Reprinted from P. Vanýsek, *Electrochim. Acta*, **40**, 2841 (1995), with permission from Elsevier Science.]

ous and organic phases. Given typical maximum values of $\Delta G_{\text{transfer, i}}^{0\alpha\rightarrow\beta}$, this window is generally smaller than 0.6 to 0.7 V (29).

If an ion with a smaller Gibbs energy of transfer than that of the other ions is introduced into one of the phases, it will transfer at smaller values of $\Delta_\alpha^\beta\phi$ within the potential window governed by the other ions. For example, when tetramethylammonium ion (TMA$^+$) is added to the aqueous phase, its $\Delta_\alpha^\beta\phi_i^0$ value is such that it transfers more readily than TBuA$^+$ between the water and nitrobenzene (Figure 6.8.2*b*). When the concentration of this ion is small (typically 0.1 to 1 m*M*), the rate of transfer across the interface is usually governed by the rate of mass transfer of the ion to the interface. Under these conditions, a scan of current *vs.* potential drop across the interface resembles a typical cyclic voltammogram (Figure 6.8.3*B*).

Such voltammograms show the same characteristics as those of nernstian faradaic waves at the metal/solution interface, that is, peak potential independent of v, peak current proportional to $v^{1/2}$, peak splitting of 59 mV/$|z_i|$, and proportionality of peak current with concentration. Such measurements are often complicated by uncompensated resistance effects because of the high resistance of the organic phase. In almost all cases investigated, the voltammograms do not show effects of slow ion transport across the interface; that is, they are reversible. Thus, measurements like these can be used to find Gibbs energies of transfer, diffusion coefficients, and solution concentrations. By exploiting ITIES, voltammetric electrodes can be prepared for ions that are not electroactive in the faradaic sense. For example, a voltammetric lithium ion electrode can be fabricated based on Li$^+$ transfer between water and an immiscible oil (*o*-nitrophenylphenylether) containing a crown ether to facilitate specific ion transport (33).

6.9 REFERENCES

1. J. E. B. Randles, *Trans. Faraday Soc.*, **44**, 327 (1948).

2. A Sevcik, *Coll. Czech. Chem. Commun.*, **13**, 349 (1948).

3. R. S. Nicholson and I. Shain, *Anal. Chem.*, **36**, 706 (1964).

4. W. H. Reinmuth, *J. Am. Chem. Soc.*, **79**, 6358 (1957).

5. H. Matsuda and Y. Ayabe, *Z. Electrochem.*, **59**, 494 (1955).

6. Y. P. Gokhshtein, *Dokl. Akad. Nauk SSSR*, **126**, 598 (1959).

7. J. C. Myland and K. B. Oldham, *J. Electroanal. Chem.*, **153**, 43 (1983).

8. A. C. Ramamurthy and S. K. Rangarajan, *Electrochim. Acta*, **26**, 111 (1981).

9. D. O. Wipf and R. M. Wightman, *Anal. Chem.*, **60**, 2460 (1988).

10. C. P. Andrieux, D. Garreau, P. Hapiot, J. Pinson, and J.-M. Savéant, *J. Electroanal. Chem.*, **243**, 321 (1988).

11. C. Amatore in "Physical Electrochemistry—Principles, Methods, and Applications," I. Rubinstein, Ed., Marcel Dekker, New York, 1995, p. 191.

12. J.-M. Savéant, *Electrochim. Acta*, **12**, 999 (1967).

13. W. M. Schwarz and I. Shain, *J. Phys. Chem.*, **70**, 845 (1966).

14. R. S. Nicholson, *Anal. Chem.*, **37**, 1351 (1965).

15. Y. P. Gokhshtein and A. Y. Gokhshtein, in "Advances in Polarography," I. S. Longmuir, Ed., Vol. 2, Pergamon Press, New York, 1960, p. 465; *Dokl. Akad. Nauk SSSR*, **128**, 985 (1959).

16. D. S. Polcyn and I. Shain, *Anal. Chem.*, **38**, 370 (1966).

17. F. Ammar and J.-M. Savéant, *J. Electroanal. Chem.*, **47**, 215 (1973).

18. J. B. Flanagan, S. Margel, A. J. Bard, and F. C. Anson, *J. Am. Chem. Soc.*, **100**, 4248 (1978).

19. P. T. Kissinger, J. B. Hart, and R. N. Adams, *Brain Res.*, **55**, 20 (1973).

20. J. C. Imbeaux and J.-M. Savéant, *J. Electroanal. Chem.*, **44**, 1969 (1973).

21. K. B. Oldham and J. Spanier, *J. Electroanal. Chem.*, **26**, 331 (1970).

22. K. B. Oldham, *Anal. Chem.*, **44**, 196 (1972).

23. K. B. Oldham, *Anal. Chem.*, **45**, 39 (1973).

24. R. J. Lawson and J. T. Maloy, *Anal. Chem.*, **46**, 559 (1974).

25. P. E. Whitson, H. W. Vanden Born, and D. H. Evans, *Anal. Chem.*, **45**, 1298 (1973).

26. J. H. Carney and H. C. Miller, *Anal. Chem.*, **45**, 2175 (1973).

27. J.-M. Savéant and D. Tessier, *J. Electroanal. Chem.*, **65**, 57 (1975).

28. L. Nadjo, J.-M. Savéant, and D. Tessier, *J. Electroanal. Chem.*, **52**, 403 (1974).

29. H. H. J. Girault and D. J. Schiffrin, *Electroanal. Chem.*, **15**, 1 (1989).

30. C. Gavach and F. Henry, *Compt. Rend. Acad. Sci.*, **C274**, 1545 (1972).

31. Z. Samec, V. Mareček, J. Koryta, and M. W. Khalil, *J. Electroanal. Chem.*, **83**, 393 (1977).

32. P. Vanýsek, *Electrochim. Acta*, **40**, 2841 (1995).

33. S. Sawada, T. Osakai, and M. Senda, *Anal. Sci.*, **11**, 733 (1995).

▶ 6.10 PROBLEMS

6.1 Derive (6.2.6) from (6.2.4) and (6.2.5).

6.2 Show that equations (6.2.8) and (6.2.9) lead directly to (5.4.26).

6.3 From the data in Table 6.3.1 plot the linear potential sweep voltammograms, that is, $\pi^{1/2}\chi(bt)$ *vs.* potential for a one-step, one-electron process with several values of k^0, given $\alpha = 0.5$, $T = 25°C$, $v = 100$ mV/s, and $D_O = 10^{-5}$ cm^2/s. Compare these results with those for a nernstian reaction shown in Figure 6.2.1.

6.4 T. R. Mueller and R. N. Adams (see R. N. Adams, "Electrochemistry at Solid Electrodes," Marcel Dekker, New York, 1969, p. 128) suggested that by measurement of $i_p/v^{1/2}$ for a nernstian linear potential sweep voltammetric curve, and by carrying out a potential step experiment in the same solution at the same electrode to obtain the limiting value of $it^{1/2}$, the n value of an electrode reaction can be determined without the need to know A, C_O^*, or D_O. Demonstrate that this is the case. Why would this method be unsuitable for irreversible reactions?

6.5 The oxidation of *o*-dianisidine (*o*-DIA) occurs in a nernstian 2*e* reaction. For a 2.27 mM solution of *o*-DIA in 2 M H$_2$SO$_4$ at a carbon paste electrode of area 2.73 mm^2 with a scan rate of 0.500 V/min, $i_p = 8.19$ μA. Calculate the D value for *o*-DIA. What i_p is expected for $v = 100$ mV/s? What i_p will be obtained for $v = 50$ mV/s and 8.2 mM *o*-DIA?

6.6 Figure 6.10.1 shows a cyclic voltammogram taken for a solution containing benzophenone (BP) and tri-*p*-tolylamine (TPTA), both at 1 mM in acetonitrile. Benzophenone can be reduced inside the working range of acetonitrile and TPTA can be oxidized. However, benzophenone cannot be
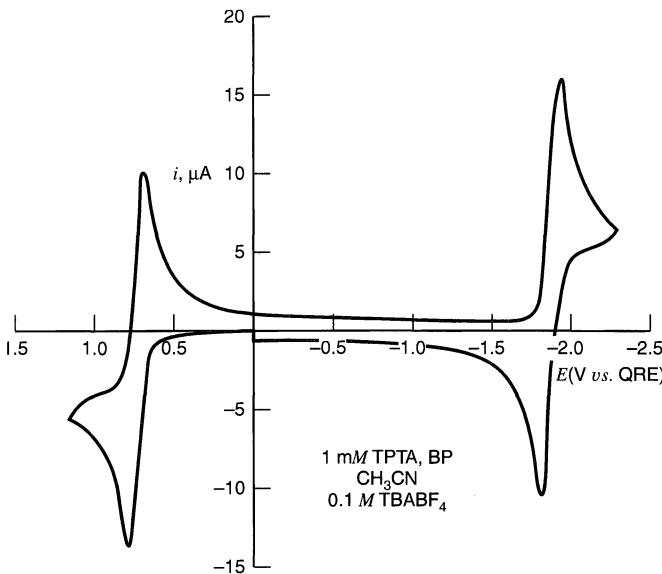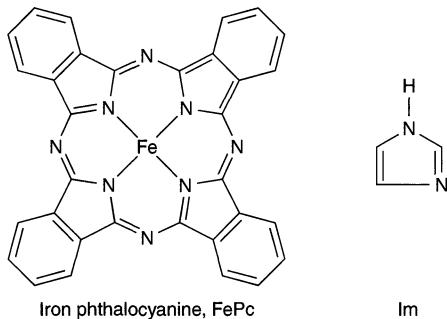
Figure 6.10.1
Cyclic voltammogram of benzophenone and tri-*p*-tolylamine in acetonitrile. [From P. R. Michael, PhD Thesis, University of Illinois at Urbana-Champaign, 1977, with permission.]

oxidized, and TPTA cannot be reduced. The scan shown here begins at 0.0 V *vs.* QRE and first moves toward positive potentials. Account for the shape of the voltammogram.

(a) Assign the voltammetric features between $+0.5$ and 1.0 V and between -1.5 and -2.0 V to appropriate electrode reactions. Comment on the heterogeneous and homogeneous kinetics pertaining to these electrode reactions.

(b) Why does the falloff in current appear between 0.7 and 1.0 V *vs.* QRE?

(c) What constitutes the anodic and cathodic currents seen at -1.0 V *vs.* QRE?

6.7 K. M. Kadish, L. A. Bottomley, and J. S. Cheng presented results of a study of the interactions between Fe(II) phthalocyanine (FePc) and various nitrogen bases, such as imidazole (Im).

Iron phthalocyanine, FePc   Im

The work was carried out in dimethylsulfoxide (DMSO) containing 0.1 *M* tetraethylammonium perchlorate (TEAP). Some results are shown in Figure 6.10.2. In (*a*), couples I and II both show peak potentials and current functions that are invariant with scan rate. Interpret the voltammetric properties of the system before and after addition of imidazole.

6.8 Consider the electrochemical reduction of molecular oxygen in an aprotic solvent such as pyridine or acetonitrile. In general, a cyclic voltammogram like that in Figure 6.10.3 is obtained. A sampled-current voltammogram on a 4-s timescale at a mercury electrode (i.e., a polarogram, Section 7.2) gives a linear plot of *E vs.* log $[(i_d - i)/i]$ with a slope of 63 mV. The reduction product at -1.0 V *vs.* SCE gives an ESR signal. If methanol is added in small quantities, the cyclic voltammogram shifts toward positive potentials, the forward peak rises in magnitude, and the reverse peak disappears. These trends continue with increasing methanol concentration until a limit is
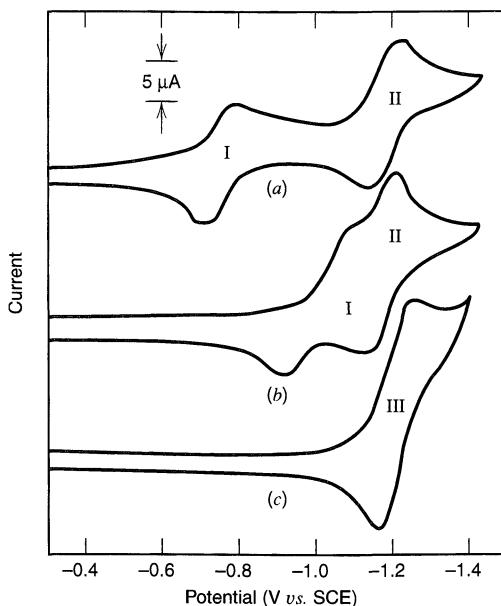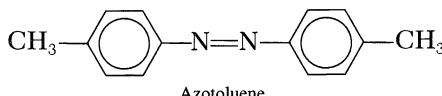
Figure 6.10.2 Cyclic voltammograms of 1.18 mM FePc in Me$_2$SO/imidazole mixtures containing 0.1 M TEAP. Scan rate 0.100 V/s. Imidazole concentrations: (a) 0.00 M; (b) 0.01 M; (c) 0.95 M. [Reprinted with permission from K. M. Kadish, L. A. Bottomley, and J. S. Cheng, *J. Am. Chem. Soc.*, **100**, 2731 (1978). Copyright 1978, American Chemical Society.]

reached with reduction near -0.4 V *vs.* SCE. The polarogram under these limiting conditions is approximately twice as high as it was in methanol-free solution, and the wave slope is 78 mV.

(a) Identify the reduction product in methanol-free solution.

(b) Identify the reduction product under limiting conditions in methanol-containing solution.

(c) Comment on the charge-transfer kinetics in methanol-free solution.

(d) Explain the voltammetric responses.

6.9 Cyclic voltammetry was studied for a DMF solution containing 0.68 mM azotoluene and 0.10 M TBAP at 25°C. The working electrode was a Pt disk with $A = 1.54$ mm^2, and the reference electrode was an SCE. A typical cyclic voltammogram is shown in Figure 6.10.4, and other data are tabulated below.

$$CH_3 - \underset{}{\bigcirc} - N{=}N - \underset{}{\bigcirc} - CH_3$$

Azotoluene

Coulometry shows that the first reduction step involves one electron. Work up these data and discuss what information is obtained about the reversibility of the reactions, stability of products, dif-
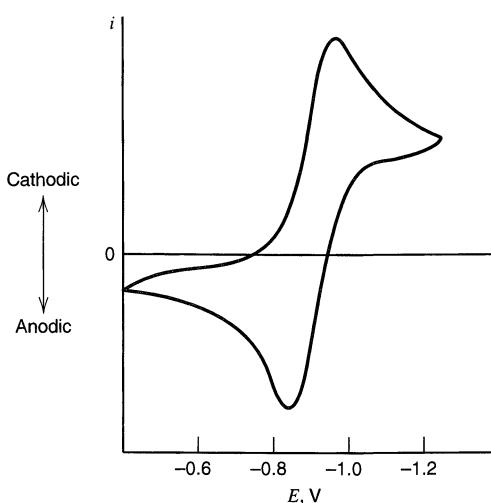
Figure 6.10.3 Cyclic voltammogram at an HMDE of oxygen in pyridine with 0.2 M TBAP. Frequency 0.1 Hz. [Reprinted with permission from M. E. Peover and B. S. White, *Electrochim. Acta*, **11**, 1061 (1966). Copyright 1966, Pergamon Press PLC.]

i

10 µA

0

−0.8   −1.0   −1.2   −1.4   −1.6   −1.8   −2.0   −2.2   −2.4
E/(V *vs.* SCE)
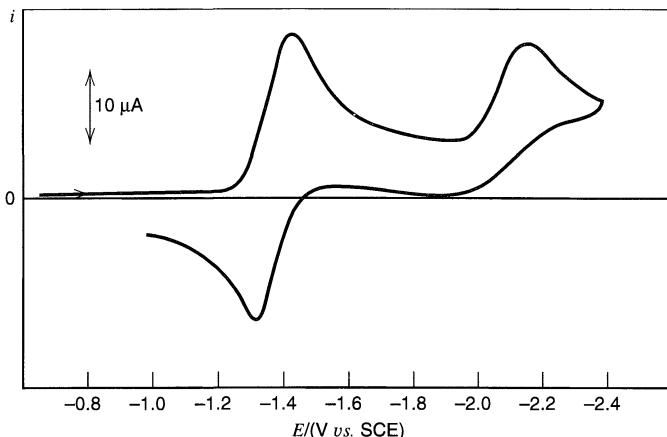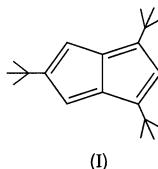
Figure 6.10.4
Cyclic voltammogram
of azotoluene in
N,N-dimethylformamide.
[See J. L. Sadler and
A. J. Bard, *J. Am. Chem.
Soc.*, **90**, 1979 (1968).]

fusion coefficients, etc. (This is a set of actual data, so don't expect numbers to conform *exactly* to theoretical treatments.)

Scan rate (mV/sec)	First Wave[a]				Second Wave		
	i_{pc} (μA)	i_{pa} (μA)	$-E_{pc}$ (V *vs.* SCE)	$-E_{pa}$ (V *vs.* SCE)	i_{pc} (μA)	$-E_{pc}$ (V *vs.* SCE)	$-E_{p/2}$ (V *vs.* SCE)
430	8.0	8.0	1.42	1.36	7.0	2.10	2.00
298	6.7	6.7	1.42	1.36	6.5	2.09	2.00
203	5.2	5.2	1.42	1.36	4.7	2.08	2.00
91	3.4	3.4	1.42	1.36	3.0	2.07	1.99
73	3.0	2.9	1.42	1.36	2.8	2.06	1.98

[a]For scan reversed 100 mV past E_{pc}.

6.10 R. W. Johnson described the electrochemical behavior of 1,3,5-tri-*tert*-butylpentalene (I).

(I)

Solutions of I in CH_3CN with 0.1 *M* tetra-*n*-butylammonium perchlorate (TBAP) were subjected to polarographic and cyclic voltammetric examination. The results were as follows:

   Polarography.[9] one wave at $E_{1/2} = -1.46$ V *vs.* SCE. Wave slope of 59 mV.

   Cyclic voltammetry. Illustrated in Figure 6.10.5; the scan starts at 0.0 V *vs.* SCE and moves first in a positive direction.

In addition, bulk electrolysis at +1.0 V produced a green solution giving a well-resolved ESR spectrum, and bulk electrolysis at −1.6 V gave a magenta solution that also produced a well-resolved ESR spectrum. Both bulk transformations were carried out in CH_2Cl_2.

(a) Describe the chemistry of the system.

(b) Account for the shape of the cyclic voltammetric curve. Identify all peaks.

(c) Interpret the polarogram and relate the cyclic voltammogram to it.

(d) What would you expect the diffusion current constant for the polarogram to be (in conventional units)? Take $D_I = 2 \times 10^{-5}$ cm^2/s.

---

[9]Polarography is sampled-current voltammetry at a dropping mercury electrode. The time scale is normally 1–4 s. See Sections 7.1 and 7.2.
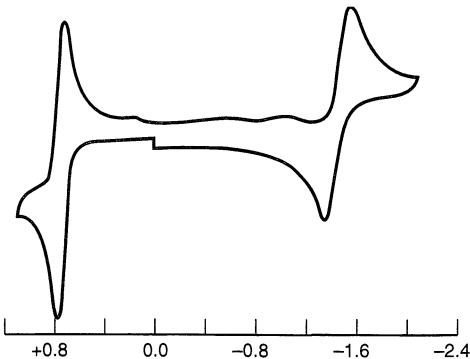
Figure 6.10.5 Cyclic voltammogram of I in CH$_3$CN with 0.1 M TBAP at a Pt electrode *vs.* SCE and at a scan rate of 500 mV/s. [Reprinted with permission from R. W. Johnson, *J. Am. Chem. Soc.*, **99**, 1461 (1977). Copyright 1977, American Chemical Society.]

(e) Make sketches showing the expected variations with v of forward peak current and ΔE_p for the couple responsible for the green solution. Do the same for the couple responsible for the magenta solution.

6.11. Sketch the distribution diagrams for the water/1,2-DCE system (concentration of ion in water/total concentration of that ion *vs. E*) for the four ions (Li$^+$, Cl$^-$, TPAs$^+$, TPB$^-$) using the following $\Delta G_{\text{transfer,i}}^{0\alpha\rightarrow\beta}$ values (kJ/mol): Li$^+$, 48.2; Cl$^-$, 46.4; TPAs$^+$, −35.1; TPB$^-$, −35.1. Use this plot to predict the current-potential behavior, such as that shown in Figure 6.8.3A.

6.12 (a) A study of the heterogeneous electron-transfer rate for the oxidation of ferrocene in acetonitrile (0.5 M TBABF$_4$) produced the following [M. V. Mirkin, T. C. Richards, and A. J. Bard, *J. Phys. Chem.*, **97**, 7672 (1993)]: $k^0 = 3.7$ cm/s and $D_R = 1.70 \times 10^{-5}$ cm^2/s. Calculate ψ and ΔE_p for the cyclic voltammetric oxidation of ferrocene at 25°C, assuming $D_R = D_O$, at scan rates of 3, 30, 100, 200, 300, and 600 V/s.

(b) The results tabulated below were reported for ΔE_p as a function of v for the oxidation of 2 mM ferrocene in acetonitrile (0.1 M TBABF$_4$) at a 25-μm diameter Au electrode [I. Noviandri et. al., *J. Phys. Chem.*, **103**, 6713 (1999)]. How do you account for these results based on the calculations in part (a)?

v(V/s)	3.2	32	102	204	297	320	640
ΔE_p(mV)	77	94	96	120	134	158	300

7

POLAROGRAPHY AND PULSE VOLTAMMETRY

In Chapter 5, we laid a foundation for understanding controlled-potential methods generally and potential step methods in particular. The focus there was on broadly applicable concepts, so we restricted our view of voltammetry to the basic sampled-current idea. Building on that development of fundamentals, we followed in Chapter 6 with a full treatment of potential sweep methods, including cyclic voltammetry, which has become so important in practice. Now we return to voltammetry based on potential step waveforms. Originating historically with *dc polarography* (the simplest form of voltammetry at the dropping mercury electrode), this group of methods has become quite diverse as more complex schemes have been devised for applying potential steps and sampling currents. The name *pulse voltammetry* is often used to encompass the group aside from dc polarography. We have already encountered *normal pulse voltammetry* (NPV) as the most straightforward version of sampled-current voltammetry. NPV is often carried out with a dropping mercury electrode, in which case it is called *normal pulse polarography* (NPP).

Because these methods are so deeply rooted in the polarographic tradition and even now are frequently used with polarographic electrodes, we begin with a discussion of phenomena at dropping mercury electrodes and then develop the subject through conventional polarography and into various forms of pulse voltammetry.

▶ 7.1 BEHAVIOR AT POLAROGRAPHIC ELECTRODES

7.1.1 The Dropping Mercury and Static Drop Electrodes

An instrument of enormous importance to the history of electroanalytical chemistry is the *dropping mercury electrode* (DME), which was invented by Heyrovský (1) for measurements of surface tension (Section 13.2.1). Using the DME, he discovered a form of voltammetry, which he named "polarography" and which became the foundation for most of the methods discussed in this book. Heyrovský was recognized with the Nobel Prize in Chemistry for his achievement. The term *polarography* has since become a general name for voltammetry at a dropping mercury electrode. In this book, we refer to the historic form as *dc polarography* or *conventional polarography*.

Figure 7.1.1 depicts a classical dropping mercury electrode. Several excellent discussions of the construction and operation of the electrode are available (2–6). A capillary with an internal diameter of $\sim 5 \times 10^{-3}$ cm is fed by a head of mercury 20 to 100 cm high. Mercury issues through the capillary to form a nearly spherical drop, which grows until its weight can no longer be supported by the surface tension. A mature drop typically has a diameter on the order of 1 mm. If electrolysis occurs during the drop's
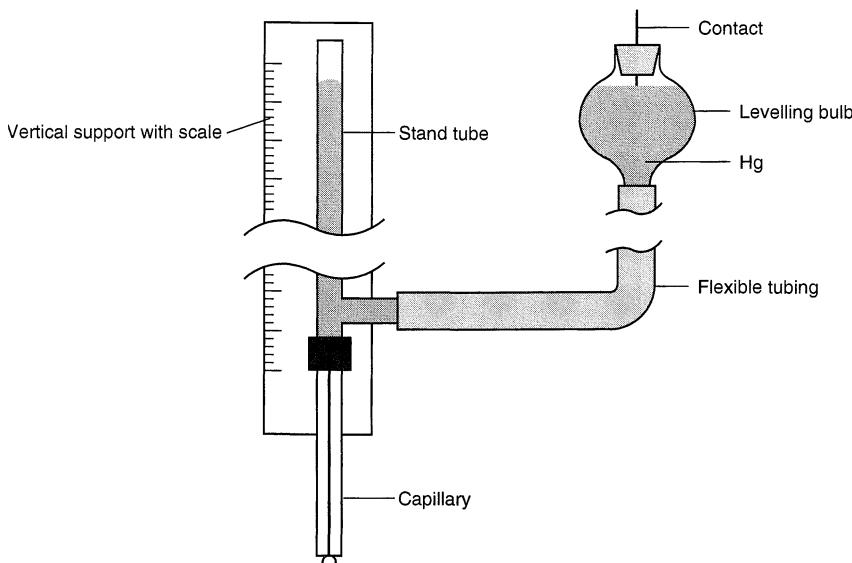
Figure 7.1.1 A dropping mercury electrode.

growth, the current has a time dependence that reflects both the expansion of the spherical electrode and the depletion effects of electrolysis. Upon falling, the drop stirs the solution and largely (but not completely[1]) erases the depletion effects, so that each drop is born into fresh solution. If the potential does not change much during the lifetime of a drop (2–6 s), the experiment is indistinguishable from a step experiment in which the potential transition coincides with the birth of a new drop. Each drop's lifetime is itself a new experiment.

The classical DME has two principal disadvantages. First, it has a constantly changing area, which complicates the treatment of diffusion and creates a continuous background current from double-layer charging. Second, its time scale is controlled by the lifetime of the drop, which cannot be varied conveniently outside the range of 0.5–10 s.

By 1980, Princeton Applied Research Corporation, later followed by others, had commercialized a replacement for the classical DME that does not suffer these drawbacks (7, 8). The *static mercury drop electrode* (SMDE, Figure 7.1.2) is an automated device in which the mercury flow is controlled by a valve. A head of only about 10 cm drives mercury through a wide-bore capillary when the valve is opened in response to an electrical signal. A drop is extruded in less than 100 ms, then growth is stopped by closure of the valve. The drop remains in place until a mechanical, solenoid-driven *drop knocker* dislodges it upon receiving another electronic signal. The SMDE can serve as a *hanging mercury drop electrode* (HMDE) or, in a repetitive mode, as a replacement for the DME. In the latter role, it retains all of the important advantages of the DME (Section 7.1.3), and it has the added feature that the area does not change at the time of measurement. Most contemporary polarographic work is carried out with SMDEs.

In the sections below, we will discuss polarographic concepts first in the context of the DME, then with reference to the SMDE.

---

[1]Additional fine points about behavior at the DME are discussed in Section 5.3 of the first edition.
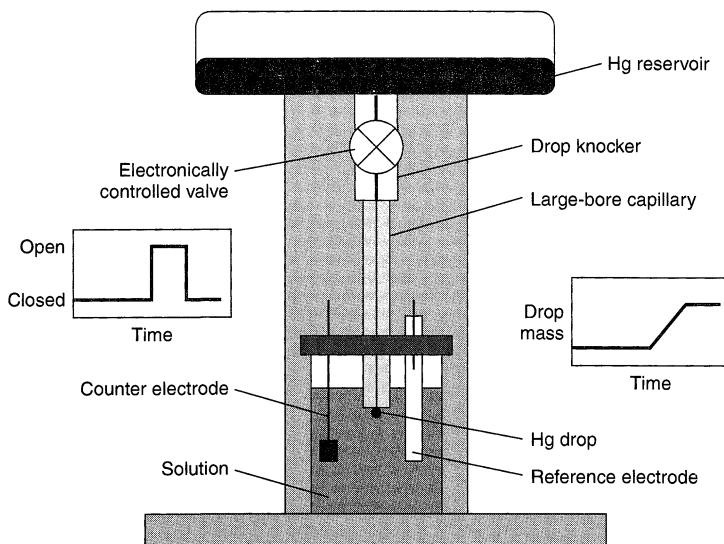
Figure 7.1.2 Schematic diagram of a static mercury drop electrode. The typical unit includes a cell stand, as shown here, and facilities for stirring and deaeration of the solution by bubbling with an inert gas. These functions are normally controlled electronically by an automated potentiostat, which also manages the issuance and dislodgment of the mercury drops and applies the potential program that they experience while they are active as working electrodes. When a new drop is needed, the old one is dislodged by a command to the drop knocker, then the electronically controlled valve is opened for 30–100 ms (see graph on left). The drop is formed during this brief period (see graph on right), then it remains indefinitely stable in size as it is employed as the working electrode.

7.1.2 Diffusion-Limited Responses at the DME and SMDE

(a) The Ilkovič Equation

Let us consider the current that flows during a single drop's lifetime when a DME is held at a potential in the mass-transfer-controlled region for electrolysis. That is, we seek the diffusion-limited current, essentially as we did in Section 5.2 for stationary planar and spherical electrodes. The problem was solved by Koutecký (9, 10), but the treatment requires consideration of the relative convective movement between the electrode and solution during drop growth. The mathematics are rather complicated and give little intuitive feel for the effects involved in the problem. The treatment we will follow, originally due to Lingane and Loveridge (11), makes no pretense to rigor. It is only an outline to the problem, but it highlights the differences between a DME and a stationary electrode (3, 11–14).

The typical values of drop lifetime and drop diameter at maturity ensure that linear diffusion holds at a DME to a good approximation [Section 5.2.2(c)]. Thus, we begin by invoking the Cottrell relation, (5.2.11), while remembering that for the moment we are considering electrolysis only at potentials on the diffusion-limited portion of the voltammetric response curve. Since the drop area is a function of time, we must determine $A(t)$ explicitly. If the rate of mercury flow from the DME capillary (mass/time) is m and the density of mercury is d_{Hg}, then the weight of the drop at time t is

$$mt = \tfrac{4}{3}\pi r_0^3 d_{Hg} \tag{7.1.1}$$

The drop's radius and its area are then given by

$$r_0 = \left(\frac{3mt}{4\pi d_{\text{Hg}}}\right)^{1/3} \tag{7.1.2}$$

$$A = 4\pi\left(\frac{3mt}{4\pi d_{\text{Hg}}}\right)^{2/3} \tag{7.1.3}$$

Substitution into the Cottrell relation gives

$$i_{\text{d}} = \left[4\pi^{1/2}F\left(\frac{3}{4\pi d_{\text{Hg}}}\right)^{2/3}\right]nD_O^{1/2}C_O^* m^{2/3}t^{1/6} \tag{7.1.4}$$

In addition to the effect of the changing area, which progressively enlarges the diffusion field, there is a second consideration that we might call the "stretching effect." That is, at any time t, expansion of the drop causes the existing diffusion layer to stretch over a still larger sphere, much like the membrane of an expanding balloon. This has the effect of making the layer thinner than it otherwise would be, so that the concentration gradient at the electrode surface is enhanced and larger currents flow. It turns out that the result is the same as if the effective diffusion coefficient were $(7/3)D_O$; hence (7.1.4) requires multiplication by $(7/3)^{1/2}$:

$$i_{\text{d}} = \left[4\left(\frac{7\pi}{3}\right)^{1/2}F\left(\frac{3}{4\pi d_{\text{Hg}}}\right)^{2/3}\right]nD_O^{1/2}C_O^* m^{2/3}t^{1/6} \tag{7.1.5}$$

Evaluating the constant in brackets, we have

$$\boxed{i_{\text{d}} = 708nD_O^{1/2}C_O^* m^{2/3}t^{1/6}} \tag{7.1.6}$$

where i_{d} is in amperes, D_O in cm^2/s, C_O^* in mol/cm^3, m in mg/s, and t in seconds. Alternatively, i_{d} can be taken in μA, and C_O^* in mM.

Ilkovič was first to derive (7.1.6); hence this famous relation bears his name (12–16). His approach was much more exact than ours has been, as was that of MacGillavry and Rideal (17), who provided an alternative derivation a few years afterward. Actually the Lingane–Loveridge approach is not independent of these more rigorous treatments, for they arrived at the $(7/3)^{1/2}$ stretching coefficient merely by comparing the bracketed factor in (7.1.4) with the factor 708 given by Ilkovič and by MacGillavry and Rideal. All three treatments are based on linear diffusion.

Figure 7.1.3 is an illustration of the current-time curves for several drops as predicted by the Ilkovič equation. Immediately apparent is that the current is a monotonically *increasing* function of time, in direct contrast to the Cottrell decay found at a stationary planar electrode. Thus, the effects of drop expansion (increasing area and stretching of the diffusion layer) more than counteract depletion of the electroactive substance near the electrode. Two important consequences of the increasing current-time function are that the current is greatest and its rate of change is lowest just at the end of the drop's life. As we will see, these aspects are helpful for applications of the DME in sampled-current voltammetric experiments.

Dc polarograms, as obtained in historic practice, are records of the current flow at a DME as the potential is scanned linearly with time, but sufficiently slowly (1–3 mV/s) that the potential remains essentially constant during the lifetime of each drop. This constancy of potential is the basis for the descriptor "dc" in the name of the method. In more modern practice, the potential is applied as a *staircase* function, such that there is a small shift in potential (normally 1–10 mV) at the birth of each drop, but the potential otherwise
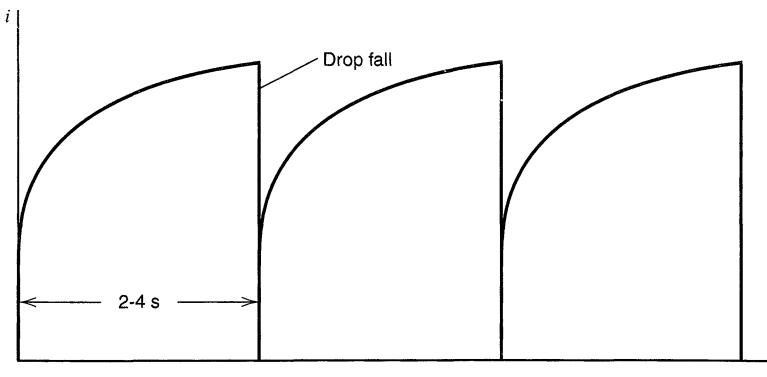
Figure 7.1.3 Current growth during three successive drops of a DME.

remains constant as a drop grows through its lifetime. The current oscillations arising from the growth and fall of the individual drops are ordinarily quite apparent if the current is recorded continuously. A typical case is shown in Figure 7.1.4. The most easily measured current is that which flows just before drop fall, and within the linear approximation it is given by

$$(i_d)_{max} = 708nD_O^{1/2}C_O^*m^{2/3}t_{max}^{1/6}$$
(7.1.7)

where t_{max} is the lifetime of a drop (usually called the *drop time* and often symbolized merely as t).[2,3]

(b) Transient Behavior at the SMDE

In most respects, the SMDE presents a much simpler situation than the classical DME, because the drop is not growing during most of its life. In parallel with our discussion of diffusion-controlled currents at the DME, we confine our view now to the situation where the SMDE is held constantly at a potential in the mass-transfer controlled region. In the earliest stages of a drop's life (on the order of 50 ms), when the valve controlling mercury flow is open and the drop is growing, the system is convective. Mass transfer and current flow are not described simply. After the valve closes, and the drop stops growing, the current becomes controlled by the spherical diffusion of electroactive species.

---

[2]Much of the older polarographic literature involves measurements of the *average* current, $\bar{i}_d$, flowing during a drop's lifetime. This practice grew up when recording was typically carried out by damped galvanometer that responded to the average current. From the Ilkovič equation, one can readily find $\bar{i}_d$ to be six-sevenths of the maximum current:

$$\bar{i}_d = 607\, nD_O^{1/2}C_O^*m^{2/3}\, t_{max}^{1/6}$$

The first edition has more on average currents, including a discussion of Koutecký's treatment of the effects of sphericity (pp. 150–152).

[3]Sometimes polarographic current-potential curves show peaks, called *polarographic maxima*, which can greatly exceed the limiting currents due to diffusion. These excess currents arise at the DME from convection around the growing mercury drop. The convection apparently comes about (a) because differences in current density at different points on the drop (e.g., at the shielded top versus the accessible bottom) cause variations in surface tension across the interface, or (b) because the inflow of mercury causes disturbances of the surface. Surfactants, such as gelatin or Triton X-100, termed *maximum suppressors*, have been found experimentally to eliminate these maxima and are routinely added in small quantities to test solutions when the maxima themselves are not of primary interest. Convective maxima are rarely important in polarography at an SMDE.
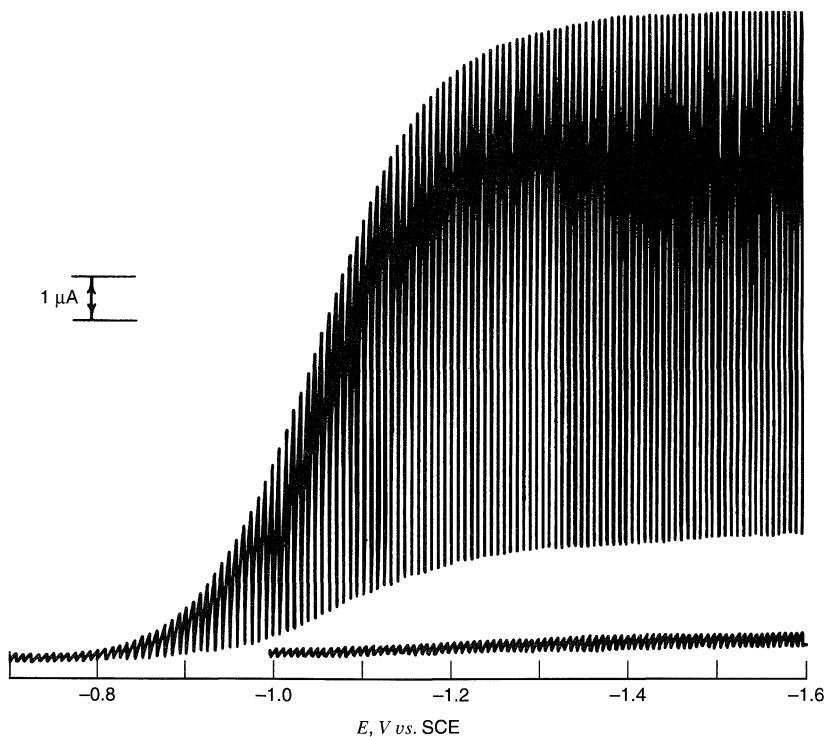
Figure 7.1.4 Polarogram for 1 mM CrO_4^{2-} in deaerated 0.1 M NaOH, recorded at a DME. The Ilkovič equation describes current flow in the plateau region, at potentials more negative than about -1.3 V. The lower curve is the residual current observed in the absence of CrO_4^{2-}. The recorder was fast enough to follow the current oscillations through most of each drop's life, but not at the moment of drop fall, as one can see by the fact that the trace does not reach the zero-current line before starting a fresh rise with the new drop.

This system is similar to that treated in Section 5.2.2, but the parallel is not exact because of the drop growth and convection in the early part of the experiment. After the drop becomes static, the current declines with time toward an asymptote. This behavior differs markedly from that at the DME, where the current rises with time because of continuous expansion of the drop. If the current at the SMDE is sampled electronically at a time τ after the birth of the drop, then the current sample is given approximately from (5.2.18) as,

$$i_d(\tau) = nFAD_OC_O^* \left[\frac{1}{(\pi D_O\tau)^{1/2}} + \frac{1}{r_0} \right] \tag{7.1.8}$$

where r_0 is the radius of the mercury droplet. This equation cannot describe the experiment reliably in the early stage, but it becomes a better descriptor at later times, as the period of growth becomes a smaller portion of the whole experiment.

In practice, an SMDE is rarely operated in this dc polarographic mode, precisely because of the unfavorable current-time profile during the life of each drop and the poor control of mass transfer in the formative stage, when currents are high. Instead, better measurement conditions are created by manipulating the potential carefully during the life of each drop. During the period when the drop is born and brought to maturity, the potential is controlled at a value where there is no significant electroactivity. After the drop becomes static the potential is changed to a value where a current measurement can be

taken. If this change involves stepping the potential to a value in the mass-transfer-controlled region, the experiment fulfills all of the conditions assumed in Section 5.2.2 without being compromised by the growth of the drop. If the current is then sampled at time τ, measured with respect to the leading edge of the potential step (rather than the birth of the drop), then the sampled current is given rigorously by (7.1.8). This experiment is known as *normal pulse polarography* and is described in more detail in Section 7.3.2. A *normal pulse polarogram* is recorded by imposing a slightly larger potential step on each successive drop and making a plot of the sampled current *vs.* step potential, essentially exactly as outlined in Figure 5.1.3.

Usually the sampling time τ is short enough that the diffusion layer thickness remains small compared to r_0, so that the second (spherical) term of (7.1.8) is negligible. Thus, the sampled limiting-current, based on linear diffusion, is given by the Cottrell equation,

$$i_d(\tau) = \frac{nFAD_O^{1/2}C_O^*}{\pi^{1/2}\tau^{1/2}} \tag{7.1.9}$$

which is the SMDE's analogue to the Ilkovič equation. Because the current declines with increasing sampling time, it is advantageous to keep that time to a minimum. A typical pulse width (and sampling time) is 50 ms.

Normal pulse polarography can also be carried out with a DME as discussed in Section 7.3.2.
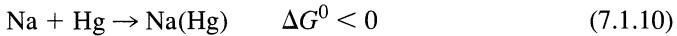
7.1.3 Polarographic Analysis

The DME and SMDE share many advantages for practical electroanalysis (3, 6, 18, 19). The dropping action is very reproducible, and the surface is continuously renewed. These factors make high-precision measurements possible (5), and the latter carries the additional advantage that the electrode is not permanently modified by material that deposits in or on the electrode (as does occur by adsorption of species from solution or in the course of electrodeposition of metals). The current-time curves at the DME, which feature minimal rates of current change as the maximum current is approached (and also a maximum current identified with the end of drop life), are well adapted to sampled-current voltammetry. The favorable time profile is sacrificed at the SMDE in favor of shorter sampling times, shorter drop times, faster runs, and higher currents. With either electrode, sampled-current voltammetry is convenient for multicomponent analysis, because current plateaus are obtained in the mass-transfer-limited region of each wave; hence flat (or at least linear) baselines apply to each of several successive waves (Sections 5.6 and 7.1.5). The repeated dropping and stirring action make it possible, in effect, to carry out a succession of step experiments with a constant potential or a slowly varying ramp applied to the electrode. With a DME, sampling can be carried out just by observing the locus of maximum currents on the current-potential curve, and this is the basis for dc polarography in the classic form. With the SMDE, sampling must be done electronically, but it is easy to accomplish.

Another important advantage of the DME or SMDE is the very high overpotential for hydrogen discharge on mercury surfaces. In many media, this process is the cathodic background reaction; thus the high overpotential means that the background limit is pushed to more negative potentials, and it becomes possible to observe electrode reactions that occur at rather extreme potentials. An example is the reduction of the sodium ion to sodium amalgam in basic aqueous media, which is observable as a clean wave well before the background limit is reached. The exothermicity and the vigor of sodium's reaction with water testifies to the much smaller *energy change* involved in the reduction of H^+

compared with the reduction of Na^+. It is the sluggish *kinetics* of the former that makes possible observations of higher-energy processes, such as the latter.

Actually, this particular case is aided by another nice feature of the DME or SMDE, namely the ability to form amalgams. Since sodium amalgam is spontaneously formed:

$$Na + Hg \rightarrow Na(Hg) \qquad \Delta G^0 < 0 \qquad (7.1.10)$$

the amalgam lies at a lower position on the free energy scale than metallic sodium. The free energy for Na^+ reduction to Na(Hg) is therefore less than for reduction to the metal, and the standard potential is correspondingly more positive. This is a general feature of electrode processes that involve reductions to amalgams, and it, like the high hydrogen overpotential, contributes to a widening of the range of processes that can be studied at the DME and SMDE.

The chief disadvantage of polarographic methods lies in the inability of mercury electrodes to operate at potentials much more positive than 0.0 V *vs.* SCE. The anodic limit, which arises from the oxidation of mercury, is always near that potential, although it depends somewhat on the medium.

Quantitative polarographic analysis is based on the linear linkage between the diffusion current and bulk concentration of the electroactive species. In general, the most precise measurements of concentration are carried out by constructing a calibration curve with a set of standard solutions. In routine work, $\pm 1\%$ precision can be obtained (3, 6, 18, 19); however, Lingane (5) showed that $\pm 0.1\%$ is possible with careful precautions. His work demonstrated that most sources of imprecision involve temperature effects of some sort. Chief among them is the temperature dependence of mass transport itself, for the diffusion coefficient increases by 1–2% per degree. Even at the 1% precision level, thermostating of the cell is required. For more details on actual measurements, the literature should be consulted (3, 16, 18, 19).

Standard addition and internal standard methods are also used in concentration measurements. They are implemented in the obvious ways and usually are capable of precision of a few percent.

Unique to dc polarographic analysis, and to the DME, is the "absolute" method for evaluating concentrations, which was advocated by Lingane (20). A rearrangement of the Ilkovič equation for maximum currents, placing all the experimental variables (i_d, t_{max}, m, and C_O^*) on one side, gives

$$(I)_{max} = \frac{(i_d)_{max}}{m^{2/3} t_{max}^{1/6} C_O^*} = 708 n D_O^{1/2} \qquad (7.1.11)$$

This *diffusion current constant*, $(I)_{max}$, is independent of the specific values of m, t_{max}, and C_O^* used in the measurement. Since it depends only on n and D_O, it is a constant of the electroactive substance and the medium in much the same way that molar absorptivity, ε, is a constant of the system for optical measurements. Given $(I)_{max}$ for the system at hand, one can evaluate C_O^* simply by measuring i_d, t_{max}, and m. No standards are needed. The method is not wholly accurate, because (7.1.7) is itself an approximation. Many workers have reported diffusion current constants and large tabulations exist (21–25).

Because the DME is now in declining use, diffusion current constants are rarely reported in new literature; however the data in older literature[4] remain useful in characteriz-

---

[4]Since the older work was often based on average limiting currents, many reported diffusion current constants are defined from the version of the Ilkovič equation for average currents, which gives:

$$\bar{I} = \frac{\bar{i}_d}{m^{2/3} t_{max}^{1/6} C_O^*} = 607 n D_O^{1/2}$$

Thus $\bar{I} = (6/7)(I)_{max}$.

ing electrode processes, particularly as indicators of n-values or diffusion coefficients. In general, one-electron, two-electron, and three-electron reactions have constants in the ranges of 1.5–2.5, 3.0–4.5, and 4.5–7.0, respectively, whenever media with water-like viscosities (~1 cP) are employed. This criterion can be extended to other media via *Walden's Rule* (14), which notes that for most substances the diffusion coefficients in two media, 1 and 2, are related to the viscosities η_1 and η_2 by

$$D_1 \eta_1 \approx D_2 \eta_2 \qquad (7.1.12)$$

Thus

$$\frac{(I_1)_{max}}{(I_2)_{max}} = \frac{\bar{I}_1}{\bar{I}_2} \approx \left(\frac{\eta_2}{\eta_1}\right)^{1/2} \qquad (7.1.13)$$

All of this rests upon the fact that diffusion coefficients for most ions and small molecules have similar values in a single medium. Exceptions include H^+ and OH^- in aqueous media, oxygen generally, polymers, and large biomolecules. Even though $(I)_{max}$ or $\bar{I}$ can be used conveniently to estimate D values, discretion is needed because of the limitations in the Ilkovič equation.

In its basic "dc" mode, polarographic analysis is carried out most precisely in the range from 0.1 to 10 mM. Comments above about precision generally apply to this region. Above 10 mM, electrode processes tend to cause such large alterations in solution composition near the electrode that density gradients arise, convection becomes a problem, and currents may be erratic. Also, such concentrated samples can produce large currents, which can be accompanied by large iR_u, leading to inaccurate potentials and broadened waves. At the other end of the working range, useful measurements can sometimes be carried out near 10^{-5} M; however charging current (Section 7.1.5) becomes a severe interference at the DME and effectively sets the detection limit for dc polarography, whether the sampling is done visually or electronically. The SMDE is usually employed with the more sophisticated polarographic methods discussed in Section 7.3, which are preferred to dc polarography because they provide better sensitivities and background suppression.

7.1.4 Effect of Mercury Column Height at a DME

In work with a dropping mercury electrode, the height of the mercury column above the capillary tip governs the pressure driving mercury through the DME, thus it is a key determinant of m (13, 14). In turn, m controls the drop time t_{max}, because the maximum mass that the surface tension can support (mt_{max}) is a constant defined by

$$mt_{max} g = 2\pi r_c \gamma \qquad (7.1.14)$$

where g is the gravitational acceleration, r_c is the radius of the capillary, and γ is the surface tension of the mercury water interface.

The first edition covered this topic in greater detail[5] and included a demonstration that m is inversely proportional to a *corrected column height*, h_{corr}, which is obtained from the actual height by applying two small adjustments.

The Ilkovič relation shows that the diffusion-limited current is proportional to $m^{2/3} t_{max}^{1/6}$, which in turn is proportional to $h_{corr}^{2/3} h_{corr}^{-1/6} = h_{corr}^{1/2}$. This square-root dependence of the limiting current on corrected column height is characteristic of processes that are limited by the rate of diffusion, and it is used as a diagnostic criterion to distinguish this

---

[5]First edition, p. 155.

case from other kinds of current limitation. For example, the current could be limited by the amount of space available on an electrode surface for adsorption of a faradaic product, or it might be limited by the rate of production of an electroreactant in a preceding homogeneous chemical reaction.

Column height is not of interest in work with an SMDE, because mercury does not flow at the time when currents are sampled. The test for diffusion control at an SMDE is to vary the sampling time and to examine whether the limiting current varies as the inverse square-root of sampling time. This procedure, like testing for dependence of limiting current on the square-root of column height at a DME, has its origin in the time dependence of the diffusion-layer thickness (Section 5.2.1).

7.1.5 Residual Current

In the absence of an electroactive substance of interest, and between the anodic and cathodic background limits, a *residual current* flows (3, 6, 14, 26). It is composed of a current due to double-layer charging and a current caused by low-level oxidation or reduction of components in the system. The residual faradaic currents arise from (a) trace impurities, (such as heavy metals, electroactive organics, or oxygen), (b) from the electrode material (which often undergoes slow, potential-dependent faradaic reactions), or (c) from the solvent and supporting electrolyte (which can produce small currents over a wide potential span via reactions that, at more extreme potential, become greatly accelerated and determine the background limits).

The nonfaradaic current (often called the *charging* or *capacitive current*) can make the residual current rather large at a DME, even in highly purified systems where the faradaic component is small. Because the DME is always expanding, new surface appears continuously. It must be charged to reflect the potential of the electrode as a whole; therefore a charging current, i_c, is always required.

An expression for it can be obtained as follows. The charge on the double layer is given by

$$q = -C_i A(E - E_z) \tag{7.1.15}$$

where C_i is the integral capacitance of the double layer (Section 13.2.2) and A is the electrode area. The difference $E - E_z$ is the potential of the electrode relative to the potential where the excess charge on the electrode is zero. That point, E_z, is called the *potential of zero charge* (the PZC; see Section 13.2.2). One can think of the expansion at the DME as creating new surface in an uncharged state, which then requires charging from the PZC to the working potential. By differentiating (7.1.15), one obtains

$$i_c = \frac{dq}{dt} = C_i(E_z - E)\frac{dA}{dt} \tag{7.1.16}$$

since C_i and E are both effectively constant during a drop's lifetime. From (7.1.3), dA/dt can be obtained, and one finds that

$$\boxed{i_c = 0.00567 C_i(E_z - E)m^{2/3}t^{-1/3}} \tag{7.1.17}$$

where i_c is in μA if C_i is given in μF/cm^2. Typically, C_i is 10 to 20 μF/cm^2. Several important conclusions can be drawn from (7.1.17):

    1.   The average charging current over a drop's lifetime is about the same magnitude as the average faradaic current for an electroactive substance present at the 10^{-5}

M level; thus we understand why the ratio of limiting current to residual current degrades badly at a DME in this concentration range. Charging current, more than any other factor, limits detection in dc polarography at a DME to concentrations above $5 \times 10^{-6} M$ or so (Section 7.3.1).

2. Note that if C_i and t_{max} are not strongly varying functions of potential, i_c is linear with E. As shown in Figure 7.1.5, experimental residual current curves actually are fairly linear over wide ranges, and this behavior provides the justification for the common practice of measuring i_d for a polarographic wave by extrapolating the baseline residual current as shown in Figure 7.1.6. Note also that the capacitive current vanishes and changes sign at $E = E_z$ (see also Figure 7.3.3).

3. Another important contrast between i_c and i_d is in their time dependencies. As we have seen, i_d increases monotonically and reaches its maximum value at t_{max}. The charging current decreases monotonically as $t^{-1/3}$ [see (7.1.17)], because the rate of area increase slows as the drop ages. Thus, the charging current is at its minimal value at t_{max}. This contrast underlies some approaches to increasing polarographic sensitivity by discriminating against i_c in favor of i_d. We will discuss them in Section 7.3.

Since an SMDE has a fixed area as the current is sampled, $dA/dt = 0$, and the charging current due to drop expansion is zero. Thus, equation 7.1.17 does not apply to an
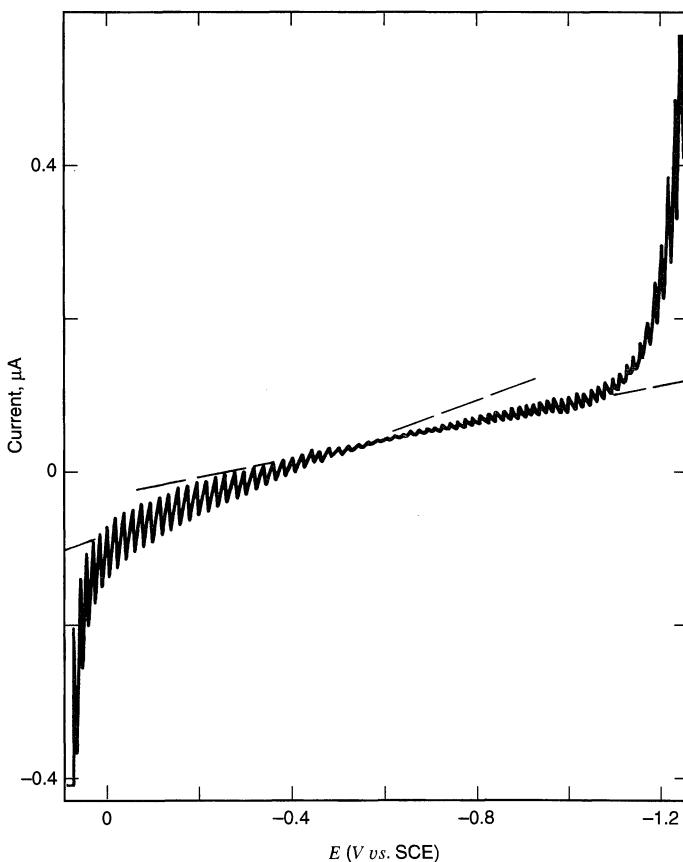
Figure 7.1.5 Residual current curve for 0.1 M HCl. The sharply increasing currents at potentials more positive than 0 V and more negative than −1.1 V arise from oxidation of mercury and reduction of H^+, respectively. The current between 0 V and −1.1 V is largely capacitive. The PZC is near −0.6 V *vs.* SCE. (From L. Meites, "Polarographic Techniques," 2nd ed., Wiley-Interscience, New York, 1965, p. 101, with permission.)
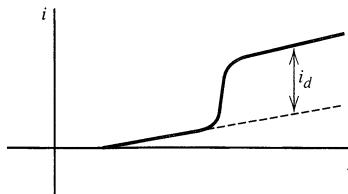
Figure 7.1.6 Method for obtaining i_d from a wave superimposed on a sloping baseline of residual current.

SMDE. In most experiments with an SMDE, the residual current is almost entirely of faradaic origin and is often controlled by the purity of the solvent-supporting electrolyte system (Section 7.3.2).

▶ 7.2 POLAROGRAPHIC WAVES

7.2.1 Reversible Systems

In Section 7.1.2, we saw that, to a first approximation, current flow at the DME can be treated as a linear diffusion problem. The time dependence of the area is taken into account directly in terms of $m^{2/3}t^{-1/6}$, and a multiplicative factor, $(7/3)^{1/2}$, accounts for increased mass transport due to the "stretching" of the diffusion layer. These concepts apply equally well to $i(t)$ at a potential on the rising portion of the wave, as expressed in (5.4.17). Consequently the wave shape found for sampled-current voltammetry, (5.4.22), applies also to polarography at the DME, which is in essence a sampled-current voltammetric experiment if the rate of potential sweep is sufficiently slow that E is virtually constant during a drop's lifetime (27, 28) [see also Section 5.4.2(b)].

Similarly, the surface concentrations are described by (5.4.29) and (5.4.30); hence (5.4.31) and (5.4.32) are valid for the DME. In this case, however, the maximum diffusion current is given by (7.1.7), and the analogues to (5.4.65) and (5.4.66) are

$$(i)_{max} = 708nD_O^{1/2}m^{2/3}t_{max}^{1/6}[C_O^* - C_O(0, t)] \tag{7.2.1}$$

$$(i)_{max} = 708nD_R^{1/2}m^{2/3}t_{max}^{1/6}C_R(0, t) \tag{7.2.2}$$

Obviously these relations still follow the forms

$$(i)_{max} = nFAm_O[C_O^* - C_O(0, t)] \tag{7.2.3}$$

$$(i)_{max} = nFAm_R[C_R(0, t) - C_R^*] \tag{7.2.4}$$

where m_O is now $[(7/3)D_O/\pi t_{max}]^{1/2}$ and m_R is defined analogously.

The SMDE adheres in detail to the treatment of Sections 5.4.1 and 5.4.3, provided that the sampling time τ is short enough for linear diffusion to apply, as is true in normal practice.

Section 5.4.4, dealing with applications of reversible sampled-current voltammograms, applies very generally to dc polarography at the DME or to normal pulse polarography at the SMDE.

7.2.2 Irreversible Systems

This section concerns special characteristics of irreversible waves at a DME (28, 29, 30). Polarography at an SMDE adheres to the results of Section 5.5.1, provided that linear diffusion effectively applies, as is normally true.

Koutecký treated the totally irreversible system at the DME and expressed the result as (29, 30)

$$\frac{i}{i_d} = F_2(\chi)$$ (7.2.5)

where $\chi = (12/7)^{1/2} k_f t_{max}^{1/2}/D_O^{1/2}$ and $F_2(\chi)$ is a numeric function computed from a power series. Table 7.2.1 gives some representative values. One can analyze an irreversible polarogram by finding i/i_d at various points on the wave, then, from the Koutecký function, finding the corresponding values of χ. From these, one obtains k_f as a function of E, which can be further distilled to k^0 and α, if the mechanism is understood well enough to make these parameters meaningful (e.g., there is a one-step, one-electron reaction or the initial step in an n-electron process is an irreversible rate-determining electron transfer; see Section 3.5.4).

A simplified method for treating totally irreversible polarographic waves was proposed by Meites and Israel (28, 31). From the definition of χ and k_f,

$$\chi = \left(\frac{12}{7}\right)^{1/2} \frac{k_f^0 t_{max}^{1/2}}{D_O^{1/2}} e^{-\alpha f E}$$ (7.2.6)

where k_f^0 is the value of k_f at $E = 0$ on the potential scale in use. Its value is $k^0 \exp(\alpha f E^{0'})$. One can take logarithms of (7.2.6) and rearrange the result to

$$E = \frac{2.303RT}{\alpha F} \log \frac{k_f^0 t_{max}^{1/2}}{D_O^{1/2}} - \frac{2.303RT}{\alpha F} \log \left(\frac{7}{12}\right)^{1/2} \chi$$ (7.2.7)

From Koutecký's values of $F_2(\chi)$, Meites and Israel found that the equation

$$\log \left(\frac{7}{12}\right)^{1/2} \chi \approx -0.130 + 0.9163 \log \frac{i}{i_d - i}$$ (7.2.8)

is valid for $0.1 < (i/i_d) < 0.94$. Substitution into (7.2.7) gives, at 25°C,

$$E = E_{1/2} + \frac{0.0542}{\alpha} \log \left(\frac{i_d - i}{i}\right)$$ (7.2.9)

TABLE 7.2.1   Shape Function of a Totally Irreversible Wave[a]

χ	i/i_d	χ	i/i_d
0.05	0.0428	1.4	0.5970
0.1	0.0828	1.6	0.6326
0.2	0.1551	1.8	0.6623
0.3	0.2189	2.0	0.6879
0.4	0.2749	2.5	0.7391
0.5	0.3245	3.0	0.773
0.6	0.3688	4.0	0.825
0.7	0.4086	5.0	0.8577
0.8	0.4440	10.0	0.9268
0.9	0.4761	20.0	0.9629
1.0	0.5050	50.0	0.9851
1.2	0.5552	∞	1

[a]Originally reported in references 29 and 30.

with

$$E_{1/2} = \frac{0.059}{\alpha} \log\left(1.349\frac{k_f^0 t_{max}^{1/2}}{D_O^{1/2}}\right) = E^{0'} + \frac{0.059}{\alpha} \log\left(1.349\frac{k^0 t_{max}^{1/2}}{D_O^{1/2}}\right) \qquad (7.2.10)$$

A plot of E vs. log $[(i_d - i)/i]$ for an irreversible system should be linear with a slope of 54.2/α mV at 25°C. Also, it is easily shown that $|E_{3/4} - E_{1/4}| = 51.7/\alpha$ mV at the same temperature.[6]

Since α is usually between 0.3 and 0.7, both the wave slope and the Tomeš criterion for a totally irreversible system are normally significantly larger than for a reversible system. These figures of merit are not without ambiguity, however. Consider the predicted wave slope of 63.8 mV for $\alpha = 0.85$. Within the precision of normal measurements, one could diagnose the system as either reversible or irreversible. It is always a good idea to examine reversibility by a method, such as cyclic voltammetry, that allows a view of the electrode reaction in both directions.

Figure 7.2.1 is a display of actual data reported by Meites and Israel (31) for the polarographic reduction of chromate, which behaves as though it is reduced with a rate-determining initial electron transfer.

The shapes and positions of irreversible waves can furnish only kinetic information. One may be able to determine such parameters as k_f, k_b, k^0, or α, but thermodynamic results, such as $E^{0'}$ and free energies, are not available (28, 33, 34). As a rule of thumb, a system with $k^0 > 2 \times 10^{-2}$ cm/s appears reversible on the classical polarographic time scale of a few seconds when D is on the order of 10^{-5} cm^2/s. A heterogeneous charge transfer with $k^0 < 3 \times 10^{-5}$ cm/s will behave in a totally irreversible manner under the same conditions, and one can evaluate the rate parameters as described above. Systems with k^0 between these limits are quasireversible, and some kinetic information can be obtained from them through the treatment prescribed by Randles (33, 34). Naturally, the precision of the kinetic information deteriorates as the reversible limit is approached. See Section 5.5.4 for much more information about the interpretation of irreversible waves.
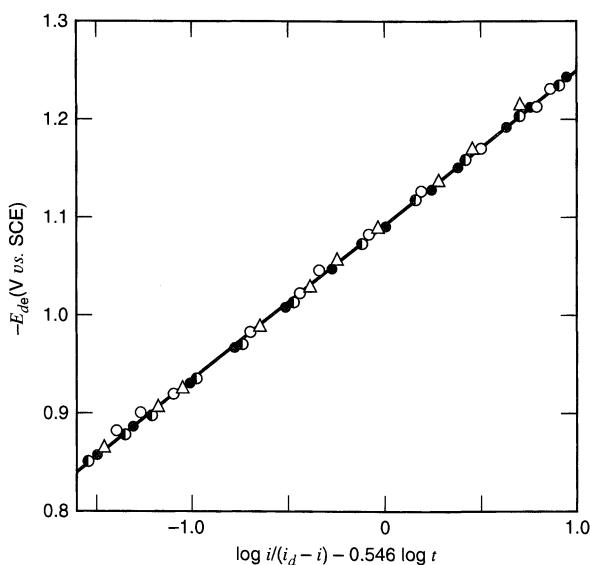
Figure 7.2.1 Wave slope plot for the reduction of 1.0 mM CrO$_4^-$ in 0.1 M NaOH. The different symbols refer to curves recorded with different drop times at -0.80 V vs. SCE: $t_{max} = 7.5$ s (open circles), 5.5 s (triangles), 4.1 s (half-filled circles), and 3.4 s (filled circles). See Figure 7.1.4 for an actual polarogram for this system. [Reprinted with permission from L. Meites and Y. Israel, *J. Am. Chem. Soc.*, **83**, 4903 (1961). Copyright 1961, American Chemical Society.]

[6]Corrections for electrode sphericity are available. See the original literature for details (28, 32).

7.3 PULSE VOLTAMMETRY

The phrase "pulse voltammetry" encompasses a sizable suite of methods whose practice has changed substantially since the first edition appeared. The methods originated in a classical polarographic context and were based on the desire to suppress the charging current arising from continuous expansion of the mercury drop at the DME. Since 1980, practice has departed from the DME, because the SMDE has become the dominant electrode for practical polarographic work and because the use of these methods at stationary electrodes has become more common (35).

We will consider five subtopics: tast polarography and staircase voltammetry, normal pulse voltammetry, reverse pulse voltammetry, differential pulse voltammetry, and square wave voltammetry. Tast polarography, normal pulse voltammetry, and differential pulse voltammetry form a sequence of development rooted historically in polarography at the DME. To illustrate the motivating concepts, we will introduce each of these methods within the polarographic context, but in a general way, applicable to both the DME and SMDE. Then we will turn to the broader uses of pulse methods at other electrodes. Reverse pulse voltammetry and square wave voltammetry were later innovations and will be discussed principally outside the polarographic context.

7.3.1 Tast Polarography and Staircase Voltammetry

The tast method (6, 36–38) is considered here not because it is widely practiced, for it makes sense only with the DME and it holds no advantages with respect to more advanced pulse methods, but because this method furnishes a useful starting point for understanding the sampling strategies that are integral to pulse voltammetry.

In describing current flow at the DME, we noted that the limiting faradaic current increases monotonically during the life of the drop and is described approximately by the Ilkovič equation (Section 7.1.2), whereas the charging current decreases steadily (Section 7.1.5). This contrast is illustrated in Figure 7.3.1. Clearly one can optimize the ratio of
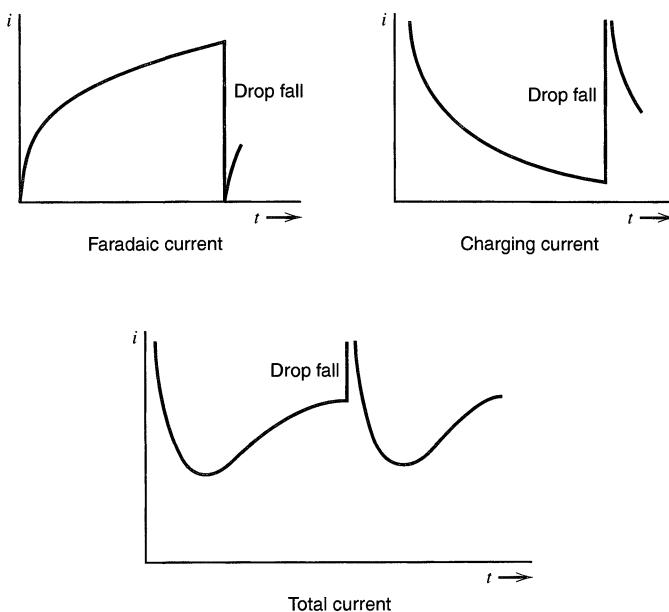
Figure 7.3.1
Superposition of capacitive and faradaic currents of a comparable size at a DME.

faradaic to charging current—and thus the sensitivity—by sampling the current at the instant just before drop fall.

Tast polarography features precisely this scheme. At a fixed time τ after the birth of a drop, the current is sampled electronically, and this sample is presented to a recording system (e.g., a computer interface, a recording oscilloscope, or a chart recorder) as a constant readout, until it is replaced at the sampling time during the next drop. The potentiostat is active at all times, and the potential is changed in small steps according to a *staircase* program (Figure 7.3.2), as in conventional polarography. Typically τ is 2–6 s and ΔE is a few mV.[7] The record of the experiment is a trace of the sampled currents *vs.* potential, which is equivalent to time. Figure 7.3.3*b* shows an example for 10^{-5} *M* Cd^{2+} in 0.01 *M* HCl. The drop time is enforced at a fixed value by dislodging each drop mechanically just after the current sample is taken. This procedure allows an even drop time over the entire potential range. Figure 7.3.4 is a diagram of the experimental arrangement.

Since the potentiostat is always active and the potential is constant during a drop's lifetime, the actual current flow at the electrode is the same as that observed in conventional polarography with a controlled drop time. The difference is that the recording system is fed only signals proportional to the sampled currents. The faradaic component of the limiting sampled current must be

$$i_d(\tau) = 708nD_O^{1/2}C_O^* m^{2/3}\tau^{1/6} \tag{7.3.1}$$

whereas the charging component is

$$i_c(\tau) = 0.00567C_i(E_z - E)m^{2/3}\tau^{-1/3} \tag{7.3.2}$$

The improvements in this method yield detection limits near 10^{-6} *M*, perhaps slightly lower than those of conventional polarography. Since tast measurements are only sampled-current presentations of conventional polarographic currents, all conclusions about the shapes of waves and all diagnostics developed for conventional measurements of maximum currents apply to the tast technique.
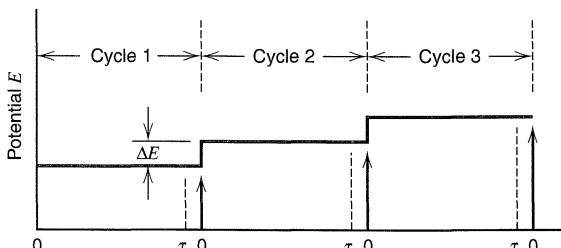
Figure 7.3.2 Staircase waveform and sampling scheme for tast polarography and staircase voltammetry. The experiment is a series of cycles in which a potential is established and held constant for a period, a current sample is taken at time τ after the start of the period, then the potential is changed by an amount ΔE. In tast polarography, the mercury drop is dislodged at the end of each cycle, as indicated by the vertical arrows. In staircase voltammetry, this step is omitted. The time between the current sample, drop dislodgment, and the change in potential is exaggerated here. Usually it is negligible and the cycle period is essentially the same as τ.

---

[7]One can alternatively apply a slow potential ramp to the working electrode, such that the potential changes only 3–10 mV during the life of the drop.
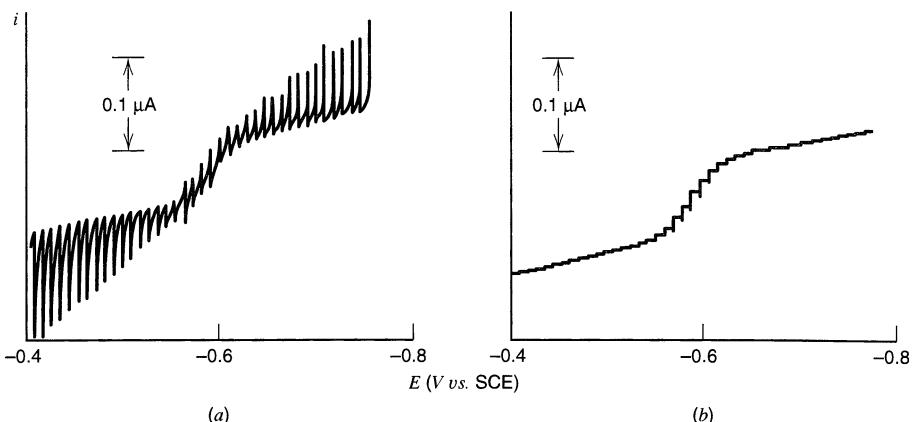
Figure 7.3.3 Polarograms at a DME for 10^{-5} M Cd^{2+} in 0.01 M HCl. (*a*) Conventional dc mode. (*b*) Tast mode. Note that the tast method eliminates the sharp nonfaradaic spikes appearing at each drop fall. The PZC is near -0.5 V in this experiment, hence the charging current spikes appear "anodic" at more positive potentials and "cathodic" at more negative ones.

Tast polarography can also be carried out at an SMDE; however there is no value in doing so. The faradaic current at an SMDE follows a Cottrell-like decay; therefore it is at its lowest value at the end of the drop's life. In the interest of larger signals and a shorter scanning time for the whole polarogram, one needs to use the shortest possible drop time. Because drop formation proceeds quickly and with some convective disruption, the current-time profile does not adhere precisely to the theory for spherical diffusion, and the limiting currents are not as interpretable in fundamental terms as at a DME. Discrimination against charging current is automatic, because the electrode does not have a changing area at any time when sampling would occur, so there rarely is an appreciable charging current with the staircase waveform. This point is discussed in greater detail in Section 7.3.2.

The tast method is designed for a periodically renewed electrode, so it is not even conceptually applicable to a stationary electrode, such as a Pt disk or an HMDE. However, *staircase voltammetry* (35), based on closely related concepts, can find use at such electrodes. The experiment is outlined in Figure 7.3.2. The sampling time and cycle duration are no longer limited by the growth and fall of a mercury droplet; hence one can vary them over a wide range. Times as short as microseconds are possible. One also has the freedom to vary ΔE considerably. This parameter defines the density of current samples along the potential axis, thus it controls the "resolution" of the voltammetry. Of
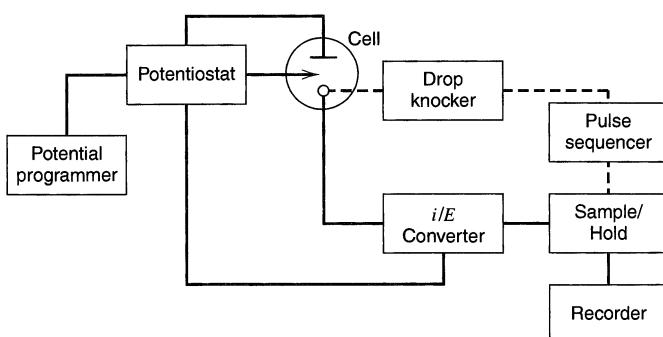
Figure 7.3.4 Schematic experimental arrangement for tast polarography. Staircase voltammetry is carried out at a stationary electrode with the same system except the drop knocker.

course, τ defines the kinetic time scale. If τ is also the cycle period, then the ratio $\Delta E/\tau$ is a *scan rate*, v, describing the speed with which the experiment gathers data over a given potential range.

Since staircase voltammetry does not involve periodic renewal, each cycle inherits its initial conditions from the preceding cycle, and the response from any sample is generally affected by the prior history of the experiment. The most common manifestation is found in the diffusion-limited region of a voltammogram, where samples in successive cycles do not produce a plateau, as they do in polarography, but instead decline as the depletion of electroactive species near the electrode becomes cumulatively greater. Thus the typical staircase voltammogram of a simple system is peak-shaped, rather than wave-shaped.

Staircase voltammetry has many features in common with the potential sweep methods described in Chapter 6. In most systems, the response in a staircase experiment with good potential resolution ($\Delta E < 5$ mV) is very similar to that from a linear sweep experiment with the same scan rate, especially if attention is given to the time in each period when sampling is done (39, 40). Thus one can often analyze results on the basis of the extensive theory available for linear sweep voltammetry and cyclic voltammetry (Chapters 6 and 12).[8]

In principle, one can suppress the charging current background by using the staircase method in place of a linear sweep. This can be true if the measurement is not demanding with respect to resolution or scan rate. For reasons discussed in the next section, τ must be several times the cell time constant to eliminate charging current from the sample. It is not always possible to meet that condition in staircase experiments because of the tradeoff between resolution and speed. There is no problem with a scan at 100 mV/s having 5 mV resolution, because the sampling time would be 50 ms, which is much longer than the cell time constants of most systems of interest. On the other hand, a scan at 1 V/s with 1 mV resolution requires $\tau = 1$ ms, which is not long enough to allow charging current to decay fully in most practical situations. Thus a charging current contribution would normally exist in the staircase experiment, and the relative advantage is muted. This reality and two drawbacks related to signal-to-noise (i.e., minimal faradaic response at the sampling time and noise effects associated with sampling over a narrow time window) have limited the adoption of staircase voltammetry *vis a vis* linear sweep methods.

7.3.2 Normal Pulse Voltammetry

(a) General Polarographic Context

Since tast measurements record the current only during a very small time period late in a drop's life, the faradaic current flow that occurs before the sampling period serves no useful purpose. Actually it works to the detriment of sensitivity because it depletes the region near the electrode of the substance being measured and necessarily reduces its flux to the surface at the time of actual measurement. *Normal pulse polarography* (NPP) was invented to eliminate this effect by forestalling electrolysis prior to the measurement period (6, 35, 41–44). Figure 7.3.5 is an outline of the way in which this goal is achieved with either a DME or an SMDE.

---

[8]In fact, many instruments now generate "linear" scan waveforms as staircase functions with very small ($<$ 0.2 mV) ΔE, because it is simpler to do so with digital control systems. When ΔE is reduced below the level of the noise on the waveform, the distinction between staircase and linear functions is lost.
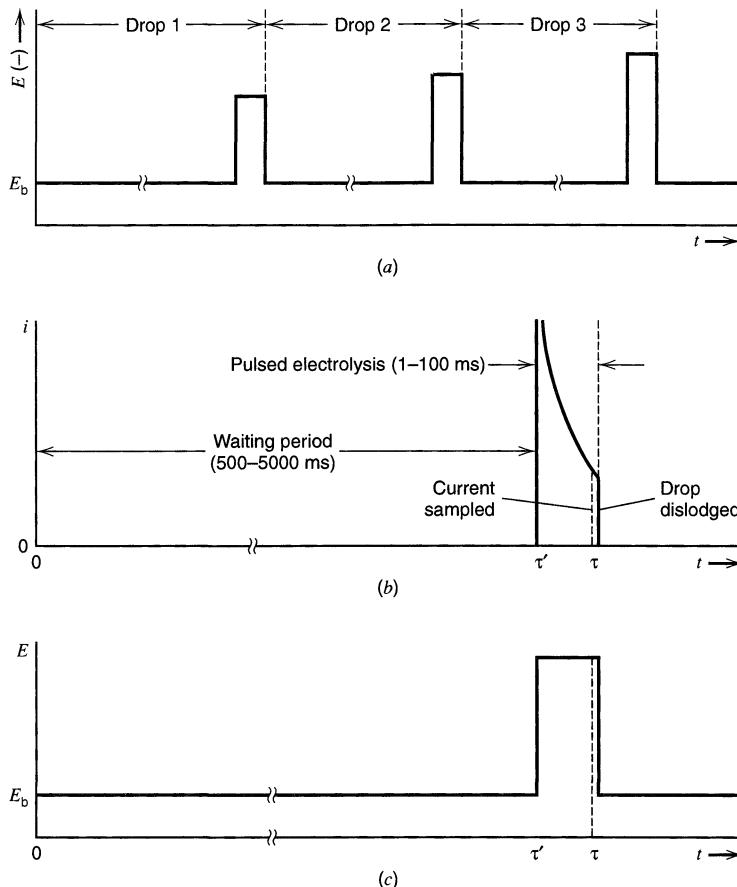
Figure 7.3.5 Sampling scheme for normal pulse polarography. (*a*) Potential program. (*b*) Current and (*c*) potential during a single drop's lifetime.

For most of the life of each mercury drop, the electrode is held at a base potential, E_b, at which negligible electrolysis occurs. After a fixed waiting period, τ', measured from the birth of the drop, the potential is changed abruptly to value E for a period typically about 50 ms in duration. The potential pulse is ended by a return to the base value, E_b. The current is sampled at a time τ near the end of the pulse, and a signal proportional to this sampled value is presented as a constant output to a recording system until the sample taken in the next drop lifetime replaces it. The drop is dislodged just after the pulse ends, then the whole cycle is repeated with successive drops, except that the step potential is made a few mV more extreme with each additional cycle. The output is a plot of sampled current *vs.* step potential E, and it takes the form shown in Figure 7.3.6*a*. A block diagram of the apparatus is shown in Figure 7.3.7.

This experiment, first performed by Barker and Gardner (41), is immediately recognizable as a sampled-current voltammetric measurement exactly on the model described in Sections 5.1, 5.4, and 5.5. *Normal pulse voltammetry* (NPV) is the more general name for the method, which may also be applied at nonpolarographic electrodes, as discussed in Section 7.3.2(d).

Since electrolysis during the waiting time is negligible, the initially uniform concentration distribution in solution is preserved until the pulse is applied. Even though the electrode is approximately spherical, it acts as a planar surface during the short time of
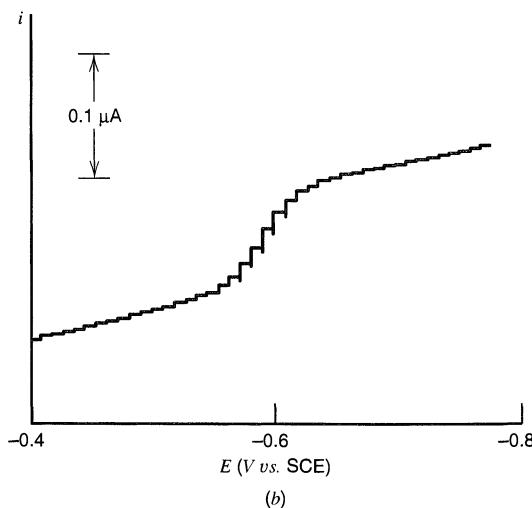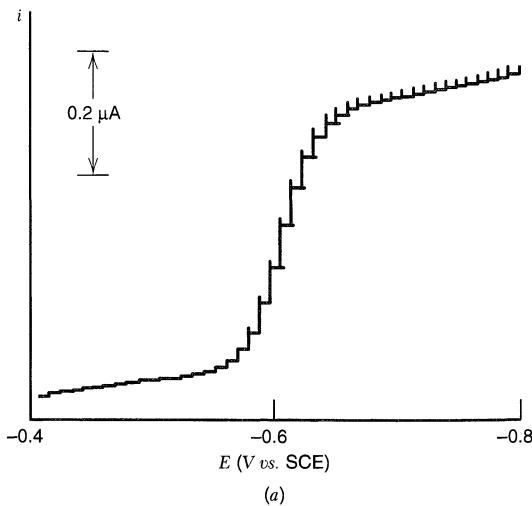
Figure 7.3.6 Polarograms at a DME for 10^{-5} M Cd^{2+} in 0.01 M HCl. (*a*) Normal pulse mode. (*b*) Tast mode.

the actual electrolysis (Section 5.2.2); therefore the sampled faradaic current on the plateau is

$$i_d = \frac{nFAD_O^{1/2}C_O^*}{\pi^{1/2}(\tau - \tau')^{1/2}} \qquad (7.3.3)$$

where $(\tau - \tau')$ is time measured from the pulse rise.

(b) Behavior at a DME

In comparing this current to that measured in a tast experiment at a DME, it is useful to recall (from Section 7.1.2) that (7.3.1) can be rewritten as

$$(i_d)_{\text{tast}} = \frac{nFA(7/3)^{1/2}D_O^{1/2}C_O^*}{\pi^{1/2}\tau^{1/2}} \qquad (7.3.4)$$

thus (42)

$$\frac{(i_d)_{\text{pulse}}}{(i_d)_{\text{tast}}} = \left(\frac{3}{7}\right)^{1/2}\left(\frac{\tau}{\tau - \tau'}\right)^{1/2} \qquad (7.3.5)$$
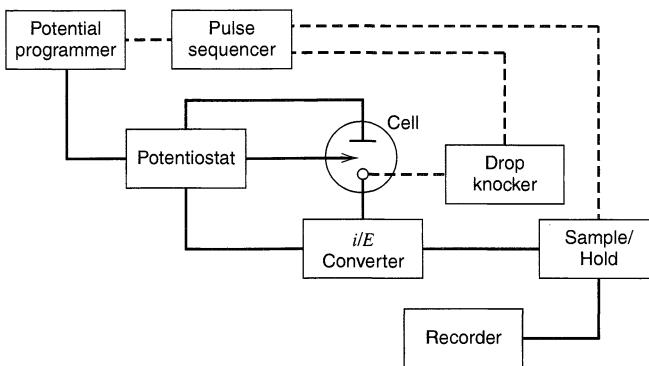
Figure 7.3.7 Schematic experimental arrangement for normal pulse polarography.

for experiments in which the current-sampling times for both methods are equal to τ. For the typical values of $\tau = 4$ s, and $(\tau - \tau') = 50$ ms, this ratio is about 6; thus the expected increase in faradaic current is substantial. Figure 7.3.6 is a comparison of results obtained by normal pulse and tast polarography at a DME for a solution of 10^{-5} M Cd^{2+} in 0.01 M HCl. The larger sampled currents obtained with the pulse method are obvious.

For reasons discussed below, the charging current contributing to the sampled total current comes almost completely from the continuous expansion of the electrode's area at potential E. It therefore is identical to that contributing to tast measurements at the same potential (eq. 7.3.2), provided that τ and m are the same for the two types of measurement. Thus, normal pulse polarography preserves entirely the sensitivity improvements achieved in tast polarography by discrimination against the charging current. In addition, the pulse method gains enhanced sensitivity through increased faradaic currents, by comparison to those observed in tast or conventional polarography. Detection limits are usually between 10^{-6} and 10^{-7} M.

Normal pulse polarography has been used widely as an analytical tool for the measurement of low-level concentrations of heavy metals and organics, particularly in environmental samples (6, 35, 43, 44, 45). Section 7.3.6 deals specifically with its application to practical analysis.

(c) Behavior at an SMDE

One of the important concepts behind the normal pulse method loses its significance with a static mercury drop electrode, because a continuous charging current, characteristic of a DME, does not exist at an SMDE.

In electrochemical measurements, charging current arises when the electrode area, the electrode potential, or the interfacial capacitance varies with time. Normally interfacial structure is either static or changes as quickly as the potential; hence there is rarely an appreciable contribution to charging current from a time dependence in capacitance *per se*. With the waveform shown in Figure 7.3.5, dE/dt is zero except on the edges of the steps; therefore the charging current exists only in response to the potential change at those edges, and it decays away exponentially according to the cell time constant R_uC_d (Section 1.2.4). After five cell time constants, the charging process is more than 99% complete, and charging current is usually negligible. Therefore, if $\tau - \tau'$ is larger than $5R_uC_d$, the sampled charging current will not include an appreciable contribution from dE/dt. In many media, the cell time constant at a DME or an SMDE is a few tens of microseconds to a few milliseconds (Section 5.9.1); hence this condition is easy to fulfill within normal operational conditions for NPP. Consequently, charging current in NPP is

almost always based on changes in the area of the electrode and is proportional to dA/dt. At a DME, dA/dt is never zero, and the charging current contributes to the background current according to (7.3.2); but at an SMDE, dA/dt is always zero except in the few tens of milliseconds required to form the drop.

We now see that when the current is actually sampled at an SMDE, charging current from all sources is normally reduced to insignificance, and the background current comes from other faradaic processes, typically involving the electrode itself, the solvent, the supporting electrolyte, or impurities in solution, such as oxygen.

Because the pulse width is relatively short, the sphericity of the SMDE does not normally manifest itself, and the faradaic current follows the Cottrell decay given as (7.3.3). The sampled signal in NPP at an SMDE is essentially the same as at a DME of the same mature electrode radius.

There are three important operational advantages in performing NPP at an SMDE *vs.* a DME: (a) The complete elimination of the charging current produces generally lower background currents and improved detection limits. (b) The elimination of the charging current also reduces the slope in the background current and consequently allows better definition of wave heights, leading to improved precision. (c) It is much easier to employ short drop times (1 s or smaller) at an SMDE; hence one can record polarograms with a time saving of 75% or more, relative to performance at a DME.

(d) Behavior at Nonpolarographic Electrodes

An essential idea behind the normal pulse voltammetric method is the cyclic renewal of the diffusion layer. With either the DME or SMDE, renewal is achieved by the stirring accompanying the fall of an expended mercury drop and its replacement by a fresh drop. At other electrodes, renewal may not be easily accomplished.

Operationally, NPV is carried out at a nonpolarographic electrode, such as a Pt disk, using the waveform and sampling scheme given in Figure 7.3.5, but without any step corresponding to drop dislodgment. Thus, the electrode and its diffusion layer are taken through cycle after cycle of pulsing and sampling. Progressive depletion of the electroactive species can occur and products can build up, either in the diffusion layer or on the surface of the electrode. These effects generally cause degradation of the NPP response. By three different means, cyclic renewal can be achieved so that well-behaved voltammograms are obtained:

1. *Chemically reversible systems.* If any electrode process carried out during the pulses can be reversed effectively at E_b, renewal will be accomplished by electrolysis when the potential returns to the base potential after each pulse. Because the electrode is normally held at E_b for a long time compared to the pulse duration, the products of the pulse can be essentially fully recollected and returned to the initial state. It is not important that the electrode kinetics be fast enough to be called "reversible," only that the chemistry can be efficiently reversed at the base potential.

2. *Convective renewal.* When normal pulse voltammetry is carried out in a convective system, as at a rotating disk, one can rely on stirring to renew the diffusion layer while the potential is held at E_b. This can be true even if the chemistry cannot be reversed electrolytically, as in the case where the species created in the pulse decays to an inactive product. The convection can also affect the current sampled in each pulse, so that the theoretical expectation based on diffusion theory is exceeded. However the error is often either irrelevant (as in analytical applications where calibration is possible) or fairly small (because a pulse of short

duration creates a diffusion layer that remains largely confined to a relatively stagnant layer of solution).

3. *Diffusive renewal.* Even without convection or electrolytic reversal, it is possible to obtain cyclic renewal of the diffusion layer simply by waiting long enough at the base potential for diffusion to replace the consumed electroreactant (46).

If the diffusion layer can be renewed, the result is essentially as discussed earlier for NPP at the SMDE. Detection limits are typically poorer than at an SMDE because most solid electrodes are afflicted by background currents from slow faradaic processes associated with the electrode surface itself.[9] If the diffusion layer cannot be effectively renewed, the polarographic wave will not show a plateau, but instead will pass through a peak, then droop at more extreme potentials as cumulative depletion of the electroreactant is manifested. The curve resembles a linear sweep voltammogram for essentially the reasons governing responses in LSV (Section 6.1).

(e) Wave Shapes
Since normal pulse polarography was historically viewed as an analytical (rather than diagnostic) tool, the shapes of waves were not a focus of interest and did not receive detailed attention. Nonetheless, the theory for them does exist (Sections 5.4 and 5.5), since NPP is the prototype of the sampled-current voltammetric method. The characteristic time scale of milliseconds is, of course, much shorter than the ~3-s time scale of conventional polarography. It is, therefore, possible for a chemical system to behave reversibly in a conventional polarographic experiment and quasireversibly or irreversibly in the normal pulse mode. Many systems that show sluggish electrode kinetics behave in just this way. Notice also that the reverse behavior can be seen, too. If a system shows fast electrode kinetics, but the product of the electrode reaction decays on a 1-s time scale, then the normal pulse experiment will show reversibility, because little product decay will occur during the measurement; yet the conventional polarogram will show the kinds of distortion that are characteristic of homogeneous reactions following charge transfer (see Chapter 12). At a nonpolarographic electrode, the diagnosis of wave shapes is dependent on effective renewal of the diffusion layer. It is not practical to analyze NPV waves in systems where renewal cannot be achieved.

7.3.3 Reverse Pulse Voltammetry
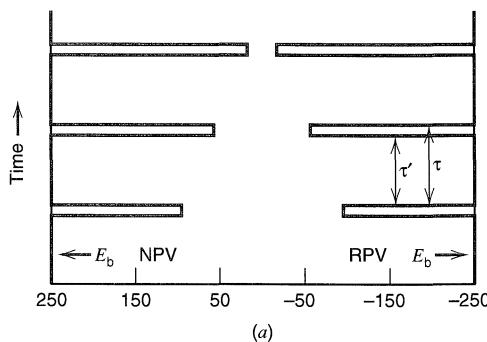
In the normal pulse experiment, the usual practice is to select a base potential E_b in a region where the electroactive species of interest does not react at the electrode. The scan is made by allowing pulses in successive cycles to reach first into the potential range surrounding $E^{0'}$ and eventually into the diffusion-limited region. If we take the usual reversible case of $O + ne \rightleftarrows R$, with O present in the bulk and R absent, then E_b would be set perhaps 200 mV more positive than $E^{0'}$, and the pulses would be made in a negative

---

[9]The surfaces of electrodes often undergo faradaic transformations, such as the formation or reduction of oxides on metals or the electrochemical conversion of oxygen-containing functional groups on the edges of graphite planes. Many of these processes take place slowly and over sizable potential ranges; consequently, they give rise to background currents that can last a long time after the potential or the medium is changed. There can also be a slowly decaying nonfaradaic background if the electrode is subject to potential-dependent adsorption of a species of low concentration in the electrolyte. Background currents of this kind are often said to arise from "surface processes." In general, such currents are much larger at solid electrodes than at mercury, unless the solid electrode is held for a long time (even several minutes or an hour) at a fixed potential in an unchanging medium.

direction (Figure 7.3.8a). In the time before each pulse is applied, negligible faradaic current flows and a uniform concentration profile, extending from the bulk to the surface, prevails.

In *reverse pulse voltammetry* or *reverse pulse polarography* (47), the potential waveform and sampling scheme are identical with those of the normal pulse method (Figure 7.3.5). The differences (Figure 7.3.8a) are (a) that the base potential is placed in the diffusion-limited region for electrolysis of the species present in the bulk, and (b) that the pulses are made "backward" through the region of $E^{0'}$ and then into range where the species present in the bulk is not electroactive. For the specific case mentioned above, the base potential would be placed 200 mV or more on the negative side of $E^{0'}$ and the pulses would be made in a positive direction. During the long period τ', when the potential is at E_b, species O is electrolytically converted at the diffusion-controlled rate; hence its concentration profile is drawn down to zero at the electrode surface, while R is produced at the electrode and a layer of it extends outward. The pulses work on this non-uniform concentration profile, which is dominated by the presence of R, not O, near the electrode. As the pulses reach more positive potentials, they become capable of oxidizing the R produced in the holding period at E_b, and anodic current samples are obtained at τ. When the pulses become more positive than $E^{0'}$ by 200 mV or more, the electrolysis of R proceeds at the diffusion-limited rate and does not change further with step potential, so that an anodic plateau is established (Figure 7.3.8b). This method is clearly a reversal experiment, because the focus is on the detection and behavior of the product from a prior, initiating electrolysis.

The normal pulse experiment involves essentially a zero faradaic current at step potentials near E_b (Figure 7.3.8b), because O does not react at the electrode until the pulses reach the region of $E^{0'}$. The analogous situation is quite different in RPV, where a signifi-

Figure 7.3.8 (a)
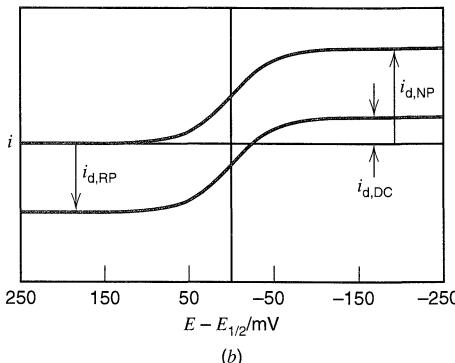
Figure 7.3.8 (b)

Figure 7.3.8 Reverse pulse voltammetry *vs.* normal pulse voltammetry in a simple reversible one-electron system. (a) Waveforms and placement of E_b. The polarographic versions of these methods involve dislodgment and regrowth of the mercury drop electrode at the end of each pulse. (b) Voltammograms of $i(\tau)$ *vs.* pulse potential: NPV (*upper*), RPV (*lower*).

cant cathodic current is sampled near the base potential. This current arises because O is consumed electrolytically at the diffusion-controlled rate at potentials near E_b. Pulses of small amplitude, not reaching into the region of $E^{0'}$, do not change the rate at which O is electrolyzed; hence the same current sample is obtained for all such pulses. The situation is as though a tast experiment were being carried out at the potential of the pulse, with current sampling at time τ. If semi-infinite linear diffusion applies, the cathodic plateau current (at the "base" of the RPV wave), shown as $i_{d,DC}$ in Figure 7.3.8b, is given by the Cottrell equation as

$$i_{d,DC} = \frac{nFAD_O^{1/2}C_O^*}{\pi^{1/2}\tau^{1/2}} \tag{7.3.6}$$

The anodic plateau current $i_{d,RP}$ can be predicted from the results of Section 5.7.2, which dealt with reversal experiments involving a diffusion-controlled forward electrolysis and a diffusion-controlled collection of the product in a reversal step. This is exactly the situation in RPV when the steps reach the main plateau of the wave, and the current flow is described by equation 5.7.15, which can be reexpressed in terms of the time parameters of RPV as

$$-i_{d,RP} = \frac{nFAD_O^{1/2}C_O^*}{\pi^{1/2}}\left[\frac{1}{(\tau - \tau')^{1/2}} - \frac{1}{\tau^{1/2}}\right] \tag{7.3.7}$$

The first term of this equation is recognizable from (7.3.3) as the diffusion-limited current for the NPV experiment, $i_{d,NP}$, while the second term is $i_{d,DC}$ [from (7.3.6)]; thus upon rearrangement

$$\boxed{i_{d,DC} - i_{d,RP} = i_{d,NP}} \tag{7.3.8}$$

The left side of (7.3.8) is the height of the whole reverse pulse voltammogram, which is found now to be the same as the height of the normal pulse voltammogram taken with the same timing characteristics.

These principles are valid regardless of the electrode employed, as long as semi-infinite linear diffusion can be assumed and renewal of the concentration profile can be accomplished in each cycle. For a stationary planar electrode, the relationships worked out above apply directly. For an SMDE, they apply to the extent that $i_{d,DC}$ is the Cottrell current for an electrolysis of duration τ and is not disturbed by the convection associated with the establishment of the drop. For a DME, the picture is complicated by the steady expansion of area, but it turns out (47, 48) that (7.3.8) is still a good approximation if $i_{d,DC}$ is understood as the Ilkovič current for time τ [(7.3.1) or (7.3.4)] and the pulse width is short compared to the preelectrolysis time [i.e., $(\tau - \tau')/\tau' < 0.05$].

For a reversible system, the shape of the RPV wave can be derived from the general double-step response given in (5.7.14). We confine our view to the situation where the forward electrolysis always takes place in the diffusion limited region, so that $\theta' = \exp[nf(E_b - E^{0'})] \approx 0$. Then we have for the current sampled in a reverse pulse to any value of E:

$$-i_{RP} = \frac{nFAD_O^{1/2}C_O^*}{\pi^{1/2}}\left[\left(1 - \frac{1}{1 + \xi\theta''}\right)\left(\frac{1}{(\tau - \tau')^{1/2}}\right) - \frac{1}{\tau^{1/2}}\right] \tag{7.3.9}$$

where $\theta'' = \exp[nf(E - E^{0'})]$. Of the three terms in (7.3.9), the first and the third together are $-i_{d,RP}$, as defined in (7.3.7), and the second is $-i_{d,NP}/(1 + \xi\theta'')$; thus

$$i_{RP} = i_{d,RP} + \frac{i_{d,NP}}{1 + \xi\theta''} \tag{7.3.10}$$

Substitution for $i_{d,NP}$ according to (7.3.8) and rearrangement gives

$$\xi\theta'' = \frac{i_{d,DC} - i_{RP}}{i_{RP} - i_{d,RP}} \qquad (7.3.11)$$

By taking the natural logarithm and defining $E_{1/2} = E^{0'} + (RT/nF) \ln (D_R^{1/2}/D_O^{1/2})$, we obtain

$$\boxed{E = E_{1/2} + \frac{RT}{nF} \ln \left(\frac{i_{d,DC} - i_{RP}}{i_{RP} - i_{d,RP}} \right)} \qquad (7.3.12)$$

which is identical to the shape function for a reversible composite wave worked out in Section 1.4.2(b). We have now established, as one suspects by a glance at Figure 7.3.8*b* that the half-wave potential, the total height, and the wave slope of the RPV wave are all exactly as for the corresponding NPV wave. These results were derived here for a system where simple semi-infinite linear diffusion applies; however Osteryoung and Kirowa-Eisner (47) show that they apply at a DME, too.

The principal use of RPV is to characterize the product of an electrode reaction, especially with respect to stability. It is obvious that if species R decays appreciably during the period of the experiment, particularly on the time scale of the pulse, it cannot be fully available to be reoxidized during the pulse. Consequently, the anodic plateau current must be smaller in magnitude than expected from (7.3.7). If the decay is very fast, R will be completely unavailable and the anodic plateau current will be zero. The ratio of plateau heights in RPV and NPV quantifies the stability, and with proper theory, one can obtain the rate constant for the following chemistry. Chapter 12 covers this kind of issue for many different mechanisms and methods.

As in the application just discussed, the focus in RPV is often on the magnitude of the wave heights, rather than wave shapes and positions. One can think of RPV as a way to present double potential step chronoamperometric data conveniently on a potential axis, because the features of interest are rooted in chronoamperometric theory, as we have already seen for the derivations done in this section. Thus one can make direct and confident use of the extensive published results for double-step chronoamperometry to treat data from RPV in various chemical situations.

7.3.4 Differential Pulse Voltammetry

(a) General Polarographic Context
Sensitivities even better than those of normal pulse voltammetry can be obtained with the small-amplitude pulse scheme shown in Figures 7.3.9 and 7.3.10, which show the basis for *differential pulse voltammetry* (DPV) (6, 35, 41–45). The figures focus on the
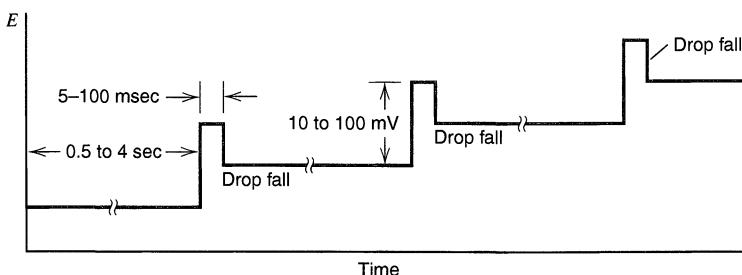
Figure 7.3.9 Potential program for several drops in a differential pulse polarographic experiment. The 10–100 mV potential change late in the drop lifetime is the pulse height, ΔE.
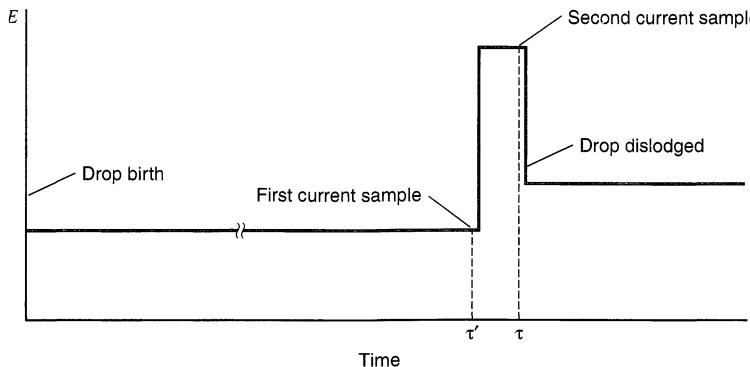
Figure 7.3.10
Events for a single drop
of a differential pulse
polarographic experiment.

special case of *differential pulse polarography* (DPP), but the waveform and measurement strategy are general for the method in its broader sense. DPP resembles normal pulse polarography, but several major differences are evident: (a) The base potential applied during most of a drop's lifetime is not constant from drop to drop, but instead is changed steadily in small increments. (b) The pulse height is only 10 to 100 mV and is maintained at a constant level with respect to the base potential. (c) Two current samples are taken during each drop's lifetime. One is at time τ', immediately before the pulse, and the second is at time τ, late in the pulse and just before the drop is dislodged. (d) The record of the experiment is a plot of the current difference, $\delta i = i(\tau) - i(\tau')$, versus the base potential. Obviously the name of the method is derived from its reliance on this differential current measurement. The pulse width ($\sim$50 ms) and the waiting period for drop growth (0.5 to 4 s) are both similar to the analogous periods in the normal pulse method.

Figure 7.3.11 is a block diagram of the experimental system and Figure 7.3.12*a* is an actual polarogram for 10^{-6} M Cd^{2+} in 0.01 M HCl. For comparison, the normal pulse response from the same system is given in Figure 7.3.12*b*.

Note that the differential measurement gives a peaked output, rather than the wavelike response to which we have grown accustomed. The underlying reason is easily understood qualitatively. Early in the experiment, when the base potential is much more positive than $E^{0'}$ for Cd^{2+}, no faradaic current flows during the time before the pulse,
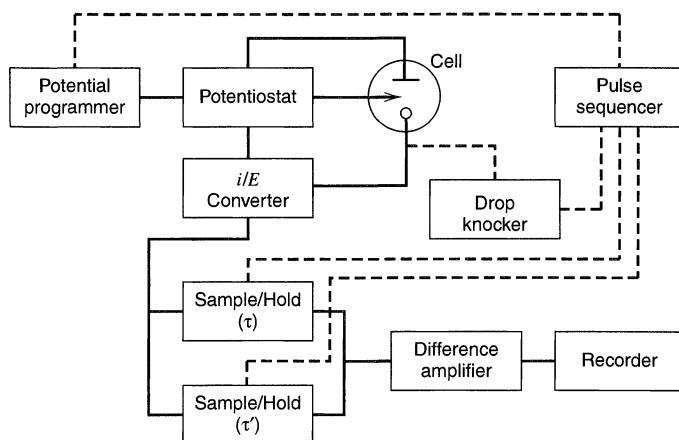
Figure 7.3.11 Schematic experimental arrangement for differential pulse polarography. For clarity, this diagram shows the functions as they would be organized in separate electronic stages in a free-standing DPP unit. In contemporary instruments, a computer performs many of the roles delineated here, including sequencing, recording of data, calculation of difference signals, and display of results.

(a)

(b)
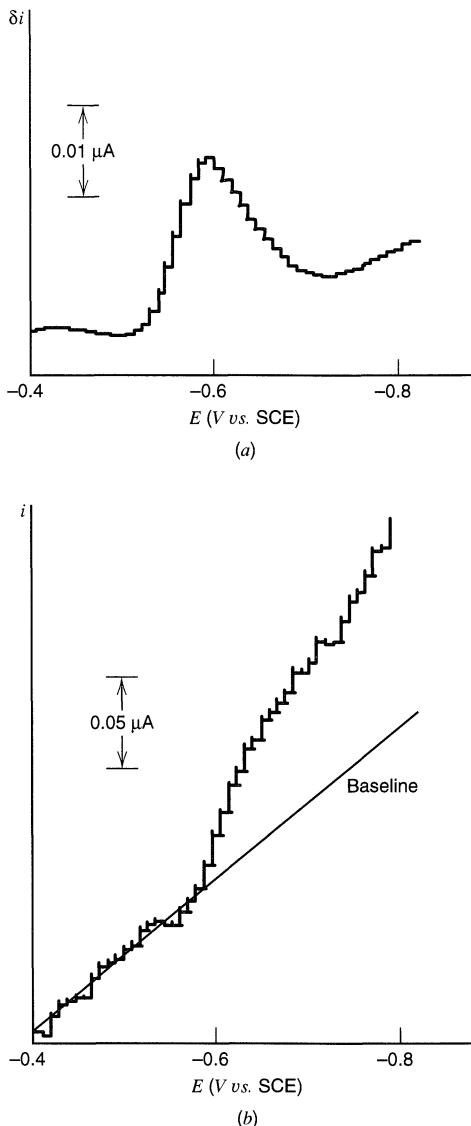
Figure 7.3.12 Polarograms at a DME for $10^{-6}\,M\,\text{Cd}^{2+}$ in 0.01 M HCl. (a) Differential pulse mode, $\Delta E = -50$ mV. (b) Normal pulse mode.

and the change in potential manifested in the pulse is too small to stimulate the faradaic process. Thus $i(\tau) - i(\tau')$ is virtually zero, at least for the faradaic component. Late in the experiment, when the base potential is in the diffusion-limited-current region, Cd^{2+} is reduced during the waiting period at the maximum possible rate. The pulse cannot increase the rate further; hence the difference $i(\tau) - i(\tau')$ is again small. Only in the region of $E^{0'}$ (for this reversible system) is an appreciable faradaic difference current observed. There the base potential is such that Cd^{2+} is reduced during the waiting period at some rate less than the maximum, since the surface concentration $C_O(0, t)$ is not zero. Application of the pulse drives $C_O(0, t)$ to a lower value; hence the flux of O to the surface and the faradaic current are both enhanced. Only in potential regions where a small potential difference can make a sizable difference in current flow does the differential pulse technique show a response.

The shape of the response function and the height of the peak can be treated quantitatively in a straightforward manner. Note that the events during each drop's lifetime actually comprise a double-step experiment. From the birth of the drop at $t = 0$ until the application of the pulse at $t = \tau'$, the base potential E is enforced. At later times, the potential is $E + \Delta E$, where ΔE is the pulse height. Each drop is born into a solution of the bulk composition, but generally electrolysis occurs during the period before τ' and the pulse operates on the concentration profiles that prior electrolysis creates. This situation is analogous to that considered in Section 5.7, and it can be treated by the techniques developed there. Even so, we will not take that approach, because the essential simplicity of the problem is obscured.

Instead, we begin by noting that the preelectrolysis period τ' is typically 20–100 times longer than the pulse duration $\tau - \tau'$. Thus the preelectrolysis establishes a thick diffusion layer, and the pulse is able to modify only a small part of it. In fact, the experiment can be approximated by assuming that the pulse cannot distinguish the actual finite concentration profiles appearing at its start from those of a semi-infinite homogeneous solution with bulk concentrations equal to the values of $C_O(0, t)$ and $C_R(0, t)$ enforced by potential E. The role of the preelectrolysis is therefore to set up "apparent bulk concentrations" that vary during successive drops from pure O to pure R (or vice versa), as the scan is made. For a given drop, we take the differential faradaic current as the current that would flow at time $\tau - \tau'$ after a potential step from E to $E + \Delta E$.

Now let us restrict our consideration to a nernstian system in which R is initially absent. The results from Section 5.4.1 show that the surface concentrations during preelectrolysis at potential E are

$$C_O(0, t) = C_O^*\left(\frac{\xi\theta}{1 + \xi\theta}\right) \qquad C_R(0, t) = C_O^*\left(\frac{\xi}{1 + \xi\theta}\right) \tag{7.3.13}$$

where $\theta = \exp[nf(E - E^{0'})]$. We regard these values as the apparent bulk concentrations $(C_O^*)_{app}$ and $(C_R^*)_{app}$ for the pulse. Since the system is nernstian, they are in equilibrium with potential E. The problem is now simply to find the faradaic current flow after a step from equilibrium to $E + \Delta E$ in a homogeneous medium of bulk concentrations $(C_O^*)_{app}$ and $(C_R^*)_{app}$.

Through the approach of Section 5.4.1 (see also Problem 5.10), that current is straightforwardly found to be

$$i = \frac{nFAD_O^{1/2}}{\pi^{1/2}t^{1/2}} \cdot \frac{[(C_O^*)_{app} - \theta'(C_R^*)_{app}]}{(1 + \xi\theta')} \tag{7.3.14}$$

where $\theta' = \exp[nf(E + \Delta E - E^{0'})]$. Substitution according to (7.3.13) gives

$$i = \frac{nFAD_O^{1/2}C_O^*}{\pi^{1/2}t^{1/2}} \cdot \frac{(\xi\theta - \xi\theta')}{(1 + \xi\theta)(1 + \xi\theta')} \tag{7.3.15}$$

It is convenient (42) to introduce the parameters P_A and σ, where

$$P_A = \xi \exp\left[\frac{nF}{RT}\left(E + \frac{\Delta E}{2} - E^{0'}\right)\right] \tag{7.3.16}$$

and

$$\sigma = \exp\left(\frac{nF}{RT}\frac{\Delta E}{2}\right) \tag{7.3.17}$$

In this notation, $\xi\theta = P_A/\sigma$ and $\xi\theta' = P_A\sigma$; thus

$$i = \frac{nFAD_O^{1/2}C_O^*}{\pi^{1/2}t^{1/2}}\left[\frac{P_A(1 - \sigma^2)}{(\sigma + P_A)(1 + P_A\sigma)}\right] \tag{7.3.18}$$

and we take the differential faradaic current $\delta i = i(\tau) - i(\tau')$ as

$$\delta i = \frac{nFAD_O^{1/2}C_O^*}{\pi^{1/2}(\tau - \tau')^{1/2}}\left[\frac{P_A(1 - \sigma^2)}{(\sigma + P_A)(1 + P_A\sigma)}\right] \tag{7.3.19}$$

The bracketed factor describes δi as a function of potential. When E is far more positive than $E^{0'}$, P_A is large and δi is virtually zero. When E is much more negative then $E^{0'}$, P_A approaches zero, and so does δi. Through the derivative $d(\delta i)/dP_A$ one can easily show (42) that δi is maximized at $P_A = 1$, which implies that

$$E_{max} = E^{0'} + \frac{RT}{nF}\ln\left(\frac{D_R}{D_O}\right)^{1/2} - \frac{\Delta E}{2} = E_{1/2} - \frac{\Delta E}{2} \tag{7.3.20}$$

Since ΔE is small, the potential of maximum current lies close to $E_{1/2}$. Also, given that ΔE is negative in this experiment, we see that the peak anticipates $E_{1/2}$ by $\Delta E/2$.

The height of the peak is

$$(\delta i)_{max} = \frac{nFAD_O^{1/2}C_O^*}{\pi^{1/2}(\tau - \tau')^{1/2}}\cdot\left(\frac{1 - \sigma}{1 + \sigma}\right) \tag{7.3.21}$$

where the quotient $(1 - \sigma)/(1 + \sigma)$ decreases monotonically with diminishing $|\Delta E|$ and reaches zero for $\Delta E = 0$. When ΔE is negative δi is positive (or cathodic), and vice versa. The quotient's maximum magnitude, which applies at large pulse amplitudes, is unity. In that limit, $(\delta i)_{max}$ is equal to the faradaic current sampled on top of the normal pulse voltammetric wave obtained under the same timing conditions. As (7.3.3) notes, that current is $nFAD_O^{1/2}C_O^*/\pi^{1/2}(\tau - \tau')^{1/2}$. Under usual conditions, ΔE is not large enough to realize this greatest possible $(\delta i)_{max}$. Table 7.3.1 shows the influence of $|\Delta E|$ on $(1 - \sigma)/(1 + \sigma)$, which is also the ratio of the peak height to the limiting value. For analysis, a typical ΔE is 50 mV, which gives a peak current from 45% to 90% of the limiting value, depending on n.

The width of the peak at half height, $W_{1/2}$, increases as the pulse height grows larger, because differential behavior can be seen over a greater range of base potential. Normally

TABLE 7.3.1 Effect of Pulse Amplitude on Peak Height[a]

ΔE, mV	$(1 - \sigma)/(1 + \sigma)$		
	$n = 1$	$n = 2$	$n = 3$
-10	0.0971	0.193	0.285
-50	0.453	0.750	0.899
-100	0.750	0.960	0.995
-150	0.899	0.995	—
-200	0.960	—	—

[a]From E. P. Parry and R. A. Osteryoung, *Anal. Chem.*, **37**, 1634 (1965).

one refrains from increasing $|\Delta E|$ much past 100 mV, because resolution is degraded unacceptably. The precise form of $W_{1/2}$ as a function of ΔE is complicated and is of no real use. However, it is of interest to note the limiting width as ΔE approaches zero. By simple algebra that turns out to be (42)

$$W_{1/2} = 3.52RT/nF \qquad (7.3.22)$$

At 25°C, the limiting widths for $n = 1, 2$, and 3 are 90.4, 45.2, and 30.1 mV, respectively. Real peaks are wider, especially if the pulse height is comparable to or larger than the limiting width.

Since the faradaic current measured in differential pulse polarography is never larger than the faradaic wave height found in the corresponding normal pulse experiment, the sensitivity gain in the differential method obviously does not come from enhanced faradaic response. Instead, the improvement comes from a reduced contribution from background currents. If the background current from interfacial capacitance or from competing faradaic processes does not change much from the first current sample to the second, then the subtractive process producing δi tends to cancel the background contribution.

(b) Behavior at a DME

Because dA/dt is never zero at the DME, capacitive currents contribute to the background and require consideration. We assume that the current samples $i(\tau)$ and $i(\tau')$ are taken at constant potential, so that the charging current arises entirely from dA/dt. From (7.1.17), we express these contributions as

$$i_c(\tau) = 0.00567C_i(E_z - E - \Delta E)m^{2/3}\tau^{-1/3} \qquad (7.3.23)$$
$$i_c(\tau') = 0.00567C_i(E_z - E)m^{2/3}\tau'^{-1/3} \qquad (7.3.24)$$

thus the contribution to the differential current is

$$\delta i_c = i_c(\tau) - i_c(\tau') = 0.00567C_i m^{2/3}\tau^{-1/3}\left[(E_z - E - \Delta E) - \left(\frac{\tau}{\tau'}\right)^{1/3}(E_z - E)\right] \quad (7.3.25)$$

where C_i has been taken as constant over the range from E to $E + \Delta E$. For the usual operating conditions, $(\tau/\tau')^{1/3}$ is very close to unity; hence the bracketed factor is approximately $-\Delta E$:

$$\boxed{\delta i_c \approx -0.00567C_i\Delta E m^{2/3}\tau^{-1/3}} \quad . \qquad (7.3.26)$$

For a negative scan δi is positive, and vice versa. A comparison between (7.3.2) and (7.3.26) shows that the capacitive contribution to differential pulse measurements differs from that in tast and normal pulse polarography by the factor $\Delta E/(E_z - E)$. Over most regions of polarographic operation ΔE is smaller than $E_z - E$ by an order of magnitude or more. Note also that the capacitive background in differential pulse polarography is flat, insofar as C_i is constant over a potential range. In contrast, normal pulse and tast measurements feature a sloping background because of the dependence on $(E_z - E)$. This difference is apparent in Figure 7.3.12, and the greater ease in evaluating the differential faradaic response is obvious.

Background currents also arise at a DME from electrolysis of impurities in solution (frequently from O_2, even in deaerated solutions) or from slow faradaic reactions of major system components (such as H^+). It is often true that the rates of these processes do not change greatly as the potential shifts from E to $E + \Delta E$ and with the elapse of time from τ' to τ within a given measurement cycle; thus the subtraction of current samples does

help to suppress the faradaic background, but normally does not eliminate it altogether, as we will see in Section 7.3.6. In practical analysis by DPP at the DME, the faradaic background is often the dominant factor limiting sensitivity.

The improvements manifested in the differential method yield sensitivities that are often an order of magnitude better than those of normal pulse polarography. Detection limits as low as 10^{-8} M can be achieved, but doing so requires close attention to selection of the medium. See Section 7.3.6 for more details.

(c) Behavior at an SMDE

Under normal experimental conditions for DPP at an SMDE, there is no appreciable charging current contribution, because dE/dt and dA/dt are both essentially zero at the moment of sampling. The faradaic current from the process of interest is the same as at a DME of equal mature drop size and is given by (7.3.19). Faradaic contributions to the background are normally also the same at an SMDE *vs.* a DME of equal drop size, because these faradaic processes are usually not affected by the history of the drop's evolution. Since the SMDE preserves the DME's sensitivity to the sample while eliminating one component of background, there is a sensitivity advantage at the SMDE in any situation where the charging current background at the DME is appreciable. Otherwise the SMDE and DME will provide comparable performance with respect to sensitivity.

An important additional advantage of the SMDE lies in the rapid formation and stabilization of the drop, which allow the use of preelectrolysis times as short as 500 ms. This time controls the duration of the scan; and the use of a short preelectrolysis period can save much time in practical analysis, often 80% of the scan time required for DPP at a DME.

(d) Behavior at Nonpolarographic Electrodes

DPV can be carried out quite successfully at a stationary electrode, such as a Pt disk or an HMDE, even though such systems do not allow physical renewal of the solution near the electrode with each measurement cycle. As we have seen above, the DPV method is based on the concept of using the preelectrolysis at potential E to establish "apparent" bulk concentrations, which are then interrogated with the pulse. If the system is kinetically reversible, the preelectrolysis can establish those conditions as well as at a renewed electrode, despite the fact that the effects of prior cycles are not erased from the diffusion layer. In fact, because the changes in potential from cycle to cycle are small, the cumulative effect of successive cycles is gradually to thicken the diffusion layer in a manner that supports the assumptions used in the treatment of wave shape and peak height given in Section 7.3.4(a).

At solid electrodes of all kinds, the background is rarely dominated by charging current, but rather by faradaic processes involving the electrode material, solvent, or supporting electrolyte. DPV allows for moderation of background contributions by taking the difference between current samples. Even so, the residual background is typically higher than at mercury, and one cannot usually achieve the sensitivity that can be obtained in DPP.

On the other hand, one has the freedom to use shorter preelectrolysis times and pulse widths at stationary electrodes *vs.* the DME or SMDE, because one does not have to wait for drop formation. This feature is used to advantage in the practice of square wave voltammetry, which is covered in Section 7.3.5.

(e) Peak Shapes

In the course of deriving the peak height for DPP in Section 7.3.4(a), we also derived the shape of the peak for a reversible system in the limit of small ΔE, and we discussed the

effects of larger ΔE. The results and conclusions of that section are valid for a reversible reaction at any type of electrode at which semi-infinite linear diffusion applies.

We will not treat the application of differential measurements to irreversible systems. Instead we will note only that, as $|\Delta E|$ tends toward zero, the response in any differential scan approaches the derivative of the normal pulse voltammogram. This fact is easily demonstrated for the reversible system (see Problem 7.7). If a system shows irreversibility because of slow heterogeneous kinetics, one can still expect to see a differential response, but the peak will be shifted from $E^{0'}$ toward more extreme potentials by an activation overpotential (i.e., toward the negative for a cathodic process and toward the positive for an anodic one). Also, the peak width will be larger than for a reversible system, because the rising portion of an irreversible wave extends over a larger potential range. Since the maximum slope on the rising portion is smaller than in the corresponding reversible case, $(\delta i)_{max}$ will be smaller than the value predicted by (7.3.21). If the irreversibility is caused by following chemistry, the peak will also be broad and low, but will be less extreme than $E^{0'}$ for reasons discussed in Chapter 12.

The range of time scales for the differential pulse experiment is the same as for normal pulse voltammetry, hence a given system ordinarily shows the same degree of reversibility toward either approach. However, the degree of reversibility toward pulse methods may differ from that shown toward conventional polarography for reasons discussed in Section 7.3.2.

7.3.5 Square Wave Voltammetry

Exceptional versatility is found in a method called *square wave voltammetry* (SWV), which was invented by Ramaley and Krause (49), but has been developed extensively in recent years by the Osteryoungs and their coworkers (35, 45, 50). One can view it as combining the best aspects of several pulse voltammetric methods, including the background suppression and sensitivity of differential pulse voltammetry, the diagnostic value of normal pulse voltammetry, and the ability to interrogate products directly in much the manner of reverse pulse voltammetry. It also offers access to a wider range of time scales than can be achieved by any of the pulse polarographic techniques. An extensive review by Osteryoung and O'Dea (50) provides many details beyond the introduction given here.

(a) Experimental Concept and Practice
Square wave voltammetry is normally carried out at a stationary electrode; such as an HMDE, and involves the waveform and measurement scheme shown in Figure 7.3.13. As in other forms of pulse voltammetry, the electrode is taken through a series of measurement cycles; however there is no renewal of the diffusion layer between cycles. In contrast to NPV, RPV, and DPV, square wave voltammetry has no true polarographic mode.[10] The waveform can be viewed as a special case of that used for DPV (Figure 7.3.9), in which the preelectrolysis period and the pulse are of equal duration, and the pulse is opposite from the scan direction. However, the interpretation of results is facilitated by considering the waveform as consisting of a staircase scan, each tread of which is superimposed by a symmetrical double pulse, one in the forward direction and one in the

---

[10]Sometimes the term *square wave polarography* is applied to the application of SWV at a slowly growing mercury drop issuing from a DME; however this practice is distant from the conventional meaning of polarography, which is built upon the dropping action and periodic renewal of the electrode during the experiment.
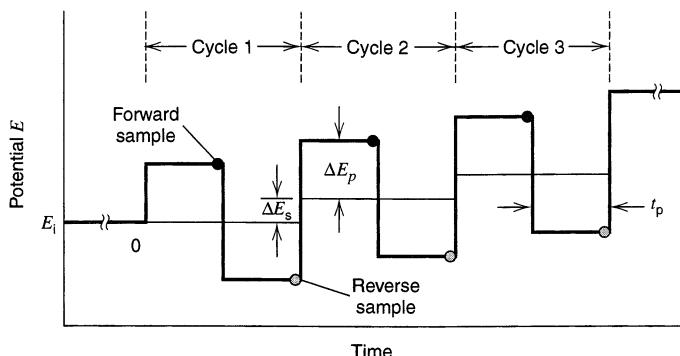
Figure 7.3.13 Waveform and measurement scheme for square wave voltammetry. Shown in bold is the actual potential waveform applied to the working electrode. The light intervening lines indicate the underlying staircase onto which the square wave can be regarded as having been superimposed. In each cycle, a forward current sample is taken at the time indicated by the solid dot, and a reverse current sample is taken at the time marked by the shaded dot.

reverse. Over many cycles, the waveform is a bipolar square wave superimposed on the staircase, and this view gives rise to the name of the method.[11]

Figure 7.3.13 helps to define the principal parameters. The square wave is characterized by a pulse height, ΔE_p, measured with respect to the corresponding tread of the staircase, and a pulse width t_p. Alternatively, the pulse width can be expressed in terms of the square wave frequency, $f = 1/2t_p$. The staircase shifts by ΔE_s at the beginning of each cycle; thus the scan rate $v = \Delta E_s/2t_p = f\Delta E_s$. The scan begins at an initial potential, E_i, which can be applied for an arbitrary time to initialize the system as desired.

Current samples are taken twice per cycle, at the end of each pulse. The *forward current sample*, i_f, arises from the first pulse per cycle, which is in the direction of the staircase scan. The *reverse current sample*, i_r, is taken at the end of the second pulse, which is in the opposite direction. A *difference current* Δi is calculated as $i_f - i_r$. There is diagnostic value in the forward and reverse currents; hence they are preserved separately. Consequently, the result of a single SWV run is three voltammograms showing forward, reverse, and difference currents *vs.* the potential on the corresponding staircase tread.

Square wave voltammetry is always performed using a computer-controlled potentiostatic system with functional elements organized essentially as in Figure 7.3.11. The computer provides for operator interaction, synthesizes the waveform, sequences the sampling and logging of data, computes difference currents, and handles reporting of results, either graphically or otherwise. In many systems, the computer also controls the electrode, especially if an SMDE is involved.

---

[11]Many years ago, Barker (51, 52) invented a method that he called "square wave polarography," in which a quite different experimental strategy is used. A small-amplitude, high-frequency square wave is superimposed on the slowly changing ramp or staircase used in polarography, and a current sampling scheme is employed to detect the averaged response to many cycles of the square wave for each drop at the DME. This method is based on the idea of achieving a "steady-state" in the form of a repeated current cycle as a response to additional potential cycles, and it has an interpretation similar to ac polarography (Chapter 10). It has been generalized to electrodes other than the DME and is also encountered as "square wave voltammetry." To avoid confusion, it is sometimes called *steady-state square wave voltammetry* or *Barker square wave voltammetry* (BSWV), while the method of interest here is called *transient square wave voltammetry* or *Osteryoung square wave voltammetry* (OSWV). OSWV is far more powerful and widely used. The term "transient" refers to the fact that a steady state is not reached in OSWV because the square wave is applied about a changing central value at a stationary electrode.

In general, t_p defines the experimental time scale; ΔE_s fixes the spacing of data points along the potential axis, and these parameters together determine the time required for a full scan. In normal practice, ΔE_s is significantly less than ΔE_p, which defines the span of interrogation in each cycle and therefore determines the resolution of voltammetric features along the potential axis. Only t_p is varied over a wide range, typically 1–500 ms (f = 1–500 Hz). Osteryoung and O'Dea (50) suggest that ΔE_s = 10/n mV and ΔE_p = 50/n mV suffice generally. With ΔE_s = 10 mV and t_p = 1–500 ms, the scan proceeds at 5 V/s to 10 mV/s; thus the recording of a full voltammogram is quick compared to the performance of most pulse methods and is comparable in duration to typical cyclic voltammetric runs (Chapter 6).

(b) Theoretical Prediction of Response

Since the diffusion layer is not renewed at the beginning of each measurement cycle, it is not possible to treat each cycle in isolation, and theoretical treatments of SWV are intrinsically much more complex than for other forms of pulse voltammetry. The initial condition for each cycle is the complex diffusion layer that has evolved from all prior pulses, and it is a function, not only of the details of the waveform, but also of the kinetics and mechanisms of the chemistry linked to the electrode process. The considerations are similar to those that we encountered in Section 5.7 as we treated double-step responses, and the mathematical device of superposition can be applied to the extended step waveforms of SWV in the simpler cases.

Let us now consider the prototypical case in which the electrode reaction $O + ne \rightleftarrows R$ exhibits reversible kinetics and the solution contains O, but not R, in the bulk. The solution has been homogenized and the initial potential E_i is chosen well positive of $E^{0'}$, so that the concentration profiles are uniform as the SWV scan begins. The experiment is fast enough to confine behavior to semi-infinite linear diffusion at most electrodes, and we assume its applicability here. These circumstances imply that we can invoke Fick's second law for both O and R, the usual initial and semi-infinite conditions, and the flux balance at the electrode surface, exactly as in (5.4.2)–(5.4.5). The final boundary condition needed to solve the problem comes from the potential waveform, which is linked to the concentration profile through the nernstian balance at the electrode. It is convenient to consider the waveform as consisting of a series of half cycles with index m beginning from the first forward pulse, which has $m = 1$. Then,

$$E_m = E_i - \left[\mathrm{Int}\left(\frac{m+1}{2}\right) - 1 \right] \Delta E_s + (-1)^m \, \Delta E_p \qquad \text{(for } m \geq 1) \qquad (7.3.27)$$

where Int[$(m+1)/2$] denotes truncation of the ratio to the highest integer. The nernstian balance at the surface can be expressed [as in (5.4.6)] for each half cycle in the following way:

$$\theta_m = \frac{C_O(0,t)}{C_R(0,t)} = \exp[nf\,(E_m - E^{0'})] \qquad (7.3.28)$$

The solution can be obtained analytically (49, 50, 53) and the sampled current for the mth half cycle turns out to be

$$i_m = \frac{nFAD_O^{1/2}C_O^*}{\pi^{1/2}t_p^{1/2}} \sum_{i=1}^{m} \frac{Q_{i-1} - Q_i}{(m-i+1)^{1/2}} \qquad (7.3.29)$$

where

$$Q_i = \frac{\xi\theta_i}{1 + \xi\theta_i} \quad (i > 0) \qquad Q_0 = 0 \qquad (7.3.30)$$

and $\xi = (D_O/D_R)^{1/2}$. The sum in (7.3.29), which runs over all half cycles preceding and including the one of interest, manifests the prior history of electrolysis. Odd values of m correspond to forward current samples and even values denote reverse current samples.

In much of the theory of SWV, currents are represented dimensionlessly by normalizing with the factor preceding the sum in (7.3.29). This factor is obviously the Cottrell current for time t_p, which is the plateau current sampled in an NPV experiment with pulse width t_p [see (7.3.3)]. Designating this current as i_d, we can define the dimensionless current sample, ψ_m, for the mth cycle as

$$\psi_m = \frac{i_m}{i_d} = \sum_{i=1}^{m} \frac{Q_{i-1} - Q_i}{(m - i + 1)^{1/2}} \qquad (7.3.31)$$

The dimensionless difference current, $\Delta\psi_m$, is given by subtraction of pairs of samples, with the odd m taken first:

$$\Delta\psi_m = \frac{\Delta i_m}{i_d} = \psi_m - \psi_{m+1} \qquad (7.3.32)$$

where m covers only odd values.

Figure 7.3.14 shows dimensionless current transients and current samples for the experiment that we have been discussing. The currents are small in the early cycles, because the staircase potential is too far positive of $E^{0'}$ for the forward pulse to reach the region where electrolysis can occur. In the middle of the figure, the staircase has moved into the region of $E^{0'}$, so that the rate of electrolysis is a strong function of potential. The forward pulse significantly amplifies the rate of reduction of O, and the reverse pulse actually reverses that reduction, so that an anodic current flows. The right side of the figure corresponds to cycles in which the staircase potential has become considerably negative of $E^{0'}$, and electrolysis begins to occur at the diffusion-controlled rate regardless of potential. Then neither the forward pulse nor the reverse affects the current much, and the samples become similar. The sampled current in the forward pulses is smaller than in the middle of
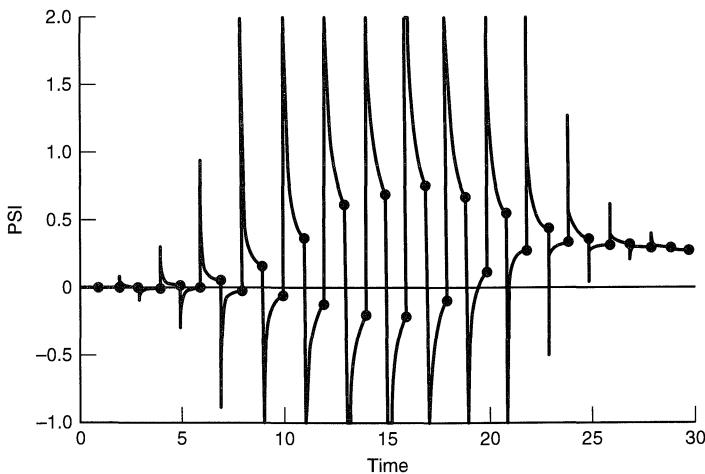
Figure 7.3.14 Dimensionless current response throughout an SWV experiment for the reversible O/R system with R absent from the bulk and with the scan beginning well positive of $E^{0'}$. Cathodic currents are upward. The time axis corresponds to the half-cycle index m, and the staircase potential reaches $E^{0'}$ near $m = 15$. Sampled currents are shown as points. $n\Delta E_p = 50$ mV and $n\Delta E_s = 30$ mV. [Reprinted from J. Osteryoung and J. J. O'Dea, *Electroanal. Chem.*, **14**, 209 (1986), by courtesy of Marcel Dekker, Inc.]
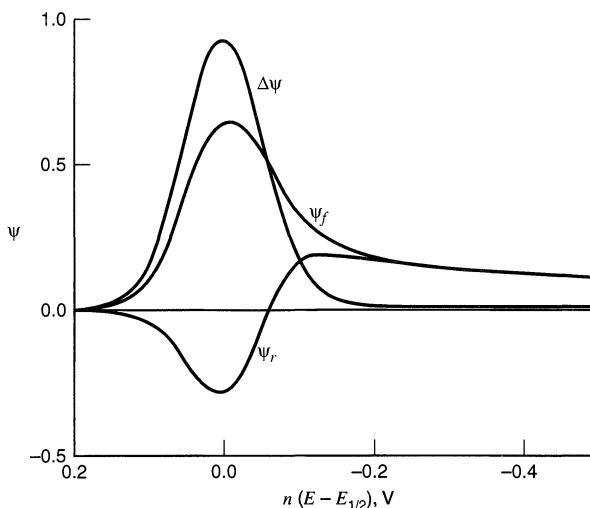
Figure 7.3.15 Dimensionless square wave voltammograms for the reversible O/R case with R absent from the bulk. $n\Delta E_p = 50$ mV and $n\Delta E_s = 10$ mV. Forward currents (ψ_f), reverse currents (ψ_r), and difference currents ($\Delta\psi$) vs. a potential axis referred to the "reversible" $E_{1/2} = E^{0'} + (RT/nF) \ln(D_R/D_O)^{1/2}$. Note that $n(E_m - E_{1/2}) = (RT/F) \ln \xi\theta_m$. [Reprinted from J. Osteryoung and J. J. O'Dea, *Electroanal. Chem.*, **14**, 209 (1986), by courtesy of Marcel Dekker, Inc.]

the diagram because the cumulative effect of electrolysis through many cycles is to deplete the diffusion layer and to slow the rate at which O arrives. The continued falloff of sampled current at the right extreme of the figure is caused by this effect. It is clear that the difference current reaches a peak near $E^{0'}$ and is small on either side.

Figure 7.3.15 contains a dimensionless representation of the voltammograms that would be derived from an experiment like that just described. The forward and reverse currents resemble a cyclic voltammogram and have much of the same diagnostic value, while the difference current resembles the response from DPV and has similar sensitivity.

The difference current voltammogram reaches a peak at $E_{1/2} = E^{0'} + (RT/nF) \ln(D_R/D_O)^{1/2}$ and has a dimensionless peak current, $\Delta\psi_p$, that depends on n, ΔE_p, and ΔE_s as presented in Table 7.3.2. The actual peak current, Δi_p, is therefore

$$\Delta i_p = \frac{nFAD_O^{1/2}C_O^*}{\pi^{1/2}t_p^{1/2}} \Delta\psi_p \qquad (7.3.33)$$

Since the Cottrell factor is the plateau current in an NPV experiment having the same pulse width, $\Delta\psi_p$ gauges the peak height in SWV relative to the limiting response in NPV, just as the ratio $(1 - \sigma)/(1 + \sigma)$ does for DPV [see (7.3.21)]. For the normal operating conditions of $\Delta E_p = 50/n$ mV and $\Delta E_s = 10/n$ mV, the SWV peak is 93% of the corresponding NPV plateau height. For DPV, the comparable figure is only about 45%

TABLE 7.3.2   Dimensionless Peak Current (ψ_p) vs. SWV Operating Parameters[a]

	$n\Delta E_s$/mV			
$n\Delta E_p$/mV	1	5	10	20
0[b]	0.0053	0.0238	0.0437	0.0774
10	0.2376	0.2549	0.2726	0.2998
20	0.4531	0.4686	0.4845	0.5077
50	0.9098	0.9186	0.9281	0.9432
100	1.1619	1.1643	1.1675	1.1745

[a]Data from reference 50.

[b]$\Delta E_p = 0$ corresponds to staircase voltammetry.

(Table 7.3.1), so the SWV method is slightly more sensitive than DPV. This is true because the reverse pulses near $E^{0'}$ produce an anodic current, which enlarges Δi.

More complicated systems, involving slow heterogeneous kinetics, coupled homogeneous reactions or equilibria (e.g., as in Chapter 12), or more complex forms of mass transfer (e.g., at a UME, Section 5.3), are most easily treated by digital simulation. Osteryoung and O'Dea (50) discuss the application of SWV to a wide range of such phenomena.

Figure 7.3.16 contains data for a system involving the oxidation of $Fe(CN)_6^{4-}$ in a positive-going scan at a small Pt disk. The results have been treated theoretically by assuming reversibility at all frequencies and by adjusting two parameters, the radius of the disk, r_0, and $E_{1/2} = E^{0'} + (RT/nF) \ln(D_R/D_O)^{1/2}$, to provide the best fit. The change in behavior with frequency is rooted in the fact that the diffusion pattern at a UME can deviate from the semi-infinite linear case, as discussed in Section 5.3. The validity of the model is supported by the consistency of these parameters for runs at different frequencies and by the quality of the fit. This example illustrates the typical manner of comparing SWV results with theory.

(c) Background Currents

The considerations involved in understanding background currents in SWV are exactly those encountered in the treatment of DPV. If t_p is greater than five cell time constants, there is no appreciable charging current contribution, either to the individual current samples or to the differences. Faradaic background processes do contribute and often control the detection limits of SWV. At solid electrodes or near background limits, the effects on the forward and reverse currents can be sizable, but they are often suppressed effectively in the difference currents.
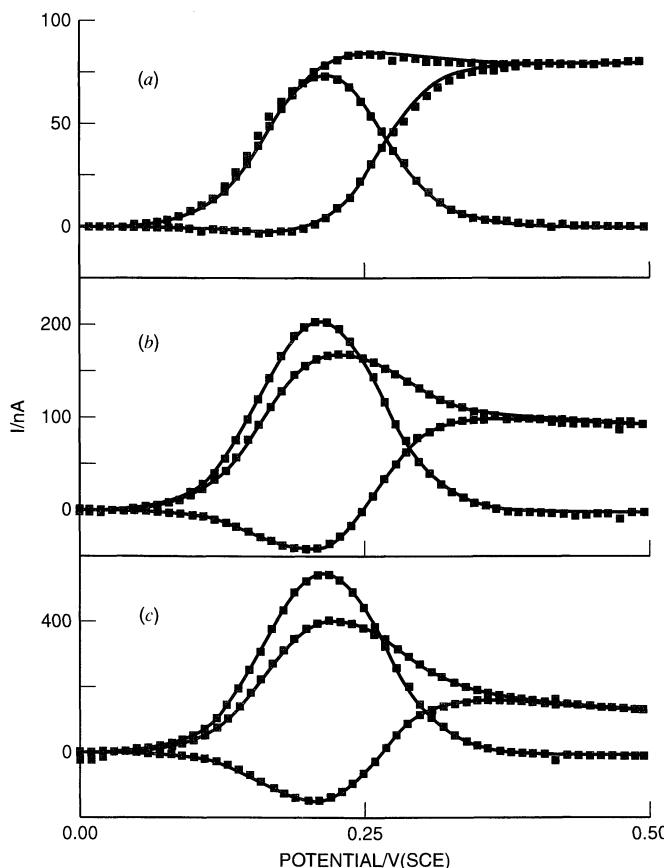
Figure 7.3.16 Square wave voltammograms at a Pt disk UME in a solution of 20 mM $Fe(CN)_6^{4-}$ also containing 2 M KNO_3. Each scan was made from 0.0 V to 0.50 V with $\Delta E_p = 50$ mV and $\Delta E_s = 10$ mV with frequencies of (a) 5 Hz, (b) 60 Hz, (c) 500 Hz. Points are experimental; curves are fitted to give r_0 and $E_{1/2}$, respectively, as: (a) 11.9 μm, 0.2142 V, (b) 12.4 μm, 0.2137 V, (c) 12.2 μm, 0.2147 V. [Reprinted from D. Whelan, J. J. O'Dea, J. Osteryoung, and K. Aoki, *J. Electroanal. Chem.*, **202**, 23 (1986), with permission from Elsevier Science.]

(d) Applications

Osteryoung and O'Dea (50) have proposed the broad diagnostic use of SWV in a way similar to that for which cyclic voltammetry (Chapters 6 and 12) has been so successful. Indeed SWV does have a high information content, especially when one considers the voltammograms of forward and reverse currents, and it has the power to interrogate electrode processes over a wide potential span in a reasonable time. Its strengths with respect to CV are derived especially from its ability to suppress the background. In general, systems can be examined at substantially lower concentrations than with CV. Moreover, there is normally much less distortion of the response by the background, so that fitting of data to theoretical models can be done with greater accuracy. On the whole, SWV is better than CV for evaluating quantitative parameters for systems that are understood mechanistically. SWV also has weaknesses with respect to CV: For most practitioners CV is more intuitively interpretable in chemical terms. Also, because the reversal in CV covers a large span of potentials, it can more readily highlight linkages between processes occurring at widely separated potentials. Finally, CV offers a considerably wider range of time scales than SWV as presently practiced.

For practical analysis, SWV is generally the best choice among all pulse methods, because it offers background suppression with the effectiveness of DPV, sensitivity slightly greater than that of DPV, much faster scan times, and applicability to a wider range of electrode materials and systems. The most reproducible behavior and lowest detection limits are generally found at mercury surfaces, so an SMDE working as an HMDE is quite effective with SWV. In the next section, we will continue this discussion of practical analysis in more general terms applicable to pulse methods as a group.

7.3.6 Analysis by Pulse Voltammetry

The differential pulse and square wave techniques are among the most sensitive means for the direct evaluation of concentrations, and they find wide use for trace analysis. When they can be applied, they are often far more sensitive than molecular or atomic absorption spectroscopy or most chromatographic approaches. In addition, they can provide information about the chemical form in which an analyte appears. Oxidation states can be defined, complexation can often be detected, and acid-base chemistry can be characterized. This information is frequently overlooked in competing methods. The chief weakness of pulse analysis, common to most electroanalytical techniques, is a limited ability to resolve complex systems. Moreover, analysis time can be fairly long, particularly if deaeration is required.

Pulse measurements are sufficiently sensitive that one must pay special attention to impurity levels in solvents and supporting electrolytes. Contamination from the electrolyte can be reduced by lowering its concentration from the usual 0.1 to 1 M range to 0.01 M or even 0.001 M. The lower limit is fixed by the maximum cell resistance that can be tolerated, if it is not set first by chemical considerations, such as the role of the supporting electrolyte in complexation or pH determination. In most analyses, aqueous media are used, both for convenience and for compatibility with the chemistry of sample preparation; however, other solvents can provide superior working ranges and merit consideration for new applications. The working range for any medium is much narrower for trace analysis by differential pulse polarography or square wave voltammetry than for conventional polarography, simply because the residual faradaic background becomes intolerably high at less extreme potentials. This point is clear from the data in Figure 7.3.17.

Under some circumstances, pulse techniques can produce distorted views of a sample's composition. Note that a fundamental assumption underlying analysis by normal pulse polarography is that the solution's composition near the working electrode at the start of each pulse is the same as that of the bulk. This assumption can hold only if negligible electrolysis occurs at the working electrode during the waiting period before τ'.
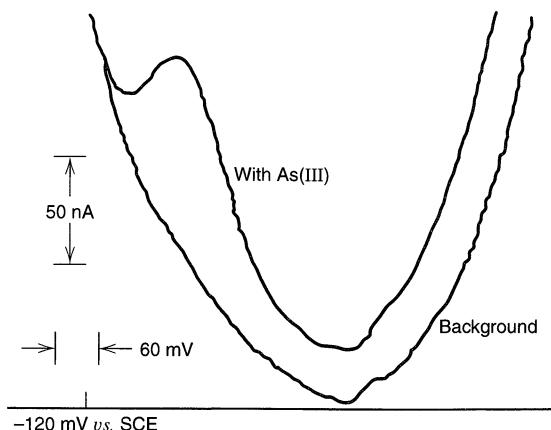
Figure 7.3.17   Differential pulse polarogram for 4.84×10^{-7} M As(III) in 1 M HCl containing 0.001% Triton X-100. $t_{max} = 2$ s, $\Delta E = -100$ mV. [From J. G. Osteryoung and R. A. Osteryoung, *Am. Lab.*, **4** (7), 8 (1972), with permission.]
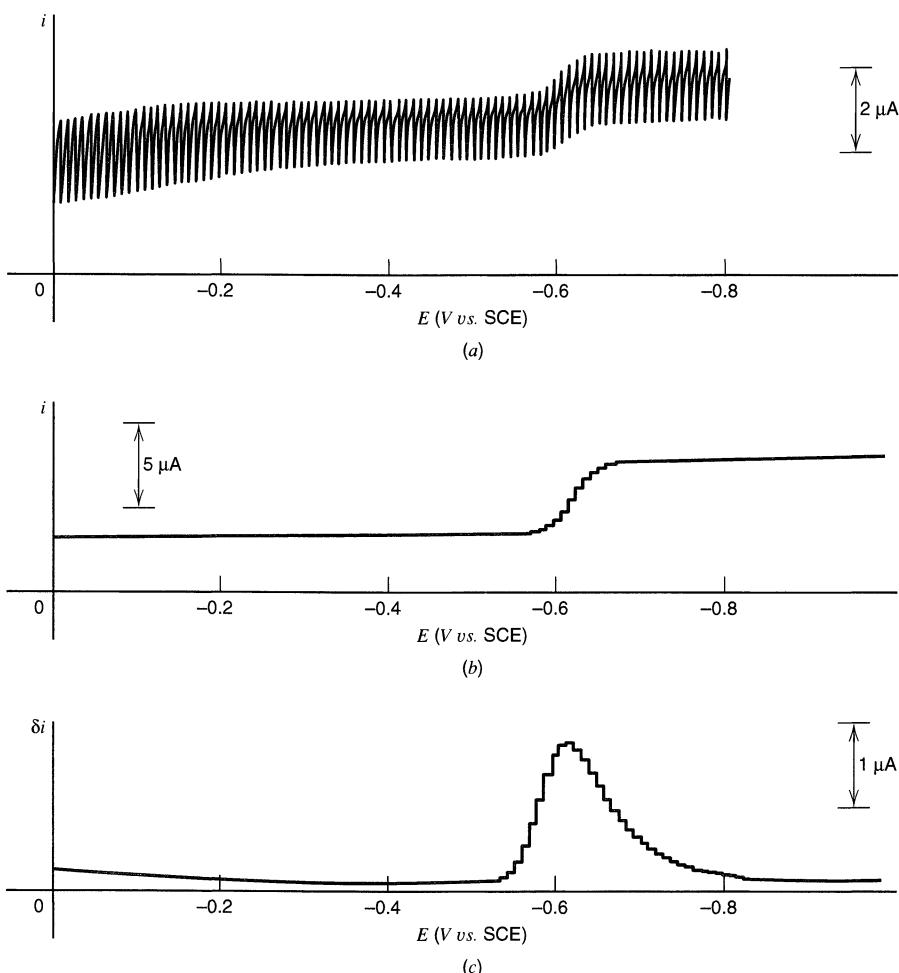
Figure 7.3.18   Polarograms at a DME of 10^{-3} M Fe^{3+} and 10^{-4} M Cd^{2+} in 0.1 M HCl. (*a*) Conventional dc mode. (*b*) Normal pulse mode, $E_b = -0.2$ V *vs.* SCE. (*c*) Differential pulse mode, $\Delta E = -50$ mV.

Therefore, the base potential must be either the equilibrium value itself or in a range over which the electrode behaves as an IPE (46). Otherwise, electrolysis modifies the solution's composition near the electrode before the pulse begins.

Figure 7.3.18 is a display of conventional and pulse polarograms for 1 mM Fe^{3+} and 10^{-4} M Cd^{2+} in 0.1 M HCl. Since $E^{0'}$ for Fe^{3+}/Fe^{2+} is more positive than the anodic limit of the DME, no wave is seen for that couple, yet the diffusion-limited reduction current for Fe^{3+} is recorded from the positive end of the working range. In the conventional polarogram (Figure 7.3.18a), the limiting current for Fe^{3+} is about five times greater than that of Cd^{2+}, as expected from the ratio of concentrations and n values. This response contrasts markedly with that from a normal pulse experiment (Figure 7.3.18b) in which E_b was -0.2 V $vs.$ SCE. The limiting current for Fe^{3+} is actually smaller than that for Cd^{2+}, because electrolysis at the base potential depletes the diffusion layer of Fe^{3+} before the pulse has a chance to measure it faithfully. Since the wave height for Cd^{2+} is unaffected, this effect would be alarming only if an accurate picture of the concentration ratio $C^*_{Fe^{3+}}/C^*_{Cd^{2+}}$ were desired. It can actually be useful for suppressing the response of a concentrated interferent.

Differential pulse polarography also produces an ambiguous record for this kind of situation, as shown in Figure 7.3.18c. A peak is seen only for the Cd^{2+} reduction, because the trace covers potentials only on the negative side of the Fe^{3+} wave. We note again that the differential pulse polarogram approximates the derivative of the normal pulse record; hence distinct peaks will not be seen in DPV (or in SWV) unless distinct waves appear in NPV.

Aside from this type of problem, DPV and SWV are particularly well-suited to the analysis of multicomponent systems because their readout format usually allows the separation of signals from individual components along a common baseline. This point is illustrated in Figure 7.3.19. Note also from that figure that pulse methods are applicable to a much richer variety of analytes than heavy metal species.

Although pulse techniques were developed specifically for the DME, they can be employed analytically with other kinds of electrodes. As important examples, one can cite differential pulse anodic stripping at a hanging mercury drop or at a thin mercury film on a rotating substrate. See Section 11.8 for details.
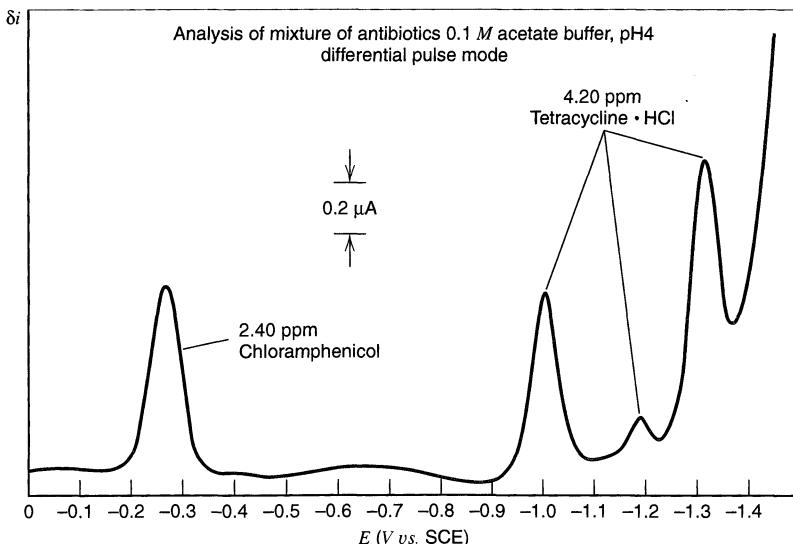
Figure 7.3.19 Differential pulse polarogram for a mixture of tetracycline and chloramphenicol. $\Delta E = -25$ mV. [From Application Note AN-111, EG&G Princeton Applied Research, Princeton, NJ, with permission.]

7.4 REFERENCES

1. J. Heyrovský, *Chem. Listy*, **16**, 256 (1922).

2. I. M. Kolthoff and J. J. Lingane, "Polarography," 2nd ed., Wiley-Interscience, New York, 1952, Chap. 17.

3. J. J. Lingane, "Electroanalytical Chemistry," 2nd ed., Wiley-Interscience, New York, 1958, Chap. 11.

4. L. Meites, "Polarographic Techniques," 2nd ed., Wiley-Interscience, New York, 1958, Chap. 2.

5. J. J. Lingane, *Anal. Chim. Acta*, **44**, 411 (1969).

6. A. Bond, "Modern Polarographic Methods in Analytical Chemistry," Marcel Dekker, New York, 1980.

7. W. M. Peterson, *Am. Lab.*, **11** (12), 69 (1979).

8. Z. Kowalski, K. H. Wong, R. A. Osteryoung, and J. Osteryoung, *Anal. Chem.*, **59**, 2216–2218 (1987).

9. J. Koutecký, *Czech. Cas. Fys.*, **2**, 50 (1953).

10. J. Koutecký and M. von Stackelberg in "Progress in Polarography," Vol. 1, P. Zuman and I. M. Koltoff, Eds., Wiley-Interscience, New York, 1962.

11. J. J. Lingane and B. A. Loveridge, *J. Am. Chem. Soc.*, **72**, 438 (1950).

12. P. Delahay, "New Instrumental Methods in Electrochemistry," Wiley-Interscience, New York, 1954, Chap. 3.

13. I. M. Kolthoff and J. J. Lingane, *op. cit.*, Chap. 4.

14. L. Meites, *op. cit.*, Chap. 3.

15. D. Ilkovič, *Coll. Czech. Chem. Commun.*, **6**, 498 (1934).

16. D. Ilkovič, *J. Chim. Phys.*, **35**, 129 (1938).

17. D. MacGillavry and E. K. Rideal, *Rec. Trav. Chim.*, **56**, 1013 (1937).

18. I. M. Kolthoff and J. J. Lingane, *op. cit.*, Chap. 18.

19. L. Meites, *op. cit.*, Chaps. 5 and 7.

20. J. J. Lingane, *Ind. Eng. Chem., Anal. Ed.*, **15**, 588 (1943).

21. I. M. Kolthoff and J. J. Lingane, *op. cit.*, Vol. 2.

22. L. Meites, *op. cit.*, Appendices B and C.

23. L. Meites, Ed., "Handbook of Analytical Chemistry," McGraw-Hill, New York, 1963, pp. 4–43 to 5–103.

24. A. J. Bard and H. Lund, Eds., "Encyclopedia of the Electrochemistry of the Elements," Marcel Dekker, New York, 1973–1986.

25. L. Meites and P. Zuman, "Electrochemical Data," Wiley, New York, 1974.

26. I. M. Kolthoff and J. J. Lingane, *op. cit.*, Chap. 9.

27. I. M. Kolthoff and J. J. Lingane, *op. cit.*, Chap. 11.

28. L. Meites, *op. cit.*, Chap. 4.

29. J. Koutecký, *Chem. Listy*, **47**, 323 (1953); *Coll. Czech. Chem. Commun.*, **18**, 597 (1953).

30. J. Weber and J. Koutecký, *Coll. Czech. Chem. Commun.*, **20**, 980 (1955).

31. L. Meites and Y. Israel, *J. Electroanal. Chem.*, **8**, 99 (1964).

32. J. Koutecký and J. Čížek, *Coll. Czech. Chem. Commun.*, **21**, 863 (1956).

33. J. E. B. Randles, *Can. J. Chem.*, **37**, 238 (1959).

34. J. E. B. Randles in "Progress in Polarography," I. M. Kolthoff and P. Zuman, Eds., Wiley-Interscience, 1962, Chap. 6.

35. J. Osteryoung, *Accts. Chem. Res.*, **26**, 77, (1993).

36. E. Wahlin, *Radiometer Polarog.*, **1**, 113 (1952).

37. E. Wahlin and A. Bresle, *Acta Chem. Scand.*, **10**, 935 (1956).

38. L. Meites, *op. cit.*, Chap. 10.

39. R. Bilewicz, K. Wikiel, R. Osteryoung, and J. Osteryoung, *Anal. Chem.*, **61**, 965 (1989).

40. P. He, *Anal. Chem.*, **67**, 986 (1995).

41. G. C. Barker and A. W. Gardner, *Z. Anal. Chem.*, **173**, 79 (1960).

42. E. P. Parry and R. A. Osteryoung, *Anal. Chem.*, **37**, 1634 (1964).

43. J. G. Osteryoung and R. A. Osteryoung, *Am. Lab.*, **4** (7), 8 (1972).

44. J. B. Flato, *Anal. Chem.*, **44** (11), 75A (1972).

45. R. A. Osteryoung and J. Osteryoung, *Phil. Trans. Roy. Soc. London, Ser. A*, **302**, 315 (1981).

46. J. L. Morris, Jr., and L. R. Faulkner, *Anal. Chem.*, **49**, 489 (1977).

47. J. Osteryoung and E. Kirowa-Eisner, *Anal. Chem.*, **52**, 62–66 (1980).

48. K. B. Oldham and E. P. Parry, *Anal. Chem.*, **42**, 229 (1970).

49. L. Ramaley and M. S. Krause, Jr., *Anal. Chem.*, **41**, 1362 (1969).

50. J. Osteryoung and J. J. O'Dea, *Electroanal. Chem.*, **14**, 209 (1986).

51. G. C. Barker and J. L. Jenkins, *Analyst*, **77**, 685 (1952).

52. G. C. Barker in "Proceedings of the Congress on Modern Analytical Chemistry in Industry," St. Andrews, Scotland, 1957, pp. 209–216.

53. J. H Christie, J. A. Turner, and R. A. Osteryoung, *Anal. Chem.*, **49**, 1899 (1977).

➤ 7.5 PROBLEMS

7.1 The following measurements were made on a reversible polarographic wave at 25°C. The process could be written $O + ne \rightleftarrows R$

E(volts *vs.* SCE)	$\bar{i}(\mu A)$
−0.395	0.48
−0.406	0.97
−0.415	1.46
−0.422	1.94
−0.431	2.43
−0.445	2.92

$\bar{i}_d = 3.24\ \mu A$
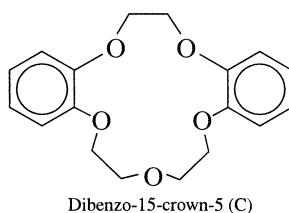
Calculate (a) the number of electrons involved in the electrode reaction, and (b) the formal potential (*vs.* NHE) of the couple involved in the electrode reaction, assuming $D_O = D_R$.

7.2 The following data were obtained for an apparently totally irreversible polarographic wave:

E(volts *vs.* SCE)	$i\ (\mu A)$
−0.419	0.31
−0.451	0.62
−0.491	1.24
−0.515	1.86
−0.561	2.48
−0.593	2.79
−0.680	3.10
−0.720	3.10

The overall reaction is known to be $O + 2e \rightarrow R$; and $m = 1.26$ mg/s, $t_{max} = 3.53$ s (constant at all potentials), and $C_O^* = 0.88$ mM. Assume the initial step in the mechanism is a rate-determining one-electron transfer. (a) Use Table 7.2.1 to determine k_f at each potential. From these values, determine α, and k_f^0 (i.e., the value of k_f at $E = 0.0$ V *vs.* NHE). (b) Use the treatment of Meites and Israel to obtain the same information. (c) Calculate $C_O(0, t)$ for each i. Plot $C_O(0, t)$ as a function of potential. On the same graph plot the i values listed above.

7.3 Consider a material A, which can be reduced at a dropping mercury electrode to form B. A 1-mM solution of A in acetonitrile shows a wave with $E_{1/2}$ at −1.90 V *vs.* SCE. The wave slope is 60.5 mV at 25°C and $(I)_{max} = 2.15$ in the usual units. When dibenzo-15-crown-5 is added to the solution, the polarographic behavior changes.

Dibenzo-15-crown-5 (C)

The following observations were made:

Concentration of C, M	$E_{1/2}$, V	Wave Slope, mV	$(I)_{max}$
10^{-3}	-2.15	60.3	2.03
10^{-2}	-2.21	59.8	2.02
10^{-1}	-2.27	59.8	2.04

What interpretation can be made of these results? Can any thermodynamic data be derived from the data? Can you suggest the identity of species A?

7.4 A polarogram of molecular oxygen in air-saturated 0.1 M KNO_3 is like that of Figure 5.6.2. The concentration of O_2 is about 0.25 mM. At $E = -0.4$ V $vs.$ SCE, $(i_d)_{max} = 3.9$ μA, $t_{max} = 3.8$ s, and $m = 1.85$ mg/s. At $E = -1.7$ V $vs.$ SCE, $(i_d)_{max} = 6.5$ μA, $t_{max} = 3.0$ s, and $m = 1.85$ mg/s. Calculate $(I)_{max}$ at each potential. Is the ratio of the two values what you expect? Explain any discrepancy in chemical terms. Calculate the diffusion coefficient for O_2 using the more appropriate constant. Defend your choice of the two.

7.5 Consider an analysis for the toxic ion Tl(I) in waste water that also contains Pb(II) and Zn(II) in 10 to 100-fold excesses. Outline any obstacles that would impede a polarographic determination and suggest means for circumventing them without implementing separation techniques. For 0.1 M KCl, $E_{1/2}(Tl^+/Tl) = -0.46$ V, $E_{1/2}(Pb^{2+}/Pb) = -0.40$ V, and $E_{1/2}(Zn^{2+}/Zn) = -0.995$ V $vs.$ SCE.

7.6 Sketch the normal pulse voltammogram expected for a substance undergoing an irreversible electrode reaction at a gold disk (e.g., $O_2 \rightarrow H_2O_2$ in 1 M KCl). Assume that the reduced form is not initially present and that no electrolysis occurs at the base potential in the starting solution. Explain the shape of the trace. (Note that the *location* of the trace on the potential axis is not of interest here.) Do the same for the case in which the electrode reaction is reversible. How would the curves differ if the disk were rotated during the recording of the polarograms?

7.7 (a) Show that the derivative of a reversible sampled-current voltammetric wave is

$$\frac{di}{dE} = \frac{n^2 F^2 A C_O^*}{RT\pi^{1/2}\tau^{1/2}} \frac{\xi\theta}{(1 + \xi\theta)^2}$$

(b) Show that (7.3.19) approaches this form for $\delta i/\Delta E \approx di/dE$ as $\Delta E \rightarrow 0$.

CHAPTER

8

CONTROLLED-CURRENT TECHNIQUES

8.1 INTRODUCTION

We discussed in Chapters 5–7 methods in which the potential of an electrode was controlled (or was the independent variable), while the current (the dependent variable) was determined as a function of time. In this chapter we consider the opposite case, where the current is controlled (frequently held constant), and the potential becomes the dependent variable, which is determined as a function of time. The other conditions assumed in Chapters 5–7, such as small ratio of electrode area to solution volume and semi-infinite diffusion, are also assumed here. We do not treat UMEs, because the behavior in the steady-state regime is not a function of whether the applied signal is a controlled potential or current. The experiment is carried out by applying the controlled current between the working and auxiliary electrodes with a current source (called a *galvanostat*) and recording the potential between the working and reference electrodes (e.g., with a recorder, oscilloscope, or other data acquisition device) (Figure 8.1.1). These techniques are generally called *chronopotentiometric* techniques, because E is determined as a function of time, or *galvanostatic* techniques, because a small constant current is applied to the working electrode.

8.1.1 Comparison with Controlled-Potential Methods

Since the general aspects of controlled-potential and controlled-current experiments are so similar, we might consider the basic differences between the two types of experiments and the relative advantages of each. The instrumentation for controlled-current experiments is simpler than the potentiostats required in controlled-potential ones, since no feedback from the reference electrode to the control device is required. Although constant-current sources constructed from operational amplifiers are frequently used, a simple circuit employing a high-voltage power supply (e.g., a 400-V power supply or several 90-V batteries) and a large resistor can be adequate. The mathematical treatment also differs from what we have already seen. In controlled-current exper-
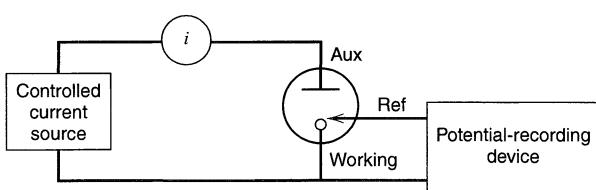
Figure 8.1.1 Simplified block diagram of apparatus for chronopotentiometric measurements.

305

iments, the surface boundary condition is based on the known current or fluxes (i.e., the concentration gradients) at the electrode surface, while in controlled-potential methods, the concentrations at $x = 0$ (as functions of E) provide the boundary conditions. Usually the mathematics involved in solving the diffusion equations in controlled-current problems are much simpler, and closed-form analytical solutions are usually obtained.

A fundamental disadvantage of controlled-current techniques is that double-layer charging effects are frequently larger and occur throughout the experiment in such a way that correction for them is not straightforward. Treating data from multicomponent systems and stepwise reactions is also more complicated in controlled-current methods, and the waves observed in E-t transients are usually less well-defined than those of potential sweep i-E curves.

Controlled-current methods can be of particular value when the process being studied is the background process, such as solvated electron formation in liquid ammonia or reduction of quaternary ammonium ion in an aprotic solvent. A simple method for determination of the thickness of metal films is by anodic stripping at constant current. Working with background processes in a controlled-potential mode is often difficult.

8.1.2 Classification and Qualitative Description

Different types of constant-current techniques are illustrated in Figure 8.1.2. Let us first consider *constant-current chronopotentiometry* (Figure 8.1.2*a*) in the context of the anthracene (An) system used as an example in Section 5.1.1. The steady current, i, applied to the electrode causes the anthracene to be reduced at a constant rate to the anion radical, $An^{\overline{\cdot}}$. The potential of the electrode moves to values characteristic of the couple and varies with time as the $An/An^{\overline{\cdot}}$ concentration ratio changes at the electrode surface. The process can be regarded as a titration of the An in the vicinity of the electrode by the continuous flux of electrons, resulting in an E-t curve like that obtained for a potentiometric titration (E as a function of titrant added, $i \cdot t$). Eventually, after the concentration of An drops to zero at the electrode surface, the flux of An to the surface is insufficient to accept all of the electrons being forced across the electrode-solution interface. The potential of the electrode will then rapidly shift toward more negative values until a new, second reduction process can start. The time after application of the constant current when this potential transition occurs is called the *transition time*, τ. It is related to the concentration and the diffusion coefficient and is the chronopotentiometric analogue of the peak or limiting current in controlled-potential experiments. The shape and location of the E-t curve is governed by the reversibility, or the heterogeneous rate constant, of the electrode reaction.

Instead of a constant current, one can apply a current that varies as a known function of time (e.g., $i = \beta t$, a current ramp; Figure 8.1.2*b*). Although this technique, called *programmed current chronopotentiometry*, can be treated theoretically with little difficulty, it has been employed infrequently. The current can also be reversed after some time (*current reversal chronopotentiometry*, Figure 8.1.2*c*). For example, if in the case considered above, the current is suddenly changed to an anodic current of equal magnitude at, or before, the transition time, the $An^{\overline{\cdot}}$ formed during the forward step will start oxidizing. The potential will move in a positive direction as the $An/An^{\overline{\cdot}}$ concentration ratio increases. When the $An^{\overline{\cdot}}$ concentration falls to zero at the electrode surface, a potential transition toward positive potentials occurs, and a reverse transition time can be measured. In an extension of this technique the current can be continuously reversed at each transition, resulting in *cyclic chronopotentiometry* (Figure 8.1.2*d*). Finally, as in the treatment of

Excitation

Response

(a)

(b)

(c)

(d)
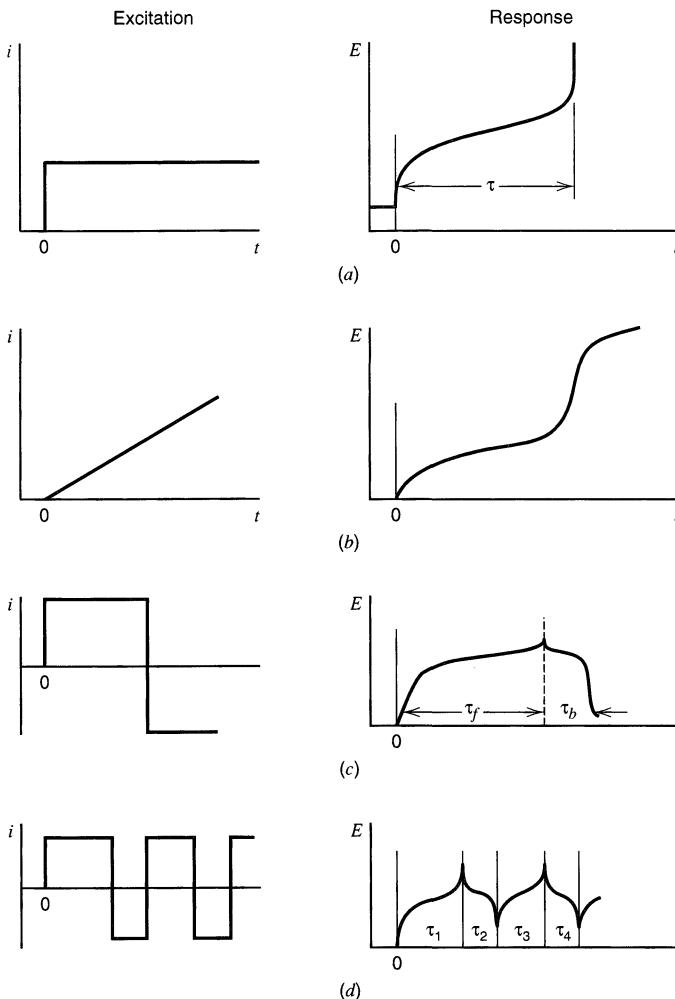
Figure 8.1.2 Different types of controlled-current techniques. (a) Constant-current chronopotentiometry. (b) Chronopotentiometry with linearly increasing current. (c) Current reversal chronopotentiometry. (d) Cyclic chronopotentiometry.

controlled-potential data, the derivatives of the E-t curves can be obtained or differential methods can be employed.[1]

▶ ## 8.2 GENERAL THEORY OF CONTROLLED-CURRENT METHODS

8.2.1 Mathematics of Semi-Infinite Linear Diffusion

We again consider the simple electron-transfer reaction, $O + ne \rightarrow R$. A planar working electrode and an unstirred solution are assumed, with only species O initially present at a concentration C_O^*. These conditions are the same as those in Section 5.4.1, so that the diffusion equations and general boundary conditions, (5.4.2) to (5.4.5), apply:

$$\frac{\partial C_O(x, t)}{\partial t} = D_O\left[\frac{\partial^2 C_O(x, t)}{\partial x^2}\right] \tag{8.2.1}$$

---

[1]These latter methods are employed infrequently and are discussed in more depth in the first edition, Sections 7.4.3 and 7.6.

$$\frac{\partial C_R(x, t)}{\partial t} = D_R\left[\frac{\partial^2 C_R(x, t)}{\partial x^2}\right] \tag{8.2.2}$$

$$\left.\begin{array}{r}\text{At } t = 0 \text{ (for all } x)\\ \text{and}\\ \text{as } x \to \infty \text{ (for all } t)\end{array}\right\} C_O(x, t) = C_O^* \qquad C_R(x, t) = 0 \tag{8.2.3}$$

$$D_O\left[\frac{\partial C_O(x, t)}{\partial x}\right]_{x=0} + D_R\left[\frac{\partial C_R(x, t)}{\partial x}\right]_{x=0} = 0 \tag{8.2.4}$$

Since the applied current $i(t)$ is presumed known, the flux at the electrode surface is also known at any time, by the equation [see (4.4.29)]:

$$D_O\left[\frac{\partial C_O(x, t)}{\partial x}\right]_{x=0} = \frac{i(t)}{nFA} \tag{8.2.5}$$

This boundary condition involving the concentration *gradient* allows the diffusion problem to be solved without reference to the rate of the electron-transfer reaction, in contrast with the concentration-potential boundary conditions required for controlled-potential methods. Although in many controlled-current experiments the applied current is constant, the more general case for any arbitrarily applied current, $i(t)$, can be solved readily and includes the constant-current case, as well as reversal experiments and several others of interest.

For species O, application of the Laplace transform method to (8.2.1) and (8.2.3) yields

$$\bar{C}_O(x, s) = \frac{C_O^*}{s} + A(s) \exp\left[-\left(\frac{s}{D_O}\right)^{1/2} x\right] \tag{8.2.6}$$

The transform of (8.2.5) is

$$D_O\left[\frac{\partial \bar{C}_O(x, s)}{\partial x}\right]_{x=0} = \frac{\bar{i}(s)}{nFA} \tag{8.2.7}$$

By taking the indicated derivative of (8.2.6) and substituting in (8.2.7) to eliminate $A(s)$, we have

$$\bar{C}_O(x, s) = \frac{C_O^*}{s} - \left[\frac{\bar{i}(s)}{nFAD_O^{1/2}s^{1/2}}\right] \exp\left[-\left(\frac{s}{D_O}\right)^{1/2} x\right] \tag{8.2.8}$$

By substitution of the known function, $\bar{i}(s)$, and employing the inverse transform, $C_O(x, t)$ can be obtained. Similarly, the following expression for $\bar{C}_R(x, s)$ can be derived:

$$\bar{C}_R(x, s) = \left[\frac{\bar{i}(s)}{nFAD_R^{1/2}s^{1/2}}\right] \exp\left[-\left(\frac{s}{D_R}\right)^{1/2} x\right] \tag{8.2.9}$$

Note that direct inversion of (8.2.8) and (8.2.9) using the convolution property leads to (6.2.8) and (6.2.9). These integral forms are also convenient for solving controlled-current problems.

8.2.2 Constant-Current Electrolysis—The Sand Equation

If $i(t)$ is constant, then $\bar{i}(s) = i/s$ and (8.2.8) becomes

$$\bar{C}_O(x, s) = \frac{C_O^*}{s} - \left[\frac{i}{nFAD_O^{1/2}s^{3/2}}\right] \exp\left[-\left(\frac{s}{D_O}\right)^{1/2} x\right] \tag{8.2.10}$$

The inverse transform of this equation yields the expression for $C_O(x, t)$:

$$C_O(x, t) = C_O^* - \frac{i}{nFAD_O} \left\{ 2\left(\frac{D_O t}{\pi}\right)^{1/2} \exp\left(-\frac{x^2}{4D_O t}\right) - x \operatorname{erfc}\left[\frac{x}{2(D_O t)^{1/2}}\right] \right\} \quad (8.2.11)$$

Typical concentration profiles at various times during a constant-current electrolysis are given in Figure 8.2.1. Note that $C_O(0, t)$ decreases continuously, yet $[\partial C_O(x, t)/\partial x]_{x=0}$ is constant at all times after the onset of electrolysis.

An expression for $C_O(0, t)$ can be obtained by setting $x = 0$ in (8.2.11), or directly by inverse transform of (8.2.8) with $x = 0$:

$$\overline{C}_O(0, s) = \frac{C_O^*}{s} - \frac{i}{nFAD_O^{1/2} s^{3/2}} \quad (8.2.12)$$

to yield

$$C_O(0, t) = C_O^* - \frac{2it^{1/2}}{nFAD_O^{1/2} \pi^{1/2}} \quad (8.2.13)$$
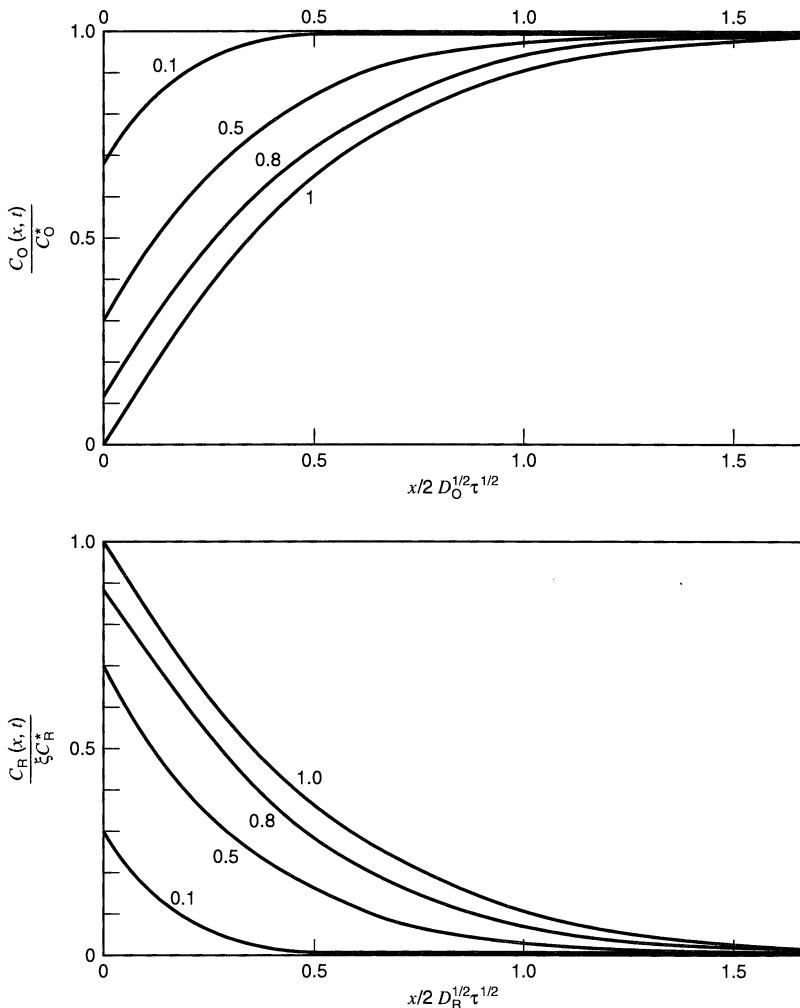
Figure 8.2.1 Concentration profiles of O and R (in dimensionless form) at various values of t/τ indicated on the curves.

At the transition time, τ, $C_O(0, t)$ drops to zero and (8.2.13) becomes

$$\frac{i\tau^{1/2}}{C_O^*} = \frac{nFAD_O^{1/2}\pi^{1/2}}{2} = 85.5\,nD_O^{1/2}A\,\frac{\text{mA-s}^{1/2}}{\text{m}M}\,(\text{with } A \text{ in cm}^2) \qquad (8.2.14)$$

This equation, known as the *Sand equation*, was first derived by H. J. S. Sand (1).

As discussed in Section 8.1.2, the flux of O to the electrode surface beyond the transition time is not large enough to satisfy the applied current, and the potential shifts to a more extreme value where another electrode process can occur (Figure 8.2.2). The actual shape of the E-t curve is discussed in the next sections.

The measured value of τ at known i (or better, the values of $i\tau^{1/2}$ obtained at various currents) can be used to determine n, A, C_O^* or D_O. For a well-behaved system, the *transition time constant*, $i\tau^{1/2}/C_O^*$, is independent of i or C_O^*. A lack of constancy in this parameter indicates complications to the electrode reaction from coupled homogeneous chemical reactions (Chapter 12), adsorption (Chapter 14), or measurement artifacts, such as double-layer charging or the onset of convection (Section 8.3.5).

Note that (8.2.11) can be written in a convenient form with dimensionless groupings $C_O(x, t)/C_O^*$, t/τ, and $\chi_O = x/[2(D_O t)^{1/2}]$ for $(0 \le t \le \tau)$:

$$\frac{C_O(x, t)}{C_O^*} = 1 - \left(\frac{t}{\tau}\right)^{1/2}[\exp(-\chi_O^2) - \pi^{1/2}\chi_O\,\text{erfc}(\chi_O)] \qquad (8.2.15)$$

$$\frac{C_O(0, t)}{C_O^*} = 1 - \left(\frac{t}{\tau}\right)^{1/2} \qquad (8.2.16)$$

In a similar way, the following equations hold for $C_R(x, t)$ when $(0 \le t \le \tau)$:

$$\frac{C_R(x, t)}{C_R^*} = \xi\left(\frac{t}{\tau}\right)^{1/2}[\exp(\chi_R^2) - \pi^{1/2}\chi_R\,\text{erfc}(\chi_R)] \qquad (8.2.17)$$

where $\chi_R = x/[2(D_R t)^{1/2}]$ and $\xi = (D_O/D_R)^{1/2}$. Accordingly,

$$C_R(0, t) = \frac{2it^{1/2}}{nFA\pi^{1/2}D_R^{1/2}} = \xi\left(\frac{t}{\tau}\right)^{1/2}C_O^* \qquad (8.2.18)$$

See Figure 8.2.1.
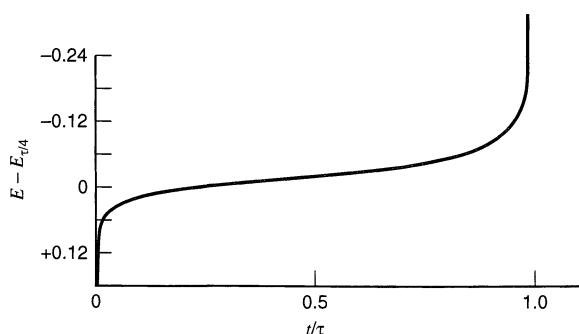
Figure 8.2.2 Theoretical chronopotentiogram for a nernstian electrode process.

8.2.3 Programmed Current Chronopotentiometry

It is possible to use currents that are programmed to vary with time in a special way, rather than remaining constant (2, 3). For example, a current that increases linearly with time could be used:

$$i(t) = \beta t \tag{8.2.19}$$

The treatment follows that for a constant-current electrolysis. In this case the transform is

$$\bar{i}(s) = \frac{\beta}{s^2} \tag{8.2.20}$$

so that (8.2.8) becomes, at $x = 0$,

$$\bar{C}_O(0, s) = \frac{C_O^*}{s} - \frac{\beta}{nFAD_O^{1/2}s^{5/2}} \tag{8.2.21}$$

$$C_O(0, t) = C_O^* - \frac{2\beta t^{3/2}}{nFAD_O^{1/2}\Gamma(5/2)} \tag{8.2.22}$$

where $\Gamma(5/2)$ is the mathematical gamma function, equal with this argument to 1.33. This same treatment can be employed with any power function of time.

A particularly interesting applied current is one varying with the square root of time:

$$i(t) = \beta t^{1/2} \tag{8.2.23}$$

$$\bar{i}(s) = \frac{\beta \pi^{1/2}}{2s^{3/2}} \tag{8.2.24}$$

$$\bar{C}_O(0, s) = \frac{C_O^*}{s} - \frac{\beta \pi^{1/2}}{2nFAD_O^{1/2}s^2} \tag{8.2.25}$$

$$C_O(0, t) = C_O^* - \frac{\beta \pi^{1/2} t}{2nFAD_O^{1/2}} \tag{8.2.26}$$

Again, defining the transition time τ as that time when $C_O(0, t) = 0$, an expression equivalent to the constant-current Sand equation results, but with τ (rather than $\tau^{1/2}$) proportional to C_O^* and β:

$$\frac{\beta \tau}{C_O^*} = 2nFA\pi^{-1/2}D_O^{1/2} \tag{8.2.27}$$

Because this current excitation function is fairly difficult to generate, the technique has not been used very much. Nevertheless, it would be advantageous for stepwise electron-transfer reactions and multicomponent systems (see Section 8.5).

▶ 8.3 POTENTIAL–TIME CURVES IN CONSTANT-CURRENT ELECTROLYSIS

8.3.1 Reversible (Nernstian) Waves

For rapid electron transfer, a nernstian relationship links the potential with the surface concentrations of O and R (Sections 3.4.5 and 3.5.3). Substitution of the expressions for $C_O(0, t)$ and $C_R(0, t)$, equations 8.2.16 and 8.2.18, into (3.5.21) yields (4)

$$\boxed{E = E_{\tau/4} + \frac{RT}{nF} \ln \frac{\tau^{1/2} - t^{1/2}}{t^{1/2}}} \tag{8.3.1}$$
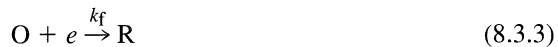
where $E_{\tau/4}$, the *quarter-wave potential*, is

$$E_{\tau/4} = E^{0'} - \frac{RT}{2nF} \ln \frac{D_O}{D_R} \tag{8.3.2}$$

Thus $E_{\tau/4}$ is the chronopotentiometric equivalent of the voltammetric $E_{1/2}$ value (Figure 8.2.2). The test for reversibility of an E-t curve is a linear plot of E vs. log $[(\tau^{1/2} - t^{1/2})/t^{1/2}]$ having a slope of $59/n$ mV, or a value of $|E_{\tau/4} - E_{3\tau/4}| = 47.9/n$ mV (at 25°C).

8.3.2 Totally Irreversible Waves

For a totally irreversible one-step, one electron reaction

$$O + e \overset{k_f}{\rightarrow} R \tag{8.3.3}$$

the current is related to the potential by either of the following equations (5):

$$i = nFAk_f^0 C_O(0, t) \exp\left[\frac{-\alpha FE}{RT}\right] \tag{8.3.4a}$$

$$i = nFAk^0 C_O(0, t) \exp\left[\frac{-\alpha F(E - E^{0'})}{RT}\right] \tag{8.3.4b}$$

When the expression for $C_O(0, t)$, (8.2.16), is substituted into these equations, the following expressions result:

$$E = \frac{RT}{\alpha F} \ln\left(\frac{FAC_O^* k_f^0}{i}\right) + \frac{RT}{\alpha F} \ln\left[1 - \left(\frac{t}{\tau}\right)^{1/2}\right] \tag{8.3.5a}$$

$$E = E^{0'} + \frac{RT}{\alpha F} \ln\left(\frac{FAC_O^* k^0}{i}\right) + \frac{RT}{\alpha F} \ln\left[1 - \left(\frac{t}{\tau}\right)^{1/2}\right] \tag{8.3.5b}$$

Equivalent expressions can be obtained by using the Sand equation and substituting for $\tau^{1/2}$:

$$E = \frac{RT}{\alpha F} \ln\left[\frac{2k_f^0}{(\pi D_O)^{1/2}}\right] + \frac{RT}{\alpha F} \ln[\tau^{1/2} - t^{1/2}] \tag{8.3.6a}$$

$$\boxed{E = E^{0'} + \frac{RT}{\alpha F} \ln\left[\frac{2k^0}{(\pi D_O)^{1/2}}\right] + \frac{RT}{\alpha F} \ln[\tau^{1/2} - t^{1/2}]} \tag{8.3.6b}$$

Thus, for a totally irreversible reduction wave, the whole E-t wave shifts toward more negative potentials with increasing current, with a tenfold increase in current causing a shift of $2.3RT/\alpha F$ (or $59/\alpha$ mV at 25°C). Note that uncompensated resistance between the reference and working electrodes will also cause the E-t curve to shift with increasing i. For a totally irreversible wave, $|E_{\tau/4} - E_{3\tau/4}| = 33.8/\alpha$ mV at 25°C.

8.3.3 Quasireversible Waves

For the quasireversible one-step, one-electron process,

$$O + e \underset{k_b}{\overset{k_f}{\rightleftarrows}} R \tag{8.3.7}$$

a general E-t relationship is found from combining the current-overpotential equation, (3.4.10), with the equations for $C_O(0, t)$, (8.2.16), and $C_R(0, t)$, (8.2.18). A bulk concen-

tration of R, C_R^*, is required, so that a starting equilibrium potential can be defined (6, 7). This requirement adds the term C_R^* to (8.2.18). The overall result is

$$\frac{i}{i_0} = \left[1 - \frac{2i}{FAC_O^*}\left(\frac{t}{\pi D_O}\right)^{1/2}\right]e^{-\alpha f\eta} - \left[1 + \frac{2i}{FAC_R^*}\left(\frac{t}{\pi D_R}\right)^{1/2}\right]e^{(1-\alpha)f\eta} \qquad (8.3.8)$$

Alternative forms can be written in terms of the current density, j, and the heterogeneous rate constants,

$$j = k_f\left[FC_O^* - 2j\left(\frac{t}{\pi D_O}\right)^{1/2}\right] - k_b\left[FC_R^* + 2j\left(\frac{t}{\pi D_R}\right)^{1/2}\right] \qquad (8.3.9a)$$

or, when $C_R^* = 0$,

$$j = Fk_fC_O^* - \frac{2jt^{1/2}}{\pi^{1/2}}\left(\frac{k_f}{D_O^{1/2}} + \frac{k_b}{D_R^{1/2}}\right) \qquad (8.3.9b)$$

where k_f and k_b are defined in (3.3.9) and (3.3.10).

Usually, the study of the kinetics of quasireversible electrode reactions by constant-current techniques (generally called the *galvanostatic or current step* method) involves small current perturbations, and the potential change from the equilibrium position is also small. When both O and R are initially present, the linearized current-potential-concentration characteristic, (3.5.33), can be employed. Combination with equations 8.2.13 and 8.2.18 (with the latter modified by an added term, C_R^*) yields

$$-\eta = \frac{RT}{F}i\left[\frac{2t^{1/2}}{FA\pi^{1/2}}\left(\frac{1}{C_O^*D_O^{1/2}} + \frac{1}{C_R^*D_R^{1/2}}\right) + \frac{1}{i_0}\right] \qquad (8.3.10)$$

The same result can be obtained by linearization of (8.3.8). Thus, a plot of η vs. $t^{1/2}$, for small values of η, will be linear, and i_0 can be obtained from the intercept. This method is the constant-current analog of the potential step method discussed in Section 5.5.1(c).

8.3.4 General Effects of Double-Layer Capacity

Because the potential is changing during the application of the current step, there is always a nonfaradaic current that contributes to charging of the double-layer capacitance. If $dA/dt = 0$, then i_c is given by

$$i_c = -AC_d(d\eta/dt) = -AC_d(dE/dt) \qquad (8.3.11)$$

Thus, of the total applied constant current, i, only a portion, i_f, goes to the faradaic reaction:

$$i_f = i - i_c \qquad (8.3.12)$$

Since dE/dt is a function of time, i_c and i_f also vary with time, even when i is constant. This situation can be treated as a case of programmed current chronopotentiometry if an explicit form of dE/dt or $d\eta/dt$ is known.

For the case where the one-step, one-electron process applies and the general η-t expression can be linearized, then (8.3.10) can be adapted as follows (8):

$$-\eta = \frac{RT}{F}i\left[\frac{2t^{1/2}}{\pi^{1/2}}N - \frac{RT}{F}AC_dN^2 + \frac{1}{i_0}\right] \qquad (8.3.13)$$

where

$$N = \frac{1}{FA}\left(\frac{1}{C_O^* D_O^{1/2}} + \frac{1}{C_R^* D_R^{1/2}}\right) \tag{8.3.14}$$

The intercept of the η-$t^{1/2}$ plot allows the determination of $1/i_0$ only when this term is appreciable compared to $(RT/F)AC_dN^2$ (8). To overcome this limitation for fast electron-transfer reactions, where i_0 is large, the galvanostatic double-pulse method has been proposed (Section 8.6).

8.3.5 Practical Issues in the Measurement of Transition Time

As discussed in Section 8.3.4, the presence of a finite double-layer capacity results in a charging current contribution proportional to dE/dt (equation 8.3.11) and causes i_f to differ from the total applied current, i. This effect, which is largest immediately after application of the current and near the transition (where dE/dt is relatively large), affects the overall shape of the E-t curve and makes measurement of τ difficult and inaccurate. A number of authors have examined this problem and have proposed techniques for measuring τ from distorted E-t curves or for correcting values obtained in the presence of significant double-layer effects.

In the simplest approach, i_c is assumed to be constant for $0 < t < \tau$. This is not strictly so, of course, since dE/dt and C_d (a function of E) change throughout the E-t curve (9, 10); however the approximation leads to

$$i = i_f + i_c \tag{8.3.15}$$

$$\frac{i\tau^{1/2}}{C_O^*} = \frac{i_f \tau^{1/2}}{C_O^*} + \frac{i_c \tau}{C_O^* \tau^{1/2}} \tag{8.3.16}$$

where $i_f \tau^{1/2}/C_O^*$ is the "true" chronopotentiometric constant, a, equal to $nFAD_O^{1/2}\pi^{1/2}/2$. In the last term, $i_c\tau$ is the total number of coulombs needed to charge an average double-layer capacitance from the initial potential to the potential at which τ is measured (ΔE), so that $i_c\tau \approx (C_d)_{avg}\,\Delta E$, and is represented by a correction factor b. Thus the final equation is

$$i\tau^{1/2}/C_O^* = a + b/C_O^*\tau^{1/2} \tag{8.3.17}$$

Plots based on (8.3.17) can thus be used to extract a and b from the observed data (e.g., a plot of $i\tau$ vs. $\tau^{1/2}$ yields a slope aC_O^* and an intercept b).

An equation of this form can also be used to correct for formation of an oxide film (e.g., on a platinum electrode during an electrochemical oxidation) and for electrolysis of adsorbed material in addition to diffusing species. Under these conditions, (8.3.15) becomes (10):

$$i = i_f + i_c + i_{ox} + i_{ads} \tag{8.3.18}$$

where i_{ox} is the current going to formation (or reduction) of the oxide film and i_{ads} is the current required for the adsorbed material. A treatment similar to that given above again yields (8.3.17), where b is now an overall correction factor including $Q_{ox} = i_{ox}\tau$ and $Q_{ads} = nF\Gamma$, where Γ is the number of moles of adsorbed species per square centimeter (Section 14.3.7). Although these approximations are rough, treatments of actual experimental data by (8.3.17) yield fairly good results, even at rather low concentrations and short transition times, where these surface effects are most important (11).
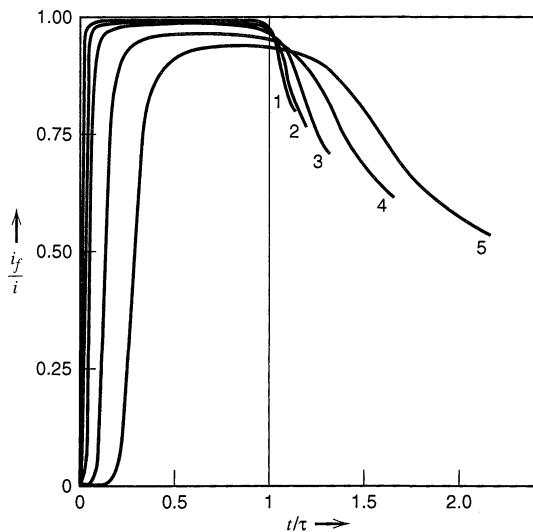
Figure 8.3.1 Fraction of total current contributing to the faradaic process (i_f/i) *vs.* time for a nernstian electrode process. K values of (*1*) 5×10^{-4}; (*2*) 10^{-3}; (*3*) 2×10^{-3}; (*4*) 5×10^{-3}; (*5*) 0.01. [From W. T. de Vries, *J. Electroanal. Chem.*, **17**, 31 (1968), with permission.]

A more rigorous approach involves only the assumption that C_d is independent of E (12–14). In this case, one must solve the diffusion equation, (8.2.1), beginning with the usual boundary conditions, (8.2.3). The flux condition, (8.2.5), is replaced by

$$i = nFAD_O\left(\frac{\partial C_O}{\partial x}\right)_{x=0} + AC_d\left(\frac{dE}{dt}\right) \tag{8.3.19}$$

In addition, one needs the appropriate *i-E* characteristic (i.e., for a reversible, totally irreversible, or quasireversible reaction). The resulting nonlinear integral equation must be evaluated numerically. Alternatively, the problem can be addressed by digital simulation techniques. Figures 8.3.1 and 8.3.2 illuminate the effects of different relative contributions of double-layer charging on i_f (at constant i) and on the *E-t* curves of a nernstian reaction. The charging contribution is represented there by the dimensionless parameter, K, defined as

$$K = \left(\frac{RT}{nF}\right)\frac{C_d}{nFC_O^*(\pi D_O\tau)^{1/2}} \tag{8.3.20}$$
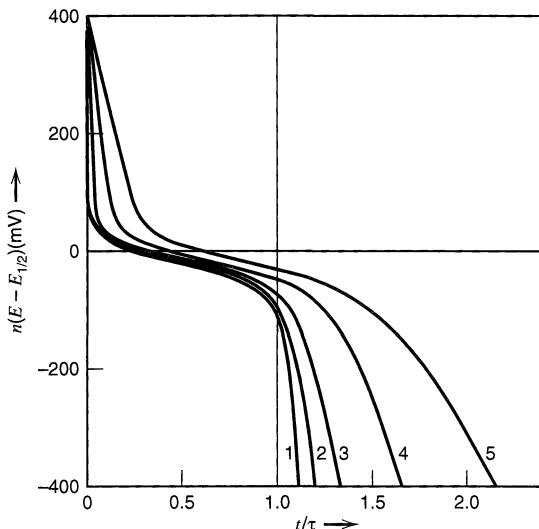
Figure 8.3.2 Effect of double-layer capacitance on chronopotentiograms for a nernstian electrode reaction. Values of K as in Figure 8.3.1. [From W. T. de Vries, *J. Electroanal. Chem.*, **17**, 31 (1968), with permission.]

7 mm

14 mm

(a)

1   2   3

(b)
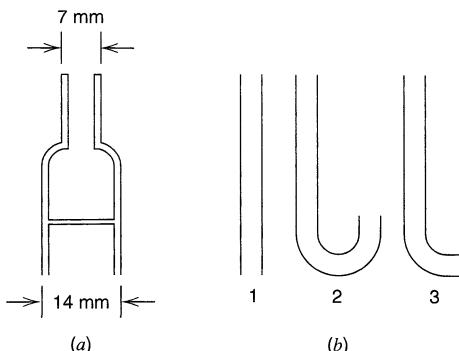
Figure 8.3.3 (*a*) Shielded electrode for maintaining linear diffusion and suppressing convection. (*b*) Tubes to which shielded electrode is attached to provide: (*1*) horizontal electrode, diffusion upward; (*2*) horizontal electrode, diffusion downward; (*3*) vertical electrode. [Reprinted with permission from A. J. Bard, *Anal. Chem.*, **33**, 11 (1961). Copyright 1961, American Chemical Society.]

The effect of double-layer charging is clearly most important at small τ values (see equation 8.3.20). Problems with distorted E-t curves and the difficulty of obtaining corrected τ values have discouraged the use of controlled-current methods as opposed to controlled-potential ones.

In both controlled-current and controlled-potential methods, problems develop at long experimental times because of the onset of convection and the nonlinearity of diffusion. Convective effects, caused by motion of the solution with respect to the electrode, can arise by accidental vibrations transmitted to the cell (e.g., by hood fans, vacuum pumps, passing traffic) or as a result of density gradients building up at the electrode surface because of differences in density between reactants and products (so-called "natural convection"). Convective effects can be minimized by using electrodes with glass mantles (shielded electrodes; Figure 8.3.3) and by orienting the electrode horizontally so that the denser species is always below the less dense one (15, 16). Vertically oriented electrodes (e.g., foils or wires) often suffer from convection effects even at not very long times (e.g., 60 to 80 s). The shielded electrode also has the virtue of constraining diffusion to lines normal to the electrode surface so that true linear diffusion conditions are approached. An unshielded electrode, such as a platinum disk imbedded in glass can show appreciable "sphericity" effects when the diffusion layer thickness is not negligible with respect to the electrode dimensions; that is, material can diffuse to the unshielded electrode from the sides. This effect causes increases in the transition time (or anomalously large currents in controlled-potential methods). With properly oriented shielded electrodes, however, linear diffusion conditions can be maintained for 300 s or longer.

▶ 8.4 REVERSAL TECHNIQUES

8.4.1 Response Function Principle

A useful technique for treating reversal methods in chronopotentiometry (and other techniques in electrochemistry) is based on the *response function principle* (2, 17). This method, which is also used to treat electrical circuits, considers the system's response to a perturbation or excitation signal, as applied in Laplace transform space. One can write the general equation (2)

$$\overline{R}(s) = \overline{\Psi}(s)\overline{S}(s) \tag{8.4.1}$$

where $\overline{\Psi}(s)$ is the excitation function transform, $\overline{R}(s)$ is the response transform, which describes how the system responds to the excitation, and $\overline{S}(s)$ is the system transform, which

connects the excitation and the response. For example for current excitation we can write, from (8.2.8) at $x = 0$,

$$\overline{C}_O(0, s) = C_O^*/s - [nFAD_O^{1/2}s^{1/2}]^{-1}\overline{i}(s) \qquad (8.4.2)$$

or

$$C_O^* - \overline{C}_O(0, s) = [nFAD_O^{1/2}s^{1/2}]^{-1}\overline{i}(s) \qquad (8.4.3)$$

In this case $\overline{\Psi}(s) = \overline{i}(s)$ (the transform of the applied current perturbation), $\overline{R}(s) = C_O^* - \overline{C}_O(0, s)$, the transform of the concentration response to the perturbation, and $\overline{S}(s) = [nFAD_O^{1/2}s^{1/2}]^{-1}$, which is characteristic of the system under excitation (semi-infinite linear diffusion). For controlled-current problems involving different systems (e.g., spherical or cylindrical diffusion, first-order kinetic complications) other system transforms would be employed.[2] We have illustrated how this equation could be employed for constant and programmed current methods, using appropriate $\overline{i}(s)$ functions. We now extend its use to reversal techniques.

8.4.2 Current Reversal (18, 19)

Consider a solution where only O is present initially at a concentration C_O^*, semi-infinite linear diffusion conditions prevail, and a constant cathodic current i is applied for a time t_1 (where $t_1 \leq \tau_1$, with τ_1 being the forward transition time). At t_1 the current is reversed, that is, the direction of the current is changed from cathodic to anodic, so that R formed during the forward step is oxidized to O, and the time τ_2 (measured from t_1) at which C_R at the electrode surface drops to zero is noted. At τ_2, the *reverse transition time*, the potential shows a rapid change toward positive values. We desire an expression for τ_2. This is most easily accomplished using the "zero shift theorem" of Section A.1.7. Since for $0 < t \leq t_1$, $i(t) = i$, and for $t_1 < t \leq t_1 + \tau_2$, $i(t) = -i$, the expression for the current, using step function notation, is

$$i(t) = i + S_{t_1}(t)(-2i) \qquad (8.4.4)$$

so that the transform is given by

$$\overline{i}(s) = \frac{i}{s} - \frac{(2e^{-t_1 s})i}{s} = \left(\frac{i}{s}\right)(1 - 2\,e^{-t_1 s}) \qquad (8.4.5)$$

Introducing this into (8.4.3), we obtain

$$\frac{C_O^*}{s} - \overline{C}_O(0, s) = \left(\frac{i}{s}\right)(1 - 2\,e^{-t_1 s})(nFAD_O^{1/2}s^{1/2})^{-1} \qquad (8.4.6)$$

The analogous expression for $\overline{C}_R(0, s)$ [see (8.2.9)] is

$$\overline{C}_R(0, s) = \left(\frac{i}{s}\right)(1 - 2\,e^{-t_1 s})(nFAD_R^{1/2}s^{1/2})^{-1} \qquad (8.4.7)$$

The inverse transform of (8.4.7) yields an expression for $C_R(0, t)$ at any time [recall that $S_{t_1}(t) = 0$ for $t \leq t_1$; $S_{t_1}(t) = 1$ for $t > t_1$; Section A.1.7]:

$$C_R(0, t) = \frac{2i}{nFA\pi^{1/2}D_R^{1/2}}[t^{1/2} - 2S_{t_1}(t)(t - t_1)^{1/2}] \qquad (8.4.8)$$

At $t = t_1 + \tau_2$, $C_R(0, t) = 0$, so that $(t_1 + \tau_2)^{1/2} = 2\tau_2^{1/2}$ and

$$\boxed{\tau_2 = t_1/3} \qquad (8.4.9)$$

---

[2]This approach, and transform methods in general, are useful only for linear problems; hence second-order reactions or nonlinear complications cannot be treated by this technique.
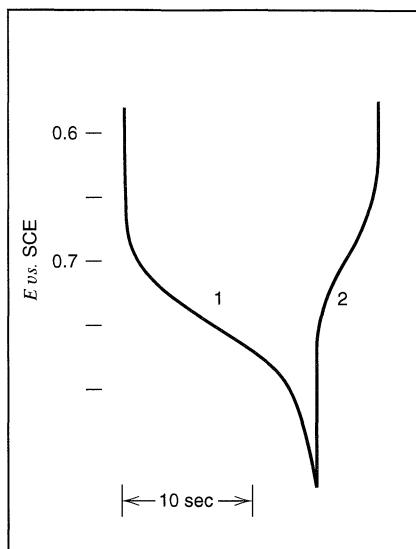
Figure 8.4.1 Typical experimental chronopotentiogram with current reversal. Oxidation of diphenylpicrylhydrazyl (DPPH) followed by reduction of the stable radical cation, $DPPH^{+}$. Solution was acetonitrile containing 1.04 mM DPPH and 0.1 M NaClO$_4$. The current was 100 μA, and a shielded platinum electrode of area 1.2 cm^2 was employed. [Reprinted with permission from E. Solon and A. J. Bard, *J. Am. Chem. Soc.*, **86**, 1926 (1964). Copyright 1964, American Chemical Society.]

Thus the reverse transition time (for stable R) is always 1/3 that of the forward time (Figure 8.4.1) up to and including τ_1, independent of D_O, D_R, C_O^*, and the rate of the electron transfer (assuming it is sufficiently rapid to show a reverse transition, that is, is not totally irreversible). The factor of 1/3 means that of the total amount of R generated during the forward step (equal to it_1/nF mol), only one-third returns to the electrode during the backward step up to τ_2, with the remainder diffusing into the bulk solution. At first thought, one might wonder at the independence of τ_2/t_1 on D_R. If D_R is very large, then a larger amount might be expected to diffuse away. However, a large D_R also implies that a larger amount will diffuse back during the reverse step, and the mathematics demonstrates that this exactly compensates for the diffusion away from the electrode. Thus the τ_2/t_1 ratio of 1/3 in chronopotentiometry is the analog of $i_r(2\tau)/i_f(\tau) = 0.293$ in potential step reversal (Section 5.7) and $i_{pc}/i_{pa} = 1.00$ in cyclic voltammetry (Section 6.5.1). Expressions can also be written for the potential-time behavior by combining the appropriate kinetic relationship with the equations for $C_O(0, t)$ and $C_R(0, t)$. For example, for a nernstian wave, $E_{0.215\tau_2} = E_{\tau/4}$. For a quasireversible system the separation between $E_{\tau/4}$ and $E_{0.215\tau_2}$ can be used to determine k^0 (20).

▶ 8.5 MULTICOMPONENT SYSTEMS AND MULTISTEP REACTIONS (19, 21–23)

Consider a solution containing two reducible substances, O_1 and O_2, at concentrations C_1^* and C_2^*, respectively, where the reduction $O_1 + n_1e \rightarrow R_1$ occurs first, and then, at more negative potentials, $O_2 + n_2e \rightarrow R_2$. Again, assuming semi-infinite linear diffusion, the following response-function equations can be written:

$$n_1FAD_1^{1/2}\left[\frac{C_1^*}{s} - \overline{C}_1(0, s)\right] = \frac{\overline{i}_1(s)}{s^{1/2}} \tag{8.5.1}$$

$$n_2FAD_2^{1/2}\left[\frac{C_2^*}{s} - \overline{C}_2(0, s)\right] = \frac{\overline{i}_2(s)}{s^{1/2}} \tag{8.5.2}$$

where $\bar{i}_1(s)$ and $\bar{i}_2(s)$ are the transforms of the individual currents [$i_1(t)$ and $i_2(t)$] involved in the reduction of O_1 and O_2, respectively. Since the total applied current, $i(t)$, is $i_1(t) + i_2(t)$, then $\bar{i}(s) = \bar{i}_1(s) + \bar{i}_2(s)$, and from (8.5.1) and (8.5.2),

$$n_1 D_1^{1/2}\left[\frac{C_1^*}{s} - \overline{C}_1(0, s)\right] + n_2 D_2^{1/2}\left[\frac{C_2^*}{s} - \overline{C}_2(0, s)\right] = \frac{\bar{i}(s)}{FAs^{1/2}} \tag{8.5.3}$$

This equation is true at all times.

For the period when the potential is not sufficiently negative for O_2 reduction to occur (i.e., when $t \leq \tau_1$), $\overline{C}_2(0, s) = C_2^*/s$, $\bar{i}_2(s) = 0$, and (8.5.3) becomes identical to the simple equation (8.4.3), so that up to τ_1 the behavior is unaffected by the presence of O_2. For $t > \tau_1$, $\overline{C}_1(0, s) = 0$, so that (8.5.3) becomes

$$\frac{n_1 D_1^{1/2} C_1^*}{s} + n_2 D_2^{1/2}\left[\frac{C_2^*}{s} - \overline{C}_2(0, s)\right] = \frac{\bar{i}(s)}{FAs^{1/2}} \tag{8.5.4}$$

The second transition time ($t = \tau_1 + \tau_2$) occurs when the concentration of O_2 drops to zero at the electrode surface, that is, $\overline{C}_2(0, s) = 0$. Thus, for a constant current, $\bar{i}(s) = i/s$, and (8.5.4) for this time becomes

$$\frac{n_1 D_1^{1/2} C_1^*}{s} + \frac{n_2 D_2^{1/2} C_2^*}{s} = \frac{i}{FAs^{3/2}} \tag{8.5.5}$$

Inversion yields

$$\boxed{(n_1 D_1^{1/2} C_1^* + n_2 D_2^{1/2} C_2^*)\left(\frac{FA\pi^{1/2}}{2}\right) = i(\tau_1 + \tau_2)^{1/2}} \tag{8.5.6}$$

For example, for the special case $n_1 D_1^{1/2} C_1^* = n_2 D_2^{1/2} C_2^*$, $\tau_2 = 3\tau_1$. Thus, while in controlled-potential voltammetric methods two substances at equal concentration with equal diffusion coefficients show two waves of equal height, in chronopotentiometry unequal transition times arise. The long second transition results from the continued diffusion of O_1 to the electrode after τ_1, so that only a fraction of the applied current is available for reduction of O_2 (Figure 8.5.1).

Similar reasoning shows that for a stepwise process:

$$O + n_1 e \rightarrow R_1 \tag{8.5.7}$$

$$R_1 + n_2 e \rightarrow R_2 \tag{8.5.8}$$
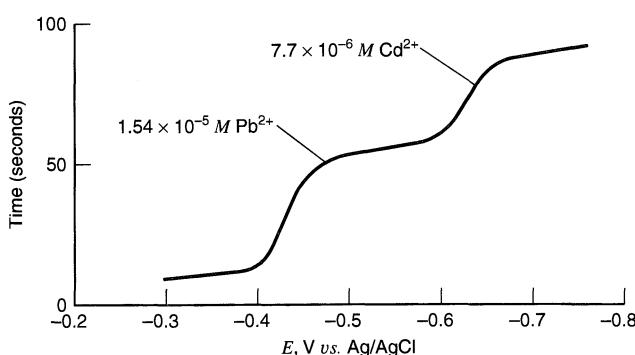
Figure 8.5.1 Consecutive reduction of Pb(II) and Cd(II) at a mercury pool electrode. Note that if E-t curve is plotted in this manner, it resembles a voltammogram. [Reprinted with permission from C. N. Reilley, G. W. Everett, and R. H. Johns, *Anal. Chem.*, **27**, 483 (1955). Copyright 1955, American Chemical Society.]
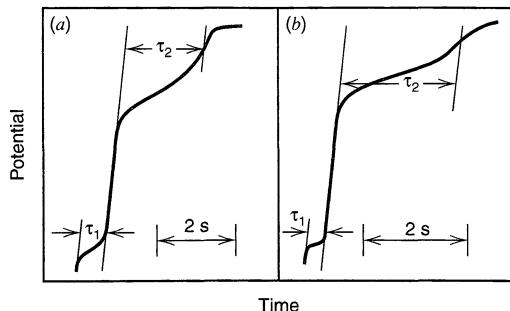
Figure 8.5.2 *E-t* curves for stepwise reduction of oxygen and uranyl ion at mercury electrode. (*a*) 1 *M* LiCl solution saturated with oxygen at 25°C. $O_2 + 2H_2O + 2e \rightarrow H_2O_2 + 2OH^-$; $H_2O_2 + 2e \rightarrow 2OH^-$; $\tau_2/\tau_1 \approx 3$. (*b*) 10^{-3} *M* uranyl nitrate in 0.1 *M* KCl + 0.01 *M* HCl. $U(VI) + e \rightarrow U(V)$; $U(V) + 2e \rightarrow U(III)$; $\tau_2/\tau_1 \approx 8$. [Reprinted with permission from T. Berzins and P. Delahay, *J. Am. Chem. Soc.*, **75**, 4205 (1953). Copyright 1953, American Chemical Society.]

the transition time ratio is given by

$$\frac{\tau_2}{\tau_1} = \frac{2n_2}{n_1} + \left(\frac{n_2}{n_1}\right)^2 \tag{8.5.9}$$

Thus for $n_2 = n_1$, $\tau_2 = 3\tau_1$ (Figure 8.5.2). By use of the response-function principle one can show (Problem 8.4) that if a current of the form $i(t) = \beta t^{1/2}$ is used, then equal transition times result when $n_2 = n_1$.

▶ 8.6 THE GALVANOSTATIC DOUBLE PULSE METHOD

In Section 8.3.4, we saw that the single-pulse galvanostatic method cannot be used for fast electron-transfer reactions (i.e., those with large i_0), because the current is primarily nonfaradaic during the initial moments following the application of the current step, and it contributes mostly to charging C_d. Gerischer and Krause (24) developed a *galvanostatic double pulse method* (GDP), in which two constant-current pulses are applied to the electrode (Figure 8.6.1). The first (large) pulse I_1, applied for $0 < t < t_1$, mainly serves to charge the double layer to a potential that becomes the point of interrogation by a second, smaller pulse of current i_2. The basic idea is to use the short first pulse (typically 0.5 to 1 μs long) to drive the system to an overpotential that exactly supports the second current. Then η will not change when i_2 is applied, and there is no significant effect from charging the double layer during the second phase. A block diagram of apparatus for this technique is shown in Figure 8.6.2.

Some faradaic current does flow during the first pulse, and its effects must be taken into account. The theory of the GDP method was extended along that line by Matsuda, et al. (25). Valuable instrumental advances were later made by Aoyagi and coworkers (26–28).
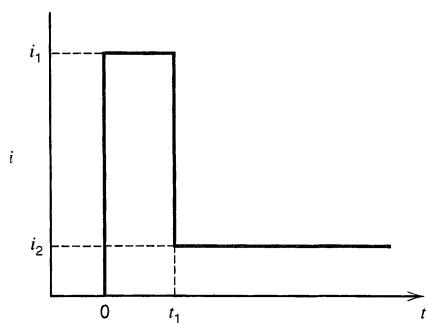
Figure 8.6.1 Excitation waveform for the galvanostatic double pulse method.
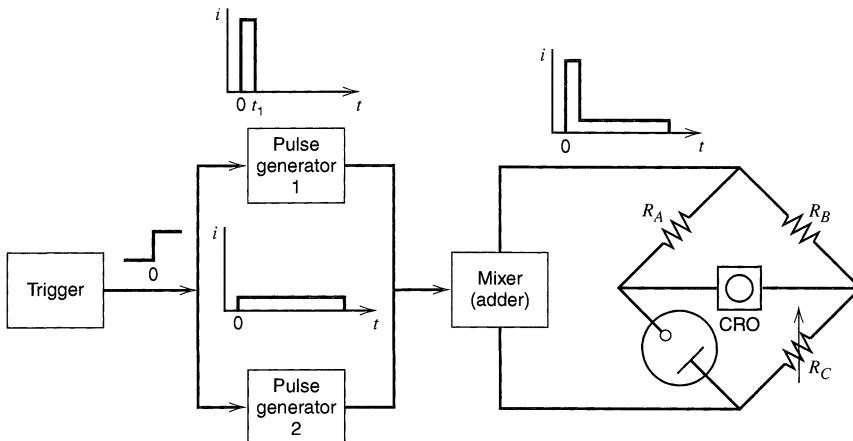
Figure 8.6.2   Block diagram for galvanostatic double-pulse method. A two-electrode cell (i.e., with a common counter/reference electrode) is placed in a bridge circuit for compensation of the cell ohmic resistance, R_Ω. The bridge is adjusted with $R_A = R_B$, $R_C = R_\Omega$, $R_A \gg R_\Omega$ so that the pulse generators produce an essentially constant current through the cell. Provision is sometimes made in double pulse circuits, however, for a three-electrode cell and potentiostatic control of the working electrode before the application of the galvanostatic pulse. For details of such apparatus, see references 26–28.

When the ratio of pulse heights (i_1/i_2) is adjusted properly, and this is determined by trial and error, the E-t curve following the cessation of the first pulse is horizontal (Figure 8.6.3). Under these conditions, the overpotential for a quasireversible one-step, one-electron process is given by (25)

$$-\eta = \frac{RT}{F}\frac{i_2}{i_0}\left[1 + \frac{4Ni_0}{3\pi^{1/2}}t_1^{1/2} + \left(1 - \frac{9\pi}{32}\right)\left(\frac{4Ni_0}{3\pi^{1/2}}\right)^2 t_1 + \ldots \right] \qquad (8.6.1)$$

(a)   (b)
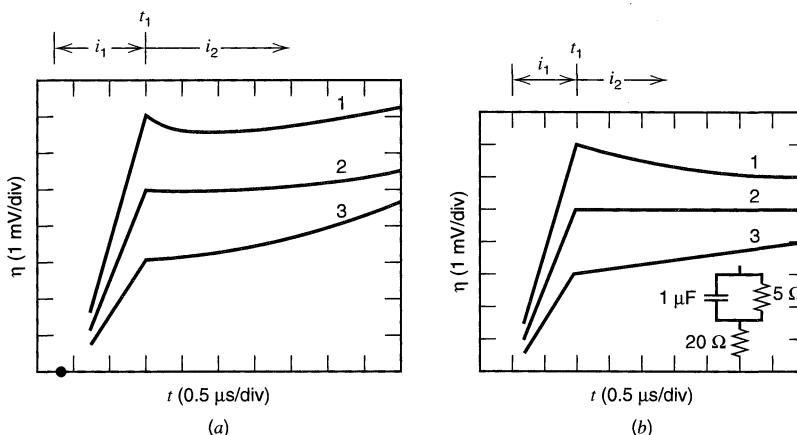
Figure 8.6.3   (a) Overpotential-time traces for galvanostatic double-pulse method for reduction of 0.25 mM Hg$_2^{2+}$ in 1 M HClO$_4$ at an HMDE. Ratio i_2/i_1 was (1) 7.8, (2) 5.3, (3) 3.2; (2) shows the desired response for utilization of (8.6.2). (b) Voltage-time traces for constant-current double pulses applied to equivalent circuit shown. i_1 was (1) 7.6, (2) 5.5, (3) 3.3 mA; and $i_2 = 1$ mA. [From M. Kogoma, T. Nakayama, and S. Aoyagi, *J. Electroanal. Chem.*, **34**, 123 (1972), with permission.]

or, at sufficiently small values of t_1,

$$-\eta \approx \frac{RT}{F} i_2 \left(\frac{1}{i_0} + \frac{4N}{3\pi^{1/2}} t_1^{1/2} \right) \qquad (8.6.2)$$

Thus one can carry out a series of experiments with different pulse widths t_1, and plot the value of η at the onset of i_2 vs. $t_1^{1/2}$ to obtain the exchange current from the intercept. Note the similarity between (8.3.10) and (8.6.2). The $t^{1/2}$ term in each case accounts for electrolytic modification of the surface concentrations. In the situation yielding (8.3.10), η was induced by current i; but in this case it is first induced by i_1 and then supported by i_2.

The differential double-layer capacitance can also be obtained from these data by the equation:

$$C_d = \lim_{t_1 \to 0} \frac{Ft_1 i_0}{RTA} \left(\frac{i_1}{i_2} \right) \left(1 - \frac{4Ni_0 t_1^{1/2}}{3\pi^{1/2}} \right)^{-1} \qquad (8.6.3)$$

This relation rests on the idea that the total charge in the first step, $i_1 t_1$, is purely non-faradaic in the limit of very short t_1.

The GDP method does not require knowledge of the diffusion coefficients for reactant and products, or of the C_d value, for the calculation of i_0. Measurements using instrumentation developed by Aoyagi and coworkers suggest that rate constants of very rapid electrode reactions (~ 1 cm/s) can be determined using this technique.

▶ 8.7 CHARGE STEP (COULOSTATIC) METHODS

8.7.1 Principles

In the *charge-step* (or *coulostatic*) *method*, a very short-duration (e.g., 0.1 to 1 μs) current pulse is applied to the cell, and the variation of the electrode potential with time after the pulse (i.e., at open circuit) is recorded. The length of the current pulse is chosen to be sufficiently short that it causes only charging of the electrical double layer, so that even a very fast charge-transfer reaction does not proceed to an appreciable extent during this time. The pulse then serves only to inject a charge increment, Δq, and, in fact, under these conditions the method of charge injection or the actual shape of the injecting pulse (the coulostatic impulse) is unimportant. For example, the charge can be injected by discharging a small capacitor across the electrochemical cell (Figure 8.7.1) or with a pulse generator connected to the cell by a capacitor or switching diodes.
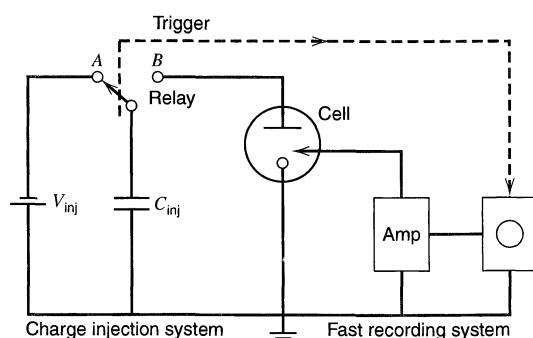
Figure 8.7.1 Circuit for charge-step or coulostatic method. In practice, the cell may be held initially at a potential E_{eq} by means of a potentiostat that is disconnected immediately before the charge injection.

For the circuit in Figure 8.7.1, when the relay is in position A, the capacitor, C_{inj}, is charged by the voltage source, V_{inj}, until the capacitor is charged by an amount

$$\Delta q = C_{inj} V_{inj} \qquad (8.7.1)$$

For example, for $V_{inj} = 10$ V and $C_{inj} = 10^{-9}$ F, $\Delta q = 0.01~\mu C$. When the relay switches to position B the charge is delivered to the electrochemical cell. Because the double-layer capacitance, C_d, is much larger than C_{inj}, essentially all of the charge will flow into the cell. The time required for this charge injection will depend on the cell resistance, R_Ω (Figure 8.7.2), with the time constant for injection being essentially $C_{inj} R_\Omega$ (Problem 8.6). This injected charge causes the potential of the electrode to deviate from its original value E_{eq} to a value $E(t = 0)$, where

$$E(t = 0) - E_{eq} = \eta(t = 0) = \frac{-\Delta q}{C_d} \qquad (8.7.2)$$

The charge on C_d now discharges through the faradaic impedance (i.e., the heterogeneous electron-transfer process), and the open circuit potential moves back toward E_{eq} as $\eta(t)$ decreases to zero. Since the total external current i is zero, we have from (8.3.11) and (8.3.12),

$$i_f = -i_c = C_d\left(\frac{d\eta}{dt}\right) \qquad (8.7.3)$$

or

$$\eta(t) = \eta(t = 0) + \frac{1}{C_d}\int_0^t i_f \, dt \qquad (8.7.4)$$

Solution of (8.7.4) with the appropriate expression for i_f yields the desired expression for the variation of E (or η) with t. Note that if no faradaic reaction is possible at $E(t = 0)$ (i.e., at an ideally polarized electrode), C_d remains charged and the potential will not decay [i.e., for $i_f = 0$, $E = E_{eq} + \eta(t = 0)$ at all t].

We will now examine the E-t behavior following a coulostatic impulse for several cases of interest. Details of the theoretical treatments have been given by Delahay (29, 30) and Reinmuth (31, 32) and their coworkers, who first described the application of this technique.

(a)

(b)
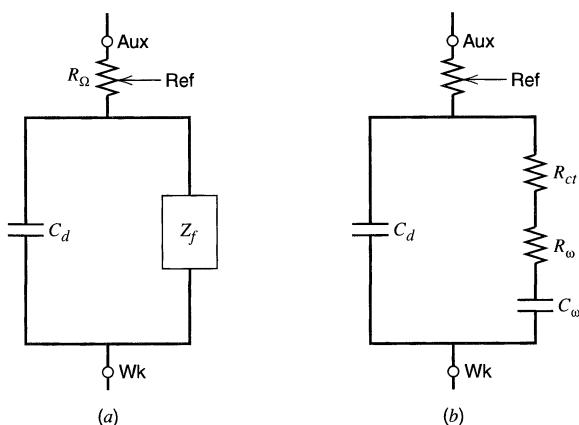
Figure 8.7.2 Equivalent circuit of cell with (a) R_Ω, the solution resistance, C_d, the double-layer capacitance, and Z_f, the faradaic impedance. The faradaic impedance represents the effect of the heterogeneous electron-transfer process. Often Z_f is broken down into the components shown in (b), where the charge-transfer resistance R_{ct} manifests the kinetics of heterogeneous charge transfer, and the components of the Warburg impedance, R_w and C_w, manifest diffusional mass transfer (see Section 10.1.3).

8.7.2 Small-Signal Analysis

When a chemically reversible, but kinetically sluggish, system is being investigated and the potential excursion is sufficiently small, that is, when $\eta(t = 0) << RT/nF$ and mass-transfer effects are absent, one can use the linearized $i\text{-}\eta$ relation, (3.5.49),

$$-\eta = \frac{RT}{nFi_0} i \tag{8.7.5}$$

to describe i_f in (8.7.4). Thus,

$$\eta(t) = \eta(t = 0) - \frac{nFi_0}{RTC_d} \int_0^t \eta(t)dt \tag{8.7.6}$$

This equation can be solved readily by the Laplace transform method (Problem 8.7) to yield

$$\eta(t) = \eta(t = 0) \exp\left(\frac{-t}{\tau_c}\right) \tag{8.7.7}$$

$$\tau_c = \frac{RTC_d}{nFi_0} = R_{ct}C_d \tag{8.7.8}$$

Thus under these conditions, the potential relaxes exponentially toward E_{eq} with a time constant τ_c, governed by the rate of the charge-transfer reaction (Figure 8.7.3). This result can also be obtained from the equivalent circuit in Figure 8.7.2b by noting that R_w and C_w are negligible, so that C_d discharges only through the charge-transfer resistance R_{ct}, given by (3.5.50), with a time constant C_dR_{ct}. When (8.7.7) holds, a plot
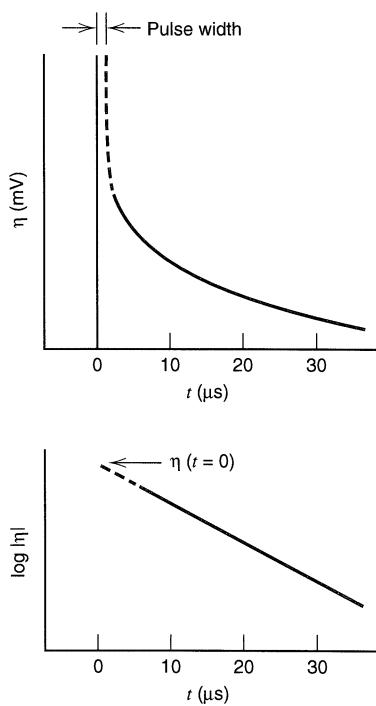
Figure 8.7.3 Typical coulostatic relaxation curves for a totally irreversible reaction.

of $\ln |\eta|$ vs. t is linear with an intercept $|\eta(t = 0)|$ [which can be used to determine C_d by (8.7.2)] and a slope $-1/\tau_c$, which yields the charge-transfer resistance and the exchange current.

On the other hand, when R_{ct} is negligible compared to the mass-transfer impedance, which is the case for a nernstian system, the following expression applies:

$$\eta(t) = \eta(t = 0) \exp\left(\frac{t}{\tau_D}\right) \text{erfc}\left[\left(\frac{t}{\tau_D}\right)^{1/2}\right] \tag{8.7.9}$$

$$\tau_D^{1/2} = \frac{RTC_d}{n^2F^2}\left(\frac{1}{C_O^*D_O^{1/2}} + \frac{1}{C_R^*D_R^{1/2}}\right) \tag{8.7.10}$$

The general small-signal expression for the case where both charge and mass-transfer terms are significant is (32)

$$\boxed{\eta(t) = \frac{\eta(t = 0)}{\gamma - \beta}\left[\gamma \exp(\beta^2 t) \text{erfc}(\beta t^{1/2}) - \beta \exp(\gamma^2 t) \text{erfc}(\gamma t^{1/2})\right]} \tag{8.7.11}$$

$$\boxed{\beta, \gamma = \frac{\tau_D^{1/2}}{2\tau_c} \pm \frac{(\tau_D/4\tau_c) - 1]^{1/2}}{\tau_c^{1/2}}} \tag{8.7.12}$$

(where the + is associated with β and the − with γ). Note that $\beta + \gamma = \tau_D^{1/2}/\tau_c$ and $\beta\gamma = 1/\tau_c$.

Clearly the analysis of experimental data for the determination of i_0 is easiest when (8.7.7) applies; this requires that $\tau_c \gg \tau_D$. Detailed discussions of the analysis of coulostatic data and relaxation curves have appeared (33, 34).

8.7.3 Large Steps—Coulostatic Analysis

Consider the application of a charge step sufficiently large that the potential changes from E_{eq} to a value, $E(t = 0)$, corresponding to the diffusion plateau of the voltammetric wave. We assume that the double-layer capacity, C_d, is independent of potential in this region. The faradaic current that flows under these conditions at a planar electrode is given by (5.2.11). Introduction of this expression into (8.7.4) yields

$$E(t) = E(t = 0) + \left(\frac{nFAD_O^{1/2}C_O^*}{\pi^{1/2}C_d}\right)\int_0^t t^{-1/2} dt \tag{8.7.13}$$

$$\boxed{\Delta E = E(t) - E(t = 0) = \frac{2nFAD_O^{1/2}C_O^*t^{1/2}}{\pi^{1/2}C_d}} \tag{8.7.14}$$

The sign of ΔE is positive, since the electrode relaxes from a more negative initial potential toward more positive values. A plot of ΔE vs. $t^{1/2}$ is linear with a zero intercept and a slope $2nFAD_O^{1/2}C_O^*/(\pi^{1/2}C_d)$, which is proportional to the solution concentration (Figure 8.7.4).

This method has been suggested for the determination of small concentrations of electroactive materials (35, 36), but it has not been widely applied, probably because it requires recording of the E-t curve and is less readily automated than, for example, pulse voltammetry.
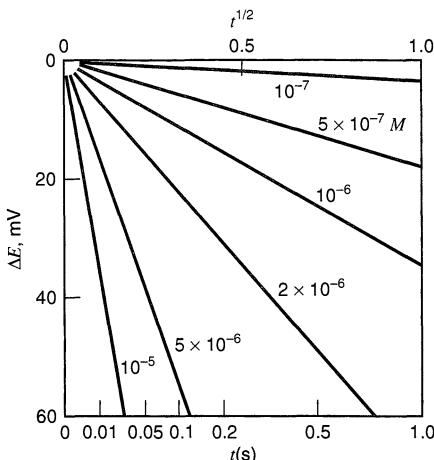
Figure 8.7.4 ΔE *vs. t* curves for a planar electrode for several values of C_O^*, with $n = 2$, $D = 10^{-5} cm^2/s$, and $C_d = 20 \, \mu F/cm^2$. [Reprinted with permission from P. Delahay, *Anal. Chem.*, **34**, 1267 (1962). Copyright 1962, American Chemical Society.]

The technique can also be extended to cover large potential excursions to the rising portion of the voltammetric wave. For example, for a reversible process, the appropriate equation for the faradaic current would be (5.4.16), as long as measurements are made at small ΔE values so that E remains close to $E(t = 0)$ and the surface concentrations do not change appreciably during the measurement. A plot of the slope of the ΔE *vs.* $t^{1/2}$ curve at any potential *vs.* E then yields a charge-step voltammogram that resembles an ordinary voltammogram (37). Because the coulostatic method requires the determination of a slope at each data point, incremental changes in Δq to cause changes in potential, and renewal of initial conditions before each step, it requires digital computer control and data acquisition.

8.7.4 Application of Charge-Step Methods

The charge-step or coulostatic methods described here have some advantages in the study of electrode reactions. Since the measurement is made at open circuit with no net external current flow, the ohmic drop is not of importance and measurements can be made in highly resistive media. Moreover, because the relaxation occurs by discharge of the double-layer capacitance, the usual competition between faradaic and charging current is replaced by an equality of i_c and i_f, and C_d no longer interferes in the measurement. However, some fundamental limitations still exist in charge-step measurements. High values of R_Ω increase the time required to deliver charge to the cell. Also, the high voltage, V_{inj}, appears across the cell at the instant of charge injection and tends to overload the measuring amplifier, which must be adjusted to a high sensitivity to determine the small changes in ΔE. An amplifier capable of rapid recovery from overloads is required, and parasitic oscillations caused by stray capacitance and unmatched impedances generally occur following the pulse. Thus, in general, measurements cannot be made for a time interval of about 0.5 μs following the pulse. The technique appears to be useful for the determination of i_0 values up to about 0.1 A/cm^2 or k^0 values up to 0.4 cm/s. A discussion of the experimental conditions and reviews of applications of charge-step methods have appeared (34, 38).

8.7.5 Coulostatic Perturbation by Temperature Jump

The potential of an electrode can be perturbed in a manner directly analogous to the coulostatic approach described above by an abrupt change in a variable other than charge,

such as the pressure or solution composition, that will shift the electrode from equilibrium. Probably the most straightforward way of doing this is by changing the electrode temperature (i.e., by a temperature jump) (39–42). This is conveniently effected by using a thin (e.g., 1–25 μm) metal film on a dielectric like glass and irradiating the film from the backside (through the dielectric) with a pulsed laser (41, 42). The film is sufficiently thick that no light penetrates the film and all of the absorbed light is converted to heat. Under these conditions photoemission of electrons into the solution (39, 40), as discussed in Section 18.3.1, does not occur. A schematic diagram of the apparatus used is shown in Figure 8.7.5. By using a fast laser and thin metal film, measurements in the nanosecond domain are possible.

The rapid temperature change of the electrode perturbs the equilibrium at the electrode–solution interface and causes a change in the potential of the electrode measured with respect to a reference electrode. The change in the open-circuit potential, ΔE_t, and its relaxation with time are used to obtain kinetic information about the electrode reaction. A number of different phenomena come into play to cause the potential shift with temperature (e.g., temperature dependence of the double-layer capacitance and the Soret potential arising from the temperature gradient between the electrode and the bulk electrolyte), but the response can be treated by a general master equation (40):

$$\Delta E_t = a\Delta T_t^* + k_\mathrm{m} b \int_0^t \exp[-k_\mathrm{m}(t - \tau)] \, \Delta T_\tau^* \, d\tau \qquad (8.7.15)$$

where ΔT_t^* is the temperature change normalized by a factor that accounts for heat losses and temperature distribution, $a\Delta T_t^*$ represents the initial potential response in the absence of interfacial electron transfer, and the second term accounts for the electron-transfer relaxation and its associated rate constant, k_m. The time dependence of the temperature change can be treated by a least-squares procedure to extract values of a, b, and k_m. This approach has been used, for example, to measure the effect of alkyl chain length in a mixed organized film of alkyl thiols, some with ferrocene terminations (see Section 14.5.2), on the rate of electron transfer from the ferrocene moiety, where k_m values on the order of 10^7–10^8 s^{-1} were found (43).
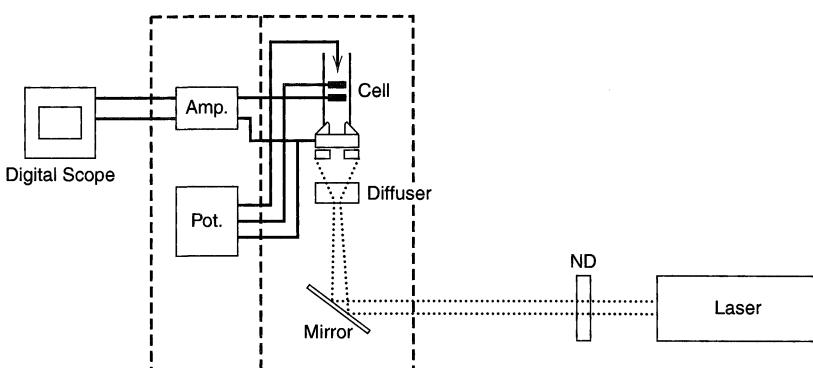
Figure 8.7.5 Schematic diagram of apparatus employed for the temperature-jump method. The laser pulse is passed through a neutral density filter (ND) and irradiates the thin film electrode at the bottom of the cell. The dark rectangles are an auxiliary electrode and a QRE for measurement of the potential change. The potentiostat (Pot.), which adjusts the electrode potential before irradiation, is disconnected immediately before the laser pulse. The change in potential is measured with a fast amplifier (Amp.). [Reprinted from J. F. Smalley, L. Geng, S. W. Feldberg, L. C. Rogers, and J. Leddy, *J. Electroanal. Chem.*, **356**, 181 (1993), with permission from Elsevier Science.]

▷ **8.8 REFERENCES**

1. H. J. S. Sand, *Phil. Mag.*, **1**, 45 (1901).

2. R. W. Murray and C. N. Reilley, *J. Electroanal. Chem.*, **3**, 64, 182 (1962).

3. A. Molina, *Curr. Top. Electrochem.* **3**, 201 (1994).

4. Z. Karaoglanoff, *Z. Elektrochem.*, **12**, 5 (1906).

5. P. Delahay and T. Berzins, *J. Am. Chem. Soc.*, **75**, 2486 (1953).

6. L. B. Anderson and D. J. Macero, *Anal. Chem.*, **37**, 322 (1965).

7. Y. Okinaka, S. Toshima, and H. Okaniwa, *Talanta*, **11**, 203 (1964).

8. P. Delahay and T. Berzins, *J. Chem. Phys.*, **23**, 972 (1955); *J. Am. Chem. Soc.*, **77**, 6448 (1955); *Z Elektrochem.*, **59**, 792 (1955).

9. J. J. Lingane, *J. Electroanal. Chem.*, **1**, 379 (1960).

10. A. J. Bard, *Anal. Chem.*, **35**, 340 (1963).

11. P. E. Sturrock, G. Privett, and A. R. Tarpley, *J. Electroanal. Chem.*, **14**, 303 (1967).

12. W. T. de Vries, *J. Electroanal. Chem.*, **17**, 31 (1968).

13. R. S. Rodgers and L. Meites, *J. Electroanal. Chem.*, **16**, 1 (1968).

14. M. L. Olmstead and R. S. Nicholson, *J. Phys. Chem.*, **72**, 1650 (1968).

15. A. J. Bard, *Anal. Chem.*, **33**, 11 (1961).

16. H. A. Laitinen and I. M. Kolthoff, *J. Am Chem. Soc.*, **61**, 3344 (1939).

17. H. B. Herman and A. J. Bard, *Anal. Chem.*, **35**, 1121 (1963).

18. A. C. Testa and W. H. Reinmuth, *Anal. Chem.*, **33**, 1320, 1324 (1961).

19. T. Berzins and P. Delahay, *J. Am. Chem. Soc.*, **75**, 4205 (1953).

20. F. H. Beyerlein and R. S. Nicholson, *Anal. Chem.*, **40**, 286 (1968).

21. P. Delahay and G. Mamantov, *Anal. Chem.*, **27**, 478 (1955).

22. C. N. Reilley, G. W. Everett, and R. H. Johns, *Anal. Chem.*, **27**, 483 (1955).

23. H. B. Herman and A. J. Bard, *Anal. Chem.*, **36**, 971 (1964).

24. H. Gerischer and M. Krause, *Z. Physik. Chem.*, N.F., **10**, 264 (1957); **14**, 184 (1958).

25. H. Matsuda, S. Oka, and P. Delahay, *J. Am. Chem. Soc.*, **81**, 5077 (1959).

26. M. Kogoma, T. Nakayama, and S. Aoyagi, *J. Electroanal. Chem.*, **34**, 123 (1972).

27. T. Rohko, M. Kogoma, and S. Aoyagi, *J. Electroanal. Chem.*, **38**, 45 (1972).

28. M. Kogoma, Y. Kanzaki, and S. Aoyagi, *Chem. Instr.*, **7**, 193 (1976).

29. P. Delahay, *J. Phys. Chem.*, **66**, 2204 (1962); *Anal. Chem.*, **34**, 1161 (1962).

30. P. Delahay and A. Aramata, *J. Phys. Chem.*, **66**, 2208 (1962).

31. W. H. Reinmuth and C. E. Wilson, *Anal. Chem.*, **34**, 1159 (1962).

32. W. H. Reinmuth, *Anal. Chem.*, **34**, 1272 (1962).

33. J. M. Kudirka, P. H. Daum, and C. G. Enke, *Anal. Chem.*, **44**, 309 (1972).

34. H. P. van Leeuwen, *Electrochim. Acta*, **23**, 207 (1978).

35. P. Delahay, *Anal. Chem.*, **34**, 1267 (1962).

36. P. Delahay and Y. Ide, *Anal. Chem.*, **34**, 1580 (1962).

37. J. M. Kudirka, R. Abel, and C. G. Enke, *Anal. Chem.*, **44**, 425 (1972).

38. H. P. van Leeuwen, *Electroanal. Chem.*, **12**, 159 (1982).

39. V. A. Benderskii, S. D. Babenko, and A. G. Krivenko, *J. Electroanal. Chem.*, **86**, 223 (1978).

40. V. A. Benderskii, I. O. Efimov, and A. G. Krivenko, *J. Electroanal. Chem.*, **315**, 29 (1991).

41. J. F. Smalley, C. V. Krishnan, M. Goldman, S. W. Feldberg, and I. Ruzic, *J. Electroanal. Chem.*, **248**, 255 (1988).

42. J. F. Smalley, L. Geng, S. W. Feldberg, L. C. Rogers, and J. Leddy, *J. Electroanal. Chem.*, **356**, 181 (1993).

43. J. F. Smalley, S. W. Feldberg, C. E. D. Chidsey, M. R. Linford, M. D. Newton, and Y. P. Liu, *J. Phys. Chem.*, **99**, 13141 (1995).
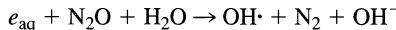
▷ **8.9 PROBLEMS**

8.1 Derive equation 8.3.13 under the assumptions given in the text.

8.2 For current reversal chronopotentiometry involving the forward reduction of a species O under conditions of semi-infinite linear diffusion, the reverse transition time can be made equal to forward

electrolysis time by a proper choice of currents during the forward (reduction) reaction, i_f, and the reverse (oxidation) reaction, i_r. Find the ratio i_f/i_r that will yield, $\tau_r = t_f$.

8.3 An analyst determines a mixture of lead and cadmium at a mercury pool cathode by chronopotentiometry. In the cell used in the determination, a 1.00 mM solution of Pb^{2+} reduced at a current of 273 mA yielded $\tau = 25.9$ s and $E_{\tau/4} = -0.38$ V $vs.$ SCE. A 0.69 mM solution of Cd^{2+} reduced with a current of 136 mA gave $\tau = 42.0$ s and $E_{\tau/4} = -0.56$ V $vs.$ SCE. An unknown mixture of Pb^{2+} and Cd^{2+} reduced at a current of 56.5 mA produced a double wave, with $\tau_1 = 7.08$ s and $\tau_2 = 7.00$ s. Calculate the concentrations of Pb^{2+} and Cd^{2+} in the mixture. Neglect double-layer and other background effects.

8.4 Show that if one uses programmed current chronopotentiometry with $i(t) = \beta t^{1/2}$, then the stepwise reduction of a substance with $n_1 = n_2$ gives $\tau_1 = \tau_2$.

8.5 Examine the results in Figure 8.4.1. Estimate the transition times and work up the data to yield information about the electrode reaction.

8.6 Consider the circuit in Figure 8.9.1, which is characteristic of that used for the injection of charge in a coulostatic experiment. C_{inj} is initially charged completely with a 10-V battery. At equilibrium, after the switch is closed, how much charge will reside on C_d and on C_{inj}? About how long will it take to charge C_d?

8.7 Solve (8.7.6) by the Laplace transform method to yield (8.7.7).

8.8 Derive the equation for the large-step coulostatic response in the diffusion limited region, analogous to (8.7.14), for a spherical indicator electrode.

8.9 Consider a 1 mM solution of cadmium in 0.1 M HCl, which is being examined coulostatically at a hanging mercury drop 0.05 cm^2 in area. The formal potential for the $Cd^{2+}/Cd(Hg)$ couple is -0.61 V $vs.$ SCE. Suppose the electrode is initially at rest at -0.4 V $vs.$ SCE, then a sufficient charge is applied to shift its potential instantaneously to -1.0 V $vs.$ SCE. Assume the differential and integral double-layer capacitances to be 10 $\mu F/cm^2$. How much charge is required for the initial potential excursion? How long would it take for the potential to fall back to -0.9 V after the charge injection? Take $D = 10^{-5}$ cm^2/s.

8.10 Barker et al. [*Faraday Disc. Chem. Soc.*, **56**, 41 (1974)] performed experiments in which 15-ns pulses from a frequency-doubled ruby laser were used to illuminate a mercury pool working electrode. Each light pulse caused ejection of electrons from the electrode. Ejected electrons seem to travel about 50 Å before becoming solvated and available for reaction.

When electrons are emitted into a solution of N_2O in water containing 1 M KCl, the following reaction occurs:

$$e_{aq} + N_2O + H_2O \rightarrow OH\cdot + N_2 + OH^-$$

The hydroxyl radicals are easily reduced at the electrode at potentials more negative than -1.0 V $vs.$ SCE.
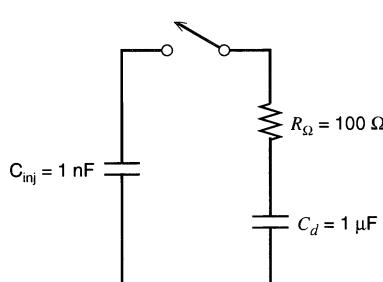
Figure 8.9.1
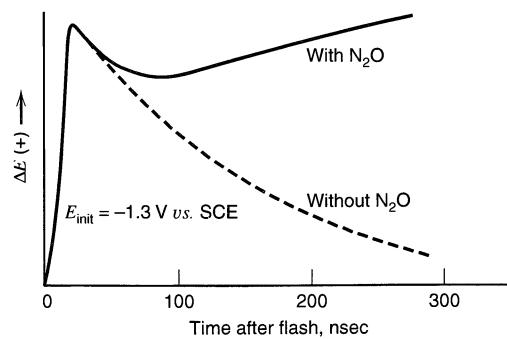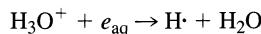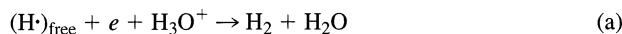
Figure 8.9.2

The response of the illuminated working electrode to the flash is followed coulostatically. Curves like those shown in Figure 8.9.2 can be obtained. Explain their shapes. ΔE is measured with respect to the initial potential.
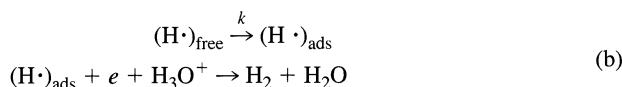
8.11 Barker's technique (Problem 8.10) can also be used to create hydrogen atoms and to study their electrochemistry. The reaction producing them in acid media is

$$H_3O^+ + e_{aq} \rightarrow H\cdot + H_2O$$

Investigators studying the hydrogen discharge reaction have often suggested that H· is an intermediate and that hydrogen gas is produced by reducing it further in a fast heterogeneous process:

$$(H\cdot)_{free} + e + H_3O^+ \rightarrow H_2 + H_2O \tag{a}$$

or

$$(H\cdot)_{free} \overset{k}{\rightarrow} (H\cdot)_{ads}$$
$$(H\cdot)_{ads} + e + H_3O^+ \rightarrow H_2 + H_2O \tag{b}$$

Whether H· is free or adsorbed has been debated. Barker addressed the question by comparing, in effect, the rate of H· electroreduction to the rate of its homogeneous reaction with ethanol (leading to electroinactive products). He found [*Ber. Bunsenges. Phys. Chem.*, **75**, 728 (1971)] that the fraction of H· undergoing electroreduction was independent of potential from -0.9 V to -1.3 V *vs.* SCE. What do his observations tell us about the choice between (a) and (b)?

9

METHODS INVOLVING FORCED CONVECTION— HYDRODYNAMIC METHODS

9.1 INTRODUCTION

There are many electrochemical techniques in which the electrode moves with respect to the solution. These involve systems where the electrode is itself in motion (e.g., rotating disks, rotating wires, streaming mercury electrodes, rotating mercury electrodes, vibrating electrodes) or ones where there is forced solution flow past a stationary electrode (conical, tubular, screen, and packed-bed electrodes in fluid streams, channel electrodes, bubbling electrodes). Indeed the DME is actually such a system, but was treated as a stationary electrode by the approximate method described in Chapter 7. Methods involving convective mass transport of reactants and products are sometimes called *hydrodynamic* methods; for example, the techniques involving measurement of limiting currents or *i-E* curves are called *hydrodynamic amperometry* and *voltammetry*, respectively.

The advantage of hydrodynamic methods is that a steady state is attained rather quickly, and measurements can be made with high precision (e.g., with digital voltmeters), often without the need for recorders or oscilloscopes. Moreover, at steady state, double-layer charging does not enter the measurement. Also, the rates of mass transfer at the electrode surface in these methods are typically larger than the rates of diffusion alone, so that the relative contribution of mass transfer to electron-transfer kinetics is often smaller.[1] Even though it might first appear that the valuable time variable is lost in steady-state convective methods, this is not so, because time enters the experiment as the rotation rate of the electrode or the solution velocity with respect to the electrode. Dual-electrode techniques can be employed to provide the same kind of information that reversal methods do in stationary electrode techniques. These methods are also of interest in the continuous monitoring of flowing liquids, and in treatments of large-scale reactors, such as those employed for electrosynthesis (see Section 11.6).

Construction of hydrodynamic electrodes that provide known, reproducible mass-transfer conditions is more difficult than for stationary electrodes. The theoretical treatments involved in these methods are also more difficult and involve solving a

---

[1]Although diffusional fluxes at ultramicroelectrodes can often exceed those available by convection at larger electrodes.

hydrodynamic problem (e.g., determining solution flow velocity profiles as functions of rotation rates, solution viscosities, and densities) before the electrochemical one can be tackled. Rarely can closed-form or exact solutions be obtained. Even though the number of possible electrode configurations and flow patterns in these methods is limited only by the imagination and resources of the experimenter, the most convenient and widely used system is the rotating disk electrode. This electrode is amenable to rigorous theoretical treatment and is easy to construct with a variety of electrode materials. Most of what follows deals with it and its variations.

▶▶ 9.2 THEORETICAL TREATMENT OF CONVECTIVE SYSTEMS

The simplest treatments of convective systems are based on a diffusion layer approach. In this model, it is assumed that convection maintains the concentrations of all species uniform and equal to the bulk values beyond a certain distance from the electrode, δ. Within the layer $0 \leq x \leq \delta$, no solution movement occurs, and mass transfer takes place by diffusion. Thus, the convection problem is converted to a diffusional one, in which the adjustable parameter δ is introduced. This is basically the approach that was used in Chapter 1 to deal with the steady-state mass transport problem. However, it does not yield equations that show how currents are related to flow rates, rotation rates, solution viscosity, and electrode dimensions. Nor can it be employed for dual-electrode techniques or for predicting relative mass-transfer rates of different substances. A more rigorous approach begins with the convective-diffusion equation and the velocity profiles in the solution. They are solved either analytically or, more frequently, numerically. In most cases, only the steady-state solution is desired.

9.2.1 The Convective-Diffusion Equation

The general equation for the flux of species j, $\mathbf{J}_j$, is (equation 4.1.9)

$$\mathbf{J}_j = -D_j \nabla C_j - \frac{z_j F}{RT} D_j C_j \nabla \phi + C_j \mathbf{v} \tag{9.2.1}$$

where on the right-hand side, the first term represents diffusion, the second, migration, and the last, convection. For solutions containing an excess of supporting electrolyte, the ionic migration term can be neglected; we will assume this to be the case for most of this chapter (see, however, Section 9.3.5). The velocity vector, $\mathbf{v}$, represents the motion of the solution and is given in rectilinear coordinates by

$$\mathbf{v}(x, y, z) = \mathbf{i} v_x + \mathbf{j} v_y + \mathbf{k} v_z \tag{9.2.2}$$

where $\mathbf{i}$, $\mathbf{j}$, and $\mathbf{k}$ are unit vectors, and v_x, v_y, and v_z are the magnitudes of the solution velocities in the x, y, and z directions at point (x, y, z). Similarly, in rectilinear coordinates,

$$\nabla C_j = \mathbf{grad}\ C_j = \mathbf{i} \frac{\partial C_j}{\partial x} + \mathbf{j} \frac{\partial C_j}{\partial y} + \mathbf{k} \frac{\partial C_j}{\partial z} \tag{9.2.3}$$

The variation of C_j with time is given by

$$\frac{\partial C_j}{\partial t} = -\nabla \cdot \mathbf{J}_j = \mathbf{div}\ \mathbf{J}_j \tag{9.2.4}$$

By combining (9.2.1) and (9.2.4), assuming that migration is absent and that D_j is not a function of x, y, and z, we obtain the general convective-diffusion equation:

$$\frac{\partial C_j}{\partial t} = D_j \nabla^2 C_j - \mathbf{v} \cdot \nabla C_j \tag{9.2.5}$$

The forms for the Laplacian operator, ∇^2, are given in Table 4.4.2. For example, for one-dimensional diffusion and convection, (9.2.5) is

$$\frac{\partial C_j}{\partial t} = D_j \frac{\partial^2 C_j}{\partial y^2} - v_y \frac{\partial C_j}{\partial y} \tag{9.2.6}$$

Note that in the absence of convection (i.e., $\mathbf{v} = 0$ or $v_y = 0$), (9.2.5) and (9.2.6) are reduced to the diffusion equations. Before the convective-diffusion equation can be solved for the concentration profiles, $C_j(x, y, z)$, and subsequently for the currents from the concentration gradients at the electrode surface, expressions for the velocity profile, $\mathbf{v}(x, y, z)$, must be obtained in terms of x, y, z, rotation rate, and so on.

9.2.2 Determination of the Velocity Profile

Although it is beyond the scope of this chapter to treat hydrodynamics in any depth, a brief discussion of some of the concepts, terms, and equations is included to provide some feeling for the approach and the results that follow. For an incompressible fluid (i.e., a fluid whose density is constant in time and space), the velocity profile is obtained by two differential equations with appropriate boundary conditions. The *continuity equation*,

$$\nabla \cdot \mathbf{v} = \mathbf{div} \, \mathbf{v} = 0 \tag{9.2.7}$$

is a statement of incompressibility, whereas the *Navier–Stokes equation*,

$$d_s \frac{d\mathbf{v}}{dt} = -\nabla P + \eta_s \nabla^2 \mathbf{v} + \mathbf{f} \tag{9.2.8}$$

represents Newton's first law ($\mathbf{F} = m\mathbf{a}$) for a fluid. The left side of (9.2.8) represents $m\mathbf{a}$ (per unit volume, since d_s is the density), and the right side represents the forces on a volume element (P is the pressure; η_s, the viscosity; and $\mathbf{f}$ the force/volume exerted on an element of the fluid by gravity). The term $\eta_s \nabla^2 \mathbf{v}$ represents frictional forces. This equation is usually written in the form

$$\frac{d\mathbf{v}}{dt} = \frac{-1}{d_s} \nabla P + \nu \nabla^2 \mathbf{v} + \frac{\mathbf{f}}{d_s} \tag{9.2.9}$$

where $\nu = \eta_s/d_s$ is called the *kinematic viscosity* and has units of cm^2/s. Values for various solutions are given in Table 9.2.1. The term $\mathbf{f}$ represents the effect of natural convection arising from the buildup of density gradients in the solution.

Two different types of fluid flow are usually considered in hydrodynamic problems (Figure 9.2.1). When the flow is smooth and steady, and occurs as if separate layers (*laminae*) of the fluid have steady and characteristic velocities, the flow is said to be *laminar*. For example, the flow of water through a smooth pipe is typically laminar, with the flow velocity being zero right at the walls (because of friction between the fluid and the wall) and having some maximum value in the middle of the pipe. The velocity profile under these conditions is typically parabolic. When the flow involves unsteady and chaotic motion, in which only on the average is there a net flow in a particular direction, it is termed

TABLE 9.2.1   Kinematic Viscosities of 0.1 M TEAP Solutions at 25.0°C^a

Solution	ν, cm^2/s
H_2O	0.009132
H_2O (0.1 M KCl)^b	0.008844
MeCN	0.004536
DMSO	0.01896
Pyridine	0.009518
DMF	0.008971
N,N-Dimethylacetamide	0.01067
HMPA	0.03530
D_2O	0.01028

^{a}From M. Tsushima, K. Tokuda, and T. Ohsaka, *Anal. Chem.*, **66**, 4551 (1994).
^{b}Contains KCl instead of TEAP.

turbulent. This type of flow might result from a barrier being placed in a pipe to obstruct the flow stream.

The solution of the hydrodynamic equations requires modeling the system, writing the equations in the appropriate coordinate system (linear, cylindrical, etc.), specifying the boundary conditions, and usually, solving the problem numerically. In electrochemical problems, only the steady-state velocity profile is of interest; therefore (9.2.9) is solved for $d\mathbf{v}/dt = 0$.

Often, the equations are rewritten in terms of dimensionless groups of variables. One that occurs in many hydrodynamic problems is the *Reynolds number*, Re, which relates a characteristic velocity, v_{ch} (cm/s), and a characteristic length, l (cm), for the system of interest. In general terms, it is given by

$$\text{Re} = v_{ch}l/\nu \tag{9.2.10}$$

The Reynolds number is proportional to fluid velocity, so high values imply high flow or electrode rotation rates. For flow rates below a level characterized by a certain critical Reynolds number, Re_{cr}, the flow remains laminar. When $\text{Re} > \text{Re}_{cr}$ the flow regime becomes turbulent.

General treatments of the formulation and solution of hydrodynamic problems, especially as they relate to problems in electrochemistry, are available (1–6).

Laminar flow   Turbulent flow
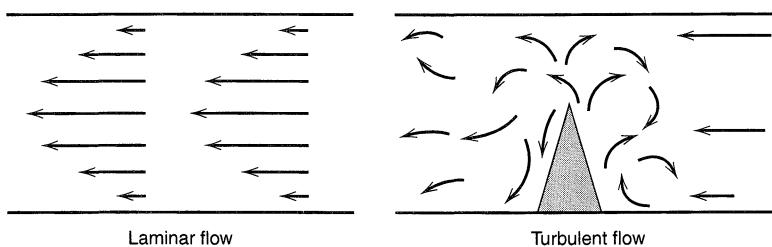
Figure 9.2.1 Types of fluid flow. Arrows represent instantaneous local fluid velocities.

▶ 9.3 ROTATING DISK ELECTRODE

The *rotating disk electrode* (RDE) is one of the few convective electrode systems for which the hydrodynamic equations and the convective-diffusion equation have been solved rigorously for the steady state. This electrode is rather simple to construct and consists of a disk of the electrode material imbedded in a rod of an insulating material. For example, a commonly used form involves a platinum wire sealed in glass tubing with the sealed end ground smooth and perpendicularly to the rod axis. More frequently, the metal is imbedded into Teflon, epoxy resin, or another plastic (Figure 9.3.1). Although the literature suggests that the shape of the insulating mantle is critical and that exact alignment of the disk is important (7), these factors are usually not troublesome in practice, except perhaps at high rotation rates, where turbulence and vortex formation may occur. It is more important that there is no leakage of the solution between the electrode material and the insulator. The rod is attached to a motor directly by a chuck or by a flexible rotating shaft or pulley arrangement and is rotated at a certain frequency, f (revolutions per second). The more useful descriptor of rotation rate is the angular velocity, ω (s^{-1}), where $\omega = 2\pi f$. Electrical connection is made to the electrode by means of a brush contact; the noise level observed in the current at the RDE depends on this contact. Carbon–silver (Graphalloy) materials are frequently used. Details of the construction and application of RDEs are given in several reviews (7–11); RDEs are available commercially.

9.3.1 The Velocity Profile at the RDE

The velocity profile, **v**, of a fluid near a rotating disk was obtained by von Karman and Cochran by solving the hydrodynamic equations under steady-state conditions (1). The spinning disk drags the fluid at its surface along with it and, because of centrifugal force, flings the solution outward from the center in a radial direction. The fluid at the disk surface is replenished by a flow normal to the surface. Because of the symmetry of the system, it is convenient to write the hydrodynamic equations in terms of the cylindrical coordinates y, r, and ϕ (Figure 9.3.2). For cylindrical coordinates,

$$\mathbf{v} = \boldsymbol{\mu}_1 v_r + \boldsymbol{\mu}_2 v_y + \boldsymbol{\mu}_3 v_\phi \tag{9.3.1}$$

$$\boldsymbol{\nabla} = \boldsymbol{\mu}_1(\partial/\partial r) + \boldsymbol{\mu}_2(\partial/\partial y) + (\boldsymbol{\mu}_3/r)(\partial/\partial\phi) \tag{9.3.2}$$
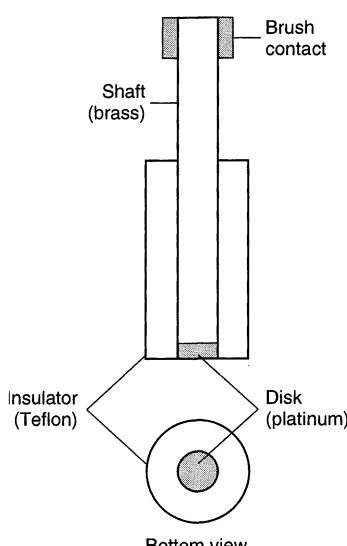
Figure 9.3.1 Rotating disk electrode.
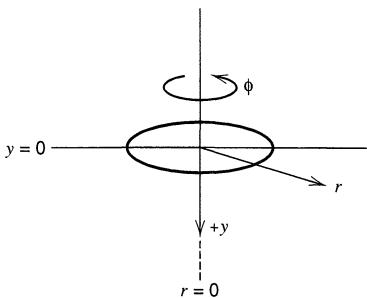
Figure 9.3.2 Cylindrical polar coordinates for the rotating disk.

where $\boldsymbol{\mu}_1$, $\boldsymbol{\mu}_2$, and $\boldsymbol{\mu}_3$ are unit vectors in the directions of positive changes of r, y, and ϕ at a given point. In contrast to the usual cartesian vectors, $\mathbf{i}$, $\mathbf{j}$, and $\mathbf{k}$, the vectors $\boldsymbol{\mu}_1$, $\boldsymbol{\mu}_2$, and $\boldsymbol{\mu}_3$ have directions that depend on the position of the point; thus the divergence and the Laplacian take on more complex forms. In particular,

$$\nabla \cdot \mathbf{v} = \frac{1}{r^2}\left[\frac{\partial}{\partial r}(v_r r^2) + \frac{\partial}{\partial y}(v_y r^2) + \frac{\partial}{\partial \phi}v_\phi\right] \tag{9.3.3}$$

$$\nabla^2 = \frac{1}{r}\left[\frac{\partial}{\partial r}\left(r\frac{\partial}{\partial r}\right) + \frac{\partial}{\partial y}\left(r\frac{\partial}{\partial y}\right) + \frac{\partial}{\partial \phi}\left(\frac{1}{r}\frac{\partial}{\partial \phi}\right)\right] \tag{9.3.4}$$

It is assumed that gravitational effects are absent ($\mathbf{f} = 0$) and that there are no special flow effects at the edge of the disk. At the disk surface ($y = 0$), $v_r = 0$, $v_y = 0$, and $v_\phi = \omega r$. This implies that the solution is dragged along at the surface of the disk at the angular velocity, ω. In the bulk solution ($y \to \infty$), $v_r = 0$, $v_\phi = 0$, and $v_y = -U_0$. Thus, far from the disk, there is no flow in the r and ϕ directions, but the solution flows at a limiting velocity, U_0, toward the disk, with U_0 determined by the solution of the problem.

The treatment by von Karman and Cochran yielded values of the velocities in the form of infinite series based on the dimensionless variable γ, where

$$\gamma = \left(\frac{\omega}{\nu}\right)^{1/2}y \tag{9.3.5}$$

The results for small values of y ($\gamma \ll 1$) are

$$v_r = r\omega F(\gamma) = r\omega\left(a\gamma - \frac{\gamma^2}{2} - \tfrac{1}{3}b\gamma^3 + \cdots\right) \tag{9.3.6}$$

$$v_\phi = r\omega G(\gamma) = r\omega(1 + b\gamma + \tfrac{1}{3}a\gamma^3 + \cdots) \tag{9.3.7}$$

$$v_y = (\omega\nu)^{1/2}H(\gamma) = (\omega\nu)^{1/2}\left(-a\gamma^2 + \frac{\gamma^3}{3} + \frac{b\gamma^4}{6} + \cdots\right) \tag{9.3.8}$$

in which $a = 0.51023$ and $b = -0.6159$. Suitable equations for the velocities at greater distances from the electrode ($\gamma \gg 1$) are given by Levich (1).

For the rotating disk electrode as employed in electrochemical studies, the important velocities are v_r and v_y (Figure 9.3.3). Near the surface of the rotating disk, $y \to 0$ (or $\gamma \to 0$), and these velocities are given by:

$$v_y = (\omega\nu)^{1/2}(-a\gamma^2) = -0.51\omega^{3/2}\nu^{-1/2}y^2 \tag{9.3.9}$$

$$v_r = r\omega(a\gamma) = 0.51\omega^{3/2}\nu^{-1/2}ry \tag{9.3.10}$$
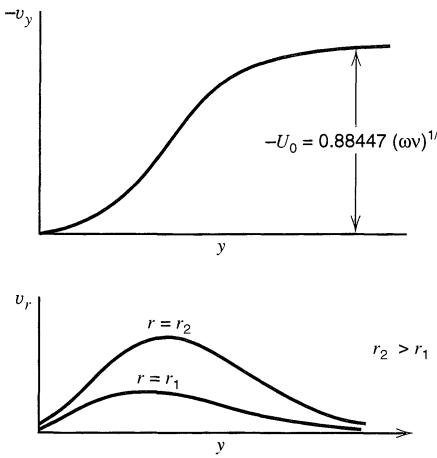
Figure 9.3.3 Variation of normal (v_y) and radial (v_r) fluid velocities as functions of y and r.

A vector representation of the flow velocities is shown in Figure 9.3.4. The limiting velocity in the y direction, U_0, is

$$U_0 = \lim_{y \to \infty} v_y = -0.88447(\omega\nu)^{1/2} \tag{9.3.11}$$

At $\gamma = (\omega/\nu)^{1/2}y = 3.6$, $v_y \approx 0.8U_0$. The corresponding distance, $y_h = 3.6(\nu/\omega)^{1/2}$, is called the *hydrodynamic* (or sometimes the *momentum* or *Prandtl*) *boundary layer thickness* and roughly represents the thickness of the layer of liquid dragged by the rotating disk. For water ($\nu \approx 0.01$ cm^2/s) at $\omega = 100$ and 10^4 s^{-1}, y_h is 0.036 and 3.6×10^{-3} cm, respectively.

9.3.2 Solution of the Convective-Diffusion Equation

Once the velocity profile has been determined, the convective-diffusion equation, (9.2.5), for the rotating disk electrode, written in convenient coordinates and with appropriate boundary conditions, can be solved. Let us first consider the steady-state lim-
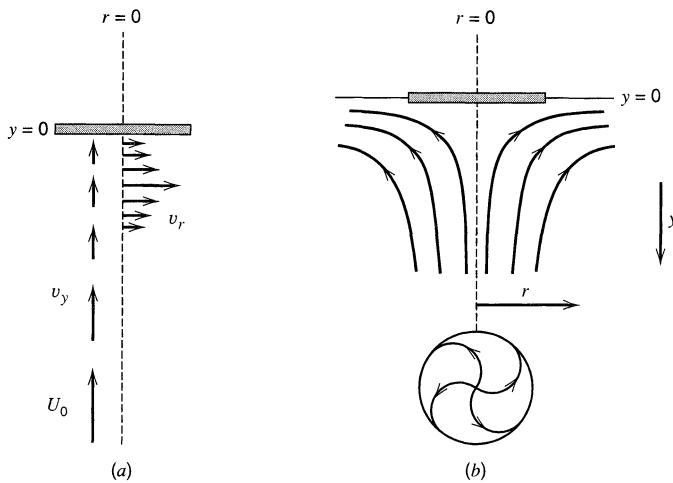
Figure 9.3.4 (*a*) Vector representation of fluid velocities near a rotating disk. (*b*) Schematic resultant streamlines (or flows).

iting current. When ω is fixed and a steady velocity profile has been attained, a potential step in the limiting current region [i.e., where $C_O(y = 0) \approx 0$] will cause the appearance of a current transient similar to that observed in the absence of convection. However, in contrast to the transient that appears in an unstirred solution at a planar electrode, which decays toward zero, the current at the RDE decays to a steady-state value. In the limit, the concentrations near the electrode are no longer functions of time, $\partial C_O/\partial t = 0$, and the steady-state convective-diffusion equation, written in terms of cylindrical coordinates, becomes

$$v_r\left(\frac{\partial C_O}{\partial r}\right) + \frac{v_\phi}{r}\left(\frac{\partial C_O}{\partial \phi}\right) + v_y\left(\frac{\partial C_O}{\partial y}\right) = D_O\left[\frac{\partial^2 C_O}{\partial y^2} + \frac{\partial^2 C_O}{\partial r^2} + \frac{1}{r}\frac{\partial C_O}{\partial r} + \frac{1}{r^2}\left(\frac{\partial^2 C_O}{\partial \phi^2}\right)\right]$$

(9.3.12)

For the limiting current condition, at $y = 0$, $C_O = 0$, and $\lim_{y\to\infty} C_O = C_O^*$. For reasons of symmetry, C_O is not a function of ϕ; therefore, $\partial C_O/\partial \phi = (\partial^2 C_O/\partial \phi^2) = 0$. Also, v_y does not depend on r (see equation 9.3.8), and at $y = 0$, $(\partial C_O/\partial r) = 0$. Thus, across the face of the disk electrode, that is, $0 \le r \le r_1$, where r_1 is the disk radius, $(\partial C_O/\partial r) = 0$ for all y. These considerations lead to a considerable simplification in (9.3.12), yielding

$$v_y\left(\frac{\partial C_O}{\partial y}\right) = D_O\frac{\partial^2 C_O}{\partial y^2}$$

(9.3.13)

or, by substitution of the value of v_y from (9.3.9) and rearrangement,

$$\frac{\partial^2 C_O}{\partial y^2} = \frac{-y^2}{B}\frac{\partial C_O}{\partial y}$$

(9.3.14)

where $B = D_O\omega^{-3/2}\nu^{1/2}/0.51$. This equation can be solved directly by integration. To make the job easier, let $X = \partial C_O/\partial y$, so that $\partial X/\partial y = \partial^2 C_O/\partial y^2$. At $y = 0$, $X = X_0 = (\partial C_O/\partial y)_{y=0}$. Then (9.3.14) becomes

$$\frac{\partial X}{\partial y} = \left(\frac{-y^2}{B}\right)X$$

(9.3.15)

$$\int_{X_0}^{X}\left(\frac{dX}{X}\right) = \left(\frac{-1}{B}\right)\int_0^y y^2\, dy$$

(9.3.16)

$$\frac{X}{X_0} = \exp\left(\frac{-y^3}{3B}\right)$$

(9.3.17)

$$\frac{\partial C_O}{\partial y} = \left(\frac{\partial C_O}{\partial y}\right)_{y=0}\exp\left(\frac{-y^3}{3B}\right)$$

(9.3.18)

Integrating once more, we can write

$$\int_0^{C_O^*} dC_O = \left(\frac{\partial C_O}{\partial y}\right)_{y=0}\int_0^\infty \exp\left(\frac{-y^3}{3B}\right) dy$$

(9.3.19)

where the limits are set for a concentration profile with $C_O(y = 0) = 0$, that is for limiting-current conditions. The definite integral on the right side is obtained by making the substitution $z = y^3/3B$, and is $(3B)^{1/3}\Gamma(4/3)$ or $0.8934(3B)^{1/3}$. Thus,

$$C_O^* = \left(\frac{\partial C_O}{\partial y}\right)_{y=0} 0.8934\left(\frac{3D_O\omega^{-3/2}\nu^{1/2}}{0.51}\right)^{1/3}$$

(9.3.20)

The current is the flux at the electrode surface, that is,

$$i = nFAD_O\left(\frac{\partial C_O}{\partial y}\right)_{y=0} \tag{9.3.21}$$

where, under the chosen current conditions, $i = i_{l,c}$. From (9.3.20) and (9.3.21), we obtain the *Levich equation*:

$$i_{l,c} = 0.62nFAD_O^{2/3}\omega^{1/2}\nu^{-1/6}C_O^* \tag{9.3.22}$$

This equation applies to the totally mass-transfer-limited condition at the RDE and predicts that $i_{l,c}$ is proportional to C_O^* and $\omega^{1/2}$. One can define the *Levich constant* as $i_{l,c}/\omega^{1/2}C_O^*$, which is the RDE analog of the diffusion current constant or current function in voltammetry or the transition time constant in chronopotentiometry.

Recall that the simple steady-state diffusion layer model yielded (see equation 1.4.9)

$$i_{l,c} = nFAm_OC_O^* = nFA\left(\frac{D_O}{\delta_O}\right)C_O^* \tag{9.3.23}$$

Thus, for the RDE

$$m_O = \frac{D_O}{\delta_O} = 0.62D_O^{2/3}\omega^{1/2}\nu^{-1/6} \tag{9.3.24}$$

$$\delta_O = 1.61D_O^{1/3}\omega^{-1/2}\nu^{1/6} \tag{9.3.25}$$

The concepts and results of the diffusion-layer model can often be used in RDE problems and, when needed, the appropriate value of δ_O can be substituted to yield the final equations.[2]

While the Levich equation (9.3.22) suffices for many purposes, improved forms based on derivations utilizing more terms in the velocity expression are available (12).

9.3.3 The Concentration Profile

The concentration profile for the limiting-current condition can be obtained from (9.3.19) by integrating between 0 and $C_O(y)$; thus,

$$\int_0^{C_O(y)} dC_O = C_O(y) = \left(\frac{\partial C_O}{\partial y}\right)_{y=0}\int_0^y \exp\left(\frac{-y^3}{3B}\right) dy \tag{9.3.26}$$

From (9.3.20) we have

$$\left(\frac{\partial C_O}{\partial y}\right)_{y=0} = \frac{C_O^*}{0.8934}(3B)^{-1/3} \tag{9.3.27}$$

This can be put in a more convenient form by letting $u^3 = y^3/3B$, so that $dy = du(3B)^{1/3}$. Then (9.3.26) becomes

$$C_O(y) = \left(\frac{C_O^*}{0.8934}\right)\int_0^Y \exp(-u^3) du \tag{9.3.28}$$

[2]From the expression for the hydrodynamic boundary layer, y_h, and (9.3.25), we obtain $y_h/\delta_O \approx 2(\nu/D)^{1/3}$. For H_2O, $\nu = 0.01$ cm^2/s, $D_O \approx 10^{-5}$ cm^2/s, so that $\delta_O \approx 0.05$ y_h. The dimensionless ratio (ν/D) occurs frequently in hydrodynamic problems and is called the *Schmidt number*, Sc.

where $Y = y/(3B)^{1/3}$. The concentration profile for C_O under these conditions is shown in Figure 9.3.5.

9.3.4 General Current-Potential Curves at the RDE

For nonlimiting-current conditions, only a change in integration limits in (9.3.19) is required. In general, at $y = 0$, $C_O = C_O(y = 0)$ and $(\partial C_O/\partial y)_{y=0}$ is given by an analogue to (9.3.20), which yields

$$C_O^* - C_O(y = 0) = \left(\frac{\partial C_O}{\partial y}\right)_{y=0} \int_0^\infty \exp\left(\frac{-y^3}{3B}\right) dy \tag{9.3.29}$$

Thus,

$$i = 0.62nFAD_O^{2/3}\omega^{1/2}v^{-1/6}[C_O^* - C_O(y = 0)] \tag{9.3.30}$$

or, from (9.3.22),

$$i = i_{l,c}\left[\frac{C_O^* - C_O(y = 0)}{C_O^*}\right] \tag{9.3.31a}$$

Alternatively, (9.3.30) can be written in terms of δ_O, as defined in (9.3.25), to yield

$$i = \frac{nFAD_O[C_O^* - C_O(y = 0)]}{\delta_O} = nFAm_O[C_O^* - C_O(y = 0)] \tag{9.3.31b}$$

Note that this equation is identical to that derived from the steady-state model in Section 1.4.

The current-potential curves for the simple reaction $O + ne \rightleftarrows R$ at the RDE can be derived from (9.3.31a) and the equivalent expression for the reduced form:

$$i = i_{l,a}\left[\frac{C_R^* - C_R(y = 0)}{C_R^*}\right] \tag{9.3.32}$$

where

$$i_{l,a} = -0.62nFAD_R^{2/3}\omega^{1/2}v^{-1/6}C_R^* \tag{9.3.33}$$
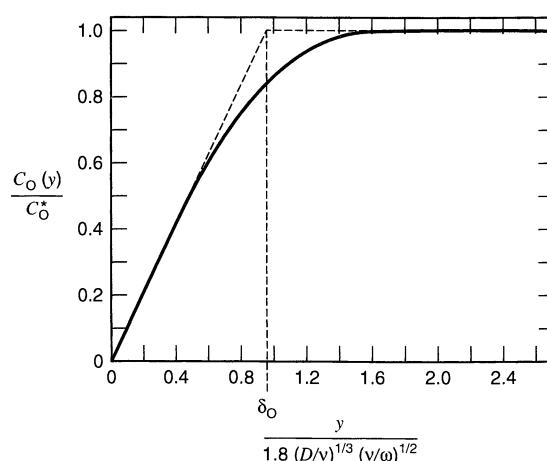
Figure 9.3.5 Concentration profile of species O given in terms of dimensionless coordinates.

For a nernstian reaction, combination of the Nernst equation for the O,R couple with the equations for the various currents yields the familiar voltammetric wave equation:

$$E = E_{1/2} + \frac{RT}{nF} \ln \frac{(i_{l,c} - i)}{(i - i_{l,a})}$$

(9.3.34)

where

$$E_{1/2} = E^{0'} + \frac{RT}{nF} \ln \left(\frac{D_R}{D_O}\right)^{2/3}$$

(9.3.35)

Note that the shape of the wave for a reversible reaction is independent of ω. Thus, since i_l varies as $\omega^{1/2}$, i at any potential should also vary as $\omega^{1/2}$. A deviation of a plot of i vs. $\omega^{1/2}$ from a straight line intersecting the origin suggests that a kinetic limitation is involved in the electron-transfer reaction. For example, for a totally irreversible one-step, one-electron reaction, the disk current is

$$i = FAk_f(E)C_O(y = 0)$$

(9.3.36)

where $k_f(E) = k^0 \exp[-\alpha f(E - E^{0'})]$. From (9.3.31),

$$i = FAk_f(E)C_O^* \left(1 - \frac{i}{i_{l,c}}\right)$$

(9.3.37)

or, with rearrangement and defining

$$i_K = FAk_f(E)C_O^*$$

(9.3.38)

one obtains the *Koutecký–Levich equation*:

$$\frac{1}{i} = \frac{1}{i_K} + \frac{1}{i_{l,c}} = \frac{1}{i_K} + \frac{1}{0.62nFAD_O^{2/3}\omega^{1/2}\nu^{-1/6}C_O^*}$$

(9.3.39)

Here, i_K represents the current in the absence of any mass-transfer effects, that is, the current that would flow under the kinetic limitation if the mass transfer were efficient enough to keep the concentration at the electrode surface equal to the bulk value, regardless of the electrode reaction. Clearly, $i/\omega^{1/2}C$ is a constant only when i_K [or $k_f(E)$] is very large. Otherwise, a plot of i vs. $\omega^{1/2}$ will be curved and tend toward the limit $i = i_K$ as $\omega^{1/2} \to \infty$ (Figure 9.3.6). A plot of $1/i$ vs. $1/\omega^{1/2}$ should be
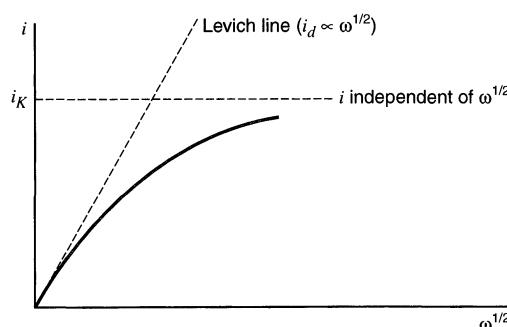
Figure 9.3.6 Variation of i with $\omega^{1/2}$ at an RDE (at constant E_D) for an electrode reaction with slow kinetics.

linear and can be extrapolated to $\omega^{-1/2} = 0$ to yield $1/i_K$. Determination of i_K at different values of E then allows determination of the kinetic parameters k^0 and α (Figure 9.3.7). A typical application of this procedure is illustrated in Figure 9.3.8, which shows such plots for the reduction of O_2 to HO_2^- at a gold electrode in alkaline solution.

It is instructive to consider a more general derivation of (9.3.39), since the RDE can be used to study the kinetics of processes other than electron transfer at modified electrode surfaces (see Section 14.4). When mass transport and another process occur in series, the rates of both processes must be the same at steady state. Thus, for the case where electron transfer at the electrode surface is the rate-limiting process,

$$D[C_O^* - C_O(y = 0)]/\delta_O = k(E)C_O(y = 0) = i/nFA \tag{9.3.40}$$

It is left as an exercise for the reader (Problem 9.10) to show that solving this equation for $C_O(y = 0)$ and use of equations (9.3.23) and (9.3.38) lead to (9.3.39). For another rate-limiting process (e.g., diffusion of an electroreactant through a film coated on the electrode), the term $k(E)C_O(y = 0)$ would be replaced by the appropriate expression. This would yield an equation in the general form of the Koutecký–Levich equation, with the extrapolation to $\omega^{-1/2} \to 0$ allowing the determination of the kinetic parameter for that process [see, for example, Section 14.4.2].

For a quasireversible one-step, one-electron reaction, a general current-potential relationship can be derived in a similar manner. The i-η equation, (3.4.10), can be written

$$\frac{i}{i_0} = \left[\frac{C_O(y = 0)}{C_O^*}\right]b^{-\alpha} - \left[\frac{C_R(y = 0)}{C_R^*}\right]b^{1-\alpha} \tag{9.3.41}$$

where $b = \exp(F\eta/RT)$. This equation, combined with (9.3.31) and (9.3.32), yields

$$\frac{1}{i} = \frac{b^\alpha}{1 - b}\left(\frac{1}{i_0} + \frac{b^{-\alpha}}{i_{l,c}} - \frac{b^{1-\alpha}}{i_{l,a}}\right) \tag{9.3.42}$$

which can be reexpressed as

$$\frac{1}{i} = \frac{b^\alpha}{1 - b}\left[\frac{1}{i_0} + \frac{1}{0.62FA\nu^{-1/6}\omega^{1/2}}\left(\frac{b^{-\alpha}}{D_O^{2/3}C_O^*} + \frac{b^{1-\alpha}}{D_R^{2/3}C_R^*}\right)\right] \tag{9.3.43}$$
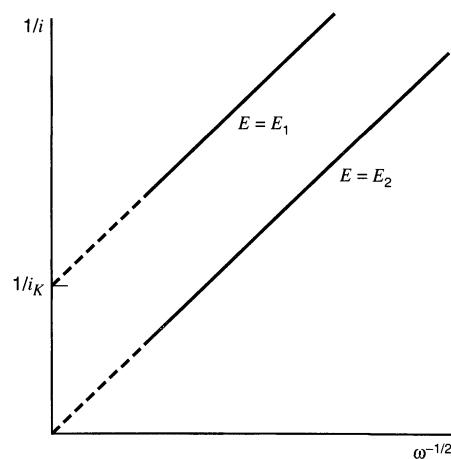
Figure 9.3.7 Koutecký–Levich plots at potential E_1, where the rate of electron transfer is sufficiently slow to act as a limiting factor, and at E_2, where electron transfer is rapid, for example, in the limiting-current region. The slope of both lines is $(0.62nFAC_O^*D_O^{2/3}\nu^{-1/6})^{-1}$.

(a)

(b)
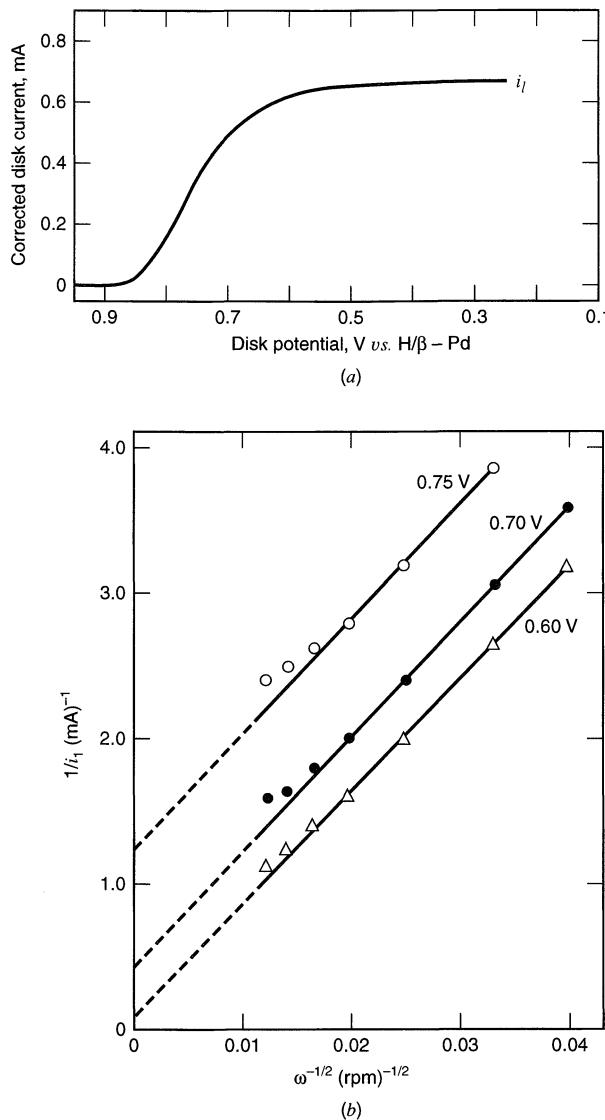
Figure 9.3.8 (a) i_D vs. E at 2500 rpm and (b) Koutecký–Levich plots for the reduction of O_2 to HO_2^- at a gold electrode in O_2-saturated ($\sim$1.0 mM) 0.1 M NaOH at an RDE (A = 0.196 cm^2). The potential was swept at 1 V/min. T = 26°C. (i_1 represents the corrected current attributable to O_2 reduction.) [From R. W. Zurilla, R. K. Sen, and E. Yeager, *J. Electrochem. Soc.*, **125**, 1103 (1978). Reprinted by permission of the publisher, The Electrochemical Society, Inc.]

Thus, $1/i$ vs. $\omega^{-1/2}$ at a given value of η is predicted to be linear for this case as well, and the intercept of the plot allows the determination of kinetic parameters.

Alternative forms of (9.3.39) and (9.3.43) are sometimes given in the literature and are listed here for convenience. If the more general kinetic relation for the one-step, one-electron process, equation 3.2.8, is used in the derivation, then the equation for $1/i$ at the disk becomes

$$\frac{1}{i} = \frac{1}{FA(k_f C_O^* - k_b C_R^*)}\left[1 + \frac{D_O^{-2/3}k_f + D_R^{-2/3}k_b}{0.62\nu^{-1/6}\omega^{1/2}}\right] \tag{9.3.44}$$

If the reverse (e.g., anodic) reaction can be ignored, then (9.3.44) yields

$$i = \frac{FAk_f C_O^*}{1 + k_f/(0.62\nu^{-1/6}D_O^{2/3}\omega^{1/2})} = \frac{FAk_f C_O^*}{1 + k_f \delta_O/D_O} \tag{9.3.45}$$

where δ_O is as defined in (9.3.25). This equation, easily derived from (9.3.40), is useful in defining the conditions for kinetic or mass-transfer control at the RDE. When $k_f \delta_O/D_O \ll 1$, the current is completely under kinetic (or activation) control. When $k_f \delta_O/D_O \gg 1$, the mass-transfer-controlled equation results. Thus, if the RDE is to be used for kinetic measurements, $k_f \delta_O/D_O$ should be small, say less than 0.1; that is, $k_f \leq 0.1D_O/\delta_O$.

Applications of RDE techniques to electrochemical problems have been reviewed (7–10, 12, 13).

9.3.5 Current Distribution at the RDE

In the preceding derivations, we assumed that the resistance of the solution was very small. With this condition, the current density is expected to be uniform across the disk and independent of the radial distance. Although this is frequently the case in real systems, the actual current distribution depends on the solution resistance, as well as the mass- and charge-transfer parameters of the electrode reaction. This topic has been treated by Newman (14) and discussed by Albery and Hitchman (15).

Consider first the *primary current distribution*, which represents the distribution when the surface overpotentials (activation and concentration) are neglected, and the electrode is taken as an equipotential surface. For a disk electrode of radius r_1 embedded in a large insulating plane with a counter electrode at infinity, the potential distribution under such conditions is as shown in Figure 9.3.9. The current flows in a direction perpendicular
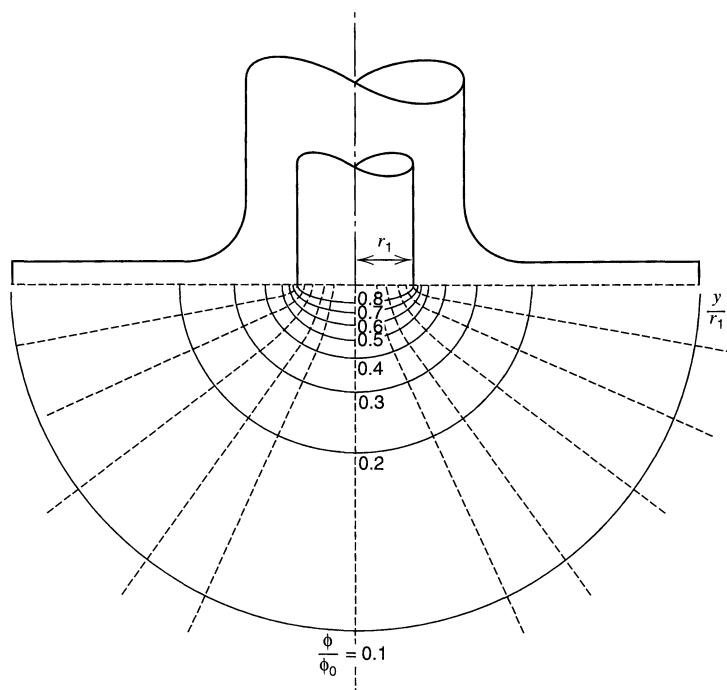
Figure 9.3.9 Primary current distribution at an RDE. Solid lines show lines of equal potential at values of ϕ/ϕ_0, where ϕ_0 is the potential at the electrode surface; that is, ϕ represents the potential of the disk measured against an infinitesimal reference electrode (whose presence does not perturb the current distribution) located at different indicated points in solution. Dotted lines are lines of current flow. The number of lines per unit length represents the current density j. Note that j is higher toward the edge of the disk than at the center. [From J. Newman, *J. Electrochem. Soc.*, **113**, 501 (1966). Reprinted with permission of the publisher, The Electrochemical Society, Inc.]

to the equipotential surfaces, and the current density is not uniform across the disk surface, but is instead much larger at the edge ($r = r_1$) than at the center ($r = 0$). This situation arises because the ionic flux at the edge occurs from the side, as well as from the direction normal to the disk. The total current flowing to the disk under total resistive control is (4, 14)

$$i = 4\kappa r_1(\Delta E) \qquad (9.3.46)$$

where κ is the specific conductivity of the bulk solution, and ΔE is the potential difference in solution between the disk and counter electrodes. Thus, the overall resistance, R_Ω, is

$$R_\Omega = 1/4\kappa r_1 \qquad (9.3.47)$$

When electrode kinetics and mass-transfer effects are included, the current distribution (now called the *secondary current distribution*) is more nearly uniform than the primary one. Albery and Hitchman (15) have shown that the current distribution can be considered in terms of the dimensionless parameter, ρ, given by

$$\rho = \frac{R_\Omega}{R_E} \qquad (9.3.48)$$

where R_E is the electrode resistance due to both charge transfer and concentration polarization. The secondary current distribution as a function of ρ is shown in Figure 9.3.10. Note that as $\rho \to \infty$ (i.e., high solution resistance and small R_E), the current distribution

Curve	ρ
1	0.079
2	0.204
3	0.393
4	0.899
5	1.571
6	2.594
7	3.927
8	5.918
9	15.708
10	∞
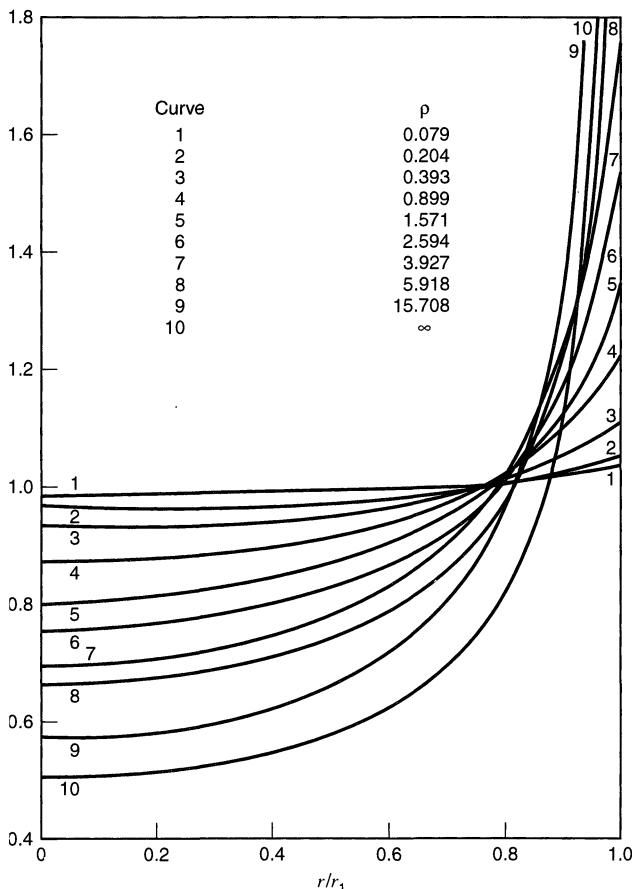
Figure 9.3.10 Secondary current distribution at an RDE. [From J. Newman, *J. Electrochem. Soc.*, **113**, 1235 (1966) as modified by W. J. Albery and M. L. Hitchman, "Ring-Disc Electrodes," Clarendon, Oxford, 1971, Chap. 4, with permission of the publishers, The Electrochemical Society, Inc., and Oxford University Press.]

approaches the primary one. Conversely, for small values of ρ (highly conductive solutions and large R_E) a fairly uniform current distribution is obtained. To avoid a nonuniform distribution, the conditions must be such that $\rho < 0.1$ (15). By taking

$$R_E + R_\Omega = \frac{dE}{di} \tag{9.3.49}$$

(where dE/di is the slope of the current-potential curve at a given value of E) and combining with (9.3.47) and (9.3.48), we obtain the condition for a uniform distribution (15):

$$\frac{di}{dE} < 0.36 r_1 \kappa \tag{9.3.50}$$

A plot of the values of di/dE that satisfy this condition at different values of r_1 and κ, taken from Albery and Hitchman, is shown in Figure 9.3.11. Note that at the limiting current, di/dE approaches zero, so that a uniform current distribution is always obtained in this circumstance.

9.3.6 Considerations in Experimental Application of the RDE

The equations derived for the RDE will not apply at very small or very large values of ω. When ω is small, the hydrodynamic boundary layer [$y_h \approx 3(\nu/\omega)^{1/2}$] becomes large, and when it approaches the disk radius r_1, the approximations break down. Thus, the
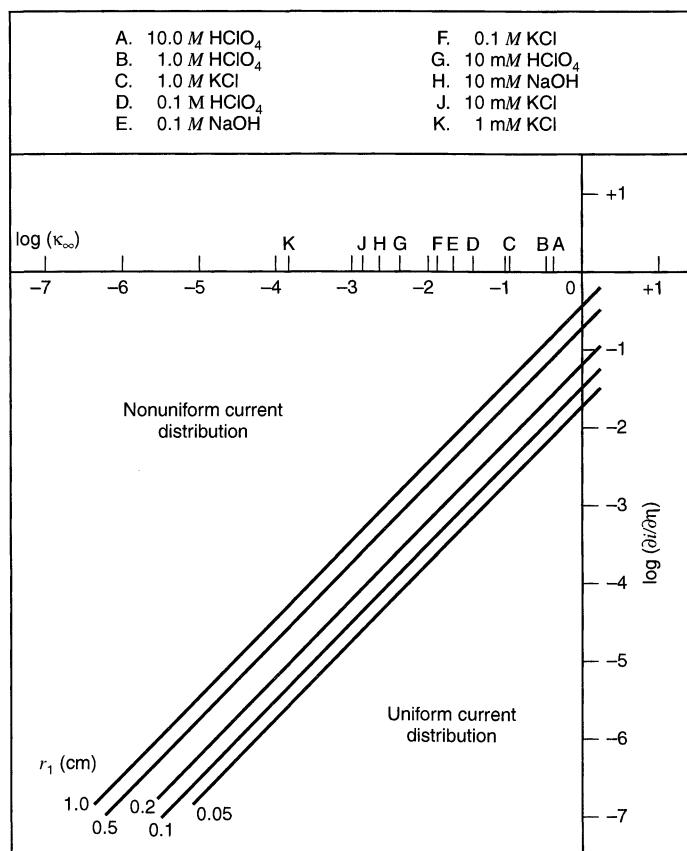
Figure 9.3.11 Diagnostic plot for the uniformity of current distribution at an RDE. Conductivities of some typical background electrolytes at 25°C in aqueous solution are marked on log (κ_∞) scale in the figure. *Note:* $di/d\eta$ is in units of Ω^{-1}; κ_∞ is bulk electrolyte conductivity in $\Omega^{-1}\text{cm}^{-1}$. [From W. J. Albery and M. L. Hitchman, "Ring-Disc Electrodes," Clarendon, Oxford, 1971, Chap. 4, by permission of Oxford University Press.]

lower limit for ω is obtained from the condition $r_1 > 3(\nu/\omega)^{1/2}$; that is, $\omega > 10\nu/r_1^2$. For $\nu = 0.01$ cm^2/s and $r_1 = 0.1$ cm, ω should be larger than 10 s^{-1}. Another problem occurs when recording *i-E* curves at the RDE at low values of ω. The derivation involved an assumed steady-state concentration at the electrode surface (i.e., $(\partial C_O/\partial t = 0)$. Thus, the rate at which the electrode potential is scanned (V/s) must be small with respect to ω to allow the steady-state concentrations to be achieved. If the scan rate is too large for a given ω, the *i-E* curves will not have the S-shape predicted by, for example, (9.3.34), but will instead show a peak, as in linear scan voltammetry at a stationary electrode. The question of transients and the time response at the RDE is covered further in Section 9.5.1.

The upper limit for ω is governed by the onset of turbulent flow. This occurs at the RDE at a critical Reynolds number, Re$_{cr}$, larger than about 2×10^5 (7, 13). In this system, v_{ch} is the velocity of the edge of the disk ωr_1, and the characteristic distance l is r_1 itself. Thus, from (9.2.10),

$$\mathrm{Re} = \frac{v_{ch} l}{\nu} = \frac{\omega r_1^2}{\nu} \tag{9.3.51}$$

and the condition for nonturbulent flow is $\omega < 2 \times 10^5 \nu/r_1^2$. For the r_1 and ν values assumed, ω should be less than 2×10^5 s^{-1}. The transition to turbulent flow can occur at much lower values of ω when the surface of the disk is not perfectly polished, when there are small bends or eccentricities in the RDE shaft, or when the cell walls are too close to the electrode surface. Also, at very high rotation rates, there can be excessive splashing or the formation of a vortex around the electrode. In practice, the maximum rotation rates are frequently at 10,000 rpm or at $\omega \approx 1000$ s^{-1}. Thus, the ranges of ω and f are limited in most RDE studies to 10 s$^{-1} < \omega < 1000$ s^{-1} or 100 rpm $< f < 10,000$ rpm.

The theory developed for the RDE also assumes that the disk is precisely centered on the axis of rotation. If the disk is located off the axis of rotation, either because of the way it is constructed (Figure 9.3.12) or because the shaft connecting the disk electrode to the rotator is bent, the observed currents will be larger than those for the centered disk. This result comes about because the disk continually sweeps into a wider area of solution and gains an additional mass-transfer contribution from radial diffusion in a manner analogous to that found with the rotating ring electrode (Section 9.4.1). The theory for this situation has been developed (16) and yields a limiting current density, $j_{\lim}$, of

$$j_{\lim} = 1.027(i_{l,c}/A)\varepsilon^{1/3} \tag{9.3.52}$$

where $i_{l,c}$ is given by (9.3.22), and ε is an eccentricity factor ($\varepsilon = R/r$), as shown in Figure 9.3.12.
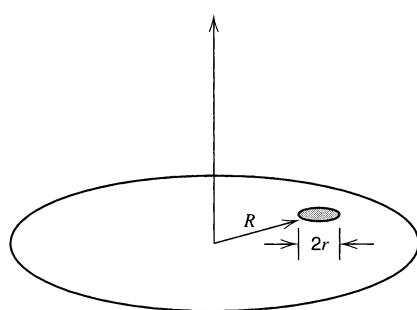
Figure 9.3.12 A rotating disk electrode where the electrode, with radius r, is offset from the axis of rotation by a distance R.

In standard RDE theory, one also assumes a negligible radial diffusion contribution to the current at the edges of the disk. This is true if the disk radius is sufficiently large that diffusion to it can be treated as simple linear diffusion. When the disk electrode radius falls in the ultramicroelectrode regime, this is no longer the case, so different equations will apply to the rotating microdisk, as discussed in Section 9.7.

▷ ## 9.4 ROTATING RING AND RING-DISK ELECTRODES

Reversal techniques are obviously not available with the RDE, since the product of the electrode reaction is continuously swept away from the surface of the disk. At the RDE, reversal of the direction of the potential sweep under conditions where the scan rate is sufficiently slow compared to ω (i.e., when no peak is seen during the forward scan) will just retrace the *i-E* curve of the forward scan. Information equivalent to that available from reversal techniques at a stationary electrode is obtained by the addition of an independent ring electrode surrounding the disk (Figure 9.4.1). By measuring the current at the ring electrode, some knowledge about what is occurring at the disk electrode surface can be obtained. For example, if the potential of the ring is held at the foot of the wave for O + $ne \rightarrow$ R, product R, formed at the disk, will be swept over to the ring by the radial flow, where it will be oxidized back to O (or be *collected*).

The ring can also be used alone as an electrode (the *rotating ring electrode*), such as when the disk is disconnected. Mass transfer to a ring electrode is larger than to a disk at a

Electrode material
(e.g., platinum)

Insulator
(e.g., Teflon)

Shaft and ring material
(e.g., brass)
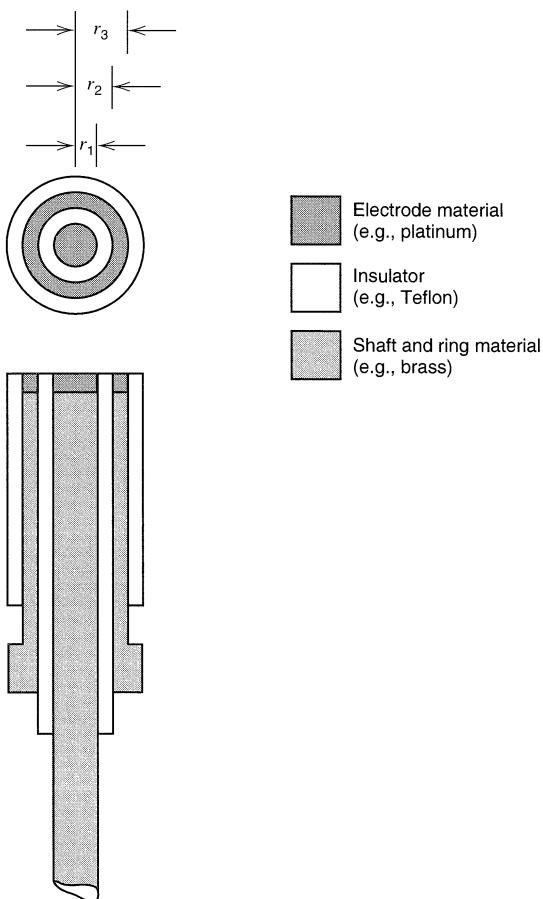
Figure 9.4.1   Ring-disk electrode.

given A and ω, because flow of fresh solution occurs radially from the area inside the ring, as well as normally from the bulk solution.

The theoretical treatment of ring electrodes is more complicated than that of the RDE, since the radial mass-transfer term must be included in the convective-diffusion equation. While the mathematics sometimes become difficult in these problems, the results are still easy to understand and to apply. The problem will only be outlined here; details of the mathematical treatment are given in references 7 and 15.

9.4.1 Rotating Ring Electrode

Consider a ring electrode with an inner radius r_2 and outer radius r_3 [$A_r = \pi(r_3^2 - r_2^2)$]. This could be, for example, the RRDE illustrated in Figure 9.4.1 with the disk electrode at open circuit. When this electrode is rotated at an angular velocity, ω, the solution flow velocity profile is that discussed in Section 9.3.1. The steady-state convective-diffusion equation that must be solved is

$$v_r\left(\frac{\partial C_O}{\partial r}\right) + v_y\left(\frac{\partial C_O}{\partial y}\right) = D_O\left(\frac{\partial^2 C_O}{\partial y^2}\right) \tag{9.4.1}$$

This is obtained from (9.3.12). As with the RDE, symmetry considerations require that the concentrations be independent of ϕ, so that the derivatives in ϕ vanish. In addition, the mass transfer by diffusion in the radial direction, represented by the terms $D_O[(\partial^2 C_O/\partial r^2) + (1/r)(\partial C_O/\partial r)]$, is, at usual flow rates, small compared to convection in the radial direction, $(v_r \partial C_O/\partial r)$; hence the diffusive terms are neglected. The boundary conditions for the limiting ring current are:

$$
\begin{aligned}
C_O &= C_O^* && \text{for} && y \to \infty \\
C_O &= 0 \text{ at } y = 0 && \text{for} && r_2 \le r < r_3 \\
\frac{\partial C_O}{\partial y} &= 0 \text{ at } y = 0 && \text{for} && r < r_2
\end{aligned}
$$

When the values of v_r and v_y are introduced [see (9.3.9) and (9.3.10)], we obtain

$$(B'ry)\left(\frac{\partial C_O}{\partial r}\right) - B'y^2\left(\frac{\partial C_O}{\partial y}\right) = D_O\left(\frac{\partial^2 C_O}{\partial y^2}\right) \tag{9.4.2}$$

$$r\left(\frac{\partial C_O}{\partial r}\right) - y\left(\frac{\partial C_O}{\partial y}\right) = \left(\frac{D_O}{B'}\right)\frac{1}{y}\left(\frac{\partial^2 C_O}{\partial y^2}\right) \tag{9.4.3}$$

where $B' = 0.51\,\omega^{3/2}\nu^{-1/2}$. The current at the ring electrode is given by[3]

$$i_R = nFD_O 2\pi \int_{r_2}^{r_3}\left(\frac{\partial C_O}{\partial y}\right)_{y=0} r\,dr \tag{9.4.4}$$

---

[3]The area of an infinitesimal section of ring of thickness δr at a radius r is $\pi(r + \delta r)^2 - \pi r^2 \approx 2\pi r(\delta r)$. The current through this section is

$$\frac{(i_R)_{\delta r}}{nFA} = \frac{(i_R)_{\delta r}}{nF2\pi r\delta r} = D_O\left(\frac{\partial C_O}{\partial y}\right)_{y=0}$$

The total ring current is the summation of $(i_R)_{\delta r}$.

$$i_R = \sum_{r=r_2}^{r_3}(i_R)_{\delta r} = nFD_O 2\pi \sum_{r=r_2}^{r_3}(\partial C_O/\partial y)_{y=0}\,r\delta r$$

which yields, as $\delta r \to 0$, eq. (9.4.4).

The solution to these equations yields the limiting ring current (17):

$$i_{R,l,c} = 0.62nF\pi(r_3^3 - r_2^3)^{2/3} D_O^{2/3}\omega^{1/2}\nu^{-1/6}C_O^*$$

(9.4.5)

or, in general,

$$i_R = i_{R,l,c}\{[C_O^* - C_O(y = 0)]/C_O^*\}$$

(9.4.6)

This can be written in terms of the disk current (9.3.30), which would be observed under identical conditions for a disk of radius r_1 to yield

$$i_R = i_D \frac{(r_3^3 - r_2^3)^{2/3}}{r_1^2}$$

(9.4.7)

or

$$\frac{i_R}{i_D} = \beta^{2/3} = \left(\frac{r_3^3}{r_1^3} - \frac{r_2^3}{r_1^3}\right)^{2/3}$$

(9.4.8)

Notice that for given reaction conditions (C_O^* and ω), a ring electrode will produce a larger current than a disk electrode of the same area. Thus, the analytical sensitivity of a ring electrode (i.e., the current caused by a mass-transfer-controlled reaction of an electroactive species divided by the residual current) is better than that of a disk electrode, and this is especially true of a thin ring electrode. However, it is usually more difficult to construct a rotating ring electrode than an RDE.

9.4.2 The Rotating Ring-Disk Electrode

In a *rotating ring-disk electrode* (RRDE), the current-potential characteristics of the disk are unaffected by the presence of the ring, and the properties of the disk are as described in Section 9.3. (In fact, if the disk current is found to change upon variation of the ring potential or current, one should suspect a defective RRDE or an undesirable coupling of the ring and disk through solution uncompensated resistance). Since RRDE experiments involve the examination of two potentials (that of the disk, E_D, and that of the ring, E_R) and two currents (i_D and i_R), the representation of the results involves more dimensions than for experimental results involving a single working electrode. RRDE experiments are usually carried out with a *bipotentiostat* (Section 15.4.4), which allows separate adjustment of E_D and E_R (Figure 9.4.2a). However, since most RRDE measurements involve steady-state conditions, it is possible to use an ordinary potentiostat to control the ring circuit and a simple floating power supply in the disk circuit (Figure 9.4.2b).
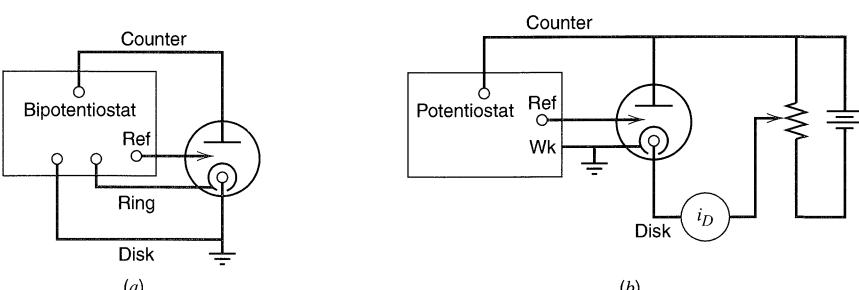
Figure 9.4.2 Block diagram of RRDE apparatus. (*a*) Bipotentiostat. (*b*) Ordinary (three-electrode) potentiostat and voltage divider.

Several different types of experiments are possible at the RRDE, The most common are *collection* experiments, where the disk generated species is observed at the ring, and *shielding* experiments, where the flow of bulk electroactive species to the ring is perturbed because of the disk reaction.

(a) Collection Experiments

Consider the experiment in which the disk is held at a potential E_D, where the reaction O $+ ne \rightarrow$ R produces a cathodic current i_D, while the ring is maintained at a sufficiently positive potential, E_R, that any R reaching the ring is rapidly oxidized (R $\rightarrow$ O $+ ne$), so that the concentration of R at the ring surface is essentially zero. We are interested in the magnitude of the ring current, i_R, under these conditions; that is, we want to know how much of the disk-generated R is collected at the ring. The approach is again to solve the steady-state ring convective-diffusion equation, (9.4.3), this time for species R:

$$r\left(\frac{\partial C_R}{\partial r}\right) - y\left(\frac{\partial C_R}{\partial y}\right) = \left(\frac{D_R}{B'}\right)\frac{1}{y}\left(\frac{\partial^2 C_R}{\partial y^2}\right) \tag{9.4.9}$$

The boundary conditions are more complex because of the structure of the system:

1. At the disk $(0 \le r < r_1)$, the flux of R is related to that of O by the usual conservation equation:

$$D_R\left(\frac{\partial C_R}{\partial y}\right)_{y=0} = -D_O\left(\frac{\partial C_O}{\partial y}\right)_{y=0} \tag{9.4.10}$$

From the results in Section 9.3.2,

$$\left(\frac{\partial C_R}{\partial y}\right)_{y=0} = \frac{-i_D}{nFAD_R} = \frac{-i_D}{\pi r_1^2 nFD_R} \tag{9.4.11}$$

2. In the insulating gap region $(r_1 \le r < r_2)$, no current flows, so that

$$\left(\frac{\partial C_R}{\partial y}\right)_{y=0} = 0 \tag{9.4.12}$$

3. At the ring $(r_2 \le r < r_3)$, under limiting current conditions,

$$C_R(y = 0) = 0 \tag{9.4.13}$$

We assume that R is initially absent from the bulk solution ($\lim_{y\to\infty} C_R = 0$) and that the bulk concentration of O is C_O^*. As in (9.4.4), the ring current is given by

$$i_R = nFD_R 2\pi \int_{r_2}^{r_3} \left(\frac{\partial C_R}{\partial y}\right)_{y=0} r\, dr \tag{9.4.14}$$

This problem can be solved in terms of dimensionless variables using the Laplace transform method and results have been given in terms of Airy functions (18, 19). It turns out that the ring current is related to the disk current by a quantity N, the *collection efficiency*,

$$\boxed{N = \frac{-i_R}{i_D}} \tag{9.4.15}$$

that depends only on r_1, r_2, and r_3 and is *independent* of ω, C_O^*, D_O, D_R, etc. The collection efficiency can be calculated from

$$N = 1 - F(\alpha/\beta) + \beta^{2/3}[1 - F(\alpha)] - (1 + \alpha + \beta)^{2/3}\{1 - F[(\alpha/\beta)(1 + \alpha + \beta)]\} \tag{9.4.16}$$

where $\alpha = (r_2/r_1)^3 - 1$, β is given by (9.4.8), and the F values are defined by

$$F(\theta) = \left(\frac{\sqrt{3}}{4\pi}\right) \ln\left\{\frac{(1 + \theta^{1/3})^3}{1 + \theta}\right\} + \frac{3}{2\pi} \arctan\left(\frac{2\theta^{1/3} - 1}{3^{1/2}}\right) + \frac{1}{4} \qquad (9.4.17)$$

The function $F(\theta)$ and values of N for different ratios r_2/r_1 and r_3/r_2 are tabulated in reference 18. One can also determine N experimentally for a given electrode, by measuring $-i_R/i_D$ for a system where R is stable. Once N is determined, it is a known constant for that RRDE. For example, for an RRDE with $r_1 = 0.187$ cm, $r_2 = 0.200$ cm, and $r_3 = 0.332$ cm, $N = 0.555$; that is, 55.5% of the product generated at the disk is collected at the ring. Qualitatively, N becomes larger as the gap thickness $(r_2 - r_1)$ decreases and as the ring size $(r_3 - r_2)$ increases. The concentration profiles of R in the vicinity of the RRDE surface are shown in Figure 9.4.3.

In a typical collection experiment, one plots i_D and i_R as functions of E_D (at a constant E_R) (Figure 9.4.4a). Stability of the product is assured if N is independent of i_D and ω. If R decomposes at a rate sufficiently high that some is lost in its passage from disk to ring, the collection efficiency will be smaller and will be a function of ω, i_D, or C_O^*. Information about the rate and mechanism of decay of R can thus be obtained from RRDE collection experiments (see Chapter 12). Information about the reversibility of the electrode reaction can be obtained by plotting the ring voltammogram (i_R vs. E_R) at a constant value of E_D, and comparing the $E_{1/2}$ with that of the disk voltammogram (Figure 9.4.4b).

(b) Shielding Experiments

The current at the ring electrode for the reduction of O to R when the disk is at open circuit is given by (9.4.5) to (9.4.8). The limiting current at the ring with $i_D = 0$, denoted $i_{R,l}^0$, is given by (9.4.8), which is rewritten as

$$i_{R,l}^0 = \beta^{2/3} i_{D,l} \qquad (9.4.18)$$

where $i_{D,l}$ is the limiting current that could be achieved at the disk electrode if it were active.

If the disk current is changed to a finite value, i_D, the flux of O to the ring will be decreased. The extent of this decrease will be the same as the flux of stable product R to the ring in a collection experiment—Ni_D. Hence the limiting ring current $i_{R,l}$ is given by

$$\boxed{i_{R,l} = i_{R,l}^0 - Ni_D} \qquad (9.4.19)$$
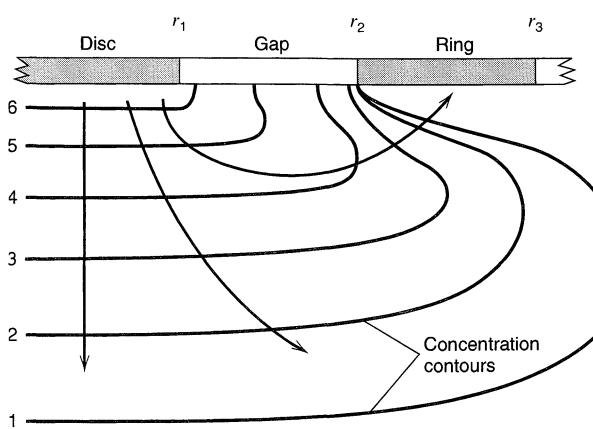
Figure 9.4.3 Concentration profiles of species R at an RRDE. Concentrations increase from curve 1 to curve 6. For the disk ($0 \leq r < r_1$), $\partial C_R/\partial r = 0$; in the gap ($r_1 \leq r < r_2$), $(\partial C_R/\partial y)_{y=0} = 0$; and at ring surface ($r_2 \leq r < r_3$), $C_R(y = 0) = 0$. [From W. J. Albery and M. L. Hitchman, "Ring-Disc Electrodes," Clarendon, Oxford, 1971, Chap. 3, by permission of Oxford University Press.]
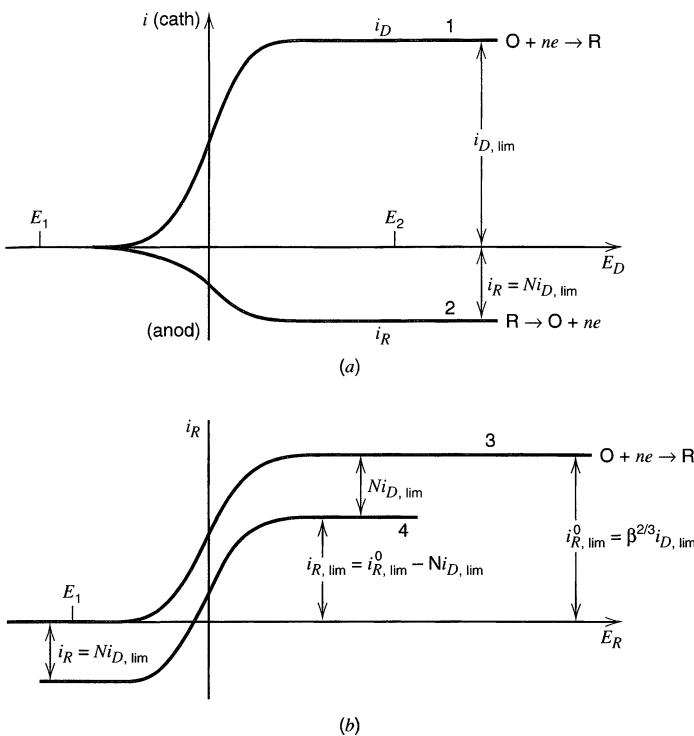
Figure 9.4.4 (*a*) Disk voltammogram. (*1*) i_D vs. E_D and (*2*) i_R vs. E_D with $E_R = E_1$. (*b*) Ring voltammograms. (*3*) i_R vs. E_R, $i_D = 0$ ($E_D = E_1$) and (*4*) i_R vs. E_R, $i_D = i_{D,l,c}$ ($E_D = E_2$).

(This equation holds for any value of i_D, including $i_D = 0$ and $i_D = i_{D,l}$.) Using (9.4.18), we have for the special case $i_D = i_{D,l}$:

$$i_{R,l} = i_{R,l}^0 (1 - N\beta^{-2/3}) \tag{9.4.20}$$

Thus, when the disk current is at its limiting value, the ring current is decreased by the factor $(1 - N\beta^{-2/3})$. This factor, always less than unity, is called the *shielding factor*. These relations are easier to understand when the complete *i-E* curves are considered (Figure 9.4.4*b*). One sees that the effect of switching i_D from 0 to $i_{D,l}$ is to shift the entire ring voltammogram (i_R vs. E_R), which is assumed to be reversible, by the amount $Ni_{D,l}$.

Other dual electrode systems that operate at steady state and show similar shielding and collection effects include microelectrode arrays and the scanning electrochemical microscope (SECM). With microelectrode arrays (Section 5.9.3), one monitors diffusion between two neighboring electrodes. In a similar way, one can use the SECM (Section 16.4) to study diffusion between an ultramicroelectrode tip and substrate electrode. In both of these systems, convective effects are absent and the time for interelectrode transit is governed by the distance between the electrodes.

9.5 TRANSIENTS AT THE RDE AND RRDE

Although a major advantage of rotating disk electrode techniques, compared to stationary electrode methods, is the ability to make measurements at steady state without the need to consider the time of electrolysis, the observation of current transients at the disk or ring following a potential step can sometimes be of use in understanding an electrochemical system. For example the adsorption of a component,

A, on the disk electrode can be studied by noticing the transient shielding of the ring current for the electrolysis of A upon stepping the disk potential to a value where A is adsorbed.

9.5.1 Transients at the RDE

The treatment of the non-steady-state problem at the RDE requires solution of the usual disk convective-diffusion equation, (9.3.14), but with inclusion of the $\partial C/\partial t$ term, that is,

$$\frac{\partial C_O}{\partial t} = D_O\left(\frac{\partial^2 C_O}{\partial y^2}\right) - B'y^2\left(\frac{\partial C_O}{\partial y}\right) \tag{9.5.1}$$

where $B' = 0.51\omega^{3/2}\nu^{-1/2}$. This has been accomplished by approximation methods (20, 21) and by digital simulation (22). For a potential step to the limiting current region of the i-E curve, the instantaneous value of i_l, denoted $i_l(t)$, is given approximately by (20)

$$R(t) = \frac{i_l(t)}{i_l(ss)} = 1 + 2\sum_{m=1}^{\infty}\exp\left(\frac{-m^2\pi^2 D_O t}{\delta_O^2}\right) \tag{9.5.2}$$

where $i_l(ss)$ is the value of i_l as $t \rightarrow \infty$, and δ_O is given in (9.3.25). An implicit approximate equation for $R(t)$ obtained by the "method of moments" has also been proposed (21):

$$\frac{D_O t}{\delta_O^2} = \frac{1}{6}\left(\frac{1.8049}{1.6116}\right)^2\left\{\frac{1}{2}\ln\left(\frac{1 - R(t)^3}{[1 - R(t)]^3}\right) + \sqrt{3}\left[\frac{\pi}{6} - \arctan\left(\frac{2R(t) + 1}{\sqrt{3}}\right)\right]\right\} \tag{9.5.3}$$

Both of these results are in good agreement with the digital simulation (22); a typical disk transient is shown in Figure 9.5.1. At short times, when the diffusion layer thickness is much thinner than δ_O, the potential step transient follows that for a stationary electrode [equation 5.2.11]. The time required for the current to attain its steady-state value can be obtained from the curve in Figure 9.5.1. The current is within 1% of $i_l(ss)$ at a time τ when

$$\omega\tau(D/\nu)^{1/3}(0.51)^{2/3} \geq 1.3 \tag{9.5.4}$$

or, taking $(D/\nu)^{1/3} \approx 0.1$, when $\omega\tau > 20$. Thus for $\omega = 100$ s (or a rotation rate of about 1000 rpm), $\tau \approx 0.2$ s.
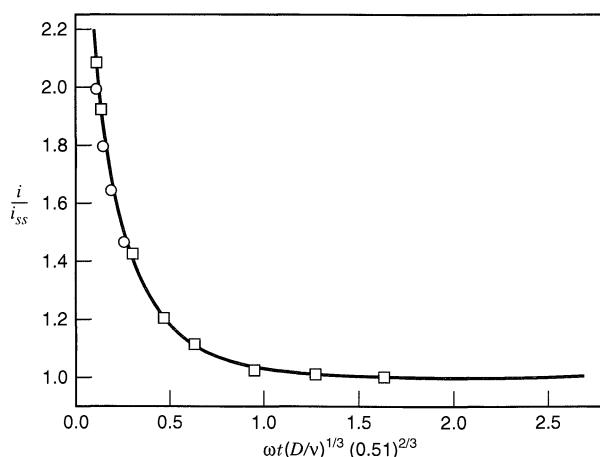
Figure 9.5.1 Disk-current transient for potential step at the disk: Curve is simulated; points are from theoretical equations given by Bruckenstein and Prager (◯) and Siver (▢). [From K. B. Prater and A. J. Bard, *J. Electrochem. Soc.*, **117**, 207 (1970), with permission of the publisher, The Electrochemical Society, Inc.]

9.5.2 Transients at the RRDE

Consider the experiment in which the ring of the RRDE is maintained at a potential where oxidation of species R to O can occur, and the disk is at open circuit or at a potential where no R is produced. If R is then generated at the disk by a potential step to an appropriate value or by a constant current step, a certain time will be required for R to transit the gap from the outside of the disk to the inside edge of the ring (the *transit time*, t'). An additional time will be required until the disk current attains its steady-state value. The rigorous solution for the ring current transient, $i_R(t)$, involves solving the non-steady-state form of (9.4.9):

$$\frac{\partial C_R}{\partial t} = D_R\left(\frac{\partial^2 C_R}{\partial y^2}\right) + B'y^2\left(\frac{\partial C_R}{\partial y}\right) - B'ry\left(\frac{\partial C_R}{\partial r}\right) \tag{9.5.5}$$

This rather difficult problem is discussed by Albery and Hitchman (23), and several approaches to the solution and approximate equations are given. These may also be obtained by the digital simulation method (see Appendix B.5) (22), and Figure 9.5.2 is a display of typical simulated ring-current transients for both a current step [to $i_{D,l}(ss)$] and a potential step to the limiting-current region at the disk electrode. Note that the ring current rises more rapidly when a potential step is applied. This effect can be attributed to the large instantaneous current that flows at the disk electrode when the potential is stepped (Figure 9.5.1).

An approximate value for the transit time can be obtained by the method suggested by Bruckenstein and Feldman (24). The radial velocity near the electrode surface is given by (9.3.10), which can be written

$$v_r = \frac{dr}{dt} = 0.51\omega^{3/2}\nu^{-1/2}ry \tag{9.5.6}$$

A molecule of R generated at the edge of the disk ($r = r_1$) must diffuse normal to the disk to reach the ring, since v_r is zero at $y = 0$. It is then swept in a radial direction and then moves by diffusion and convection in the y direction to reach the inner edge of the ring. This path can be described by some average trajectory and some time-dependent distance y from the electrode surface. Integration of (9.5.6) yields

$$\ln\left(\frac{r_2}{r_1}\right) = 0.51\omega^{3/2}\nu^{-1/2}\int_0^{t'} y\, dt \tag{9.5.7}$$
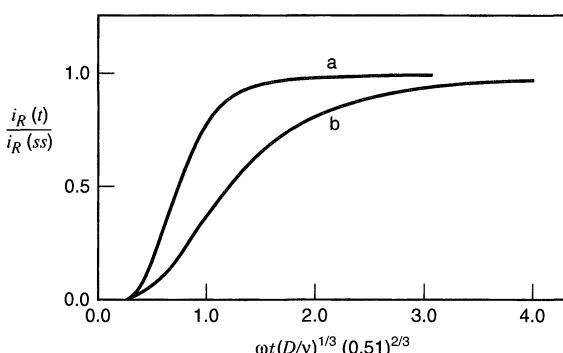
Figure 9.5.2 Simulated ring-current transients. *Curve a*: Potential step at the disk. *Curve b*: Current step at the disk. [From K. B. Prater and A. J. Bard, *J. Electrochem. Soc.*, **117**, 207 (1970), with permission of the publisher, The Electrochemical Society, Inc.]

If one uses the approximation $y \approx (Dt)^{1/2}$, substitutes this value in (9.5.7), and carries out the integration, the result is[4]

$$\omega t' = 3.58(\nu/D)^{1/3} \left[\log\left(\frac{r_2}{r_1}\right) \right]^{2/3} \tag{9.5.8}$$

With $(D/\nu)^{1/3} = 0.1$, $\omega = 100 \text{ s}^{-1}$, and an electrode with $r_2/r_1 = 1.07$ (representing a rather narrow gap), the transit time from (9.5.8) is about 30 ms. Simulated ring transients for electrodes of different geometries are shown in Figure 9.5.3; the points on the curves represent the t' values calculated from (9.5.8). This t' more closely represents the time required for the ring current to attain about 2% of the steady value.

A study of ring-current transients can be useful in determining adsorption of a disk-generated intermediate at the disk, since this will cause a delay in the appearance of this species at the ring (25). The transients can also be used in a qualitative way to study electrode processes. Consider a "shielding transient" experiment described by Bruckenstein and Miller (26) concerning the reduction of oxygen at a copper-ring/platinum-disk electrode (Figure 9.5.4). Oxygen is reduced more readily on Pt than on Cu. If the electrode is immersed in an air-saturated solution containing 0.2 M H_2SO_4 and 2×10^{-5} M Cu(II), no reaction occurs at the disk with E_D at 1.00 V vs. SCE. If E_R is held at -0.25 V vs. SCE, there is a cathodic ring current of about 11 μA due to the reaction Cu(II) + $2e \rightarrow$ Cu. Oxygen is not reduced at the copper ring at this potential (even though the reversible potential for the reaction $O_2 + 4H^+ + 4e \rightarrow H_2O$ is much more positive), because the kinetics are very slow. If E_D is now stepped to 0.0V, a cathodic disk current of about 700 μA flows. This current represents reduction of oxygen at the platinum disk and also plating of copper by reduction of the Cu(II). This plating of copper on the platinum substrate occurs at potentials more positive than those where copper would deposit on bulk copper and is called *underpotential deposition* (Section 11.2.1). The reduction of Cu(II) at the disk shields the ring, so that a drop in i_R is observed. As copper deposits on the disk, however, the reduction of oxygen is hindered, and the disk current falls. After about a monolayer of copper has deposited on the disk, further underpotential deposition is no longer possible, Cu(II) reduction at the disk ceases, and the ring current returns to its unshielded value.
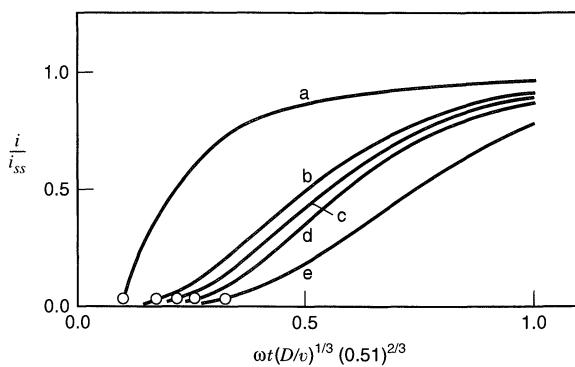
Figure 9.5.3 Simulated ring transients for electrodes of different geometries $(r_2/r_1, r_3/r_1)$. *Curve a*: 1.02, 1.04. *Curve b*: 1.05, 1.07. *Curve c*: 1.07, 1.48. *Curve d*: 1.09, 1.52. *Curve e*: 1.13, 1.92. Points show transit times, t', calculated from (9.5.8). [From K. B. Prater and A. J. Bard, *J. Electrochem. Soc.*, **117**, 207 (1970), with permission of the publisher, The Electrochemical Society, Inc.]

[4]Different choices of y [e.g., $2(Dt)^{1/2}$] or a different method of carrying out the integration will result in an alternative value of the constant. For example, Bruckenstein and Feldman (24) considered the case in which the species diffuses outward for $t < t'/2$, then back toward the surface for $t'/2 < t \leq t'$. Then the constant in (9.5.8) is 4.51.
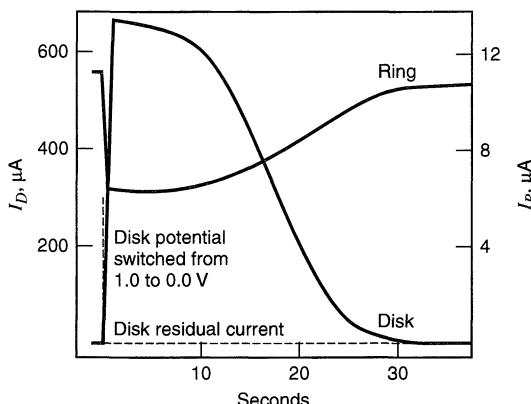
Figure 9.5.4 Time dependence of the oxygen reduction current at the disk and the Cu(II) reduction current at the ring of a platinum ring-disk electrode. Solution: 0.2 M H_2SO_4 and 2 × 10^{-5} M Cu(II) with air saturation. Rotation speed, 2500 rpm. Disk potential held at 0.00 V *vs*. SCE for $t > 0$; ring potential $= -0.25$ V *vs*. SCE at all t. Disk area, 0.458 cm^2; $\beta^{2/3} = 0.36$; collection efficiency, 0.183. [Reprinted with permission from S. Bruckenstein, and B. Miller, *Accts. Chem. Res.*, **10**, 54 (1977). Copyright 1977, American Chemical Society.]

This rather simple experiment demonstrates quite clearly the "poisoning" of the oxygen reduction process by copper. Incidentally, Cu(II) is a rather common impurity in distilled water and mineral acids, and this experiment demonstrates that underpotential deposition of a monolayer of copper from solutions containing as little as 1 ppm Cu can drastically affect the behavior of a platinum electrode. Adsorption of small amounts of other impurities (i.e., organic molecules) can also have an effect on solid-electrode behavior. Thus, electrochemical experiments often require making great efforts to establish and maintain solution purity.

The RRDE can also be used to study electrochemical processes at electrodes modified with thin polymer films (Chapter 14). In this application, the polymer film is prepared on the disk, and the ring monitors the flux of ions from the film during a potential sweep. For example, the flux of the cation, 1,3-dimethylpyridinium, from a film of polypyrrole/poly(styrenesulfonate) was monitored at the ring electrode, as the disk was cycled in an acetonitrile solution over the potential region where reduction and oxidation of the film occurred (27).

▶ 9.6 MODULATED RDE

9.6.1 Hydrodynamic Modulation

For all of the methods discussed so far in this chapter, we have assumed that the rotation rate of the electrode is constant and at its steady-state value of ω when measurements of currents are carried out. However, it can also be useful to measure currents under conditions when ω is changing with time.

The simplest case involves a monotonic variation of ω as a function of time (e.g., $\omega \propto t^2$) and an automatic plotting of i_D vs. $\omega^{1/2}$. These "automated Levich plots" can be of value compared to manual (and possibly more precise) point-by-point measurements, especially when the electrode surface is changing with time (e.g., during an electrode-position, or with impurity or product adsorption) and a rapid scan is needed. This technique and related methods have been reviewed (28).

Another useful technique features the sinusoidal variation of $\omega^{1/2}$ [called *sinusoidal hydrodynamic modulation*]. Consider an RDE whose rotation rate is varied sinusoidally about a fixed center speed, ω_0, at a frequency σ, so that the instantaneous value of $\omega^{1/2}$ is given by

$$\omega^{1/2} = \omega_0^{1/2} + \Delta\omega^{1/2} \sin(\sigma t) \tag{9.6.1}$$

For example, consider the case where $\omega_0^{1/2} = 19.4 \text{ s}^{-1/2}$ ($\omega_0 = 376 \text{ s}^{-1}$, rotation rate = 3600 rpm), $\Delta\omega^{1/2} = 1.94 \text{ s}^{-1/2}$ (i.e., $\Delta\omega = 3.8 \text{ s}^{-1}$, equivalent to 36 rpm), and the modulation frequency is 3 Hz [$\sigma = 6\pi \text{ s}^{-1}$]. In this situation, ω varies between 380 and 372 s^{-1} (between 3636 and 3564 rpm) three times per second (Figure 9.6.1). $\Delta\omega$ is always smaller than ω_0, and is usually only about 1% of ω_0. The usable modulation frequency depends on the inertia and response of the motor-electrode system and is usually 3 to 6 Hz.

If the system follows the Levich equation, (9.3.22), the current is given by

$$i(t) = A'[\omega_0^{1/2} + \Delta\omega^{1/2} \sin(\sigma t)] \tag{9.6.2}$$

where $A' = 0.62nFAD_O^{2/3}\nu^{-1/6}C_O^* = i_{\omega_0}/\omega_0^{1/2}$. Thus,

$$i(t) = i_{\omega_0}\left[1 + \left(\frac{\Delta\omega}{\omega_0}\right)^{1/2} \sin \sigma t\right] \tag{9.6.3}$$

and the amplitude of the modulated current is[5]

$$\boxed{\Delta i = (\Delta\omega/\omega_0)^{1/2}i_{\omega_0}} \tag{9.6.4}$$

This varying component of the disk current is most conveniently recorded after filtering and passage through a lock-in amplifier or full-wave rectifier (Figure 9.6.2).

Although the Δi value is much smaller in magnitude than i_{ω_0}, it has the very important advantage of being free of contributions from processes that do not depend on the mass-transfer rate. Thus, Δi is essentially independent of double-layer charging and is unaffected by oxidation and reduction of the electrode or of adsorbed species. More-
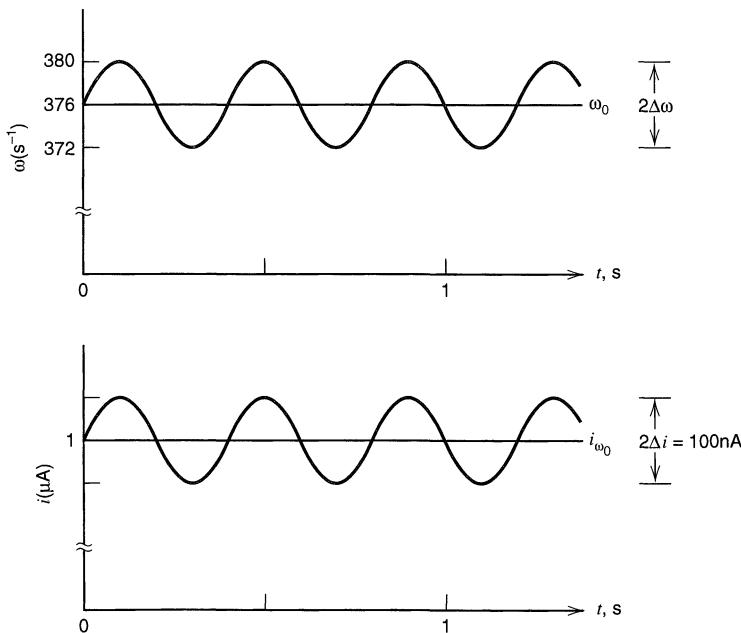
Figure 9.6.1
Representation of $\Delta\omega$ and Δi for a sinusoidally hydrodynamically modulated RDE.

[5]This equation was derived for limiting-current conditions. It is also valid for currents in the rising portion of a reversible wave. It will not be valid if the rate of change in ω is comparable to the rate of hydrodynamic relaxation. Thus, $\Delta\omega/\omega_0$ and σ are usually kept small.
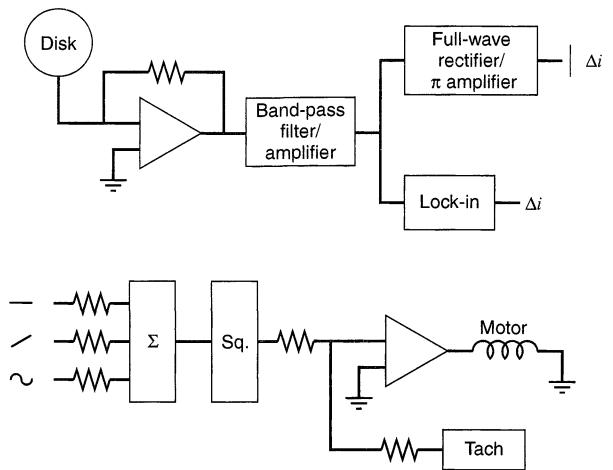
Figure 9.6.2 Schematic of speed control and disk-current processing circuitry. Only the current follower of the conventional three-electrode potentiostat that controls the disk electrode is shown. [Reprinted with permission from B. Miller, and S. Bruckenstein, *Anal. Chem.*, **46**, 2026 (1974), Copyright 1974, American Chemical Society.]

over, it is relatively insensitive to the anodic and cathodic background currents. Sinusoidal hydrodynamic modulation is a useful technique for the determination of very low (submicromolar) concentrations with the RDE, for studies in the presence of surface complications, and for measurements near the background limits of the solvent/supporting-electrolyte system. Shown in Figure 9.6.3 are results from a study in which 0.2 μM Tl(I) was reduced at an amalgamated gold RDE (which can be used when a mercury-like surface is desired) (29). Even though the faradaic current for the Tl(I) reduction cannot be distinguished from the residual current on the i_D-E scan, a clear reduction wave is found by measuring Δi. It is also possible to obtain kinetic information from hydrodynamic modulation experiments, by employing σ values where deviations from Levich behavior occur (30).

9.6.2 Thermal Modulation

The RDE can also be modulated thermally by irradiating the back of the disk electrode with a laser (Figure 9.6.4) (31). This method is the RDE analog of the temperature jump
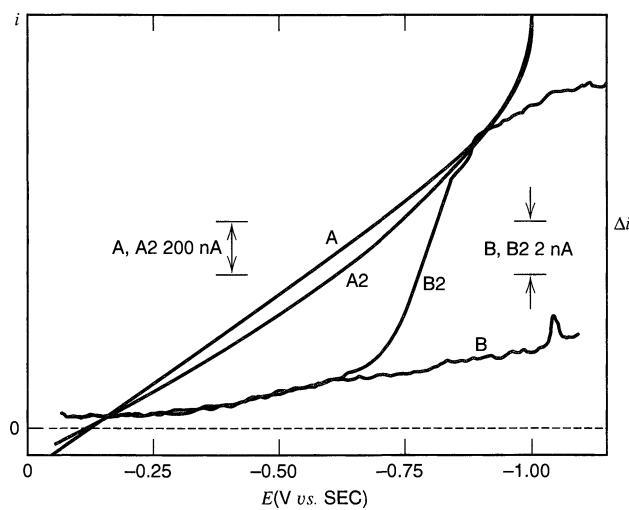
Figure 9.6.3 Controlled-potential cathodic scans of Tl(I) at an amalgamated gold disk. All A traces are RDE curves, all B traces are HMRDE curves. (A, B) 0.01 M HClO$_4$; $(A2, B2)$ 2.0 × 10^{-7} M Tl$^+$ in 0.01 M HClO$_4$. Current sensitivities indicated by markers; zero current for all curves is the dashed line. For all curves, $\omega_0^{1/2} = 60$ rpm$^{1/2}$. For B curves, $\Delta\omega^{1/2} = 6$ rpm$^{1/2}$, $\sigma/2\pi = 3$ Hz, averaging time constant = 3 s, and scan rate = 2 mV/s. [Reprinted with permission from B. Miller, and S. Bruckenstein, *Anal. Chem.*, **46**, 2026 (1974). Copyright 1974, American Chemical Society.]
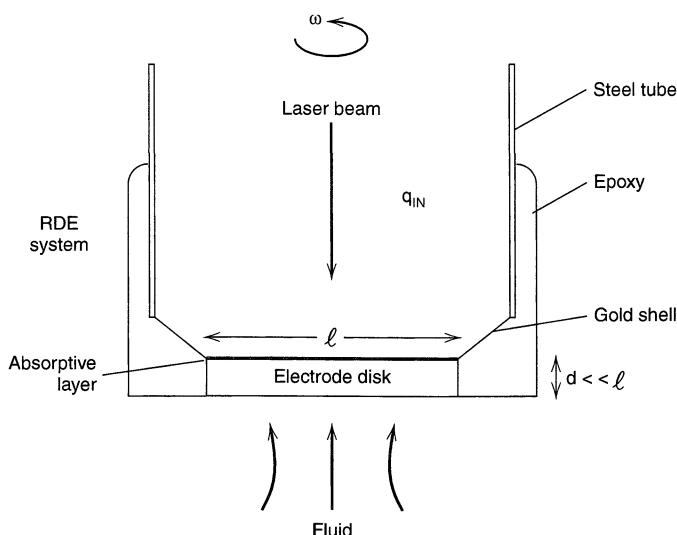
Figure 9.6.4 Schematic diagram of the apparatus employed for temperature modulation of the RDE. The laser pulse irradiates a disk electrode coated with an absorptive layer. [Reprinted with permission from J. L. Valdes, and B. Miller, *J. Phys. Chem.* **92**, 525 (1988). Copyright 1988, American Chemical Society.]

experiment discussed in Section 8.7.5. Experiments for both constant and modulated irradiation of the electrode have been carried out. In the constant mode, the irradiating beam represents a heat input (on the order of 25–200 mW), while heat is carried away from the electrode surface by thermal diffusion and convection into the solution. Eventually, a steady-state disk temperature is attained. This temperature change is proportional to $\omega^{-1/2}$ (since a higher rotation rate results in more heat being carried away from the electrode surface). The temperature change at the electrode surface will cause a change in a number of parameters, such as D (see Section 8.7.5), that affect i_D; hence the disk current is modulated by the heating of the laser beam. A theoretical analysis shows that the magnitude of the current change, Δi_D, is proportional to the laser heat input, but is relatively independent of ω (31).

In the periodically modulated version of this experiment (32), the laser heating is carried out sinusoidally at a frequency of 5 to 20 Hz, and the resulting sinusoidally varying current, Δi_D, is detected with a lock-in amplifier, as in hydrodynamic modulation. The variation of Δi_D with E is called *thermal modulation voltammetry* (TMV). Near $E^{0'}$, Δi_D shows a peak whose magnitude for a nernstian reaction is a function of the ratio of the entropic energy of the electrode reaction divided by the activation energy of the mass transport process. While the method is capable of extracting thermodynamic information about a reaction, both the theory and the experimental set-up is sufficiently complex that it has not yet found widespread use.

▷ 9.7 CONVECTION AT UMEs

One advantage of ultramicroelectrodes (Section 5.3) is that mass transport to the electrode by radial diffusion is high, even in the absence of convection. For a microdisk electrode of radius r, the mass-transfer coefficient is:

$$m_O = 4D/\pi r \tag{9.7.1}$$

However, the mass-transfer coefficient can be increased above this level by introducing convective flow, for example, by rotating the electrode or rapidly flowing a solution to it. This might be useful in measurements of rapid heterogeneous electron-transfer kinetics, where the radial diffusion alone is insufficient to remove mass-transfer limitations.

As noted in Section 9.3.6, the theory developed earlier for the RDE does not hold for UMEs where there is significant radial diffusion to the edges of the electrode. Although no
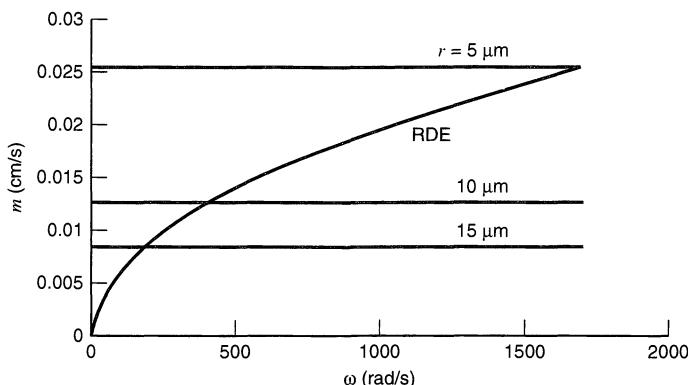
Figure 9.7.1 The effect of angular rotation rate, ω, on the mass-transfer coefficient, m, for an RDE. The horizontal lines indicate the mass-transfer coefficients for unrotated UMEs of different radii, r. Calculations assume $D = 1.0 \times 10^{-5}$ cm^2/s and $\nu = 0.01$ cm^2/s. [Adapted from data in X. Gao, and H. S. White, *Anal. Chem.*, **67**, 4057 (1995).]

theoretical treatments exist for the rotating UME, one can obtain a good concept of the behavior by considering the limiting situations at low and high rotation rates (33, 34). As $\omega \to 0$, the behavior approaches that of a stationary UME, while as $\omega \to \infty$, the usual RDE dependency on $\omega^{1/2}$ should be observed. Shown in Figure 9.7.1 is the dependency of the mass-transfer coefficient for an RDE on ω, along with m for electrodes with radii of 5, 10, and 15 μm. Clearly, for the larger radii, mass transport can be enhanced by rotating the electrode, but the electrode of 5-μm radius shows a larger mass-transfer coefficient than can be attained for an RDE at any experimentally accessible rotation rate. Rotation of UMEs of larger radii (e.g., 15 μm) might be useful, however, when solutions of high resistivity are used (34) or where studies of polymer films (Section 14.4.2) are of interest (33). An additional problem that arises with rotating UMEs (33, 34) is that the electrode itself is often offset from the rotation axis during construction and the rotation may cause flexing of the shaft with additional offset, causing the effect discussed in Section 9.3.6. Note that it is also possible to increase the effective mass-transfer rate to a UME by using it in the positive feedback mode with a scanning electrochemical microscope, as discussed in Section 16.4.2.

Convective flow to UMEs can also be attained by flowing the solution past a stationary electrode. For example, flow can be directed normal to the electrode from a nozzle positioned nearby (Figure 9.7.2) (35). This configuration is sometimes called a *wall jet* or
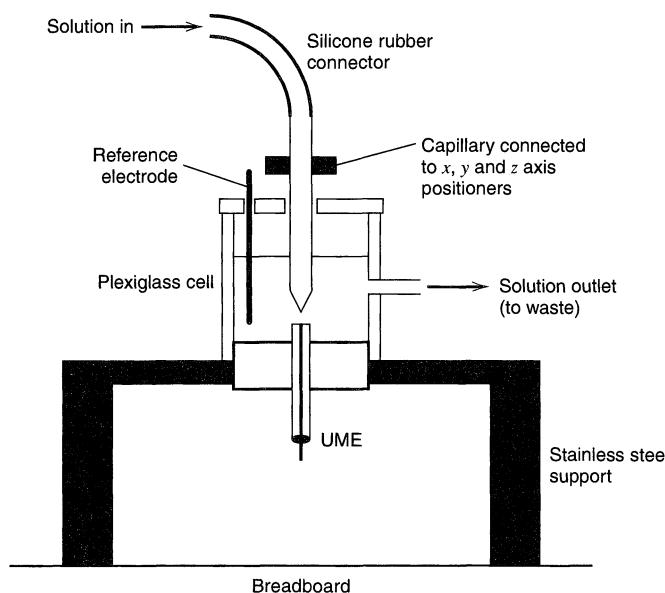
Figure 9.7.2 Schematic drawing of arrangement for wall jet or microjet electrode. [Reprinted with permission from J. V. Macpherson, S. Marcar, and P. R. Unwin, *Anal. Chem.*, **66**, 2175 (1994). Copyright 1994, American Chemical Society.]

microjet electrode. A jet of solution fed by gravity or pumped from a small nozzle (e.g., 50–100 μm diameter) impinges on the ultramicroelectrode (e.g., 25 μm diameter). The mass-transfer coefficient for this configuration is proportional to the square root of the volume flow rate and can be as large as 0.55 cm/s, equivalent to that of an ultramicroelectrode with a radius of 150 nm in the absence of convection (35). Another arrangement involves placement of the ultramicroelectrode in a flow channel with the solution flow parallel to the electrode surface (36). An example is a microband electrode 12 μm thick and 0.2 cm long positioned across a channel 116 μm high and 0.2 cm wide (36). In this configuration, an effective mass-transfer coefficient of 0.5 cm/s can be attained with volume flow velocities near 3.7 cm³/s. Flow cells of this type are useful as detectors, for example, in liquid chromatography (see Section 11.6.4). They have found less use in electrochemical studies, probably because of the technical problems involved in setting up systems with solution flow.

▶ 9.8 ELECTROHYDRODYNAMICS AND RELATED PHENOMENA

There are many phenomena involving convection in electrochemical systems (6). While it is beyond the scope of this monograph to treat these in any depth, we will give a brief overview as an introduction to more detailed treatments. In general, electrohydrodynamics deals with fluid motion induced by electric fields. *Electroosmosis* is one important example.

Our previous examples of convective flow dealt with fluid flow induced by a pressure gradient (Section 9.2.2). At steady state, in the absence of gravitational effects (natural convection), the fluid velocity, **v**, could be obtained from the equation

$$\eta_s \nabla^2 \mathbf{v} = \nabla P \tag{9.8.1}$$

Similarly, the force generated by the interaction of an electric field on excess charge density in a fluid can induce fluid flow, that is,
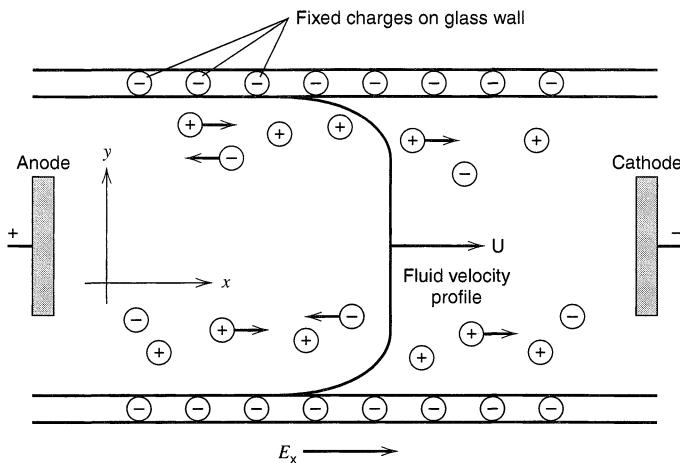
$$\eta_s \nabla^2 \mathbf{v} = -\rho_E \mathscr{E} \tag{9.8.2}$$

where $\mathscr{E}$ is the electric field (V/cm) and ρ_E is the charge per unit volume.

9.8.1 Electroosmotic Flow

Let us consider the application of an electric field along a glass capillary tube filled with an electrolyte solution, as shown schematically in Figure 9.8.1. The walls of the capillary tube will be charged at most pH values, because of protonation/deprotonation equilibria involving surface Si-OH groups. At a pH above about 3, the surface charge will be negative. This charge causes the formation of a diffuse layer of counter (positive) charge in solution, just as at a charged electrode surface (Chapter 13). When an electric field is applied along the capillary axis, this excess charge (in the form of electrolyte cations) will move toward the cathode and the net viscous drag on the solvent will induce convection of the solution. In most cases, the radius of the tube will be large compared to the thickness of the diffuse layer, so that curvature can be neglected, and the flow considered as taking place in a planar channel. Then, (9.8.2) can be written (6) in terms of the field, $\mathscr{E}_x$, along the axis of the capillary,

$$\eta_s \frac{\partial^2 v}{\partial y^2} = -\rho_E \mathscr{E}_x = \varepsilon \varepsilon_0 \frac{\partial^2 \phi}{\partial y^2} \mathscr{E}_x \tag{9.8.3}$$

Figure 9.8.1
Representation of electroosmotic flow of a fluid (e.g., water) in a glass capillary. Only ions near the glass walls are shown. Note that the velocity profile here is flatter (so-called "plug flow") than the parabolic profile seen with an external pressure drop along a tube.

where the charge density has been obtained from the Poisson equation, (13.3.5),

$$\rho_E = -\varepsilon\varepsilon_0 \frac{\partial^2 \phi}{\partial y^2} \tag{9.8.4}$$

A single integration of (9.8.3), with $\partial v/\partial y = 0$ and $\partial \phi/\partial y = 0$ far from the walls ($y \to \infty$), yields

$$\eta_s(\partial v/\partial y) = \varepsilon\varepsilon_0(\partial \phi/\partial y)\mathscr{E}_x \tag{9.8.5}$$

A second integration from a position near the wall, where $v = 0$ and $\phi = \zeta$, to the middle of the channel, where $v = U$ and $\phi = 0$, gives the *Helmholtz–Smoluchowski equation*:

$$U = -\varepsilon\varepsilon_0 \zeta \mathscr{E}_x/\eta_s \tag{9.8.6}$$

The parameter ζ is called the *zeta potential*, which is the potential in a not-very-well-defined position in the diffuse layer called the *shear plane* (37), and U is the *electroosmotic solution velocity* past a plane charged surface. For $\zeta = 0.1$ V and $\mathscr{E}_x = 100$ V/cm in an aqueous solution, $U \sim 0.1$ cm/s.

Electroosmosis is one of several *electrokinetic effects* that deal with phenomena associated with the relative motion of a charged solid and a solution. A related effect is the *streaming potential* that arises between two electrodes placed as in Figure 9.8.1 when a solution streams down the tube (essentially the inverse of the electroosmotic effect). Another is *electrophoresis*, where charged particles in a solution move in an electric field. These effects have been studied for a long time (37, 38). Electrophoresis is widely used for separations of proteins and DNA (gel electrophoresis) and many other substances (capillary electrophoresis).

9.8.2 Other Electrohydrodynamic Phenomena

Electrokinetic effects are not usually of importance in the type of electrochemical experiments considered in this monograph, because the electric fields at the walls of the glass cells are small and significant convection is not induced. Although electrohydrodynamic flow can be induced by the interaction of an electric field with the diffuse layer near an electrode surface, the fields in the diffuse layer near the electrode surface are not sufficiently large in most electrochemical experiments to produce measurable fluid flow. However experiments in which very large fields are intentionally applied can produce

convection (39, 40). Related experiments involve the effects of applied magnetic fields on electrochemical processes (39, 41). Hydrodynamic instabilities can produce convective patterns in thin-layer cells with resistive solutions. For example, a form of convection in thin-layer cells (sometimes called the *Felici instability*) can produce hexagonal patterns during ECL experiments (Section 18.1) in organic solvents with very low concentrations of supporting electrolyte (42, 43).

▶ 9.9 REFERENCES

1. V. G. Levich, "Physicochemical Hydrodynamics," Prentice-Hall, Englewood Cliffs, NJ, 1962.

2. R. B. Bird, W. E. Stewart, and E. N. Lightfoot, "Transport Phenomena," Wiley, New York, 1960.

3. J. N. Agar, *Disc. Faraday Soc.*, **1**, 26 (1947).

4. J. Newman, *Electroanal. Chem.*, **6**, 187 (1973).

5. J. S. Newman, "Electrochemical Systems," 2nd ed., Prentice-Hall, Englewood Cliffs, NJ, 1991.

6. R. F. Probstein, "Physicochemical Hydrodynamics—An Introduction," 2nd ed., Wiley, New York, 1994.

7. A. C. Riddiford, *Adv. Electrochem. Electrochem. Engr.*, **4**, 47 (1966).

8. R. N. Adams, "Electrochemistry at Solid Electrodes," Marcel Dekker, New York, 1969, pp. 67–114.

9. C. Deslouis and B. Tribollet, *Adv. Electrochem. Sci. Engr.*, **2**, 205 (1992).

10. W. J. Albery, C. C. Jones, and A. R. Mount, *Compr. Chem. Kinet.*, **29**, 129 (1989).

11. V. Yu. Filinovskii and Yu. V. Pleskov, *Compr. Treatise Electrochem.*, **9**, 293 (1984).

12. J. S. Newman, *J. Phys. Chem.*, **70**, 1327 (1966).

13. V. Yu. Filinovskii and Yu. V. Pleskov, *Prog. in Surf. Membrane Sci.*, **10**, 27 (1976).

14. J. Newman, *J. Electrochem. Soc.*, **113**, 501, 1235 (1966).

15. W. J. Albery and M. L. Hitchman, "Ring-Disc Electrodes," Clarendon, Oxford, 1971, Chap. 4.

16. C. M. Mohr and J. Newman, *J. Electrochem. Soc.*, **122**, 928 (1975).

17. V. G. Levich, *op. cit.*, p. 107.

18. W. J. Albery and M. Hitchman, *op. cit.*, Chap. 3.

19. W. J. Albery and S. Bruckenstein, *Trans. Faraday Soc.*, **62**, 1920 (1966).

20. Yu. G. Siver, *Russ. J. Phys. Chem.*, **33**, 533 (1959).

21. S. Bruckenstein and S. Prager, *Anal. Chem.*, **39**, 1161 (1967).

22. K. B. Prater and A. J. Bard, *J. Electrochem. Soc.*, **117**, 207 (1970).

23. W. J. Albery and M. Hitchman, *op. cit.*, Chap. 10.

24. S. Bruckenstein and G. A. Feldman, *J. Electroanal. Chem.*, **9**, 395 (1965).

25. S. Bruckenstein and D. T. Napp, *J. Am. Chem. Soc.*, **90**, 6303 (1968).

26. S. Bruckenstein and B. Miller, *Accts. Chem. Res.*, **10**, 54 (1977).

27. C. A. Salzer, C. M. Elliott, and S. M. Hendrickson, *Anal. Chem.*, **71**, 3677 (1999).

28. S. Bruckenstein and B. Miller, *J. Electrochem. Soc.*, **117**, 1032 (1970).

29. B. Miller and S. Bruckenstein, *Anal. Chem.*, **46**, 2026 (1974).

30. K. Tokuda, S. Bruckenstein, and B. Miller, *J. Electrochem. Soc.*, **122**, 1316 (1975).

31. J. L. Valdes and B. Miller, *J. Phys. Chem.*, **92**, 525 (1988).

32. J. L. Valdes and B. Miller, *J. Phys. Chem.*, **93**, 7275 (1989).

33. T. E. Mallouk, V. Cammarata, J. A. Crayston, and M. S. Wrighton, *J. Phys. Chem.*, **90**, 2150 (1986).

34. X. Gao and H. S. White, *Anal. Chem.*, **67**, 4057 (1995).

35. J. V. Macpherson, S. Marcar, and P. R. Unwin, *Anal. Chem.*, **66**, 2175 (1994).

36. N. V. Rees, R. A. W. Dryfe, J. A. Cooper, B. A. Coles, R. G. Compton, S. G. Davies, and T. D. McCarthy, *J. Phys. Chem.*, **99**, 7096 (1995).

37. A. W. Adamson, "Physical Chemistry of Surfaces," Wiley-Interscience, New York, 1990, pp. 213–226.

38. D. A. MacInnes, "The Principles of Electrochemistry," Dover, New York, 1961, Chap. 23.

39. J.-P. Chopart, A. Olivier, E. Merienne, J. Amblard, and O. Aaboubi, *Electrochem. Solid State Lett.*, **1**, 139 (1998).

40. D. A. Saville, *Annu. Rev. Fluid Mech.*, **29**, 27 (1997).

41. J. Lee, S. R. Ragsdale, X. Gao, and H. S. White, *J. Electroanal. Chem.*, **422**, 169 (1997).

42. H. Schaper and E. Schnedler, *J. Phys. Chem.*, **86**, 4380 (1982).

43. M. Orlik, J. Rosenmund, K. Doblhofer, and G. Ertl, *J. Phys. Chem.*, **102**, 1397 (1998).

⯈ 9.10 PROBLEMS

9.1 Consider an RDE with a disk radius, r_1, of 0.20 cm, immersed in an aqueous solution of a substance A ($C_A^* = 10^{-2}$ M, $D_A = 5 \times 10^{-6}$ cm^2/s) and rotated at 100 rpm. A is reduced in a 1e reaction. $\nu \approx 0.01$ cm^2/s. Calculate: v_r and v_y at a distance 10^{-3} cm normal to the disk surface at the edge of the disk; v_r and v_y at the electrode surface; U_0; $i_{l,c}$; m_A; δ_A; and the Levich constant.

9.2 What dimensions (r_2 and r_3) can a rotating ring electrode have to produce the same limiting current as an RDE with $r_1 = 0.20$ cm? (Note that many possible combinations of r_2 and r_3 are suitable.) What is the area of the ring electrode?

9.3 From the data in Figure 9.3.8, calculate the diffusion coefficient for O_2 in 0.1 M NaOH and k_f for the reduction of oxygen at 0.75 V. Assume a totally irreversible initial electron transfer at the RDE. Take $\nu = 0.01$ cm^2/s.

9.4 Figure 9.10.1 contains current-potential curves at an RRDE for a solution of 5 mM CuCl$_2$ in 0.5 M KCl showing (1) i_D vs. E_D and (2) i_R vs. E_R. For the electrode used there, $N = 0.53$.
   (a) Analyze these data to determine D, β, and any other possible information about the electrode reaction at the first reduction step [Cu(II) + e → Cu(I)].
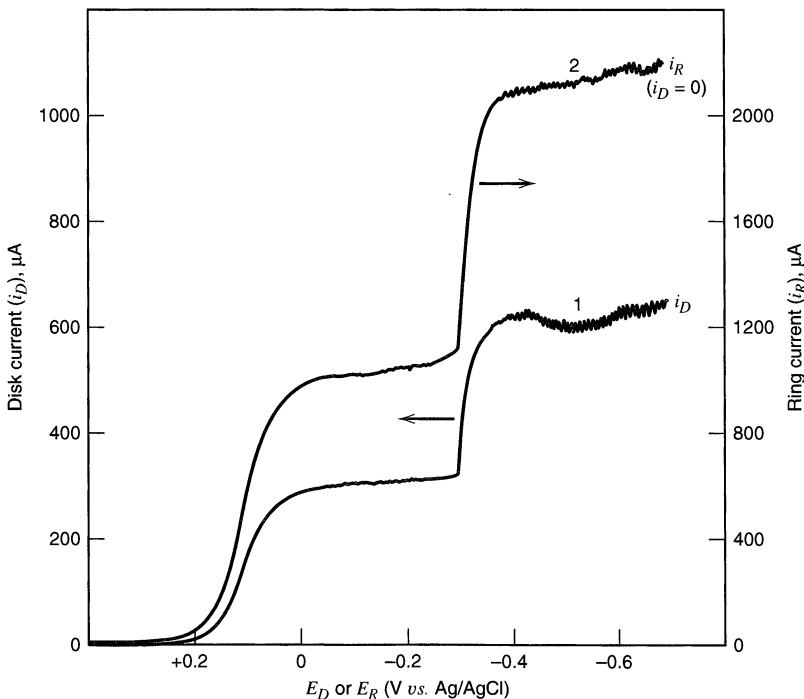
Figure 9.10.1 Voltammograms at an RRDE. *Curve 1*: i_D vs. E_D. *Curve 2*: i_R vs. E_R (at $i_D = 0$). Solution contained 5 mM CuCl$_2$ and 0.5 M KCl. $\omega = 201$ s^{-1}; disk area = 0.0962 cm^2; $\nu = 0.011$ cm^2/s.

(b) If the ring voltammogram were obtained with $E_D = -0.10$ V, what value of $i_{R,l,c}$ (at $E_R = -0.10$ V) would be expected?

(c) If E_R is held at $+0.4$ V and $E_D = -0.10$ V, what value of i_R is expected?

(d) What process occurs at the second wave? Account for this wave shape.

(e) Assume the ring is held at $+0.4$ V. Sketch the expected plot of i_R vs. E_D as E_D is scanned from $+0.4$ to -0.6 V.

9.5 The ring voltammograms for an RRDE in 5 mM $K_3Fe(CN)_6$ and 0.1 M KCl are shown in Figure 9.10.2. From the information in these curves, calculate N for this electrode and D for $Fe(CN)_6^{3-}$. What is the predicted slope of i_D vs. $\omega^{1/2}$? What are the predicted values of the limiting disk current ($i_{D,l,c}$) and ring current ($i_{R,l,c}$ with $i_D = 0$ and $i_D = i_{D,l,c}$) at 5000 rpm? Assume $\nu = 0.01$ cm^2/s.

9.6 Experiments are performed at an RRDE with the following dimensions: $r_1 = 0.20$ cm, $r_2 = 0.22$ cm, $r_3 = 0.32$ cm. A disk voltammogram (i_D vs. E_D) is to be recorded for a rotation rate of 2000 rpm. What maximum potential sweep rate should be employed to prevent non-steady-state effects from occurring? What is the transit time with this electrode?

9.7 The diffusion coefficient of an electroactive species can be obtained from a limiting-current measurement at an RDE and a transient measurement (e.g., a potential step measurement) at the same electrode (at $\omega = 0$) under identical conditions. It is not necessary to know the electrode area, n, or C^*. Explain how this is accomplished and discuss the possible errors in this procedure.

9.8 S. Bruckenstein and P. R. Gifford [*Anal. Chem.*, **51**, 250 (1979)] proposed that ring electrode shielding measurements at the RRDE could be employed for the analysis of micromolar solutions by using the equation

$$\Delta i_{R,l} = 0.62 nF\pi r_1^2 D^{2/3} \nu^{-1/6} \omega^{1/2} NC^*$$

where $\Delta i_{R,l}$ represents the change in the limiting ring current for $i_D = 0$ and $i_D = i_{D,l}$. (a) Derive this equation. (b) A plot of $i_{R,l}$ vs. E_D is given in Figure 9.10.3 for the reduction of Bi(III) to Bi(0) in 0.1 M HNO$_3$. Mass-transfer limited reduction of Bi(III) occurs at -0.25 V. From the data on the curve during the forward scan (E_D varied from $+1.0$ to -0.2 V), calculate N for this RRDE. Explain the large ring current transient observed during the reverse scan (E_D from -0.2 to $+1.0$ V).

9.9 The effective time scale for kinetic measurements at a rotating disk electrode is $\sim 1/\omega$. What range of effective times is available for the usual range of rotation rates of an RDE? UMEs provide an al-
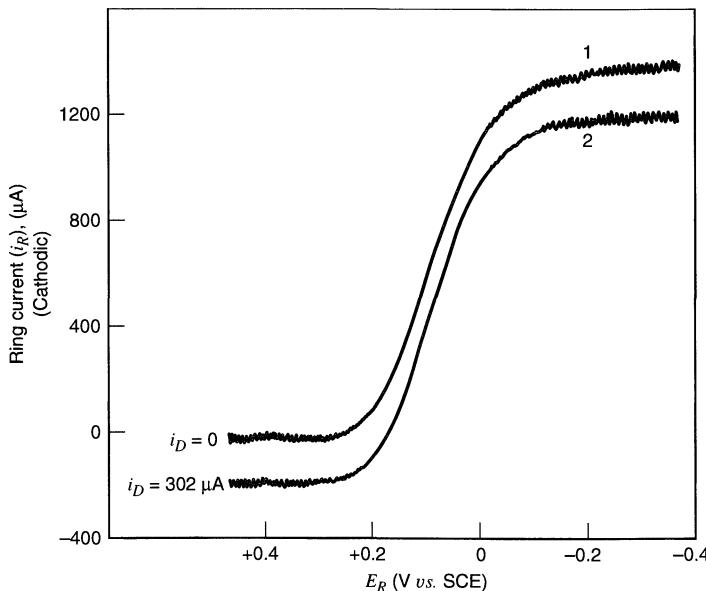
Figure 9.10.2 Ring voltammograms (i_R vs. E_R) with (*1*) $i_D = 0$ and (*2*) i_D at its limiting value, 302 μA, for an RRDE with $r_2 = 0.188$ cm and $r_3 = 0.325$ cm, rotated at 48.6 rps in a solution of 5.0 mM $K_3Fe(CN)_6$ and 0.10 M KCl.
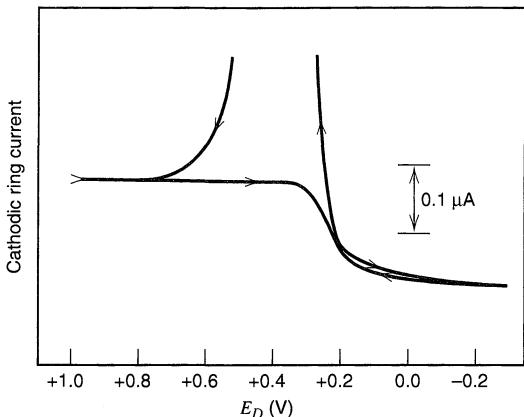
Figure 9.10.3 $i_{R,l,c}$ vs. E_D for reduction of Bi(III) to Bi(0) for a solution containing 4.86×10^{-7} M Bi(III) and 0.1 M HNO$_3$. The ring electrode was held at -0.25 V, and the disk potential was scanned from $+1.0$ V at 200 mV/s. For this electrode, the slope of $i_{D,l,c}$ vs. $C^*_{Bi(III)}$ is 0.934 $\mu A/\mu M$. [Reprinted with permission from S. Bruckenstein, and P. R. Gifford, *Anal. Chem.*, **51**, 250 (1979). Copyright 1979, American Chemical Society.]

ternative steady-state electrode system for electrochemical studies. What range of UME radii yields the same effective time range as that calculated for the RDE? Can stationary UMEs be extended to even shorter times than an RDE at its maximum useful rotation rate? Explain.

9.10 Show how eq. (9.3.40) leads to (9.3.39).

10

TECHNIQUES BASED ON CONCEPTS OF IMPEDANCE

▶ 10.1 INTRODUCTION

In previous chapters we have discussed ways of studying electrode reactions through large perturbations on the system. By imposing potential sweeps, potential steps, or current steps, we typically drive the electrode to a condition far from equilibrium, and we observe the response, which is usually a transient signal. Another approach is to perturb the cell with an alternating signal of small magnitude and to observe the way in which the system follows the perturbation at steady state. Many advantages accrue to these techniques. Among the most important are (a) an experimental ability to make high-precision measurements because the response may be indefinitely steady and can therefore be averaged over a long term, (b) an ability to treat the response theoretically by linearized (or otherwise simplified) current-potential characteristics, and (c) measurement over a wide time (or frequency) range (10^4 to 10^{-6} s or 10^{-4} to 10^6 Hz). Since one usually works close to equilibrium, one often does not require detailed knowledge about the behavior of the *i-E* response curve over great ranges of overpotential. This advantage leads to important simplifications in treating kinetics and diffusion.

In deriving the theory below, we will rely frequently on analogies between the electrochemical cell and networks of resistors and capacitors that are thought to behave like the cell. This feature may seem at times to disembody the interpretation from the chemical system, so let us emphasize beforehand that the ideas and the mathematics used in the interpretation are basically simple. We will do our best to tie them to the chemistry at every possible point, and we hope readers will avoid letting the details of interpretation obscure their view of the great power and beauty of these methods.

10.1.1 Types of Techniques (1–12)

The prototypical experiment is the *faradaic impedance* measurement, in which the cell contains a solution with both forms of a redox couple, so that the potential of the working electrode is fixed. For example, one might use 1 mM Eu^{2+} and 1 mM Eu^{3+} in 1 M NaClO$_4$. A mercury drop of fixed area might be employed as the working electrode, and it might be paired with a nonpolarizable reference such as an SCE, which would act also as the counter electrode. It is probably easiest to understand the measurement of impedance by considering the classical approach with an impedance bridge. The cell is inserted as the unknown impedance into one arm of an impedance bridge, and the bridge is balanced by adjusting R and C in the opposite arm of the bridge, as shown in Figure 10.1.1.

ac source
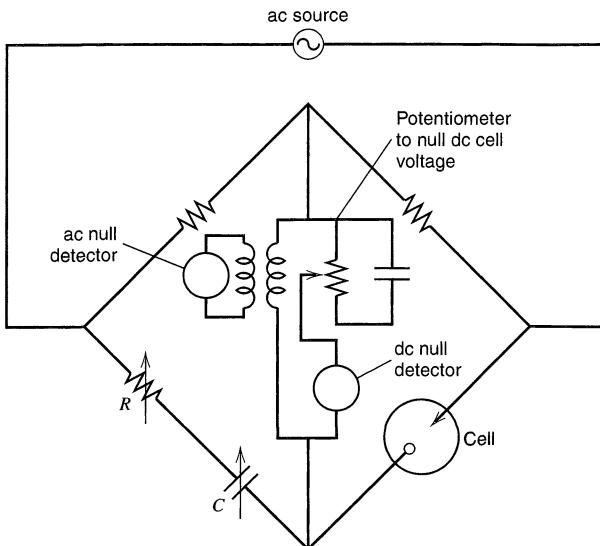
Figure 10.1.1 A bridge circuit for measurements of electrochemical impedance.

This operation determines the values of R and C that, in series, behave as the cell does at the measurement frequency. The impedance is measured as a function of the frequency of the ac source. The technique where the cell or electrode impedance is plotted *vs.* frequency is called *electrochemical impedance spectroscopy* (EIS). In modern practice, the impedance is usually measured with lock-in amplifiers or frequency-response analyzers, which are faster and more convenient than impedance bridges. Such approaches are introduced in Section 10.8. The job of theory is to interpret the equivalent resistance and capacitance values in terms of interfacial phenomena. The mean potential of the working electrode (the "dc potential") is simply the equilibrium potential determined by the ratio of oxidized and reduced forms of the couple. Measurements can be made at other potentials by preparing additional solutions with different concentration ratios. The faradaic impedance method, including EIS, is capable of high precision and is frequently used for the evaluation of heterogeneous charge-transfer parameters and for studies of double-layer structure.

A variation on the faradaic impedance method is *ac voltammetry* (or, with a DME, *ac polarography*). In these experiments, a three-electrode cell is used in the conventional manner, and the potential program imposed on the working electrode is a dc mean value, E_{dc}, which is scanned slowly with time, plus a sinusoidal component, E_{ac}, of perhaps 5-mV peak-to-peak amplitude. The measured responses are the magnitude of the ac component of the current at the frequency of E_{ac} and its phase angle with respect to E_{ac}.[1] A typical experimental arrangement is shown schematically in Figure 10.1.2. As we will see presently, this measurement is equivalent to determining the faradaic impedance. The role of the dc potential is to set the mean surface concentrations of O and R. In general, this potential differs from the true equilibrium value; hence $C_O(0, t)$ and $C_R(0, t)$ differ from C_O^* and C_R^*, and a diffusion layer exists. Note, however, that since E_{dc} is effectively steady, this layer soon becomes so thick that its dimensions greatly exceed those of the diffusion zone affected by the rapid perturbations from E_{ac}. Thus, the mean surface con-

---

[1]Alternatively, one could measure the current components in phase with E_{ac} and 90° out of phase with E_{ac}. They provide equivalent information.
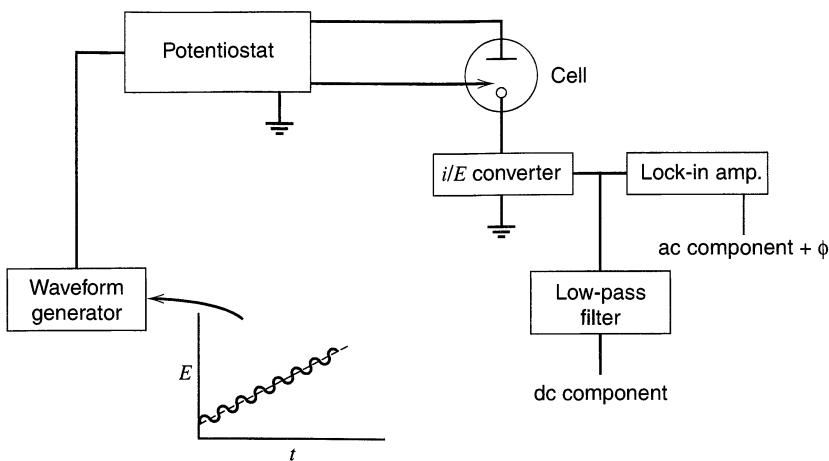
Figure 10.1.2 Schematic diagram of apparatus for an ac voltammetric experiment.

centrations $C_O(0, t)$ and $C_R(0, t)$ look like bulk concentrations to the ac part of the experiment. This same effect is exploited in DPP (see Section 7.3.4). One usually starts with a solution containing only one redox form, for example Eu^{3+}, and obtains continuous plots of the ac current amplitude and the phase angle *vs.* E_{dc}. In effect, these plots represent the faradaic impedance at continuous ratios of $C_O(0, t)$ and $C_R(0, t)$, all recorded without changing the solution. The amplitude plot is also useful for analytical measurements of concentration.

EIS and ac voltammetry normally involve excitation signals, E_{ac}, of very low amplitude, and they depend essentially on the fact that current-overpotential relations are virtually linear at low overpotentials. In a linear system, excitation at frequency ω provides a current also of frequency ω (and only of frequency ω). On the other hand, a nonlinear *i-E* relation gives a distorted response that is not purely sinusoidal; but it is still periodic and can be represented as a superposition (Fourier synthesis) of signals at frequencies ω, 2ω, 3ω, ... The current-overpotential function for an electrode reaction is nonlinear over moderate ranges of overpotential, and the effects of this nonlinearity can be observed and put to use. For example, consider *second* (and higher) *harmonic ac voltammetry*, which is nearly the same as the first harmonic ac experiment described above. It differs in that one detects an ac component current at 2ω, 3ω, ... , etc., instead of the component at the excitation frequency ω. *Faradaic rectification* features excitation with a purely sinusoidal source and measurement of the dc component of current flow. *Intermodulation voltammetry* depends on the mixing properties of a nonlinear characteristic. One excites with two superimposed signals at frequencies ω_1 and ω_2 and observes the current at the combination frequencies (sidebands or beat frequencies) $\omega_1 + \omega_2$ and $\omega_1 - \omega_2$. A big advantage common to all techniques based on nonlinearity is comparative freedom from charging currents. The double-layer capacitance is generally much more linear than the faradaic impedance; hence charging currents are largely restricted to the excitation frequencies.

10.1.2 Review of ac Circuits

A purely sinusoidal voltage can be expressed as

$$e = E \sin \omega t \tag{10.1.1}$$
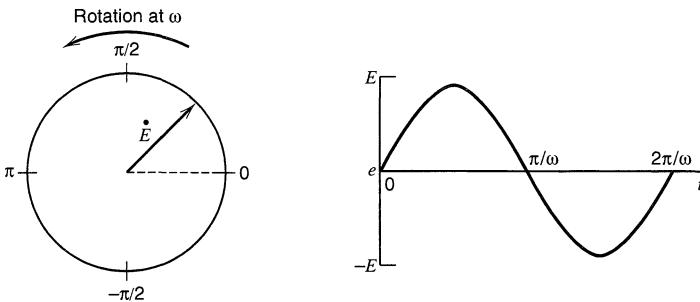
Figure 10.1.3 Phasor diagram for an alternating voltage, $e = E \sin \omega t$.

where ω is the angular frequency, which is 2π times the conventional frequency in Hz. It is convenient to think of this voltage as a rotating vector (or *phasor*) quantity like that pictured in Figure 10.1.3. Its length is the amplitude E and its frequency of rotation is ω. The observed voltage at any time, e, is the component of the phasor projected on some particular axis (normally that at $0°$) .

One frequently wishes to consider the relationship between two related sinusoidal signals, such as the current, i, and the voltage, e. Each is then represented as a separate phasor, $\dot{I}$ or $\dot{E}$, rotating at the same frequency. As shown in Figure 10.1.4, they generally will not be in phase; thus their phasors will be separated by a *phase angle*, ϕ. One of the phasors, usually $\dot{E}$, is taken as a reference signal, and ϕ is measured with respect to it. In the figure, the current lags the voltage. It can be expressed generally as

$$i = I \sin(\omega t + \phi) \tag{10.1.2}$$

where ϕ is a signed quantity, which is negative in this case.

The relationship between two phasors at the same frequency remains constant as they rotate; hence the phase angle is constant. Consequently, we can usually drop the references to rotation in the phasor diagrams and study the relationships between phasors simply by plotting them as vectors having a common origin and separated by the appropriate angles.

Let us apply these concepts to the analysis of some simple circuits. Consider first a pure resistance, R, across which a sinusoidal voltage, $e = E \sin \omega t$, is applied. Since Ohm's law always holds, the current is $(E/R)\sin \omega t$ or, in phasor notation,

$$\dot{I} = \frac{\dot{E}}{R} \tag{10.1.3}$$

$$\dot{E} = \dot{I}R \tag{10.1.4}$$

The phase angle is zero, and the vector diagram is that of Figure 10.1.5.
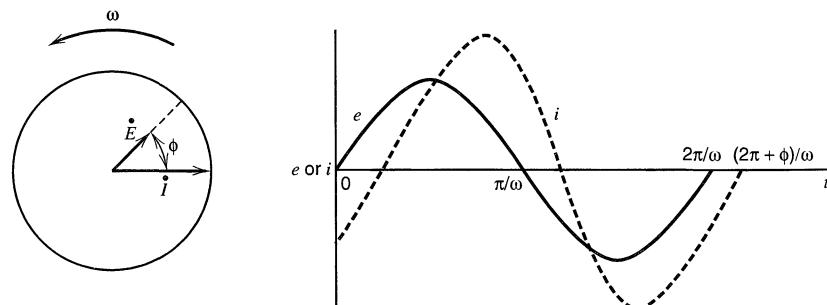
Figure 10.1.4 Phasor diagram showing the relationship between alternating current and voltage signals at frequency ω.
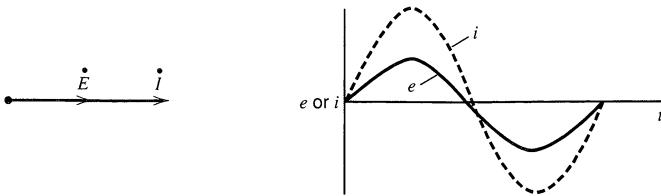
Figure 10.1.5
Relationship between the voltage across a resistor and current through the resistor.

Suppose we now substitute a pure capacitance, C, for the resistor. The fundamental relation of interest is then $q = Ce$, or $i = C(de/dt)$; thus

$$i = \omega CE \cos \omega t \tag{10.1.5}$$

$$i = \frac{E}{X_C} \sin\left(\omega t + \frac{\pi}{2}\right) \tag{10.1.6}$$

where X_C is the *capacitive reactance*, $1/\omega C$.

The phase angle is $\pi/2$, and the current leads the voltage, as shown in Figure 10.1.6. Since the vector diagram has now expanded to a plane, it is convenient to represent phasors in terms of complex notation. Components along the ordinate are assigned as imaginary and are multiplied by $j = \sqrt{-1}$. Components along the abscissa are real. Introducing complex notation here is only a bookkeeping measure to help keep the vector components straight. We handle them mathematically as "real" or "imaginary," but both types are real in the sense of being measurable by phase angle. In circuit analysis, it turns out to be advantageous to plot the current phasor along the abscissa as shown in Figure 10.1.6, even though the current's phase angle is measured experimentally with respect to the voltage. If that is done, it is clear that

$$\dot{E} = -jX_C\dot{I} \tag{10.1.7}$$

Of course, this relation must hold regardless of where $\dot{I}$ is plotted with respect to the abscissa, since only the relationship between $\dot{E}$ and $\dot{I}$ is significant. A comparison of equations 10.1.4 and 10.1.7 shows that X_C must carry dimensions of resistance, but, unlike R, its magnitude falls with increasing frequency.

Now consider a resistance, R, and a capacitance, C, in series. A voltage, $\dot{E}$, is applied across them, and at all times it must equal the sum of the individual voltage drops across the resistor and the capacitor; thus

$$\dot{E} = \dot{E}_R + \dot{E}_C \tag{10.1.8}$$

$$\dot{E} = \dot{I}(R - jX_C) \tag{10.1.9}$$

$$\dot{E} = \dot{I}\mathbf{Z} \tag{10.1.10}$$
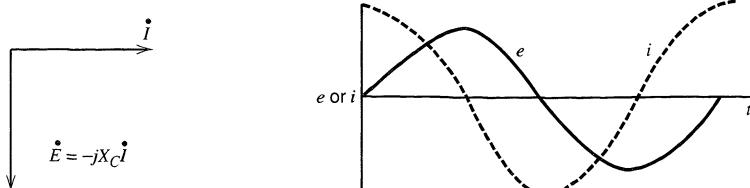
Figure 10.1.6
Relationship between an alternating voltage across a capacitor and the alternating current through the capacitor.

In this way we find that the voltage is linked to the current through a vector $\mathbf{Z} = R - jX_C$ called the *impedance*. Figure 10.1.7 is a display of the relationships between these various quantities. In general the impedance can be represented as[2]

$$\mathbf{Z}(\omega) = Z_{Re} - jZ_{Im}$$ (10.1.11)

where Z_{Re} and Z_{Im} are the real and imaginary parts of the impedance. For the example here, $Z_{Re} = R$ and $Z_{Im} = X_C = 1/\omega C$. The magnitude of $\mathbf{Z}$, written $|Z|$ or Z, is given by

$$|Z|^2 = R^2 + X_C^2 = (Z_{Re})^2 + (Z_{Im})^2$$ (10.1.12)

and the phase angle, ϕ, is given by

$$\tan \phi = Z_{Im}/Z_{Re} = X_C/R = 1/\omega RC$$ (10.1.13)

The impedance is a kind of generalized resistance, and equation 10.1.10 is a generalized version of Ohm's law. It embodies both (10.1.4) and (10.1.7) as special cases. The phase angle expresses the balance between capacitive and resistive components in the series circuit. For a pure resistance, $\phi = 0$; for a pure capacitance, $\phi = \pi/2$; and for mixtures, intermediate phase angles are observed.

The variation of the impedance with frequency is often of interest and can be displayed in different ways. In a *Bode plot*, log $|Z|$ and ϕ are both plotted against log ω. An alternative representation, a *Nyquist plot*, displays Z_{Im} vs. Z_{Re} for different values of ω. Plots for the series *RC* circuit are shown in Figures 10.1.8 and 10.1.9. Similar plots for a parallel *RC* circuit are shown in Figures 10.1.10 and 10.1.11.

More complex circuits can be analyzed by combining impedances according to rules analogous to those applicable to resistors. For impedances in series, the overall impedance is the sum of the individual values (expressed as complex vectors). For impedances in parallel, the inverse of the overall impedance is the sum of the reciprocals of the individual vectors. Figure 10.1.12 shows a simple application.
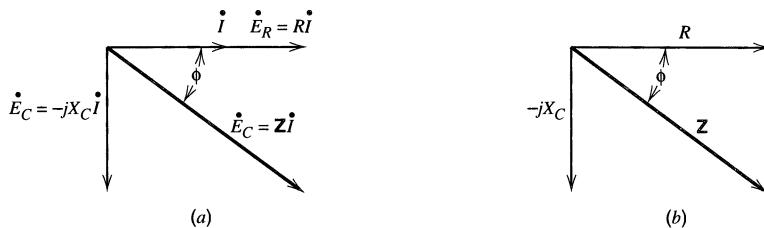
Figure 10.1.7 (*a*) Phasor diagram showing the relationship between the current and the voltages in a series *RC* network. The voltage across the whole network is $\dot{E}$, and $\dot{E}_R$ and $\dot{E}_C$ are its components across the resistance and the capacitance. (*b*) An impedance vector diagram derived from the phasor diagram in (*a*).

[2]In many treatments, the definition of impedance is taken as $\mathbf{Z} = Z_{Re} + jZ_{Im}$, but we can simplify matters with the definition in (10.1.11). In electrochemistry, the imaginary impedance is almost always capacitive and therefore negative. With our definition of $\mathbf{Z}$, we can generally work with positive values and expressions for Z_{Im}, and impedance plots appear naturally in the first quadrant. Our choice is in accord with the general, although sometimes implicit, practice in the field. In reviewing other literature, it is wise to take note of the definition of $\mathbf{Z}$.
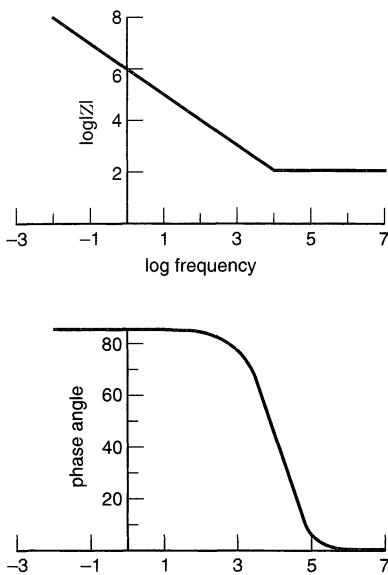
Figure 10.1.8   Bode plots for a series RC circuit with $R = 100\ \Omega$ and $C = 1\ \mu F$.

Sometimes it is advantageous to analyze ac circuits in terms of the *admittance*, **Y**, which is the inverse impedance, $1/\mathbf{Z}$, and therefore represents a kind of conductance. The generalized form of Ohm's law, (10.1.10), can then be rewritten as $\dot{I} = \dot{E}\mathbf{Y}$. These concepts are especially useful in the analysis of parallel circuits, because the overall admittance of parallel elements is simply the sum of the individual admittances.

Later we will be interested in the vector relationship between **Z** and **Y**. If **Z** is written in its polar form (Section A.5):

$$\mathbf{Z} = Z e^{j\phi} \tag{10.1.14}$$

then the admittance is

$$\mathbf{Y} = \frac{1}{Z} e^{-j\phi} \tag{10.1.15}$$

Here we see that **Y** is a vector with magnitude $1/Z$ and a phase angle equal to that of **Z**, but opposite in sign. Figure 10.1.13 is a picture of the arrangement.
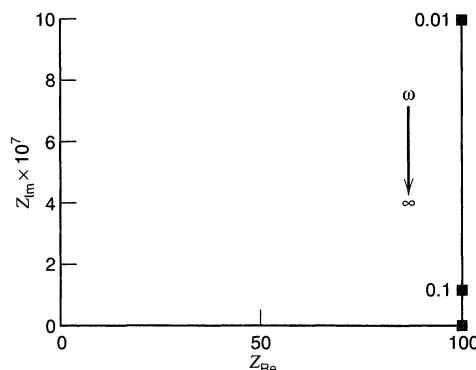
Figure 10.1.9   Nyquist plot for a series RC circuit with $R = 100\ \Omega$ and $C = 1\ \mu F$.
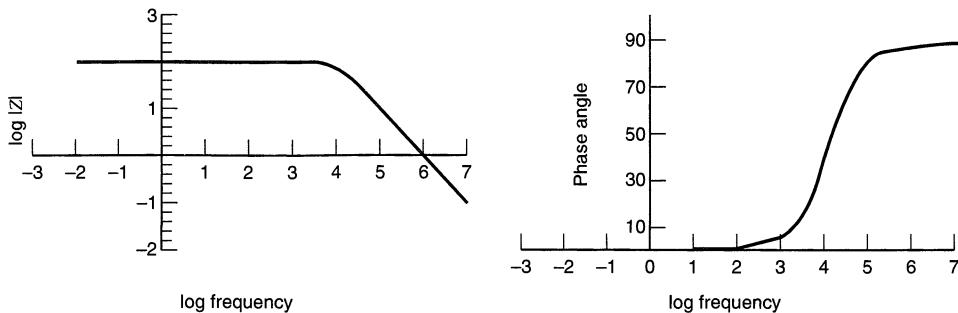
Figure 10.1.10 Bode plots for a parallel RC circuit with $R = 100 \ \Omega$ and $C = 1 \ \mu F$.
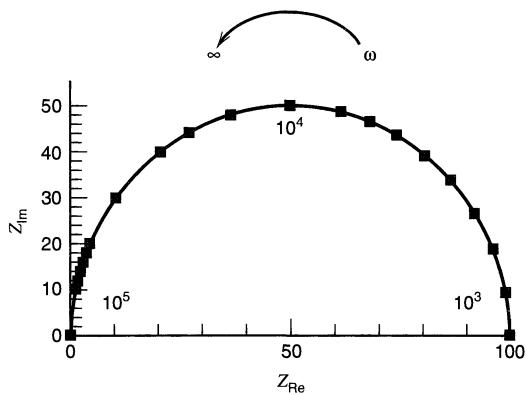
Figure 10.1.11 Nyquist plot for a parallel RC circuit with $R = 100 \ \Omega$ and $C = 1 \ \mu F$.

$$Z_p = \frac{Z_2 Z_3}{Z_2 + Z_3}$$

$$Z_T = Z_1 + \frac{Z_2 Z_3}{Z_2 + Z_3}$$
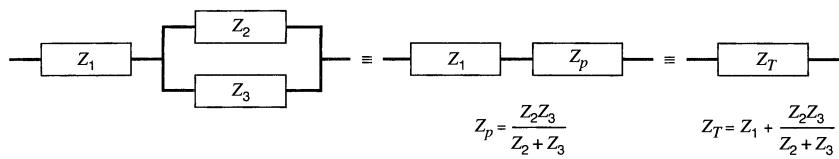
Figure 10.1.12 Calculation of a total impedance from component impedances.
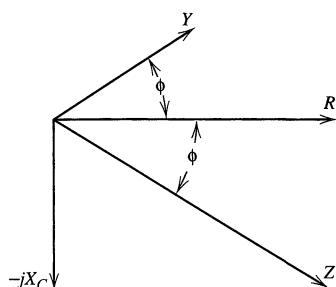
Figure 10.1.13 Relationship between the impedance, **Z**, and the admittance, **Y**.

10.1.3 Equivalent Circuit of a Cell (1, 4, 13, 14)

In a general sense, an electrochemical cell can be considered simply an impedance to a small sinusoidal excitation; hence we ought to be able to represent its performance by an *equivalent circuit* of resistors and capacitors that pass current with the same amplitude and phase angle that the real cell does under a given excitation. A frequently used circuit, called the *Randles equivalent circuit*, is shown in Figure 10.1.14a. The parallel elements are introduced because the total current through the working interface is the sum of distinct contributions from the faradaic process, i_f, and double-layer charging, i_c. The double-layer capacitance is nearly a pure capacitance; hence it is represented in the equivalent circuit by the element C_d. The faradaic process cannot be represented by simple linear circuit elements like, R and C, whose values are independent of frequency. It must be considered as a general impedance, Z_f. Of course, all of the current must pass through the solution resistance; therefore R_Ω is inserted as a series element to represent this effect in the equivalent circuit.[3]

The faradaic impedance has been considered in the literature in various ways. Figure 10.1.14b shows two equivalences that have been made. The simplest representation is to take the faradaic impedance as a series combination comprising the *series resistance*, R_s, and the *pseudocapacity*, C_s.[4] An alternative is to separate a pure resistance, R_{ct}, the *charge-transfer resistance* (Sections 1.3 and 3.4.3), from another general impedance, Z_w, the *Warburg impedance*, which represents a kind of resistance to mass transfer. In contrast to R_Ω and C_d, which are nearly ideal circuit elements, the components of the faradaic impedance are not ideal, because they change with frequency, ω. A given equivalent circuit represents cell performance at a given frequency, but not at other frequencies. In fact, a chief objective of a faradaic impedance experiment is to discover the frequency dependencies of R_s and C_s. Theory is then applied to transform these functions into chemical information.

The circuits considered here are based on the simplest electrode processes. Many others have been devised in order to account for more complex situations, for example, those involving adsorption of electroreactants, multistep charge transfer, or homogeneous

(a)

(b)
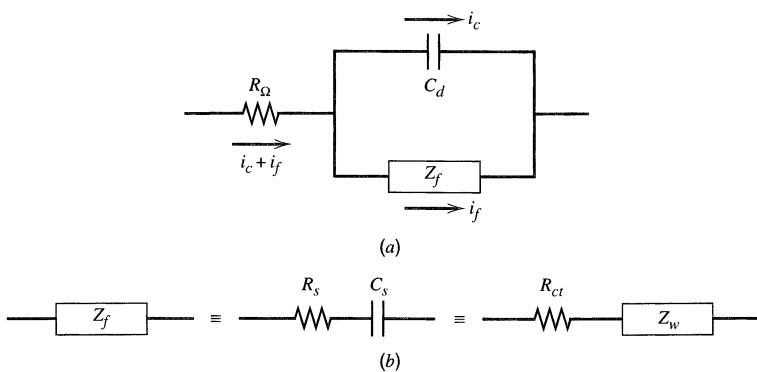
Figure 10.1.14
(a) Equivalent circuit of an electrochemical cell.
(b) Subdivision of Z_f into R_s and C_s, or into R_{ct} and Z_w.

---

[3]In the faradaic impedance measurements described above (Section 10.1.1), the impedance determined by the bridge is a whole-cell impedance and includes contributions from the counter electrode's interface. Processes at the counter electrode are not usually of interest; hence the impedance at that interface is intentionally reduced to insignificance by employing a counter electrode of large area.

[4]In some treatments, R_s is called the *polarization resistance*. However, that name is applied to other variables in electrochemistry, so we avoid it here.

chemistry. It is important to understand that equivalent circuits drawn for electrochemical cells are not unique. Moreover, only in the simplest cases can one identify individual circuit elements with processes that occur in the electrochemical cell. This is especially true for equivalent circuits that represent more complicated processes, such as, coupled homogeneous reactions or the behavior of adsorbed intermediates. In fact even the simple $R_\Omega C_d$ circuit in the absence of a faradaic process at low electrolyte concentration shows *frequency dispersion* (i.e., variation of R_Ω and C_d with frequency) (15). For specific information, the original or review literature should be consulted (1, 4, 8–14, 16).

▶ 10.2 INTERPRETATION OF THE FARADAIC IMPEDANCE

10.2.1 Characteristics of the Equivalent Circuit

The measurement of the cell characteristics in a bridge yields values of R_B and C_B that in series are equivalent to the whole cell impedance, including the contributions from R_Ω and C_d, which are often not of interest in studies focused on the faradaic process. In general, one desires to separate the faradaic impedance from R_Ω and C_d. It is possible to do so by considering the frequency dependencies of R_B and C_B, or by evaluating R_Ω and C_d from separate experiments in the absence of the electroactive couple.[5] Techniques for making such determinations are considered in Section 10.4. For the moment, let us assume that the faradaic impedance, expressed as the series combination R_s and C_s, is evaluable from the total impedance (see Figure 10.1.14).

Now consider the behavior of this impedance as a sinusoidal current is forced through it. The total voltage drop is

$$E = iR_s + \frac{q}{C_s} \tag{10.2.1}$$

hence

$$\frac{dE}{dt} = R_s \frac{di}{dt} + \frac{i}{C_s} \tag{10.2.2}$$

If the current is

$$i = I \sin \omega t \tag{10.2.3}$$

then

$$\frac{dE}{dt} = (R_s I \omega) \cos \omega t + \left(\frac{I}{C_s}\right) \sin \omega t \tag{10.2.4}$$

This equation is the link we will use to identify R_s and C_s in electrochemical terms. We will find that the response of the electrode process to the current stimulus, (10.2.3), will also give dE/dt having the form of (10.2.4). That is, sine and cosine terms will appear; thus R_s and C_s can be identified by equating the coefficients of those terms in the electrical and chemical equations.

10.2.2 Properties of the Chemical System (1, 4, 13, 14)

For our standard system, $O + ne \rightleftarrows R$, with both O and R soluble, we can write

$$E = E[i, C_O(0, t), C_R(0, t)] \tag{10.2.5}$$

---

[5]However, O and R must not affect R_Ω and C_d appreciably if separate experiments are used.

hence,

$$\frac{dE}{dt} = \left(\frac{\partial E}{\partial i}\right)\frac{di}{dt} + \left[\frac{\partial E}{\partial C_O(0, t)}\right]\frac{dC_O(0, t)}{dt} + \left[\frac{\partial E}{\partial C_R(0, t)}\right]\frac{dC_R(0, t)}{dt} \qquad (10.2.6)$$

or

$$\frac{dE}{dt} = R_{ct}\frac{di}{dt} + \beta_O\frac{dC_O(0, t)}{dt} + \beta_R\frac{dC_R(0, t)}{dt} \qquad (10.2.7)$$

where

$$R_{ct} = \left(\frac{\partial E}{\partial i}\right)_{C_O(0,t),C_R(0,t)} \qquad (10.2.8)$$

$$\beta_O = \left[\frac{\partial E}{\partial C_O(0, t)}\right]_{i,C_R(0,t)} \qquad (10.2.9)$$

$$\beta_R = \left[\frac{\partial E}{\partial C_R(0, t)}\right]_{i,C_O(0,t)} \qquad (10.2.10)$$

Obtaining an expression for dE/dt depends on our ability to evaluate the six factors on the right of (10.2.7). The three parameters R_{ct}, β_O, and β_R depend specifically on the kinetic properties of the electrode reaction. Special cases will be considered later. The remaining three factors [the derivatives of i, C_O^* and C_R^*] can be evaluated generally for current flow according to (10.2.3). One of them is trivial:

$$\frac{di}{dt} = I\omega \cos \omega t \qquad (10.2.11)$$

The others are evaluated by considering mass transfer.[6]
   Assuming semi-infinite linear diffusion with initial conditions $C_O(x, 0) = C_O^*$ and $C_R(x, 0) = C_R^*$, we can write from our experience in Section 8.2.1 that

$$\overline{C}_O(0, s) = \frac{C_O^*}{s} + \frac{\overline{i}(s)}{nFAD_O^{1/2}s^{1/2}} \qquad (10.2.12)$$

$$\overline{C}_R(0, s) = \frac{C_R^*}{s} - \frac{\overline{i}(s)}{nFAD_R^{1/2}s^{1/2}} \qquad (10.2.13)$$

Inversion by convolution gives

$$C_O(0, t) = C_O^* + \frac{1}{nFAD_O^{1/2}\pi^{1/2}}\int_0^t \frac{i(t - u)}{u^{1/2}}\,du \qquad (10.2.14)$$

$$C_R(0, t) = C_R^* - \frac{1}{nFAD_R^{1/2}\pi^{1/2}}\int_0^t \frac{i(t - u)}{u^{1/2}}\,du \qquad (10.2.15)$$

---

[6]Note that the equivalent impedance was analyzed just above in terms of current as it is usually defined for circuit analysis. That is, a positive change in E causes a positive change in i. On the other hand, the electrochemical current convention followed elsewhere in this book denotes cathodic currents as positive; hence a *negative* change in E causes a positive change in i. If we adhere to this convention now, confusion will reign when we try to make comparisons between the electrical equivalents and the chemical systems. We must have a common basis for the current. Since the interpretations of the measurements are closely linked to electronic circuit analysis, it is advantageous to adopt the electronic convention. *For this chapter, then, we take an anodic current as positive.*
   This expedient will turn out not to cause much trouble, because we never really follow the instantaneous sign of the current in ac experiments. Instead, we measure the amplitude of the sinusoidal component and its phase angle with respect to the sinusoidal potential. Of course the phase angle would depend on our choice of current convention, but it is advantageous even here to take the electronic custom, because the electronic devices used to measure phase angle are based on it.

From (10.2.3), we can substitute for $i(t - u)$; hence the problem becomes one of evaluating the integral common to both of these relations.

We begin with the trigonometric identity:

$$\sin \omega(t - u) = \sin \omega t \cos \omega u - \cos \omega t \sin \omega u \qquad (10.2.16)$$

which implies that

$$\int_0^t \frac{I \sin \omega(t - u)}{u^{1/2}} du = I \sin \omega t \int_0^t \frac{\cos \omega u}{u^{1/2}} du - I \cos \omega t \int_0^t \frac{\sin \omega u}{u^{1/2}} du \qquad (10.2.17)$$

Now let us consider the range of times in which we are interested. Before the current is turned on, the surface concentrations are C_O^* and C_R^*, and after a few cycles we can expect them to reach a *steady state* in which they cycle repeatedly through constant patterns. We can be sure of this point because no net electrolysis takes place in any full cycle of current flow. Our interest is not in the transition from initial conditions to steady state, but in the steady state itself. The two integrals on the right side of (10.2.17) embody the transition period. Because $u^{1/2}$ appears in their denominators, the integrands are appreciable only at short times. After a few cycles, each integral must reach a constant value characteristic of the steady state. We can obtain it by letting the integration limits go to infinity:

$$\int_{\substack{\text{Steady} \\ \text{state}}} \frac{I \sin \omega(t - u)}{u^{1/2}} du = I \sin \omega t \int_0^\infty \frac{\cos \omega u}{u^{1/2}} du - I \cos \omega t \int_0^\infty \frac{\sin \omega u}{u^{1/2}} du$$

$$(10.2.18)$$

It is easy to show that both integrals on the right side of (10.2.18) are equal to $(\pi/2\omega)^{1/2}$; hence we have by substitution into (10.2.14) and (10.2.15)

$$C_O(0, t) = C_O^* + \frac{I}{nFA(2D_O\omega)^{1/2}} (\sin \omega t - \cos \omega t) \qquad (10.2.19)$$

$$C_R(0, t) = C_R^* - \frac{I}{nFA(2D_R\omega)^{1/2}} (\sin \omega t - \cos \omega t) \qquad (10.2.20)$$

Now we can evaluate the derivatives of the surface concentrations as required above:[7]

$$\frac{dC_O(0, t)}{dt} = \frac{I}{nFA} \left(\frac{\omega}{2D_O}\right)^{1/2} (\sin \omega t + \cos \omega t) \qquad (10.2.21)$$

$$\frac{dC_R(0, t)}{dt} = -\frac{I}{nFA} \left(\frac{\omega}{2D_R}\right)^{1/2} (\sin \omega t + \cos \omega t) \qquad (10.2.22)$$

10.2.3 Identification of R_s and C_s

By substitution of (10.2.11), (10.2.21), and (10.2.22) into (10.2.7), we obtain

$$\frac{dE}{dt} = \left(R_{ct} + \frac{\sigma}{\omega^{1/2}}\right) I\omega \cos \omega t + I\sigma\omega^{1/2} \sin \omega t \qquad (10.2.23)$$

---

[7]In general, we ought to consider the current as $i = i_{dc} + I \sin \omega t$, where i_{dc} is steady or varies only slowly with time. However, we are interested now in derivatives of surface concentrations, and they will be dominated by the higher-frequency ac signal. Relations (10.2.21) and (10.2.22) will still apply to a very high approximation. This is a mathematical manifestation of the way in which the ac part of the experiment can usually be uncoupled from the dc part.

where

$$\sigma = \frac{1}{nFA\sqrt{2}}\left(\frac{\beta_O}{D_O^{1/2}} - \frac{\beta_R}{D_R^{1/2}}\right) \qquad (10.2.24)$$

It is easy to identify R_s and C_s by comparison with (10.2.4):

$$\boxed{R_s = R_{ct} + \sigma/\omega^{1/2}} \qquad (10.2.25)$$

$$\boxed{C_s = \frac{1}{\sigma\omega^{1/2}}} \qquad (10.2.26)$$

The complete evaluation of R_s and C_s depends on finding relations for R_{ct}, β_O, and β_R.

We will see below that R_{ct} is primarily determined by the heterogeneous charge-transfer kinetics, and we have already observed above that the terms $\sigma/\omega^{1/2}$ and $1/\sigma\omega^{1/2}$ come from mass-transfer effects. Recognition of this situation has led to a division of the faradaic impedance into the charge-transfer resistance, R_{ct}, and the Warburg impedance, Z_w, as shown in Figure 10.1.14b. Equations 10.2.25 and 10.2.26 demonstrate that this latter impedance can be regarded as a frequency-dependent resistance, $R_w = \sigma/\omega^{1/2}$, in series with the pseudocapacitance, $C_w = C_s = 1/\sigma\omega^{1/2}$. Thus the total faradaic impedance, Z_f, can be written

$$Z_f = R_{ct} + R_w - j/(\omega C_w) = R_{ct} + [\sigma\omega^{-1/2} - j(\sigma\omega^{-1/2})] \qquad (10.2.27)$$

with the term in brackets representing the Warburg impedance.

10.3 KINETIC PARAMETERS FROM IMPEDANCE MEASUREMENTS (1, 4, 6, 8–14, 16)

From the description of the faradaic impedance experiment given in Section 10.1, it is clear that measurements are made with the working electrode's mean potential at equilibrium. Since the amplitude of the sinusoidal perturbation is small, we can use the linearized i-η characteristic to describe the electrical response to the departure from equilibrium. For a one-step, one-electron process, $O + e \underset{k_b}{\overset{k_f}{\rightleftarrows}} R$, the linearized relationship is (3.4.30), which can be rewritten in terms of the electronic current convention as

$$\eta = \frac{RT}{F}\left[\frac{C_O(0, t)}{C_O^*} - \frac{C_R(0, t)}{C_R^*} + \frac{i}{i_0}\right] \qquad (10.3.1)$$

hence

$$\boxed{R_{ct} = \frac{RT}{Fi_0}} \qquad (10.3.2)$$

$$\beta_O = \frac{RT}{FC_O^*} \qquad (10.3.3)$$

$$\beta_R = -\frac{RT}{FC_R^*} \qquad (10.3.4)$$

Now we see that

$$R_s - \frac{1}{\omega C_s} = R_{ct} = \frac{RT}{Fi_0} \qquad (10.3.5)$$

so that the exchange current, and therefore k^0, can be evaluated easily when R_s and C_s are known. The bridge method allows a precise definition of these electrical equivalents; thus it can yield kinetic data of very high quality.

Equation 10.3.5 shows that one can, in principle, evaluate i_0 from data taken at a single frequency. However, doing so is not really wise, because one has no experimental assurance that the equivalent circuit actually mirrors the performance of the system. The best way to check for agreement is to examine the frequency dependence of the impedance. For example, (10.2.25) and (10.2.26) predict that R_s and $1/\omega C_s$ should both be linear with $\omega^{-1/2}$ and should have a common slope, σ, which is quantitatively predictable from the constants of the experiment; that is,

$$\sigma = \frac{RT}{F^2 A \sqrt{2}} \left(\frac{1}{D_O^{1/2} C_O^*} + \frac{1}{D_R^{1/2} C_R^*} \right) \qquad (10.3.6)$$

Figure 10.3.1 is a display of these relationships.

The plot of R_s should have an intercept, R_{ct}, from which i_0 can be evaluated. Extrapolation to the intercept is equivalent to estimating the system's performance at infinite frequency. The Warburg impedance drops out at high frequencies, because the time scale is so short that diffusion cannot manifest itself as a factor influencing the current. Since the surface concentrations never change significantly from the mean values [see (10.2.19) and (10.2.20)], charge-transfer kinetics alone dictate the current.

If the linear behavior typified in Figure 10.3.1 is not observed, then the electrode process is not as simple as we assume here, and a more complex situation must be considered. The availability of this kind of check for internal consistency is an extremely important asset of the impedance technique. See Section 10.4 for more details.

The conclusions of the foregoing discussion are also applicable to a quasireversible multistep mechanism, for which R_{ct} is defined as

$$R_{ct} = \frac{RT}{nFi_0} \qquad (10.3.7)$$

See Section 3.5.4(d) for more about the interpretation of i_0 in such a system.

Let us now consider the general impedance properties of a reversible system, which is an important limiting case. When charge-transfer kinetics are very facile, $i_0 \to \infty$; hence $R_{ct} \to 0$. Thus $R_s \to \sigma/\omega^{1/2}$. The corresponding impedance plot is shown in Figure 10.3.2a.
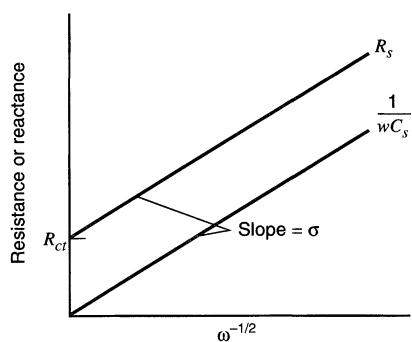
Figure 10.3.1 Dependence of R_s and $1/\omega C_s$ on frequency.
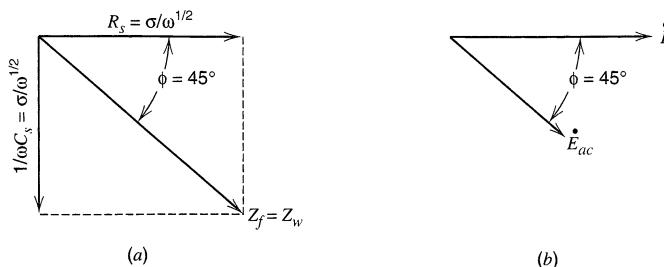
Figure 10.3.2 (*a*) Vector diagram showing the components of the faradaic impedance for a reversible system. (*b*) Phase relationship between the ac current and the ac component of potential.

Since the resistance and the capacitive reactance are exactly equal, the magnitude of the faradaic impedance is

$$Z_f = \left(\frac{2}{\omega}\right)^{1/2} \sigma \tag{10.3.8}$$

which is the magnitude of the Warburg impedance alone.

Since this is a mass-transfer impedance that applies to any electrode reaction, it is a minimum impedance. If kinetics are observable, another factor, R_{ct}, contributes, and Z_f must be greater, as Figure 10.3.3*a* depicts. Thus the amplitude of the sinusoidal current flowing in response to a given excitation signal, $\dot{E}_{ac}$, is maximal for a reversible system and decreases correspondingly for more sluggish kinetics. If the heterogeneous redox process is very immobile, R_{ct} and Z_f are so large that there is only a very small ac component to the current, and the limit of detection sets the lower bound on rate constants that can be measured by this approach. See Section 10.4.2 for more details about quantitative working ranges.

It is interesting also to examine the effect of concentration, which is manifested through σ. In general, higher concentrations reduce the mass-transfer impedance, as we would expect intuitively. Of greater interest, however, is the effect of the concentration ratio C_O^*/C_R^*. One can change it experimentally in order to vary the equilibrium potential for a series of impedance measurements. Both large and small ratios imply that one of the concentrations is small; hence σ and Z_f must be large. The current response to $\dot{E}_{ac}$ is not very great, because the supply of one reagent is insufficient to permit a high reaction rate for the cyclic, reversible electrode process that causes the ac current. Large rates can be achieved only when both electroreactants are present at comparable concentrations; hence we expect Z_f to be minimal near $E^{0'}$. Impedance measurements are most easily made in that potential region, and they gradually become more difficult as one departs from it ei-
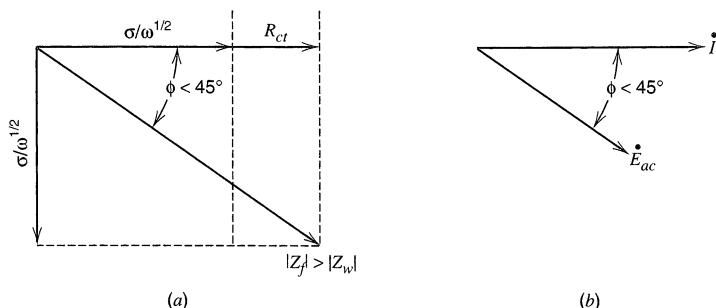
Figure 10.3.3 (*a*) Vector diagram showing the effect of R_{ct} on the impedance. (b) Phase relationship between $\dot{I}$ and $\dot{E}$ for a system with significant R_{ct}.

ther positively or negatively. This effect presages the shape of the ac voltammetric response, which will be derived in Section 10.5.

A final point of interest is the phase angle between the current phasor, $\dot{I}_{ac}$, and the potential, $\dot{E}_{ac}$. Since $\dot{I}_{ac}$ lies along R_s and $\dot{E}_{ac}$ lies along Z_f, the phase angle is readily calculated as

$$\phi = \tan^{-1}\frac{1}{\omega R_s C_s} = \tan^{-1}\frac{\sigma/\omega^{1/2}}{R_{ct} + \sigma/\omega^{1/2}} \tag{10.3.9}$$

For the reversible case, $R_{ct} = 0$; hence $\phi = \pi/4$ or 45°. A quasireversible system shows $R_{ct} > 0$; hence $\phi < \pi/4$. However, ϕ must always be greater than zero, unless $R_{ct} \rightarrow \infty$; but then the reaction would be so sluggish that little alternating current would flow anyway in a conventional impedance measurement. This sensitivity of ϕ to kinetics suggests that R_{ct} might be extracted from the phase angle. It can be, and often it is, by ac voltammetric experiments. Before we proceed to a discussion of them, let us note that since $0 \le \phi \le 45°$, there is always a component of i_{ac} that is in-phase (0°) with $\dot{E}_{ac}$, and it can be measured with a phase-sensitive detector (e.g., a lock-in amplifier) referenced to $\dot{E}_{ac}$. This feature is extremely useful as a basis for discriminating against charging current in ac voltammetry.

Even though this section has been developed with the assumption that the electrode reaction is a one-step, one-electron process, many of the conclusions apply generally for chemically reversible multi-electron mechanisms. The nernstian limit is still described by (10.3.8) and Figure 10.3.2, but with σ given by

$$\sigma = \frac{RT}{n^2 F^2 A \sqrt{2}} \left(\frac{1}{D_O^{1/2} C_O^*} + \frac{1}{D_R^{1/2} C_R^*} \right) \tag{10.3.10}$$

When charge-transfer kinetics manifest themselves in a chemically reversible n-electron system, they do so in the manner discussed in relation to Figure 10.3.3. The kinetic effects can be expressed in terms of a charge-transfer resistance R_{ct} defined operationally as in (10.2.8). Further analysis of R_{ct}, such as to obtain the rate constant of the RDS, requires knowledge of the i-E characteristic for the mechanism, which can, however, be difficult to develop (see Section 3.5.4).

10.4 ELECTROCHEMICAL IMPEDANCE SPECTROSCOPY

In Section 10.3, we concentrated on the components of the faradaic impedance, R_s and C_s. We assumed that they can be extracted readily from direct measurements of the total impedance, which also includes the solution resistance, R_Ω, and the double-layer capacitance, C_d. In this section we will consider measurements of the total cell or electrode impedance as a function of ω and methods of extracting the faradaic impedance, R_Ω, and C_d from the results.

At a given frequency, the equivalent circuit of the cell can be taken as in Figure 10.1.14, but we measure its impedance as a resistance value R_B and the capacitance value C_B in series [or equivalently as $Z_{Re} = R_B$ and $Z_{Im} = 1/\omega C_B$]. One approach to obtaining the faradaic impedance from these values is to measure the cell impedance in a separate experiment under identical conditions, but in the absence of the electroactive couple. This measurement should yield the values of R_Ω and C_d (assuming they are not changed by the presence of the electroactive species), since the faradaic path is inactive. One can then subtract these graphically or analytically from the R_B and C_B values. This approach is

often used when impedance bridge measurements are made and was discussed in some detail in the first edition.[8] A more direct approach involves a study of the way in which the total impedance $\mathbf{Z} = R_B - j/(\omega C_B) = Z_{Re} - jZ_{Im}$ varies with frequency. From this variation, one can extract R_Ω, C_d, R_s, and C_s directly. This method circumvents the need for separate measurements without the electroactive species, and it eliminates the need to assume that the electroactive species has no effect on the nonfaradaic impedance.

10.4.1 Variation of Total Impedance (4, 16)

The electrochemical impedance spectroscopic approach, which is largely based on similar methods used to analyze circuits in electrical engineering practice, was developed by Sluyters and coworkers (4) and later extended by others (8–12). It deals with the variation of total impedance in the complex plane [as represented in Nyquist plots (Section 10.1.2)]. Let us consider this approach for our standard system.

The measured total impedance of the cell, $\mathbf{Z}$, is expressed as the series combination of R_B and C_B. These two elements provide the real and imaginary components of $\mathbf{Z}$, that is, $Z_{Re} = R_B$ and $Z_{Im} = 1/\omega C_B$. The electrochemical system is described theoretically in terms of an equivalent circuit such as that in Figure 10.1.14. Its impedance is readily written down according to the methods of Section 10.1.2. The real part, which must equal the measured Z_{Re}, is

$$Z_{Re} = R_B = R_\Omega + \frac{R_s}{A^2 + B^2} \tag{10.4.1}$$

where $A = (C_d/C_s) + 1$ and $B = \omega R_s C_d$. Similarly,

$$Z_{Im} = \frac{1}{\omega C_B} = \frac{B^2/\omega C_d + A/\omega C_s}{A^2 + B^2} \tag{10.4.2}$$

Substitution for R_s and C_s by (10.2.25) and (10.2.26) provides

$$Z_{Re} = R_\Omega + \frac{R_{ct} + \sigma\omega^{-1/2}}{(C_d\sigma\omega^{1/2} + 1)^2 + \omega^2 C_d^2(R_{ct} + \sigma\omega^{-1/2})^2} \tag{10.4.3}$$

$$Z_{Im} = \frac{\omega C_d(R_{ct} + \sigma\omega^{-1/2})^2 + \sigma\omega^{-1/2}(\omega^{1/2}C_d\sigma + 1)}{(C_d\sigma\omega^{1/2} + 1)^2 + \omega^2 C_d^2(R_{ct} + \sigma\omega^{-1/2})^2} \tag{10.4.4}$$

Chemical information can be extracted by plotting Z_{Im} vs. Z_{Re} for different ω. For simplicity let us first consider the limiting behavior at high and low ω.

(a) Low-Frequency Limit
As $\omega \to 0$, the functions (10.4.3) and (10.4.4) approach the limiting forms:

$$Z_{Re} = R_\Omega + R_{ct} + \sigma\omega^{-1/2} \tag{10.4.5}$$
$$Z_{Im} = \sigma\omega^{-1/2} + 2\sigma^2 C_d \tag{10.4.6}$$

Elimination of ω between these two gives

$$\boxed{Z_{Im} = Z_{Re} - R_\Omega - R_{ct} + 2\sigma^2 C_d} \tag{10.4.7}$$

Thus, the plot of Z_{Im} vs. Z_{Re} should be linear and have unit slope, as shown in Figure 10.4.1. The extrapolated line intersects the real axis at $R_\Omega + R_{ct} - 2\sigma^2 C_d$. One can see

---

[8]First edition, pp. 347–349.
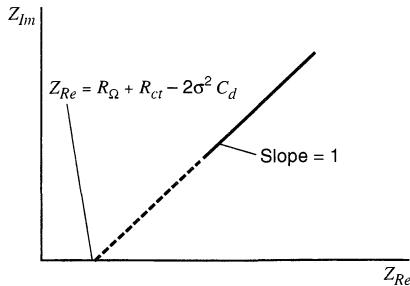
Figure 10.4.1 Impedance plane plot for low frequencies.

from (10.4.5) and (10.4.6) that the frequency dependence in this regime comes only from Warburg impedance terms; thus the linear correlation of Z_{Re} and Z_{Im} is characteristic of a diffusion-controlled electrode process. As the frequency rises, the charge-transfer resistance, R_{ct}, and the double-layer capacitance become more important elements, and we can expect a departure from (10.4.7).

(b) High-Frequency Limit

At very high frequencies, the Warburg impedance becomes unimportant in relation to R_{ct}, and the equivalent circuit converges to that of Figure 10.4.2. The impedance is

$$\mathbf{Z} = R_\Omega - j\left(\frac{R_{ct}}{R_{ct}C_d\omega - j}\right) \tag{10.4.8}$$

which has the components

$$Z_{Re} = R_\Omega + \frac{R_{ct}}{1 + \omega^2 C_d^2 R_{ct}^2} \tag{10.4.9}$$

$$Z_{Im} = \frac{\omega C_d R_{ct}^2}{1 + \omega^2 C_d^2 R_{ct}^2} \tag{10.4.10}$$

Elimination of ω from this pair of equations yields

$$\left(Z_{Re} - R_\Omega - \frac{R_{ct}}{2}\right)^2 + Z_{Im}^2 = \left(\frac{R_{ct}}{2}\right)^2 \tag{10.4.11}$$

Hence Z_{Im} vs. Z_{Re} should give a circular plot centered at $Z_{Re} = R_\Omega + R_{ct}/2$ and $Z_{Im} = 0$ and having a radius of $R_{ct}/2$. Figure 10.4.3 depicts the result.

The general features of the plot are readily grasped intuitively. The imaginary component to the impedance in the circuit of Figure 10.4.2 comes solely from C_d. Its contribution falls to zero at high frequencies, because it offers no impedance. All of the current is charging current, and the only impedance it sees is the ohmic resistance. As the frequency drops, the finite impedance of C_d manifests itself as a significant Z_{Im}. At very low frequencies, the capacitance C_d offers a high impedance; hence current flow passes mostly
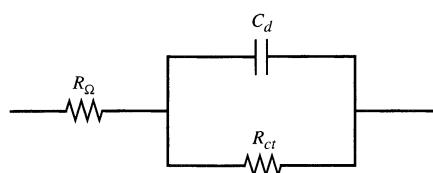
Figure 10.4.2 Equivalent circuit for a system in which the Warburg impedance is unimportant.
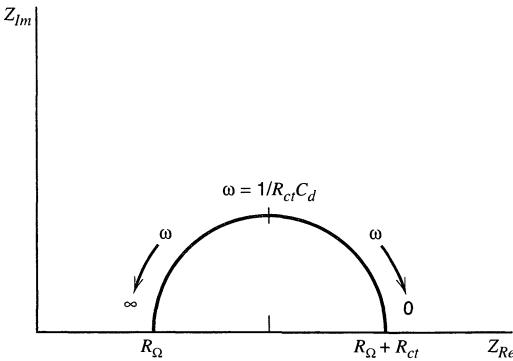
Figure 10.4.3 Impedance plane plot for the equivalent circuit of Figure 10.4.2.

through R_{ct} and R_Ω. Thus the imaginary impedance component falls off again. In general, we can expect to see a departure from this plot in this lower-frequency regime, because the Warburg impedance will become important.

(c) Application to Real Systems
An actual plot of impedance in the complex plane will combine the features of our two limiting cases as in Figure 10.4.4. However, both regions may not be well defined for any given system. The determining feature is the charge-transfer resistance, R_{ct}, and its relation to the Warburg impedance, which is controlled by σ. If the chemical system is kinetically sluggish, it will show a large R_{ct}, and may display only a very limited-frequency region where mass transfer is a significant factor. This case is shown in Figure 10.4.5a. At the other extreme, R_{ct} might be inconsequentially small by comparison to the ohmic resistance and the Warburg impedance over nearly the whole available range of σ. Then the system is so kinetically facile that mass transfer always plays a role, and the semicircular region is not well defined. An example is shown in Figure 10.4.5b.

10.4.2 Limits to Measurable k^0 by the Faradaic Impedance Method (1–6, 9–12)

The foregoing paragraphs highlight the limitations in interpreting impedance data, and they lead naturally to the idea that k^0 must fall in some fairly well-defined range in
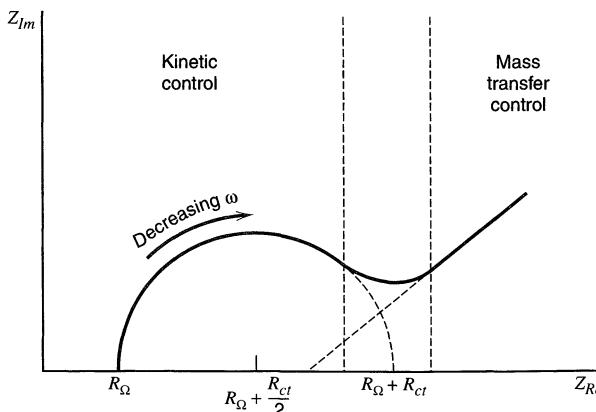
Figure 10.4.4 Impedance plot for an electrochemical system. Regions of mass-transfer and kinetic control are found at low and high frequencies, respectively.
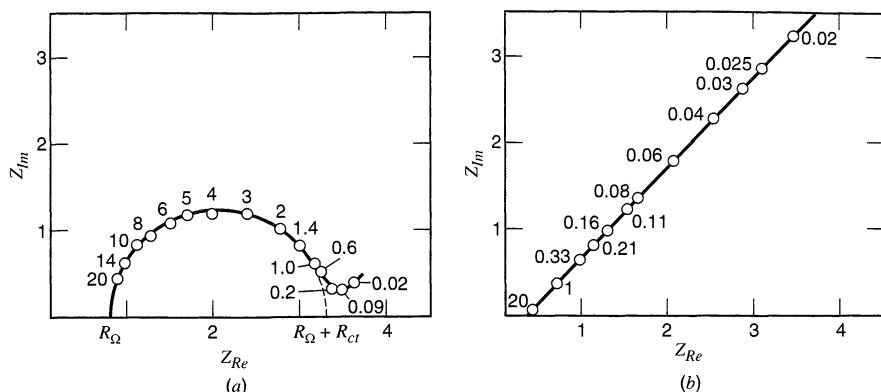
Figure 10.4.5 Impedance plane plots for actual chemical systems. Numbers by points are frequencies in kHz. (a) For the electrode reaction $Zn^{2+} + 2e \rightleftarrows Zn(Hg)$. $C^*_{Zn^{2+}} = C^*_{Zn(Hg)} = 8 \times 10^{-3}$ M. Electrolyte was 1 M $NaClO_4$ plus 10^{-3} M $HClO_4$. (b) For the electrode reaction $Hg_2^{2+} + 2e \rightleftarrows Hg$ in 1 M $HClO_4$. $C_{Hg_2^{2+}} = 2 \times 10^{-3}$ M. [From J. H. Sluyters and J. J. C. Oomen, *Rec. Trav. Chim. Pays-Bas*, **79**, 1101 (1960), with permission.]

order to be reliably measured by an impedance method. We can define the range semi-quantitatively.

(a) Upper Limit

The parameter R_{ct} must make a significant contribution to R_s hence $R_{ct} \geq \sigma/\omega^{1/2}$. Substituting from (10.3.2), (10.3.6), and (3.4.7) and assuming $D_O = D_R$ and $C^*_O = C^*_R$, we obtain the condition that $k^0 \leq (D\omega/2)^{1/2}$. The highest practical value of ω is determined by the cell time constant, $R_u C_d$, which must remain much smaller than the cycle period of the applied ac stimulus. With a UME, one can do useful work at several MHz, so that $\omega \leq 10^7$ s^{-1}, and with $D \sim 10^{-5}$ cm^2/s, we have $k^0 \leq 7$ cm/s.[9] In addition, there are requirements that $C_s \geq C_d$ and $R_s \geq R_\Omega$.

(b) Lower Limit

For very large R_{ct}, the Warburg impedance is negligible, and the equivalent circuit of Figure 10.4.2 can be applied. One problem here is that R_{ct} cannot be so large that all the current takes the path through C_d. That is, $R_{ct} \leq 1/\omega C_d$ or $k^0 \geq RTC_d\omega/F^2 C^* A$. If we choose the most favorable conditions of $C^* = 10^{-2}$ M and $\omega = 2\pi \times 1$ Hz,[10] then at $T = 298$ K and with $C_d/A = 20$ μF/cm^2, we obtain $k^0 \geq 3 \times 10^{-6}$ cm/s.

---

[9]The reductions and oxidations of aromatic species to anion and cation radicals in aprotic solvents are generally among the fastest known heterogeneous charge-transfer reactions. The values of k^0 can exceed 1 cm/s. See references 17 and 18 for measurements of such systems by impedance methods.

[10]It is also essential that the period of the ac stimulus not be so long that convection becomes a factor within a few cycles. The lower frequency limit was set here at 1 Hz because convection would become a problem in the range of several seconds in most liquid systems with water-like viscosity. Current equipment for EIS can operate at much lower frequencies (as low as 10 μHz) and can be usefully applied in the low-frequency (long-time) regime when the processes being examined are not controlled by convection. Examples include transport or reaction at a solid–solid interfaces or diffusion and reaction in extremely viscous media, such as glasses or polymers.

10.4.3 Other Applications of Electrochemical Impedance Spectroscopy

The approach discussed above for EIS of a simple heterogeneous electron-transfer reaction of solution components can be applied to more complicated electrochemical systems, like those with coupled homogeneous reactions or with adsorbed intermediates. In such cases Nyquist plots can be obtained and compared to theoretical models based on the appropriate equations representing the rates of the various processes and their contributions to the current. It may be useful in these cases to represent the system by an equivalent circuit involving different components (resistors, capacitors, inductors). However, such equivalent circuits are not unique and one cannot easily guess the form or structure of the equivalent circuit from the processes involved in the reaction scheme (19). Electrode surface roughness and heterogeneity can also be significant factors in the ac response in EIS. Indeed, even for simple electron-transfer reactions, measurements that can be made usefully with a smooth and homogeneous mercury electrode are often not possible with solid electrodes.

EIS has been applied to a variety of electrochemical systems, including those involved in corrosion, electrodeposition, polymer films, and semiconductor electrodes. Representative studies can be found in EIS symposia proceedings (20–22).

▶ 10.5 AC VOLTAMMETRY

We noted in Section 10.1 that ac voltammetry is basically a faradaic impedance technique in which the mean potential, E_{dc}, is imposed potentiostatically at arbitrary values that usually differ from the equilibrium value. Ordinarily, E_{dc} is varied systematically (e.g., linearly) on a long time scale compared to that of the superimposed ac variation, $\dot{E}_{ac}$ (10 Hz to 100 kHz). The output is a plot of the magnitude of the ac component of the current $vs.$ E_{dc}. The phase angle between the alternating current and $\dot{E}_{ac}$ is also of interest.

Treatments of this problem are greatly simplified by uncoupling the long-term diffusion due to E_{dc} from the rapid diffusional fluctuations due to $\dot{E}_{ac}$. We do that by recognizing that E_{dc} sets up mean surface concentrations that look like bulk values to the ac perturbation because of the difference in time scale. In Section 10.3, we defined the faradaic impedance in terms of bulk concentrations; thus the current response in ac voltammetry as a function of E_{dc} is readily obtained by substituting the surface concentrations imposed by E_{dc} directly into these impedance relations. Since this strategy is simple and intuitive, we will pursue it. More rigorous treatments are available in the literature for the interested reader (2, 3, 5). The results are the same by either approach.

The mean surface concentrations enforced by E_{dc} depend on many factors: (a) the way in which E_{dc} is varied; (b) whether or not there is periodic renewal of the diffusion layer; (c) the applicable current-potential characteristic; and (d) homogeneous or heterogeneous chemical complications associated with the overall electrode reaction. For example, one could vary E_{dc} in a sequential potentiostatic manner with periodic renewal of the diffusion layer, as in sampled-current voltammetry. This is the technique that is actually used in ac $polarography$, which features a DME and effectively constant E_{dc} during the lifetime of each drop. Alternatively one could use a stationary electrode and a fairly fast sweep without renewal of the diffusion layer. Both techniques have been developed and are considered below. The effects of different kinds of charge-transfer kinetics will also be examined here, but the effects of homogeneous complications are deferred to Chapter 12. Throughout the discussion, one should keep in mind that the chief strength of ac

voltammetry is the access it gives to exceptionally precise quantitative information about electrode processes. Diagnostic aspects certainly exist, but they are more subtle than with other methods.

10.5.1 ac Polarography in a Reversible System

Let us consider the ac response at a renewable stationary mercury drop electrode immersed in a solution containing initially only species O in the nernstian process $O + ne \rightleftarrows R$. The dc potential starts at a value considerably more positive than $E^{0'}$ and is scanned slowly in a negative direction. During the lifetime of a single drop, E_{dc} is effectively constant; hence the dc part of the experiment is conventional polarography and is treated as a series of individual step experiments (see Sections 7.1 and 7.2).

Since the charge-transfer resistance is completely negligible, (10.3.10) always applies where

$$\sigma = \frac{RT}{n^2 F^2 A \sqrt{2}} \left[\frac{1}{D_O^{1/2} C_O(0, t)_m} + \frac{1}{D_R^{1/2} C_R(0, t)_m} \right] \tag{10.5.1}$$

and the mean concentrations $C_O(0, t)_m$ and $C_R(0, t)_m$ are determined by the nernstian relation:

$$\frac{C_O(0, t)_m}{C_R(0, t)_m} = \theta_m = \exp\left[\frac{nF}{RT} (E_{dc} - E^{0'}) \right] \tag{10.5.2}$$

The arguments that led to (5.4.29) and (5.4.30) apply equally to the dc part of this experiment; hence we write

$$C_O(0, t)_m = C_O^* \left(\frac{\xi \theta_m}{1 + \xi \theta_m} \right) \tag{10.5.3}$$

$$C_R(0, t)_m = C_O^* \left(\frac{\xi}{1 + \xi \theta_m} \right) \tag{10.5.4}$$

where ξ is $D_O^{1/2}/D_R^{1/2}$, as usual. Thus the faradaic impedance is obtained by substitution into (10.5.1) and then into (10.3.8):

$$Z_f = \frac{RT}{n^2 F^2 A \omega^{1/2} D_O^{1/2} C_O^*} \left(\frac{1}{\xi \theta_m} + 2 + \xi \theta_m \right) \tag{10.5.5}$$

Let us note now that $\xi \theta_m$ can be written

$$\xi \theta_m = e^a \tag{10.5.6}$$

where

$$a = \frac{nF}{RT} (E_{dc} - E_{1/2}) \tag{10.5.7}$$

and $E_{1/2}$ is the reversible half-wave potential defined in (5.4.21):

$$E_{1/2} = E^{0'} + \frac{RT}{nF} \ln \frac{D_R^{1/2}}{D_O^{1/2}} \tag{10.5.8}$$

By substitution from (10.5.6), we find that the term in parentheses in (10.5.5) is $e^{-a} + 2 + e^a$, which is also $4 \cosh^2(a/2)$. Thus we have

$$Z_f = \frac{4RT}{n^2 F^2 A \omega^{1/2} D_O^{1/2} C_O^*} \cosh^2\left(\frac{a}{2} \right) \tag{10.5.9}$$

In Section 10.3 we saw that the faradaic current for a reversible system leads $\dot{E}_{ac}$ by exactly 45°. If $\dot{E}_{ac} = \Delta E \sin \omega t$, then

$$i_{ac} = \frac{\Delta E}{Z_f} \sin\left(\omega t + \frac{\pi}{4}\right) \qquad (10.5.10)$$

and the amplitude of this current, which is the chief observable, is simply

$$\boxed{I = \frac{\Delta E}{Z_f} = \frac{n^2 F^2 A \omega^{1/2} D_O^{1/2} C_O^* \, \Delta E}{4RT \, \cosh^2(a/2)}} \qquad (10.5.11)$$

Figure 10.5.1 is a display of the ac polarogram defined by this equation. The bell shape derives from the factor $\cosh^{-2}(a/2)$, and it reflects the potential dependence of the impedance, Z_f. The maximum in the current occurs at $a/2 = 0$ or at $E_{dc} = E_{1/2}$, which is near $E^{0'}$. As one moves away from that potential, either positively or negatively, the impedance rises sharply and the current falls off. The physical basis for this behavior was outlined in Section 10.3. In effect, the current is controlled by the limiting reagent, that is, the smaller of the two surface concentrations. At potentials far from $E^{0'}$, where only small amounts of one reagent can exist at the surface, only small currents can flow.

The peak current at $E_{dc} = E_{1/2}$ comes easily from (10.5.11). Since $\cosh(0) = 1$,

$$\boxed{I_p = \frac{n^2 F^2 A \omega^{1/2} D_O^{1/2} C_O^* \, \Delta E}{4RT}} \qquad (10.5.12)$$

From this relation and (10.5.11) one can show straightforwardly that the shape of the ac polarogram adheres to

$$\boxed{E_{dc} = E_{1/2} + \frac{2RT}{nF} \ln\left[\left(\frac{I_p}{I}\right)^{1/2} - \left(\frac{I_p - I}{I}\right)^{1/2}\right]} \qquad (10.5.13)$$

(See Problem 10.1.)

The same results hold for the DME, where one must account for the effect of drop growth on the polarogram. The use of linear diffusion relations for the dc part of the
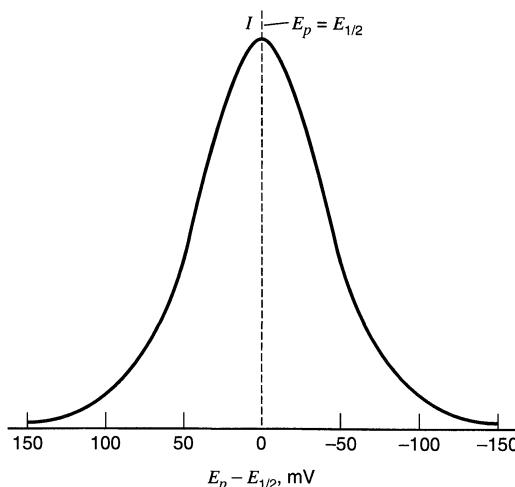
Figure 10.5.1   Shape of a reversible ac voltammetric peak for $n = 1$.

experiment has already been justified (see Section 7.1.2), and that justification is even more valid for the ac part because of its shorter time scale. Thus the peculiarities of the expanding sphere are felt only in the changing area A with time, and that factor is directly accountable by substitution of (7.1.3) into (10.5.11). Since A grows as $t^{2/3}$ as the drop ages, the current also shows the same dependence. Thus we can expect the current to oscillate as successive drops grow and fall. Maxima should be observed at the end of each drop's life. Experimental results in Figure 10.5.2 bear out these expectations. Measurements carried out on the envelope of the ac polarogram can be treated by all relations derived above, provided that A is defined as the area just before drop fall.

A number of important properties of the reversible ac voltammogram can be deduced from (10.5.11)–(10.5.13). Among them are the direct proportionalities between I_p and n^2, $\omega^{1/2}$, and C_O^*. There is also a proportionality to ΔE; however, this relation is a limited one, because the linearized i-E characteristic underlying the derivation of Z_f becomes invalid if ΔE is too large. For linearity within a few percent, ΔE must be less than about $10/n$ mV. Not surprisingly, the width of the peak at half height also depends on ΔE if large values are used. If it is kept below $10/n$ mV, there is a constant width of $90.4/n$ mV at 25°C. At larger ΔE the peaks are broader.

10.5.2 Voltammetric ac Response to Quasireversible and Irreversible Systems

When heterogeneous kinetics become sluggish enough to be visible, one requires a more elaborate theory to predict the voltammetric ac response. Even for a one-step, one-electron process, the general case in which k^0 can adopt any value is very complex. The reader is referred to the literature for complete discussions (2, 3, 5). Here we examine

Alternating Current

−0.650   −0.550

E(V $vs.$ SCE)
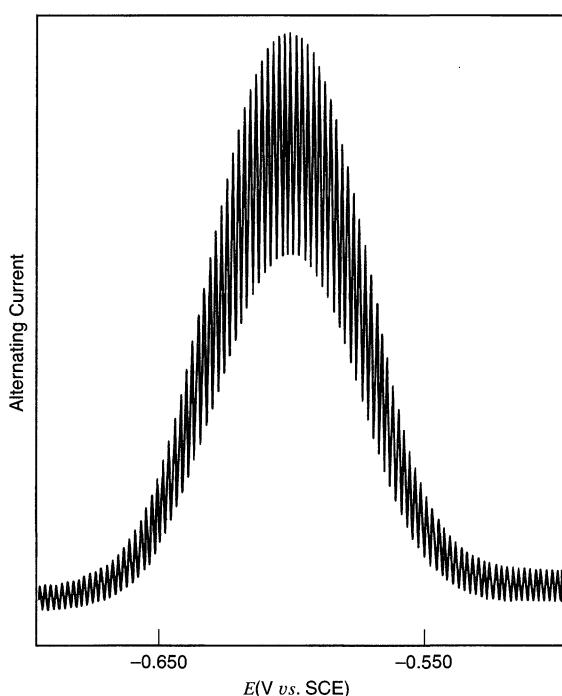
Figure 10.5.2   An ac polarogram for $3 \times 10^{-3}\, M$ Cd^{2+} in $1.0\, M$ Na_2SO_4. $\Delta E = 5$ mV, $\omega/2\pi = 320$ Hz. [Reprinted with permission from D. E. Smith, *Anal Chem.*, **35**, 1811 (1963). Copyright 1963, American Chemical Society.]

an important special case in detail, and it will provide us with a good intuitive understanding of the kinetic effects of interest.

That special case is the situation in which the dc response from a one-step, one-electron system is effectively nernstian, whereas the ac response is not. This situation is frequently seen in real systems because the time scales of the two aspects can differ so greatly. That is, k^0 can be sufficiently large that the mean surface concentrations are kept in the ratio dictated in E_{dc} through the nernstian balance, (10.5.2), even though that rate constant is not large enough to assure a negligible charge-transfer resistance to the much faster ac perturbation.

The faradaic impedance in this situation involves both R_{ct} and σ, and the magnitude can be written from (10.2.27):

$$Z_f = \left[\left(R_{ct} + \frac{\sigma}{\omega^{1/2}} \right)^2 + \left(\frac{\sigma}{\omega^{1/2}} \right)^2 \right]^{1/2} \tag{10.5.14}$$

The parameters R_{ct} and σ can both be defined through the assumption of dc reversibility, which allows us to use the same mean surface concentrations as in the previous section. They are defined by (10.5.3) and (10.5.4); thus we can develop σ by substitution into (10.5.1). Rearrangements equivalent to those used in obtaining (10.5.9) then yield

$$\sigma = \frac{4RT}{\sqrt{2}F^2 A D_O^{1/2} C_O^*} \cosh^2\left(\frac{a}{2}\right) \tag{10.5.15}$$

where we have recognized that $n = 1$.

The charge-transfer resistance, R_{ct}, is given by (10.3.2) in terms of the exchange current, i_0. Normally we speak of i_0 as an equilibrium property defined by bulk concentrations of O and R according to (3.4.6). However, since the mean surface concentrations act like bulk values for the ac process, we can recognize an effective exchange current for ac perturbation that would be given by

$$(i_0)_{eff} = FAk^0 [C_O(0, t)_m]^{(1-\alpha)} [C_R(0, t)_m]^\alpha \tag{10.5.16}$$

By determining the mean surface concentrations, E_{dc} controls $(i_0)_{eff}$ and, therefore, R_{ct}. A more explicit expression of this dependence is obtained by substitution from (10.5.3), (10.5.4), and (10.5.6), as above:

$$(i_0)_{eff} = FAk^0 C_O^* \xi^\alpha \left(\frac{e^{\beta a}}{1 + e^a} \right) \tag{10.5.17}$$

where $\beta = (1 - \alpha)$. Since $R_{ct} = RT/F(i_0)_{eff}$, we have

$$R_{ct} = \frac{RT}{F^2 Ak^0 C_O^* \xi^\alpha} \left(\frac{1 + e^a}{e^{\beta a}} \right) \tag{10.5.18}$$

Now that R_{ct} and σ are available, we can write Z_f as a function of E_{dc} by substitution into (10.5.14). That operation is straightforward, but it yields a rather messy expression. Perhaps more instructive is to examine limiting behavior for high and low frequencies, which can be discerned from (10.5.14).

At very low frequencies, R_{ct} is small compared to $\sigma/\omega^{1/2}$; hence the system looks reversible. This is not surprising; after all we are bringing the time domain of the ac process toward that of the dc perturbation, which evokes a reversible response. Everything we found in the previous section about the reversible ac response should also apply to the quasireversible system at the low-frequency limit.

As the frequency is elevated, R_{ct} becomes appreciable in comparison to $\sigma/\omega^{1/2}$; hence reversibility is vitiated. The ac time domain has become shortened enough to strain the

heterogeneous kinetics. Finally, at the high-frequency limit, R_{ct} greatly exceeds $\sigma/\omega^{1/2}$, and Z_f approaches R_{ct} itself. The amplitude of the alternating current is then

$$I = \frac{\Delta E}{R_{ct}} = \frac{F^2 A k^0 C_O^* \Delta E \xi^\alpha}{RT}\left(\frac{e^{\beta a}}{1 + e^a}\right) \qquad (10.5.19)$$

This equation describes the shape of the ac polarogram. In general, the response as a function of dc potential is bell-shaped, much as in the reversible situation. This point is seen by noting the behavior of the factor in parentheses as a becomes large either positively or negatively. However, positive deviations from $E_{1/2}$ do not evoke the same response as negative deviations; that is, the response is not symmetric and the bell shape is skewed.

The peak is easily found by differentiating (10.5.19) with respect to a. The maximum is reached when $e^a = \beta/\alpha$, or

$$E_{dc} = E_{1/2} + \frac{RT}{F}\ln\frac{\beta}{\alpha} \qquad (10.5.20)$$

The peak current amplitude is therefore

$$I_p = \frac{F^2 A k^0 C_O^* \Delta E \xi^\alpha}{RT}\beta^\beta \alpha^\alpha \qquad (10.5.21)$$

These equations, together with those describing the reversible, low-frequency limit, give a good picture of the behavior of the system as ω changes. The peak current is at first linear with $\omega^{1/2}$, but with increasing frequency that dependence is reduced until, at the high-frequency limit, I_p becomes independent of ω. It is easy to see from preceding developments that the frequency dependence reflects the mass transport effects manifested in the Warburg impedance. The lack of a frequency dependence in (10.5.19) and (10.5.21) comes about because the current is totally controlled at high ω by heterogeneous kinetics. Mass transfer plays no role. Not surprisingly, then, I_p is proportional to k^0 at high ω, and it is totally insensitive to k^0 at low ω. The proportionalities between I_p and ΔE and C_O^* hold at all frequencies.

Note also that since kinetic control of I at high frequencies implies a faradaic impedance that greatly exceeds the Warburg impedance at those frequencies, the current must be much smaller than that for a truly reversible system, which shows only the Warburg impedance at any frequency. The general reduction in ac response in quasireversible systems is illustrated in Figure 10.5.3. The k^0 values for all curves shown there are sufficiently great that the assumption of dc reversibility holds. It is easy to see the trend in responses with decreasing k^0; hence one recognizes that there will be a rather small ac response if k^0 falls below 10^{-4} to 10^{-5} cm/s. Systems showing totally irreversible dc polarograms can be almost invisible to the ac experiment. This fact is useful for analytical work (see Section 10.7).[11]

---

[11]The totally irreversible case does yield an ac current, contrary to the impression one might gain from this line of argument. The current arises from the simple modulation of the dc wave (23, 24). Since the shape of that wave is independent of k^0 (Section 5.5), the ac peak height is also independent of k^0. The peak lies near the half-wave potential of the dc wave; hence it is shifted substantially from $E^{0'}$ by an amount related to the size of k^0.
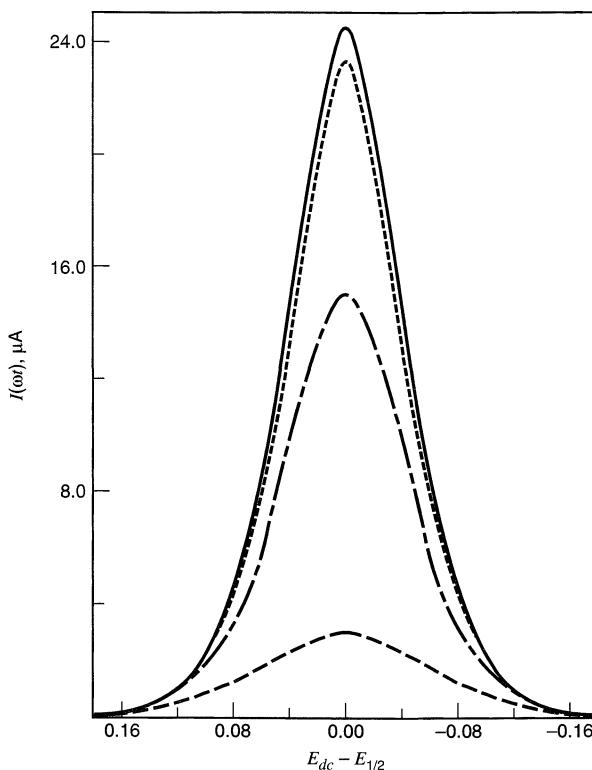
Figure 10.5.3 Calculated ac polarograms for quasireversible one-step, one-electron systems. Curves (from the top) are for $k^0 \to \infty$, $k^0 = 1$, $k^0 = 0.1$, and $k^0 = 0.01$ cm/s. Other parameters are as follows: $\omega = 2500 \text{ s}^{-1}$, $\alpha = 0.500$, $D = 9 \times 10^{-6} \text{ cm}^2/\text{s}$, $A = 0.035$ cm^2, $C_O^* = 1.00 \times 10^{-3} M$, $T = 298$ K, $\Delta E = 5.00$ mV. The curves show the faradaic current at t_{max}. [Reprinted from D. E. Smith, *Electroanal. Chem.*, **1**, 1 (1966), by courtesy of Marcel Dekker, Inc.]

The position of the peak is also of interest. Relations derived above show that there is a slight shift with increasing frequency. At low ω, the peak comes at $E_{dc} = E_{1/2}$, just as for a reversible system at any frequency. As ω becomes greater, the peak potential deviates from this value until it reaches the limiting position defined by (10.5.20). Since α and β are generally comparable, we can expect the extent of this shift, $(RT/F) \ln (\beta/\alpha)$, to be quite small. In other words, the peak potential for an ac polarogram is always near the formal potential for the couple, provided dc reversibility applies.

The phase angle of $\dot{I}_{ac}$ with respect to $\dot{E}_{ac}$ is of great interest as a source of kinetic information. This point was suggested in Section 10.3, and it is rooted in equation 10.3.9. We can rewrite that relation as

$$\cot \phi = 1 + \frac{R_{ct}\omega^{1/2}}{\sigma} \tag{10.5.22}$$

Substitution from (10.5.15) and (10.5.18) and rearrangement gives

$$\cot \phi = 1 + \frac{(2D_O^\beta D_R^\alpha \omega)^{1/2}}{k^0} \left[\frac{1}{e^{\beta a}(1 + e^{-a})} \right] \tag{10.5.23}$$

The bracketed factor shows that $\cot \phi$ depends on the dc potential. Large positive and negative values of a force $\cot \phi$ to unity, and hence there must be a maximum in this quantity near the peak of the polarogram. The precise position is easily found by differentiation, and one ascertains that $e^{-a} = \beta/\alpha$ at that point. Thus,

$$E_{dc} = E_{1/2} + \frac{RT}{F} \ln \frac{\alpha}{\beta} \tag{10.5.24}$$

This maximum point is independent of nearly all experimental variables, for example, ΔE, C_O^*, and, most notably, A and ω. The difference between $E_{1/2}$ and the potential of maximum cot ϕ provides access to the transfer coefficient α.

Actual cot ϕ data are shown in Figure 10.5.4 for TiCl₄ in oxalic acid solution (25). The electrode reaction is the one-electron reduction of Ti(IV) to Ti(III). Note that the potential of maximum cot ϕ is independent of frequency, as predicted above.

Plots of cot ϕ vs. $\omega^{1/2}$ yield k^0, once α is known from the position of $[\cot \phi]_{max}$ and the diffusion coefficients are known from other measurements. This point is easily seen from (10.5.23), which holds for any value of E_{dc}. In practice, these plots are usually made for special values of E_{dc} that give simplified forms of the linear relation.

A convenient procedure is to choose $E_{dc} = E_{1/2}$, for then $a = 0$, and we have

$$[\cot \phi]_{E_{1/2}} = 1 + \left(\frac{D_O^\beta D_R^\alpha}{2}\right)^{1/2} \frac{\omega^{1/2}}{k^0} \tag{10.5.25}$$

If one can take $D_O = D_R = D$, then $D_O^\beta D_R^\alpha = D$, and the slope of this particular plot becomes independent of α. Figure 10.5.5 is an example in which the data from Figure 10.5.4 at $E_{dc} = E_{1/2} = -0.290$ V vs. SCE have been plotted vs. $\omega^{1/2}$.

Another simplified version of (10.5.23) can be obtained for the potential of maximum cot ϕ. By substituting $e^{-a} = \beta/\alpha$, we obtain

$$[\cot \phi]_{max} = 1 + \frac{(2D_O^\beta D_R^\alpha)^{1/2}}{k^0\left[\left(\dfrac{\alpha}{\beta}\right)^{-\alpha} + \left(\dfrac{\alpha}{\beta}\right)^{\beta}\right]} \omega^{1/2} \tag{10.5.26}$$

The product of the diffusion coefficients can usually be simplified as above, but α still must be known for an evaluation of k^0, because of the bracketed factor.

Quantitative information about heterogeneous charge-transfer kinetics obtained from ac polarographic data nearly always comes from the behavior of cot ϕ with po-
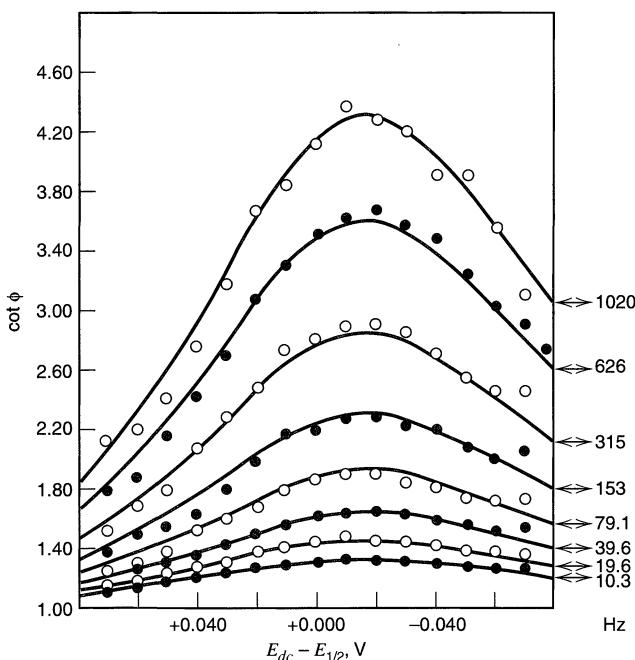
Figure 10.5.4 Dependence of the phase angle on E_{dc}. The system is 3.36 mM TiCl₄ in 0.200 M H₂C₂O₄. $\Delta E = 5.00$ mV, $T = 25°C$. Points are experimental; curves are predicted from experimental parameters by (10.5.23). [Reprinted with permission from D. E. Smith, *Anal. Chem.*, **35**, 610 (1963). Copyright 1963, American Chemical Society.]
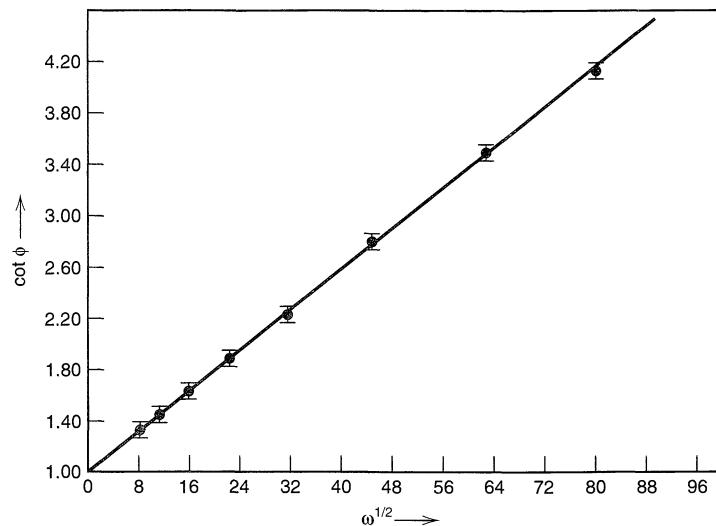
Figure 10.5.5 Plot of cot ϕ vs. $\omega^{1/2}$ for 3.36 mM TiCl$_4$ in 0.200 mM H$_2$C$_2$O$_4$. $E_{dc} = E_{1/2} = -0.290$ V vs. SCE. $\Delta E = 5.00$ mV, $T = 25°C$. [Reprinted with permission from D. E. Smith, *Anal. Chem.*, **35**, 610 (1963). Copyright 1963, American Chemical Society.]

tential and frequency, rather than from the heights, shapes, or positions of the polarograms. One reason for this favor toward cot ϕ is that many experimental variables do not have to be controlled closely or even be known. Among them are C_O^*, ΔE, and A. Freedom from knowing A can be a significant advantage. However, the most important reason for evaluating kinetics through cot ϕ is that relations (10.5.23) to (10.5.26) hold for any quasireversible or irreversible system. We have derived them for the situation in which dc reversibility applies; however, they hold regardless of that condition. Demonstrations of this point are available in the literature (3, 5). Their unconditional validity is a big asset, for it frees the experimenter from having to achieve special limiting conditions.

As in the previous section, we have assumed semi-infinite linear diffusion to a planar electrode throughout the mathematical discussion here. With a reversible dc process, the effects of sphericity and drop growth at the DME are exactly as discussed in Section 10.5.1. In general, the sphericity has a negligible impact and drop growth can be accommodated by using an explicit expression for A as a function of time. If dc reversibility does not apply, these factors influence the ac response in more complex ways (3, 5, 23). The reader is referred to the literature for details.

10.5.3 Linear Sweep ac Voltammetry at Stationary Electrodes (26, 27)

The previous two sections have dealt generally with ac voltammetry as recorded by the application of E_{dc} in successive steps and with a renewal of the diffusion layer between each step. The DME permits the most straightforward application of that technique, but other electrodes can be used if there is a means for stirring the solution between steps so that the diffusion layer is renewed. On the other hand, this requirement for periodic renewal is inconvenient when one wishes to use stationary electrodes, such as metal or carbon disks, or a hanging mercury drop. Then one prefers to apply E_{dc} as a ramp and to renew the diffusion layer only between scans. In this section, we will examine the expected ac voltammograms for reversible and quasireversible systems when E_{dc} is imposed as a linear sweep and we will compare them with the results obtained above for effectively constant E_{dc}.

The strategy is exactly that used before. The time domains associated with variations in E_{dc} and $\dot{E}_{ac}$ are assumed to differ greatly, so that the diffusional aspects of the two parts of the experiment can be uncoupled. This assumption will hold as long as the scan rate, v, is not too large compared to the ac frequency (28). More precisely, $dE_{dc}/dt = v$ should be much smaller than the amplitude of $d\dot{E}/dt$, which is $\Delta E\omega$. Then, we can take the mean surface concentrations enforced by E_{dc} as effective bulk values for the ac perturbation, just as we did earlier. The current amplitude and phase angle then follow easily from the impedance properties.

(a) Reversible Systems

Let us consider a completely nernstian system $O + ne \rightleftarrows R$ in which R is initially absent. The starting potential for the linear sweep is rather positive with respect to $E^{0'}$, and the scan direction is negative. Semi-infinite linear diffusion is assumed. The mean surface concentrations, $C_O(0, t)_m$ and $C_R(0, t)_m$, are exactly those obtained in the analogous linear sweep experiment without superposed ac excitation, and they adhere always to the nernstian relation (10.5.2).

The arguments leading to equation 5.4.26 show that it applies without reference to the kinetic properties of the electrode reaction or the nature of the excitation waveform. For the present purpose, we can rewrite it as

$$D_O^{1/2}C_O(0, t)_m + D_R^{1/2}C_R(0, t)_m = C_O^* D_O^{1/2} \qquad (10.5.27)$$

Substitution from (10.5.2) then reveals that the mean surface concentrations are exactly as given in (10.5.3) and (10.5.4). In other words, those relations, which were derived earlier expressly for step excitation, have been shown here to apply regardless of the manner by which E_{dc} is attained.[12]

This conclusion is very important because it implies that all relations and all qualitative conclusions presented in Section 10.5.1 also hold for linear sweep ac voltammetry of reversible systems at a stationary electrode.

(b) Quasireversible Systems

An important special case of quasireversibility is the situation in which a one-step, one-electron process is sufficiently facile to maintain a reversible dc response, but not facile enough to show a negligible charge-transfer resistance, R_{ct}, to the ac perturbation.

If the dc response is nernstian, (10.5.2) and (10.5.27) hold, and the mean surface concentrations are given by (10.5.3) and (10.5.4), which are the same relations used in the treatment of Section 10.5.2. Thus, all of the equations and qualitative conclusions reached there for quasireversible ac polarograms also apply to the corresponding linear sweep ac voltammograms.

These precise parallels between linear sweep voltammetry and ac polarography no longer persist when there is a lack of dc reversibility. Treating such a case is more complex than the situations we have examined above because the mean surface concentrations are affected by the concentration profiles throughout the diffusion layer, and the surface values applicable at any potential generally depend on the waveform used to attain that potential (26, 27).

Linear sweep ac voltammetry allows precise, rapid kinetic measurements at solid electrodes. It can therefore be used to characterize these electrodes themselves, which

---

[12]Equation 10.5.27 is based on semi-infinite linear diffusion; hence this conclusion applies strictly only to planar electrodes. Work at an SMDE can be affected by sphericity (27).

may be of considerable interest, or to study electrode processes operating outside the working range of mercury or taking place in controlled environments where the DME or SMDE may be inconvenient.

10.5.4 Cyclic ac Voltammetry (26, 27)

Cyclic ac voltammetry is a simple extension of the linear sweep technique; one simply adds the reversal scan in E_{dc}. This technique retains the best features of two powerful, complementary methodologies. Conventional cyclic voltammetry is especially informative about the qualitative aspects of an electrode process. However, the response waveforms lend themselves poorly to quantitative evaluations of parameters. Cyclic ac voltammetry retains the diagnostic utility of conventional cyclic measurements, but it does so with an improved response function that permits quantitative evaluations as precise as those obtainable with the usual ac approaches. Although this technique is not widely employed, it can be a useful adjunct to dc cyclic voltammetry.

Treatments of cyclic ac voltammetry follow the familiar pattern. The ac and dc time scales are independently variable, but are assumed to differ markedly. Then a treatment of the dc aspect yields mean surface concentrations, which are used to calculate faradaic impedances that define the ac response by amplitude and phase angle. The electrode is assumed to be stationary and the solution is regarded as quiescent for the duration of the dc cycle.

(a) Reversible Systems

Cyclic ac voltammograms for completely nernstian systems are easy to predict on the basis of results from the previous section. The mean surface concentrations, $C_O(0, t)_m$ and $C_R(0, t)_m$, adhere to (10.5.3) and (10.5.4) unconditionally; hence at any potential they are the same for both the forward and reverse scans. The cyclic ac voltammogram should therefore show superimposed forward and reverse traces of ac current amplitude $vs.$ E_{dc}. We expect a peak-shaped voltammogram that adheres in every way to the conclusions reached in Section 10.5.1 about the general ac voltammetric response to a reversible system at a planar electrode.

Figure 10.5.6 contrasts the responses from the ac and dc versions of cyclic voltammetry for the purely nernstian case. Kinetic reversibility is shown in the dc experiment by a
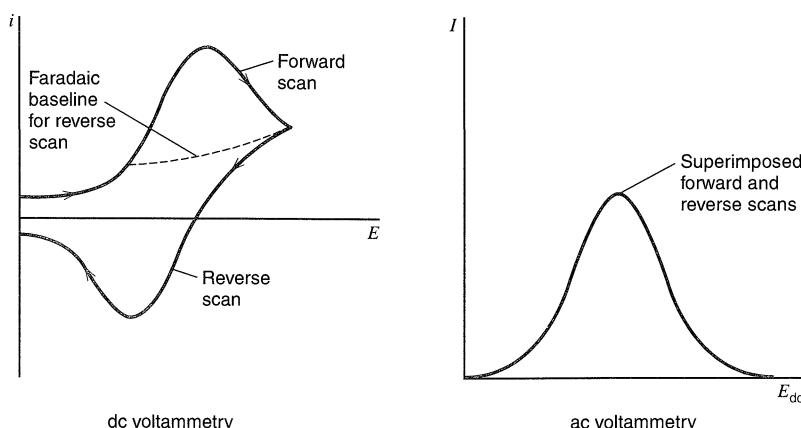
Figure 10.5.6 Comparison of response wave forms for cyclic dc and cyclic ac voltammetry for a reversible system.

peak separation near $60/n$ mV (25°C), regardless of scan rate. In the ac experiment, it is shown by identical forward and reverse peak potentials and by peak widths of $90/n$ mV (25°C), again regardless of scan rate. Chemical stability of the reduced form is demonstrated in the dc experiment by a peak current ratio, $|i_{p,r}/i_{p,f}|$, of unity. Given charge-transfer reversibility, the same thing is shown by the ratio of peak ac current amplitudes, $|I_{p,r}/I_{p,f}|$. The advantage in the ac experiment is that the reversal response has an obvious baseline for quantitative measurements, whereas the baseline for reversal currents in the dc response is more difficult to fix.

(b) Quasireversible Systems

It continues to be helpful to consider two separate cases of quasireversibility in a one-step, one-electron reaction. In both, a significant polarization resistance is manifested in the ac response, but in one instance the dc aspect appears reversible, whereas more generally it is not.

When dc reversibility obtains, a theoretical description is straightforward, because the mean surface concentrations still adhere to (10.5.3) and (10.5.4), regardless of the manner in which the dc potential determining them was established. Thus the forward and the reverse traces again overlap precisely. The shape of the peak and its position adhere to the relations derived in Section 10.5.2, where this kinetic case was considered in detail.

If dc reversibility does not hold, then the situation becomes quite complex. The mean surface concentrations at a given dc potential tend to depend on the way in which that potential is reached. In general, the surface concentrations at any E_{dc} will differ for forward and reverse scans; therefore we can expect the corresponding traces to differ in the voltammogram. In the dc cyclic voltammogram, increasingly sluggish electron transfer causes greater splitting of the forward and reverse peaks, because larger activation overpotentials are needed to motivate charge transfer. This splitting also manifests the fact that the surface concentrations undergo the transition from nearly pure O to virtually pure R in different potential regions for the two scan directions. Since the ac voltammogram shows a response only in the potential regions where such transition takes place, we can expect the cyclic ac voltammogram to show split peaks that are largely aligned with the forward and reverse dc voltammetric peaks. The standard potential $E^{0'}$ will lie between them. Some traces are shown in Figure 10.5.7.

Evidently there is a *crossover potential*, E_{co}, where both scans yield the same response. This potential can be rigorously shown to lie at

$$E_{co} = E_{1/2} + \frac{RT}{F} \ln \frac{\alpha}{1 - \alpha} \qquad (10.5.28)$$

regardless of the details of dc polarization (26). It serves as a convenient source for the evaluation of α. The amplitude and the phase angle of the ac response at E_{co} are totally independent of the dc process. In this respect E_{co} is a unique potential, and it may be the most convenient point for evaluating k^0 by a plot of cot ϕ vs. $\omega^{1/2}$. One can also derive k^0 from the separation of forward and reverse peaks in the ac voltammogram (26, 27).

Figure 10.5.8 is a display of an actual cyclic ac voltammogram for ferric acetylacetonate, Fe(acac)$_3$, in acetone containing 0.1 M tetraethylammonium perchlorate. Since this system is very nearly reversible to the dc process, the peak splitting is quite small, but easily detectable. The convenience of the waveform for quantitative work is also readily apparent.
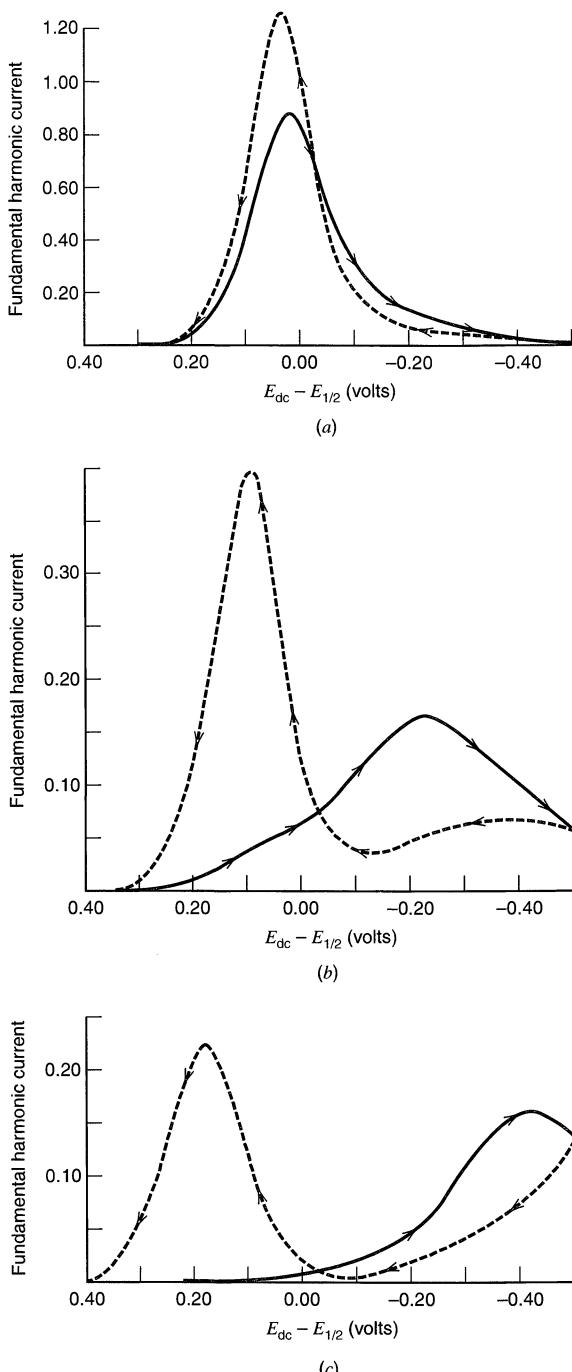
Figure 10.5.7 Predicted cyclic ac voltammograms for systems with non-nernstian dc behavior. (a) $k^0 = 4.4 \times 10^{-3}$ cm/s. (b) 4.4×10^{-4} cm/s, (c) 4.4×10^{-5} cm/s. For $\omega/2\pi = 400$ Hz, $n = 1$, $T = 298$ K, $A = 0.30$ cm^2, $C_O^* = 1.00$ mM, $D_O = D_R = 1.00 \times 10^{-5}$ cm^2/s, $v = 50$ mV/s, $\Delta E = 5.00$ mV, and $\alpha = 0.5$. Ac amplitude given as the normalized function $IRT/n^2F^2A(2\omega D_O)^{1/2}C_O^*\Delta E$. [Reprinted with permission from A. M. Bond et al., *Anal. Chem.*, **48**, 872 (1976). Copyright 1976, American Chemical Society.]

(c) Homogeneous Chemical Complications

Conventional cyclic voltammetry's greatest utility is in the diagnosis of electrode reactions involving chemical complications, and the ac variant is also useful in meeting this kind of problem. The ratio $I_{p,r}/I_{p,f}$ is a sensitive indicator of product stability, just as the dc voltammetric ratio $|i_{p,r}/i_{p,f}|$ is. However, the ac ratio is easier to measure precisely, and it lends itself well to quantitative evaluation of homogeneous rate constants.
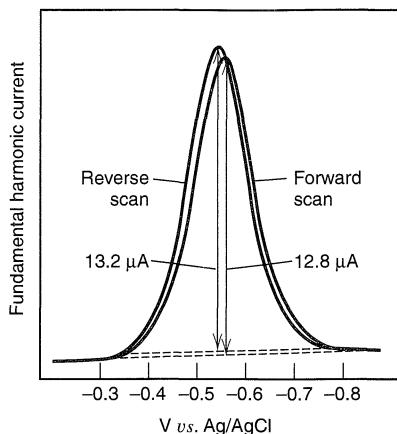
Figure 10.5.8 Cyclic ac voltammogram for 1.0 mM tris(acetylacetonate)Fe(III) in acetone containing 0.1 M tetraethylammonium perchlorate. Working electrode was a platinum disk. $T = 25°C$, $\Delta E = 5$ mV, $v = 100$ mV/s, $\omega/2\pi = 400$ Hz. (Reprinted with permission from A. M. Bond et al., *Anal. Chem.*, **48**, 872 (1976). Copyright 1976, American Chemical Society.]

Actual results (29) for a complicated case involving two interrelated couples are shown in Figure 10.5.9. The species of interest are the complexes $Mo(CO)_2(DPE)_2$, where DPE is diphenylphosphinoethane. These complexes exist in *cis* and *trans* forms which are oxidized at different potentials. Moreover, the oxidized *cis* form (cis^+) homogeneously converts to the oxidized *trans* form ($trans^+$). That is,

$$trans - e \rightleftarrows trans^+ \tag{10.5.29}$$

$$cis - e \rightleftarrows cis^+ \tag{10.5.30}$$

$$cis^+ \overset{k}{\rightarrow} trans^+ \tag{10.5.31}$$

The voltammograms of Figure 10.5.9 were obtained with a solution initially containing only *cis*-$Mo(CO)_2(DPE)_2$. Close study of these curves shows that the diagnostic utility of the dc voltammogram is preserved in the ac traces. In fact, it may be a bit more obvious from the ac curves that cis^+ does not decay completely during the experiment.

10.6 HIGHER HARMONICS (3, 5, 7)

To this point, we have found that excitation of an electrochemical system by a signal, $\dot{E}_{ac} = \Delta E \sin \omega t$ produces a sinusoidal current response at the same frequency. That result rests on the fact that only the linearized current-potential relation has been used. The remaining terms in the Taylor expansion of current *vs.* potential were dropped (Section 3.4.6). If we include them, we find that the current response is not purely sinusoidal, but instead comprises a whole series of sinusoidal signals at ω, 2ω, 3ω, . . . , which are summed together. The current component at 2ω is the *second harmonic* response, while that at 3ω is the *third harmonic*, etc.[13] These higher harmonics arise from *curvature* in the *i-E* relation.

Each harmonic is individually detectable by circuits employing tuned amplifiers or lock-in amplifiers. The most common arrangement is a variant of ac voltammetry, as might be implemented according to Figure 10.6.1. The cell is excited exactly as in ac voltammetry, but the lock-in amplifier is tuned to 2ω and detects only that current contribution. The result is a trace of $I(2\omega)$ *vs.* E_{dc}.

---

[13]This nomenclature differs from that used in electrical engineering, where the signal at ω is the *fundamental* and that at 2ω is the *first harmonic*. We will adhere to the usual electrochemical usage.
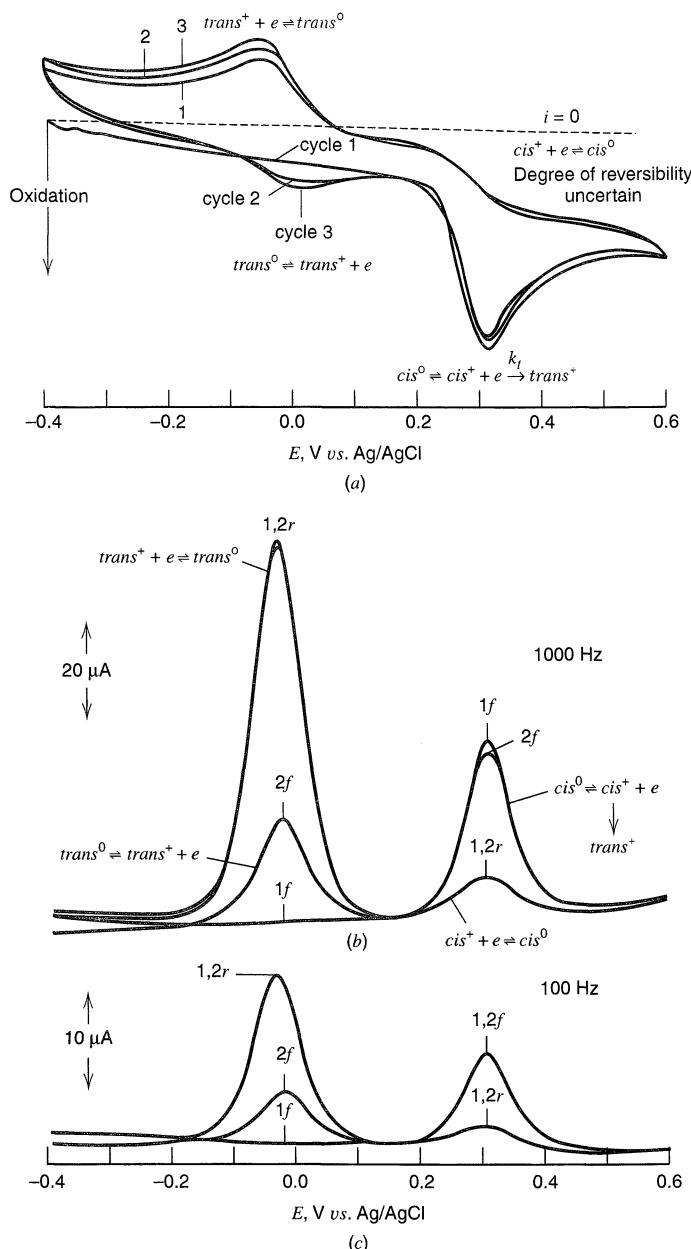
Figure 10.5.9 (*a*) Cyclic dc voltammograms of *cis*-Mo(CO)$_2$(DPE)$_2$ in acetone containing 0.1 *M* tetraethylammonium perchlorate. Solution was saturated with the molybdenum species. $v = 100$ mV/s. Anodic currents are plotted downward. (*b, c*) Cyclic ac voltammograms at the same platinum wire electrode. $v = 100$ mV/s, $\Delta E = 5$ mV. *Notation*: *nf*, scan number *n* in forward direction; *nr*, scan number *n* in reverse direction. [From A. M. Bond, *J. Electroanal. Chem.*, **50**, 285 (1974), with permission.]

An exact treatment of higher harmonic response is straightforward, but it is rather lengthy, so we will leave it to the specialized literature. Instead we will follow an intuitive approach that will reveal most of the distinctive features of second-harmonic ac voltammetry. For simplicity, we consider only a reversible system in which R is initially absent.

The mean surface concentrations, $C_O(0, t)_m$ and $C_R(0, t)_m$, are set by the value of E_{dc} and are given by (10.5.3) and (10.5.4). Figure 10.6.2 is a graphical display of $C_R(0, t)_m$. The ac response is determined by the way in which $\dot{E}_{ac}$ causes small perturbations in the surface concentrations about those mean values. The fundamental (or first-harmonic)
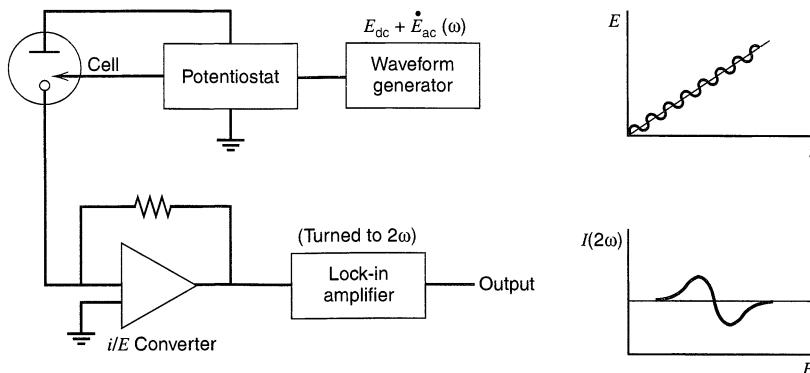
Figure 10.6.1 Block diagram of apparatus for recording a second-harmonic ac voltammogram.

component is controlled essentially by the linear elements of variation, which are the slopes $\partial C_O(0, t)_m/\partial E$ and $\partial C_R(0, t)_m/\partial E$. The higher harmonics reflect curvature; hence they are sensitive to the second and higher derivatives. Comprehension of this point allows us to predict the general shape of the second harmonic response.

Consider potentials E_1, E_3, and E_5 in Figure 10.6.2. Since they have the common feature that the curvature in $C_O(0, t)_m$ and $C_R(0, t)_m$ is zero, there is no second harmonic current. Of course, E_1 and E_5 lie at extreme values where there is also no fundamental response; but E_3 lies at the inflection point $E = E_{1/2}$, where the fundamental response is greatest. The potentials E_2 and E_4 are at points of maximum curvature, hence they should be the potentials of peak second-harmonic current. If we detect only the magnitude $I(2\omega)$, then we can expect a double-peaked voltammogram like that of Figure 10.6.3a.

Let us note, though, that the curvature at E_2 is opposite to that at E_4. This difference implies that the second harmonic component undergoes a 180° phase shift when E_{dc} passes through the null point at $E_{1/2}$. Phase-sensitive detection of $I(2\omega)$ at a fixed phase angle will therefore produce a sign inversion at $E_{1/2}$. Figure 10.6.3b is an example. In general, a nernstian reaction detected at any phase angle will show positive and negative lobes that are symmetrical around the point of intersection with the potential axis. The dc potential corresponding to this intersection is $E_{1/2}$ at all phase angles (Figure 10.6.4) (30). The responses at a given phase angle compared to the same phase angle plus 90° are symmetrical around the potential axis only at 0° and 180°.
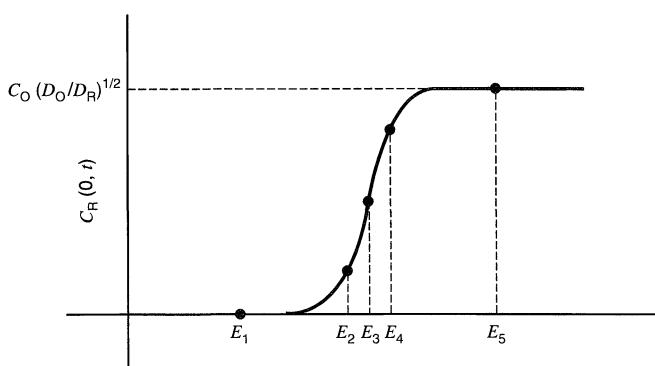
Figure 10.6.2
Dependence of the surface concentration of species R on the electrode potential.
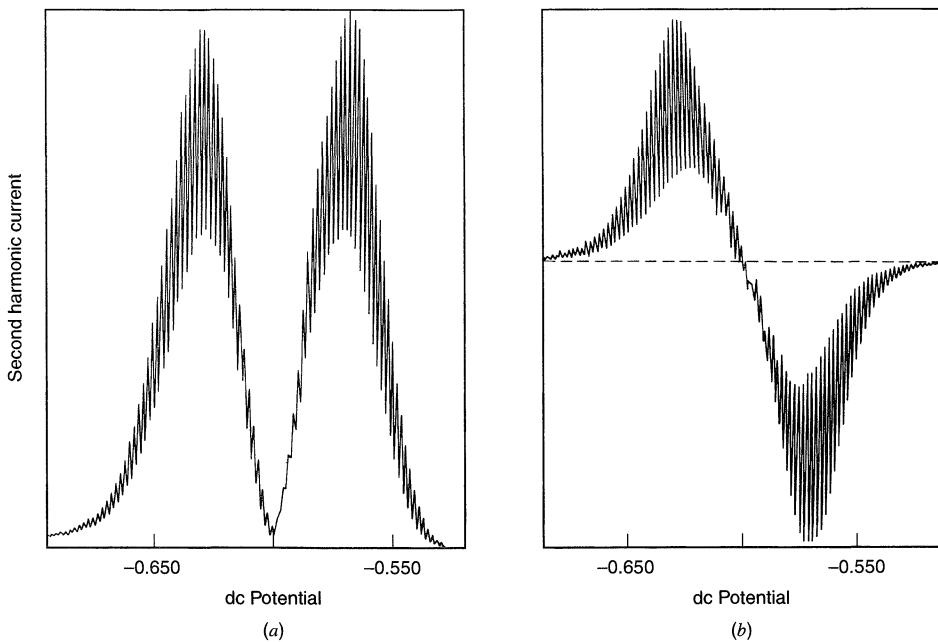
Figure 10.6.3 Second-harmonic ac polarograms for 3 mM Cd^{2+} in 1.0 M Na_2SO_4. $\omega/2\pi$ = 80 Hz, ΔE = 5 mV. (*a*) Total ac amplitude *vs.* E_{dc} (*vs.* SCE). (*b*) Phase-selective polarogram showing the ac amplitude at 0° with respect to $\dot{E}_{ac}$. [Reprinted with permission from D. E. Smith, *Anal. Chem.*, **35**, 1811 (1963). Copyright 1963, American Chemical Society.]

The exact solution of this problem is

$$i(2\omega) = \frac{n^3 F^3 A C_O^* (2\omega D_O)^{1/2} \Delta E^2 \sinh(a/2)}{16 R^2 T^2 \cosh^3(a/2)} \sin\left(2\omega t - \frac{\pi}{4}\right) \qquad (10.6.1)$$

where a is defined in (10.5.7). This equation embodies the proportionalities of C_O^*, $\omega^{1/2}$, and $D_O^{1/2}$ that we have come to expect of diffusion-controlled processes. The phase angle of 45° has the same origin. Note, however, that $i(2\omega)$ is proportional to ΔE^2. This dependence manifests the greater importance of nonlinear effects for perturbations of larger magnitude. The two peak potentials are located at $E_{dc} = E_{1/2} \pm 34/n$ mV at 25°C.

Second-harmonic techniques are useful for analytical purposes and for the quantitative evaluation of heterogeneous kinetic parameters (3, 5, 7, 31). Applications in both areas are attractive, because the double-layer capacitance is a rather linear element and contributes very small second-harmonic currents. Second-harmonic voltammetry has also been used to investigate electrode reactions with coupled homogeneous reactions. In particular, it has been proposed as a method of obtaining the standard potential for a reaction even in the presence of a fast following reaction that consumes the product. However, the fact that a second harmonic response is obtained does not imply that the effects of the following reaction have been eliminated, because one will obtain such a response from simple modulation of the (nonlinear) dc wave. To extract a valid standard potential, one must insure that the observed response shows all of the characteristics of a nernstian process (see Figure 10.6.4) (30). Harmonics above the second have been examined briefly, but have not been applied to any great extent.
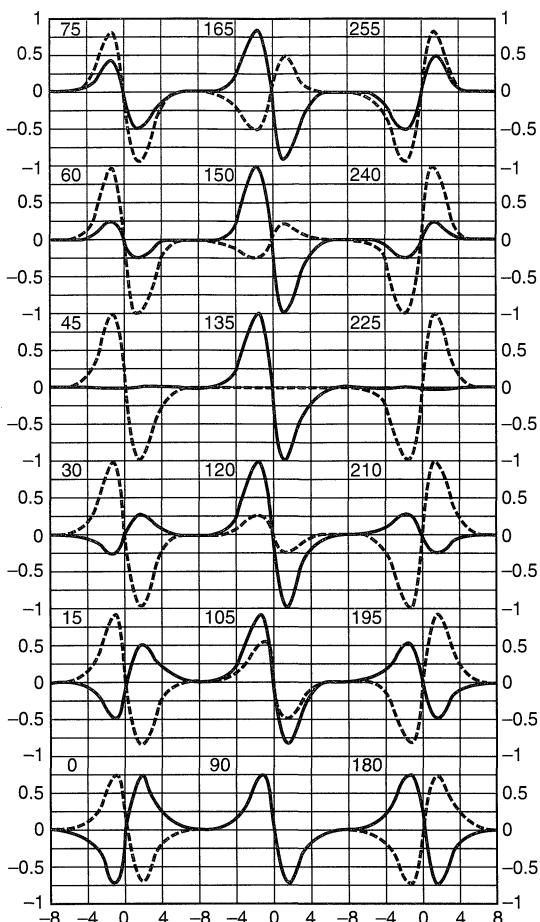
Figure 10.6.4 Theoretical second-harmonic responses for a nernstian reaction as a function of phase angle (solid line) and at that same angle plus 90° (dashed line). The horizontal axis is $-(RT/F)(E - E^{0'})$ and the vertical axis is the second harmonic current normalized to the maximum response. The calculation assumes $D_O = D_R$ and $\Delta E = 25$ mV. [Reprinted with permission from C. P. Andrieux, P. Hapiot, J. Pinson, and J.-M. Savéant, *J. Am. Chem. Soc.*, **115**, 7783 (1993). Copyright 1993, American Chemical Society.]

10.7 CHEMICAL ANALYSIS BY AC VOLTAMMETRY

Both fundamental and second-harmonic ac voltammetry are attractive as analytical techniques because they offer good sensitivities. Detection limits for the polarographic variants can reach the order of 10^{-7} *M*. Such performance is possible because both methods have ready means for discrimination against capacitive currents (5, 7).

In the fundamental mode, one employs phase-sensitive detection to measure the current component in phase with the excitation signal $\dot{E}_{ac}$. We noted in Section 10.3 that there is generally a faradaic contribution to this current, and Figure 10.7.1 reinforces the idea pictorially. In contrast, the charging current is ideally 90° out of phase with $\dot{E}_{ac}$, since it passes through a purely capacitive element. It therefore has no projection in phase with $\dot{E}_{ac}$. Thus we expect the current in phase to be purely faradaic, whereas the current at 90° (the *quadrature current*) contains a second faradaic component plus the nonfaradaic contribution. By taking the current in phase as the analytical signal, we discriminate effectively against the capacitive interference.

The limitation to this scheme is imposed partially by the uncompensated resistance, R_Ω. Since the charging current passes through R_Ω and C_d in series, this current does not lead $\dot{E}_{ac}$ by exactly 90°, but instead by some smaller angle. Thus the current in phase with
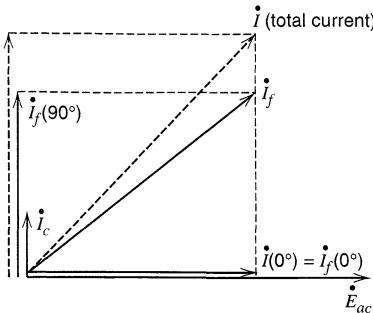
Figure 10.7.1 Phasor diagram showing the relationships between the faradaic ($\dot{I}_f$) and capacitive ($\dot{I}_c$) components to the total current ($\dot{I}$). Note that $\dot{I}_f$ has a component along $\dot{E}_{ac}$, whereas $\dot{I}_c$ does not.

$\dot{E}_{ac}$ must contain a nonfaradaic element, which becomes significant to the measurement as the analyte concentration drops.

Second-harmonic ac voltammetry gains its freedom from nonfaradaic interference from the relative linearity of the double-layer capacitance as a circuit element. There is consequently only a very small second-harmonic capacitive current, although it too can become important at low analyte concentrations.

The shapes of the voltammograms generated in ac measurements are convenient for analysis. Detection of the fundamental current produces a peak whose height is readily measured and is linear with concentration. Phase-selective second-harmonic voltammetry gives the second-derivative waveform of Figure 10.6.3b. The peak-to-peak amplitude is linear with concentration and can be read with high precision. It is also relatively unaffected by the background signal (31).

Analytical measurements are usually carried out at excitation frequencies ranging from 10 Hz to 1 kHz, although Bond has noted that frequencies in the upper part of this range allow fuller exploitation of certain aspects of selectivity that are unique to ac methods (32). Their basis is the discrimination against the much smaller response from irreversible systems.

For example, one can effect a significant saving in analysis time by working directly with aerated solutions. Since the reduction of oxygen in most aqueous solutions is irreversible, it does not interfere with determinations made by ac voltammetry. Also, one can often control the medium in order to introduce selectivity toward certain analytes. Transition metals are especially susceptible to such manipulation because their electrode kinetics are often strongly affected by coordination. Thus, one can enhance their ac responses or mask them from the voltammogram by intelligent choice of electrolyte composition. Since many supporting electrolytes show irreversible reductions, there is considerable freedom to manipulate composition without introducing serious interferences.

▶ 10.8 INSTRUMENTATION FOR ELECTROCHEMICAL IMPEDANCE SPECTROSCOPY

Impedance measurements can be made in either the frequency domain with a frequency response analyzer (FRA) or in the time domain using Fourier transformation with a spectrum analyzer. Commercial instrumentation and software is available for these measurements and the analysis of the data.

10.8.1 Frequency Domain Measurements (8, 9, 11)

The basic principles of a FRA in measuring the impedance of an electrochemical cell are shown in the block diagram in Figure 10.8.1. The FRA generates a signal $e(t) =$
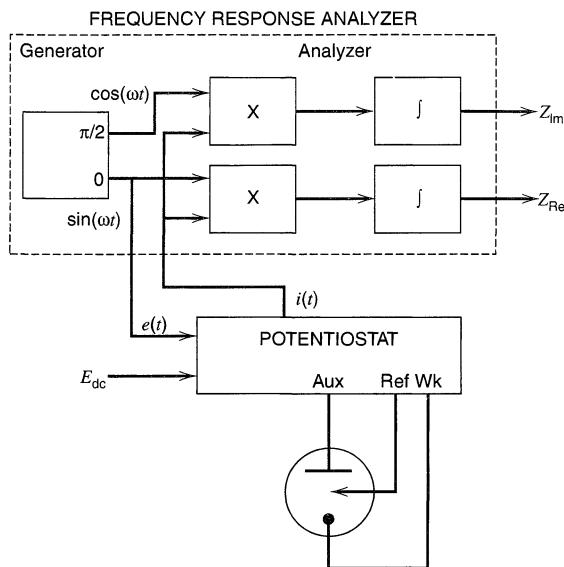
Figure 10.8.1 System for measuring the impedance of an electrochemical cell based on a frequency response analyzer (FRA).

$\Delta E \sin(\omega t)$ which is fed to the potentiostat. This is added to E_{dc} and fed to the cell. In practice, care must be taken to avoid phase and amplitude errors that can be introduced by the potentiostat, particularly at higher frequencies. The resulting current, $i(t)$, or more precisely a voltage signal proportional to the current, is fed to the analyzer, mixed with the input signal, and integrated over several signal periods to yield signals that are proportional to the real and imaginary parts of the impedance (or equivalently the magnitude and phase angle of the impedance). Commercial frequency response analyzers are available with a frequency range of 10 μHz to 20 MHz. Means are provided for sweeping the frequency over a given range and storing the resulting impedance data.

10.8.2 Time Domain Measurements and Fourier Transform Analysis

In time domain measurements, the electrochemical system is subjected to a potential variation that is the resultant of many frequencies, like a pulse or white noise signal, and the time-dependent current from the cell is recorded. The stimulus and the response can be converted via Fourier transform methods to spectral representations of amplitude and phase angle *vs.* frequency, from which the desired impedance can be computed as a function of frequency.

Applications of the Fourier transformation to spectroscopy have become widespread and are familiar to most chemists. They are attractive because they allow one to interpret experiments in which several different excitation signals are applied to a chemical system at the same time. The responses to those signals are superimposed on each other, but the Fourier transformation provides a means for resolving them. This capacity for simultaneous measurement is sometimes called the *multiplex advantage* of transform methods, and it is of great importance to applications in electrochemistry (see also Section A.6).

By now it should be clear that fully characterizing an electrochemical process by impedance methods can be a tedious operation, because one requires information at a set of frequencies ranging over 2 to 3 decades and at a set of potentials ranging over $E^{0'} \pm 100$ mV. For example, the data in Figure 10.5.4 alone required eight ac polarograms, each scanned with the tuned circuitry set to a different frequency and each having the in-phase

and quadrature currents separately recorded. Not only does the operation require time and patience, but also there is the danger that the surface properties of the system will change during the procedure.

One can employ an alternative in which excitation signals of all desired frequencies are brought to bear at once (33–37). The idea is outlined in Figure 10.8.2, which shows that the excitation signal, $\dot{E}_{ac}$, is actually a noise waveform, rather than a pure sinusoid. As before, $\dot{E}_{ac}$ is superimposed on a virtually constant level, E_{dc}. Of course $\dot{E}_{ac}$ will stimulate a current flow showing related "noisy" variations. During a brief period, lasting perhaps 100 ms, the output of the follower and the output of the i/E converter are digitized simultaneously and stored in a computer's memory.

Fourier transformation of these two transients gives the distribution of harmonics that comprise the signals. One therefore knows the amplitude of excitation and the corresponding amplitude and phase angle for current flow at each frequency in the Fourier distributions. In other words, one has the faradaic impedance as a function of ω for the potential E_{dc}. All of this can be obtained with a 100-ms period of data acquisition even on a single drop at a DME; hence it is feasible to repeat the whole procedure, perhaps on subsequent drops, so that more precise ensemble-averaged results are obtained. Changing E_{dc} for each complete set of measurements then provides the potential distribution, that is, $\dot{E}(E_{dc}, \omega)$.

In practice, it is desirable to have a special kind of excitation noise. Smith and his coworkers (34, 36) demonstrated that the best choice is an odd-harmonic, phase-varying pseudorandom white noise of the type displayed in Figure 10.8.3. This noise is the superposition of signals at several frequencies (15 in the example), all of which are odd harmonics of the lowest frequency. The choice of odd harmonics ensures that second-

$$I(\omega_1), \phi(\omega_1), E(\omega_1) \rightarrow Z(\omega_1)$$
$$I(\omega_2), \phi(\omega_2), E(\omega_2) \rightarrow Z(\omega_2)$$
$$\vdots$$
$$I(\omega_n), \phi(\omega_n), E(\omega_n) \rightarrow Z(\omega_n)$$
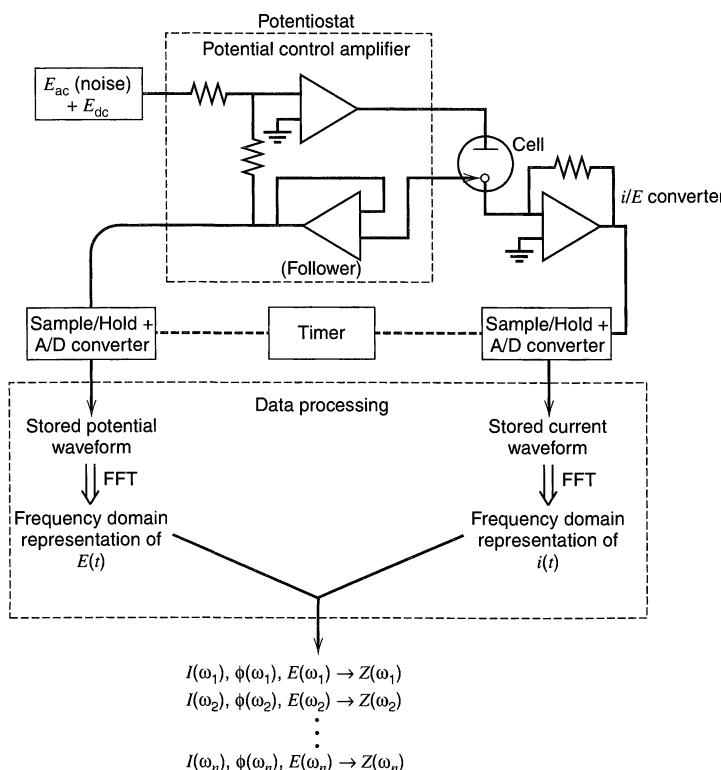
Figure 10.8.2 Schematic diagram showing apparatus and data-processing steps used in on-line Fourier analysis of ac voltammetric data. The steps in the large dashed box are carried out in a computer, usually by the fast Fourier transform (FFT) algorithm (see Section A.6).
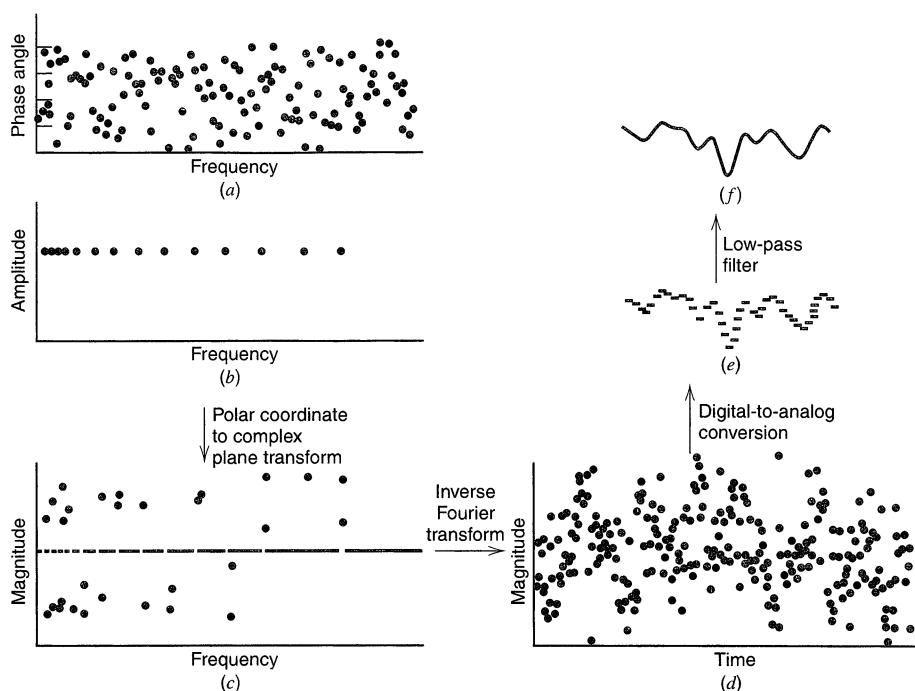
Figure 10.8.3 Procedure for generating a complex excitation waveform. (*b*) Shows the chosen amplitudes for the various frequencies and (*a*) shows randomized phase angles. In (*c*) there is a complex plane representation of the arrays in (*a*) and (*b*). (*d*) The time domain representation, which is subjected to digital/analog conversion to produce (*e*); and in turn, low-pass filtering yields (*f*). Only a small part of the waveform period is shown in (*e*) and (*f*). [From S. C. Creason et al., *J. Electroanal. Chem.*, **47**, 9 (1973), with permission.]

harmonic components will not appear in the currents measured for the 15 fundamental frequencies. The amplitudes of the 15 excitation frequencies are equal ("white" noise) so that each carries equal weight; and their phase angles are randomized, so that the total excitation signal does not show large swings in amplitude.

Despite these demands, it is easy to generate such special noise by inverting the scheme for signal analysis. The method is sketched in Figure 10.8.3. One starts with the amplitude and phase-angle arrays, which have been tailored in the computer according to specifications. These are transformed into the complex plane; then the fast inverse Fourier transform is invoked, so that one obtains a digital representation of the time-domain noise signal. Feeding these numbers sequentially to a digital-to-analog (D/A) converter at the desired rate yields an analog signal, which is filtered and sent to the potentiostat's input. Repeated passage through the D/A conversion and filtering steps yields a repetitive excitation waveform, which is applied continuously until a single measurement pass is completed. A new waveform with different randomized phase angles is generated for the next pass, and so on.

The quality of the results from these experiments is illustrated in Figure 10.8.4 by data for the $Cr(CN)_6^{3-}/Cr(CN)_6^{4-}$ couple. The run represents an average of 64 measurement passes, each taken on one DME drop and each requiring ~ 2 s for acquisition and reduction of the data. Compare the range of cot ϕ and its precision in this figure with that of the good manual data in Figure 10.5.5.
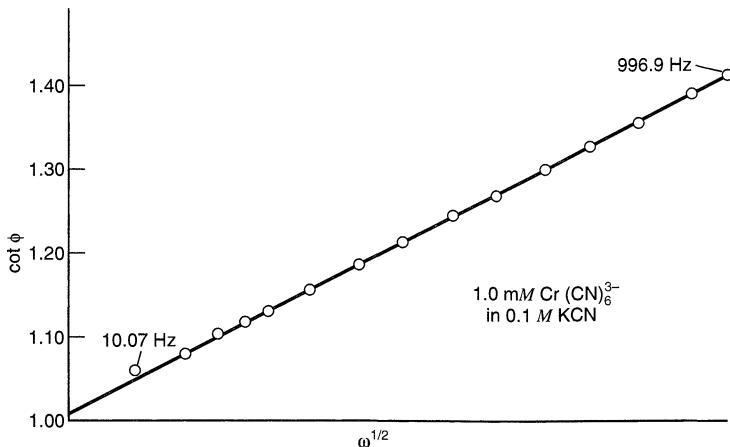
Figure 10.8.4 cot ϕ vs. $\omega^{1/2}$ for the chromicyanide system. Data were obtained with a phase-varying, 15-component, odd-harmonic complex waveform. [From S. C. Creason et al., *J. Electroanal. Chem.*, **47**, 9 (1973), with permission.]

The ability of the Fourier transformation to dissect a complex waveform into its components can also be used to obtain higher harmonics (35, 36). In this case, one might excite with a pure sinusoid at frequency ω and examine the transformed current waveform. It will provide the dc current, the current and phase angle at the fundamental frequency ω, as well as amplitudes and phase angles of the higher harmonics. Repeating measurement passes at various values of E_{dc} allows one to trace out all of the corresponding voltammograms from data obtained on a single run.

In addition to its applications as an integral component of the measurement process, the Fourier transformation can be extremely useful for various signal-conditioning operations, such as smoothing, convolution, and correlation. Smith et al. have discussed the possibilities in this area at some length, and the interested reader is urged to pursue their discussions (36, 38).

▶ 10.9 ANALYSIS OF DATA IN THE LAPLACE PLANE

There are many instances in electrochemistry when we find it very difficult to obtain an explicit relationship between current, potential, and time. Either the system itself is intrinsically complex (e.g., a quasireversible charge transfer involving adsorbed and diffusing reactant species) or the experimental conditions are less than ideal (e.g., step experiments carried out on a time domain so short that the rise time of the potentiostat is not negligible). It is usually true in these and other cases that much simpler relationships exist in the Laplace domain between the perturbations and the observables. Thus it can be useful to transform the data and carry out the analysis in transform space (39–42).

As an example, consider the case of potential steps applied to a one-step, one-electron system containing only electroactive species O, which is reduced quasireversibly. In Section 5.5.1, we treated this case conventionally and found that the current-time function was

$$i = FAk_f C_O^* \exp(H^2 t) \, \text{erfc}(Ht^{1/2}) \qquad (10.9.1)$$

where $H = k_f/D_O^{1/2} + k_b/D_R^{1/2}$. The complex time dependence embodied in (10.9.1) is difficult to handle in the analysis of real data; hence various attacks based on linearization or

extrapolation were devised. On the other hand, we could use all of the data without introducing such approximations by considering the transformed current:

$$\bar{i}(s) = \frac{FAk_f C_O^*}{s^{1/2}(H + s^{1/2})} \tag{10.9.2}$$

We might plot, for example, the function $1/\bar{i}(s)s^{1/2}$ vs. $s^{1/2}$. The slope and intercept of the resulting linear function would provide k_f and H. In doing this, we have elected to analyze the system in the s domain, rather than the time domain.

To implement such a plan, we must be able to obtain the function $\bar{i}(s)$ from the measured curve $i(t)$. That can be done by considering the definition of the Laplace transformation (Section A.1):

$$\bar{i}(s) = \int_0^\infty i(t) e^{-st} dt \tag{10.9.3}$$

In a practical situation, $i(t)$ is usually a collection of data points. Thus, $\bar{i}(s)$ is calculated for a given value of s by multiplying each point by e^{-st} and then performing a numeric integration of the resulting curve. Algorithms for carrying out this task on a computer have been published (42). The whole process is repeated for each desired s value, and the final result is a new collection of data points describing $\bar{i}(s)$, just as the original data described $i(t)$. Since s has dimensions of frequency, $\bar{i}(s)$ is sometimes called a representation of the current in the frequency domain.

Many applications of this strategy are based on extensions of the concepts of impedance developed earlier in this chapter (41–43). However, the excitation waveform is usually an impulse in potential (rather than a periodic perturbation), and a transient current is measured. One records both $E(t)$ and $i(t)$ as observed functions. Then both are subjected to transformations, and comparisons are made in the frequency domain between $\bar{E}(s)$ and $\bar{i}(s)$. Ratios of the form $\bar{i}(s)/\bar{E}(s)$ are *transient impedances*, which can be interpreted in terms of equivalent circuits in exactly the fashion we have come to understand. The advantages of this approach are (a) that the analysis of data is often simpler in the frequency domain, (b) that the multiplex advantage applies, and (c) the waveform $E(t)$ does not have to be ideal or even precisely predictable. The last point is especially useful in high-frequency regions, where potentiostat response is far from perfect. Laplace domain analyses have been carried out for frequency components above 10 MHz.

In general, it is useful to regard s as a complex number $s = \sigma + j\omega$ in these analyses (41, 42). Then one can calculate real-axis and imaginary-axis frequency domain representations of a function. For example, the *real-axis transform* of $E(t)$ is

$$\boxed{\bar{E}(\sigma) = \int_0^\infty E(t) e^{-\sigma t} dt} \tag{10.9.4}$$

and the *imaginary-axis transform* is

$$\boxed{\bar{E}(j\omega) = \int_0^\infty E(t) e^{-j\omega t} dt = \int_0^\infty E(t) \cos \omega t \, dt - j \int_0^\infty E(t) \sin \omega t \, dt} \tag{10.9.5}$$

Note that the real-axis transform of any function is strictly real, but the imaginary-axis transform is complex. It has both real and imaginary components. Since one can transform experimental potential and current transients in this way, one can calculate a *real-axis transient impedance*, $Z(\sigma) = \bar{i}(\sigma)/\bar{E}(\sigma)$, and an *imaginary-axis transient impedance*, $Z(j\omega) = \bar{i}(j\omega)/\bar{E}(j\omega)$. Since $Z(j\omega)$ is complex, we can break it into real and imaginary components $Z(j\omega)_{Re}$ and $Z(j\omega)_{Im}$. One can easily show that $Z(j\omega)$ is the same as the conventional

impedance (comprising resistances and reactances) that we have already discussed. These various functions are useful for the analysis of electrical response in terms of equivalent circuits. In general, all of the various transform functions contain the same chemical information; however, one of them may be more readily applied to data analysis. Since this treatment involves a complex s domain, it is often called *Laplace plane analysis*.

Consider as an example, a double-layer capacitance C_d in series with an uncompensated solution resistance R_u. The overall system obeys

$$E(t) = i(t) R_u + \frac{1}{C_d} \int_0^t i(t)\, dt \tag{10.9.6}$$

or, in the frequency domain,

$$\overline{E}(s) = \overline{i}(s)\left(R_u + \frac{1}{C_d s} \right) \tag{10.9.7}$$

Thus the various impedances are[14]

$$Z(\sigma) = R_u + \frac{1}{C_d \sigma} \tag{10.9.8}$$

$$Z(j\omega)_{Re} = R_u \qquad Z(j\omega)_{Im} = \frac{1}{\omega C_d} \tag{10.9.9}$$

and the phase angle ϕ, defined by the real and imaginary components of $Z(j\omega)$, is given by

$$\tan \phi = \frac{1}{\omega R_u C_d} \tag{10.9.10}$$

Thus we have four simple frequency domain relationships that allow the evaluation of R_u and C_d. It is probably most convenient to use $Z(\sigma)$ for that purpose, but the availability of the other functions is useful for cross-checking the validity of one's equivalent circuit as a model for any given chemical system.

An interesting application of Laplace plane analysis comes from the work by Pilla and Margules on ionic transport through biological membranes (43). Their experimental arrangement involved the use of the membrane as a separator between two solutions containing separate electrodes. A small voltage pulse was applied across the membrane and the transient current was measured. Transformation of the voltage and current functions allowed the calculation of the impedances described above.

The equivalent circuits used in the analysis are shown in Figure 10.9.1. The elements correspond to solution resistance, interfacial capacitances, and impedances associated with the transport of ions through the membrane and across the boundary between the solution and the membrane.

Figure 10.9.2 is an illustration of the behavior of $Z(\sigma)$ at high frequencies in an actual system (43). At these frequencies, both of the circuits in Figure 10.9.1 look essentially like a series combination of C_d and R_e, because the impedance of C_d would be much lower than the impedances of the parallel arms involving resistances. Thus $Z(\sigma)$ should adhere to (10.9.8), where R_u is the same as R_e for this example. The intercept and the slope of Figure 10.9.2 therefore allow a determination of R_e and C_d.

Data at lower frequencies contain information about the arms parallel to C_d, but extracting it requires correction for the effects of R_e and C_d. This is accomplished in Figure 10.9.3. The basis for that analysis is left as an exercise in Problem 10.10.

[14]See the footnote concerning the definition of impedance in (10.1.11).
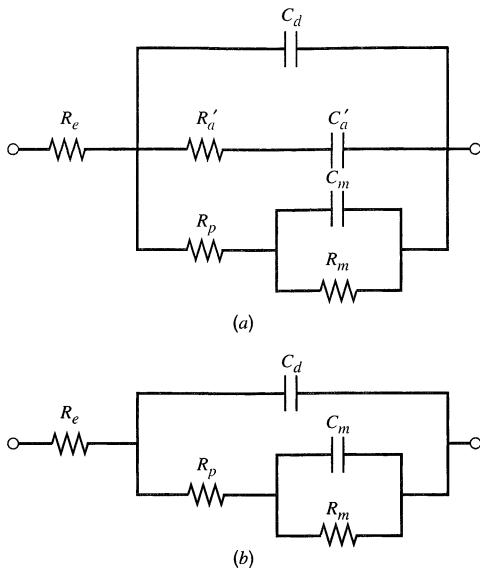
Figure 10.9.1 Equivalent circuits used to analyze the transient behavior of the toad urinary bladder membrane. R_e represents electrolyte resistance and C_d is the dielectric capacitance of the membrane. The branches involving R_p, C_m, and R_m are used to account for the transfer of charge across the membrane boundaries. They are analogous to R_{ct} and Z_w in electrode reactions. In circuit A, R'_a and C'_a model the effects of adsorption. [From A. A. Pilla and G. S. Margules, *J. Electrochem. Soc.*, **124**, 1697 (1977), reprinted by permission of the publisher, The Electrochemical Society, Inc.]
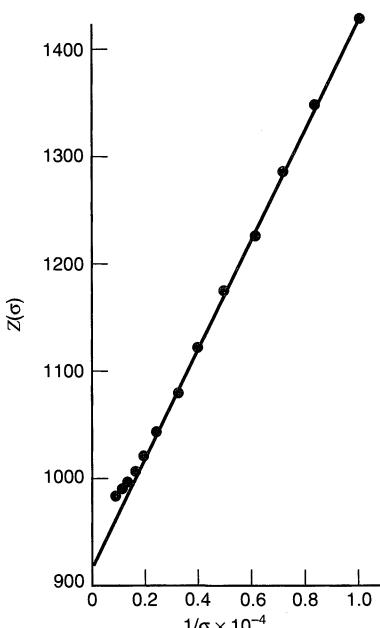
Figure 10.9.2 High-frequency plot of $Z(\sigma)$ vs. $1/\sigma$ for the toad urinary bladder membrane. [From A. A. Pilla and G. S. Margules, *J. Electrochem. Soc.*, **124**, 1697 (1977), reprinted by permission of the publisher, The Electrochemical Society, Inc.]
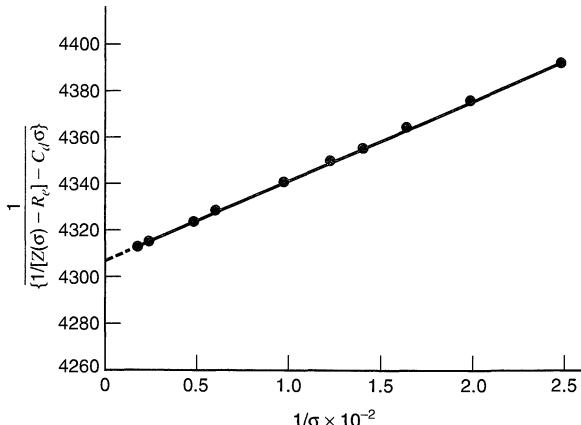
Figure 10.9.3 Intermediate-frequency plot of real-axis impedance data for the toad urinary bladder membrane. [From A. A. Pilla and G. S. Margules, *J. Electrochem. Soc.*, **124**, 1697 (1977), reprinted by permission of the publisher, The Electrochemical Society, Inc.]

▷ 10.10 REFERENCES

1. P. Delahay, "New Instrumental Methods in Electrochemistry," Wiley-Interscience, New York, 1954, Chap. 7.

2. B. Breyer and H. H. Bauer, "Alternating Current Polarography and Tensammetry," Vol. 13 in the series "Chemical Analysis," P. J. Elving and I. M. Kolthoff, Eds., Wiley-Interscience, New York, 1963.

3. D. E. Smith, *Electroanal. Chem.*, **1**, 1 (1966).

4. M. Sluyters-Rehbach and J. H. Sluyters, *Electroanal. Chem.*, **4**, 1 (1970).

5. D. E. Smith, *Crit. Rev. Anal. Chem.*, **2**, 247 (1971).

6. D. D. Macdonald, 'Transient Techniques in Electrochemistry," Plenum, New York, 1977.

7. A. M. Bond, "Modern Polarographic Methods in Analytical Chemistry," Marcel Dekker, New York, 1980.

8. C. Gabrielli, "Identification of Electrochemical Processes by Frequency Response Analysis," Solartron Instrument Group, Solarton-Schlumberger, Farnborough, Hampshire, England, Ref. 004/83, 1980.

9. F. Mansfeld and W. J. Lorenz in "Techniques for Characterization of Electrodes and Electrochemical Processes," R. Varma and J. R. Selman, Eds., Wiley, New York, 1991, Chap. 12.

10. D. D. Macdonald in " Techniques for Characterization of Electrodes and Electrochemical Processes," R. Varma and J. R. Selman, Eds., Wiley, New York, 1991, Chap. 11.

11. C. Gabrielli in "Physical Electrochemistry," I. Rubinstein, Ed., Marcel Dekker, New York, 1995, Chap. 6.

12. A. Lasia, *Mod. Asp. Electrochem.*, **32** (1999), Chap. 2.

13. (a) J. E. B. Randles, *Disc. Faraday Soc.*, **1**, 11 (1947); (b) D. C. Grahame, *J. Electrochem. Soc.*, **99**, C370 (1952).

14. (a) L. Pospisil and R. de Levie, *J. Electroanal. Chem.*, **22**, 227 (1969); (b) H. Moreira and R. de Levie, *ibid.*, **29**, 353 (1971); **35**, 103 (1972).

15. (a) D. C. Grahame, *J. Am. Chem. Soc.*, **68**, 301 (1946); (b) G. C. Barker, *J. Electroanal. Chem.*, **12**, 495 (1966).

16. R. D. Armstrong, M. F. Bell, and A. A. Metcalfe, in "Electrochemistry" (A Specialist Periodical Report), Vol. 6, H. R. Thirsk, Senior Reporter, The Chemical Society, London, 1978.

17. H. Kojima and A. J. Bard, *J. Electroanal. Chem.*, **63**, 117 (1975).

18. H. Kojima and A. J. Bard, *J. Am. Chem. Soc.*, **97**, 6317 (1975).

19. R. de Levie, *Ann. Biomed. Eng.*, **20**, 337 (1992).

20. C. Gabrielli, Ed., "Proceedings of the First International Symposium on Electrochemical Impedance Spectroscopy," *Electrochim. Acta*, **35** (10) (1990).

21. D. D. Macdonald, Ed., "Proceedings of the Second International Symposium on Electrochemical Impedance Spectroscopy," *Electrochim. Acta*, **38** (14) (1993).

22. J. Vareecken, Ed., "Proceedings of the Third International Symposium on Electrochemical Impedance Spectroscopy," *Electrochim. Acta*, **41** (7/8) (1996).

23. B. Timmer, M. Sluyters-Rehbach, and J. H. Sluyters, *J. Electroanal. Chem.*, **14**, 169, 181 (1967).

24. D. E. Smith, and T. G. McCord, *Anal. Chem.*, **40**, 474 (1968).

25. D. E. Smith, *Anal. Chem.*, **35**, 610 (1963).

26. A. M. Bond, R. J. O'Halloran, I. Ruzic, and D. E. Smith, *Anal. Chem.*, **48**, 872 (1976).

27. A. M. Bond, R. J. O'Halloran, I. Ruzic, and D. E. Smith, *Anal. Chem.*, **50**, 216 (1978).

28. W. L. Underkofler and I. Shain, *Anal. Chem.*, **37**, 218 (1965).

29. A. M. Bond, *J. Electroanal. Chem.*, **50**, 285 (1974).

30. C. P. Andrieux, P. Hapiot, J. Pinson, and J.-M. Savéant, *J. Am. Chem. Soc.*, **115**, 7783 (1993).

31. H. Blutstein, A. M. Bond, and A. Norris, *Anal. Chem.*, **46**, 1754 (1974).

32. A. M. Bond, *Anal. Chem.*, **45**, 2026 (1973).

33. H. Kojima and S. Fujiwara, *Bull. Chem. Soc. Jpn.*, **44**, 2158 (1971).

34. S. C. Creason, J. W. Hayes, and D. E. Smith, *J. Electroanal. Chem.*, **47**, 9 (1973).

35. D. E. Glover and D. E. Smith, *Anal. Chem.*, **45**, 1869 (1973).

36. D. E. Smith, *Anal. Chem.*, **48**, 221A, 517A (1976).

37. J. Házì, D. M. Elton, W. A. Czerwinski, J. Schiewe, V. A. Vincente-Beckett, and A. M. Bond, *J. Electroanal. Chem.*, **437**, 1 (1997).

38. J. W. Hayes, D. E. Glover, D. E. Smith, and M. W. Overton, *Anal. Chem.*, **45**, 277 (1973).

39. M. D. Wijnen, *Rec. Trav. Chim.*, **79**, 1203 (1960).

40. E. Levart and E. Poirier d'Ange d'Orsay, *J. Electroanal. Chem.*, **19**, 335 (1968).

41. A. A. Pilla, *J. Electrochem. Soc.*, **117**, 467 (1970).

42. A. A. Pilla in "Computers in Chemistry and Instrumentation," Vol. 2, "Electrochemistry," J. S. Mattson, H. B. Mark, Jr., and H. C. MacDonald, Eds., Marcel Dekker, New York, 1972.

43. A. A. Pilla and G. S. Margules, *J. Electrochem. Soc.*, **124**, 1697 (1977).

▷ 10.11 PROBLEMS

10.1 Derive equation 10.5.13, describing the shape of a reversible polarographic wave, from equation 10.5.11.

10.2 Derive formulas for converting a parallel resistance-capacitance network (R_p and C_p in parallel) to a series equivalent (R_s and C_s in series).

10.3 The faradaic impedance is sometimes represented as a resistance and a capacitance in parallel rather than in series. Find the expressions for the components of the parallel representation of this impedance in terms of R_{ct}, β_O, β_R, and ω. [*Hint.* Use known expressions for series elements and equations for series-to-parallel circuit conversion (Problem 10.2).]

10.4 The faradaic impedance method is employed to study the reaction $O + e \rightleftarrows R$ by imposing a small sinusoidal signal (5 mV) to the cell, and measuring the equivalent series resistance R_B and capacitance C_B of the cell. The following data are obtained for $C_O^* = C_R^* = 1.00$ mM, $T = 25°C$, and $A = 1$ cm^2:

Frequency ($\omega/2\pi$) (Hz)	R_B (Ω)	C_B (μF)
49	146.1	290.8
100	121.6	158.6
400	63.3	41.4
900	30.2	25.6

In a separate experiment under exactly the same conditions, but in the absence of the electroactive species, the cell resistance R_Ω is found to be 10 Ω, and the double-layer capacity of the electrode C_d is found to be 20.0 μF. (a) From these data calculate at each frequency R_s and C_s and the phase angle ϕ between the components of the faradaic impedance. (b) Calculate i_0 and k^0 for the reaction, and estimate D (assuming $D_O = D_R$).

10.5 Derive (10.4.5) and (10.4.6) from (10.4.3) and (10.4.4).

10.6 Derive (10.4.11) from (10.4.9) and (10.4.10).

10.7 From the data in Figures 10.5.4 and 10.5.5, evaluate α and k^0 for the reduction of Ti(IV) to Ti(III) at a DME in oxalic acid solution. From other experiments, we know that $n = 1$ and $D_O = 6.6 \times 10^{-6}$ cm^2/s. Assume $D_O = D_R$.

10.8 The reduction of nitrobenzene to its radical anion in N,N-dimethylformamide is reported to occur with $k^0 = 2.2 \pm 0.3$ cm/s (see reference 18). The value of D_O is given as 1.02×10^{-5} cm^2/s at $22 \pm 2°$C, where k^0 was evaluated. The transfer coefficient, α, is 0.70. Calculate the phase angles expected for $\omega/2\pi = 10, 100, 1000,$ and 10,000 Hz. Draw the corresponding plot of cot ϕ vs. $\omega^{1/2}$ for $E = E_{1/2}$. Describe a means for obtaining cot ϕ from the in-phase and quadrature phase-selective polarograms, and comment on the frequency range where it might be experimentally feasible to obtain cot ϕ values sufficiently precise to allow a determination of k^0 for the system at hand.

10.9 Devise and justify an equivalent circuit for a system in which O and R are bound to the surface of the electrode as the result of a chemical modification. Follow the steps in Sections 10.2 and 10.3 to evaluate the expected frequency dependence of the faradaic impedance for the case in which the electrode reaction is nernstian. What phase angle is expected?

10.10 Derive the equation underlying Figure 10.9.3. First show how the quantity plotted on the ordinate can be regarded as $Z(\sigma)$ corrected for the effects of R_e and C_d. Then derive the expression for $Z(\sigma)$ for the remaining elements of circuit (b) in Figure 10.9.1. Consider the behavior at low and intermediate frequencies with respect to Figure 10.9.3.

10.11 Plot the amplitude and phase arrays [analogous to segments (a) and (b) of Figure 10.8.3] for generating a complex waveform having components at 100, 200, 300, ... Hz, all with phase angles equal to $\pi/2$. Let these arrays have 128 elements, with the zeroth element representing the dc level and the 127th element representing $\omega/2\pi = 1270$ Hz. What disadvantages would the waveform resulting from your arrays have with respect to that generated in Figure 10.8.3? Would your waveform have any advantages?

11

BULK ELECTROLYSIS METHODS

The methods described in Chapters 5 to 10 generally employ conditions featuring a small ratio of electrode area, A, to solution volume, V. These allow the experiments to be carried out over fairly long time periods without appreciable changes of the concentrations of the reactant and the products in the bulk solution, and they allow the semi-infinite boundary condition (e.g., $C_O(x, t) = C_O^*$ as $x \to \infty$) to be maintained over repeated trials. For example, consider a 5×10^{-3} M solution of O with $V = 100$ cm^3 and $A = 0.1$ cm^2. Assume that during 1 hour of experimentation an average current of about 100 μA flows (i.e., current density, j, of 1 mA cm^{-2}). During this time period only 0.36 C of electricity will be passed, and the bulk concentration of electroactive species will have decreased by less than 1%.

There are circumstances, however, where one desires to alter the composition of the bulk solution appreciably by electrolysis; these include analytical measurements (e.g., electrogravimetric or coulometric methods), techniques for removal or separation of solution components, and electrosynthetic methods. These *bulk* (or *exhaustive*) *electrolysis* methods are characterized by large A/V conditions and as effective mass-transfer conditions as possible. Thus, if all of the conditions of the previous example hold, except that the electrode area is 100 cm^2 (so that the total current is 0.1 A, assuming the same $j = 1$ mA cm^{-2}), the electroactive species can be completely electrolyzed in less than 10 minutes (assuming $n = 1$ and the occurrence of only a single electrode process, that is, 100% current efficiency; see Section 11.2.2). Although bulk electrolytic methods are generally characterized by large currents and experimental time scales on the order of minutes and hours, the basic principles governing electrode reactions described in the previous chapters still apply.

▷ 11.1 CLASSIFICATION OF TECHNIQUES

The methods can be classified by the controlled parameter (E or i) and by the quantities actually measured or the process carried out. Thus in *controlled-potential* techniques the potential of the working electrode is maintained constant with respect to a reference electrode. Since the potential of the working electrode controls the degree of completion of an electrolytic process in most cases, controlled-potential techniques are usually the most desirable for bulk electrolysis. However, these methods require potentiostats with large output current and voltage capabilities and they need stable reference electrodes, carefully placed to minimize uncompensated resistance effects. Placement of the auxiliary electrode to provide a fairly uniform current distribution across the surface of the working electrode is usually desirable, and the auxiliary electrode is often placed in a separate

compartment isolated from the working-electrode compartment by a sintered-glass disk, ion-exchange membrane, or other separator.

In *controlled-current* techniques, the current passing through the cell is held constant (or is sometimes programmed to change with time or in response to some indicator electrode signal). Although these techniques frequently involve simpler instrumentation than controlled-potential methods, they require either a special set of chemical conditions in the cell or specific detection methods to signal completion of the electrolysis and to ensure 100% current efficiency. For preparative electrolysis (or *electrosynthesis*), constant-current methods can sometimes be used, as long as measures are taken to ensure that the electrode potential does not move into a region where undesirable side reactions occur.

The general considerations and models employed in electroanalytical bulk electrolysis methods are also often applicable to large-scale and flow electrosynthesis, to galvanic cells, batteries, and fuel cells, and to electroplating.

Bulk electrolysis methods are also classified according to purpose. For example, one form of analysis involves determination of the weight of a deposit on the electrode (*electrogravimetry*). In this case 100% current efficiency is not required, but the substance of interest must be deposited in a pure, known form. In *coulometry*, the total quantity of electricity required to carry out an exhaustive electrolysis is determined. The quantity of material or number of electrons involved in the electrode reaction can then be determined by Faraday's laws, if the reaction occurred with 100% current efficiency. For *electroseparations*, electrolysis is used to remove, selectively, constituents from the solution.

Several related bulk electrolysis techniques should be mentioned. In *thin-layer electrochemical methods* (Section 11.7) large A/V ratios are attained by trapping only a very small volume of solution in a thin (20–100 μm) layer against the working electrode. The current level and time scale in these techniques are similar to those in voltammetric methods. *Flow electrolysis* (Section 11.6), in which a solution is exhaustively electrolyzed as it flows through a cell, can also be classified as a bulk electrolysis method. Finally there is *stripping analysis* (Section 11.8), where bulk electrolysis is used to preconcentrate a material in a small volume or on the surface of an electrode, before a voltammetric analysis. We also deal in this chapter with detector cells for liquid chromatography and other flow techniques. While these cells do not usually operate in a bulk electrolysis mode, they are often thin-layer flow cells that are related to the other cells described.

General treatments of bulk electrolysis techniques, as well as numerous examples of their application to analysis and separations, are contained in references 1–4.

▶ 11.2 GENERAL CONSIDERATIONS IN BULK ELECTROLYSIS

11.2.1 Extent or Completeness of an Electrode Process

The extent or degree of completion of a bulk electrolytic process can be predicted for nernstian reactions from the applied electrode potential and a suitable form of the Nernst equation.

(a) Both Forms Soluble in Solution
Consider the overall reduction reaction

$$O + ne \rightleftarrows R \tag{11.2.1}$$

$$E = E^{0'} + \left(\frac{RT}{nF}\right)\ln\left(\frac{C_O}{C_R}\right) \tag{11.2.2}$$

where both O and R are soluble and R is initially absent. Let C_i be the initial concentration of O, V_s be the volume of the solution, and x be the fraction of O reduced to R at the electrode potential, E. Then

$$\text{moles O at equilibrium} = V_s C_i (1 - x) \tag{11.2.3}$$

$$\text{moles R at equilibrium} = V_s C_i x \tag{11.2.4}$$

and (11.2.2) to (11.2.4) yield

$$E = E^{0'} + \left(\frac{RT}{nF}\right) \ln\left[\frac{(1 - x)}{x}\right] \tag{11.2.5}$$

or

$$\text{fraction of O reduced} = x = \{1 + 10^{[(E-E^{0'})n/0.059]}\}^{-1} \ (\text{at } 25°C) \tag{11.2.6}$$

For example, for 99% completeness of reduction of O to R (i.e., $x = 0.99$) the potential of the working electrode should be

$$E = E^{0'} + \frac{0.059}{n} \log\left(\frac{0.01}{0.99}\right) \approx E^{0'} - \frac{(0.059)(2)}{n} \tag{11.2.7}$$

or $118/n$ mV more negative than $E^{0'}$ at 25°C.

(b) Deposition as an Amalgam
Consider the reaction

$$O + ne \underset{}{\overset{\text{Hg}}{\rightleftarrows}} R(\text{Hg}) \tag{11.2.8}$$

where R(Hg) represents an amalgam of R, that is, R dissolved in a mercury electrode of volume, V_{Hg}, the situation is similar to that where both forms are soluble in solution, except that $E_a^{0'}$, the formal potential for the reaction in (11.2.8), replaces $E^{0'}$, and C_R represents the concentration of R in the mercury electrode (assumed to be below the saturation value). This results in the equation:

$$E = E_a^{0'} + \frac{RT}{nF} \ln\left[\frac{(V_s C_i (1 - x)/V_s)}{(V_s C_i x/V_{\text{Hg}})}\right] \tag{11.2.9}$$

$$E = E_a^{0'} + \frac{RT}{nF} \ln\left(\frac{V_{\text{Hg}}}{V_s}\right) + \frac{RT}{nF} \ln \frac{1 - x}{x} \tag{11.2.10}$$

(c) Deposition of a Solid
For the reaction

$$O + ne \rightleftarrows R \ (\text{solid}) \tag{11.2.11}$$

when more than a monolayer of R is deposited on an inert electrode (e.g., copper on a platinum electrode) or the deposition is carried out on an electrode made of R (e.g., copper on a copper electrode), the activity of R, a_R, is constant and equal to unity. Thus the Nernst equation yields

$$E = E^0 + \frac{RT}{nF} \ln[\gamma_O C_i (1 - x)] \tag{11.2.12}$$

where γ_O is the activity coefficient of species O. When less than a monolayer of R is deposited on an inert substrate, $a_R \neq 1$, and an expression for a_R as a function of coverage by R must be used in the Nernst equation. It is sometimes assumed (5) that a_R is proportional to the fraction, θ, of the electrode surface covered with R. Thus, for example,

$$a_R \approx \gamma_R \theta = \gamma_R \frac{A_R}{A} = \frac{\gamma_R N_R A_a}{A} \tag{11.2.13}$$

where A is the electrode area, A_R is the area occupied by R, A_a is the cross-sectional area of a molecule of R, and N_R is the number of molecules of R deposited on the electrode. At equilibrium, N_R is given by

$$N_R = V_s C_i x N_A \tag{11.2.14}$$

where N_A is Avogadro's number. This then yields, when combined with (11.2.13) and the Nernst equation,

$$E = E^0 + \frac{RT}{nF} \ln \left(\frac{\gamma_O A}{\gamma_R V_s N_A A_a} \right) + \frac{RT}{nF} \ln \left(\frac{1-x}{x} \right) \tag{11.2.15}$$

Thus, within this very simplified model, the shape of the deposition curve follows that of the case of soluble components or an amalgam [(11.2.5) or (11.2.10)], even though a solid is deposited (Figure 11.2.1).

The deposition begins at potentials more positive than values where deposition of R occurs on bulk R. Consider, for example, the deposition of Ag on a 1-cm^2 Pt electrode from a 0.01-L solution containing 10^{-7} M Ag$^+$. Let $A_a = 1.6 \times 10^{-16}$ cm^2 and $\gamma_O = \gamma_R$. The potential for deposition of one-half of the silver (which forms about 0.05 monolayer) is $E = 0.35$ V, compared to $E = 0.43$ V required for the same amount of deposition on a silver electrode. Deposition at potentials before that predicted by the Nernst equation with $a_R = 1$ is called *underpotential deposition*. The situation is much more complicated than the above treatment suggests, since the deposition potential depends on the nature of the substrate (material and pretreatment) and on adsorption of O. Also, the treatment assumes that formation of a second layer does not start until the first is complete. However, this is frequently not the case; atoms of metal will often aggregate, rather than deposit on a foreign surface, and dendrites will form. Reviews on the nature of underpotential deposition and the deposition of solids in general are available (6–10).
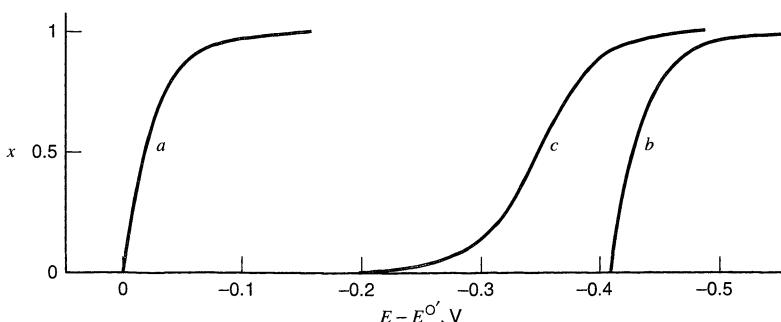
Figure 11.2.1 Fraction of a metal M$^+$ (e.g., Ag$^+$) deposited (x) as a function of potential. *Curve a*: 1 M Ag$^+$ on Ag. *Curve b*: 10^{-7} M Ag$^+$ on Ag. *Curve c*: 10^{-7} M Ag$^+$ on Pt, according to (11.2.15).

For slow electron-transfer (irreversible) processes, the eventual extent of the electrode process will be governed by equilibrium considerations and the Nernst equation, but the rate of electrolysis will be small at the potentials predicted in the previous sections and long-duration electrolyses would result. For these processes, reduction must be carried out at somewhat more negative potentials; the actual potential is usually selected on the basis of experimental current-potential curves taken under conditions near those for the intended bulk electrolysis. Processes that are controlled by the rate of a homogeneous reaction, such as

$$A \xrightarrow{k} O \qquad O + ne \rightleftharpoons R \tag{11.2.16}$$

may be slow and independent of the potential chosen. In that case, the potential is selected for complete conversion of O to R, and other steps are taken, for example, an increase in temperature or addition of a catalyst, to increase the rate of the preceding reaction. Catalysts (or *mediators*) are sometimes added to carry out electrolyses of substances that themselves undergo very slow electron-transfer rates at the electrode but react rapidly with the mediator. For example, many enzymes, (e.g., cytochromes) are reduced very slowly at an electrode. The addition of a mediator, such as methyl viologen, which is reduced reversibly at an electrode and whose reduced form reacts rapidly with the enzyme, can enable the reduction (11, 12). This strategy, which is related to the coulometric titration technique (see Section 11.4.2), can also be used with other irreversible electrode reactions.

11.2.2 Current Efficiency

When two or more faradaic reactions can occur simultaneously at an electrode, the fraction of the total current (i_{total}) going to the rth process is called the *instantaneous current efficiency*:

$$\text{Instantaneous current efficiency for } r\text{th process} = i_r/i_{total} \tag{11.2.17}$$

A current efficiency of unity (or 100%) implies that only one process is occurring at an electrode. When one considers the result of an electrolysis over some period of time, the *overall current efficiency* represents the fraction of the total charge involved in the rth process:

$$\text{Overall current efficiency for } r\text{th process} = Q_r/Q_{total} \tag{11.2.18}$$

It is generally desirable for bulk electrolytic processes to be carried out with high current efficiency. This requires that the working electrode potential and other conditions be chosen so that no side reactions occur (e.g., reduction or oxidation of solvent, supporting electrolyte, electrode material, or impurities). In electrogravimetric methods, 100% current efficiency is usually not necessary, as long as the side reactions do not produce insoluble products. In coulometric titrations at constant current, 100% *titration efficiency* (rather than current efficiency) is required; the distinction is discussed in Section 11.4.2.

11.2.3 Electrolysis Cells

Bulk electrolysis techniques, because of the longer duration of the experiments and the larger currents involved, usually present more problems in cell design than transient experiments. Typical bulk electrolysis cells are shown in Figure 11.2.2.
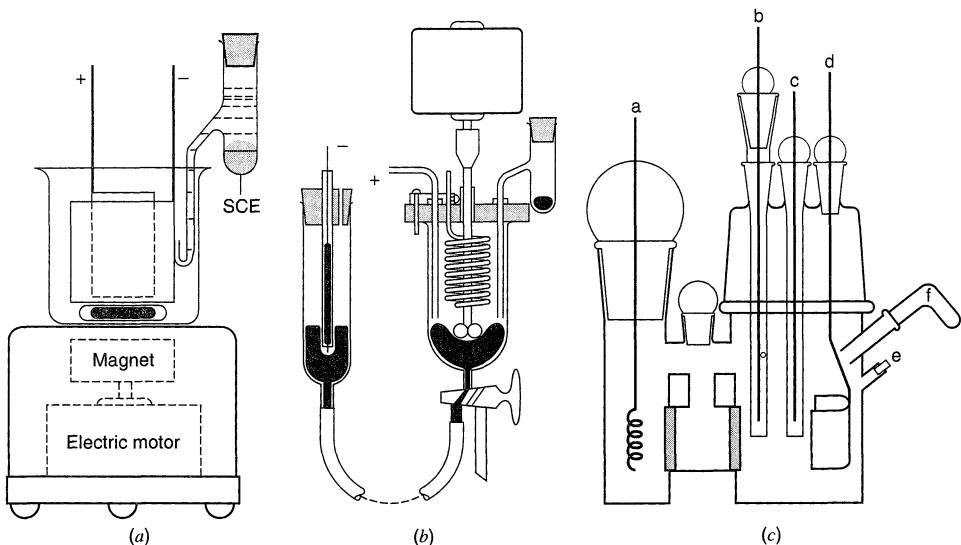
Figure 11.2.2 Typical cells for bulk electrolysis. (*a*) Undivided cell for controlled-potential separations and electrogravimetric analysis at a solid cathode. [From J. J. Lingane, *Anal Chim. Acta*, **2**, 584 (1948), with permission.] (*b*) Undivided cell for coulometric analysis at mercury cathode with a silver anode. [Reprinted with permission from J. J. Lingane, *J. Am. Chem. Soc.*, **67**, 1916 (1945). Copyright 1945, American Chemical Society.] (*c*) Three-compartment cell, with ground-glass joints, for coulometric and voltammetric studies on a vacuum line. (*a*) Platinum wire auxiliary electrode; (*b*) silver wire reference electrode in separate compartment; (*c*) gold voltammetric working microelectrode; (*d*) platinum foil coulometric working electrode; (*e*) silicone rubber septum for sample injection; (*f*) rotatable side arm for solid sample addition. Arm and joint for attachment of cell to the vacuum line are not shown. [Reprinted with permission from W. H. Smith and A. J. Bard, *J. Am. Chem. Soc.*, **97**, 5203 (1975). Copyright 1975, American Chemical Society.]

(a) Electrodes and Geometry

Solid electrodes usually are wire gauzes or foil cylinders, although packed beds of powders, slurries, or fluidized beds are sometimes used. The aim is to have as large a working electrode area as possible. Mercury electrodes generally take the form of pools.

Auxiliary electrode placement is not usually a problem with small electrodes and low currents, as in voltammetric experiments, but it is of critical importance in bulk electrolysis cells. With large electrodes and an asymmetrically placed auxiliary electrode, the solution resistance is different between the auxiliary and different parts of the working electrode. The varying iR drops along the different current paths produce a nonuniform potential across the working electrode surface, as shown in Figure 11.2.3, and as a consequence there is a nonuniform current density on the working electrode surface. These effects can cause undesired side reactions or ineffective use of the total electrode area.

The proper placement of the tip of the reference electrode salt bridge is also important. In general, it should be located at the position of highest current density directly under the auxiliary electrode compartment. Good potential control is often difficult in bulk electrolysis cells because the fluctuations in the large currents result in large changes in the uncompensated resistive drop. The long term stability of the reference electrode potential is also important (see also Section 15.6).
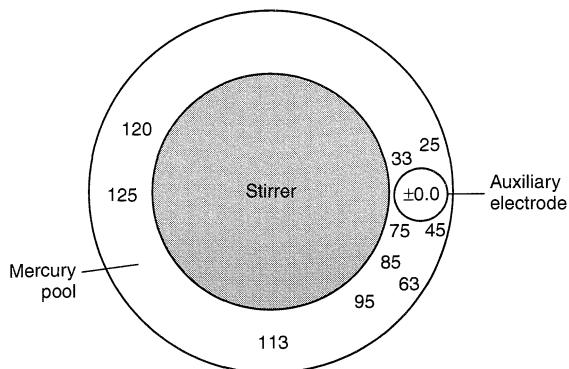
Figure 11.2.3 Potential distribution in mV at surface of ring-shaped mercury pool electrode using an unsymmetrical auxiliary electrode. Solution: 0.5 M H_2SO_4; total cell current: 40 mA; pool: 1.5 in. o.d., 1.0 in. i.d. Small circle shows position of the auxiliary electrode's fritted-glass separator, situated 4 mm above the pool surface. [Reprinted with permission from G. L. Booman and W. B. Holbrook, *Anal. Chem.*, **35**, 1793 (1963). Copyright 1963, American Chemical Society.]

(b) Separators

Because soluble products of the electrode reaction at the auxiliary electrode may be reactive at the working electrode, the two electrodes are usually placed in separate compartments. These compartments can be separated by sintered (or fritted) glass disks or ion-exchange membranes (or, less frequently, filter paper, asbestos mats, or porous ceramics). Choosing a separator that does not allow intermixing of *anolyte* and *catholyte* and also does not contribute appreciably to the cell resistance is often of major importance. Separator design is often critical in the fabrication of galvanic cells and batteries. Sometimes the judicious choice of the auxiliary electrode reaction, for example, when solid products or innocuous gaseous products are formed, allows cells without separators to be used. Examples of these are the use of silver anodes in halide media (e.g., $Ag + Cl^- \rightleftarrows AgCl + e$) or hydrazine as an "anodic depolarizer" at platinum anodes ($N_2H_4 \rightarrow N_2 + 2H^+ + 2e$).

(c) Cell Resistance

High cell resistances are very deleterious in experiments involving high currents, because large values of i^2R mean wasted power, a need for high voltage output of potentiostat or power supply, and undesirable heat evolution. Moreover, in cells with high resistance, it may not be possible to place the reference electrode tip close enough to the working electrode to avoid large uncompensated iR-drops. Cell design for the minimization of cell resistance is especially important when nonaqueous solvents are employed (e.g., acetonitrile, N,N-dimethylformamide, tetrahydrofuran, and ammonia), because they have lower dielectric constants than aqueous media, and hence inherently lower solution conductivities.

▶ 11.3 CONTROLLED-POTENTIAL METHODS

11.3.1 Current-Time Behavior

The current-potential characteristics described for stirred solutions (Section 1.4.2 and Chapter 9) generally apply to these electrolysis conditions as well, except that C_O^*, the bulk concentration, is a function of time, decreasing during the electrolysis. Thus i-E curves taken repeatedly during an electrolysis (assumed to be taken at such a rapid rate that no appreciable change of C_O^* occurs during the potential scan) will show a continuously decreasing i_l as C_O^* decreases (Figure 11.3.1).

Background current
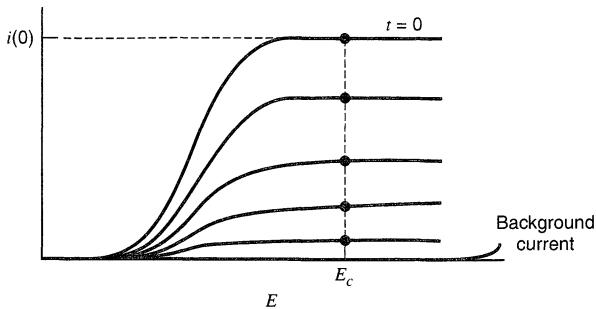
Figure 11.3.1 Current-potential curves at different times during a controlled-potential bulk electrolysis at $E = E_c$.

Consider the electrolysis of O, initially present in bulk solution at a concentration $C_O^*(0)$, by the reaction $O + ne \rightarrow R$, at an electrode of area A held at a potential E_c in the limiting current region. The current at any time is given by (1.4.9):

$$i_l(t) = nFAm_O C_O^*(t) \tag{11.3.1}$$

The current also indicates the total rate of consumption of O, dN_O/dt (mol/s), due to electrolysis (assuming 100% current efficiency):

$$i_l(t) = -nF\left[\frac{dN_O(t)}{dt}\right] \tag{11.3.2}$$

where N_O is the total number of moles of O in the system. If one assumes that the solution is completely homogeneous (i.e., one neglects the small volume of the diffusion layer, $\delta_O A$, in the vicinity of the electrode surface, where C_O is smaller than C_O^*), then

$$C_O^*(t) = \frac{N_O(t)}{V} \tag{11.3.3}$$

where V is the total solution volume. Equations 11.3.2 and 11.3.3 yield

$$i_l(t) = -nFV\left[\frac{dC_O^*(t)}{dt}\right] \tag{11.3.4}$$

Equating the two relations for $i_l(t)$, we obtain

$$\frac{dC_O^*(t)}{dt} = -\left(\frac{m_O A}{V}\right)C_O^*(t) = -pC_O^*(t) \tag{11.3.5}$$

with the initial condition, $C_O^*(t) = C_O^*(0)$ at $t = 0$. Equation 11.3.5 is characteristic of a first-order, homogeneous chemical reaction, where $p = m_O A/V$ is analogous to the first-order rate constant. The solution to this ordinary differential equation is

$$\boxed{C_O^*(t) = C_O^*(0)\exp(-pt)} \tag{11.3.6}$$

and using (11.3.1), we obtain the i-t behavior:

$$\boxed{i(t) = i(0)\exp(-pt)} \tag{11.3.7}$$

where $i(0)$ is the initial current (13). Thus a controlled-potential bulk electrolysis is like a first-order reaction, with the concentration and the current decaying exponentially with time during the electrolysis (Figure 11.3.2) and eventually attaining the background
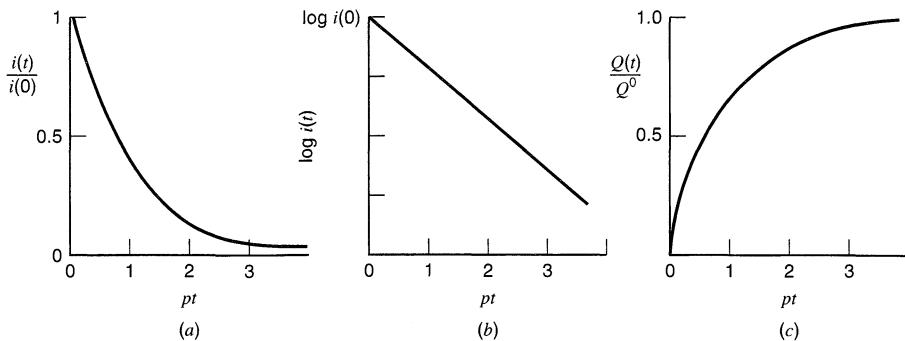
Figure 11.3.2 (*a*) Current-time curve during controlled-potential electrolysis (in dimensionless form). (*b*) log $i(t)$ vs. t. (*c*) Q vs. t.

(residual) current level. Equation 11.3.7 can be used to determine the duration of the electrolysis for a given conversion:

$$\frac{-p}{2.3} t = \log\left[\frac{C_O^*(t)}{C_O^*(0)}\right] = \log\left[\frac{i(t)}{i(0)}\right] \tag{11.3.8}$$

For 99% completion of electrolysis, $C_O^*(t)/C_O^*(0) = 10^{-2}$, and $t = 4.6/p$; for 99.9% completion, $t = 6.9/p$. With effective stirring, $m_O \approx 10^{-2}$ cm/s, so that for $A(\text{cm}^2) \approx V(\text{cm}^3)$, $p \approx 10^{-2}$ s^{-1}, and a 99.9% electrolysis would require ~690 s or ~12 minutes. Typically bulk electrolyses are slower than this, requiring 30 to 60 minutes, although cell designs with very large A/V and very effective stirring (e.g., using ultrasonics) with a p of ~10^{-1} s^{-1} have been described (14). For effective rates of electrolysis, A should be as large as possible and, in many practical devices (e.g., preparative cells or fuel cells and other power sources), porous electrodes and flow systems are employed (see Section 11.6).

The total quantity of electricity $Q(t)$ consumed in the electrolysis is given by the area under the *i-t* curve (Figure 11.3.2*c*):

$$Q(t) = \int_0^t i(t)\, dt \tag{11.3.9}$$

Electrolysis at controlled potential is the most efficient method of carrying out a bulk electrolysis, because the current is always maintained at the maximum value (for given cell conditions) consistent with 100% current efficiency. Note that the rate of electrolysis is independent of $C_O^*(0)$, so that electrolysis of a 0.1 M solution of O and a 10^{-6} M solution of O should require the same amount of time, given the same values of E, A, V, and m_O.

11.3.2 Electrogravimetric Methods

The determination of a metal by selective deposition on an electrode, followed by weighing, is among the oldest of electroanalytical methods [Cruikshank (1801); W. Gibbs (1864)]. In controlled-potential methods, the potential of the solid electrode is adjusted to a value where the desired plating reaction occurs and no interfering reaction leading to the deposition of another insoluble substance takes place.

The sensitivity of an electrogravimetric method is limited by the difficulty in determining the small difference in weight between the electrode itself and the electrode plus

deposit. The technique also requires the washing and drying of the electrode and is, of course, limited to electrode reactions involving the formation of insoluble substances. For these reasons, many electrogravimetric determinations have been supplanted by coulometric ones (see Section 11.3.4), except for situations where 100% current efficiency cannot be attained.

Electrogravimetric determinations also require smooth and adherent metal platings and deposits. The physical characteristics of a deposit depend on the form of the metal ion in the solution, the presence of adsorbable surface-active agents in the solution, and other factors, some not completely understood. The reader is referred to references 15–17 and books on electroplating (18) for a detailed discussion of these factors. Depositions from solutions of complex ions frequently are smoother than those obtained from solutions containing only the aquo-form. For example, brighter deposits are obtained from solutions of Ag^+ in a CN^- medium [containing $Ag(CN)_2^-$] than from a nitrate medium. The addition of surface-active agents ("brighteners"), such as gelatin, often leads to improved deposits. It has been reported that organic additives are sometimes occluded with the metal deposit, leading to positive errors in electrogravimetric analysis. This error is apparently smaller when depositions are carried out under controlled-potential conditions. Hydrogen evolution during deposition also leads to a rougher deposit. Deposits at very large current densities tend to be less adherent and rougher than those obtained at lower ones.

Some metals determined by electrogravimetric methods and their deposition potentials are given in Table 11.3.1. Detailed discussions of the methods and applications of electrogravimetric methods are available (1, 3, 19, 20). Electrogravimetry can also be carried out with the quartz crystal microbalance as described in Section 17.5.

TABLE 11.3.1 Deposition Potentials (V *vs*. SCE) for Various Metals in Different Media at a Platinum Electrode[a]

	Supporting Electrolyte				
Metal	0.2 M H$_2$SO$_4$	0.4 M NaTart + 0.1 M NaHTart	1.2 M NH$_3$ + 0.2 M NH$_4$Cl	0.4 M KCN + 0.2 M KOH	EDTA + NH$_4$OAc[b]
Au	+0.70	(+0.50)[d]	—	−1.00	+0.40
Hg	+0.40	(+0.25)[d]	−0.05	−0.80	+0.30
Ag	+0.40	(+0.30)[b]	−0.05	−0.80	+0.30
Cu	−0.05	−0.30	−0.45	−1.55	−0.60
Bi	−0.08	−0.35	—	(−1.70)[d]	−0.60
Sb	−0.33	−0.75	—	−1.25	−0.70
Sn[c]	—	—	—	—	—
Pb	—	−0.50	—	—	−0.65
Cd	−0.80	−0.90	−0.90	−1.20	−0.65
Zn	—	−1.10	−1.40	−1.50	—
Ni	—	—	−0.90	—	—
Co	—	—	−0.85	—	—

[a]Adapted from table given in reference 3.
[b]5 g NH$_4$OAc + 200 mL H$_2$O (pH ≈ 5); [EDTA]:[metal] = 3:1.
[c]Tin can be deposited from solutions of Sn(II) in HCl or HBr media.
[d]Metal deposits obtained are not suitable for electrogravimetric analysis.

11.3.3 Electroseparations

In an electrochemical separation, the quantitative deposition of one metal (M_1) on a solid or mercury electrode is desired without appreciable deposition of a second metal (M_2). The considerations of Section 11.2.1, concerning the degree of completion of electrolysis as a function of potential, apply. If $E_{a1}^{0'}$ is the formal potential for the n_1-electron reduction and if $V_{Hg} = V_s$, then complete (i.e., $\geq 99.9\%$) deposition of M_1 as an amalgam requires $E \leq E_{a1}^{0'} - 0.18/n_1$ V at 25°C. For $\leq 0.1\%$ deposition of M_2, $E \geq E_{a2}^{0'} + 0.18/n_2$ V. Therefore, the separation between the formal potentials must be at least $0.18 \ (n_1^{-1} + n_2^{-1})$ (Figure 11.3.3). If $|E_{a2}^{0'} - E_{a1}^{0'}|$ is smaller than this, a separation at the 99.9% level cannot be accomplished. In that case changing the supporting electrolyte to one that complexes one or both of the metals will often give an improved separation. The potential range for a successful separation can best be found by determining the i-E curve on a voltammetric electrode under the same conditions (concentrations, supporting electrolyte, temperature) considered for the separation.

Although electrogravimetric analyses are rarely carried out with a mercury electrode, this electrode is often used for electroseparations. Metals that can be deposited at a mercury electrode are shown in Figure 11.3.4.

11.3.4 Coulometric Measurements

In controlled-potential coulometry the total number of coulombs consumed in an electrolysis is used to determine the amount of substance electrolyzed. To enable a coulometric method, the electrode reaction must satisfy the following requirements: (a) it must be of known stoichiometry; (b) it must be a single reaction or at least have no side reactions of different stoichiometry; (c) it must occur with close to 100% current efficiency.

A block diagram of the apparatus used in controlled-potential coulometry is shown in Figure 11.3.5. The potentiostat generally needs an output power capability of 100 W (e.g., 1 A at 100 V or 5 A at 20 V). The current is monitored during the electrolysis, so that the background current can be determined and the completion of electrolysis observed. The shape of the i-t curve can be diagnostic of the mechanism of the electrode reaction or experimental problems. For example, if the final current following electrolysis is constant, but appreciably higher than the preelectrolysis background current of the supporting electrolyte solution alone, a reaction of the electrolysis product may be regenerating starting material or another electroactive substance (see Section 12.7). This symptom can also indicate leakage of material from the auxiliary electrode compartment. If the current at the start of the electrolysis remains constant for some time before showing the usual exponential decay (Figure 11.3.2a), the output current or voltage of the potentiostat is probably in-
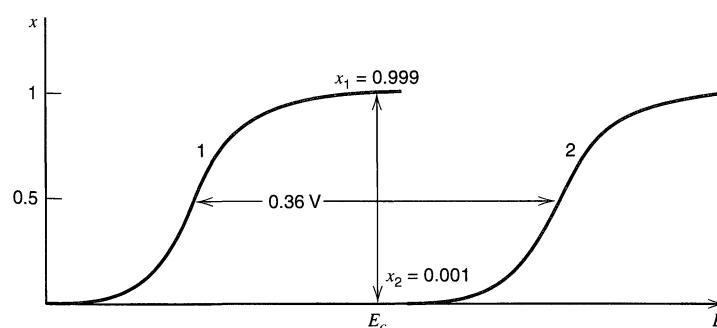
Figure 11.3.3 Conditions for complete separation of metals M_1 and M_2 at a mercury electrode ($n_1 = n_2 = 1$).

Ia	IIa	IIIa	IVa	Va	VIa	VIIa	VIII			1b	IIb	IIIb	IVb	Vb	VIb	VIIb	0
H																	He
Li	Be											B	C	N	O	F	Ne
Na	Mg											Al	Si	P	S	Cl	Ar
K	Ca	Sc	Ti	V	Cr	Mn	Fe	Co	Ni	Cu	Zn	Ga	Ge	As	Se	Br	Kr
Rb	Sr	Y	Zr	Nb	Mo	Tc	Ru	Rh	Pd	Ag	Cd	In	Sn	Sb	Te	I	Xe
Cs	Ba	La^a	Hf	Ta	W	Re	Os	Ir	Pt	Au	Hg	Tl	Pb	Bi	Po	At	Rn
Fr	Ra	Ac^b															

Note: Heavy solid lines enclose elements that can be quantitatively deposited in the mercury cathode. Broken lines enclose elements that are quantitatively separated from the electrolyte, but are not quantitatively deposited in the mercury. Light lines enclose elements that are incompletely separated.
^{a}Also elements 58 to 71 (partial deposition of lanthanum and neodymium has been reported).
^{b}Also elements 90 to 103.

Figure 11.3.4 Metals deposited at a mercury electrode. [Reprinted with permission from J. A. Maxwell and R. P. Graham, *Chem. Rev.*, **46**, 471 (1950). Copyright 1950, American Chemical Society.]

sufficient to maintain the working electrode at the chosen potential, given the electrolysis conditions (electrode area, C_O^*, cell resistance, stirring rate).

Several different types of coulometers are available. Formerly chemical types (gravimetric, titrimetric, and gas) were used. These can be related directly to a chemical primary standard (e.g., the silver coulometer) and are capable of high accuracy and precision. However, they are inconvenient and time-consuming to use and are now rarely employed. Operational amplifier integrator circuits or digital circuits are usually used to determine total charge. These give a direct readout in coulombs (or if desired, in equivalents) and can be employed to record Q-t curves during electrolysis; see, for example, Fig-
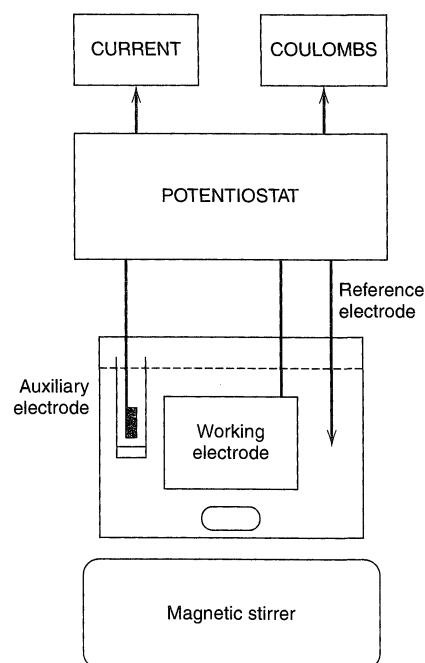
Figure 11.3.5 Block diagram of typical controlled-potential coulometry apparatus.

ure 11.3.2c. The shape of this curve for an uncomplicated electrolysis is immediately obtained from (11.3.7) and (11.3.9):

$$Q(t) = \frac{i(0)}{p}(1 - e^{-pt}) = Q^0(1 - e^{-pt}) \qquad (11.3.10)$$

where Q^0 is the value of Q at the completion of the electrolysis ($t \rightarrow \infty$), and is given by

$$Q^0 = nFN_O = nFVC_O^*(0) \qquad (11.3.11)$$

where N_O represents the total number of moles of O initially present. Equation 11.3.11 is just a statement of Faraday's law and is the basis for any coulometric method of analysis.

There have been numerous applications of controlled-potential coulometry to analysis. Many electrodeposition reactions that are the basis of electrogravimetric determinations can be employed in coulometry as well. However, some electrogravimetric determinations can be used when the electrode reactions occur with less than 100% current efficiency, for example, the plating of tin on a solid electrode. Coulometric determinations can, of course, also be based on electrode reactions in which soluble products or gases are formed (e.g., reduction of Fe(III) to Fe(II), oxidation of I^- to I_2, oxidation of N_2H_4 to N_2, reduction of aromatic nitro compounds). Many reviews concerned with controlled-potential coulometric analysis have appeared (1, 20–22); some typical applications are given in Table 11.3.2.
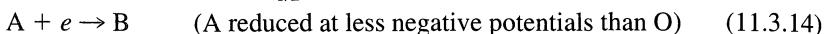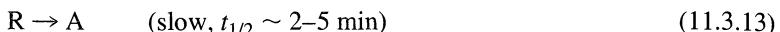
Controlled-potential coulometry is also a useful method for studying the mechanisms of electrode reactions and for determining the n-value for an electrode reaction

TABLE 11.3.2 Typical Controlled-Potential Coulometric Determinations

Substance	Working Electrode	Supporting Electrolyte[a]	Control Potential (V vs. SCE)	Overall Reaction
Li	Hg	0.1 M TBAP (CH_3CN)	−2.16	Li(I) → Li(Hg)
Cr	Pt	1 M H_2SO_4	+0.50	Cr(VI) → Cr(III)
Fe	Pt	1 M H_2SO_4	+0.20	Fe(III) → Fe(II)
Zn	Hg	2 M NH_3 1 M $(NH_4)_3$ Citrate	−1.45	Zn(II) → Zn(Hg)
Te^{2-}	Hg	1 M NaOH	−0.60	Te^{2-} → Te
Br^-	Ag on Pt	0.2 M KNO_3 (MeOH)	0.0	Ag + Br^- → AgBr
I^-	Pt	1 M H_2SO_4	+0.70	$2I^-$ → I_2
U	Hg	0.5 M H_2SO_4	−0.325	U(VI) → U(IV)
Pu	Pt	1 M H_2SO_4	+0.70	Pu(III) → Pu(IV)
Ascorbic acid	Pt	0.2 M phthalate buffer, pH 6	+1.09	Oxdn. n = 2
DDT	Hg		−1.60	Redn. n = 2
Aromatic hydrocarbons (e.g., diphenylanthracene)	Hg or Pt	0.1 M TBAP (DMF)		Redn. Ar → $Ar^{\cdot-}$
Aromatic nitro-compounds	Hg	0.5 M LiCl (DMSO)		Redn. $ArNO_2$ → $ArNO_2^{\cdot-}$

[a]With water as solvent, unless indicated otherwise.

without prior knowledge of electrode area or diffusion coefficient. (Note that in voltammetric methods if n is to be determined from the limiting current, D and A usually must be known.[1] To determine n from potential measurements, knowledge about the reversibility of the reaction is required.) However, because the time scale of coulometric measurements ($\sim$10–60 min) is at least one or two orders of magnitude longer than that of voltammetric methods, perturbing homogeneous chemical reactions following the electron transfer, which might not affect the voltammetric measurement, may be important in coulometry (see Section 12.7). For example, consider the reaction sequence:

$$O + e \rightleftharpoons R \tag{11.3.12}$$

$$R \rightarrow A \qquad \text{(slow, } t_{1/2} \sim \text{2–5 min)} \tag{11.3.13}$$

$$A + e \rightarrow B \qquad \text{(A reduced at less negative potentials than O)} \tag{11.3.14}$$

This sequence occurs, for example, in the reduction of o-iodonitrobenzene (O = $IPhNO_2$) in liquid ammonia (with 0.1 M KI as supporting electrolyte). A voltammetric experiment (e.g., cyclic voltammetry at scan rates of 50 to 500 mV/s) shows a one-electron reaction with formation of the radical anion (R = $IPhNO_2^{-\cdot}$), which is stable on this time scale. However, controlled-potential coulometric reduction shows n-values approaching 2 for reductions requiring 1-hour durations. In this time, the radical anion loses an I^- to form the radical (A = $\cdot PhNO_2$) which is reduced at these potentials (to B = $^-:PhNO_2$); this then protonates to form nitrobenzene.

▶ 11.4 CONTROLLED-CURRENT METHODS

11.4.1 Characteristics of Controlled-Current Electrolysis

The course of a bulk electrolysis under controlled-current conditions can be ascertained from consideration of i-E curves like those in Figure 11.4.1. As long as the applied current i_{app} is less than the limiting current at a given bulk concentration $i_l(t)$, the electrode reaction proceeds with 100% current efficiency. As the electrolysis proceeds, the bulk concentration of O, $C_O^*(t)$, decreases and $i_l(t)$ decreases (linearly with time). When

$$C_O^*(t) = \frac{i_{app}}{nFAm_O} \tag{11.4.1}$$

$i_{app} = i_l(t)$. At longer times, $i_{app} > i_l(t)$, and the potential shifts to a new, more negative value, where an additional electrode reaction can occur; this reaction contributes the additional current $i_{app} - i_l(t)$. The current efficiency thus drops below 100%. Since the potential is now sufficiently negative to be on the mass-transfer-controlled plateau of the O $\rightarrow$ R reduction, the electrolysis of O occurs as if it were being carried out under controlled-potential conditions. Thus the current contribution for this reaction decays exponentially, as in (11.3.7) (Figure 11.4.2). If i_{app} is larger than the initial limiting current, the rate of electrolysis of O will be essentially the same as if the reduction were carried out under controlled-potential conditions, but with much lower current efficiency.[2]

---

[1]An exception is highlighted in Problem 5.19.

[2]Sometimes a constant-current electrolysis will be somewhat faster than a controlled potential one under apparently identical conditions, because gas evolution (e.g., hydrogen or oxygen), occurring during the electrolysis, leads to effective stirring at the electrode surface and produces larger mass-transfer rates (i.e., a larger m_O).
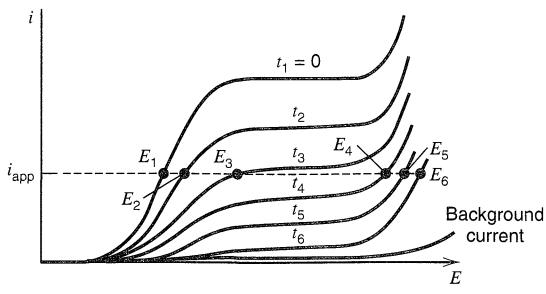
Figure 11.4.1 Current-potential curves at different times (increasing from t_1 to t_6) during bulk electrolysis with an applied constant current, i_{app}. The electrode potential shifts from E_1 to E_6 during the course of the electrolysis, with the largest shift occurring (between curves *3* and *4*) when $i_{app} = i_l$.

The selectivity of a constant-current separation is obviously intrinsically poorer than the corresponding controlled-potential method, since at some time during the electrolysis the potential must shift into a more negative region where a new electrode reaction occurs and, for example, a second metal could be deposited. One method of avoiding the interfering reaction would be to use an i_{app} less than 1% of the initial i_l, so that 99% of the O would be reduced before the potential shift occurred. This method would lead to a very prolonged electrolysis. Another method that is sometimes employed involves the use of a "cathodic depolarizer," a substance that is introduced into the solution to be reduced more easily (i.e., at less negative potentials) than any interfering substance. For example, consider the reduction of Cu(II) in the presence of Pb(II) (Figure 11.4.3). If NO_3^- is added to the solution, it will be reduced preferentially before the Pb(II) reduction occurs, and will prevent the deposition of lead along with the copper. In this case NO_3^- is said to play the role of a cathodic depolarizer. (The term *depolarizer* implies that the substance fixes the potential, by its own reduction, at a certain desired value.) Hydrogen ion often also plays the role of a depolarizer.

Generally, except for the simpler apparatus involved, controlled-current electrolysis offers no advantages over controlled-potential methods. With the commercial availability of suitable potentiostats, controlled-current methods are being used less frequently in analysis and lab-scale preparative electrolysis. For large-scale electrosynthesis or separations involving very high currents, especially in flow systems where the reactants are
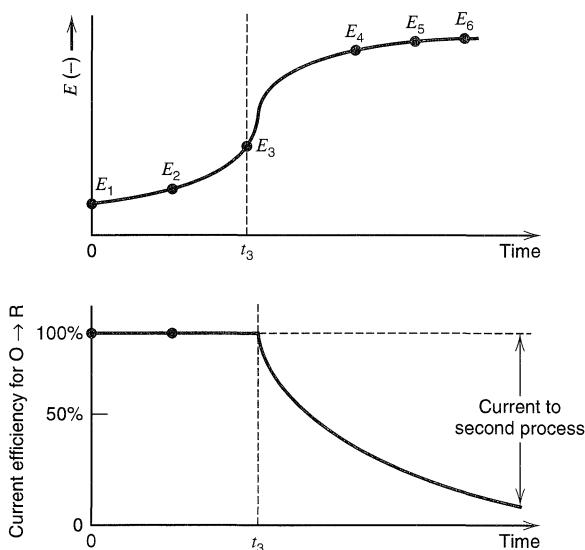
Figure 11.4.2 Potential and current efficiency for the electrolysis illustrated in Figure 11.4.1.
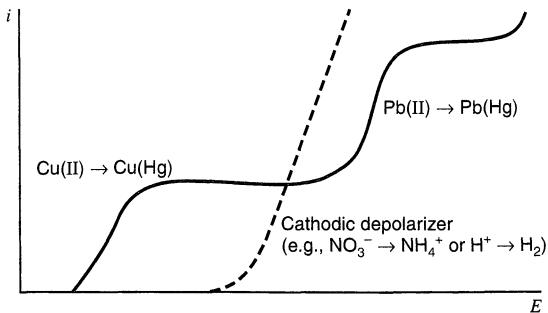
Figure 11.4.3 Schematic i-E curves illustrating action of a cathodic depolarizer in limiting the negative potential excursion of the working electrode and preventing codeposition of lead in the separation of copper.

continually added to the cell and products removed, the simplicity of constant-current methods is a great advantage. Here some degree of control of the working electrode potential can be obtained by regulation of the rate of solution flow or addition of reactant. Most industrial electrolytic apparatus (e.g., for the chloralkali process and aluminum production) operate under controlled-current conditions (see Problem 11.14).

11.4.2 Coulometric Methods

A constant-current coulometric method is attractive because a stable constant-current source is easy to construct and the total number of coulombs consumed in an electrolysis can be calculated readily from the duration of the electrolysis, τ, by

$$Q = i_{app}\tau \tag{11.4.2}$$

However, to use a coulometric method for a determination, the reaction of interest must proceed with nearly 100% efficiency. To illustrate how this is accomplished in a constant-current format, consider the coulometric determination of Fe^{2+} by oxidation at a platinum electrode to Fe^{3+} in an H_2SO_4 medium (Figure 11.4.4). If a constant current is applied to the Pt anode, then as described in Section 11.4.1, when the i_l for Fe^{2+} oxidation falls below i_{app}, the current efficiency would fall below 100% and part of the applied current would go to a secondary process (e.g., oxygen evolution). However, if Ce^{3+} is added to the solution, when the current efficiency for the *direct* oxidation of Fe^{2+} falls below 100%, the next process to occur is $Ce^{3+} \rightarrow Ce^{4+} + e$. The Ce^{4+} so produced is capable of oxidizing any Fe^{2+} remaining in the bulk solution by the fast reaction

$$Ce^{4+} + Fe^{2+} \rightarrow Ce^{3+} + Fe^{3+} \tag{11.4.3}$$
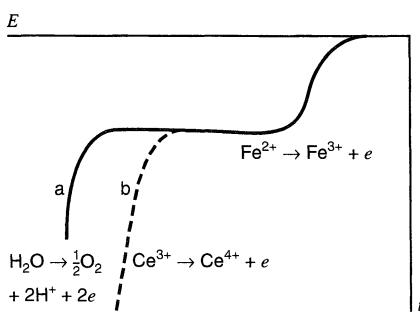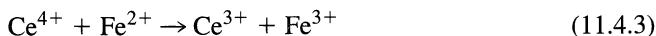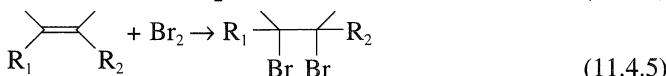
Figure 11.4.4 Schematic i-E curves for Fe^{2+} in $1\ M\ H_2SO_4$ in the absence (*curve a*) and in the presence (*curve b*) of excess Ce^{3+}.

Thus some Fe^{2+} is *indirectly* oxidized to Fe^{3+}, and the *titration efficiency* for the oxidation of Fe^{2+} is maintained. This then resembles an ordinary titration of Fe^{2+} with Ce^{4+}, in that a true equivalence point is reached. For this reason this technique is usually called a *coulometric titration* (of Fe^{2+} with the electrogenerated titrant, Ce^{4+}). Note that some end-point detection technique (as is also required in an ordinary titration) must be used to indicate when the oxidation of Fe^{2+} is complete, since neither the current nor the potential of the working electrode is a good indicator of the course of the reaction.

The requirements for the coulometric *intermediate* or *titrant* (e.g., Ce^{4+}) are that it be generated with a high current efficiency and that it react rapidly and completely with the substance being determined (Fe^{2+}). In some cases, such as the $Fe^{2+}-Ce^{4+}$ titration, the generation of the intermediate accounts for only part of the total electricity consumed. In others, such as the coulometric titration of olefins with electrogenerated Br_2 (generated by oxidation of Br^-), all of the current goes to the generation of the intermediate, which then reacts with the substance being titrated, that is,

$$2Br^- \rightarrow Br_2 + 2e \tag{11.4.4}$$

$$\underset{R_1 \quad\quad R_2}{>\!\!=\!\!<} + Br_2 \rightarrow R_1 \underset{Br\ Br}{-\!\!\!\!\!\!\diagup\!\!\!\diagup\!\!-} R_2 \tag{11.4.5}$$

A block diagram of the apparatus used in coulometric titrations is shown in Figure 11.4.5. The cell is composed of a working electrode and an auxiliary electrode in separate compartments. End-point detection is often made by an electrometric method (Section 11.5); hence indicator electrodes suited to the particular end-point detection technique are also located within the cell. The constant-current source can be simply a high-voltage (e.g., 400 V) power supply and a resistor. This will produce essentially a constant current as long as the reversible cell potential and cell resistance are small compared to the applied voltage and circuit resistance. Electronic constant-current sources (*amperostats* or *galvanostats*) based on operational amplifier circuitry are also frequently used (see Section 15.5). Whenever current is switched to the cell, a timer is actuated, so that the total electrolysis time can be recorded. Typically the applied current is in the range of 10 μA to 200 mA and titration times are 10 to 100 s.

The solution conditions and the end-point detection system are usually chosen based on the same criteria used for an ordinary titration (e.g., fast, definite, single, complete titration reaction and sensitive end-point detection). The current density range for
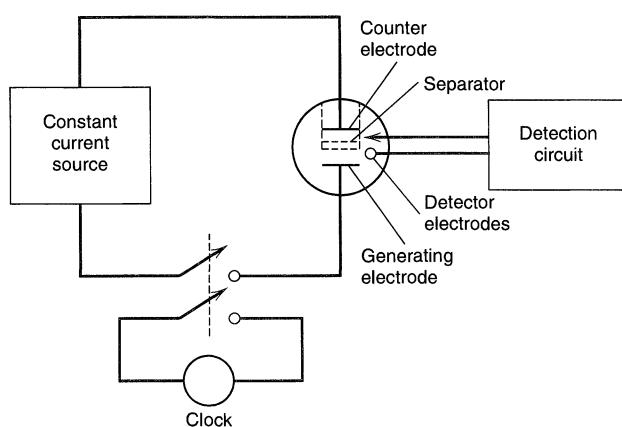
Figure 11.4.5 Apparatus for coulometric titrations.

generation of the titrant can be determined by taking i-E curves of the supporting electrolyte system with and without the titrant precursor species (A) present (23, 24) (Figure 11.4.6). The current efficiency for the generation of titrant (B) can be estimated by the equation

$$\text{Current efficiency} = \frac{100T}{T + S} \tag{11.4.6}$$

(assuming the process A $\pm$ ne $\rightarrow$ B does not affect the background electrolysis process). A plot of current efficiency as a function of current density can be prepared and, from this, the optimum region for titrant generation can be established. The current to be used is selected by consideration of the amount of substance to be determined and a convenient electrolysis time. Then an electrode area is calculated to give the needed current density. For example, the determination of 0.1 μequiv of a substance requires $\sim 10^4$ μC, or a current of 100 μA for 100 s. Thus, if the optimum generation current density is 1 mA cm^{-2}, a generating electrode area of 0.1 cm^2 would be used.

Coulometric titrations can be applied to a number of different types of determinations, including acid-base, precipitation, complexation, and redox titrations. Some typical examples are given in Table 11.4.1; detailed descriptions of the scope and nature of coulometric titrations are given in references 20 and 25–27.

Coulometric titrations offer a number of advantages over conventional titrations with standard solutions: (a) Very small amounts of substances can be determined without the use of ultramicrovolumetric techniques. For example, a titration with i_{app} = 10 μA and t = 100 s is quite easy and corresponds to about 10^{-8} mol (n = 1), or only a few micrograms, of titratable material. Indeed, with growing interest in nanometer scale chemistry, there should be greater interest in delivery of chemical reagents electrochemically (28). Note that a current of 1 pA represents, for an n = 1 reaction, a flux of 10^{-17} mol/s. (b) Standard solutions need not be prepared or stored. Standardizations using primary standards are not necessary. (c) Substances that are unstable or inconvenient to use because of volatility or reactivity can be employed as titrants, for example, Br$_2$, Cl$_2$, Ti^{3+}, Sn^{2+}, Cr^{2+}, Ag^{2+}, and Karl Fischer reagent. (d) The titrations are easily automated, since it is easier to control an electric current and monitor time than it is to control a buret valve and record volume. (e) They can be performed remotely (e.g., in the analysis of radioactive materials) and under an inert atmosphere more easily. (f) Dilution effects do not occur during the titration, making end-point location simpler.
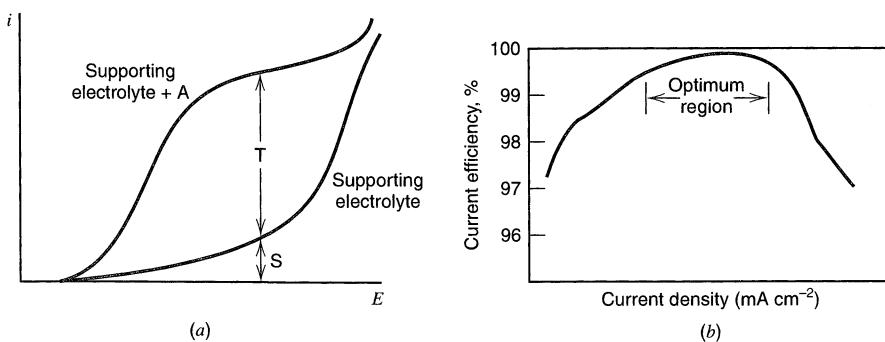
Figure 11.4.6 (a) Use of i-E curves for estimating current efficiency at given potential and current density. (b) Typical plot of current efficiency as a function of current density for an electrogenerated titrant.

**TABLE 11.4.1 Typical Electrogenerated Titrants
and Substances Determined by Coulometric Titration**

Electrogenerated Titrant	Generating Electrode and Solution	Typical Substances Determined
Oxidants		
Bromine	Pt/NaBr	As(III), U(IV), NH_3, olefins, phenols, SO_2, H_2S, Fe(II)
Iodine	Pt/KI	H_2S, SO_2, As(III), water (Karl Fischer), Sb(III)
Chlorine	Pt/NaCl	As(III), Fe(II), various organics
Cerium(IV)	$Pt/Ce_2(SO_4)_3$	U(IV), Fe(II), Ti(III), I^-
Manganese(III)	$Pt/MnSO_4$	Fe(II), H_2O_2, Sb(III)
Silver(II)	$Pt/AgNO_3$	Ce(III), V(IV), $H_2C_2O_4$
Reductants		
Iron(II)	$Pt/Fe_2(SO_4)_3$	Mn(III), Cr(VI), V(V), Ce(IV), U(VI), Mo(VI)
Titanium(III)	$Pt/TiCl_4$	Fe(III), V(V,VI), U(VI), Re(VIII), Ru(IV), Mo(VI)
Tin(II)	$Au/SnBr_4(NaBr)$	I_2, Br_2, Pt(IV), Se(IV)
Copper(I)	Pt/Cu(II)(HCl)	Fe(III), Ir(IV), Au(III), Cr(VI), IO_3^-
Uranium(V),(IV)	Pt/UO_2SO_4	Cr(VI), Fe(III)
Chromium(II)	$Hg/CrCl_3(CaCl_2)$	O_2, Cu(II)
Precipitation and Complexation Agents		
Silver(I)	$Ag/HClO_4$	Halide ions, S^{2-}, mercaptans
Mercury(I)	$Hg/NaClO_4$	Halide ions, xanthate
EDTA	$Hg/HgNH_3Y^{2-a}$	Metal ions
Cyanide	$Pt/Ag(CN)_2^-$	Ni(II), Au(III,I), Ag(I)
Acids and Bases		
Hydroxide ion	$Pt(-)Na_2SO_4$	Acids, CO_2
Hydrogen ion	$Pt(+)/Na_2SO_4$	Bases, CO_3^{2-}, NH_3

$^a Y^{4-}$ is ethylenediamine-tetra-acetate anion.

Another broad field of applications involves continuous coulometric titrators which are employed in process stream analyzers. In these the generating current is continuously adjusted to maintain a small excess of electrogenerated titrant to react with material in the incoming liquid or gaseous sample stream. The level of generating current is a measure of the instantaneous concentration of the titrated substance (29, 30). Coulometric titration methods have also been used in chromatographic detectors and for determination of homogeneous reaction rates (31).

▶ 11.5 ELECTROMETRIC END-POINT DETECTION (32–37)
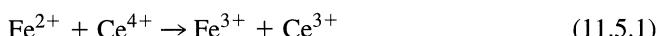
11.5.1 Classification

Electrometric methods are employed to detect the end points of conventional titrations, as well as those of the coulometric titrations described in Section 11.4. These detection methods typically involve two small electrodes in an indicator circuit that is electrically separate from the generating circuit that would be present for a coulometric titration. All electrometric methods are based on measurements of either the potential difference between the two electrodes in the indicator circuit (*potentiometric methods*) or the current passing in that circuit (*amperometric methods*). Further classification is based on the

nature of the two electrodes. One of them may be nonpolarizable (i.e., a reference electrode), or both electrodes may be polarizable. Thus for potentiometric methods one has: (a) $i = 0$, one nonpolarizable electrode (ordinary potentiometry); (b) constant applied current, one polarizable electrode ("one-electrode potentiometry"); (c) constant applied current, two polarizable electrodes ("two-electrode potentiometry"). Similarly for amperometric methods we can define (a) constant applied voltage, one polarizable electrode ("one-electrode amperometry"); (b) constant applied voltage, two polarizable electrodes ("two-electrode amperometry"). The polarizable, or *indicator*, electrode can be any steady-state voltammetric electrode, for example, a DME, a platinum microelectrode in stirred solution, an RDE, and so on. The reference electrode is usually a facile one, such as an SCE with a low-resistance junction, so that with the usual small currents employed, iR drops are small and two-electrode systems can be employed. (Three-electrode potentiometric and amperometric systems are possible, but they are rarely used). The shapes and characteristics of the titration curves (E or i vs. fraction titrated, f) depend on the i-E curves for the indicator electrode(s) at different points during the titration. These depend on the composition of the solution at a given value of f and on the reversibility of the different couples in the solution.

11.5.2 Current-Potential Curves During Titration

Consider the titration of Fe^{2+} with Ce^{4+} by the reaction

$$Fe^{2+} + Ce^{4+} \rightarrow Fe^{3+} + Ce^{3+} \tag{11.5.1}$$

Assume that this is the typical manual titration of a solution initially containing Fe^{2+} with added titrant Ce^{4+}. For simplicity, we will neglect dilution effects and assume both the Fe^{3+}/Fe^{2+} and Ce^{4+}/Ce^{3+} couples behave nearly reversibly at a platinum microelectrode. Schematic i-E curves obtained at different values of f (where $f =$ moles Ce^{4+} added/moles Fe^{2+} initially present) are shown in Figure 11.5.1. Initially ($f = 0$), the cell contains only Fe^{2+}, and only the anodic wave for Fe^{2+} oxidation is observed. During the titration ($0 < f < 1$) the solution contains Fe^{2+}, Fe^{3+}, and Ce^{3+}, while after the equivalence point ($f > 1$) the solution contains Fe^{3+}, Ce^{3+}, and Ce^{4+}. The titration curves for the different potentiometric and amperometric methods can be derived from these i-E curves. These are discussed in more detail in the first edition.[3] We describe here representative examples of the more widely used end-point methods.

11.5.3 Potentiometric Methods

One-electrode potentiometry involves the measurement of the potential of an indicator electrode with respect to a reference (nonpolarizable) electrode either at open circuit or with a small anodic or cathodic current applied to the indicator electrode. These three possibilities are shown in Figure 11.5.2 for the Fe^{2+}–Ce^{4+} titration, and the resulting titration curves are shown in Figure 11.5.3. The $i = 0$ curve, (*a*), is the usual potentiometric titration curve, showing the equilibrium potential of the solution (E_{eq}) as a function of f. When a small anodic current is impressed on the indicator electrode, the measured potential at a given f will be somewhat more positive than E_{eq} [curve (*c*)]. When a small cathodic cur-

---

[3]First edition, Section 10.5.
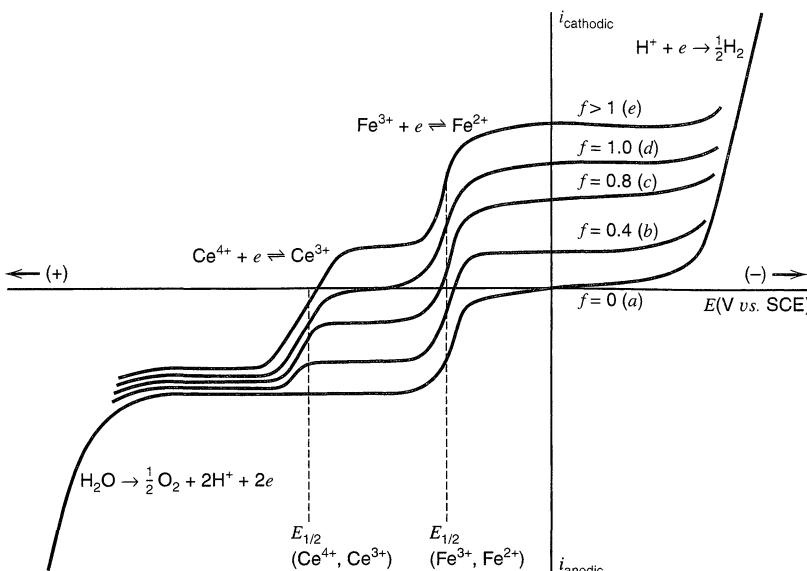
Figure 11.5.1 Idealized current-potential curves at a platinum electrode during titration of Fe^{2+} with Ce^{4+} at different fractions, f, of Fe^{2+} titrated. (a) $f = 0$; only an anodic wave for $Fe^{2+} \rightarrow Fe^{3+}$ is observed. (b), (c) $0 < f < 1$; the solution contains Fe^{2+}, Fe^{3+}, and Ce^{3+}. A composite wave for Fe^{3+}, Fe^{2+} couple, as well as an anodic wave for $Ce^{3+} \rightarrow Ce^{4+} + e$, are observed. (d) $f = 1$; the solution contains Fe^{3+} and Ce^{3+}. There is a cathodic wave for $Fe^{3+} + e \rightarrow Fe^{2+}$ and an anodic wave for oxidation of cerous. (e) $f > 1$; the solution contains Fe^{3+}, Ce^{3+}, and Ce^{4+}. A composite wave for the Ce^{4+}, Ce^{3+} couple and a cathodic wave for ferric ion are observed. The curves drawn are representative of those obtained for a steady-state voltammetric technique, for example, an RDE or a microelectrode in stirred solution. [Adapted from J. J. Lingane, "Electroanalytical Chemistry," 2nd ed., Wiley-Interscience, New York, 1958.]

rent is applied, the potential will be more negative than E_{eq} [curve (b)]. If the applied currents are small, the break in the E vs. f titration curve with applied current will only be slightly displaced from that of the E_{eq} vs. f curve. The advantage of potentiometric end-point detection methods with applied current (or polarized electrodes) is that a steady potential is sometimes attained more rapidly under these conditions compared to measurements at open circuit. This is particularly true in titrations involving couples that show irreversible behavior. In these cases, the shapes of the titration curves will be somewhat different from those depicted for reversible reactions. They are left as an exercise for the reader (see Problem 11.3).

In *two-electrode potentiometry* the titration curve can be derived by considering that the small constant current applied between two polarizable electrode must be the same at the anode and cathode. The result is a curve of E vs. f that shows a peak at the equivalence point.

11.5.4 Amperometric Methods

One-electrode amperometry involves maintaining the potential of the indicator electrode at a constant value with respect to a reference electrode and determining the current as a function of f. Consider again the Ce^{4+}–Fe^{2+} titration, this time, however,
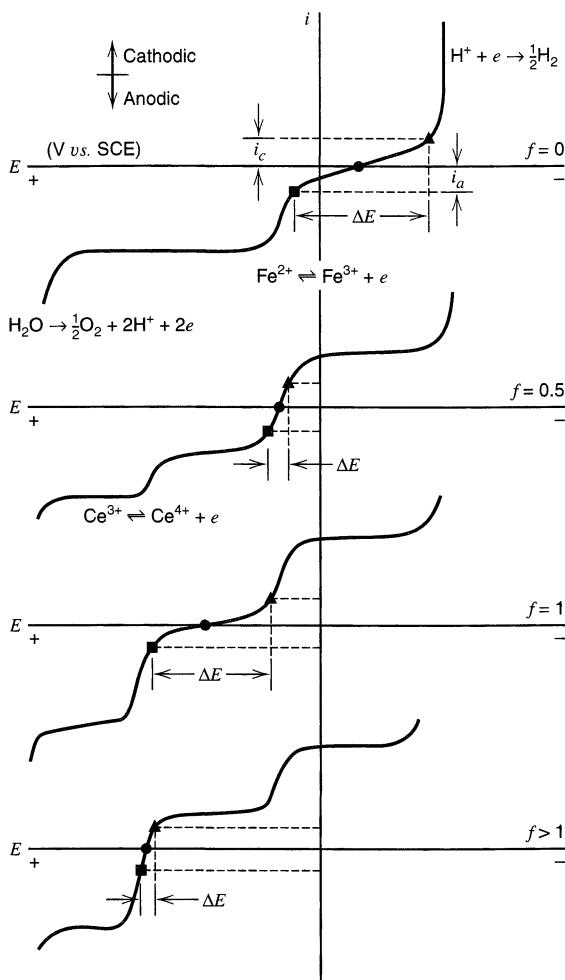
Figure 11.5.2 Current-potential curves at a platinum electrode during titration of Fe^{2+} with Ce^{4+} at different fractions titrated, f, illustrating the potential attained by this indicator electrode (*vs.* SCE) at (*a*) zero current (●); (*b*) small applied cathodic current, i_c (▲); (*c*) small applied anodic current, i_a (■). (The magnitudes of the actual applied currents used in a titration would be much smaller than those shown here, which are exaggerated for clarity.)
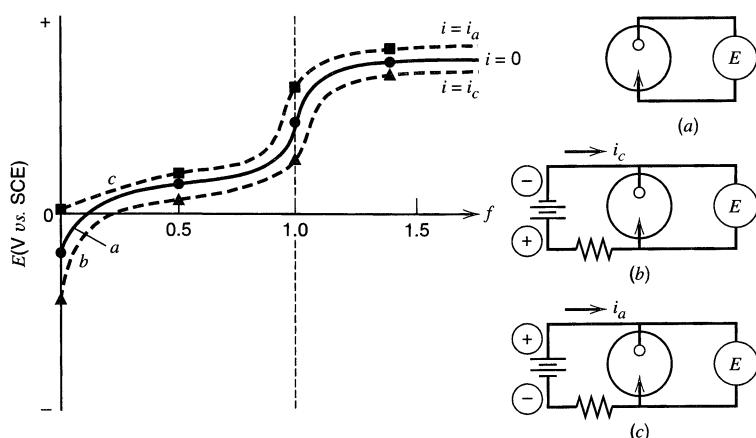
Figure 11.5.3 Potentiometric titration curves for a platinum indicator electrode *vs.* SCE (reference) with impressed current of: *Curve a*, 0. *Curve b*, i_c. *Curve c*, i_a. Points on curves correspond to those in Figure 11.5.2. The corresponding circuits for these end-point detection methods are illustrated in (*a*) to (*c*). The meter, E, is assumed to have a high input impedance, and the voltage source/resistor combination is chosen so that the applied currents are essentially constant.

with the potential of the indicator electrode maintained at a value on the plateau of the i-E curve for Fe^{2+} oxidation (E_1 in Figure 11.5.4). The current during the titration is shown in Figure 11.5.5. In this titration, the current changes from anodic to cathodic at $f = 1$. Note that for this titration, holding the potential of the indicator electrode in the region of E_1 is the only way of obtaining an informative titration curve.[4] If the indicator electrode is held at other potentials, a useful titration curve usually would not result.

Several different types of amperometric titration curves are possible. For example, one can titrate a metal ion that shows a voltammetric wave (e.g., Pb^{2+}) with a titrant that causes its precipitation (e.g., $Cr_2O_7^{2-}$). If the potential is held at the plateau of the voltammetric wave, the current will decrease during the titration and remain at the residual current level for $f > 1$.

Two-electrode amperometry involves the use of two indicator electrodes with a small constant potential impressed between them. Since they are in the same current loop, the anodic current in one will be equal in magnitude to the cathodic current in the other. The
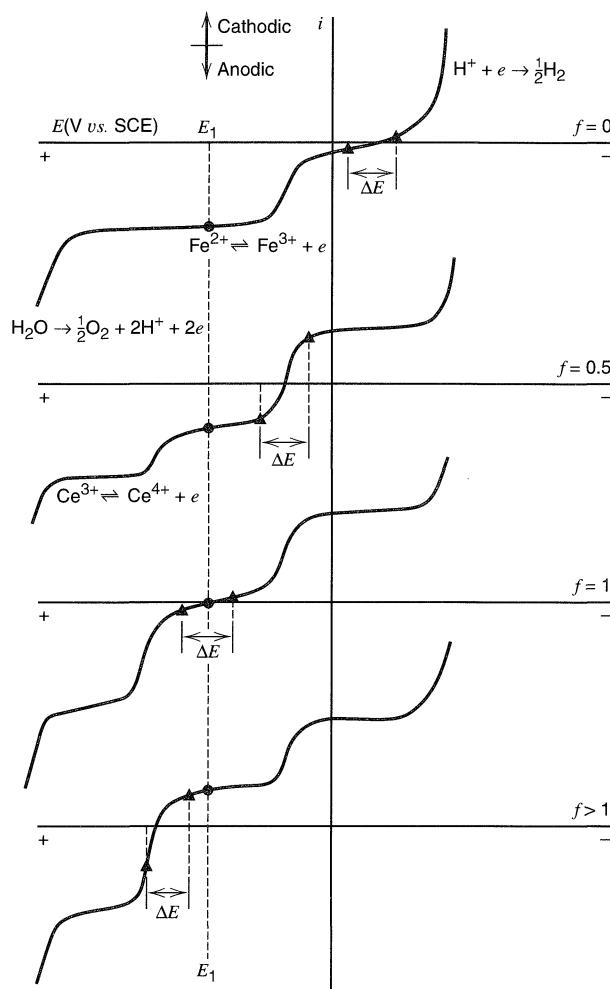
Figure 11.5.4 Current-potential curves at a platinum electrode during titration of Fe^{2+} with Ce^{4+} at different fractions titrated, f, illustrating the currents attained (*a*) for an indicator electrode at potential E_1 (●); (*b*) when a constant potential difference ΔE is impressed across two identical indicator electrodes (▲).

[4]Unless the mass-transfer coefficients for the various species (e.g., Fe^{2+} and Fe^{3+} *vs.* Ce^{3+} and Ce^{4+}) are quite different (see Problem 11.9).
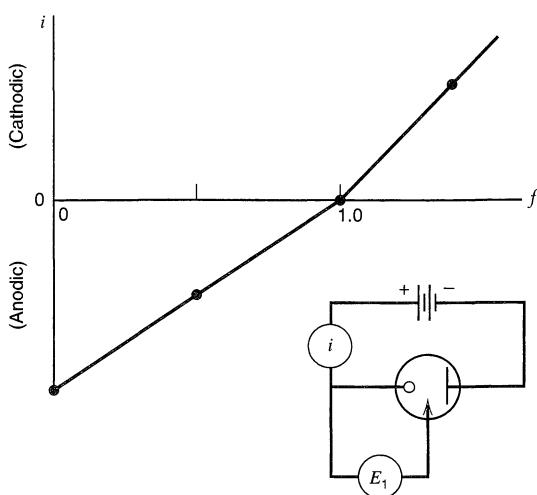
Figure 11.5.5 One-electrode amperometric titration curve (dilution neglected) for titration of Fe^{2+} with Ce^{4+} with the platinum indicator electrode held at E_1 in Figure 11.5.4.

potential of each will thus shift during a titration to maintain the condition $i_c = |i_a|$. For example, for the Fe^{2+}–Ce^{4+} titration with two platinum electrodes held at a potential difference, ΔE (~50 mV) (Figure 11.5.4), the titration curve that results is shown in Figure 11.5.6.

The shape of the two-electrode amperometric titration curve depends strongly on the reversibility of the electrode reactions of the titrant and titrate systems. For example, if the titrate involves reversible electrode reactions (e.g., I_3^-/I^-) and the titrant electrode reactions are irreversible (e.g., $S_2O_3^{2-}/S_4O_6^{2-}$), the current in the titration is similar to that in Figure 11.5.6, except that it remains at the residual current level for $f > 1$. These titration curves are sometimes said to involve "dead-stop" end points, since the current falls essentially to zero at the end point and remains there. This type of end-point detection was applied in some of the earliest amperometric methods; in fact, it was discovered and used before the theoretical basis for these titrations was established. We leave it to the reader to work out the titration curves (potentiometric and amperometric) that result for other different cases involving reversible and irreversible couples as titrants and titrates.

The amperometric titration curves for coulometric titrations have somewhat different shapes than the ones for the manual titrations described, because usually one form of the couple exists in large excess. For example, in the titration of Fe^{2+} with electrogenerated Ce^{4+}, Ce^{3+} will be present from the start at a concentration that is large compared to that of the Fe^{2+}. Titrations for multicomponent systems can be treated in a similar manner. In all cases the curves can be derived by consideration of the i-E curves that arise during the titration.
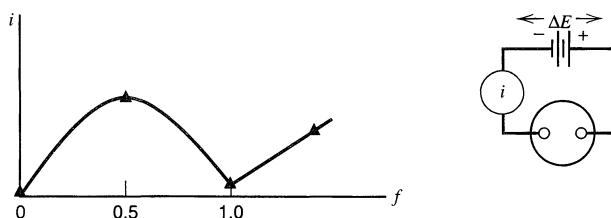
Figure 11.5.6 Two-electrode amperometric titration of Fe^{2+} with Ce^{4+} with a constant potential difference, ΔE, impressed between two platinum indicator electrodes (see Figure 11.5.4).

➤ 11.6 FLOW ELECTROLYSIS

11.6.1 Introduction

An alternative method of bulk electrolysis involves flowing the solution to be electrolyzed continuously through a porous working electrode (38) of large surface area. Flow electrolytic methods can result in high efficiencies and rapid conversions and are especially convenient where large amounts of solution are to be treated. Flow methods are of use in industrial situations (e.g., removal of metals such as copper from waste streams) and have been broadly applied to electrosynthesis, separations, and analysis.

The flow electrolysis cell (Figure 11.6.1) contains a working electrode of large surface area, composed, for example, of screens of fine mesh metal or beds of conductive material (e.g., graphite or glassy carbon grains, metal shot, or powder). If a divided cell is not necessary, as in metal deposition, the counter electrode can be interleaved with the working electrode and insulated from it with simple separators. Divided cells require more complex structures (including separators such as porous glass, ceramics, or ion-exchange membranes) and careful placement of the counter and reference electrodes to minimize iR drops. The cells are designed to show high conversions with a minimum length of electrode and maximum flow velocities.

11.6.2 Mathematical Treatment (39)

Consider a flow-through porous electrode of length L (cm) and cross-sectional area A (cm^2) immersed in a stream of volumetric flow rate v (cm^3/s) (Figure 11.6.2). The *linear flow velocity* of the stream, U (cm/s), is given by

$$U = \frac{v}{A} \tag{11.6.1}$$

The reaction being carried out at the electrode, $O + ne \rightarrow R$, is assumed to occur with 100% current efficiency. The inlet concentration of O is $C_O(\text{in})$, and $C_R(\text{in})$ is assumed to be zero. At the outlet, the concentrations are $C_O(\text{out})$ and $C_R(\text{out})$. The overall conversion of O to R in passage through the electrode is i/nF (mol/s) or i/nFv (mol/cm^3). If R is the fraction of O converted ($R = 0$, no conversion; $R = 1$, 100% conversion), then

$$C_O(\text{out}) = C_O(\text{in})(1 - R) \tag{11.6.2}$$

$$C_R(\text{out}) = C_O(\text{in})\, R \tag{11.6.3}$$

$$C_O(\text{out}) = C_O(\text{in}) - \frac{i}{nFv} \tag{11.6.4}$$

$$R = \frac{i}{nFvC_O(\text{in})} = 1 - \frac{C_O(\text{out})}{C_O(\text{in})} \tag{11.6.5}$$

We desire an expression for the dependence of the current on flow velocity and electrode parameters. The *total internal area* of the electrode, which encompasses the sum of the areas of all of the pores, is a (cm^2), and the total electrode volume is LA (cm^3). Porous electrodes are frequently characterized by their *specific area*, s, given by

$$s \ (cm^{-1}) = a \ (cm^2)/LA \ (cm^3) \tag{11.6.6}$$
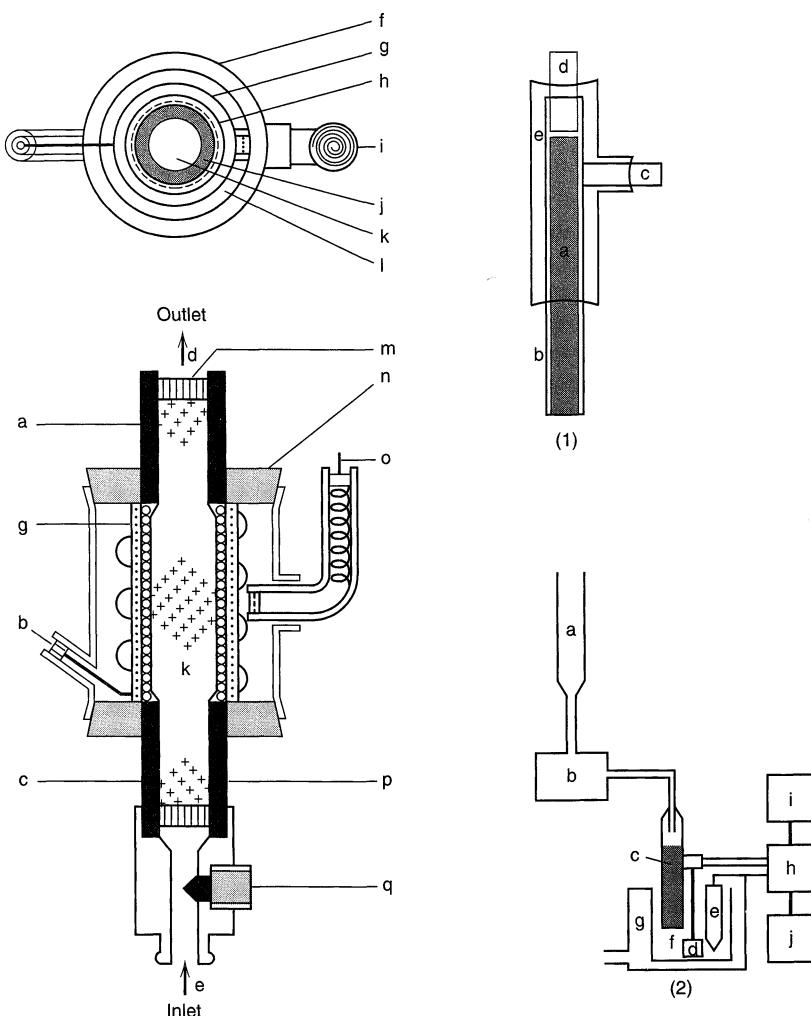
Figure 11.6.1 Flow electrolytic cells. *Left:* Cell utilizing glassy carbon granule working electrode (k), silver auxiliary electrode (g), Ag/AgCl reference electrode (o, i) with porous glass separator (h). Other components are (a, c) lead for working electrode; (b) lead to auxiliary electrode; (d) solution outlet; (e) solution inlet; (f) glass or plastic tube; (j, p) porous carbon tube; (l) saturated KCl solution; (m) silicone rubber. [Reprinted with permission from T. Fujinaga and S. Kihara, *CRC Crit. Rev. Anal. Chem.*, **6**, 223 (1977). Copyright, CRC Press, Inc., Boca Raton, FL.] *Right:* Cell with Reticulated Vitreous Carbon (RVC™), a conductive foam-type material available in several porosities. (*1*) (a) RVC cylinder, (b) heat-shrink tubing, (c) graphite rod sidearm, (d) glass tube, (e) glass and epoxy support. (*2*) Schematic diagram of complete apparatus. (a) Solution reservoir, (b) pump, (c) RVC electrode, (d) platinum electrode, (e) SCE reference electrode, (f) downstream reservoir, (g) runover collector, (h) potentiostat, (i) recorder, (j) digital voltmeter. [Reprinted with permission from A. N. Strohl and D. J. Curran, *Anal. Chem.*, **51**, 353 (1979). Copyright 1979, American Chemical Society.]
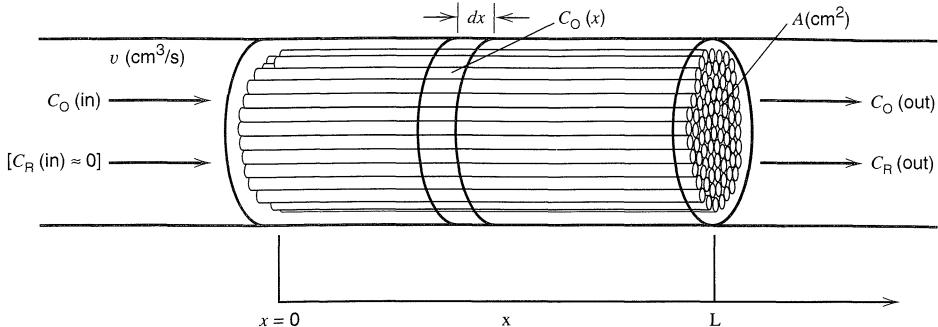
Figure 11.6.2 Schematic diagram of the working electrode of a flow electrolysis cell.

(see example, Figure 11.6.3). The concentration of O decreases continuously with distance from the front face of the electrode ($x = 0$), and the local current density at a given location, $j(x)$, varies with x. The net conversion in a slab of thickness dx is $j(x)sA\,dx/nF$ (mol/s), where under mass-transfer-controlled, limiting-current conditions (see Section 1.4.2),

$$j(x) = nFm_O C_O(x) \tag{11.6.7}$$

The variation in concentration at x is then

$$-dC_O(x)(\text{mol/cm}^3) = \frac{j(x)sA\,dx}{nFv} \tag{11.6.8}$$

Combining (11.6.7) and (11.6.8) then yields

$$-\frac{dC_O(x)}{dx} = \frac{m_O C_O(x)sA}{v} \tag{11.6.9}$$

$$\int_{C_O(\text{in})}^{C_O(x)} \frac{dC_O(x)}{C_O(x)} = \frac{-m_O sA}{v} \int_0^x dx \tag{11.6.10}$$

$$C_O(x) = C_O(\text{in}) \exp\left(\frac{-m_O sA}{v} x\right) \tag{11.6.11}$$

$$j(x) = nFm_O C_O(\text{in}) \exp\left(\frac{-m_O sA}{v} x\right) \tag{11.6.12}$$

The total current in the electrode is then

$$i = \int_0^L j(x)sA\,dx = nFm_O C_O(\text{in})sA \int_0^L \exp\left(\frac{-m_O sAx}{v}\right) dx \tag{11.6.13}$$

$$i = nFC_O(\text{in})v\left[1 - \exp\left(\frac{-m_O sAL}{v}\right)\right] \tag{11.6.14}$$

This can be combined with (11.6.5) to yield (39a)

$$\boxed{R = 1 - \exp\left(\frac{-m_O sAL}{v}\right)} \tag{11.6.15}$$

The mass-transfer coefficient m_O is a function of flow velocity, U, and is sometimes given as

$$m_O = bU^\alpha \tag{11.6.16}$$
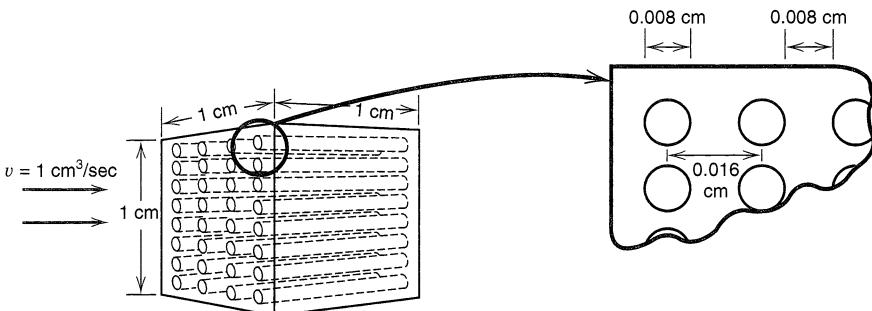
Figure 11.6.3 Ideal porous electrode illustrating calculation of the specific area, s, and porosity, ε. Consider the electrode as a cube $1 \times 1 \times 1$ (cm), containing straight pores, each 0.008 cm in diameter, spaced at centers 0.016 cm apart. The total number of pores, N, on a 1-cm^2 face is ~3900; the internal area of each pore is $2\pi rL = \pi(0.008 \text{ cm})(1 \text{ cm}) = 0.025 \text{ cm}^2$; the total internal electrode area is $a = (3900)(0.025 \text{ cm}^2) = 98 \text{ cm}^2$; the total internal electrode volume is 1 cm^3; the specific area is $s = 98 \text{ cm}^2/1 \text{ cm}^3 = 98 \text{ cm}^{-1}$; the facial area of each pore is $\pi r^2 = 5.0 \times 10^{-5} \text{ cm}^2$; the total open area on face is $a_p = (3900)(5.0 \times 10^{-5} \text{ cm}^2) = 0.2 \text{ cm}^2$; the porosity is $\varepsilon = 0.2 \text{ cm}^2/1 \text{ cm}^2 = 0.2$. If the volumetric flow rate is $v = 1 \text{ cm}^3/s$, the linear flow velocity is $U = 1 \text{ cm}^3/s /1 \text{ cm}^2 = 1 \text{ cm/s}$, and the interstitial velocity is $W = 1 \text{ cm/s} /0.2 = 5 \text{ cm/s}$.

where b is a proportionality factor and α is a constant (frequently having values between 0.33 and 0.5 for laminar flow and increasing up to nearly 1 for turbulent flow). With this equation and (11.6.1), equations 11.6.14 and 11.6.15 take the forms

$$i = nFAUC_O(\text{in})[1 - \exp(-bU^{\alpha-1}sL)] \tag{11.6.17}$$
$$R = 1 - \exp(-bU^{\alpha-1}sL) \tag{11.6.18}$$

Thus the conversion efficiency, R, increases with decreasing flow velocity and increasing specific area and length of electrode. From (11.6.11) it can be seen that the concentration of O varies exponentially with distance along the electrode with

$$\boxed{C_O(\text{out}) = C_O(\text{in}) \exp\left(\frac{-m_O sAL}{v}\right)} \tag{11.6.19}$$

The local current density, $j(x)$, is highest at the front face of the electrode and decreases exponentially with x.

These equations can also be cast in a form comparable with those for batch bulk electrolysis. If the total front-surface, open area of the pores is a_p, then the *porosity*, is defined as (see Figure 11.6.3)

$$\varepsilon = \frac{a_p}{A} \tag{11.6.20}$$

The linear flow velocity, which is U in the liquid stream, increases upon entering the electrode to an *interstitial velocity*, W, given by

$$W = \frac{U}{\varepsilon} = \frac{v}{A\varepsilon} = \frac{v}{a_p} \tag{11.6.21}$$

A volume element of solution moves down a pore at this velocity and, if it entered the electrode at time $t = 0$, then at time t it will be a distance x, given by

$$x = Wt = \frac{Ut}{\varepsilon} \tag{11.6.22}$$

This allows the equations to be formulated in terms of time, so that substitution of (11.6.22) into (11.6.11) yields

$$C_O(t) = C_O(\text{in}) \exp\left(\frac{-m_O s}{\varepsilon} t\right)$$ (11.6.23)

This equation is of the same form as that for a batch electrolysis, (11.3.6), with $m_O s/\varepsilon = p$ (compared to $m_O A/V = p$). Thus, the cell factor, p, increases with increasing mass-transfer rate, increasing specific area, and decreasing porosity. The length of porous electrode required for a given conversion R can be obtained from (11.6.15):

$$L = -\frac{v}{m_O sA} \ln(1 - R)$$ (11.6.24)

The time for an element of solution to transit the electrode, τ, sometimes called the *residence time* is derived from (11.6.22) and (11.6.24) as

$$\tau = \frac{L\varepsilon}{U} = p^{-1} \ln(1 - R)$$ (11.6.25)

An alternative simplified approach to the efficiency of electrolysis in a porous electrode (40) is based on the time t' required for O in the center of a pore of radius r to diffuse to the wall:

$$t' \approx \frac{r^2}{2D_O}$$ (11.6.26)

The time required to move through the electrode down a pore of length L is given by [see (11.6.21) and (11.6.22)]

$$t = \frac{La_p}{v}$$ (11.6.27)

If this time is greater than or equal to t', a high conversion ($R \approx 1$) will be attained. From (11.6.26) and (11.6.27), we find that the flow velocity required for high conversion must satisfy the expression:

$$v \leq \frac{2a_p L D_O}{r^2}$$ (11.6.28)

For example, for a porous silver electrode with $A = 0.2$ cm^2, $\varepsilon = 0.5$, $L = 50$ μm, $r = 2.5$ μm, $D_O = 5 \times 10^{-6}$ cm^2/s, $a_p = \varepsilon A = 0.1$ cm^2, the maximum flow velocity for $R \approx 1$ is 0.1 cm^3/s, with a residence time in the electrode of ~ 5 ms.

The simple treatment given here can be employed to find general conditions of an efficient flow electrolysis involving limiting current conditions. However, we have neglected (a) resistive drops in the electrode and in the solution in the pores, (b) kinetic limitations to the electron-transfer reaction, and (c) the possibility of a current efficiency less than unity. Treatments taking these other effects into account are available (41–43); they usually result in equations requiring numerical solution.

Flow cells operating at $R = 1$ are convenient for the continuous analysis of liquid streams, since the measured current is directly proportional to the concentration of the substance undergoing electrolysis, that is, from (11.6.5), $C_O(\text{in}) = i/nFv$. Since this is actually a continuous coulometric analysis, such an analytical method is absolute and does not require calibration or knowledge of mass-transfer parameters, electrode area, etc. (44).

A chromatographic method based on flow electrolysis has also been described (45). Here, as in elution chromatography methods, a sample containing metal ions is introduced into a stream of flowing electrolyte solution with the potential of the porous working electrode maintained constant. Deposition of a metal ion on the column results in a current-time trace that allows determination of the amount of metal ion. Electrolytic chromatographic methods, where a gradient in potential is maintained along the length of the porous working electrode, are also available.

11.6.3 Dual-Electrode Flow Cells

Flow cells that incorporate two working electrodes in the flow channel have also been described (Figure 11.6.4 *a*). These can be considered as the flow coulometric equivalent of the rotating ring-disk electrode, where convective flow carries material from the first working electrode to the second. This strategy has been used in the coulometric analysis of plutonium, where the two working electrodes were large beds of glassy carbon particles, with the first electrode used to adjust the oxidation state of the plutonium to a single known level [Pu(IV)] and the second used for the coulometric analysis [Pu(IV) + $e \rightarrow$ Pu(III)] (45). This type of system can also be used to analyze for the products produced at the first electrode (the *generator electrode*), by electrolysis at the second (the *collector electrode*). The most obvious case involves reversal electrolysis, such as with O + $ne \rightarrow$ R taking place at the generator and R $\rightarrow$ O + ne occurring at the collector.

In this application, thin, but efficient, working electrodes separated by a small gap, g, are desired. A system (Figure 11.6.4 *b*) involving porous silver disk working electrodes (50-μm average pore diameter) separated by a gap of 200 μm with porous Teflon material has been described (40). In this mode of operation, each working electrode is provided with its own auxiliary and reference electrode (so that this constitutes a six-electrode cell), and two separate potential control circuits must be used. The characteristics of these working electrodes are those given immediately after (11.6.28), and the estimated maximum flow velocity for good conversion ($\sim$0.1 cm^3/s) was approximately confirmed experimentally by carrying out the reduction of Fe(III) to Fe(II) in an oxalate medium on one working electrode and noting where the current began to deviate from that predicted by (11.6.5) with $R = 1$. At this flow rate the transit time across the gap is about 40 ms and high collection efficiencies (i.e., $i_{collector}/i_{generator}$) were found even for flow rates where $R < 1$. The authors suggested that such a system might be useful for studying homogeneous reactions coupled to the electron-transfer reaction. For example, if the product of the reaction at the generator electrode (R) decomposes (e.g., R $\rightarrow$ A), then not only will the collector current for the oxidation of R be smaller, but also product A will appear in the effluent and can be determined there by any of a number of analytical methods. Application of this cell to a study of the isomerization of the radical anion of diethylmaleate in N,N-dimethylformamide solution was reported.

11.6.4 Electrochemical Detectors for Liquid Chromatography

An important application of flow cells is their use as detectors in liquid chromatography (LC), capillary zone electrophoresis (CZE), and flow injection (FI) methods (46–50). Such cells may be coulometric ones, where all of the material flowing into the cell is electrolyzed, but more frequently they are amperometric or voltammetric cells, sometimes utilizing UMEs as described in Section 9.7.
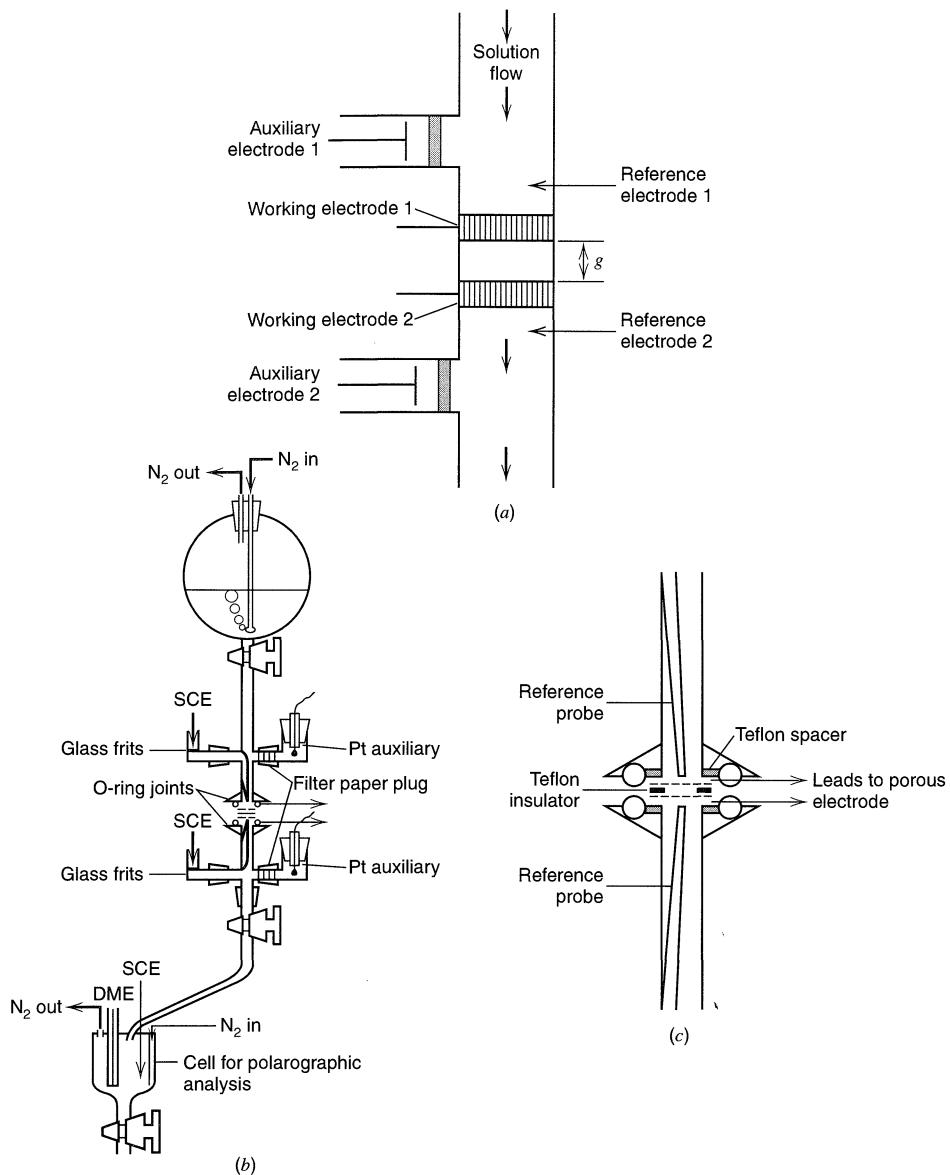
Figure 11.6.4 (*a*) Schematic representation of a dual-electrode flow cell. (*b*) Actual complete dual-electrode flow cell assembly. Solution flows by gravity from upper reservoir. For greater clarity, the "O-ring joint" portion of the cell with the dual working electrodes is shown in exploded form. A close-up view of this portion with the porous silver electrodes is shown in (*c*). [From J. V. Kenkel and A. J. Bard, *J. Electroanal. Chem.*, **54**, 47 (1974), with permission.]

Many different cell geometries and flow arrangements have been used in the design of LC detectors. The general requirements are (51): well-defined hydrodynamics, low dead volume, high mass-transfer rate, high signal/noise, robust design, and reproducible working and reference electrode responses. An important factor is the nature of the solution flow with respect to the electrode. Several typical arrangements are shown in Figure 11.6.5. The solution of the hydrodynamic equations that govern the cell currents follows
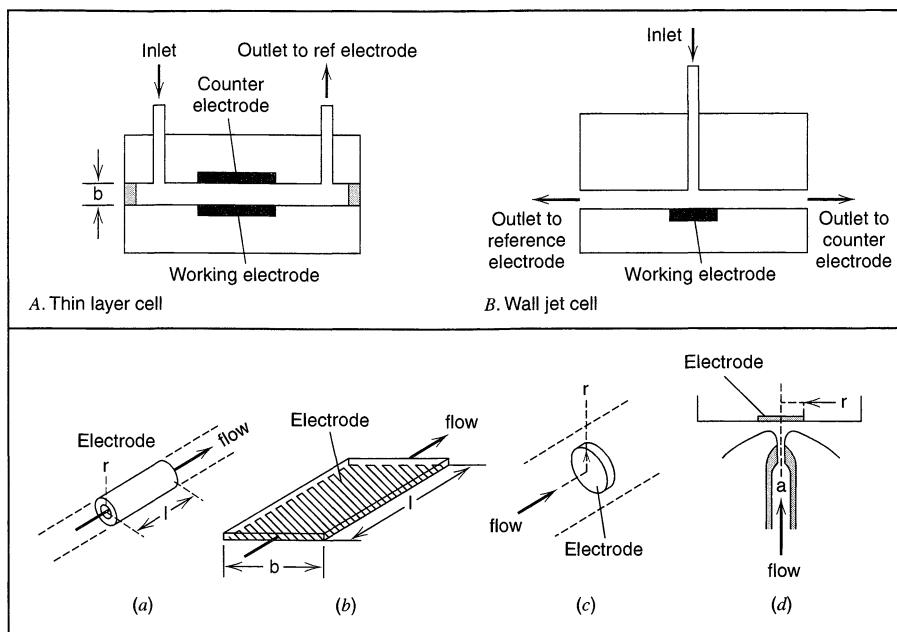
Figure 11.6.5 Typical cell arrangements and electrode geometries for electrochemical flow cells. *Top*: (*A*) Thin-layer cell. (*B*) Wall-jet cell. *Bottom*: Various electrode geometries: (a) tubular electrode; (b) planar electrode with parallel flow; (c) planar electrode with perpendicular flow; (d) wall-jet electrode. [Reprinted from H. Gunasingham and B. Fleet, *Electroanal. Chem.*, **16**, 89 (1989), by courtesy of Marcel Dekker, Inc.]

the methodology discussed in Chapter 9 (51, 52), and the general equations for the mass-transfer-limited currents for different cell geometries are given in Table 11.6.1.

A large number of particular cell designs and electrode materials have been proposed (46). Two thin-layer cell arrangements are shown in Figure 11.6.6. Electrode materials are frequently different forms of carbon (e.g., carbon paste or glassy carbon), or Pt, Au, or Hg, although other metals, such as Cu, Ni, and Pb find application for particular analyses (e.g., amino acids, carbohydrates). Within the basic thin-layer design format, one has different choices as to the placement of the reference and auxiliary electrodes (Figure 11.6.7).

TABLE 11.6.1   Limiting Currents for Different Cell Geometries[a]

Electrode Geometry	Limiting Current Equation[b]
Tubular	$i = 1.61nFC(DA/r)^{2/3}v^{1/3}$
Planar, parallel flow in channel	$i = 1.47nFC(DA/b)^{2/3}v^{1/3}$
Planar, perpendicular flow	$i = 0.903nFCD^{2/3}v^{-1/6}A^{3/4}U^{1/2}$
Wall jet	$i = 0.898nFCD^{2/3}v^{-5/12}a^{-1/2}A^{3/8}v^{3/4}$

[a] Adapted from J. M. Elbicki, D. M. Morgan, and S. G. Weber, *Anal. Chem.*, **56**, 978 (1984). See Figure 11.6.5 for illustration of types.

[b] a = diameter of jet inlet, A = electrode area, b = channel height, C = concentration, D = diffusion coefficient, v = kinematic viscosity, r = radius of tubular electrode, v = average volume flow rate (cm^3/s), U = flow velocity (cm/s).
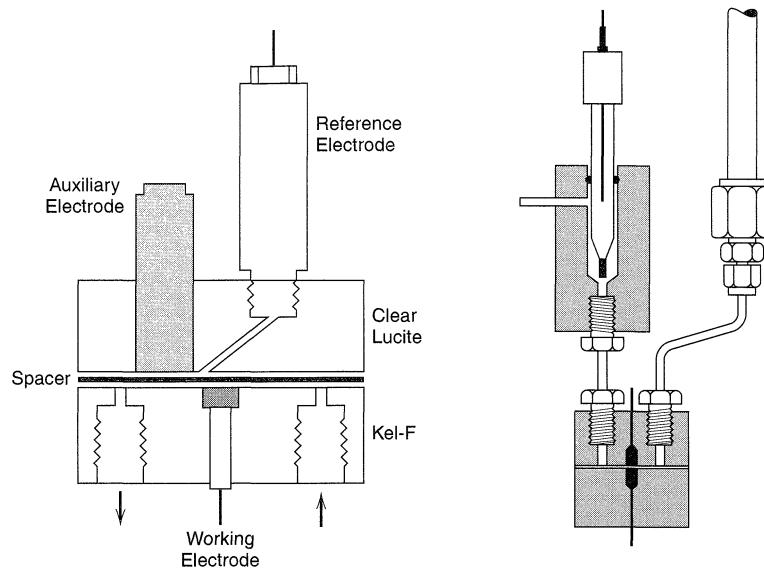
Figure 11.6.6 Thin-layer LC detector cells. *Left*: Cell with auxiliary and reference electrodes in thin-layer portion downstream from working electrode. [Reprinted from J. A. Wise, W. R. Heineman and P. T. Kissinger, *Anal. Chim. Acta*, **172**, 1 (1985), with permission from Elsevier Science.] *Right*: Cell with facing working and auxiliary electrodes and reference electrode downstream in flow channel. [Courtesy of Bioanalytical Systems, Inc.]

The design in Figure 11.6.7*A* is the simplest, but produces a nonuniform current distribution across the electrode surface and high uncompensated resistive drop to the reference electrode. The design in Figure 11.6.7*B* produces a uniform current density, but still shows uncompensated resistive drop. In this arrangement, potentially interfering products could be formed at the auxiliary electrode and react at the detector working electrode to produce an unwanted current. However, such interference will not occur if the flow velocity is sufficiently high to carry the detected electroactive species through the cell in a short time compared to the time needed for the working electrode-generated product to diffuse across the cell (perpendicular to the solution flow direction). At the expense of greater complexity in cell design and maintenance, a separator membrane can be added between the two parallel electrodes, as shown in Figure

PARALLEL PLATE FLOW CELLS
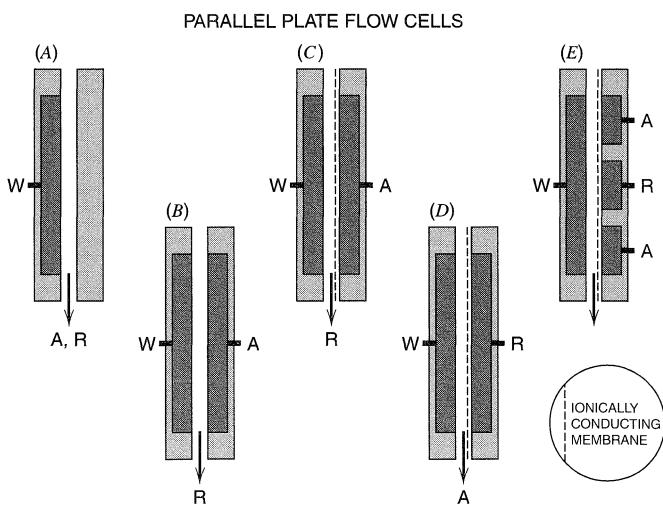
Figure 11.6.7 Different geometries for thin-layer electrochemical detector cells involving different placements of the working (W), auxiliary (A) and reference (R) electrodes. [Reprinted from S. M. Lunte, C. E. Lunte, and P. T. Kissinger, in "Laboratory Techniques in Electroanalytical Chemistry," 2nd ed., P. T. Kissinger and W. R. Heineman, Eds., Marcel Dekker, New York, 1996, by courtesy of Marcel Dekker, Inc.]

11.6.7C. In principle the reference electrode can be placed nearer the working electrode, as shown in Figures 11.6.7D and E, but this is difficult with conventional reference electrodes.

The simplest electrochemical technique for use in LC cells is amperometry, where the working electrode potential is fixed at a value where the compounds of interest are oxidized or reduced, and they are detected by the current flow as they pass from the chromatographic column to the cell (Figure 11.6.8). A key issue is sensitivity, which is related to the current produced by the electroactive eluent compared to the background current at the electrode from impurities and solvent processes. A detection limit at about the 0.1 pmol level can be achieved for oxidizable substances. Higher detection limits, at the 1 pmol level, are found with reducible substances because of higher background currents from oxygen reduction and other processes. Amplification of the response is possible when the cell configuration is that in Figure 11.6.7B and the redox couple is reversible. In this case, the detector behaves as a thin-layer cell (Section 11.7), and the reaction at electrode A (e.g., $O + e \rightarrow R$) is just the reverse of that at W (e.g., $R - e \rightarrow O$). Many more electrons are passed per molecule of R in this redox cycling than for detection at a single electrode. The efficiency of the cycling depends upon the flow rate and the spacing between electrodes A and W (53).

Greater selectivity and better information for qualitative identification can be obtained with the detector electrode operated in the voltammetric mode, where its potential is scanned over a given potential window during elution. However, the detection limits
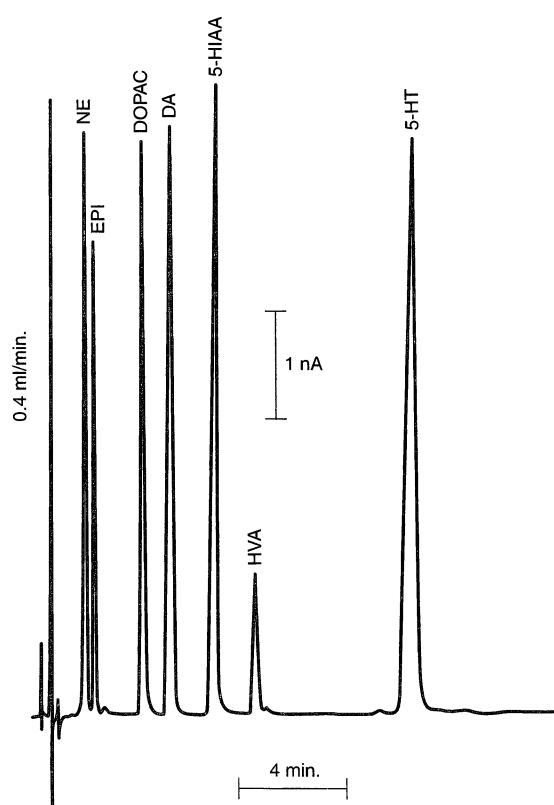
Figure 11.6.8 Liquid chromatographic separation of tryptophan and tyrosine metabolites using amperometric detection with a glassy carbon working electrode at 0.65 V *vs.* Ag/AgCl in a thin-layer cell. NE, norepinephrine; EPI, epinephrine; DOPAC, 3,4-hydroxyphenylacetic acid; DA, dopamine; 5-HIAA, 5-hydroxyindole-3-acetic acid; HVA, homovanillic acid; 5-HT, serotonin (5-hydroxytryptamine). [From T. Huang and P. T. Kissinger, *Curr. Separations*, **14**, 114 (1996), with permission.]

are much higher in the voltammetric mode because of the large background current, which arises partly from double-layer charging, but also very significantly from slow faradaic processes associated with adaptation of the electrode surface to a changing potential. [See the related footnote in Section 7.3.2(d)]. The situation can be improved by use of square wave or staircase voltammetric approaches, but the best sensitivity is always associated with an electrode operating at a fixed potential in a mobile phase of unchanging composition.

An alternative approach is to utilize cells with dual working electrodes maintained at different potentials (53), monitoring the current at each simultaneously (Figure 11.6.9). If the electrodes are placed side-by-side, perpendicular to the solution flow (*parallel* arrangement), each is exposed to the same sample components, with one used to establish a background current level and the other to detect the species of interest. The electrode can also be arranged along the direction of solution flow, in a manner similar to the cells in Section 11.6.3 (*series* arrangement). In this case the downstream working electrode monitors (*collects*) products from the upstream one. This can be used to improve selectivity by detecting products that show better separations in potential than the original eluted compounds. It can also discriminate between compounds that produce electroactive products from those that do not.

An important problem with such flow cells is electrode fouling with continued use. Although the LC column is effective in removing some impurities that can foul the electrode surface, sometimes the electrode reaction itself, such as in the oxidation of phenols, will form insulating layers on the electrode surface. In such a case it is frequently neces-
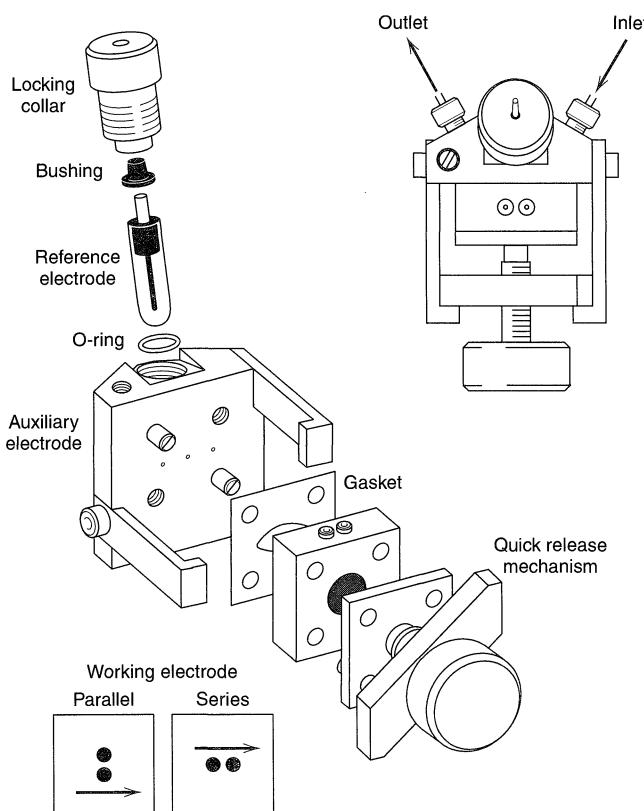
Figure 11.6.9 Cell with dual working electrodes and cross-flow design [Reprinted from S. M. Lunte, C. E. Lunte, and P. T. Kissinger, in "Laboratory Techniques in Electroanalytical Chemistry," 2nd ed., P. T. Kissinger and W. R. Heineman, Eds., Marcel Dekker, New York, 1996, by courtesy of Marcel Dekker, Inc.]

sary to clean the electrodes by cycling the potential between anodic and cathodic limits or to use other types of potential programs to obtain reproducible behavior. Such cycling can oxidize and desorb surface impurities and return the electrode surface to a reproducible state. Automated operation in this mode is sometimes called *pulsed amperometric detection* (PAD) (54–56).

Analogous detector cells can be used in flow injection and CZE measurements. However, CZE cell design is more complicated because of the very small volumes needed and the presence of a high applied electric field and the associated current flow that drives the electrophoretic separation. The detector electrodes are usually carbon fiber UMEs that are placed outside of the electrophoresis field (57, 58).

▷ 11.7 THIN-LAYER ELECTROCHEMISTRY

11.7.1 Introduction

An alternative approach to obtaining bulk electrolysis conditions and a large A/V ratio, even with no convective mass transfer, involves decreasing V, so that a very small solution volume (a few μL) is confined to a thin layer (2–100 μm) at the electrode surface. A schematic diagram of a thin-layer cell and some typical actual cell configurations are shown in Figure 11.7.1. As long as the cell thickness, l, is smaller than the diffusion layer thickness for a given experimental time, that is, $l << (2Dt)^{1/2}$, mass transfer within the cell can be neglected, and special bulk electrolysis equations result. At shorter times, dif-

(a)

(b)
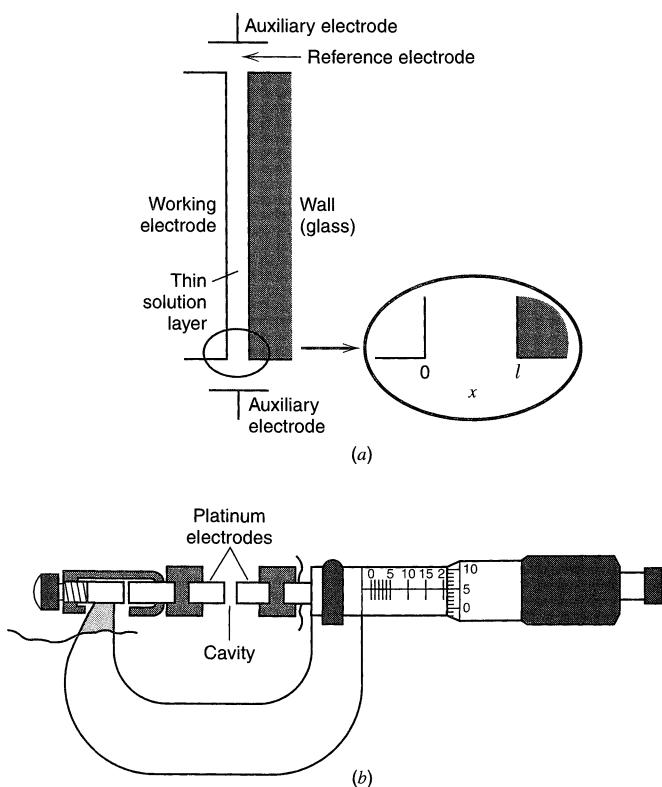
Figure 11.7.1 (*a*) Schematic diagram of a single-electrode thin-layer cell. (*b*) Micrometer, twin-electrode thin-layer cell with adjustable solution layer thickness.

(c)

(d)
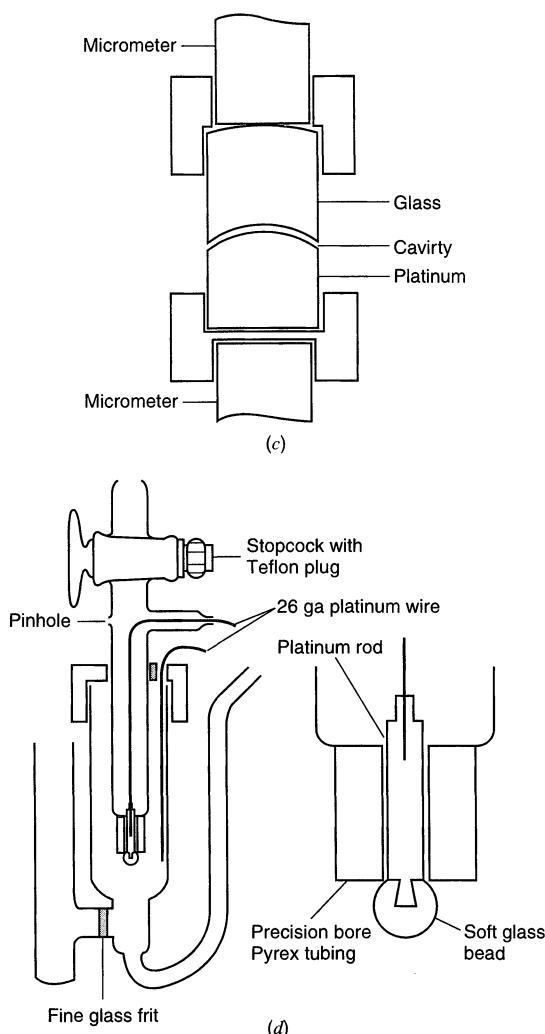
Figure 11.7.1 Continued (c) Close-up of electrode portion for single-electrode configuration of (b). (d) Capillary-wire single-electrode thin-layer electrode. The solution layer is contained in the small space between the metal rod and the inner surface of the precision-bore capillary. The layer thickness is typically 2.5×10^{-3} cm. The metal rod may be positioned within the capillary to a high degree of concentricity by machining three small flanges onto the surface of the rod near each end. Highly reproducible rinsing and filling are accomplished by alternately applying and releasing nitrogen pressure with the stopcock. [From A. T. Hubbard and F. C. Anson, *Electroanal. Chem.*, **4**, 129 (1970), by courtesy of Marcel Dekker, Inc.]

fusion in the cell must be considered. Thin-layer electrochemical cells were first utilized in the early 1960s, and their theory and applications have been reviewed in depth (59–64).

11.7.2 Potential Step (Coulometric) Methods

Consider the twin-working-electrode, thin-layer cell (Figure 11.7.1b), with the potential stepped from a value E_1, where no current flows, to E_2, where the reaction $O + ne \rightarrow R$ is virtually complete and the concentration of O at the electrode surface is essentially zero. To obtain the current-time behavior and the concentration profile one must solve the diffusion equation

$$\frac{\partial C_O(x, t)}{\partial t} = D_O\left(\frac{\partial^2 C_O(x, t)}{\partial x^2}\right) \tag{11.7.1}$$

with the boundary conditions

$$C_O(x, 0) = C_O^* \qquad\qquad t = 0; 0 \le x \le l \tag{11.7.2}$$

$$C_O(0, t) = C_O(l, t) = 0 \qquad t > 0 \tag{11.7.3}$$

Note that in this case the semi-infinite boundary condition used for the analogous experiment in Section 5.2 has been replaced by the condition for C_O at l. Solution of these equations by the Laplace transform method yields (63)[5]

$$C_O(x, t) = \frac{4C_O^*}{\pi} \sum_{m=1}^{\infty} \left(\frac{1}{2m-1}\right) \exp\left[\frac{-(2m-1)^2\pi^2D_Ot}{l^2}\right] \sin\frac{(2m-1)\pi x}{l} \qquad (11.7.4)$$

At later times, the concentration profile can be obtained from consideration of only the $m = 1$ term, since the $(2m - 1)^2$ factor in the exponential causes the terms for $m = 2$, $3, \ldots$ to be small for $\pi^2 D_O t/l^2 \gg 1$. Then

$$C_O(x, t) \approx \frac{4C_O^*}{\pi} \exp\left(\frac{-\pi^2D_Ot}{l^2}\right) \sin\frac{\pi x}{l} \qquad (11.7.5)$$

Typical concentration profiles are as given in Figure 11.7.2a.
  With A including both active surfaces,

$$i(t) = nFAD_O\left[\frac{\partial C_O(x, t)}{\partial x}\right]_{x=0} \qquad (11.7.6)$$

$$i(t) = \frac{4nFAD_OC_O^*}{l} \sum_{m=1}^{\infty} \exp\left[\frac{-(2m-1)^2\pi^2D_Ot}{l^2}\right] \qquad (11.7.7)$$

or at later times,

$$i(t) \approx i(0) \exp(-pt) \qquad (11.7.8)$$

with

$$p = \frac{\pi^2D_O}{l^2} = \frac{\pi^2D_OA}{Vl} = \frac{m_OA}{V}$$

$$m_O = \frac{\pi^2D_O}{l} \quad \text{and} \quad i(0) = \frac{4nFAC_O^*m_O}{\pi^2}$$

Note that the form of (11.7.8) is the same as (11.3.7), which would be followed for the thin-layer cell if the concentration within the cell could be considered completely uniform
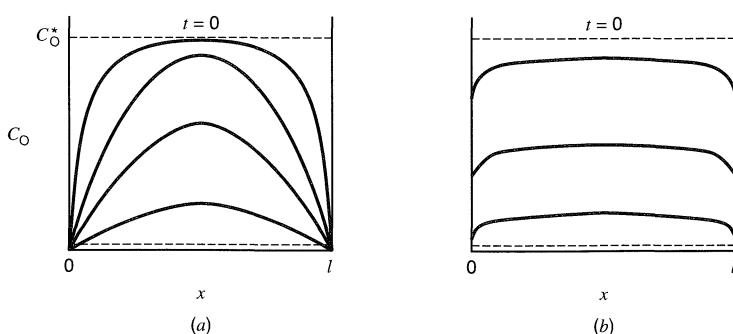
Figure 11.7.2
Concentration of O during reduction of O in twin-electrode thin-layer cell.
(a) Actual profiles.
(b) Neglecting mass transfer in cell.

---

[5]For a thin-layer cell with the solution constrained between a single working electrode and inert boundary, as in Figure 11.7.1a, the condition at the inert boundary is $[\partial C_O(x, t)/\partial x]_{x=l} = 0$.

throughout the electrolysis (as in Figure 11.7.2*b*). Finally, the total charge passed by the electrolytic reaction is

$$Q(t) = nFVC_O^* \left\{ 1 - \frac{8}{\pi^2} \sum_{m=1}^{\infty} \left(\frac{1}{2m-1} \right)^2 \exp\left[\frac{-(2m-1)^2\pi^2 D_O t}{l^2} \right] \right\} \quad (11.7.9)$$

$$Q(t) \approx nFVC_O^* \left(1 - \frac{8}{\pi^2} e^{-pt} \right) \qquad \text{(later times)} \qquad (11.7.10)$$

$$Q(t \to \infty) = nFVC_O^* = nFN_O \qquad (11.7.11)$$

Equation 11.7.11 is the same as the coulometry equation (11.3.11), and it indicates that determinations of N_O or n are possible without the necessity of knowing D_O. The electrolysis rate constant in a thin-layer cell, p, can be quite large. For example, for $D = 5 \times 10^{-6}$ cm^2/s and $l = 10^{-3}$ cm, $p = 49$ s^{-1} and the electrolysis will be 99% complete in less than 0.1 s. In actual experiments the measured charge will be larger than that given by (11.7.9) to (11.7.11), because contributions from double-layer charging, electrolysis of adsorbed species, and background reactions will be included (see Section 14.3.7)

11.7.3 Potential Sweep Methods

Consider again the reaction and initial conditions of Section 11.7.2, but now for the situation where the working electrode potential is swept from an initial value E_i, where no reaction occurs, toward negative values. Under conditions where the concentrations of O and R can be considered uniform $[C_O(x, t) = C_O(t)$ and $C_R(x, t) = C_R(t)$ for $0 \le x \le l]$, the current is given, as in (11.3.4), by

$$i = -nFV \left[\frac{dC_O(t)}{dt} \right] \qquad (11.7.12)$$

For a nernstian reaction,

$$E = E^{0'} + \frac{RT}{nF} \ln \frac{C_O(t)}{C_R(t)} \qquad (11.7.13)$$

$$C_O^* = C_O(t) + C_R(t) \qquad (11.7.14)$$

Combination of these two equations yields

$$C_O(t) = C_O^* \left\{ 1 - \left[1 + \exp\left(\frac{nF}{RT}(E - E^{0'}) \right) \right]^{-1} \right\} \qquad (11.7.15)$$

Differentiation of (11.7.15) and substitution into (11.7.12), with the sweep rate, v, recognized as $-(dE/dt)$, yields the expression for the current:

$$i = \frac{n^2F^2vVC_O^*}{RT} \frac{\exp\left[\left(\frac{nF}{RT} \right)(E - E^{0'}) \right]}{\left\{ 1 + \exp\left[\left(\frac{nF}{RT} \right)(E - E^{0'}) \right] \right\}^2} \qquad (11.7.16)$$

The peak current occurs at $E = E^{0'}$ and is given by

$$i_p = \frac{n^2F^2vVC_O^*}{4RT} \qquad (11.7.17)$$

A typical scan voltammogram in a thin-layer cell is shown in Figure 11.7.3. Note that the peak current is directly proportional to v, but the total charge under the i-E curve, given by (11.7.11), is independent of v.

The rigorous solution for this problem, accounting for nonuniform concentrations within the cell, can be derived (63). It has been shown that the approximate form, (11.7.16), will hold at sufficiently small values of v, that is, when

$$|v| \le \frac{RT}{nF} \frac{\pi^2 D}{3l^2} \log\left(\frac{1 - \varepsilon}{1 + \varepsilon}\right) \tag{11.7.18}$$

where ε is the relative error tolerated in calculation of i_p.

For a totally irreversible one-step, one-electron reaction, the current is given by

$$\frac{i}{FA} = k_f C_O(t) \tag{11.7.19}$$

where $k_f = k^0 \exp[(-\alpha F/RT)(E - E^{0'})]$.

By combining (11.7.19) with (11.7.12) we obtain

$$\frac{dC_O(t)}{dt} = -\left[\frac{A k_f(t)}{V}\right] C_O(t) \tag{11.7.20}$$

In a potential sweep experiment, $E(t) = E_i - vt$ (see equation 6.2.1); therefore, with $f = F/RT$,

$$k_f(t) = k^0 \exp[-\alpha f(E_i - E^{0'})] \exp(\alpha f v t) \tag{11.7.21}$$

By substitution of (11.7.21) into (11.7.20) and integration between $t = 0$ ($C_O = C_O^*$) and t [$C_O = C_O(t)$], under the conditions that $k^0 \exp[-\alpha f(E_i - E^{0'})] \to 0$ (i.e., an initial po-
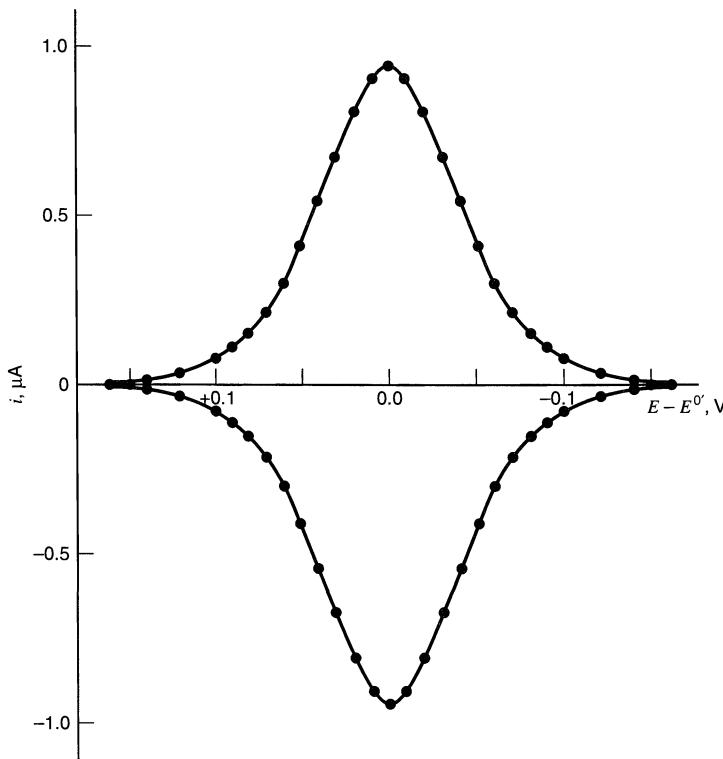
Figure 11.7.3 Cyclic current-potential curve for a nernstian reaction with $n = 1$, $V = 1.0\ \mu L$, $|v| = 1$ mV/s, $C_O^* = 1.0$ mM, $T = 298$ K. [From A. T. Hubbard and F. C. Anson, *Electroanal. Chem.*, **4**, 129 (1970), by courtesy of Marcel Dekker, Inc.]
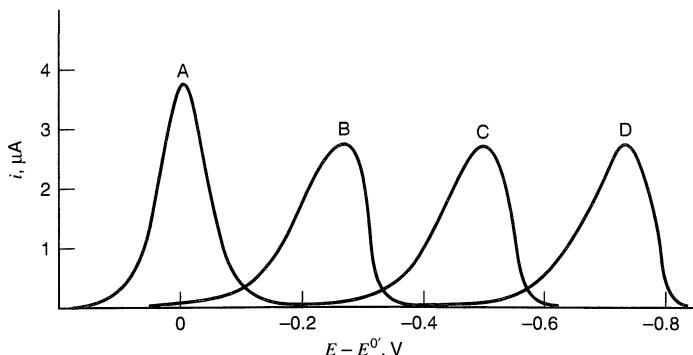
Figure 11.7.4 Theoretical cathodic current-potential curves for one-step, one-electron irreversible reactions according to (11.7.24) for several values of k^0. *Curve A*: reversible reaction (shown for comparison). *Curve B*: $k^0 = 10^{-6}$. *Curve C*: $k^0 = 10^{-8}$. *Curve D*: $k^0 = 10^{-10}$ cm/s. The values assumed in making the plots were $|v| = 2$ mV/s, $A = 0.5$ cm^2, $C_O^* = 1.0$ mM, $\alpha = 0.5$, $V = 2.0$ μL. [From A. T. Hubbard, *J. Electroanal. Chem.*, **22**, 165 (1969), with permission.]

tential well positive of $E^{0'}$), the following expressions for $C_O(E)$ and $i(E)$ are obtained (63, 64):

$$C_O(E) = C_O^* \exp\left(\frac{-RT}{\alpha F}\frac{Ak_f}{Vv}\right) \tag{11.7.22}$$

$$i(E) = FAk_f C_O^* \exp\left(\frac{-RT}{\alpha F}\frac{Ak_f}{Vv}\right) \tag{11.7.23}$$

or, substituting for k_f,

$$i(E) = FAk^0 C_O^* \exp\left\{-\alpha f(E - E^{0'}) - \frac{Ak^0}{\alpha f Vv}\exp[-\alpha f(E - E^{0'})]\right\} \tag{11.7.24}$$

Typical i-E curves for a totally irreversible reduction of O to R in a thin-layer cell are shown in Figures 11.7.4 and 11.7.5. The peak potential [obtained by differentiating (11.7.24) and setting the result equal to zero] occurs at

$$E_{pc} = E^{0'} + \frac{RT}{\alpha F}\ln\left(\frac{ARTk^0}{\alpha F Vv}\right) \tag{11.7.25}$$
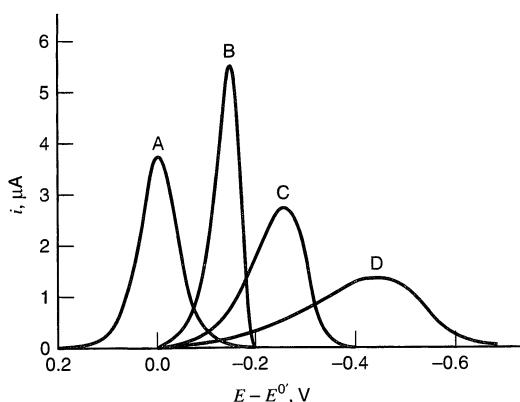
Figure 11.7.5 Theoretical cathodic current-potential curves for one-step, one-electron irreversible reactions for several values of α. *Curve A*: reversible reaction. *Curve B*: $\alpha = 0.75$, $k^0 = 10^{-6}$ cm/s. *Curve C*: $\alpha = 0.5$, $k^0 = 10^{-6}$ cm/s. *Curve D*: $\alpha = 0.25$, $k^0 = 10^{-6}$ cm/s. The values assumed in making the graphs were: $|v| = 2$ mV/s, $A = 0.5$ cm^2, $C_O^* = 1.0$ mM, $V = 2.0$ μL. [From A. T. Hubbard, *J. Electroanal. Chem.*, **22**, 165 (1969), with permission.]

The peak current is still proportional to v and C_O^* and is

$$i_{pc} = \frac{\alpha F^2 V v C_O^*}{2.718RT}$$

(11.7.26)

Thin-layer methods have been suggested for determination of kinetic parameters of electrode reactions (63–65), but they have not been widely used for this purpose. A difficulty in these methods, especially when nonaqueous solutions or very low supporting electrolyte concentrations are employed, is the high resistance of the thin layer of solution. Since the reference and auxiliary electrodes are placed outside the thin-layer chamber, one can have seriously nonuniform current distributions and high uncompensated iR drops (producing for example, nonlinear potential sweeps) (66, 67). Although cell designs that minimize this problem have been devised (63, 64), careful control of the experimental conditions is required in kinetic measurements. Thin-layer cells have been applied in a number of electrochemical studies, including investigations of adsorption, electrodeposition, complex reaction mechanisms, and n-value determinations. They have also become very popular in spectroelectrochemical studies (see Chapter 17).

The theory and mathematical treatments used for thin-layer cells find application in other electrochemical problems. For example, the deposition of metals (as amalgams) into thin films of mercury and their subsequent stripping (Section 11.8) is fundamentally a thin-layer problem. Similarly the electrochemical oxidation or reduction of thin films (e.g., oxides, adsorbed layers, and precipitates) follows an analogous treatment (see Section 14.3). Thin-layer concepts are also directly applicable to synthetically modified electrodes featuring electroactive species bound to the surface (Chapter 14). In many problems involving surface films, mass transfer truly is negligible over wide time domains and problems with uncompensated resistance are minimal; thus relatively fast experiments can be performed. Finally, the observed behavior with a scanning electrochemical microscope (Section 16.4), where electrochemistry is examined in the gap between an electrode (tip) and a conducting or insulating substrate can be thought of as that of a leaky thin-layer cell.

▷ 11.8 STRIPPING ANALYSIS

11.8.1 Introduction

Stripping analysis is an analytical method that utilizes a bulk electrolysis step (*preelectrolysis*) to preconcentrate a substance from solution into the small volume of a mercury electrode (a hanging mercury drop or a thin film) or onto the surface of an electrode. After this electrodeposition step, the material is redissolved ("stripped") from the electrode using some voltammetric technique (most frequently LSV or DPV). If the conditions during the preelectrolysis step are maintained constant, exhaustive electrolysis of the solution is not necessary and, by proper calibration and with fixed electrolysis times, the measured voltammetric response (e.g., peak current) can be employed to find the solution concentration. This process is represented schematically in Figure 11.8.1. The major advantage of the method, as compared to direct voltammetric analysis of the original solution, is the preconcentration of the material to be analyzed on or within the electrode (by factors of 100 to >1000), so that the voltammetric (stripping) current is less perturbed by charging or residual impurity currents. The technique is especially useful for the analysis of very dilute solutions (down to 10^{-10} to 10^{-11} M). Stripping analysis is most frequently used for the determination of metal ions by cathodic deposition, fol-
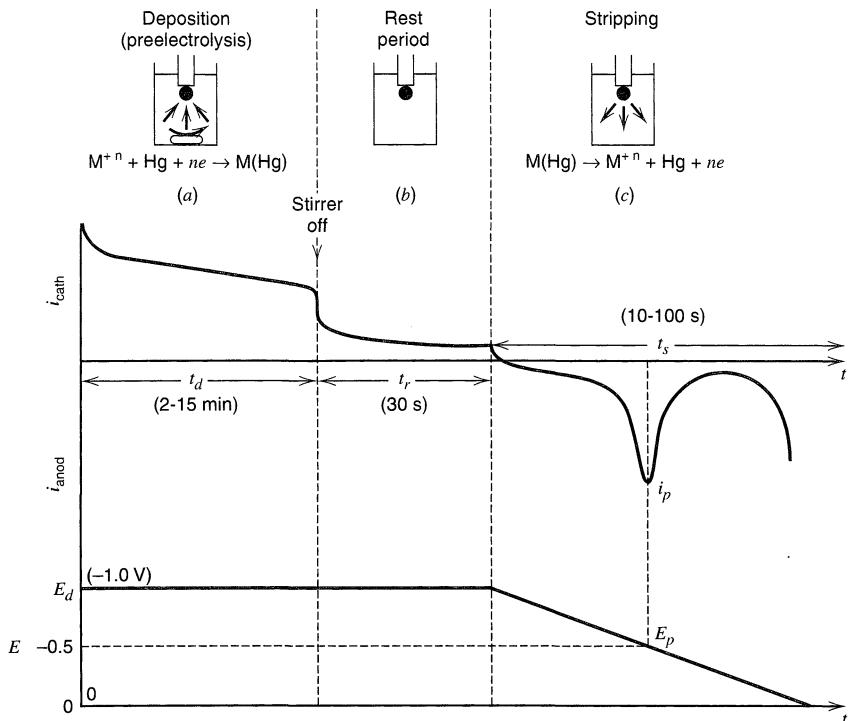
Figure 11.8.1 Principle of anodic stripping. Values shown are typical ones used; potentials and E_p are typical of Cu^{2+} analysis. (*a*) Preelectrolysis at E_d; stirred solution. (*b*) Rest period; stirrer off. (*c*) Anodic scan ($v = 10$–100 mV/s). [Adapted from E. Barendrecht, *Electroanal. Chem.*, **2**, 53 (1967), by courtesy of Marcel Dekker, Inc.]

lowed by anodic stripping with a linear potential scan and, therefore, is sometimes called *anodic stripping voltammetry* (ASV) or, less frequently, *inverse voltammetry*. The basic theoretical principles and some typical applications will be described here. Several complete reviews describing the history, theory, and experimental methodology of this technique have appeared (68–74).

11.8.2 Principles and Theory

The mercury electrode used in stripping analysis is either a conventional HMDE or a mercury film electrode (MFE). In current practice, the MFE is typically deposited onto a rotating glassy carbon or wax-impregnated graphite disk. One usually adds mercuric ion (10^{-5}–10^{-4} M) directly to the analyte solution, so that during the preelectrolysis, the mercury codeposits with the species to be determined. The resulting mercury films are often less than 100 Å thick. Since the MFE has a much smaller volume than the HMDE, the MFE shows a higher sensitivity. There is evidence that mercury electrodes with platinum contacts dissolve some platinum on prolonged contact, with possible deleterious effects; hence platinum is usually avoided. Solid electrodes (e.g., Pt, Ag, C) are used (less frequently) without mercury for ions that cannot be determined at mercury (e.g., Ag, Au, Hg).

The *electrodeposition step* is carried out in a stirred solution at a potential E_d, which is several tenths of a volt more negative than $E^{0'}$ for the least easily reduced metal ion to be determined. The relevant equations generally follow those for a bulk electrolysis (see

Section 11.3.1). However, since the electrode area is so small, and t_d is much smaller than the time needed for exhaustive electrolysis, the current remains essentially constant (at i_d) during this step, and the number of moles of metal deposited is then $i_d t_d / nF$. Because the electrolysis is not exhaustive, the deposition conditions (stirring rate, t_d, temperature) must be the same for the sample and standards to achieve high accuracy and precision.

With an HMDE, one observes a *rest period*, when the stirrer is turned off, the solution is allowed to become quiescent, and the concentration of metal in the amalgam becomes more uniform. The *stripping step* is then carried out by scanning the potential linearly toward more positive values.

When an MFE is used, the stirring during deposition is controlled by rotation of the substrate disk. A rest period usually is not observed, and rotation continues during the stripping step.

The behavior governing the *i-E* curve during the anodic scan depends on the type of electrode employed. For an HMDE of radius r_0, the concentration of reduced form, M, at the start of the scan is uniform throughout the drop and is given by

$$C_M^* = \frac{i_d t_d}{nF(4/3)\pi r_0^3} \tag{11.8.1}$$

When the sweep rate v is sufficiently high that the concentration in the middle of the drop ($r = 0$) remains at C_M^* at the completion of the scan, then the behavior is essentially that of semi-infinite diffusion and the basic treatment of Section 6.2 applies (75). Correction must be made for the sphericity of the drop [see (6.2.23)]. In this case the spherical correction term must be subtracted from the planar term, since the concentration gradient builds up inside the drop and the area of the extended diffusion field decreases with time. Thus, the equations that apply for a reversible stripping reaction at the HMDE are (75)

$$i = nFAC_M^* \left[(\pi D_M \sigma)^{1/2} \chi(\sigma t) - \frac{D_M \phi(\sigma t)}{r_0} \right] \tag{11.8.2}$$

$$i_p = AD_M^{1/2} C_M^* \left[(2.69 \times 10^5) n^{3/2} v^{1/2} - \frac{(0.725 \times 10^5) n D_M^{1/2}}{r_0} \right] \tag{11.8.3}$$

where i_p is in A, A in cm^2, D_M in cm^2/s, C_M^* in mol/cm^3, v in V/s, and r_0 in cm; the functions $\chi(\sigma t)$ and $\phi(\sigma t)$, where $\sigma = nFv/RT$, are tabulated in Table 6.2.1. These equations hold for the usual HMDE for $v > 20$ mV/s, and clearly, under these conditions, a large fraction of the deposited metal remains in the drop. A comparison of the *i-E* curve predicted by (11.8.2) and a typical experimental stripping voltammogram at an HMDE is shown in Figure 11.8.2 (76). At very large scan rates the spherical term becomes negligible and linear diffusion scan behavior, with i_p proportional to $v^{1/2}$, results. Practical stripping measurements are usually carried out in this regime. At smaller rates, when the diffusion layer thickness exceeds r_0, the finite electrode volume and depletion of M at $r = 0$ must be considered. At the limit of very small v, when the drop is completely depleted of M during the scan, the behavior approaches that of a thin-layer cell or MFE (see below) with i_p proportional to v.

Because the volume and thickness of the mercury film on an MFE are small, the stripping behavior with this electrode follows thin-layer behavior more closely (see Section 11.7), and depletion effects predominate. The theoretical treatment for the MFE has appeared (77, 78); a diagram of the model employed is shown in Figure
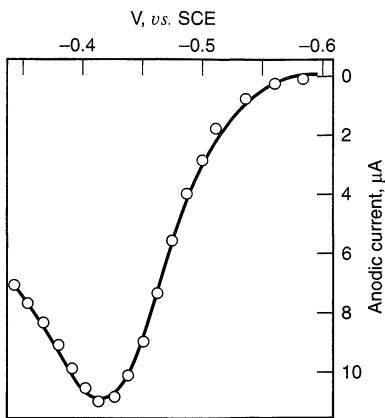
Figure 11.8.2 Experimental anodic stripping *i-E* curve for thallium. Experimental conditions: $1.0 \times 10^{-5} M$ Tl^+, $0.1 M$ KCl solution, $E_d = -0.7$ V *vs.* SCE, $t_d = 5$ min, $v = 33.3$ mV/s. Circles are theoretical points calculated from (11.8.2). [Reprinted with permission from I. Shain and J. Lewinson, *Anal. Chem.*, **33**, 187 (1961). Copyright 1961, American Chemical Society.]

11.8.3. If the stripping reaction is assumed to be reversible, the Nernst equation holds at the surface:

$$C_{M^{+n}}(0, t) = C_M(0, t) \exp\left[\frac{nF}{RT}(E_i - E^{0'} + vt)\right] \qquad (11.8.4)$$

The solution of the diffusion equations with this condition and the initial and boundary conditions shown in Figure 11.8.3 leads to an integral equation that must be solved numerically. Typical results for i_p for films of different thicknesses, l, as a function of v are shown in Figure 11.8.4*a*. At small v and l, thin-layer behavior predominates and $i_p \propto v$. For high v and large l, semi-infinite linear diffusion behavior predominates and $i_p \propto v^{1/2}$. The limits of these zones are shown in Figure 11.8.4*b*. MFEs used in current practice fall within the region where thin-layer behavior can be expected for virtually all usual sweep rates ($\leq$500 mV/s). An approximate equation for the peak current in the thin-layer region based on a diffusion layer approximation in solution has also been proposed (79):

$$|i_p| = \frac{n^2 F^2 |v| lAC_M^*}{2.7RT} \qquad (11.8.5)$$

Notice the similarity between this expression and the corresponding limiting thin-layer equation (11.7.17) (where $Al = V$).
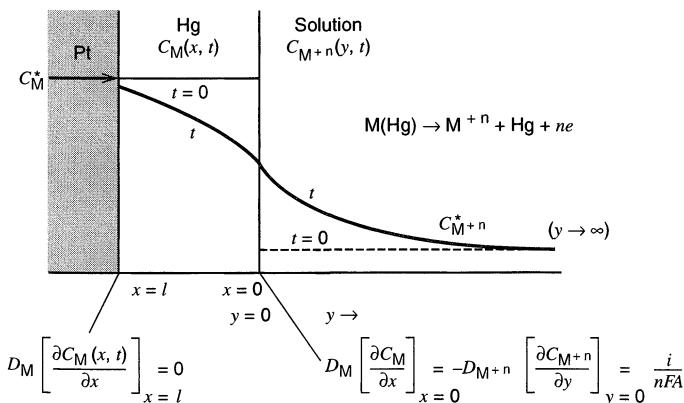
Figure 11.8.3 Notation, initial conditions, and boundary conditions for theoretical treatment of MFE.
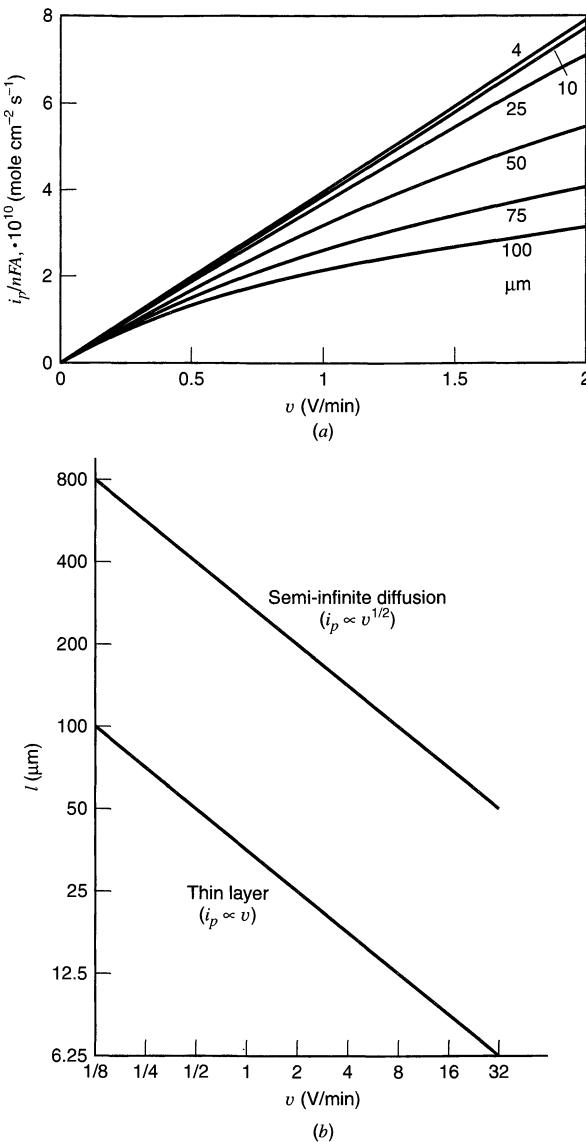
Figure 11.8.4 (*a*) Calculated variation of peak current with scan rate for different thickness of MFE. (*b*) Zones where semi-infinite diffusion and thin-layer equations apply at MFE. [From W. T. de Vries, *J. Electroanal. Chem.*, **9**, 448 (1965), with permission.]

11.8.3 Applications and Variations

The technique of controlled-potential cathodic deposition followed by anodic stripping with a linear potential sweep has been applied to the determinations of a number of metals (e.g., Bi, Cd, Cu, In, Pb, and Zn) either alone or in mixtures (Figure 11.8.5). An increase in sensitivity can be obtained by using pulse polarographic, square wave, or coulostatic stripping techniques. Other variants, such as stripping by a potential step, current step, or more elaborate programs (e.g., an anodic potential step for a short time followed by a cathodic sweep) have also been proposed (68–74).

Important interferences that sometimes occur with mercury electrodes involve (a) reactions of the metals with the substrate material (e.g., Pt or Au) or with the mercury (e.g., Ni–Hg), or (b) formation of an intermetallic compound between two metals deposited into the mercury at the same time (e.g., Cu–Cd or Cu–Ni). These effects are much
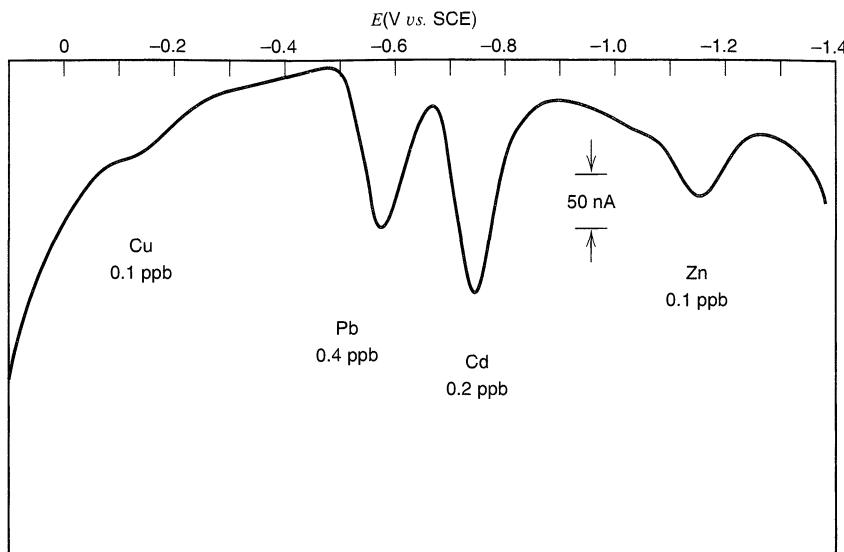
Figure 11.8.5 Anodic stripping analysis of a solution containing 2×10^{-9} M Zn, Cd, Pb, and Cu at an MFE (mercury-plated, wax-impregnated graphite electrode). Stripping carried out by differential pulse voltammetry.

more serious with mercury films than with hanging drops, because MFEs feature fairly concentrated amalgams and a high ratio of substrate area to film volume. They can be overriding concerns in the choice between an MFE and an HMDE.

On the other hand, MFEs offer much better sensitivity in linear sweep stripping and better control of mass transfer during the deposition step. If an HMDE is chosen (e.g., to reduce interferences), one can use differential pulse stripping to obtain sensitivities comparable to those attained by LSV at an MFE.

Since stripping at an MFE gives total exhaustion of the thin film, the voltammetric peaks are narrow and can allow baseline resolution of multicomponent systems. Thin-layer properties and the sharpness of the peaks permit relatively fast stripping sweeps, which in turn shorten analysis times. In contrast, the falloff in current past the peak in a stripping voltammogram obtained at an HMDE comes from diffusive depletion, rather than exhaustion, and it continues for quite some time. Thus the peaks are broader, and overlap of adjacent peaks is more serious. (Compare, for example, Figures 11.8.6*a* and 11.8.6*d*.) This problem is usually minimized for the HMDE by using slow sweep rates, at a cost of lengthened analysis time.

Cathodic stripping analysis can also be carried out for species (usually anions) that deposit in an anodic preelectrolysis. For example, the halides (X^-) can be determined at mercury by deposition as Hg_2X_2. Deposition on solid electrodes is also possible. In this case, surface problems (e.g., oxide films) and underpotential deposition effects often appear. On the other hand, the sensitivity for stripping from a solid electrode is very high, since the deposit can be removed completely, even at high scan rates. Stripping of films has often been used to determine the thickness of coatings (e.g., Sn on Cu) and oxide layers (e.g., CuO on Cu).[6]

---

[6]In fact, one of the earliest electroanalytical (coulometric) methods was the determination of the thickness of tin coatings on copper wires (80).
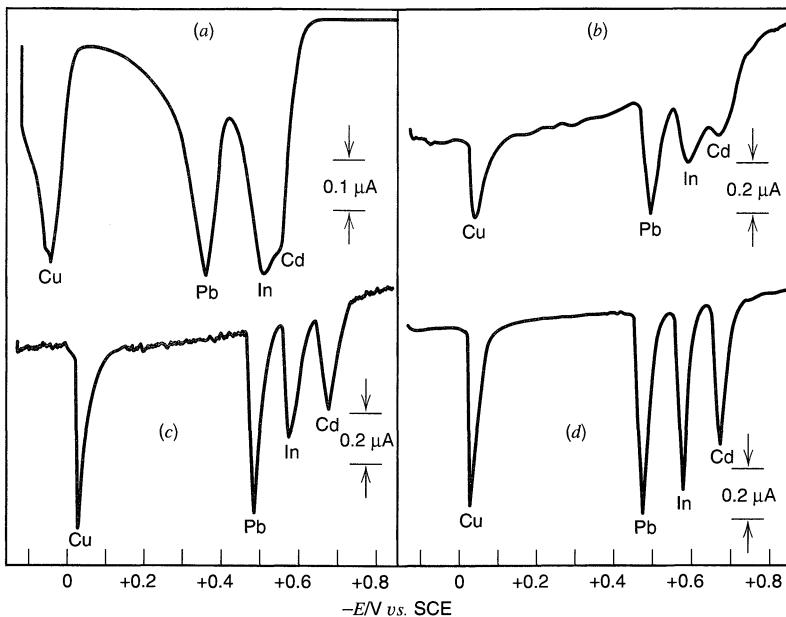
Figure 11.8.6 Stripping curves for 2×10^{-7} M Cd^{2+}, In^{3+}, Pb^{2+}, and Cu^{2+} in 0.1 M KNO_3. $|v| = 5$ mV/s. (*a*) HMDE, $t_d = 30$ min. (*b*) Pyrolytic graphite, $t_d = 5$ min. (*c*) Unpolished glassy carbon, $t_d = 5$ min. (*d*) Polished glassy carbon, $t_d = 5$ min. For (*b*) to (*d*), $\omega/2\pi = 2000$ rpm and Hg^{2+} was added at 2×10^{-5} M. [From T. M. Florence, *J. Electroanal. Chem.*, **27**, 273 (1970), with permission.]

Another variation involves the stripping or electrolysis of species that have sponta-neously adsorbed on the surface of an electrode without the preelectrolysis step. This technique, called *adsorptive stripping voltammetry*, can be applied, for example, to sul-fur-containing species, organic compounds, and certain metal chelates that adsorb on Hg and Au (74, 81). Examples include cysteine (and proteins that contain this amino acid), dissolved titanium in the presence of the chelator solochrome violet RS, and the drug diazepam. The amounts found by this method would necessarily be limited to monolayer levels. However, similar approaches can be employed with thicker polymer layers that can interact with solution species. Related experiments are described in Chapter 14.

▷ 11.9 REFERENCES

1. J. J. Lingane, "Electroanalytical Chemistry," 2nd. ed., Wiley-Interscience, New York, 1958, Chaps. 13–21.

2. P. Delahay, "New Instrumental Methods in Electrochemistry," Wiley-Interscience, New York, 1954, Chaps. 11–14.

3. N. Tanaka, in "Treatise on Analytical Chem-istry," Part I, Vol. 4, I. M. Kolthoff and P. J. Elv-

ing, Eds., Wiley-Interscience, New York, 1963, Chap. 48.

4. E. Leiva, *Electrochim. Acta*, **41**, 2185 (1996).

5. (a) L. B. Rogers and A. F. Stehney, *J. Elec-trochem. Soc.*, **95**, 25 (1949); (b) J. T. Byrne and L. B. Rogers, *ibid.*, **98**, 452 (1951).

6. D. M. Kolb, *Adv. Electrochem. Electrochem. Engr.*, **11**, 125 (1978).

7. N. Tanaka, *op. cit.*, pp. 2241–2443.

8. H. Gerischer, D. M. Kolb, and M. Prazanyski, *Surf. Sci.*, **43**, 662 (1974); **51**, 323 (1975); *J. Electroanal. Chem.*, **54**, 25 (1974); and references therein.

9. V. A. Vincente and S. Bruckenstein, *Anal. Chem.*, **45**, 2036 (1973); *J. Electroanal. Chem.*, **82**, 187 (1977); and references therein.

10. E. Schmidt, M. Christen, and P. Beyelar, *J. Electroanal. Chem.*, **42**, 275 (1973) and references therein.

11. For example, M. Ito and T. Kuwana, *J. Electroanal. Chem.*, **32**, 415 (1971).

12. W. R. Heineman and T. Kuwana, *Biochem. Biophys. Res. Commun.*, **50**, 892 (1973).

13. J. J. Lingane, *J. Am. Chem. Soc.*, **67**, 1916 (1945); *Anal. Chim. Acta.*, **2**, 584 (1948).

14. A. J. Bard, *Anal. Chem.*, **35**, 1125 (1963).

15. J. A. Harrison and H. R. Thirsk, *Electroanal. Chem.*, **5**, 67–148 (1971).

16. J. O'M. Bockris and A. Damjanovic, *Mod. Asp. Electrochem.*, **3**, 224 (1964).

17. M. Fleischmann and H. R. Thirsk, *Adv. Electrochem. Electrochem. Engr.*, **3**, 123 (1963).

18. F. A. Lowenheim, "Modern Electroplating," 3rd ed., Wiley, New York, 1974; "Electroplating," McGraw-Hill, New York, 1978.

19. H. J. S. Sand, "Electrochemistry and Electrochemical Analysis," Blackie, London, 1940.

20. Biennial reviews in *Anal. Chem.* (up to 1974). (a) S. E. Q. Ashley, **21**, 70 (1949); **24**, 91 (1952). (b) D. D. DeFord, **26**, 135 (1954); **28**, 660 (1956); **30**, 613 (1958); **32**, 31R (1960). (c) A. J. Bard, **34**, 57R (1962); **36**, 70R (1964); **38**, 88R (1966); **40**, 64R (1968); **42**, 22R (1970). (d) D. G. Davis, **44**, 79R (1972); **46**, 21R (1974).

21. G. A. Rechnitz, "Controlled Potential Analysis," Pergamon, New York, 1963.

22. J. E. Harrar, *Electroanal. Chem.*, **8**, 1 (1975).

23. J. J. Lingane, "Electroanalytical Chemistry," *op. cit.*, pp. 488–495.

24. J. J. Lingane, C. H. Langford, and F. C. Anson, *Anal. Chim. Acta.*, **16**, 165 (1959).

25. J. J. Lingane, "Electroanalytical Chemistry," *op. cit.*, Chap. 21.

26. H. L. Kies, *J. Electroanal. Chem.*, **4**, 257 (1962).

27. D. DeFord and J. W. Miller, in "Treatise on Analytical Chemistry," Part I, Vol. 4, I. M. Kolthoff and P. J. Elving, Eds., Wiley-Interscience, New York, 1963, Chap. 49.

28. A. J. Bard in "Chemistry at the Nanometer Scale," *Proc. of the Welch Foundation 40th Conf. Chem. Res.*, Robert A. Welch Foundation, Houston, 1996, p. 235.

29. P. A. Shaffer, Jr., A. Briglio, Jr., and J. A. Brockman, Jr., *Anal. Chem.*, **20**, 1008 (1948).

30. R. S. Braman, D. D. DeFord, T. N. Johnston, and L. J. Kuhns, *Anal. Chem.*, **32**, 1258 (1960).

31. J. Janata and H. B. Mark, Jr., *Electroanal. Chem.*, **3**, 1 (1969).

32. J. J. Lingane, "Electroanalytical Chemistry," *op. cit.*, Chaps. 5–8, 12 and references to the older literature contained therein.

33. C. N. Reilley and R. W. Murray (Chap. 43) and N. H. Furman (Chap. 45) in "Treatise on Analytical Chemistry," Part I, Vol. 4, I. M. Kolthoff and P. J. Elving, Eds., Wiley-Interscience, New York, 1963.

34. J. T. Stock, "Amperometric Titrations," Interscience, New York, 1965.

35. W. D. Cooke, C. N. Reilley, and N. H. Furman, *Anal. Chem.*, **23**, 1662 (1951).

36. I. M. Kolthoff and J. J. Lingane, "Polarography," 2nd ed., Vol. 2, Interscience, New York, 1952, Chap. 47.

37. L. Meites, "Polarographic Techniques," 2nd ed., Wiley-Interscience, New York, 1965, Chap. 9.

38. R. de Levie, *Adv. Electrochem. Electrochem. Engr.*, **6**, 329 (1967).

39. The treatment given here basically follows that outlined in the following papers and references contained therein:

    (a) R. E. Sioda, *Electrochim. Acta*, **13**, 375 (1968); **15**, 783 (1970); **17**, 1939 (1972); **22**, 439 (1977).

    (b) R. E. Sioda, *J. Electroanal. Chem.*, **34**, 399, 411 (1972); **56**, 149 (1974).

    (c) R. E. Sioda and T. Kambara, *J. Electroanal. Chem.*, **38**, 51 (1972).

    (d) I. G. Gurevich and V. S. Bagotsky, *Electrochim. Acta*, **9**, 1151 (1964).

    (e) I. G. Gurevich, V. S. Bagotsky, and Yu. R. Budeka, *Electrokhim.*, **4**, 321, 874, 1251 (1968).

    (f) R. E. Sioda and K. B. Keating, *Electroanal. Chem.*, **12**, 1 (1982).

40. J. V. Kenkel and A. J. Bard, *J. Electroanal. Chem.*, **54**, 47 (1974).

41. J. A. Trainham and J. Newman, *J. Electrochem. Soc.*, **124**, 1528 (1977).

42. R. Alkire and R. Gould, *ibid.*, **123**, 1842 (1976).

43. B. A. Ateya and L. G. Austin, *ibid.*, **124**, 83 (1977).

44. E. L. Eckfeldt, *Anal. Chem.*, **31**, 1453 (1959).

45. T. Fujinaga and S. Kihara, *CRC Crit. Rev. Anal. Chem.*, **6**, 223 (1977).

46. S. M. Lunte, C. E. Lunte, and P. T. Kissinger, in "Laboratory Techniques in Electroanalytical Chemistry," 2nd ed., P. T. Kissinger and W. R. Heineman, Eds., Marcel Dekker, New York, 1996.

47. D. C. Johnson and W. R. LaCourse, *Anal. Chem.*, **62**, 589A (1990).

48. D. M. Radzik and S. M. Lunte, *CRC Crit. Rev. Anal. Chem.*, **20**, 317 (1989).

49. P. C. White, *Analyst*, **109**, 677 (1984).

50. P. Jandik, P. R. Haddad, and P. E. Sturrock, *CRC Crit. Rev. Anal. Chem.*, **20**, 1 (1988).

51. H. Gunasingham and B. Fleet, *Electroanal. Chem.*, **16**, 89 (1989).

52. J. M. Elbicki, D. M. Morgan, and S. G. Weber, *Anal. Chem.*, **56**, 978 (1984).

53. D. A. Roston, R. E. Shoup, and P. T. Kissinger, *Anal. Chem.*, **54**, 1417A (1982).

54. M. B. Jensen and D. C. Johnson, *Anal. Chem.*, **69**, 1776 (1997).

55. D. C. Johnson and W. R. LaCourse, *Anal. Chem.*, **62**, 589A (1990).

56. W. R. LaCourse, *Analysis*, **21**, 181 (1993).

57. R. A. Wallingford and A. G. Ewing, *Anal. Chem.*, **59**, 1762 (1987).

58. X. Huang, R. N. Zare, S. Sloss, and A. G. Ewing, *Anal. Chem.*, **63**, 189 (1991).

59. E. Schmidt and H. R. Gygax, *Chimia*, **16**, 156 (1962).

60. J. H. Sluyters, *Rec. Trav. Chim.*, **82**, 100 (1963).

61. C. R. Christensen and F. C. Anson, *Anal. Chem.*, **35**, 205 (1963).

62. C. N. Reilley, *Pure Appl. Chem.*, **18**, 137 (1968).

63. A. T. Hubbard and F. C. Anson, *Electroanal. Chem.*, **4**, 129 (1970).

64. A. T. Hubbard, *CRC Crit. Rev. Anal. Chem.*, **2**, 201 (1973).

65. A. T. Hubbard, *J. Electroanal. Chem.*, **22**, 165 (1969).

66. G. M. Tom and A. T. Hubbard, *Anal. Chem.*, **43**, 671 (1971).

67. I. B. Goldberg and A. J. Bard, *Anal. Chem.*, **38**, 313 (1972).

68. I. Shain, in "Treatise on Analytical Chemistry," Part I, Vol. 4, I. M. Kolthoff and P. J. Elving, Eds., Wiley-Interscience, New York, 1963, Chap. 50.

69. E. Barendrecht, *Electroanal. Chem.*, **2**, 53–109 (1967).

70. R. Neeb, "Inverse Polarographie and Voltammetrie," Akademie-Verlag, Berlin, 1969.

71. J. B. Flato, *Anal. Chem.*, **44** (11), 75A (1972).

72. T. R. Copeland and R. K. Skogerboe, *Anal. Chem.*, **46**, 1257A (1974).

73. F. Vydra, K. Štulík, and E. Juláková, "Electrochemical Stripping Analysis," Halsted, New York, 1977.

74. J. Wang, "Stripping Analysis: Principles, Instrumentation, and Applications," VCH, Dearfield Beach, FL, 1985.

75. W. H. Reinmuth, *Anal. Chem.*, **33**, 185 (1961).

76. I. Shain and J. Lewinson, *Anal. Chem.*, **33**, 187 (1961).

77. W. T. de Vries and E. Van Dalen, *J. Electroanal. Chem.*, **8**, 366 (1964).

78. W. T. de Vries, *J. Electroanal. Chem.*, **9**, 448 (1965).

79. D. K. Roe and J. E. A. Toni, *Anal. Chem.*, **37**, 1503 (1965).

80. G. G. Grower, *Proc. Am. Soc. Testing Mater.*, **17**, 129 (1917).

81. J. Wang, *Electroanal. Chem.*, **16**, 1 (1989).

▷ 11.10 PROBLEMS

11.1 Based on the curves in Figure 11.10.1, consider the titration of Sn^{2+} with I_2 using one-electrode amperometry. Sketch the resulting titration curves for a platinum indicator electrode maintained at (a) $+0.2$ V, (b) -0.1 V, and (c) -0.4 V *vs.* SCE.

11.2 Based on the curves in Figure 11.10.1, how could one determine a mixture of Br_2 and I_2 by titration with Sn^{2+} using one-electrode amperometry? Sketch the current-potential curves that would be obtained for various stages of the titration and the amperometric titration curves that would result from the method you propose. Sketch the titration curve of a mixture of Br_2 and I_2 by titration with Sn^{2+} using two-electrode amperometry with an impressed voltage of 100 mV.
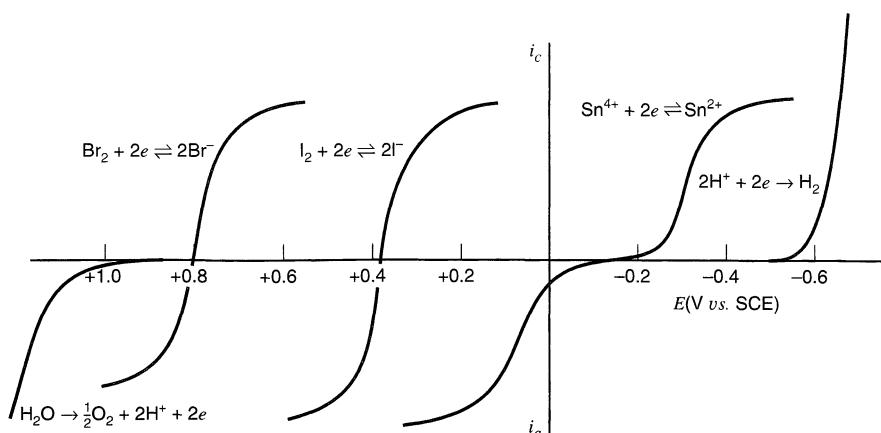
Figure 11.10.1   Idealized current-potential curves for several systems at a platinum electrode.

11.3   Based on the curves in Figure 11.10.1, sketch the titration curves for the titrations in Problems 11.1 and 11.2 for one- and two-electrode potentiometry with a small impressed current.

11.4   Fifty milliliters of a $ZnSO_4$ solution are transferred to an electrolytic cell with a mercury cathode, and enough solid potassium nitrate is added to make the solution 0.1 M in KNO_3. The electrolysis of Zn^{2+} is carried to completion at a potential of -1.3 V $vs.$ SCE with the passage of 241 C. Calculate the initial concentration of zinc ion.

11.5   Iodide is to be titrated coulometrically at constant current at a silver electrode. The sample is 1.0 mM NaI contained in a pH 4 acetic acid solution with 0.1 M sodium acetate having a total volume of 50 mL.

(a) Describe the course of the titration. What generating current do you recommend and what total titration time is expected?

(b) Consider the current-potential curves that would be recorded at a rotated platinum disk upon scanning from the cathodic background limit ($ca.$ -0.5 V) to the anodic limit (at $ca.$ $+1.5$ V $vs.$ SCE). Draw curves for the 0%, 50%, 100%, and 150% titration points. Label the waves with the electrode processes that cause them. All electrode reactions other than the background discharges are reversible. The following information is useful:

Reaction	E^0, volts $vs.$ SCE
$Ag^+ + e \rightleftharpoons Ag$	$+0.56$
$I_3^- + 2e^- \rightleftharpoons 3I^-$	$+0.30$
$AgI + e \rightleftharpoons Ag + I^-$	-0.39

(c) Sketch amperometric titration curves for:

 (1) One polarized electrode at -0.3 V $vs.$ SCE.

 (2) One polarized electrode at $+0.4$ V $vs.$ SCE.

 (3) Two polarized electrodes with 100-mV potential difference.

 The indicator electrodes are rotated platinum microelectrodes.

11.6   Iodide in the solution in Problem 11.5 can also be determined by controlled-potential oxidation to iodine at a platinum electrode. What potential should be used for this oxidation (see Figure 11.10.1)? How many coulombs will be passed?

11.7   The following is a standard procedure for the assay of uranium samples: (1) Dissolution of the sample in acid to produce UO_2^{2+} as the chloride. (2) Reduction of the UO_2^{2+} solution by passage through a Jones reductor (amalgamated zinc). This solution is perhaps 0.1 M in H_2SO_4. Reduction takes place to U^{3+}. (3) Stirring in air to give U^{4+}. (4) Addition of Fe^{3+} and Ce^{3+} in excess and coulometric titration to an end point.
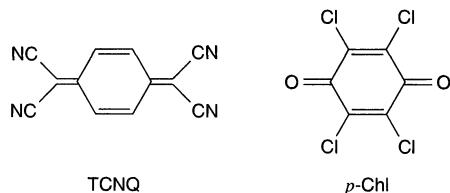
(a) Suppose the solution after treatment (3) contains ~ 1 mM U^{4+}. Fe^{3+} and Ce^{3+} are added in quantities that yield 4 and 50 mM concentrations of iron and cerium species, respectively. Sulfuric acid is also added to bring its concentration to 1 M. Draw the current-potential curve that would be recorded at a rotating platinum disk immersed in this solution. The anodic background limit is $+1.7$ V $vs.$ NHE and the cathodic limit is at -0.2 V $vs.$ NHE.

(b) Explain the chemistry of step (4) and the setup for the coulometric titration.

(c) Sketch current-potential curves for points at which the titration is 0%, 50%, 100%, and 150% complete.

(d) Sketch amperometric titration curves for one polarized electrode operated at $+0.3$ V and at $+0.9$ V $vs.$ NHE, and for two polarized electrodes separated by 100 mV.

(e) Sketch the null current potentiometric responses on a quantitative potential scale.

The following information may be useful:
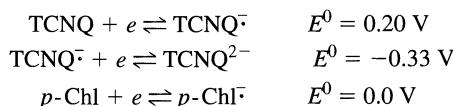
Reaction	Formal Potential, V $vs.$ NHE
1. $Ce^{4+} + e \rightleftharpoons Ce^{3+}$	1.44
2. $Fe^{3+} + e \rightleftharpoons Fe^{2+}$	0.77
3. $UO_2^{2+} + e \rightleftharpoons UO_2^{+}$	0.05
4. $UO_2^{+} + 4H^{+} + e \rightarrow U^{4+} + 2H_2O$	0.62
5. $U^{4+} + e \rightleftharpoons U^{3+}$	-0.61

All reactions except 4 are reversible. That process will not show a wave at platinum before the cathodic background limit is reached.

11.8 A molecule of interest in research is tetracyanoquinodimethane (TCNQ):

TCNQ   p-Chl

Samples of high purity are often required. Suppose you wish to develop a technique for assaying the purity of TCNQ samples. Describe a means for accomplishing this goal by coulometric titration with electrogenerated anion radicals of p-chloranil (p-Chl). Acetonitrile containing tetra-n-butylammonium perchlorate would be a suitable medium. Its background limits at platinum are -2.5 V and $+2$ V $vs.$ SCE. The following reduction potentials are relevant:

$$TCNQ + e \rightleftharpoons TCNQ^{\bar{\cdot}} \qquad E^0 = 0.20 \text{ V}$$
$$TCNQ^{\bar{\cdot}} + e \rightleftharpoons TCNQ^{2-} \qquad E^0 = -0.33 \text{ V}$$
$$p\text{-Chl} + e \rightleftharpoons p\text{-Chl}^{\bar{\cdot}} \qquad E^0 = 0.0 \text{ V}$$
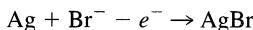
All of these processes are reversible.

(a) Specify the details of the cell, the starting composition of the solution, and the chemical processes taking place at the electrodes and in homogeneous solution.

(b) Draw the current-potential curves that would be recorded at a rotating platinum disk if the titration were stopped at the 0%, 50%, 100%, and 150% points.

(c) Sketch titration curves for: (1) amperometric detection with one polarized electrode at 1.0 V; (2) amperometric detection with one polarized electrode at 0.1 V; and (3) amperometric detection with two polarized electrodes separated by 100 mV.

11.9 Consider carrying out a one-electrode amperometric titration for the system Fe^{2+}–Ce^{4+} as shown in Figure 11.5.1 at several widely different potentials and sketch the amperometric titration curves that result. Consider, in each case, situations in which (a) the mass-transfer coefficients for all species

are equal and (b) those for iron ions are 25% larger than those for cerium species. Which curves would be useful in a practical titration?

11.10 When a solution of volume 100 cm^3 containing metal ion, M^{2+} at a concentration 0.010 M is electrolyzed with a rapid scan at a large-area (10 cm^2) rotating disk electrode, a limiting current of 193 mA is observed for reduction to metal M. Calculate the value of the mass transport coefficient $m_{M^{2+}}$, in cm/s. If an electrolysis of the solution is carried out at this electrode at controlled potential in the limiting current region, what time will be required for 99.9% of the M^{2+} to be plated out? How many coulombs will be required for this electrolysis?

11.11 If the solution in Problem 11.10 is electrolyzed at a constant current of 80 mA under the same conditions: (a) What is the concentration of M^{2+} remaining in solution when the current efficiency drops below 100%? (b) How long does it take to reach this point? (c) How many coulombs have been passed to this point? (d) How much longer will it take to decrease the M^{2+} concentration to 0.1% of its initial value? What is the overall current efficiency for removal of 99.9% of M^{2+} by this constant-current electrolysis?

11.12 A solution of volume 200 cm^3 contains 1.0×10^{-3} M X^{2+} and 3.0×10^{-3} M Y^{2+}, where X and Y are metals. The solution is to be electrolyzed at a mercury pool electrode of area 50 cm^2 and volume 100 cm^3. Under the stirring conditions and cell geometry, both X^{2+} and Y^{2+} have mass-transfer coefficients m of 10^{-2} cm/s. The polarographic $E_{1/2}$ values for reduction of X^{2+} and Y^{2+} to the metal amalgams are -0.45 and -0.70 V vs. SCE, respectively. (a) A current-potential curve for the solution is taken under the above conditions. (Assume no changes in concentrations of X^{2+} and Y^{2+} during the scan.) Make a neat, labeled, quantitatively correct sketch of the i-E curve that would be obtained. (b) If the electrolysis is to be performed at a controlled potential, at what potentials can X^{2+} be quantitatively deposited (less than 0.1% left in solution) leaving Y^{2+} behind in solution (less than 0.1% Y^{2+} deposited in mercury)? (c) How long will it take to carry out this electrolysis at controlled potential?

11.13 Consider a chronopotentiometric experiment dealing with two components that are reversibly reduced in waves separated by 500 mV. Derive an expression for the second transition time in an experiment carried out in a thin-layer cell. Compare and contrast the properties of multicomponent systems in thin-layer chronopotentiometry with those of the semi-infinite method.

11.14 In the electrolytic production of aluminum, the reduction of Al$_2$O$_3$ (alumina) in a bath of molten cryolite (Na$_3$AlF$_6$) ($T \approx 1000°C$) is carried out at constant current with carbon electrodes. A charge of alumina is placed in the cell and the electrolysis carried out until the voltage across a cell rises sharply, signaling the need to add additional alumina. Explain this behavior.

11.15 Suppose bromide ion is to be determined at very low concentrations. This is done by depositing bromide on a silver electrode, which is held at a potential where the following reaction occurs:

$$Ag + Br^- - e^- \rightarrow AgBr$$

(A typical deposition potential is $+0.2$ V vs. SCE.) Stripping is carried out by scanning in a negative direction to reverse the deposition. In general, it is observed that the response during stripping shows a complex dependence on deposition time, as shown in Figure 11.10.2. Explain this effect. What problems would be present in quantitative analysis? How could they be surmounted? [See H. A. Laitinen and N. H. Watkins, *Anal. Chem.*, **47**, 1352 (1975) for similar results in determinations of lead.]

11.16 A study of seawater by stripping analysis reveals an anodic copper peak having a height of 0.13 μA when deposition is carried out at -0.5 V. However, deposition at -1.0 V yields a larger peak of 0.31 μA. Account for these results. Standard addition of 10^{-7} M Cu^{2+} elevates the peaks in both cases by 0.24 μA. Comment on the feasibility of obtaining polarograms of any type on this solution. What responses would you expect for dc, normal pulse, and differential pulse experiments? Would any of these supply useful analytical information?

11.17 An analysis for lead at the HMDE gives rise to a peak current of 1 μA under conditions in which the deposition time is held constant at 5 min and the sweep rate is 50 mV/s . What currents would be observed for sweep rates of 25 and 100 mV/s ?
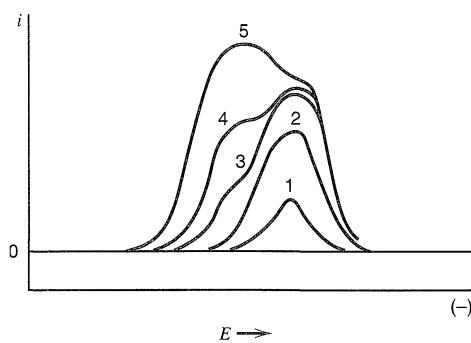
Figure 11.10.2 Cathodic stripping of AgBr from a silver electrode following anodic deposition. Curves 1 to 5 involve successively longer deposition times.
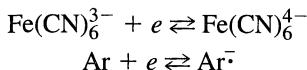
The same solution gives a peak current of 25 μA at a 100-Å thick mercury film electrode on glassy carbon when the deposition time is 1 min, the electrode rotation rate is 2000 rpm, and the sweep rate is 50 mV/s. What currents would be observed for sweep rates of 25 and 100 mV/s under otherwise unchanged conditions? Compare this situation to the one observed for a deposition time of 1 min, a sweep rate of 50 mV/s, and a rotation rate of 4000 rpm? Suppose the film thickness were varied by the use of different concentrations of mercuric ion in the analyte. What effect would one see on the peak current under otherwise constant conditions?

12

ELECTRODE REACTIONS WITH COUPLED HOMOGENEOUS CHEMICAL REACTIONS

12.1 CLASSIFICATION OF REACTIONS

The previous chapters dealt with a number of electrochemical techniques and the responses obtained when the electroactive species (O) is converted in a heterogeneous electron-transfer reaction to the product (R). This reaction is often a simple one-electron transfer, such as an outer-sphere reaction where no chemical bonds in species O are broken and no new bonds are formed. Typical reactions of this type are

$$Fe(CN)_6^{3-} + e \rightleftarrows Fe(CN)_6^{4-}$$
$$Ar + e \rightleftarrows Ar^{\cdot -}$$

where Ar is an aromatic species and $Ar^{\cdot -}$ is a radical anion. In many cases the electron-transfer reaction is coupled to homogeneous reactions that involve species O or R. For example, O may not be present initially at an appreciable concentration, but may be produced during the electrode reaction from another, nonelectroactive species. More frequently, R is not stable and reacts (e.g., with solvent or supporting electrolyte). Sometimes a substance that reacts with product R is intentionally added so that the rate of the reaction can be determined by an electrochemical technique or a new product can be produced. In this chapter, we will survey the general classes of coupled homogeneous chemical reactions and discuss how electrochemical methods can be used to elucidate the mechanisms of these reactions.

Electrochemical methods are widely applied to the study of reactions of organic and inorganic species, since they can be used to obtain both thermodynamic and kinetic information and are applicable in many solvents. Moreover, as described below, reactions can be examined over a wide time window by electrochemical techniques (submicroseconds to hours). Finally, these methods have the special feature that the species of interest (e.g., R) can be synthesized in the vicinity of the electrode by the electron-transfer reaction and then be immediately detected and analyzed electrochemically.

The initial investigations of coupled chemical reactions were carried out by Brdička, Wiesner, and others of the Czechoslovakian polarographic school in the 1940s; since that time countless papers dealing with the theory and application of dif-

ferent electroanalytical techniques to the study of coupled reactions have appeared. It is beyond the scope of this textbook to attempt to treat this area exhaustively. The reader is instead referred to monographs and review articles dealing with different aspects of it (1–9).

Before discussing the electrochemical techniques themselves, let us consider some general pathways that typify the overall electrochemical reactions of many soluble organic and inorganic species. We represent our general stable reactant as RX and consider what reactions can occur following an initial one-electron oxidation or reduction (Figure 12.1.1). For example, if RX is an organic species, R can be a hydrocarbon moiety (alkyl, aryl) and X can represent a substituent (e.g., H, OH, Cl, Br, NH_2, NO_2, CN, CO_2^-, . . .). In some cases, the product of the one-electron reaction is stable and leads to production of a radical ion (path 1). Often the addition of an electron to an antibonding orbital or the removal of an electron from a bonding orbital will weaken a chemical bond. This can lead to a rearrangement of the molecule (path 3) or, if X is a good "leaving group," reaction paths 6 and 7 can occur. Sometimes, for example, with an olefinic

(a) General reduction paths

(b) General oxidation paths
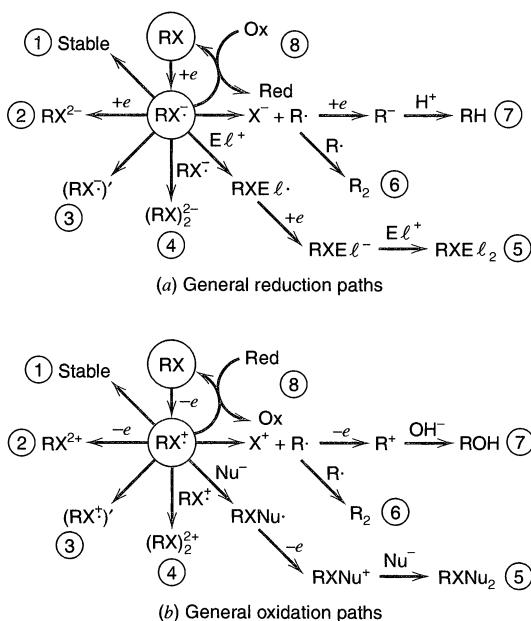
Figure 12.1.1 Schematic representation of possible reaction paths following reduction and oxidation of species RX. (a) Reduction paths leading to (1) a stable reduced species, such as a radical anion; (2) uptake of a second electron (EE); (3) rearrangement (EC); (4) dimerization (EC$_2$); (5) reaction with an electrophile, $E\ell^+$, to produce a radical followed by an additional electron transfer and further reaction (ECEC); (6) loss of X^- followed by dimerization (ECC$_2$); (7) loss of X^- followed by a second electron transfer and protonation (ECEC); (8) reaction with an oxidized species, Ox, in solution (EC'). (b) Oxidation paths leading to (1) a stable oxidized species, such as a radical cation; (2) loss of a second electron (EE); (3) rearrangement (EC); (4) dimerization (EC$_2$); (5) reaction with a nucleophile, Nu$^-$, followed by an additional electron transfer and further reaction (ECEC); (6) loss of X^+ followed by dimerization (ECC$_2$); (7) loss of X^+ followed by a second electron transfer and reaction with OH$^-$ (ECEC); (8) reaction with a reduced species, Red, in solution (EC'). Note that charges shown on products, reactants, and intermediates are arbitrary. For example, the initial species could be RX$^-$, the attacking electrophile could be uncharged, etc.

reactant, dimerization takes place (path 4) (with the possibility of further oligimeriza-tion and polymerization reactions). Finally, reactions of intermediates with solution components are possible. These include the reaction of $RX^{\bar{\cdot}}$ with an electrophile, $E\ell^+$ (i.e., a Lewis acid like H^+, CO_2, SO_2) or of $RX^{\dot{+}}$ with a nucleophile, Nu^- (i.e., a Lewis base like OH^-, CN^-, NH_3) (path 5). An electron-transfer reaction with a nonelectroac-tive species present in solution (Ox or Red) can also occur (path 8). In general, the addi-tion of an electron produces a species that is more basic than the parent so that protonation can occur (i.e., $RX^{\bar{\cdot}}$ in path 5 with $E\ell^+$ being H^+). Likewise, removal of an electron from a molecule produces a species that is more acidic than the parent, so that loss of a proton can occur (i.e., $RX^{\dot{+}}$ in path 7 with X^+ being H^+). Similar path-ways take place following an initial electron-transfer reaction with an organometallic species or coordination compound. For example, oxidation or reduction can be followed with loss of a ligand or rearrangement.

It is convenient to classify the different possible reaction schemes by using letters to signify the nature of the steps. "E" represents an electron transfer at the electrode sur-face, and "C" represents a homogeneous chemical reaction (10). Thus a reaction mecha-nism in which the sequence involves a chemical reaction of the product after the electron transfer would be designated an *EC reaction*. In the equations that follow, substances designated X, Y, and Z are assumed to be not electroactive in the potential range of in-terest. It is also convenient to subdivide the different types of reactions into (1) those that involve only a single electron-transfer reaction at the electrode and (2) those that involve two or more E-steps.

12.1.1 Reactions with One E Step

(a) CE Reaction (Preceding Reaction)

$$Y \rightleftarrows O \qquad (12.1.1)$$

$$O + ne \rightleftarrows R \qquad (12.1.2)$$

Here the electroactive species, O, is generated by a reaction that precedes the electron transfer at the electrode. An example of the CE scheme is the reduction of formaldehyde at mercury in aqueous solutions. Formaldehyde exists as a nonreducible hydrated form, $H_2C(OH)_2$, in equilibrium with the reducible form, $H_2C=O$:

$$H_2C{\overset{\displaystyle OH}{\underset{\displaystyle OH}{\big\langle}}} \rightleftarrows H_2C=O + H_2O \qquad (12.1.3)$$
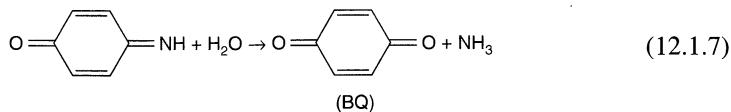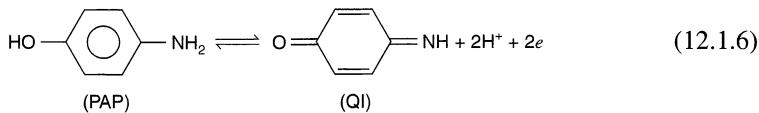
The equilibrium constant of (12.1.3) favors the hydrated form. Thus the forward reaction in (12.1.3) precedes the reduction of $H_2C=O$, and under some conditions the current will be governed by the kinetics of this reaction (yielding a so-called *kinetic current*). Other examples of this case involve reduction of some weak acids and the conjugate base an-ions, the reduction of aldoses, and the reduction of metal complexes.

(b) EC Reaction (Following Reaction)

$$O + ne \rightleftarrows R \qquad (12.1.4)$$

$$R \rightleftarrows X \qquad (12.1.5)$$

In this case the product of the electrode reaction, R, reacts (e.g., with solvent) to pro-duce a species that is not electroactive at potentials where the reduction of O is occurring.

An example of this scheme is the oxidation of p-aminophenol (PAP) at a platinum electrode in aqueous acidic solutions:

$$ \text{(PAP)} \qquad\qquad \text{(QI)} \qquad\qquad (12.1.6) $$

$$ \text{(BQ)} \qquad (12.1.7) $$
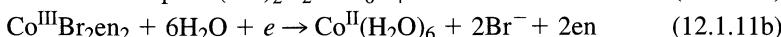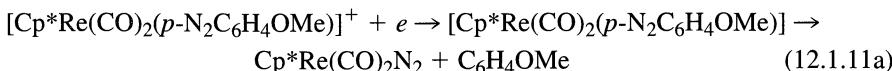
where the quinone imine (QI) formed in the initial electron-transfer reaction undergoes a hydrolysis reaction to form benzoquinone (BQ), which is neither oxidized nor reduced at these potentials. This type of reaction sequence occurs quite frequently, since the electrochemical oxidation or reduction of a substance often produces a reactive species. For example, the one-electron reductions and oxidations that are characteristic of organic compounds in aprotic solvents [e.g., in acetonitrile (CH_3CN) or N,N-dimethylformamide ($Me_2NHC{=}O$)] produce radicals or radical ions that tend to dimerize:

$$ R + e \rightleftharpoons R^{\bar{\cdot}} \tag{12.1.8} $$

$$ 2R^{\bar{\cdot}} \rightarrow R_2^{2-} \tag{12.1.9} $$

e.g., where R is an activated olefin, such as diethyl fumarate (see Figure 12.1.1, path 4). In this example, the reaction that follows the electron transfer is a second-order reaction, and this case is sometimes designated as an EC_2 reaction. Sometimes, yet another chemical reaction follows the first; for example, in the dimerization of olefins, there is a concluding (two-step) protonation process:

$$ R_2^{2-} + 2H^+ \rightarrow R_2H_2 \tag{12.1.10} $$
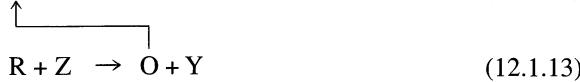
This sequence is an ECC (or EC_2C) reaction. The products of one-electron transfers can also rearrange (see Figure 12.1.1, path 3), because a bond is weakened. For similar reasons, electron transfers can also lead to loss of ligands, substitution, or isomerization in coordination compounds. Examples include

$$ [Cp^*Re(CO)_2(p\text{-}N_2C_6H_4OMe)]^+ + e \rightarrow [Cp^*Re(CO)_2(p\text{-}N_2C_6H_4OMe)] \rightarrow $$

$$ Cp^*Re(CO)_2N_2 + C_6H_4OMe \tag{12.1.11a} $$

$$ Co^{III}Br_2en_2 + 6H_2O + e \rightarrow Co^{II}(H_2O)_6 + 2Br^- + 2en \tag{12.1.11b} $$

(where $Cp^* = \eta^5\text{-}C_5Me_5$ and en = ethylenediamine). In many cases, the product formed in the following reaction can undergo an additional electron-transfer reaction, leading to an ECE sequence, discussed in Section 12.1.2(b).

(c) Catalytic (EC′) Reaction

$$ O + ne \rightleftarrows R \tag{12.1.12} $$

$$ R + Z \rightarrow O + Y \tag{12.1.13} $$

A special type of EC process involves reaction of R with a nonelectroactive species, Z, in solution to regenerate O (Figure 12.1.1, path 8). If species Z is present in large excess compared to O, then (12.1.13) is a pseudo-first-order reaction. An example of this
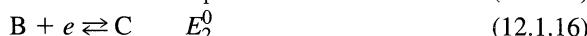
scheme is the reduction of Ti(IV) in the presence of a substance that can oxidize Ti(III), such as NH_2OH or ClO_3^-:

$$Ti(IV) + e \rightarrow Ti(III)$$

$$\underset{ClO_3^-,\ NH_2OH}{\uparrow \underline{\hspace{3cm}}|} \tag{12.1.14}$$
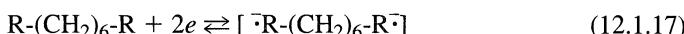
Since hydroxylamine and chlorate ion can be reduced by Ti(III), they should be reducible directly at the mercury electrode at the potentials needed to generate Ti(III); however, the direct reductions do not occur because the rates at the electrode are very small. Other examples of EC′ reactions are the reduction of Fe(III) in the presence of H_2O_2 and the oxidation of I^- in the presence of oxalate. An important EC′ reaction involves reductions at mercury where the product can reduce protons or solvent (a so-called "catalytic" hydrogen reaction).

12.1.2. Reactions with Two or More E Steps

(a) EE Reaction

$$A + e \rightleftarrows B \qquad E_1^0 \tag{12.1.15}$$

$$B + e \rightleftarrows C \qquad E_2^0 \tag{12.1.16}$$

The product of the first electron-transfer reaction may undergo a second electron-transfer step at potentials either more or less negative than that for the first step (Figure 12.1.1, path 2). Of particular interest is the case where the second electron transfer is thermodynamically easier than the first. In this situation, a multielectron overall response arises. In general, the addition of an electron to a molecule or atom results in a species that is more difficult to reduce, considering only the electrostatics; that is, R^- is more difficult to reduce than R. Similarly, R^+ is more difficult to oxidize than R. In the gas phase, the ionization potential (IP) for R^+ is almost always much higher, by 5 eV or more, than that for R (e.g., Zn, $IP_1 = 9.4$ eV and $IP_2 = 18$ eV). Thus one would generally expect a species to undergo stepwise one-electron reduction or oxidation reactions. However, if one or more electron-transfer steps involve significant structural change such as a rearrangement or a large change in solvation, then the standard potentials of the electron-transfer reactions can shift to promote the second electron transfer and produce an apparent multielectron wave. Thus one can argue that the oxidation of Zn proceeds in an apparent two-electron reaction to Zn^{2+}, because this species is much more highly solvated and stabilized than Zn^+. Apparent multielectron-transfer reactions are also observed when there are several identical groups on a molecule that do not interact with one another, such as,

$$R\text{-}(CH_2)_6\text{-}R + 2e \rightleftarrows [\ ^-R\text{-}(CH_2)_6\text{-}R^-] \tag{12.1.17}$$

where R = 9-anthryl or 4-nitrophenyl. This same principle holds in the reduction or oxidation of many polymers, such as $(CH_2\text{-}CHR')_x$, where R′ is an electroactive group like ferrocene. The electrochemical response appears as a single wave, representing an x-electron EEE ... (or xE) reaction. This result contrasts sharply with the multistep electron-transfer behavior found with fullerene (C_{60}), which shows six resolved, one-electron cathodic waves (an overall 6E sequence), where each step is thermodynamically more difficult than the preceding one (11).

Whenever more than one electron-transfer reaction occurs in the overall sequence, such as in an EE reaction sequence, one must consider the possibility of solution-phase electron-transfer reactions, such as for (12.1.15) and (12.1.16), the *disproportionation* of B:

$$2B \rightleftarrows A + C \tag{12.1.18}$$
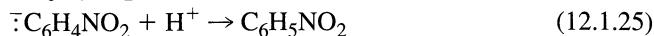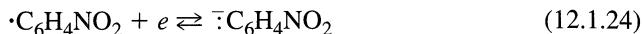
or the reverse reaction (the *comproportionation* of A and C).

(b) ECE Reaction

$$O_1 + n_1 e \rightleftharpoons R_1 \qquad E_1^0 \tag{12.1.19}$$

$$R_1 \xrightarrow{(+Z)} O_2 \tag{12.1.20}$$

$$O_2 + n_2 e \rightleftharpoons R_2 \qquad E_2^0 \tag{12.1.21}$$

When the product of the following chemical reaction is electroactive at potentials of the O_1/R_1 electron-transfer reaction, a second electron-transfer reaction can take place (Figure 12.1.1, paths 5 and 7). An example of this scheme is the reduction of a halonitroaromatic compound in an aprotic medium (e.g., in liquid ammonia or N,N-dimethylformamide), where the reaction proceeds as follows ($X = Cl, Br, I$):

$$XC_6H_4NO_2 + e \rightleftharpoons XC_6H_4NO_2^{-\cdot} \tag{12.1.22}$$

$$XC_6H_4NO_2^{-\cdot} \rightarrow X^- + \cdot C_6H_4NO_2 \tag{12.1.23}$$

$$\cdot C_6H_4NO_2 + e \rightleftharpoons {}^{\cdot \cdot}C_6H_4NO_2 \tag{12.1.24}$$

$${}^{\cdot \cdot}C_6H_4NO_2 + H^+ \rightarrow C_6H_5NO_2 \tag{12.1.25}$$

Since protonation follows the second electron-transfer step, this is actually an ECEC reaction sequence. The assignment of such a sequence is not as straightforward as it might first appear, however. Because species O_2 is more easily reduced than O_1 (i.e., $E_1^0 < E_2^0$), species R_1 diffusing away from the electrode is capable of reducing O_2. Thus, for the example mentioned above, the following reaction can occur:

$$XC_6H_4NO_2^{-\cdot} + \cdot C_6H_4NO_2 \rightleftharpoons XC_6H_4NO_2 + {}^{\cdot \cdot}C_6H_4NO_2 \tag{12.1.26}$$
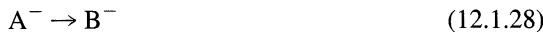
It is not simple to distinguish between this case, where the second electron transfer occurs in bulk solution [sometimes called the *DISP mechanism*], and the true ECE case where the second electron transfer occurs at the electrode surface (12).

Another variety of this type of reaction scheme, which we will designate ECE′, occurs when the reduction of O_2 takes place at more negative potentials than O_1 (i.e., $E_1^0 > E_2^0$). In this case the reaction observed at the first reduction wave is an EC process; however, the second reduction wave will be characteristic of an ECE reaction.

(c) $\overrightarrow{E}\overleftarrow{C}E$ Reaction

This case occurs when the product of a chemical reaction following the reduction of A at the electrode is *oxidized* at potentials where A is reduced (hence the backward arrow on the second E) (13):

$$A + e \rightleftharpoons A^- \tag{12.1.27}$$

$$A^- \rightarrow B^- \tag{12.1.28}$$

$$B^- - e \rightleftharpoons B \tag{12.1.29}$$

Charges are explicitly indicated here only to emphasize the different directions of the two E steps. As with EE and ECE reactions, one needs to include the possibility of a solution electron-transfer reaction also taking place:

$$A^- + B \rightleftharpoons B^- + A \tag{12.1.30}$$
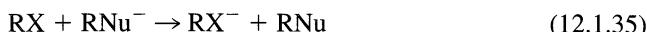
An example of this case is the reduction of $Cr(CN)_6^{3-}$ in 2 M NaOH (in the absence of dissolved CN^-). In this case, reduction of the kinetically inert $Cr(CN)_6^{3-}$ (A) to the labile $Cr(CN)_6^{4-}$ (A$^-$) causes rapid loss of CN^- to form $Cr(OH)_n(H_2O)_{6-n}^{2-n}$ (B$^-$) which is immediately oxidized to $Cr(OH)_n(H_2O)_{6-n}^{3-n}$ (B). Additional reactions of this type include isomerizations and other structural changes that occur on electron transfer.

Note that the overall reaction for this scheme is simply A → B, with no net transfer of electrons. Thus, at a suitable potential, the electrode accelerates a reaction that presumably would proceed slowly without the electrode. An interesting extension of this mechanism is the *electron-transfer-catalyzed substitution* reaction (equivalent to the organic chemist's $S_{RN}1$ mechanism) (7, 14):

$$RX + e \rightleftarrows RX^- \qquad (12.1.31)$$
$$RX^- \rightarrow R + X^- \qquad (12.1.32)$$
$$R + Nu^- \rightarrow RNu^- \qquad (12.1.33)$$
$$RNu^- - e \rightleftarrows RNu \qquad (12.1.34)$$

along with the occurrence of the solution phase reaction

$$RX + RNu^- \rightarrow RX^- + RNu \qquad (12.1.35)$$

Again the overall reaction does not involve any net transfer of electrons and is equivalent to the simple substitution reaction

$$RX + Nu^- \rightarrow RNu + X^- \qquad (12.1.36)$$

(d) Square Schemes

Two electron-transfer reactions can be coupled to two chemical reactions in a cyclic pattern called a "square scheme" (15):

$$
\begin{array}{ccc}
A^\circ + e^\circ & \rightleftarrows & {}^\circ A^- \\
\Updownarrow & & \Updownarrow \\
B^\circ + e^\circ & \rightleftarrows & {}^\circ B^-
\end{array}
\qquad (12.1.37)
$$
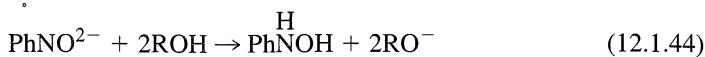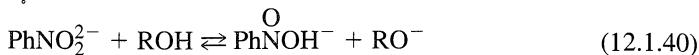
This mechanism often occurs when there is a structural change on reduction, such as a *cis-trans* isomerization. An example of this scheme for an oxidation reaction is found in the electrochemistry of *cis*-$W(CO)_2(DPE)_2$ [where DPE = 1,2-*bis*(diphenylphosphino)ethane], where the cis-form (C) on oxidation yields C^+, which isomerizes to the *trans* species, T^+. More complex reaction mechanisms result from coupling several square schemes together to form *meshes* (e.g., *ladders* or *fences*) (8).

(e) Other Reaction Patterns

Under the subheadings above, we have considered some of the more important general electrode reactions involving coupled homogeneous and heterogeneous steps. A great variety of other reaction schemes is possible. Many can be treated as combinations or variants of the general cases that we delineated above. In all schemes, the observed behavior depends on the reversibility or irreversibility of the electron transfer and the homogeneous reactions (i.e., the importance of the back reactions). For example, subclasses of EC reactions can be distinguished depending on whether the reactions are reversible (r), quasireversible (q), or irreversible (i); thus we can differentiate E_rC_r, E_rC_i, E_qC_i, etc. There has been much interest and success since the 1960s in the elucidation of complex reaction schemes by application of electrochemical methods, along with identification of intermediates by spectroscopic techniques (see Chapter 17) and judicious variation of solvent and reaction conditions. A complex example is the reduction of nitrobenzene ($PhNO_2$) to phenylhydroxylamine in liquid ammonia in the presence of proton donor (ROH), which has been analyzed as an EECCEEC process (16):

$$PhNO_2 + e \rightleftarrows PhNO_2^{\cdot -} \qquad (12.1.38)$$
$$PhNO_2^{\cdot -} + e \rightleftarrows PhNO_2^{2-} \qquad (12.1.39)$$

$$PhNO_2^{2-} + ROH \rightleftarrows PhN\overset{O}{O}H^- + RO^- \tag{12.1.40}$$

$$PhN\overset{O}{O}H^- \rightarrow PhNO \text{ (nitrosobenzene)} + OH^- \tag{12.1.41}$$

$$PhNO + e \rightleftarrows PhNO^{\cdot -} \tag{12.1.42}$$

$$PhNO^{\cdot -} + e \rightleftarrows PhNO^{2-} \tag{12.1.43}$$

$$PhNO^{2-} + 2ROH \rightarrow PhN\overset{H}{O}H + 2RO^- \tag{12.1.44}$$

12.1.3 Effects of Coupled Reactions on Measurements

In general, a perturbing chemical reaction can affect the primary measured parameter of the forward reaction (e.g., the limiting or peak current in voltammetry), the forward reaction's characteristic potentials (e.g., $E_{1/2}$ or E_p), and the reversal parameters (e.g., i_{pa}/i_{pc}). A qualitative understanding of how different types of reactions affect the different parameters of a given technique is useful in choosing reaction schemes as candidates for more detailed analysis in a given situation. We assume here that the characteristics of the unperturbed electrode reaction (O + ne ⇌ R) have already been determined, so we focus now on how the perturbing coupled reaction affects these characteristics.

(a) Effect on Primary Forward Parameters (i, Q, τ, . . .)
The extent to which the limiting current for the forward reaction (O + ne → R) is affected by the coupled reaction depends on the reaction scheme. For an EC reaction, the flux of O is not changed very much, so that any index of that flux, such as the limiting current (or Q_f or τ_f), is only slightly perturbed. On the other hand, the limiting current for a catalytic reaction (EC′) will be increased, because O is continuously replenished by the reaction. The extent of this increase will depend on the duration (or characteristic time) of the experiment. For very short-duration experiments, this limiting current will be near that for the unperturbed reaction, since the regenerating reaction will not have sufficient time to regenerate O in appreciable amounts. For longer-duration experiments, the limiting current will be larger than in the unperturbed case. Similar considerations apply to the ECE mechanism, except that for longer-duration experiments an upper bound for the limiting current is reached.

(b) Effect on Characteristic Potentials ($E_{1/2}$, E_p, . . .)
The manner in which the potential of the forward reaction is affected depends not only on the type of coupled reaction and experimental duration, but also on the reversibility of electron transfer. Consider the E_rC_i case; that is, a reversible (nernstian) electrode reaction followed by an irreversible chemical reaction:

$$O + ne \rightleftarrows R \rightarrow X \tag{12.1.45}$$

The potential of the electrode during the experiment is given by the Nernst equation:

$$E = E^{0'} + \frac{RT}{nF} \ln \frac{C_O(x=0)}{C_R(x=0)} \tag{12.1.46}$$

where $C_O(x=0)/C_R(x=0)$ is determined by the experimental conditions. The effect of the following reaction is to decrease $C_R(x=0)$ and hence to increase $C_O(x=0)/C_R(x=0)$. Thus the potential will be more positive at any current level than in the absence of the perturbation, and the wave will shift toward positive potentials. (This case was considered with steady-state approximations in Section 1.5.2.) For an EC reaction

where the electron transfer is totally irreversible, the following reaction causes no change in characteristic potential, because the *i-E* characteristic contains no term involving $C_R(x = 0)$.

(c) Effect on Reversal Parameters (i_{pa}/i_{pc}, τ_r/τ_f, . . .)
Reversal results are usually very sensitive to perturbing chemical reactions. For example, in the E_rC_i case for cyclic voltammetry, i_{pa}/i_{pc} would be 1 in the absence of the perturbation (or in chronopotentiometry τ_r/τ_f would be 1/3). In the presence of the following reaction, $i_{pa}/i_{pc} < 1$ (or $\tau_r/\tau_f < 1/3$) because R is removed from near the electrode surface by reaction, as well as by diffusion. A similar effect will be found for a catalytic (EC′) reaction, where not only is the reverse contribution decreased, but the forward parameter is increased.

12.1.4 Time Windows and Accessible Rate Constants

The previous discussion makes it generally clear that the effect of a perturbing reaction on the measured parameters of an electrode process depends on the extent to which that reaction proceeds during the course of the electrochemical experiment. Consequently, it is valuable to be able to compare characteristic time for reaction with a characteristic time for observation. The characteristic lifetime of a chemical reaction with rate constant k can be taken as $t'_1 = 1/k$ for a first-order reaction or $t'_2 = 1/kC_i$ for a second-order (e.g., dimerization) reaction, where C_i is the initial concentration of reactant. One can easily show that t'_1 is the time required for the reactant concentration to drop to 37% of its initial value in a first-order process, and that t'_2 is the time required for the concentration to drop to one-half of C_i in a second-order process. Each electrochemical method is also described by a characteristic time, τ, which is a measure of the period during which a stable electroactive species can communicate with the electrode. If this characteristic time is small compared to t'_1 or t'_2, then the experimental response will be largely unperturbed by the coupled chemistry and will reflect only the heterogeneous electron transfer. If $t' \ll \tau$, the perturbing reaction will have a large effect.

For a given method with a particular apparatus, a certain range of τ (a *time window*) exists. The shortest useful τ is frequently determined by double-layer charging and instrumental response (which can be governed by the excitation apparatus, the measuring apparatus, or the cell design). The longest available τ is often governed by the onset of natural convection or changes in the electrode surface. The achievable time window is different for the different electrochemical techniques (Table 12.1.1). To study a coupled reaction, one must be able to find conditions that place the reaction's characteristic lifetime within the time window of the chosen technique. Potential step and voltammetric methods are applicable to reactions that are fast enough to occur within the diffusion layer near the electrode surface. Thus these methods would be useful for studying first-order reactions with rate constants of about 0.02 to 10^7 s^{-1}. To reach the upper limit, a UME would have to be employed, where the characteristic time is governed by the electrode radius, r_0, and is $\sim r_0^2/D$. Rapid reactions can also be studied by ac methods and with the SECM (where the characteristic time depends on the spacing between the tip and substrate, d, and is $\sim d^2/D$). Coulometric methods are applicable to slower reactions that take place outside of the diffusion layer. The main strategy adopted in studying a reaction is to systematically change the experimental variable controlling the characteristic time of the technique (e.g., sweep rate, rotation rate, or applied current) and then to determine how the forward parameters (e.g., $i_p/v^{1/2}C$, $i\tau^{1/2}/C$, or $i_l/\omega^{1/2}C$), the characteristic potentials (e.g., E_p and $E_{1/2}$), and the reversal parameters (i_{pa}/i_{pc}, i_r/i_f, Q_r/Q_f) respond. The directions and extents of variation of these provide *diagnostic criteria* for establish-

TABLE 12.1.1 Approximate Time Windows for Different Electrochemical Techniques

Technique	Time parameter	Usual range of parameter[a]	Time window (s)[b]
ac Impedance	$1/\omega = (2\pi f)^{-1}$ (s) (f = freq. in Hz)	$\omega = 10^{-2} - 10^{5}$ s^{-1}	10^{-5}–100
Rotating disk electrode voltammetry	$1/\omega = (2\pi f)^{-1}$ (s)^c (f = rotation rate, in r/s)	$\omega = 30$–1000 s^{-1}	10^{-3}–0.03
Scanning electrochemical microscopy	d^2/D	d = 10 nm–10 μm	10^{-7}–0.1
Ultramicroelectrode at steady state	r_0^2/D	$r_0 = 0.1$–25 μm	10^{-5}–1
Chronopotentiometry	t(s)	10^{-6}–50 s	10^{-6}–50
Chronoamperometry	τ (Forward phase duration, s)	10^{-7}–10 s	10^{-7}–10
Chronocoulometry	τ (Forward phase duration, s)	10^{-7}–10 s	10^{-7}–10
Linear scan voltammetry	RT/Fv (s)	$v = 0.02$–10^6 V/s	10^{-7}–1
Cyclic voltammetry	RT/Fv (s)	$v = 0.02$–10^6 V/s	10^{-7}–1
dc Polarography	t_{max} (drop time, s)	1–5 s	1–5
Coulometry	t (electrolysis duration, s)	100–3000 s	100–3000
Macroscale electrolysis	t (electrolysis duration, s)	100–3000 s	100–3000

[a]This represents a readily available range; these limits can often be extended to shorter times under favorable conditions. For example, potential and current steps in the nanosecond range and potential sweeps above 10^6 V/s have been reported.
[b]This time window should be considered only approximate. A better description of the conditions under which a chemical reaction will cause a perturbation of the electrochemical response can be given in terms of the dimensionless rate parameter, λ, discussed in Section 12.3.
[c]This is sometimes also given in a term that includes the kinematic viscosity, ν, and diffusion coefficient, D, (both with units of cm^2/s), such as, $(1.61)^2\nu^{1/3}/(\omega D^{1/3})$.

ing the type of mechanism involved, and the measurements themselves provide data for evaluation of the magnitudes of the rate constants of the coupled reactions.

▶ 12.2 FUNDAMENTALS OF THEORY FOR VOLTAMMETRIC AND CHRONOPOTENTIOMETRIC METHODS

12.2.1 Basic Principles

The theoretical treatments for the different voltammetric methods (e.g., polarography, linear sweep voltammetry, and chronopotentiometry) and the various kinetic cases generally follow the procedures described previously. The appropriate partial differential equations (usually the diffusion equations modified to take account of the coupled reactions producing or consuming the species of interest) are solved with the requisite initial and boundary conditions. For example, consider the E_rC_i reaction scheme:

$$O + ne \rightleftarrows R \text{ (at electrode)} \tag{12.2.1}$$

$$R \xrightarrow{k} Y \text{ (in solution)} \tag{12.2.2}$$

For species O, the unmodified diffusion equation still applies, since O is not involved directly in reaction (12.2.2); thus

$$\frac{\partial C_O(x, t)}{\partial t} = D_O\left[\frac{\partial^2 C_O(x, t)}{\partial x^2}\right] \tag{12.2.3}$$

For the species R, however, Fick's law must be modified because, at a given location in solution, R is removed not only by diffusion but also by the first-order chemical reaction. Since the rate of change of the concentration of R caused by the chemical reaction is

$$\left[\frac{\partial C_R(x, t)}{\partial t}\right]_{\text{chem.rxn.}} = -kC_R(x, t) \tag{12.2.4}$$

the appropriate equation for species R is

$$\frac{\partial C_R(x, t)}{\partial t} = D_R\left[\frac{\partial^2 C_R(x, t)}{\partial x^2}\right] - kC_R(x, t) \tag{12.2.5}$$

The initial conditions, assuming only O is initially present, are, as usual,

$$C_O(x, 0) = C_O^* \qquad C_R(x, 0) = 0 \tag{12.2.6}$$

The usual boundary conditions for the flux at the electrode surface

$$D_O\left[\frac{\partial C_O(x, t)}{\partial x}\right]_{x=0} = -D_R\left[\frac{\partial C_R(x, t)}{\partial x}\right]_{x=0} \tag{12.2.7}$$

and as $x \to \infty$,

$$\lim_{x \to \infty} C_O^*(x, t) = C_O^* \quad {}^\circ \quad {}^\circ \lim_{x \to \infty} C_R(x, t) = 0 \tag{12.2.8}$$

also apply. The sixth needed boundary condition depends on the particular technique and the reversibility of the electron-transfer reaction (12.2.1), just as described in Chapters 5–10. For example, for a potential step experiment to the limiting cathodic current region, $C_O(0, t) = 0$. For a step to an arbitrary potential, assuming (12.2.1) is reversible, the requisite condition is [see (5.4.6)]

$$\frac{C_O(0, t)}{C_R(0, t)} = \theta = \exp\left[\frac{nF}{RT}(E - E^{0'})\right] \tag{12.2.9}$$

and, for chronopotentiometry,
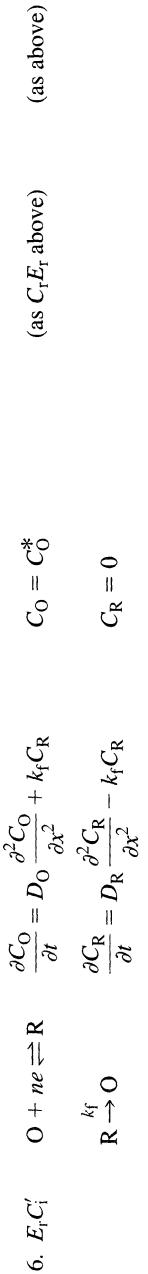
$$D_O\left[\frac{\partial C_O(x, t)}{\partial t}\right]_{x=0} = \frac{i}{nFA} \tag{12.2.10}$$

Note that equations need not be written for species Y, since its concentration does not affect the current or the potential. If reaction (12.2.2) were reversible, however, the concentration of species Y would appear in the equation for $\partial C_R(x, t)/\partial t$, and an equation for $\partial C_Y(x, t)/\partial t$ and initial and boundary conditions for Y would have to be supplied (see entry 3 in Table 12.2.1). Generally, then, the equations for the theoretical treatment are deduced in a straightforward manner from the diffusion equation and the appropriate homogeneous reaction rate equations. In Table 12.2.1, equations for several different reaction schemes and the appropriate boundary conditions for potential-step, potential-sweep, and current-step techniques are given.
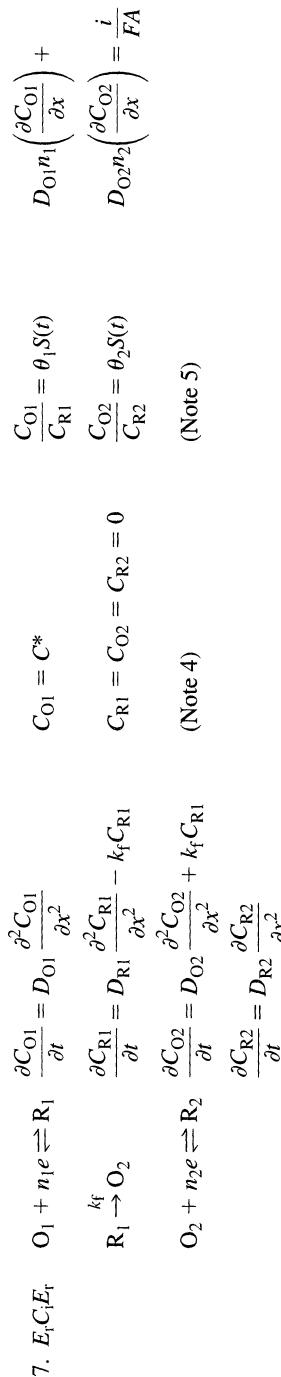
Solutions of the equations appropriate for a given reaction scheme are obtained by (a) approximation methods, (b) Laplace transform or related techniques to yield closed form solutions, (c) digital simulation methods, and (d) other numerical methods. Approximation methods, such as those based on the reaction layer concept as described in Section 1.5.2, are sometimes useful in showing the dependence of measured variables on various parameters and in yielding rough values of rate constants. With the availability of digital simulation methods, they are now rarely used. Laplace transform techniques can sometimes be employed with first-order coupled chemical reactions, often with judicious substitutions and combinations of the equations. Only rarely can closed-form solutions be obtained, such as in Section 12.2.2. For most reaction schemes, direct numerical solution

TABLE 12.2.1 Modified Diffusion Equations and Boundary Conditions for Several Different Coupled Homogeneous Chemical Reactions in Voltammetry

Case	Reactions	Diffusion equations (all x and t)	General initial and semi-infinite boundary conditions ($t = 0$ and $x \to \infty$)	Potential step and sweep boundary conditions (at $x = 0$)	Current step boundary conditions (at $x = 0$)
1. C_rE_r	$Y \underset{k_b}{\overset{k_f}{\rightleftharpoons}} O$ $O + ne \rightleftharpoons R$	$\dfrac{\partial C_Y}{\partial t} = D_Y \dfrac{\partial^2 C_Y}{\partial x^2} - k_f C_Y + k_b C_O$ $\dfrac{\partial C_O}{\partial t} = D_O \dfrac{\partial^2 C_O}{\partial x^2} + k_f C_Y - k_b C_O$ $\dfrac{\partial C_R}{\partial t} = D_R \dfrac{\partial^2 C_R}{\partial x^2}$	$C_O/C_Y = K$ $C_O + C_Y = C^*$ $C_R = 0$ (Note 1)	$\dfrac{C_O}{C_R} = \theta S(t)$ (Note 2)	$\dfrac{\partial C_O}{\partial x} = \dfrac{i}{nFAD_O}$
2. C_rE_i	$Y \underset{k_b}{\overset{k_f}{\rightleftharpoons}} O$ $O + ne \to R$	(as above)	(as above)	$D_O\left(\dfrac{\partial C_O}{\partial x}\right) = k' C_O e^{bt}$ (Note 3)	(as above)
3. E_rC_r	$O + ne \rightleftharpoons R$ $R \underset{k_b}{\overset{k_f}{\rightleftharpoons}} Y$	$\dfrac{\partial C_O}{\partial t} = D_O \dfrac{\partial^2 C_O}{\partial x^2}$ $\dfrac{\partial C_R}{\partial t} = D_R \dfrac{\partial^2 C_R}{\partial x^2} - k_f C_R + k_b C_Y$ $\dfrac{\partial C_Y}{\partial t} = D_Y \dfrac{\partial^2 C_Y}{\partial x^2} + k_f C_R - k_b C_Y$	$C_O = C_O^*$ $C_R = C_Y = 0$ (Note 1)	(as C_rE_r above)	(as above)
4. E_rC_i	$O + ne \rightleftharpoons R$ $R \overset{k_f}{\to} Y$	(as above, with $k_b = 0$) (equation for C_Y not required)	(as above)	(as C_rE_r above)	(as above)
5. E_rC_{2i}	$O + ne \rightleftharpoons R$ $2R \overset{k_f}{\to} X$	$\dfrac{\partial C_O}{\partial t} = D_O \dfrac{\partial^2 C_O}{\partial x^2}$ $\dfrac{\partial C_R}{\partial t} = D_R \dfrac{\partial^2 C_R}{\partial x^2} - k_f C_R^2$	(as above)	(as C_rE_r above)	(as above)

6. E_rC_i' $O + ne \rightleftharpoons R$

$$R \xrightarrow{k_f} O$$

$$\frac{\partial C_O}{\partial t} = D_O \frac{\partial^2 C_O}{\partial x^2} + k_f C_R$$

$$\frac{\partial C_R}{\partial t} = D_R \frac{\partial^2 C_R}{\partial x^2} - k_f C_R$$

$C_O = C_O^*$

$C_R = 0$

[Note 1(a)]

(as C_rE_r above)

(as above)

---

7. $E_rC_iE_r$ $O_1 + n_1e \rightleftharpoons R_1$

$$R_1 \xrightarrow{k_f} O_2$$

$$O_2 + n_2e \rightleftharpoons R_2$$

$$\frac{\partial C_{O1}}{\partial t} = D_{O1}\frac{\partial^2 C_{O1}}{\partial x^2}$$

$$\frac{\partial C_{R1}}{\partial t} = D_{R1}\frac{\partial^2 C_{R1}}{\partial x^2} - k_f C_{R1}$$

$$\frac{\partial C_{O2}}{\partial t} = D_{O2}\frac{\partial^2 C_{O2}}{\partial x^2} + k_f C_{R1}$$

$$\frac{\partial C_{R2}}{\partial t} = D_{R2}\frac{\partial^2 C_{R2}}{\partial x^2}$$

$C_{O1} = C^*$

$C_{R1} = C_{O2} = C_{R2} = 0$

(Note 4)

$\dfrac{C_{O1}}{C_{R1}} = \theta_1 S(t)$

$\dfrac{C_{O2}}{C_{R2}} = \theta_2 S(t)$

(Note 5)

$$D_{O1}n_1\left(\frac{\partial C_{O1}}{\partial x}\right) + D_{O2}n_2\left(\frac{\partial C_{O2}}{\partial x}\right) = \frac{i}{FA}$$

(Note 1)   (a) $D_O\left(\dfrac{\partial C_O}{\partial x}\right)_{x=0} = -D_R\left(\dfrac{\partial C_R}{\partial x}\right)_{x=0}$ · · (b) $D_Y\left(\dfrac{\partial C_Y}{\partial x}\right)_{x=0} = 0$

(Note 2)   For potential sweep, $\theta = \exp\left[\dfrac{nF}{RT}(E_i - E^{0'})\right]$ · · $S(t) = \exp\left(-\dfrac{nF}{RT}vt\right)$ · · E_i = initial potential v = scan rate

     For potential step to potential E, $\theta = \exp\left[\dfrac{nF}{RT}(E - E^{0'})\right]$ · · $S(t) = 1$

(Note 3)   For sweep from E_i at scan rate v or for step to E_i with $v = 0$, $k' = k_0\exp\left[\dfrac{-\alpha F}{RT}(E_i - E^{0'})\right]$ · · $b = \dfrac{\alpha F}{RT}v$

(Note 4)   There are two flux balance equations analogous to that in Note 1(a), one written for each of the redox couples.

(Note 5)   For potential sweep, $\theta_j = \exp\left[\dfrac{n_j F}{RT}(E_i - E_j^{0'})\right]$ · · $E_j^{0'}$ pertains to $O_j + n_j e \rightleftharpoons R_j$

     For potential step, $\theta_j = \exp\left[\dfrac{n_j F}{RT}(E - E_j^{0'})\right]$

of the differential equations or digital simulation, especially when higher-order reactions are involved, is the method of choice. Commercial computer programs, such as, DigiSim (17), ELSIM (18), and CVSIM (19), are available for some methods. A brief discussion of digital simulation with coupled homogeneous reactions is given in Section B.3.

For rotating disk electrode studies, the appropriate kinetic terms are added to the convective-diffusion equations. For ac techniques, the equations in Table 12.2.1 are solved for $C_O(0, t)$ and $C_R(0, t)$ in a form obtained by convolution [equivalent to (10.2.14) and (10.2.15) for the appropriate case]. Substitution of the current expression, (10.2.3), then yields the final relationships.

12.2.2 Solution of the E_rC_i Scheme in Current Step (Chronopotentiometric) Methods

To illustrate the analytical approach to solving problems involving coupled chemical reactions and the treatment of the theoretical results, we consider the E_rC_i scheme for a constant-current excitation. Although chronopotentiometric methods are now rarely used in practice to study such reactions, this is a good technique for illustrating the Laplace transform method, the nature of the changes caused by the coupled reaction, and the "zone diagram" approach for visualizing the effects of changes in time scale and rate constant. Analogous principles apply for cyclic voltammetry, where only numerical solutions are available. The equations governing the E_rC_i case are given as entry 4 in Table 12.2.1 and were discussed in Section 12.2.1.

(a) Forward Reaction
The equation for $C_O(x, t)$ is the same as that in the absence of the following reaction, that is, (8.2.13):

$$C_O(0, t) = C_O^* - \frac{2it^{1/2}}{nFAD_O^{1/2}\pi^{1/2}} \tag{12.2.11}$$

Thus, the forward transition time, τ_f [when $C_O(0, t) = 0$], is unperturbed, and $i\tau_f^{1/2}/C_O^*$ is a constant given by (8.2.14). However, $C_R(x, t)$ is affected by the following reaction, and this causes the $E-t$ curve to be different. The Laplace transform of (12.2.5) with initial condition (12.2.6) yields

$$s\overline{C}_R(x, s) = D_R\left[\frac{d^2\overline{C}_R(x, s)}{dx^2}\right] - k\overline{C}_R(x, s) \tag{12.2.12}$$

$$\left[\frac{d^2\overline{C}_R(x, s)}{dx^2}\right] = \left[\frac{(s + k)}{D_R}\right]\overline{C}_R(x, s) \tag{12.2.13}$$

Solution of this equation with the boundary condition $\lim_{x \to \infty} C_R(x, s) = 0$ gives

$$\overline{C}_R(x, s) = \overline{C}_R(0, s) \exp\left[-\left(\frac{s + k}{D_R}\right)^{1/2} x\right] \tag{12.2.14}$$

With the boundary condition

$$-D_R\left[\frac{\partial \overline{C}_R(x, s)}{\partial x}\right]_{x=0} = \frac{\overline{i}(s)}{nFA} \tag{12.2.15}$$

this finally yields

$$\overline{C}_R(0, s)(s + k)^{1/2}D_R^{1/2} = \frac{\overline{i}(s)}{nFA} \tag{12.2.16}$$

For the forward step at constant current,

$$\bar{i}(s) = \frac{i}{s} \tag{12.2.17}$$

$$\bar{C}_R(0, s) = \frac{i}{nFAD_R^{1/2}s(s + k)^{1/2}} \tag{12.2.18}$$

and, from the inverse transform,

$$C_R(0, t) = \frac{i}{nFAD_R^{1/2}k^{1/2}} \, \text{erf}[(kt)^{1/2}] \tag{12.2.19}$$

(b) Potential-Time Behavior

From (8.2.14) and (12.2.11),

$$C_O(0, t) = \frac{2i(\tau^{1/2} - t^{1/2})}{nFAD_O^{1/2}\pi^{1/2}} \tag{12.2.20}$$

For a reversible electron-transfer reaction, the Nernst equation applies, that is,

$$E = E^{0'} + \left(\frac{RT}{nF}\right) \ln \frac{C_O(0, t)}{C_R(0, t)} \tag{12.2.21}$$

The E–t curve is obtained from (12.2.19) to (12.2.21):

$$E = E^{0'} + \frac{RT}{nF} \ln \frac{2}{\pi^{1/2}} \left(\frac{D_R}{D_O}\right)^{1/2} \frac{(kt)^{1/2}(\tau^{1/2} - t^{1/2})}{\text{erf}[(kt)^{1/2}]t^{1/2}} \tag{12.2.22}$$

$$E = E^{0'} + \frac{RT}{2nF} \ln\left(\frac{D_R}{D_O}\right) + \frac{RT}{nF} \ln\left\{\frac{2}{\pi^{1/2}} \frac{(kt)^{1/2}}{\text{erf}[(kt)^{1/2}]}\right\} + \frac{RT}{nF} \ln\left(\frac{\tau^{1/2} - t^{1/2}}{t^{1/2}}\right) \tag{12.2.23}$$

This can be written

$$\boxed{E = E_{1/2} - \frac{RT}{nF} \ln \Xi + \frac{RT}{nF} \ln\left(\frac{\tau^{1/2} - t^{1/2}}{t^{1/2}}\right)} \tag{12.2.24a}$$

$$\Xi = \frac{\pi^{1/2}}{2} \frac{\text{erf}[(kt)^{1/2}]}{(kt)^{1/2}} \tag{12.2.24b}$$

The term $(RT/nF) \ln \Xi$ represents the perturbation caused by the chemical reaction.

It is instructive to examine the limiting behavior of Ξ as a function of the dimensionless product kt. For $(kt)^{1/2} < 0.1$, $\text{erf}[(kt)^{1/2}] \approx 2(kt)^{1/2}/\pi^{1/2}$ (see Section A.3), or $\Xi = 1$, and the second term of (12.2.24a) is zero. In other words, the following reaction will have no effect for sufficiently small k or short times. This condition can be considered to define the *pure diffusion-controlled zone*. As $(kt)^{1/2}$ increases, Ξ becomes smaller, so that the E–t curve is shifted toward more positive potentials. For example, when $(kt)^{1/2} = 1$, $\text{erf}[(kt)^{1/2}] = 0.84$, $\Xi = 0.75$ and the wave is shifted 7 mV on the potential axis in a positive direction. When $(kt)^{1/2} \geq 2$, $\text{erf}[(kt)^{1/2}]$ approaches the asymptote of 1, so that $\Xi = 1/2(\pi/kt)^{1/2}$. This represents the limiting region for large k or t, and leads to the E–t equation for the *pure kinetic zone*:

$$E = E_{1/2} + \left(\frac{RT}{nF}\right) \ln\left(\frac{2k^{1/2}}{\pi^{1/2}}\right) + \left(\frac{RT}{nF}\right) \ln(\tau^{1/2} - t^{1/2}) \tag{12.2.25}$$

Note that this equation is very similar in form to that for a totally irreversible electron-transfer reaction with no coupled chemical reaction, (8.3.6), and predicts a linear variation of E with $\ln(\tau^{1/2} - t^{1/2})$ in this zone. This equation can also be written as

$$E = E_{1/2} + \left(\frac{RT}{nF}\right) \ln\left(\frac{2}{\pi^{1/2}}\right) + \left(\frac{RT}{2nF}\right) \ln(kt) + \left(\frac{RT}{nF}\right) \ln\left(\frac{\tau^{1/2} - t^{1/2}}{t^{1/2}}\right) \tag{12.2.26}$$

or, at $t = \tau/4$, $E = E_{\tau/4}$, where

$$E_{\tau/4} = E_{1/2} + \left(\frac{RT}{nF}\right) \ln\left(\frac{2}{\pi^{1/2}}\right) + \left(\frac{RT}{2nF}\right) \ln(kt) \tag{12.2.27}$$

A plot of $E_{\tau/4}$ vs. log (kt) is shown in Figure 12.2.1. Note that the limiting diffusion and kinetic zones are described by the solid lines,[1] and the dashed curve represents the exact equation, (12.2.24). Of course, the boundaries of these zones depend on the approximation employed, and the applicability of the limiting equations depends on the accuracy of the electrochemical measurements. For example, if potential measurements are made to the nearest 1 mV, the pure kinetic zone will be reached (for $n = 1$ and 25°C) when 25.7 ln $[\mathrm{erf}(kt)^{1/2}] \leq 1$ mV or when $(kt)^{1/2} \geq 1.5$.

(c) Current Reversal

The treatment involving current reversal employs the same equations and utilizes the zero-shift-theorem method, as in Section 8.4.2. Thus, for reversal of current at time t_1 (where $t_1 \leq \tau_1$),

$$i(t) = i - S_{t_1}(t)(2i) \tag{12.2.28}$$

where $S_{t_1}(t)$ is the step function, equal to 0 $(t \leq t_1)$ and 1 $(t > t_1)$. Then

$$\bar{i}(s) = \left(\frac{i}{s}\right)(1 - 2 e^{-t_1 s}) \tag{12.2.29}$$

and from (12.2.16),

$$\overline{C}_R(0, s) = \frac{i}{nFAD_R^{1/2}}\left[\frac{1}{s(s + k)^{1/2}} - \frac{2 e^{-t_1 s}}{s(s + k)^{1/2}}\right] \tag{12.2.30}$$
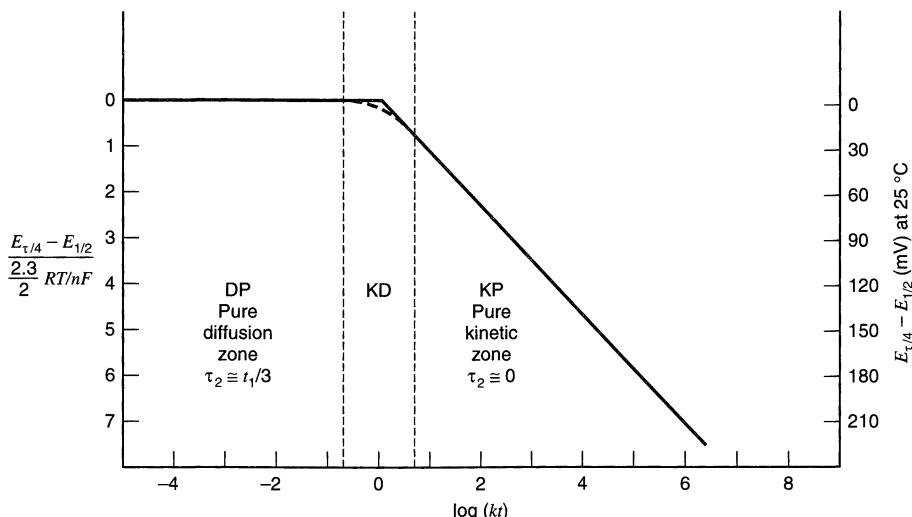
Figure 12.2.1 Variation of $E_{\tau/4}$ with log(kt) for chronopotentiometry with the E_rC_i reaction scheme. Zone KD is a transition region between the pure diffusion and pure kinetic situations.

---

[1]The concept of using zone diagrams to describe behavior within a given mechanistic framework was developed extensively by Savéant and coworkers. Many examples are covered below. The labels given to the zones (e.g., DP, KD, and KP in Figure 12.2.1) are typically derived from their work and are based on their French-language abbreviations.
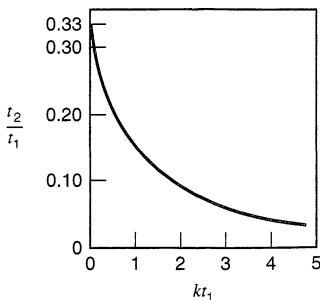
Figure 12.2.2 Variation of τ_2/t_1 with kt_1 for chronopotentiometry with the E_rC_i reaction scheme.

The inverse transform yields

$$C_R(0, t) = \frac{i}{nFAD_R^{1/2}}\left[\frac{\text{erf}(kt)^{1/2}}{k^{1/2}} - S_{t_1}(t)\frac{2}{k^{1/2}}\text{erf}\{[k(t - t_1)]^{1/2}\}\right] \qquad (12.2.31)$$

At the reverse transition time, $t = t_1 + \tau_2$, $C_R(0, t) = 0$, so that

$$\boxed{\text{erf}\{[k(t_1 + \tau_2)]^{1/2}\} = 2\,\text{erf}[(k\tau_2)^{1/2}]}$$

Let us again examine the limiting behavior. When kt_1 is small (diffusion zone), $\text{erf}[(k\tau_2)^{1/2}]$ approaches $2(k\tau_2)^{1/2}/\pi^{1/2}$ and $\text{erf}\{[k(t_1 + \tau_2)]^{1/2}\}$ approaches $2[k(t_1 + \tau_2)]^{1/2}/\pi^{1/2}$. Under these conditions (12.2.32) becomes identical to the equation for unperturbed reversal chronopotentiometry and $\tau_2 = t_1/3$ (see equation 8.4.9). When kt_1 is large (kinetic zone), τ_2 approaches 0. The variation of τ_2/t_1 with kt_1 is shown in Figure 12.2.2 (20–22). Note that kinetic information can be obtained from reversal measurements only in the intermediate zone ($0.1 \le kt_1 \le 5$). The actual value of k is obtained by determining τ_2/t_1 for different values of t_1 and fitting the data to the *working curve* shown in Figure 12.2.2 (23). Kinetic information can also be obtained in the kinetic zone from the shift of potential with τ_1; however, $E^{0'}$ must be known for the electron-transfer step before an actual value of k can be determined.

The treatment given here is typical of those required for other reaction schemes and techniques. These treatments result in the establishment of (a) diagnostic criteria for distinguishing one mechanistic scheme from another and (b) working curves or tables that can be used to evaluate rate constants. A survey of results is given in Section 12.3.

12.3 THEORY FOR TRANSIENT VOLTAMMETRY AND CHRONOPOTENTIOMETRY

We examine here the theoretical treatments for cyclic voltammetry and other transient techniques (chronoamperometry, chronopotentiometry) for a broad set of reaction schemes, all of which are introduced in Section 12.2. When one wants to investigate an electrochemical reaction scheme, one almost always turns first to CV. Although all transient methods can, in principle, explore the same *i-E-t* space to obtain the needed data, cyclic voltammetry allows one to see easily the effects of E and t on the current in a single experiment (Figure 6.1.1). Moreover, correction of the faradaic current for capacitive effects and adsorption is relatively straightforward with CV (compared, for example, to chronopotentiometry). If capacitive effects are so large that good CV behavior is not obtained, methods such as square wave or pulse voltammetry might be preferable. On the other hand, CV suffers from the fact that heterogeneous kinetics can affect the observed response and can complicate the extraction of accurate rate constants for homogeneous re-

actions. Measurements in which the potential is stepped to values where the heterogeneous reaction is mass-transfer controlled, like potential step and rotating disk electrode methods, do not have this problem. Thus, after a reaction mechanism has been elucidated and semiquantitative results have been obtained by CV, one often turns to other methods, like chronocoulometry or RDE methods, to obtain better values of kinetic parameters.

In the sections that follow, we first examine typical cyclic voltammetric responses for the different reaction mechanisms and then show how consideration of zone diagrams and theoretical responses can be used to recognize the reaction scheme and extract kinetic parameters. After the discussion of CV, other transient techniques for the same reaction scheme are discussed. We will not describe results in detail, but rather attempt to show important limiting cases and equations that are useful for recognizing a given reaction sequence and estimating rate constants.

12.3.1 Preceding Reaction—C_rE_r

$$Y \underset{k_b}{\overset{k_f}{\rightleftarrows}} O \tag{12.3.1}$$

$$O + ne \rightleftarrows R \tag{12.3.2}$$

$$K = k_f/k_b = C_O(x, 0)/C_Y(x, 0) \tag{12.3.3}$$

The behavior of this system depends on the magnitudes of both first-order rate constants, k_f and k_b (s^{-1}), and the equilibrium constant, K. It is convenient to describe the reactions in terms of dimensionless parameters related to the rate constants of the reactions (or the characteristic reaction lifetimes) and the duration of the experiment. For the C_rE_r case in the context of a potential step experiment of duration t, these are conveniently expressed by K and $\lambda = (k_f + k_b)t$. For different methods and mechanisms, λ is defined in particular ways, as given in Table 12.3.1.

It is instructive to think about the behavior according to the zone diagram (24) in Figure 12.3.1, which defines how the electrochemical parameters are affected by λ and K, and when the limiting behavior will be observed within a given accuracy. When K is large (e.g., $K \geq 20$), the equilibrium in (12.3.1) lies so far to the right that most of the material exists in the electroactive form, O. The preceding reaction then has little effect on the electrochemical response, which is essentially the unperturbed nernstian behavior. Similarly, when k_f and k_b are small compared to the experimental time scale (e.g., $\lambda < 0.1$), the preceding reaction cannot occur appreciably on the experimental time scale. Thus it again has little effect and a nernstian response results, but with the effective initial concentration of O, $C_O(x, 0)$, being given by

$$C_O(x, 0) = \frac{C^*K}{(K + 1)} \tag{12.3.4}$$

TABLE 12.3.1 Dimensionless Parameters for Various Methods

Technique	Time parameter(s)	Dimensionless kinetic parameter, λ, for C_rE_r	E_rC_i	E_rC_i'
Chronoamperometry and polarography	t	$(k_f + k_b)t$	kt	$k'C_Z^*t$
Linear sweep and cyclic voltammetry	$1/v$	$\dfrac{(k_f + k_b)}{v}\left(\dfrac{RT}{nF}\right)$	$\dfrac{k}{v}\left(\dfrac{RT}{nF}\right)$	$\dfrac{k'C_Z^*}{v}\left(\dfrac{RT}{nF}\right)$
Chronopotentiometry	τ	$(k_f + k_b)\tau$	$k\tau$	$k'C_Z^*\tau$
Rotating disk electrode	$1/\omega$	$(k_f + k_b)/\omega^a$	k/ω	$k'C_Z^*\omega$

^{a}Or $\delta/\mu = 1.61\ k^{1/2}\nu^{1/6}/\omega^{1/2}D^{1/6}$.
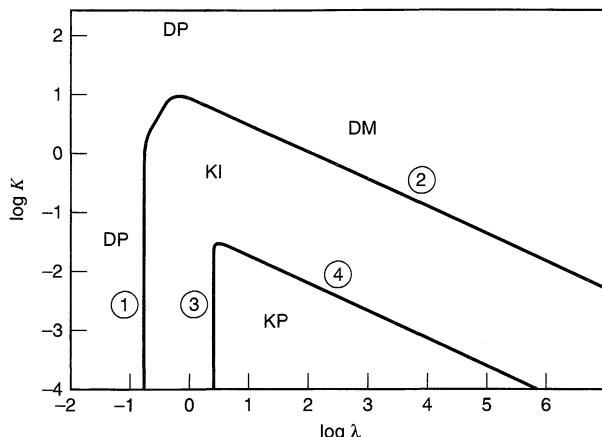
Figure 12.3.1 C_rE_r reaction diagram with zones for different types of electrochemical behavior as a function of K and λ (defined in Table 12.3.1). The zones are DP, pure diffusion; DM, diffusion modified by equilibrium constant of preceding reaction; KP, pure kinetics; and KI, intermediate kinetics. The circled numbers correspond to the boundaries calculated in Section 12.3.1(c). [Adapted with permission from J.-M. Savéant and E. Vianello, *Electrochim. Acta*, **8**, 905 (1963). Copyright 1963, Pergamon Press PLC.]

where

$$C_O(x, 0) + C_Y(x, 0) = C^* \tag{12.3.5}$$

When λ is very large, (12.3.1) is so mobile that it can always be considered at equilibrium. In this case, the behavior is yet again nernstian, but the wave is shifted along the potential axis from its unperturbed position by an extent that depends on the magnitude of K, as discussed in Sections 1.5.1 and 5.4.4. This shift is a thermodynamic effect reflecting the energy by which species O is stabilized by the equilibrium. The extent of this zone, in the upper-right portion of Figure 12.3.1, depends on K and λ. When K is small and λ is large, the reaction is so fast that the reactants can be considered to be at steady-state values within the reaction layer near the electrode surface, and the differential equations governing the system can be solved by setting the derivatives with respect to time equal to zero (the "reaction-layer treatment"). This is the pure kinetic zone. A more quantitative description of how the limits of these zones are chosen is given in Section 12.3.1(c).

(a) Linear Sweep and Cyclic Voltammetric Methods
The shape of the i–E curve depends on the values of K and λ; that is, on the region of interest in Figure 12.3.1 (24, 25). Curves for this scheme with $K = 10^{-3}$, $k_f = 10^{-2}$ s^{-1}, $k_b = 10$ s^{-1}, and scan rates, v, of 0.01 to 10 V/s (λ of 26 to 0.026) are shown in Figure 12.3.2. It is instructive to correlate these curves to the appropriate points in the zone diagram (Figure 12.3.1). In all cases, log $K = -3$. At the high scan rate ($v = 10$ V/s, log $\lambda = -1.6$), the operating point is in the DP region, and a diffusion-controlled voltammogram with little contribution from the preceding reaction is observed. The behavior appears essentially as an unperturbed reversible reaction with an initial concentration of O determined by the small equilibrium constant of reaction (12.3.1). As v decreases, one proceeds horizontally at the log $K = -3$ level across the zone diagram toward larger log λ values. At $v = 1$ V/s (log $\lambda = -0.6$), the operating point is in the KI region. We enter the KP region at still smaller scan rates, such as $v = 0.01$ V/s (log $\lambda = 1.6$). In this region, the response is totally governed by the rate at which O is supplied by the forward re-
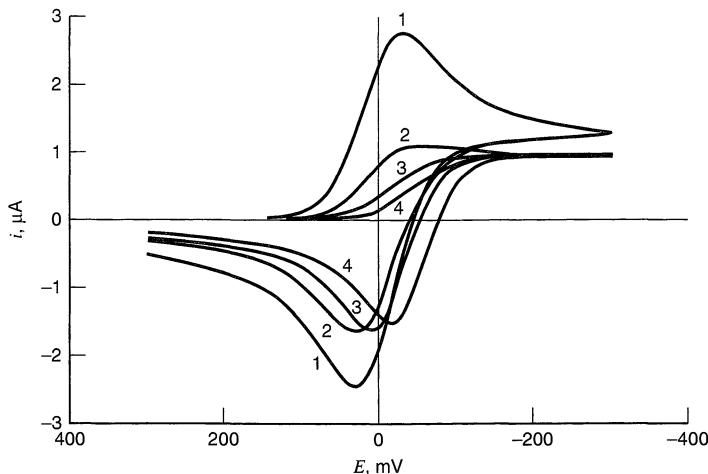
Figure 12.3.2 Cyclic voltammograms for the C_rE_r case. $A \rightleftarrows B$; $B + e \rightleftarrows C$, where $E_{B/C}^{0'} = 0$ V, $C^* = 1$ mM, $A = 1$ cm^2, $D_A = D_B = D_C = 10^{-5}$ cm^2/s, $K = 10^{-3}$, $k_f = 10^{-2}$ s^{-1}, $k_b = 10$ s^{-1}, $T = 25°C$, and scan rates, v of (1) 10; (2) 1; (3) 0.1; (4) 0.01 V/s.

action, rather than by diffusion. The current attains a steady-state value, indicated by the cathodic plateau independent of the scan rate.

Since the observed i-E response depends upon K, k_f, k_b, and v, in addition to D, C, and n, a full representation of the CV behavior in terms of these parameters would involve a large number of plots. The results can be given more economically by plotting in terms of the dimensionless parameters K and λ and by normalizing the current, as shown in Figure 12.3.3.

As discussed in the introduction to this section, the behavior is diffusion-controlled in regions DP and DM.

In the pure kinetic region (KP), the i-E curve takes on an S-shape (rather than the usual peak-shape) and the current attains a steady-state value, i_L, independent of v, given by

$$i_L = nFAD^{1/2}C^*K(k_f + k_b)^{1/2} \qquad (12.3.6)$$

In this region, the half-peak (i.e., half-plateau) potential $E_{p/2}$ is given by

$$E_{p/2} = E^{0'} - 0.277RT/nF - (RT/2nF) \ln \lambda \qquad (12.3.7)$$

The shift of $E_{p/2}$ with v is

$$dE_{p/2}/d \ln v = RT/2nF \qquad (12.3.8)$$

thus at 25°C a tenfold increase in v causes the reduction peak to shift by 29/n mV in the positive direction. As v increases (so that λ decreases) and the system enters the zone of intermediate kinetics (zone KI, Figure 12.3.1), the shift of $E_{p/2}$ with scan rate becomes smaller and finally is independent of v in the diffusion zone (DP). The shift of $E_{p/2}$ with the dimensionless parameter $K\lambda$ is shown in Figure 12.3.4 (25). A working curve showing the ratio of the kinetic peak current, i_k, to the diffusion-controlled current, i_d (attained at very slow scan rates), has been proposed (25) (Figure 12.3.5) and has been shown to fit the empirical equation

$$\frac{i_k}{i_d} = \frac{1}{1.02 + 0.471/K\sqrt{\lambda}} \qquad (12.3.9)$$
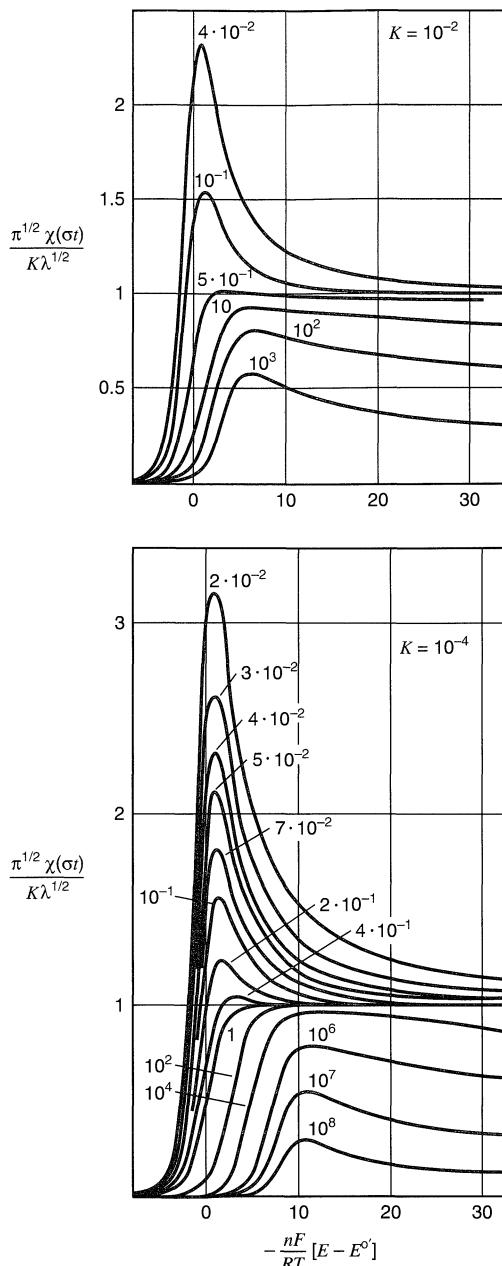
Figure 12.3.3 Curves of current [plotted as $\pi^{1/2}\chi(\sigma t)/K\lambda^{1/2}$, where $\chi(\sigma t)$ is defined as in (6.2.16)] vs. potential at $K = 10^{-2}$ (upper) and $K = 10^{-4}$ (lower), at different values of $\lambda = (RT/nF)[(k_f + k_b)/v]$ shown on each curve for the C_rE_r reaction scheme. [Reprinted with permission from J.-M. Savéant and E. Vianello, *Electrochim. Acta*, **8**, 905 (1963). Copyright 1963, Pergamon Press PLC.]

In cyclic voltammetry, the anodic portion on the reverse scan is not affected as much as the forward response by the coupled reaction (Figure 12.3.2). The ratio of i_{pa}/i_{pc} (with i_{pa} measured from the extension of the cathodic curve as described in Section 6.5) increases with increasing scan rate as shown in the working curve in Figure 12.3.6 (25). The actual i–E curves can be drawn using series solutions or a table given by Nicholson and Shain (25) or by digital simulation.

(b) Polarographic and Chronoamperometric Methods
The current of interest is that at the limiting current plateau, that is, for $C_O(0, t) = 0$. For a planar electrode, assuming equal diffusion coefficients for all species ($D_O = D_Y = D$)
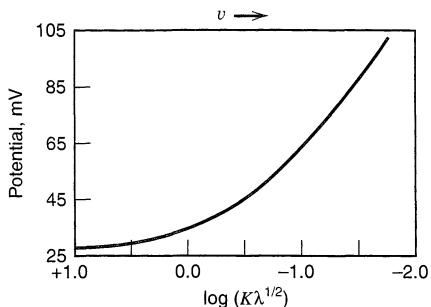
Figure 12.3.4 Variation of $E_{p/2}$ with $K\lambda^{1/2}$ for the C_rE_r reaction scheme. Potential axis is $n(E_{p/2} - E_{1/2}) - (RT/F) \ln[K/(1 + K)]$. $v\rightarrow$ shows direction of increasing scan rate. [Reprinted with permission from R. S. Nicholson and I. Shain, *Anal. Chem.*, **36**, 706 (1964). Copyright 1964, American Chemical Society.]

and the chemical equilibrium favoring Y [$K << 1$, $C_Y(x, 0) \approx C^*$], the current is given by (26)

$$i = nFAC^*D^{1/2}k_f^{1/2}K^{1/2} \exp(k_f K t) \, \mathrm{erfc}[(k_f K t)^{1/2}] \tag{12.3.10}$$

Letting $(k_f K t)^{1/2} = Z$, this can be written

$$i = nFAD^{1/2}C^*t^{-1/2}Z \exp(Z^2) \, \mathrm{erfc}(Z) \tag{12.3.11}$$

Note that this is of the same form as the current for a totally irreversible wave [see (5.5.27)]. For large values of k_f, the function $Z \exp(Z^2) \, \mathrm{erfc}(Z)$ approaches $\pi^{-1/2}$ and the current becomes the diffusion-controlled value, i_d (equation 5.2.11); hence the behavior is in the diffusion zone on the right side in Figure 12.3.1. Equation 12.3.11 can be written

$$\frac{i}{i_d} = \pi^{1/2}Z \exp(Z^2) \, \mathrm{erfc}(Z) \tag{12.3.12}$$

[Compare with (5.5.28) and Figure 5.5.2.] For small values of the argument Z, $\exp(Z^2) \, \mathrm{erfc}(Z) \approx Z$, and (12.3.12) yields the same current given in equation 12.3.6 with $K << 1$, that is,

$$i = i_d \pi^{1/2}(k_f K t)^{1/2} = nFAD^{1/2}C^*(k_f K)^{1/2} \tag{12.3.13}$$

which is independent of t and governed by the rate of conversion of Y to O.

These equations hold for polarography as well (within the expanding plane approximation) with $t = t_{max}$ (the drop time) and the area A given by (7.1.3). The approach of Section 7.2.2 applies. Treatments taking account of spherical diffusion and unequal diffusion coefficients have also been presented (27, 28). Note how the limiting current in po-
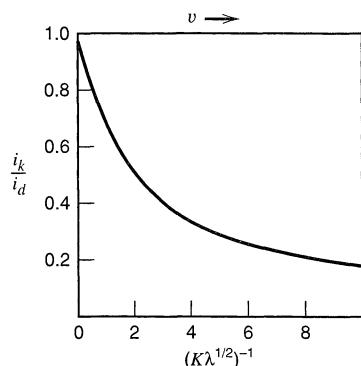
Figure 12.3.5 Working curve of i_k/i_d vs. $(K\lambda^{1/2})^{-1}$ for the C_rE_r reaction scheme. [Reprinted with permission from R. S. Nicholson and I. Shain, *Anal. Chem.*, **36**, 706 (1964). Copyright 1964, American Chemical Society.]
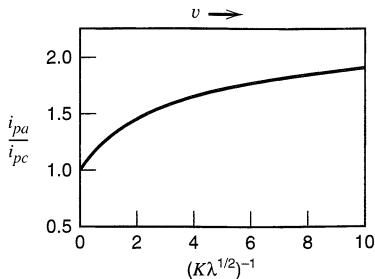
Figure 12.3.6 Ratio of anodic to cathodic peak currents as a function of the kinetic parameters for the C_rE_r reaction scheme. [Reprinted with permission from R. S. Nicholson and I. Shain, *Anal. Chem.*, **36**, 706 (1964). Copyright 1964, American Chemical Society.]

larography varies with t_{max} or the height of the mercury column, h_{corr}. For large k_f (in the diffusion region), i varies as $t_{max}^{1/6}$ or as $h_{corr}^{1/2}$. For small k_f, where (12.3.13) applies, i is independent of both t_{max} and h_{corr}.

(c) Chronopotentiometric Methods

The i-τ behavior is governed by the following equation (29–31)

$$i\tau^{1/2} = \frac{nFAC^*(\pi D)^{1/2}}{2} - \frac{i}{2K}\left[\frac{\pi}{(k_f + k_b)}\right]^{1/2} \mathrm{erf}(\lambda^{1/2}) \tag{12.3.14}$$

The first term on the right is the value for the diffusion-controlled reaction, $i\tau_d^{1/2}$. Using the definition of λ (Table 12.3.1), this equation can then be written

$$i\tau^{1/2} = i\tau_d^{1/2} - \frac{i\tau^{1/2}\pi^{1/2}}{2K\lambda^{1/2}}\mathrm{erf}(\lambda^{1/2}) \tag{12.3.15}$$

or

$$\boxed{i\tau^{1/2} = \frac{i\tau_d^{1/2}}{1 + \dfrac{0.886\,\mathrm{erf}(\lambda^{1/2})}{K\lambda^{1/2}}}} \tag{12.3.16}$$

The variation of $i\tau^{1/2}$ with $\lambda^{1/2}$ for several different values of K is shown in Figure 12.3.7. This equation is also useful in examining the limiting behavior of $i\tau^{1/2}$ and defining the different zones of interest as in Figure 12.3.1. Consider $\lambda^{1/2} \leq 0.4$, where $\mathrm{erf}(\lambda^{1/2})/\lambda^{1/2}$ approaches the limiting value of $2/\pi^{1/2}$ (within *ca.* 5%) and (12.3.16) yields $(i\tau^{1/2}/i\tau_d^{1/2}) \approx K/(1 + K)$, which is the diffusion-controlled response corrected by calculat-
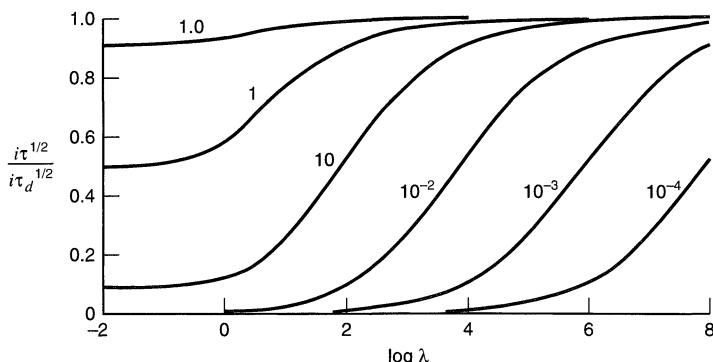
Figure 12.3.7 Variation of $i\tau^{1/2}/i\tau_d^{1/2}$ with λ for various values of K (indicated on curve) for chronopotentiometric study of the C_rE_r reaction scheme.

ing $C_O(x, 0)$ from C^*. Thus this condition, or log $\lambda < -0.8$, defines the left boundary (line 1). For large λ (e.g., $\lambda^{1/2} \geq 1.4$), erf($\lambda^{1/2}$) ≈ 1 and (12.3.16) yields

$$\frac{i\tau^{1/2}}{i\tau_d^{1/2}} = \left(1 + \frac{0.886}{K\lambda^{1/2}}\right)^{-1} \tag{12.3.17}$$

This condition gives diffusion-controlled behavior when $0.886/K\lambda^{1/2} \leq 0.05$, or log $K = 1.25 - (1/2)$ log λ; this represents the right boundary (line 2). The pure kinetic region is also defined by large λ values, this time as $K \to 0$. One can set the boundary by using $\lambda^{1/2} \geq 1.4$ (line 3) and the condition that the second term on the right predominates in (12.3.17). Thus $0.886/K\lambda^{1/2} \geq 10$ or log $K = -1/2$ log $\lambda - 1.05$ (line 4). Note that the exact locations of these boundaries depend on the levels of approximations used. Moreover, in this pure kinetic region, (12.3.14) becomes

$$i\tau^{1/2} = i\tau_d^{1/2} - \frac{i\pi^{1/2}}{2K(k_f + k_b)^{1/2}} \tag{12.3.18}$$

so that a plot of $i\tau^{1/2}$ vs. i in this region is a straight line of slope $-\pi^{1/2}/2K(k_f + k_b)^{1/2}$. This behavior is evident in the plots shown in Figure 12.3.8.

For simple reversal chronopotentiometry, the ratio of reversal transition time τ_2 to the forward time τ_1 is 1/3, just as in the diffusion-controlled case, independent of the rate constants. However, for cyclic chronopotentiometry the transition times for the third (τ_3) and subsequent reversals differ from those of the diffusion-controlled case (31).

12.3.2 Preceding Reaction—C_rE_i

This scheme is the same as that in Section 12.3.1, except that the electron-transfer reaction (12.3.2) is totally irreversible and is governed by the charge-transfer parameters α and k^0. The limiting current behavior in chronoamperometric and polarographic methods will not be perturbed by irreversibility in the electron-transfer reaction; since the potential is stepped to a value sufficiently beyond the equilibrium value that reaction (12.3.2) proceeds rapidly. Thus the results will be the same as in Section 12.3.1(b). This case illustrates an important advantage of chronoamperometric methods: that the potential can be chosen to eliminate complexities in the analysis of the behavior caused by the heterogeneous electron-transfer
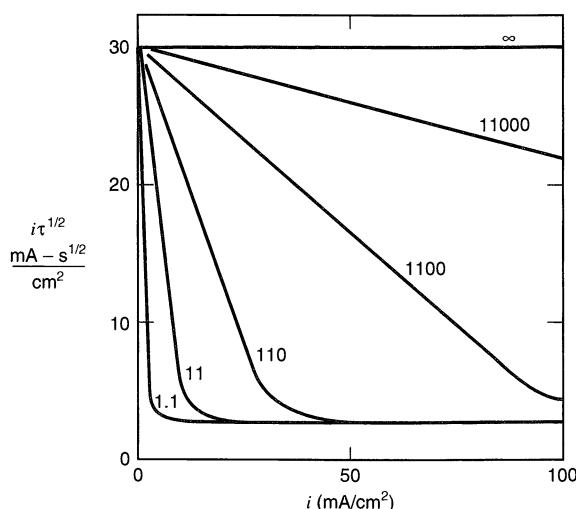
Figure 12.3.8 Variation of $i\tau^{1/2}$ with i, for various values of $(k_f + k_b)$ (in s^{-1}). Calculated for $K = 0.1$, $C^* = 0.11$ mM, and $D = 10^{-5}$ cm^2/s. [Reprinted with permission from P. Delahay and T. Berzins, *J. Am. Chem. Soc.*, **75**, 2486 (1953). Copyright 1953, American Chemical Society.]

step. On the other hand, once the rate constants of the homogeneous reactions have been deduced, potential steps to less extreme potentials can provide information about α and k^0. This requires solution of the more complex problem where the boundary condition for $C_O(0, t)$ is governed by the heterogeneous reaction rate. This problem will not be examined here.

The C_rE_i case has been treated for linear sweep voltammetry (25). Because of the irreversibility of the electron transfer, no anodic current is observed on the reverse scan and cyclic voltammetric behavior need not be considered. Typical i–E curves are shown in Figure 12.3.9. The limiting behavior again depends on the magnitude of the kinetic parameter $K\lambda_i^{1/2}$, where λ_i is the λ factor of Table 12.3.1, with n set to $\alpha n = \alpha$ for a one-electron "E" step:

$$\lambda_i = \frac{k_f + k_b}{v}\left(\frac{RT}{\alpha F}\right) \tag{12.3.19}$$

When λ_i is small, the behavior is the same as that of the unperturbed irreversible one-step, one-electron reaction, as described in Section 6.3, except that the concentration of O is given by $C^*[K/(1 + K)]$. This represents the limiting behavior at high scan rates. For large λ_i and large values of $K\lambda_i^{1/2}$, the preceding reaction can be considered to be essentially at equilibrium at all times, and again the i–E behavior becomes that of the unperturbed irreversible case in Section 6.3, with the wave shifted (from the position it would have had without the preceding reaction) in a negative direction by an amount $(RT/\alpha F) \ln[K/(1 + K)]$. For small values of $K\lambda_i^{1/2}$ (but with large λ_i), the behavior depends on k^0, as well as K and λ_i, and the i–E curve no longer shows a peak, but instead has an S-shape with a current plateau. This is the pure kinetic region where the limiting current becomes independent of v, as in the case of the C_rE_r scheme. Under these conditions the current is given by (25)

$$i = \frac{FAC^*D^{1/2}\,K(k_f + k_b)^{1/2}}{1 + \left[\dfrac{\pi D^{1/2}\alpha f v(K + 1)}{k^0(k_f + k_b)^{1/2}}\right]\exp[\alpha f(E - E^{0'})]} \tag{12.3.20}$$

Nicholson and Shain (25) suggest that for all ranges of $K\lambda_i^{1/2}$ the kinetic parameters can be obtained by fitting the kinetic peak (or plateau) current for the C_rE_i case, i_k, to that for the diffusion-controlled peak current for an irreversible charge transfer, i_d (equation 6.3.12), by the empirical equation

$$\frac{i_k}{i_d} = \frac{1}{1.02 + 0.531/K\sqrt{\lambda_i}} \tag{12.3.21}$$
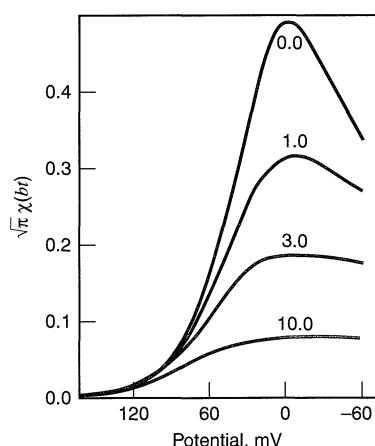
Figure 12.3.9 Curves of current [plotted as $\pi^{1/2}\chi(bt)$, where $\chi(bt)$ is defined as in (6.3.6)] vs. potential at different values of $(K\lambda_i^{1/2})^{-1}$ (shown on curves). The potential scale is $\alpha(E - E^{0'}) + (RT/F)\ln[(\pi Db)^{1/2}/k^0] - (RT/F)\ln[K/(1 + K)]$. $b = \alpha F v/RT$; $\lambda_i = (k_f + k_b)/b$. [Reprinted with permission from R. S. Nicholson and I. Shain, *Anal. Chem.*, **36**, 706 (1964). Copyright 1964, American Chemical Society.]

[compare to (12.3.9)]. For the more general C_rE_q case, the best approach is via digital simulation for different values of the parameters.

For chronopotentiometry, the behavior of τ is again like the C_rE_r case, since the wave will shift to sufficiently negative values to maintain the electron-transfer reaction rate at the value required by the applied constant current, and the treatment in Section 12.3.1 applies.

12.3.3 Following Reaction—E_rC_i

This case for the chronopotentiometric method was treated in Section 12.2.2, and the zones for pure diffusion behavior (DP) and pure kinetic behavior (KP) were derived in terms of the dimensionless kinetic parameter λ (Table 12.3.1): DP, $\lambda < 0.1$; KP, $\lambda > 5$ (Figure 12.2.1). These zones generally apply with the other techniques as well.
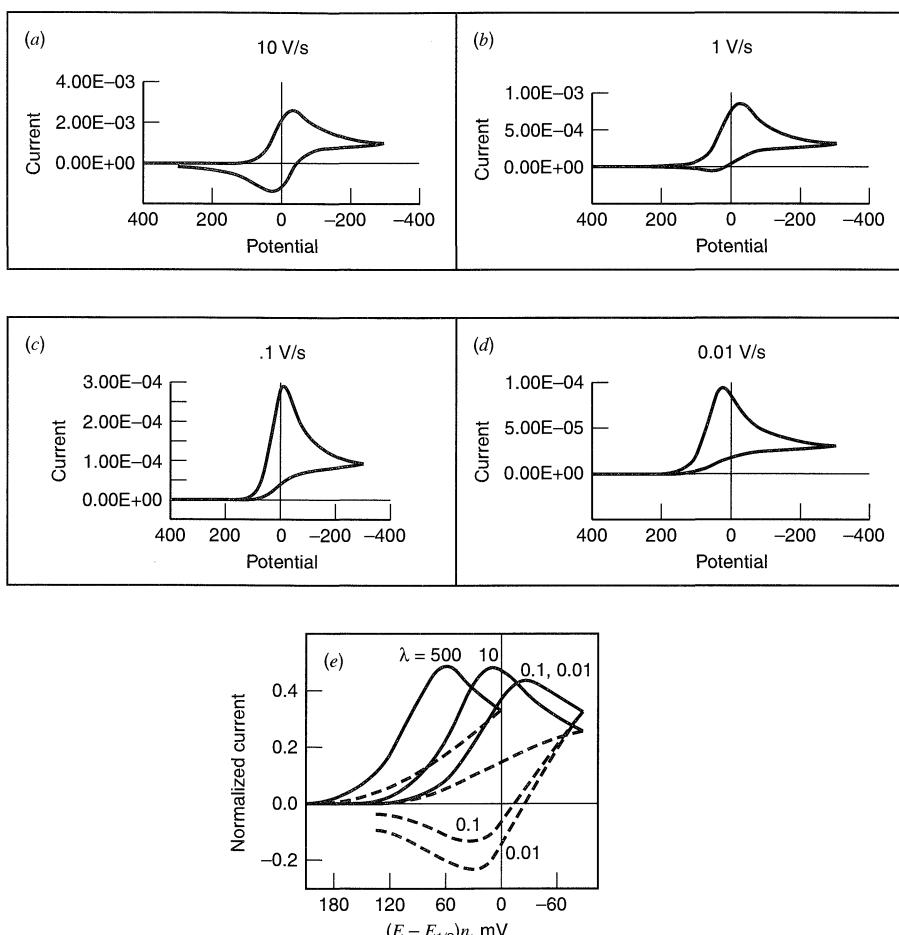
Figure 12.3.10 Cyclic voltammograms for E_rC_i case at 25°C. $A + e \rightleftarrows B$; $B \rightarrow C$. (a–d) System where $E^0_{A/B} = 0$ V, $C^*_A = 1$ mM, $C^*_B = 0$, $A = 1$ cm^2, $D_A = D_B = 10^{-5}$ cm^2/s, and $k_f = 10$ s^{-1} at scan rates v of (a) 10, (b) 1, (c) 0.1, and (d) 0.01 V/s. Current in amperes; potential in mV. Note that the vertical scale changes from panel to panel. (e) Normalized current for several values of $\lambda = kRT/nFv$. [Part (e) reprinted with permission from R. S. Nicholson and I. Shain, *Anal. Chem.*, **36**, 706 (1964). Copyright 1964, American Chemical Society.]
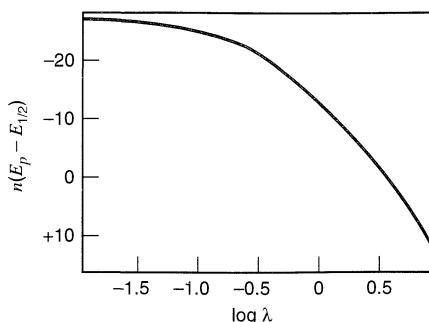
Figure 12.3.11 Variation of peak potential as a function of λ for the E_rC_i case. [Reprinted with permission from R. S. Nicholson and I. Shain, *Anal. Chem.*, **36**, 706 (1964). Copyright 1964, American Chemical Society.]

(a) Linear Sweep and Cyclic Voltammetric Methods

Typical curves for this case, both as they would appear in an experimental trial and in normalized form, are given in Figure 12.3.10. At small values of λ, essentially reversible behavior is found. For large values of λ (in the KP region), no current is observed on scan reversal and the shape of the curve is similar to that of a totally irreversible charge transfer, (6.3.6). In this region the current function changes only slightly with scan rate (i.e., $i_p/v^{1/2}$ increases by about 5% for λ changing from 1 to 10). The peak, which is generally positive of the reversible E_p value because of the following reaction, shifts in a negative direction (toward the reversible curve) with increasing v (Figure 12.3.11).

In the KP region, E_p is given by

$$E_p = E_{1/2} - \frac{RT}{nF} 0.780 + \frac{RT}{2nF} \ln \lambda \qquad (12.3.22)$$

so that the wave shifts toward negative potentials by about $30/n$ mV (at 25°C) for a tenfold increase in v. In the intermediate region of λ (KO), that is, $5 > \lambda > 0.1$, information can be obtained from the ratio of anodic and cathodic peak currents i_{pa}/i_{pc}; these are determined as described in Section 6.5.1. Nicholson and Shain (25) plotted the ratio i_{pa}/i_{pc} as a function of $k\tau$, where τ is the time between $E_{1/2}$ and the switching potential E_λ. By fitting the observed values to a working curve (Figure 12.3.12), a value of k_f can be estimated (assuming $E_{1/2}$ can be determined by experiments at sufficiently high scan rates). Note, however, that reversal data yield kinetic information only over a small range of λ. It is sometimes useful to extend the scan to more extreme potentials to see if the products of the following reaction are electroactive. For example, Figure 12.3.13 shows the cyclic voltammograms for the same reaction and conditions as in Figure 12.3.10b, but with the scan extended to more positive potentials to show waves for the oxidation of species C and, on the second reversal, the reduction of its oxidation product, D.
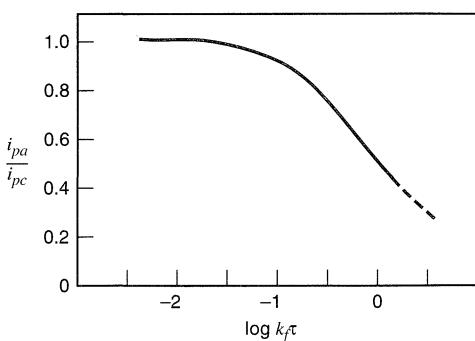
Figure 12.3.12 Ratio of anodic to cathodic peak current as a function of $k_f\tau$, where τ is the time between $E_{1/2}$ and the switching potential E_λ. [Reprinted with permission from R. S. Nicholson and I. Shain, *Anal. Chem.*, **36**, 706 (1964). Copyright 1964, American Chemical Society.]
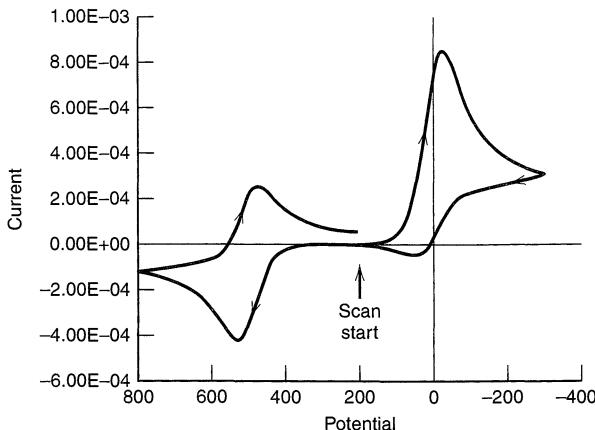
Figure 12.3.13 Cyclic voltammograms for the E_rC_i case. $A + e \rightleftarrows B$; $B \rightarrow C$ (as in Figure 12.3.10b, $v = 1$ V/s), with the scan extended to show the waves for the couple $D + e = C$, $E^0_{D/C} = 0.5$ V.

(b) Chronoamperometric Methods

Since the forward reaction for a potential step to the limiting current region is unperturbed by the irreversible following reaction, no kinetic information can be obtained from the polarographic diffusion current or the limiting chronoamperometric i–t curve. Some kinetic information is contained in the rising portion of the i–E wave and the shift of $E_{1/2}$ with t_{max}. Since this behavior is similar to that found in linear potential sweep methods, these results will not be described separately. The reaction rate constant k can be obtained by reversal techniques (see Section 5.7) (32, 33). A convenient approach is the potential step method, where at $t = 0$ the potential is stepped to a potential where $C_O(x = 0) = 0$, and at $t = \tau$ it is stepped to a potential where $C_R(x = 0) = 0$. The equation for the ratio of i_a (measured at time t_r) to i_c (measured at time $t_f = t_r - \tau$) (see Figure 5.7.3) is

$$-\frac{i_a}{i_c} = \phi[k\tau, (t_r - \tau)/\tau] - \left[\frac{(t_r - \tau)/\tau}{1 + (t_r - \tau)/\tau}\right]^{1/2} \qquad (12.3.23)$$

where ϕ represents a rather complicated function involving a confluent hypergeometric series. Working curves can be derived from (12.3.23) showing i_a/i_c as a function of $k\tau$ (i.e., λ) and $(t_r - \tau)/\tau$ (Figure 12.3.14). Similar working curves have been obtained by digital simulation of this case for both chronoamperometry and chronocoulometry (33). These curves can be employed to obtain the rate constant k if a value of τ can be employed that yields a λ in the useful range.

(c) Chronopotentiometric Methods

The equations governing τ, the E–t curve, and single reversal experiments are given in Section 12.2.2. Cyclic chronopotentiometry shows a continuous decrease in the relative transition times on repeated reversals because of the irreversible loss of R during the course of the experiment (22).

(d) Other E_rC Mechanisms

The E_rC case has been treated for a number of variations in addition to the irreversible first-order following reaction discussed here. For example, the case where the product R dimerizes:

$$2R \xrightarrow{k_2} R_2 \qquad (12.3.24)$$

has been treated for several techniques (33–37). This case can be distinguished from the first-order one by the dependence of the electrochemical response on C_O^*. Also, the varia-
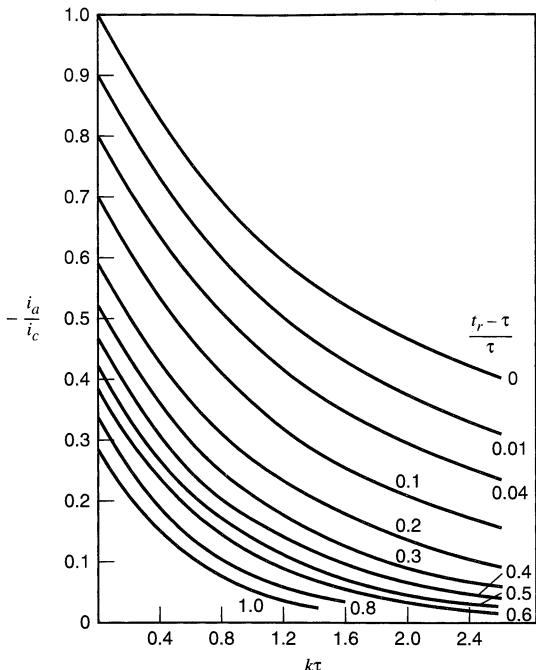
Figure 12.3.14 Working curves for double potential step chronoamperometry for the E_rC_i case. i_a = anodic current measured at time t_r; i_c = cathodic current measured at time $t_f = t_r - \tau$; time of potential reversal = τ. [Reprinted with permission from M. Schwarz and I. Shain, *J. Phys. Chem.*, **69**, 30 (1965). Copyright 1965, American Chemical Society.]

tion of $i_p/v^{1/2}$, E_p, . . . with the dimensionless kinetic parameter [which for this second-order reaction is $\lambda_2 = k_2 C_O^* t_1$ or $\lambda_2 = k_2 C_O^* (RT/nFv)$] is different. For example, for linear sweep voltammetry in the KP region, the peak potential equation is (35, 37)

$$E_p = E_{1/2} - \frac{RT}{nF} 0.902 + \frac{RT}{3nF} \ln(\tfrac{2}{3}\lambda_2) \tag{12.3.25}$$

so that E_p shifts 20 mV (at 25°C) for a tenfold change in scan rate. Other EC schemes, for example, for a reversible following reaction (E_rC_r) (25, 35), or where the product R can react with starting material O (33, 38), have also been discussed.

12.3.4 Following Reaction—E_qC_i

When the rate of the charge-transfer reaction is sufficiently slow, the observed behavior depends on k^0 and α [for reaction (12.2.1) considered as a one-electron process] as well as the kinetic parameter λ for the following reaction. This case can be important even with fast charge-transfer reactions because, as shown in the discussion of E_rC_i reactions, the irreversible following reactions cause the voltammetric wave to shift toward positive values, and this shift away from $E^{0'}$ causes a decrease in the rate of the charge-transfer reaction. We consider here only the cyclic voltammetric method (39, 40). It is convenient to define a dimensionless parameter Λ related to k^0 (40):

$$\Lambda = \frac{k^0}{D^{1/2} v^{1/2}} \left(\frac{RT}{F}\right)^{1/2} \tag{12.3.26}$$

and to illustrate the general behavior by a zone diagram (Figure 12.3.15), showing the effect of Λ and λ. The different zones can be explained as follows. For $\lambda < 0.1$, the following reaction has no effect and the behavior is characteristic of reversible (DP), quasireversible (QR), or totally irreversible (IR) electron transfers, as described in Chapter 6. Similarly, for large Λ values (i.e., the upper portion of Figure 12.3.15), the reaction
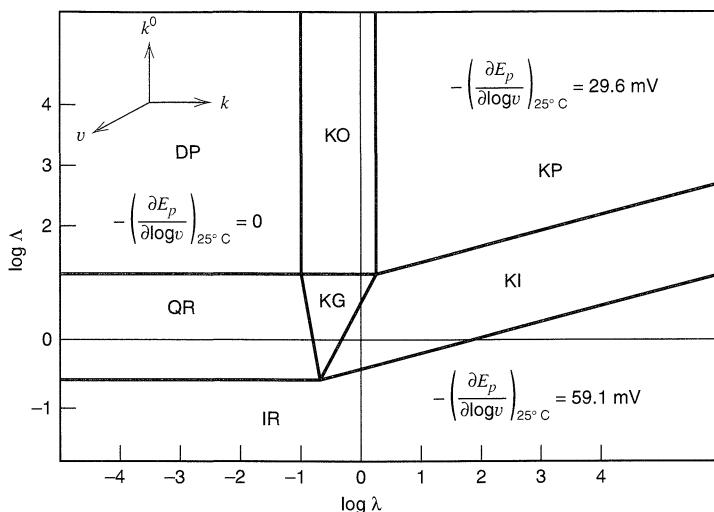
Figure 12.3.15 Zone diagram for the one-electron E_qC_i case: $\lambda = (k/v)(RT/F)$; $\Lambda = k^0(RT/F)^{1/2}/(Dv)^{1/2}$. [Adapted from L. Nadjo and J.-M. Savéant, *J. Electroanal. Chem.*, **48**, 113 (1973), with permission.]

can be considered essentially reversible and the behavior corresponds to that in Section 12.3.3 (regions DP, KO, and KP). The effects of joint electron transfer and chemical irreversibility are mainly manifest in zone KG ($-0.7 < \log \Lambda < 1.3$, $-1.2 < \log \lambda < 0.8$). Tables with values of the electrochemical parameters as functions of Λ and λ are given in reference 40. For example, E_p as a function of λ and Λ in this region is shown in Figure 12.3.16. Clearly apparent is the change in $(\partial E_p/\partial \log v)$ at 25°C from zero at low Λ and λ values to $30/n$ mV with increasing λ and to $59/n$ mV with increasing Λ.
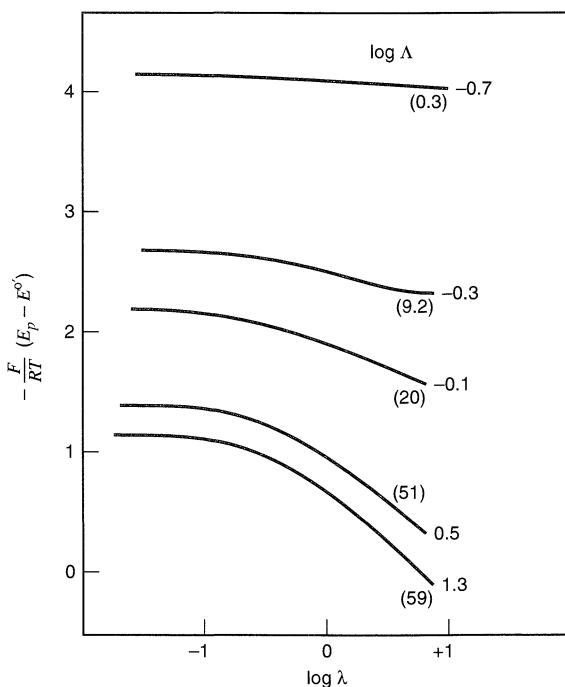
Figure 12.3.16 Variation of E_p for the one-electron E_qC_i case in the intermediate kinetics region (KG) as a function of $\log \lambda$, at several values of $\log \Lambda$. Parenthesized numbers indicate limiting slope of each curve. [Data from L. Nadjo and J.-M. Savéant, *J. Electroanal. Chem.*, **48**, 113 (1973).]

12.3.5 Catalytic Reaction—E_rC_i'

In the catalytic reaction scheme, a species Z, usually nonelectroactive, reacts in the following chemical reaction to regenerate starting material. Thus the problem would involve consideration of a second-order reaction and the diffusion of species Z.

$$O + ne \rightleftharpoons R \tag{12.3.27}$$

$$R + Z \xrightarrow{k'} O + Y \tag{12.3.28}$$

In most treatments, it is assumed that Z is present in large excess ($C_Z^* \gg C_O^*$), so that its concentration is essentially unchanged during the voltammetric experiment, and (12.3.28) can be considered a pseudo-first-order reaction. Under these conditions, the kinetic parameter of interest is

$$\lambda = k' C_Z^* t \quad \text{or} \quad \lambda = \frac{k' C_Z^*}{v}\left(\frac{RT}{nF}\right).$$

(a) Linear Sweep and Cyclic Voltammetric Methods

Typical voltammograms for this case, treated in several papers (24, 25), are shown in Figures 12.3.17 and 12.3.18. Note that at sufficiently negative potentials all of the curves tend to a limiting value of current i_∞, independent of v, given by

$$i_\infty = nFAC_O^*(Dk'C_Z^*)^{1/2} \tag{12.3.29}$$

This limiting current arises when the rate of removal of O by the electrolysis is exactly compensated by the rate of production of O by (12.3.28), so that $C_O(x = 0)$ attains a value independent of time (or v). In this KP region, when λ becomes large, the i-E curve loses its peak-shaped appearance and becomes a wave. The equation for the wave in this region is

$$i = \frac{nFAC_O^*(Dk'C_Z^*)^{1/2}}{1 + \exp\left[\dfrac{nF}{RT}(E - E_{1/2})\right]} \tag{12.3.30}$$
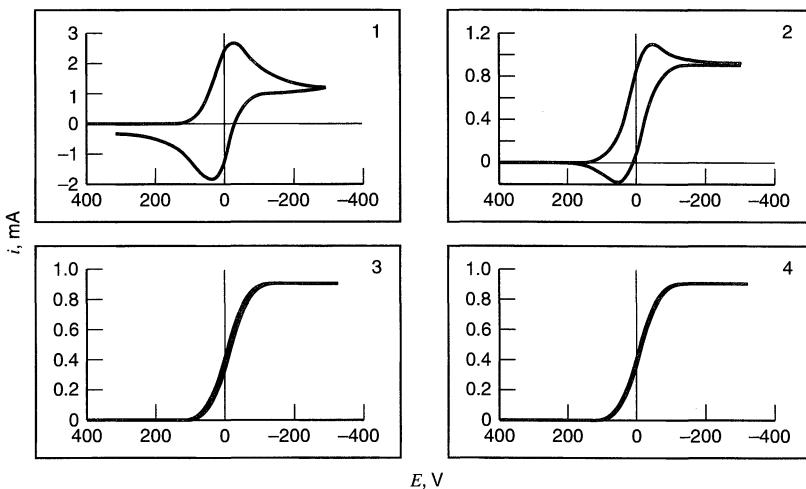
Figure 12.3.17 The E_rC_i' case: $A + e \rightleftharpoons B$; $B + Z \rightarrow A + Y$. Cyclic voltammograms for the system where $E_{A/B}^{0'} = 0$ V, $C_A^* = 1$ mM, $C_B^* = 0$, $C_Z^* = 1$ M, $A = 1$ cm^2, $D_A = D_B = D_Z = 10^{-5}$ cm^2/s, $T = 25°C$, and $k_f = 10$ s^{-1} at scan rates, v, of (1) 10, (2) 1, (3) 0.1, and (4) 0.01 V/s.

$$\frac{\pi^{1/2} \chi(\sigma t)}{\lambda^{1/2}}$$

$$-\frac{nF}{RT} (E - E^{o\prime})$$
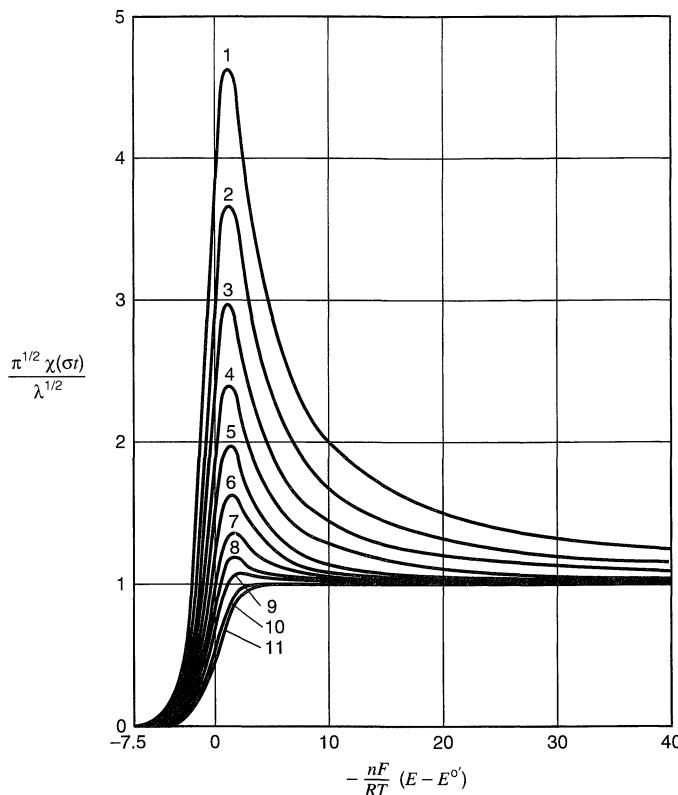
Figure 12.3.18 The E_rC_i' case: $A + e \rightleftarrows B$; $B + Z \rightarrow A + Y$. Linear sweep voltammograms for various values of $\lambda = (RT/nF\upsilon)k'C_Z^*$:
(1) 1.00×10^{-2};
(2) 1.59×10^{-2};
(3) 2.51×10^{-2};
(4) 3.98×10^{-2};
(5) 6.30×10^{-2};
(6) 1.00×10^{-1};
(7) 1.59×10^{-1};
(8) 2.51×10^{-1};
(9) 3.98×10^{-1};
(10) 1.00; (11) ∞.
[Reprinted with permission from J.-M. Savéant and E. Vianello, *Electrochim. Acta,* **10**, 905 (1965). Copyright 1965, Pergamon Press PLC.]

or, from (12.3.29) and (12.3.30),

$$E = E_{1/2} + \frac{RT}{nF} \ln\left(\frac{i_\infty - i}{i}\right) \tag{12.3.31}$$

Thus in the KP region the analysis of the wave is quite easy and leads immediately to $E_{1/2}$ and k'.

The peak (or plateau) current variation with scan rate changes from a $\upsilon^{1/2}$ dependence in the DP zone to independence in the KP zone as shown by a plot of i/i_d vs. λ (Figure 12.3.19). The half-peak potential $E_{p/2}$ is independent of λ at both high and low values of λ and shows a maximum value of $\Delta E_{p/2} /\Delta \log \upsilon$ in the KI region of about $24/n$ mV at $25°C$ (Figure 12.3.20).

$$\frac{i}{i_d}$$

$$\lambda^{1/2}$$
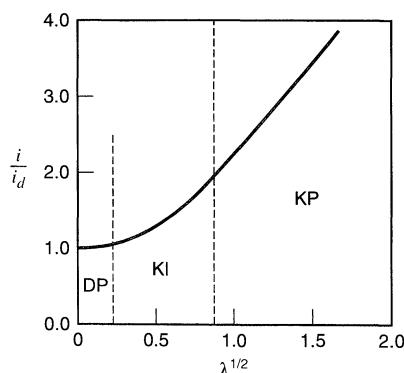
Figure 12.3.19 Ratio of kinetic peak current for the E_rC_i' reaction scheme to diffusion-controlled peak current as a function of $\lambda^{1/2}$. [Adapted with permission from R. S. Nicholson and I. Shain, *Anal. Chem.*, **36**, 706 (1964). Copyright 1964, American Chemical Society.]
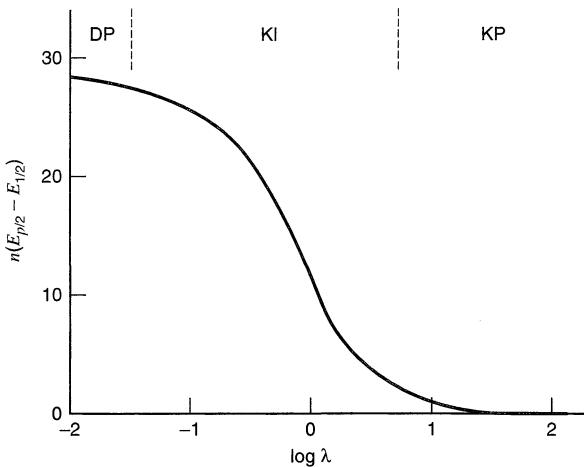
Figure 12.3.20 Variation of half-peak potential with λ in the E_rC_i' case.

For cyclic scans, the ratio of i_{pa}/i_{pc} (with i_{pa} measured from the extension of the cathodic curve) is always unity, independent of λ, even in the KP region, where on the reverse scan the current tends to retrace the forward scan current (Figure 12.3.17).

A more complicated variation of the EC' scheme, largely studied by voltammetry, is the situation where reaction (12.3.28) is reversible, but the product Y is unstable and undergoes a fast following reaction (Y → X). This instability of Y tends to drive reaction (12.3.28) to the right, so the observed behavior resembles that of the E_rC_i scheme. In this case, the O/R couple mediates the reduction of species Z, with the ultimate production of species X, and the process is called *redox catalysis*. By selecting a mediator couple whose E^0 lies positive of that of the Z/Y couple and noting changes in the cyclic voltammetric response with v and the concentration of Z, one can find the rate constant for the decomposition of Y to X, even if it is too rapid to measure by direct electrochemistry of Z (i.e., as an EC reaction) (8, 9).

This approach has been used to study the mechanism of a bond-breaking reaction following electron transfer (a *dissociative electron transfer*). Consider, for example, the case where species Z is an aryl halide, ArX, that becomes reduced by the electrogenerated reductant to yield the ultimate products Ar and X^-. This result can occur either by a *concerted path*, where bond cleavage occurs simultaneously with electron transfer, or by a *stepwise path*, where the radical anion, $ArX^{-\cdot}$, is an intermediate. Investigations of such reactions have been carried out by redox catalysis, and theoretical analysis of the structural and thermodynamic factors that affect the reaction path have been described (14, 41, 42). Similar considerations apply to oxidation reactions, such as of $C_2O_4^{2-}$ to form two molecules of CO_2.

(b) Chronoamperometric Methods

The limiting current for a chronoamperometric experiment $[C_O(x = 0) = 0]$ is given by (43–45)

$$\boxed{\frac{i}{i_d} = \lambda^{1/2}\left[\pi^{1/2}\,\mathrm{erf}(\lambda^{1/2}) + \frac{\exp(-\lambda)}{\lambda^{1/2}}\right]} \tag{12.3.32}$$

where i_d is the diffusion-controlled current in the absence of the following reaction, (5.2.11). This equation can be used to define the limiting regions of behavior. For small values of λ (e.g., $\lambda < 0.05$), $\mathrm{erf}(\lambda^{1/2}) \approx 2\lambda^{1/2}/\pi^{1/2}$ and $i/i_d \approx 1$ (DP region); here the cat-

alytic reaction has no effect. For $\lambda > 1.5$, $\text{erf}(\lambda^{1/2}) \to 1$, $\exp(-\lambda)/\lambda^{1/2} \to 0$, and equation (12.3.32) becomes

$$\frac{i}{i_d} = \pi^{1/2}\lambda^{1/2} \tag{12.3.33}$$

This defines the pure kinetic region (KP). The chronoamperometric response can be employed to determine λ (or $k'C_Z^*$) from a suitable working curve based on (12.3.32) (Figure 12.3.21).

(c) Chronopotentiometric Methods

The solution to this case (46) yields the following expressions for the concentrations ($t < \tau$) with $k = k'C_Z^*$:

$$C_O(0, t) = C_O^* - \frac{i}{nFAD^{1/2}k^{1/2}} \text{erf}[(kt)^{1/2}] \tag{12.3.34}$$

$$C_R(0, t) = C_O^* - C_O(0, t) \tag{12.3.35}$$

At the transition time, $C_O(0, t) = 0$ and, from the expression for the transition time (τ_d) in the absence of the perturbing reaction, (8.2.14), one obtains

$$\left(\frac{\tau}{\tau_d}\right)^{1/2} = \frac{2\lambda^{1/2}}{\pi^{1/2}\,\text{erf}(\lambda^{1/2})} \tag{12.3.36}$$

Note that the limiting values of τ/τ_d in the DP and KP regions can be obtained by consideration of the behavior at small and large λ values (see Problem 12.6). A plot showing this behavior is given in Figure 12.3.22. Note the similarity of the limiting behavior for $\lambda > 1.5$, (12.3.36), to the corresponding equation for chronoamperometry, (12.3.33), as well as the similarity of the working curves. The $E–t$ curves can be derived by substitution of the expressions for $C_O(0, t)$ and $C_R(0, t)$ into the Nernst equation (see Problem 12.7).

The equation for the reverse transition time in terms of τ_f in this case is the same as for the E_rC_i case (equation 12.2.32) (34, 47, 48), so that simple reversal experiments cannot distinguish between these cases. However, the variation of τ with i immediately differentiates between the E_rC_i and E_rC_i' cases.
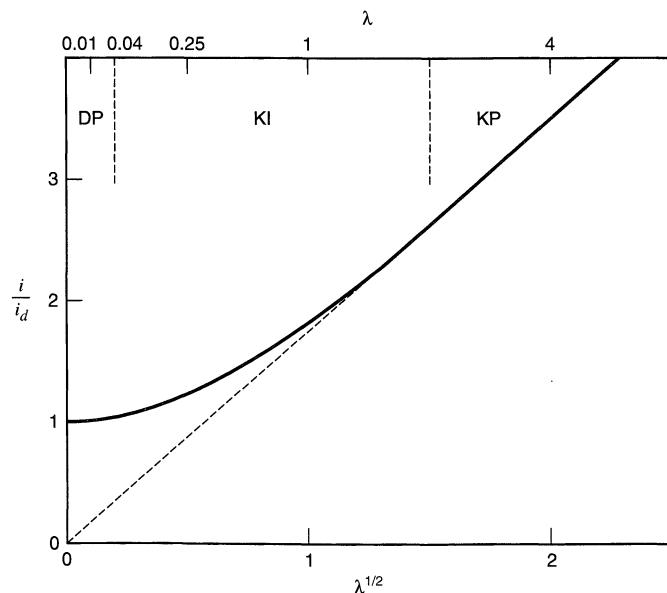
Figure 12.3.21 Chronoamperometric working curve for the E_rC_i' case (eq. 12.3.32) for various values of $\lambda^{1/2}$, where $\lambda = k'C_Z^*t$. Dashed line is the KP-region limiting line, (12.3.33).
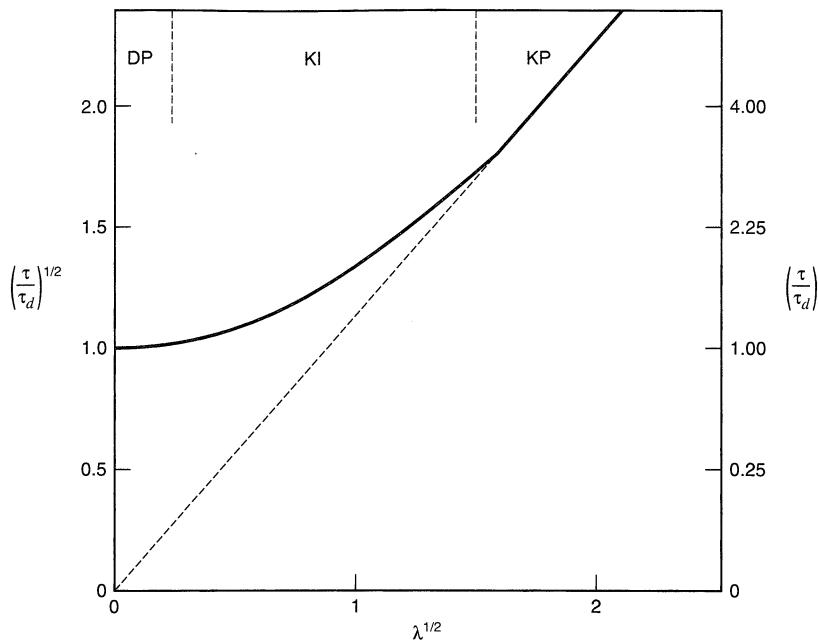
Figure 12.3.22 Variation of $(\tau/\tau_d)^{1/2}$ with $\lambda^{1/2}$ for E_rC_i' case in chronopotentiometry ($\lambda = k'C_Z^*\tau$). Dashed line is limiting behavior in the KP region.

12.3.6 E_rE_r Reactions

We now consider cases in which there are two (or more) heterogeneous electron-transfer reactions.

$$A + e \rightleftarrows B \qquad E_1^0 \qquad (12.3.37)$$
$$B + e \rightleftarrows C \qquad E_2^0 \qquad (12.3.38)$$

The simplest case is that where both electron-transfer reactions are rapid. Let us consider the cyclic voltammetric behavior for this situation. The appearance of the voltammogram depends upon the location of the standard potentials, E_1^0 and E_2^0, and the spacing between them, $\Delta E^0 = E_2^0 - E_1^0$ (Figure 12.3.23) (49).

Typical voltammograms, the variation of the peak current function for the first (cathodic) wave, and the peak splitting between the cathodic and anodic reversal waves
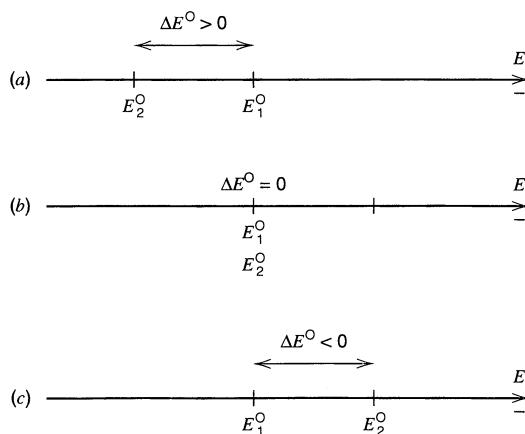
Figure 12.3.23 Different cases for the E_rE_r reaction scheme depending upon relative values of E_2^0 and E_1^0, as expressed by $\Delta E^0 = E_2^0 - E_1^0$.

(ΔE_p) at 25°C are shown in Figure 12.3.24. When $\Delta E^0 > 100$ mV, the second electron step occurs much more easily than the first, and one observes a single wave with characteristics indistinguishable from a single, nernstian, two-electron transfer (i.e., $\Delta E_p = 29$ mV, peak current function, $\pi^{1/2}\chi(\sigma t)n^{3/2} = 1.26$). As discussed in Sections 3.5 and 12.1, the actual occurrence of a simultaneous transfer of two electrons is, however, very unlikely. As ΔE^0 decreases, one observes a single wave with an increasing ΔE_p until ΔE^0 reaches about -80 mV, where a suggestion of two waves can be seen. The two waves become resolvable at $\Delta E^0 = -125$ mV, where each wave takes on the characteristics of a one-electron transfer [i.e., $\Delta E_p = 58$ mV, peak current function, $\pi^{1/2}\chi(\sigma t)n^{3/2} = 0.446$]. A characteristic of an E_rE_r reaction is the independence of these parameters with scan rate. Under these conditions, the working curves in Figure 12.3.25 can be employed to estimate ΔE^0.

It is instructive to consider the chemical and structural factors that affect ΔE^0. When the successive electron transfers involve a single molecular orbital, and no large structural changes occur upon electron transfer, then one expects two well-spaced waves ($\Delta E^0 \ll -125$ mV). For example, the reduction of aromatic hydrocarbons like anthracene occurs with two waves spaced on the order of 500 mV apart (Figure 12.3.26a). However, if transfer occurs to two different groups (two different orbitals) in a molecule (Figure 12.3.26b), then closer spacing between the waves, and even a single wave, can result. Consider a molecule with two identical groups, A, linked in some manner (e.g., with a hydrocarbon chain). When an electron is added to one A group, the energy required to add the second electron depends upon the extent of interaction between the groups. If there is no interaction between them, $\Delta E^0 = -35.6$ mV (at 25°C), where the curve crosses the dashed line in Figure 12.3.25b. Thus one observes the characteristic splitting of a one-electron transfer ($\Delta E_p = 58$ mV at 25°C), even though a single wave involving two electron transfers is recorded. Note that a lack of interaction is not represented by $\Delta E^0 = 0$, because statistical (entropic) factors make the second electron transfer slightly more diffi-
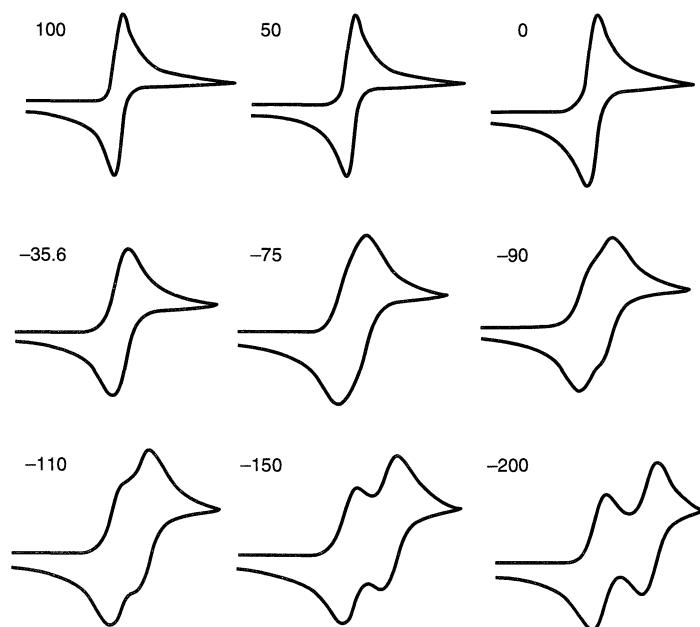
Figure 12.3.24 Changing shapes of cyclic voltammograms for the E_rE_r reaction scheme at different values of ΔE^0.
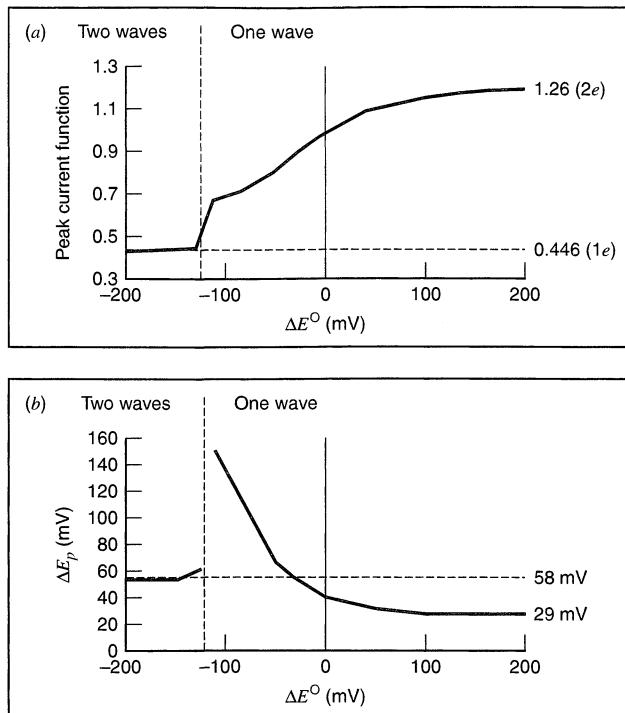
Figure 12.3.25 (a) Peak current function $[\pi^{1/2}\chi(\sigma t)n^{3/2}]$ and (b) ΔE_p vs. ΔE^0 for the E_rE_r reaction scheme. The discontinuity in the curve in (b) at negative values of ΔE^0 occurs when two waves are resolved.

cult, in terms of free energy, than the first. It turns out that $\Delta E^0 = -(2RT/F) \ln 2$ (50, 51). If the groups interact repulsively, then a greater peak splitting is observed. This effect can be seen, for example, in the voltammetry of α,ω-9,9'-dianthrylalkanes (Figure 12.3.27). Values of ΔE^0 larger than -35.6 mV result when there are attractive interactions, so that the second electron transfer occurs more easily than the first. This almost always requires a major structural rearrangement or large solvation or ion pairing effects occurring as a result of the first electron-transfer step (52).
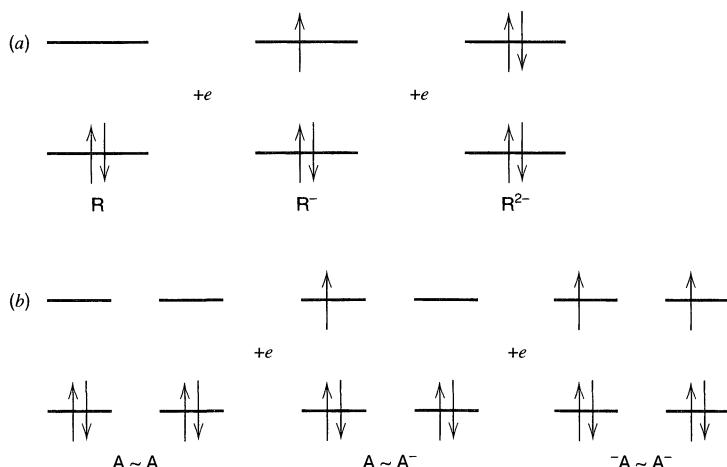
Figure 12.3.26 (a) Stepwise addition of electrons to the same molecular orbital in a molecule, R, usually yielding two separated waves. (b) Addition to two separate groups, A, on a molecule, A~A, where the spacing between the waves depends upon the extent of interaction between the groups.
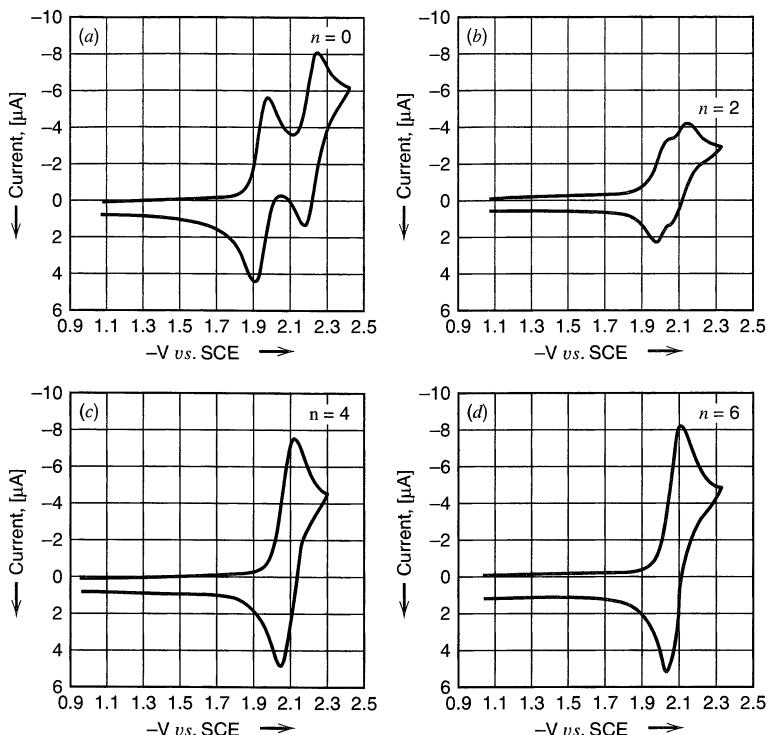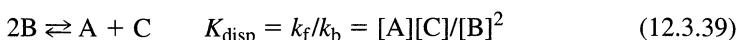
Figure 12.3.27 Cyclic voltammograms for the reduction of α,ω-9,9'-dianthrylalkanes (i.e., An-$(CH_2)_n$-An, where An = anthracene) in 1:1 benzene:acetonitrile containing 0.1 M tetra-n-butylammonium perchlorate at a Pt electrode. As alkane chain length, n ($n = 0, 2, 4, 6$), lengthens, the voltammograms show a decreasing repulsive interaction. [From K. Itaya, A. J. Bard, and M. Szwarc, *Z. Physik. Chem. N. F.*, **112**, 1 (1978), with permission.]

Whenever an E_rE_r reaction takes place, one must consider the possibility of a disproportionation-comproportionation equilibrium,

$$2B \rightleftarrows A + C \qquad K_{disp} = k_f/k_b = [A][C]/[B]^2 \tag{12.3.39}$$

also developing in the solution near the electrode. The extent of the reaction, as measured by the equilibrium constant, K_{disp}, is governed by ΔE^0:

$$(RT/F) \ln K_{disp} = \Delta E^0 = E_2^0 - E_1^0 \tag{12.3.40}$$

For example, for two well-separated waves ($\Delta E^0 < 0$), K_{disp} is small, and reaction (12.3.39) lies to the left (i.e., the comproportionation of A and C dominates the disproportionation of B). Thus, at potentials of the second wave, C diffusing away from the electrode can reduce A diffusing towards it, so that the concentration profiles of A, B, and C are perturbed from those that would exist if the solution phase reaction did not occur. However, for the E_rE_r reaction scheme, the observed voltammogram is independent of the rates of the forward and back reactions in (12.3.39), because, at any given potential, the average oxidation state in any layer of solution near the electrode remains the same (53). At potentials of the second wave, species A, which would take two electrons, is removed by the comproportionation reaction, but two B molecules are produced, and each of these would take one electron for no net change. This is not true, however, if the heterogeneous rate constants for the electron transfer are slow (Section 12.3.7) or in ECE reactions (Section 12.3.8).

The same considerations apply for reactions involving more than two electron transfers, that is, $E_rE_rE_r \ldots$ schemes. The observed behavior can vary from a set of n resolved

one-electron waves to a single n-electron wave. For example, a solution of C_{60} shows up to 6 separated one-electron waves, attributed to the addition of electrons to three degenerate orbitals in the molecule. However, for solutions of many polymers, such as poly(vinylferrocene) (PVF), only a single wave is observed, with a ΔE_p characteristic of a one-electron process and a peak height governed by the degree of polymerization and the total number of electrons added per molecule (51). This behavior is consistent with the lack of interaction among ferrocene centers on a polymer chain. For example, the oxidation of PVF containing (on the average) 74 ferrocene units per molecule produces a 74-electron wave whose shape is essentially that of a nernstian one-electron-transfer reaction.

12.3.7 E_qE_q Reactions

The treatment of EE reactions becomes more complex when one or both of the electron-transfer reactions are quasireversible. Even in the simplest case, where $n_1 = n_2 = 1$ and $\alpha_1 = \alpha_2 = 0.5$, the cyclic voltammetric behavior depends upon three parameters, ΔE^0, k_1^0, and k_2^0 (rather than the single parameter ΔE^0 for the E_rE_r scheme in Section 12.3.6). These three parameters can be represented in different ways, for example, in terms of dimensionless aggregates like $\Lambda_1 = k_1^0/[Dv(F/RT)]^{1/2}$ and k_1^0/k_2^0.

Consider the special case of an E_rE_q reaction, where the first electron transfer is fast (nernstian) and the second somewhat slower. The cyclic voltammetric behavior, such as for $\Delta E^0 = 0$ as shown in Figure 12.3.28, depends upon the scan rate. At smaller scan rates (curve A), a single wave with behavior approaching the E_rE_r case, is seen. As the scan rate is increased (i.e., as Λ_2 decreases), the first electron-transfer wave remains reversible and centered on E^0, but the slower second electron transfer results in a
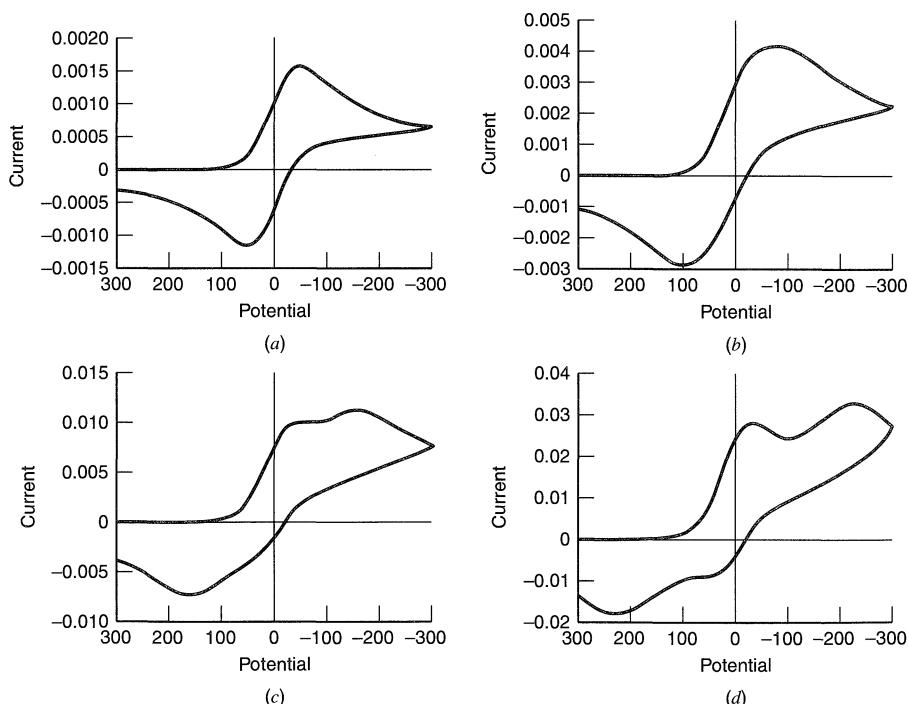
Figure 12.3.28   Representative behavior for an E_rE_q reaction. System with $\Delta E^0 = 0$, $E_1^0 = 0$, $n_1 = n_2 = 1$, $\alpha_1 = \alpha_2 = 0.5$, $k_1^0 = 10^4$ cm/s, $k_2^0 = 10^{-2}$ cm/s, $D = 10^{-5}$ cm^2/s, $C = 1$ mM, $A = 1$ cm^2, $T = 25°C$, and scan rates, v, of (a) 1; (b) 10; (c) 100; (d) 1000 V/s. Rate constants for (12.3.39) are assumed to be zero. Current in amperes; potential in mV.
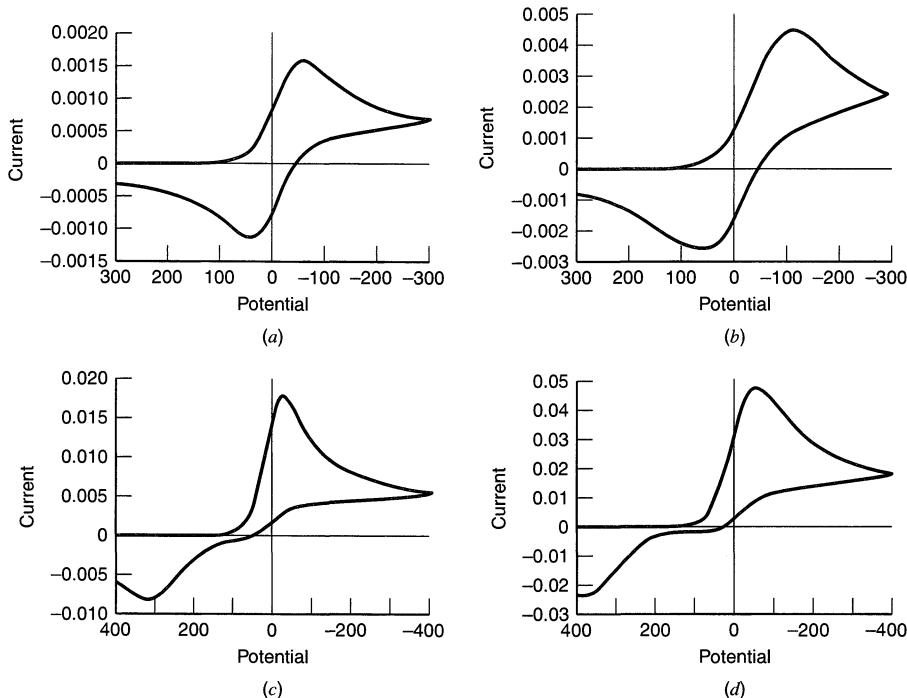
Figure 12.3.29 Representative behavior for an E_rE_q reaction. System with all parameters as in Figure 12.3.28, except $\Delta E^0 = 150$ mV. Scan rates of (a) 1; (b) 10; (c) 100; (d) 1000 V/s. Rate constants for (12.3.39) are assumed to be zero.
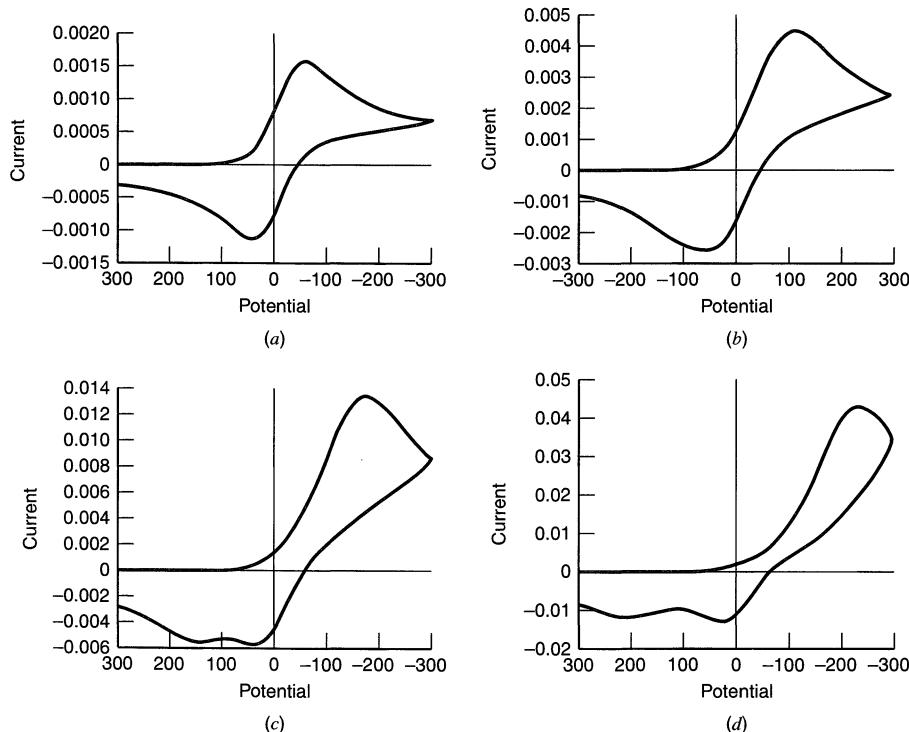
Figure 12.3.30 Representative behavior for an E_qE_r reaction. System with $\Delta E^0 = 0$, $n_1 = n_2 = 1$ $\alpha_1 = \alpha_2 = 0.5$, $k_1^0 = 10^{-2}$ cm/s, $k_2^0 = 10^4$ cm/s, $D = 10^{-5}$ cm^2/s, $C = 1$ mM, $A = 1$ cm^2, $T = 25°$C and scan rates, v, of (a) 1; (b) 10; (c) 100; (d) 1000 V/s. Current in amperes; potential in mV.

second wave splitting away from the first (curves C and D), with larger splitting found at higher scan rates. The situation is somewhat different for an E_rE_q reaction where the second electron transfer occurs more easily than the first, for example, for $\Delta E^0 = 150$ mV (Figure 12.3.29). In this case, when species B is formed, it is readily reduced to C, because the reaction is occurring at potentials well negative of E_2^0. Thus at high scan rates (curves C and D) the cathodic wave is not split and reversibility is not seen at the potential of the first wave.

The E_qE_r reaction is another special case, where the first electron transfer is now the rate-determining step. The general trend in this case (Figure 12.3.30) is a shift in E_{pc} to more negative values with increasing scan rate, without splitting of the cathodic wave. The anodic wave splits at higher scan rates because the oxidation of species B to A occurs at more positive potentials.

A general treatment of the E_qE_q scheme is probably best carried out through digital simulations, although attempts have been made to give working curves, such as of ΔE_p or i_{pa}/i_{pc} vs. Λ_1 at different values of ΔE^0 and $k_1^0/k_2^0 = \Lambda_1/\Lambda_2$ (54). The situation is made even more complicated, however, by the fact that the observed voltammogram is affected (unlike the E_rE_r case) by a disproportionation-comproportionation equilibrium, (12.3.39), so yet another variable (the rate constant for the homogeneous disproportionation reaction) must be considered. The effect of this rate constant for an E_rE_q reaction is shown in Figure 12.3.31. For the conditions given in this example, the disproportionation has little

(a)

(b)

(c)
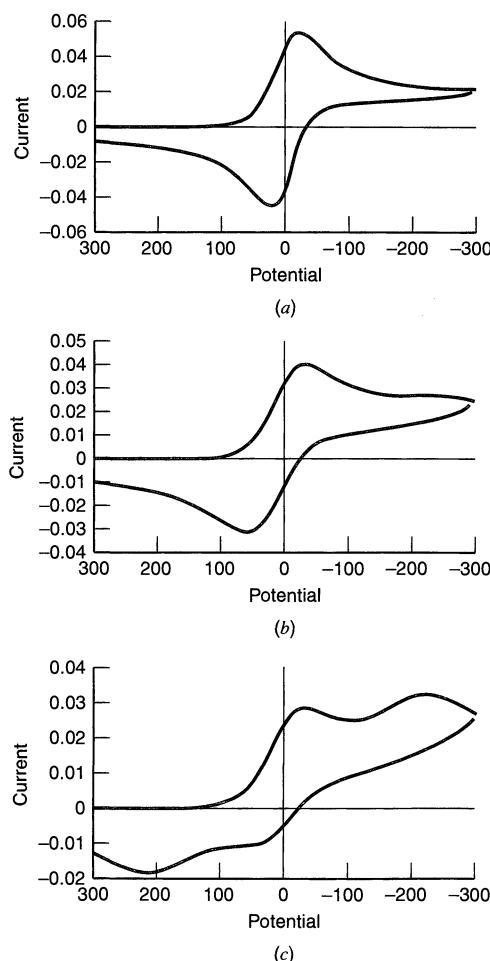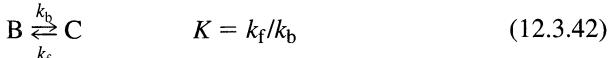
Figure 12.3.31 Representative behavior for the E_rE_q process shown in Figure 12.3.28D including a disproportionation reaction. $\Delta E^0 = 0$, $E_1^0 = 0$, $n_1 = n_2 = 1$, $\alpha_1 = \alpha_2 = 0.5$, $k_1^0 = 10^4$ cm/s, $k_2^0 = 10^{-2}$ cm/s, $D = 10^{-5}$ cm^2/s, $C = 1$ mM, $A = 1$ cm^2, $T = 25°C$, and $v = 1000$ V/s. Disproportionation rate constant of (a) 10^{10}; (b) 10^8; (c) 10^6 $M^{-1}s^{-1}$. Current in amperes; potential in mV.

effect as long as its rate constant is less than about $10^{-6}\,M^{-1}s^{-1}$. However, large changes are noted for larger values of the rate constant, since this solution phase reaction can assist in equilibrating the reactant species at the electrode surface, thus causing the behavior to appear more similar to that found at smaller scan rates.

12.3.8 ECE Reactions

The general ECE reaction scheme is[2]

$$A + e \rightleftharpoons B \qquad\qquad E_1^0 \qquad\qquad (12.3.41)$$

$$B \overset{k_b}{\underset{k_f}{\rightleftharpoons}} C \qquad\qquad K = k_f/k_b \qquad\qquad (12.3.42)$$

$$C + e \rightleftharpoons D \qquad\qquad E_2^0 \qquad\qquad (12.3.43)$$

$$B + C \overset{k_d}{\rightarrow} A + D \qquad\qquad\qquad (12.3.44)$$

In the case of greatest interest, $E_2^0 \gg E_1^0$, so that species C is much easier to reduce than species A. Typically, $\Delta E^0 = E_2^0 - E_1^0 \geq 180$ mV. In the opposite limiting case, when the second reaction occurs at significantly more negative potentials than the first ($\Delta E^0 \leq -180$ mV), sequential stepwise addition of electrons results in two voltammetric waves. The first wave is based on an EC sequence that can be analyzed as described in Section 12.3.3, without consideration of the second electron-transfer step.

Reaction (12.3.44) is included in the scheme because species B is capable of reducing species C in a homogeneous reaction near the electrode surface. With $\Delta E^0 \geq 180$ mV, (12.3.44) can be taken as irreversible to the right. Because species B and C are at the same oxidation level, this reaction can be considered to be a disproportionation reaction, and ECE-schemes that include it are denoted ECE/DISP mechanisms.

(a) Linear Scan and Cyclic Voltammetric Methods
For the ECE case under consideration here, only a single wave (wave I, reduction of A and C) is observed on the first (cathodic) scan (Figure 12.3.32). This wave occurs near E_1^0, since any C formed at this potential is immediately reduced to D. On the reverse scan, a reversal wave (II) is observed for oxidation of B if reaction (12.3.42) is not too rapid (Figure 12.3.32b). As the reverse scan continues, a second reversal wave (III) is seen representing oxidation of D to C. Another reversal of the scan reveals a corresponding cathodic wave (IV) for the reduction of C to D. The relative sizes of waves II, III, and IV depend upon the magnitudes of the rate constants in the reaction scheme, k_f, k_b, and k_d. The curves shown in Figure 12.3.32 are for an $E_rC_iE_r$ sequence where $k_f = k_d = 0$ and the dimensionless parameter of interest is $\lambda = (RT/Fv)k_b$. A zone diagram for this case can be given in terms of the normalized peak current of wave I, n_{app}, as a function of λ (Figure 12.3.33), where

$$n_{app} = i_p/FAC_A^*(\pi D\sigma)^{1/2}\chi(\sigma t) = i_p(I)/[i_p(I)(\lambda = 0)] \qquad (12.3.45)$$

When λ is small (region DP), B is stable, and $n_{app} \approx 1$. In this region, waves III and IV are very small. For large λ (region KP), essentially all B is converted to C which immediately reacts to form D; therefore $n_{app} \approx 2$, and waves III and IV are prominent. The quantitative treatment of this scheme has been described (55, 56).

---

[2]To be consistent with much of the published work in this field, the rate constant for the forward reaction in (12.3.42) is labeled by k_b, and the equilibrium constant K is defined as shown.
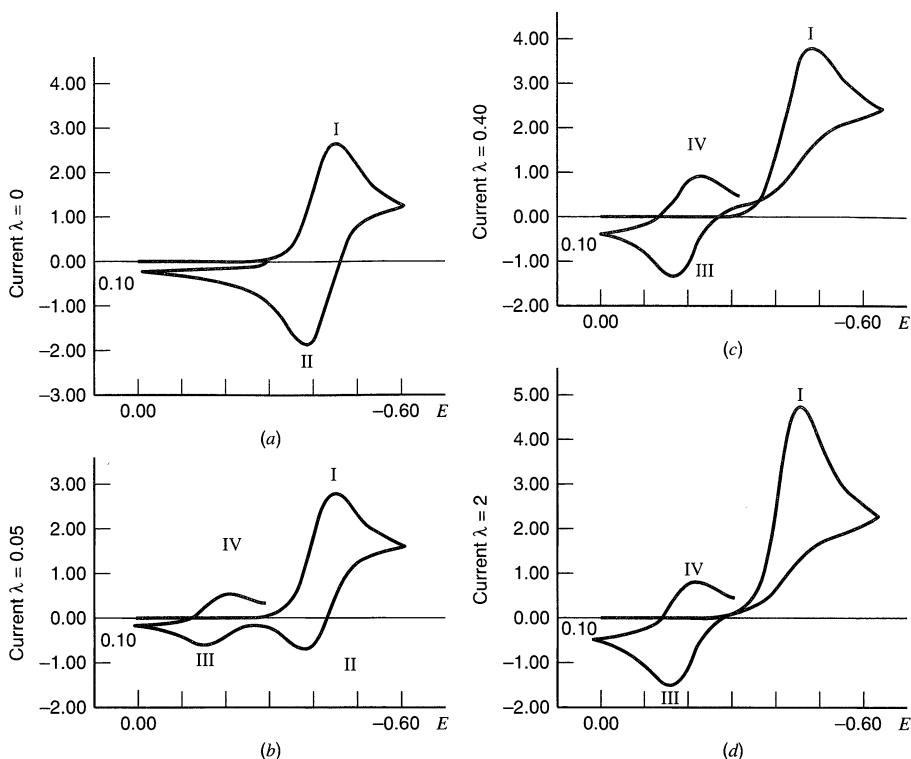
Figure 12.3.32 Cyclic voltammograms for the $E_rC_iE_r$ case obtained by digital simulation for $E_1^0 = -0.44V$, $E_2^0 = -0.20$ V for different values of $\lambda = (k_b/v)(RT/F)$; $n_1 = n_2 = 1$. (a) $\lambda = 0$ (unperturbed nernstian reaction); (b) $\lambda = 0.05$; (c) $\lambda = 0.40$; (d) $\lambda = 2$.

When reaction 12.3.42 is reversible, the overall process is denoted as $E_rC_rE_r$, and the observed voltammetric behavior depends upon both K and $\lambda = (RT/Fv)(k_f + k_b)$. The zone diagram for this case is shown in Figure 12.3.34 (57, 58). When K is large, species B is always favored and a simple one-electron process is observed (region DO). At the opposite limit, when K is such that conversion of B to C takes place and λ is large, nernstian behavior is again found, but with a two-electron wave seen for the overall reaction

$$A + 2e \rightleftarrows D \qquad (12.3.46)$$
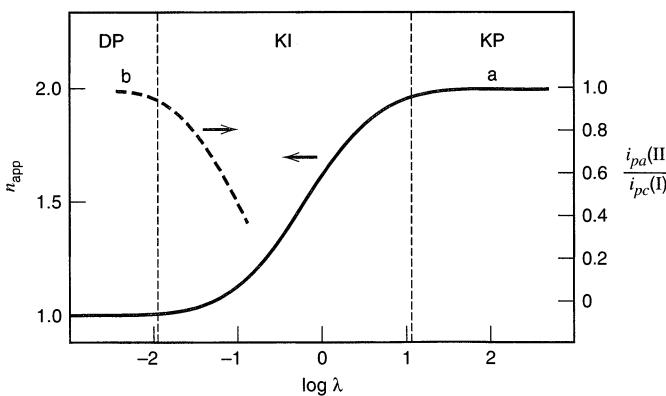
Figure 12.3.33 Variation of n_{app} and $i_{pa}(II)/i_{pc}(I)$ with λ in cyclic voltammetry for the $E_rC_iE_r$ system shown in Figure 12.3.32. n_{app} defined in (12.3.45). Zones showing limiting behavior also indicated.
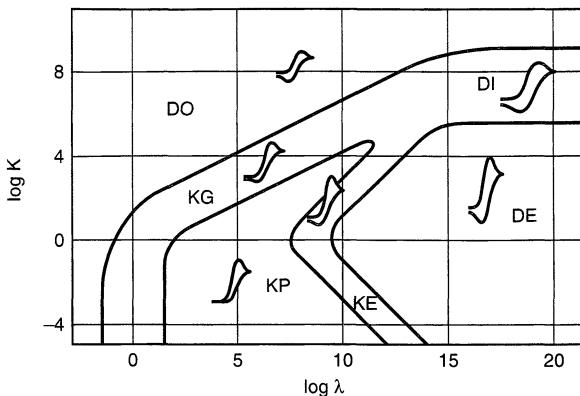
Figure 12.3.34 Zone diagram for the $E_rC_rE_r$ mechanism, where $K = k_f/k_b = C_B/C_C$ and $\lambda = (RT/Fv)(k_f + k_b)$. [Reprinted from J.-M. Savéant, C. P. Andrieux, and L. Nadjo, *J. Electroanal. Chem.*, **41**, 137 (1973), with permission from Elsevier Science.]

(region DE). By combining the relevant thermodynamic data for this set of reactions, one finds that the standard potential of (12.3.46), E^{0*}, is given by

$$E^{0*} = (E_1^0 + E_2^0)/2 - (RT/2nF) \ln K \qquad (12.3.47)$$

The observed wave in the DE region occurs at this potential. For smaller values of λ, one traverses different regions where kinetics control the observed behavior. The special case of the $E_rC_iE_r$ sequence can be seen in this diagram where K is very small (e.g., log $K = -4$).

In general, one must also take account of the disproportionation reaction, (12.3.44). Limiting cases where this reaction dominates for the conversion of A to D [i.e., where the second electron-transfer reaction at the electrode, (12.3.43), does not occur] are denoted as DISP schemes (12, 59). Although (12.3.43) is thermodynamically favored, it might not occur to a significant extent because species C does not reach the electrode. This happens, for example, when k_b is small, so that C is produced some distance from the electrode, and k_d is large, so that C diffusing towards the electrode mainly reacts with B diffusing away from it.

These DISP schemes can be divided into two subcases: DISP1, where (12.3.42) is the rate-determining-step; and DISP2, where (12.3.44) is the rate-determining-step and (12.3.42) is at equilibrium. A simplified zone diagram can be drawn (neglecting the intermediate regions) in terms of the parameters K and $p = k_d C_A^*/[(k_f + k_b)^{1/2}(RT/Fv)^{1/2}]$, where the different limiting cases apply (Figure 12.3.35) (7). A more complete diagram is
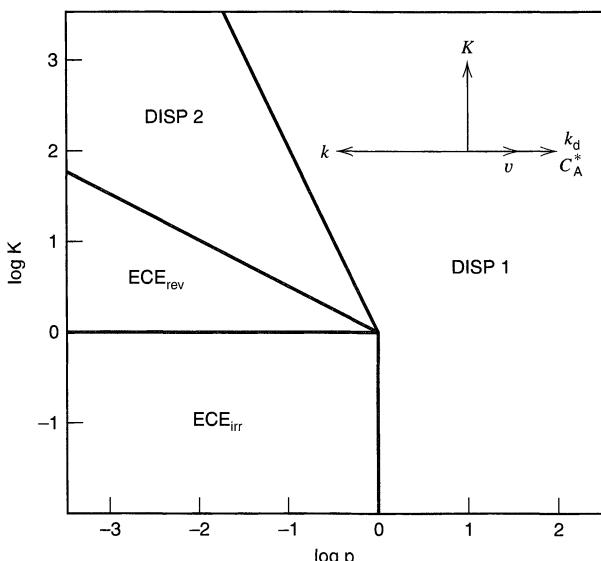
Figure 12.3.35 Simplified zone diagram showing where different limiting ECE and DISP cases apply in terms of the parameters K and $p = k_d C_A^* /[(k_f + k_b)^{3/2}(RT/Fv)^{1/2}]$. [From C. P. Andrieux and J.-M. Savéant, in "Investigation of Rates and Mechanisms of Reactions," Part II, 4th ed., C. F. Bernasconi, Ed., Wiley-Interscience, New York, 1986, with permission.]

shown in the following section covering chronoamperometric methods. Clearly the general behavior of this system is complicated, and collection of voltammetric data over a wide range of the experimental variables C_A^* and v is required to confirm the mechanism and extract the kinetic parameters (k_d, k_f, and k_b). Note also that the above treatment assumed a rather large ΔE^0 value. For $0 \leq \Delta E^0 < 180$ mV, the waves for the two half-reactions will begin to overlap. Theoretical voltammograms are usually obtained by digital simulation for different values of ΔE^0, k_d, k_f, k_b, C_A^*, and v.

This system becomes even more complex when the heterogeneous kinetics of the electron-transfer reactions are taken into account. While a theoretical treatment has been given with either one or both of these reactions assumed to be totally irreversible (55), such complications are rarely dealt with in practice.

(b) Chronoamperometric Methods

There are two limiting cases for this scheme, assuming a step to potentials where $C_A(x = 0) = C_C(x = 0) = 0$. For $\lambda \to 0$, the behavior approaches the simple unperturbed reaction involving only (12.3.41), that is, equation (5.2.11) with $n = 1$ (zone DP) (Figure 12.3.33, with $\lambda = k_b t$). For $\lambda \to \infty$, the behavior again approaches diffusion control with both electron transfers occurring, that is, equation (5.2.11) with $n = 2$, denoted $(it^{1/2})_\infty$ (zone KP). For intermediate values of λ, the following equation applies (60):

$$(it^{1/2})/(it^{1/2})_\infty = 1 - (e^{-\lambda/2}) \tag{12.3.48}$$

Thus, zone DP is attained when $\lambda < 0.05$, while KP results when $\lambda > 3$. An alternative expression for this behavior is

$$n_{app} = 2 - e^{-\lambda} \tag{12.3.49}$$

A general treatment of the ECE-DISP system for chronoamperometry has also appeared (59) with zone diagrams (including some three-dimensional ones) to describe the behavior under various conditions. For example, the general case for pure kinetic conditions is shown in Figure 12.3.36.
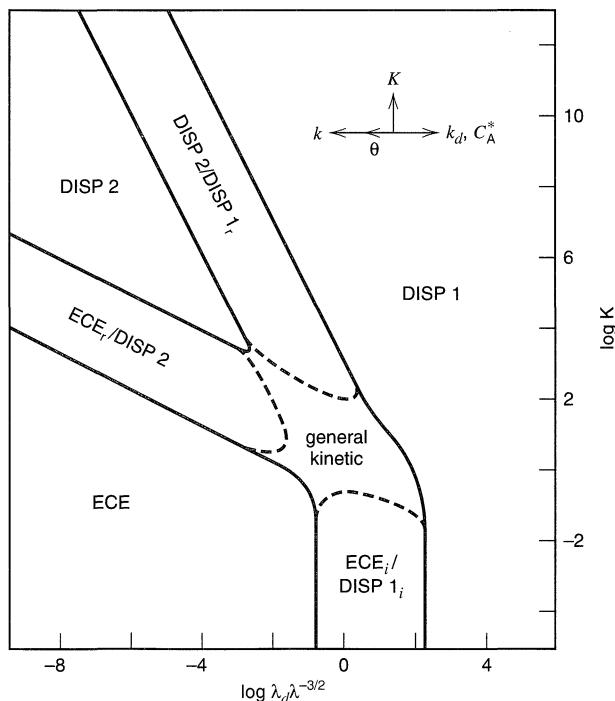
Figure 12.3.36 Zone diagram for the ECE-DISP scheme for chronoamperometry in terms of K, $\lambda_d = k_d t$, and $\lambda = (k_f + k_b)t$. This diagram also applies to voltammetry when the characteristic time in the λ expressions, t, is replaced by (RT/Fv). Compare with the simplified diagram in Figure 12.3.35. [Reprinted from C. Amatore and J.-M. Savéant, *J. Electroanal. Chem.*, **102**, 21 (1979), with permission from Elsevier Science.]
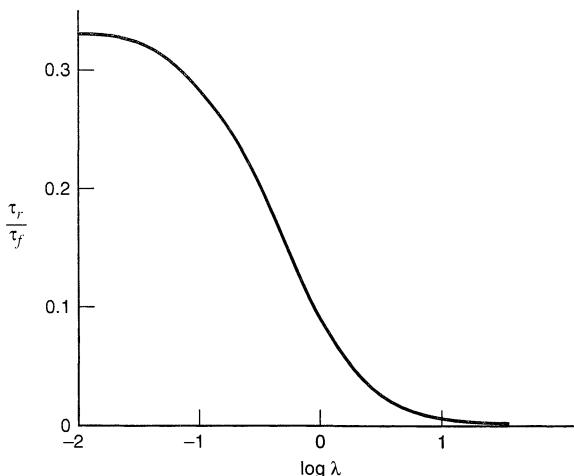
Figure 12.3.37 Variation of τ_r/τ_f with λ for chronopotentiometry in the $E_rC_iE_r$ reaction with $n_1 = n_2$. [Data from H. B. Herman and A. J. Bard, *J. Phys. Chem.*, **70**, 396 (1966).]

While the ECE reaction can be studied by dc polarography (61–63), the limited time window in this method greatly restricts its utility.

(c) Chronopotentiometric Methods

For constant current experiments on $E_rC_iE_r$ systems with $\Delta E^0 > 0$, the results are analogous to those found in chronoamperometry and linear scan voltammetry (10, 64). For small λ in zone DP, as $i \to \infty$, (8.2.14) applies with $n = 1$. In zone KP with large λ as $i \to 0$, (8.2.14) again holds with $n = 2$. The overall dependence of $i\tau^{1/2}$ on λ involves a rather complicated expression; the general trend is similar to that in Figure 12.3.33. On current reversal, only B is oxidized near the forward wave, and the ratio of transition times τ_r/τ_f as a function of λ is shown in Figure 12.3.37.

12.3.9 Other Reaction Schemes

It is beyond the scope of this work to consider the many other reaction schemes (e.g., $\overrightarrow{E}\overleftarrow{C}\overrightarrow{E}$, electron-transfer catalyzed reactions, square schemes) that have been treated theoretically and applied to actual systems. Details of the appropriate equations and procedures to treat these cases, as well as references to the original literature, can be found in reviews (7–9, 14, 65–68). Many applications of electrochemical techniques to the elucidation of organic (69, 70) and inorganic (71, 72) reaction mechanisms have appeared.

12.4 ROTATING DISK AND RING-DISK METHODS

The rotating disk electrode (RDE) discussed in Chapter 9 has proven to be very useful in studies of coupled homogeneous reactions. The information content of the experimental results is high, since the coupled reactions cause perturbations in the limiting current, the half-wave potential, and the ring current at the RRDE; and an intuitive appreciation of the interpretation of the $i–E$ curves is easy to attain. Also, by working at potentials in the limiting current region, complications caused by slow heterogeneous electron-transfer steps can be avoided. Although rigorous theoretical treatments at the RDE, and especially the RRDE, are rather difficult, a number of reaction schemes have been investigated, and the successful application of digital simulation methods has allowed even complex reaction schemes to be treated.

An important advantage of the RDE is that measurements are made under steady-state (i.e., time-independent) conditions. Thus, the general approaches described in Sections 1.4.2 and 1.5 can be applied, with the appropriate choices of m (the mass-transfer coefficient) and μ (the reaction layer thickness). Moreover, equations of the same form are found with other steady-state techniques and can be found by replacing $m = 0.62D^{2/3}\omega^{1/2}\nu^{-1/6}$ for the RDE with m for the particular technique. For example, $m = D/r_0$ at hemispherical UMEs at long times (or slow sweep rates).

12.4.1 Theoretical Treatments

As with LSV or CV, the mass-transfer equations for the various species must be changed to take account of loss or production of material because of the coupled reactions. Thus for the CE mechanism [(12.3.1) and (12.3.2)] at the RDE, (9.3.13) becomes

$$v_y\left(\frac{\partial C_O}{\partial y}\right) = D_O\left(\frac{\partial^2 C_O}{\partial y^2}\right) + k_f C_Y - k_b C_O \tag{12.4.1}$$

This must be solved with the appropriate boundary conditions. For investigations at the RRDE, the radial convective terms must be included as well. Thus, in the treatment of the $E_r C_i$ scheme at the RRDE [(12.2.1) and (12.2.2)], where product R is oxidized at the ring electrode, the appropriate equation for R is

$$v_y\left(\frac{\partial C_R}{\partial y}\right) + v_r\left(\frac{\partial C_R}{\partial r}\right) = D_R\left(\frac{\partial^2 C_R}{\partial y^2}\right) - kC_R \tag{12.4.2}$$

The solution of this equation would then follow as described in Section 9.4. The modifications of the mass-transfer equations for the different cases generally follow those used in voltammetric methods as shown in Table 12.2.1. Appropriate dimensionless parameters are listed in Table 12.3.1. It is usually not possible to solve these equations analytically, so various approximations (e.g., the reaction layer approach, as described in Section 1.5.2), digital simulations, or other numerical methods must be employed. The behavior of systems at the RDE can be analyzed by means of the zone diagrams employed for voltammetry (Section 12.3) by redefining the parameter λ. This is accomplished by replacing (RT/nFv) with the term $\delta^2/D [= (1.61)^2\nu^{1/3}/\omega D^{1/3}]$ (7).

12.4.2 Preceding Reaction—$C_r E_r$

The solution for the limiting current at the RDE for the reaction scheme in (12.3.1)–(12.3.3) has been obtained (73). To solve the convective-diffusion equations it was assumed that the reactions were rapid, so that $(D/\nu)^{1/3} << (k_f + k_b)/\omega$. With this condition, the limiting current is given by

$$i = \frac{nFADC^*}{1.61\,D^{1/3}\omega^{-1/2}\nu^{1/6} + D^{1/2}/Kk^{1/2}} \tag{12.4.3}$$

where $k = k_f + k_b$ and $C^* = C_O^* + C_Y^*$. The first term in the denominator is δ, the Nernst diffusion layer thickness:

$$\delta = 1.61D^{1/3}\omega^{-1/2}\nu^{1/6} = D/m \tag{12.4.4}$$

and the second term, which also has dimensions of length, contains the so-called reaction layer thickness μ

$$\mu = (D/k)^{1/2} \tag{12.4.5}$$

Parameters for the reaction can be determined from the variation of i with ω. Note that at small ω, the first term of the denominator predominates ($\delta \gg \mu/K$), and the observed current is the mass-transfer-controlled limiting current i_l (equation 9.3.22). At high ω ($\delta \ll \mu/K$), the pure kinetic current results:

$$i = nFAD^{1/2}C^*Kk^{1/2} \tag{12.4.6}$$

The current under these conditions is independent of ω and is identical to that found for linear scan voltammetry and chronoamperometry, (12.3.6). Equation 12.4.3 can also be written in the form (74)

$$\boxed{\frac{i}{\omega^{1/2}} = \frac{i_l}{\omega^{1/2}} - i\left(\frac{D^{1/6}}{1.61\, \nu^{1/6}Kk^{1/2}}\right)} \tag{12.4.7}$$

so that a plot of $i/\omega^{1/2}$ vs. i can be used to obtain $K(k_f + k_b)^{1/2}$. This case has also been treated for the rotating ring electrode (75).

12.4.3 Following Reaction—E_rC_i

A steady-state treatment of this case using the reaction layer concept was given in Section 1.5.2. The limiting cathodic current is not affected by the following reaction, but the curve is shifted toward positive potentials because of the following reaction, with $E_{1/2}$ becoming a function of ω. The theoretical equation based on a more exact treatment of this case is (76)

$$E_{1/2} = E^{0'} + \left(\frac{RT}{nF}\right)\ln\left(\frac{\delta}{\mu}\right)\coth\left(\frac{\delta}{\mu}\right) \tag{12.4.8}$$

where $\delta/\mu = 1.61\, k^{1/2}\nu^{1/6}D^{-1/6}\omega^{-1/2}$. When δ/μ becomes large (i.e., for $k/\omega > 100$), $\coth(\delta/\mu) \to 1$, and (12.4.8) becomes

$$\boxed{E_{1/2} = E^{0'} + \left(\frac{RT}{nF}\right)\ln(1.61\, D^{-1/6}\nu^{1/6}) + \frac{RT}{2nF}\ln\left(\frac{k}{\omega}\right)} \tag{12.4.9}$$

Note that the equation from the approximate treatment, (1.5.25), becomes the same as (12.4.9) by choosing $\mu = (D/k)^{1/2}$ (the same reaction layer thickness defined in Section 12.4.2). The limits of applicability of these equations have been examined (76, 77). Note also the similarity between (12.4.9) and the voltammetric equation (12.3.22). (Recall that $\lambda = k/\omega$ for the RDE.)

The RRDE is especially useful in the study of EC reactions. The ring is set at a potential where the mass-transfer-controlled oxidation of R back to O [the reverse of (12.2.1)] occurs, and one evaluates k from the difference between the measured (kinetic) collection efficiency N_K ($= -i_r/i_d$) and the value N found in the absence of the perturbing reaction (see Section 9.4.2). An approximate treatment of steady-state kinetic collection efficiencies for thin-ring/thin-gap electrodes, later extended to a wider range of electrode geometries, has been presented (78–80). For such electrodes two approximate equations were suggested (78): For $4.5 < \kappa < 3.5$

$$N_K \approx 1.75\kappa^{-3}\exp[-4\kappa^3(r_2 - r_1)/r_1] \tag{12.4.10}$$

For $\kappa < 0.5$

$$\frac{N}{N_K} = 1 + 1.28\left(\frac{\nu}{D}\right)^{1/3}\left(\frac{k}{\omega}\right) \tag{12.4.11}$$
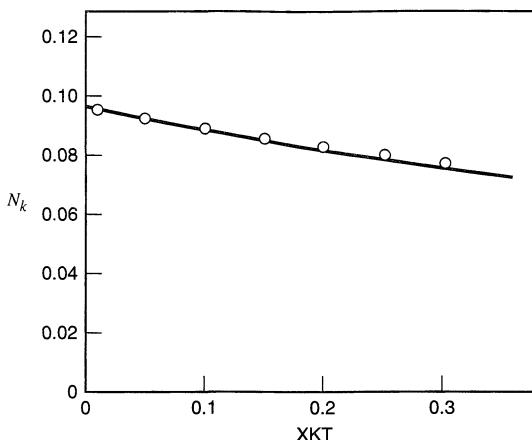
Figure 12.4.1 Collection efficiency *vs.* **XKT** $[= \kappa^2 = k\nu^{1/3}/\omega D^{1/3}(0.51)^{2/3}]$. Curve obtained from digital simulation of an E_rC_i reaction at thin-ring/thin-gap electrode $(r_2/r_1 = 1.02, r_3/r_2 = 1.02)$. Points show N_K calculated from (12.4.11). [From K. B. Prater and A. J, Bard, *J. Electrochem. Soc.*, **117**, 335 (1970), reprinted by permission of the publisher, The Electrochemical Society, Inc.]

where

$$\kappa = k^{1/2}\omega^{-1/2}D^{-1/6}\nu^{1/6}(0.51)^{-1/3} \tag{12.4.12}$$

and r_1 and r_2 are the radii of the disk and inner edge of the ring, respectively (see Figure 9.4.1). These expressions hold, however, only for electrodes where $r_2/r_1 \approx r_3/r_1$, which are very difficult to construct in practice. An alternate, more complicated expression for N_K was therefore suggested (79, 80):

$$N_K = N - (\beta')^{2/3}(1 - U_*A_1^{-1}) + \tfrac{1}{2}A_1^{-1}A_2^2\kappa^2U_*(\beta')^{4/3} - 2A_2\kappa^2T_2 \tag{12.4.13}$$

where $A_1 = 1.288$, $A_2 = 0.643\ \nu^{1/6}D^{1/3}$, $\beta' = 3\ln(r_3/r_2)$, $U_* = \kappa^{-1}\tanh(A_1\kappa)$, and T_2 is a rather complicated small factor approximately equal to $0.718\ln(r_2/r_1)$.

The problem of the E_rC_i reaction has also been attacked using digital simulation methods (81) (Appendix B). In this approach, no approximations need be made about electrode geometry. However, a separate simulation is required for each electrode geometry and each value of κ. Results from typical simulations of N_K as a function of the simulation parameter XKT $(= \kappa^2)$ are shown in Figures 12.4.1 and 12.4.2, which also contain predictions from the approximate equations in the appropriate regions. The range of rate constants that can be measured by the RRDE technique generally is, with rather generous limits, $0.3 < \kappa < 5$ (80). As can be seen in Figure 12.4.2 when $\kappa < 0.3$, $N_K \approx N$; while for $\kappa > 5$, $N_K \to 0$ and the ring current becomes too small to measure. For the usual range of ω, D, and ν, the range of measurable rate constants is approximately $0.03 < k < 10^3\ \text{s}^{-1}$.
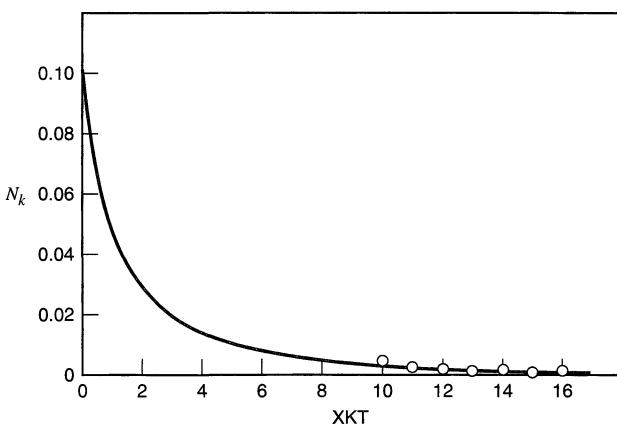
Figure 12.4.2 N_K *vs.* **XKT** as in Figure 12.4.1: Points show calculations from (12.4.10). [From K. B. Prater and A. J. Bard, *J. Electrochem. Soc.*, **117**, 335 (1970), reprinted by permission of the publisher, The Electrochemical Society, Inc.]

Theoretical treatments are also available for E_rC_i schemes involving second-order reactions (81, 82), as well as for the disk and ring transients in this reaction scheme (81).

12.4.4 Catalytic Reaction—E_rC_i'

A solution based on the reaction layer approach for this mechanism [see (12.3.27) and (12.3.28)] follows closely that given for the C_rE_r reaction discussed in Section 12.4.2 (73). Under the conditions that $\delta >> \mu$ (i.e., that $\omega(D/\nu)^{1/3} << 3k'C_Z^*$), a limiting kinetic current, independent of ω, is found:

$$i = nFAD^{1/2}C_O^*(k'C_Z^*)^{1/2} \qquad (12.4.14)$$

Note that this equation is the same as (12.3.29). This limiting current holds only in the region of small ω. When λ $(= k'C_Z^*/\omega)$ becomes small, the behavior approaches the mass-transfer-controlled limiting current. Results of a digital simulation of the catalytic case (83) are shown in Figure 12.4.3. Other treatments of the E_rC_i' case at the RDE, as well as variations of this mechanism, have also appeared (84–86). The treatment of the E_rC_i' case for the RRDE by digital simulation techniques showed that the results (i.e., plots of N_K vs. **XKT**) are indistinguishable from those of the E_rC_i case for first- or pseudo-first-order reactions (83).

12.4.5 ECE Reactions

The behavior of systems at the RDE undergoing the general ECE/DISP scheme (Section 12.3.8) can be analyzed by means of the zone diagrams employed for voltammetry with the appropriate expressions for λ and λ_d. Most RDE treatments, however, have been concerned with the $E_rC_iE_r$ sequence, which has been treated at several different levels of approximation. Karp (87) proposed the following equation for the limiting current:

$$i = i_l\left[2 - \frac{\tanh(\delta/\mu)}{\delta/\mu}\right] \qquad (12.4.15)$$

$$\frac{n_{app}}{n} = 2 - \frac{\tanh(\delta/\mu)}{\delta/\mu} \qquad (12.4.16)$$

where $n_1 = n_2 = n$, i_l is the n-electron mass-transfer-limiting current given in (9.3.22), and δ and μ are as defined in (12.4.4) and (12.4.5). Filinovskii (88) proposed the equation

$$i = 0.94\, i_l\left[2 - \frac{(1 + \delta^2/1.9\, \mu^2)^{1/2}}{1 + \delta^2/\mu^2}\right] \qquad (12.4.17)$$
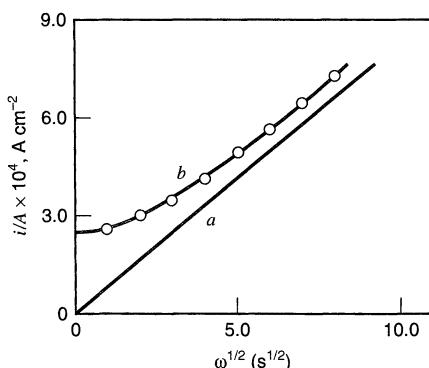
Figure 12.4.3 Simulated disk current for the catalytic reaction E_rC_i'. *Curve a*: In absence of a following reaction. *Curve b*: In the presence of a following reaction with $k_2 = 145\ M^{-1}s^{-1}$ and $C_Z^* = 10\ C_O^*$. Points are experimental data from study of reduction of Fe^{3+} in the presence of H_2O_2 (85). [From K. B. Prater and A. J. Bard, *J. Electrochem. Soc.*, **117**, 1517 (1970), reprinted by permission of the publisher, The Electrochemical Society, Inc.]
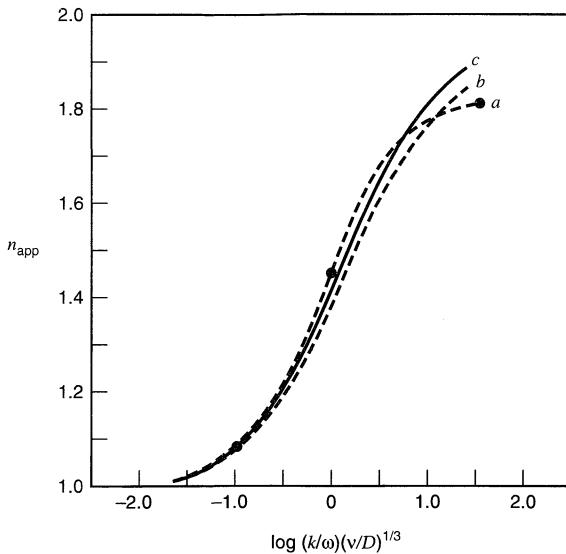
Figure 12.4.4 Variation of n_{app} with $\log(k\omega^{-1}\nu^{1/3}D^{-1/3}) = \log(\delta^2/2.6\mu)$ for $E_rC_iE_r$ mechanism. *Curve a*: Equation 12.4.17 divided by i_l. *Curve b*: Equation 12.4.16. *Curve c*: Digital simulation (83).

which gives n_{app}/n upon division of both sides by i_l. Digital simulations of this reaction scheme at the RDE were also carried out (83, 89); these included cases with a second-order intervening reaction and the possibility of a disproportionation reaction between species B and C. A reaction layer treatment was also employed to relate shifts in half-wave potentials to elucidation of the ECE/DISP1 scheme (90). A comparison of the results of different treatments is given in Figure 12.4.4. A digital simulation of the RRDE behavior for this case for first- and second-order intervening reactions has been reported (83). As in other RRDE treatments of reactions with kinetic complications, the results depend on the electrode geometry. The variation of N_K with the kinetic parameters for a typical RRDE electrode (with an unperturbed collection efficiency, N, of 0.55) is shown in Figure 12.4.5.
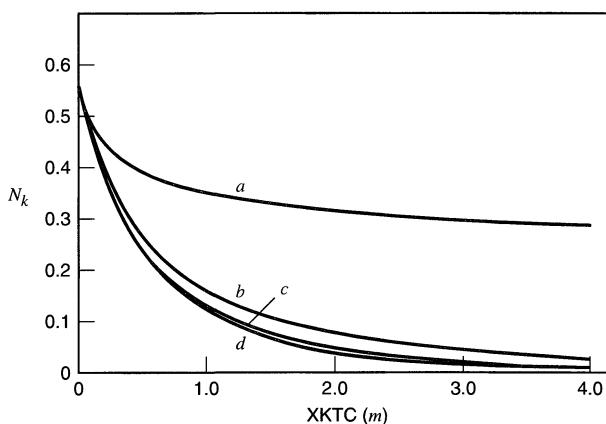
Figure 12.4.5 Variation of N_K with kinetic parameters for an RRDE ($r_2/r_1 = 1.13$; $r_3/r_2 = 1.69$) for the following ECE mechanism: $O_1 + n_1e \rightarrow R_1$, $R_1 + Z \rightarrow O_2 + Y$, $O_2 + n_2e \rightarrow R_2$, with $n_1 = n_2$ and k_2 as the rate constant for the middle step. **XKTC** $= k_2C_{O_1}^*\omega^{-1}\nu^{1/3}D^{-1/3}(0.51)^{-2/3}$; $m = C_Z^*/C_{O_1}^*$. *Curve a*: $m = 0.1$. *Curve b*: $m = 1.0$. *Curve c*: $m = 10$. *Curve d*: First order.
[From K. B. Prater and A. J. Bard, *J. Electrochem. Soc.*, **117**, 1517 (1970), reprinted by permission of the publisher, The Electrochemical Society, Inc.]

▶ 12.5 UME TECHNIQUES

The behavior of a UME depends upon the time scale of the experiment. At very short times, when $Dt \ll r_0^2$, it behaves like a planar electrode. Measurements of rapid reactions are possible in this time regime, since double-layer charging effects are greatly diminished (Section 5.9.1), and the treatments of Section 12.2 apply. However, the steady-state currents or voltammograms at a UME (when $Dt \gg r_0^2$) can also be employed to study coupled homogeneous reactions. In this case, the response is similar to that for an RDE at steady state. (The behavior in the intermediate time region is complicated and rarely used in practice). A given UME operating in the steady-state mode has the disadvantage of having only a single characteristic time ($\sim r_0^2/D$) and thus a restricted time window for obtaining kinetic information. To illustrate this concept, consider the study of an ECE reaction. When the intervening reaction, (12.3.42), is fast, and the reaction layer thickness, μ, is small compared to the diffusion layer thickness ($\sim r_0$), all reactions will occur within the diffusion layer and $n_{app} = 2$. When the reaction is slow, so that μ is large compared to r_0, the occurrence of (12.3.42) will have essentially no effect, and $n_{app} = 1$. It is only when the reaction layer thickness is of the order of r_0 that useful kinetic information can be obtained. Thus, data at several electrodes of different r_0 must be obtained to span the needed time regime in an investigation of a single reaction, while with an RDE, a single electrode can be employed at different rotation rates.

The equations governing the steady-state current as a function of r_0 can be obtained by solving the ordinary differential equations for spherical diffusion governing the appropriate kinetic scheme or by using the reaction layer approximation (7, 91–94). The relevant behavior at microspherical electrodes in any time regime can also be obtained through digital simulation (17).

Generation/collection experiments, analogous to those at the RRDE, can be carried out with pairs of microband electrodes. In this case, the relevant time parameter is that required for the electrogenerated species to diffuse across the gap, d, separating the microbands (95). Because of the small spacing attainable with microbands, this time can be smaller than that typically found at the RRDE at usual rotation rates. However, the fixed gap width implies that a given pair of microbands is characterized by a narrow time window ($\sim d^2/D$), thus requiring that a given reaction be studied at several electrode pairs. Equivalent studies of coupled reactions can be carried out by scanning electrochemical microscopy (SECM) (Section 16.4.4), where d is continuously variable down to very small values (96).

▶ 12.6 SINE WAVE METHODS

Although there have been numerous theoretical treatments for the effects of coupled homogeneous chemical reactions on the measured faradaic impedance or ac voltammetric response, these methods generally have not found very wide application to studies of coupled chemistry. This is mainly the result of the rather complicated, often cumbersome, general equations describing the measured ac response in terms of frequency and kinetic parameters. In addition, ac responses such as current amplitude and phase angle, do not provide as clear a qualitative or semiquantitative feeling for the nature of the coupled reaction as do voltammetric responses. For most mechanisms, the added chemistry (beyond the heterogeneous electron transfers) produces an intrinsic irreversibility that may not allow a steady-state response to be achieved. Thus, the measurements may depend upon the duration of the experiment. Finally, the higher frequencies employed in ac methods frequently bring the electron-transfer reactions from nernstian behavior into the quasireversible regime. While this can be helpful in determining heterogeneous rate constants, it complicates the interpretation of the results and the elucidation of the pathway of the overall reaction. On

the other hand, ac methods have a high inherent precision, and with the advent of computer-controlled data acquisition and Fourier transform techniques, they are capable of defining an electrode reaction over a wide frequency range in a rather short time. A discussion of the faradaic impedance and ac voltammetry for the C_rE_r mechanism, with examples of the effect of the heterogeneous electron-transfer rate on the observed response, is given in the first edition.[3] Reviews on this subject are also available (97–99).

▷ 12.7 CONTROLLED-POTENTIAL COULOMETRIC METHODS

The bulk electrolytic methods described in Section 11.3.4 are especially useful for examining the effects of slower reactions coupled to the electron-transfer reaction. Since the time window of such methods is about 100 to 3000 s, reactions with first-order rate constants of the order of 10^{-2} to 10^{-4} s^{-1} can be studied. Moreover, by analysis of the solution following electrolysis (e.g., by spectroscopic, chromatographic, or electrochemical methods), the products of the reactions, and hence the overall reaction scheme, can be determined. The experiments are usually carried out at potentials corresponding to the limiting current plateau, so that the kinetics of the electron-transfer reactions do not enter the analysis of results. Finally, the theoretical treatments for this technique and the analysis of the experimental results are frequently much simpler than those for the voltammetric methods.

12.7.1 Theoretical Treatments

The theory for the different reaction schemes involves ordinary (rather than partial) differential equations, because the electrolyzed solution is assumed to be essentially homogeneous (see Section 11.3.1). The concentrations are functions of t during the bulk electrolysis, but not of x. The measured responses in coulometry are the i–t curves and the apparent number of electrons n_{app} consumed per molecule of electroactive compound. From the quantity of electricity passed during the electrolysis $Q(t)$, n_{app} can be calculated as

$$n_{app} = \frac{Q(t)}{FN_O} = \frac{Q(t)}{FV[C_O^*(0) - C_O^*(t)]} \tag{12.7.1}$$

where N_O is the amount (moles) of O consumed; $C_O^*(0)$ is the initial concentration of O; $C_O^*(t)$ is the concentration at time t; and V is the total volume of solution. In coulometric experiments under limiting current conditions, electrode reactions are treated as first-order chemical reactions [see (11.3.5)], so that for the electron-transfer step $O + ne \rightarrow R$,

$$\frac{dC_O^*(t)}{dt} = -pC_O^*(t) \tag{12.7.2}$$

where $p = m_O A/V$, A is the electrode area (cm^2), and m_O is the mass-transfer constant for O (cm/s), which is a function of D_O and the convective conditions during the electrolysis. The current at any time is calculated using (11.3.1):

$$i(t) = nFAm_O C_O^*(t) \tag{12.7.3}$$

As an example of a theoretical treatment involving a coupled reaction, let us consider the catalytic reaction (E_rC_i'):

$$O + ne \overset{p}{\rightleftharpoons} R \tag{12.7.4}$$

$$R + Z \overset{k'}{\rightarrow} O + Y \tag{12.7.5}$$

---

[3]First edition, pp. 471–475.

where we assume $C_Z^*(0) \gg C_O^*(0)$, so that (12.7.5) represents a pseudo-first-order reaction with $k = k'C_Z^*(0)$. The equations governing the system are

$$\frac{dC_O^*(t)}{dt} = -pC_O^*(t) + kC_R^*(t) \tag{12.7.6}$$

$$\frac{dC_R^*(t)}{dt} = pC_O^*(t) - kC_R^*(t) \tag{12.7.7}$$

with the initial conditions that $C_O^*(0) = C_i$ and $C_R^*(0) = 0$. From the stoichiometry of the process,

$$C_R^*(t) = C_i - C_O^*(t) \tag{12.7.8}$$

Substitution of this value of $C_R^*(t)$ into (12.7.6) and integration of the resulting equation yields

$$C_O^*(t) = C_i\left\{\frac{\gamma + \exp[-p(1 + \gamma)t]}{1 + \gamma}\right\} \tag{12.7.9}$$

where $\gamma = k/p$. The i–t behavior is obtained by combining (12.7.3) and (12.7.9) to yield

$$\boxed{\frac{i(t)}{i(0)} = \frac{\gamma + \exp[-p(1 + \gamma)t]}{1 + \gamma}} \tag{12.7.10}$$

Note that in this case the current does not decay to zero (or the background level), as in the case of the unperturbed reaction ($k \to 0$), but instead decays to a steady-state value, i_{ss}, where

$$\frac{i_{ss}}{i(0)} = \frac{\gamma}{(1 + \gamma)} \tag{12.7.11}$$

(Figure 12.7.1). Thus, γ can be determined from $i_{ss}/i(0)$. Since the current does not decay to background, no time-independent n_{app} value is attained for the EC′ case, and n_{app} keeps increasing during the electrolysis. From (12.7.1) and (12.7.10) and the fact that

$$Q(t) = \int_0^t i(t)\, dt \tag{12.7.12}$$

the n_{app} equation is derived:

$$n_{app} = n\left[\frac{1}{1 + \gamma} + \frac{p\gamma t}{1 - e^{-p(1+\gamma)t}}\right] \tag{12.7.13}$$
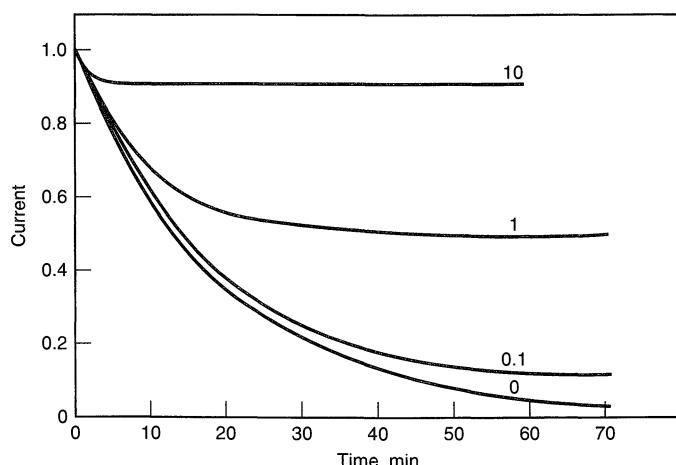
Figure 12.7.1   Current-time behavior for catalytic reaction case; $p = 0.05$ min^{-1} and k/p values indicated on the curves. [Reprinted from A. J. Bard and K. S. V. Santhanam, *Electroanal. Chem.*, **4**, 215 (1970), by courtesy of Marcel Dekker, Inc.]

The diagnostic criteria for the EC′ case in coulometry are (a) a current that does not decay to background and (b) a continually increasing n_{app} (with n_{app} values that are larger than expected). Further details about EC′ reactions in coulometry are available (100–102).

We will now briefly consider the results of theoretical treatments for other cases of coupled chemical reactions in coulometry. Detailed reviews have appeared (103, 104).

12.7.2 Preceding Reaction—C_rE_r

When the electroactive species is generated by a preceding reaction [see (12.3.1) to (12.3.3)], the n_{app} value for complete electrolysis is unperturbed, that is, $n_{app} = n$. However, the i–t behavior is changed from the simple exponential decay behavior, because the current is partially controlled by the rate of conversion of Y to O. The current is given by (105, 106)

$$\frac{i}{nFVp(C_O)_i} = C_1 e^{-(L-G)t} + (1 - C_1)e^{-(L+G)t} \qquad (12.7.14)$$

where

$$L = 0.5(k_f + k_b + p)$$
$$G = (L^2 - k_f p)^{1/2}$$
$$C_1 = G + L - p/2G$$
$$(C_O)_i = \frac{K}{1 + K} C^*$$

Typical log i–t curves are shown in Figure 12.7.2. The initial current is governed by the equilibrium concentration of O, $(C_O)_i$, and the initial decay is governed by the rate of electrolysis of existing O, hence p. The limiting rate is determined by the rate of conversion of Y to O, hence k_f.
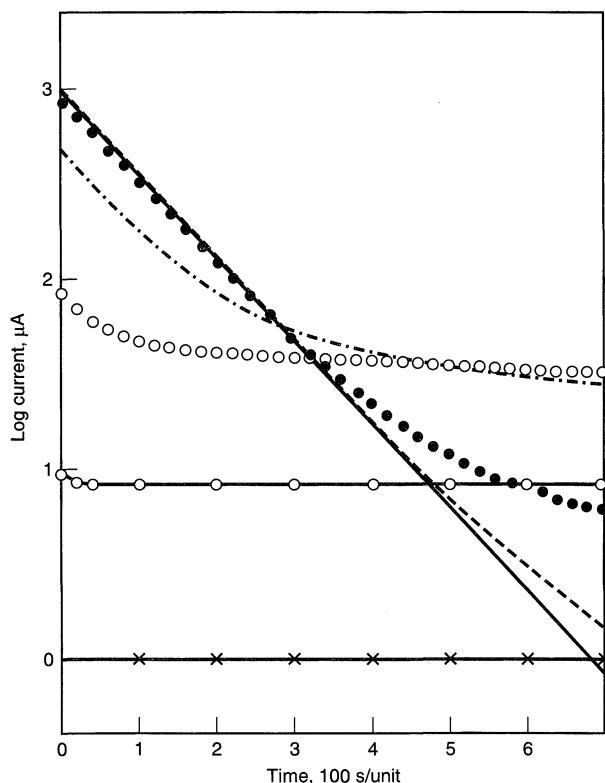
Figure 12.7.2 Current-time behavior for the preceding reaction for different values of $K = k_f/k_b$, calculated for $(C_O)_i + (C_Y)_i = 10^{-4} M$, $p = 0.01$ s^{-1}, and $k_f = 10^{-3}$ s^{-1}. (–×–) $K = 0.001$; (–O–) $K = 0.01$; (O) $K = 0.1$; (·—·—) $K = 1.0$; (●) $K = 10.0$; (---) $K = 100.0$; (—) $K \to \infty$. [Reprinted with permission from A. J. Bard and E. Solon, *J. Phys. Chem.*, **67**, 2326 (1963). Copyright 1963, American Chemical Society.]

12.7.3 Following Reaction (E_rC_i) and Reversal Coulometry

An irreversible following reaction does not perturb the forward i–t curve or the n_{app} value. However, by stepping the potential after the forward electrolysis ($O + ne \rightarrow R$) has proceeded for a time, t_1, to a value where the back oxidation occurs ($R \rightarrow O + ne$) and by determining the relative amounts of electricity passed during the forward step (Q_f) and the reversal step (Q_b), information about the rate of the following reaction ($R \xrightarrow{k} Y$) can be obtained. For the forward electrolysis (107),

$$Q_f = nFVC_O^*(0)[1 - \exp(-pt_1)] \tag{12.7.15}$$

This equation yields (11.3.11) as $t_1 \rightarrow \infty$. For the back electrolysis carried out for a time t_2 in the absence of the perturbing reaction,

$$Q_b/Q_f = 1 - \exp[-p(t_2 - t_1)] \tag{12.7.16}$$

Clearly when $(t_2 - t_1) \rightarrow \infty$, $Q_b = Q_f$.

In the presence of the following reaction,

$$Q_b = \frac{nFVpC_R(t_1)}{(p + k)} \{1 - \exp[-(p + k)(t_2 - t_1)]\} \tag{12.7.17}$$

where $C_R(t_1)$ is the concentration of R at the start of the reverse electrolysis and is given by

$$C_R(t_1) = \frac{pC_O^*(0)}{(k - p)} [\exp(-pt_1) - \exp(-kt_1)] \quad \degree \quad \degree \quad k \neq p \tag{12.7.18a}$$

$$C_R(t_1) = pC_O^*(0)t_1 \exp(-pt_1) \quad \degree \quad \degree \quad\quad\quad k = p \tag{12.7.18b}$$

The rate constant, k, can be evaluated from (12.7.17) and (12.7.18) or, more simply, by allowing the back reaction to proceed to completion to yield Q_b^0 [when$(t_2 - t_1) \rightarrow \infty$]. Under these conditions,

$$\frac{Q_b^0}{Q_f} = \frac{p^2}{k^2 - p^2} \left\{ \frac{1 - \exp[(p - k)t_1]}{\exp(pt_1) - 1} \right\} \quad\quad k \neq p \tag{12.7.19a}$$

$$\frac{Q_b^0}{Q_f} = \frac{pt_1}{2[\exp(pt_1) - 1]} \quad\quad k = p \tag{12.7.19b}$$

Similar treatments have been presented for reversal coulometry with reversible reactions and dimerizations following the electron-transfer reaction (107).

12.7.4 $E_rC_iE_r$ Reactions

The ECE reaction shown in Table 12.7.1 (where $\Delta E^0 > 0$) is characterized by an n_{app} value of n_1 at short times, when the intervening reaction cannot occur to an appreciable extent, and of $n_1 + n_2$ at longer times. The i–t curve for this case, assuming the same p value for each electron-transfer step, is (106, 108, 109)

$$\frac{i}{FVC_O^*(0)p \exp(-pt)} = n_1 + \frac{n_2pk}{k - p} \left\{ t - \frac{[1 - e^{-(k-p)t}]}{k - p} \right\} \tag{12.7.20}$$

Typical i–t curves for different values of k/p are shown in Figure 12.7.3. When $k/p \ll 1$ and $kt_1 \ll 1$, $n_{app} = n_1$ and the simple exponential decay of current is observed. For long

TABLE 12.7.1 **Diagnostic Criteria in Controlled Potential Coulometry for Different Reaction Mechanisms**

Reaction Mechanism	$n_{app}^{\ b}$	Reversal Coulometry^c	$\log i - t^d$
No kinetic effects			
$O + ne \rightarrow R$	$n_{app} = n$	$Q_b^0 = Q_f$	Linear, slope p
Catalytic reaction			
$O + ne \rightarrow R$	$n_{app} > n$	$0 \leqq Q_b^0 < Q_f$	Concave upward; current reaches steady-state value. If the electrolysis is interrupted and resumed, current will be higher than value at interruption.
$R + Z \xrightarrow{k} O$			
$O + ne \rightarrow R$	$n_{app} > n$	$0 \leqq Q_b^0 < Q_f$	Linear or concave downward
$R + Z \xrightarrow{k_1} O$	$n_{app} = f(C_O)_i$		
$R + X \xrightarrow{k_2} Y$			
Preceding reaction			
$Y \underset{k_b}{\overset{k_f}{\rightleftharpoons}} O$	$n_{app} = n$	$Q_b^0 = Q_f$	Concave upward
$O + ne \rightarrow R$			
Coupling reaction			
$O + ne \rightarrow R$	$n/2 < n_{app} < n$	$Q_b^0 < Q_f$	Linear slope $> p$
$R + O \xrightarrow{k} Y$	$n_{app} = f(C_O)_i$		
or			
$R + O \xrightarrow{k_1} Y$	$n/2 < n_{app} < n$	$Q_b^0 < Q_f$	Linear slope $> p$
$R + Z \xrightarrow{k_2} X$	$n_{app} = f(C_O)_i$		
Competing reaction			
$O + ne \rightarrow R$	$n_{app} < n$	$Q_b^0 = Q_f$	Linear slope $> p$
$O + Z \xrightarrow{k} X$	n_{app} is a function of time between mixing of solution and electrolysis, and $(C_O)_i$		
Following reaction			
$O + ne \rightarrow R$	$n_{app} = n$	$Q_b^0 < Q_f$	Linear slope $= p$
$R \xrightarrow{k} Y$			
or			
$R \underset{k_b}{\overset{k_f}{\rightleftharpoons}} Y$			
$2R \xrightarrow{k} X$			
Consecutive reaction			
$O \xrightarrow{+n_1e} I \xrightarrow{+n_2e} R$	$n_{app} = n_1 + n_2$	$Q_b^0 = Q_f$	Linear or concave upward
$O \xrightarrow{+n_1e} I \xrightarrow{+n_2e} R$ $\Big\downarrow k$ $\rightarrow X$	$n_1 < n_{app} < n_1 + n_2$	$Q_b^0 < Q_f$	Linear or concave upward

TABLE 12.7.1 *(continued)*

ECE reactions

$$O_1 \xrightarrow{n_1 e} R_1 \xrightarrow{k_1} O_2 \xrightarrow{n_2 e} R_2 \quad n_{app} = n_1 + n_2$$

$$Q_b^0 = Q_f\left(\frac{n_2}{n_1 + n_2}\right) \quad \text{Linear, concave upward or downward}$$

(irreversible
intervening
reaction)

$$O_1 \xrightarrow{n_1 e} R_1 \xrightarrow{k_1} O_2 \xrightarrow{n_2 e} R_2 \quad n_1 < n_{app} < n_1 + n_2$$
$$\quad\quad \downarrow{k_2}$$
$$\quad\quad\;\; Z$$

$$Q_b^0 < Q_f\left(\frac{n_2}{n_1 + n_2}\right) \quad \text{Linear, concave upward or downward}$$

$$O_1 \xrightarrow{n_1 e} R_1 \xrightarrow{k_1} O_2 \xrightarrow{n_2 e} R_2 \quad n_1 < n_{app} < n_1 + n_2$$

$$2R_1 \xrightarrow{k_2} X \quad\quad\quad n_{app} = f(C_O)_i$$

$$Q_b^0 < Q_f\left(\frac{n_2}{n_1 + n_2}\right) \quad \text{Linear, concave upward or downward}$$

(irreversible
intervening
reactions)

---
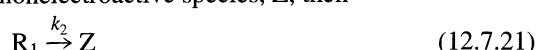
[a]From A. J. Bard and K. S. V. Santhanam, *Electroanal. Chem.*, **4**, 215–315 (1970) with permission.
[b]Where n_{app} is a function of initial concentration of O, $(C_O)_i$, it is so indicated.
[c]Assuming all electrochemical steps are reversible.
[d]Current decays to background, unless noted otherwise.

electrolysis times, $n_{app} = n_1 + n_2$. When there are additional reactions that occur, the n_{app} values can be nonintegral even for long electrolysis times. For example, if the product of the first reduction, R_1, decomposes to a nonelectroactive species, Z, then

$$R_1 \xrightarrow{k_2} Z \tag{12.7.21}$$

in addition to its decomposition to O_2; then (108)

$$n_{app} = n_1 + \frac{n_2}{1 + (k_2/k)} \tag{12.7.22}$$

This reaction path would lead to nonintegral n_{app} values.

A number of other reaction schemes in coulometry have been treated (103, 104). The diagnostic criteria for various reaction mechanisms are given in Table 12.7.1 (103).
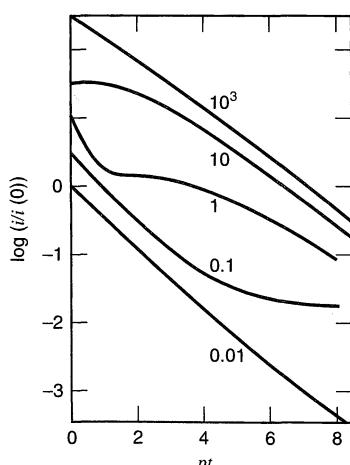
Figure 12.7.3 Variation of $i/i(0)$ with t for an ECE mechanism with $p = 10^{-3}\,\text{s}^{-1}$. Value of k/p shown on each curve. The ordinate scale pertains to the lowermost curve, for which $k/p = 0.01$. Each successive curve above this is shifted upward 0.5 unit on the ordinate. [From S. Karp and L. Meites, *J. Electroanal. Chem.*, **17**, 253 (1968), with permission.]

12.8 REFERENCES
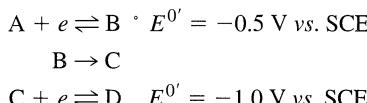
1. Z. Galus, "Fundamentals of Electrochemical Analysis," 2nd ed., Wiley, New York, 1994.

2. P. Delahay, "New Instrumental Methods in Electrochemistry," Wiley-Interscience, New York, 1954.

3. I. M. Kolthoff and J. J. Lingane, "Polarography," 2nd ed., Wiley-Interscience, New York, 1952.

4. D. D. Macdonald, "Transient Techniques in Electrochemistry," Plenum, New York, 1977.

5. D. Pletcher, *Chem. Soc. Rev.*, **4**, 471 (1975).

6. D. H. Evans, *Accts. Chem. Res.*, **10**, 313 (1977).

7. C. P. Andrieux and J.-M. Savéant, in "Investigation of Rates and Mechanisms of Reactions," Part II, 4th ed., C. F. Bernasconi, Ed., Wiley-Interscience, New York, 1986, Part 2, Vol. 6, pp. 305–390.

8. D. H. Evans, *Chem. Rev.*, **90**, 739 (1990).

9. C. P. Andrieux, P. Hapiot, and J.-M. Savéant, *Chem. Rev.*, **90**, 723 (1990).

10. A. C. Testa and W. H. Reinmuth, *Anal. Chem.*, **33**, 1320 (1961).

11. Q. Xie, E. Perez-Cordero, and L. Echegoyen, *J. Am. Chem. Soc.*, **114**, 3978 (1992).

12. C. Amatore and J.-M. Savéant, *J. Electroanal. Chem.*, **85**, 27 (1977).

13. S. W. Feldberg, and L. Jeftic, *J. Phys. Chem.*, **76**, 2439 (1972).

14. J.-M. Savéant, in "Advances in Physical Organic Chemistry," D. Bethell, Ed., Academic, New York, 1990, Vol. 26, pp. 1–130.

15. J. Jacq, *J. Electroanal. Chem.*, **29**, 149 (1971).

16. W. H. Smith and A. J. Bard, *J. Am. Chem. Soc.*, **97**, 5203 (1975).

17. (a) DigiSim is a cyclic voltammetry simulator sold by Bioanalytical Systems, Inc. (b) M. Rudolph, D. P. Reddy, and S. W. Feldberg, *Anal. Chem.*, **66**, 589A (1994).

18. (a) ELSIM simulates various electrochemical responses and is sold by Technical Software Distributors. (b) L. K. Bieniasz, *Computers Chem.*, **17**, 355 (1993).

19. CVSIM, a cyclic voltammetry simulator, is available with the monograph, D. K. Gosser, Jr., *Cyclic Voltammetry: Simulation and Analysis of Reaction Mechanisms*, VCH, New York, 1994.

20. A. C. Testa and W. H. Reinmuth, *Anal. Chem.*, **32**, 1512 (1960).

21. O. Dracka, *Coll. Czech. Chem. Commun.*, **25**, 338 (1960).

22. H. B. Herman and A. J. Bard, *Anal. Chem.*, **36**, 510 (1964).

23. D. A. Tryk and S. M. Park, *Anal. Chem.*, **51**, 585 (1979).

24. J.-M. Savéant and E. Vianello, *Electrochim. Acta*, **8**, 905 (1963); **12**, 629 (1967).

25. R. S. Nicholson and I. Shain, *Anal. Chem.*, **36**, 706, (1964).

26. J. Koutecký and R. Brdička, *Coll. Czech. Chem. Commun.*, **12**, 337 (1947).

27. J. Koutecký and J. Čížek, *Coll. Czech. Chem. Commun.*, **21**, 836 (1956).

28. J. Koutecký *Coll. Czech. Chem. Commun.*, **19**, 857 (1954).

29. P. Delahay and T. Berzins, *J. Am. Chem. Soc.*, **75**, 2486 (1953).

30. W. H. Reinmuth, *Anal. Chem.*, **33**, 322 (1961).

31. A. J. Bard and H. B. Herman, "Polarography—1964," G. J. Hills, Ed., Wiley-Interscience, New York, 1966, p. 373.

32. W. M. Schwarz and I. Shain, *J. Phys. Chem.*, **69**, 30 (1965).

33. W. V. Childs, J. T. Maloy, C. P. Keszthelyi, and A. J. Bard, *J. Electrochem. Soc.*, **118**, 874 (1971).

34. M. L. Olmstead and R. S. Nicholson, *Anal. Chem.*, **41**, 851 (1969).

35. J.-M. Savéant and E. Vianello, *Electrochim. Acta*, **12**, 1545 (1967).

36. M. L. Olmstead, R. T. Hamilton, and R. S. Nicholson, *Anal. Chem.*, **41**, 260 (1969).

37. R. S. Nicholson, *Anal. Chem.*, **37**, 667 (1965).

38. C. P. Andrieux, L. Nadjo, and J.-M. Savéant, *J. Electroanal. Chem.*, **26**, 147 (1970).

39. D. H. Evans, *J. Phys. Chem.*, **76**, 1160 (1972).

40. L. Nadjo and J.-M. Savéant, *J. Electroanal. Chem.*, **48**, 113 (1973).

41. J.-M. Savéant in "Advances in Physical Organic Chemistry," Vol. 35, T. Tidwell, Ed., Academic, New York, 2000 (in press).

42. C. Costentin, M. Robert, and J.-M. Savéant, *J. Phys. Chem.*, **104**, 7492 (2000).

43. P. Delahay and G. L. Steihl, *J. Am. Chem.*, **74**, 3500 (1952).

44. S. L. Miller, *J. Am. Chem. Soc.*, **74**, 4130 (1952).

45. Z. Pospíšil, *Coll. Czech. Chem. Commun.*, **12**, 39 (1947).

46. P. Delahay, C. C. Mattax, and T. Berzins, *J. Am. Chem.*, **76**, 5319 (1954).

47. O. Fischer, O. Dracka and E. Fischerova, *Coll. Czech. Chem. Commun.*, **26**, 1505 (1961).

48. C. Furlani and G. Morpurgo, *J. Electroanal. Chem.*, **1**, 351 (1960).

49. D. S. Polcyn and I. Shain, *Anal. Chem.*, **38**, 370 (1966).

50. F. Ammar and J.-M. Savéant, *J. Electroanal. Chem.*, **47**, 215 (1973).

51. J. B. Flanagan, S. Margel, A. J. Bard, and F. C. Anson, *J. Am. Chem. Soc.*, **100**, 4248 (1978).

52. J. Phelps and A. J. Bard, *J. Electroanal. Chem.*, **68**, 313 (1976).

53. C. P. Andrieux and J.-M. Savéant *J. Electroanal. Chem.*, **28**, 339 (1970).

54. K. Hinkelmann and J. Heinze, *Ber. Bunsenges. Phys. Chem.*, **91**, 243 (1987) and references therein.

55. R. S. Nicholson and I. Shain, *Anal. Chem.*, **37**, 178 (1965).

56. J.-M. Savéant, *Electrochim., Acta*, **12**, 753 (1967).

57. M. Mastragostino, L. Nadjo, and J.-M. Savéant, *Electrochim. Acta*, **13**, 721 (1968).

58. J.-M. Savéant, C. P. Andrieux, and L. Nadjo, *J. Electroanal. Chem.*, **41**, 137 (1973).

59. C. Amatore and J.-M. Savéant, *J. Electroanal. Chem.*, **102**, 21 (1979).

60. G. S. Alberts and I. Shain, *Anal. Chem.*, **35**, 1859 (1963).

61. J. Koutecký, *Coll. Czech. Chem. Commun.*, **18**, 183 (1953).

62. R. S. Nicholson, J. M. Wilson, and M. L. Olmstead, *Anal. Chem.*, **38**, 542 (1966).

63. J.-M. Savéant, *Bull. Chem. Soc. France*, **1967**, 91.

64. H. B. Herman and A. J. Bard, *J. Phys. Chem.*, **70**, 396 (1966).

65. B. W. Rossiter and J. F. Hamilton, Eds., "Physical Methods of Chemistry," 2nd ed., Vol. II., "Electrochemical Methods," Wiley-Interscience, New York, 1986.

66. J. Heinze, *Angew. Chem. Int. Ed. Engl.*, **23**, 831 (1984).

67. J.-M. Savéant, *Accts. Chem. Res.*, **13**, 323 (1980).

68. D. H. Evans and K. M. O'Connell, *Electroanal. Chem.*, **14**, 113 (1986).

69. M. D. Hawley, in "Laboratory Techniques in Electroanalytical Chemistry, 2nd ed.," P. T. Kissinger and W. R. Heineman, Eds., Marcel Dekker, New York, 1996, Chap. 21.

70. H. Lund and M. M. Baizer, Eds., "Organic Electrochemistry," 3rd ed., Marcel Dekker, New York, 1991.

71. W. E. Geiger, in "Laboratory Techniques in Electroanalytical Chemistry," 2nd ed., P. T. Kissinger and W. R. Heineman, Eds., Marcel Dekker, New York, 1996, Chap. 23.

72. N. G. Connelly and W. E. Geiger, *Adv. Organomet. Chem.*, **23**, 1 (1984).

73. J. Koutecký and V. G. Levich, *Zhur. Fiz. Khim.*, **32**, 1565 (1958); *Dokl. Akad. Nauk SSSR*, **117**, 441 (1957).

74. W. Vielstich and D. Jahn, *Z. Elektrochem.*, **32**, 2437 (1958).

75. H. Matsuda, *J. Electroanal. Chem.*, **35**, 77 (1972).

76. L. K. J. Tong, K. Liang, and W. R. Ruby, *J. Electroanal. Chem.*, **13**, 245 (1967).

77. S. A. Kabakchi and V. Yu. Filinovskii, *Elektrokhim.*, **8**, 1428 (1972).

78. W. J. Albery and S. Bruckenstein, *Trans. Faraday Soc.*, **62**, 1946 (1966).

79. W. J. Albery, M. L. Hitchman, and J. Ulstrup, *Trans. Faraday Soc.*, **64**, 2831 (1968).

80. W. J. Albery, M. L. Hitchman, "Ring-Disc Electrodes," Clarendon, Oxford, 1971.

81. K. B. Prater and A. J. Bard, *J. Electrochem. Soc.*, **117**, 335 (1970).

82. W. J. Albery and S. Bruckenstein, *Trans. Faraday Soc.*, **62**, 2584 (1966).

83. K. B. Prater and A. J. Bard, *J. Electrochem. Soc.*, **117**, 1517 (1970).

84. P. Beran and S. Bruckenstein, *J. Phys. Chem.*, **72**, 3630 (1968).

85. D. Haberland and R. Landsberg, *Ber. Bunsenges. Phys. Chem.*, **70**, 724 (1966).

86. F. Kermiche-Aouanouk and M. Daguenet, *Electrochim. Acta*, **17**, 723 (1972).

87. S. Karp, *J. Phys. Chem.*, **72**, 1082 (1968).

88. V. Yu. Filinovskii, *Elektrokhim.*, **5**, 635 (1969).

89. L. S. Marcoux, R. N. Adams, and S. W. Feldberg, *J. Phys. Chem.*, **73**, 2611 (1969).

90. R. G. Compton, R. G. Harland, P. R. Unwin, and A. M. Waller, *J. Chem. Soc., Faraday Trans. 1*, **83**, 1261 (1987).

91. C. G. Phillips, *J. Electroanal. Chem.*, **296**, 255 (1990).

92. G. Denuault and D. Pletcher, *J. Electroanal. Chem.*, **305**, 131 (1991).

93. K. B. Oldham, *J. Electroanal. Chem.*, **313**, 3 (1991).

94. Z. Qiankun and C. Hongyuan, *J. Electroanal. Chem.*, **346**, 471 (1993).

95. T. V. Shea and A. J. Bard, *Anal. Chem.*, **59**, 2101 (1987).

96. (a) P. R. Unwin and A. J. Bard, *J. Phys. Chem.*, **95**, 7814 (1991); (b) F. Zhou, P. R. Unwin, and A. J. Bard, *ibid.*, **96**, 4917 (1992); (c) D. Treichel, M. V. Mirkin, and A. J. Bard, *ibid.*, **98**, 5751 (1994).

97. D. E. Smith, *Electroanal. Chem.*, **1**, 1 (1966).

98. D. E. Smith, *CRC Crit. Rev. Anal. Chem.*, **2**, 247 (1971).

99. M. Sluyters-Rehbach and J. H. Sluyters, *Electroanal. Chem.*, **4**, 1 (1970).

100. D. H. Geske and A. J. Bard, *J. Phys. Chem.*, **63**, 1957 (1959).

101. L. Meites and S. A. Moros, *Anal. Chem.*, **31**, 23 (1959).

102. G. A. Rechnitz and H. A. Laitinen, *Anal. Chem.*, **33**, 1473 (1961).

103. A. J. Bard and K. S. V. Santhanam, *Electroanal. Chem.*, **4**, 215 (1970).

104. L. Meites in "Techniques of Chemistry," A. Weissberger and B. W. Rossiter, Eds., Wiley-Interscience, New York, 1971, Part IIA, Vol. I, Chap. IX.

105. A. J. Bard and E. Solon, *J. Phys. Chem.*, **67**, 2326 (1963).

106. R. I. Gelb and L. Meites, *J. Phys. Chem.*, **68**, 630 (1964).

107. A. J. Bard and S. V. Tatwawadi, *J. Phys. Chem.*, **68**, 2676 (1964).

108. A. J. Bard and J. S. Mayell, *J. Phys. Chem.*, **66**, 2173 (1962).

109. S. Karp and L. Meites, *J. Electroanal. Chem.*, **17**, 253 (1968).

▷ 12.9 PROBLEMS

12.1 Consider the following system:

$$A + e \rightleftharpoons B \quad E^{0'} = -0.5 \text{ V } vs. \text{ SCE}$$

$$B \rightarrow C$$

$$C + e \rightleftharpoons D \quad E^{0'} = -1.0 \text{ V } vs. \text{ SCE}$$
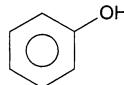
The half-life of B is 100 ms. Both charge-transfer reactions have large values of k^0. Draw the expected cyclic voltammograms for scans beginning at 0.0 V *vs.* SCE and reversing at −1.2 V. Show curves for rates of 50 mV/s, 1 V/s, and 20 V/s.

12.2 Draw a rough quantitative graph of collection efficiency *vs.* rotation rate for an RRDE at which the electrode reaction for the previous problem is carried out. Assume electrolysis occurs in the mass-transfer-limited region. The collection efficiency is 0.45 for Fe(II) $\rightleftharpoons$ Fe(III) + *e*.

12.3 The data below were recorded from a series of cyclic voltammetric experiments designed to elucidate the mechanism of the electrode reaction involving reduction of a certain compound. Formulate a mechanism to explain the behavior of the diagnostic functions, then briefly rationalize as many of the trends in the data as you can in terms of your mechanism. The switching potential was held constant at −1.400 V *vs.* SCE.

Scan rate, v V/s	$E_{p/2}$ (cathodic) V *vs.* SCE	$E_{p/2}$ (anodic) V *vs.* SCE	$\dfrac{i_p \text{ (anodic)}}{i_p \text{ (cathodic)}}$	$i_p \text{ (cathodic)}/v^{1/2}$ $\mu A\text{-s}^{1/2} \text{ V}^{-1/2}$
0.1	−1.253	−1.17	0.1	35
2.0	−1.260	−1.185	0.51	34.4
10	−1.265	−1.197	0.84	33.0
20	−1.270	−1.208	0.91	32.8
100	−1.271	−1.212	1.01	32.6
200	−1.270	−1.212	1.01	32.7

12.4 Consider a material A, which can be reduced at a DME to substance B. A 1 m*M* solution of A in acetonitrile shows a polarographic wave at −1.90 V *vs.* SCE. The wave has a slope of 60.5

mV at 25°C and it gives $(I_d)_{max} = 1.95$. When phenol is added to the system, the behavior changes:
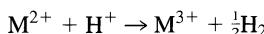
Phenol (C)

Rationalize the observations in the following table. Can you suggest the nature of A and B?
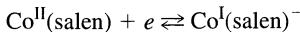
Concentration of C, M	$E_{1/2}$	Wave slope, mV	$(I_d)_{max}$
10^{-3}	-1.88	61.4	2.81
10^{-2}	-1.85	61.9	3.85
10^{-1}	-1.82	61.8	3.87

12.5 Cyclic voltammetry is often used to obtain information about standard potentials for correlative studies of molecular properties (e.g., ionization potentials, electron affinities, molecular orbital calculations, etc.). How is a standard potential extracted from data of this sort? Are assumptions involved? What kind of error would appear if the electrode process were EC? What if it involved slow electron transfer to a chemically stable product?

12.6 Derive the limiting values of $(\tau/\tau_d)^{1/2}$ for chronopotentiometry with a following catalytic reaction $(E_r C_i')$ for large and small λ values; see (12.3.36). What is the slope of the line of $(\tau/\tau_d)^{1/2}$ vs. $\lambda^{1/2}$ in the KP region of Figure 12.3.22?

12.7 Derive the equation for the E–t curve for chronopotentiometry with a following catalytic reaction $(E_r C_i')$. See (12.3.34) and (12.3.35). Show that as $k \to 0$, the E–t curve for a nernstian electrode reaction is approached. What is the limiting (KP) behavior as $\lambda \to \infty$? Plot a curve showing how $E_{\tau/4}$ varies with λ.

12.8 The limiting current, i_∞, in linear sweep voltammetry with an $E_r C_i'$ reaction scheme, (12.3.29), can be derived by noting that steady-state conditions apply, that is $[\partial C_O(x, t)/\partial t] = [\partial C_R(x, t)/\partial t] = 0$, and that $C_O(x, t) + C_R(x, t) = C_O^*$ (taking $D_O = D_R = D$). Carry out the derivation.

12.9 The controlled-potential reduction of a $0.01\ M\ M^{3+}$ solution in $1\ M$ HCl produces M^{2+}. When the electrolysis is carried out in a volume of $100\ cm^3$ at a 50-cm^2 electrode with $m = 10^{-2}\ cm/s$, it is noticed that the current decays to a steady-state value, 24.5 mA, significantly higher than the preelectrolysis residual current (500 μA) in $1\ M$ HCl at this potential. This effect is attributed to the reaction

$$M^{2+} + H^+ \to M^{3+} + \tfrac{1}{2}H_2$$
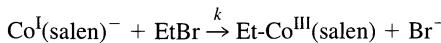
which regenerates M^{3+}. What is the pseudo-first-order rate constant for this reaction? What is the steady-state concentration of M^{2+} in solution during electrolysis?

12.10 G. Costa, A. Puxeddu, and E. Reisenhofer (*J. Chem. Soc. Dalton*, **1973**, 2034) studied the cyclic voltammetric reduction of the complex Co^{III} (salen) in DMF at a mercury electrode [where (salen) is the chelating ligand N,N'-ethylenebis(salicylideneiminate)]. In the absence of any additive, a 0.20 mM solution of the complex gives a typical reversible cyclic voltammogram corresponding to

$$Co^{II}(salen) + e \rightleftarrows Co^{I}(salen)^-$$

When ethyl bromide (EtBr) is added, the irreversible reaction below occurs:

$$Co^{I}(salen)^- + EtBr \xrightarrow{k} Et\text{-}Co^{III}(salen) + Br^-$$

where Et-Co^{III}(salen) is reduced at more negative potentials than Co^{II}(salen). To measure k, the ratio i_{pa}/i_{pc} was determined at concentrations of EtBr where the following reaction was pseudo-first-order, $k' = k[EtBr]$. When the time τ between $E_{1/2}$ and the switching potential E_λ was 32 ms, the i_{pa}/i_{pc} ratio was 0.7 at 0°C with 13.3 mM EtBr. Calculate k and k'.

12.11 Consider curve 1 in Figure 12.3.2, taken at $v = 10$ V/s. What is the approximate concentration of O at the start of the scan? Calculate i_p by assuming that the preceding reaction does not affect the behavior, and compare the result to the observed value of i_p.

12.12 The voltammograms in Figures 12.3.2 (CE), 12.3.10 (EC), and 12.3.17 (EC′) all involve nernstian electrode reactions with coupled chemical reactions. In each case, the total concentration of starting compound is 1 mM and $D = 10^{-5}$ cm^2/s. From the data in these figures, prepare a plot of i_{pc} vs. $v^{1/2}$ for each mechanism, and include the line for an uncomplicated nernstian electron transfer reaction (E_r). Justify the behavior in terms of the reactions occurring in each case.

13

DOUBLE-LAYER STRUCTURE AND ADSORPTION

In Chapter 1, we introduced some elementary ideas about the double layer, including notions about its capacitance and structure. In the remainder of the text to this point, we have made repeated references to its influence on electrode processes and electrochemical measurements. It is time now to delve into this aspect of electrochemical science in more detail. Here our goal is to examine the kinds of experimental measurements that can illuminate the structure of the double layer, as well as the important structural models and their implications for electrode kinetics.

13.1 THERMODYNAMICS OF THE DOUBLE LAYER

A great deal of our knowledge about the double layer comes from measurements of macroscopic, equilibrium properties, such as interfacial capacitance and surface tension. In general, we are interested in the way in which these properties change with potential and with the activities of various species in the electrolyte. The next section will deal with experimental aspects in some detail. For the moment, we will concentrate on the theory that we use to suggest and interpret experiments. Since our concern now is with macroscopic, equilibrium properties, we can expect a thermodynamic treatment to describe the system rigorously without a postulated model. This is an important aspect, because it implies that we can obtain data that any successful structural model must rationalize.

We begin by developing the *Gibbs adsorption isotherm*, which describes interfaces in general, and from that we obtain the *electrocapillary equation*, which describes the properties of electrochemical interfaces more particularly.

13.1.1 The Gibbs Adsorption Isotherm

Suppose we have an interface of surface area A separating two phases, α and β. A segment of the system is depicted in Figure 13.1.1. The region between the two solid lines is the interfacial zone, whose composition and properties concern us. To the right of BB′, there is pure phase β; and to the left of AA′, the system is purely α. Because intermolecular forces are exerted only over a short range, the interfacial zone is just a few hundred angstroms thick, and we can regard the interfacial perturbations on α and β as properties of a surface. The lines AA′ and BB′ can be defined anywhere, provided they contain all segments of the system that differ from the pure α and β phases as a result of the interfacial perturbation.
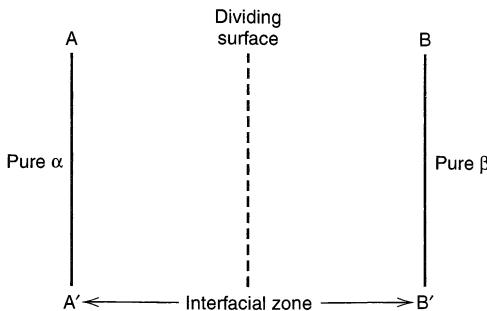
Figure 13.1.1 Schematic diagram of an interfacial region separating phases α and β.

Let us now compare the real interfacial zone with an imaginary *reference interfacial zone*. In the reference zone, we will define a *dividing surface*, which is shown as the dotted line in Figure 13.1.1. The position we choose for the dividing surface is arbitrary and has no impact on the final results (see Problem 13.1), but it is convenient to think of it as coinciding with the actual interfacial surface. In this reference system, we imagine that the pure, unperturbed phase α extends to the dividing surface from the left, while the pure phase β extends to it from the right.

The reason for defining the reference system is that the properties of the interface are governed by *excesses* and *deficiencies* in the concentrations of components; that is, we are concerned with *differences* between the quantities of various species in the actual interfacial region, with respect to the quantities we would expect if the existence of the interface did not perturb the pure phases, α and β. These differences are called *surface excess* quantities. For example, the surface excess in the number of moles of any species, such as potassium ions or electrons, would be

$$n_i^{\sigma} = n_i^{S} - n_i^{R} \tag{13.1.1}$$

where n_i^{σ}, is the excess quantity and n_i^{S} and n_i^{R} are the numbers of moles of species i in the interfacial region for the actual system and the reference system, respectively. Surface excess quantities can be defined for any extensive variable.

One of those variables is the electrochemical free energy, which can be considered profitably in a general way (1–4). For the reference system, the electrochemical free energy depends on the usual variables: temperature, pressure, and the molar quantities of all components. That is, $\overline{G}^{R} = \overline{G}^{R}(T, P, n_i^{R})$. The surface area has no impact on $\overline{G}^{R}$ because the interface does not perturb phases α and β. There is, therefore, no energy of interaction. On the other hand, we know from experience that real systems have a tendency to minimize or maximize the interfacial area; hence the free energy of the actual system, $\overline{G}^{S}$, must depend on the area. Thus, $\overline{G}^{S} = \overline{G}^{S}(T, P, A, n_i^{S})$.

The total differentials are

$$d\overline{G}^{R} = \left(\frac{\partial \overline{G}^{R}}{\partial T}\right) dT + \left(\frac{\partial \overline{G}^{R}}{\partial P}\right) dP + \sum_i \left(\frac{\partial \overline{G}^{R}}{\partial n_i^{R}}\right) dn_i^{R} \tag{13.1.2}$$

$$d\overline{G}^{S} = \left(\frac{\partial \overline{G}^{S}}{\partial T}\right) dT + \left(\frac{\partial \overline{G}^{S}}{\partial P}\right) dP + \left(\frac{\partial \overline{G}^{S}}{\partial A}\right) dA + \sum_i \left(\frac{\partial \overline{G}^{S}}{\partial n_i^{S}}\right) dn_i^{S} \tag{13.1.3}$$

We consider experiments only at constant temperature and pressure; hence the first two terms in each expression can be dropped. The partial derivatives $(\partial \overline{G}^{R}/\partial n_i^{R})$ are the electrochemical potentials $\overline{\mu}_i$, which we encountered earlier in Section 2.2.4. Since equilibrium applies, this potential is constant throughout the system for any given species.

Since it is the same in the interfacial zone as in the pure phases, α and β, it must also be true that

$$\overline{\mu}_i = \left(\frac{\partial \overline{G}^R}{\partial n_i^R}\right) = \left(\frac{\partial \overline{G}^S}{\partial n_i^S}\right) \tag{13.1.4}$$

We can also give a name to the partial derivative $(\partial \overline{G}^S / \partial A)$. It is the *surface tension* γ. The surface tension is a measure of the energy required to produce a unit area of new surface, for example, by dividing the system more finely. Doing this requires that atoms or molecules previously in the bulk of their phases be brought to the new interface. They have fewer binding interactions with neighbors in their original phase, but may have new ones with neighbors in the opposite phase. Thus, the surface tension depends on the chemical identity of both α and β.

Now we can write the differential *excess free energy* as

$$d\overline{G}^\sigma = d\overline{G}^S - d\overline{G}^R = \gamma dA + \sum_i \overline{\mu}_i \, d(n_i^S - n_i^R) \tag{13.1.5}$$

and from (13.1.1) we have

$$d\overline{G}^\sigma = \gamma \, dA + \sum_i \overline{\mu}_i \, dn_i^\sigma \tag{13.1.6}$$

This equation tells us that the interfacial free energy can be described (under our conditions of constant temperature and pressure) by the variables A and n_i, all of which are extensive. This feature allows us to invoke Euler's theorem,[1] which yields

$$\overline{G}^\sigma = \left(\frac{\partial \overline{G}^\sigma}{\partial A}\right) A + \sum_i \left(\frac{\partial \overline{G}^\sigma}{\partial n_i^\sigma}\right) n_i^\sigma \tag{13.1.7}$$

$$\overline{G}^\sigma = \gamma A + \sum_i \overline{\mu}_i n_i^\sigma \tag{13.1.8}$$

Let us find the total differential, $d\overline{G}^\sigma$, from this expression.

$$d\overline{G}^\sigma = \gamma \, dA + \sum_i \overline{\mu}_i \, dn_i^\sigma + A \, d\gamma + \sum_i n_i^\sigma \, d\overline{\mu}_i \tag{13.1.9}$$

Clearly (13.1.6) and (13.1.9) must be equivalent; hence the last two terms in (13.1.9) must sum to zero:

$$A \, d\gamma + \sum_i n_i^\sigma \, d\overline{\mu}_i = 0 \tag{13.1.10}$$

In general, it is more convenient to speak of excesses per unit area of surface; therefore, we now introduce the *surface excess concentration*, $\Gamma_i = n_i^\sigma / A$. Then (13.1.10) is reexpressed as

$$\boxed{-d\gamma = \sum_i \Gamma_i \, d\overline{\mu}_i} \tag{13.1.11}$$

which is the *Gibbs adsorption isotherm*. It already hints that measurements of surface tension will play an important role in elucidating interfacial structure, but to see the experimental ramifications we need to specialize it to an electrochemical situation. That is our next job.

---

[1]We say that $\overline{G}$ is an *extensive function* of the *extensive variables* A and n_i. By this, we mean that the electrochemical free energy depends linearly on the physical extent of the system. If we double the size of the system by doubling A and all the n_i, then $\overline{G}$ doubles. Mathematically, such behavior implies that $\overline{G}(A, n_i)$ is a *linear homogeneous function* of A and n_i. The *Euler theorem* (5) applies generally to homogeneous functions and, for linear ones, it allows us to define the function itself in terms of derivatives and variables as in (13.1.7).

13.1.2 The Electrocapillary Equation

Let us now consider a specific chemical system in which a mercury surface contacts an aqueous KCl solution. The potential of the mercury is controlled with respect to a reference electrode having no liquid junction with the test solution. Suppose also that the aqueous phase contains a neutral species, M, that might be interfacially active. For example, the cell could be

$$Cu'/Ag/AgCl/K^+, Cl^-, M/Hg/Ni/Cu \qquad (13.1.12)$$

We will focus on the interface between the mercury electrode and the aqueous solution.

In writing the Gibbs adsorption isotherm for this case, it is useful to group terms relating separately to components of the mercury electrode, ionic components of the solution, and neutral components of the solution. Since excesses of charge can exist on the electrode surface, we need to consider a surface excess of electrons on the mercury. It could be either positive or negative. Thus

$$\begin{aligned} -d\gamma = &(\Gamma_{Hg}\, d\bar{\mu}_{Hg} + \Gamma_e\, d\bar{\mu}_e^{Hg}) \\ &+ (\Gamma_{K^+}\, d\bar{\mu}_{K^+} + \Gamma_{Cl^-}\, d\bar{\mu}_{Cl^-}) \\ &+ (\Gamma_M\, d\bar{\mu}_M + \Gamma_{H_2O}\, d\bar{\mu}_{H_2O}) \end{aligned} \qquad (13.1.13)$$

where $\bar{\mu}_e^{Hg}$ refers to electrons in the mercury phase.

There are some important linkages between electrochemical potentials:

$$\bar{\mu}_e^{Hg} = \bar{\mu}_e^{Cu} \qquad (13.1.14)$$

$$\bar{\mu}_{KCl} = \mu_{KCl} = \bar{\mu}_{K^+} + \bar{\mu}_{Cl^-} \qquad (13.1.15)$$

Moreover,

$$\bar{\mu}_{H_2O} = \mu_{H_2O} \qquad (13.1.16)$$

$$\bar{\mu}_M = \mu_M \qquad (13.1.17)$$

By further recognizing that $d\bar{\mu}_{Hg} = d\bar{\mu}_{Hg}^0 = 0$, we can reexpress (13.1.13) as

$$-d\gamma = \Gamma_e\, d\bar{\mu}_e^{Cu} + [\Gamma_{K^+}\, d\bar{\mu}_{KCl} - \Gamma_{K^+}\, d\bar{\mu}_{Cl^-} + \Gamma_{Cl^-}\, d\bar{\mu}_{Cl^-}] + [\Gamma_M\, d\mu_M + \Gamma_{H_2O}\, d\mu_{H_2O}] \qquad (13.1.18)$$

Now we consider the important fact that our reference electrode responds to one of the components of the aqueous phase. From the equilibrium at the reference interface, we have

$$\bar{\mu}_{AgCl} + \bar{\mu}_e^{Cu'} = \bar{\mu}_{Ag} + \bar{\mu}_{Cl^-} \qquad (13.1.19)$$

Since $d\bar{\mu}_{AgCl} = d\bar{\mu}_{Ag} = 0$,

$$d\bar{\mu}_e^{Cu'} = d\bar{\mu}_{Cl^-} \qquad (13.1.20)$$

Substituting (13.1.20) into (13.1.18) and regrouping terms, we obtain

$$-d\gamma = \Gamma_e\, d\bar{\mu}_e^{Cu} - [\Gamma_{K^+} - \Gamma_{Cl^-}]\, d\bar{\mu}_e^{Cu'} + \Gamma_{K^+}\, d\mu_{KCl} + \Gamma_M\, d\mu_M + \Gamma_{H_2O}\, d\mu_{H_2O} \qquad (13.1.21)$$

The excess charge density on the metallic side of the interface is

$$\sigma^M = -F\Gamma_e \qquad (13.1.22)$$

An equal, but opposite charge density resides on the solution side:

$$\sigma^S = -\sigma^M = F(\Gamma_{K^+} - \Gamma_{Cl^-}) \qquad (13.1.23)$$

In addition,

$$d\overline{\mu}_e^{Cu} - d\overline{\mu}_e^{Cu'} = -Fd(\phi^{Cu} - \phi^{Cu'}) = -FdE_- \tag{13.1.24}$$

where E_- is the potential of the mercury electrode with respect to the reference. We follow convention in attaching a negative subscript to signify that the reference electrode responds to an anionic component of our system. Invoking (13.1.22)–(13.1.24) converts (13.1.21) into

$$-d\gamma = \sigma^M \, dE_- + \Gamma_{K^+} \, d\mu_{KCl} + \Gamma_M \, d\mu_M + \Gamma_{H_2O} \, d\mu_{H_2O} \tag{13.1.25}$$

Now we must recognize that all of the parameters in this equation are not independent. We cannot change the chemical potentials of KCl, M, and H_2O separately (e.g., by changing the concentrations). If one of them changes, it affects the others. A consequence of this fact is that Γ_{K^+}, Γ_M, and Γ_{H_2O} are not independently measurable. Can we convert (13.1.25) into an expression of measurable and independently controllable quantities?

We can, by recognizing the Gibbs–Duhem relation for the aqueous phase. It says that for any phase at constant T and P (5),

$$\sum_i X_i \, d\mu_i = 0 \tag{13.1.26}$$

where i ranges over all components and the X_i are mole fractions. For our aqueous phase,

$$X_{H_2O} \, d\mu_{H_2O} + X_{KCl} \, d\mu_{KCl} + X_M \, d\mu_M = 0 \tag{13.1.27}$$

Between (13.1.25) and (13.1.27), we can eliminate $d\mu_{H_2O}$ to give

$$-d\gamma = \sigma^M \, dE_- + \left[\Gamma_{K^+} - \frac{X_{KCl}}{X_{H_2O}} \Gamma_{H_2O}\right] d\mu_{KCl} + \left[\Gamma_M - \frac{X_M}{X_{H_2O}} \Gamma_{H_2O}\right] d\mu_M \tag{13.1.28}$$

The bracketed quantities are measurable parameters called *relative surface excesses*. They are symbolized separately as

$$\boxed{\Gamma_{K^+(H_2O)} = \Gamma_{K^+} - \frac{X_{KCl}}{X_{H_2O}} \Gamma_{H_2O}} \tag{13.1.29}$$

$$\boxed{\Gamma_{M(H_2O)} = \Gamma_M - \frac{X_M}{X_{H_2O}} \Gamma_{H_2O}} \tag{13.1.30}$$

Thus we now learn that we cannot measure the absolute surface excess of K^+, but only its excess relative to water. For example, a zero relative excess does not imply a lack of adsorption of K^+, but only that K^+ and H_2O are adsorbed to the same degree. That is, K^+ and H_2O are adsorbed in the same mole ratio that they have in the bulk electrolyte. A positive relative excess means that K^+ is adsorbed to a greater degree than water, not in absolute molar quantities, but with respect to the amounts available in the bulk electrolyte.

Water is taken here as the *reference component*. It is advantageous to select the solvent S in any electrolyte as the reference component, because one then does not have to be concerned with its activity. Also, one can sometimes argue that the quantities $(X_i/X_S)\Gamma_S$ are negligibly small, so that measured relative surface excesses can be regarded as absolute surface excesses. This assumption is not rigorous, of course, but may be sound from a practical viewpoint in many experimental situations involving dilute solutions.

These considerations bring us to the final statement of the *electrocapillary equation* for our experimental system (1–4):

$$\boxed{-d\gamma = \sigma^M \, dE_- + \Gamma_{K^+(H_2O)} \, d\mu_{KCl} + \Gamma_{M(H_2O)} \, d\mu_M} \tag{13.1.31}$$

Other systems would have similar equations involving terms for other components. More general statements of the electrocapillary equation are available in the specialized literature (4).

Equation 13.1.31 is a relation involving experimentally significant quantities; that is, every quantity is either controllable or measurable. It is our key to an experimental attack on double-layer structure.

▶ 13.2 EXPERIMENTAL EVALUATION OF SURFACE EXCESSES AND ELECTRICAL PARAMETERS

13.2.1 Electrocapillarity and the DME

It is not obvious why (13.1.31) is called an electrocapillary equation. The name is a historic artifact derived from the early application of this equation to the interpretation of measurements of surface tension at mercury–electrolyte interfaces (1–4, 6–8). The earliest measurements of this sort were carried out by Lippmann, who invented a device called a capillary electrometer for the purpose (9). Its principle involves null balance. The downward pressure created by a mercury column is controlled so that the mercury–solution interface, which is confined to a capillary, does not move. In this balanced condition, the upward force exerted by the surface tension exactly equals the downward mechanical force. Because the method relies on null detection, it is capable of great precision. Elaborated approaches are still used. These instruments yield *electrocapillary curves*, which are simply plots of surface tension versus potential.

A more familiar device for achieving the same end is the DME, which actually was invented by Heyrovský (10) for the measurement of surface tension. Of course, its utility eventually far surpassed its original purpose (see Chapter 7). Figure 7.1.1 is a diagram of a typical device.

The weight of the drop at the end of its life is gmt_{max} where m is the mass flow rate of mercury issuing from the capillary, g is the gravitational acceleration, and t_{max} is the lifetime of the drop. This force is counterbalanced by the surface tension γ acting around the circumference of the capillary, whose radius is r_c; thus

$$t_{max} = \frac{2\pi r_c}{mg} \gamma \tag{13.2.1}$$

One can easily see that the drop time t_{max} is directly proportional to γ; hence a plot of t_{max} vs. potential has the same shape as the true electrocapillary curve. The ordinate is simply multiplied by a constant factor, which can be separately taken into account. Sometimes these plots of drop time are also called electrocapillary curves.

It is difficult to overstate the importance of these devices to our current understanding of interfacial structure. We have already seen that the thermodynamic relations bearing on the issue emphasize surface tension. Since good measurements of surface tension are made far more conveniently at liquid–metal electrodes, work with mercury and amalgams dominated research in this area for decades. Mercury offers other advantages too. It has a large hydrogen overpotential; hence there is a wide potential range for which only nonfaradaic processes are significant. It is a liquid; therefore, surface features such as grain boundaries do not enter the picture. At the DME, a fresh surface is exposed every few seconds, so that problems with progressive contamination of the working surface are minimized. These advantages also extend to the use of mercury surfaces for faradaic electrochemistry, but they are overwhelmingly favorable for probing interfacial structure. Let us now see how electrocapillary curves can reveal part of that structure.

13.2.2 Excess Charge and Capacitance

Again, we take up the specific chemical system discussed in Section 13.1.2. From its electrocapillary equation, (13.1.31), it is clear that

$$\sigma^M = -\left(\frac{\partial \gamma}{\partial E_-}\right)_{\mu_{KCl}, \mu_M} \tag{13.2.2}$$

hence the excess charge on the electrode is the slope of the electrocapillary curve at any potential (1–4, 6–8). Figure 13.2.1 is a plot of the drop time of a DME in 0.1 M KCl $vs.$ potential. It has the nearly parabolic shape that is usually characteristic of these curves, although there are significant variations in the curves as the electrolyte is changed (Figure 13.2.2).

A feature common to all of the curves is the existence of a maximum in surface tension. The potential at which it occurs is the *electrocapillary maximum* (ECM) and is an extremely important point in the system. Since the slope of the curve is zero there, it is the *potential of zero charge* (PZC), where $\sigma^M = \sigma^S = 0$.

At more negative potentials, the electrode surface has a negative excess charge, and at more positive potentials there is a positive surface charge. The units of electronic charge composing any excess repel each other; hence they counteract the usual tendency of the surface to contract, and they weaken the surface tension. Plots of surface charge can be made by differentiating electrocapillary curves. Some examples are shown in Figure 13.2.3.

The capacitance of the interface characterizes its ability to store charge in response to a perturbation in potential. One definition is based on the small change in charge density resulting from a small alteration in potential:

$$C_d = \left(\frac{\partial \sigma^M}{\partial E}\right) \tag{13.2.3}$$

This *differential capacitance* is obviously the slope of the plot of σ^M $vs.$ E at any point. Figure 13.2.4 helps to clarify the definition. One can see there and in Figure 13.2.3 that C_d is not constant with potential, as it is for an ideal capacitor.
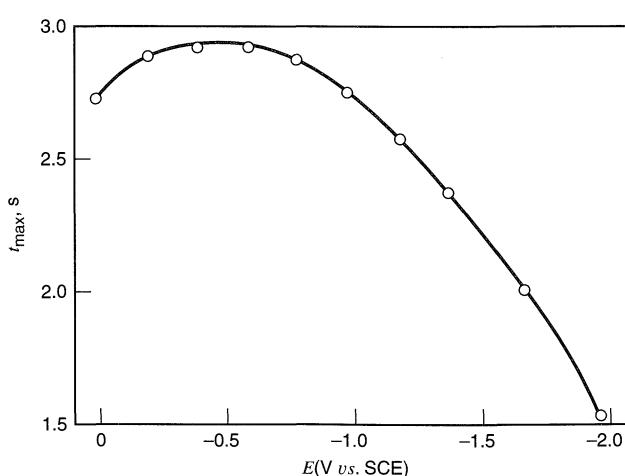
Figure 13.2.1
Electrocapillary curve of drop time $vs.$ potential at a DME in 0.1 M KCl. [Data of L. Meites, $J.\ Am.\ Chem.\ Soc.,$ **73**, 2035 (1951).]
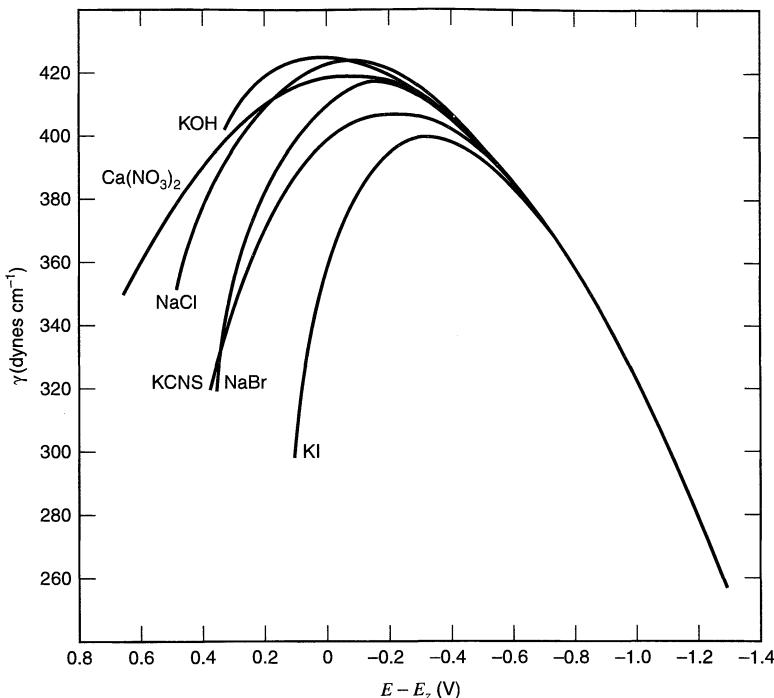
Figure 13.2.2   Electrocapillary curves of surface tension *vs.* potential for mercury in contact with solutions of the indicated electrolytes at 18°C. The potential is plotted with respect to the PZC for NaF. [Reprinted with permission from D. C. Grahame, *Chem. Rev.*, **41**, 441 (1947). Copyright 1947, American Chemical Society.]

The variation in C_d with E causes us to define an *integral capacitance*, C_i (sometimes denoted K), which is the ratio of the total charge density, σ^M, at potential E to the total potential difference placing it there. That is,

$$C_i = \frac{\sigma^M}{(E - E_z)}$$ (13.2.4)

where E_z is the PZC. Figure 13.2.4 contains a graphical interpretation of C_i. It is related to C_d by the equation

$$C_i = \frac{\int_{E_z}^{E} C_d \, dE}{\int_{E_z}^{E} dE}$$ (13.2.5)

hence it is an average of C_d over the potential range from E_z to E.

The differential capacitance is the more useful quantity, in part because it is precisely measurable by impedance techniques (see Chapter 10). As we will see in Section 13.3, capacitance measurements have played crucial roles in the formulation of structural models for the double layer.

We can now understand that these measurements are largely equivalent to electrocapillary information. The capacitances can be obtained from the electrocapillary curves by double differentiation, whereas the electrocapillary curves can be constructed from differential capacitances by double integration (11, 12):

$$\gamma = \int\int_{E_z}^{E} C_d \, dE$$ (13.2.6)
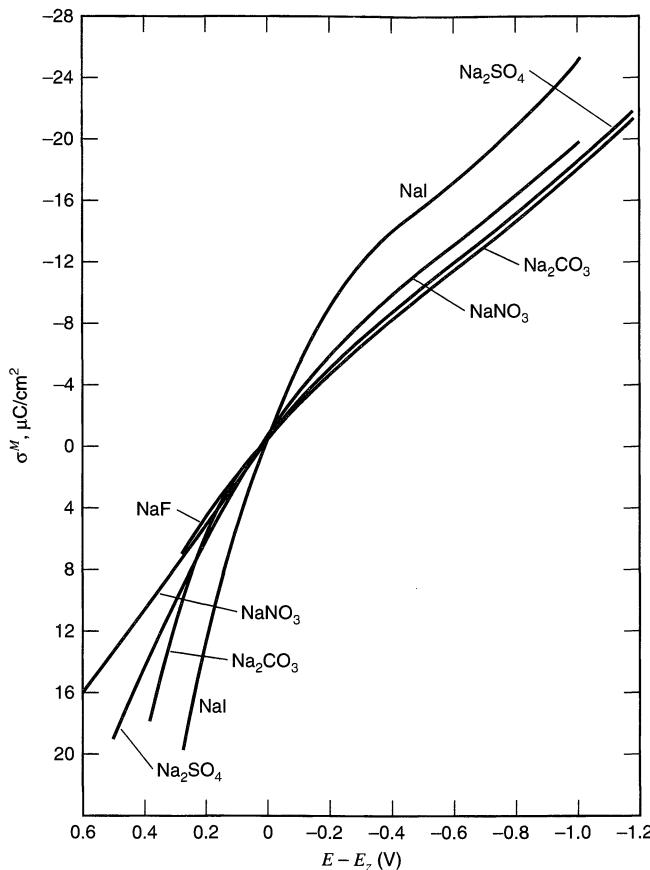
Figure 13.2.3 Charge density on the electrode *vs.* potential for mercury immersed in 1 *M* solutions of the indicated electrolytes at 25°C. The potentials are plotted with respect to the PZC for each electrolyte. [Reprinted with permission from D. C. Grahame, *Chem. Rev.*, **41**, 441 (1947). Copyright 1947, American Chemical Society.]

The latter procedure requires separate knowledge of the PZC. Capacitances may be more generally useful primary data because the generation of σ^M *vs.* E and γ *vs.* E from them involves integration, which averages out random experimental variations. In contrast, differentiation of surface tension accentuates them. In addition, capacitance measurements can be made straightforwardly at solid electrodes, where γ is much less accessible.
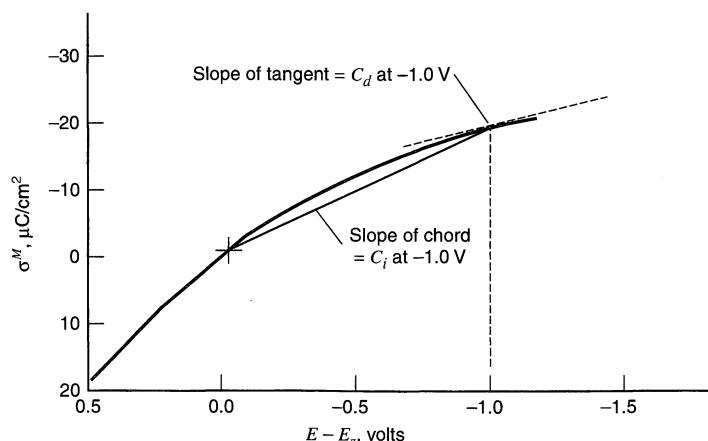
Figure 13.2.4 Schematic plot of charge density *vs.* potential illustrating the definitions of the integral and differential capacitances.

13.2.3 Relative Surface Excesses

Returning now to the electrocapillary equation, (13.1.31), we find that the relative surface excess of potassium ion at the interface considered there is given by (1–4, 6–8)

$$\Gamma_{K^+(H_2O)} = -\left(\frac{\partial \gamma}{\partial \mu_{KCl}}\right)_{E_-,\mu_M} \tag{13.2.7}$$

Since

$$\mu_{KCl} = \mu_{KCl}^0 + RT \ln a_{KCl} \tag{13.2.8}$$

we have

$$\boxed{\Gamma_{K^+(H_2O)} = \frac{-1}{RT}\left(\frac{\partial \gamma}{\partial \ln a_{KCl}}\right)_{E_-,\mu_M}} \tag{13.2.9}$$

This relation implies that we can evaluate $\Gamma_{K^+(H_2O)}$ at any potential E_- by measuring the surface tension for several KCl activities, while we hold the activity of M constant. The relative surface excess of chloride can then be evaluated from the charge balance in (13.1.23).

A relation analogous to (13.2.9) can be readily derived for the neutral species M; hence its relative surface excess can be evaluated by the effect of its activity on γ.

Figure 13.2.5 is a graph of the relative surface excesses for the components of a 0.1 M KF solution in contact with mercury. Note that at potentials positive of E_z the surface excess of F^- is positive and that of K^+ is negative. This negative surface excess of K^+ simply implies that the concentration of K^+ in the vicinity of the mercury/solution interface is smaller than that in the bulk solution. The opposite condition holds for potentials negative of E_z. The behavior of KF solutions thus conforms to what we would expect based on simple electrostatics. We can contrast this behavior with that of a 0.1 M KBr solution shown in Figure 13.2.6. Note here that at potentials positive of E_z (i.e., for $\sigma^M > 0$), Γ_{K^+} is positive. The reason for this interesting behav-
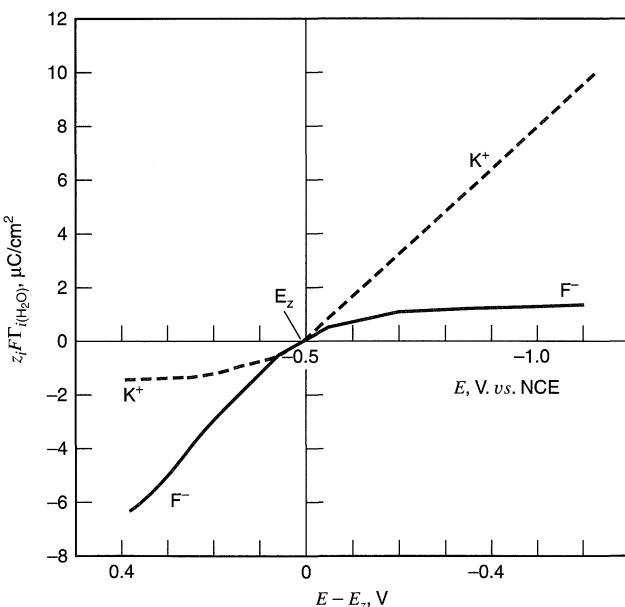
Figure 13.2.5 Surface excesses *vs.* potential for mercury in 0.1 M KF. Potentials are referenced both to a NCE and the potential of zero charge, E_z. [From data in D. C. Grahame and B. A. Soderberg, *J. Chem. Phys.*, **22**, 449 (1954).]
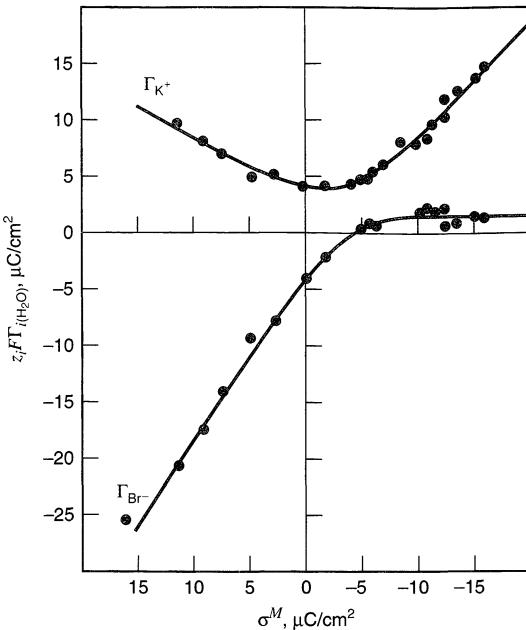
Figure 13.2.6 Surface excesses *vs.* charge density on the electrode for mercury in 0.1 *M* KBr. [Reprinted with permission from M. A. V. Devanathan and S. G. Canagaratna, *Electrochim. Acta*, **8**, 77 (1963). Copyright 1963, Pergamon Press PLC.]

ior is connected with specific adsorption of Br⁻ on mercury. We will discuss this in Section 13.3.4.

▶ 13.3 MODELS FOR DOUBLE-LAYER STRUCTURE

Now that we have seen how some of the basic facts about charge and molar excesses can be obtained for an interface, we would like to develop a picture of the way in which the excesses are arrayed. However, we cannot gain a structural view from purely thermodynamic quantities. Our recourse is to postulate a model, predict its properties, and compare them to the known facts of real systems. If significant differences are found, the model must be revised and tested again. Here we will consider several models that have been proposed for interfacial structure (2–4, 6–8, 13–19).

13.3.1 The Helmholtz Model

Since the metallic electrode is a good conductor, it supports no electric fields within itself at equilibrium. In Chapter 2, we saw that this fact implies that any excess charge on a metallic phase resides strictly at the surface. Helmholtz, who was the first to think consequentially about charge separation at interfaces, proposed that the counter-charge in solution also resides at the surface. Thus there would be two sheets of charge, having opposite polarity, separated by a distance of molecular order. In fact, the name *double layer* arises from Helmholtz's early writings in this area (20–22).

Such a structure is equivalent to a parallel-plate capacitor, which has the following relation between the stored charge density, σ, and the voltage drop, V, between the plates (23):

$$\sigma = \frac{\varepsilon\varepsilon_0}{d}V \qquad (13.3.1)$$
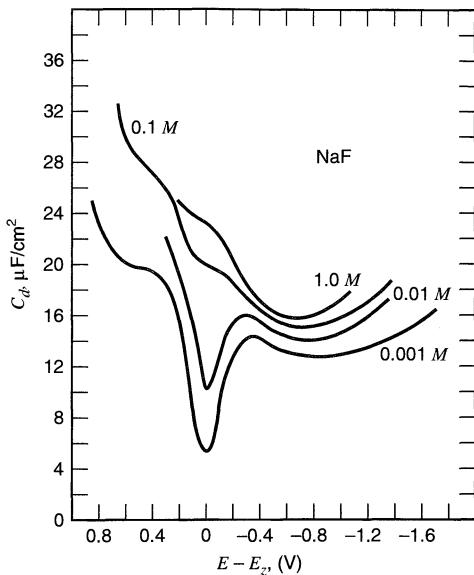
Figure 13.3.1 Differential capacitance *vs.* potential for NaF solutions in contact with mercury at 25°C. [Reprinted with permission from D. C. Grahame, *Chem. Rev.*, **41**, 441 (1947). Copyright 1947, American Chemical Society.]

where ε is the dielectric constant of the medium, ε_0 is the permittivity of free space, and d is the interplate spacing.[2] The differential capacitance is therefore

$$\frac{\partial \sigma}{\partial V} = C_d = \frac{\varepsilon \varepsilon_0}{d} \tag{13.3.2}$$

The weakness of this model is immediately apparent in (13.3.2), which predicts that C_d is a constant. We know from our earlier discussion that it is not a constant in real systems. Figure 13.3.1 is a dramatic illustration for interfaces between mercury and sodium fluoride solutions of various concentrations. Variations in C_d with potential and concentration suggest that either ε or d depends on these variables; hence a more sophisticated model is clearly in order.

---

[2]Here and elsewhere in this book we use the electrical relations appropriate to SI units, which lead to the following definition of Coulomb's law (24):

$$F = \frac{qq'}{4\pi\varepsilon\varepsilon_0 r^2}$$

The force F (in newtons) between two charges q and q' (in coulombs) is therefore related to the distance of charge separation r (in meters), the dielectric constant of the medium ε (dimensionless) and the *permittivity of free space* ε_0. The last parameter is a measured constant equal to $8.85419 \times 10^{-12}\,\mathrm{C^2N^{-1}m^{-2}}$. This system has the advantage that the electrical variables are measured in common units. An alternative is the electrostatic system, where Coulomb's law is

$$F = \frac{qq'}{\varepsilon r^2}$$

The force F (in dynes) is related here to the charges (in statcoulombs) by the dielectric constant ε and the separation distance (in cm). Equations for the electrostatic system can be converted to corresponding relations for SI units by replacing ε with $4\pi\varepsilon\varepsilon_0$, and vice versa. Many treatments of interfacial structure involve electrostatic units. They are recognizable by the absence of ε_0 and the *appearance* of multiples of 4π in the results. In some treatments, $\varepsilon\varepsilon_0$ is denoted as a single quantity, usually ε, called the *permittivity* of the medium.

13.3.2 The Gouy–Chapman Theory

Even though the charge on the electrode is confined to the surface, the same is not necessarily true of the solution. Particularly at low concentrations of electrolyte, one has a phase with a relatively low density of charge carriers. It may take some significant thickness of solution to accumulate the excess charge needed to counterbalance σ^M. A finite thickness would arise essentially because there is an interplay between the tendency of the charge on the metallic phase to attract or repel the carriers according to polarity and the tendency of thermal processes to randomize them.

This model therefore involves a *diffuse layer* of charge in the solution like that described earlier in Section 1.2.3 (2–4, 6–8, 15, 16). The greatest concentration of excess charge would be adjacent to the electrode, where electrostatic forces are most able to overcome the thermal processes, while progressively lesser concentrations would be found at greater distances as those forces become weaker. Thus, an average distance of charge separation replaces d in the capacitance expression (13.3.2). Also, we can expect that average distance to show dependences on potential and electrolyte concentration. As the electrode becomes more highly charged, the diffuse layer should become more compact and C_d should rise. As the electrolyte concentration rises, there should be a similar compression of the diffuse layer and a consequent rise in capacitance. Note that these qualitative trends are actually seen in the data of Figure 13.3.1.

Gouy and Chapman independently proposed the idea of a diffuse layer and offered a statistical mechanical approach to its description (25–27). We outline the attack here.

Let us start by thinking of the solution as being subdivided into laminae, parallel to the electrode and of thickness dx, as shown in Figure 13.3.2. All of these laminae are in thermal equilibrium with each other. However, the ions of any species i are not at the same energy in the various laminae, because the electrostatic potential ϕ varies. The laminae can be regarded as energy states with equivalent degeneracies; hence the number concentrations of species in two laminae have a ratio determined by a Boltzmann factor. If we take a reference lamina far from the electrode, where every ion is at its bulk concentration n_i^0, then the population in any other lamina is

$$n_i = n_i^0 \exp\left(\frac{-z_i e\phi}{\pmb{k}T}\right) \tag{13.3.3}$$

where ϕ is measured with respect to the bulk solution. The other quantities in (13.3.3) are the charge on the electron, e, the Boltzmann constant, $\pmb{k}$, the absolute temperature, T, and the (signed) charge, z_i, on ion i.
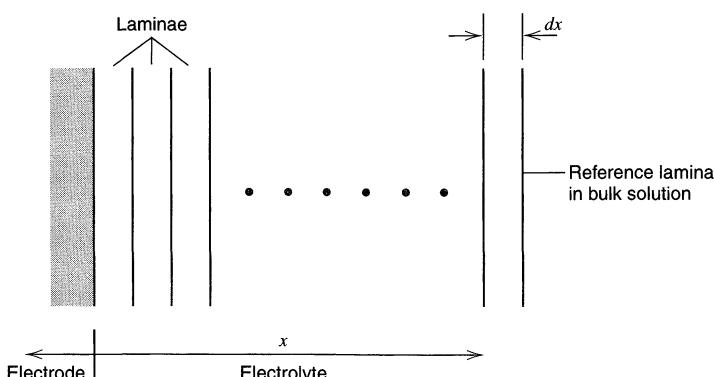
Figure 13.3.2 View of the solution near the electrode surface as a series of laminae.

The total charge per unit volume in any lamina is then

$$\rho(x) = \sum_i n_i z_i e$$

$$= \sum_i n_i^0 z_i e \, \exp\left(\frac{-z_i e \phi}{kT}\right)$$

(13.3.4)

where i runs over all ionic species. From electrostatics, we know that $\rho(x)$ is related to the potential at distance x by the Poisson equation (28):

$$\rho(x) = -\varepsilon\varepsilon_0 \frac{d^2\phi}{dx^2}$$

(13.3.5)

hence (13.3.4) and (13.3.5) can be combined to yield the *Poisson–Boltzmann equation*, which describes our system:

$$\frac{d^2\phi}{dx^2} = -\frac{e}{\varepsilon\varepsilon_0} \sum_i n_i^0 z_i \, \exp\left(\frac{-z_i e \phi}{kT}\right)$$

(13.3.6)

Equation 13.3.6 is treated by noting that

$$\frac{d^2\phi}{dx^2} = \frac{1}{2} \frac{d}{d\phi}\left(\frac{d\phi}{dx}\right)^2$$

(13.3.7)

hence,

$$d\left(\frac{d\phi}{dx}\right)^2 = -\frac{2e}{\varepsilon\varepsilon_0} \sum_i n_i^0 z_i \, \exp\left(\frac{-z_i e \phi}{kT}\right) d\phi$$

(13.3.8)

Integration gives

$$\left(\frac{d\phi}{dx}\right)^2 = \frac{2kT}{\varepsilon\varepsilon_0} \sum_i n_i^0 \, \exp\left(\frac{-z_i e \phi}{kT}\right) + \text{constant}$$

(13.3.9)

and the constant is evaluated by recognizing that at distances far from the electrode $\phi = 0$ and $(d\phi/dx) = 0$. Thus,

$$\left(\frac{d\phi}{dx}\right)^2 = \frac{2kT}{\varepsilon\varepsilon_0} \sum_i n_i^0 \left[\exp\left(\frac{-z_i e \phi}{kT}\right) - 1 \right]$$

(13.3.10)

Now it is useful to specialize the model to a system containing only a symmetrical electrolyte.[3] Applying this limitation yields

$$\frac{d\phi}{dx} = -\left(\frac{8kTn^0}{\varepsilon\varepsilon_0}\right)^{1/2} \sinh\left(\frac{ze\phi}{2kT}\right)$$

(13.3.11)

The details of the transformation from (13.3.10) to (13.3.11) are left to Problem 13.2. In (13.3.11), n^0 is the number concentration of each ion in the bulk, and z is the *magnitude* of the charge on the ions.

(a) The Potential Profile in the Diffuse Layer
Equation (13.3.11) can be rearranged and integrated in the following manner:

$$\int_{\phi_0}^{\phi} \frac{d\phi}{\sinh(ze\phi/2kT)} = -\left(\frac{8kTn^0}{\varepsilon\varepsilon_0}\right)^{1/2} \int_0^x dx$$

(13.3.12)

---

[3]That is, an electrolyte having only one cationic species and one anionic species, both with charge magnitude z. Sometimes symmetrical electrolytes, for example, NaCl, HCl, and $CaSO_4$, are called "$z:z$ electroytes."

where ϕ_0 is the potential at $x = 0$ relative to the bulk solution. In other words, ϕ_0 is the potential drop across the diffuse layer. The result is

$$\frac{2kT}{ze}\ln\left[\frac{\tanh(ze\phi/4kT)}{\tanh(ze\phi_0/4kT)}\right] = -\left(\frac{8kTn^0}{\varepsilon\varepsilon_0}\right)^{1/2} x \tag{13.3.13}$$

or,

$$\frac{\tanh(ze\phi/4kT)}{\tanh(ze\phi_0/4kT)} = e^{-\kappa x} \tag{13.3.14}$$

where

$$\kappa = \left(\frac{2n^0 z^2 e^2}{\varepsilon\varepsilon_0 kT}\right)^{1/2} \tag{13.3.15a}$$

For dilute aqueous solutions ($\varepsilon = 78.49$) at 25°C, this equation can be expressed as

$$\kappa = (3.29 \times 10^7)zC*^{1/2} \tag{13.3.15b}$$

where $C*$ is the bulk $z:z$ electrolyte concentration in mol/L and κ is given in cm^{-1}.

Equation 13.3.14 describes the potential profile in the diffuse layer in a general way, and in Figure 13.3.3 there are calculated profiles for several different values of ϕ_0. The potential always decays away from the surface. At large ϕ_0 (a highly charged electrode), the drop is precipitous, because the diffuse layer is relatively compact. As ϕ_0 becomes smaller, the decline is more gradual.

In fact, the form is exponential in the limit of small ϕ_0. If ϕ_0 is sufficiently low that $(ze\phi_0/4kT) < 0.5$, then $\tanh(ze\phi/4kT) \approx ze\phi/4kT$ everywhere, and

$$\phi = \phi_0 e^{-\kappa x} \tag{13.3.16}$$

This relation is a good approximation for $\phi_0 \leq 50/z$ mV at 25°C.
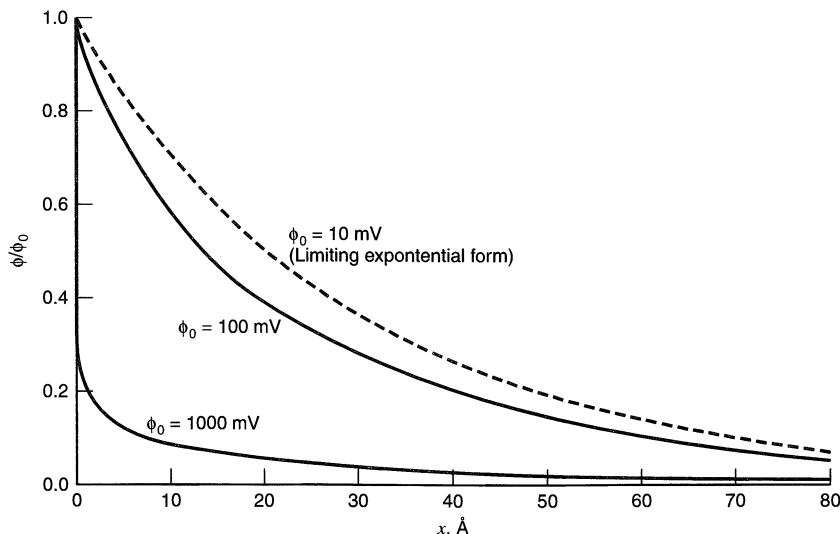
Figure 13.3.3 Potential profiles through the diffuse layer in the Gouy–Chapman model. Calculated for a 10^{-2} M aqueous solution of a $1:1$ electrolyte at 25°C. $1/\kappa = 30.4$ Å. See equations 13.3.14 to 13.3.16.

TABLE 13.3.1 Characteristic Thickness of the Diffuse Layer[a]

$C^*(M)$[b]	$1/\kappa(\text{Å})$
1	3.0
10^{-1}	9.6
10^{-2}	30.4
10^{-3}	96.2
10^{-4}	304

[a]For a 1:1 electrolyte at 25°C in water.
[b]$C^* = n^0/N_A$ where N_A is Avogadro's number.

Note that the reciprocal of κ has units of distance and characterizes the spatial decay of potential. It can be regarded as a kind of characteristic thickness of the diffuse layer. Table 13.3.1 provides values $1/\kappa$ for several concentrations of a 1:1 electrolyte. The diffuse layer is clearly quite thin by comparison to the distance scale encountered in typical diffusion layers for faradaic experiments. It becomes thicker as the concentration of electrolyte falls, as we anticipated in the qualitative discussion above.

(b) The Relation Between σ^M and ϕ_0

Suppose we now imagine a Gaussian surface in the shape of a box placed in our system as shown in Figure 13.3.4. One end is at the interface. The sides are perpendicular to this end and extend far enough into the solution that the field strength $d\phi/dx$ is essentially zero. The box therefore contains all of the charge in the diffuse layer opposite the portion of the electrode surface adjacent to the end.

From the Gauss law (Section 2.2.1), this charge is

$$q = \varepsilon\varepsilon_0 \oint_{\text{surface}} \mathscr{E} \cdot d\mathbf{S} \tag{13.3.17}$$

Since the field strength, $\mathscr{E}$, is zero at all points on the surface except the end at the interface [where the magnitude of the field strength is $(d\phi/dx)_{x=0}$ at every point], we have

$$q = \varepsilon\varepsilon_0 \left(\frac{d\phi}{dx}\right)_{x=0} \int_{\substack{\text{end}\\\text{surface}}} dS \tag{13.3.18}$$

Electrode surface

Gaussian enclosure

End surface
Area = A

$\dfrac{d\phi}{dx} = 0$

Surface against electrode
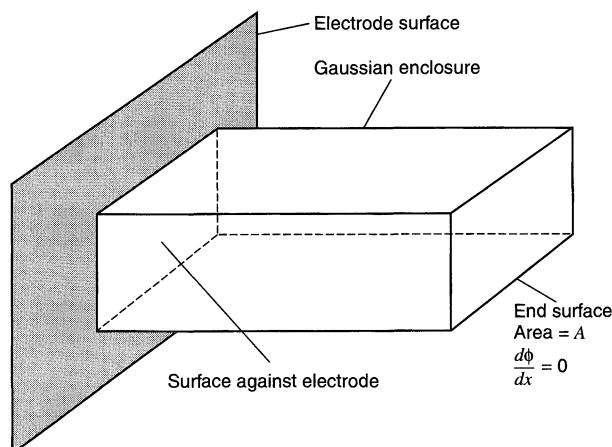
Figure 13.3.4 A Gaussian box enclosing the charge in the diffuse layer opposite an area, A, of the electrode surface.

or

$$q = \varepsilon\varepsilon_0 A \left(\frac{d\phi}{dx}\right)_{x=0} \tag{13.3.19}$$

Substituting from (13.3.11) and recognizing that q/A is the solution phase charge density σ^S, we obtain

$$\sigma^M = -\sigma^S = (8 k T \varepsilon\varepsilon_0 n^0)^{1/2} \sinh\left(\frac{ze\phi_0}{2kT}\right) \tag{13.3.20a}$$

For dilute aqueous solutions at 25°C, the constants can be evaluated to give

$$\sigma^M = 11.7C^{*1/2} \sinh(19.5z\phi_0) \tag{13.3.20b}$$

where C^* is in mol/L for σ^M in $\mu C/cm^2$. Note that ϕ_0 is related monotonically to the state of charge on the electrode.

(c) Differential Capacitance

Now we are in a position to predict the differential capacitance by differentiating (13.3.20):

$$C_d = \frac{d\sigma^M}{d\phi_0} = \left(\frac{2z^2 e^2 \varepsilon\varepsilon_0 n^0}{kT}\right)^{1/2} \cosh\left(\frac{ze\phi_0}{2kT}\right) \tag{13.3.21a}$$

For dilute aqueous solutions at 25°C, this equation can be written,

$$C_d = 228zC^{*1/2} \cosh(19.5z\phi_0) \tag{13.3.21b}$$

where C_d is in $\mu F/cm^2$ and the bulk electrolyte concentration C^* is in mol/L. Figure 13.3.5 is a graph of the way in which C_d varies with potential according to the dictates of (13.3.21). There is a minimum at the PZC and a steep rise on either side.
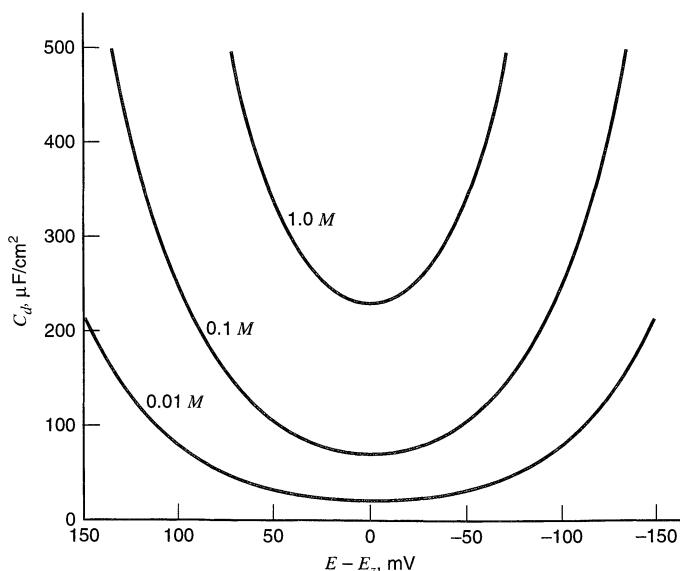
Figure 13.3.5 Predicted differential capacitances from the Gouy–Chapman theory. Calculated from (13.3.21) for the indicated concentrations of a 1:1 electrolyte in water at 25°C. Note the very restricted potential scale. The predicted capacitance rises very rapidly at more extreme potentials relative to E_z.

The predicted V-shaped capacitance function does resemble the observed behavior in NaF at low concentrations and at potentials not too far from the PZC (see Figure 13.3.1). However, the actual system shows a flattening in capacitance at more extreme potentials, and the valley at the PZC disappears altogether at high electrolyte concentrations. Moreover, the actual capacitance is usually much lower than the predicted value. The partial success of the Gouy–Chapman theory suggests that it has elements of truth, but its failures are significant and indicate major defects. We will see in the next section that one of those defects is related to the finite size of the ions in the electrolyte.

13.3.3 Stern's Modification

The reason for the unlimited rise in differential capacitance with ϕ_0 in the Gouy–Chapman model is that the ions are not restricted with respect to location in the solution phase. They are considered as point charges that can approach the surface arbitrarily closely. Therefore, at high polarization, the effective separation distance between the metallic and solution-phase charge zones decreases continuously toward zero.

This view is not realistic. The ions have a finite size and cannot approach the surface any closer than the ionic radius. If they remain solvated, the thickness of the primary solution sheath would have to be added to that radius. Still another increment might be necessary to account for a layer of solvent on the electrode surface. For example, see Figure 1.2.3. In other words, we can envision a *plane of closest approach* for the centers of the ions at some distance x_2.

In systems with low electrolyte concentration, this restriction would have little impact on the predicted capacitance for potentials near the PZC, because the thickness of the diffuse layer is large compared to x_2. However, at larger polarizations or with more concentrated electrolytes, the charge in solution becomes more tightly compressed against the boundary at x_2, and the whole system begins to resemble the Helmholtz model. Then we can expect a corresponding leveling of the differential capacitance. The plane at x_2 is an important concept and is called the *outer Helmholtz plane* (OHP).

This interfacial model (2–4, 6–8, 15, 16), first suggested by Stern (29), can be treated by extending the considerations of the last section. The Poisson–Boltzmann equation, (13.3.6), and its solutions, (13.3.10) and (13.3.11), still apply at distance $x \geq x_2$. Now the potential profile in the diffuse layer of a $z:z$ electrolyte is given by

$$\int_{\phi_2}^{\phi} \frac{d\phi}{\sinh(ze\phi/2\textit{k}T)} = -\left(\frac{8\textit{k}Tn^0}{\varepsilon\varepsilon_0}\right)^{1/2} \int_{x_2}^{x} dx \tag{13.3.22}$$

or

$$\boxed{\frac{\tanh(ze\phi/4\textit{k}T)}{\tanh(ze\phi_2/4\textit{k}T)} = e^{-\kappa(x-x_2)}} \tag{13.3.23}$$

where ϕ_2 is the potential at x_2 with respect to the bulk solution, and κ is defined by (13.3.15).

The field strength at x_2 is given from (13.3.11):

$$\left(\frac{d\phi}{dx}\right)_{x=x_2} = -\left(\frac{8\textit{k}Tn^0}{\varepsilon\varepsilon_0}\right)^{1/2} \sinh\left(\frac{ze\phi_2}{2\textit{k}T}\right) \tag{13.3.24}$$

Since the charge density at any point from the electrode surface to the OHP is zero, we know from (13.3.5) that this same field strength applies throughout that interval. Thus the

potential profile in the compact layer is linear. Figure 13.3.6b is a summary of the situation. Now we find the total potential drop across the double layer to be

$$\phi_0 = \phi_2 - \left(\frac{d\phi}{dx}\right)_{x=x_2} x_2 \tag{13.3.25}$$

Note also that all of the charge on the solution side resides in the diffuse layer, and its magnitude can be related to ϕ_2 by considering a Gaussian box exactly as we did above.[4]

$$\sigma^M = -\sigma^S = -\varepsilon\varepsilon_0\left(\frac{d\phi}{dx}\right)_{x=x_2} = (8kT\varepsilon\varepsilon_0 n^0)^{1/2} \sinh\left(\frac{ze\phi_2}{2kT}\right) \tag{13.3.26}$$

To find the differential capacitance, we substitute for ϕ_2 by (13.3.25):

$$\sigma^M = (8kT\varepsilon\varepsilon_0 n^0)^{1/2} \sinh\left[\frac{ze}{2kT}\left(\phi_0 - \frac{\sigma^M x_2}{\varepsilon\varepsilon_0}\right)\right] \tag{13.3.27}$$

Differentiation and rearrangement (Problem 13.4) gives

$$C_d = \frac{d\sigma^M}{d\phi_0} = \frac{(2\varepsilon\varepsilon_0 z^2 e^2 n^0/kT)^{1/2} \cosh(ze\phi_2/2kT)}{1 + (x_2/\varepsilon\varepsilon_0)(2\varepsilon\varepsilon_0 z^2 e^2 n^0/kT)^{1/2} \cosh(ze\phi_2/2kT)} \tag{13.3.28}$$

(a)

x, Å

(b)
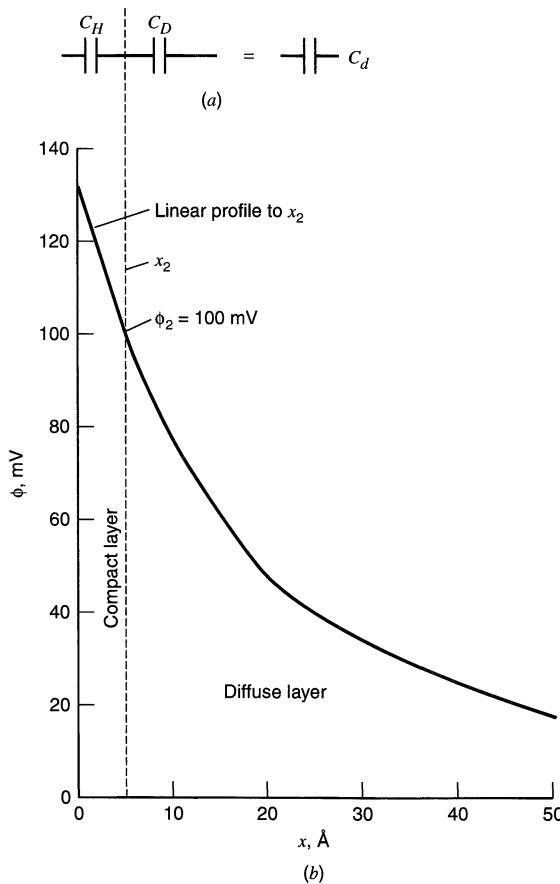
Figure 13.3.6 (a) A view of the differential capacitance in the Gouy–Chapman–Stern (GCS) model as a series network of Helmholtz-layer and diffuse-layer capacitances. (b) Potential profile through the solution side of the double layer, according to GCS theory. Calculated from (13.3.23) for 10^{-2} M 1:1 electrolyte in water at 25°C.

[4] See (13.3.15b), (13.3.20b), and (13.3.21b) for evaluations of the constants for aqueous solutions at 25°C.

which is more simply stated as the inverse:

$$\frac{1}{C_d} = \frac{x_2}{\varepsilon\varepsilon_0} + \frac{1}{(2\varepsilon\varepsilon_0 z^2 \, e^2 n^0/kT)^{1/2} \cosh(ze\phi_2/2kT)} \qquad (13.3.29)$$

This expression says that the capacitance is made up of two components that can be separated in the reciprocal, exactly as one would find for two capacitors in series. Thus we can identify the terms in (13.3.29) as the reciprocals of component capacitances, C_H and C_D, which can be depicted as in Figure 13.3.6a:

$$\frac{1}{C_d} = \frac{1}{C_H} + \frac{1}{C_D} \qquad (13.3.30)$$

By comparing the terms of (13.3.29) with (13.3.2) and (13.3.21), it is clear that C_H corresponds to the capacitance of the charges held at the OHP, whereas C_D is the capacitance of the truly diffuse charge.

The value of C_H is independent of potential, but C_D varies in the V-shaped fashion we found in the last section. The composite capacitance C_d shows a complex behavior and is governed by the *smaller* of the two components. Near the PZC in systems with low electrolyte concentration, we expect to see the V-shaped function characteristic of C_D. At larger electrolyte concentrations, or even at large polarizations in dilute media, C_D becomes so large that it no longer contributes to C_d and one sees only the constant capacitance of C_H. Figure 13.3.7 is a schematic picture of this behavior.

This model, known as the *Gouy–Chapman–Stern* (GCS) *model*, gives predictions that account for the gross features of behavior in real systems. There are still discrepancies, in that C_H is not truly independent of potential. Figure 13.3.1 is a plain illustration. This aspect must be handled by refinements to the GCS theory that take into account the structure of the dielectric in the compact layer, saturation (i.e., full polarization) of that dielectric in the strong interfacial field, differences in x_2 for anionic and cationic excesses, and other similar matters (2–4, 6–8, 13, 15–18, 30). The theory also neglects ion pairing (or ion–ion correlation) effects in the double layer and strong nonspecific interactions of the ions with the surface charge on the electrode. The latter effect can be described in terms of "ion condensation" in the electrical double layer and can be treated by a model in which the surface charge is considered as an "effective surface charge," smaller than the actual charge on the electrode because of the condensed ionic counter charge (30, 31). These types of effects are not easily probed by measurements of capacitance or surface tension, but may be addressed by alternative methods of studying the interface, as discussed in Chapters 16 and 17.
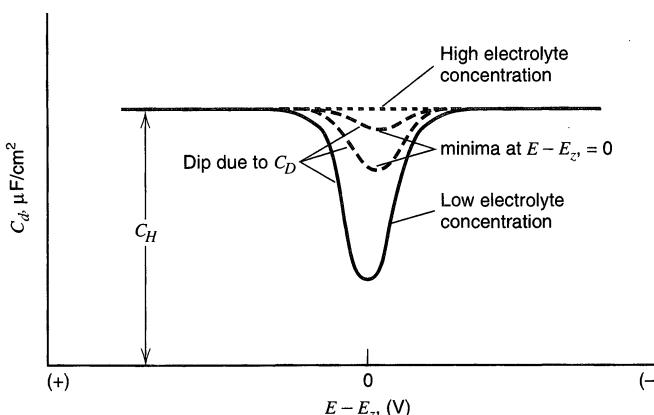
Figure 13.3.7 Expected behavior of C_d according to GCS theory as the electrolyte concentration changes.

Often one must also consider the influence of charged or uncharged species that are adsorbed by chemical interactions with the electrode surface. That issue is our next concern.

13.3.4 Specific Adsorption

In constructing models for interfacial structure, we have so far considered only long-range electrostatic effects as the basis for creating the excesses of charge found in the solution phase. Aside from the magnitude of the charges on the ions, and possibly their radii, we have been able to ignore their chemical identities. They are said to be *nonspecifically adsorbed*.[5]

However, there is more to the picture. Consider the data in Figure 13.2.2. Note that at potentials more negative than the PZC, the surface tension follows the kind of decline we have come to expect, and the decline is the same regardless of the composition of the system. This result is predictable from the GCS theory. On the other hand, the curves at potentials more positive than the PZC diverge markedly from each other. The behavior of the system in the positive region depends specifically on the composition. Since the deviations in behavior occur for potentials where anions must be in excess, we suspect that some sort of *specific adsorption* of anions takes place on mercury (2–4, 6–8, 13, 16–19, 32). Specific interactions would have to be very short-range in nature; hence we gather that specifically adsorbed species are tightly bound to the electrode surface in the manner depicted in Figure 1.2.3. The locus of their centers is the *inner Helmholtz plane* (IHP), at distance x_1 from the surface.

What experimental approaches are available for detecting and quantifying specific adsorption? Perhaps the most straightforward approach is through relative surface excesses. Turning now to Figure 13.2.6, we note several peculiarities. First, there are positive relative excesses of bromide at potentials negative of the PZC and potassium at values more positive than the PZC. At the PZC itself, positive excesses of both species are found. None of these features is accountable within an electrostatic model, such as the basic GCS theory.

The identity of the specifically adsorbed ion is revealed by considering the slopes of $z_i F \Gamma_{i(H_2O)}$ *vs.* σ^M in key regions. It is always true that

$$\sigma^M = -[F\Gamma_{K^+(H_2O)} - F\Gamma_{Br^-(H_2O)}] \tag{13.3.31}$$

In the absence of specific adsorption, the charge on the electrode is counterbalanced by an excess of one ion and a deficiency of the other, as we see in the negative region of Figure 13.2.6. If the electrode becomes even more negative, the excess charge is accommodated by a growth in *both the excess and the deficiency*, so that $F\Gamma_{K^+(H_2O)}$ does not grow as fast as σ^M. In other words, the slope of $F\Gamma_{K^+(H_2O)}$ *vs.* σ^M in the negative region should have a magnitude no greater than unity. By similar reasoning, we conclude that the slope magnitude of $-F\Gamma_{Br^-(H_2O)}$ *vs.* σ^M should also be less than or equal to unity in the positive region.

The data of Figure 13.2.6 show that the system is well-behaved in this respect at potentials much more negative than the PZC. However, in the positive region, there is *superequivalent adsorption* of bromide. The slope $d(-F\Gamma_{Br^-(H_2O)})/d\sigma^M$ exceeds unity in magnitude; hence a change in charge on the electrode is countered by more than an equivalent charge of Br$^-$. This evidence points strongly to specific adsorption of bromide at potentials more positive than the PZC. The existence of a positive excess of K$^+$ in the same

---

[5]Note that nonspecifically adsorbed species are not really adsorbed at all in the terms usually meant by the word adsorption. There is no close-range interaction in this case.

region is explained by the necessity to compensate partially the superequivalence of adsorbed bromide. Apparently, the forces responsible for specific adsorption are strong enough to withstand the opposing coulombic field in at least part of the negative region, as one may infer from the positive excess of bromide in the zone of small negative σ^M.

Another indicator of specific adsorption of charged species is the *Esin–Markov effect*, which is manifested by a shift in the PZC with a change in electrolyte concentration (33). Table 13.3.2 provides data compiled by Grahame (2). The magnitude of the shift is usually linear with the logarithm of electrolyte activity, and the slope of the linear plot is the *Esin–Markov coefficient* for the condition of $\sigma^M = 0$. Similar results are obtained at nonzero, but constant, electrode charge densities; hence the Esin–Markov coefficient can be written generally as

$$\frac{1}{RT}\left(\frac{\partial E_{\pm}}{\partial \ln a_{\text{salt}}}\right)_{\sigma^M} = \left(\frac{\partial E_{\pm}}{\partial \mu_{\text{salt}}}\right)_{\sigma^M} \tag{13.3.32}$$

Nonspecific adsorption provides no mechanism for the electrode potential to depend on the concentration of the electrolyte, so the Esin–Markov coefficient should be zero in the absence of specific adsorption.

Now consider a system in which the anion is specifically adsorbed and the electrode is being held at the PZC. If we introduce more of the same electrolyte, more anions will be adsorbed; hence σ^S becomes nonzero and must be balanced. Since the electrode is more polarizable than the solution, the countercharge is induced there. To regain the condition $\sigma^M = 0$, the potential must be shifted to a more negative value, so that the charge excess of specifically adsorbed anions is exactly counterbalanced by an opposing excess charge in the diffuse layer. Thus specific adsorption of anions is indicated by negative shifts in potential at constant charge density, whereas specific cationic adsorption is revealed by positive shifts, as the electrolyte concentration is elevated.

TABLE 13.3.2   Potentials of Zero Charge in Various Electrolytes[a]

Electrolyte	Concentration, M	E_z, V *vs.* NCE[b]
NaF	1.0	−0.472
	0.1	−0.472
	0.01	−0.480
	0.001	−0.482
NaCl	1.0	−0.556
	0.3	−0.524
	0.1	−0.505
KBr	1.0	−0.65
	0.1	−0.58
	0.01	−0.54
KI	1.0	−0.82
	0.1	−0.72
	0.01	−0.66
	0.001	−0.59

[a]From D. C. Grahame, *Chem. Rev.*, **41**, 441 (1947).
[b]NCE = normal calomel electrode.

From the data in Table 13.3.2, we see that chloride, bromide, and iodide all appear to be specifically adsorbed, but fluoride is not. It is clear now why sodium and potassium fluoride solutions in contact with mercury are the standard systems for testing the GCS theory of nonspecific adsorption.

It is obvious that specific adsorption will also introduce a capacitive component and should also be detectable by the study of C_d. In fact, we could anticipate that changes in the degree of specific adsorption with changes in potential would be highlighted by examining the derivative of C_d that is, $\partial C_d / \partial E$. Some of the most general approaches to the analysis of interfacial structure are based on these ideas. Since their details are beyond our scope, the interested reader is urged to pursue them in the literature.

Specific ionic adsorption can alter the potential profile in the interfacial zone to an extreme degree. Figure 13.3.8 is a set of curves presented by Grahame (2) for a mercury interface with 0.3 M NaCl. Note particularly the traces for the most positive potentials. These profiles can influence electrode kinetics by mechanisms considered in Section 13.7 below.

Neutral molecules are also interesting as adsorbates, because they influence or participate in faradaic processes (2–4, 6–8, 13, 16–19, 34). They can be detected and studied by the methods we have outlined above (see Problem 13.6). An interesting aspect of their behavior is that adsorption from aqueous solutions is often effective only at potentials relatively near the PZC. The usual rationale for this phenomenon rests on a recognition that adsorption of a neutral molecule requires the displacement of water molecules from the surface. When the interface is strongly polarized, the water is tightly bound and its displacement by a less dipolar substance is energetically unfavorable. Adsorption can take
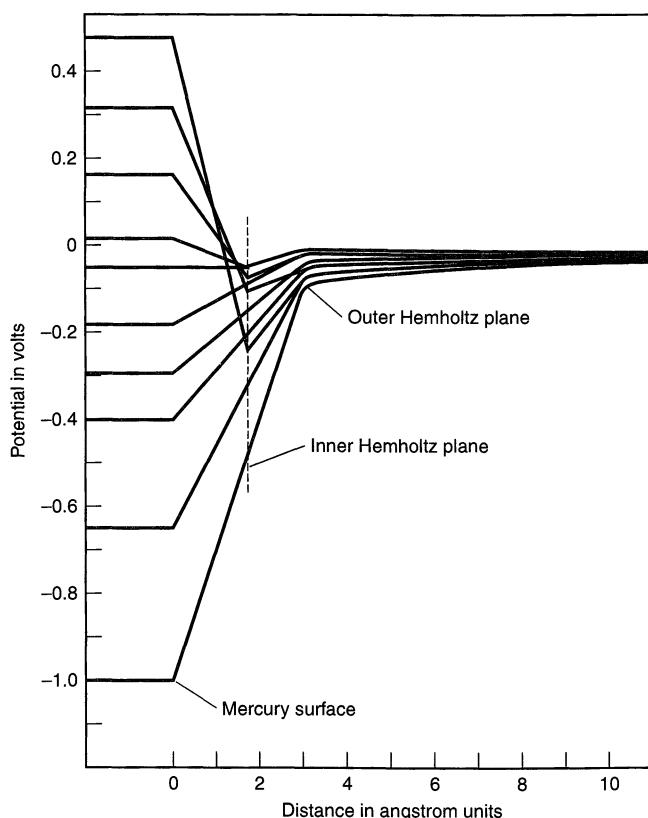
Figure 13.3.8 Calculated potential profiles in the double layer for mercury in contact with aqueous 0.3 M NaCl at 25°C. Potentials given with respect to the PZC in NaF. At positive electrode potentials the profile has a sharp minimum because chloride is specifically adsorbed. [Reprinted with permission from D. C. Grahame, *Chem. Rev.*, **41**, 441 (1947). Copyright 1947, American Chemical Society.]

place only near the PZC, where the water can be removed more easily. The applicability of this rationale in any given case obviously depends on the electrical properties of the specific neutral species at hand (19).

▶ 13.4 STUDIES AT SOLID ELECTRODES

13.4.1 The Double Layer at Solids

Most of the work in the previous sections of this chapter has dealt with mercury electrodes for the reasons discussed in Section 13.2.1. However, electrochemists are also interested in studying the interfacial structure of solids, because most electrochemical studies are carried out with solid electrodes (e.g., platinum or carbon). Such studies are difficult, because there are problems in reproducing a surface and in keeping it clean. Impurities in solution can diffuse to the electrode surface and adsorb, thereby significantly changing the interfacial properties. Moreover, the surfaces of solids, unlike those of mercury, are not atomically smooth, but have defects, such as dislocation lines, with a density of at least 10^5 to 10^7 cm^{-2}. In comparison, a typical metal surface density has about 10^{15} atoms cm^{-2}. Especially important to the understanding of solid electrodes has been the use of so-called "well-defined" metal electrodes, that is, single crystal metals with very carefully prepared surfaces of known orientation (35).

Measurements of the surface tension and surface stress of solids are not easy. Some attempts have been made to measure the surface energy, or at least to determine the PZC, of solid electrodes attached to piezoelectric materials (36, 37). More often there is a reliance on studies of differential capacitance (Section 13.4.3) (35, 38). In principle, these measurements could provide all of the information needed to describe the surface charges and relative excesses; however, one must first know the PZC. Evaluating it for a solid electrode/electrolyte system is not straightforward, and indeed, as discussed below, the PZC is not uniquely defined for a polycrystalline electrode. The most widely used approach is to evaluate the potential of minimum differential capacitance in a system involving dilute electrolyte. The identification of this potential as the PZC rests on the Gouy–Chapman–Stern theory discussed in Section 13.3.

Surface excesses of electroactive species are often examined by methods sensitive to the faradaic reactions of the adsorbed species. Cyclic voltammetry, chronocoulometry, polarography, and thin layer methods are all useful in this regard. Discussions of their application to this type of problem are provided in Section 14.3. In addition to these electrochemical methods for studying the solid electrode/electrolyte interface, there has been intense activity in the utilization of spectroscopic and microscopic methods (e.g., surface enhanced Raman spectroscopy, infrared spectroscopy, scanning tunneling microscopy) as probes of the electrode surface region; these are discussed in Chapters 16 and 17.

There has also been growing interest in the investigation of metals in ultrahigh vacuum environments that have coadsorbed water and other species in an attempt to model the double layer (39).

13.4.2 Well-Defined Single-Crystal Electrode Surfaces

Most of the reported electrochemistry with solid electrodes involves polycrystalline materials. Such electrodes consist of a variety of small domains with different crystal faces and edges presented to the contacting electrolyte. As discussed below, different crystal faces exhibit different properties (e.g., PZC or work function) so that the behavior observed at a polycrystalline electrode represents an average of that for a number of different crystal

planes and sites. The desire to obtain a better understanding of solid electrode interfaces, if possible with an atomic-level perspective, has led to studies with single-crystal electrodes having clean, well-defined, and well-ordered surfaces (35, 40, 41).

Single crystals of metals can be grown by zone-refining and are commercially available. Many of the metals used as electrodes, that is, Pt, Pd, Ag, Ni, Cu, form face-centered cubic (FCC) crystal structures. These can be cut to expose different crystal faces (index planes), as indicated in Figure 13.4.1. The low-index crystal faces, that is, the (100), (110), and (111) planes, are shown in this figure, and are the surfaces most frequently used as electrodes, because they tend to be stable and can be polished to yield fairly smooth, uniform surfaces. The higher-index planes, shown in Figure 13.4.2, have smaller atomically smooth terraces, with many more exposed edges and kink sites. Crystals are cut along a particular index plane after careful orientation with an x-ray or laser beam. Alternative approaches to obtaining well-defined crystal faces include flame annealing or vacuum evaporation. In the flame annealing method, a small wire (e.g., Pt, Pd, Au) is melted in a hydrogen-oxygen flame and then cooled to produce a small metal bead with eight clear (111) facets in an octahedral configuration (42). Vacuum evaporation on the proper substrate (e.g., Au on mica or glass) under carefully
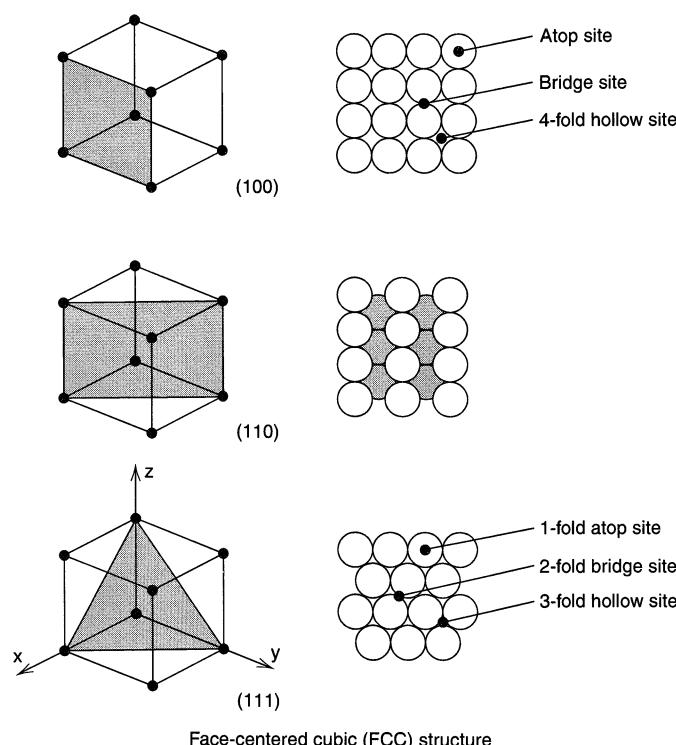
Figure 13.4.1 The atomic structure of the low-Miller-index surfaces, that is, the (100), (110), and (111) faces, of a face-centered cubic crystal obtained by cutting along the planes shown on the left. The *Miller indices* are obtained by noting the intersection of the plane of interest with the principal axes (x, y, z) shown in the lower left diagram. The Miller indices (hkl) are the smallest integers h, k, and l such that $h:k:l = (1/p):(1/q):(1/r)$, where p, q, and r are the coordinates of the intersections with the x, y, and z axes, respectively. For example, if a plane intersects the axes at $x = 2$, $y = 2$, $z = 2$, then $h:k:l = (1/2):(1/2):(1/2) = 1:1:1$, so this is the (111) plane. The atomic arrangements for the indicated planes are shown on the right. The shaded atoms in the (110) face are in the plane below the unshaded (surface) atoms. The names used for the different sites on the surfaces are also indicated.
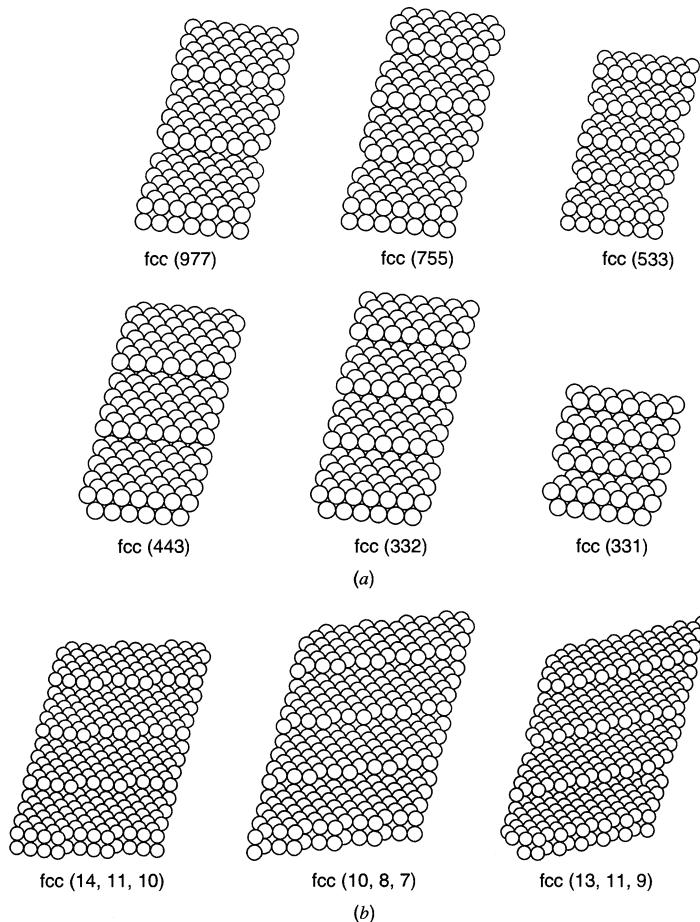
Figure 13.4.2 The atomic structure of several high-Miller-index stepped surfaces, showing terraces, step edges, and kink sites. [From G. A. Somorjai in "Photocatalysis—Fundamentals and Applications," N. Serpone and E. Pelizzetti, Eds., Wiley, New York, 1989, p. 265, with permission.]

controlled conditions can also produce (111) regions of atomic smoothness. Such surfaces can be characterized by low-energy electron diffraction and the other techniques described in Chapters 16 and 17. One should be aware that even the most carefully prepared surfaces are not atomically smooth over areas larger than a few square micrometers, and they inevitably show step edges and defect sites (as seen by scanning tunneling microscopy).

Moreover, surfaces can reconstruct. When a solid is cleaved, the surface atoms are no longer subjected to the same bonding forces and will sometimes undergo a change in configuration to minimize the surface energy. This *reconstruction* of an electrode can be a function of potential and the extent of specific adsorption.

Carbon is another widely used electrode material. The well-defined form of carbon is highly oriented pyrolytic graphite (HOPG), which consists of sheets of hexagonally close-packed (HCP) carbon atoms in a layered or stacked structure (Figure 13.4.3). The carbon atoms are strongly bonded to each other within the HCP surface (the basal plane), which atomically is similar to the FCC (111) plane. Bonding to the next (lower) layer of atoms involves van der Waals forces and is much weaker. Thus HOPG is easily cleaved along the basal plane to expose a fresh, smooth, HCP surface.
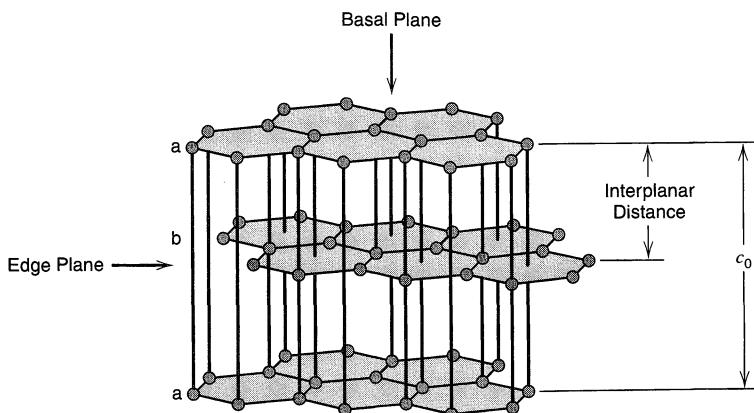
Figure 13.4.3 Structure of highly oriented pyrolytic graphite. The interplanar distance between the a and b layers is 3.35 Å. Note that the unit cell distance, c_0, is 6.70 Å, because of the abab . . . stacking arrangement. [Adapted from A. J. Bard, "Integrated Chemical Systems," Wiley, New York, 1994, p. 132, with permission.]

Pt (100)

$\mu C \cdot cm^{-2}$

$(Q_O)_{des} = 212$

$(Q_H)_{des} = 205$

Pt (111)

$(Q_O)_{des} = 95$

$(Q_H)_{des} = 240$

Pt (110)

$(Q_O)_{des} = 195$

$(Q_H)_{des} = 200$
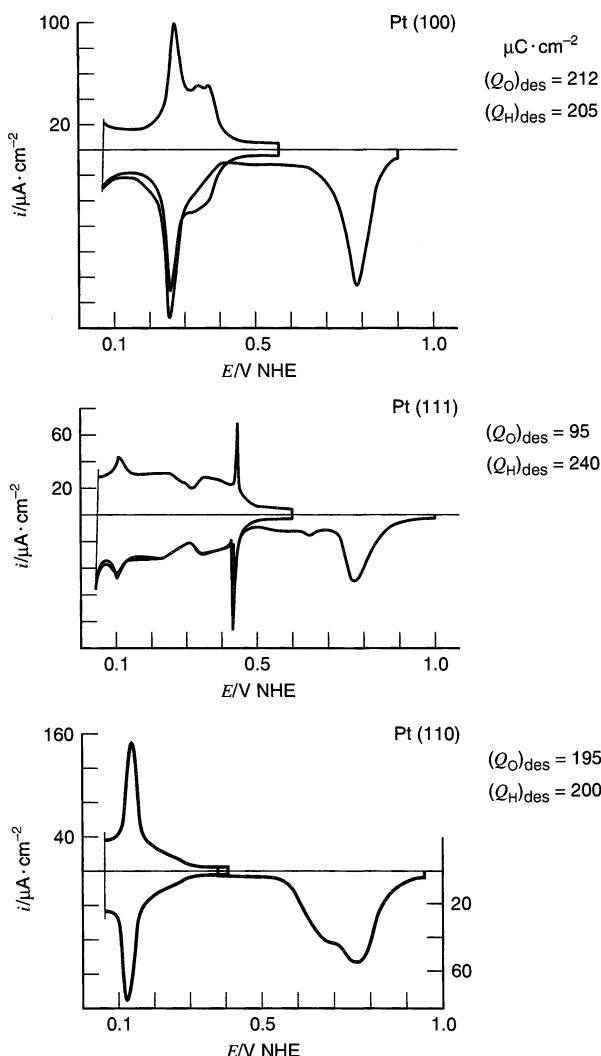
Figure 13.4.4 First cyclic voltammograms of flame treated platinum of different orientations in 0.5 M H_2SO_4 at 50 mV/s. Positive potentials are plotted to the right, and anodic currents up. Compare these to the voltammogram of a polycrystalline electrode, Figure 13.6.1. Q_H and Q_O represent the areas under the hydrogen and oxygen desorption peaks, respectively. [Reprinted with permission from J. Clavilier in "Electrochemical Surface Science: Molecular Phenomena at Electrode Surfaces," M. Soriaga, Ed., ACS Books, Washington, D.C., 1988, p. 205. Copyright 1988, American Chemical Society.]

Studies with single-crystal electrodes and well-defined surfaces have demonstrated that the properties (e.g., PZC and work function) of solid electrodes can depend strongly on the index plane presented to the solution. For example, with a silver electrode there is a significant difference between the PZC on Ag(111) (-0.69 V *vs.* SCE) and Ag(110) (-0.98 V *vs.* SCE). Since a polycrystalline electrode presents many different exposed crystal faces to a solution, different sites on the same surface can carry a different charge. For example on a silver electrode held at -0.8 V *vs.* SCE, the (111) sites will be negative of their PZC and carry a negative charge, while the (110) sites will carry a positive charge (38). In addition the catalytic and adsorptive properties of solid surfaces can depend upon the crystal face. A striking example is the difference in cyclic voltammograms for reductive adsorption and oxidative desorption of hydrogen on the different surfaces of platinum (Figure 13.4.4).

13.4.3 The Solid Metal–Solution Interface

Information about the PZC and the nature of the solid/electrolyte interface can be obtained from capacitance measurements with scrupulous care in electrode surface preparation and solution purity (35). For example, capacitance curves for Ag (100) at different concentrations of two electrolytes, KPF_6 and NaF, are shown in Figure 13.4.5. The essential inde-
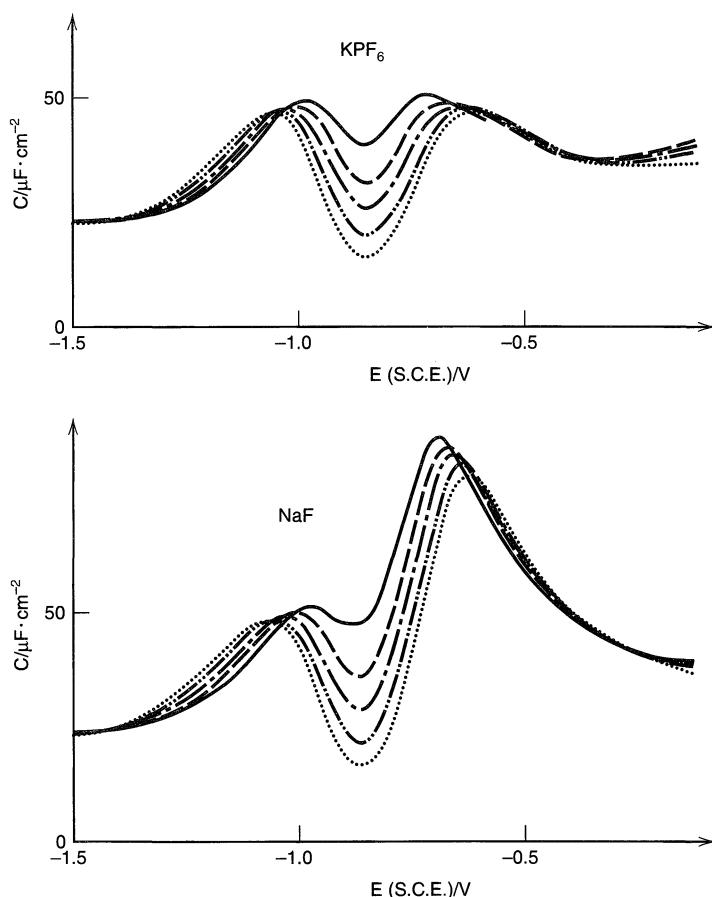
Figure 13.4.5 Capacitance curves for Ag(100) in aqueous solutions of (*a*) KPF_6 and (*b*) NaF for different concentrations of electrolyte: Top to bottom, 100, 40, 20, 10, and 5 m*M*. $v = 5$ mV/s. $\omega/2\pi = 20$ Hz. [Reprinted from G. Valette, *J. Electroanal. Chem.*, **138**, 37 (1982), with permission from Elsevier Science.]

pendence of the minimum in capacitance with the electrolyte and concentration suggests that the species are only weakly specifically adsorbed on Ag (if they are adsorbed at all) and that the PZC can be identified with the capacitance minimum. Note, however, the differences in behavior with the same electrolyte for different crystal faces of Ag (Figure 13.4.6). Identification of the capacitance minimum with the PZC clearly suggests that the PZC depends upon the crystal face exposed to the solution. The capacitance of a model polycrystalline electrode, with the assumption that the surface was 46% (110), 23% (100) and 31% (111) is also shown. The PZC in this case is close to that of the (110) surface. The situation is more complicated with a real polycrystalline electrode surface with exposed high-index planes and defect sites.

Another complication with solid electrodes is the possibility that the surface can reconstruct, even during a potential scan (43). As an example, consider a Au(100) electrode. When this surface is heated in a flame, it undergoes reconstruction to form a surface layer of the close-packed form, a slightly-buckled (111) arrangement often called a (5 × 20) surface from its LEED (low-energy electron diffraction) pattern. This surface structure is maintained when the electrode is immersed in a solution of 0.01 M HClO$_4$. When the potential of the electrode is cycled to more positive potentials, the reconstructed surface is maintained as long as the potential is not larger than about +0.5 V $vs.$ SCE, and the capacitance curve is representative of the (5 × 20) surface (Figure 13.4.7b). If the potential is cycled to +0.7 V, the surface converts to the original (100) surface [with a (1 × 1) LEED pattern]. The original reconstruction is said to have been *lifted*. Accompanying this
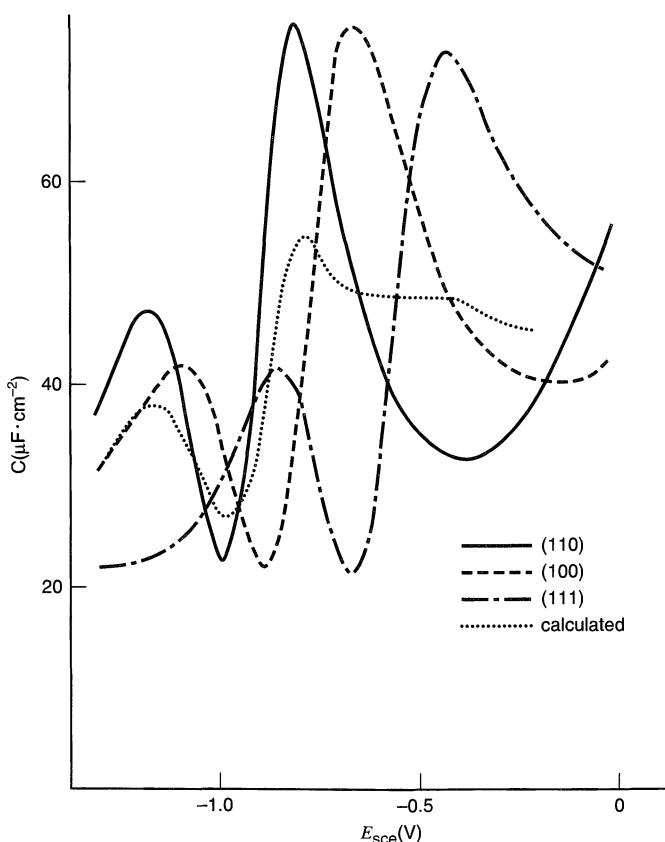
Figure 13.4.6
Capacitance curves for the (111), (100) and (110) faces of Ag in 10 mM NaF. $v = 5$ mV/s. $\omega/2\pi = 20$ Hz. The "calculated" curve is for a model polycrystalline Ag electrode (see text). [Original data from G. Valette and A. Hamelin, *J. Electroanal. Chem.*, **45**, 301 (1973). Figure reprinted from A. Hamelin, *Mod. Asp. Electrochem.*, **16**, 1 (1985), with permission.]

Legend for figure:
——— (110)
- - - - - (100)
—·—·— (111)
············ calculated

Axis labels: $C(\mu F \cdot cm^{-2})$ vertical with values 60, 40, 20; horizontal axis $E_{sce}(V)$ with values −1.0, −0.5, 0
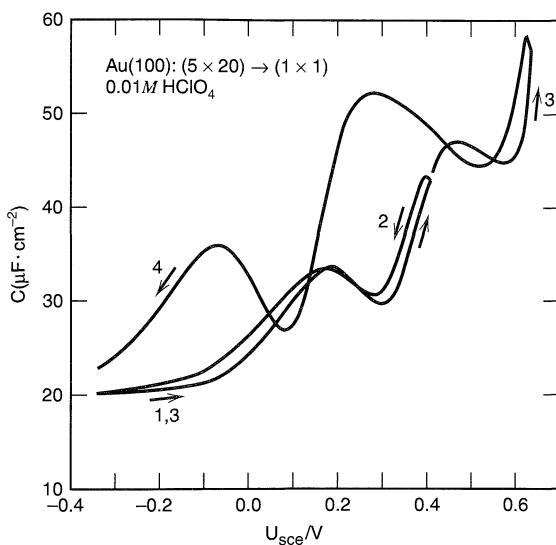
Figure 13.4.7 Capacitance curves for an Au(100) electrode with a reconstructed (5 × 20) surface in 0.01 M HClO$_4$ at $v = 10$ mV/s. The abscissa is potential $vs.$ SCE. Numbers refer to the sequence of scans. The (5 × 20) reconstructed surface is maintained in scans 1 and 2 to a potential of about 0.4 V $vs.$ SCE. However on scan 3, beyond 0.6 V, the surface reverts to the original Ag(100)–(1 × 1) surface. [Reprinted from D. M. Kolb and J. Schneider, *Electrochim. Acta*, **31**, 929 (1986), with permission from Elsevier Science.]

change is a large change in the capacitance curve and a shift in the PZC. Similar effects have been seen with other surfaces and suggest that surface structure can change significantly during potential sweeps.

13.5 EXTENT AND RATE OF SPECIFIC ADSORPTION

In the preceding sections, we have discussed *nonspecific adsorption*, where long-range electrostatic forces perturb the distribution of ions near the electrode surface, and *specific adsorption*, where a strong interaction between the adsorbate and the electrode material causes the formation of a layer (partial or complete) on the electrode surface. The difference between nonspecific and specific adsorption is analogous to the difference between the presence of an ion in the ionic atmosphere of another, oppositely charged, ion in solution (e.g., as modeled by the Debye–Hückel theory) and the formation of a bond between the two solution species (as in a complexation reaction).

Nonspecific adsorption of an electroactive species can affect the electrochemical response, because it affects the concentration of the species, as well as the potential distribution, near the electrode. These consequences are described in Section 13.7.

Specific adsorption can have several effects. If an *electroactive* species is adsorbed, the theoretical treatment of a given electrochemical method must be modified to account for the presence of the reactive species at the electrode surface in a relative amount higher than the bulk concentration at the start of the experiment. In addition, specific adsorption can change the energetics of the reaction, for example, adsorbed O may be more difficult to reduce than dissolved O. The effects of specific adsorption in different electrochemical methods are discussed in Section 14.3.

Specific adsorption of an *electroinactive* species can also alter the electrochemical response, for example, by forming a blocking layer on the electrode surface. However, adsorption may also increase the reactivity of a species, for example, by causing dissociation of an unreactive material into reactive fragments, such as in the adsorption of aliphatic hydrocarbons on a platinum electrode. In this case, the electrode behaves as a catalyst for the redox reaction, and this phenomenon is usually called *electrocatalysis* (see Section 13.6 and Chapter 14).

13.5.1 Nature and Extent of Specific Adsorption

Electrocapillary methods, described in Sections 13.2 and 13.3, are very useful in the determination of relative surface excesses of specifically adsorbed species on mercury. As discussed in Section 13.4, such methods are less straightforward with solid electrodes. For electroactive species and products of electrode reactions, the faradaic response can frequently be used to determine the amount of adsorbed species (Section 14.3). Nonelectrochemical methods can also be applied to both electroactive and electroinactive species. For example, the change in concentration of an adsorbable solution species after immersion of a large-area electrode and application of different potentials can be monitored by a sensitive analytical technique (e.g., spectrophotometry, fluorimetry, chemiluminescence) that can provide a direct measurement of the amount of substance that has left the bulk solution upon adsorption (7, 44). Radioactive tracers can be employed to determine the change in adsorbate concentration in solution (45). Radioactivity measurements can also be applied to electrodes removed from the solution, with suitable corrections applied for bulk solution still wetting the electrode (45). A general problem with such direct methods is the sensitivity and precision required for accurate determinations, since the bulk concentration changes caused by adsorption are usually rather small (see Problem 13.7).

The amount of material in a monolayer of adsorbate depends on the size of the adsorbing molecule and its orientation on the electrode surface. Atoms or molecules can adsorb on the surface in different ways and in different patterns. If the molecules adsorb in a pattern that is in exact correspondence with the surface atoms, the adsorption is said
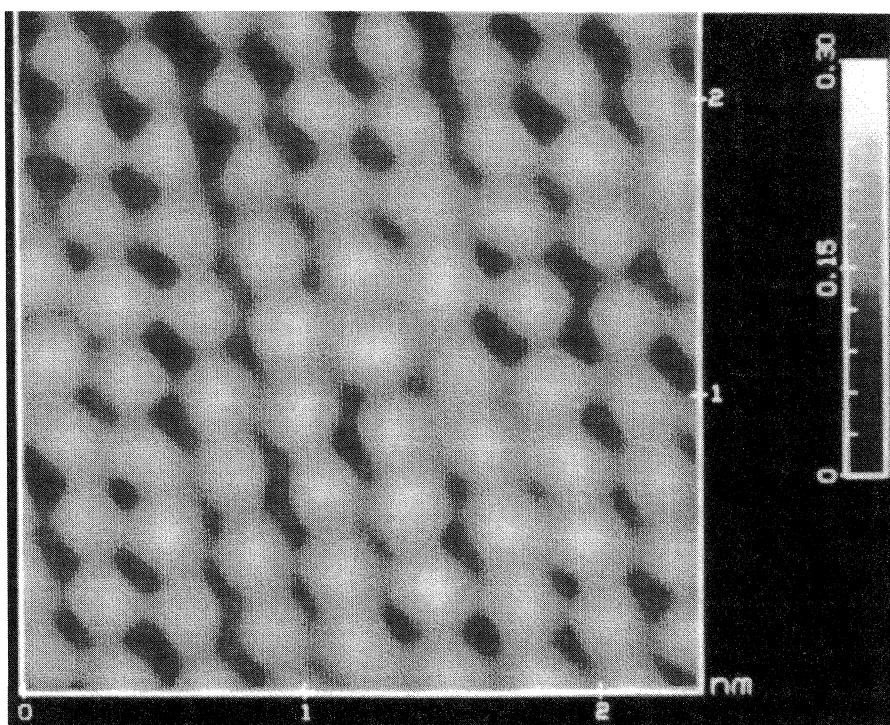
Figure 13.5.1 Scanning tunneling microscope image of a 23 Å × 23 Å region of an Au (111) surface prepared by evaporation of Au on a mica substrate. [Reprinted with permission from Y.-T. Kim, R. L. McCarley, and A. J. Bard, *J. Phys. Chem.*, **96**, 7416 (1992). Copyright 1992, American Chemical Society.]

to be *commensurate*. For example, there are 1.5×10^{15} Au atoms/cm^2 on the surface of gold (111), with an interatom spacing of 2.9 Å (Figure 13.5.1). If adsorbate atoms took *atop sites* (Figure 13.4.1) on each gold atom (denoted as a *1 × 1 superlattice*), the surface coverage would be 2.5×10^{-9} mol/cm^2. Generally the molecular dimensions of adsorbates are too large to pack in this way and they are more widely spaced on the surface. When iodine or 4-aminothiophenol adsorb on the Au (111) surface they presumably are in *3-fold hollow sites*. However, they are too large to fit into every vacant site, so they seem to be spaced into every other site as suggested in Figure 13.5.2. Simple geometry indicates that the distance between adjacent adsorbate molecules is $\sqrt{3}$ times the Au to Au spacing, or 5.0 Å. Moreover, a row of adsorbate molecules is at an angle of 30° with respect to a row of Au atoms in the underlayer. Thus this structure is called ($\sqrt{3} \times \sqrt{3}$)R30°. The number of adsorbate molecules in this case is one-third that of the gold atoms, or 8.3×10^{-10} mol/cm^2. Lower coverages are found with larger molecules. Typically, for low molecular weight substances, coverages lie in the range of 10^{-9} to 10^{-10} mol/cm^2. This represents an easily measurable amount of charge (>10 μC/cm^2), so that electrochemical measurements of adsorbed electroactive materials can detect fractions of monolayers (see Section 14.3).

(a)

(b)
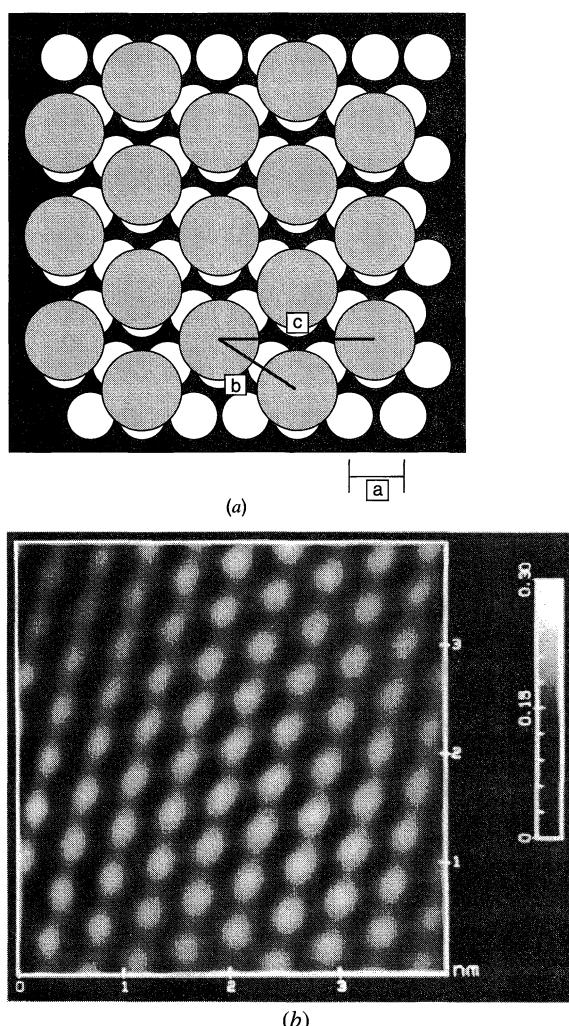
Figure 13.5.2 (*a*) Schematic representation of an adsorbed layer with a ($\sqrt{3} \times \sqrt{3}$)R30° structure on a gold (111) surface. (*b*) Scanning tunneling microscope image of a 40 Å × 40 Å region of a 4-aminothiophenol monolayer on an Au (111) surface. Note difference in spacing compared to that in Figure 13.5.1 [Part *b* reprinted with permission from Y.-T. Kim, R. L. McCarley, and A. J. Bard, *J. Phys. Chem.*, **96**, 7416 (1992). Copyright 1992, American Chemical Society.]

Note that the coverages quoted above are for an atomically smooth surface. The surfaces of essentially all solid electrodes, including single-crystal surfaces, are much rougher because of steps, plateaus and defects, and so will show larger coverages per unit projected area. The ratio of the actual area of an electrode to the projected area (the area assuming the electrode is perfectly smooth) is called the *roughness factor* (see Section 5.2.3). Even apparently smooth and polished solid electrodes have roughness factors of 1.5 to 2 or more.

There has also been interest in studying adsorbed layers on the electrode surfaces by spectrometric methods, either with the electrode immersed in the solution (e.g., by ellipsometry, surface enhanced Raman spectroscopy, scanning tunneling microscopy) or after removal (*emersion*) of the electrode from solution. These methods are useful, since they can supply information about the structure of the adsorbed layer. They are discussed briefly in Chapter 17.

13.5.2 Adsorption Isotherms

The relationship between the amount of substance i adsorbed on the electrode per unit area, Γ_i, the activity in bulk solution, a_i^b, and the electrical state of the system, E or q^M, at a given temperature, is given by the *adsorption isotherm*. This is obtained from the condition of equality of electrochemical potentials for bulk and adsorbed species i at equilibrium

$$\bar{\mu}_i^A = \bar{\mu}_i^b \tag{13.5.1}$$

where the superscripts A and b refer to adsorbed i and bulk i, respectively. Thus

$$\bar{\mu}_i^{0,A} + RT \ln a_i^A = \bar{\mu}_i^{0,b} + RT \ln a_i^b \tag{13.5.2}$$

where the $\bar{\mu}_i^0$ terms are the standard electrochemical potentials. The standard free energy of adsorption, $\Delta\bar{G}_i^0$, which is a function of the electrode potential, is defined as

$$\Delta\bar{G}_i^0 = \bar{\mu}_i^{0,A} - \bar{\mu}_i^{0,b} \tag{13.5.3}$$

Thus

$$a_i^A = a_i^b \, e^{-\Delta\bar{G}_i^0/RT} = \beta_i a_i^b \tag{13.5.4}$$

where (4)

$$\beta_i = \exp\left(\frac{-\Delta\bar{G}_i^0}{RT}\right) \tag{13.5.5}$$

Equation 13.5.4 is a general form of an adsorption isotherm, with a_i^A being a function of a_i^b and β_i. Different specific isotherms result from different assumptions or models for the relationship between a_i^A and Γ_i. A number have been proposed (4, 7, 34, 46); some commonly used ones are discussed below.

The *Langmuir isotherm* involves assumptions of (a) no interactions between the absorbed species on the electrode surface, (b) no heterogeneity of the surface, and (c) at high bulk activities, saturation coverage of the electrode by adsorbate (e.g., to form a monolayer) of amount Γ_s. Thus

$$\boxed{\frac{\Gamma_i}{\Gamma_s - \Gamma_i} = \beta_i a_i^b} \tag{13.5.6}$$

Isotherms are sometimes written in terms of the fractional coverage of the surface, $\theta = \Gamma_i/\Gamma_s$; the Langmuir isotherm in this form is

$$\frac{\theta}{1 - \theta} = \beta_i a_i^b \tag{13.5.7}$$

The Langmuir isotherm can be written in terms of the concentration of species i in solution by including activity coefficients in the β term. This yields

$$\Gamma_i = \frac{\Gamma_s \beta_i C_i}{1 + \beta_i C_i} \qquad (13.5.8)$$

If two species, i and j, are adsorbed competitively, the appropriate Langmuir isotherms are

$$\Gamma_i = \frac{\Gamma_{i,s} \beta_i C_i}{1 + \beta_i C_i + \beta_j C_j} \qquad (13.5.9)$$

$$\Gamma_j = \frac{\Gamma_{j,s} \beta_j C_j}{1 + \beta_i C_i + \beta_j C_j} \qquad (13.5.10)$$

where $\Gamma_{i,s}$ and $\Gamma_{j,s}$ represent the saturation coverages of i and j, respectively. These equations can be derived from a kinetic model assuming independent coverages of θ_i and θ_j, with the rate of adsorption of each species proportional to the free area, $1 - \theta_i - \theta_j$, and the solution concentrations, C_i and C_j. The rate of desorption of each is assumed to be proportional to θ_i and θ_j.

Interactions between adsorbed species complicate the problem by making the energy of adsorption a function of surface coverage. Isotherms that include this possibility are the *logarithmic Temkin isotherm*:

$$\boxed{\Gamma_i = \frac{RT}{2g} \ln(\beta_i a_i^b) \qquad (0.2 < \theta < 0.8)} \qquad (13.5.11)$$

and the *Frumkin isotherm*:

$$\boxed{\beta_i a_i^b = \frac{\Gamma_i}{\Gamma_s - \Gamma_i} \exp\left(-\frac{2g\Gamma_i}{RT}\right)} \qquad (13.5.12)$$

The Frumkin isotherm arises from the assumption that the electrochemical free energy of adsorption, defined in (13.5.3), is linearly related to Γ_i:

$$\Delta \overline{G}_i^0 \text{ (Frumkin)} = \Delta \overline{G}_i^0 \text{ (Langmuir)} - 2g\Gamma_i \qquad (13.5.13)$$

The parameter g typically has units of J/mol per mol/cm^2, and it expresses the way in which increased coverage changes the adsorption energy of species i. If g is positive, the interactions between neighboring adsorbed molecules on the surface are attractive; and if g is negative, the interactions are repulsive. As $g \to 0$, the Frumkin isotherm approaches the Langmuir isotherm. This isotherm can also be written in the form (including activity coefficients in the β term)

$$\beta_i C_i = \frac{\theta}{1 - \theta} \exp(-g'\theta) \qquad (13.5.14)$$

where $g' = 2g\Gamma_s/RT$. The range of g' is generally $-2 \le g' \le 2$; g' may also be a function of potential (34).

13.5.3 Rate of Adsorption

The adsorption of a species i from solution upon creation of a fresh electrode surface (e.g., at a fresh mercury drop at a DME) follows a general behavior analogous to that of an electrode reaction. If the rate of adsorption at the surface is rapid, equilibrium is established at the electrode surface, and the amount of substance adsorbed at a given time, $\Gamma_i(t)$, is related to the concentration of the adsorbate at the electrode surface, $C_i(0, t)$, by the ap-

propriate isotherm. The rate of buildup of the adsorbed layer to its equilibrium value, Γ_i, is then governed by the rate of mass transfer to the electrode surface. This situation, for mass transfer by diffusion and convection using the diffusion layer approximation, has been treated for a linearized isotherm (47). When $\beta C_i \ll 1$, the isotherm in (13.5.8) can be expressed in a linear form to yield (see Problem 13.8)

$$\Gamma_i = \Gamma_s \beta_i C_i = b_i C_i \tag{13.5.15}$$

where $b_i = \beta_i \Gamma_s$. This equation becomes the boundary condition for the problem, that is,

$$\Gamma_i(t) = b_i C_i(0, t) \tag{13.5.16}$$

The other needed equations are Fick's second law for i, and the conditions $C_i(x, 0) = C_i^*$, and $\lim_{x \to \infty} C_i(x, t) = C_i^*$. Moreover, the amount of material adsorbed at t is related to the flux of i at the electrode surface:

$$\Gamma_i(t) = \int_0^t D_i \left[\frac{\partial C_i(x, t)}{\partial x} \right]_{x=0} dt \tag{13.5.17}$$

The solution to this problem for a stationary plane electrode (semi-infinite linear diffusion) is (47)

$$\frac{C_i(x, t)}{C_i^*} = 1 - \exp\left(\frac{x}{b_i} + \frac{D_i t}{b_i^2} \right) \mathrm{erfc} \left[\frac{x}{2(D_i t)^{1/2}} + \frac{(D_i t)^{1/2}}{b_i} \right] \tag{13.5.18}$$

$$\frac{\Gamma_i(t)}{\Gamma_i} = 1 - \exp\left(\frac{D_i t}{b_i^2} \right) \mathrm{erfc} \left[\frac{(D_i t)^{1/2}}{b_i} \right] \tag{13.5.19}$$

This function is plotted in Figure 13.5.3.

Note that under the conditions of the linearized isotherm, $\Gamma_i(t)/\Gamma_i$ is independent of C_i^*. A consequence is that for realistic values of D_i and b_i a rather long time is required to attain equilibrium coverage [i.e., for $\Gamma_i(t)/\Gamma_i \approx 1$; see Problem 13.9]. Adsorption equilibrium may not be attained at the DME at the usual drop times or at a stationary electrode during a linear potential sweep at moderate rates from initial potentials where adsorption does not occur.

The assumption of a linear isotherm is, of course, valid only over a limited concentration range. The use of the full adsorption isotherm may require numerical solution of the problem; the results of such treatments are in qualitative agreement with that for the linearized isotherm (48, 49) (see Figure 13.5.4). The rate of attainment of equilibrium is clearly seen to depend on the bulk concentration C_i^*, however.

Of course, the rate of adsorption can be increased by stirring the solution. For the linearized isotherm in stirred solution (47),

$$\frac{\Gamma_i(t)}{\Gamma_i} = 1 - \exp\left(\frac{-m_i t}{b_i} \right) \tag{13.5.20}$$
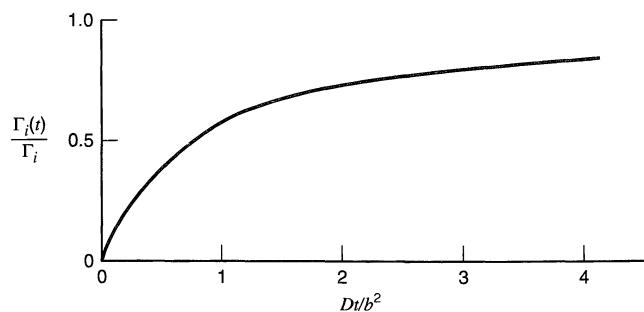
Figure 13.5.3 Attainment of equilibrium coverage, Γ_i, for diffusion-controlled adsorption under conditions of a linearized isotherm; see (13.5.19). $b = \beta \Gamma_s$.
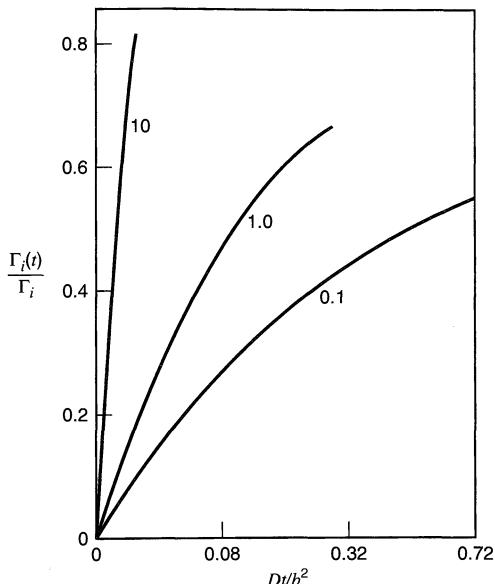
Figure 13.5.4 Attainment of equilibrium coverage, Γ_i, for diffusion-controlled adsorption under a Langmuir isotherm at several values of bC^*/Γ_s (indicated on curves). [Reprinted with permission from W. H. Reinmuth, *J. Phys. Chem.*, **65**, 473 (1961). Copyright 1961, American Chemical Society.]

where $m_i = D_i/\delta_i$ is the mass-transfer coefficient. Other treatments of mass-transfer-controlled kinetics have been reviewed (16).

The case where the rate of adsorption at the electrode is governed by the adsorption process itself has also been treated, with the assumptions of a logarithmic Temkin isotherm and Temkin kinetics (4, 34, 50). The results of this approach have not been widely applied, although measurements of adsorption rates have been attempted (51). Delahay (34) concludes that the inherent rate of adsorption, at least on mercury from aqueous solution, usually is rapid, so that the overall rate is frequently governed by mass transfer.

13.6 EFFECT OF ADSORPTION OF ELECTROINACTIVE SPECIES

The adsorption of electroinactive species on an electrode surface (sometimes referred to as "getting crap on the electrode") occurs frequently. Such adsorption can inhibit (or poison) an electrode reaction (e.g., by formation of an impervious layer that blocks a portion of the electrode surface), or it can accelerate the electrode reaction (e.g., by double-layer effects, as discussed in Section 13.7, or as in the anion induced adsorption of metal ions discussed in Section 14.3.6). Indeed, in many studies with solid electrodes, one observes a slow change in the electrochemical response with time, which can be ascribed to the buildup of adsorbed impurities on the electrode surface at a rate limited by their diffusion from the bulk solution. Moreover, in aqueous solutions, metals form layers of adsorbed oxygen (or equivalently, oxide film monolayers) or adsorbed hydrogen, and they can affect the electrochemical behavior. A great advantage of mercury electrodes is the possibility of easily renewing the surface, and thus allowing repetitive measurements at surfaces essentially free of adsorbed films.

At solids, reproducible surface behavior can sometimes be attained by preceding an experiment with a program of potential steps to values where desorption of impurities occurs or where oxide films are formed and then reduced. Applying such a program is sometimes described as "activating" the electrode surface (52). Several reviews have appeared dealing with these topics (34, 53–57).

An adsorbed film may inhibit an electrode reaction by completely blocking the electrode surface so that reaction only occurs at the uncovered fraction, $(1 - \theta)$. Alternatively,

the reaction may occur also at the filmed portion of the electrode, for example, by penetration of the reactive species or by transfer of electrons through the film, but at a reduced rate compared to the free surface. It is even possible that the sites of adsorbed material promote the electrode reaction. These effects are sometimes treated by assuming that the rate constant for a heterogeneous electron transfer, k^0, is a linear function of the coverage θ (53):

$$k^0 = k^0_{\theta=0}(1 - \theta) + k^0_c\theta \qquad (13.6.1)$$

where $k^0_{\theta=0}$ is the standard rate constant at the bare surface and k^0_c that at the filmed portions. For complete blockage by the film, $k^0_c = 0$; while for catalysis by the filmed area, $k^0_c > k^0_{\theta=0}$. Actual attempts at experimental verification of this equation under conditions of equilibrium coverage are few. A study of the reduction of Zn(II) on Zn(Hg) with blockage by adsorbed alcohols, such as amyl alcohol, thymol, and cyclohexanol, showed such a linear dependence at small coverages, but significant deviations were observed at higher coverages (58). In this case, correction for ϕ_2 effects (see Section 13.7) and the determination of the extent of coverage at higher alcohol concentrations caused some difficulty in obtaining corrected rate constants. Other studies at mercury electrodes that also failed to confirm (13.6.1) have been reported (59, 60).

The effect of adsorbed substances on solid electrodes has been the subject of numerous investigations because of the technological implications of such adsorption. This is especially true for noble metals that are used as electrodes or electrocatalysts in fuel cells and other applications (52, 61). For example, the current-potential curve for a platinum electrode in an aqueous solution shows peaks for the formation and oxidation of both adsorbed hydrogen and adsorbed oxygen (Figure 13.6.1). Measurement of the areas under the peaks, assuming they represent monolayer coverage, have been suggested as a means of determining the "true" (as opposed to "geometric" or "projected") area of the electrode
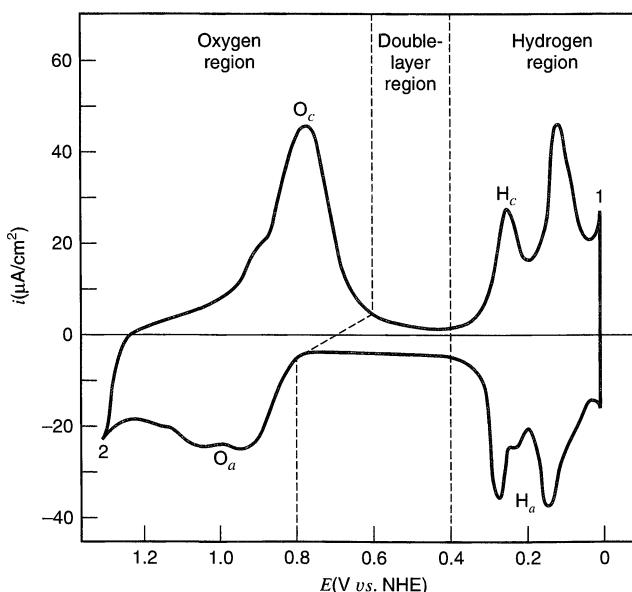
Figure 13.6.1 Cyclic voltammogram for a smooth platinum electrode in 0.5 M H_2SO_4. Peaks H_c: formation of adsorbed hydrogen. Peaks H_a: oxidation of adsorbed hydrogen. Peaks O_a: formation of adsorbed oxygen or a platinum oxide layer. Peak O_c: reduction of the oxide layer. Point 1: start of bulk hydrogen evolution. Point 2: start of bulk oxygen evolution. The shape, number, and size of the peaks for adsorbed hydrogen depend on the crystal faces of platinum exposed (62), pretreatment of electrode, solution impurities, and supporting electrolyte. See also Figure 13.4.4.

(Section 5.2.3). Many substances can adsorb onto a platinum electrode and inhibit the hydrogen electrode reactions. Evidence for this effect is the decrease in the area under the adsorbed hydrogen region of the *i-E* curve when such substances (e.g., compounds of mercury and arsenic, carbon monoxide, and many organic substances) are added to the system. Alternatively, the formation of an adsorbed oxygen (or oxide) layer on platinum inhibits many oxidation processes (e.g., the oxidation of hydrogen, oxalic acid, hydrazine, and a number of organic substances). Adsorption of electroinactive substances plays an important role in electrodeposition processes, where they can act as brighteners (see Section 11.3.2). Adsorbed organic molecules (such as acridine or quinoline derivatives) can also act as corrosion inhibitors by decreasing the rates of any of the reactions that may occur at a metal surface (e.g., metal dissolution or oxygen reduction).

▶ 13.7 DOUBLE-LAYER EFFECTS ON ELECTRODE REACTION RATES

13.7.1 Introduction and Principles

The fact that the structure of the double layer and the specific adsorption of ions can affect the kinetics of electrode reactions was recognized as early as 1933 (63). Such effects can give rise to a number of apparent anomalies. For example, the rate constant, k^0, for a given heterogeneous electron-transfer step might be a function of the nature of the supporting electrolyte ions or the supporting electrolyte concentration, even when no apparent bulk reaction involving electrolyte ions (e.g., complexation or ion pairing) occurs. Nonlinear Tafel plots (see Section 3.4.3) can be observed. Sometimes rather spectacular effects can be observed in the *i-E* curves. For example, in the reduction of anionic species (e.g., $S_2O_8^{2-}$), the current on the diffusion plateau can drop at a certain potential, with a resulting minimum in the *i-E* curve.

These effects can be understood and interpreted in terms of the variation of potential in the double-layer region, as discussed in Section 13.3. The basic concepts were described by Frumkin (7), and this effect is sometimes called the *Frumkin effect*.

If we assume that the species undergoing reduction, O^z, in the one-step, one-electron reaction

$$O^z + e \rightleftarrows R^{z-1} \tag{13.7.1}$$

is not specifically adsorbed, then its position of closest approach to the electrode is the OHP ($x = x_2$) (see Section 13.3.3). The potential at the OHP, ϕ_2, is not equal to the potential in solution, ϕ^S, because of the potential drop through the diffuse layer (and possibly because some ions are specifically adsorbed). These potential differences in the double layer, as shown for example in Figure 13.3.6, can affect the electrode reaction kinetics in two ways.

    (a) If $z \neq 0$, the concentration of O^z at x_2 will be different from that immediately outside the diffuse layer, C_O^b, which for our calculations can be regarded as the concentration "at the electrode surface."[6] Thus from (13.3.3),

$$C_O(x_2, t) = C_O^b \, e^{-zF\phi_2/RT} \tag{13.7.2}$$

---

[6]In this section, we need to distinguish two separate meanings of "the concentration at the electrode surface." For electrode kinetics, the relevant distance scale is angstroms; thus "$x = 0$" is very near the interface, and $C_O(0, t)$ must be understood essentially as $C_O(x_2, t)$. When the focus is on diffusion, "$x = 0$" is the inner boundary of the diffusion layer. Since the diffuse layer thickness ($\sim 1/\kappa$, see Table 13.3.1) is normally much smaller than the diffusion layer thickness (typically micrometers even for dilute solutions and rather short experimental durations), this plane is operationally quite close to the electrode. Thus, in equations derived from diffusion theory, $C_O(0, t)$ is what we mean here as C_O^b.

An alternate way of expressing this idea is to note that when the electrode has a positive charge (i.e., $q^M > 0$), $\phi_2 > 0$, and anions (e.g., $z = -1$) will be attracted to the electrode surface, while cations (e.g., $z = +1$) will be repelled. For $q^M < 0$, the opposite effect will hold, while at the PZC, $q^M = 0$, $\phi_2 = 0$, and $C_O(x_2, t) = C_O^b$.

(b) The potential difference driving the electrode reaction is not $\phi^M - \phi^S$ (as in Section 3.4), but instead $\phi^M - \phi^S - \phi_2$; thus the effective electrode potential is $E - \phi_2$.

Consider the rate equation for a totally irreversible one-step, one-electron reaction as written previously (e.g., in Section 3.3):

$$\frac{i}{FA} = k^0 C_O(0, t) e^{-\alpha f(E - E^{0'})} \tag{13.7.3}$$

Let us now apply the correction in (13.7.2) and that for E. The equation written in terms of the true rate constant, k_t^0, is then

$$\frac{i}{FA} = k_t^0 C_O^b e^{-zf\phi_2} e^{-\alpha f(E - \phi_2 - E^{0'})} \tag{13.7.4}$$

or

$$\boxed{\frac{i}{FA} = k_t^0 e^{(\alpha - z)f\phi_2} C_O^b e^{-\alpha f(E - E^{0'})}} \tag{13.7.5}$$

By comparison of (13.7.3) and (13.7.5), noting that $C_O^b \approx C_O(0, t)$, we find

$$\boxed{k_t^0 = k^0 \exp\left[\frac{-(\alpha - z)F\phi_2}{RT}\right]} \tag{13.7.6}$$

This important relationship, in which the exponential term is sometimes called the *Frumkin correction*, allows the calculation of the true (or corrected) standard rate constant k_t^0 from the apparent one k^0. In a similar way, a true exchange current, $i_{0,t}$, can be defined as in (3.4.6):

$$i_{0,t} = FAk_t^0 C_O^{*(1-\alpha)} C_R^{*\alpha} \tag{13.7.7}$$

$$\boxed{i_{0,t} = i_0 \exp\left[\frac{-(\alpha - z)F\phi_2}{RT}\right]} \tag{13.7.8}$$

Alternative, and somewhat more rigorous, derivations of (13.7.6) and (13.7.8) can be obtained using the approach based on electrochemical potentials (34, 64), as outlined in the first edition.[7]

The overall effect of the double layer on kinetics (sometimes also referred to as "the ϕ_2 effect" or, in the Russian literature, as "the ψ effect") is that the apparent quantities, k^0 and i_0, are functions of potential, through the variation of ϕ_2 with $E - E_z$. They are functions of supporting electrolyte concentration as well, since ϕ_2 depends on it. Correction of apparent rate data to find the potential- and concentration-independent k_t^0 or $i_{0,t}$ therefore involves obtaining a value of ϕ_2 for the given experimental conditions based on some model for the double-layer structure (see Section 13.3).

---

[7]First edition, Sections 3.4 and 12.7.1.

13.7.2 Double-Layer Effects in the Absence of Specific Adsorption of Electrolyte

Corrections for the ϕ_2 effect can be made most readily for the mercury electrode, since the variation of σ^M with E and electrolyte concentration can be obtained from electrocapillary curves, as discussed in Section 13.2. In the absence of specific adsorption of electrolyte, ϕ_2 can then be calculated by assuming that the GCS model applies [from (13.3.26)]. Such corrections are less frequently attempted at solid electrodes because data about the double-layer structure at them is often lacking. Typical results showing such corrections for the reduction of Zn(II) at a Zn(Hg) electrode in aqueous solution (58) and for the reduction of several aromatic compounds in N,N-dimethylformamide solution (65) are given in Table 13.7.1. Note that for the Zn(II) reduction, where $z = 2$, and $\alpha = 0.60$, the i_0 value is larger than $i_{0,t}$ for negative ϕ_2 values, since the negative charge on the electrode attracts the positively charged zinc ion and this effect outweighs the kinetic effect of the potential drop in the diffuse double layer. On the other hand, for reduction of uncharged aromatic compounds, $z = 0$, $\alpha \approx 0.5$, and ϕ_2 is negative, so that k_t^0 is larger than k^0.

The correction factors in several different possible cases for the actual ϕ_2 values observed for a mercury electrode in NaF (66) are shown in Table 13.7.2. Clearly these factors can be quite large, especially at low concentrations of supporting electrolyte and at potentials distant from E_z. A number of other cases and details about the treatment of experimental data are discussed in more extensive reviews (16, 34).

While these results involving double-layer corrections are very useful in explaining supporting electrolyte effects on rate constants, we must be aware of several limitations in this treatment. The absence of specific adsorption of electrolyte, reactants, and products is a rather rare occurrence. The limitations of the GCS model, as well as the general lack of

TABLE 13.7.1 Typical Experimental Results Showing Corrections of Heterogeneous Electron-transfer Rate Data for Double-Layer Effects

A. Zn(II) Reduction at Zn(Hg)[a]

Supporting Electrolyte/M	ϕ_2/mV	i_0/mA cm^{-2}	$i_{0,t}$/mA cm^{-2}
0.025 Mg(ClO$_4$)	-63.0	12.0	0.39
0.05	-56.8	9.0	0.41
0.125	-46.3	4.7	0.38
0.25	-41.1	2.7	0.29

B. Reduction of Aromatics at Mercury in 0.5 M TBAP in DMF[b]

Compound	$E_{1/2}$/V vs. SCE	α	ϕ_2/mV	k^0/cm s^{-1}	k_t^0/cm s^{-1}
Benzonitrile	-2.17	0.64	-83	0.61	4.9
Phthalonitrile	-1.57	0.60	-71	1.4	7.5
Anthracene	-1.82	0.55	-76	5	26
p-Dinitrobenzene	-0.55	0.61	-36	0.9$_3$	2.2

[a]Data from reference 58, $T = 26 \pm 1°C$, $C_{Zn(II)} = 2$ mM, $C_{Zn(Hg)} = 0.048$ M. Exchange currents determined by galvanostatic method. $\alpha = 0.60$. Final column calculated according to (13.7.8). In the original literature, this case was analyzed under the assumption that it had a $2e$ RDS, so the authors found $\alpha = 0.3$. Treating it as a multistep process (Section 3.5), one finds best agreement with a mechanism having the first electron transfer upon reduction as the RDS with $\alpha = 0.6$.

[b]From reference 65, $T = 22 \pm 2°C$, concentration of compounds ~ 1 mM. Rate constants measured by ac impedance method. Final column calculated according to (13.7.6).

TABLE 13.7.2 Double-Layer Data for Mercury Electrode in NaF Solutions and Frumkin Correction Factors for Several Cases[a]

$E - E_z$ (V)	σ^M ($\mu C/cm^2$)	ϕ_2 (V)	Frumkin correction factors ($\alpha = 0.5$)[b]		
			$z = 0$	$z = 1$	$z = -1$
0.010 M NaF ($E_z = -0.480$ V $vs.$ NCE)					
-1.4	-23.2	-0.189	0.025	39.5	1.6×10^{-5}
-1.0	-16.0	-0.170	0.037	27.3	4.9×10^{-5}
-0.5	-8.0	-0.135	0.072	13.8	3.8×10^{-4}
0	0	0	1.0	1.0	1.0
$+0.5$	11.5	0.153	19.6	0.051	7.5×10^3
0.10 M NaF ($E_z = -0.472$ V $vs.$ NCE)					
-1.4	-24.4	-0.133	0.075	13.3	4.3×10^{-4}
-1.0	-17.0	-0.114	0.11	9.2	1.3×10^{-3}
-0.5	-8.9	-0.083	0.20	5.0	7.9×10^{-3}
0	0	0	1.0	1.0	1.0
$+0.5$	13.2	0.102	7.3	0.14	3.8×10^2
1 M NaF ($E_z = -0.472$ V $vs.$ NCE)					
-1.4	-25.7	-0.078	0.22	4.6	1.1×10^{-2}
-1.0	-18.0	-0.062	0.30	3.3	2.6×10^{-2}
-0.5	-9.8	-0.039	0.47	2.1	0.10
0	0	0	1.0	1.0	1.0
$+0.5$	14.9	0.054	2.9	0.35	23

[a]σ^M and ϕ_2 data taken from compilation (66) based on Grahame's data.
[b]Correction factor $= \exp[(\alpha - z)f\phi_2]$.

a single "plane of closest approach" when the electrolyte contains a number of different ions, leads to uncertainties in the correct values for ϕ_2 and x_2. Indeed these uncertainties often lead to sufficient differences in correction factors as to hinder a comparison of measured apparent rate constants with those predicted by different theories of electron transfer (65). In addition, the GCS model involves average potentials in the vicinity of the electrode and ignores the discrete nature of charges in solution. Such "discreteness of charge effects" have been treated and invoked to account for failures in the usual double-layer corrections (67).

13.7.3 Double-Layer Effects with Specific Adsorption of Electrolyte

When an ion from the supporting electrolyte (e.g., Cl^- or I^-) is specifically adsorbed, ϕ_2 is perturbed from the value calculated strictly from diffuse double-layer corrections. Specific adsorption of an anion will cause ϕ_2 to be more negative, while specific adsorption of a cation will cause ϕ_2 to be more positive. In principle, these effects could be taken into account using the Frumkin correction factor; however, the location of the plane of closest approach for the reacting species and the actual potential at the OHP often cannot be defined, and qualitative, rather than quantitative, explanations of these effects are usually given. Specific adsorption of an ion may also result in blocking of the electrode surface, as discussed in Section 13.6, and may inhibit the reaction, independent of the ϕ_2 effect. Consider the case of the polarographic reduction of CrO_4^{2-} at the DME. Because $z = -2$, the rate of reaction is very sensitive to ϕ_2 effects (68). The addition of quaternary
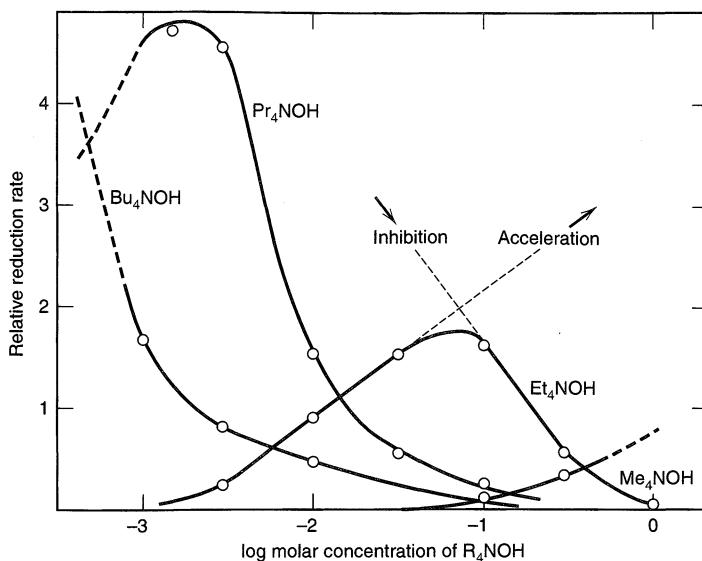
Figure 13.7.1 Variation of the rate of reduction of chromate (0.2 mM) in the presence of different tetra-alkylammonium hydroxides (R$_4$NOH) at -0.75 V *vs.* SCE and 25°C. (Me, methyl; Et, ethyl; Pr, propyl; Bu, butyl). [From L. Gierst, J. Tondeur, R. Cornelissen, and F. Lamy, *J. Electroanal. Chem.*, **10**, 397 (1965), with permission.]

ammonium (R$_4$N$^+$) hydroxides at low concentrations greatly accelerates the reduction, because R$_4$N$^+$ is specifically adsorbed from aqueous solutions, and this adsorption makes ϕ_2 more positive (Figure 13.7.1). At higher concentrations, however, the rate is decreased. This effect is attributed to blocking of the electrode surface and is clearly of more importance as the size of the R-group increases (Bu > Pr > Et > Me). Studies of the effects of double-layer structure on reaction rates, although frequently complicated, can provide information about details of the electrode reaction mechanism, the location of the reacting species, and the nature of the reacting site. See, for example, studies on the electroreduction of complex ions at a mercury electrode (69).

13.8 REFERENCES

1. P. Delahay, "Double Layer and Electrode Kinetics," Wiley-Interscience, New York, 1965, Chap. 2.

2. D. C. Grahame, *Chem. Rev.*, **41**, 441 (1947).

3. R. Parsons, *Mod. Asp. Electrochem.*, **1**, 103 (1954).

4. D. M Mohilner, *Electroanal. Chem.*, **1**, 241 (1966).

5. I. M. Klotz and R. M. Rosenberg, "Chemical Thermodynamics," 4th ed., Benjamin/Cummins, Menlo Park, CA, 1986.

6. D. C. Grahame, *Annu. Rev. Phys. Chem.*, **6**, 337 (1955).

7. B. E. Conway, "Theory and Principles of Electrode Processes," Ronald, New York, 1965, Chaps. 4 and 5.

8. R. Payne in "Techniques of Electrochemistry," Vol. 1, E. Yeager and A. J. Salkind, Eds., Wiley-Interscience, New York, 1972, pp. 43ff.

9. G. Lippmann, *Compt. Rend.*, **76**, 1407 (1873).

10. J. Heyrovský, *Chem. Listy*, **16**, 246 (1922).

11. J. Lawrence and D. M. Mohilner, *J. Electrochem. Soc.*, **118**, 259, 1596 (1971).

12. D. M. Mohilner, J. C. Kreuser, H. Nakadomari, and P. R. Mohilner, *J. Electrochem. Soc.*, **123**, 359 (1975).

13. D. J. Schiffrin in "Electrochemistry" (A Specialist Periodical Report), Vols. 1–3, G. J. Hills, Senior Reporter, Chemical Society, London, 1971–1973.

14. I. Morcos in "Electrochemistry" (A Specialist Periodical Report), Vol. 6, H. R. Thirsk, Senior Reporter, Chemical Society, London, 1978, p. 65ff.

15. P. Delahay, *op. cit.*, Chap. 3.

16. R. Parsons, *Adv. Electrochem. Electrochem. Engr.*, **1**, 1 (1961).

17. R. Payne, *J. Electroanal. Chem.*, **41**, 277 (1973).

18. R. M. Reeves, *Mod. Asp. Electrochem.*, **9**, 239 (1974).

19. F. C. Anson, *Accts. Chem. Res.*, **8**, 400 (1975).

20. H. L. F. von Helmholtz, *Ann. Physik*, **89**, 211 (1853).

21. G. Quincke, *Pogg. Ann.*, **113**, 513 (1861).

22. H. L. F. von Helmhotz, *Ann. Physik*, **7**, 337 (1879).

23. D. Halliday and R. Resnick, "Physics," 3rd ed., Wiley, New York, 1978, p. 664.

24. E. M. Pugh and E. W. Pugh, "Principles of Electricity and Magnetism," 2nd ed., Addison-Wesley, Reading, Mass., 1970, Chap. 1.

25. G. Gouy, *J. Phys. Radium*, **9**, 457 (1910).

26. G. Gouy, *Compt. Rend.*, **149**, 654 (1910).

27. D. L. Chapman, *Phil. Mag.*, **25**, 475 (1913).

28. E. M. Pugh and E. W. Pugh, *op. cit.*, pp. 69, 146.

29. O. Stern, *Z. Elektrochem.*, **30**, 508 (1924).

30. (a) S. L. Carnie and G. M. Torrie in "Advances in Chemical Physics," I. Prigogine and S. A. Rice, Eds., Wiley-Interscience, New York, 1984, Vol. 56, pp. 141–253; (b) L. Blum, *ibid.*, Vol. 78, 1990, pp. 171–222; (c) P. Attard, *ibid.*, Vol. 92, 1996, pp. 1–159.

31. P. Attard, *J. Phys. Chem.*, **99**, 14174 (1995).

32. P. Delahay, *op. cit.*, Chap. 4.

33. O. A. Esin and B. F. Markov, *Acta Physicochem. USSR*, **10**, 353 (1939).

34. P. Delahay, *op. cit.*, Chap. 5.

35. A. Hamelin, in *Mod. Asp. Electrochem.*, **16**, 1 (1985).

36. A. V. Gokhshtein, *Russ. Chem. Rev.*, **44**, 921 (1975).

37. R. E. Malpas, R. A Fredlein, and A. J. Bard, *J. Electroanal. Chem.*, **98**, 339 (1979).

38. R. Parsons, *Chem. Rev.*, **90**, 813 (1990).

39. F. T. Wagner in "Structure of Electrified Interfaces," J. Lipkowski and P. N. Ross, Eds., VCH, New York, 1993, Chap. 9.

40. R. M. Ishikawa and A. T. Hubbard, *J. Electroanal. Chem.*, **69**, 317 (1976).

41. A. T. Hubbard, *Chem. Rev.*, **88**, 633 (1988).

42. (a) J. Clavilier, R. Fauré, G. Guinet, and D. Durand, *J. Electroanal. Chem.*, **107**, 205 (1980); (b) J. Clavilier, D. El Achi, and A. Rodes, *Chem. Phys.*, **141**, 1 (1990).

43. D. M. Kolb in "Structure of Electrified Interfaces," J. Lipkowski and P. N. Ross, Eds., VCH, New York, 1993, Chap. 3.

44. B. E. Conway, T. Zawidzki, and R. G. Barradas, *J. Phys. Chem.*, **62**, 676 (1958).

45. N. A. Balashova and V. E. Kazarinov, *Electroanal. Chem.*, **3**, 135 (1969).

46. R. Parsons, *Trans. Faraday Soc.*, **55**, 999 (1959); *J. Electroanal. Chem.*, **7**, 136 (1964).

47. P. Delahay and I. Trachtenberg, *J. Am. Chem. Soc.*, **79**, 2355 (1957).

48. P. Delahay and C. T. Fike, *J. Am. Chem. Soc.*, **80**, 2628 (1958).

49. W. H. Reinmuth, *J. Phys. Chem.*, **65**, 473 (1961).

50. P. Delahay and D. M. Mohilner, *J. Am. Chem. Soc.*, **84**, 4247 (1962).

51. W. Lorenz, *Z. Elektrochem.*, **62**, 192 (1958).

52. S. Gilman, *Electroanal. Chem.*, **2**, 111 (1967).

53. J. Heyrovský and J. Kuta, "Principles of Polarography," Academic, New York, 1966.

54. C. N. Reilley and W. Stumm, in "Progress in Polarography," P. Zuman and I. M. Kolthoff, Eds., Wiley-Interscience, New York, 1962, Vol. 1, pp. 81–121.

55. H. W. Nurnberg and M. von Stackelberg, *J. Electroanal. Chem.*, **4**, 1 (1962).

56. A. N. Frumkin, *Dokl Akad. Nauk. S.S.S.R.*, **85**, 373 (1952); *Electrochim. Acta*, **9**, 465 (1964).

57. R. Parsons, *J. Electroanal. Chem.*, **21**, 35 (1969).

58. A. Aramata and P. Delahay, *J. Phys. Chem.*, **68**, 880 (1964).

59. T. Biegler and H. A. Laitinen, *J. Electrochem. Soc.*, **113**, 852 (1966).

60. K. K. Niki and N. Hackerman, *J. Phys. Chem.*, **73**, 1023 (1969); *J. Electroanal. Chem.*, **32**, 257 (1971).

61. R. Woods, *Electroanal. Chem.*, **9**, 1 (1976).

62. P. N. Ross, Jr., *J. Electrochem. Soc.*, **126**, 67 (1979).

63. A. N. Frumkin, *Z. Physik. Chem.*, **164A**, 121 (1933).

64. D. M. Mohilner and P. Delahay, *J. Phys. Chem.*, **67**, 588 (1963).

65. H. Kojima and A. J. Bard, *J. Am. Chem. Soc.*, **97**, 6317 (1975).

66. C. D. Russell, *J. Electroanal. Chem.*, **6**, 486 (1963).

67. W. R. Fawcett and S. Levine, *J. Electroanal. Chem.*, **43**, 175 (1973).

68. L. Gierst, J. Tondeur, R. Cornelissen, and F. Lamy, *J. Electroanal. Chem.*, **10**, 397 (1965).

69. M. J. Weaver and T. L. Satterberg. *J. Phys. Chem.*, **81**, 1772 (1977).

▷ 13.9 PROBLEMS

13.1 Prove that relative surface excesses are independent of the position of the dividing surface used in the reference system chosen for the thermodynamic treatment of the interface.

13.2 Derive the special case (13.3.11) from (13.3.10).

13.3 Present an argument, based only on Gaussian boxes, for a linear potential profile inside the compact layer.

13.4 Obtain (13.3.29) from (13.3.27).

13.5 Why do we view adsorbed neutral species as being intimately bound to the electrode surface, rather than being collected in the diffuse layer?

13.6 Interpret the data in Figures 13.9.1 and 13.9.2. How do the traces in Figure 13.9.2 relate to those in Figure 13.9.1? What implications can be derived from the flat region in the electrocapillary curves in the presence of n-heptyl alcohol? Construct a chemical model to explain the very low differential capacitance from -0.4 to -1.4 V in the presence of n-heptyl alcohol. Can you provide a formal (i.e., mathematical) rationale for the sharp peaks in C_d? Can you rationalize them chemically?
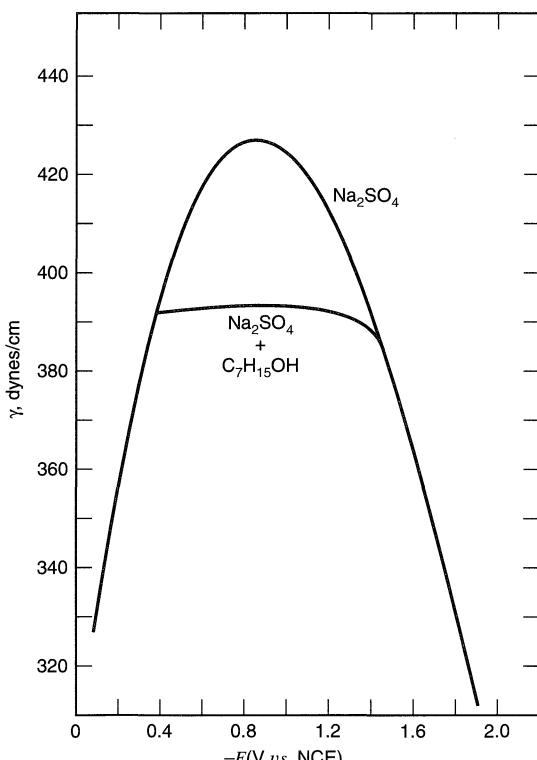
Figure 13.9.1 Electrocapillary curves for mercury in contact with 0.5 M Na_2SO_4 in the presence and absence of n-heptanol. Data from G. Gouy, *Ann. Chim. Phys.*, **8**, 291 (1906). [Reprinted with permission from D. C. Grahame, *Chem. Rev.*, **41**, 441 (1947). Copyright 1947, American Chemical Society.]
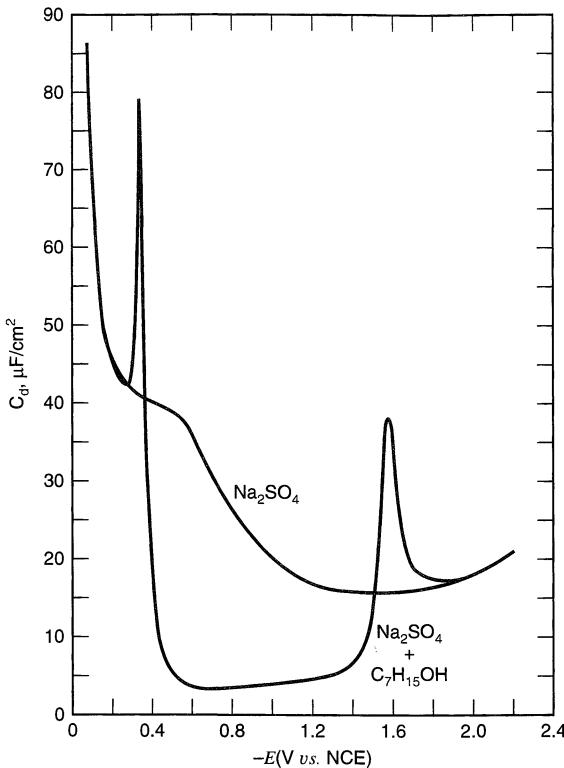
Figure 13.9.2 Differential capacitance curves corresponding to the systems of Figure 13.9.1. [Reprinted with permission from D. C. Grahame, *Chem. Rev.*, **41**, 441 (1947). Copyright 1947, American Chemical Society.]

13.7 A solution containing a certain organic compound, Z, at a concentration of 1.00×10^{-4} M shows a UV absorbance, $\mathscr{A}$, of 0.500 when measured at 330 nm in a spectrophotometric cell of path length 1.00 cm. Into 50 cm^3 of this solution, a platinum electrode with a surface area of 100 cm^2 is immersed. If the amount of Z adsorbed corresponds to 1.0×10^{-9} mol/cm^2, what will be the absorbance of this solution after adsorption equilibrium occurs?

13.8 The adsorption of a certain substance, X, follows a Langmuir isotherm. Saturation coverage of the material is 8×10^{-10} mol/cm^2 and $\beta = 5 \times 10^7$ cm^3/mol (assuming $a_i = C_i$). At what concentration of X will the electrode surface be half covered (i.e., $\theta = 0.5$)? Sketch the adsorption isotherm of the substance. At what concentrations of X will the linearized isotherm be valid to ~1%?

13.9 For the substance X in Problem 13.8, under linearized conditions and taking $D = 10^{-5}$ cm^2/s, how long after immersion will be required for the surface of a plane electrode to attain half of the equilibrium coverage (see Figure 13.5.3)? How long will be required to attain half of equilibrium coverage if the solution is stirred and $m = 10^{-2}$ cm/s?

13.10 Derive, using a kinetic model, the Langmuir isotherms for the simultaneous adsorption of two species, i and j [see (13.5.9) and (13.5.10)].

13.11 Calculate the values of σ^M corresponding to various values of ϕ_2 (from -0.2 to $+0.2$ V) for a mercury electrode in 0.01 M NaF based on the GCS model. (a) Plot ϕ_2 vs. σ^M. (b) From the variation of σ^M with $E - E_z$, shown in Table 13.7.2, prepare a plot of ϕ_2 vs. $E - E_z$.

13.12 Because of the Frumkin effect, Tafel plots are not linear and have the following varying slopes in the cathodic region:

$$f\left[-\alpha + (\alpha - z)\left(\frac{\partial \phi_2}{\partial \eta}\right)\right]$$

(a) Derive this equation. (b) Asada, Delahay, and Sundaram [*J. Am. Chem. Soc.*, **83**, 3396 (1961)] suggested that a plot of $\ln[i \exp(zF\phi_2/RT)]$ against $\phi_2 - \eta$ (a "corrected Tafel plot") is linear and has a slope of $\alpha F/RT$. Show, by suitable manipulation of the equations, that this is so.

13.13 Aramata and Delahay (58) found that for a solution containing 2 mM Zn(II) and 0.025 M Ba(ClO$_4$)$_2$ at a Zn(Hg) electrode containing 0.048 M Zn, the apparent exchange current density was 9.1 mA/cm^2. At the equilibrium potential for this system, $\phi_2 = -60.8$ mV. Calculate $i_{0,t}$ and k_t^0, given $\alpha = 0.60$ and $z = +2$. See Table 13.7.1, footnote a.

13.14 Write a spreadsheet program for the Frumkin isotherm, (13.5.14), to calculate θ vs. C_i curves for g' = −2, 0, and 2. Discuss how attractive ($g' = 2$) and repulsive ($g' = -2$) interactions affect the isotherm.

13.15 The potential dependence of adsorption can be treated by expanding $\Delta \overline{G}_i^0$, as is usually done for electrochemical potentials, into a standard free energy of adsorption at $E = 0$ (against an arbitrary reference electrode) and the potential dependence, $z_i F(\phi^A - \phi^b)$. (See equation 13.5.3.) This yields for the Langmuir isotherm

$$\frac{\theta}{1-\theta} = a_i^b \exp(-\Delta G_{ads}^0/RT) \exp(-z_i FE/RT)$$

which is sometimes written

$$\frac{\theta}{1-\theta} = C_i K_{i,ads} \exp(-z_i FE/RT)$$

where $K_{i,ads}$ is the "equilibrium constant for adsorption." Derive these equations. What do they predict about the effect of potential on the adsorption of anions and cations? What is neglected in this model (e.g., to account for the behavior of neutral species)? Derive the equivalent expression for the Frumkin isotherm.

14

ELECTROACTIVE LAYERS AND MODIFIED ELECTRODES

14.1 INTRODUCTION—INTELLECTUAL AND TECHNOLOGICAL MOTIVATIONS

Chapter 13 was largely concerned with adsorbed species that are not electroactive. In this chapter we consider electroactive monolayers and thicker films on conductive substrates; these are frequently called *chemically modified electrodes*. This area of electrochemistry has been a very active one in recent years, and a number of reviews discussing the preparation, characterization, and electrochemical behavior of chemically modified electrodes are available (1–14). These electrodes are often prepared by the modification of a conductive substrate to produce an electrode suited to a particular function, whose properties are different from those of the unmodified substrate. Modified electrodes can be prepared in several different ways, as discussed in Section 14.2, including irreversible adsorption, covalent attachment of a monolayer, and coating the electrode with films of polymers or other materials.

The strong, and sometimes irreversible, adsorption of a species to an electrode surface will often change the electrochemical behavior of an electrode. For example, the adsorption of CN^- on Pt increases the hydrogen overpotential and thus extends the range of the electrode to more negative potentials in electroanalytical applications. Conversely, adsorption of alkaloids and proteins on Hg decreases the hydrogen overpotential; polarographic waves produced in this way with solutions containing cobalt ions and small amounts of proteins or other sulfhydryl-containing species (Brdička waves) were investigated many years ago (15). Purposeful covering of electrode surfaces with adsorbed layers or films can also change the electron-transfer rates at an electrode surface. For example, a Pt electrode immersed in an acidic solution containing Sn(IV), when subjected to potentials where hydrogen is evolved, becomes coated with a layer of hydrous tin oxide because of the pH increase at the electrode surface. This layer increases the hydrogen overpotential and allows a Pt electrode to be used for the coulometric generation of Sn(II) from Sn(IV), a process not possible at a bare Pt electrode because of concomitant hydrogen evolution (16).

In the 1970s, interest arose in the modification of electrode surfaces by covalent attachment of monolayers of different species to electrode surfaces. Electrodes modified with thicker polymeric films and inorganic layers were introduced later. Paralleling this work was activity in the field of electronically conductive polymers and organic metals, many of which can be produced electrochemically. More complex structures (bilayers, arrays, biconductive films) have also been prepared.

Interest in chemically modified electrodes is based mainly on possible applications. Electrocatalysis has been of prime interest. For example, an electrode of an inexpensive and rugged material that could reduce oxygen to water effectively at a potential near the thermodynamic one would find wide use in fuel cells, batteries, and other electrochemical systems. Modified electrodes involving materials that change color upon oxidation and reduction could be employed in electrochromic devices, such as displays or "smart" windows and mirrors. There are also examples of surface films that emit light upon electrochemical excitation (electrogenerated chemiluminescence, Chapter 18). These have the potential for use as active displays. Another application of modifying layers is to protect the underlying substrate from corrosion or chemical attack during use. Layers of different materials on semiconductor electrodes have been suggested for this application. Modified electrodes can also serve as analytical sensors and reference electrodes. Finally, there is growing interest in molecular electronic devices, that is, electrochemical systems that can mimic the behavior of diodes, transistors, and electrical networks.

In addition to these applications, however, studies with modified electrodes have proven useful in the characterization of electron- and mass-transfer processes in polymers and other materials (as discussed in Section 14.4) and in gaining insight into how surface structures can be designed to carry out specified reactions or processes.

▶ 14.2 TYPES, PREPARATION, AND PROPERTIES OF FILMS AND MODIFIED ELECTRODES

14.2.1 Substrates

The *substrate* is the platform upon which the modifying layer assembled. Typically it is a material that is also used in an unmodified form as an electrode, such as a metal (Pt, Au), carbon, or a semiconductor (SnO_2). Generally substrates are chosen for good mechanical and chemical stability and are frequently pretreated before modification, such as by polishing or by a chemical or electrochemical procedure which prepares the surface for subsequent modification steps, as discussed below. For applications where extreme smoothness of the surface is important, materials like HOPG, single crystals of metals, or metal films evaporated on a mica substrate can be used. In other applications a high surface area may be desired; this can sometimes be obtained by extended electrochemical cycling of the electrode or by forming the electrode by sintering of small particles.

14.2.2 Monolayers

Monolayers can be formed on electrode surfaces by irreversible adsorption or covalent attachment, or, in the form of organized assemblies, by Langmuir–Blodgett transfer and self-assembly techniques.

(a) Irreversible Adsorption
As discussed in Section 13.5, many substances spontaneously adsorb on a substrate surface from solution, generally because the substrate environment is energetically more favorable than that in solution (Figure 14.2.1). For example, sulfur-containing species are strongly held on mercury, gold, and other metal surfaces, because of strong metal–sulfur interactions. When a mercury electrode is placed in contact with a solution containing only small ($<\mu M$) amounts of cystine or a sulfur-containing protein, such as bovine serum albumin, a monolayer forms on the Hg surface. Electrochemical oxidation and reduction of the surface species can then be observed. Strong adsorption from aqueous solu-

(a)

(b)
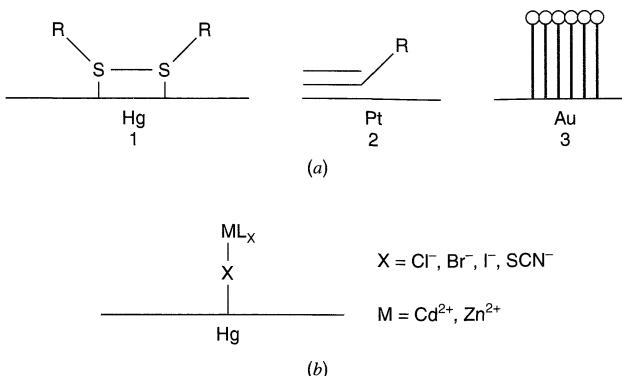
Figure 14.2.1 Examples of specific adsorption on electrodes. (a) Adsorption of (1) a disulfide or protein on Hg; (2) an olefin on Pt; (3) an organized Langmuir-Blodgett film on Au. (b) Adsorption of a metal ion or complex through an anionic ligand bridge. [From A. J. Bard, "Integrated Chemical Systems," Wiley, New York, 1994, with permission.]

tions of some ions (e.g., halides, SCN^-, CN^-) and many organic compounds (especially those containing aromatic rings, double bonds, and long hydrocarbon chains) takes place on metal or carbon surfaces. A typical example (displayed below in Figure 14.3.3) is that of 9,10-phenanthraquinone (PAQ), which forms a monolayer on the basal plane of pyrolytic graphite simply by immersion into a solution of the PAQ in 1 M $HClO_4$ (17). The electrochemical response shows that 37 μC of charge/cm^2 of electrode surface is passed during the reduction and reoxidation steps; this is equivalent to 1.9×10^{-10} mol PAQ/cm^2 or 1.1×10^{14} molecules/cm^2 (for a two-electron redox process). Adsorption of metal ions that normally would not adsorb can take place by anion-induced adsorption (Figure 14.2.1b). In this case the strong adsorption of an anion (e.g., SCN^- on Hg) that can act as a ligand for a particular metal, M, will induce its adsorption on the substrate.
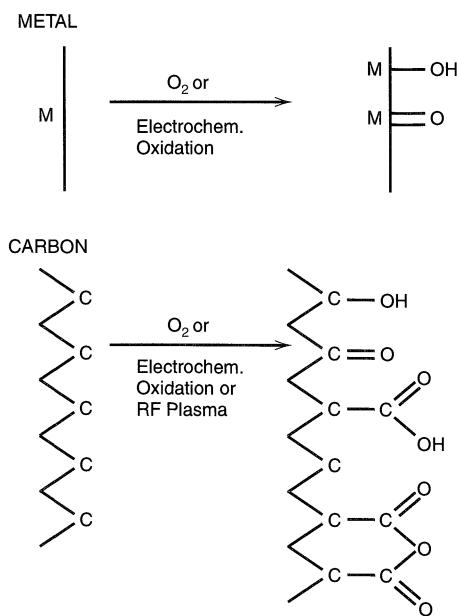
Figure 14.2.2 Formation of functional groups on a metal or a carbon surface via oxidation before treatment with linking agents. [From A. J. Bard, "Integrated Chemical Systems," Wiley, New York, 1994, with permission.]

(b) Covalent Attachment

Stronger attachment to the substrate surface can be accomplished by covalent linking of the desired component to surface groups present on, or formed on, the substrate. These covalent linking procedures frequently employ organosilanes and other linking agents and are discussed in detail in several references (2, 8, 12). The substrate surface is usually pre-treated, e.g., by an oxidative reaction, to form surface groups (Figure 14.2.2). The surface is then treated with the linking agent and the desired component. Favorite components linked to electrode surfaces in this way, because they show easily detected electrochemical reactions, include various ferrocenes, viologens, and $M(bpy)_x^{n+}$ species (M = Ru, Os, Fe). Typical covalent attachments and the electrochemical responses of the layers are shown in Figure 14.2.3. A table listing many examples of such electrodes is given in reference 2.
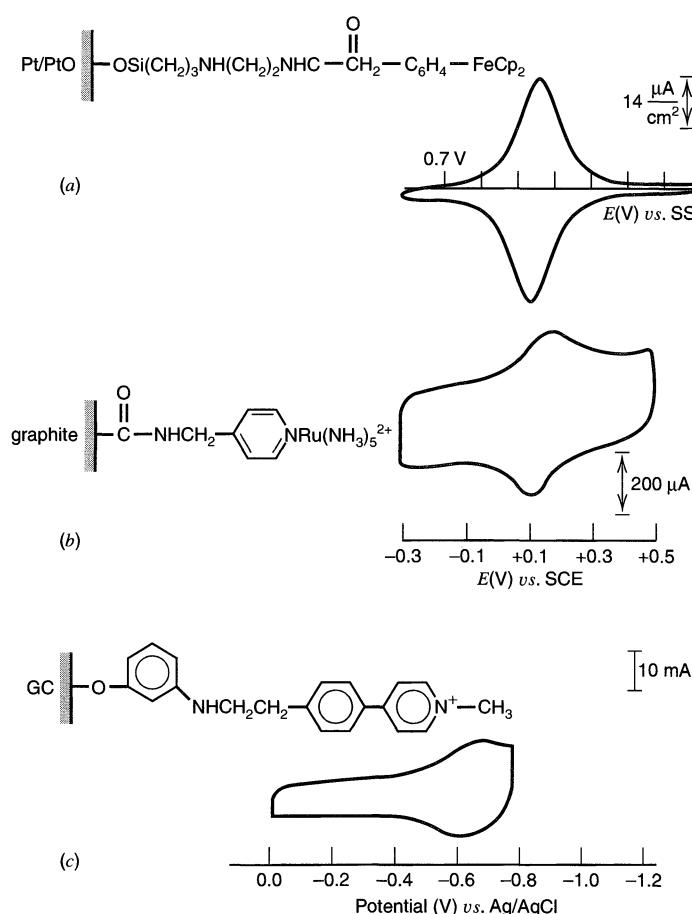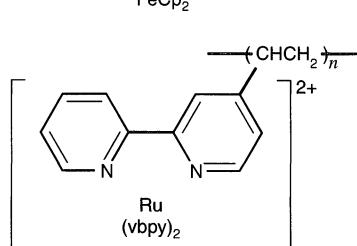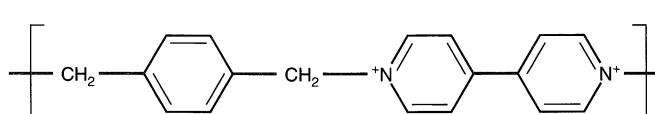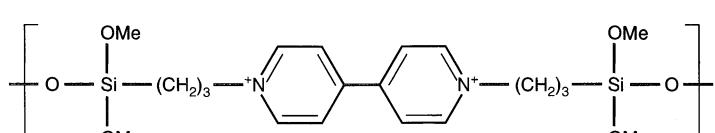
Figure 14.2.3 Cyclic voltammograms of electrodes modified by covalent attachment of monolayers of different types. (*a*) Pt electrode with attached ferrocene, 200 mV/s. [Reprinted with permission from J. R. Lenhard and R. W. Murray, *J. Am. Chem. Soc.*, **100**, 7870 (1978). Copyright 1978, American Chemical Society.] (*b*) Graphite with attached py-$Ru(NH_3)_5$, 5 V/s. [Reprinted with permission from C. A. Koval and F. C. Anson, *Anal. Chem.*, **50**, 223 (1978). Copyright 1978, American Chemical Society.] (*c*) Glassy carbon with attached viologen, 100 mV/s. [Reprinted from D. C. S. Tse, T. Kuwana, and G. P. Royer, *J. Electroanal. Chem.*, **98**, 345 (1979), with permission from Elsevier Science.]

(c) Organized Assemblies

Monolayers of surface-active compounds [Langmuir–Blodgett (LB) films] can be transferred from the liquid/air interface to a substrate surface. For example, an organized monolayer can be formed on an SnO_2 surface by using a film balance to transfer molecules consisting of a viologen head group with a long chain hydrocarbon tail (18). Alternatives to LB films are self-assembled monolayer films that can be formed without a film balance. We define *self-assembly* as a spontaneous process leading to a structure with some degree of order imposed by lateral interactions among the component molecules. Good examples involve layers of organosulfur (e.g., thiol) compounds with long chain alkyl groups on Au. The thiol head-groups bind tightly to the gold, and the lateral interactions between neighboring alkyl chains create a regular structure in which the chains are extended in parallel at an angle from the normal (see Figures 3.6.7 and 14.5.6). Self-

TABLE 14.2.1   Typical Polymers Used for Electrode Modification[a]

Name	Structure	Abbreviation
	Electroactive Polymers	
Poly(vinylferrocene)		PVF
Poly[Ru(vbpy)$_3^{2+}$][b]		
Poly(xylylviologen)		
Polymerized viologen organosilane		PQ^{2+}
	Ion-exchange Polymers (Polyelectrolytes)	
Nafion		NAF
Poly(styrenesulfonate)		PSS

(continued)
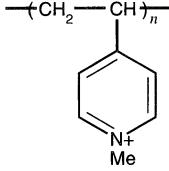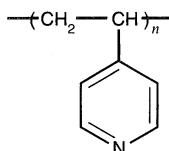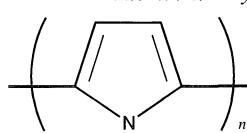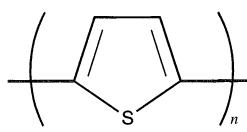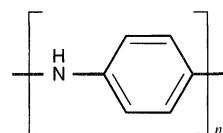
assembled alkyl siloxane monolayers can be formed by treating surfaces containing hydroxyl groups with long chain alkyl trichlorosilanes (19).

14.2.3 Polymers

(a) Types

By using polymeric modifying layers, fairly thick films, containing many more electroactive sites than a monolayer, can be formed on an electrode surface. Several different types of polymers have been used to modify electrode surfaces (Table 14.2.1). *Electroactive polymers* contain oxidizable or reducible groups covalently linked to the polymer backbone. Typical examples are poly(vinylferrocene) and polymerized $Ru(vbpy)_3^{2+}$. *Coordinating (ligand-bearing) polymers*, such as poly(4-vinylpyridine), contain groups that can

TABLE 14.2.1 *(continued)*

Name	Structure	Abbreviation
	Ion-exchange Polymers (Polyelectrolytes)	
Quaternized poly (4-vinylpyridinium)	$-(CH_2-CH)_n-$ N+ Me	QPVP
	Coordinating Polymer	
Poly(4-vinylpyridine)	$-(CH_2-CH)_n-$ N	PVP
	Electronically Conducting Polymers[c]	
Polypyrrole	N	PP
Polythiophene	S	PT
Polyaniline	H N	PANI

[a]Adapted from A. J. Bard, "Integrated Chemical Systems," Wiley, New York, 1994, pp 142–143.
[b]vbpy = 4-vinyl-2,2'-bipyridine.
[c]Shown in the reduced (nonconductive) state. These polymers become conductive after oxidation and the incorporation of anions.

coordinate to species like metal ions and bring them into the polymer matrix. *Ion-exchange polymers (polyelectrolytes)* contain charged sites that can bind ions from solution via an ion-exchange process; typical examples are Nafion, polystyrene sulfonate, and protonated poly(4-vinylpyridine). *Electronically conductive polymers*, such as polypyrrole and polyaniline, can also be considered as ion-exchange materials, since the polymer redox processes are usually accompanied by incorporation of ions into the polymer network. *Biological polymers*, such as enzymes and other proteins, are often useful in sensor applications. *Blocking polymers* are formed from the monomers, such as by oxidation of phenols, to produce impermeable layers and blocked or passivated surfaces.

(b) Preparation

Polymer films can be formed on an electrode surface from solutions of either the polymer or the monomer. Methods that start with dissolved polymer include cast or dip coating, spin coating, electrodeposition, and covalent attachment via functional groups. Starting with the monomer, one can produce films by thermal, electrochemical, plasma, or photochemical polymerization.

14.2.4 Inorganic Films

Different types of inorganic materials, such as metal oxides, clays, and zeolites, can also be deposited on electrode surfaces. Such films are of interest, because they frequently show well-defined structures (e.g., they have unique pore or interlayer sizes), they are thermally and chemically very stable, and are usually inexpensive and readily available. A few examples will be described.

(a) Metal Oxides

Films of oxides can be produced by anodization of metal electrodes. For example, Al_2O_3 forms on an aluminum anode immersed in a solution of H_3PO_4. The thickness of the film can be controlled by the applied potential and the time of anodization. Such a film can be used as a support for other materials, such as poly(vinylpyridine) (PVP). Oxide films of other metals, such as Ti, W, and Ta, can be produced in a similar way. Oxide films can also be produced by CVD, vacuum evaporation and sputtering, and deposition from colloidal solution. Related inorganic films are those of polyoxometallates (iso- and heteropolyacids and their salts) (20). For example, the heteropolyanion $P_2W_{17}MoO_{62}K_6$ shows a number of reduction waves at a glassy carbon electrode. A wide variety of metallic polyanionic species (e.g., of W, Mo, V) exist and have a rich chemistry. Films of such materials are interesting for their electrocatalytic possibilities.

(b) Clays and Zeolites

Clays and zeolites, both naturally-occurring and synthetic, are aluminosilicates with well-defined structures that usually show ion-exchange properties (10, 21). In addition to their high stability and low cost, they often show catalytic properties and have been widely used as heterogeneous catalysts. Clay layers can be "pillared" by treatment with appropriate inorganic or organic agents, such as polyoxyanions of Fe, Al, or Zr, to form structures between the silicate layers that maintain the interlayer spacing at a given value (e.g., ~ 17 Å). Films of clay can be cast on substrate surfaces and will remain intact when they are used as electrodes. Electroactive cations, such as $Ru(bpy)_3^{2+}$ or MV^{2+}, can be exchanged into the clay film and show typical cyclic voltammetric responses of surface-confined species. Zeolites are aluminosilicates with structures consisting of well-defined cages and pores. These also show ion-exchange properties and can be employed as modifying layers

on electrode surfaces. For example, a suspension of zeolite Y particles, $\sim$1 μm diameter, containing a small amount of polystyrene as a binder in THF can be used to cast a film on a SnO_2 electrode surface. The film, of about 60 μm total thickness, shows most of the polystyrene forming a porous layer at the outer (solution) surface of the film, with only a first few micrometers of zeolite on the inner (electrode) side active for electrochemical reactions. Ions, such as $Ru(bpy)_3^{2+}$ and $Co(CpCH_3)_2^+$, can be incorporated into the film by soaking the formed electrode in the appropriate solution or by pre-soaking the zeolite particles before the film is cast.

(c) Transition-Metal Hexacyanides
Thin films of materials such as Prussian Blue (PB) (a lattice of ferric ferrocyanide) and related materials can be formed on electrode surfaces and show interesting properties (22). PB can be deposited on a suitable substrate by electrochemical reduction in a solution of $FeCl_3$ and $K_3Fe(CN)_6$. The resulting blue film, which is often given the formula $KFe^{III}Fe^{II}(CN)_6$, can be oxidized in a KCl solution to form $Fe^{III}Fe^{III}(CN)_6$ (Berlin Green) and reduced to form $K_2Fe^{II}Fe^{II}(CN)_6$ (Everitt's salt). PB electrodes show electrocatalytic properties (e.g., for the reduction of oxygen) and the color changes that occur suggest possible electrochromic applications. Other metal ferricyanide films have also been studied. For example, a film of nickel ferricyanide can be deposited by oxidizing a nickel electrode in the presence of ferricyanide.

14.2.5 Biologically Related Materials

Many electrodes modified with biologically-derived materials have been described, usually in connection with the preparation of electrochemical sensors (23). The basic approach in such biosensors involves the immobilization of a biologically sensitive coating (e.g., an enzyme, antibody, DNA) which can interact with ("recognize") a target analyte, and in the process, produce an electrochemically detectable signal. Probably the most highly developed are electrodes containing surface-confined enzymes (24). Related types of electrodes involve suspensions of bacteria and slices of tissue. In many cases, the enzyme or suspension is simply held in the vicinity of the electrode by a permeable polymer membrane, such as a dialysis membrane. Alternative methods of immobilization include entrapment in a gel, encapsulation, adsorption, and covalent linkage.

14.2.6 Composites and Multilayer Assemblies

In addition to the modified electrodes described in the previous sections, which usually involve a conductive substrate and a single film of modifying material, more complicated structures have been described. Typical examples (Figure 14.2.4) include multiple films of different polymers (e.g., bilayer structures), metal films formed on the polymer layer (sandwich structures), multiple conductive substrates under the polymer film (electrode arrays), intermixed films of ionic and electronic conductor (biconductive layers), and polymer layers with porous metal or minigrid supports (solid polymer electrolyte or iongate structures) (6, 7). These often show different electrochemical properties than the simpler modified electrodes and may be useful in applications such as switches, amplifiers, and sensors.

    Porous metal films, such as Pt or Au, can be deposited on free-standing polymer membranes or on polymer films on an electrode surface by chemical reduction or by evaporation in vacuum. For example, a porous film of Pt can be deposited on a Nafion
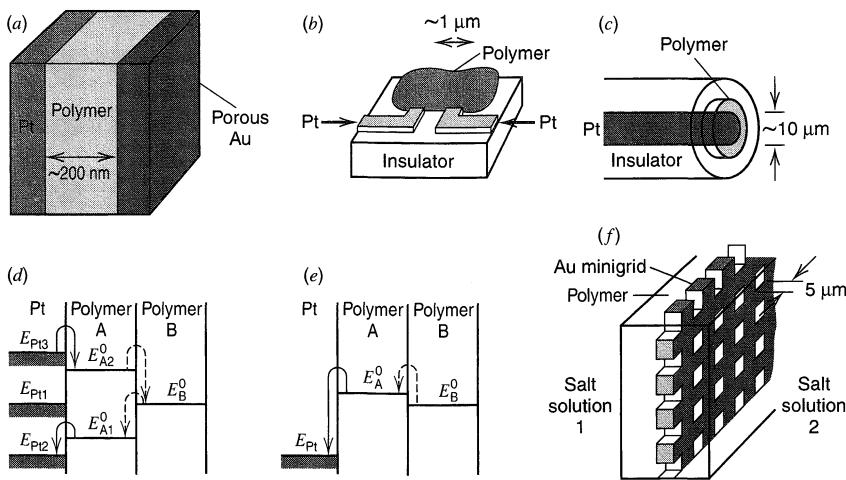
Figure 14.2.4 More complex modified electrode structures based on electroactive polymers. (*a*) Sandwich electrode; (*b*) array electrode; (*c*) microelectrode; (*d, e*) bilayer electrodes; (*f*) ion-gate electrode. [Reprinted with permission from C. E. D. Chidsey and R. W. Murray, *Science*, **231**, 25 (1986), copyright 1986, American Association for the Advancement of Science.]

membrane by clamping it between a solution of $PtCl_6^{2-}$ and a solution of a reducing agent, such as hydrazine. The reducing agent diffuses through the membrane and causes precipitation of metallic Pt on the membrane surface and partially within the membrane structure as well. Such structures are of interest as electrodes in *solid polymer electrolyte* (SPE) cells, employed, for example, in fuel cells and for water electrolysis. In the former application two porous Pt films on either side of a Nafion membrane form the anode (for hydrogen oxidation) and the cathode (for oxygen reduction). Deposition of a porous metal on top of a polymer film formed on a conductive substrate leads to a structure in which a thin polymer film is sandwiched between two electronically conductive films, at least one of which is porous to solution or gas phase species. While this structure is formally similar to that used in SPE electrolysis, the polymer films in these are much thinner and are usually deposited on a nonporous conducting substrate before formation of the second, porous, metal layer.

A bilayer structure usually consists of two different films deposited on a substrate, one overlying the other. A typical system consists of a Pt substrate with an electrodeposited film of poly-$[Ru(vbpy)_3^{2+}]$ on which a film of poly-$[Os(bpy)_2(vbpy)_2^{2+}]$ is electrodeposited (25).[1] Another type of sandwich structure involves a pair of closely spaced electrodes such as in an electrode array (26), bridged by a polymer film. Alternatively, a different polymer can be deposited on each electrode of an array pair to form a bilayer-like arrangement having a junction where the films meet. Three-electrode devices of this type can produce a structure functionally equivalent to a field effect transistor (FET) (27).

Multicomponent structures containing both electronic and ionic conductors, called *biconductive films* (or mixed conductivity composites), can be fabricated electrochemically. Interest in these stems from the possibility of improving the rates of charge transport through the films and of incorporating catalysts or semiconductor particles within an ionically conducting polymer layer. An early example of this kind of structure was the deposition of the electronically conducting solid tetrathiafulvalenium bromide (TTF^+Br^-) within a Nafion

[1]vbpy = 4-vinyl-2,2'-bipyridine.

layer on an electrode (28). Electronically conductive polymers can also be deposited within ionically conductive supports. For example, polypyrrole can be formed inside Nafion or clay layers by electrochemical oxidation of a pyrrole solution (29). These films show electrochemical and mechanical properties that are different from those of the single component (Nafion or polypyrrole). Biconductive films are also formed when metal clusters are produced within ionic polymers, for example, the deposition of Cu and Ag at poly[Ru(bpy)$_2$(vpy)$_2$]$^{2+}$ (30).

▶ 14.3 ELECTROCHEMICAL RESPONSES OF ADSORBED MONOLAYERS

14.3.1 Principles

The electrochemical response (e.g., the voltammetric i-E curve) for the electrode reaction $O + ne \rightarrow R$ can be affected quite significantly by the adsorption of O or R. In this section, we will examine the consequences of strong or weak adsorption of either or both species. First we consider the behavior of an electroactive species, O, when it is so strongly adsorbed that the contribution of dissolved O to the response is negligible, as well as the case where both adsorbed O and dissolved O undergo electrode reactions.

The treatment of such problems is more complicated than those involving only dissolved species, because one must choose an adsorption isotherm, which involves the introduction of additional parameters and, in general, nonlinear equations. In addition, the treatment must include assumptions about (a) the degree to which adsorption equilibrium is attained before the start of the electrochemical experiment (i.e., how long after the formation of a fresh electrode surface the experiment is initiated) and (b) the relative rate of electron transfer to the adsorbed species compared to that for the dissolved species. These effects complicate the evaluation of the voltammetric data and make the extraction of desired mechanistic and other information more difficult. Thus adsorption is often considered a nuisance to be avoided, when possible, by changing the solvent or changing concentrations. However, adsorption of a species is sometimes a prerequisite for rapid electron transfer (as in forms of electrocatalysis), and can be of major importance in processes of practical interest (e.g., the reduction of O$_2$, the oxidation of aliphatic hydrocarbons, or the reduction of proteins). Our discussion here will deal with the basic principles and several important cases.

The equations governing the voltammetric method (e.g., assuming only species O is present initially) include the same ones as used previously, namely the mass-transfer equations [such as (5.4.2)] and the initial and semi-infinite conditions (5.4.3) and (5.4.4). However, the flux condition at the electrode surface is different, because the net reaction involves the electrolysis of diffusing O as well as O adsorbed on the electrode, to produce R that diffuses away and R that remains adsorbed. The general flux equation is then

$$D_O\left[\frac{\partial C_O(x, t)}{\partial x}\right]_{x=0} - \frac{\partial \Gamma_O(t)}{\partial t} = -\left[D_R\left(\frac{\partial C_R(x, t)}{\partial x}\right)_{x=0} - \frac{\partial \Gamma_R(t)}{\partial t}\right] = \frac{i}{nFA} \quad (14.3.1)$$

where $\Gamma_O(t)$ and $\Gamma_R(t)$ are the amounts of O and R adsorbed at time t (mol/cm^2). The introduction of these terms requires additional equations relating Γ to C. Most frequently, one assumes the Langmuir (or linearized Langmuir) isotherms, for example, see (13.5.9) and (13.5.10):

$$\Gamma_O(t) = \frac{\beta_O \Gamma_{O,s} C_O(0, t)}{1 + \beta_O C_O(0, t) + \beta_R C_R(0, t)} \quad (14.3.2)$$

$$\Gamma_R(t) = \frac{\beta_R \Gamma_{R,s} C_R(0, t)}{1 + \beta_O C_O(0, t) + \beta_R C_R(0, t)} \quad (14.3.3)$$

Initial conditions must also be supplied, for example,

$$(t = 0) \qquad \Gamma_O = \Gamma_O^* \qquad \Gamma_R = 0 \tag{14.3.4}$$

The other equations appropriate to the given electrochemical method and the rates of electron transfer are then added and a solution of the problem is attempted.

14.3.2 Cyclic Voltammetry: Only Adsorbed O and R Electroactive—Nernstian Reaction

Let us consider the case where adsorbed O, but not dissolved O, is electroactive (31–33). This could be the case when the sweep rate, v, is so large that O does not have time to diffuse appreciably to the electrode surface [i.e., $D_O(\partial C_O(0, t)/\partial x)_{x=0} \ll \partial \Gamma_O(t)/\partial t$]. Alternatively, the wave for adsorbed O could be shifted to potentials well before the reduction wave for dissolved O. The conditions for such behavior will be given below. There are also cases where adsorption is so strong that the adsorbed layer of O can form even when the solution concentration is so small that the contribution to the current from dissolved O is negligible. We also assume that within the range of potentials of the wave, the Γ's are independent of E. Under these conditions, (14.3.1) becomes

$$-\frac{\partial \Gamma_O(t)}{\partial t} = \frac{\partial \Gamma_R(t)}{\partial t} = \frac{i}{nFA} \tag{14.3.5}$$

Equation (14.3.5) implies that reduction of adsorbed O produces adsorbed R with no adsorption or desorption occurring during the scan. This equation, along with (14.3.4), yields

$$\Gamma_O(t) + \Gamma_R(t) = \Gamma_O^* \tag{14.3.6}$$

From (14.3.2) and (14.3.3),

$$\frac{\Gamma_O(t)}{\Gamma_R(t)} = \frac{\beta_O \Gamma_{O,s} C_O(0, t)}{\beta_R \Gamma_{R,s} C_R(0, t)} = \frac{b_O C_O(0, t)}{b_R C_R(0, t)} \tag{14.3.7}$$

with $b_O = \beta_O \Gamma_{O,s}$, $b_R = \beta_R \Gamma_{R,s}$. If the reaction is nernstian, so that

$$\frac{C_O(0, t)}{C_R(0, t)} = \exp\left[\left(\frac{nF}{RT}\right)(E - E^{0'})\right] \tag{14.3.8}$$

then (14.3.7) yields

$$\frac{\Gamma_O(t)}{\Gamma_R(t)} = \left(\frac{b_O}{b_R}\right) \exp\left[\left(\frac{nF}{RT}\right)(E - E^{0'})\right] \tag{14.3.9}$$

From (14.3.5), (14.3.6), and (14.3.9), with

$$\frac{i}{nFA} = \frac{-\partial \Gamma_O(t)}{\partial t} = \left[\frac{\partial \Gamma_O(t)}{\partial E}\right]v \tag{14.3.10}$$

and $E = E_i - vt$, the equation for the i-E curve is obtained:

$$i = \frac{n^2 F^2}{RT} \frac{vA\Gamma_O^*(b_O/b_R) \exp[(nF/RT)(E - E^{0'})]}{\{1 + (b_O/b_R) \exp[(nF/RT)(E - E^{0'})]\}^2} \tag{14.3.11}$$

Note the similarity between this equation and that derived for a thin-layer cell (11.7.16). This is readily understandable, since the sample is fully converted without mass-transfer limitations in both cases. In the thin-layer cell, VC_O^* moles of O are elec-

trolyzed during the potential sweep, compared to $A\Gamma_O^*$ moles of adsorbed O on the electrode surface. Thus the i-E curve (Figure 14.3.1) has the same shape as that in Figure 11.7.3. The peak current is given by

$$i_p = \frac{n^2F^2}{4RT}\, vA\Gamma_O^*$$

(14.3.12)

and the peak potential by

$$E_p = E^{0'} - \left(\frac{RT}{nF}\right)\ln\left(\frac{b_O}{b_R}\right) = E_a^{0'}$$

(14.3.13)

The peak current, and indeed the current at each point on the wave, is proportional to v, in contrast to the $v^{1/2}$ dependence observed for nernstian waves of diffusing species. The proportionality between i and v is the same as that observed for a purely capacitive current [see (6.2.25)], and this fact has led to some treatments of adsorption in terms of pseudocapacitances (32, 34). The area under the reduction wave, corrected for any residual current, represents the charge required for the full reduction of the layer, that is, $nFA\Gamma_O^*$. The anodic wave on scan reversal is the mirror image of the cathodic wave reflected across the potential axis. For an ideal nernstian reaction under Langmuir isotherm conditions, $E_{pa} = E_{pc}$, and the total width at half-height of either the cathodic or anodic wave is given by

$$\Delta E_{p,1/2} = 3.53 \frac{RT}{nF} = \frac{90.6}{n}\,\text{mV}\,(25°\text{C})$$

(14.3.14)
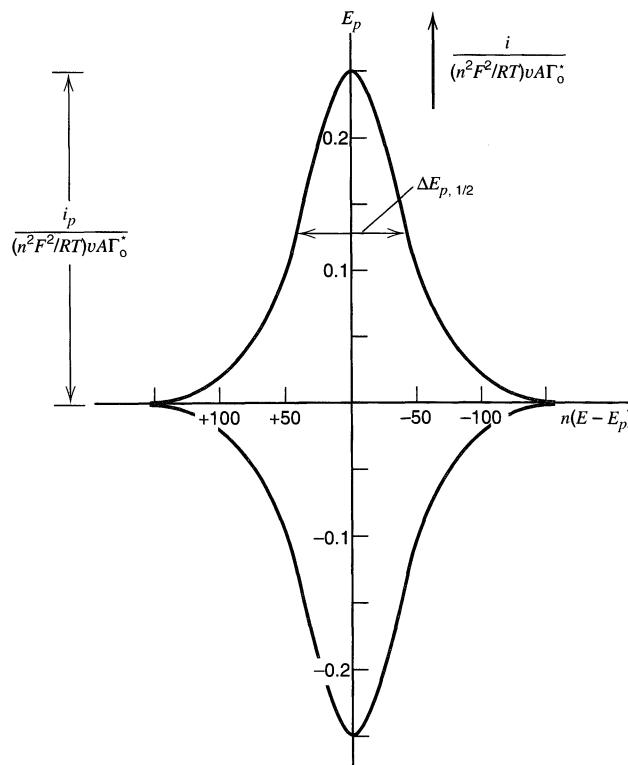
Figure 14.3.1 Cyclic voltammetric curve for reduction and subsequent reoxidation of adsorbed O; see (14.3.11). Current is given in normalized form and the potential axis is shown for 25°C.

The location of E_p with respect to $E^{0'}$ depends on the relative strength of adsorption of O and R according to the principles of stabilization discussed in Section 5.4.4. If $b_O = b_R$, $E_p = E^{0'}$. If O is adsorbed more strongly ($b_O > b_R$), the wave is displaced toward negative potentials, beyond the position where the reversible wave of a diffusing species would occur. For this reason, it is termed a *postwave*. If R is adsorbed more strongly ($b_R > b_O$), the wave occurs at more positive potentials than $E^{0'}$ and is called a *prewave*. The wave shape observed for this case in experimental studies depends strongly on the actual isotherm and rarely shows the ideal shape in Figure 14.3.1.

When lateral interactions exist between O and R in the film, the shape of the *i-E* curve depends upon the energies of the interactions of O with O, R with R, and O with R. The exact shape of the curve depends upon how these interactions are taken into account. For example, if a Frumkin-type isotherm (35, 36) is assumed, the relevant expression is:

$$\exp\left[\frac{nF}{RT}(E - E_a^{0'})\right] = \frac{\theta_O}{\theta_R}\exp[2\nu\theta_O(a_{OR} - a_O) + 2\nu\theta_R(a_R - a_{OR})] \quad (14.3.15)$$

where a_{OR}, a_O, and a_R are the O–R, O–O, and R–R interaction parameters ($a_i > 0$ for an attractive interaction and $a_i < 0$ for a repulsive one), ν is the number of water molecules displaced from the surface by adsorption of one O or R, and θ_O and θ_R are the fractional coverages of O and R, respectively. The expression for the *i-E* curve is then (37)

$$i = \frac{n^2F^2Av\Gamma_O^*}{RT}\left[\frac{\theta_R(1 - \theta_R)}{1 - 2\nu g\theta_T\theta_R(1 - \theta_R)}\right] \quad (14.3.16)$$

where $\theta_T = (\theta_O + \theta_R)$, $g = a_O + a_R - 2a_{OR}$, $\Gamma_O^* = \Gamma_O + \Gamma_R$, $\theta_i = \Gamma_i/\Gamma_O^*$. The potential variation in (14.3.16) arises through the variation of θ_R with E, via (14.3.9). Typical *i-E* curves based on (14.3.16) are given in Figure 14.3.2. The curve shape is governed by the interaction parameter, $\nu g\theta_T$. When this is 0, the behavior is that of Figure 14.3.1 and the width at half height, $\Delta E_{p,1/2}$, is 90.6/n mV (T = 25°C). When $\nu g\theta_T > 0$, $\Delta E_{p,1/2} < 90.6/n$; when $\nu g\theta_T < 0$, $\Delta E_{p,1/2} > 90.6/n$. An example of an experimental voltammogram compared to a theoretical treatment involving interaction parameters is shown in Figure 14.3.3.

The equations given above, based on the Frumkin isotherm, assume a random distribution of O and R sites in the film. If the film is structured, such as in an organized monolayer deposited by the L-B technique, there will be an ordered distribution of the sites. Under these conditions, a statistical mechanical approach is needed to account for the interactions and to find the *i-E* curve (38). For negative values of the interaction parameter in a structured film, a double wave results, even for a single electrode reaction, while the random distribution produces only a single broadened wave.

The above approaches to treatments of nonideal surface films rely upon empirical adjustable parameters to produce waves with the shapes of experimental ones. By taking into account the interfacial potential distribution (related to such factors as the dielectric constants of film and solution, the concentrations of electroactive adsorbate and supporting electrolyte, and the film thickness) the shape of the cyclic voltammetric curves can also be modeled without the need for such parameters (39).

The treatment discussed in this section also applies to covalently attached monolayers and thicker films under some conditions, although in actual studies of modified surfaces the voltammetric waves frequently deviate from the above behavior, which is still rather idealized. Often there is severe asymmetry or strong departure from a bell shape (40). Rarely can actual experimental voltammograms of thicker films be described simply in terms of parameters like those discussed here. The overall situation is usually much more complicated, with factors such as inhomogeneity of the film, finite mass and charge transport through the film, and structural and resistive changes in the film during oxidation and reduction coming into play. Some of these factors will be considered in Section 14.4.
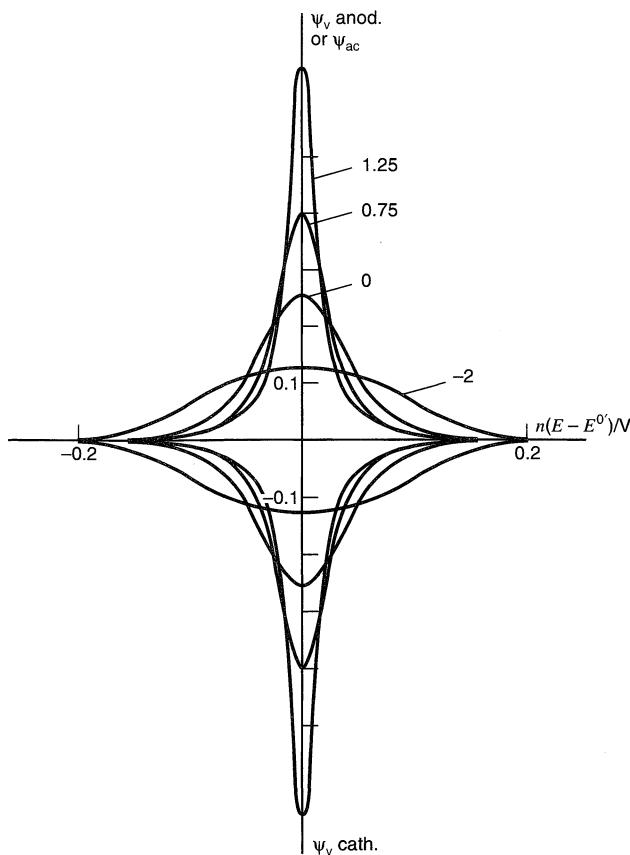
Figure 14.3.2 Effect of interactions on cyclic voltammetric wave shape for a thin layer on an electrode. A Frumkin isotherm is assumed, and values of $\nu g \theta_T$ are shown on each curve. The curve with $\nu g \theta_T = 0$ corresponds to that in Figure 14.3.1. [Reprinted from E. Laviron, *J. Electroanal. Chem.*, **100**, 263 (1979), with permission from Elsevier Science.]
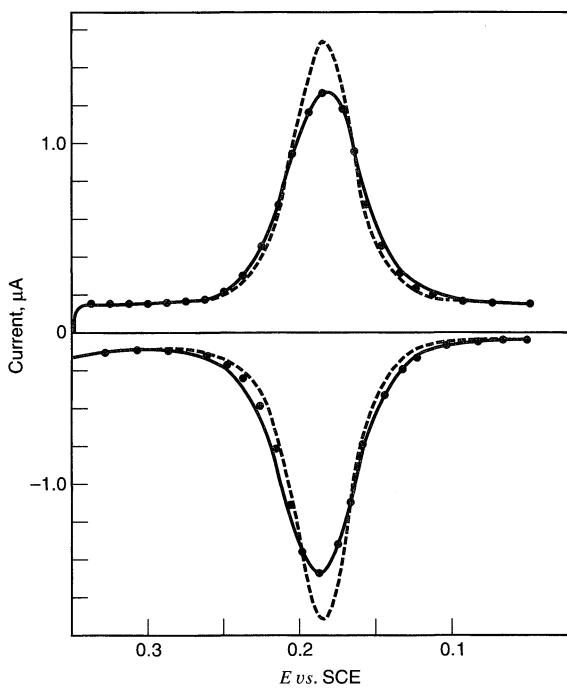
Figure 14.3.3 Experimental and theoretical cyclic voltammograms for reduction and reoxidation of 9,10-phenanthrenequinone irreversibly adsorbed on a pyrolytic graphite electrode. $\Gamma_O = 1.9 \times 10^{-10}$ mol/cm^2; $v = 50$ mV/s in 1 M HClO$_4$. (—) experimental voltammogram; (----) theoretical voltammogram calculated from (14.3.11); (●) calculated including nonideality parameters. [Reprinted with permission from A. P. Brown and F. C. Anson, *Anal. Chem.*, **49**, 1589 (1977). Copyright 1977, American Chemical Society.]

14.3.3 Cyclic Voltammetry: Only Adsorbed O Electroactive—Irreversible Reaction

For the case where adsorbed O is reduced in a totally irreversible one-step, one-electron reaction (32, 33), the langmuirian-nernstian boundary condition (14.3.9) is replaced by a kinetic one, similar to that used for dissolved reactants [e.g., (6.3.1)]:

$$\frac{i}{FA} = k_f \Gamma_O(t) \tag{14.3.17}$$

Note that for adsorbed reactants, k_f has units of s^{-1}, although it can still be given in the form of (3.3.9), or for the potential sweep experiment [see (6.3.3)]:

$$k_f = k_{fi} \, e^{at} \tag{14.3.18}$$

where $k_{fi} = k^0 \exp[-\alpha f(E_i - E^{0'})]$ and $a = \alpha f v$. Like k_f, the standard rate constant, k^0, for a surface bound species has units of s^{-1}. By combining (14.3.10) with (14.3.17) and (14.3.18), we obtain

$$\frac{d\Gamma_O(t)}{dt} = -k_{fi} \, e^{at} \Gamma_O(t) \tag{14.3.19}$$

This is solved with the initial condition that at $t = 0$, $\Gamma_O(t) = \Gamma_O^*$, and the results are the expressions for $\Gamma_O(t)$ and the i-E curve:

$$\Gamma_O(t) = \Gamma_O^* \exp\left(\frac{k_f}{a}\right) \tag{14.3.20}$$

$$\boxed{i = FAk_f \Gamma_O^* \exp\left[\left(\frac{RT}{\alpha F}\right)\left(\frac{k_f}{v}\right)\right]} \tag{14.3.21}$$

Note that these equations were obtained under the usual assumption that the sweep was started at sufficiently positive potentials that $k_{fi} \to 0$, hence $\exp(k_{fi}/a) \to 1$. The potential dependence of the current is obtained by substitution for k_f. Again note the similarity between these equations and those in the thin-layer case [equations 11.7.22 and 11.7.23]. The shapes of the i-E curves (Figure 14.3.4a) are independent of v and k^0 and follow closely those shown in Figures 11.7.4 and 11.7.5 with suitable minor modifications of parameters. The peak values are given by

$$\boxed{i_p = \frac{\alpha F^2 A v \Gamma_O^*}{2.718 RT}} \tag{14.3.22}$$

$$\boxed{E_p = E^{0'} + \frac{RT}{\alpha F} \ln\left(\frac{RT}{\alpha F} \frac{k^0}{v}\right)} \tag{14.3.23}$$

$$\Delta E_{p,1/2} = 2.44\left(\frac{RT}{\alpha F}\right) = \frac{62.5}{\alpha} \text{ mV } (25°C) \tag{14.3.24}$$

Again i_p is proportional to v, but the wave is shifted negatively from the reversible value and is distorted from its symmetrical shape. An experimental example of such a wave is shown in Figure 14.3.4b.

The treatment for the general case of a quasireversible one-step, one-electron reaction follows that given above, but involves consideration of the back reaction [i.e., use of (3.2.8)] as well as the adsorption isotherms for both O and R. This case, as well as vari-

$$\frac{i}{(F^2/RT)\alpha A v \Gamma_o^*}$$

0.4

0.3

0.2

0.1

+150   +100   +50   0   −50

$\alpha(E - E_p)$, mV

(a)

0.1 μA

0.4   0.5   0.6

E, Volts

(b)
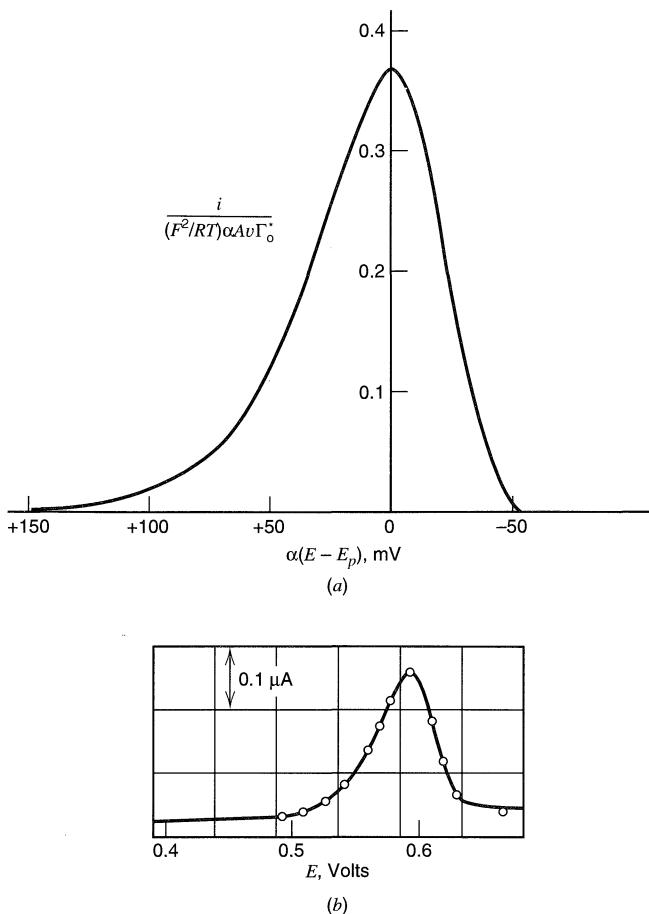
Figure 14.3.4   Experimental and theoretical linear sweep voltammograms for a system where adsorbed O is irreversibly reduced. (a) Theoretical curve; see (14.3.21). (b) Experimental curve for reduction of 5 μM *trans*-4,4'-dipyridyl-1,2-ethylene in aqueous 0.05 M H_2SO_4 at mercury drop electrode ($A = 0.017$ cm²); $v = 0.1$ V/s. [From E. Laviron, *J. Electroanal. Chem.*, **52**, 355 (1974), with permission. Upper frame adapted for the one-step, one-electron case.]

ants where coupled chemical reactions are associated with the electron-transfer reactions, have been discussed rather extensively in the literature (32, 33, 41, 42 and references therein).

14.3.4   Cyclic Voltammetry: Both Dissolved and Adsorbed Species Electroactive

When both the dissolved and adsorbed species are electroactive, the theoretical treatment involves the use of the full flux equation (14.3.1), along with adsorption isotherms, the usual diffusion equations, and the initial and semi-infinite conditions, as discussed in Chapter 6. Since the partial differential equations involving mass transfer must be employed, the mathematical treatment is more complicated and we consider here only the case for a nernstian electron-transfer reaction where either O (reactant) or R (product) is adsorbed, but not both (43).

(a) Product (R) Strongly Adsorbed
For this case $\beta_O \rightarrow 0$ and β_R is reasonably large (i.e., $\beta_R C^* \geq 100$). Initially $C_O = C_O^*$, $C_R = 0$, $\Gamma_R^* = 0$. The equations to be solved are the diffusion equations for O and R, the total flux equation (14.3.1), the adsorption isotherm (14.3.3), and (since the electrode reaction is assumed nernstian) equation 14.3.8. We assume that adsorption equilibrium is
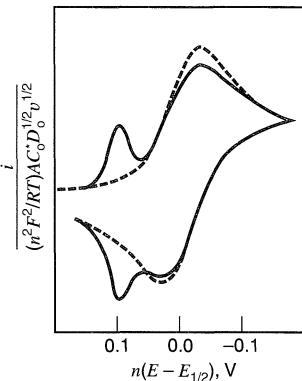
Figure 14.3.5 Cyclic voltammogram for reduction when the product is strongly adsorbed, showing a prepeak. The dashed line gives behavior in absence of adsorption. [Reprinted with permission from R. H. Wopschall and I. Shain, *Anal. Chem.*, **39**, 1514 (1967). Copyright 1967, American Chemical Society.)

maintained at all times. The solution to the problem generally follows that described in Section 6.2 (43). In their treatment, Wopschall and Shain also consider the possibility of a variation of β_R with potential, that is,

$$\beta_R = \beta_R^0 \exp\left[\left(\frac{\sigma_R n F}{RT}\right)(E - E_{1/2})\right] \tag{14.3.25}$$

where σ_R represents a parameter that shows how $\Delta \overline{G}_i^0$ varies with potential; $\sigma_R = 0$ implies that β_R is independent of E.

The results can be summarized as follows. A *prewave* (or *prepeak*) of the same shape and general properties as that described in Section 14.3.2 appears (Figure 14.3.5), representing the reduction of dissolved O to form a layer of adsorbed R. This response occurs at potentials more positive than the diffusion-controlled wave, because the free energy of adsorption of R makes reduction of O to adsorbed R easier than to R in solution. The prepeak is followed by the wave for reduction of dissolved O to dissolved R. While the latter resembles that observed in the absence of adsorption, it is perturbed by the depletion of species O at the foot of the diffusion wave during reduction of O to adsorbed R. The larger the value of β_R, the more the prepeak precedes the diffusion peak (Figure 14.3.6).
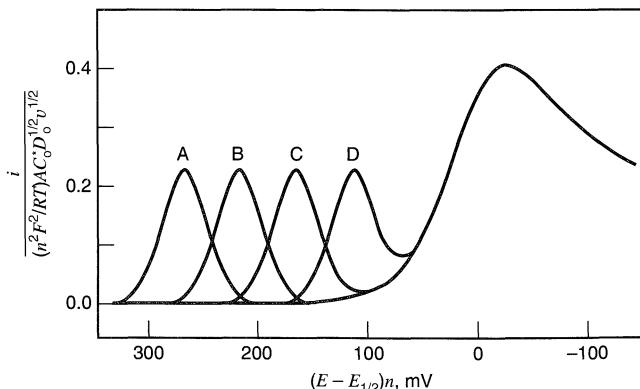
Figure 14.3.6 Variation of linear scan voltammograms for reduction when the product is strongly adsorbed. Calculated for $C_O^*(\pi D_O)^{1/2}/[4\Gamma_{R,s}(nFv/RT)^{1/2}] = 1$, $\sigma_R F/RT = 0.05$ mV^{-1}, and $4\Gamma_{R,s}\beta_R^0$ $(nFv/RT)^{1/2}/(\pi D_R)^{1/2}$ values of: *curve A*, 2.5×10^6; *curve B*, 2.5×10^5; *curve C*, 2.5×10^4; *curve D*, 2.5×10^3. [Reprinted with permission from R. H. Wopschall and I. Shain, *Anal. Chem.*, **39**, 1514 (1967). Copyright 1967, American Chemical Society.]
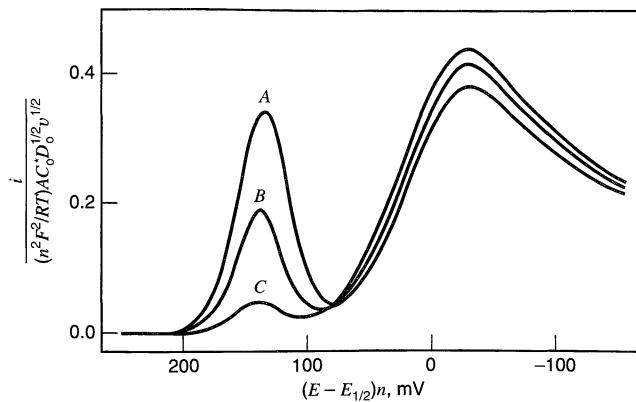
Figure 14.3.7 Effect of scan rate and $\Gamma_{R,s}$ on linear scan voltammograms when the product is strongly adsorbed. Calculated for $\sigma_R F/RT = 0.05$ mV^{-1}, $\beta_R^0 C_O^*(D_O/D_R)^{1/2} = 2.5 \times 10^5$ and values of $4\Gamma_{R,s} v^{1/2} (nF/RT)^{1/2}/C_O^*(\pi D_O)^{1/2}$ of: *curve A*, 1.6; *curve B*, 0.8; *curve C*, 0.2. Note that with all parameters constant except v, relative scan rates are 64:16: 1. [Reprinted with permission from R. H. Wopschall and I. Shain, *Anal. Chem.*, **39**, 1514 (1967). Copyright 1967, American Chemical Society.]

Since the peak current for the prepeak, $(i_p)_{ads}$, increases with v, while that for the diffusion wave, $(i_p)_{diff}$, varies with $v^{1/2}$, $(i_p)_{ads}/(i_p)_{diff}$ increases with increasing v (Figure 14.3.7). In a similar way, $(i_p)_{ads}/(i_p)_{diff}$ increases with $\Gamma_{R,s}$ at a given C_O^*. However, $(i_p)_{ads}/(i_p)_{diff}$ decreases with increasing C_O^* (Figure 14.3.8). At very low concentrations (assuming significant amounts of R are still adsorbed), only the prepeak is observed. As C_O^* increases, the prepeak increases, because Γ_R increases. However, $(i_p)_{ads}$ essentially attains a limiting value as Γ_R approaches $\Gamma_{R,s}$, and then the diffusion peak grows with respect to the adsorption peak. The width of the prepeak at half height, $\Delta E_{p,1/2}$, is a function of σ_R, and varies from $90.6/n$ to $7.5/n$ mV for $\sigma_R F/RT$ increasing from 0 to 0.4 mV^{-1}.
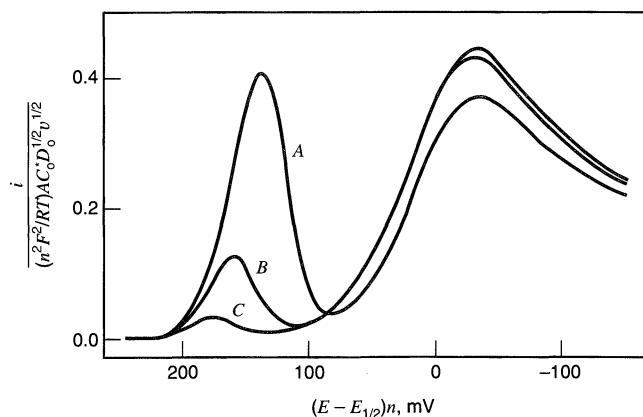
Figure 14.3.8 Effect of C_O^* on linear scan voltammograms when the product is strongly adsorbed. Calculated for $\sigma_R F/RT = 0.05$ mV^{-1}, $4\Gamma_{R,s}\beta_R^0 v^{1/2}(nF/RT)^{1/2}/(\pi D_R)^{1/2} = 1.0 \times 10^6$, and $C_O^*(\pi D_O)^{1/2}/[4\Gamma_{R,s} v^{1/2}(nF/RT)^{1/2}]$ values of: *curve A*, 0.5; *curve B*, 2.0; *curve C*, 8.0. [Reprinted with permission from R. H. Wopschall and I. Shain, *Anal. Chem.*, **39**, 1514 (1967). Copyright 1967, American Chemical Society.]
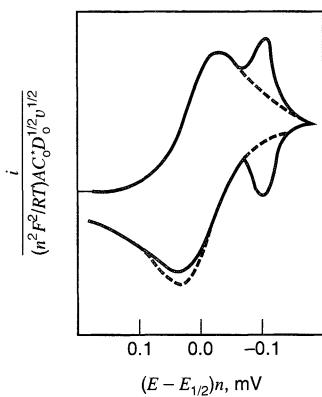
Figure 14.3.9 Cyclic voltammogram for reduction when the reactant is strongly adsorbed, showing a postpeak. Dashed line gives behavior in the absence of adsorption. [Reprinted with permission from R. H. Wopschall and I. Shain, *Anal. Chem.*, **39**, 1514 (1967). Copyright 1967, American Chemical Society.

Details concerning the derivation, results, and treatment of data are given in reference 43. A general discussion of the effect of adsorption is given in reference 44.

(b) Reactant (O) Strongly Adsorbed ($\beta_R \to 0, \beta_O C_O^* \geq 100$)

The adsorption of O results in a *postwave* (or *postpeak*), for the reduction of adsorbed O, following the peak for the diffusion-controlled reduction of O to R in solution (Figure 14.3.9). The postwave results from the greater stability with respect to reduction of adsorbed O compared to dissolved O. The general treatment and results are analogous to those discussed in subsection (a) above. The diffusion wave on the forward scan is unperturbed by the adsorption of O, since it is assumed that adsorption equilibrium has been attained and $C_O(x, t) = C_O^*$ at all x before the scan is initiated. The reduction of dissolved O presumably occurs either through the adsorbed O film or at the free surface. The postwave has the typical bell shape, as
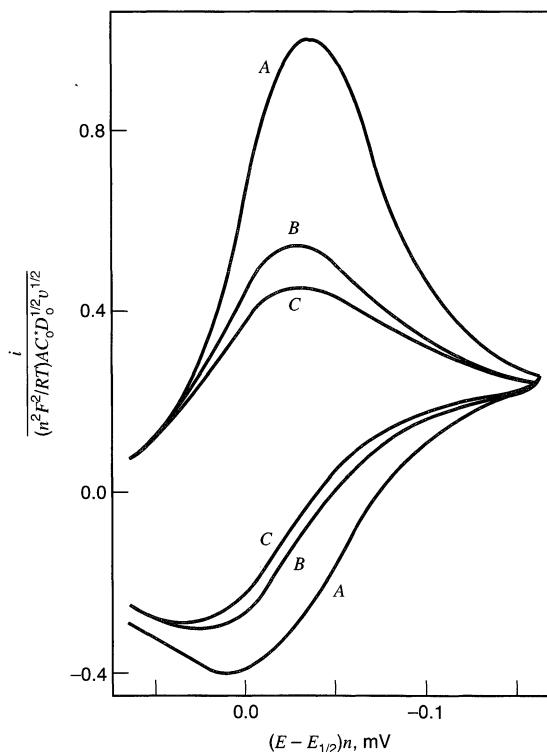
Figure 14.3.10 Effect of scan rate on cyclic voltammograms when the reactant is weakly adsorbed. Calculated for $\beta_O C_O^* = 0.01$ and $4\Gamma_{O,s}\beta_O v^{1/2}(nF/RT)^{1/2}/(\pi D_O)^{1/2}$ values of: *curve A*, 5.0; *curve B*, 1.0; *curve C*, 0.1. (Curve C corresponds to an essentially unperturbed reaction). Note that relative scan rates are 2500:100:1. [Reprinted with permission from R. H. Wopschall and I. Shain, *Anal. Chem.*, **39**, 1514 (1967). Copyright 1967, American Chemical Society.]
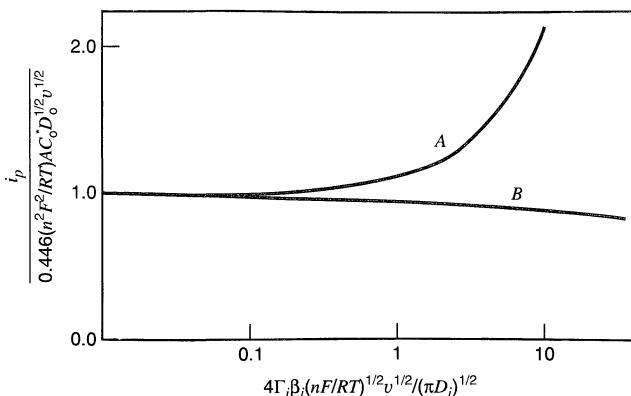
Figure 14.3.11 Variation of peak current with scan rate for linear scan voltammogram when the reactant (A) or product (B) is weakly adsorbed. *Curve A*: $\Gamma_i = \Gamma_{O,s}$, $\beta_O C_O^* = 1$. *Curve B*; $\Gamma_i = \Gamma_{R,s}$, $\beta_R C_O^* = 1$. [Reprinted with permission from R. H. Wopschall and I. Shain, *Anal. Chem.*, **39**, 1514 (1967). Copyright 1967, American Chemical Society.]

well as the properties of adsorption waves discussed in subsection (a) and in Section 14.3.2, on the forward and reverse scans. The diffusion wave on reversal is only slightly perturbed.

(c) Reactant (O) Weakly Adsorbed ($\beta_R \to 0$, $\beta_O C_O^* \le 2$)

When adsorption is weak the difference in energies for reduction of adsorbed and dissolved O is small, and a separate postwave is not observed (Figure 14.3.10). The net effect is an increase in the height of the cathodic peak compared to that in the absence of adsorption, because both adsorbed and diffusing O contribute to the current. The anodic current on reversal is also increased (but to a smaller extent), because there is a larger amount of R near the electrode at the time of scan reversal. As in the case of strong adsorption of O, the relative contribution of adsorbed O increases at increasing scan rates (Figure 14.3.11). At the very high v limit, i_p approaches a proportionality with v, while at very low v, $i_p \propto v^{1/2}$ (see Problem 14.3). Similarly the ratio, i_{pa}/i_{pc}, is a function of v,and is smaller than the value of unity, found in the absence of adsorption (Figure 14.3.12). As
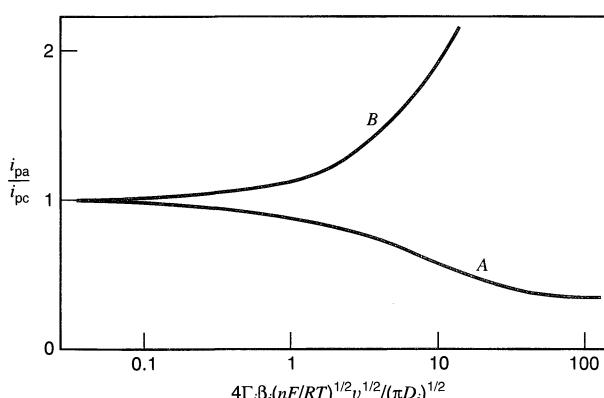
Figure 14.3.12 Peak current ratio *vs.* scan rate for cyclic voltammetry when the reactant (A) or the product (B) is weakly adsorbed. *Curve A*: $\Gamma_i = \Gamma_{O,s}$, $\beta_O C_O^* = 1$. *Curve B*: $\Gamma_i = \Gamma_{R,s}$, $\beta_R C_O^* = 1$. Reversal potential = $E_{1/2} - (180/n)$ mV. [Reprinted with permission from R. H. Wopschall and I. Shain, *Anal. Chem.*, **39**, 1514 (1967). Copyright 1967, American Chemical Society.]

with strong adsorption, the relative contribution of the effect of adsorption decreases at high bulk concentrations of O.

(d) Product (R) Weakly Adsorbed ($\beta_O = 0$, $\beta_R C_O^* \leq 2$)

When R is weakly adsorbed, the cathodic current on the forward scan is only slightly perturbed, while the anodic current on reversal is enhanced (Figure 14.3.13). The forward peak shifts slightly toward more positive potentials with increasing v, representing a decrease in dissolved R near the electrode surface because of adsorption. The effect is similar to the positive shift observed in E_{pc} when R is involved in a following reaction (e.g., E_rC_i, see Section 12.3.3). In this case i_{pa}/i_{pc} is greater than unity and decreases with decreasing v.

(e) Digital Simulations—Irreversible Electron-Transfer Reactions

A more general treatment of cyclic voltammetry involving adsorbed and dissolved reactants and products has been worked out with the aid of digital simulation techniques (45). This approach allowed application of the more general Frumkin isotherm, as well as consideration of rate limitations in the electron-transfer reactions involving the dissolved or the adsorbed species. Several representative simulations showing the effects of interactions between adsorbed reactant or irreversibility are shown in Figure 14.3.14. Feldberg (45) has pointed out that irreversibility will begin to manifest itself when $k_{diff}^0/(\pi D_O v F/RT)^{1/2} + k_{ads}^0 \Gamma_{O,s} \beta_O^{1-\alpha} \beta_R^\alpha/(\pi D_O v F/RT)^{1/2} < \beta_O C_O^*$, where the k^0s refer to the diffusing and adsorbed species. Adsorption effects on cyclic voltammetric studies of the E_rC_i reaction scheme (46) and the effects of rate-controlling adsorption have also been discussed (45, 47).
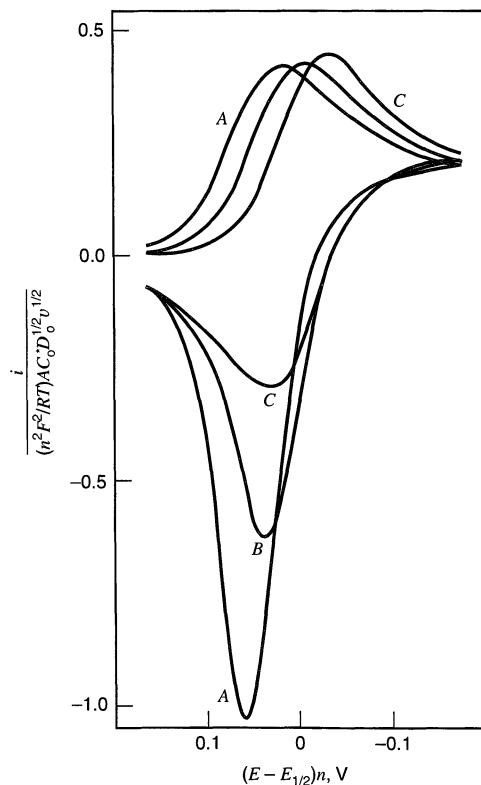
Figure 14.3.13 Effect of scan rate on cyclic voltammograms for initial reduction when the product is weakly adsorbed. Calculated for $\beta_R C_O^* = 0.01$ and $4\Gamma_{R,s}\beta_R v^{1/2}(nF/RT)^{1/2}/(\pi D_R)^{1/2}$ values of: *curve A*, 20; *curve B*, 5; *curve C*, 0.1. (Curve C corresponds to an essentially unperturbed reaction). Note that relative scan rates are 4×10^4:2500:1. [Reprinted with permission from R. H. Wopschall and I. Shain, *Anal. Chem.*, **39**, 1514 (1967). Copyright 1967, American Chemical Society.]
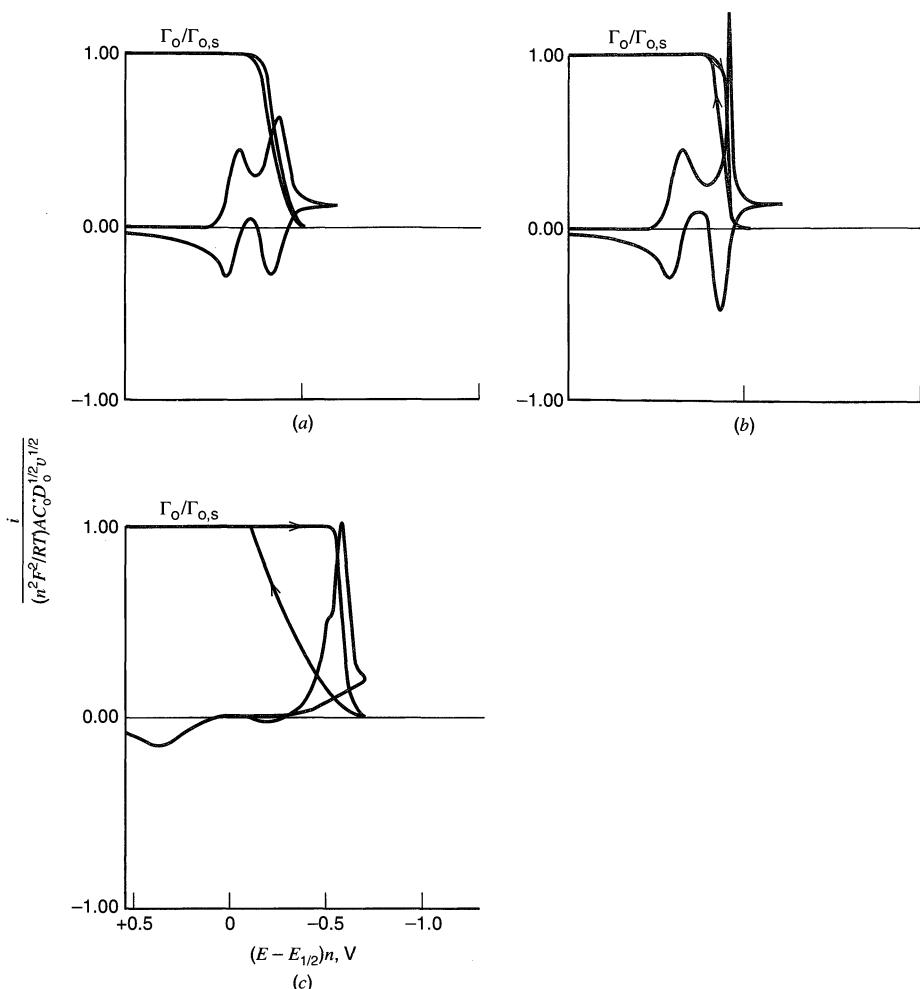
Figure 14.3.14 Simulated cyclic voltammograms for initial reduction where reactant is strongly adsorbed. $\beta_O = 10^4$. (*a*) Nernstian reaction, Langmuir isotherm. (*b*) Nernstian system, Frumkin isotherm, $2g\Gamma_{O,s}/RT = -1.5$. (*c*) Irreversible reaction, $k_{diff}^0/(\pi D_O v F/RT)^{1/2} = 1$, $\alpha = 0.5$, Frumkin case, $2g\Gamma_{O,s}/RT = 0.6$. Additional curves in the figure show variation of $\Gamma_O/\Gamma_{O,s}$ as a function of E during scan. [Reprinted from S. W. Feldberg in "Computers in Chemistry and Instrumentation," Vol. 2, "Electrochemistry," J. S. Mattson, H. B. Mark, Jr., and H. C. MacDonald, Jr., Eds., Marcel Dekker, New York, 1972, Chap. 7, by courtesy of Marcel Dekker, Inc.]

14.3.5 Adsorption in dc Polarography

While the treatment of adsorption at the DME generally follows that for linear sweep voltammetry at a stationary electrode, it is complicated by the growth of the drop with time and the continuous exposure of fresh surface. In this case, the rate of mass transfer of reactant and product (see Section 13.5.3) and the rate of adsorption can affect the height of the adsorption wave. Although the first explanation of adsorption in voltammetric methods and the explanation of prewaves and postwaves arose from the classic studies by Brdička (48, 49), dc polarography is not the method of choice in the study of adsorption. Only a brief discussion will be given here; more detailed treatments have appeared (33, 44, 50).

Let us consider the case where only product R is strongly adsorbed (i.e., the case of a prewave). After detachment of a drop, a new drop starts with a fresh surface. If the potential is in the region of the prewave, O is reduced to adsorbed R. The quantity of R adsorbed is given by [see (7.1.3)]

$$\text{moles R} = A(t)\Gamma_R(t) = (8.5 \times 10^{-3})m^{2/3}t^{2/3}\Gamma_R(t) \tag{14.3.26}$$

If the rate of reduction is diffusion limited, then

$$\text{moles R} = \frac{1}{nF}\int_0^t i_d\, dt \tag{14.3.27}$$

Substitution of the instantaneous polarographic current (7.1.6) for i_d, integration, and combination with (14.3.26) yields (51)

$$(8.5 \times 10^{-3})m^{2/3}t^{2/3}\Gamma_R(t) = (6.3 \times 10^{-3})D_O^{1/2}C_O^*m^{2/3}t^{7/6} \tag{14.3.28}$$

$$\Gamma_R(t) = 0.74D_O^{1/2}C_O^*t^{1/2} \tag{14.3.29}$$

Thus the time t_m needed to achieve saturation coverage, $\Gamma_{R,s}$, at a given concentration (assuming adsorption itself is rapid) is

$$\boxed{t_m = \frac{1.83\Gamma_{R,s}^2}{C_O^{*2}D_O}} \tag{14.3.30}$$

When the drop time, t_{max}, is less than t_m, the height of the prewave is limited by diffusion, and is governed by the Ilkovič equation (7.1.6) (Figure 14.3.15a). When $t_{max} > t_m$, the surface becomes saturated, and the current attains a limiting value i_a defined by the rate at which new area opens up. Excess O remains at the electrode surface. The value of i_a, which is independent of C_O^* and t_{max}, is obtained from the expression

$$i_a = \frac{nFd[A(t)\Gamma_{R,s}]}{dt} \tag{14.3.31}$$

$$i_a = (5.47 \times 10^2)nm^{2/3}\Gamma_{R,s}\, t^{-1/3} \tag{14.3.32}$$
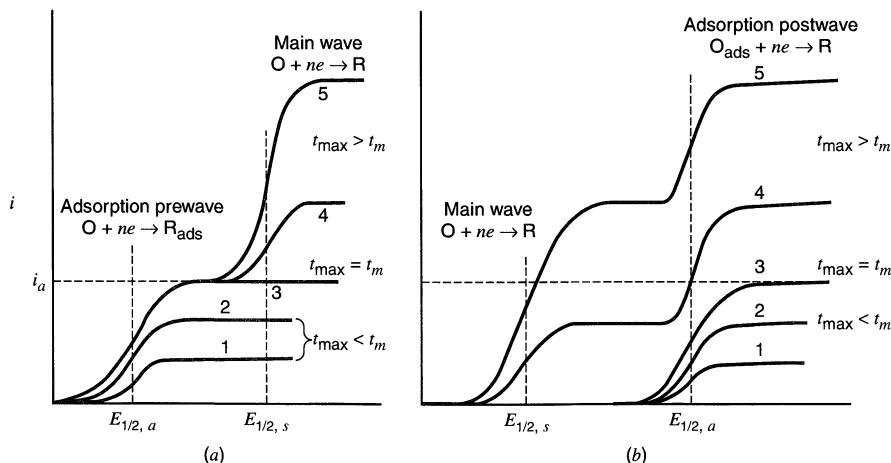
Figure 14.3.15 Polarographic current-potential curves showing (a) prewave and (b) postwave. *Curves 1, 2:* $t_{max} < t_m$; only adsorption wave observed. *Curve 3:* $t_{max} = t_m$; current attains i_a. *Curves 4, 5:* $t_{max} > t_m$; adsorption wave height remains at i_a and main wave grows. This behavior is usually observed at constant t_{max} with increasing C_O^*. $t_m = 1.83\Gamma_{R,s}^2/C_O^{*2}D_O$; $t_{max} =$ drop time.

(i_a in A; m in mg/s; t in s; $\Gamma_{R,s}$ in mol/cm^2). Note that the form of (14.3.32) is the same as that for the charging current, equation 7.1.17. Again we see the analogy between adsorption and capacitance. When the potential is scanned into the region of the main wave, the excess O at the electrode surface is reduced and the diffusion wave appears (Figure 14.3.15a). The total current for this wave is also governed by the Ilkovič equation, since all O reaching the electrode surface is reduced, either to adsorbed or dissolved R.

Because of the different dependency of the current on time for $t < t_m$ and $t > t_m$, the i-t curve at potentials of the adsorption prewave can have an unusual appearance for $t_{max} > t_m$. The current increases until $t \approx t_m$, then falls off with a $t^{-1/3}$ dependence. For a nernstian reaction, both the prewave and the main wave will have the usual reversible shapes (33). Note also, from the dependence of m and t on the corrected mercury column height, h_{corr}, [i.e., $m \propto h_{corr}$ and $t \propto h_{corr}^{-1}$, (see Section 7.1.4)] that i_a is directly proportional to h_{corr} [see (14.3.32)], compared to the $h_{corr}^{1/2}$ dependence for i_d.

A similar treatment holds for the polarographic behavior in the presence of adsorption of O, when a postwave appears (Figure 14.3.15b).

14.3.6 Chronocoulometry

It is possible in principle to determine the amount of adsorbed reactant, Γ_O, by integrating the area under the postwave in the linear sweep voltammogram, when this wave is well-separated from the main wave. In practice, it is often difficult to subtract the main wave baseline and to correct for double-layer charging. The result becomes more uncertain as the separation between the waves becomes smaller, although estimation of Γ_O at very high scan rates is still possible. Chronocoulometry, discussed in Section 5.8, provides a method for determining Γ_O independent of the relative positions of the dissolved O and adsorbed O reductions, as well as the kinetics of the reactions (52–54).

We consider the case where only O is adsorbed. The potential is stepped from a value E_i, where the amount of O adsorbed per unit area is Γ_O (which may be a function of E_i), to a value sufficiently negative that all O on the electrode surface is reduced and $C_O(0, t) \approx 0$. As shown in (5.8.2), the total charge at time t is

$$Q_f(t \leq \tau) = 2nFAC_O^*\left(\frac{D_O t}{\pi}\right)^{1/2} + nFA\Gamma_O + Q_{dl} \qquad (14.3.33)$$

where the terms on the right side of the equation represent the contributions of dissolved O, adsorbed O, and double-layer charging, respectively. As shown in Figure 5.8.1, a plot of Q_f vs. $t^{1/2}$ yields an intercept Q_f^0 given by

$$Q_f^0 = nFA\Gamma_O + Q_{dl} \qquad (14.3.34)$$

The determination of Γ_O requires an independent estimate of Q_{dl}. While the amount of charge for the supporting electrolyte solution alone, Q_{dl}', can be obtained in an experiment involving a potential step over the same region in the absence of O, often the adsorption of O perturbs C_d, so that $Q_{dl}' \neq Q_{dl}$. The proper correction can be obtained, however, by a double potential step experiment, in which the potential is returned to E_i at $t = \tau$. The charge during this reverse step, Q_r, measured as shown in Figure 5.8.2, is given by

$$Q_r(t > \tau) = 2nFAC_O^*D_O^{1/2}\pi^{-1/2}\theta + nFA\Gamma_O\left(1 - \frac{2}{\pi}\sin^{-1}\sqrt{\frac{\tau}{t}}\right) + Q_{dl} \quad (14.3.35)$$

where $\theta = \tau^{1/2} + (t - \tau)^{1/2} - t^{1/2}$. Christie et al. have shown (53) that, to a good approximation, the plot of Q_r vs. θ is linear and follows the equation

$$Q_r(t > \tau) = 2nFAC_O^* D_O^{1/2} \pi^{-1/2}\left(1 + \frac{a_1 nFA\Gamma_O}{Q_c}\right)\theta + a_0 nFA\Gamma_O + Q_{dl} \quad (14.3.36)$$

where Q_c is the total charge arising from the diffusing species during the forward step, that is,

$$Q_c = 2nFAC_O^*\left(\frac{D_O\tau}{\pi}\right)^{1/2} \quad (14.3.37)$$

and the values of a_0 and a_1 depend slightly on the range of $\theta/\tau^{1/2}$, but are usually taken as $a_0 = -0.069$ and $a_1 = 0.97$. Thus a plot of Q_r vs. θ has an intercept, Q_r^0, given by

$$Q_r^0 = a_0 nFA\Gamma_O + Q_{dl} \quad (14.3.38)$$

The value of Q_{dl} in the presence of adsorption is thus near Q_r^0, or more exactly

$$Q_{dl} = \frac{Q_r^0 - a_0 Q_f^0}{1 - a_0} \quad (14.3.39)$$

Once Q_{dl} is determined, $nFA\Gamma_O$ can be obtained from (14.3.34).

The results of a typical experiment (54) involving the reduction of Cd(II) at an HMDE are shown in Figure 14.3.16. In the absence of SCN$^-$, Cd^{2+} is not adsorbed on
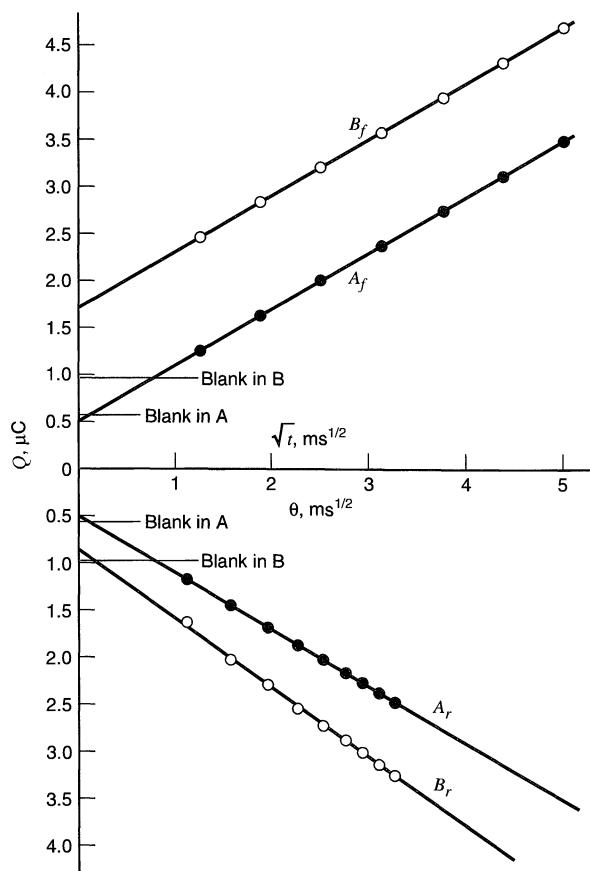
Figure 14.3.16 Double potential step chronocoulometric study of the induced adsorption of Cd(II) by SCN$^-$ at an HMDE. Potential stepped from $E_i = -0.200$ V to -0.900 V *vs.* SCE and back to E_i. A. (●) 1 mM Cd(II) in 1 M NaNO$_3$. The lines have the following slopes (S) and intercepts (Q^0): $S_f = S_r = 0.58\ \mu C/ms^{1/2}$; $Q_f^0 = 0.54\ \mu C$, $Q_r^0 = 0.55\ \mu C$. B. (○) 1 mM Cd(II) in 0.2 M NaSCN + 0.8 M NaNO$_3$. $S_f = 0.60\ \mu C/ms^{1/2}$; $Q_f^0 = 1.67$ μC; $Q_r^0 = 0.86\ \mu C$. The points labeled "blank" in A and B refer to the coulombs required to charge the double layer in the cadmium-free supporting electrolyte solutions alone. The area of HMDE was 0.032 cm^2. [From F. C. Anson, J. H. Christie, and R. A. Osteryoung, *J. Electroanal. Chem.*, **13**, 343 (1967), with permission.]

Hg, and the chronocoulometric responses show equal intercepts of Q_{dl}'. In the presence of SCN^-, Cd^{2+} is adsorbed, and the plots of Q_f vs. $t^{1/2}$ and Q_r vs. $\theta^{1/2}$ have significantly different intercepts, which allow calculation of Γ_O by using the treatment given above. The variation of Γ_O with potential can be studied by changing E_i. The variation of Γ_O at different concentrations of O (or supporting electrolyte) is often of interest. The adsorption of Cd(II) in the presence of SCN^- is an example of anion-induced adsorption, in which a specifically adsorbed substance (e.g., SCN^-, N_3^-, halide ion) binds to a metal ion in solution and promotes specific adsorption of the metal [e.g., Cd(II), Pb(II), Zn(II)] as well (55, 56) (see Section 14.2).

Chronocoulometry can also be applied to the cases discussed in Section 14.3.2 where only adsorbed species are electroactive (57). In this situation the potential step causes only double-layer charging and the electrolysis of the adsorbed species. One can estimate Q_{dl} by steps between a potential at the foot of the adsorption wave, E_i, and potentials, E_f, beyond the adsorption wave. If C_d is not a function of E in the region of the wave, the following equation results (57):

$$Q = Q_{dl} + Q_{ads} = AC_d(E_i - E_f) + nFA\Gamma_O \tag{14.3.40}$$

so that a plot of Q vs. $(E_i - E_f)$ can be employed to determine C_d and Γ_O.

14.3.7 Other Methods

Adsorption of electroactive reactant or product also affects the response in the other methods considered in previous chapters.

(a) Chronopotentiometry

In constant current step methods (58–61), the treatment depends on the order in which the adsorbed and diffusing species are electrolyzed. If only adsorbed O is electrolyzed, then the transition time τ follows the relation

$$i\tau = nFA\Gamma_O \tag{14.3.41}$$

A similar equation holds for a prewave where dissolved species O is reduced to adsorbed R. If both dissolved and adsorbed O are reduced, but with adsorbed O being reduced almost completely before reduction of the dissolved O, then the $i\tau$ equation is

$$i\tau = \frac{n^2F^2\pi D_O A^2 C_O^{*2}}{4i} + nFA\Gamma_O \tag{14.3.42}$$

If adsorbed O is reduced last (i.e., in a postwave), the situation becomes more complicated, because the two processes are not separated in time. Some of the current must be devoted to the continuing flux of diffusing O as the adsorbed O is reduced. The overall transition time is given by $\tau = \tau_1 + \tau_2$, where τ_1 is the transition time due only to diffusing species:

$$\tau_1 = \frac{n^2F^2\pi D_O A^2 C_O^{*2}}{4i^2} \tag{14.3.43}$$

and τ_2 is defined implicitly by

$$\frac{\pi nFA\Gamma_O}{i} = \tau \cos^{-1}\left(\frac{\tau_1 - \tau_2}{\tau}\right) - 2(\tau_1\tau_2)^{1/2} \tag{12.3.44}$$

For simultaneous reduction of adsorbed and dissolved species, the behavior is still more complex and depends on the form of the adsorption isotherm as well as the manner

in which the current divides between adsorbed and diffusing O. The problem is, in many ways, similar to that concerning the effect of double-layer charging in chronopotentiometry (see Section 8.3.5). For example, with the assumption that the fraction of the current contributing to the reduction of adsorbed O remains constant for $0 \leq t \leq \tau$,

$$i\tau = \frac{nFA(\pi D_O)^{1/2} C_O^*}{2} + nFA\Gamma_O \qquad (14.3.45)$$

Clearly, constant current methods are not as useful as chronocoulometric ones for determination of adsorbed reactant. However, once Γ_O is determined, the chronopotentiometric response can yield information about the order in which dissolved and adsorbed species are reduced.

(b) Coulometry in Thin-Layer Cells

Thin-layer methods (Section 11.7) are very valuable in studying irreversibly adsorbed substances (62, 63). The cells used in these studies usually are of the type shown in Figure 11.7.1d. They contain a thin layer (e.g., 40 μm) of electrolyte between a smooth cylindrical Pt electrode and surrounding precision glass tubing. The surface area of the electrode, A, is typically about 1 cm^2; hence the solution volume, V, is about 4 μL. The cell is filled quite reproducibly by capillary action and can be flushed with pressurized inert gas.

Determination of the amount of species adsorbed, Γ, depends upon the electroactivity of the adsorbate. Consider the case where a molecule is irreversibly adsorbed and does not undergo an electrochemical oxidation at potentials where the dissolved species shows a cyclic voltammetric wave. An example of this type of behavior is hydroquinone (H_2Q) in 1 M $HClO_4$. When an aliquot of solution containing a known concentration, C^0, is introduced into the thin-layer cell, ΓA moles of the H_2Q will adsorb, so the new concentration in the solution, C, will be

$$C = C^0 - \Gamma A/V \qquad (14.3.46)$$

Anodic coulometry yields the amount of charge, Q_1, required to electrolyze the dissolved material in equilibrium with the adsorbed layer. By filling and flushing the cell several more times (without removing adsorbed material from the electrode), the surface of the electrode picks up enough adsorbate to be at equilibrium with the original solution concentration, so that the solution in the cell is no longer depleted by adsorption. Anodic coulometry performed on that solution gives the charge, Q^*, corresponding to C^0. Thus

$$\Gamma = (Q^* - Q_1)/nFA \qquad (14.3.47)$$

The adsorbate layer can then be removed by oxidation at very positive potentials.

If the adsorbed molecule is electroactive and shows a voltammetric postpeak well separated from the voltammetric response of the dissolved species, it may be possible to measure Q_1 by coulometry at a potential between the peaks for the dissolved and adsorbed species, and to measure $Q^* - Q_1$ as the additional charge passed when the potential is changed to a value beyond the postpeak.

Values of Γ (mol/cm^2) are sometimes used to ascertain the orientation of the adsorbed molecules on the electrode surface. This is done by calculating the average area, σ, occupied by the molecule, where

$$\sigma \, (\text{Å}^2) = 10^{16}/(6.023 \times 10^{23} \, \Gamma) \qquad (14.3.48)$$

and comparing that number with values obtained from molecular models assuming different orientations in a close-packed, immobile structure (62) (Figure 14.3.17; see Problem 14.6).
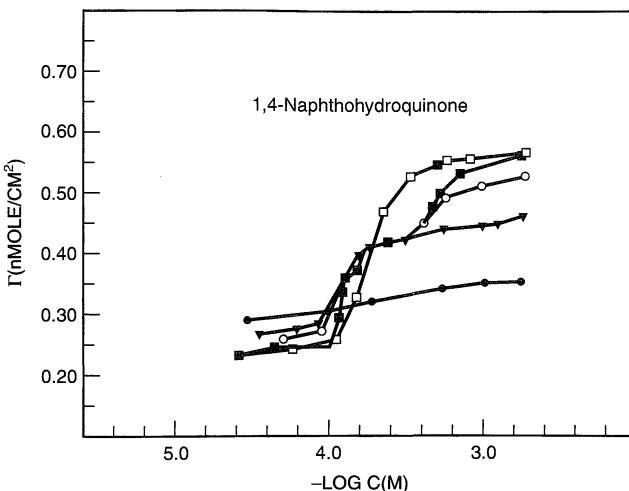
Figure 14.3.17 Adsorbed coverage of 1,4-naphthohydroquinone as a function of molar concentration in 1 M HClO$_4$ at 5, 25, 35, 45, and 65°C (top to bottom). These data were obtained for a Pt electrode in a thin-layer cell like that in Figure 11.7.1d. The existence of multiple levels of saturation coverage is evidence that the molecule adsorbs in a different geometries (e.g., flat $vs.$ edgewise) as the coverage changes. [Reprinted with permission from M. P. Soriaga, J. H. White, and A. T. Hubbard, *J. Phys. Chem.*, **87**, 3048 (1983). Copyright, 1983, American Chemical Society.]

(c) Impedance Measurements

The effect of adsorption of electroactive species in ac methods is taken into account by modification of the equivalent circuit representing the electrode reaction (44, 64–68). This is usually accomplished by adding an "adsorption impedance" in parallel with the Warburg impedance and double-layer capacitance. Expressions for this impedance have been suggested for reversible (65, 66) and irreversible (67, 68) systems, but the complexity of the resulting analysis has limited the application of these techniques.

The situation in ac polarography with adsorption of the solution component is even more complicated, since the effect of adsorption on the dc process, as well as the rate of attainment of adsorption equilibrium at the DME, must be taken into account (44, 69). If the adsorbed layer engages in reversible charge transfer at the potentials where the dissolved species gives a response, the general effect on the ac polarogram is an enhancement of the peak height and an increase in the phase angle ϕ, sometimes to values greater than the 45° characteristic of a reversible process. (Recall that slow electron-transfer kinetics or coupled chemical reactions lead to ϕ values below 45°.) The reason for the larger phase angle is that reversible charge transfer to a surface layer mimics the reversible charging and discharging of a capacitor, which involves a phase angle approaching 90° if the uncompensated resistance is not too high. The net result is similar to that discussed in Section 10.7, where the effects of double-layer charging are considered. The approach has not been applied widely to studies of adsorption itself, but one should be aware of the complications adsorption can cause in interpretation of ac (and dc) voltammetry (44, 70).

Impedance methods have been more useful in studying electron-transfer kinetics in electroactive monolayers in the absence of an electroactive solution species (71–73), such as alkylthiol layers with tethered electroactive groups (Section 14.5.2). The equivalent circuit adopted is shown in Figure 14.3.18, where the adsorbed layer is represented by $C_{ads} = (F^2 A \Gamma)/4RT$ and the electron-transfer kinetics by $R_{ct} = (2RT)/F^2 A \Gamma k_f$, so that

$$k_f = 1/(2R_{ct}C_{ads}) \tag{14.3.49}$$
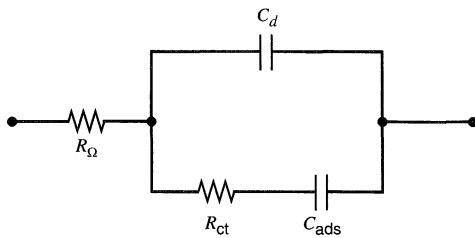
Figure 14.3.18 Equivalent circuit for an electroactive monolayer. R_Ω = solution resistance, C_d = double-layer capacitance, R_{ct} = charge-transfer resistance, and C_{ads} = capacitance of the adsorbed layer.

and values of k_f and Γ can be extracted readily from impedance spectroscopy studies. Creager and Wooster (73) propose an alternative method of treating ac voltammetric results by plotting the ratio of the ac peak current to the background (obtained by extrapolating the baseline on either side of the ac peak) as a function of frequency and fitting these results to predictions based on the equivalent circuit.

14.4 OVERVIEW OF PROCESSES AT MODIFIED ELECTRODES

In general, a complex structure is designed toward a particular end, perhaps to facilitate an electrode process (such as the electrocatalytic oxidation of methanol), or to inhibit a reaction (such as metallic corrosion), or to produce selectivity toward a particular process (such as the enzyme-catalyzed oxidative determination of glucose in whole blood). The end is
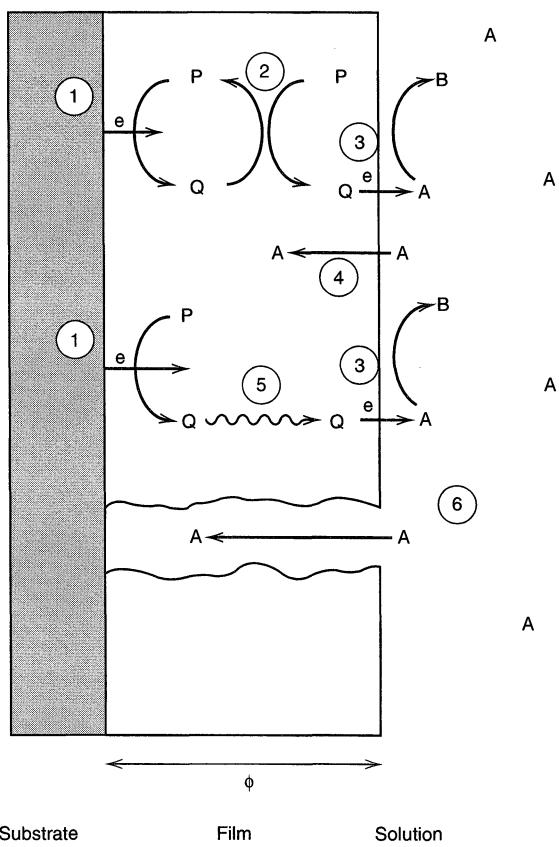
Figure 14.4.1 Schematic diagram of processes that can occur at a modified electrode. P represents a reducible substance in a film on the electrode surface and A, a species in solution. Processes shown are: (1) heterogeneous electron transfer to P to produce the reduced form, Q; (2) electron transfer from Q to another P in the film (electron diffusion or electron hopping in the film); (3) electron transfer from Q to A at the film/solution interface; (4) penetration of A into the film (where it can also react with Q or at the substrate-film interface); (5) movement (mass transfer) of Q within the film; (6) movement of A through a pinhole or channel in the film to the substrate, where it can be reduced. [From A. J. Bard, "Integrated Chemical Systems," Wiley, New York, 1994, with permission.]

achieved by developing within the structure a favorable interplay of the dynamics by which electrons are conveyed between the electrode and the species whose oxidation or reduction is ultimately required to achieve the goal. It may be necessary to employ a selective catalyst, or to restrict access to the interior of the structure, or to allow for the ready flow of electrons to more remote parts of an assembly. Many modified electrodes are based on films thicker than the monolayers considered in Section 14.3, and the theoretical treatments are more complex, because mass transfer and reaction kinetics within the film must be considered. A schematic picture of the typical situation is given in Figure 14.4.1, wherein a *primary reactant*, A, in the external solution is converted to a product, B. This can occur by mass transport of A moving through the film to the underlying electrode or by cross-reaction with a catalyst, Q, contained in the film and renewed electrochemically. Species A might react with Q either within the film or at the film/solution interface.[2]

The performance of the whole system is determined by the interrelation of several different dynamical processes; hence the behavior is intrinsically multidimensional and complex. The understanding and improvement of such systems is greatly aided by use of steady-state methods and a systematic theoretical framework. Savéant, Andrieux, and their coworkers (74) have provided the most comprehensive treatment, and the development given here follows their approach and notation.

14.4.1 General Behavior at a Rotating Disk

It is advantageous to study modified electrodes and other complex structures at steady state, precisely because of the complexity of their dynamics. By so doing, one can eliminate time as a variable and simplify the treatment considerably. One way to achieve steady state is to assemble the structure on an electrode that can be rotated. Another is to use a UME in the steady-state regime. Hydrodynamic voltammetry at the RDE yields waves for the conversion of primary reactant to product, as shown in Figure 9.3.8.

As we saw in Section 9.3.4, a Koutecký–Levich plot ($1/i_l$ vs. $1/\omega^{1/2}$) allows one to separate the effects of rate limitation within the assembly from those of convective diffusion outside. The limiting current for the voltammetric wave is expressed by

$$1/i_l = 1/i_A + 1/i_F \tag{14.4.1}$$

where i_A is simply the Levich current expressing the arrival rate of species A at the outer boundary of the film ($i_A = 0.62nFAC_A^* D_A^{2/3} \nu^{-1/6} \omega^{1/2}$), and i_F is an expression of the maximum rate at which A can be converted to B in the film. This latter current is the limit for rotation at an infinite rate, so that there is no limitation on the supply of A at the outer boundary of the structure. The Koutecký–Levich plot is a convenient means for extrapolating behavior to infinite ω, and it yields $1/i_F$ as the intercept, as shown in Figure 9.3.7.

The power of this approach in dealing with modified electrodes lies in its generality. The treatment does not require any assumption about the identity of the rate-limiting processes within the film, and there is only one constraint on the mathematical form of the kinetic relationship, which is that the overall rate of conversion of A be proportional to its concentration just outside the film. That is,

$$i_F/nFA = kC_A(y = \phi) \tag{14.4.2}$$

---

[2]In this book, the term *substrate* is used consistently in the sense of a *platform*, such as might be used to support the assembly of a larger structure. In much of the literature on modified electrodes, the same term is used in the sense of a *consumable reactant*, as often found in biochemistry. In this nomenclature, our *primary reactant*, A, is called the *substrate*.

The proportionality constant, k, describes the overall rate law and can reflect any of the parameters describing partitioning, transport, or reaction within the film. Diagnosis of the rate-controlling processes is possible by examining the dependence of k (or i_F) on experimental variables, such as the thickness of the film, ϕ, or the concentration of catalyst within the film. In the next section, we will establish a basis for describing different situations.

14.4.2 Dynamical Elements, Characteristic Currents, and Limiting Behavior

Figure 14.4.1 provides a convenient basis for introducing the principal dynamical components in complex systems. Several different types of activity can affect the rate at which A is converted to B. Each such conversion causes a transfer of n electrons; hence i/nFA is the rate in moles per unit area per second. Species A must arrive at the film–solution boundary by convective diffusion; it might enter the structure by rate limited partitioning; it might require diffusion to the electrode surface or to a redox site within the film; there might be a rate limitation in the transfer of electrons at the electrode surface or at the redox site; and there might be a need for electrons to distribute themselves among redox sites throughout the structure. Any of these processes might be rate controlling for the overall conversion. In real systems, one also has to recognize the possibility of pores or pinholes in the film through which A can diffuse to the electrode.

For diagnosis of the rate-limiting elements in any system, we need a common format for comparing the rate capacities of the different processes. In electrochemistry, it is often convenient to express rates as currents, and we will do so in considering this set of problems. Our strategy is to express, as a set of *characteristic currents*, the *maximum* rates that would be observed if each individual dynamic element, in turn, defined the rate of the overall process entirely on its own. These situations are mostly imaginary and the corresponding currents ought to be regarded as conceptual. They are indices of capacity and are not the same as the current measured in the cell under any particular set of operating conditions. They have value because they afford a convenient, systematic way to treat limiting conditions where one process controls the rate and, eventually, to help express the current that would be observed under all operating conditions. We first consider these different limiting cases, and then (in Section 14.4.3) the general case where several processes together are rate-determining.

(a) Convective Diffusion in Solution
Let us imagine a situation in which events in the film are all very fast. Then, the rate of the overall conversion of A is the same as the rate at which A arrives at the outer boundary of the structure. This is the Levich flux, $0.62C_A^* D_A^{2/3} \nu^{-1/6} \omega^{1/2}$; thus the current would be i_A. This is the maximum conversion rate that could ever be seen in any system under any operating conditions, for it is impossible to convert A any faster than it arrives.

(b) Diffusion of A within the Film
Now let us consider the situation in which convective diffusion is very fast and species A partitions into the film quickly; yet no processes operate to convert A to B inside the film (e.g., process 4 in Figure 14.4.1). If the heterogeneous conversion of A is fast, then the overall process is entirely controlled by the rate at which the primary reactant, A, can arrive at the electrode surface by diffusion through the film.

Figure 14.4.2 provides a schematic view of the situation. The concentration of A at the electrode surface is zero (because the heterogeneous kinetics are fast). Just inside
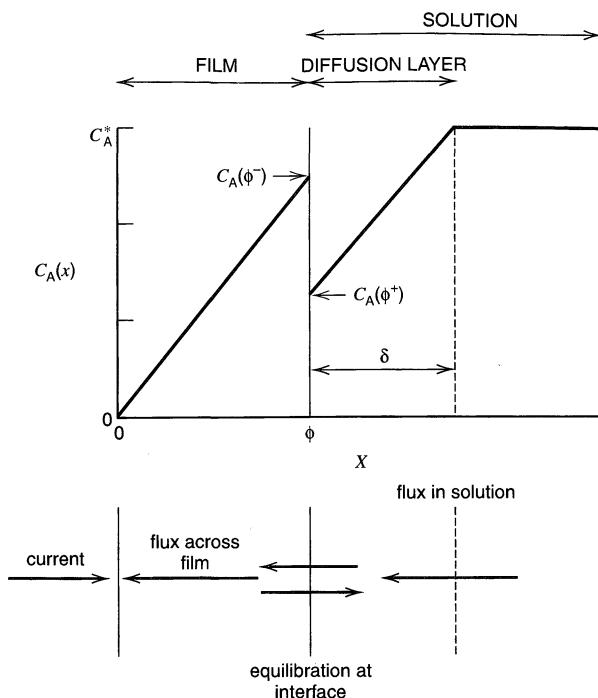
Figure 14.4.2 Steady-state concentration profiles for Case S, where the current is determined by the mass transfer of A in the film and in solution. The system is an RDE with a film of thickness ϕ on the electrode surface. The thickness of the diffusion layer in solution is $\delta = 1.61D_A^{1/3}\nu^{1/6}\omega^{-1/2}$. The various fluxes of species A are indicated by arrows. Distances are not to scale; ordinarily $\delta \gg \phi$.

the outer boundary of the film (ϕ^-), the concentration differs from that just outside the film (ϕ^+) because partitioning occurs. The concentrations are related via the partition coefficient

$$\kappa = \frac{C_A(\phi^-)}{C_A(\phi^+)} \tag{14.4.3}$$

This partitioning equilibrium applies only at the film–solution boundary. The system is at steady state; therefore the flux of A at all points in the film is constant. If the diffusion coefficient of A in the film, D_S, is uniform everywhere in the film, the slope of the concentration profile must be constant; hence the profile must be linear as shown in Figure 14.4.2.

Under conditions of very fast convective diffusion, the depletion layer outside the film would disappear, so that the concentration of A exposed to the film would become the bulk value. The largest possible concentration just inside the outer boundary is therefore κC_A^* and the maximum flux is $D_S\kappa C_A^*/\phi$. This is the greatest possible rate at which A can be converted to B when the process rests entirely upon reactant diffusion in the film, and this *reactant diffusion current*, i_S, becomes one of our conceptual descriptors of the system.[3]

$$i_S = \frac{nFAD_S\kappa C_A^*}{\phi} \tag{14.4.4}$$

---

[3]The subscript "S" is consistently used in the literature for this conceptual current and for the diffusion coefficient of A in the film. The usage is rooted in the fact that A is often called the *substrate*. See the footnote in the introduction to Section 14.4 for further relevant comment.

In the actual situation, both convective transfer of A to the film surface and diffusion of A through the film occur serially. At steady state these processes take place at equal rates, so that

$$\frac{D_S C_A(\phi^-)}{\phi} = \frac{D[C_A^* - C_A(\phi^+)]}{\delta} = \frac{i}{nFA} \tag{14.4.5}$$

where D applies to A in solution. The relevant equation for the limiting current from (14.4.3)–(14.4.5) is

$$\frac{1}{i_l} = \frac{1}{i_A} + \frac{1}{i_S} \tag{14.4.6}$$

Thus, if diffusion of A within the film is the rate-determining process, the value of i_S can be determined from the intercept of a plot i_l^{-1} vs. $\omega^{-1/2}$. An example of the situation just described involves the reduction of benzoquinone on an electrode coated with a film of poly(vinylferrocene). The results of an RDE study are shown in Figure 14.4.3. Note that the slopes of the curves of i_l^{-1} vs. $\omega^{-1/2}$ are the same in the presence and absence of film, since they are determined by mass transport only in solution (i.e., i_A). The intercepts depend upon ϕ and C_A^*, as predicted by (14.4.4).

The case where an extraction equilibrium is not attained at the film/solution interface has also been considered (75). In this case, the transport of A across the interface becomes another limiting flux, given by the expression $\chi_f C_A(\phi^+) - \chi_b C_A(\phi^-)$, where χ_f and χ_b are the rate constants for transfer of A from solution into film, and from film into solution, respectively. This situation yields the equation

$$\frac{1}{i_l} = \frac{1}{i_A} + \frac{1}{i_S} + \frac{1}{i_P} \tag{14.4.7}$$
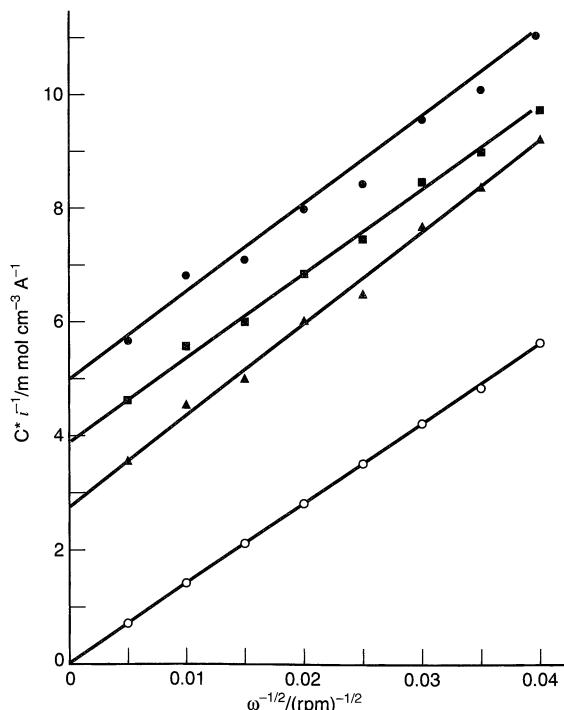
Figure 14.4.3 Experimental results for the reduction of benzoquinone (BQ) through a film of poly(vinylferrocene) on a Pt RDE. The reciprocal current [normalized for the concentration of BQ in solution: 5.82, 3.84, and 1.96 mM (top to third curves)] vs. $\omega^{1/2}$. The open circles show the results for a bare Pt RDE immersed in a solution containing 5.82 mM BQ. [Reprinted from J. Leddy and A. J. Bard, *J. Electroanal. Chem.*, **153**, 223 (1983), with permission from Elsevier Science.]

where the *permeation current*, i_P, is given by

$$i_P = nFA\chi_f \, C_A^*$$ (14.4.8)

When the flux of A across the interface, measured by i_P, is large, the limiting behavior of (14.4.6) is obtained.

The situation just discussed is sometimes called the *membrane model*, since the film behaves as a membrane through which species A must diffuse to reach the substrate surface. In Section 14.4.3, we will discuss the general case of film-mediated reduction of A in terms of a zone diagram that shows how different experimental parameters affect the observed voltammetric behavior. Within this formalism, the condition that we have just covered, where diffusion of A through the film is totally limiting is called *Case S*.

(c) Diffusion of Electrons in the Film

Many potential applications of modified electrodes involve the need to distribute electrons (or holes) throughout the structure. For example, if a given electrode process does not proceed at the electrode surface because of slow kinetics, one might still achieve success by placing a catalyst in the film. This is shown in Figure 14.4.1 by the introduction of a species P to the film that can be reduced to Q at the electrode surface. We assume that A cannot enter the film, but that electrons can move through the film by hopping from Q to P as shown as process 2 in the figure, with electron transfer to A taking place at the film/solution interface (process 3). Electrons might also reach the interface by physical diffusion of Q through the film (process 5), but here we consider the situation where this does not occur. Such would be the case, for example, when species P is an electroactive group attached to a polymer chain incorporated in the film (Section 14.2.3), so that long range motion of P and Q would be highly restricted. Note, however, that charge hopping between P and Q implies the existence of counter ions in the film that can undergo some motion to compensate charge.

Under these circumstances, the apparent rate at which Q appears to move through the film from electrode to the outer boundary of the film depends upon the rate of the electron-transfer reaction between P and Q. Considerations of analogous reactions in homogeneous solution showed that such a process is equivalent to diffusion (76, 77). The *apparent diffusion coefficient* observed for a species, D_E, is composed of contributions from the physical movement of the species (governed by its translational diffusion coefficient, D) and the electron-transfer process. When bimolecular kinetics apply and the species can be considered as points, then D_E can be estimated from the *Dahms–Ruff equation*,

$$D_E = D + k\delta^2 C_P^* b$$ (14.4.9)

where δ is the distance between sites for electron transfer, b is a numerical constant (frequently taken as $\pi/4$ or as $1/6$ for three-dimensional diffusion), and C_P^* is the total concentration of sites, oxidized and reduced. Similar and equivalent representations were given for polymer films on electrodes, where charge hopping was again treated as a diffusional process (40, 78, 79). Thus the movement of charge by electron transfer through the polymer can be treated in terms of a diffusion coefficient, D_E (sometimes also written in the literature as D_{ET} or D_{ct}), which is related to the electron-transfer kinetics, and should be distinguished from actual mass-transfer diffusion coefficients, such as D and D_S.

Now let us imagine an assembly in which electron diffusion carries the whole weight of the process by which A is converted to B. We disallow the permeation of A into the

film, so we can disregard the direct reaction of the primary reactant at the electrode surface, and we have no kinetic limitations from the dynamics of partitioning or diffusion of A in the structure. Thus we require that all electrons participating in the overall process be transported entirely across the film, where a fast reaction of A takes place.

The maximum current arises when the concentration of electrons in the film is at its largest possible value near the electrode surface, but approaches zero at the outer boundary (because species A arrives in high flux and reacts quickly). The largest possible concentration of electrons is the concentration of redox sites hosting them, C_P^*; therefore the maximum flux of electrons (formally a flux of Q outward, or of P inward, in the model of Figure 14.4.1) is $D_E C_P^*/\phi$ in moles per unit area per unit time. The corresponding *electron diffusion current*,

$$i_E = \frac{FAD_E C_P^*}{\phi}$$

(14.4.10)

is the principal expression of charge delivery capacity via electron diffusion in the system. The amount of P in the film is sometimes given in terms of a surface concentration, Γ_P, (mol cm^{-2}), $C_P^* = \Gamma_P/\phi$. This limiting case is designated *Case E*.

A more complicated example where electron transfer within a modified layer is important is in the design of an electrode for the oxidation of glucose. This reaction proceeds at a slow rate on most electrode surfaces. Placement of glucose oxidase in a film on the electrode allows glucose to be oxidized, but that process results in reduction and deactivation of the oxidase. Moreover, the fact that the glucose has been oxidized, even to the extent of one turnover, cannot be communicated to the electrode, because the kinetics of electrooxidation of the enzyme are poor. The missing element is a means for shuttling electrons from the reduced enzyme, wherever it might be located in the structure, to the electrode. A happy solution is shown in Figure 14.4.4, where Os(bpy)$_2$(PVP)Cl^{2+} (representing species P) is introduced as a electron-transfer mediator by coordination to a polymeric matrix (PVP).

(d) Cross-Reaction in the Film

It is also possible, as in the example of glucose detection, that the cross-reaction of primary reactant with redox sites in a film, that is, the rate of the reaction of A with Q, is rate-determining in the overall conversion of A. This is a common situation, so we need a means for characterizing the capacity of a system to deliver charge by cross-reaction when nothing else is limiting.

Let us imagine a system in which A partitions and permeates rapidly, so that its concentration everywhere in the film is the partitioned value in equilibrium with the concentration in solution just outside the film. Suppose also that electrons diffuse rapidly through the structure, so that their concentration is uniform. Finally, suppose that A does not react at the electrode surface. In this situation, depicted in Figure 14.4.5, A is converted to B uniformly in the film, because there is a uniform availability of electrons, reaction sites, and primary reactant.

The maximum rate of charge delivery is defined by the maximum rate of cross-reaction, which occurs when two conditions are satisfied. First, the potential of the electrode must be sufficiently negative to leave the redox sites fully reduced (if the conversion of A to B is a reduction), so that the electron concentration is C_P^*. Second, the convective-diffusion outside the film must be efficient enough to bring the concentration just outside the film-solution boundary to the bulk value. Then the concentration of A inside the film is the greatest possible value κC_A^*.

(a)

−0.1 V(SHE)   0.5 V(SHE)   0.6 V(SHE)

GLUCOSE   GLUCOSE   2[Os(bpy)$_2$(pvp)Cl]$^+$
                 OXIDASE
                 FAD+2H$^+$

$2e^-$ $2e^-$ $2e^-$ ELECTRODE

GLUCONOLACTONE   GLUCOSE   2[Os(bpy)$_2$(pvp)Cl]$^{2+}$
+2H$^+$ OXIDASE
                 FADH$_2$

(b)
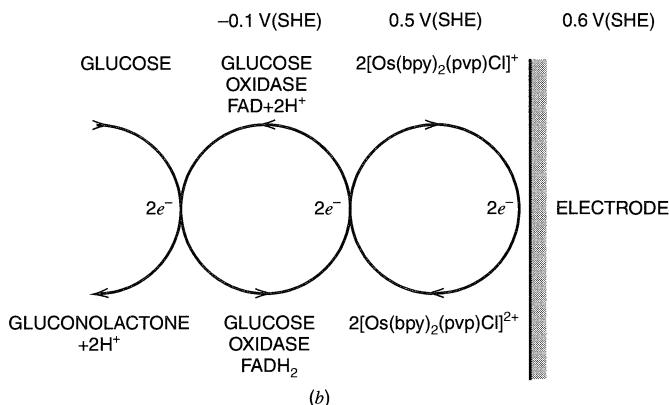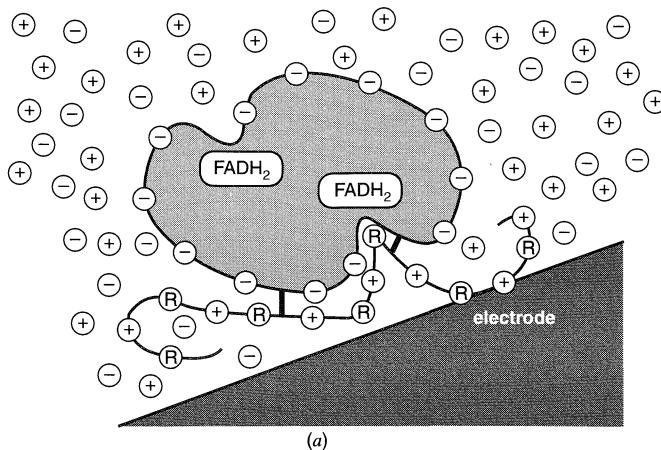
Figure 14.4.4 (*a*) Representation of an enzyme electrode based on glucose oxidase (containing FADH$_2$ centers) and a polycationic polymer incorporating redox groups, R. (*b*) The electron-transfer steps in the reaction, with approximate potentials of the electrode and the redox couples. [Reprinted with permission from A. Heller, *Accts. Chem. Res.*, **23**, 128 (1990). Copyright 1990, American Chemical Society.]

In most published treatments, the redox sites used to shuttle electrons are assumed to be the same as those where A is converted to B. This assumption is valid in many real systems and it affords a simplification, so we will use it here. The consequence is that the electron concentration is also the concentration of reaction centers. Given a bimolecular cross reaction, the greatest possible rate is $k\kappa C_A^* C_P^*$ in moles per unit volume per second.
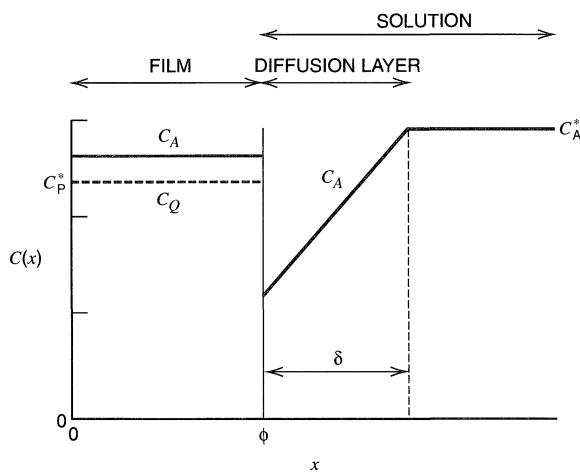
Figure 14.4.5 Schematic concentration profiles for Case R, where the rate of reaction between A (solid line) and Q (dashed line) limits the current.

The corresponding current flow, called the *cross-reaction current* i_k, is the product of this rate, the volume of the film, and charge passed per mole of reaction nF,

$$i_k = nFA\phi k\kappa C_A^* C_P^* = nFAk\Gamma_P C_A^* \qquad (14.4.11)$$

This characteristic current is the principal index of an assembly's capacity for cross-reaction. As in the previous limiting cases, the expression for the current is

$$\frac{1}{i_l} = \frac{1}{i_A} + \frac{1}{i_k} \qquad (14.4.12)$$

This limiting case is designated *Case R.*

The example of Figure 14.4.4 clearly shows that the species involved in shuttling electrons need not be the same as those engaged in cross-reaction with A; hence the redox site concentration might differ from C_P^* in Equation (14.4.11). Adaptation of that equation is straightforward, although such systems might also require an explicit consideration of the rate capacity for electron transfer between the shuttle and the cross-reaction site.

14.4.3 Interplay of Dynamical Elements

In the general case, several of the processes previously considered and illustrated in Figure 14.4.1 can contribute simultaneously to the rate of the reaction. For example, A might be reduced in the film at a rate controlled, not by a single process, but jointly by the parallel processes of its diffusion within the film and its cross-reaction with mediator Q. The overall general mathematical treatment is more complicated than for the various limiting cases discussed in Section 14.4.2 and requires a fuller discussion than can be given here (80). The different processes are represented by the characteristic currents described above:

i_A mass transport rate of A in solution to a bare electrode or the outer film boundary.

i_S maximum mass transport rate of A in the film, (14.4.4)

i_E maximum effective charge diffusion rate via the mediator Q in the film, (14.4.10)

i_P maximum mass-transfer rate of A across the film-solution interface, (14.4.8)

i_k maximum rate of electron-transfer reaction between A and Q, (14.4.11)

Schematic concentration profiles for the general case are shown in Figure 14.4.6. The limiting current with all of the processes contributing can be obtained only by numerical solution of the differential equations governing the system. However, in most experimental systems only one or two of the processes will be important. Which limiting case or subcase applies (i.e., which factors are rate-determining) is determined by the relative magnitudes of the characteristic currents, or more explicitly, by the ratios i_S^*/i_k^* and i_E/i_k^*, where

$$i_S^* = i_S\left[1 - \frac{i_l}{i_A} - \frac{i_l}{i_P}\right] \qquad (14.4.13)$$

$$i_k^* = i_k\left[1 - \frac{i_l}{i_A} - \frac{i_l}{i_P}\right] \qquad (14.4.14)$$

With knowledge of these ratios, the appropriate limiting case or subclass can be determined from the zone diagram of Figure 14.4.7.

For example, consider first the case where the reaction rate between A and Q is slow, but A can readily penetrate the film and electron diffusion in the film is rapid. This is Case
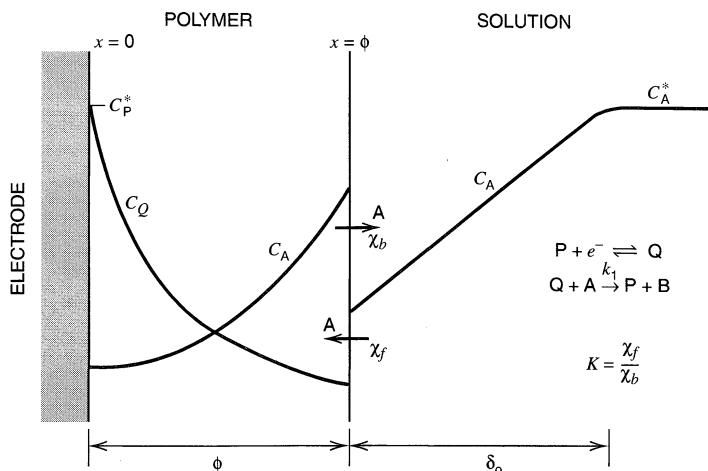
Figure 14.4.6 Schematic concentration profiles for the general case of mediated (catalytic) reduction of the primary reactant, A, by electrogenerated Q. The electrode is held at a potential where all P at the electrode surface is reduced to Q, so that the concentration of Q at the electrode surface is C_P^* ($= \Gamma_P^*/\phi$). Within the solution ($x > \phi$), the concentration profile for A is approximately linear. χ_f and χ_b are the rate constants for the transport of A into and out of the film, respectively. [Reprinted from J. Leddy, A. J. Bard, J. T. Maloy, and J.-M. Savéant, *J. Electroanal. Chem.*, **187**, 205 (1985), with permission from Elsevier Science.]
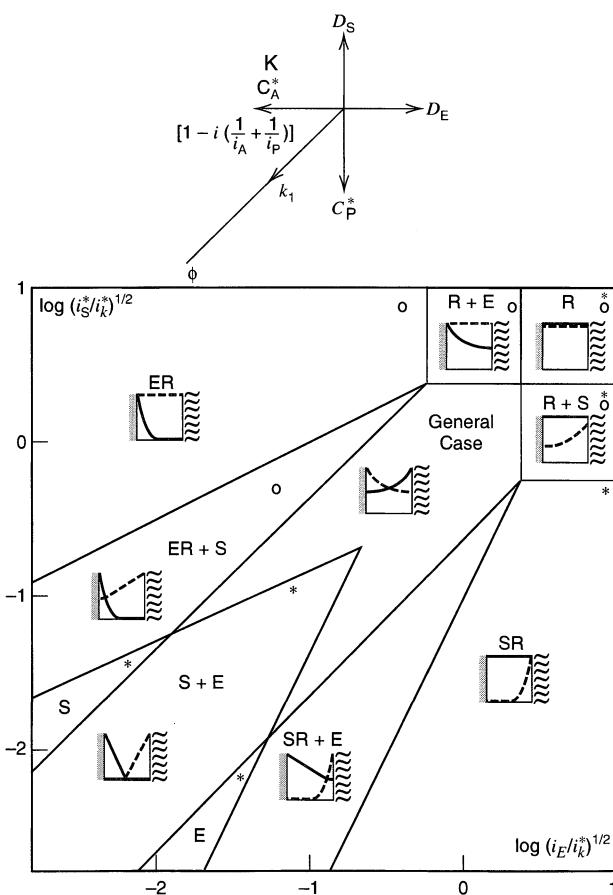
Figure 14.4.7 Zone diagram for different special cases involved in the general case of mediated reduction of a primary reactant at a film-covered electrode. Some of these cases (e.g., cases S, R, E) are discussed in the text. Cases marked * are those that produce linear plots of $(1/i_l)$ *vs.* $\omega^{-1/2}$. The experimental behavior is affected by the magnitude of various experimental parameters shown at the top of the figure. Schematic concentration profiles of the species A (dotted line) and Q (solid line) are shown for the different cases. [Reprinted from J. Leddy, A. J. Bard, J. T. Maloy, and J.-M. Savéant, *J. Electroanal. Chem.*, **187**, 205 (1985), with permission from Elsevier Science.]

R in the upper right corner of the diagram, which also shows the normalized concentration profiles of A and Q (see also Figure 14.4.5). If we now consider this case as D_S decreases, so that movement of A in the film becomes slower, we find a change in behavior, first to *Case R + S* and then to *Case SR*. In the latter case, which often occurs in practical studies, both the cross-reaction rate and diffusion of A in the film affect the behavior. The relevant expressions for the various limiting cases and subcases are given in Table 14.4.1. In this table i_1 is the plateau current corresponding to reduction of A via reaction with Q (the catalytic reaction) and i_2 represents the plateau current for the direct reduction of A. The latter is observed only in certain situations where A can penetrate the film and reach the metal substrate before it is all consumed by reaction with Q. For example, one can see in Table 14.4.1 that Case SR will produce a linear Koutecký–Levich plot ($1/i_l$ vs. $1/\omega^{1/2}$ or $1/i_l$ vs. $1/i_A$) with an intercept of $1/i_P + 1/(i_k i_S)^{1/2}$. Also, $i_2 = 0$ for this case.

In actual studies, the problem is more complicated, since one must determine which case applies from the experimental results, that is, i_l as a function of ω, Γ_P^*, C_A^*, and ϕ. Procedures and diagnostic criteria are given in reference 80. Also discussed there are several experimental studies featuring analysis of results using this approach. In addition, this reference covers situations where the catalyst and the electron carrier are different species, such as in the glucose oxidase enzyme electrode.

TABLE 14.4.1 Expressions for Plateau Currents in Koutecký–Levich Format for Various Dynamical Cases in Modified Electrode Systems[a]

† $\dfrac{1}{i_1} = \dfrac{1}{i_A} + \left\{\dfrac{1}{i_P} + \dfrac{1}{(i_k i_S)^{1/2}\tanh\left(\frac{i_k}{i_S}\right)^{1/2}}\right\}$ $(m) = 1$	† $\dfrac{1}{i_1} = \dfrac{1}{i_A} + \left\{\dfrac{1}{i_P} + \dfrac{1}{i_k}\right\}$ $(m) = 1$ $(b) = (FC_P^* C_A^* k_1 \kappa\phi)^{-1} + i_P^{-1}$	$\dfrac{1}{i_1} = \dfrac{1}{i_A} + \dfrac{1}{i_P} + \dfrac{i_1}{i_k i_E \tanh^2\left\{\frac{i_k}{i_E}\left[1 - i_1\left(\frac{1}{i_A} + \frac{1}{i_P}\right)\right]\right\}^{1/2}}$
† $\dfrac{1}{i_1 + i_2} = \dfrac{1}{i_A} + \left\{\dfrac{1}{i_P} + \dfrac{\tanh\left(\frac{i_k}{i_S}\right)^{1/2}}{(i_k i_S)^{1/2}}\right\}$ $(m) = 1$	† $\dfrac{1}{i_1 + i_2} = \dfrac{1}{i_A} + \left\{\dfrac{1}{i_P} + \dfrac{1}{i_S}\right\}$ $(m) = 1$ $(b) = \phi/FC_A^*\kappa D_S + i_P^{-1}$	† $\dfrac{1}{i_1 + i_2} = \dfrac{1}{i_A} + \left\{\dfrac{1}{i_P} + \dfrac{1}{i_S}\right\}$ $(m) = 1$ $(b) = \phi/FC_A^*\kappa D_S + i_P^{-1}$
(R + S)	(R)	(E + R)

† $\dfrac{1}{i_1} = \dfrac{1}{i_A} + \left\{\dfrac{1}{i_P} + \dfrac{1}{(i_k i_S)^{1/2}}\right\}$ $(m) = 1$ $(b) = 1/FC_A^*\kappa(C_P^* D_S k_1)^{1/2} + i_P^{-1}$ $i_2 = 0$	¶ $\left[\dfrac{1}{i_1} - \dfrac{1}{i_A}\right] = \left\{\dfrac{1}{i_P}\right\} + \dfrac{i_1}{i_k i_E}$ $(m) = (i_k i_E)^{-1}$ $(b) = i_P^{-1}$ † $\dfrac{1}{i_1 + i_2} = \dfrac{1}{i_A} + \left\{\dfrac{1}{i_P} + \dfrac{1}{i_S}\right\}$ $(m) = 1$ $(b) = \phi/FC_A^*\kappa D_S + i_P^{-1}$
(SR)	(ER)

$\dfrac{1}{i_1} = \dfrac{1}{i_A} + \dfrac{1}{i_P} + \dfrac{1}{\left[i_k i_S\left(1 - \frac{i_1}{i_E}\right)\right]^{1/2}}$ $i_2 = 0$	† Exhibits linear Koutecký–Levich behavior with (m) = slope and (b) = intercept ¶ Non-linear Koutecký–Levich behavior, but a linear form is given having (m) = slope and (b) = intercept $i_P^{-1} = 1/FC_A^*\chi_f$	¶ $\left[\dfrac{1}{i_1} - \dfrac{1}{i_A}\right] = \left\{\dfrac{1}{i_P} + \dfrac{1}{i_S}\right\} + \dfrac{i_1}{(i_k i_E)}$ $(m) = (i_k i_E)^{-1}$ $(b) = \phi/FC_A^*\kappa D_S + i_P^{-1}$ † $\dfrac{1}{i_1 + i_2} = \dfrac{1}{i_A} + \left\{\dfrac{1}{i_P} + \dfrac{1}{i_S}\right\}$ $(m) = 1$ $(b) = \phi/FC_A^*\kappa D_S + i_P^{-1}$
(SR + E)		(ER + S)

† $\dfrac{1}{i_1} = \left\{\dfrac{1}{i_E}\right\}$ $(m) = 0$ $(b) = i_E^{-1}$ $i_2 = 0$	† $\dfrac{1}{i_A} = \left\{\dfrac{i_S}{i_S + i_E}\right\}\dfrac{1}{i_A} + \left\{\dfrac{1}{i_S + i_E}\left(1 + \dfrac{i_S}{i_P}\right)\right\}$ $(b)/(m) = \phi/FC_A^*\kappa D_S + i_P^{-1}$ $i_2 = 0$	† $\dfrac{1}{i_1} = \dfrac{1}{i_A} + \left\{\dfrac{1}{i_P} + \dfrac{1}{i_S}\right\}$ $(m) = 1$ $(b) = \phi/FC_A^*\kappa D_S + i_P^{-1}$ $i_2 = 0$
(E)	(S + E)	(S)

[a] Adapted from J. Leddy, A. J. Bard, J. T. Maloy, and J. M. Savéant, *J. Electroanal. Chem.*, **187**, 205 (1985) with permission from Elsevier Science.

One can also consider the case where the cross-reaction is so fast that it occurs at a single monolayer of mediator at the film/solution interface. The limiting current is then

$$1/i_l = 1/i_A + \{i_k[1 - (i_l/i_E)]\}^{-1} \tag{14.4.15}$$

When $i_E \gg i_l$, this yields the same expression as that for Case R, (14.4.12).

▶ 14.5 BLOCKING LAYERS

While the previous sections mainly dealt with layers that contain electroactive species, layers that serve to block electron and ion transport between an electrode and a solution are also of interest. These can have practical applications, for example, to prevent corrosion of the surface or to serve as electrical insulators. Electrochemical methods are useful in establishing how well such layers block transfer to the surface and, as discussed in Section 14.5.2, can be used to study the distance dependence of electron transfer.

14.5.1 Permeation Through Pores and Pinholes

Consider an electrode covered with a film that has continuous pores or channels from the solution to the electrode (Figure 14.4.1, process 6). We can ask how the electrolysis of a species in solution at such an electrode differs from that at the bare (unfilmed) electrode. The answer depends upon the extent of coverage of the electrode by the film, the size and distribution of the pores, and the time scale of the experiment. The situation is complicated, because the pores can have different dimensions and degrees of tortuosity, and their distribution within the film may not be uniform. Thus, theoretical treatments of such films often use idealized models. The theory for electrodes of this type is closely related to that for ultramicroelectrode arrays (Section 5.9.3), which, however, often involve a better-defined geometry and uniform distribution of active sites (81, 82).

(a) Chronoamperometric Characterization
One can examine the current passed at the modified electrode during a potential step to the diffusion-limited regime for a solution species and then compare the result to the Cottrell behavior at a bare electrode (equation 5.2.11). Usually simple models, like those in Figure 14.5.1, are used.
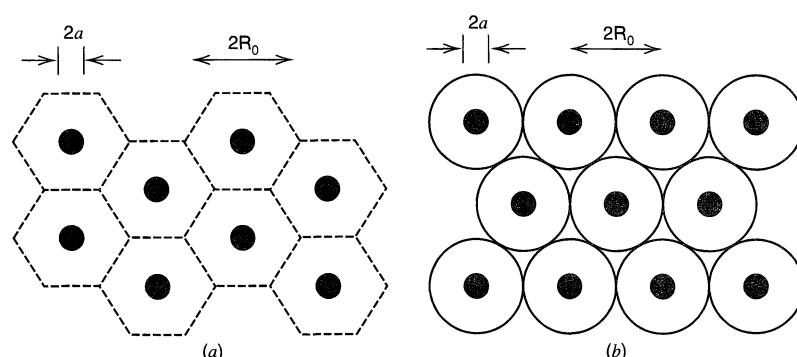
Figure 14.5.1 Idealized models for a surface with active sites (shaded) of radius a, spaced $2R_0$ apart. Shown are (a) a hexagonal array and (b) an approximation where the inactive zones are taken as circular.

Most often we consider the case where the fraction of the surface uncovered, $(1 - \theta)$, is small, the pore radius, a, is small, and the pores are spaced far apart compared to a. This is much like the situation shown in Figure 5.2.4. When the time scale of the experiment is small, so that $(Dt)^{1/2} << a$, the electrode will show a linear electrochemical response, except that the area will be $(1 - \theta)$ times that of the bare electrode, that is, electrolysis of solution species occurs directly at the substrate only within the pores of the film. At longer times, each site will show steady-state ultramicroelectrode behavior, and the current that results represents the sum of that from the individual sites. When the time is such that the diffusion layers from the individual sites grow together, overlap, and merge, the electrode behavior approaches that of the unfilmed electrode with a total area of that of the bare electrode. Thus a study of the electrochemical response as the effective time scale of the experiment is varied can provide information about θ, a, and the pore distribution.

Gueshi et al. (83) considered an electrode surface with uniformly distributed, circular, active regions of radius a inside hexagonal, inactive regions of total radius R_0. The
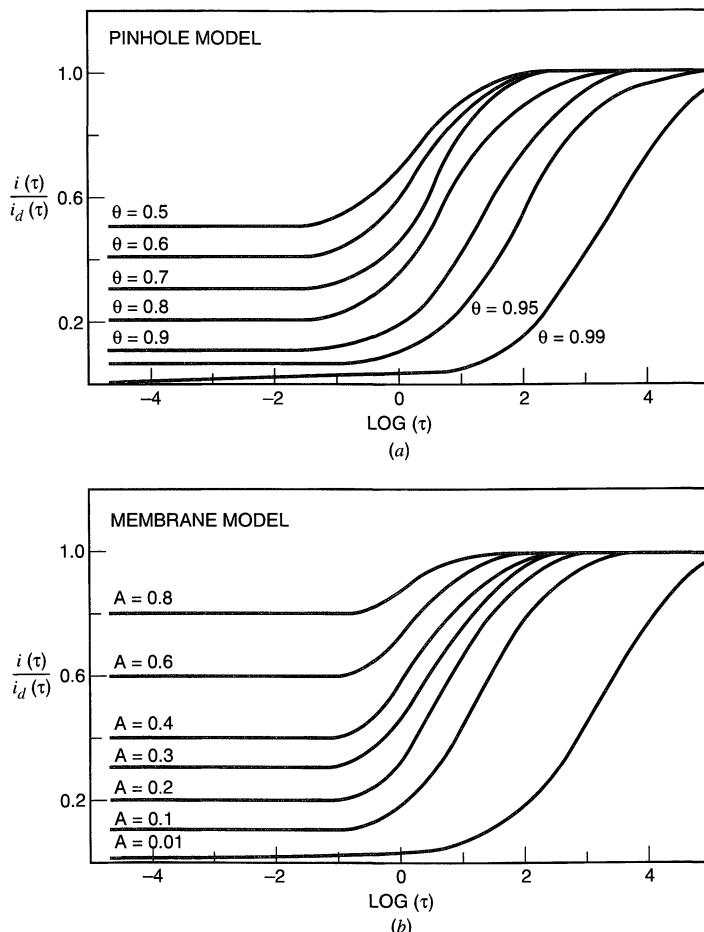
Figure 14.5.2 Working curves for chronoamperometric (potential step) experiments at electrodes covered with a blocking film assuming (a) pinhole and (b) membrane models. The curves are given in terms of dimensionless parameters [the current ratio, $i(\tau)/i_d(\tau)$, and τ (see text)] for different coverages, θ, or values of $A = \kappa(D_S/D_A)^{1/2}$. [Reprinted from J. Leddy and A. J. Bard, *J. Electroanal. Chem.*, **153**, 223 (1983), with permission from Elsevier Science.]

current at such an electrode, $i(t)$, normalized to the current at the same time at the bare electrode, is given by (84)

$$\frac{i(\tau)}{i_d(\tau)} = \frac{1}{\sigma^2 - 1} \{\sigma \exp(-\tau) - 1 + \sigma^2 (\pi T)^{1/2} \exp(T)[\text{erf}(\sigma T^{1/2}) - \text{erf}(T^{1/2})]\} \quad (14.5.1)$$

where $T = \tau/(\sigma^2 - 1)$, $\sigma = \theta/(1 - \theta)$, $\tau = \ell t$, and ℓ is a function of D, the hole size and distribution, and θ, as defined in (83). A plot of $i(\tau)/i_d(\tau)$ is given in Figure 14.5.2a for different values of θ. Note that at short times (small τ) the current ratio attains the limiting value of $1 - \theta$. At long times, when the diffusion layer grows to a thickness that is large compared to R_0, the ratio approaches unity. The location of the intermediate region depends upon θ and a, and thus a plot of $i(\tau)/i_d(\tau)$ vs. t can be used to estimate these parameters. This treatment assumes a thin film where the rate of diffusion of solution reactant through the pores is rapid and no region where steady-state microelectrode behavior is observed (i.e., R_0/a not very large). In many systems these assumptions do not hold, and more complex models are needed.

The chronoamperometric behavior of the case just considered is very similar to that seen for partitioning of the solution reactant, A, into the film and diffusion in the film with a diffusion coefficient, D_S, to the electrode surface. This is just the membrane model or Case S considered in Section 14.4.2(b). The concentration profiles for a potential step experiment where the concentration of A at the electrode/film interface, $C_A(x = 0) \approx 0$ are shown in Figure 14.5.3. The expression for the current, normalized to that at the bare electrode is (84)

$$\frac{i(\tau)}{i_d(\tau)} = u\left\{1 + 2\sum_{j=1}^{\infty}\left(\frac{1-u}{1+u}\right)^j \exp(-j^2/\tau)\right\} \quad (14.5.2)$$

where $\tau = D_S t/\phi^2$ and $u = \kappa(D_S/D_A)^{1/2}$. Plots of the normalized current vs. log τ, for different values of u, are shown in Figure 14.5.2b. Note the similarity to the pinhole model curves in Figure 14.5.2a. At short times, when the diffusion layer thickness is small compared to the film thickness, that is, $(D_S t)^{1/2} \ll \phi$, the electrolysis occurs completely within the film and is characterized by a diffusion coefficient, D_S, and an initial concentration, κC_A^*. Under these conditions the current ratio approaches $\kappa(D_S/D_A)^{1/2}$. At long times, the diffusion layer extends well into the solution phase, and the current ratio approaches unity.
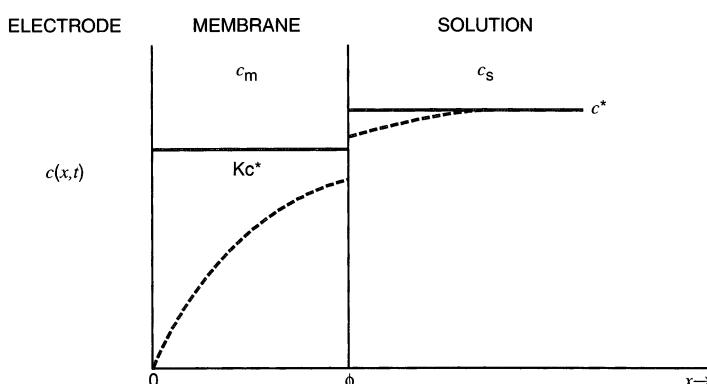
Figure 14.5.3 Concentration profiles for the membrane model of a thin film of thickness ϕ. Solid lines, initial concentrations; dashed lines, after a potential step. In this figure, K is the partition coefficient, κ, identified in the text. The situation considered is for $K = \kappa < 1$. [Reprinted from P. Peerce and A. J. Bard, *J. Electroanal. Chem.*, **112**, 97 (1980), with permission from Elsevier Science.]

A chronoamperometric investigation of this type involved poly(vinylferrocene) films (~1 μm thick), where benzoquinone or methyl viologen were the solution species whose movement through the film was studied (85). For this system, a membrane model fit the experimental results better than a pinhole model, and values of κ and D_S were estimated.

(b) RDE Studies

Given the similarity in the chronoamperometric results for the pinhole and membrane models, we would expect that the response of a solution species at an RDE with the surface covered by a blocking film with pores or pinholes would also be similar to that described in Section 14.4.2(b). Indeed the form of the equation in the latter case is (80, 85, 86):

$$1/i_l = 1/i_A + 1/i_{CD} \tag{14.5.3}$$

where the expression for the maximum current attributable to channel diffusion, i_{CD}, depends upon the details of the model used in the treatment. In one treatment (86), mainly applicable to pinholes of average radius, a, spaced so that the distance between centers is $2R_0$ (with both a and R_0 being of the order of the thickness of the diffusion layer), the following expression results:

$$i_{CD} = \frac{nFAD_A C_A^*}{\sum\limits_n A_n \tanh[x_n \delta/R_0]} \tag{14.5.4}$$

where $\delta = 1.61 D_A^{1/3} \nu^{1/6} \omega^{-1/2}$ is the thickness of the diffusion layer in solution and A_n is a function of a, R_0, and x_n, with x_n, representing the zero points of first-order Bessel functions. In the limiting case where $\delta > R_0$, $A_n \tanh[x_n \delta R_0] \rightarrow A_n$ and a linear plot following (14.5.3) would be expected.

The simple model in Figure 14.5.1b can be used to give a simpler approximation for i_{CD}. Since $\pi a^2/\pi R_0^2 \approx (1 - \theta)$, $a = R_0(1 - \theta)^{1/2}$. When the site radius and spacing are small compared to the diffusion layer thickness, so that the sites behave as a collection of p UMEs, the expression for the total limiting current is[4]

$$i_l = 4FD_A C_A^* ap = 4FD_A C_A^* pR_0(1 - \theta)^{1/2} \tag{14.5.5}$$

The total electrode area, A, is $p\pi R_0^2$, so that the current density would be

$$j_l = FD_A C_A^*(1 - \theta)^{1/2}/\gamma R_0 \tag{14.5.6}$$

where γ is a factor that depends upon the site type and distribution. For the disk array under consideration the following expression has been proposed (80, 87):

$$j_l = F(1 - \theta)^{1/2} D_A C_A^*/0.6R_0 \tag{14.5.7}$$

where θ is the fractional coverage of the electrode by the blocking film and $2R_0$ is the spacing between the sites.

(c) Voltammetry

The treatments in subsections (a) and (b) pertain to conditions where the electron-transfer reaction at the electrode surface at unblocked sites is assumed to be so fast that the surface concentration of A is essentially zero (e.g., because the potential is sufficiently negative). It is instructive to consider the shape of the whole voltammogram with a blocking film.

---

[4]An assumption here is that the diffusion layer at each of the pores remains small compared to δ, so that the limiting current at each pore is not affected by the rotation of the electrode.

The parameters that govern the shape of the cyclic voltammogram compared to that at the bare electrode are θ, υ, k^0, and R_0 (87). Basically two factors come into play. First, for a given total current, the current density at the active sites will be larger than that at the bare electrode. Since the overpotential depends upon the current density, the effects of heterogeneous electron-transfer kinetics (e.g., the overpotential required for a given current) will be larger at a partially covered electrode. Second, when individual sites behave as ultramicroelectrodes, and they are spaced apart at a sufficient distance that their diffusion layers do not overlap during the time of the scan, the voltammogram will represent that of a collection of ultramicroelectrodes and produce a steady-state voltammogram. The behavior is shown in the zone diagram in Figure 14.5.4. The appropriate dimensionless constants for disk-type active sites are:

$$\lambda = \frac{(DRT/F\upsilon)^{1/2}}{0.6R_0(1 - \theta)} \tag{14.5.8}$$

$$\Lambda = \frac{k^0(1 - \theta)}{(RT/DF\upsilon)^{1/2}} \tag{14.5.9}$$

For large values of λ, such as where the diffusion layer thickness is small compared to the size and spacing of the sites, peak-shaped cyclic voltammograms result, with an apparent decrease in the heterogeneous rate constant compared to that shown for the unblocked electrode, $k_{app}^0 = k^0(1 - \theta)$. If k^0 is sufficiently high, so that Λ is large (the upper right section of the diagram), nernstian cyclic voltammograms are obtained. If Λ is small, the voltammograms become kinetically irreversible (lower right section). For small values of λ, the behavior becomes characteristic of an ultramicroelectrode array (left side of diagram) with limiting currents in the S-shaped voltammograms given by (14.5.7).
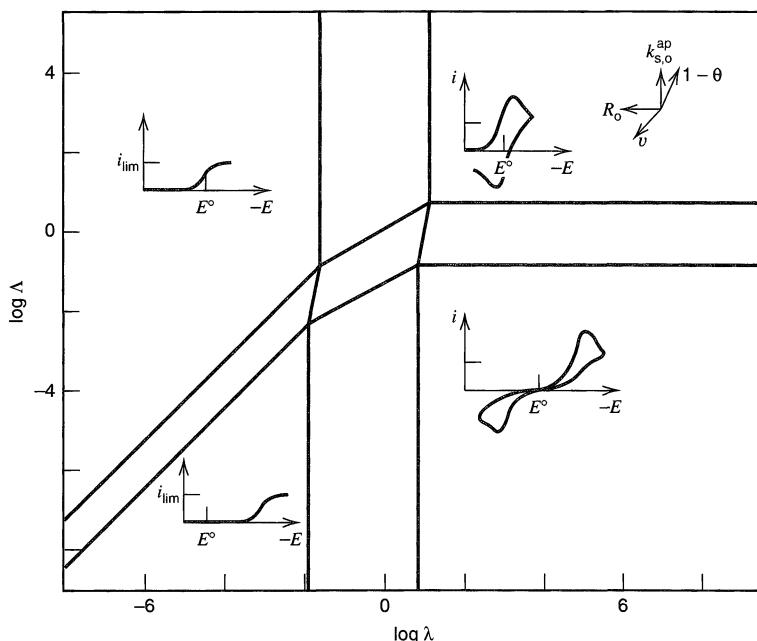
Figure 14.5.4 Zone diagram showing the characteristic cyclic voltammograms for a blocked electrode as a function of the dimensionless parameters λ and Λ and the experimental parameters θ, R_0, υ, and k^0 (indicated on the figure as $k_{s,0}^{ap}$). [Adapted from C. Amatore, J.-M. Savéant, and D. Tessier, *J. Electroanal. Chem.*, **147**, 39 (1983), with permission from Elsevier Science.]

14.5.2 Electron Transfer by Tunneling Through Blocking Films

By definition, mediated electron transfer of the type discussed in Section 14.4.2(c) cannot occur in blocking films. However for very thin films, e.g., self-assembled monolayers (SAM) of alkane thiols or oxide films, electrons can tunnel through the film and cause faradaic reactions. This phenomenon is important in electronic devices, in passivation of metal surfaces, and in fundamental studies of the distance dependence of the rate of electron transfer.

The basic concepts of electron tunneling were discussed briefly in Section 3.6.4, and the equation for the effect of tunneling on the electron-transfer rate constant, obtained from (3.6.2) and (3.6.39), can be written

$$k^0(x) = k^0(x = 0) \exp(-\beta x) \tag{14.5.10}$$

assuming β is essentially independent of potential. In some treatments the variation of β with energy, as implied in (3.6.38), is taken into account. The exponential decrease in the rate of tunneling with distance and the magnitude of β, usually on the order of 1 Å^{-1}, implies that electron tunneling will only be important with blocking films thinner than about 1.5 nm. Indeed the tunneling current through a bilayer lipid membrane (BLM), which is a model for a biological membrane and is about 3 to 4 nm thick, is negligibly small (resistance $> 10^8$ ohm cm^2). Similarly thin oxide films of metals like Ta, Si, and Al are highly resistive and can prevent electron transfer.

The formation of a blocking film on an electrode surface will decrease the capacitance compared to that of the bare electrode, since the distance of closest approach of the counter ions, d, will be increased by the thickness of the layer [see (13.3.2) and Figure 14.5.5]. The extent of blocking by the monolayer and the presence of pinholes can be assessed in a number of ways (88). To obtain the aggregate area of the pinholes one can, for example, compare the sizes of voltammetric peaks for the bare and filmed electrode (such as those for the formation and reduction of an oxide layer on Au). To obtain the spatial distribution, one can deposit a metal like Cu, then strip the film and perform microscopy on the resulting surface. A frequently used procedure is to observe the chronoamperometric or cyclic voltammetric behavior of an outer sphere species like Ru(NH$_3$)$_6^{3+}$ in solution
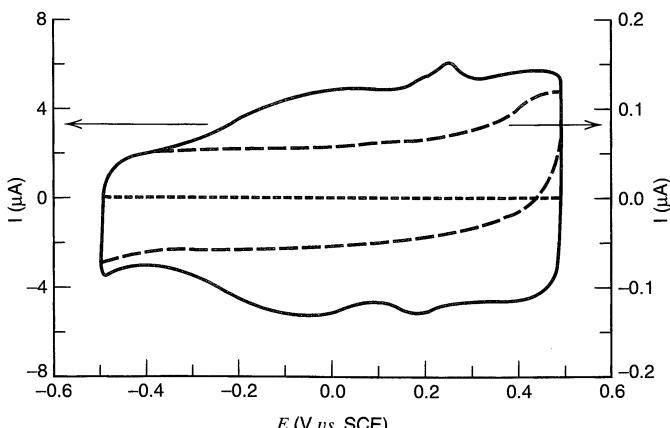
Figure 14.5.5 CV charging currents at 0.1 V/s for a bare polycrystalline gold electrode ($A \approx 1$ cm^2) in 1 M Na$_2$SO$_4$ [solid line (left current scale)] and coated with a C$_{18}$ alkyl thiol [coarse dashed line (right current scale) and fine dashed line (left current scale)]. The decrease in capacitance upon coating is by about a factor of 80. [Reprinted from H. O. Finklea, *Electroanal. Chem.*, **19**, 109 (1996), by courtesy of Marcel Dekker, Inc.]

at the electrode using the treatment in Section 14.5.1, under conditions where there is no electron tunneling through the film.

Studies of electron tunneling have generally been of two types (Figure 14.5.6). One involves a blocking film and electroactive molecules in solution. The other involves electroactive groups tethered on the opposite end of the molecule from the attachment site, usually in a mixed monolayer containing similar molecules without the electroactive group (see Figure 3.6.7). The interest in both types of studies is in determining (a) how the rate constant for electron transfer changes with distance between the electroactive center and the conductive electrode surface, and (b) how it is affected by potential or other experimental conditions. For these studies to be meaningful, it is important that there be no pinholes or defects in the films allowing direct access of electroactive solution species or tethered electroactive groups to the substrate. Moreover the films should have a well-defined and known structure, so that the distance between substrate and electroactive group is constant and known. Several studies discuss the effect of blocking monolayers on electrode reactions of outer sphere reactions of solution reactants and the treatment of the results via Marcus theory to obtain reorganization energies (λ) (88, 89). Note that in these studies of solution species, rate constants are the typical heterogeneous electron-transfer constants (cm/s). Fast reactions are difficult to study in this way because of mass-transfer limitations.

Studies of tethered electroactive species are less sensitive to pinholes than experiments with solution reactants and blocking layers, although heterogeneity and roughness of the substrate and film defects can still play a role. The rate constant, k, in this case has units of a first-order reaction (s^{-1}). Rate constants can be determined by a voltammetric method as described earlier for electroactive monolayers (Section 14.3.3). In addition potential-step chronoamperometry can be employed, in which case the current follows a simple exponential decay (88, 90, 91):

$$i(t) = kQ \exp(-kt) \qquad (14.5.11)$$
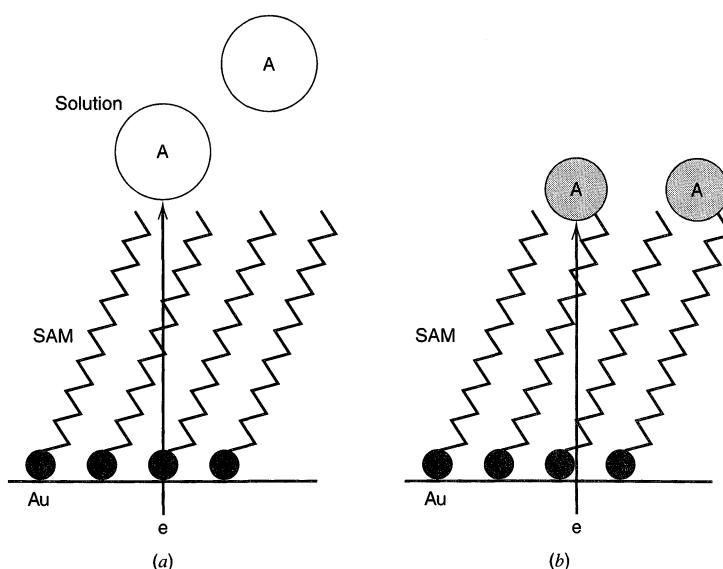
Figure 14.5.6 Types of experiments for studying electron tunneling through surface layers. (a) Through a blocking layer to a species, A, in solution. (b) To an electroactive group covalently attached to the layer. SAM = self-assembled monolayer.

where $Q = nFA\Gamma$, and Γ is the surface coverage of electroactive centers (mol/cm^2). Corrections for double-layer charging and solution resistance effects may be necessary, but they can be obviated or minimized by use of UMEs (91). Figure 14.5.7 contains a typical transient of this type for the reduction of Os(bpy)$_2$Cl(p3p)$^{3+}$ at a Pt UME, where (p3p) is 4,4'-trimethylenedipyridine (or py(CH$_2$)$_3$py). The molecule forms an adsorbed layer via the uncoordinated pyridine group on the p3p ligand. Because a UME was used, the experiment could be carried out in the microsecond regime. After decay of the double-layer charging current, a plot of $\ln[i(t)]$ *vs.* t is linear, as expected from (14.5.11), with a slope determined by the rate constant of the reaction. The dependence of $\ln k$ with overpotential for the reduction of the adsorbed $+3$ species or oxidation of the adsorbed $+2$ species follows Butler–Volmer behavior (Figure 14.5.8) in the range of low overpotential, but deviates sharply from that behavior with larger overpotentials. Note that the use of a UME and an adsorbed layer allowed the study of a very fast reaction ($k^0 \approx 10^4$ s^{-1}), where the equivalent reaction of a dissolved species probably would have been diffusion-controlled. This experimental approach also permits the use of an extraordinarily large range of overpotentials, and can therefore support quite full tests of electron-transfer theory.
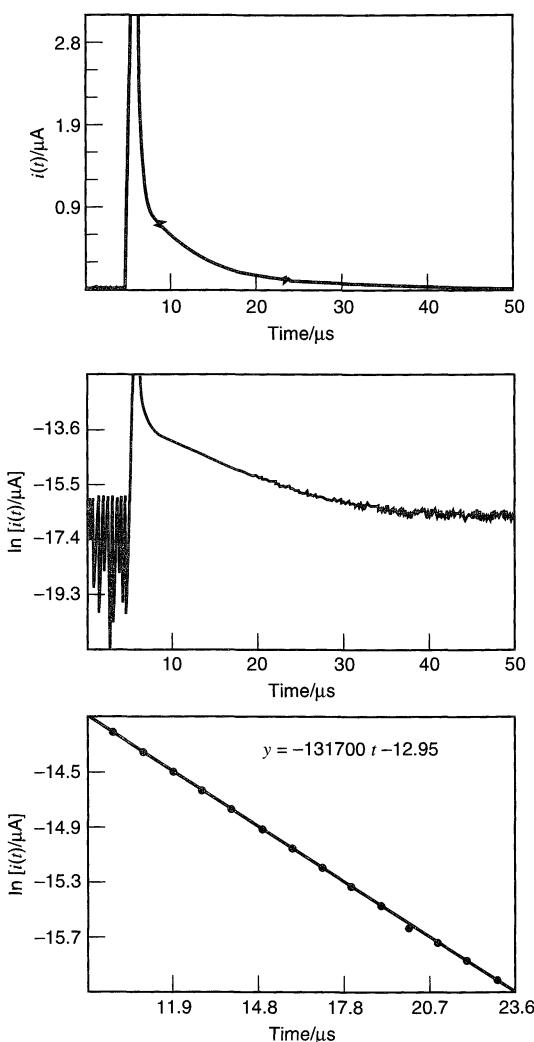
Figure 14.5.7 *Top*: Current transient for a potential step at a 5-μm radius Pt electrode with a monolayer of adsorbed Os(bpy)$_2$Cl(p3p)$^{3+}$ in DMF containing 0.1 M Et$_4$NClO$_4$. The lower frames show plots of log[$i(t)$] *vs.* t for the portion of the transient after double-layer charging. [Reprinted with permission from R. J. Forster and L. R. Faulkner, *J. Am. Chem. Soc.*, **116**, 5444 (1994). Copyright 1994, American Chemical Society.]
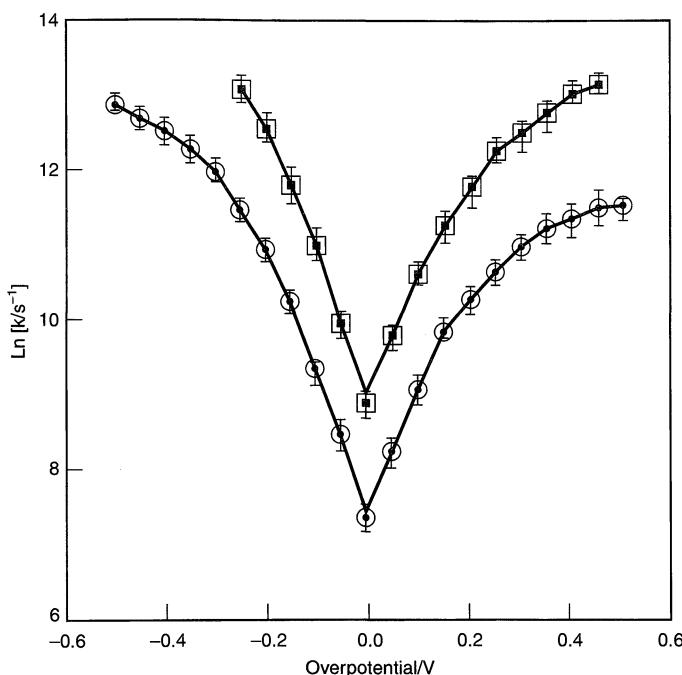
Figure 14.5.8 Dependence of ln k on overpotential. Circles show data for the reduction of a monolayer of Os(bpy)$_2$Cl(p3p)$^{3+}$ and the oxidation of Os(bpy)$_2$Cl(p3p)$^{2+}$ at a Pt UME. The external medium is 0.1 M TBAP in chloroform. Squares are for the analogous system with p2p in place of p3p, where p2p has only two methylene groups in the bridge. [Reprinted with permission from R. J. Forster and L. R. Faulkner, *J. Am. Chem. Soc.*, **116**, 5444 (1994). Copyright 1994, American Chemical Society.]

Impedance spectroscopic methods and ac voltammetry can also be used, as described in Section 14.3.7, to study electron-transfer kinetics in systems like those discussed here (71–73).

14.6 OTHER METHODS OF CHARACTERIZATION

While electrochemical methods provide powerful and sensitive ways of studying modified electrodes to provide information about electron-transfer kinetics and film porosity, they cannot provide information about structure or elemental composition. Thus complete characterization requires application of many of the nonelectrochemical methods described in Chapter 17. These encompass microscopy, high vacuum surface analysis, Raman and IR spectroscopy, and methods based on scanning probes, the quartz crystal microbalance, and measurements of contact angles.

Information about the structure of the film can be obtained by scanning electron microscopy and the different types of scanning probe microscopy. Elemental composition, which is important in monitoring surface structures, can be obtained by X-ray or UV photoelectron spectroscopy. IR spectroscopy has been very useful in determining the state of organization of monolayers. A key parameter in interpreting many electrochemical experiments is the film thickness, ϕ. This is often estimated from the amount of material on the electrode by assuming a value for the film density. Ellipsometric methods are particularly useful for determining ϕ for thin films and for monitoring film growth. The thickness can

also be determined by profilometry, atomic force microscopy, and scanning electrochemical microscopy (SECM). *In situ* methods are most useful, since solvation of a dry film can cause the thickness to change appreciably. One often assumes that the composition and properties are uniform throughout the film, so that parameters like D_S and D_E are constants. However, in many cases, especially with thicker films, the composition and diffusion coefficients may be functions of distance from the substrate or liquid interface. Few methods can provide this type of information, however, as discussed in Section 16.4.6, SECM can be used to probe inside a film and perform electrochemical experiments at a tip as a function of penetration depth.

▶ 14.7 REFERENCES

1. R. W. Murray, *Accts. Chem. Res.*, **13**, 135 (1980).

2. R. W. Murray, *Electroanal. Chem.*, **13**, 1 (1983).

3. A. J. Bard, *J. Chem. Educ.*, **60**, 302 (1983).

4. L. R. Faulkner, *Chem. Engr. News*, **62** (9), 28 (1984).

5. M. S. Wrighton, *Inorg. Chem.*, **4**, 269 (1985).

6. C. E. D. Chidsey and R. W. Murray, *Science*, **231**, 25 (1986).

7. M. S. Wrighton, *Science*, **231**, 32 (1986).

8. M. Fujihira in "Topics in Organic Electrochemistry," A. J. Fry and W. E. Britton, Eds., Plenum, New York, 1986.

9. R. W. Murray, A. G. Ewing, and R. A. Durst, *Anal. Chem.*, **59**, 379A (1987).

10. A. J. Bard and W. E. Rudzinski in "Preparative Chemistry Using Supported Reagents," P. Laszlo, Ed., Academic, San Diego, 1987, pp. 77–97.

11. I. Rubinstein in "Applied Polymer Analysis and Characterization," Vol. II, J. Mitchell, Jr., Ed., Hanser, Munich, 1992, Part III, Chap. 1.

12. R. W. Murray, Ed., "Molecular Design of Electrode Surfaces," Vol. XXII in the series, "Techniques in Chemistry," A. Weissberger, Founding Ed., Wiley-Interscience, New York, 1992.

13. G. Inzelt, *Electroanal. Chem.*, **18**, 89 (1994).

14. A. J. Bard, "Integrated Chemical Systems," Wiley, New York, 1994.

15. I. M Kolthoff and J. J. Lingane, "Polarography," Interscience, New York, 1952, p. 291.

16. A. J. Bard, *J. Electroanal. Chem.*, **2**, 117 (1962).

17. A. P. Brown and F. C. Anson, *Anal. Chem.*, **49**, 1589 (1977).

18. C.-W. Lee and A. J. Bard, *J. Electroanal. Chem.*, **239**, 441 (1988).

19. See, for example, (a) W. A. Zisman, "Advances in Chemistry Series," No. 43, American Chemical Society, Washington, DC, 1964, p. 1; (b) R. G. Nuzzo, B. R. Zegarski, and L. H. Dubois, *J. Am. Chem. Soc.*, **109**, 733 (1987); (c) M. D. Porter, T. B. Bright, D. L. Allara, and C. E. D. Chidsey, *ibid.*, 3559; (d) R. Maoz and J. Sagiv, *J. Coll. Interfac. Sci.*, **100**, 465 (1984); (e) H. O. Finklea, S. Avery, M. Lynch, and T. G. Furtsch, *Langmuir*, **3**, 409 (1987); (f) G. M. Whitesides and G. S. Ferguson, *Chemtracts-Org. Chem.*, **1**, 171 (1988) and references therein.

20. (a) B. Keita and L. Nadjo, *J. Electroanal. Chem.*, **243**, 87 (1988); (b) P. J. Kulesza, G. Roslonek, and L. R. Faulkner, *ibid.*, **280**, 233 (1990) and references therein.

21. A. J. Bard and T. Mallouk in R. W. Murray, Ed., "Molecular Design of Electrode Surfaces," *op. cit.*, p. 271.

22. (a) K. Itaya, I. Uchida, and V. D. Neff, *Accts. Chem. Res.*, **19**, 162 (1986); (b) K. Itaya, H. Akahashi, and S. Toshima, *J. Electrochem. Soc.*, **129**, 1498 (1982); (c) K. Itaya, T. Ataka, and S. Toshima, *J. Am. Chem. Soc.*, **104**, 4767 (1982).

23. (a) E. A. H. Hall, "Biosensors," Prentice-Hall, Englewood Cliffs, N. J., 1991; (b) G. A. Rechnitz, *Anal. Chem.*, **54**, 1194A, 1982; *Science*, **214**, 287 (1981); (c) M. E. Meyerhoff and Y. M. Fraticelli, *Anal. Chem.*, **54**, 27 (1982).

24. (a) L. C. Clark, Jr. and C. Lyons, *Ann. N. Y. Acad. Sci.*, **102**, 29 (1962); (b) P. W. Carr and L. D. Bowers, "Immobilized Enzymes in Analytical and Clinical Chemistry," Wiley-Interscience, New York, 1980; (c) N. Lakshminarayanaiah, "Membrane Electrodes," Academic, New York, 1976; (d) P. L. Bailey, "Analysis with Ion Selective Electrodes," Heydon, London, 1976.

25. (a) P. G. Pickup, C. R. Leidner, P. Denisevich, and R. W. Murray, *J. Electroanal. Chem.*, **164**, 39 (1984); (b) C. R. Leidner, P. Denisevich, K. W. Willman, and R. W. Murray, *ibid.*, **164**, 63 (1984).

26. (a) G. P. Kittlesen, H. S. White, and M. S. Wrighton, *J. Am. Chem. Soc.*, **106**, 7389 (1984);

(b) H. S. White, G. P. Kittlesen, and M. S. Wrighton, *ibid.*, **106**, 5375 (1984); (c) I. Fritsch-Faules and L. R. Faulkner, *Anal. Chem.*, **64**, 1118 (1992) and references therein.

27. (a) G. P. Kittlesen, H. S. White, and M. S. Wrighton, *J. Am. Chem. Soc.*, **107**, 7373 (1985); (b) E. T. Turner Jones, O. M. Chyan, and M. S. Wrighton, *ibid.*, **109**, 5526 (1987).

28. T. P. Henning, H. S. White, and A. J. Bard, *J. Am. Chem. Soc.*, **103**, 3937 (1981); **104**, 5862 (1982).

29. F.-R. F. Fan and A. J. Bard, *J. Electrochem. Soc.*, **133**, 301 (1986).

30. P. G. Pickup, K. N. Kuo, and R. W. Murray, *J. Electrochem. Soc.*, **130**, 2205 (1983).

31. E. Laviron, *Bull. Soc. Chim. France*, 3717 (1967).

32. S. Srinivasan and E. Gileadi, *Electrochim. Acta*, **11**, 321 (1966).

33. E. Laviron, *J. Electroanal. Chem.*, **52**, 355, 395 (1974).

34. B. E. Conway, "Theory and Principles of Electrode Processes," Ronald, New York, 1965, Chaps. 4 and 5.

35. A. N. Frumkin and B. B. Damaskin, *Mod. Asp. Electrochem.*, **3**, 149 (1964).

36. P. Delahay, "Double Layer and Electrode Kinetics," Interscience, New York, 1965.

37. E. Laviron, *J. Electroanal. Chem.*, **100**, 263 (1979).

38. H. Matsuda, K. Aoki, and K. Tokuda, *J. Electroanal. Chem.*, **217**, 1 (1987); **217**, 15 (1987).

39. C. P. Smith and H. S. White, *Anal. Chem.*, **64**, 2398 (1992).

40. P. J. Peerce and A. J. Bard, *J. Electroanal. Chem.*, **114**, 89 (1980).

41. H. Angerstein-Kozlowska and B. E. Conway, *J. Electroanal. Chem.*, **95**, 1 (1979).

42. V. Plichon and E. Laviron, *J. Electroanal. Chem.*, **71**, 143 (1976).

43. R. H. Wopschall and I. Shain, *Anal. Chem.*, **39**, 1514 (1967).

44. M. Sluyters-Rehbach and J. H. Sluyters, *J. Electroanal. Chem.*, **65**, 831 (1975).

45. S. W. Feldberg, in "Computers in Chemistry and Instrumentation," Vol. 2, "Electrochemistry", J. S. Mattson, H. B. Mark, Jr., and H. C. Mac-Donald, Jr., Eds., Marcel Dekker, New York, 1972, Chap. 7.

46. R. H. Wopschall and I. Shain, *Anal. Chem.*, **39**, 1535 (1967).

47. M. H. Hulbert and I. Shain, *Anal. Chem.*, **42**, 162 (1970).

48. R. Brdička, *Z. Elektrochem.*, **48**, 278, 686 (1942).

49. R. Brdička, *Coll. Czech. Chem. Commun.*, **12**, 522 (1947).

50. M. Sluyters-Rehbach, C. A. Wijnhorst, and J. H. Sluyters, *J. Electroanal. Chem.*, **74**, 3 (1976).

51. J. Koryta, *Coll. Czech. Chem. Commun.*, **18**, 206 (1953).

52. F. C. Anson, *Anal. Chem.*, **38**, 54 (1966).

53. J. H. Christie, R. A. Osteryoung, and F. C. Anson, *J. Electroanal. Chem.*, **13**, 236 (1967).

54. F. C. Anson, J. H. Christie, and R. A. Osteryoung, *J. Electroanal. Chem.*, **13**, 343 (1967).

55. F. C. Anson and D. J. Barclay, *Anal. Chem.*, **40**, 1791 (1968) and references therein.

56. H. B. Herman, R. L. McNeely, P. Surana, C. M. Elliot, and R. W. Murray, *Anal. Chem.*, **46**, 1268 (1974) and references therein.

57. M. T. Stankovich and A. J. Bard, *J. Electroanal. Chem.*, **86**, 189 (1978).

58. F. C. Anson, *Anal. Chem.*, **33**, 1123 (1961).

59. W. Lorenz, *Z. Elektrochem.*, **59**, 730 (1955).

60. W. H. Reinmuth, *Anal. Chem.*, **33**, 322 (1961).

61. S. V. Tatwawadi and A. J. Bard, *Anal. Chem.*, **36**, 2 (1964).

62. M. P. Soriaga and A. T. Hubbard, *J. Am. Chem. Soc.*, **104**, 2735 (1982).

63. G. N. Salaita and A. T. Hubbard, in R. W. Murray, Ed., "Molecular Design of Electrode Surfaces," *op. cit.*

64. M. Sluyters-Rehbach and J. H. Sluyters, *Electroanal. Chem.*, **4**, 1 (1970).

65. B. Timmer, M. Sluyters-Rehbach, and J. H. Sluyters, *J. Electroanal. Chem.*, **18**, 93 (1968).

66. P. Delahay and K. Holub, *J. Electroanal. Chem.*, **16**, 131 (1968).

67. P. Delahay, *J. Electroanal. Chem.*, **19**, 61 (1968).

68. I. Epelboim, C. Gabrielli, M. Keddam, and H. Takenouti, *Electrochim. Acta*, **20**, 913 (1975) and references therein.

69. D. E. Smith, *Electroanal. Chem.*, **1**, 1 (1966).

70. A. M. Bond, *J. Electroanal. Chem.*, **35**, 343 (1972); A. M. Bond and G. Hefter, *ibid.*, **42**, 1 (1973).

71. H. O. Finklea, M. S. Ravenscroft, D. A. Snider, *Langmuir*, **9**, 223 (1993).

72. T. M. Nahir and E. F. Bowden, *J. Electroanal. Chem.*, **410**, 9 (1996).

73. S. E. Creager and T. T. Wooster, *Anal. Chem.*, **70**, 4257 (1998).

74. (a) C. P. Andrieux, J. M. Dumas-Bouchiat, and J.-M. Savéant, *J. Electroanal. Chem.*, **131**, 1 (1982); (b) C. P. Andrieux and J.-M. Savéant, *ibid.*, **134**, 163 (1982); *ibid.*, **142**, 1 (1982); (c) C. P. Andrieux, J. M. Dumas-Bouchiat, and J.-M. Savéant, *ibid.*, **169**, 9 (1984); (d) C. P. Andrieux and J.-M. Savéant, *ibid.*, **171**, 65 (1984); (e) F. C. Anson, J.-M. Savéant, and K. Shigehara, *J. Phys. Chem.*, **87**, 214 (1983).

75. J. Leddy, A. J. Bard, J. T. Maloy, and J.-M. Savéant, *J. Electroanal. Chem.*, **187**, 205 (1985).

76. M. Majda in R. W. Murray, Ed., "Molecular Design of Electrode Surfaces," *op. cit.*, p. 159.

77. (a) H. Dahms, *J. Phys. Chem.*, **72**, 362 (1968); (b) I. Ruff and V. J. Friedrich, *ibid.*, **75**, 3297 (1971); (c) I. Ruff, V. J. Friedrich, K. Demeter, and K. Csillag, *ibid.*, **75**, 3303 (1971); (d) I. Ruff and I. Korösi-Odor, *Inorg. Chem.*, **9**, 186 (1970); (e) I. Ruff and L. Botár, *J. Chem. Phys.*, **83**, 1292 (1985).

78. E. Laviron, *J. Electroanal. Chem.*, **112**, 1 (1980).

79. C. P. Andrieux and J.-M. Savéant, *J. Electroanal. Chem.*, **111**, 377 (1980).

80. C. P. Andrieux and J.-M. Savéant in R. W. Murray, Ed., "Molecular Design of Electrode Surfaces," *op. cit.*, p. 207.

81. B. R. Scharifker, *J. Electroanal. Chem.*, **240**, 61 (1988).

82. H. Reller, E. Kirowa-Eisner, and E. Gileadi, *J. Electroanal. Chem.*, **138**, 65 (1982).

83. T. Gueshi, K. Tokuda, and H. Matsuda, *J. Electroanal. Chem.*, **89**, 247 (1978).

84. P. J. Peerce and A. J. Bard, *J. Electroanal. Chem.*, **112**, 97 (1980).

85. J. Leddy and A. J. Bard. *J. Electroanal. Chem.*, **153**, 223 (1983).

86. (a) F. Scheller, S. Müller, R. Landsberg, and H. J. Spitzer, *J. Electroanal. Chem.*, **19**, 187 (1968); (b) F. Scheller, R. Landsberg, and S. Müller, *ibid.*, **20**, 375 (1969); (c) R. Landsberg and R. Thiele, *Electrochim. Acta*, **11**, 1243 (1966).

87. C. Amatore, J.-M. Savéant, and D. Tessier, *J. Electroanal. Chem.*, **147**, 39 (1983).

88. H. O. Finklea, *Electroanal. Chem.*, **19**, 109 (1996).

89. C. J. Miller, "Physical Electrochemistry. Principles, Methods, and Applications," I. Rubinstein, Ed., Marcel Dekker, New York, 1995, Chap. 2.

90. (a) C. E. D. Chidsey, C. R. Bertozzi, T. M. Putvinski, and A. M. Mujsce, *J. Am. Chem. Soc.*, **112**, 4301 (1990); (b) C. E. D. Chidsey, *Science*, **251**, 919 (1991).

91. R. J. Forster and L. R. Faulkner, *J. Am. Chem. Soc.*, **116**, 5444 (1994).

▶ 14.8 PROBLEMS

14.1 Elliott and Murray performed chronocoulometric experiments to measure the surface excess of Tl^+ at a mercury-electrolyte interface. Of interest was the influence of bromide on the adsorption. Explain how such measurements would be carried out. The results are summarized in Figure 14.8.1. Explain the results in terms of chemical processes.

14.2 From the curves in Figure 14.3.4*b*, estimate the amount of *trans*-4,4′-dipyridyl-1,2-ethylene adsorbed per cm^2. Assume $n = 2$.

14.3 From Figure 14.3.11 for weak adsorption of a reactant, estimate the ranges of v where (a) i_p is proportional to v and (b) where i_p is proportional to $v^{1/2}$, in terms of β_O, $\Gamma_{O,s}$, and D_O, at 25°C and $\beta_O C_O^* = 1$.

14.4 The amount of adsorbed O, Γ_O, can also be determined in a double potential step chronocoulometric experiment from the ratio of the slopes of the curves for the forward (S_f) and reverse (S_r) phases. Explain how.

14.5 Using the data in Figure 14.3.16, calculate D_O and Γ_O [O is Cd(II)]. Also calculate Q_{dl} and C_d in the absence and presence of SCN^-.

14.6 A thin-layer cell with a Pt electrode (area, 1.2 cm^2) and a layer thickness of 40 μm is used to determine the amount of hydroquinone (H_2Q) adsorbed on Pt. The cell is first filled with a 0.100 mM solution of H_2Q, irreversible adsorption is allowed to occur, and a potential step chronocoulometric experiment is carried out to oxidize the dissolved H_2Q (adsorbed H_2Q is not elec-
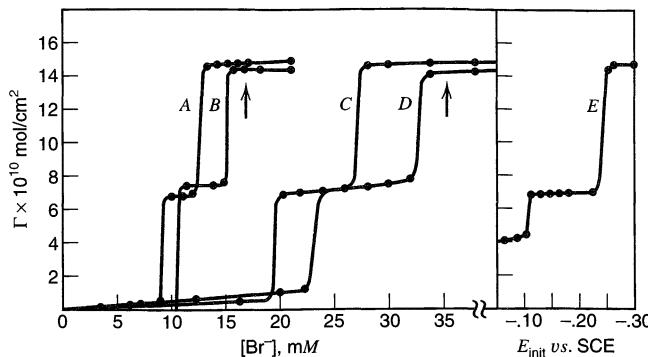
Figure 14.8.1 Surface excesses of Tl^+ at mercury in the presence of Br^-. The step potential was -0.70 V *vs*. SCE in every case. *Curve A*: 1 m*M* Tl^+, initial potential $= -0.30$ V. *Curve B*: 1 m*M* Tl^+, initial potential $= -0.20$ V. *Curve C*: 0.5 m*M* Tl^+, initial potential $= -0.30$ V. *Curve D*: 0.5 m*M* Tl^+ initial potential $= -0.20$ V; *Curve E*: 1 m*M* Tl^+, 14 m*M* Br^-. Arrows show saturation with respect to precipitation of TlBr from bulk solution. [Reprinted with permission from C. M. Elliott and R. W. Murray, *J. Am. Chem. Soc.*, **96**, 3321 (1974). Copyright 1974, American Chemical Society.]

troactive). Oxidation of H_2Q ($n = 2$) required 32 μC. This solution is flushed from the cell, which is rinsed and purged several times with fresh solution. A fresh aliquot is introduced. Another chronocoulometric experiment shows that 96 μC are now required. (a) Calculate the amount of H_2Q adsorbed, Γ (mol/cm^2), and the area each molecule occupies, σ (Å^2/molecule). (b) From the structure of the H_2Q molecule, what orientation of the molecule on the electrode seems most reasonable?

CHAPTER

15

ELECTROCHEMICAL

INSTRUMENTATION

Electrochemical instrumentation generally consists of a *potentiostat*, for enforcing a controlled potential at an electrode (or a *galvanostat*, for controlling the current through the cell), along with a *function generator*, to produce the desired perturbation, and a *recording and display system* for measuring and presenting i, E, and t. The instrument is connected to the electrochemical cell, typically a three-electrode cell consisting of working, counter, and reference electrodes. In modern instrumentation the potentiostat, as well as amplifiers and other modules employed to condition the current and potential signals, are analog devices constructed with operational amplifiers. *Analog devices* are electronic systems for handling continuous signals, such as voltages. The function generator can also be an analog device, but often the desired signal is instead generated in *digital* form with a computer and then fed to the potentiostat via a *digital-to-analog converter* (DAC). Analog signals can be recorded on strip-chart or X-Y recorders or with an oscilloscope, but signal acquisition is carried out more often with a computer via an *analog-to-digital converter* (ADC). Our goal in this chapter is to explore the basis for the usual electrochemical instruments, not to review exhaustively all approaches.

Because the chief electrochemical variables are all analog quantities (at least in the ranges of normal interest), our first concerns are with circuitry for *controlling* and *measuring* voltages, currents, and charges in the analog domain. The circuit elements best suited to these jobs are *operational amplifiers*. We must explore their properties before we can understand the way in which the amplifiers are assembled into instruments.

▶ 15.1 OPERATIONAL AMPLIFIERS

15.1.1 Ideal Properties (1–7)

Operational amplifiers are devices with special properties, and are almost always found as packaged integrated circuits. We have no interest in the contents of the amplifier; our concern is strictly with its behavior as a unit in a circuit.

In Figure 15.1.1a we note that several connections must be made to the amplifier. First there are the power lines. Usually these devices require two supplies, such as one at $+15$ V and the other at -15 V relative to a common circuit point, defined at the power supplies, called *ground*. Many measurements are made with respect to this point, which may or may not be related to *earth ground*. In addition to the power lines, there are input and output connections as shown. Usually one side of the output is connected directly to ground (i.e., is *grounded*). Most amplifiers are constructed so that neither input terminal must be at ground; that is, both can be *floating* away from ground. The important parameter is the difference in voltage between the two input terminals. In circuit diagrams, the power connections are always understood, and the amplifier is depicted as shown in Figure 15.1.1b.
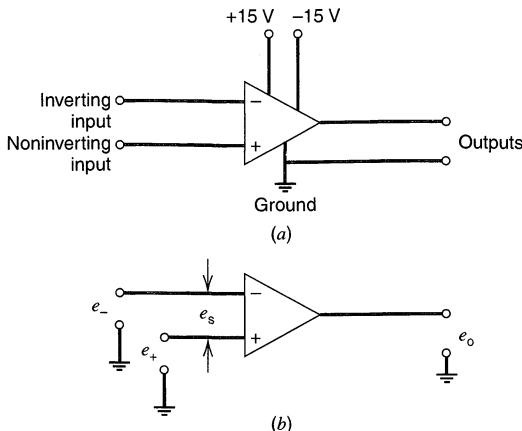
Figure 15.1.1 Schematic diagrams of operational amplifiers.

The two input terminals are labeled with signs in the manner depicted there. The top one is called the *inverting input* and the bottom one is the *noninverting input*. The fundamental property of the amplifier is that the output, e_o, is the inverted, amplified voltage difference e_s, where e_s is the voltage of the inverting input *with respect to the noninverting input*. That is,

$$e_o = -Ae_s \qquad (15.1.1)$$

where A is the *open-loop gain*.

The names of the inputs come from a different way of looking at e_s. We could picture the system as having two independent inputs, e_- and e_+, both measured with respect to ground. The output is then

$$e_o = -Ae_- + Ae_+ \qquad (15.1.2)$$

which is the sum of the inverted, amplified signal, e_-, and the noninverted, amplified signal, e_+. Equation 15.1.2 is equivalent to (15.1.1), since $e_s = e_- - e_+$.

The ideal operational amplifier has several important properties. First, its open-loop gain, A, is effectively infinite, so that the slightest input voltage, e_s, will drive the output to the limit deliverable by the power supply (usually ± 13–14 V). The reasons for desiring the highest possible amplification factor will become clear in Section 15.2. For now, let us note that if the ideal amplifier is operating in any circuit with its output anywhere in the range between the voltage limits, then the two input terminals *must be at the same voltage*.

Ideal amplifiers also have infinite input impedance, so that they can accept input voltages without drawing any current from the voltage sources. This feature enables them to measure voltages without perturbing them. On the other hand, the ideal device can also supply any desired current to its load; hence it has effectively zero output impedance. Finally, we regard the ideal amplifier as having infinite bandwidth; that is, it responds faithfully to a signal of any frequency.

In most discussions of circuitry, we assume ideal behavior, because it simplifies the approach. For most electrochemical applications, available devices perform so well that nonidealities are negligible. However, in demanding circumstances, nonideal properties may have to be recognized.

15.1.2 Nonidealities (1–7)

The characteristics of operational amplifiers are discussed in many electronics texts (2) and in the manufacturers' literature. The following are of importance:

(a) Open-Loop Gain

Actual devices have A values for dc signals ranging from 10^4 to 10^8. A typical figure for a general-purpose amplifier is 10^5. The open-loop gain is frequency-dependent. It declines at high frequencies, and this feature is one aspect bearing on the useful operating range.

(b) Bandwidth

The degradation in performance of real devices at high frequencies can be measured in several ways. The frequency at which the open-loop gain becomes unity for an input signal of small amplitude is called the *unity-gain bandwidth*. Depending on the purpose for which the device is designed, this bandwidth may be as low as 100 Hz or as high as 1 GHz. Typical values for general-purpose amplifiers are 5 to 20 MHz. Since most applications of operational amplifiers are based on a high open-loop gain, the useful bandwidth is usually one or two orders of magnitude lower than the unity-gain bandwidth.

Another parameter describing an amplifier's limitations at high frequency is the *slew rate*, which is the maximum rate of change in the output voltage in response to a large amplitude step at the input. Real values range from 100 V/s to 1000 V/μs. General-purpose devices have slew rates on the order of 20 to 75 V/μs; hence the minimum time required for a transition over their full output range would be of the order of 1 to 10 μs.

Still a third characterization of high-frequency response is the *settling time*. This figure applies to an amplifier operating in a given feedback-stabilized circuit. Often a unity-gain inverter is used (Section 15.2.2). An essentially ideal step function is applied at the input. The settling time is then measured as the time required for the output to settle within some defined error range (usually 0.1–0.01%) around the new equilibrium output value. The settling time is dependent on the circuit within which the amplifier is used.

The characteristics of present amplifiers are such that one can easily obtain accurate, reliable performance on time scales of 10 μs or greater (i.e., bandwidths less than 100 kHz). Time scales below 10 μs (bandwidths above 100 kHz) can be reached with care in circuit design and choice of components. Building reliable operational amplifier circuits like those described below for time scales under 3 μs is very difficult.

(c) Input Impedance

The range of input impedance in real devices is 10^5 to 10^{13} Ω. General-purpose amplifiers typically offer about 10^6 to 10^{12} Ω. Higher impedances are specifically sought for more demanding purposes, such as monitoring resistive voltage sources (like glass electrodes) and service in integrators.

(d) Output Limits

The *voltage limits* of the amplifier are controlled by the power supplies. They usually are quite close to the supply values. For most devices, the limits are ±13–14 V. Currents will be supplied freely to a load until the *current limits* are reached, typically at ±5–100 mA. Special devices with larger current or voltage output limits are available, but high output power in operational amplifier circuits is usually obtained by *booster stages*, as described below.

(e) Offset Voltage

In general, a zero input voltage e_s will not produce zero output voltage in a practical device. Instead there is a nonzero *offset* at the output. Most amplifiers have a provision for nulling the offset by an external adjustable resistor.

(f) Other Properties

In some applications, noise and drift characteristics of the devices and their stability with temperature may be of concern. Usually these aspects are of secondary importance in electrochemical instrumentation.

▶ 15.2 CURRENT FEEDBACK

We have already noted that a negligibly small voltage differential at the inputs will drive a practical amplifier to its limit; thus we almost never use the amplifier to deal with an input signal without elaboration of the circuit. Normally the amplifier is stabilized by feeding back part of its output to the *inverting* input. The manner in which the feedback is accomplished determines the operational properties of the whole circuit. Here our concern is with circuits involving the routing of a *current* from the output to the input (1–7).

15.2.1 Current Follower

Consider the circuit shown in Figure 15.2.1. The resistor, R_f, is the feedback element, through which there is a feedback current, i_f. The input is a current, i_{in}, which might be from a working electrode or a photomultiplier tube. From the conservation of charge (Kirchhoff's law), the sum of all the currents into the *summing point,* S, must be zero, and since a negligibly small current passes between the inputs,

$$i_f = -i_{in} \tag{15.2.1}$$

From Ohm's law,

$$\frac{e_o - e_s}{R_f} = -i_{in} \tag{15.2.2}$$

and, by substitution from (15.1.1),

$$e_o \left(1 + \frac{1}{A}\right) = -i_{in} R_f \tag{15.2.3}$$

Since the value of A is very high, the parenthesized quantity is virtually unity, and

$$\boxed{e_o \simeq -i_{in} R_f} \tag{15.2.4}$$

Thus the output voltage is proportional to the input current by a scale factor determined by R_f. The circuit is called a *current follower* or a *current-to-voltage (i/E or i/V) converter.*

The voltage of the summing point e_s is $-e_o/A$, which for a typical device lies between ± 15 V/10^5, or ± 150 μV. In other words, S is a *virtual ground.* It is not a true ground in that there is no direct connection, but it has virtually the same potential as ground. This feature is important because it allows currents to be converted to equivalent voltages while the current source is maintained at ground potential. We will utilize that virtue later in building a potentiostat.
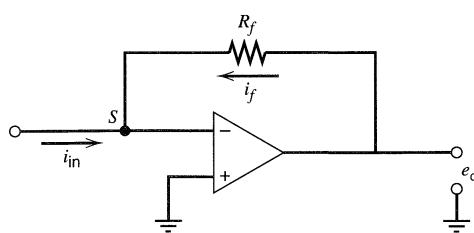
Figure 15.2.1 A current follower.

There is an easier way to analyze this circuit than we have used here. Since we recognize that the two inputs are always at virtually the same potential, it is intuitive that the noninverting input is a virtual ground. From (15.2.1), we can therefore write immediately

$$\frac{e_o}{R_f} = -i_{in} \tag{15.2.5}$$

which is the final result.

15.2.2 Scaler/Inverter

The circuit in Figure 15.2.2 differs from the current follower only in that the input current is driven through an input resistor by the voltage e_i. Our previous analysis holds exactly, but we can now reexpress i_{in} in (15.2.5) as e_i/R_i; hence

$$\boxed{e_o = -e_i \left(\frac{R_f}{R_i}\right)} \tag{15.2.6}$$

This circuit is therefore a *scaler*, in which the output is simply the inverted input multiplied by the factor (R_f/R_i). By choosing precision resistors, (R_f/R_i) can be set at any desired value, although the practical ratios for a single stage lie between ~0.01 and ~200. When $R_f = R_i$, the circuit is an *inverter*.

Note that the voltage source must be able to supply the input current, i_{in}, so that the effective input impedance of the whole circuit is R_i. Typical values are 1 to 100 kΩ.

15.2.3 Adders

In Figure 15.2.3, we consider a circuit in which three different voltage sources e_1, e_2, and e_3 supply three input currents i_1, i_2, and i_3 to the summing junction, S, through separate input resistors. The feedback arrangement is just as before. Now we write

$$i_f = -(i_1 + i_2 + i_3) \tag{15.2.7}$$

and, since the summing point is a virtual ground,

$$\frac{e_o}{R_f} = -\left(\frac{e_1}{R_1} + \frac{e_2}{R_2} + \frac{e_3}{R_3}\right) \tag{15.2.8}$$

or,

$$\boxed{e_o = -\left[e_1\left(\frac{R_f}{R_1}\right) + e_2\left(\frac{R_f}{R_2}\right) + e_3\left(\frac{R_f}{R_3}\right)\right]} \tag{15.2.9}$$
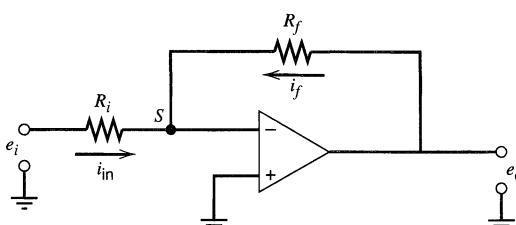
Figure 15.2.2 A scaler/inverter.
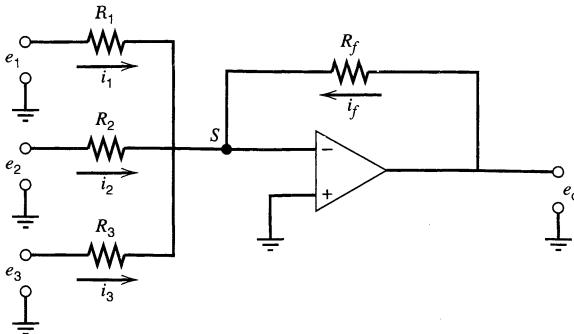
Figure 15.2.3 An adder circuit.

The output is therefore the sum of independently scaled input voltages. The scale factors are again set by selecting appropriate resistors. If all the resistances are equal, we have a simple *inverting adder*:

$$e_o = -(e_1 + e_2 + e_3) \tag{15.2.10}$$

Note that the fundamental basis of the addition is the summing of *currents* at point S. That, in turn, is simplified because S is a virtual ground.

15.2.4 Integrators

In Figure 15.2.4, we consider a capacitor, C, as a feedback element. The input is a current i_{in}. Equation 15.2.1 still holds and S is still a virtual ground; therefore, we can write by substitution into (15.2.1):

$$C\frac{de_o}{dt} = -i_{in} \tag{15.2.11}$$

or

$$e_o = -\frac{1}{C}\int i_{in}\, dt \tag{15.2.12}$$

The output is a voltage proportional to the integrated input current, which is actually the charge stored on the capacitor. *Current integrators* are useful in coulometric and chrono-coulometric experiments.

Usually one desires to discharge the capacitor before starting a new measurement. The *reset* switch in Figure 15.2.4 allows that.

If the charges are to be stored on C for more than a few seconds, one must take care to minimize losses due to leakage. They mainly occur through the dielectric in the capaci-
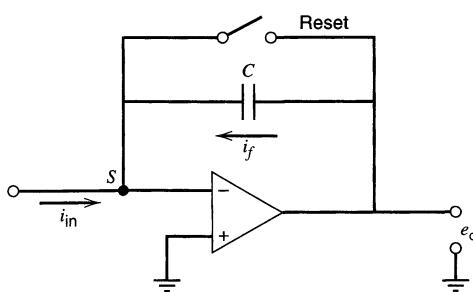
Figure 15.2.4 A current integrator.
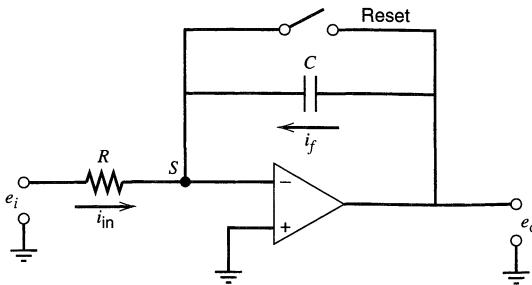
Figure 15.2.5   A voltage integrator.

tor and through the input impedance in the amplifier. One can minimize them by choosing special capacitors and using amplifiers with very high input impedances.

An input voltage can be integrated by the circuit shown in Figure 15.2.5, where the input current is driven by e_i through the resistor R. Equation 15.2.12 still holds, and we can substitute there to obtain

$$e_o = \frac{-1}{RC} \int e_i dt$$

(15.2.13)

A special type of voltage integrator is the *ramp generator,* which involves a constant e_i. If the experiment begins with a reset condition, then

$$e_o = \frac{-e_i}{RC} t$$

(15.2.14)

Such an arrangement is sometimes used to generate waveforms for linear sweep experiments. The sweep rate is controlled by the combination of e_i, R, and C; and the direction of sweep is governed by the polarity of e_i.

15.2.5   Differentiator

In Figure 15.2.6 one sees an input capacitor and a feedback resistor, which pass currents i_{in} and i_f, respectively. Starting as usual with equation 15.2.1 and substituting for the currents we obtain,

$$\frac{e_o}{R} = -C \frac{de_i}{dt}$$

(15.2.15)

or

$$e_o = -RC \left(\frac{de_i}{dt} \right)$$

(15.2.16)

The output is therefore a scaled derivative of e_i with respect to time.
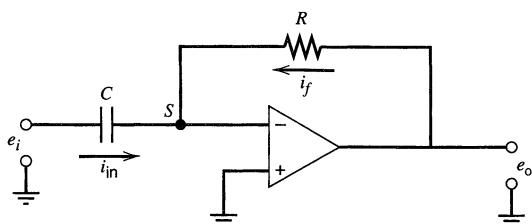
Figure 15.2.6   A differentiator.

This kind of circuit finds use in highlighting inflections in voltage-time functions. However, differentiation of analog signals tends to degrade the signal-to-noise ratio (Problem 15.5) and is usually avoided.

▶ 15.3 VOLTAGE FEEDBACK

An alternative to feeding back a current from the output is to stabilize the circuit by returning part of the output *voltage* to the inverting input (1–7). These circuits generally require negligible input currents and are especially well-suited to control functions and to the measurement of voltages. Circuits based on current feedback are, by contrast, often better suited to signal processing in the manner discussed earlier.

15.3.1 Voltage Follower

Figure 15.3.1 contains an important circuit in which the whole output voltage is returned to the input. We treat it by invoking (15.1.1) and noting that $e_s = e_o - e_i$; thus

$$e_o = -A(e_o - e_i) \tag{15.3.1}$$

or

$$e_o = \frac{e_i}{(1 + 1/A)} \tag{15.3.2}$$

Since A is very large,

$$\boxed{e_o \approx e_i} \tag{15.3.3}$$

This result could have been obtained intuitively by noting that the two inputs must be at virtually the same potential.

The circuit is called a *voltage follower*, because the output is the same as the input. Its function is to match impedances. It offers a very high input impedance and a very low output impedance; hence it can accept an input from a device that cannot supply much current (such as a glass electrode) and offer the same voltage to a significant load (e.g., a recorder). It is an intermediary that allows the measurement of a voltage without perturbing that voltage significantly.

15.3.2 Control Functions

Consider the arrangement shown in Figure 15.3.2. Because the inverting input is a virtual ground, point A is at $-e_i$ *vs.* ground. The amplifier will adjust its output to control the currents through the resistors so that this condition is maintained. We therefore have a means for controlling the voltage at a fixed point in a network of resistances, even if the resistances (or, more generally, impedances) fluctuate during the experiment. This job is precisely what we ask a potentiostat to do.
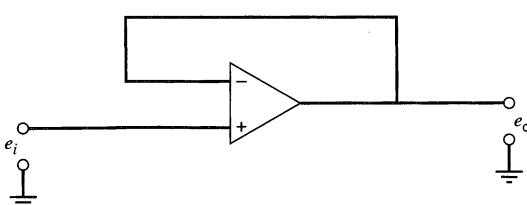
Figure 15.3.1 A voltage follower.
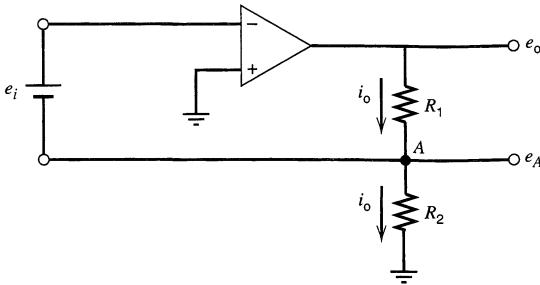
Figure 15.3.2 A circuit for controlling the potential at point A regardless of changes in R_1 and R_2. Note that the feedback circuit passes through the voltage source, which is shown for simplicity as a battery.

Since the current through R_1 must also pass through R_2, the total output voltage, e_o, is $i_o(R_1 + R_2)$. Since $i_o = -e_i/R_2$,

$$e_o = -e_i \left(\frac{R_1 + R_2}{R_2} \right) \tag{15.3.4}$$

This basic design can also be used to control the current through a load. Consider the circuit in Figure 15.3.3, which has an arbitrary load impedance, Z_L. Since the voltage at point A is $-e_i$, the current through the resistor, R, is $i_o = -e_i/R$. It passes through the load, too, and is independent of the value of Z_L or fluctuations in it. Such a circuit could be employed as a galvanostat. The cell would simply replace the load impedance (see Section 15.5).

▶ 15.4 POTENTIOSTATS

15.4.1 Basic Considerations (1, 7, 8)

From an electronic standpoint, an electrochemical cell can be regarded as a network of impedances like those shown in the equivalent circuit of Figure 15.4.1*a*, where Z_c and Z_{wk} represent the interfacial impedances at the counter and working electrodes, and the solution resistance is divided into two fractions, R_Ω and R_u, depending on the position of the reference electrode's contact with the current path (see Section 1.3.4). This representation can be distilled further into that of Figure 15.4.1*b*.

Suppose we now incorporate the cell into the circuit of Figure 15.4.2. If the cell is equivalent to the network in Figure 15.4.1*b*, then we can immediately see that the overall circuit bears a strong analogy to the control system in Figure 15.3.2. The current through the cell is controlled by the amplifier so that the reference electrode is always at $-e_i$ vs. ground. Since the working electrode is grounded,

$$e_{wk}(vs.\ \text{ref}) = e_i \tag{15.4.1}$$

regardless of fluctuations in Z_1 and Z_2.
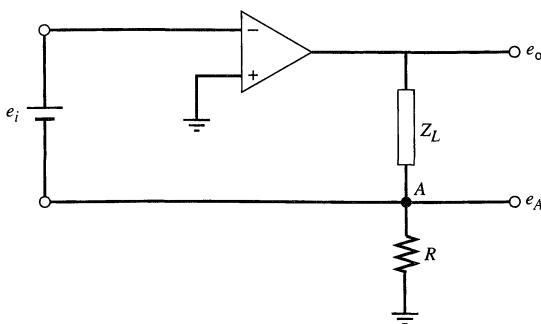
Figure 15.3.3 A circuit for controlling the current through an arbitrary load, Z_L.

(a)

(b)
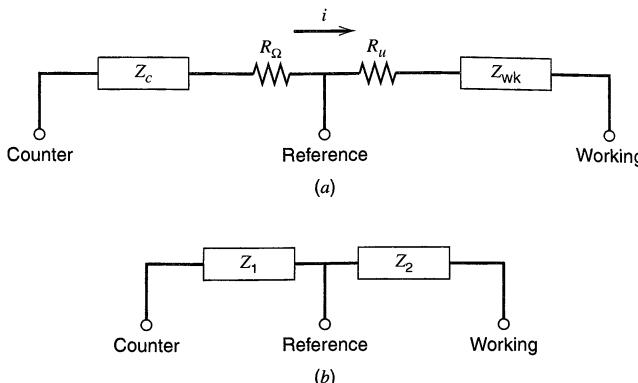
Figure 15.4.1 Views of an electrochemical cell as an impedance network tapped by connections to the three electrodes.

Figure 15.4.1 shows that the controlled voltage, e_{ref} *vs.* ground, contains a portion, iR_u, of the total voltage drop in the solution. The presence of this *uncompensated resistance loss* keeps the circuit from giving accurate control over the *true potential* of the working electrode with respect to the reference, but in many cases iR_u can be made negligibly small by careful placement of the reference electrode (see Section 1.3.4). At other times, the uncompensated resistance is a major factor in understanding experimental results. We will have more to say about it later.

15.4.2 The Adder Potentiostat (1, 7, 8)

The potentiostat of Figure 15.4.2 illustrates the basic principles of potential control and will accomplish that task as well as any of several other designs. Its drawbacks concern its input requirements. First, note that neither terminal of the potential source is a true ground; hence the function generator supplying the waveform for potential control would have to possess a differential floating output. Most waveform sources would not meet that demand.

Consider also the *form* of the desired control function. Suppose, for example, we wish to carry out an ac voltammetric experiment involving a scan from -0.5 V. The waveform needed at e_i is shown in Figure 15.4.3. It is a complicated function and could not be supplied simply. We must synthesize it by adding together a ramp, a sinusoid, and a constant offset. It is generally true that electrochemical waveforms are syntheses of several simpler signals, and therefore we need a general facility for accepting and adding basic inputs at the potentiostat itself.

The *adder potentiostat* shown in Figure 15.4.4 remedies both drawbacks of the control circuit considered above, and is by far the most widely used design. Since the currents into the summing point S must add to zero,

$$-i_{ref} = i_1 + i_2 + i_3 \qquad (15.4.2)$$
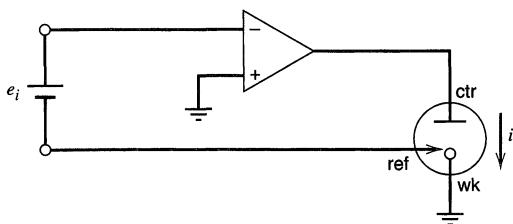
Figure 15.4.2 A simple potentiostat based on the control circuit of Figure 15.3.2.

Total waveform = Ramp + Sinusoid + Constant offset
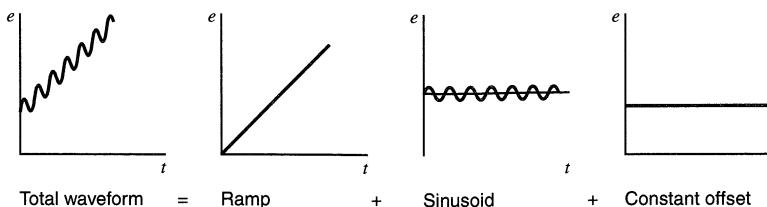
Figure 15.4.3 Synthesis of a complex waveform. For clarity, the magnitude of the sinusoid has been exaggerated and its frequency has been lowered, relative to the values usually employed.

and since S is a virtual ground,

$$-e_{ref} = e_1\left(\frac{R_{ref}}{R_1}\right) + e_2\left(\frac{R_{ref}}{R_2}\right) + e_3\left(\frac{R_{ref}}{R_3}\right) \tag{15.4.3}$$

Note that, as before, $-e_{ref}$ is the potential of the working electrode with respect to the reference. Thus the circuit maintains the working electrode at a potential equal to the weighted sum of the inputs. Usually all the resistors have the same value, and one has

$$\boxed{e_{wk}(vs.\ ref) = e_1 + e_2 + e_3} \tag{15.4.4}$$

The facility for addition of input signals allows the straightforward synthesis of complex waveforms, and each input signal is individually referred to circuit ground. Any reasonable number of signals can be added at the input. One simply requires a resistor into the summing point for each of them.

15.4.3 Refinements to the Adder Potentiostat (1, 7, 8)

There are three important deficiencies in the design of Figure 15.4.4: (a) The reference electrode must supply a significant current, i_{ref}, to the summing point; (b) there is no facility for measuring the current through the cell; and (c) the power that is available at the cell is only that available from the output of the operational amplifier. Figure 15.4.5 is a schematic of a potentiostat that remedies these deficiencies. It is a design in very common use.

A voltage follower, F, has been inserted into the feedback loop, so that the reference electrode is not loaded by the current fed into the summing point. The follower's output, e_F, is also available externally for use with a recording device. It is a convenient continuous monitor of $-e_{wk}$ (vs. ref).
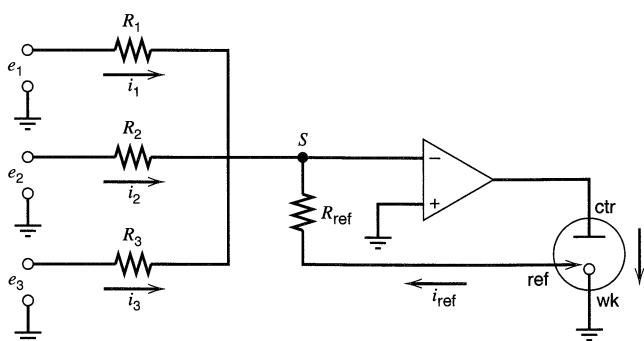
Figure 15.4.4 A basic adder potentiostat.
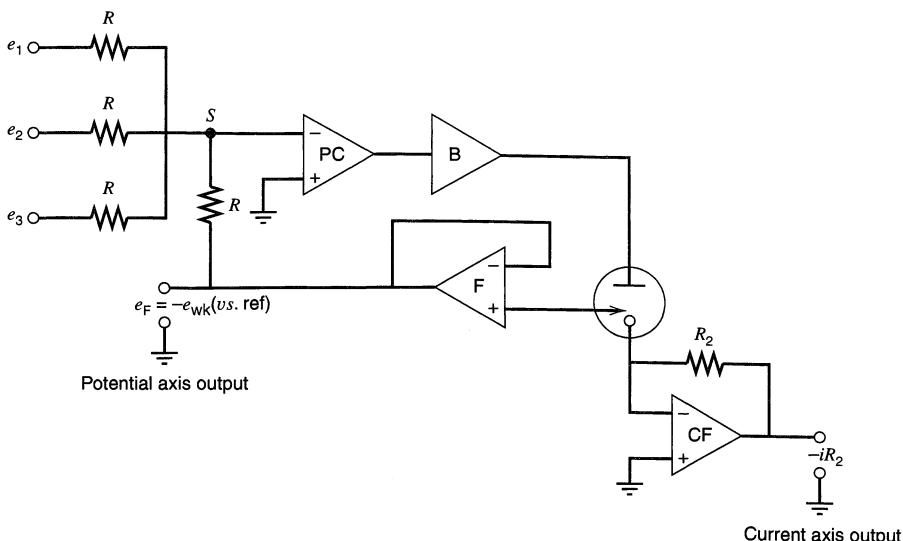
Figure 15.4.5 A full potentiostatic system based on a potential control amplifier (PC) in the adder configuration. The booster (B) is included to improve the available output voltage. If one also desires to boost the available current, then a second booster would have to be added to the current follower (CF) circuit, to make it capable of handling a cell current beyond the limits of CF.

The working electrode now feeds a current follower, whose output is proportional to the current. Note that the current follower allows the working electrode to remain at virtual ground, which is an essential condition for the operation of the system.

Increased power has been achieved by inserting a *booster amplifier* in the output loop. A booster is simply a noninverting amplifier, usually having low gain, capable of delivering higher currents or higher voltages, or both, than the operational amplifier itself. Since it is noninverting, one can consider it as an extension of the operational amplifier such that the overall open-loop gain of the combination is $A = A_{OA}A_B$, where the open-loop gain of the operational amplifier is A_{OA} and that of the booster is A_B. Then (15.1.1) applies directly and feedback principles apply as before.

15.4.4 Bipotentiostats (9, 10)

Some electrochemical experiments, such as those involving rotating ring-disk electrodes and the scanning electrochemical microscope, require simultaneous control of two working interfaces. A device that will meet this demand is called a *bipotentiostat*.

The usual approach is shown in Figure 15.4.6. One electrode is controlled in exactly the manner discussed in the previous section. The circuitry devoted to it is shown in the left half of the figure. The second electrode is controlled by the elements in the right half. There one finds a current follower (CF2) with a summing point held away from ground by some voltage difference, Δe, because its noninverting input is away from ground by Δe. This circuit uses the first electrode as a reference point for the second. We can set the first at any desired potential, e_1, with respect to the reference, then the second working electrode is offset with respect to the first by $\Delta e = e_2 - e_1$, where e_2 is the potential of the second electrode with respect to the reference. The counter electrode passes the sum of i_1 and i_2.

The remaining amplifiers (I2 and Z2) serve as inverting and zero-shifting stages. They allow one to supply the desired potential e_2 at the input without concern for the
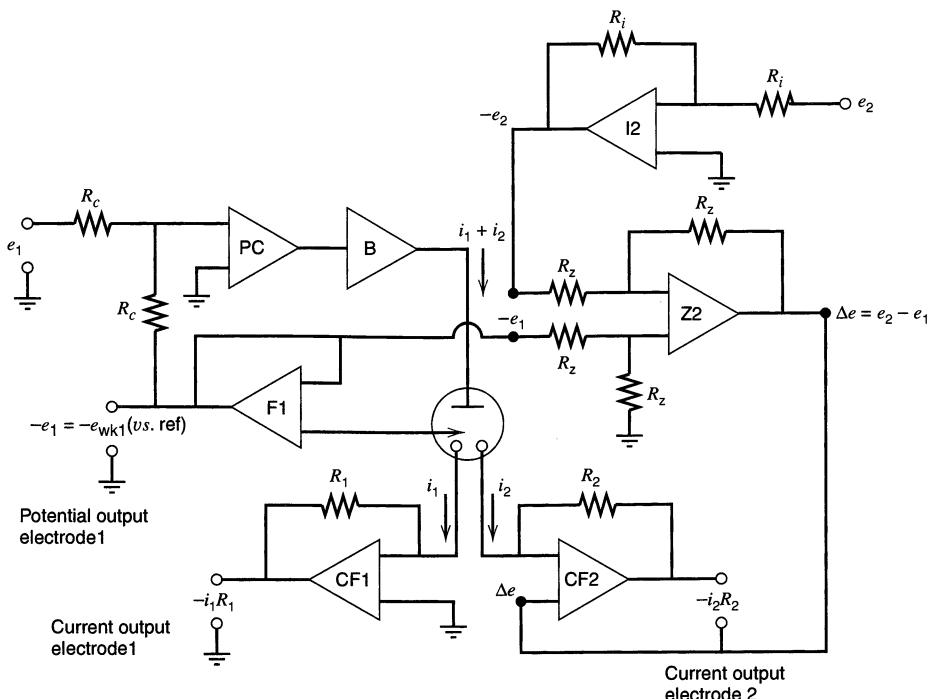
Figure 15.4.6 A bipotentiostat based on the adder concept. On the left is essentially the system of Figure 15.4.5, which is devoted to electrode 1. On the right is a network for controlling electrode 2. For large currents at both electrodes, boosters might have to be added to CF1 and CF2.

value of e_1 (see Problem 15.7). Such a convenience is valuable when one wishes to vary e_1 and e_2 independently in time.

▶ 15.5 GALVANOSTATS

Controlling the current through a cell is simpler than controlling the potential at an electrode, because only two elements of the cell, the working and counter electrodes, are involved in the control circuit. In galvanostatic experiments, one is usually interested in the potential of the working electrode with respect to a reference electrode, and circuitry is normally added to permit that measurement, but it makes no contribution to the control function.

Two different galvanostats can be derived from operational amplifier circuits that we have considered above (6, 7). The device shown in Figure 15.5.1 is strongly reminiscent
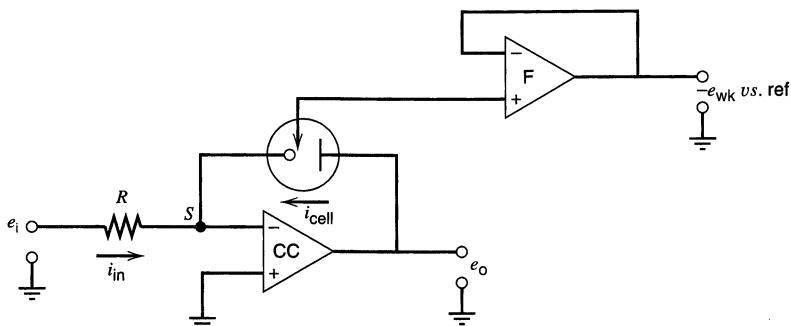
Figure 15.5.1 A simple galvanostat based on the scaler/inverter circuit.
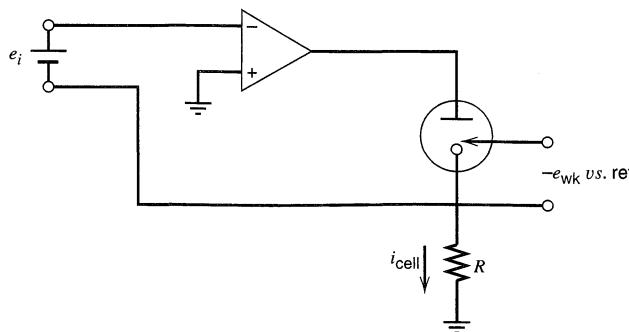
Figure 15.5.2 A galvanostat based on the circuit of Figure 15.3.3.

of the scaler/inverter discussed in Section 15.2.2. The cell has replaced the feedback resistance R_f. Summing currents at S, we have

$$i_{cell} = -i_{in} = \frac{-e_i}{R} \tag{15.5.1}$$

hence the cell current is controlled by the input voltage. It can be constant or vary in any arbitrary fashion, and the cell current will follow.

This design holds the working electrode at virtual ground, and that feature is a convenience for the measurement of the potential difference between the reference and working electrodes. The voltage follower, F, gives the reference electrode's potential versus ground, which is $-e_{wk}$ (vs. ref). Note by comparing Figures 15.5.1 and 15.4.1 that the follower's output has a contribution from uncompensated resistance equal to $i_{cell}R_u$.

The input network can be expanded by adding resistors into the summing point to create a system that will provide a cell current equal to the sum of input currents in the fashion of an adder. Each input voltage source must be capable of supplying its contribution to the cell current, as one can see from Figure 15.5.1. This requirement can create problems in systems intended for applying high currents.

In that case, the galvanostat shown in Figure 15.5.2 may be more useful. It is based on the design of Figure 15.3.3. The arbitrary impedance Z_L has been replaced by the cell. The current through the cell is

$$i_{cell} = \frac{-e_i}{R} \tag{15.5.2}$$

and this current does not have to be supplied by the voltage source e_i. A drawback is that the working electrode is off-ground by $-e_i$; hence the potential of the working electrode with respect to the reference must be measured differentially. In addition, the input voltage e_i is subject to the inflexibilities discussed earlier for Figure 15.4.2.

▶ 15.6 DIFFICULTIES WITH POTENTIAL CONTROL

The foregoing sections have outlined the principles of potential control. Here we examine some of the difficulties that can arise in measurements with real systems.

15.6.1 Effects of Solution Resistance (6, 7, 11–16)

The first set of complications pertains to experiments, such as fast transient electrochemistry or bulk electrolysis, involving the passage of large currents. The impact of solution resistance on such experiments is substantial and involves several considerations. In bulk electrolysis, current flow takes place at a high level over a long term because electrode

areas are large and mass transfer is effective. In fast transient experiments, high current pulses are encountered because dE/dt is high at some time during the measurement. At the very least, there is a capacitive component to the current. Suppose, for example, we wish to impose a 1-V step in 1 μs on an electrode having an interfacial capacitance of 2 μF. The average current in that period is 2 $\mu C/\mu s$ or 2 A. The peak current would be higher.

In both types of experiments, the potentiostat must have an adequate *power reserve*. It has to be able to supply the necessary currents (even if they are demanded only momentarily), and it must be able to force those currents through the cell. In high-current situations, the output voltage of the potentiostat is mostly dropped across the solution resistance $R_\Omega + R_u$, and the requirement can easily exceed 100 V. The limits of delivery of the potentiostat are sometimes called the *current compliance* and the *voltage compliance*. The power reserve is the product of the two compliances.

Whenever currents are passed, there is always a potential control error due to the uncompensated resistance. It was seen in Section 1.3.4 to be iR_u. If a cathodic current flows, the true working electrode potential is *less negative* than the nominal value by that amount. The opposite holds for an anodic current. Even small values of R_u, such as 1 to 10 Ω, can cause a large control error when substantial currents flow. This is one reason why large-scale electrosynthesis is not usually carried out potentiostatically. In that instance, controlling the current density is often more practical.

The control error in a fast experiment may be a transient problem existing only during brief periods of high current flow. Consider a step experiment on the equivalent circuit shown in Figure 15.6.1a, in which the working interface has only a capacitance representing the double layer. Even if an ideal control circuit exists so that e_{ref} is instantaneously stepped (from e.g., 0 V), there will be a lag in the true potential, e_{true}, because iR_u is nonzero while the double layer is charging. The actual relation (see Problem 15.8) is

$$e_{true} = e_{ref}(1 - e^{-t/R_uC_d}) \tag{15.6.1}$$

The relationship between e_{true} and e_{ref} is shown in Figure 15.6.2. Eventually e_{true} would reach e_{ref} as C_d became fully charged and the current dropped virtually to zero. However, the rise in potential at the working interface is governed by the exponential,

(a)   (b)
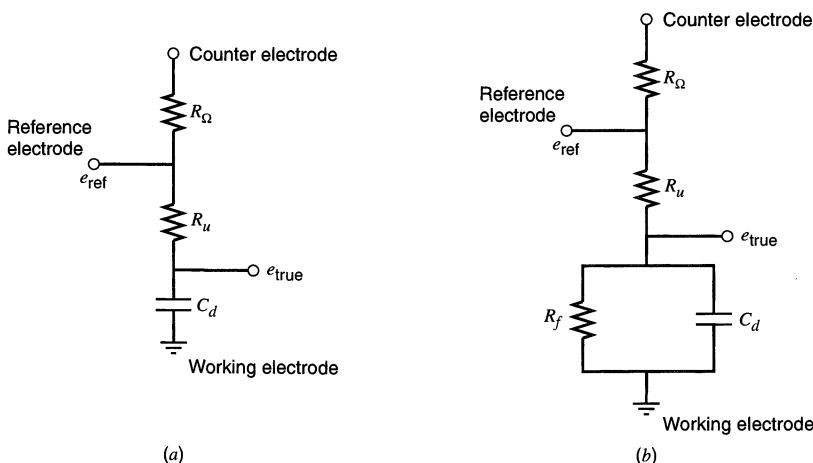
Figure 15.6.1 Simple dummy cells. (a) For a nonfaradaic system, where C_d is the double-layer capacitance and $R_u + R_\Omega$ is the solution resistance, with R_u being uncompensated. (b) For a system passing faradaic currents through R_f, as well as nonfaradaic ones through C_d.
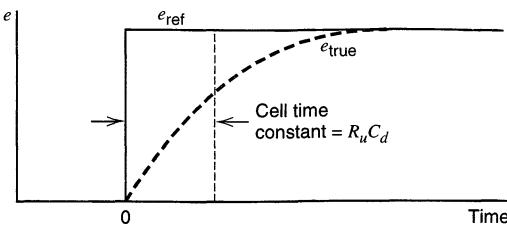
Figure 15.6.2 The effect of the cell time constant on the rise of the true working electrode potential after an instantaneous step is applied.

which is controlled by the *cell time constant*, $R_u C_d$. This time constant defines the shortest time domain over which the cell will accept a significant perturbation. The picture would not change drastically if a faradaic impedance, Z_f, were placed in parallel with C_d, but then e_{true} would never equal e_{ref} because a current would always leak through Z_f and cause a control error, iR_u. This error may or may not be significant, depending on the sizes of i and R_u (see Problem 15.9 and Figure 15.6.1*b*, where Z_f is shown as a simple resistance, R_f).

These considerations show that transient experiments will not be meaningful unless the cell time constant is small compared to the time scale of the measurement, regardless of the high-frequency characteristics of the control circuitry.

15.6.2 Cell Design and Electrode Placement (12, 14)

The time constant $R_u C_d$ can be reduced in at least three ways: (a) One can reduce the total resistance $R_\Omega + R_u$ by increasing the conductivity of the medium through an increase in supporting electrolyte concentration or solvent polarity, or through a decrease in the viscosity. (b) One can shrink the size of the working electrode to reduce C_d proportionally. (c) One can move the reference electrode tip as close as possible to the working electrode so that R_u is a smaller fraction of the total resistance $R_\Omega + R_u$, which would remain the same. All of these steps should be considered in any application, although (a) and (b) may be restricted by other experimental concerns. For example, the chemistry of the system may dictate the nature of the medium, and aspects of electrode fabrication may place significant constraints on the size of the working electrode. (See also Sections 5.9 and 11.2.3.)

When high currents pass through the electrolyte, that phase is not an equipotential volume (Section 2.2.1). Thus, the interfacial potential difference between the working electrode and the solution varies across the surface of the working electrode (Section 11.2.3). One can therefore expect a nonuniform current density over the interface. In general, current densities will be highest at points on the working electrode at closest proximity to the counter electrode. Nonuniform current densities imply that the effective working area is less than the actual area by an amount related to the absolute magnitude of the current. Such a condition is clearly unacceptable for most work depending on correlation of quantitative theory and experiment. The remedy is to design the cell so that the current paths from all points on the working electrode are equivalent. Symmetry in the design and placement of the working and counter electrodes is important in this regard. (See Section 11.2.3.)

The resistance between the working and counter electrodes directly controls the power levels required from the potentiostat and the resistive heating in bulk electrolysis that might have to be dissipated by cooling. It should be minimized by shortening the gap between the electrodes and removing impediments to current flow (such as frits or other separators) to the extent that is feasible within the constraints imposed by a desire for possible chemical isolation of the counter electrode or by a need for a spatial relationship concordant with uniform current density on the working surface.

Designing a cell for a demanding experiment is a task requiring optimization of many factors. We have space here only to outline some of the important considerations. The interested reader is referred to more specialized literature on the subject.

15.6.3 Electronic Compensation of Resistance (7, 11–16)

Since uncompensated resistance causes a potential control error equal to iR_u, it is logical to attempt automatic compensation by adding into the input of the potentiostat a correction voltage proportional to the current flow. If one were lucky, it might be possible to use a proportionality factor equal to R_u, so that the potential control error would be completely removed. This idea is the basis for *positive feedback compensation* schemes, the most common version of which is implemented in the circuit of Figure 15.6.3. The system is identical to the refined adder potentiostat of Figure 15.4.5, with the exception of the new feedback loop connecting the current follower to the potential control amplifier. The potentiometer selects some fraction f of the current follower's output for application to the input network; hence the feedback voltage is $-ifR_f$.

From the discussion in Section 15.4.2, we know that the working electrode's potential is then[1]

$$e_{wk} \,(vs.\ \text{ref}) = e_1 + e_2 + e_3 - ifR_f \tag{15.6.2}$$

The true working electrode potential versus the reference is

$$\boxed{e_{true} = e_1 + e_2 + e_3 - ifR_f + iR_u} \tag{15.6.3}$$

and this differs from the desired sum of the signal inputs $e_1 + e_2 + e_3$ by the control error $i(R_u - fR_f)$. The effect of the feedback loop has been to reduce the uncompensated resistance by the amount fR_f.

These considerations suggest that we might be able to set fR_f exactly equal to R_u and achieve total compensation. They also indicate that almost any degree of undercompensation or overcompensation is available.
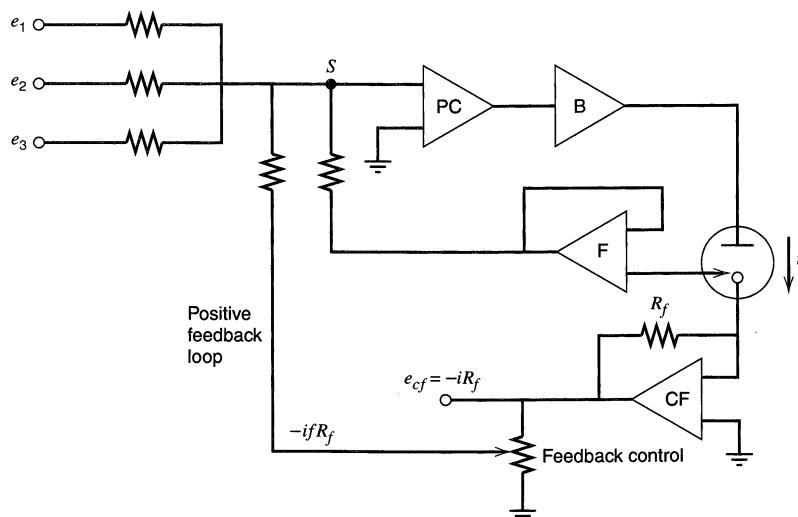
Figure 15.6.3 An adder potentiostat with positive feedback compensation.

---

[1]Note that i adheres to our usual definition for this discussion. Cathodic currents are positive.

In practice, there are problems with this scheme, because the elements of the cell and the amplifiers in the control circuit introduce phase shifts. Thus, there are significant time lags in the application of a correction signal, the establishment of a correction, and the sensing that the correction has been applied. These delays can cause the whole feedback system to overcorrect for changes in the input signal $e_1 + e_2 + e_3$. Effects such as overshoot and ringing are manifestations. In severe cases, the potentiostat will break into a high-frequency oscillation and therefore lose control completely over the cell. For reasons that are not obvious and that are too detailed for this treatment, potentiostats may require some uncompensated resistance to achieve stability. Total compensation is impractical when this is true.

In addition, there is a problem in knowing the value of R_u. The quick-and-dirty method of electronic compensation is to set the potential at a value where faradaic processes do not occur and to increase f with the potentiometer until the potentiostat starts to oscillate. Then f is decreased to a value about 10–20% below the critical f so that stability is reestablished. Since the critical f may lie either below or above full compensation, depending on the electronic properties of the whole system (cell plus potentiostat), this method must be used with care. Moreover, there is some danger that the test solution or the working electrode will undergo undesirable reactions (get "cooked") during the oscillation period.

It is preferable to measure R_u and to use the measured figure as the basis of compensation. There are a number of ways to determine R_u. One can use an impedance method like that discussed in Section 10.4.1. Another approach is the interrupter method, where the current flowing during a faradaic reaction is switched off for a few microseconds (i.e., the cell is taken to open circuit), and the instantaneous change in the potential, as the current drops to zero, is used to find iR_u. This method is based upon the fact that the relaxation of potential from faradaic processes and diffusion is slower, so that the instantaneous change in potential can be totally assigned to iR_u. A method (15) that is used with computer-controlled potentiostats (Section 15.8) involves the application of a small potential step (e.g., $\Delta E = 50$ mV) in a potential region where no faradaic reaction occurs. If the only current that flows in this region is charging current, the current response should be

$$i(t) = (\Delta E/R_u) \exp(-t/R_u C_d) \tag{15.6.4}$$

Automated analysis of the data according to this equation, such as by computing the linear regression of $\ln i(t)$ vs. t, can be used to extract R_u and C_d (see Problem 15.12). Once R_u is known, one can adjust the value of f in the positive feedback circuitry to approach unity in a systematic way while testing for early indications of potentiostatic instability. All of this can be done automatically with computer-controlled instruments.

The details of this subject and discussions of alternative approaches to compensation are covered in several good reviews (11, 12, 14–16). A reader involved in experiments requiring compensation should consult them.

Another source of uncompensated resistance, which can be important when high currents are passed or when the cell resistance is small (e.g., 0.1 Ω), is the contact resistance where the working electrode lead attaches to the working electrode. In many cases, especially where alligator clips are used, a *contact resistance*, R_c, of up to 0.3 Ω can exist. While this resistance is of little consequence at low currents, at higher current levels, iR_c can be significant. Contact resistance also exists at the reference and counter electrodes, but is usually of no consequence, since very small currents are drawn from the reference electrode and resistance at the counter electrode only means that a higher voltage is needed from the potentiostat. The working electrode contact resistance can be compen-

sated by the addition of a fourth lead, called a *high-current* or *sensing lead*, that clips on to the working electrode lead but draws no current. This lead allows the instrument to measure the voltage drop between its attachment point and ground (iR_c), so that iR_c can be subtracted from the reference potential in a manner analogous to the compensation of iR_u.

▶ 15.7 MEASUREMENT OF LOW CURRENTS

The increased use of UMEs and studies of electrochemical devices with μm- and nm-size features have led to the necessity of measurements at the pA, or even fA, level. Work with low currents involves some special considerations (17). Noise, including pickup from stray electromagnetic fields, becomes very important, and it is necessary to take steps to minimize this interference (18). In most cases with low current measurements, the electrochemical cell is enclosed in a Faraday cage, which is a grounded metal or screen box serving to shield the cell from stray fields. An operational amplifier selected for low input current (low *bias current*) is used for the current follower. Amplifiers with input currents of 25 fA are available. The time constant for a current follower circuit, such as that discussed in Section 15.2.1, is R_fC_s, where C_s is the stray shunting capacitance. Methods to compensate for C_s are available (17). It is important to minimize stray currents generated by vibrations creating static charges, by the movement of cables in the earth's magnetic field, and by electrostatic coupling to charged bodies or wires carrying current (17). Because large feedback resistors are needed to measure small currents and because the stray noise often necessitates filtering or integration of the transduced signal, measurements of small currents are especially difficult at high speed. Moreover, low currents at short times produce few electrons (Problem 15.13), a fact that implies significant uncertainty in measured values.

Commercial electrochemical instruments that measure currents down to 1 pA are available. To reach the nA and pA current ranges, conventional electrochemical instruments frequently are used in concert with a *current amplifier*, which is a module consisting of a current follower and an inverter (Figure 15.7.1). This device is placed between the working electrode and the corresponding lead from the potentiostat (which usually is the input to another current follower, CF) (19). The amplification factor is R_f/R_o, where R_f is the feedback resistance of the first amplifier and R_o is the output resistance (to CF).

Still smaller currents can be measured with commercial electrometers that can reach the fA regime. Most electrometers operate in the current feedback mode and maintain the input at virtual ground, so one can easily preserve the integrity of the potentiostatic system simply by connecting the working electrode to the input of the electrometer and establishing a common ground between the potentiostat and the electrometer. The normal working electrode lead of the potentiostat is not used in this configuration, and the output of the electrometer is fed to the recording system in place of the output of the current follower in the potentiostat.

An important advantage in low-current measurements in electrochemical systems, as discussed in Section 5.9, is that uncompensated resistance is usually not important, so that two-electrode cells can be employed. This simplifies cell design and can help to minimize stray currents and pickup. Figure 15.7.2 illustrates a typical configuration, in which a function generator is directly connected to the reference electrode. The working electrode is maintained at virtual ground, so the function generator has a potentiostatic effect. It need only be able to supply the desired waveform and the required current through the cell. The counter electrode shown in the diagram is not essential and is not present in a true two-electrode system. It is often a useful addition, because it can be much larger than the UME used as a working electrode, so that its capacitance can handle most of the cur-
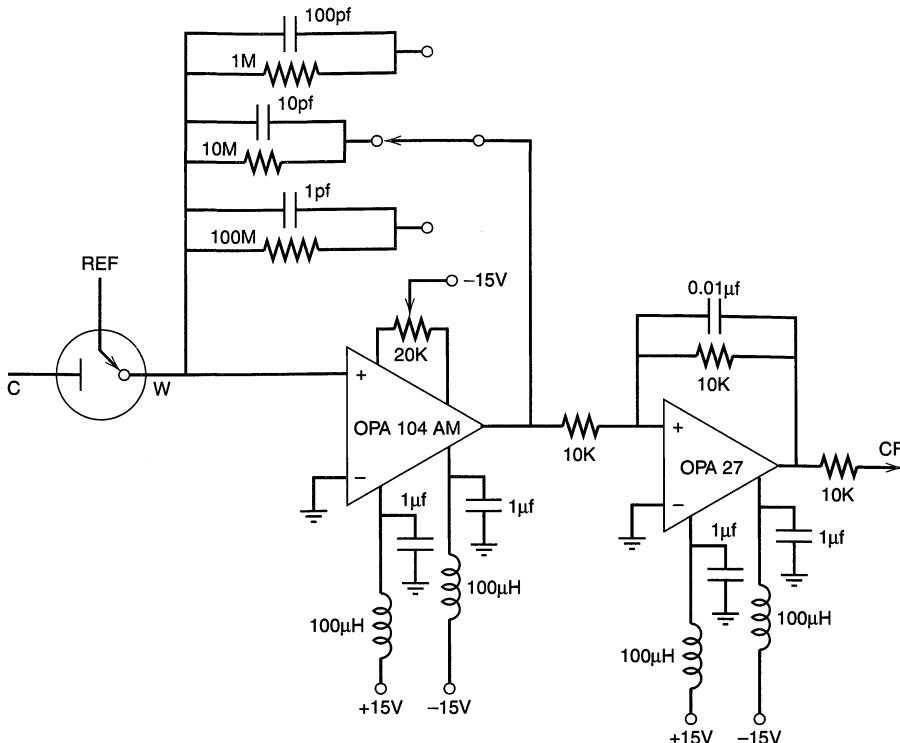
Figure 15.7.1   A low-current transducer for insertion between the working electrode and the current follower (CF) of a potentiostat. Depending on which feedback resistor is chosen in the first stage, the amplification factor in this system is 10^2, 10^3, or 10^4. The capacitors in the feedback loops provide some filtering (time constant, 100 μs). An inductor-capacitor network was inserted in each power supply connection to minimize noise coupling. [Reprinted with permission from H.-J. Huang, P. He, and L. R. Faulkner, *Anal. Chem.*, **58**, 2889 (1986). Copyright 1986, American Chemical Society.]
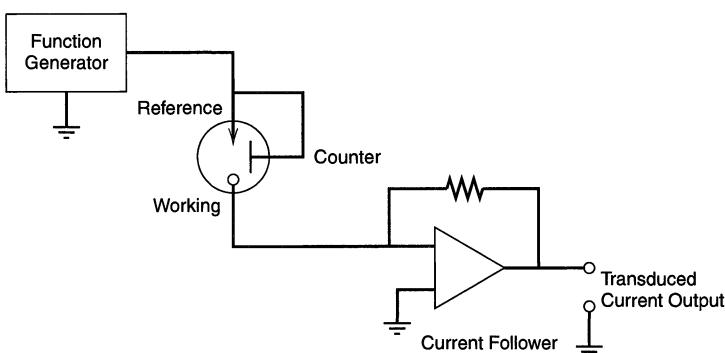
Figure 15.7.2   Alternative configuration for use with an ultramicroelectrode. The function generator produces the desired waveform and controls e_{ref} *vs.* ground, which is $-E_{wk}$ *vs.* the reference electrode. The current at the working electrode is transduced to a voltage using a current follower in the usual manner.

rent required at the reference/counter terminus. This feature spares the reference electrode from being gradually polarized over time by the accumulated effects of current flow, and it can improve the response of the system to current transients.

▶ ## 15.8 COMPUTER-CONTROLLED INSTRUMENTATION

Most electrochemical instrumentation now utilizes a microprocessor for signal generation and data acquisition, and a personal computer for interaction with the operator, overall experimental management, and analysis and display of results. While the use of computers for control of electrochemical experiments dates from the 1960s (20–23), the expense of the earlier equipment, its very modest performance, and the significant effort needed to interface to the experiment (in terms of both hardware and software) discouraged widespread use. The advent of inexpensive and powerful personal computers has led to their extensive utilization for signal generation and data acquisition in commercial and home-built electrochemical instruments. Although it is possible, in principle, to construct potentiostats that operate via digital feedback, almost all electrochemical instruments still utilize analog electronics based on operational amplifiers for potentiostats and voltage and current followers. The computer is used to generate signals, replacing analog function generators, and to acquire and display the data, replacing recorders and oscilloscopes.

Computers are versatile for generating complex waveforms (24). These are first created as numerical arrays in memory, then the number sequences are clocked out to a digital-to-analog converter (DAC) (2, 3), which produces an analog voltage proportional to the input digital number. This analog voltage is then applied to a potentiostat based on the adder design (Section 15.4.2). A good example is described in Section 10.8. The waveform in Figure 10.8.2f would be extremely difficult to synthesize in the analog domain (21, 22). Another example is the potential program for differential pulse polarography, shown in Figure 7.3.9. Analog generation of this function usually involves adding a slow ramp to the desired voltage pulses. The value of dE/dt is then never zero and one always has a charging current from that source. A computer can easily generate a more ideal waveform.

Computers are also used to control timing of different phases of experiments (e.g., deaeration of solutions, stirring, and growth of a mercury drop) and are well-suited to the performance of a series of experiments without operator attention.

In data acquisition, the electrochemical responses (potential, current, or charge) are recorded at fixed time intervals by digitizing them with an analog-to-digital converter (ADC) (2, 3). The input to the ADC, such as from the current follower, produces a number each time a conversion is triggered. These numbers are stored as an array in computer memory. The accuracy of the conversion depends on the number of bits produced for the given input voltage. An 8-bit converter (maximum accuracy of 1 part in 255) can make conversions at rates down to 3 ns/point. Conversions of 12-bit (maximum accuracy of 1 in 4095) require a time on the order of 1 μs/point. The maximum rate of data acquisition also depends upon the speed of the computer and the time needed to store a point in memory. Very fast rates can be obtained with a *transient recorder*, which is basically a fast ADC and streamlined memory logic. The signal is digitized and stored in the memory and then can be read out of memory by a computer at a rate suited to the computer. A *digital oscilloscope* is a type of transient recorder. Current equipment can acquire data at times below 1 ps/point at 14-bit resolution. Note that in employing digital data acquisition, it is important to optimize the signal levels with respect to the maximum resolution of the ADC. For example, if the ADC has an input voltage range of 0–1 V and produces corresponding numbers over the range of 0–1023, than its maximum resolution is 1 part in

1023 (i.e., 10-bit resolution). Recording signals over only a fraction of the operating range will yield a degraded resolution (e.g., only 1 part in 100 or less for signals of 0–10 mV). Under these conditions, data that should be continuous functions can appear as a series of steps. Depending on the noise level in the input signal, one can often alleviate this *quantization effect* and obtain both better accuracy and better precision by making multiple samples and conversions, then averaging the results.[2]

Several instruments built around computers are available commercially, such as from Bioanalytical Systems, CH Instruments, Cypress Instruments, and Eco Chemie. A block diagram of a typical instrument of this type is shown in Figure 15.8.1. It contains the basic features described above and in other discussions of "cybernetic" electrochemical instruments (25, 26). The major advantages of computer-based systems are found in their abilities to manage experiments with some intelligence, to store large amounts of data, to manipulate the data in complicated, often automatic, ways, and to present the results in a convenient format (e.g., as plots suitable for publication or for presentations). The data analysis function is particularly important, since very complex schemes can be applied (20–23). A good example is the Fourier analysis discussed in Section 10.8. Other possibilities include digital filtering, numerical resolution of overlapping peaks, convolution, subtraction of background current, and digital correction for uncompensated resistance.
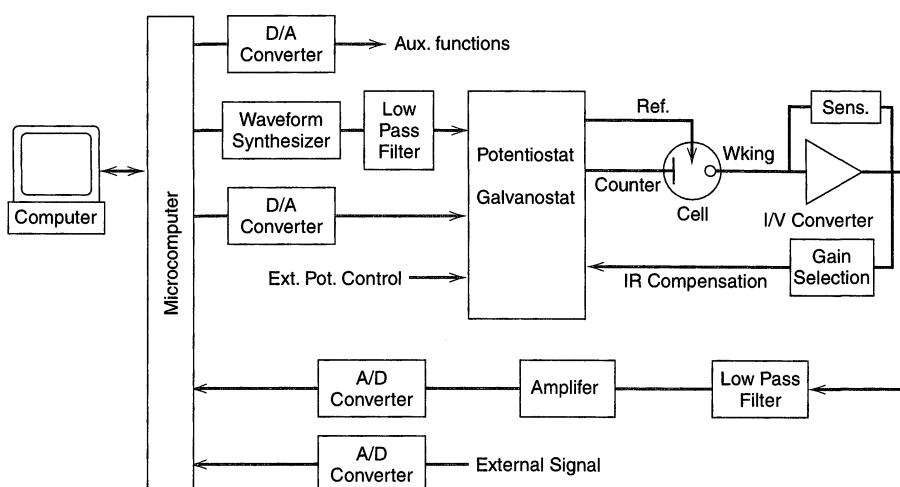
Figure 15.8.1 Block diagram of typical computer-controlled electrochemical instrument [based on the CH Instruments Model 600A]. The waveform synthesizer produces the desired scan signal (e.g., a triangular wave), and the D/A converter generates a dc bias signal. These two signals are fed to the adder potentiostat. The analog output (*Aux. Functions*) creates various operational signals, such as to dislodge drops in a SMDE or to control stirring, deaeration, and RDE rotation rates.

[2]Consider a measurement system that digitizes a 0–10 V input signal with 8-bit resolution. Upon sampling the input voltage, this system transforms the signal to a number in the range of 0–255; thus it has a resolution of 10/255 V, or 39.2 mV. Now suppose a noise-free signal of 3.92 V is presented to the input. Repeated measurement will always give the digitized result of 100 on the scale of 0–255. Of course, averaging the repeated measurements will produce the same. In fact, the identical outcome will arise for all input voltages in the 39-mV band bracketing 3.92 V. If noise is added to the signal, the behavior will not change as long as the noise remains small compared to the quantization level, because the signal always remains in the quantized band. On the other hand, noise greater than the quantization level leads to digitized values that are not uniform, so repeated sampling and averaging gives results on a scale where the quantization is smaller by a factor of n, where n is the number of averaged samples. Thus, the noise can actually be used to bring about a more continuous measurement scale.

Digital data can also be manipulated by spreadsheet programs and can be imported into digital simulation programs for comparison to theoretical curves.

While computer-based instrumentation offers unparalleled convenience and versatility, a word of caution is appropriate, because the operation of such instruments is often in a "black-box" mode. Details about how the data are acquired and then processed are often lacking. The user should periodically calibrate the instrument to ensure that currents and potentials are measured or controlled accurately within specifications. This can be done easily with a standard resistor or a dummy cell. Moreover, it is a good idea to check the response time of the instrument in situations where it might influence recorded results. Cybernetic instruments typically employ software-controlled electronic filtering in some circuits, such as the current follower; hence the instrumental time constant varies according to the experiment. The internal software normally uses a criterion that keeps the instrumental time constant an order of magnitude, or more, shorter than the characteristic time of the experiment, but an exceptionally sharp feature (e.g., a voltammetric spike or a sharp step-edge) can be distorted when recorded under conditions that would be safe for normal responses. These instruments usually allow the operator to override automatic filtering and to make other choices (including worse ones). One way to understand the effects of filtering in a given situation is to try different manual options and to examine the effects on results. In a similar manner, one should also be aware of the methods by which the instrument's software might treat the raw data, such as by averaging or algorithmic filtering, before results are displayed. Often software-based data treatments are electable by the operator. If so, it is worthwhile to experiment with the possibilities to define circumstances where they begin to distort the data significantly.

For experiments outside the scope of commercial instruments, one can relatively straightforwardly construct a specialized electrochemical instrument centered on a digital computer. The interfacing to the analog electronics is most conveniently accomplished through a commercial *data acquisition* (DAQ) *board* that plugs into an available slot in the computer. Such boards usually contain several DACs and ADCs, digital input and output (I/O), timing functions, and triggers. Alternative approaches are based on a GPIB (IEEE 488) or serial (RS-232) interface between the computer and the analog circuitry. Instrument software is needed to manage the application of signals and the acquisition of data. This can involve programming in a conventional computer language, such as C++. It is generally more convenient to use a higher graphical programming language, such as LabView (National Instruments) that allows the assembly of "virtual instruments" by manipulation of graphical symbols. Quite powerful systems can be constructed in a relatively short time with a DAQ board and operational amplifier signal-conditioning circuits (or an available analog potentiostat).

▶ 15.9 TROUBLESHOOTING ELECTROCHEMICAL SYSTEMS

We offer here some simple guidelines for checking an electrochemical system (instrument and cell) and isolating a problem, when the system does not seem to be producing the proper response. We assume (a) a three-electrode cell (e.g., Pt working electrode, Pt counter electrode, and SCE), (b) and an electrochemical instrument set up for cyclic voltammetry (e.g., as shown in Figure 15.4.5) at a scan rate of 0.1 V/s, and (c) a solution containing electrolyte and an electroactive species that should show a near-nernstian response. A typical system might be 5 mM Ru(NH$_3$)$_6^{3+}$ in 0.1 M KCl, which should produce a nice, reversible CV response at about -0.19 V *vs*. SCE at most working electrodes (Pt, Au, Hg). If the resulting current-potential response is ab-

sent (i remains at zero or is constant with E over the expected potential range (e.g., $+0.3$ to -0.5 V with the above system) or is anomalous [e.g., is excessively noisy, does not show a well-behaved peak, or is otherwise "strange" (perhaps showing a high slope or excessive capacitance)], one can follow the procedure outlined below to try to isolate the problem. We assume that the instrument has been checked to make sure that the proper current range for the electrode and the correct voltage range to encompass the redox species of interest have been selected. As a rule of thumb, the expected peak current in CV for a one-electron reaction at a scan rate of 0.1 V/s is about 200 $\mu A/cm^2$ electrode area/mM concentration. For a UME, the analogous figure is about 0.2 nA/μm radius/mM concentration.

1. With the electrochemical instrument turned off, disconnect the cell and replace it with a 10 kΩ resistor (dummy cell), with the reference and counter electrode leads connected together on one side of the resistor and the working electrode lead connected to the other side. Scan from $+0.5$ to -0.5 V with the sensitivity of the instrument set for currents of about 100 μA. The resulting scan should be a straight line that intersects the origin with maximum currents of ± 50 μA.

   A. The correct response is obtained. This means the electrochemical instrument and the leads and connections are OK, and the problem lies in the electrochemical cell. (Go to 2.)

   B. An incorrect response is obtained. There is a problem with the instrument or leads. (Go to 3.)

2. Reconnect the cell, but connect both the reference and counter electrode leads to the counter electrode and the working electrode lead to the working electrode. Run the potential scan. The response should now resemble a typical voltammogram, but shifted in potential and distorted from a nernstian response.

   A. This response is obtained. The problem lies with the reference electrode. (In the experience of the authors, most cell problems arise from bad reference electrodes.) Check to make sure the electrode salt bridge is not clogged and is immersed in the solution, that no air bubble is blocking the end of the salt bridge, and that the wire to the reference electrode is making proper contact. If none of these problems is found, replace the reference electrode with a quasi-reference (e.g., a silver wire) and see if a good voltammogram is obtained. If so, replace the reference electrode.

   B. This response is not obtained. Make sure both the counter and working electrodes are immersed in the solution and that the internal electrode leads are intact (use an ohmmeter to check continuity between lead and electrode). If the response obtained is generally satisfactory, but the waves are drawn out or otherwise strange, the problem may be with the working electrode surface. Go to 4.

3. Disconnect the leads between the instrument and the cell and replace with another set of leads or check the continuity between the instrument connector and the cell connection on either side of each lead (working, reference, counter). If the problem is not in the leads, then the instrument is at fault and must be serviced.

4. The problem may be with the working electrode surface. For example, it may contain a layer of polymer or adsorbed material that partially blocks or changes its electrochemical response. A solid electrode can be reconditioned by polishing

it with 0.05 μm alumina and then carefully washing it (sometimes with sonication). A Pt electrode can be cleaned and "activated" by cycling it in 1 M H_2SO_4 between potentials where hydrogen evolution occurs and potentials where oxygen evolution occurs, ending with the cathodic phase. After several cycles, the voltammogram of the Pt electrode should resemble that in Figure 13.6.1. Problems with working electrodes sometimes involve poor metal-to-glass seals that leave a gap and can result in a sloping baseline. Poor contacts between the inner electrode lead and the Pt can result in high resistances. A thin glass wall between the internal lead connection (e.g., solder or silver epoxy) and the solution can lead to high capacitances. Excessive noise can be caused by poor contacts either to the electrodes or at the instrument connector, or by pickup on the leads or in the cell. The latter problem can be corrected by making the leads shorter and placing the cell in a Faraday cage.

▶ 15.10 REFERENCES

1. P. T. Kissinger in "Laboratory Techniques in Electroanalytical Chemistry," 2nd ed., P. T. Kissinger and W. R. Heineman, Eds., Marcel Dekker, New York, 1996, Chap. 6.

2. P. Horowitz and W. Hill, "The Art of Electronics," 2nd ed., Cambridge University Press, Cambridge, 1989, Chap. 4.

3. R. E. Simpson, "Introductory Electronics for Scientists and Engineers," Prentice Hall, Englewood Cliffs, NJ, 1987, Chaps. 9 and 10.

4. M. C. H. McKubre and D. D. Macdonald, in "Comprehensive Treatise on Electrochemistry," R. E. White, J. O'M. Bockris, B. E. Conway, and E. Yeager, Eds., Plenum, New York, 1984, Chap. 1.

5. J. G. Graeme, G. E. Tobey, and L. P. Huelsman, Eds., "Operational Amplifiers—Design and Applications," McGraw-Hill, New York, 1971.

6. D. E. Smith, *Electroanal. Chem.*, **1**, 1 (1966).

7. R. R. Schroeder in "Computers in Chemistry and Instrumentation," Vol. 2, "Electrochemistry," J. S. Mattson, H. B. Mark, Jr., and H. C. MacDonald, Jr., Eds., Marcel Dekker, New York, 1972, Chap. 10.

8. W. M. Schwarz and I. Shain, *Anal. Chem.*, **35**, 1770 (1963).

9. D. T. Napp, D. C. Johnson, and S. Bruckenstein, *Anal. Chem.*, **39**, 481 (1967).

10. B. Miller, *J. Electrochem. Soc.*, **116**, 1117 (1969).

11. D. E. Smith, *Crit. Rev. Anal. Chem.*, **2**, 247 (1971).

12. J. E. Harrar and C. L. Pomernacki, *Anal. Chem.*, **35**, 47 (1973).

13. D. Garreau and J.-M. Savéant, *J. Electroanal. Chem.*, **86**, 63 (1978).

14. D. Britz, *J. Electroanal. Chem.*, **88**, 309 (1978).

15. P. He and L. R. Faulkner, *Anal. Chem.*, **58**, 517 (1986).

16. D. K. Roe, in "Laboratory Techniques in Electroanalytical Chemistry," P. T. Kissinger and W. R. Heineman, Eds., Marcel Dekker, New York, 1996, Chap. 7.

17. "Low Level Measurements," Keithley Instruments, Inc., Cleveland, OH, 1993.

18. R. Morrison, "Grounding and Shielding Techniques in Instrumentation," Wiley, New York, 1967.

19. H.-J. Huang, P. He, and L. R. Faulkner, *Anal. Chem.*, **58**, 2889 (1986).

20. See, for example, J. S. Mattson, H. B. Mark, and H. C. MacDonald, Eds., "Computers in Chemistry and Instrumentation," Vol. 2, "Electrochemistry," Marcel Dekker, New York, 1972, Chap. 11 (by R. A. Osteryoung), Chap. 12 (by D. E. Smith), Chap. 13 (by S. P. Perone), Chap. 1 (by P. R. Mohilner and D. M. Mohilner), Chap. 2 (by H. C. MacDonald, Jr.), Chap. 4 (by R. F. Martin and D. G. Davis), and Chap. 6 (by A. A. Pilla).

21. S. C. Creason, J. W. Hayes, and D. E. Smith, *J. Electroanal. Chem.*, **47**, 9 (1973).

22. D. E. Smith, *Anal. Chem.*, **48**, 221A, 517A (1976).

23. J. W. Hayes, D. E. Glover, D. E. Smith, and M. W. Overton, *Anal. Chem.*, **45**, 277 (1973).

24. P. He and L. R. Faulkner, *J. Electroanal. Chem.*, **224**, 277 (1987).

25. P. He, J. P. Avery, and L. R. Faulkner, *Anal. Chem.*, **54**, 1313A (1982).

26. P. He and L. R. Faulkner, *J. Chem. Inf. Comput. Sci.*, **25**, 275 (1985).

▶ 15.11 PROBLEMS

15.1 Consider a voltage follower circuit with the input leads reversed so that the feedback loop involves the noninverting input. Derive a formula linking the output e_o to the input e_i. Is e_o defined for any condition (e.g., any frequency)? Suppose the amplifier is at an equilibrium condition and a sudden positive change is made in e_i. Would e_o converge on a new equilibrium value, given a finite delay in the response of e_o to e_i? Answer these same questions for the conventional voltage follower. Is it now clear why the feedback involves the inverting input?

15.2 Devise an operational amplifier circuit that will integrate the sum of two input signals. Only one amplifier is required.

15.3 Suppose you wanted a ramp generator with a facility for stopping the sweep at any point and holding a constant output until the sweep is to be resumed. How could you fabricate such a device?

15.4 Current followers often feature a capacitor in parallel with the feedback resistor. What is its effect? Is it useful?

15.5 Suppose you have an input signal with information at $\omega/2\pi = 10$ Hz and noise at $\omega/2\pi = 60$ Hz; for example,

$$e_i = 10 \sin 2\pi(10)t + 0.1 \sin 2\pi(60)t$$

What is the signal-to-noise ratio in e_i? To what extent is the ratio degraded by analog differentiation? Calculate the improvement upon integration. Is there an optimal RC product for either differentiation or integration?

15.6 Consider the adder potentiostat of Figure 15.4.5. What would be the effect of adding a capacitor between the summing point and the booster output? Explain the mechanism for the effect by considering currents at the summing point. When might this arrangement be useful?

15.7 Show that amplifiers I2 and Z2 in Figure 15.4.6 place a voltage $e_2 - e_1$ at the noninverting input of CF2. What is the output of CF2?

15.8 Derive a formula describing current flow in the dummy cell shown in Figure 15.6.1*a* on application of a step in e_{ref} from 0 V to an arbitrary value e_{ref}. Derive equation 15.6.1 from your result.

15.9 Derive a formula describing current flow in the dummy cell shown in Figure 15.6.1*b* upon application of a step in e_{ref} from 0 V to an arbitrary value e_{ref}. Derive an equation for the true potential difference between the reference and working electrodes corrected for the drop through R_u. Is the cell time constant still a factor controlling the rise of e_{true}?

15.10 What would happen to the working electrode potential if the output of the current follower in Figure 15.4.5 reached its voltage limit under a heavy current load? Suppose this happened during a potential step. What would the effect be on the rise of the true potential difference between the working and reference electrodes?

15.11 An alternative potentiostatic circuit is shown in Figure 15.11.1. Explain its operation. What simple amplifier circuit is it based on? Evaluate its strong and weak points relative to the simple circuit of Figure 15.4.2 and the adder design of Figure 15.4.4. Design a potentiostatic system equivalent to that of Figure 15.4.5 on the basis of this circuit.
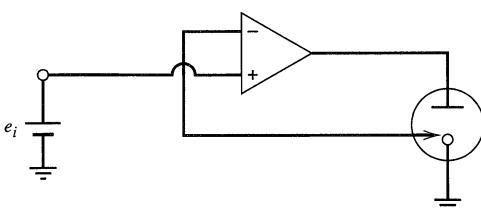
Figure 15.11.1 An alternative potentiostatic circuit.

15.12 A cell with a 0.1 cm^2 area working electrode is subjected to a 50-mV potential step in a potential region where no faradaic reaction occurs. After 1.0 ms, the current is 30 μA and after 3 ms, the current is 11 μA. What is the magnitude of the uncompensated resistance, R_u, and the double-layer capacitance, C_d?

15.13 How many electrons flow when a current of 1 pA passes for 1 μs? Do you think this current could be measured?

CHAPTER

16

SCANNING PROBE
TECHNIQUES

▶ 16.1 INTRODUCTION

The electrochemical methods discussed in the previous chapters can provide a wealth of information about the electrode–electrolyte interface and the processes that occur there. However these methods are typically macroscopic ones, that is, they are based on measurements over large areas compared to the size of a molecule or the unit cell of a crystal surface. To provide structural information about the electrode, surface microscopic methods are needed. In Chapters 16 and 17, we consider a number of other techniques that supplement the purely electrochemical methods. This chapter is devoted to scanning probe methods, and the next describes spectroscopic and other methods.

We would like a microscopic view of the electrode surface at several different levels of resolution. The optical microscope's resolution is limited by the wavelength of visible light, but can still provide useful information about the electrode surface at the micrometer level. For example, UMEs are frequently examined under an optical microscope to determine the shape and the effects of polishing on the surface. Much higher resolution can be obtained by *scanning electron microscopy* (SEM). However, the usual equipment requires that the sample be in a vacuum (i.e., SEM is an *ex situ technique*, where the electrode must be removed from the electrochemical environment), and this makes it somewhat less useful for studying structures that may form on an electrode surface during an electrochemical reaction, but may not remain stable in a gaseous or vacuum environment. The invention of *scanning tunneling microscopy* (STM) by Binnig and Rohrer in 1982 provided a new, high-resolution, tool for looking at surfaces (1), and their achievement was quickly recognized by the Nobel Prize. Later work showed that STM could be used in liquids and in electrochemical cells (i.e., it could be used as an *in situ technique*). Other forms of scanning probe microscopy, like *atomic force microscopy* (AFM), provide complimentary information about electrode surface topography and surface forces. *Scanning electrochemical microscopy* (SECM) can be used to probe surface reactions and also serves as an electrochemical tool. The principles and electrochemical applications of these different methods to electrochemical problems are described in this chapter.

▶ 16.2 SCANNING TUNNELING MICROSCOPY

16.2.1 Introduction and Principles

The STM is useful for studying surfaces, particularly well-defined and atomically smooth surfaces. It is probably the only technique available that can provide true atomic resolution of electrode surfaces in an electrochemical environment. The technique is based on

measurement of the tunneling current that flows between the electrode surface and a sharp metal tip (W or Pt) as the tip is brought close to the surface and scanned across it (Figure 16.2.1). Tunneling is a form of electronic conduction that occurs when the tip is so close to the surface that the wave functions of the tip overlap those of the substrate atoms. This current flow is not based on a faradaic process and does not produce a chemical change. The simplified expression for the tunneling current, i_{tun}, is

$$i_{tun} = (\text{constant})V \exp(-2\beta x) = V/R_{tun} \qquad (16.2.1)$$

where V is the tip-substrate bias, x is the distance between tip and surface, $\beta \approx 1 \text{ Å}^{-1}$, and R_{tun} is the effective resistance of the tunneling gap, typically 10^9 to 10^{11} ohms (see also Sections 3.6.4 and 14.5.2). In more detailed discussions and derivations of the tunneling current equation (2–4), the pre-exponential constant is related to the overlap of the density of states (filled and vacant), and β depends on the energy barrier between tip and sample, which is related to the work function of the sample. Appreciable (pA to nA) currents flow only when the tip is closer than a few nanometers from the surface under a bias of millivolts to a few volts. STM is generally used in the *constant current mode*, in which one obtains an image of a surface by moving the tip in the z-direction until a tunneling current flows and then scanning the tip across the surface (in the x-y plane) while maintaining the current constant by moving the tip up and down, that is, by varying z.

The movement of the tip is controlled by piezoelectric elements (*piezos*) whose dimensions depend upon the voltage applied to them. Thus the movement of the tip in the z-direction is controlled by the z-piezo voltage, and the constant current mode image consists of a plot of this voltage as a function of x and y position (varied by scanning the x- and y-piezos). The observed STM image basically consists of a topographic trace of the surface, affected, however, by any local variations in work function on a surface consisting of several different materials. A typical STM image is shown in Figure 16.2.2a as a topographic plot. More frequently, however, the results are presented as a color- or grayscale image, where different heights are plotted as different shades or different colors, as in Figure 16.2.2b. The spacing between tip and substrate is controlled by the applied bias and the set constant current level. A small bias and a high set current results in the tip moving very near the surface and this is needed for a high-resolution image.

To obtain high-resolution STM images, the tip must be very sharp; its movement must be controlled within fractions of an Å; and thermal changes and vibrational movements must be avoided. Atomically sharp tips can be obtained by electrochemical etching or by ju-
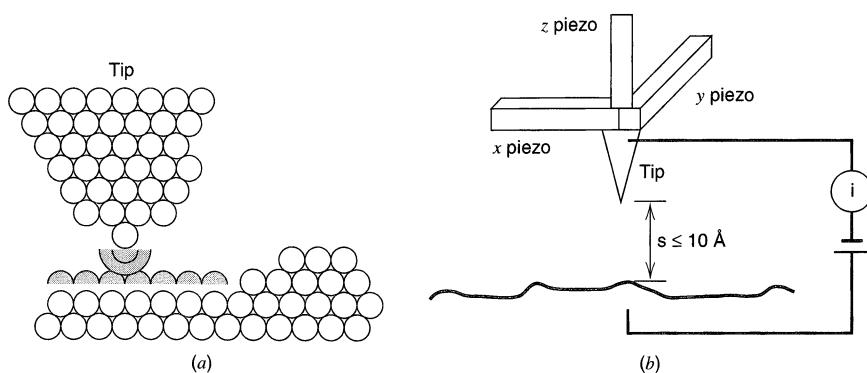
Figure 16.2.1 (*a*) Representation of tunneling between tip and sample atoms. Shaded portions denote electron distributions. (*b*) Tip attached to three piezo elements used to position the tip and scan it across a surface.
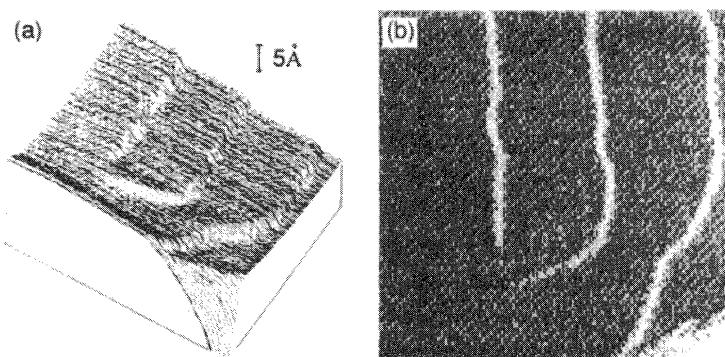
Figure 16.2.2 (*a*) Topographic plot and (*b*) gray-scale image of the same 200 nm × 200 nm region of a Au(111) film on mica, imaged at +0.7 V *vs.* NHE in 5 × 10⁻⁵ *M* HCl, 0.1 *M* HClO₄. [Reprinted with permission from D. J. Trevor, C. E. D. Chidsey, and D. N. Loiacono, *Phys. Rev. Lett.*, **62**, 929 (1989). Copyright 1989, American Physical Society.]

dicious snipping of small wires. The piezo-elements that control tip movement have dimensions that can be controlled to a resolution of better than 0.1Å. Vibrations can be minimized by proper design of the STM microscope head (usually by making the size of the tip and piezo assembly small, so that its resonant frequency is higher than those of typical building vibrations) and by mounting the head and sample on a system that damps those vibrations.

An important aspect in the design of an STM is the method used to provide for coarse approach, whereby the tip is brought to the sample surface within range of the z-piezo travel (typically several μm). This is usually accomplished by a stepping motor or *inch-worm* (a piezo-based device that by repeated extensions and clamping steps can move over a large distance) and with the aid of an optical microscope. The attainable resolution in STM usually depends upon the tip shape, which can be judged by noting the STM image obtained on standard samples, like HOPG or single-crystal gold.

It is also possible to obtain images by measuring i_{tun} with the z-piezo maintained at a given voltage (the *constant height mode*). However this mode is only useful for very smooth samples, since any small obstruction on the surface would result in a tip crash.

16.2.2 Electrochemical Applications

In electrochemical STM (ESTM), the working electrode is mounted horizontally at the bottom of a small cell that contains auxiliary and reference electrodes. The scanning tip is held above the working electrode (Figure 16.2.3). The potentials of the working electrode (E_{we}) and the tip (E_t) are controlled independently with a bipotentiostat (Section 15.4.4), where E_{we} is selected to produce the reaction of interest and E_t is adjusted to give the desired bias. Because only the tunneling current is of interest in STM, electrode reactions that occur at the tip are undesirable. Thus, in ESTM (as opposed to *ex situ* STM in air or vacuum) the tip is coated with glass or polymer, with only a very small area at the very bottom portion left exposed. The actual exposed area can be estimated, if necessary, by using the tip as a UME, noting the magnitude of the limiting current in a known solution, and applying equation 5.3.11. The tip potential is also chosen to be in a region where electrode reactions do not occur. The thickness of the electrolyte layer over the working electrode must be small, so that only the tip, and not the tip holder or a piezo, contacts the solution. This arrangement makes it difficult to keep the electrolyte solution free of oxygen, unless the whole cell and STM head are kept in an inert atmosphere, such as with a
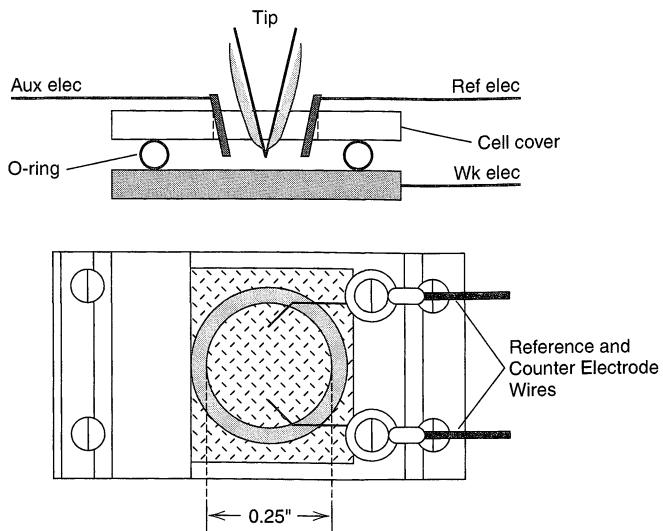
Figure 16.2.3 Cell for electrochemical STM. *Upper*: schematic diagram. *Lower*: Nanoscope III cell, top view. [Courtesy of Digital Instruments, Veeco Metrology Group].

glove bag. Further details about the experimental arrangement and techniques in ESTM can be found in reviews (5).

ESTM is usually used with HOPG and single-crystal metal and semiconductor electrodes. In many cases, one can resolve the atomic structure of the electrode and see different features (e.g., terraces and pits) on the surface. STM images of an Au electrode and of an HOPG basal plane surface are shown in Figures 13.5.1 and 16.2.4, respectively. These are maps of the electron density distribution across the surface. The observed *corrugations* depend upon this distribution and are much larger for HOPG, where the electron density is less delocalized through the material, than for Au. These distributions can sometimes be identified with the actual atomic structure of the surface, but other aspects of the sample also influence the image. For example, with HOPG only half of the surface carbon atoms are imaged, because of the nature of the underlying carbon atom layer. Half of the surface atoms are situated directly over carbon atoms in the second layer. The electron density for such surface atoms is directed downward and is less available for overlap with the tip than that for surface atoms that are located above interatomic spaces in the second layer. When
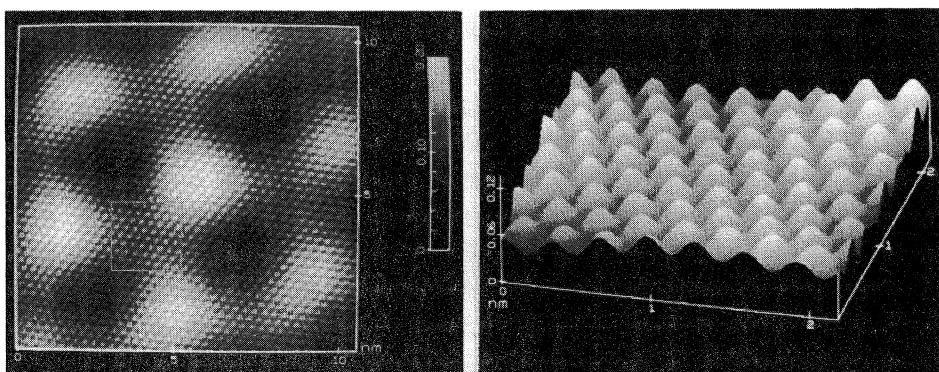
Figure 16.2.4 STM image of HOPG. Gray-scale image at low resolution (*left*) and higher resolution topographic plot (*right*). [Reprinted with permission from C.-Y. Liu, H. Chang, and A. J. Bard, *Langmuir*, **7**, 1138 (1991). Copyright 1991, American Chemical Society.]

good atomic resolution is obtained, it is possible to note the arrangements of atoms on the surface, such as on Au(111), and to determine the interatomic spacing.

The STM tip interacts with the surface both by interatomic forces and by the tip's electrical field. Thus, the tip can affect the structure of the scanned area, especially at high tunneling currents. This effect can sometimes be recognized after scanning over a given small region by decreasing the set tunneling current, increasing the x-y scan dimensions, and observing whether an image of a square perturbed region, where the earlier scanning took place, is visible.

The tip-surface interaction also makes it difficult to image molecules on an electrode surface. Isolated molecules usually cannot be seen, because they are too mobile beneath the scanning tip. If the molecules are packed in a layer on the surface, however, imaging of the adsorbed layer is possible. For example, a layer of iodine adsorbed on a Pt(111) surface is shown in Figure 16.2.5. One can recognize the $(\sqrt{3} \times \sqrt{3})$ R30° pattern of the iodine overlayer from this image (6). One can similarly image self-assembled monolayers and other close-packed layers on electrode surfaces, such as the adsorbed layer of 4-aminothiophenol on Au(111) shown in Figure 13.5.2. One difficulty with typical STM studies is that only a tiny area (for example 100 nm × 100 nm or less) of the surface is imaged in a given scan. Thus, it is difficult to know if the area seen is representative of the surface. It is necessary to examine many different areas and different electrodes to ensure that one has not, by chance, found a unique spot (e.g., one governed by an impurity).

It is almost impossible to remove a sample from the STM and then put it back and find the same place again for imaging. (Note that there are 10^9 areas 100 nm × 100 nm on a 0.1 cm^2 electrode.) An advantage of *in situ* ESTM is that the same area can be imaged over time, and even as the potential is changed, without removing the electrode from the electrochemical environment. Small drifts do occur with time, due to thermal effects and mechanical relaxation of the piezos and sample, but these can usually be recognized and accommodated. Thus, one can study the progressive change in a surface, such as by etching, corrosion, or deposition, and gain an understanding of structural changes at the atomic level in favorable cases (5). A study of the dissolution of a Cu(111) electrode is summarized in Figure 16.2.6 (7). One can see that when the electrode is held at a potential where slow etching of the Cu(111) occurs, the different terraces are gradually etched
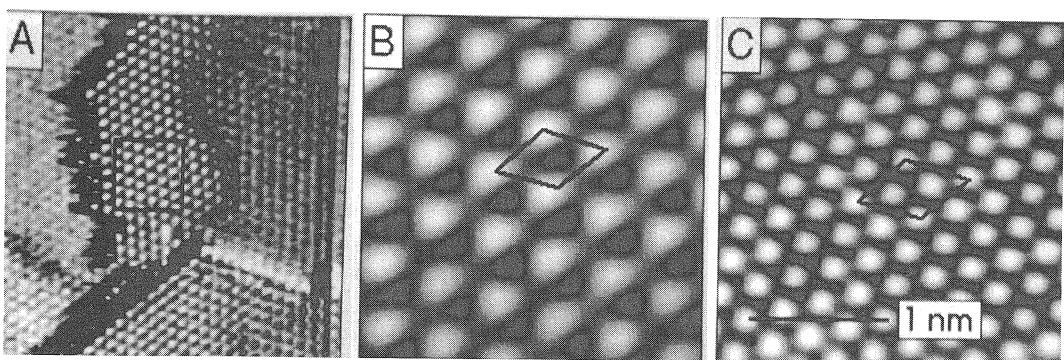
Figure 16.2.5 STM Images of Pt(111) single crystal with a $(\sqrt{3} \times \sqrt{3})$ R30°-I adlattice (adsorbed iodine) imaged in 0.1 M HClO$_4$. (*A*) 12.5 nm × 12.5 nm area; bias, 31 mV; tunneling current, 25 nm; (*B*) 2.5 nm × 2.5 nm image of boxed region in (*A*); (*C*) 2.5 nm × 2.5 nm image of the Pt(111) substrate lattice [Reprinted with permission from S.-L. Yau, C. M. Vitus, and B. C. Schardt, *J. Am. Chem. Soc.*, **112**, 3677 (1990). Copyright 1990, American Chemical Society.]
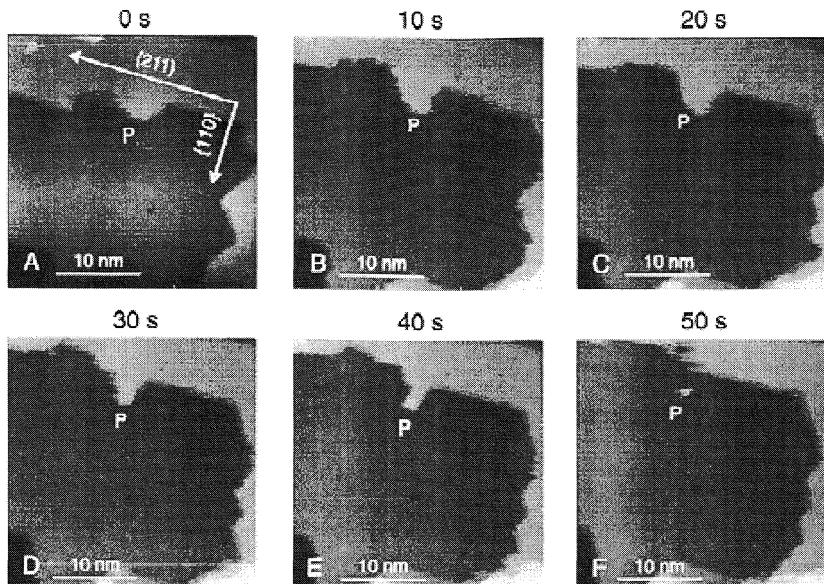
Figure 16.2.6 STM images of the surface of a Cu(111) single crystal showing the effect of electrochemical etching at different times (indicated above each image) after initiation. The arrows in *A* indicate the: {211} and {110} directions. Applied tip potential, 0 V *vs.* SCE; substrate bias, 21 mV *vs.* the tip; tip current, 9.0 nA. Note that etching is fastest along the {211} direction and that a facet (P) forms along the dissolving {211} step. The apex of the facet is pinned and dissolution occurs around the pinned point until dissolution isolates P. [Reprinted with permission from D. W. Suggs and A. J. Bard, *J. Am. Chem. Soc.*, **116**, 10725 (1994). Copyright 1994, American Chemical Society.]

away. Moreover the rate of etching is faster along the {211} direction (where the Cu atoms are less close-packed) compared to the {110} direction (Figure 16.2.7).[1] This implies that atoms along the {110} edge, which are coordinated to four other Cu atoms, are held more strongly in the lattice (i.e., have a different E^0 for oxidation) compared to those along the {211} edge, which are coordinated only to three Cu atoms.

ESTM studies have been carried out on the deposition of metals, corrosion of alloys, and oxidation of metals and HOPG.

An important limitation of STM is that a quantitative correlation between the tunneling current and useful theoretical equations is not yet possible. Thus, there is little real chemical and analytical information in the STM scans, and one gains mechanistic and structural information mainly from the interpretation of images. However, one can obtain additional information by noting how the STM behavior varies with the substrate potential (*vs.* a reference electrode) or the tip bias (between tip and substrate). An experiment of this type, involving the ESTM behavior of mixed monolayers of protoporphyrin IX (PP) and iron protoporphyrin IX (FePP) adsorbed on HOPG (9), is illustrated in Figures 16.2.8 and 16.2.9. PP is not reduced at potentials up to -0.7 V *vs.* SCE, while FePP shows a reduction wave characteristic of a surface species (Section 14.3.2) with E_p at

---

[1]The *planes* of a crystal are indicated by the Miller indices and are enclosed in parentheses, such as a (111) plane (see Figure 13.4.1). *Directions* along a plane are indicated by braces, such as the {211} direction. This is a vector where one moves the length of two lattice spacings in the *x* direction for every one in the *y* and *z* directions. The {110} direction lies in the *x-y* plane and is parallel with the intersection of any (111) plane with the *x-y* plane (8).

Top View

{110}

{211}
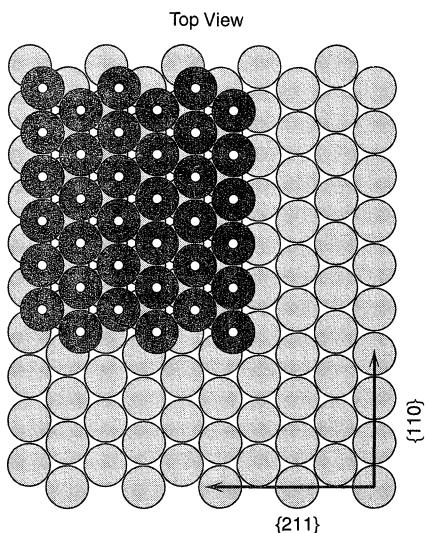
Figure 16.2.7 View of step edge on Cu(111) illustrating the atomic arrangement of the top layer (darker atoms) and the bottom layer (lighter atoms). Note that in the {211} direction the atoms are less coordinated by neighbors (and a higher density of kink sites exists) than in the {110} direction. [Reprinted with permission from D. W. Suggs and A. J. Bard, *J. Am. Chem. Soc.*, **116**, 10725 (1994). Copyright 1994, American Chemical Society.]

−0.48 V (Figure 16.2.8). As shown in this figure, with a tip bias of −0.1 V and substrate potential of −0.41 V, the tunneling current is greater when the tip is above FePP compared to PP, so FePP molecules appear brighter. The tunneling behavior is a function of potential, as shown in Figure 16.2.9, with the maximum difference between FePP and PP and the largest tunneling current (i.e., apparent height) being observed near E_p for the

(a)   (b)
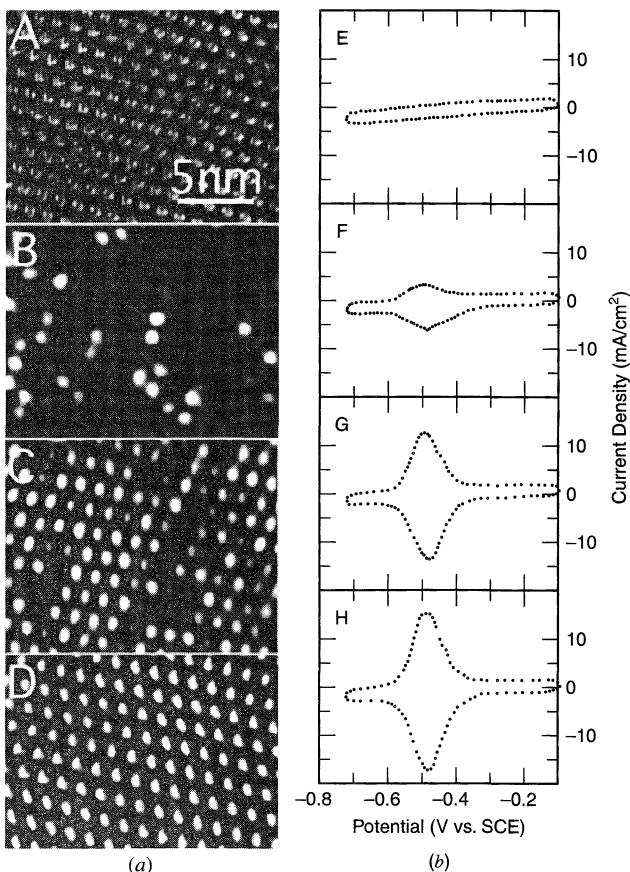
Figure 16.2.8 (a) STM images of (A–D) mixed adsorbed layers of PP and FePP on HOPG. Taken with a wax-coated Pt tip in 0.05 M $Na_2B_4O_7$ solution containing FePP and PP in the ratio of (A) 0:1 (B) 1:4 (C) 4:1 and (D) 1:0. The HOPG substrate potential was −0.41 V *vs.* SCE; the tip/substrate bias was −0.1 V; and the tunneling current was 30 pA. (b) (E–H) The corresponding cyclic voltammograms for A–D, respectively, at a sweep rate of 0.2 V/s. [Reprinted with permission from N. J. Tao, *Phys. Rev. Lett.*, **76**, 4066 (1996). Copyright 1996, American Physical Society.]
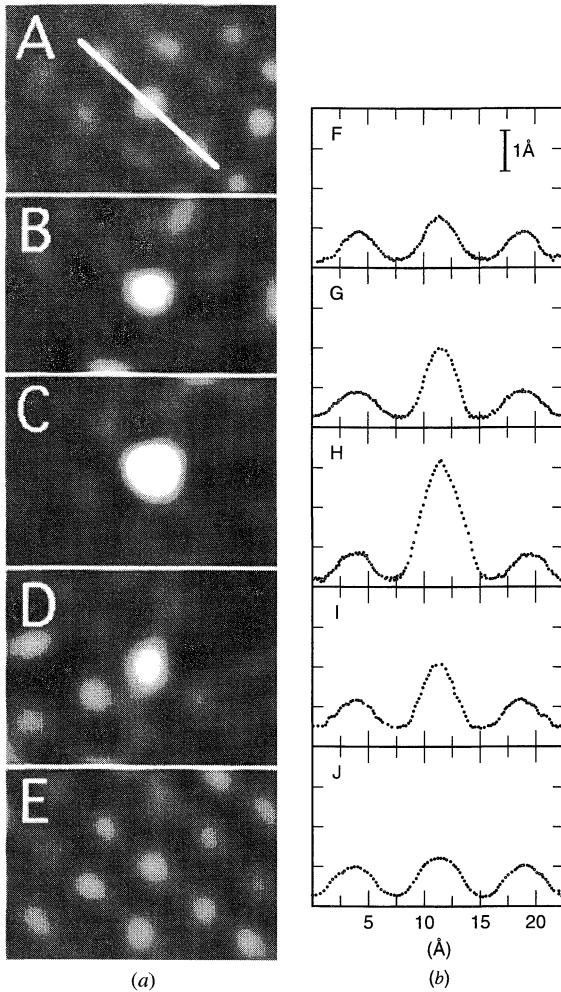
Figure 16.2.9 (*a*) STM images of FePP molecule embedded in an ordered array of PP molecules for different values of the HOPG substrate potential: (*A*) −0.15, (*B*) −0.30, (*C*) −0.42, (*D*) −0.55, and (*E*) −0.65 V *vs.* SCE, with other conditions as in Figure 16.2.8. (*b*) (*F–J*) are the corresponding cross-sections along the white line in (*A*) covering three molecules: PP/FePP/PP. The imaging was done at a constant current of 30 pA, and the response is shown as an apparent height. [Reprinted with permission from N. J. Tao, *Phys. Rev. Letters,* **76**, 4066 (1996). Copyright 1996, American Physical Society.]

FePP. The increase in current for FePP near E_p was ascribed to resonant tunneling through the molecules.

A variation of STM, called *scanning tunneling spectroscopy* (STS), can, in principle, also provide chemical information. In STS, the applied bias is modulated (e.g., 10 mV at 10 kHz) as it is slowly swept, keeping the tip position essentially constant while the variation in the tunneling current is measured. The quantity (di_{tun}/dV) (the *differential tunneling conductance*), or as it is usually plotted $(di_{tun}/dV)/(i_{tun}/V)$ is related to the density of states in the sample. This technique has not yet been applied widely for *in situ* electrochemical studies, because of difficulties with separating the desired effects from simple modulation of the faradaic component.

▶ 16.3 ATOMIC FORCE MICROSCOPY

16.3.1 Introduction and Principles

Although STM provides a high-resolution image of many surfaces, it has its limitations. It cannot be used with highly resistive substrates, because the observed current would be limited by the substrate resistance. For insulating materials on a conductive substrate, an STM image can sometimes be obtained, but the process by which such imaging occurs is

not fully understood. Moreover, in electrochemical studies, the potential applied to the tip can affect the process on the substrate immediately under the tip, which is essentially "touching" the substrate. For example, in electrodeposition studies, if the tip is held at a positive potential, it can prevent deposition of metal directly under tip as the substrate electrode is swept toward negative potentials, while deposition occurs at places remote from the tip. AFM can be useful in achieving high resolution in situations where STM suffers these limitations.

AFM is based on measurements of changing deflections of a tiny cantilever holding a sharp tip, frequently one of Si_3N_4 or SiO_2, as the tip is scanned over a surface. These deflections are caused by short-range forces between tip and surface. The measurement of these tiny movements is usually carried out by noting the position of a laser beam reflected off of the cantilever. A typical AFM arrangement is shown in Figure 16.3.1. The sample is held on the piezo scanner, which moves it in the z-direction (toward and away from the tip cantilever) as well as in the x- and y-directions. The cantilever, with an integral tip, is usually made of Si and is fabricated by photolithographic techniques. The laser beam is reflected to photocells by a metal coating on the top surface of the cantilever. Movement of the cantilever causes a change in the amount of light on each cell, creating a differential electrical signal which is recorded. Further details about the construction and operation of force microscopes, including others based on different measurement arrangements, are available (4, 10, 11).

Since the imaging process depends upon surface forces (12), it is useful to discuss these briefly. Consider a plot of cantilever deflection against z-piezo displacement (Figure 16.3.2). To begin, the tip is positioned 20 nm or more from the surface. When the tip and the surface are immersed in a solution, there is essentially no force between them at such long distances, so the cantilever is straight. The system is adjusted so that equal light falls on each photocell. As the z-piezo moves up, carrying the sample surface toward the tip, forces between tip and sample become appreciable. At distances on the order of 10 nm, the only forces between the tip and substrate are electrostatic, which can be either attractive or repulsive. Let us assume that the tip and surface have the same charge, so the force is repulsive. The upward movement of the sample and the repulsive force cause the can-
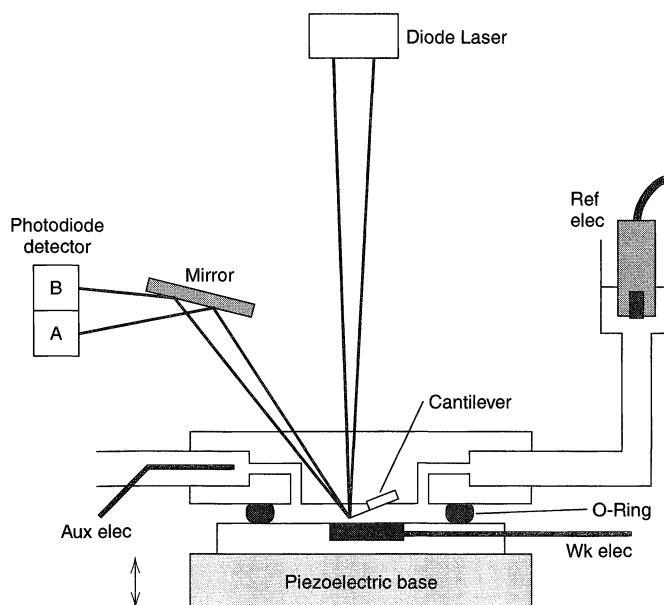
Figure 16.3.1
Electrochemical cell for AFM for Nanoscope III (Digital Instruments, Veeco Metrology Group).
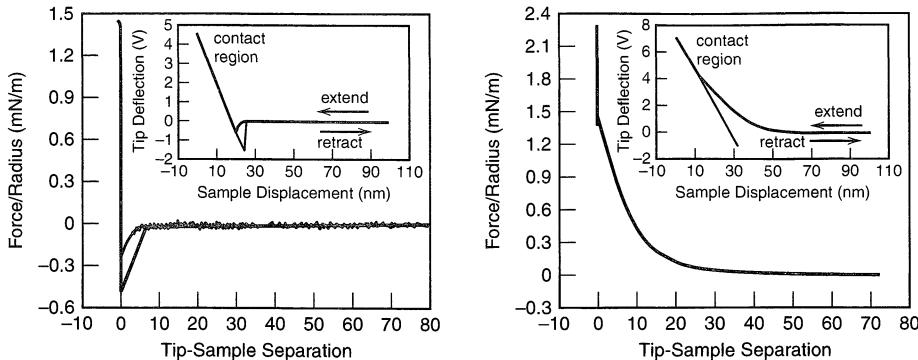
Figure 16.3.2 Cantilever displacement *vs.* z-deflection for (*left*) attractive interaction (opposite charge on tip and substrate) and (*right*) repulsive interaction (same charge on tip and substrate). The inset shows the raw data (cantilever deflection), which is converted to the force data based on the radius of the tip and the force constant of the cantilever. In this study, the tip is a SiO_2 sphere ~10 μm in diameter. [Reprinted with permission from A. Hillier, S. Kim, and A. J. Bard, *J. Phys. Chem.*, **100**, 18808 (1996). Copyright 1996, American Chemical Society].

tilever to deflect upward. From the amount of deflection and the known spring constant of the cantilever, typically of the order of 0.01 to 0.4 N/m, the repulsive force can be estimated. When the spacing between the tip and cantilever becomes very small, ~3 nm, attractive van der Waals forces come into play and the tip moves toward the substrate (i.e., the cantilever deflects downward). If the force becomes large compared to the spring constant of the cantilever times the deflection, the tip will "jump to contact" with the substrate. At "contact" the forces are repulsive, and as the z-piezo moves up, the cantilever moves up by essentially the same amount (assuming that the tip does not significantly deform the surface). This region allows one to calibrate cantilever deflection in terms of z-piezo travel.

Typically, imaging is carried out in the "contact mode" where the tip is as close as possible to the surface and the forces are repulsive. One maintains the beam deflection at a constant value by moving the z-piezo up and down and recording the piezo voltage as a function of x- and y-position. Other forms of imaging are also possible, and it is sometimes convenient, when adhesion of the tip to the surface is a problem, to use a tapping mode, where the tip position is modulated up and down during the scanning.

16.3.2 Electrochemical Applications

In electrochemistry, AFM has mainly been used to look at changes in electrode surfaces, caused, for example, by underpotential deposition (UPD), etching, or adsorption. An early example is a study of the UPD of Cu on Au(111) (13). AFM images of an Au(111) electrode immersed in either an $HClO_4$ or H_2SO_4 electrolyte containing 1 mM Cu^{2+} at different potentials are shown in Figure 16.3.3. At positive potentials (+0.7 V *vs.* Cu/1 mM Cu^{2+}), where no Cu is deposited, the Au(111) structure is observed (Figure 16.3.3A). At negative potentials (−0.1 V), bulk Cu is deposited (Figure 16.3.3B). At intermediate potentials, a UPD monolayer is seen. The structure of the monolayer depends upon the electrolyte. In perchlorate, one sees an incommensurate close-packed Cu overlayer (Figure 16.3.3C, D), and in sulfate the result is a ($\sqrt{3} \times \sqrt{3}$) R30° Cu overlayer (Figure 16.3.3E, F). AFM is able to resolve the atomic packing pattern on the different structures.
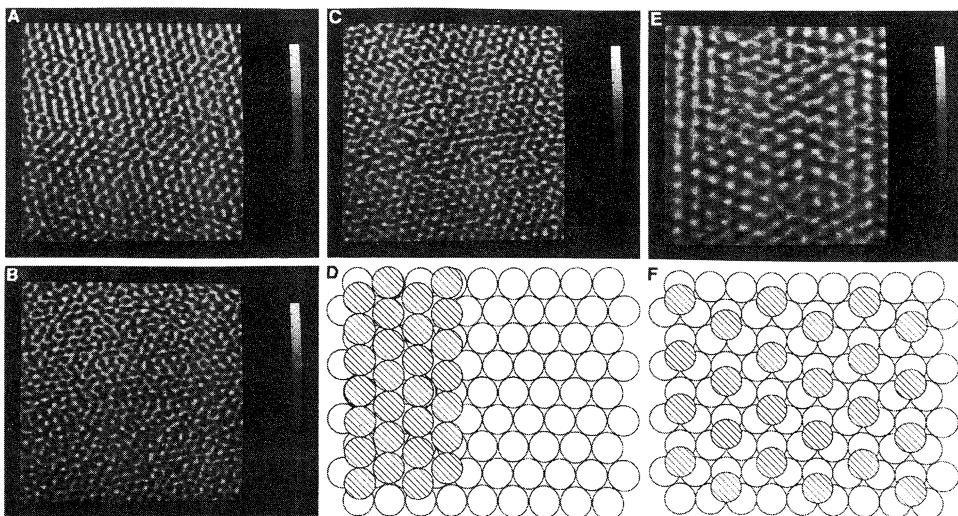
Figure 16.3.3 AFM study of Cu underpotential deposition (UPD) on an Au(111) electrode surface in 1 mM Cu^{2+} solution at different potentials. (A) At +0.7 V, showing Au(111) substrate; (B) At −0.1 V, Cu bulk deposition; (C) close packed overlayer of Cu at +0.114 V in 0.1 M HClO$_4$; (D) schematic representation of incommensurate close-packed overlayer of Cu (striped atoms) on Au substrate (light atoms); (E) ($\sqrt{3} \times \sqrt{3}$) R30° overlayer of Cu on Au observed at +0.144 V in 0.1 M sulfate solution; (F) schematic representation of Cu overlayer shown in (E). [Reprinted with permission from S. Manne, P. K. Hansma, J. Massie, V. B. Elings, and A. A. Gewirth, *Science*, **251**, 183 (1991). Copyright 1991, American Association for the Advancement of Science.]

The mechanism by which an atomic resolution image is obtained in AFM is still unclear. It is not likely that one can obtain an atomically sharp tip and image a single atom-against-atom force in the presence of the interactions from all of the other atoms in tip and substrate. More likely one is imaging the forces of one array of atoms on the tip against an array on the substrate, which generates a Moiré (interference) pattern that results in apparent atomic resolution. If so, it will be difficult to image single-atom defects, as one can by STM.

The AFM might also find use in quantitative measurements of surface forces, relating these to surface charge and other interactions (12). For example, a small silica sphere attached to the cantilever attains a charge by ionic adsorption. At pH values above 4, this surface charge is negative because of adsorption of hydroxide ions. Thus the force between the tip and an electrode, as the tip is moved through the diffuse double layer, is a measure of the surface charge on the electrode (14).

Cantilever deflections are also caused by small changes in temperature, because the usual fabrication produces a bimetallic strip configuration. Thus the AFM arrangement could be used to measure tiny thermal changes that arise in electrochemical cells. Applications of this type are just emerging.

▷ 16.4 SCANNING ELECTROCHEMICAL MICROSCOPY

16.4.1 Introduction and Principles

SECM is an electrochemical scanning probe technique where the measured current is caused by an electrochemical reaction at the tip (15). The overall apparatus for SECM is similar to that used for ESTM, that is, a bipotentiostat is used to control the tip potential

(and frequently also that of the substrate), and the tip is moved by piezo controllers. However the principles of operation and the type of information obtained by SECM differ from those of ESTM (16–18). For electrodes with radii of 1 to 25 μm, the tip is usually a small disk of Pt or C sealed in glass and polished to form a disk UME. The glass surrounding the disk is usually beveled so that the thickness of insulator surrounding the conductive disk is small. This makes it easier to position the tip so that it can be moved very close to the substrate without the insulator touching the surface. Smaller electrodes usually have a less well-defined geometry and are similar to STM tips produced by etching a wire to a sharp point and then insulating with wax or other coating. In the SECM experiment, the tip and sample (substrate) are immersed in a solution containing electrolyte, and an electroactive species (e.g., substance O at concentration C_O^* and with diffusion coefficient D_O). The cell also contains auxiliary and reference electrodes (Figure 16.4.1). When the tip is far from the substrate and a potential is applied, the steady-state current, $i_{T,\infty}$, is (see Section 5.3)

$$i_{T,\infty} = 4nFD_OC_O^*a \tag{16.4.1}$$

where a is the radius of the tip electrode (Figure 16.4.2a). When the tip is brought very near the substrate surface (within a few tip radii), the current is perturbed by two effects. First, the surface blocks diffusion of O to the tip, tending to decrease the current (Figure 16.4.2b). However, if the surface can regenerate species O, for example, because it is an electrode that can oxidize the product of the tip reaction, R, back to O, the result is a larger flux of O to the tip, which causes the current to increase (Figure 16.4.2c). Thus, the current at the tip is a function of its distance, d, from the substrate and also the rates of reactions that occur at the substrate to generate species that are electroactive at the tip. This form of operation of the SECM is called the *feedback mode*. It is also possible to work in the *collection mode*, where the tip is held close to the substrate at a potential where electroactive products produced at the substrate are detected by the tip.

16.4.2 Approach Curves

A plot of the tip current, i_T, as a function of tip-substrate separation, d, as the tip is moved from a distance several tip diameters away towards the substrate is called an *approach curve*. As suggested in the previous section, this curve provides information about the nature of the substrate. Approach curves for a disk-shaped tip in a thin insulating planar
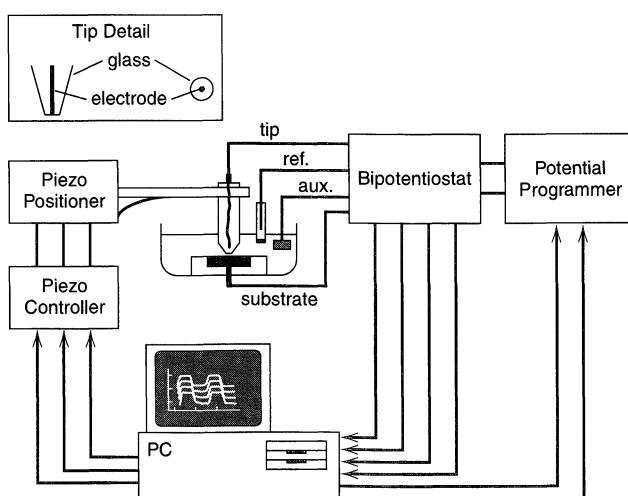
Figure 16.4.1 Schematic diagram of SECM apparatus. [Reprinted with permission from A. J. Bard, G. Denuault, C. Lee, D. Mandler, and D. O. Wipf, *Accts. Chem. Res.*, **23**, 357 (1990). Copyright 1990, American Chemical Society.]
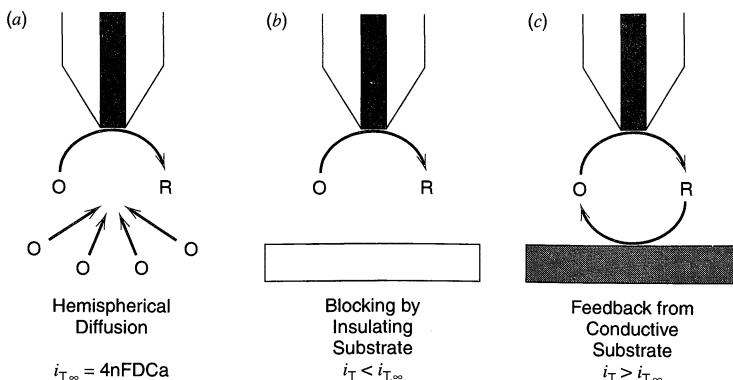
Figure 16.4.2 Principles of SECM, showing (*a*) hemispherical diffusion to the disk-shaped tip far from substrate, (*b*) blocking of diffusion by insulating substrate, (*c*) positive feedback at a conductive substrate.

sheath can be calculated by digital simulation methods, which yield the results shown in Figure 16.4.3 for a perfectly insulating substrate (no reaction of tip-generated species, R) and for an active substrate (where oxidation of R back to O occurs at a diffusion-controlled rate). These curves are presented in the dimensionless form of $i_T/i_{T,\infty}$ vs. d/a (where $I_T(L) = i_T/i_{T,\infty}$ and $L = d/a$) and are independent of disk diameter, diffusion coefficient, and solute concentration. The following approximate forms for the numerical results have been proposed for an insulating substrate:

$$I_T(L) = [0.292 + 1.5151/L + 0.6553 \exp(-2.4035/L)] \qquad (16.4.2)$$

and for a conductive substrate:

$$I_T(L) = 0.68 + 0.78377/L + 0.3315 \exp(-1.0672/L) \qquad (16.4.3)$$
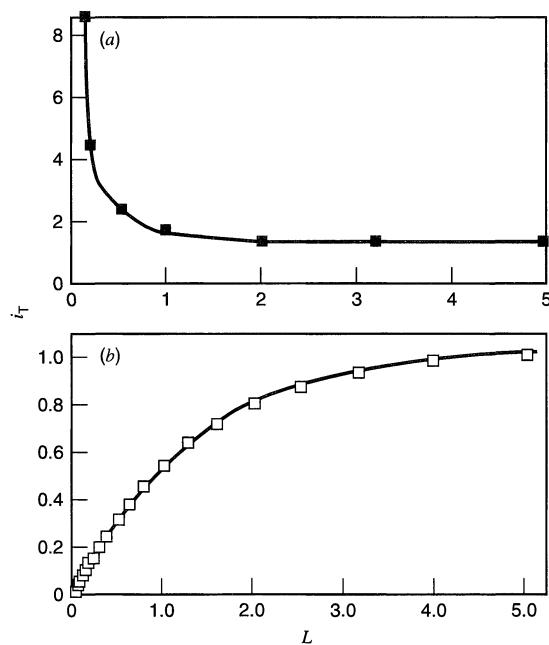
Figure 16.4.3 SECM approach curves for steady-state currents at (*a*) a conductive substrate and (*b*) an insulating substrate. I_T (normalized tip current) = $i_T/i_{T,\infty}$; L (normalized distance) = d/a. [From M. Arca, A. J. Bard, B. R. Horrocks, T. C. Richards, and D. A. Treichel, *Analyst*, **119**, 719 (1994), with permission.]

In both cases, the substrate is assumed to be much larger than the tip radius, a. The approach curves are also functions of the tip shape and can therefore provide information about tip geometry. Thus spherical or conical tips show different approach curves than disk-shaped ones. The approach curve over a conductor can also indicate when the conductive part of the tip is recessed inside the insulating sheath, which often happens with very small tips. In this case, only a small amount of positive feedback is observed before the insulating portion contacts the substrate and the i_T-value levels off. Since characterization of small tips, such as by electron microscopy, is difficult, SECM is a useful way of learning about the tip size and configuration (19).

In addition to the limiting cases described above (i.e., either no conversion or total conversion of R to O at a conductive substrate), one can calculate approach curves for different heterogeneous rate constants for conversion of R to O at the substrate (20, 21). The resulting curves, shown in Figure 16.4.4, represent the combined effects of blocking and regeneration of O, and lie between the limiting case curves of Figure 16.4.3. The rate of heterogeneous electron transfer can also be probed by recording the voltammogram, i_T vs. E, or in dimensionless form, $I_T(E, L)$ vs. θ, where $\theta = 1 + \exp[nf(E - E^{0'})]D_O/D_R$. Kinetic limitations on heterogeneous electron transfer cause the shape of the voltammogram to deviate from the reversible shape as the tip is moved closer to a conductive substrate held at a potential where oxidation of R is diffusion-controlled. An approximate equation for the voltammogram is (16):

$$I_T(E,L) = \frac{0.68 + 0.78377/L + 0.3315 \exp(-1.0672/L)}{\theta + 1/\kappa} \tag{16.4.4}$$

where

$$\kappa = \frac{k^0 \exp[-\alpha f(E - E^{0'})]}{m_O}$$

$$m_O = \frac{4D_O}{\pi a}[0.68 + 78377/L + 0.3315 \exp(-1.0672/L)] = \frac{i_T(L)}{\pi a^2 nFC_O^*}$$
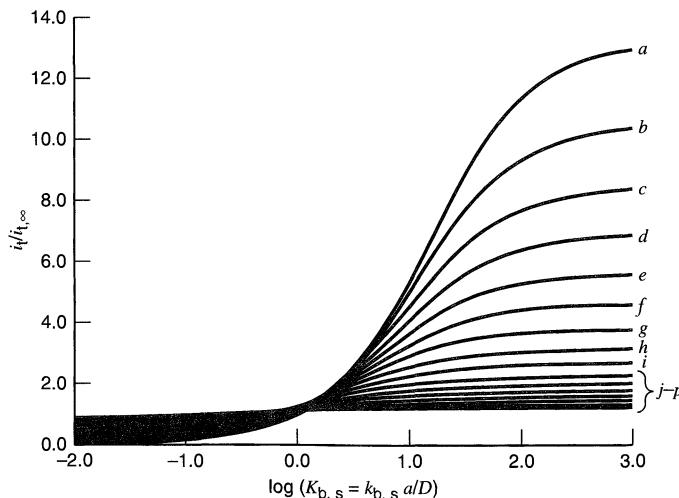
Figure 16.4.4 SECM approach curves for different values of the heterogeneous rate constant, $k_{b,s}$, for the conversion of R to O at the substrate electrode. Curves a–p correspond to $\log(d/a) = -1.2, -1.1, -1.0, \ldots, 0.3$. [Reprinted with permission from A. J. Bard, M. V. Mirkin, P. R. Unwin, and D. O. Wipf, *J. Phys. Chem.*, **96**, 1861 (1992). Copyright 1992, American Chemical Society.]

Thus the SECM is useful in probing heterogeneous kinetics at electrode surfaces, as well as other surfaces, like enzyme-containing membranes. The largest values of k^0 that can be measured are of the order of D/d. Obviously this limit depends experimentally upon d, which is the "characteristic length" in SECM. Analogous measurements at a UME in bulk solution are similarly limited and provide a maximum k^0 on the order of D/a. For example, the k^0 for the ferrocene/ferricenium couple in MeCN, often used as a reference redox couple, as measured by SECM was 3.7 cm/s (22).

16.4.3 Imaging Surface Topography and Reactivity

If the tip is scanned in the x-y plane (*rastered*) above the substrate, the surface topography can be imaged by recording the changing current (related to changes in d) *vs.* tip position in the x-y plane. With a substrate that has both conductive and insulating regions, the current response at a given d differs over the different regions. Over a conductor, $i_T > i_{T,\infty}$, while over the insulating portions, $i_T < i_{T,\infty}$. One can also differentiate between these regions by modulating the tip in the z-direction with a sinusoidal voltage applied to the z-piezo and noting the phase of the modulated tip current with respect to the modulated distance (23). Over a conductive zone, as the tip approaches the sample, the current increases, while over an insulating zone the current decreases. Thus, if one measures the modulated current, such as with a lock-in amplifier, the current over a conductor and that over an insulator are 180° out-of-phase.

The SECM can also be used to map zones of gradually varying reactivity on an electrode surface. For a reactant, R, generated at a tip as it is scanned over the substrate surface at constant d, the feedback current is a measure of the rate at which R is oxidized on different parts of the substrate (20). For example, this technique was employed to study the rate of oxidation of Fe^{2+} on a glassy carbon electrode that had gold deposited on small areas. Since the heterogeneous rate constant for Fe^{2+} oxidation on gold is higher than on carbon, the feedback current at intermediate potentials is larger when the tip is over gold than when it is over carbon; thus a map of electrode activity can be obtained. At more positive potentials, the rate of Fe^{2+} oxidation is diffusion-controlled on both gold and carbon, so the image shows a uniform reaction rate across the electrode surface.

16.4.4 Measurement of Homogeneous Reaction Kinetics

The SECM can be used in several different modes to study homogeneous reactions of products generated at either the tip or the substrate (24, 25). Such studies are analogous to other dual-electrode experiments, like those at an RRDE (Section 9.4) or at interdigitated band microelectrodes (Section 5.9.3). In feedback experiments, the effect of the coupled reaction on the tip current is studied, while in collection experiments one electrode, such as the tip, behaves as the generator electrode, producing the product of interest (R) and the other, such as the substrate electrode, is the collector, set at a potential where R is oxidized back to O. Such a mode is called the *tip generation/substrate collection* (or TG/SC) *mode*. When species R is stable and the tip is close to the substrate ($a/d < 2$), essentially all of the R is collected (i.e., oxidized) by the substrate. Under these conditions the magnitude of the steady-state anodic substrate current, i_S, is equal to the tip current, i_T, or $|i_T/i_S|$ (the *collection efficiency*) is 1. Contrast this behavior with that at the RRDE, where even with close spacing between disk and ring and with a large ring, the collection efficiency is usually much smaller, because some disk-generated product always diffuses away before being collected by the ring.

Now suppose the tip-generated species is not stable and decomposes to an electroinactive species, such as in the E_rC_i case (Chapter 12). If R reacts appreciably before it diffuses across the tip/substrate gap, the collection efficiency will be smaller than unity, approaching zero for a very rapidly decomposing R. Thus a determination of $|i_T/i_S|$ as a function of d and concentration of O can be used to study the kinetics of decomposition of R. In a similar way, this decomposition decreases the amount of positive feedback of O to the tip, so that i_T is smaller than in the absence of any kinetic complication. Accordingly, a plot of i_T vs. d can also be used to determine the rate constant for R decomposition, k. For both the collection and feedback experiments, k is determined from working curves in the form of dimensionless current vs. distance (e.g., $i_T/i_{T,\infty}$ vs. d/a) for different values of the dimensionless kinetic parameter, $K = ka^2/D$ (first-order reaction) or $K' = k'a^2C_O^*/D$ (second-order reaction).

To illustrate this technique, consider the dimerization of the acrylonitrile anion radical (AN⁻) in DMF (26). The electroreductive hydrodimerization of AN is used commercially to produce adiponitrile [$(ANH)_2$], a precursor in Nylon production. The proposed reaction mechanism, an E_rC_2 reaction [Section 12.1.1(b)], is

$$AN + e \rightarrow AN^{\bar{\cdot}} \tag{16.4.5}$$

$$2\ AN^{\bar{\cdot}} \rightarrow (AN)_2^{2-} \tag{16.4.6}$$

$$(AN)_2^{2-} + 2\ H^+ \rightarrow (ANH)_2 \tag{16.4.7}$$

The voltammogram for the reduction of AN in a DMF/0.1 M TBAPF$_6$ solution at a tip (radius, 2.5 μm) shows a reduction wave at -2.0 V vs. a QRE (Figure 16.4.5). The tip-generated species, AN⁻, is so unstable that in most experiments, such as fast scan cyclic voltammetry, one does not observe its oxidation in a reversal experiment. However
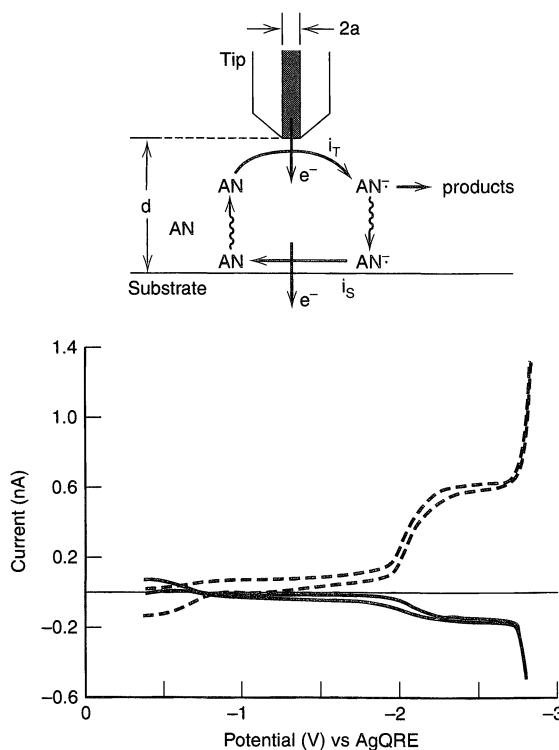
Figure 16.4.5 SECM TG/SC voltammograms. The tip ($a = 2.5$ μm) was spaced 1.36 μm from a 60-μm diameter gold electrode held at a potential of -1.75 V vs. a silver QRE (AgQRE). The tip potential was scanned at 100 mV/s to produce a voltammogram (dashed line) for the reduction of acrylonitrile (1.5 mM) in 0.1 M TBAPF$_6$. The substrate current (solid line) shows the oxidation of the radical anion of acrylonitrile generated at the tip. [Reprinted with permission from F. Zhou and A. J. Bard, *J. Am. Chem. Soc.*, **116**, 393 (1994). Copyright 1994, American Chemical Society.]

when the tip is close (1.36 μm) to a 60-μm diameter gold substrate, held at a potential of -1.75 V *vs.* QRE, where AN$^{\cdot}$ is oxidized, one sees a wave for the oxidation of the radical anion as the tip is scanned through the reduction wave. By studying the dependence of the collection efficiency on d, the rate constant of reaction (16.4.6) was found to be 6×10^7 M^{-1}s^{-1}.

It is also possible to carry out *substrate generation/tip collection* (SG/TC) *experiments*, where the tip probes the products of a reaction at the substrate. However this approach to studies of homogeneous kinetics is less straightforward, since the larger substrate electrode does not attain a steady-state condition and the collection efficiency for this case, i_T/i_S, is much less than unity, even in the absence of a homogeneous kinetic complication. This mode has been used, however, for looking at concentration profiles above a substrate (27).

16.4.5 Potentiometric Tips

The tips discussed so far have been amperometric probes, typically of Pt–Ir, that produce faradaic currents reflecting redox processes at an exposed surface. However, it is also possible to use potentiometric tips, such as ion selective electrodes based on micropipets, in an SECM (28, 29). These produce potentials (with respect to a reference electrode) that depend logarithmically on the solution activity of a specific ion. Tips of this type that can detect H$^+$, Zn^{2+}, NH$_4^+$, and K$^+$ with a resolution of a few μm have been described. Tips of this type are especially useful for detection of nonelectroactive ions, like many of those of interest in biological systems. However, such tips are passive probes, in that they detect the local activity of a given species but do not sense the presence of the substrate. They cannot be used to determine d, so they must be positioned with respect to a substrate, such as, in studying a concentration gradient at an electrode, by visual observation with a microscope, by resistance measurements, or by using a double-barrel tip that contains both an amperometric element and a potentiometric one.

16.4.6 Other Applications

SECM can also be used to study the flux of species produced at a modified electrode surface, such as one with a film of polymer (Section 14.2.3). In one type of experiment, the tip is held at a potential where it can detect an electroactive ion released from the polymer film during a redox process (30–32). For example the SECM was used to detect the release of Br$^-$ during the reduction of oxidized polypyrrole (PP) in the form, PP$^+$Br$^-$. During a reductive cyclic voltammetric scan, Br$^-$ was found to be released only in a later part of the scan, after an appreciable amount of cathodic charge had passed. This result suggested that during the early phase of the reduction the uptake of cations, rather than the release of anions, maintained charge balance in the film.

By positioning the tip close to the surface, SECM can be used to measure the flux of ions through the pores of a membrane (e.g., skin) driven by an electric current (*iontophoresis*) (33). Similarly the rate of electron and ion transfer across the liquid/liquid interface (ITIES) can be studied (34).

An emerging field in electrochemistry is the study of a single molecule or a small number of molecules (35). Since the currents or charges of single electron-transfer events cannot be detected at an electrode, some amplification process is required. The reported studies involved a tip with a radius of the order of 10 nm, coated with a thin layer of insulator (wax or polyethylene) and having a very small depression (chamber) at the end of

the tip in which a molecule can be trapped. When the tip is very close (~10 nm) to a conductive substrate, the tip-generated species diffuses to the substrate where it is converted back to the starting material. At this distance the cycling of a species between tip and substrate is sufficient to generate pA-level currents (see Problem 16.1). One can distinguish the trapping of 0, 1, or 2 molecules as they move into and out of the tip/substrate gap by the discrete current levels observed.

SECM can be particularly useful in imaging electrode surfaces and probing films on surfaces. For example, the nature of the pores in a blocking film of Ta_2O_5 on a Ta electrode was studied as a function of potential by mapping the locations where iodide could be oxidized on the substrate (with detection of iodine at the tip) (Figure 16.4.6) (36). Active sites clearly form and disappear as the oxidation of the Ta surface proceeds.

An example of probing a film in the z-direction is the study of a Nafion film containing $Os(bpy)_3^{2+}$ (37). The tip current for the oxidation of $Os(bpy)_3^{2+}$ was measured as a conical tip moved from the solution phase into the film as shown in Figure 16.4.7. The point where the tip just enters the film is signaled by the onset of current flow. The current increases until the conical section is completely in the film where a steady-state plateau current is recorded. When the tip approaches the ITO substrate, positive feedback and, finally, tunneling occurs. These measurements allowed determination of the film thickness as 220 nm and estimation of electrochemical parameters within the film. For example, by obtaining a voltammogram when the tip was inside the film (position C), it was possible to estimate the heterogeneous electron-transfer rate constant for $Os(bpy)_3^{2+}$ oxidation as 1.6×10^{-4} cm/s (37).
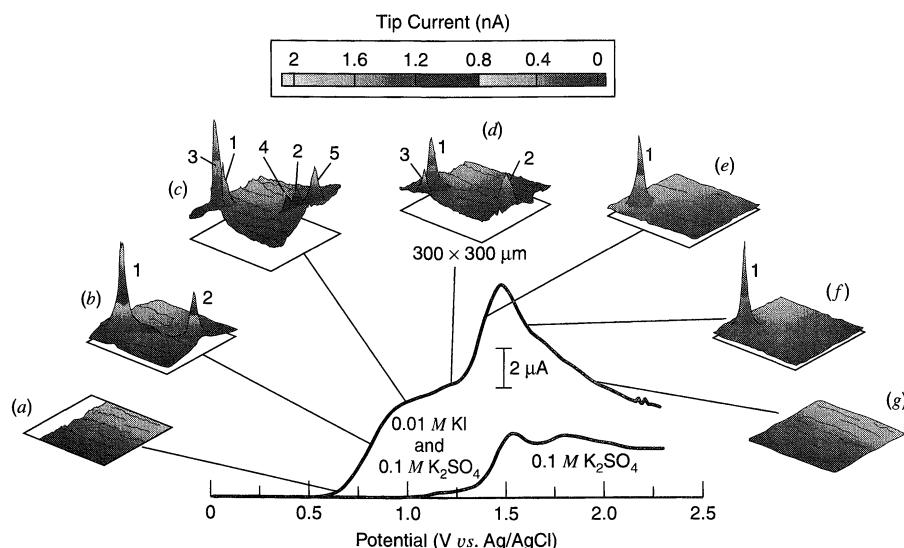
Figure 16.4.6 Image of a 300 μm $\times$ 300 μm area of a Ta electrode with a Ta_2O_5 film in a solution of 10 mM NaI and 0.1 M K_2SO_4 as the Ta potential is scanned to more positive values. The tip potential was 0.0 V $vs.$ Ag/AgCl, where any iodine formed on the substrate would be reduced. The voltammetry for the substrate in the absence of iodide is also shown. [Reprinted with permission from S. B. Basame and H. S. White, *Anal. Chem.*, **71**, 3166 (1999). Copyright 1999, American Chemical Society.]
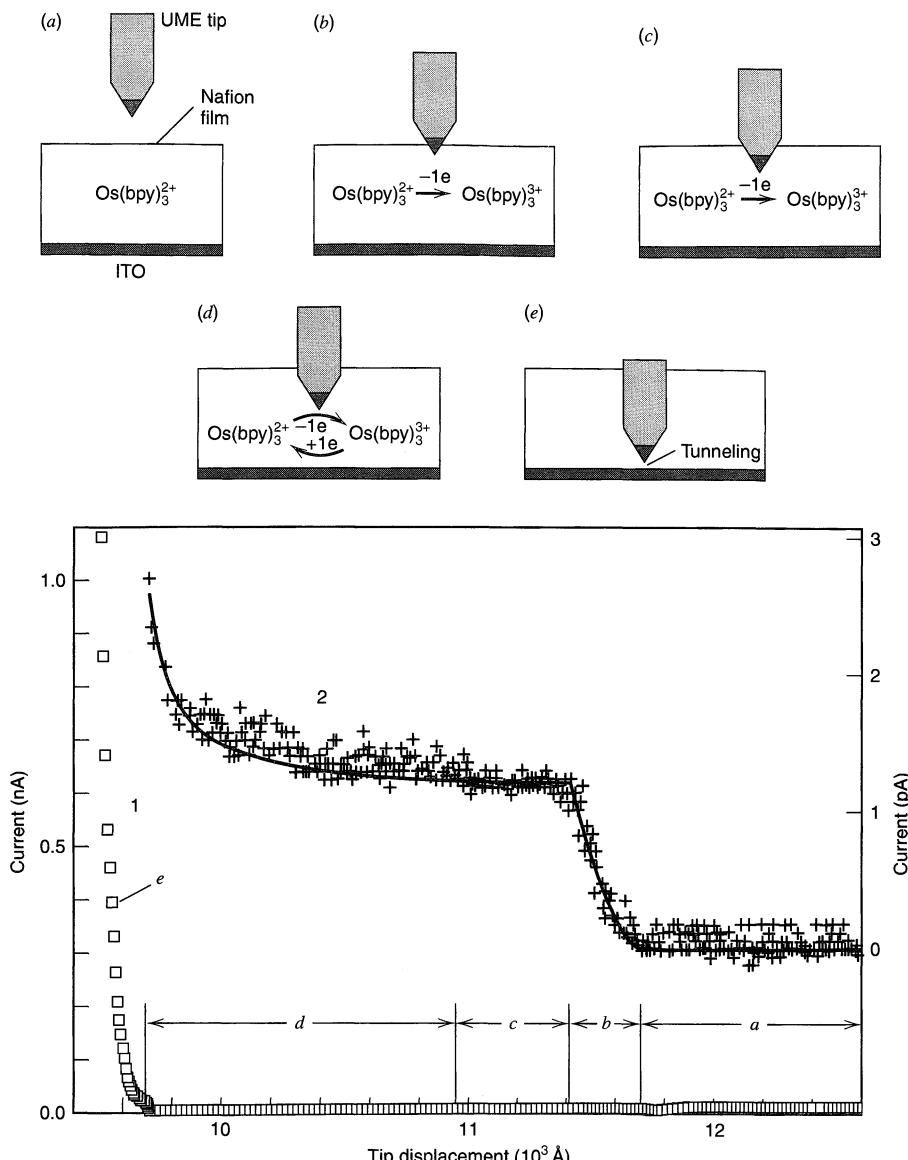
Figure 16.4.7 *Top.* Schematic representation of the five stages of the SECM current-distance experiment as a tip penetrates from solution into a Nafion film containing $Os(bpy)_3^{2+}$: (*a*) Tip in solution above film. (*b*) Tip just penetrates the film. (*c*) Conical electroactive portion of tip completely in film. (*d*) Tip near substrate where positive feedback occurs. (*e*) Tip in the tunneling region. *Bottom.* The tip current *vs.* displacement (at two different sensitivities) during the experiment, where the letters *a–e* correspond to the stages in the top part of the figure. The tip was held at 0.80 V *vs.* SCE and the ITO substrate at 0.20 V *vs.* SCE. The tip moved in the *z*-direction at 3 nm/s. [Reprinted with permission from M. V. Mirkin, F.-R. F. Fan, and A. J. Bard, *Science*, **257**, 364 (1992). Copyright 1992, American Association for the Advancement of Science.]

▷ 16.5 REFERENCES

1. G. Binnig and H. Rohrer, *Helv. Phys. Acta*, **55**, 726 (1982).

2. D. A. Bonnell, Ed., "Scanning Tunneling Microscopy and Spectroscopy—Theory, Techniques and Applications," VCH, New York, 1993.

3. C. J. Chan, "Introduction to Scanning Tunneling Microscopy," Oxford University Press, New York, 1993.

4. H. K. Wickramasinghe, Ed., "Scanned Probe Microscopy," AIP Conf. Proc. 241, American Institute Physics, New York, 1992.

5. A. J. Bard and F.-R. F. Fan, in D. A. Bonnell, Ed., *op.cit.*, Chap. 9.

6. S.-L. Yau, C. M. Vitus, and B. C. Schardt, *J. Am. Chem. Soc.*, **112**, 3677 (1990).

7. D. W. Suggs and A. J. Bard, *J. Am. Chem. Soc.*, **116**, 10725 (1994).

8. R. I. Masel, "Principles of Adsorption and Reaction on Solid Surfaces," Wiley, New York, 1996, pp. 33–36.

9. N. J. Tao, *Phys. Rev. Lett.*, **76**, 4066 (1996).

10. D. Sarid, "Scanning Force Microscopy," Oxford University Press, New York, 1994.

11. N. J. DiNardo, "Nanoscale Characterization of Surfaces and Interfaces," VCH, New York, 1994.

12. J. Israelachvili, "Intermolecular and Surface Forces," Academic, New York, 1992.

13. S. Manne, P. K. Hansma, J. Massie, V. B. Elings, and A. A. Gewirth, *Science*, **251**, 183 (1991).

14. (a) W. A. Ducker, T. J. Sneden, and R. M. Pashley, *Langmuir*, **8**, 1831 (1992); (b) A. C. Hillier, S. Kim, and A. J. Bard, *J. Phys. Chem.*, **100**, 18808 (1996).

15. A. J. Bard, F.-R. F. Fan, J. Kwak, and O. Lev, *Anal. Chem.*, **61**, 132 (1989).

16. A. J. Bard, F.-R. F. Fan, and M. V. Mirkin, *Electroanal. Chem.*, **18**, 243 (1994).

17. M. V. Mirkin, *Anal. Chem.*, **68**, 177A (1996).

18. A. J. Bard, F.-R. F. Fan, and M. V. Mirkin in "Physical Electrochemistry: Principles, Methods and Applications," I. Rubinstein, Ed., Marcel Dekker, NY, 1995, p. 209.

19. M. V. Mirkin, F.-R. F. Fan, and A. J. Bard, *J. Electroanal. Chem.*, **328**, 47 (1992).

20. D. O. Wipf and A. J. Bard, *J. Electrochem. Soc.*, **138**, 469 (1991).

21. A. J. Bard, M. V. Mirkin, P. R. Unwin, and D. O. Wipf, *J. Phys. Chem.*, **96**, 1861 (1992).

22. M. V. Mirkin, T. C. Richards, and A. J. Bard, *J. Phys. Chem.*, **97**, 7672 (1993).

23. D. O. Wipf and A. J. Bard, *Anal. Chem.*, **64**, 1362 (1992).

24. P. R. Unwin and A. J. Bard, *J. Phys. Chem.*, **95**, 7814 (1991).

25. F. Zhou, P. R. Unwin, and A. J. Bard, *J. Phys. Chem.*, **96**, 4917 (1992).

26. F. Zhou and A. J. Bard, *J. Am. Chem. Soc.*, **116**, 393 (1994).

27. R. C. Engstrom, T. Meany, R. Tople, and R. M. Wightman, *Anal. Chem.*, **59**, 2005 (1987).

28. B. R. Horrocks, M. V. Mirkin, D. T. Pierce, A. J. Bard, G. Nagy, and K. Toth, *Anal. Chem.*, **65**, 1213 (1993).

29. C. Wei, A. J. Bard, G. Nagy, and K. Toth, *Anal. Chem.*, **67**, 34 (1995).

30. M. Arca, M. V. Mirkin, and A. J. Bard, *J. Phys. Chem.*, **99**, 5040 (1995).

31. J. Kwak and F. C. Anson, *Anal. Chem.*, **64**, 250 (1992).

32. C. Lee and F. C. Anson, *Anal. Chem.*, **64**, 528 (1992).

33. E. R. Scott, H. S. White, and J. B. Phillips, *J. Membr. Sci.*, **58**, 71 (1991).

34. (a) C. Wei, A. J. Bard, and M. V. Mirkin, *J. Phys. Chem.*, **99**, 16033 (1995); (b) M. Tsionsky, A. J. Bard, and M. V. Mirkin, *J. Am. Chem. Soc.*, **119**, 10785 (1997).

35. F.-R. F. Fan and A. J. Bard, *Science*, **267**, 871 (1995).

36. S. B. Basame and H. S. White, *Anal. Chem.*, **71**, 3166 (1999).

37. M. V. Mirkin, F.-R. F. Fan, and A. J. Bard, *Science*, **257**, 364 (1992).

▷ 16.6 PROBLEMS

16.1 Assume that one molecule of a species A, reversibly oxidizable to A^+, is trapped between an SECM tip and a substrate located 10 nm from the tip. Assume also that $D_A = D_{A^+} = 5 \times 10^{-6}$ cm^2/s. (a) Use the diffusion layer approximation to find about how long it takes for A to diffuse between the

tip and the substrate. (b) About how many round-trip excursions of A would occur in 1 s? (c) If A is oxidized to A^+ at the tip and A^+ is reduced to A at the substrate, what current will result?

16.2 SECM is carried out with a disk-shaped tip of 10-μm diameter embedded in a glass insulating sheath over a Pt electrode. An experiment was carried out with a solution of species O having $C_O^* = 5.0$ mM and $D_O = 5.0 \times 10^{-6}$ cm^2/s. When the tip, at a potential where O is reduced to R at a diffusion-controlled rate, was held near the Pt surface, with the Pt electrode at a potential where R is totally oxidized to O, the ratio $i_T/i_{T,\infty}$ was 2.5. (a) At what distance, d, was the tip from the surface? (b) What is $i_{T,\infty}$? (c) If this tip is held over a glass substrate at the same d value, what would $i_T/i_{T,\infty}$ be?

16.3 Use a spreadsheet program to calculate tip voltammograms for the SECM at several different values of k^0 for $L = 0.1$, $a = 10$ μm, $D_O = D_R = 10^{-5}$ cm^2/s, $\alpha = 0.5$, and $T = 25°$C. What values of k^0 could be determined from experimental results under these conditions? How could the conditions be changed so that larger k^0 values could be measured?

16.4 SECM is used to study an E_rC_i reaction (O + $e \rightleftarrows$ R; R $\rightarrow$ Z). A 10-μm tip is used to reduce O while being positioned over a Pt electrode where R is oxidized back to O at a diffusion-controlled rate. When the tip is 0.2 μm from the surface, the approach curve shows the same feedback current as for a mediator where the product is stable. However, when the tip is 4.0 μm away, the response is close to that for an insulating substrate. Estimate the rate constant for the decomposition of R to Z. If this reaction were studied by cyclic voltammetry, approximately what scan rates would be needed to find a nernstian response? What are the advantages of SECM in studying this kind of reaction compared to CV?

16.5 Consider the same system as in Problem 16.2. Assume the tip is biased about 0.5 V with respect to the Pt substrate. At about what distance, d, will the current attributable to direct tunneling become larger than the SECM feedback current? Do you think that a tip like that described in Problem 16.2 could attain such a d value? Why?

17

SPECTROELECTROCHEMISTRY AND OTHER COUPLED CHARACTERIZATION METHODS

Recent years have seen high continued interest in studying electrode processes by experiments that involve more than the usual electrochemical variables of current, charge, and potential. Much of the motivation for this work has been to provide means for obtaining information about electrochemical systems that could not be gathered in purely electrochemical experiments. In this chapter, we will examine some of the more important approaches involving the coupling of nonelectrochemical techniques, such as various forms of spectroscopy, with an electrochemical system. Techniques are usually classified as *in situ* or *ex situ*. *In situ techniques* involve examination of the electrode surface while it is immersed in solvent in the electrochemical cell, often under potential control and during the passage of current. In *ex situ techniques* the electrode is removed from the electrochemical cell and examined, often in air or high vacuum. While *ex situ* techniques allow many types of measurements that are not possible in solution, such as the forms of surface spectroscopy discussed in Section 17.3, the nature of the electrode surface can change significantly upon removal from the cell environment. In this chapter, except in Section 17.3, we concentrate on *in situ* techniques. With such a great variety of material involved here, we cannot delve into any topic with much depth. Instead, we will simply review the basic principles, consider some typical experimental arrangements, and outline the types of chemical information that can be obtained in each case. More extensive reviews are available (1–5).

17.1 ULTRAVIOLET AND VISIBLE SPECTROSCOPY

17.1.1 Transmission Experiments

Perhaps the simplest spectroelectrochemical experiment is to direct a light beam through the electrode surface, as shown in Figure 17.1.1, and to measure absorbance changes resulting from species produced or consumed in the electrode process. Figure 17.1.2 is an illustration of two types of cells in which such experiments could be carried out.

The obvious prerequisite is an *optically transparent electrode* (OTE). Several types of OTEs have been reported (6–13). They may be thin films of a semiconductor (e.g., SnO_2 or
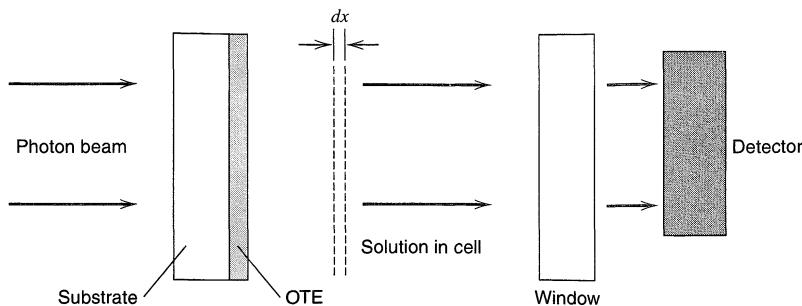
Figure 17.1.1   Schematic view of the experimental arrangement for transmission spectroelectrochemistry.

In$_2$O$_3$) or a metal (e.g., Au or Pt) deposited on a glass, quartz, or plastic substrate; or they may be fine wire mesh "minigrids" with perhaps several hundred wires per centimeter. The films are quite planar, uniform electrode surfaces, but the minigrids are not planar and have a structure involving alternating regions of opaque bulk metal and transparent openings. On the other hand, the minigrids behave like planar electrodes if the electrochemical experiment has a characteristic time long enough to allow the diffusion layer thickness to become much larger than the size of these openings. Then the diffusion field feeding the electrode is one-dimensional and has a cross-sectional area equal to the projected area of the whole electrode, including the spaces (14, 15). (See also Section 5.2.3.)

Transmission experiments may involve the study of absorbance *vs.* time as the electrode potential is stepped or scanned, or they may involve wavelength scans to provide spectra of electrogenerated species. Either of these experimental goals can be attained with cells fitting into conventional spectrophotometers; but if one wishes to follow spec-
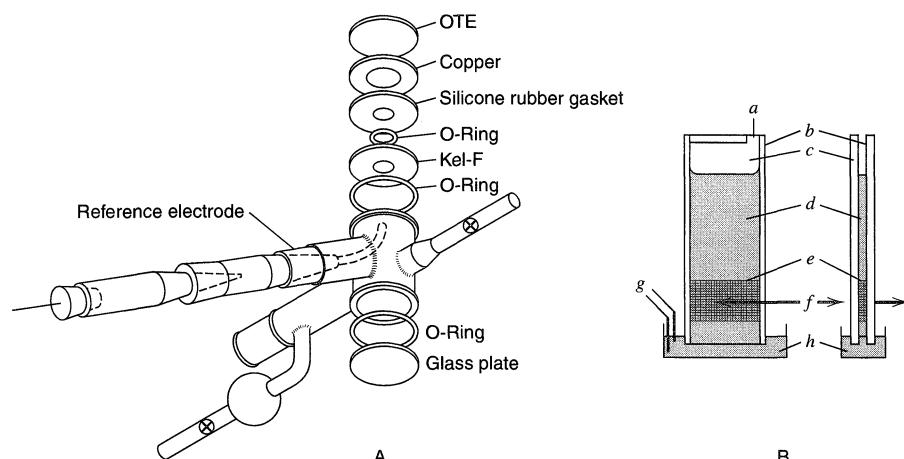
Figure 17.1.2   *A*: Cell for transmission spectroelectrochemistry involving semi-infinite linear diffusion. Light beam passes along vertical axis. [Reprinted from N. Winograd and T. Kuwana, *Electroanal. Chem.*, **7**, 1 (1974), by courtesy of Marcel Dekker, Inc.] *B*: Optically transparent thin-layer system: front and side views. (*a*) Point of suction application in changing solutions; (*b*) Teflon tape spacers; (*c*) 1 × 3 in. microscope slides; (*d*) test solution; (*e*) gold minigrid, 1 cm high; (*f*) optical beam axis; (*g*) reference and auxiliary electrodes; (*h*) cup containing test solution. [Reprinted with permission from W. R. Heineman, B. J. Norris, and J. F. Goelz, *Anal. Chem.*, **47**, 79 (1975). Copyright 1975, American Chemical Society.] A thin-layer cell that can be sealed and is useful for organic solvents has been described (16).

tral evolution over comparatively short time scales, then a rapid scanning system is needed. Apparatus permitting the acquisition of as many as 1000 spectra per second has been utilized (6, 9). With such a capability for high repetition rates, signal averaging is a practical means for improving spectral quality.

The cell in Figure 17.1.2*a* is designed for experiments involving semi-infinite linear diffusion of the electroactive species to the electrode surface (6). It is normally used for experiments in which one applies large-amplitude steps in order to carry out electrolysis in the diffusion-limited region, and one then records the change in absorbance, $\mathscr{A}$, versus time. From an electrochemical standpoint, the result is the same as that of the Cottrell experiment described in Section 5.2.1.

The absorbance change can be described by considering a segment of solution of thickness dx and cross-sectional area A, as shown in Figure 17.1.1. If species R is the only species absorbing at the monitored wavelength, and if A is uniformly illuminated, the differential absorbance registered upon passage of the light through this segment is $d\mathscr{A} = \varepsilon_R C_R(x, t)dx$, where ε_R is the molar absorptivity of R. The total absorbance is then

$$\mathscr{A} = \varepsilon_R \int_0^\infty C_R(x,t)dx \qquad (17.1.1)$$

If R is a stable species, the integral in (17.1.1) is the total amount of R produced per unit area and is equal to Q_d/nFA, where Q_d is the charge passed in electrolysis. Since Q_d is given by the integrated Cottrell equation, (5.8.1), we have

$$\mathscr{A} = \frac{2\varepsilon_R C_O^* D_O^{1/2} t^{1/2}}{\pi^{1/2}} \qquad (17.1.2)$$

which shows that the absorbance should be linear with $t^{1/2}$ as shown in Figure 17.1.3. Note that the slope of the $\mathscr{A} - t^{1/2}$ plot affords a way of measuring diffusion coefficients without independent knowledge of the area A.
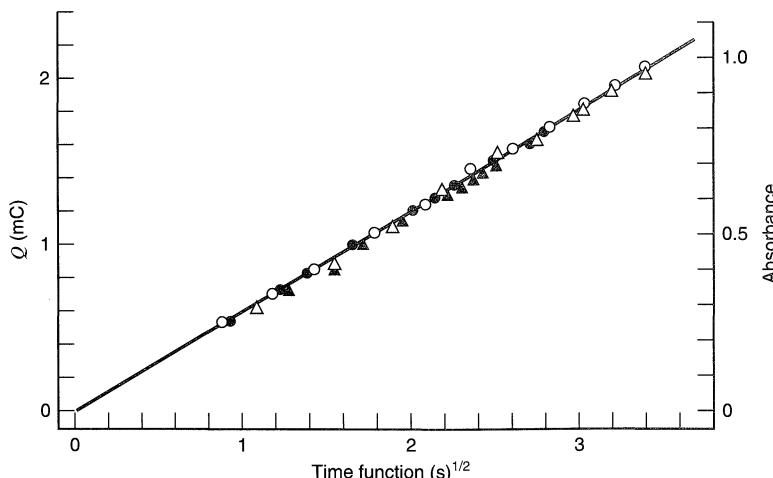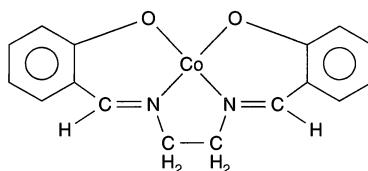
Figure 17.1.3 Responses at a 2000 wire-per-inch gold minigrid during a double potential step experiment. The solution contained 0.8 mM o-tolidine in 1 M HClO$_4$–0.5 M acetic acid. In the forward step o-tolidine was oxidized in a diffusion-controlled, two-electron process. The stable product was rereduced in the reversal. Open circles, forward step charge vs. $t^{1/2}$; filled circles, forward step absorbance vs. $t^{1/2}$; open triangles, Q_r ($t > \tau$) vs. θ (see Section 5.8.2); filled triangles, $\mathscr{A}(\tau) - \mathscr{A}$ vs. θ. The forward step duration is denoted by τ. [Reprinted with permission from M. Petek, T. E. Neal, and R. W. Murray, *Anal. Chem.*, **43**, 1069 (1971). Copyright 1971, American Chemical Society.]

Since the usual transmission experiment directly monitors the electrolytic product, it offers many of the diagnostic features of reversal chronoamperometry or reversal chrono-coulometry. In effect, $\mathcal{A}$ is a continuous index of the total amount of the monitored species still remaining in solution at the time of observation. Equation 17.1.2 describes the limiting case in which the product is completely stable. If homogeneous chemistry tends to deplete the concentration of R, different absorbance-time relations will be seen. They can be predicted (e.g., by digital simulations; see Appendix B), and curves for many mechanistic cases have been reported (17).

Another popular mode for transmission experiments involves a thin-layer system (9, 10, 13, 18) like that shown in Figure 17.1.2*b*. The working electrode is sealed into a chamber (e.g., between two microscope slides spaced perhaps 0.05–0.5 mm apart) containing the electroactive species in solution. The chamber is filled by capillarity, and the solution within it contacts additional solution in a larger container, which also holds the reference and counter electrodes. The electrolytic characteristics of the cell are naturally similar to those of the conventional thin-layer systems discussed in Section 11.7. One can do cyclic voltammetry, bulk electrolysis, and coulometry in the ordinary way, but there is also a facility for obtaining absorption spectra of species in the cell.

The particular advantage of this *optically transparent thin-layer electrode* (OTTLE) is that bulk electrolysis is achieved in a few seconds, so that (for a chemically reversible system) the whole solution reaches an equilibrium with the electrode potential, and spectral data can be gathered on a static solution composition.

Figure 17.1.4 is a display of spectra obtained for the cobalt complex with the Schiff base ligand bis(salicylaldehyde)ethylenediimine (19):
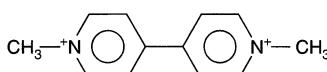
At -0.9 V *vs.* SCE, the complex contains Co(II), but at -1.45 V the metal center is reduced to Co(I). Spectra obtained in this way may be intrinsically interesting for characterizing the electronic properties of the species under scrutiny, and they may be used to obtain precise standard potentials in the manner elicited in Problem 17.1.

Spectroelectrochemical methods can be especially useful for unraveling a complex sequence of charge transfers. Figure 17.1.5 is a display from a classic example (20). The sample is a mixture of cytochrome c and cytochrome c oxidase, which is initially fully oxidized. The experiment is a coulometric titration by the electrogenerated radical cation of methyl viologen (MV^{2+}):

$$MV^{2+} + e \rightleftharpoons MV^{+\cdot} \tag{17.1.3}$$

where MV^{2+} corresponds to

In solution, one $MV^{+\cdot}$ ion can reduce a single heme site in cytochrome c or one of two in the oxidase. The spectra were recorded after 5-nanoequivalent increments of charge, and they indicate that one of the heme groups in cytochrome c oxidase is reduced first. Then $MV^{+\cdot}$ reduces the heme in cytochrome c before it deals with the second heme of the oxidase.
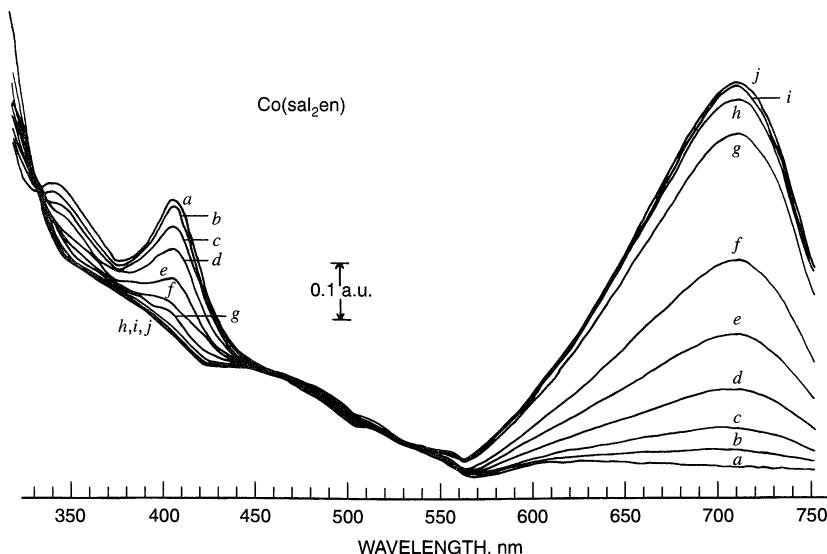
Figure 17.1.4 Spectra of the cobalt complex with the ligand bis(salicylaldehyde)ethylene-diimine, obtained at an OTTLE. Applied potentials: (*a*) −0.900, (*b*) −1.120, (*c*) −1.140, (*d*) −1.160, (*e*) −1.180, (*f*) −1.200, (*g*) −1.250, (*h*) − 1.300, (*i*) −1.400, and (*j*) − 1.450 V *vs*. SCE. [From D. F. Rohrbach, E. Deutsch, and W. R. Heineman in "Characterization of Solutes in Nonaqueous Solvents," G. Mamantov, Ed., Plenum, New York, 1978, with permission.]

This example is a good illustration of the indirect electrochemical measurements that typically have to be applied with biological macromolecules, like enzymes, which sometimes will not undergo direct charge exchange with an electrode (possibly for steric reasons). Instead, one uses smaller molecules to exchange charge heterogeneously with the electrode, and homogeneously with the macromolecules. These species are called *mediators* (9, 10, 18, 20). They provide a mechanism for enforcing and maintaining electrochemical equilibrium with the macromolecules; hence they are especially useful for characterizing standard potentials for redox centers in these species.

Many different designs have been described for transmission spectroelectrochemical cells (21). To increase the sensitivity, long path length cells, in which the light beam passes parallel to the electrode surface, have been used (22). In spectroelectrochemical flow cells, the solution flows in a thin channel between a working and counter electrodes, which are outside of the field of view of the spectrometer (23).

17.1.2 Specular Reflectance and Ellipsometry

One might guess that changes at the surface of an electrode, even minute changes, such as the adsorption of submonolayer amounts of iodide, would affect the reflecting properties of the surface, and therefore might provide information about the kinetics of surface chemistry and the nature of surface films. This approach is indeed useful and has given rise to several different experimental techniques. For the two areas covered in this section, we want to concentrate on the surface itself. We are interested in the properties of a light beam reflected from that surface, and we seek specifically to avoid any changes in the optical properties of the solution during the course of the experiment. These methods are well-suited to the direct observation of surface chemistry in an operating cell, but not in the presence of simultaneous homogeneous reactions involving absorbing species.
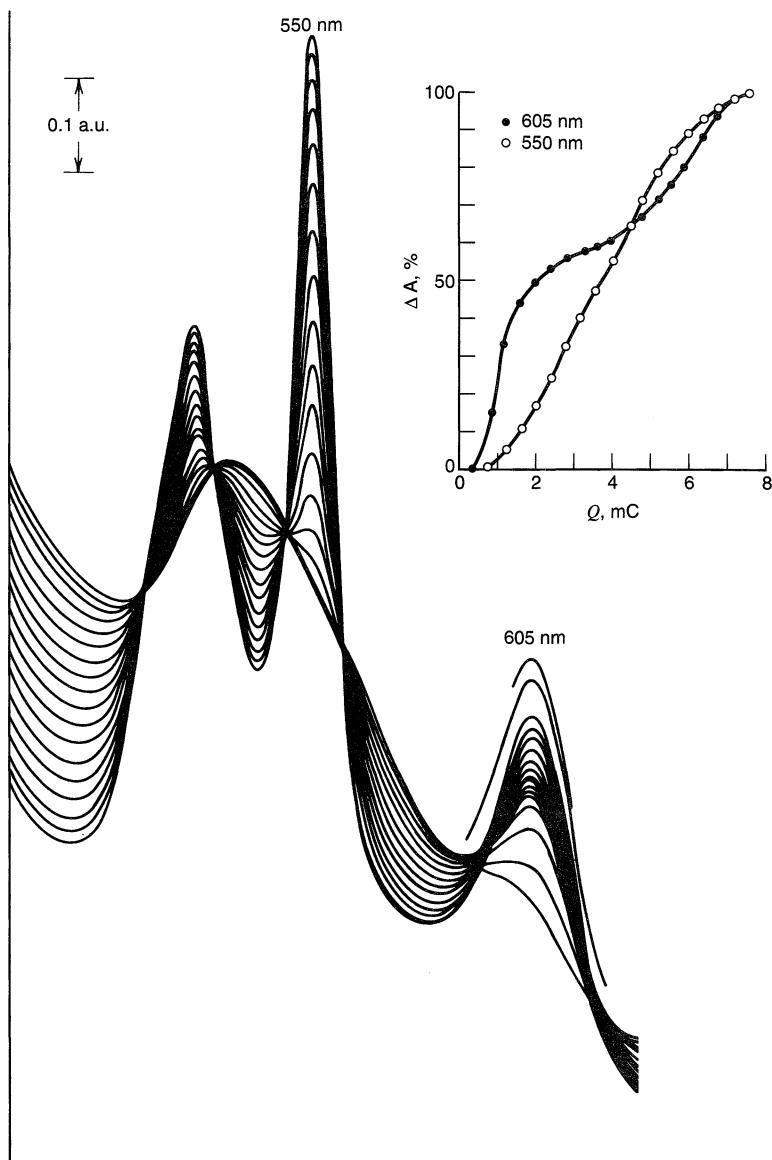
Figure 17.1.5   Coulometric titration of cytochrome c (17.5 μM) and cytochrome c oxidase (6.3 μM) by MV‡ generated at an SnO_2 OTE. Each spectrum was recorded after 5×10^{-9} equivalents of charge were passed. [From W. R. Heineman, T. Kuwana, and C. R. Hartzell, *Biochem. Biophys. Res. Comm.*, **50**, 892 (1973), with permission from Academic Press, Inc.]

(a) Optical Principles

Before we proceed further, we must review some basic concepts of optics. It is clearly beyond our scope to go very far along this line, but we will try to develop a basis for understanding the methods at hand. The reader who requires more complete information should consult more comprehensive sources (24–27).

Optical reflection is best understood in terms of the wavelike properties of light. The electric field vector associated with the wave oscillates in a plane as the wave propagates (Figure 17.1.6), and the intensity of the light is proportional to the square of the electric
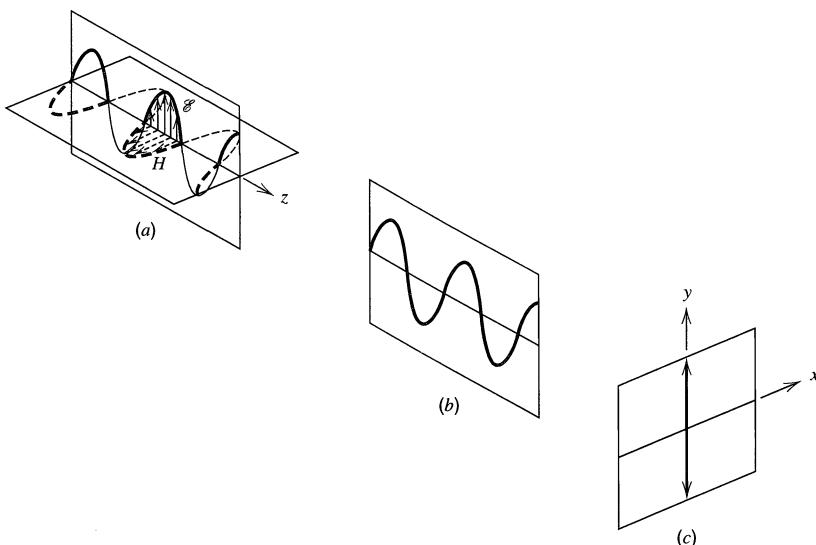
Figure 17.1.6 (*a*) Electric field and magnetic field vectors of a light wave propagating along the *z* direction. (*b*) The *plane of polarization* contains the electric field vector. (*c*) To an observer at a fixed point, a train of these waves, all oriented in the same way, would have electric field vectors along the indicated line. Such a light beam is *linearly polarized*. [From R. H. Muller, *Adv. Electrochem. Electrochem. Engr.*, **9**, 167 (1973), with permission.]

field amplitude. A magnetic field vector, oscillating in a perpendicular plane, as shown in Figure 17.1.6, accompanies the electric vector; but generally we do not have to consider its presence.

Most light sources comprise independent emitters yielding rays that are uncorrelated with each other; thus the planes of oscillation of the electric field are randomized with respect to the angle about the axis of propagation. This light is said to be *unpolarized*. However, reflection of the light from a surface, or even transmission through a window, is generally more efficient for rays having certain particular orientations with respect to the actual physical surfaces involved; hence the reflected and transmitted beams are *partially polarized*, because particular directions of oscillation predominate. By processing the beam carefully, one can achieve a *linearly* (or *plane*) *polarized* beam in which all rays have the same angle for the plane of electric field oscillation.

In reflectance studies, one usually wants to control the state of polarization with respect to the experimental apparatus. Measurements are always referred to the physical *plane of incidence*, as defined in Figure 17.1.7. If the polarization is *parallel* to this plane, then it and parameters related to it are traditionally denoted by the subscript *p*. For polarization *perpendicular* to the plane of incidence a subscript *s* is employed.

If some other angle of polarization with respect to the plane of incidence is employed, such as 45°, then one usually resolves the electric field vector into the parallel and perpendicular components. Thus, any linearly polarized beam incident on a surface can be regarded as a combination of separate beams with parallel and perpendicular polarization. Each ray in the parallel-polarized beam has a partner in the beam with perpendicular polarization, and they are locked in phase so that the orientation of the resultant electric field vector is always at the constant angle of polarization of the beam as a whole.
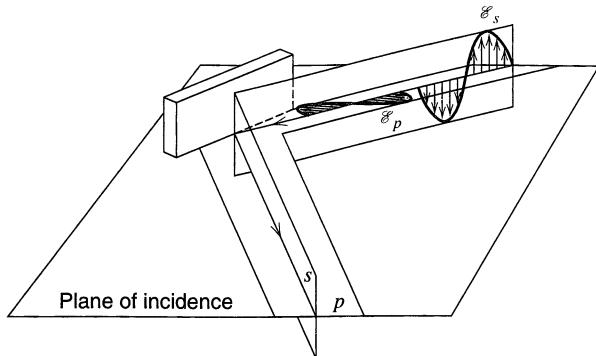
Figure 17.1.7 Reflection of polarized light from a surface. [From R. H. Muller, *Adv. Electrochem. Electrochem. Engr.*, **9**, 167 (1973), with permission.]

If a linearly polarized beam is reflected from a surface, one usually finds that the parallel and perpendicular components undergo different changes in amplitude and phase. Thus individual pairs of rays in the two beams are in phase upon incidence, but are out of phase upon reflection. This effect has interesting consequences, as shown in Figure 17.1.8. Note that now the resultant electric field vector for a ray pair is not at a fixed angle, as it was upon incidence, but instead it traces out a spiral as the wave propagates. The projection of the spiral is an ellipse; hence the light is *elliptically polarized.* The shape of the ellipse is controlled by the relative amplitudes and the phase differences of the two beams. *Circular polarization* represents the special case in which the amplitudes are equal and the phase shift is 90°.

The optical properties of any material are controlled by its *optical constants*. One of these is the *index of refraction, n*, which is

$$n = \frac{c}{v} = (\varepsilon\mu)^{1/2} \tag{17.1.4}$$

where c is the speed of light *in vacuo*, v is the speed of propagation in the medium, ε is the *optical-frequency dielectric constant*, and μ is the *magnetic permeability*. If the medium is light-absorbing, we must add the *extinction coefficient, k*, which is proportional
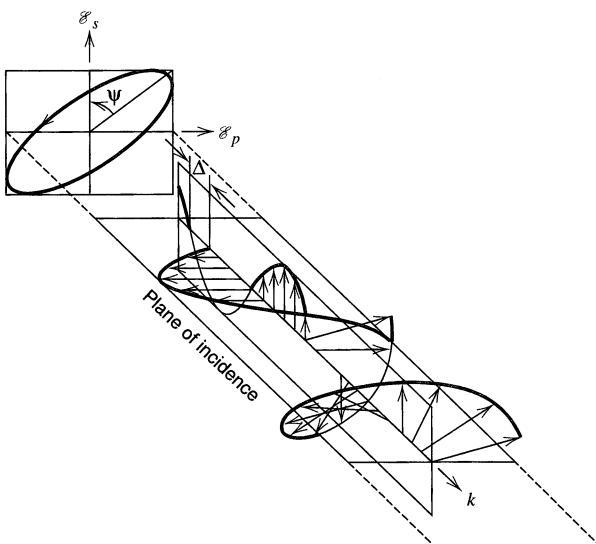
Figure 17.1.8 Elliptic polarization arising from a phase shift, Δ, between parallel and perpendicular components. [From R. H. Muller, *Adv. Electrochem. Electrochem. Engr.*, **9**, 167 (1973), with permission.]

to the *absorption coefficient*, α, which in turn characterizes the exponential falloff in light intensity upon passage through the medium. The absorbance of a thickness x of the medium is $\alpha x/2.303$, and k is related to α by

$$\alpha = \frac{4\pi k}{\lambda} \tag{17.1.5}$$

where λ is the wavelength *in vacuo* of the incident light.[1]

In the literature on reflectance, one finds that it is often convenient to work with a *complex refractive index* $\hat{n}$ defined by

$$\hat{n} = n - jk \tag{17.1.6}$$

where $j = \sqrt{-1}$. Thus the real and imaginary components of $\hat{n}$ are n and $-k$. By analogy to (17.1.4), one then defines a *complex optical-frequency dielectric constant* $\hat{\varepsilon}$ adhering to

$$\hat{n} = (\mu\hat{\varepsilon})^{1/2} \tag{17.1.7}$$

with $\hat{\varepsilon}$ expressed in terms of the real and imaginary components as

$$\hat{\varepsilon} = \varepsilon' - j\varepsilon'' \tag{17.1.8}$$

where

$$\varepsilon' = \frac{n^2 - k^2}{\mu} \quad \text{and} \quad \varepsilon'' = \frac{2nk}{\mu} \tag{17.1.9}$$

The magnetic permeability μ is nearly unity at optical frequencies for most materials. The basic optical characteristics of the phase are defined by μ, n, and k, or, alternatively, by μ, ε', and ε''. Both sets are used in the analysis of experimental results.

(b) Specular Reflectance Spectroscopy (26–32)

Measurements of specular reflectance involve the intensities of light reflected from the surface of interest. Usually the incident light is polarized either parallel (*p*) or perpendicular (*s*) to the plane of incidence, as shown in Figure 17.1.7, and a detector monitors the intensity of the reflected beam. The light is monochromatic, but is often tuned over large wavelength ranges. The surface under examination must be flat and, preferably, smooth. For our purpose, it is an electrode in an electrochemical cell.

The *reflectance*, R, is defined as the ratio of the reflected light intensity to the intensity of the incident beam. Absolute reflectances are difficult to measure and are not necessarily of interest. Instead one is usually interested in the change in reflectance ΔR induced by some change in the system, for example, in electrode potential. Experimentally, one measures only the intensity of the reflected beam, I_R. Then if the incident intensity remains constant, a change ΔI_R in the reflected beam gives $\Delta R/R = \Delta I_R/I_R$. The basic data of reflectance experiments are plots of $\Delta R/R$ *vs.* the variable of interest, which may be frequency of incident light, potential, concentration of an electroactive species, etc.

Values of $\Delta R/R$ typically range from 10^{-6} to unity, hence quite small effects are often involved. To make them experimentally accessible, various modulation schemes are used and lock-in detection is employed (26, 30, 31). In the simplest case, the light beam is chopped. In other circumstances, an experimental variable, such as the potential, may be modulated.

Specular reflectance measurements are attractive for the evaluation of the optical constants of metals and other materials, particularly in the form of films, whose properties may differ markedly from those of bulk solids. The strength of the method is the rel-

---

[1]Note that neither k nor α is the same as the *molar absorptivity*, ε, which is also frequently called the "extinction coefficient."
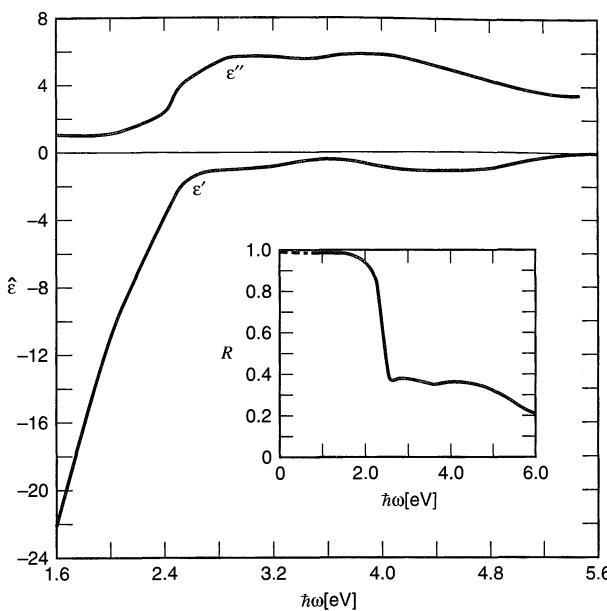
Figure 17.1.9 Dependence of the real and imaginary components of the optical-frequency dielectric constant of gold on the energy of incident photons. The normal-incidence reflectivity of gold in air is shown in the inset. [From D. M. Kolb and J. D. E. McIntyre, *Surf. Sci.*, **28**, 321 (1971), with permission.]

ative ease in obtaining results as a function of wavelength. Optical constants of materials may be of interest in their own right (e.g., in defining band structure or locating surface states; see Section 18.2), or they may be needed for a later analysis (e.g., in determining the thickness of an anodic film growing *in situ*). Figure 17.1.9 is an illustration of typical data for gold (33).
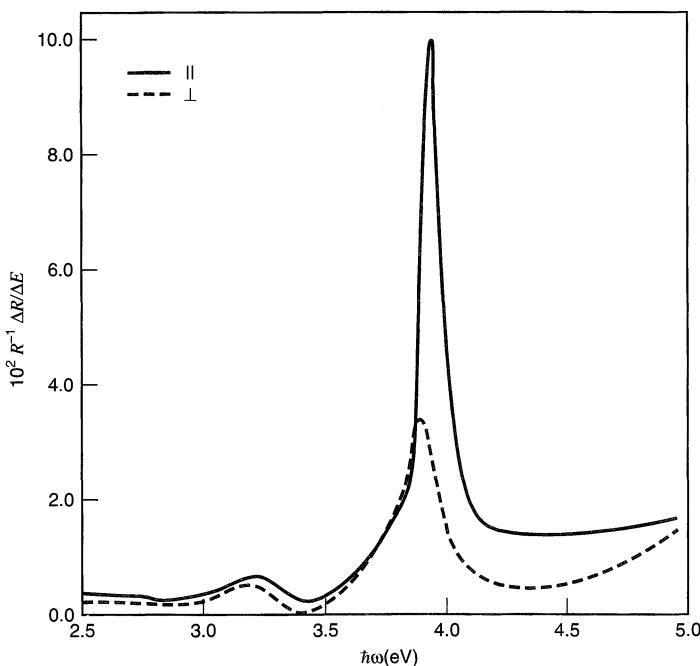
Figure 17.1.10 Electroreflectance spectra of Ag in 1 M NaClO$_4$. $E_{dc} = -0.5$ V *vs.* SCE. The potential was modulated with $\Delta E = 100$ mV rms at 27 Hz. [From J. D. E. McIntyre, *Adv. Electrochem. Electrochem. Engr.*, **9**, 61 (1973), with permission.]

The *electroreflectance* method features modulation of the potential of the electrode, usually sinusoidally, and lock-in detection of resulting reflected light intensity changes, which are proportional to dR/dE. The reported response is usually $(1/R) \times (dR/dE)$. Figure 17.1.10 illustrates typical results for electroreflectance as a function of incident light energy. These kinds of spectra reveal the electronic structure of the system in the interfacial region. The sharp peak in Figure 17.1.10 is ascribed to the effect of the high double-layer field on the optical properties of the metallic phase (26).

Probably the most important applications of specular reflectance spectroscopy in electrochemistry involve the monitoring of surface films and adsorption layers. In Figure 17.1.11 one can see the effect of specific adsorption of anions on the reflectance properties (34). Figure 17.1.12 contains data demonstrating the formation of anodic oxide films on platinum (30). Note that on platinum, the film forms at potentials more positive than 0.5 V, but the original state of the electrode is restored on the return sweep. The optical constants and thicknesses of films can be evaluated by these methods, and that information can be useful in identifying the chemical nature of the films.

(c) Ellipsometry (27, 35–40)

We saw above that reflection of linearly polarized light from a surface generally produces elliptically polarized light, because the parallel and perpendicular components are reflected with different efficiencies and different phase shifts. We can measure these changes in intensity and phase angle, and we can use them to characterize the reflecting system. That approach is called *ellipsometry*.

The basic ellipsometric parameters are defined in Figure 17.1.8. The difference in phase angle between the leading and trailing components is given by Δ, and the ratio of electric field amplitudes defines the second parameter, ψ:

$$\frac{|\mathscr{E}_p|}{|\mathscr{E}_s|} = \tan \psi \qquad (17.1.10)$$

The values of Δ and ψ may be recorded as functions of other experimental variables, such as potential or time.

Several methods for evaluating Δ and ψ exist (26, 27), but the most precise approaches rely on a null balance like that depicted in Figure 17.1.13. Light that is polarized
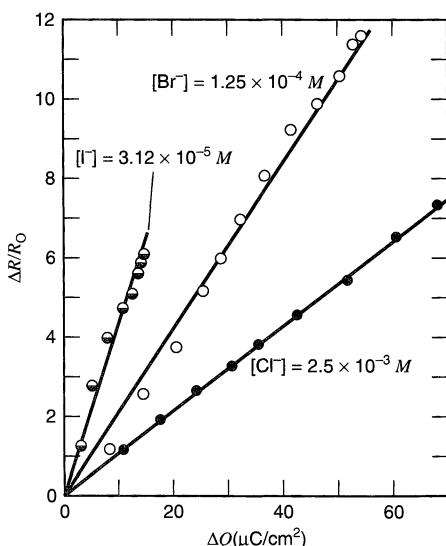
Figure 17.1.11 Reflectance changes caused by halide adsorption on gold in 0.2 M HClO$_4$. [From T. Takamura, K. Takamura, and E. Yeager, *Symp. Faraday Soc.*, **4**, 91 (1970), with permission.]
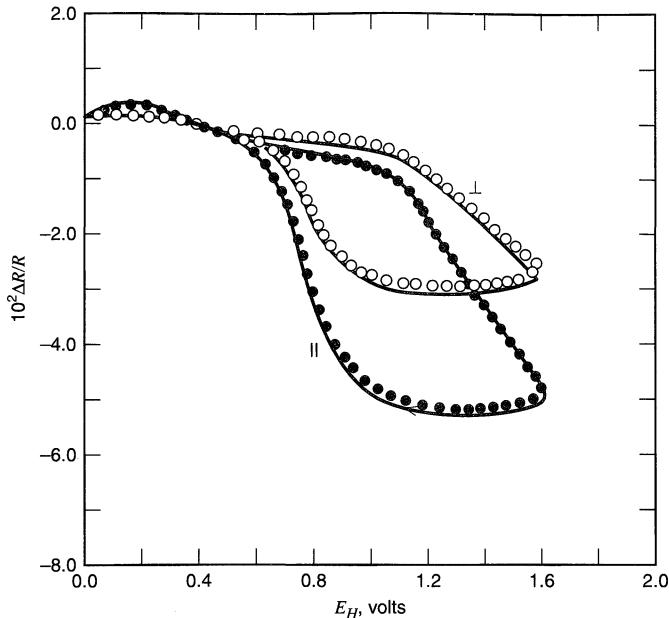
Figure 17.1.12 Reflectance change *vs.* potential for a platinum electrode in 1.0 M $HClO_4$. $v = 30$ mV/s. Separate data are shown for parallel and perpendicular polarization. The curves are for Ar-saturated solutions, and the points are for O_2-saturated solutions. Note that the reflectance changes are independent of the faradaic reduction of O_2, which takes place in the negative part of this range. [From J. D. E. McIntyre and D. M. Kolb, *Symp. Faraday Soc.*, **4**, 99 (1970), with permission.]

linearly at 45° with respect to the plane of incidence impinges on the sample. It has $|\mathscr{E}_p| = |\mathscr{E}_s|$ and $\Delta = 0$. After reflection the beam is passed through a *compensator*, which is adjusted to restore the original condition of $\Delta = 0$. The position of the compensator required for this restoration is a measure of the value of Δ induced by reflection. The resulting linearly polarized beam is then passed through a second polarizer (an *analyzer*), which is rotated until its axis of transmission is at right angles to the plane of polarization of the oncoming light. Then no light passes through the analyzer to the detector, and the condition of *extinction* is reached. The angular position of the analyzer then provides a measure
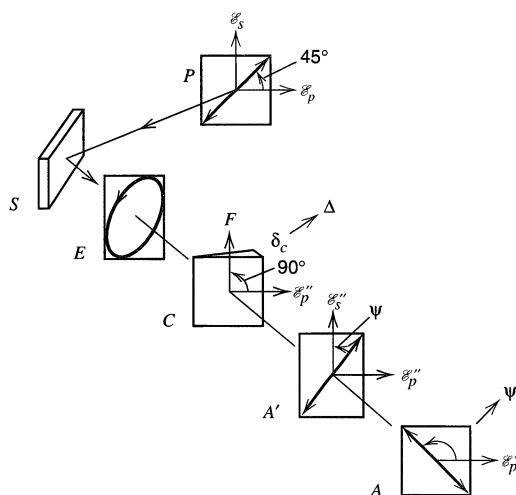
Figure 17.1.13 Schematic layout of one type of ellipsometer. Linearly polarized light (P) is incident on the sample (S). Reflection produces elliptic polarization (E), which is restored to linear polarization (A') by the compensator (C). The analyzer (A) is adjusted to achieve extinction. [From R. H. Muller, *Adv. Electrochem. Electrochem. Engr.*, **9**, 167 (1973), with permission.]

of ψ. Note that extinction will not be achieved unless the compensator and the analyzer are both correctly adjusted. These adjustments usually require tens of seconds with manual instruments.

Most ellipsometric measurements are now made with automated equipment controlled by a computer. A typical configuration of such an instrument consists of a fixed polarizer and an analyzer that is rotated continuously at 50–100 Hz. The result is a sinusoidally varying output that can be analyzed to yield the values of ψ and Δ. Instruments based on a fixed analyzer have also been described. In that case, the polarization of the incident beam is varied continuously with a photoelastic modulator. With automated ellipsometers, measurement times in the millisecond regime are possible (38–40).

Ellipsometry is widely used to study film growth on electrode surfaces. Results for a typical case, the formation of an anodic film on aluminum (41), are shown in Figure 17.1.14. Initial measurements on the substrate are found at the point marked 0.0 Å, and subsequent measurements, made at various stages of film growth, are shown as crosses. They trace out a closed figure, and then with still greater thicknesses (shown as circles), they begin to retrace the figure. With two measured parameters, Δ and ψ, and known optical constants for aluminum, one can calculate two fundamental parameters for the film at any stage of growth. In this case, since the film is assumed to be nonabsorbing ($k = 0$), the refractive index n and the thickness d can be calculated. The curve in Figure 17.1.14 is the predicted response for $n = 1.62$ and the various indicated thicknesses.

The kinetics of film growth can be studied in this manner without removing the electrode from the cell or interrupting the electrolysis. Figure 17.1.15 contains data showing three regimes of growth kinetics for the formation of a passive film on iron (42).

Ellipsometry has also been used to study the growth or changes in the characteristics of polymer films on electrodes (Chapter 14). For example, ellipsometric measurements
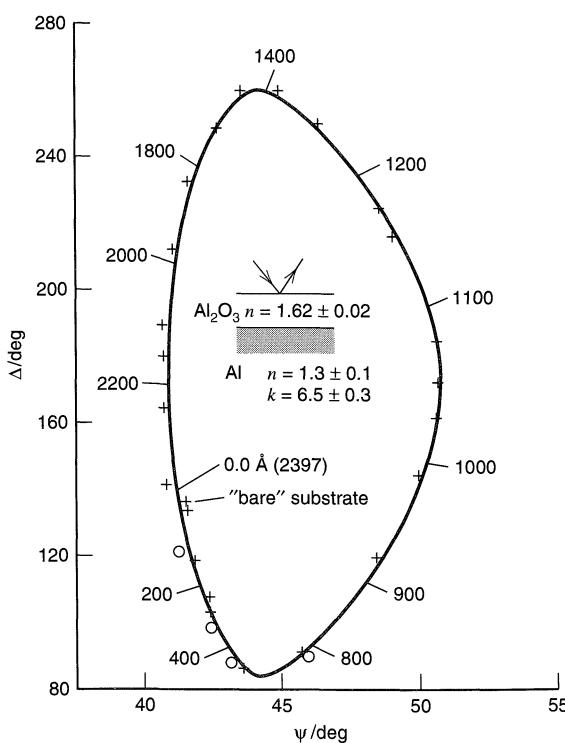
Figure 17.1.14 Ellipsometric results for anodization of aluminum in 3% tartaric acid (pH 5.5). Numbers along fitted curve indicate film thickness in Å. [From C. J. Dell'Oca and P. J. Fleming, *J. Electrochem. Soc.,* **123**, 1487 (1976), reprinted by permission of the publishers, The Electrochemical Society, Inc.]
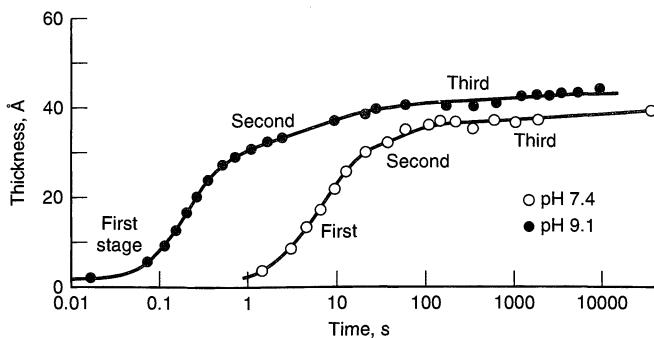
Figure 17.1.15 Growth of passive film on iron at 0.8 V *vs.* SCE. [From J. Kruger and J. P. Calvert, *J. Electrochem. Soc.*, **114**, 43 (1967), reprinted by permission of the publishers, The Electrochemical Society, Inc.]

taken during the galvanostatic growth of a polyaniline film by oxidation of aniline in aqueous HCl are shown in Figure 17.1.16 (43). The parameters were fit assuming growth of a single uniform film (constant refractive index). Note that this model shows large deviations for film thicknesses above 1400 Å (dashed line), which were ascribed to changes in the density and optical constants of the film at larger thickness. Changes in film properties with thickness during film growth or with time during conversion of a film from one state to another (e.g., the conversion of a film of neutral polypyrrole to the oxidized state) can make quantitative interpretations of the ellipsometric data difficult, since they rely on models with a number of adjustable parameters. Film roughness can also be a problem, since the surface layer in that case depends upon the refractive indices of both film and solvent.

Although ellipsometric measurements are most frequently made at a single wavelength, usually produced by a laser, and at a single angle-of-incidence, other modes of operation are possible. For example, it is possible to make measurements at multiple angles of incidence with a monochromatic source to remove ambiguities in the measured refractive index for a constant-thickness film. The film spectral response can also be obtained by making measurements at a number of wavelengths (*spectroellipsometry*), employing, for example, an optical multichannel analyzer for detection (44).
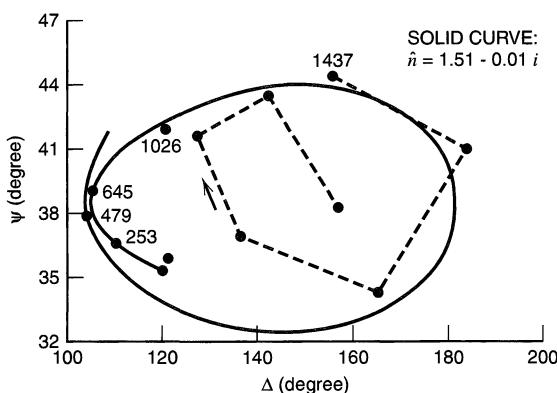
Figure 17.1.16 Experimental data (points) and fitted results (solid line) for ellipsometry during growth of a polyaniline film at a constant current of 77 μA/cm^2 in aqueous HCl, with ellipsometric readings taken for the reduced form of the film at -0.2 V *vs.* SCE. Calculated film thicknesses indicated on plot in Å. Theoretical plot deviates from fit above about 1400 Å (dashed line). [Reprinted from J. Rishpon, A. Redondo, C. Derouin, and S. Gottesfeld, *J. Electroanal. Chem.*, **294**, 73 (1990), with permission from Elsevier Science.]

17.1.3 Internal Reflection Spectroelectrochemistry (6, 8–10, 45–49)

(a) Optically Transparent Electrodes

Another approach to the optical sampling of the electrochemical interface is to utilize an OTE (Section 17.1.1) as an internal reflection element in the manner depicted in Figure 17.1.17. The light beam is directed parallel to the plane of the electrode and enters a prism that refracts it so that it passes into the electrode substrate at an angle greater than the critical angle. Then the beam travels by internal reflection through the glass until it reaches the second prism, which allows it to exit, after refraction, along its original line of propagation. The intensity of the beam is then measured. While the light is trapped within the electrode/substrate assembly, it is reflected several times from the electrode/electrolyte interface, and at each point of reflection it can interact optically with that region. Changes induced there, for example by electrolysis, cause detectable changes in the beam intensity measured by the detector, and they are the basis for *internal reflection spectroelectrochemistry* (IRS).

Mostly these experiments are concerned with light absorption by species at the interface, although other effects, such as changes in refractive index, can also be measured (6, 8, 45, 46). Absorption is possible because the electric field accompanying the light wave is not wholly contained within the electrode/substrate assembly. At the points of reflection, the field extends into the solution for a short distance. Its strength falls exponentially with distance from the interface according to the relation:

$$\langle \mathscr{E}^2 \rangle = \langle \mathscr{E}_0^2 \rangle \, e^{-x/\delta} \tag{17.1.11}$$
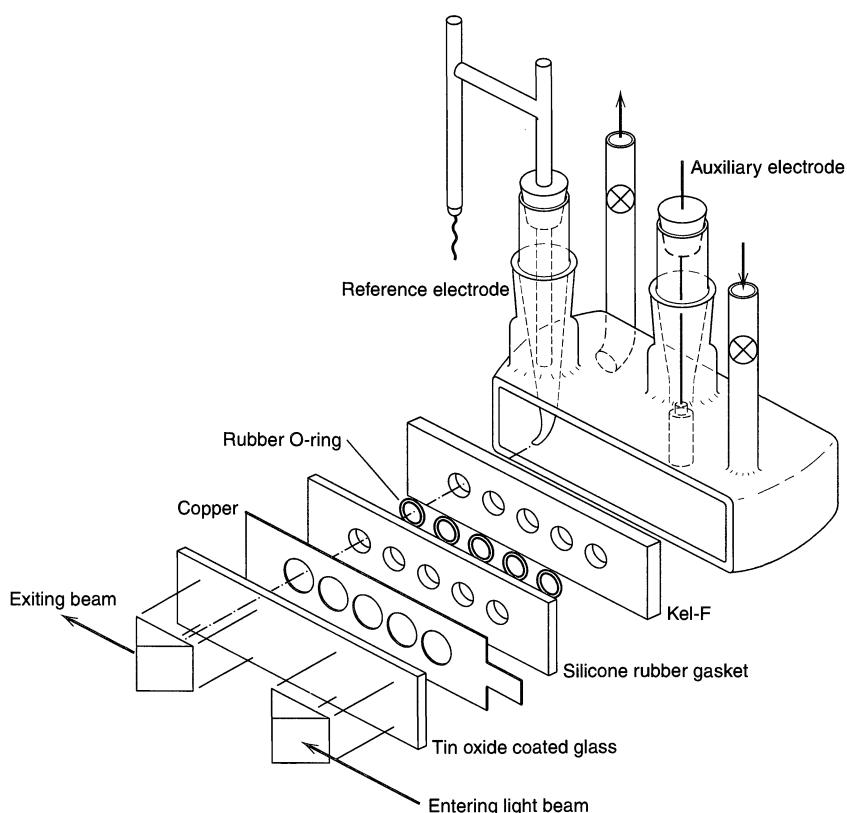
Figure 17.1.17   Cell assembly for internal reflection spectroelectrochemistry. [Adapted from N. Winograd and T. Kuwana, *J. Electroanal. Chem.*, **23**, 333 (1969), with permission.]

where $\langle \mathscr{E}_0^2 \rangle$ is the average square field amplitude at the interface, $\langle \mathscr{E}^2 \rangle$ is the average square amplitude at distance x, and δ is the *penetration depth*. This field is a manifestation of the *evanescent wave* existing on the solution side of the interface. It interacts with absorbing species, with a probability of absorption proportional to $\langle \mathscr{E}^2 \rangle$.

The penetration depth defines the distance into the solution over which optical sampling occurs. It is calculable from the optical parameters of the system (8, 45). For the usual three-phase case (e.g., SnO_2 on glass in contact with solution),

$$\delta = \frac{\lambda}{4\pi \, Im \, \xi} \qquad (17.1.12)$$

where λ is the wavelength of incident light and $Im \, \xi$ is the imaginary part of $(\hat{n}_3^2 - n_1^2 \sin^2 \theta_1)^{1/2}$, in which $\hat{n}_3$ is the complex refractive index of the solution, n_1 is the index of refraction of the substrate (usually glass), and θ_1 is the angle of incidence within the substrate. In general, the absorbing properties of the solution do not affect δ very much (8, 45, 46); hence $\hat{n}_3 \approx n_3$ for this calculation. Since typical values of δ (Problem 17.7) are 500 to 2000 Å, the IRS method is strictly sensitive to the part of the solution very near the interface.

Suppose now that only the reduced form of the O/R couple absorbs. Its absorbance is usually expressed as

$$\mathscr{A}_R(t) = N_{eff}\varepsilon_R \int_0^\infty C_R(x, t) \exp\left(\frac{-x}{\delta}\right) dx \qquad (17.1.13)$$

where the integral arises because the probability of light absorption is proportional to $\langle \mathscr{E}^2 \rangle$ and $C_R(x, t)$ at any value of x. At all points the absorbance is proportional to the molar absorptivity ε_R. The parameter N_{eff} is a sensitivity factor incorporating the number of reflections and the relationship between the incident intensity and $\langle \mathscr{E}_0^2 \rangle$. It depends on the materials used in the electrode/substrate assembly, the beam geometry, and its state of polarization. In general, N_{eff} must be evaluated empirically. Values on the order of 50 to 100 are typical.

If the electrolysis time is longer than about 1 ms, the diffusion layer is much thicker than δ; hence $C_R(x, t) \approx C_R(0, t)$ at all values of x where the exponential factor has a significant value, and

$$\boxed{\mathscr{A}_R(t) = N_{eff}\varepsilon_R\delta C_R(0, t)} \qquad (17.1.14)$$

Thus the absorbance is a measure of the surface concentration of R. The spectrum of absorbance is not the same as the conventional absorption spectrum (ε_R vs. λ), because N_{eff} and δ vary with λ and because various other optical effects associated with the electrode/substrate system complicate the picture (6, 45, 46).

For electrolyses involving time scales shorter than about 500 μs, the diffusion layer is of the same order as δ, and the absorbance is sensitive to the evolving concentration profile of R (6, 46, 47). The resulting optical transients can be useful for characterizing rather fast electrochemical processes, which are otherwise complicated severely by nonfaradaic contributions to current and charge functions. Theoretical absorbance transients can be computed from (17.1.13), once the diffusion-kinetic equations defining the concentration profile of R have been solved, either analytically or by numeric methods such as digital simulation.

Figure 17.1.18 contains data obtained in experiments of this sort (47). The electrode reaction for curve a is the oxidation of tri-p-anisylamine (TAA) to its cation radical in acetonitrile:

$$TAA - e \rightarrow TAA^{\ddagger} \qquad (17.1.15)$$
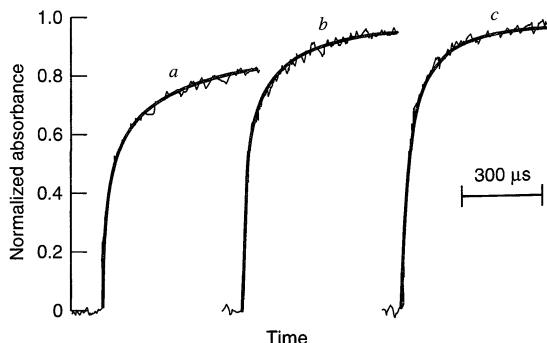
Figure 17.1.18 Transient absorbances caused by potential steps of 800-μs width from 0.40 to 0.80 V $vs.$ SCE. Pulses were repeated at 30 Hz for 2 min, and transients were averaged. *Curve a*: 0.182 mM TAA in acetonitrile. *Curve b*: 0.182 mM TAA and 0.182 mM AF. *Curve c*: 0.167 mM TAA and 0.333 mM AF. Solid curves are fitted results yielding the rate constant given in the text. [Reprinted with permission from N. Winograd and T. Kuwana, *J. Am. Chem. Soc.*, **93**, 4343 (1971). Copyright 1971, American Chemical Society.]

and the transient absorbance is due to TAA‡ generated in a step experiment involving an 800-μs width. To improve the signal-to-noise ratio, the pulses were repeated at 30 Hz for 2 min, and the 3600 transients were averaged. The results are reported in terms of *normalized absorbance*, which is the value of $\mathscr{A}(t)$ divided by the asymptotic $\mathscr{A}$ at long times [essentially provided by (17.1.14) with $C_R(0, t) = C_R^*$, assuming $D_R = D_O$]. This procedure allows cancellation of N_{eff} and ε.

Experiments b and c were performed to evaluate the rate constant for the electron transfer from TAA to acetylferricenium cation (AF$^+$):

$$\text{TAA} + \text{AF}^+ \underset{k_2}{\overset{k_1}{\rightleftharpoons}} \text{TAA}^{\ddagger} + \text{AF} \tag{17.1.16}$$

The ratio k_1/k_2 is the equilibrium constant, which is available from standard potentials. The step in potential causes oxidation of *both* TAA and AF, then the AF$^+$ diffuses out into solution and reacts with TAA, so that TAA‡ is produced faster than in the absence of AF$^+$. From the shape of the absorbance rise, one can evaluate the rate constant k_1 as 3.8 $\times 10^8 \, M^{-1} \, \text{s}^{-1}$. Note that this figure is quite large, and implies a reaction time scale that will severely tax most purely electrochemical methods.

(b) Surface Plasmon Resonance (SPR) (50, 51)

The arrangement for an SPR measurement in an electrochemical cell is shown in Figure 17.1.19. The electrode is a thin gold film ($\sim$50 nm) deposited on a glass cover slip. It is irradiated from the backside by p-polarized light from a laser via the hemispherical prism, and the reflectivity is measured as a function of the angle of incidence, θ. The result is a plot that shows a dip in reflectivity over angles of a few degrees (Figure 17.1.20). The lowest point is referred to as the *SPR minimum*. The beam, when coupled to the film via the prism in this configuration (called the *Kretschmann configuration*), causes collective excitations of electrons at the gold film/solution interface that are called *plasmons*. The intensity of the optical field associated with the plasmons decays exponentially with distance into the solution away from the electrode surface with a decay length on the order of 200 nm; thus this field is sensitive to thin layers at the gold-solution interface and provides information about the surface dielectric constant and layer thickness. It has been used to study the adsorption of biological molecules and self-assembled monolayers on
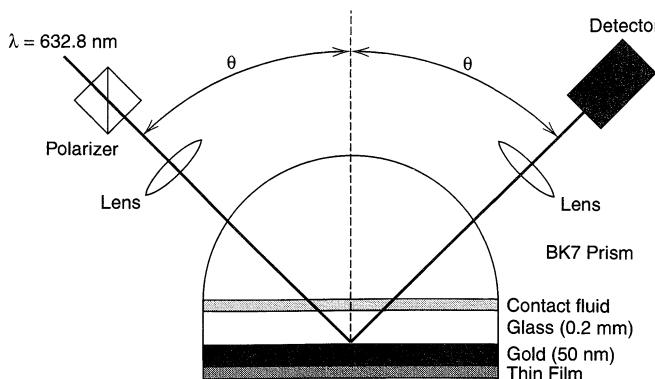
Figure 17.1.19 A prism/gold electrode arrangement for an SPR experiment. The gold film (50 nm thick) is deposited on a glass microscope cover slip and serves as the electrode. Laser light is coupled into the electrode via the hemispherical prism. The remainder of the cell is below the assembly shown here. The layer labeled "thin film" is an adsorbed layer or some other deposit on the working electrode. [Reprinted from D. G. Hanken, C. E. Jordan, B. L. Frey, and R. M. Corn, *Electroanal. Chem.*, **20**, 141 (1998), by courtesy of Marcel Dekker, Inc.]
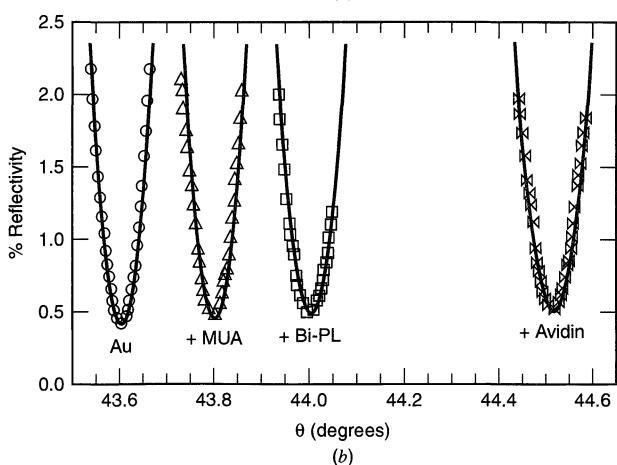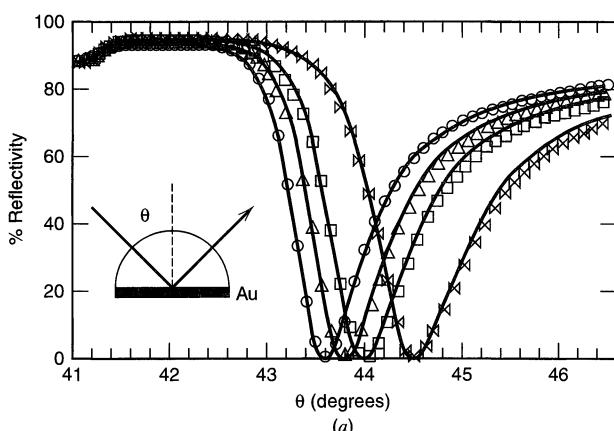
Figure 17.1.20 SPR reflectivity curves for clean gold (circles) and sequentially adsorbed monolayers of 11-mercaptoundecanoic acid (triangles), a 22% biotinylated poly-L-lysine monolayer (squares), and the protein avidin (bowties). The shift in the minimum, the SPR angle, is used to determine the thickness of the adsorbed layer. [Reprinted with permission from B. L. Frey, C. E. Jordan, S. Kornguth, and R. M. Corn, *Anal. Chem.*, **67**, 4452 (1995). Copyright 1995, American Chemical Society.]

metals, the potential distribution at an electrode surface, and electrochemical processes like underpotential deposition and electrode oxidation. For example, the change in behavior of a clean gold surface after adsorption of different layers is shown in Figure 17.1.20. Note the shift in the SPR minimum with increasing film thickness.

17.1.4 Photoacoustic and Photothermal Spectroscopy

The transmission and reflection techniques, while very powerful in characterizing changes occurring at or near the electrode surface, make rather severe demands on the type of electrode that can be used. For example, electrodes with very rough surfaces cannot be examined easily by reflection techniques, because the impinging light is largely scattered, and, of course, only transparent electrodes can be employed in transmission experiments. There has thus been interest in developing techniques for the optical investigation of solids, either *in situ* or after removal from the electrochemical cell, by detecting directly the amount of absorbed radiation through temperature changes in the electrode, rather than by analyzing properties of the transmitted or reflected beam. This goal can be reached by measuring the temperature change directly (*photothermal spectroscopy*) or by measuring the pressure fluctuations in a solution or in air induced by the periodic temperature variation resulting from a chopped light beam (*photoacoustic spectroscopy*). These techniques, which have not found widespread use in electrochemical systems, are discussed in more detail in the first edition.[2] *Photothermal deflection spectroscopy* is a related technique in which temperature or compositional changes that occur near an electrode surface are measured by the deflection of a laser beam that probes changes in refractive index near the electrode (52).

17.1.5 Second Harmonic Spectroscopy

In the optical methods described so far, the electrode is irradiated with light of frequency ω and the radiation is also detected at ω. However, nonlinear optical effects, analogous to the electrochemical effects discussed in Section 10.6, can result in the appearance of radiation at frequency 2ω. This effect occurs in noncentrosymmetric crystals and is the basis of frequency doublers used in laser systems. Symmetry is also broken at an interface, hence the generation of a second harmonic signal can be a selective probe of interfaces. This method is especially useful for solid/liquid interfaces, since the interrogating light beam can be passed through the solution without effect on the second harmonic response. The principles, theory, and application of *second harmonic generation* (SHG) to electrochemical systems has been the subject of a number of reviews (53–55).

The typical apparatus for an SHG experiment is shown in Figure 17.1.21. Since the conversion efficiencies from the fundamental to the second harmonic signal are very low, typically of the order of 10^{-12} % (55), it is necessary to use high power pulsed (ps-ns) lasers with light intensities at the surface of 10^5 to 10^8 W/cm^2. Even with these high intensities the resulting second harmonic signal is small, perhaps 5 to 50,000 photons/s, so gated photon counting or some form of signal averaging is needed in the detection electronics.

The SHG signal is sensitive to species at the interface (i.e., those within a few molecular layers from the electrode surface) and can be used to detect adsorbed species, reaction intermediates, and changes in the nature of the electrode surface. Often the response is dominated by changes in the nonlinear susceptibility of the metal surface, which is sensitive to the presence of adsorbed species, but not very effective for identifying the species.

---

[2]First edition, pp. 596–600
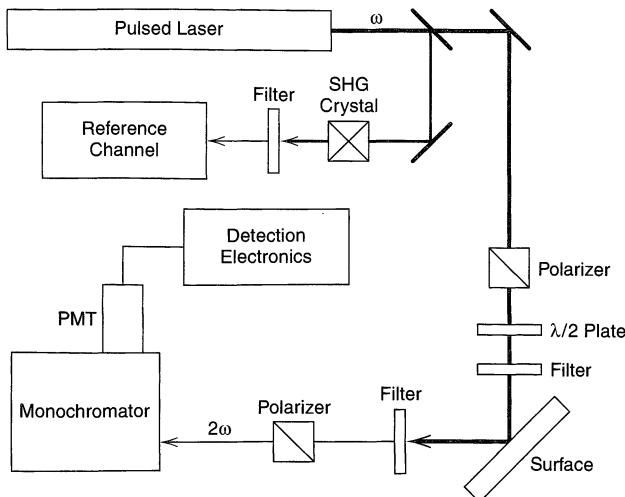
Figure 17.1.21 Experimental apparatus for SHG experiments. A small portion of the beam from a high-power pulsed laser is sent to a reference channel, after frequency doubling, to provide a signal to normalize for fluctuations in the laser intensity. The main beam is linearly polarized and filtered before impinging on the sample. The resulting beam at 2ω is separated from the fundamental by filters and a monochromator. [Reprinted with permission from R. M. Corn and D. A. Higgins, *Chem. Rev.*, **94**, 107 (1994). Copyright 1994, American Chemical Society.]
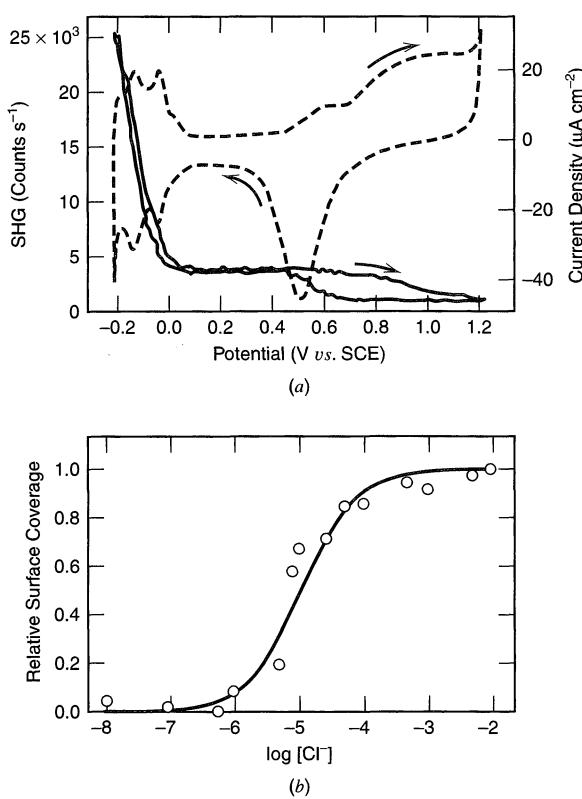
Figure 17.1.22 (*a*) Second harmonic signal (solid line) and cyclic voltammogram (dashed line) for a polycrystalline Pt electrode in 0.5 M $HClO_4$ and 1 mM KCl. (*b*) Adsorption isotherm determined from SHG response at 0.2 V at different KCl concentrations. The chloride surface coverage was taken as proportional to the metal surface nonlinear susceptibility. [Reprinted with permission from R. M. Corn and D. A. Higgins, *Chem. Rev.*, **94**, 107 (1994). Copyright 1994, American Chemical Society.]

However the generation of SHG signals during a voltammetric scan can be chemically informative when coupled to electrochemical behavior. Consider Figure 17.1.22*a*, which depicts the SHG signal during a cyclic voltammogram on a polycrystalline Pt electrode in 0.5 *M* $HClO_4$ and 1 m*M* KCl. The response indicates the changes in the electrode surface during the scan (56). The large increase at negative potentials is due to the formation of adsorbed hydrogen. The signal between 0 and 0.4 V *vs.* SCE is attributed to adsorbed chloride ions. Above 0.4 V chloride is desorbed as the layer of oxide or adsorbed hydroxyl forms. The signal at 0.2 V as a function of chloride ion concentration can be used to find the adsorption isotherm, as shown in Figure 17.1.22*b*. SHG has been used to study adsorption on many different metals, semiconductor electrodes, and underpotential deposition.

▶ 17.2 VIBRATIONAL SPECTROSCOPY

17.2.1 Infrared Spectroscopy (57–59)

In general, the electric field of incident radiation interacts with the molecular dipole. When the frequency of the radiation ($\sim 10^{13}$ Hz) resonates with a molecular vibration, absorption can occur, particularly if excitation of that vibration has an effect on the molecular dipole moment. The energy changes involved in exciting vibrational modes in this way correspond to the infrared spectral region. A full infrared spectrum consists of bands (*group frequencies*), assignable to particular moieties (e.g. $-CH_2-$, $-CH_3$, C=O), in characteristic frequency regions that are relatively independent of the other groups in the molecule. Since infrared spectroscopy probes molecular vibrations that involve changes in the dipole moment, the vibrations of polar molecular bonds generally correspond to strong infrared bands.

In *infrared spectroelectrochemistry* (IR-SEC), species are probed at the electrode surface and in a thin zone of solution near the surface. The usual configuration involves one like that shown in Figure 17.2.1, the *external reflection mode*, where the infrared radiation passes through a window and a thin layer of solution, reflects off of the electrode surface, and is detected. The solution layer between the window and electrode must be thin (1 to 100 μm) because most solvents are good absorbers of IR radiation. A typical cell configuration is shown in Figure 17.2.2. The electrode is placed at the end of a piston that can be used to adjust the spacing between electrode and window. Even with this thin layer, the absorbance of the species of interest is usually much smaller than that of the bulk solution, so modulation or difference techniques are often employed to obtain useful signals. Either the potential or the polarization of the incident radiation can be modulated.

The technique in which the potential is modulated is known as EMIRS, for *electrochemically modulated infrared reflectance spectroscopy* (60). A block diagram of the appa-
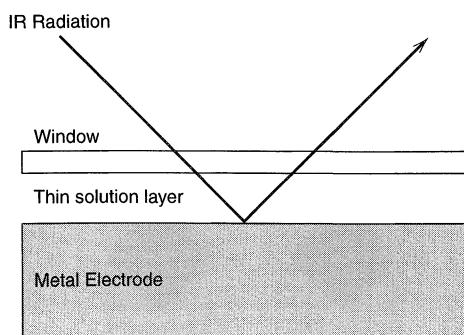
Figure 17.2.1   Diagram of the external reflectance configuration for IR-SEC. The cell window (e.g., CaF_2, Si, ZnSe) must be transparent to IR radiation and insoluble in the solution of interest.
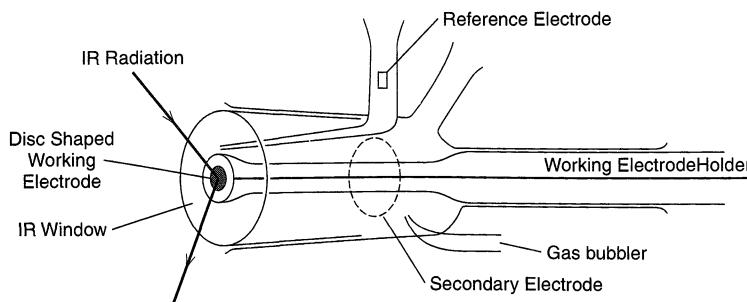
Figure 17.2.2   Spectroelectrochemical cell for IR-SEC. [Reprinted from A. Bewick, K. Kunimatsu, B. S. Pons, and J. W. Russell, *J. Electroanal. Chem.*, **160**, 47 (1984), with permission from Elsevier Science.]

ratus for this experiment is shown in Figure 17.2.3. The potential is modulated between one where the species of interest is absent and one where it is electrochemically generated. Thus the technique allows detection of the generated species while discriminating against the solvent and dissolved species, whose IR absorbances are not affected by the potential modulation. Modulation rates are generally limited to a few Hz, because the high resistance of the thin layer of solution between electrode and window results in a large cell time constant.

Most modern IR spectrometers exploit the multiplex advantages of Fourier transform (FT) approaches. The corresponding IR-SEC technique is SNIFTIRS, for *subtractively normalized interfacial Fourier transform infrared spectroscopy*.[3] The apparatus is shown schematically in Figure 17.2.4. The monochromator is replaced by an interferometer, and the signal is an interferogram, representing detected intensity as a function of mirror position in the interferometer. Because modern FTIR spectrometers can record interferograms in milliseconds, many interferograms can be recorded and signal-averaged. By inverse Fourier transformation, the averaged result is converted into a conventional infrared spectrum. Rather than modulating between two potentials, spectra are obtained separately at two potentials,
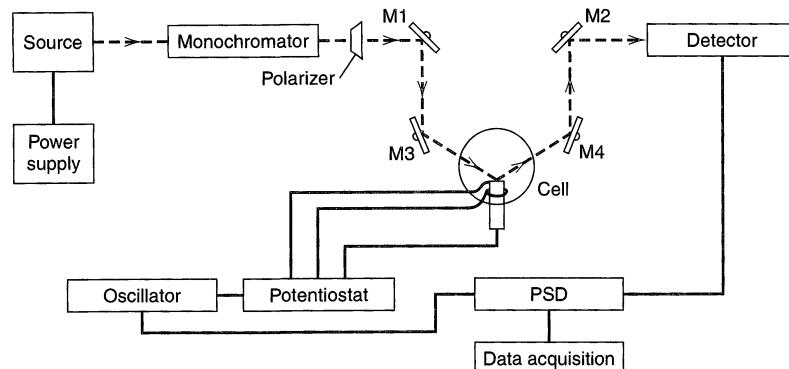
Figure 17.2.3   Block diagram for the instrumentation in an EMIRS experiment. The oscillator varies the potential of the electrode and provides a reference signal to the phase-sensitive detector (PSD). The modulated IR signal from the detector is also fed to the PSD. [Reprinted from J. K. Foley, C. Korzeniewski, J. L. Daschbach, and S. Pons, *Electroanal. Chem.*, **14**, 309 (1986), by courtesy of Marcel Dekker, Inc.]

---

[3] The same method is sometimes called PDIRS (for *potential difference infrared spectoscopy*) or SPAIRS (for *single potential alteration infrared spectroscopy*).
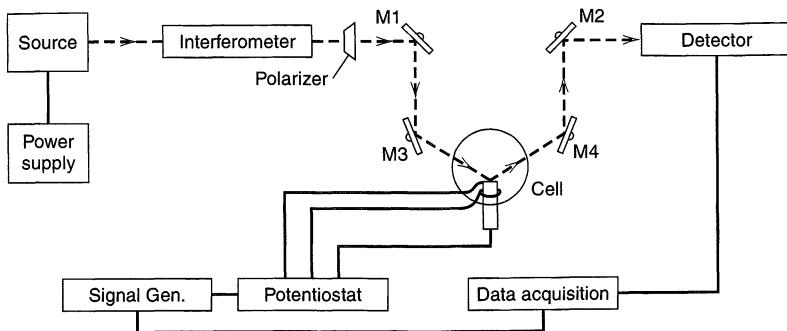
Figure 17.2.4 Block diagram for a SNIFTIRS instrument. The source, interferometer, detector, and data acquisition usually are in a commercial FTIR instrument. [Reprinted from J. K. Foley, C. Korzeniewski, J. L. Daschbach, and S. Pons, *Electroanal. Chem.*, **14**, 309 (1986), by courtesy of Marcel Dekker, Inc.]

one where the electrochemical process of interest is happening and one where it is not. Subtraction of absorbances at corresponding wavelengths gives the SNIFTERS spectrum.

Still another approach involves modulation of the polarization of the incident radiation between the *p*- and *s*-polarized waves with a photoelastic modulator (Figure 17.2.5). Only *p*-polarized light is surface-sensitive, while the randomly oriented solution molecules absorb *p*- and *s*-polarized to the same extent. This technique is called IRRAS, for *infrared reflection absorption spectroscopy*. In IRRAS, the electrode potential remains fixed during acquisition of the spectrum. FTIR spectrometers can also be used in the IRRAS configuration. Because the final result from IRRAS represents only the surface layer at a fixed potential, it has the appearance of a normal IR absorption spectrum. In contrast, the other modulation and difference techniques discussed here typically give spectra with positive and negative peaks, because the background signal is not fully removed, but instead contributes, with a negative sign, to the final result.

The IR absorption probability per molecule can be significantly increased (by a factor of 10–50) when thin (~10 nm) films of certain metals, like Ag and Au, are evaporated on the surface to form an island structure that produces sites for adsorption of the substance
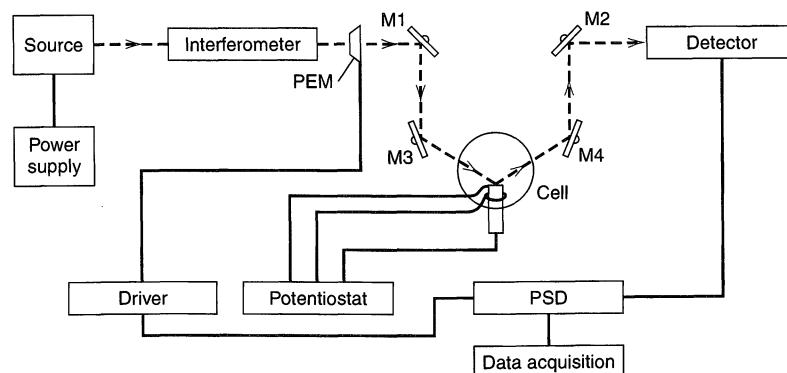
Figure 17.2.5 Block diagram for an IRRAS instrument with an FT spectrometer. The photoelastic modulator (PEM) is a crystal, such as ZnSe, whose refractive index can be changed by application of a strain by a piezoelectric transducer, thus modulating the radiation between *s*- and *p*-polarization. [Reprinted from J. K. Foley, C. Korzeniewski, J. L. Daschbach, and S. Pons, *Electroanal. Chem.*, **14**, 309 (1986), by courtesy of Marcel Dekker, Inc.]

of interest (61). This phenomenon, which is related to a more widely-studied effect in Raman spectroscopy (Section 17.2.2), results from an enhanced optical electric field through coupling of the radiation via modes in the metal and from increased polarizability of the molecules caused by chemisorption. This technique is called *surface-enhanced infrared absorption* (SEIRA).

Infrared methods have been used to study adsorbed species (reactants, intermediates, products), to examine species produced in the thin layer of solution between electrode and window, and to probe the electrical double layer. These approaches have been especially useful with species that have a high infrared absorption coefficients, like CO and CN^-. In favorable cases, information about the orientation of an adsorbed molecule and the potential dependence of adsorption can be obtained. For example, the SNIFTIRS spectrum obtained with a 0.5 mM aqueous solution of p-difluorobenzene in 0.1 M $HClO_4$ at a Pt electrode is shown in Figure 17.2.6 (62). The spectrum results from both dissolved (positive $\Delta R/R$-values) and surface adsorbed (negative $\Delta R/R$-values) p-difluorobenzene.

One can obtain vibrational spectra of only adsorbed species by taking advantage of the nonlinear effects at the interface discussed in Section 17.1.5 in connection with SHG. In the vibrational region, the technique is called *sum frequency generation* (SFG) and is carried out by irradiating the electrode/solution interface with a visible beam at a fixed frequency,
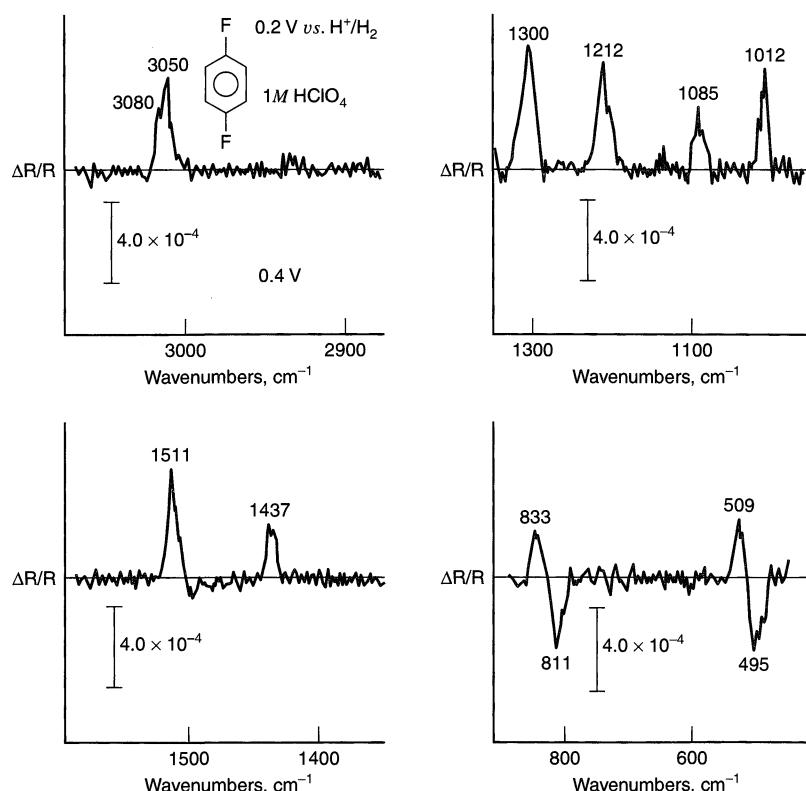
Figure 17.2.6   SNIFTIRS spectra of p-difluorobenzene in 1 M $HClO_4$ at a Pt electrode in different wavenumber regions. Each curve is a difference between spectra recorded at 0.2 and 0.4 V *vs.* NHE. The negative peaks correspond to spectral features dominant at 0.4 V, and the positive ones to features dominant at 0.2 V. [Data from S. Pons and A. Bewick, *Langmuir*, **1**, 141 (1985). Figure reprinted from J. K. Foley, C. Korzeniewski, J. L. Daschbach, and S. Pons, *Electroanal. Chem.*, **14**, 309 (1986), by courtesy of Marcel Dekker, Inc.]

ω_{vis}, and a tunable infrared beam, ω_{ir}. Because of the inherent nonlinearity of the interface, a third beam at frequency $\omega_{sf} = \omega_{vis} + \omega_{ir}$ is generated when the infrared light excites a vibrational resonance corresponding to a species at the interface (63, 64). The frequency of the infrared beam is scanned, and a signal at ω_{sf} is detected. Note that while this is a form of vibrational spectroscopy, the detected light is in the visible region, not far from ω_{vis}. For example, in a study of CO adsorbed on Pt electrodes, the visible beam was at 532 nm (18,800 cm^{-1}) and the infrared beam was scanned between 1400 and 4000 cm^{-1} (65). The reflected beam was passed through a monochromator to separate the light at ω_{sf} from the reflection of the incident light at 532 nm. One can also obtain information from the polarization of the sum-frequency output with respect to that of the visible and infrared beams.

17.2.2 Raman Spectroscopy

Raman scattering experiments usually involve excitation of a sample with light that is not absorbed by the sample. Most of this light passes directly through the system or is *elastically scattered*; that is, it is scattered without a change in photon energy (the *Rayleigh effect*). However, some photons exchange energy with the sample and are *inelastically scattered*, with a change in wavelength reflecting the loss or gain in energy. This process is the *Raman effect* (66, 67), and it provides much qualitative information about the sample from the characteristic changes in energy observed in the scattered photons.

The scattering process can be viewed in the manner depicted in Figure 17.2.7a. The incident photon can be imagined as raising a molecule to a "virtual state," which is a nonstationary state of the system. Immediate reemission without loss of energy effects Rayleigh scattering, and reemission to a final state other than the original state gives Raman scattering. Note that the Raman effect will produce light with *discrete energy differences* relative to the energy of incident light. These differences correspond to quanta of the vibrational normal modes of the molecule. Usually one studies the *Stokes lines*, which are Raman emissions at lower energy than the excitation energy. However, the scattered photon can also have more energy than the incident light by being scattered from a system with some initial vibrational activation. This *anti-Stokes* branch is generally less useful because it is usually of lower intensity.

The probability of Raman scattering depends on certain selection rules, but under most circumstances is quite small; hence experiments must involve intense light sources and
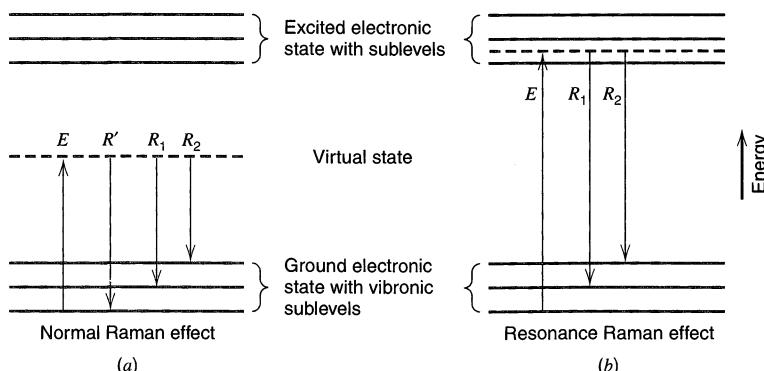
Figure 17.2.7   Schematic views of Raman scattering. Excitation (E) to a nonstationary virtual state is followed by Rayleigh scattering (R') with no change in energy, or Raman scattering (R_1 and R_2) with energy changes equal to vibrational quanta. (*a*) The normal Raman effect involves excitation in a nonabsorbing region. (*b*) The resonance Raman effect involves excitation very near an allowed absorption transition.

high sample concentrations. Raman spectroscopy provides molecular vibrational informa-
tion complementing that of IR spectroscopy. Because it is carried out with excitation and
detection in the visible region of the spectrum, it can be employed in electrochemical cells
with glass windows and aqueous solutions, both of which are strongly absorbing in the IR
region. A block diagram of a Raman spectrometer is shown in Figure 17.2.8. Since Raman
experiments always involve the measurement of small energy shifts on the order of 100 to
3000 cm^{-1} from the excitation energy, a monochromatic source is essential. Since high in-
tensity is also required, lasers are universally used. A high-resolution double or triple
monochromator is employed to separate the Raman lines from the intense Rayleigh line. In
electrochemical situations, measurements are usually made on species within the operating
cell. Dissolved species or those adsorbed on an electrode surface can be monitored.
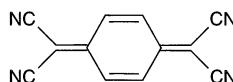
Most Raman experiments in electrochemical systems utilize techniques that result in
large enhancements of the signal. In one approach, known as *resonance Raman spec-
troscopy* (RRS) (67), very large enhancements in the scattering occur when the excitation
wavelength corresponds to an electronic transition in the molecule. Molecules adsorbed
on certain surfaces (e.g., silver or gold) also show a large enhancement in the Raman sig-
nal; this effect is employed in *surface enhanced Raman spectroscopy* (SERS) (68–70).

A schematic view of the process that occurs in RRS is given in Figure 17.2.7*b*. Exci-
tation is made within an absorption band to a virtual state nearly of the same energy as
one of the stationary states of the system. The near-resonance electronic interaction en-
ables the molecule to interact much more effectively with the light and provides an en-
hancement factor of 10^4 to 10^6 in scattering probability.

A good example of the application of RRS to the examination of a dissolved species
generated electrochemically is represented by the spectra in Figure 17.2.9 which were
recorded for the system (71),

$$TCNQ + e \rightleftharpoons TCNQ^{-} \qquad (17.2.1)$$

where TCNQ is tetracyanoquinodimethane:

The anion radical was generated by coulometric bulk reduction of a TCNQ solution. The
extremely high information content of these spectra is readily apparent. They can be used
as diagnostics and can be interpreted, in much the same manner as infrared spectra, to
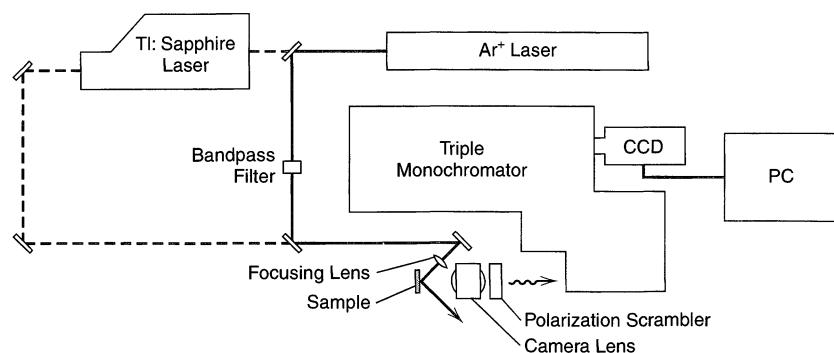
Figure 17.2.8   Block diagram of Raman spectrometer with a choice of laser excitation and
detection with a charge-coupled device (CCD). [Reprinted with permission from J. E. Pemberton in
"The Handbook of Surface Imaging and Visualization," A. T. Hubbard, Ed., CRC, Boca Raton, FL,
1995, p. 647. Copyright CRC Press, Inc., Boca Raton, FL.]
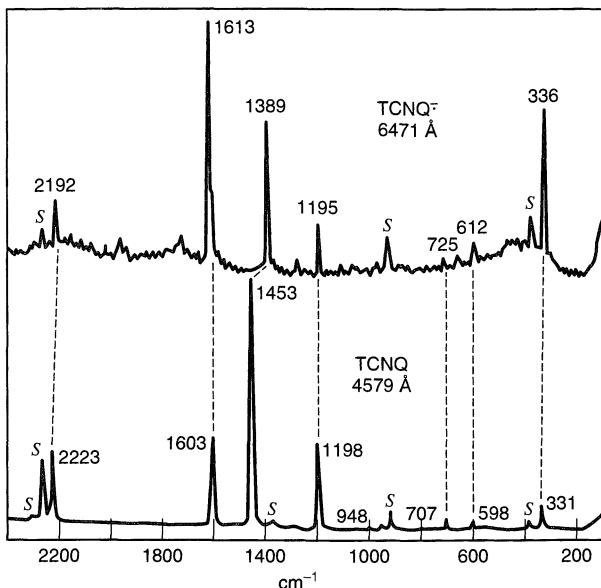
Figure 17.2.9 Resonance Raman spectra of TCNQ and electrogenerated TCNQ⁻, which was coulometrically produced by reduction at -0.10 V *vs.* SCE. Initially, TCNQ was present at 10.9 mM in acetonitrile containing 0.1 M tetra-n-butylammonium perchlorate. Excitation wavelengths are indicated. Abscissa shows frequency shift with respect to excitation line. S denotes a normal Raman band of the solvent. [Reprinted with permission from D. L. Jeanmaire and R. P. Van Duyne, *J. Am. Chem. Soc.*, **98**, 4029 (1976). Copyright 1976, American Chemical Society.]

identify unknown electrolysis products (72). Alternatively, they can be interpreted in fundamental terms for the information they contain about the electronic and vibrational properties of the species under examination (71, 73, 74).

Raman data can also be obtained on species in the diffusion layer at a faradaically active electrode (73, 75). Whole spectra are gathered as the electrode is cycled through a repeated double-step waveform involving, for example, a short period of forward electrolysis and a long reversal step.

Alternatively, transients in Raman intensity are available by observing one selected line for the duration of the experiment. An example (75) is shown in Figure 17.2.10a. Since this result is the average signal from 1000 cycles of a 50-ms period of forward electrolysis and a 950-ms reversal, the whole experiment required 1000 s. The Raman intensity quantifies the total amount of the product generated, thus it is analogous to the absorbance-time transient observed in a transmission experiment and the charge-time curve in chronocoulometry. The forward phase should yield a signal proportional to $t^{1/2}$, and reversal should produce an intensity proportional to $t^{1/2} - (t - \tau)^{1/2}$, where τ is the duration of the forward phase. The two plots should have the same slope (Problem 17.8). The graph in Figure 17.2.10b verifies the expectations. Note that these experiments are extremely selective, because the monitored Raman line is so narrow that interference from another species in solution is improbable.

Most frequently, Raman techniques are used to examine species adsorbed on surfaces. Although it is possible under favorable circumstances to obtain spectra of monolayers with unenhanced, normal Raman (NR) spectroscopy (76), such studies involve considerable difficulty, and the vast majority of reports are based on the SERS technique. In SERS the Raman signal is enhanced from 10^5 to 10^6 times when the adsorbed mole-
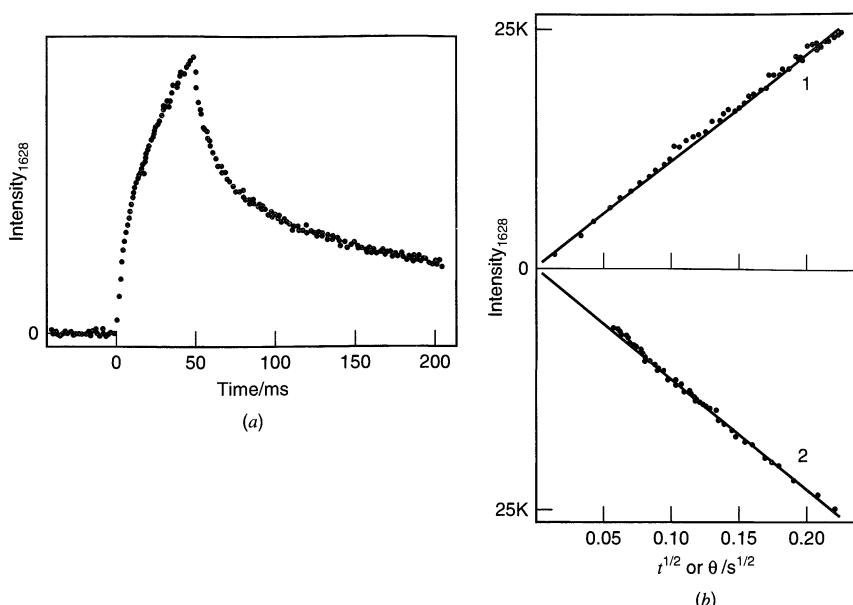
Figure 17.2.10 (a) Resonance Raman intensity transient for the cation radical of N,N,N',N'-tetramethyl-p-phenylenediamine (TMPD) produced in a 50-ms step and rereduced in a 950-ms step. Average of 1000 experiments. Intensity is for the 1628 cm^{-1} line of TMPD$\cdot^{+}$ under excitation at 6120 Å. [TMPD] = 3.0 mM in CH$_3$CN. (b) Plots of the forward-phase intensity (1) vs. $t^{1/2}$ and reverse-phase intensity (2) vs. $\theta = t^{1/2} - (t - \tau)^{1/2}$. Data from transient in (a). [From D. L. Jeanmaire and R. P. Van Duyne, *J. Electroanal. Chem.*, **66**, 235 (1975), with permission.]

cule is on a roughened surface of Ag, Cu, or Au. In the first experimental observation of this effect, with pyridine on Ag (77), a silver electrode was roughened electrochemically (to increase the surface area) by repeatedly scanning or stepping the potential of the electrode between regions where oxidation and reduction occurs (called in the SERS literature an "oxidation-reduction cycle" or ORC). This process creates a surface with asperities on the nanometer and atomic scales. The serendipitous choice of Ag and the roughening step in the original experiment turned out to be critical for the surface enhancement phenomenon. That a large enhancement effect was occurring under these experimental conditions was realized only later (78, 79), and the origin of the enhancement and applications of SERS in electrochemical systems have been the subject of numerous subsequent studies (68–70, 80–82).

The surface enhancement is ascribed to the occurrence of two separate effects, electromagnetic and chemical (70). The electromagnetic effect arises from small surface structures arising in the ORC that cause strong local increases of the electric fields of the excitation and scattered radiation via surface plasmon waves. The chemical effect is attributed to interactions between the adsorbed molecule and the metal surface which lead to electronic (charge-transfer) transitions between molecule and metal. The result is a resonance-Raman-like effect. Since both effects operate only over very small distances, SERS is specific for molecules at the electrode surface.

As an example of a SERS study in an electrochemical environment, consider the behavior of Os(NH$_3$)$_5$py^{3+} (py = pyridine) adsorbed on a silver electrode (83). In a typical experiment, the electrode was immersed in a solution containing 0.1 mM Os(NH$_3$)$_5$py^{3+}, 0.1 M NaBr, and 0.1 M HCl, and an ORC was carried out. SERS spectra were recorded with excitation at 647 or 514 nm as a function of electrode potential over the range −150
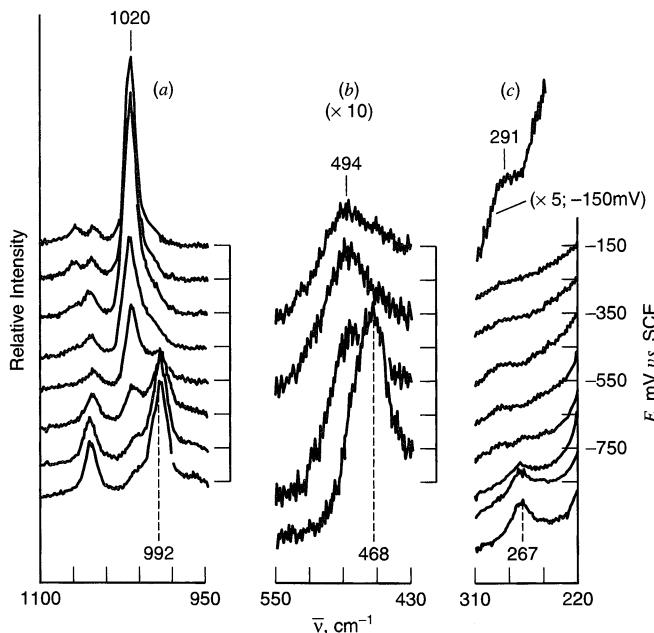
Figure 17.2.11 SER spectra for $Os(NH_3)_5py^{3+}$ adsorbed on an Ag electrode as a function of potential (scale at right) in three different wavelength regions with 514.5 nm laser excitation. Solution contained 0.1 mM $Os(NH_3)_5py^{3+}$, 0.1 M NaBr, and 0.1 M HCl. [Reprinted with permission from S. Farquharson, M. J. Weaver, P. A. Lay, R. H. Magnuson, and H. Taube, *J. Am. Chem. Soc.*, **105**, 3350 (1983). Copyright 1983, American Chemical Society]

to −850 mV *vs.* SCE (Figure 17.2.11). At −150 mV (topmost spectra), the adsorbed species is present in the +3 state and shows, for example, a prominent peak at 1020 cm^{-1}, ascribed to the symmetric pyridine ring breathing mode. Upon reduction at more negative potentials, such as −750 mV, this peak disappears and is replaced by one at 992 cm^{-1} (and another peak at 1053 cm^{-1} grows in) characteristic of this complex in the +2 state. These results were reversible with electrode cycling, and a plot of peak heights at 1020 and 992 cm^{-1} as a function of potential could be correlated to the redox potential of the +3/+2 couple. In this system, the changes in the Raman bands of the pyridine ligand can be attributed to changes in the oxidation state of the metal center, but adsorbed molecules show SERS spectra that are functions of the electrode potential even when changes in oxidation state do not occur. For example, for methanol adsorbed on Ag, the position and relative intensities of the C–O and C–H vibrational bands change with the applied potential over the range of −0.05 to −1.0 V (69).

A limitation to the application of SERS to electrochemical systems is the specificity of the enhancement effect to Ag, Au, and Cu. However, since the electromagnetic part of the enhancement is maintained over distances of several nanometers, it has been possible to coat a SERS active metal with a thin layer of another metal that is exposed to the adsorbing molecules and still obtain enhanced signals (69). For example, by constant-current deposition, it is possible to deposit pinhole-free layers of Pd on Au with a thickness corresponding to 3.5 monolayers and to study the adsorption of species on the Pd by SERS. The spectra of adsorbed benzene on such an electrode are shown in Figure 17.2.12 (84). The symmetric ring-breathing mode of benzene adsorbed on Pd appears at 950 cm^{-1}, shifted considerably from that found either for liquid benzene (992 cm^{-1}) or for benzene adsorbed on Au (975 cm^{-1}). Deuterated benzene (C_6D_6) behaves similarly and shows the expected shift in the band to lower frequency. The attenuation of the enhancement effect with thickness of the Pd overlayer was reported to be only a factor of 4–5 for thicknesses of 3–30 monolayers.

An interesting recent finding (85) from observations of individual silver particles bearing adsorbed molecules (e.g., rhodamine 6G) is that "hot" particles with a size range
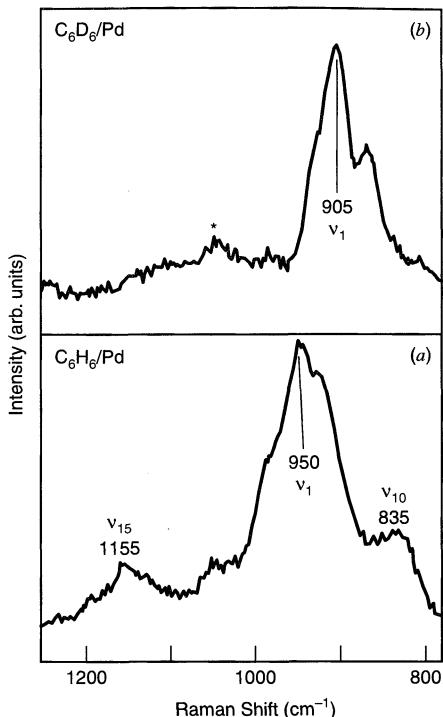
Figure 17.2.12 SER spectra for (a) benzene and (b) benzene-d_6 on a Pd film, 3.5 monolayers thick, on roughened Au. The potential was -0.2 V *vs.* SCE in an aqueous 0.5 M H_2SO_4 solution containing 10 mM benzene. Excitation, 647.1 nm at 20–40 mW. The feature marked by an asterisk is ascribed to an impurity. [Reprinted with permission from S. Zou, C. T. Williams, E. K.-Y. Chen, and M. J. Weaver, *J. Am. Chem. Soc.*, **120**, 3811 (1998). Copyright 1998, American Chemical Society.]

of 80–100 nm showed much larger enhancement factors ($\sim 10^{14}$) with excitation at 514.5 nm than those typical for a large roughened surface. This enormous enhancement permitted the observation of Raman spectra from single molecules.

17.3 ELECTRON AND ION SPECTROMETRY

Powerful surface analysis techniques, based on the detection of charged particles (electrons and ions) following irradiation of the sample with photons, electrons, or ions, have been developed, largely for the characterization of materials and microelectronics (2, 86–90). Some of these techniques and their general principles are illustrated and listed in Figure 17.3.1. Important considerations include the size of the irradiating spot (which governs the spatial resolution of the technique), the sensitivity (minimum detectable amounts), and the depth of the zone that is sampled. These are compared for various techniques in Figure 17.3.2.

A common feature of all of these methods is that measurement is carried out in *ultra-high vacuum* (UHV) ($<10^{-8}$ torr); thus any electrode surface to be examined must be removed from the cell, possibly rinsed, dried of solvent, and then place *in vacuo*. Electrodes cannot be examined *in situ*, since liquids will absorb and block the beams of electrons and ions. The sample must be transferred into a system where there is no electrolyte. This always raises the possibility that the analyzed interface differs significantly from the one in the cell, which is the actual point of interest. For example, hydrated solids will lose water in vacuum and may change composition. Also, exposure of the electrode to the air during transfer can cause oxidation of surface species. Special apparatus has been designed to minimize the problems of exposure to the atmosphere by allowing the sample to be removed from the cell in an inert atmosphere and moved directly into the UHV (Figure 17.3.3), but one must always be alert to artifacts engendered by the transfer.
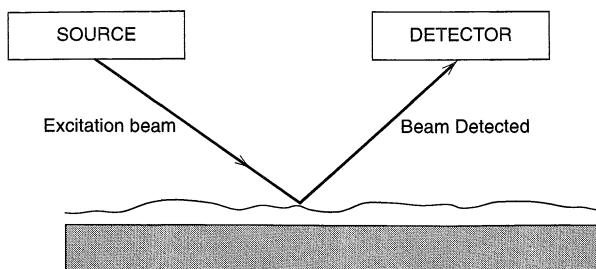
Figure 17.3.1 General principle of ultrahigh vacuum surface spectroscopic techniques. [From A. J. Bard, "Integrated Chemical Systems," Wiley, New York, 1994, p. 102, with permission.]

Technique	Abbreviation	Excitation	Detection
X-ray photoelectron spectroscopy	XPS	Photons (X-ray)	Electrons
UV photoelectron spectroscopy	UPS	Photons (UV)	Electrons
Auger electron spectroscopy	AES	Electrons	Electrons
Low-energy electron diffraction	LEED	Electrons	Electrons
High-resolution electron energy loss spectroscopy	HREELS	Electrons	Electrons
Rutherford backscattering	RBS	H^+ or He^+ ions	H^+ or He^+ ions
Secondary ion mass spectroscopy	SIMS	Ions	Ions
Laser desorption mass spectroscopy	LDMS	Photons	Ions
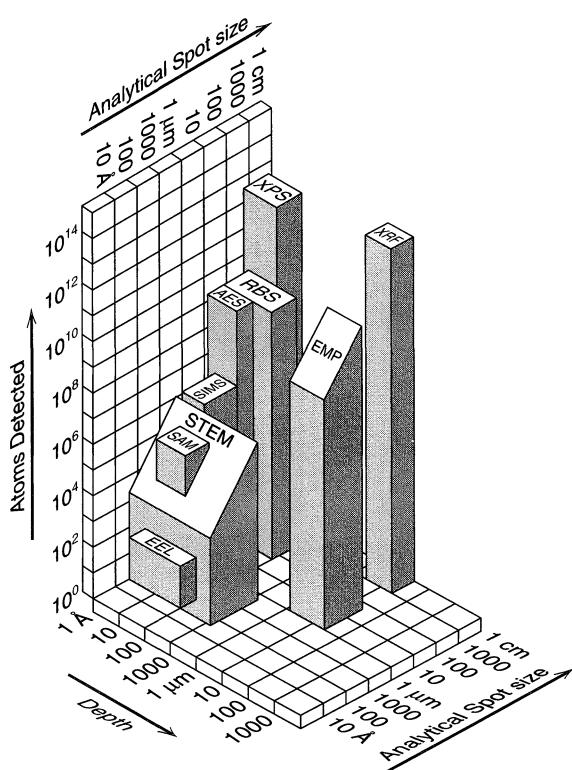
Figure 17.3.2 Detection limits, sampling depth, and spot size for several surface spectroscopic techniques. XRF (x-ray fluorescence); EMP (electron microprobe); EEL (electron energy loss), SAM (scanning Auger microprobe); STEM (scanning transmission electron microscopy). Other abbreviations in Figure 17.3.1. This figure is meant to provide a graphic summary of the relative capabilities of different methods; modern instruments have somewhat better quantitative performance characteristics than the 1986 values given here. [From A. J. Bard, "Integrated Chemical Systems," Wiley, New York, 1994, pp. 103, with permission; adapted from "Texas Instruments Materials Characterizations Capabilities," Texas Instruments, Richardson, TX, 1986, with permission.]
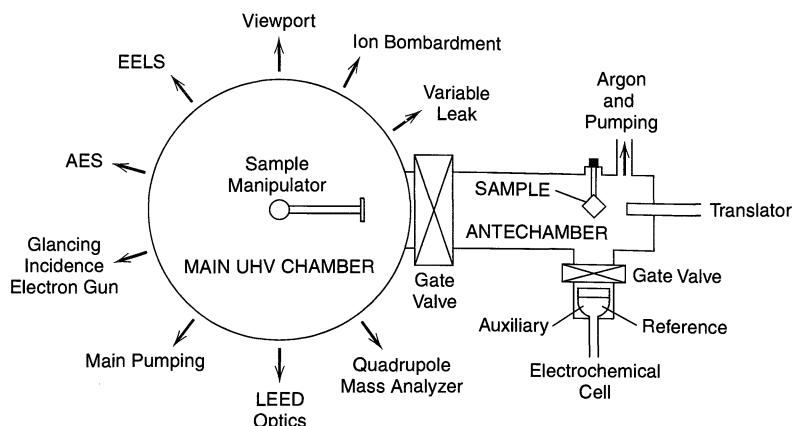
Figure 17.3.3 Schematic diagram of apparatus that allows electrochemical preparation of sample in an antechamber under argon and then direct transfer into a UHV chamber for surface spectroscopic examination. [Reprinted from A. T. Hubbard, E. Y. Cao, and D. A. Stern in "Physical Electrochemistry," I. Rubinstein, Ed., Marcel Dekker, New York, 1995, Chap. 10, by courtesy of Marcel Dekker, Inc..]

17.3.1 X-Ray Photoelectron Spectroscopy (88, 91–97)

If one irradiates a sample with monochromatic X-rays (e.g., the Al K_α line at 1486.6 eV or the Mg K_α line at 1253.6 eV), electrons will be ejected from the sample into the surrounding vacuum. Some of these electrons are removed from deep core levels of atoms making up the lattice, and they are of particular interest to us now (Figure 17.3.4a). If the atoms are sufficiently close to the surface (<20 Å), there is a high probability that the electrons will escape without being inelastically scattered and suffering the consequent loss in kinetic energy. We are interested in the distribution of unscattered electrons *vs.*
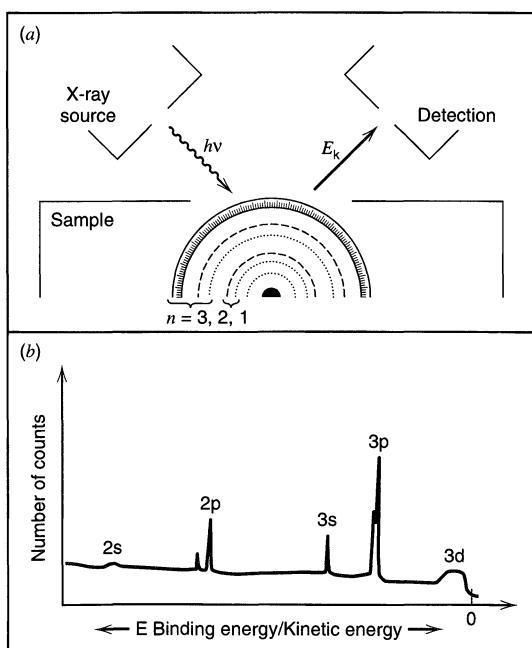
Figure 17.3.4 Schematic representation of (*a*) the electron emission process and (*b*) the resulting photoelectron spectrum. One X-ray photon will cause ejection of one electron. The resulting kinetic energy of that electron depends upon which core or valence electron has been ejected. [From J. J. Pireaux and R. Sporken in M. Grasserbauer and H. W. Werner, Eds., "Analysis of Microelectronic Materials and Devices," Wiley, New York, 1991, with permission.]

their kinetic energy *in vacuo*, that is, the *photoelectron spectrum*. This approach is called *X-ray photoelectron spectroscopy* (XPS).

The energy of the photon that ejects an electron must be conserved and can be separated into four terms (95):

$$hv = E_b + E_k + E_r + \phi_{sp} \qquad (17.3.1)$$

The two most important of these are the kinetic energy E_k of the electron in the spectrometer and the energy required to remove the electron from the initial state, that is, the *binding energy*, E_b. Since the value of E_b is discrete and is well-defined for different atomic levels, one can expect discrete kinetic energies E_k corresponding to these levels; hence the photoelectron spectrum shows a peak corresponding to each level (Figure 17.3.4*b*). The binding energy associated with a given peak is approximately $hv - E_k$. Minor corrections for the *recoil energy*, E_r, at the site of ejection (usually very small) and for the *spectrometer work function*, ϕ_{sp} (3–4 eV), must be applied for accurate binding energy assignment. A schematic diagram of an X-ray photoelectron spectrometer is shown in Figure 17.3.5.

From an analytical standpoint, the utility of XPS is that it provides atomic information about the surface region without seriously damaging that region. Some information about oxidation states is also available, because the binding energy of an electron in a given orbital is affected slightly by its electronic environment. Thus, one can see, for example, separate peaks for 1s electrons derived from nitrogen in its amide and nitro forms (see below). In general, the surface and thin-film analytical tools discussed here are not very informative about the chemical forms in which atoms are present, and the ability of XPS to supply such information has made it useful for electrochemical applications.

XPS signals can be detected for atoms throughout the periodic table, except helium and hydrogen. The sensitivity limits are on the order of 0.1 atomic percent, except for lighter elements, which are often detectable only above 1 to 10%.

The characterization of anodic oxide films is one area where XPS has been extremely useful. Figure 17.3.6 contains spectra for platinum samples that have been oxidized in three different ways (98). Curve *a* represents a sample reduced in H_2, then exposed to O_2
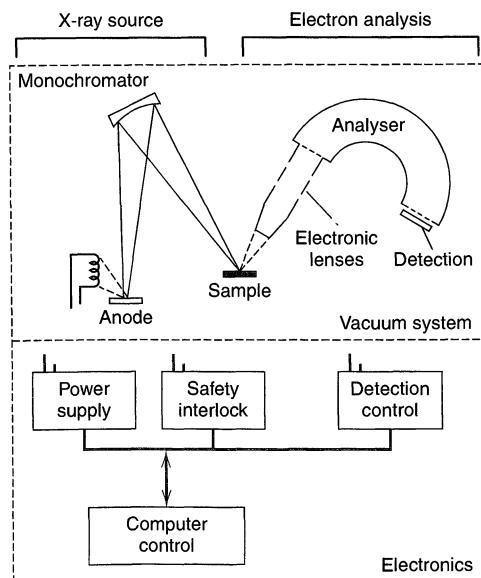
Figure 17.3.5   Schematic diagram of X-ray photoelectron spectrometer with an electrostatic hemispherical analyzer. The detector is usually a channel electron multiplier. [From J. J. Pireaux and R. Sporken in M. Grasserbauer and H. W. Werner, Eds., "Analysis of Microelectronic Materials and Devices," Wiley, New York, 1991, with permission.]
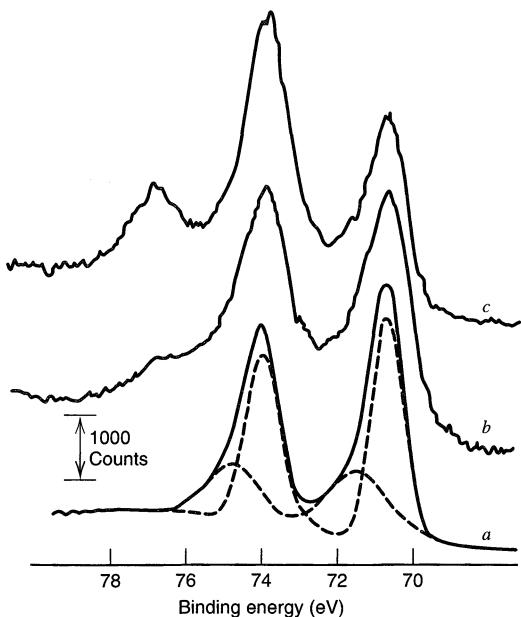
Figure 17.3.6 XPS responses for Pt 4f levels. Platinum foil treated by (*a*) H_2 reduction at 400°C for 10 hr, H_2 desorption at 400°C (10^{-5} torr) for 5 hr, then exposure to pure O_2 (1 atm) at ambient temperature, (*b*) electrochemical oxidation at +1.2 V, and (*c*) at +2.2 V *vs.* SCE. For (*b*) and (*c*), electrolyte was 1 *M* $HClO_4$. Curves have been displaced vertically for clarity. [Reprinted with permission from K. S. Kim, N. Winograd, and R. E. Davis, *J. Am. Chem. Soc.*, **93**, 6296 (1971). Copyright 1971, American Chemical Society.]

at ambient temperature. The two peaks arise from Pt 4f(7/2) and 4f(5/2) orbitals, and each is resolved into two components. The larger is assigned to platinum, and the smaller to platinum associated with adsorbed oxygen atoms. The electrochemically oxidized samples (curves *b* and *c*) show structure at higher binding energies, manifesting a more positive platinum center. This feature is assigned to the oxides PtO and PtO_2. Resolution of the curves permits an estimate of the relative contributions of the various forms as shown in Table 17.3.1.

XPS peaks are often broad and show severe overlap like that present in Figure 17.3.6, so curve resolution is widely practiced. Obviously it must be done with care, preferably with foreknowledge of the actual single-component spectra of the substances to which components in mixtures are assigned.

Another electrochemical domain to which XPS has made major contributions is surface modification (Chapter 14). Figure 17.3.7*a* contains data showing the effect of treating a glassy carbon surface with γ-aminopropyltriethoxysilane to produce an "amine functionalized" carbon surface (99). The rise of the silicon and nitrogen peaks and the

TABLE 17.3.1 Estimated Compositions of Oxidized Platinum Surfaces[a]

| Species | Binding Energy, eV | | Relative Peak Areas[b] | | |
	4f (7/2)	4f (5/2)	+0.7 V	+1.2 V	+2.2 V
Pt	70.7	74.0	56	39	34
PtO_{ads}	71.6	74.9	39	37	24
PtO	73.3	76.6	<5	24	22
PtO_2	74.1	77.4	0	0	20

[a]From K. S. Kim, N. Winograd, and R. E. Davis, *J. Am. Chem. Soc.*, **93**, 6296 (1971).

[b]Oxidation carried out at indicated potential (*vs.* SCE) for 3 min.
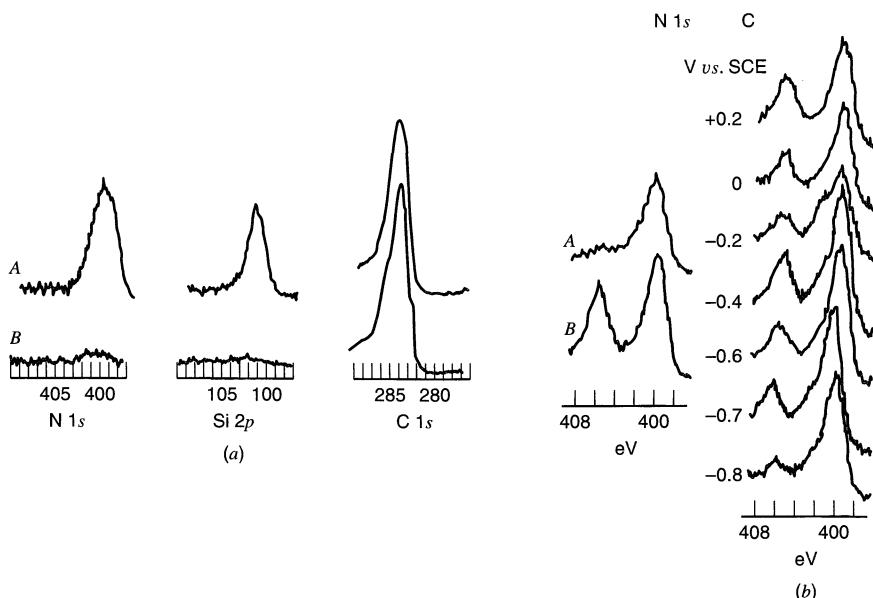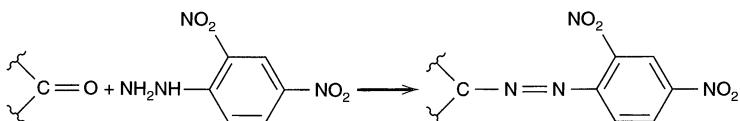
Figure 17.3.7 XPS responses for derivatized glassy carbon electrodes. (*a*) *Curves A*, following treatment with γ-aminopropyltriethoxysilane. *Curves B*, unreacted surfaces. (*b*) Nitrogen 1*s* spectra for surfaces treated with DNPH: *A*, derivatized electrode cycled between 0 and − 1.2 V *vs.* SCE; *B*, fresh modified electrode; *C*, a series of samples held at indicated potentials for 3 min. [Reprinted with permission from C. M. Elliott and R. W. Murray, *Anal. Chem.*, **48**, 1247 (1976). Copyright 1976, American Chemical Society.]

drop in carbon response show the presence of the reagent on the surface. This kind of information is extremely useful in following a surface synthesis.

A similar case (99) is involved in Figure 17.3.7*b*. Dinitrophenylhydrazine (DNPH) was reacted with the surface to produce what is thought to be a hydrazone derivative of a quinoidal surface site:

The XPS spectrum in Figure 17.3.7*b*, *Curve B*, shows separate peaks due to nitro nitrogen at high binding energy and the less oxidized nitrogen at lower energy. Holding the electrode at potentials more negative than about −0.8 V *vs.* SCE eliminates the peak due to the nitro form and elevates the remaining peak; thus it appears that the nitro functions are reduced in a faradaic process.

Considerable attention has been devoted recently to the phenomenon of *underpotential deposition* of metal adatoms (Section 11.2.1) and to the nature of the interaction between the adatom and its substrate. In Figure 17.3.8, one can see that the binding energy of Cu 2*p*(3/2) electrons for Cu adatoms on Pt differs markedly from the value for bulk copper (100, 101). The *negative* shift in binding energy suggests that the deposited copper is not in an oxidized form, but instead is metallic atom in a distinctive electronic environment.

The principles and apparatus for *ultraviolet photoelectron spectroscopy* (UPS) are similar to those of XPS, except that excitation is with an ultraviolet source, usually a He

Cu $2p_{3/2}$

(a)

(b)

935.0   933.0   931.0

Binding energy/eV
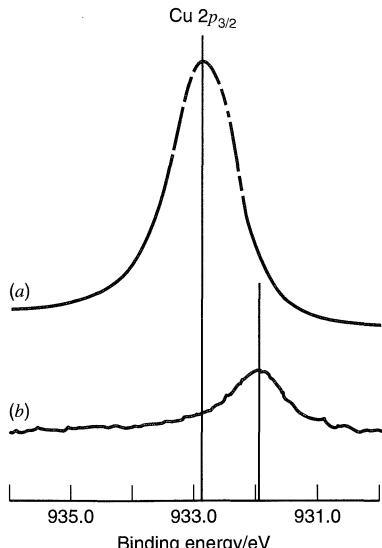
Figure 17.3.8   XPS responses for copper. (a) Bulk metal cleaned by etching with beam of Ar^+ *in situ*. (b) Copper deposited at underpotential on platinum. [From J. S. Hammond and N. Winograd, *J. Electroanal. Chem.*, **80**, 123 (1977), with permission.]

discharge. Since the excitation energies are much lower (e.g., for He, 21.2 and 40.8 eV), UPS mainly involves valence band electrons.

17.3.2   Auger Electron Spectrometry (91–93, 96, 102, 103)

If a vacancy is created in an atomic core level, for example, by irradiation with X-rays, as above, or with electrons, then an electron from an upper level can be expected to fill the hole. Figure 17.3.9 is a schematic view of the process in which a K-shell vacancy in silicon is filled by an L_1 electron. The energy difference liberated by this relaxation is 1690 eV, and it can be released wholly in the form of a photon (*X-ray fluorescence*) or by ejecting an *Auger electron* from the atom. In the example of Figure 17.3.9, the Auger electron comes from the $L_{2,3}$ shell.
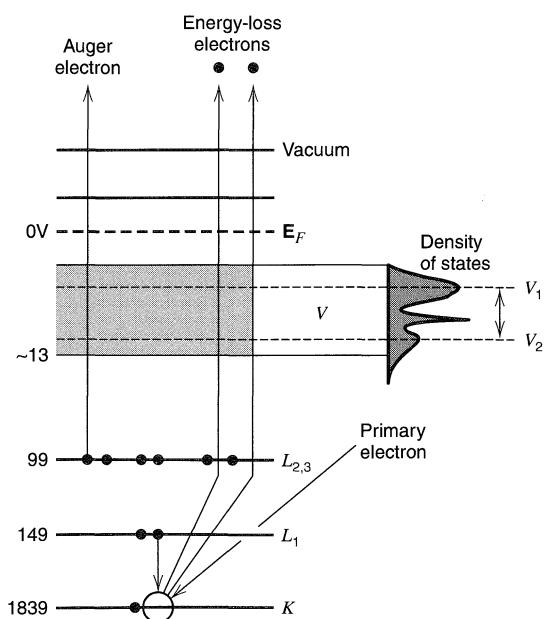
Figure 17.3.9   Schematic view of the Auger emission process from silicon. The atom is ionized initially by an incident electron. That electron and one from the K shell leave the sample as "energy loss electrons." The energies of the levels relative to the Fermi level, E_F (Sections 3.6.3 and 18.2), are given on the left. [From C. C. Chang in "Characterization of Solid Surfaces," P. F. Kane and G. B. Larrabee, Eds., Plenum, New York, 1974, Chap. 20, with permission.]

The required energy loss of 1690 eV is divided into the energy required to remove the electron from the sample (mostly its binding energy) and the kinetic energy it retains upon entering the vacuum. Since the total energy of the transition and the binding energy are well-defined values, the kinetic energy of the Auger electron *in vacuo* is also well-defined. By measuring the distribution of electrons *vs.* kinetic energy, one can obtain a spectrum showing sharp peaks at the discrete Auger energies. Each Auger line is characteristic of the originating atom and can be used analytically to indicate the presence of that species.

Auger transitions are conventionally labeled with a three-letter notation indicating, respectively, the shell of the primary vacancy, the shell of the filling electron, and the shell from which the Auger electron was emitted. Thus the transition in Figure 17.3.9 would be called the KL_1L_2 or KL_1L_3 process. Any given atom may show several Auger transitions, hence several lines in the spectrum.

If the electron is scattered inelastically during its passage through the sample, its kinetic energy *in vacuo* will differ from the characteristic Auger energy, and it will contribute only to the broad continuum on which the Auger lines are superimposed. Thus, Auger electron spectrometry (AES) is strictly a surface technique, in that atoms only within about 20 Å from the surface can contribute unscattered electrons.

In most instruments, an electron beam, which can be focused to a smaller spot size than an X-ray beam (see Figure 17.3.2), is used to excite the sample. The spectrum of emitted and scattered electrons, including Auger electrons, is analyzed according to kinetic energy in a manner that produces a derivative readout, so that the sharp Auger structure is more easily seen on the broad continuum (Figure 17.3.10).

AES signals can be seen for all elements except hydrogen and helium, but (in contrast to XPS) the line positions are insufficiently resolved to indicate the oxidation state except in very few cases. Detection limits are usually about 0.1 to 1 atomic percent. The electron beam can damage the sample in some cases.

Some instruments, called *scanning Auger microprobes* (SAM) offer two-dimensional scan control (*rastering*) of the electron beam, so that analysis can be carried out as a function of surface position. The spatial resolution is controlled by the beam diameter, which can be as small as 50 nm.

A very useful feature on most equipment is a facility for obtaining Auger response as a function of depth into a sample. This technique, called *depth profiling*, is carried out by etching the sample with a beam of high-energy ions (e.g., Ar^+) from an ion gun through a sputtering process. After etching for a period, an Auger spectrum can be recorded. Alter-
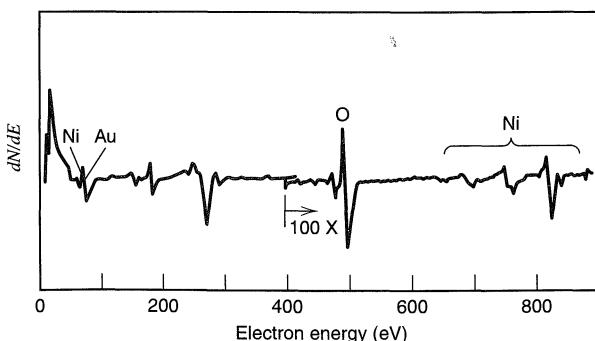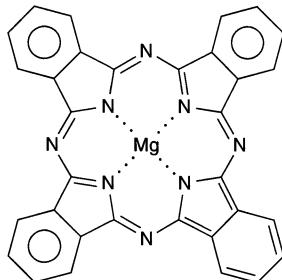
Figure 17.3.10 Derivative Auger spectrum of nickel oxide on the surface of gold-plated nickel. The oxide is sufficiently thin that the 69-eV peak of Au is visible. Additional peaks from 150 to 300 eV are from S, Cl, and C contamination of the surface. [From S. H. Kulpa and R. P. Frankenthal, *J. Electrochem. Soc.*, **124**, 1588 (1977), reprinted by permission of the publisher, The Electrochemical Society, Inc.]

natively, one can record an Auger line intensity *vs.* etching time to follow the distribution of a particular element with depth. The chief artifacts that can arise with this procedure are homogenization of the sample by the high-energy ion beam and *differential sputtering*, which involves removal of one component at a faster rate than another.

AES is widely employed for the characterization of anodic films, particularly among investigators interested in corrosion. The spectrum in Figure 17.3.10 relates to a study of the tarnishing of nickel in air, in which the Auger depth profiling method was used to measure film composition and thickness as a function of ambient conditions during exposure of the sample (104). Figure 17.3.11 contains depth profiles for an anodic film formed on GaAs (105). The results in (*a*) show that the electrochemically formed oxide region actually comprises four distinct zones with varying arsenic-to-gallium ratios. Heat treatment (Figure 17.3.11*b*) changes the profiles considerably and particularly enhances the gallium-rich surface zone. Results of this sort are useful in advancing technology that depends on the properties of films such as passivating layers or insulating barriers.

Auger techniques have also proven useful in the characterization of electrochemically induced changes in thin-film electrodes. An example concerns films (500–2000 Å thick) of magnesium phthalocyanine (MgPc) deposited over a gold contact layer on a glass substrate (106):

Since the phthalocyanines may be useful in electrocatalytic systems, their properties as electrode materials are of interest and have been studied in this manner (107–109). At
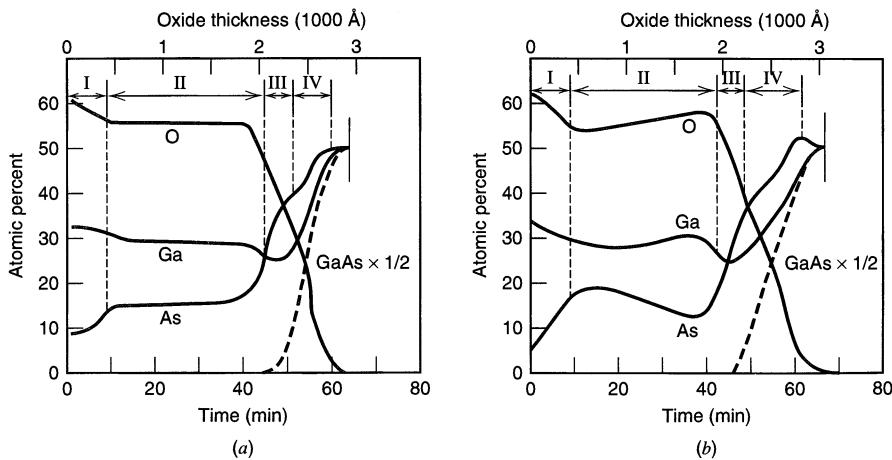
Figure 17.3.11   AES depth profiles for GaAs anodized in H_3PO_4 solutions. Ordinate has been corrected for relative Auger intensities and differential sputtering rates. Abscissa is sputtering time. Thickness scales are approximate. Roman numerals indicate different compositional regions in the oxide layer. Bulk GaAs is at rightmost limit. (*a*) From electrochemical treatment only. (*b*) With added annealing step at 250°C. [From C. C. Chang, B. Schwartz, and S. P. Murarka, *J. Electrochem. Soc.*, **124**, 922 (1977), reprinted by permission of the publisher, The Electrochemical Society, Inc.]
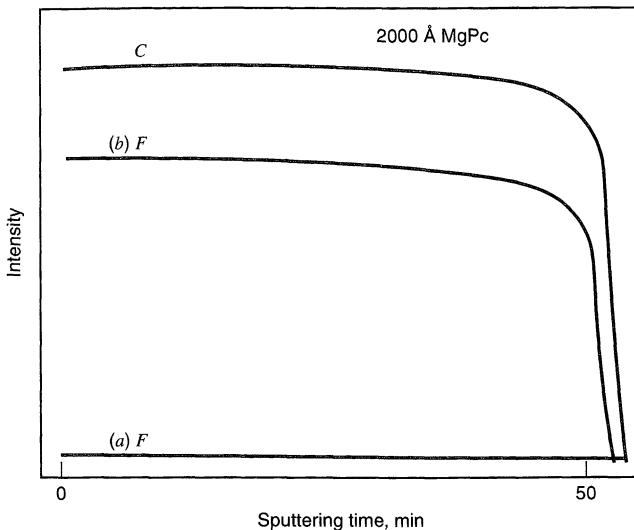
Figure 17.3.12 AES depth profiles for carbon and fluorine in 2000-Å-thick MgPc films. Carbon profiles of separate samples were normalized to a common curve. (*a*) MgPc film immersed in aqueous 0.1 *M* KPF$_6$. (b) MgPc film oxidized in 0.1 *M* KPF$_6$ solution.

potentials more positive than about 0.6 V *vs.* SCE, one generally finds that MgPc films undergo large-scale oxidation and change color. Figure 17.3.12 is a set of Auger depth profiles showing that the charges created within the film upon oxidation are counterbalanced by anions extracted from the electrolyte. Accommodating the ions probably requires rather substantial changes in lattice properties.

17.3.3 Low-Energy Electron Diffraction (90, 110–112)

Electrons traveling *in vacuo* at kinetic energies in the range from 10 to 500 eV have de Broglie wavelengths on the order of angstroms; hence one could expect a monochromatic beam of these electrons to be reflected from an ordered solid in a diffraction pattern that provides information about the structure of the solid. This effect is the basis of *low-energy electron diffraction* (LEED).

A LEED experiment differs significantly from other types of diffraction experiments, in that the probing beam cannot penetrate the sample to a distance greater than a few angstroms without being scattered inelastically and losing energy. Thus it is incapable of sampling the three-dimensional order of the solid, and any observed diffraction is due to the *two-dimensional order of the surface.* Thus LEED is a very specific tool for examining the geometric pattern of atoms on a surface, and it has been widely used for studies of adsorption from the gas phase and catalysis of gas-phase/solid-surface reactions. LEED is also employed to characterize electrode surfaces, especially single-crystal electrodes that produce well-defined diffraction patterns (90, 113–117).

Figure 17.3.13 is a schematic diagram of a typical apparatus. The chamber is always at ultrahigh vacuum ($<10^{-8}$ torr), so that the surface remains clean during the experiment. Electrons are directed toward the sample in a beam and are reflected diffractively along certain well-defined lines. The grids filter out inelastically scattered electrons (at lower energy) and then allow the diffracted ones to accelerate toward a luminescent screen. Bright spots on the screen can be observed and photographed from the viewing port. The arrangement of this system also allows AES experiments to be done by changing the signals on the grids and the energy of the electron beam. One very frequently finds combined LEED/Auger systems in use, because it is convenient to be able to monitor surface contamination or adsorption by AES during LEED studies.
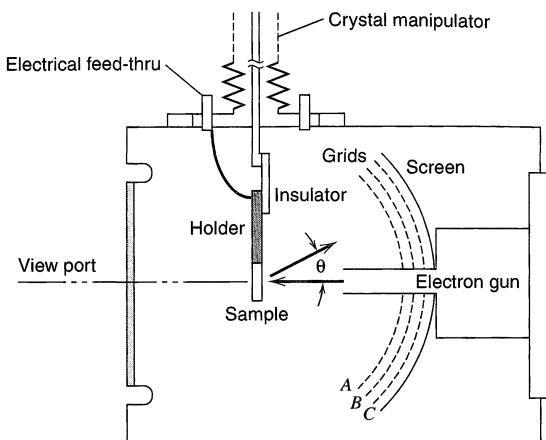
Figure 17.3.13 Schematic diagram of a LEED apparatus. [From G. A. Somorjai and H. H. Farrell, *Adv. Chem. Phys.*, **20**, 215 (1971), with permission.]

Different spot patterns can be interpreted in terms of different surface structures in a fairly straightforward manner. There is a standard notation for describing the structures and their corresponding patterns (110, 111, 118), but it is beyond our scope to delve into it here.

In electrochemical experiments, LEED is used to define the structure of a single-crystal electrode surface [e.g., the (100) face of platinum] before its use in a cell, and to monitor changes that may have taken place upon immersion or electrochemical treatment. One often finds, for example, that a single-crystal surface will *reconstruct*, to yield a new surface arrangement, upon contact with an electrochemical medium at certain potentials (e.g., see Figure 13.4.7) (113, 116).

17.3.4 High Resolution Electron Energy Loss Spectroscopy (90, 119)

High resolution electron energy loss spectroscopy (HREELS) is a form of surface vibrational spectroscopy in which the difference in energies between an impinging and a scattered electron beam provides information about the vibrational modes of a surface species. The apparatus is similar to that used in AES, in that an electron beam serves as the excitation source. However, because one must make precise measurements with resolutions in the meV range, the excitation electron beam is made monochromic to within 2–5 meV by use of an electrostatic energy analyzer. The scattered beam is at lower energy because of vibrational excitation of sample surface species; typically these energy losses range up to 5000 cm^{-1} (equivalent to 600 meV). Thus, a plot of the reflected intensity as a function of the difference in energy between the excitation and scattered beams (the energy loss) presents a vibrational spectrum. Because the low energy electron beam does not penetrate the surface (penetration depth < 1 nm), HREELS shows higher surface sensitivity than infrared or Raman spectroscopy. Typically the selection rules for scattering by surface dipoles are such that only totally symmetric modes are active.

As an example of HREELS applied to an electrochemical system, consider the results in Figure 17.3.14, which shows spectra of SCN$^-$ adsorbed on an Ag(111) single crystal. The spectrum depends upon the potential applied during the adsorption step. At -0.3 V a band for the C—S stretch at 772 cm^{-1} is seen, while adsorption at $+0.14$ V shows a band attributable to the C≡N stretch. AES and LEED measurements were useful in this experiment to indicate the structure and orientation of the SCN$^-$ layer. These measurements were carried out by transferring the single-crystal electrode between the electrochemical cell and the UHV chamber with apparatus like that shown in Figure 17.3.3.
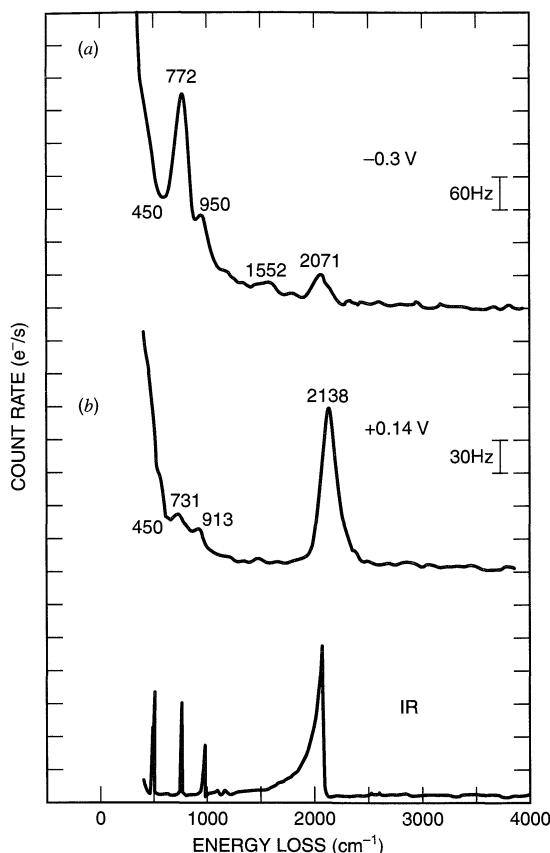
Figure 17.3.14   HREELS spectra of SCN⁻ adsorbed on Ag(111) from a solution of 0.1 mM KSCN and 10 mM KF/HF (pH 3) at (a) −0.3 V and (b) 0.14 V. Beam energy, 4 eV; beam current, 200 pA; resolution about 12 meV; incidence and detection angles, 62°. Bottom curve is IR spectrum of solid KSCN in Nujol (with Nujol peaks subtracted). [Reprinted from E. Y. Cao, P. Gao, J. Y. Gui, F. Lu, D. A. Stern, and A. T. Hubbard, *J. Electroanal. Chem.*, **339**, 311 (1992), with permission from Elsevier Science.]

17.3.5 Mass Spectrometry

Electrochemists often use mass spectrometry as a tool for the identification of electrolysis products *ex situ*, but the approach is conventional and requires no amplification here. Mass spectrometry (MS) can also be used to sample volatile species produced at a porous electrode connected directly to a mass spectrometer. Alternatively, the solution in the electrochemical cell can be introduced into the mass spectrometer inlet by a thermospray or electrospray approach. Moreover, electrodes can be removed from the cell and introduced into a UHV chamber and their surface examined by MS using conventional desorption techniques, such as laser or thermal desorption, or bombardment of the surface with an ion beam (secondary-ion mass spectrometry or SIMS) to produce the ions that are mass-analyzed.

The first workers who directly coupled an electrochemical cell to the inlet of a mass spectrometer used a Pt working electrode prepared on a porous glass membrane treated with a Teflon dispersion to make it nonwetting (120). This porous electrode could sustain a differential pressure of 1 atm without liquid leaking through the membrane. The response time for detecting the gaseous products produced at the electrode by MS was about 20 s (121). A number of improvements have been made in the original design, notably by adding a differential pumping system with turbomolecular pumps to allow faster transfer of products into the ionization chamber of the mass spectrometer (Figure 17.3.15a,b) (122, 123). Response times in these systems can be as small as 50 ms, so that real-time analysis of reaction products during a potential sweep is possible. This tech-

(a)

(b)

(c)
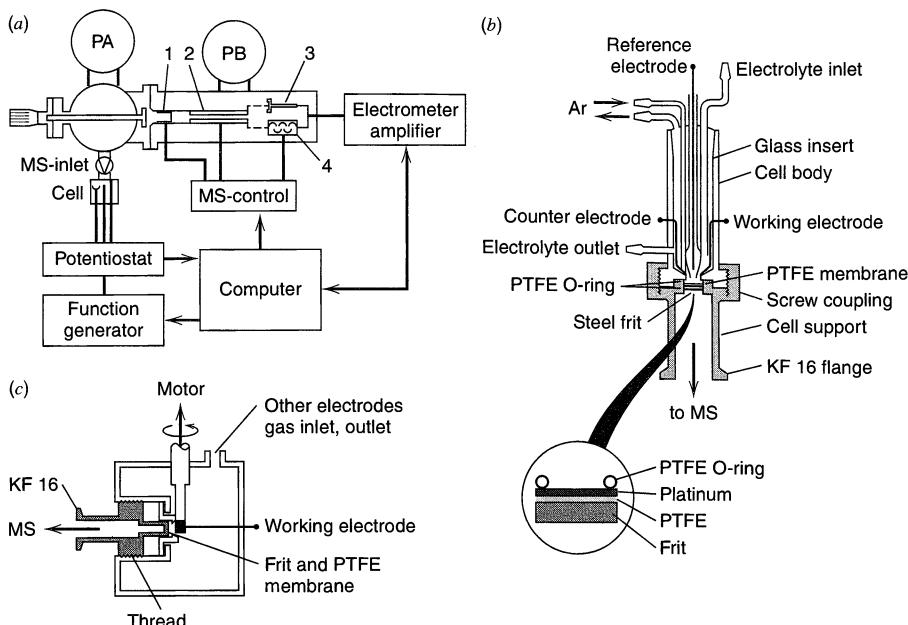
Figure 17.3.15 *Top left (a)*: Schematic diagram of apparatus for DEMS. The chamber connected directly to the electrochemical cell and the mass spectrometer (MS) are pumped differentially by turbo pumps PA and PB. Electrolysis products are passed into the ionization chamber (1), analyzed in the quadrupole mass filter (2), and detected with either a Faraday cup (3) or electron multiplier (4). *Right (b)*: Electrochemical cell for on-line mass spectrometry with a porous electrode. Electrode shown is Pt with Teflon (PTFE)-treated glass frit. [Reprinted from B. Bittins-Cattaneo, E. Cattaneo, P. Königshoven, and W. Vielstich, *Electroanal. Chem.*, **17**, 181 (1991), by courtesy of Marcel Dekker, Inc.] *Bottom left (c)*: Electrochemical cell with a rotating cylinder electrode and sampling with separate inlet to MS. [Reprinted from S. Wasmus, E. Cattaneo, and W. Vielstich, *Electrochim. Acta.*, **35**, 771 (1990), with permission from Elsevier Science.]

nique is sometimes called differential electrochemical mass spectrometry (DEMS) (122). An alternative arrangement, compatible with more conventional electrode materials, uses a Teflon membrane inlet to the mass spectrometer that is placed close (~0.3 mm) to a rotating cylindrical electrode (Figure 17.3.15c). A number of studies with these techniques have been reported (122). For example, they are useful in characterizing fuel cell catalysts involved in the oxidation of methanol and formic acid (Figure 17.3.16).

One can also couple the electrochemical cell to the mass spectrometer through an interface similar to that used for coupling liquid chromatography columns. In this arrangement the electrolyte flows past the working electrode, such as a Pt gauze or reticulated vitreous carbon, directly to the interface with the MS. In the *thermospray* (TSP) *ionization technique*, the solution is passed to a heated vaporizer ($T \approx 290°C$) at flow rates of a few cm^3/s to produce a jet that enters the spectrometer (124, 125). The time between formation of a product at an electrode and detection of a mass signal ranges from 500 ms to several seconds. It is also possible to use an electrospray ion source interface and to study the electrochemical reactions that occur at the metal capillary of the electrospray source (126, 127).

Also of interest to electrochemistry is SIMS, which is another *ex situ* UHV method for surface and thin-film characterization (93, 103, 128, 129). This approach involves the bombardment of a surface with a high-energy primary ion beam (e.g., 15 keV Cs^+), which etches the surface by sputtering and produces *secondary ions* derived from the sur-
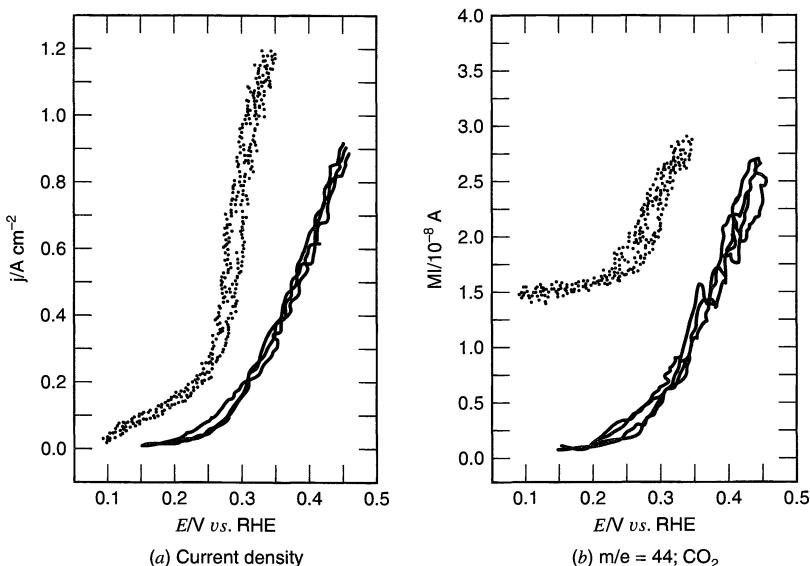
Figure 17.3.16   Results for oxidation of formic acid (dotted curves) and methanol (solid curves) at a fuel-cell anode (Pt/Ru) with phosphoric-acid-doped polybenzimidazole polymer electrolyte, 170°C. (*a*) current density and (*b*) mass signal for CO_2 at a scan rate of 1 mV/s. [From M. Weber, J.-T. Wang, S. Wasmus, and R. F. Savinell, *J. Electrochem. Soc.*, **143**, L158 (1996), reprinted by permission of the publisher, The Electrochemical Society, Inc.]

face constituents. These ions are detected mass spectrometrically. Two-dimensional characterization can be carried out by scanning the primary beam, and depth profiles can be obtained by monitoring a single ion intensity *vs.* sputtering time. SIMS offers much better detection limits (10^{-4}–10^{-8} atomic percent) than XPS or AES. However, SIMS is not a true surface technique, because the efficiency of secondary-ion production is determined by the three-dimensional properties of the thin ion-implanted layer created by the primary beam (130,131). Artifacts in depth profiles arise at interfaces from this aspect. Alternative approaches for mass spectrometric examination of an electrode surface after transfer into the UHV sample chamber utilize thermal desorption (132) and laser desorption (133) to produce ions of surface species for analysis.

▶ 17.4 MAGNETIC RESONANCE METHODS

17.4.1 Electron Spin Resonance

Electron spin resonance (ESR, also known as *electron paramagnetic resonance*, EPR) is used for the detection and identification of electrogenerated products or intermediates that contain an odd number of electrons; that is, radicals, radical ions, and certain transition metal species. Because ESR spectroscopy is a very sensitive technique, allowing detection of radical ions at about the 10^{-8} *M* level under favorable circumstances, and because it produces information-rich, distinctive, and easily interpretable spectra, it has found extensive application to electrochemistry, especially in studies of aromatic compounds in nonaqueous solutions. Also, electrochemical methods are particularly convenient for the generation of radical ions; thus they have been used frequently by ESR spectroscopists for the preparation of samples for study. Several reviews dealing with the principles of ESR and the application to electrochemical investigations have appeared (134–138).

ESR measurements are based on the absorption of radiation of frequency, ν, by a paramagnetic species contained in a magnetic field, H. The magnetic field causes a splitting of the unpaired electron energy levels by an amount $g\mu_{\mathrm{B}}H$ (Figure 17.4.1a), where g is the spectroscopic splitting or g *factor* (which depends on the orbital and electronic environment of the electron; $g \approx 2$ for a free electron and most organic radical species), and μ_{B} is a constant called the *Bohr magneton* (5.788×10^{-5} eV/T). When the field is such that the relation

$$\Delta \mathbf{E} = h\nu = g\mu_{\mathrm{B}}H \qquad (17.4.1)$$

is satisfied, transitions between these levels are observed by absorption of the incident radiation, which is normally in the microwave region. Spectra are recorded by measuring the absorption as a function of H while the magnetic field strength is scanned. The structure found in ESR spectra (*hyperfine structure*) arises from additional splitting of the energy levels by neighboring protons and other nuclei (e.g., N^{14}, P^{31}) having magnetic moments that interact with the unpaired electron. Detailed descriptions of the principles of ESR and the interpretation of ESR spectra are given in many reviews and monographs (139–141).

The apparatus and applications of ESR in electrochemistry were discussed in some detail in the first edition.[4] A commercial ESR apparatus is usually employed with cells
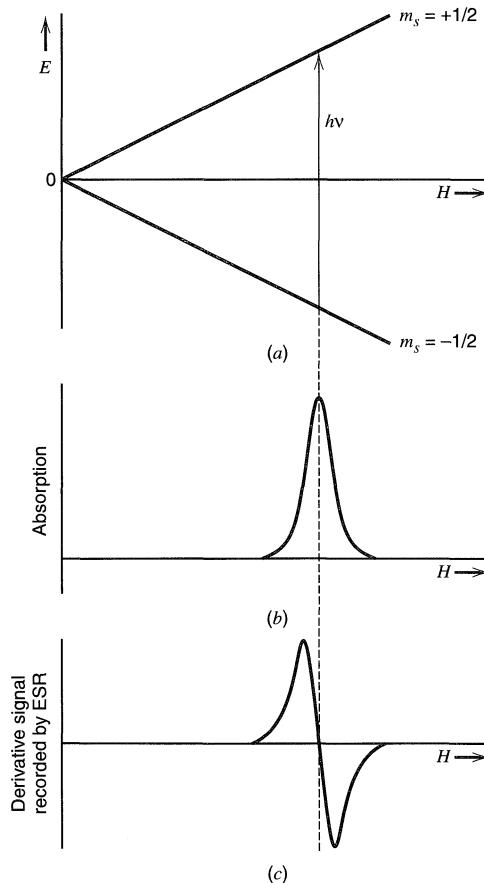
Figure 17.4.1 Principles of the ESR experiment. (*a*) Energy-level diagram of a free electron in a magnetic field. (*b*) ESR absorption *vs*. magnetic field. (*c*) Derivative ESR signal obtained after phase-sensitive detection.

[4]First edition, pp. 615–621.

configured so that electrochemistry can be carried out directly in the ESR cavity. Most electrochemical ESR cells, such as those shown in Figure 17.4.2, contain a large-area working electrode, with smaller auxiliary and reference electrodes positioned as fully as possible outside of the sensitive region (which depends upon cavity shape) (142–144). Such cells allow experiments in which the ESR signal and the electrolysis current can be monitored simultaneously as functions of potential or time [simultaneous electrochemical-ESR (SEESR) experiments].

In general, ESR is very useful in identifying the presence of radical ions in an electrochemical reaction. More detailed analysis of the hyperfine splitting can provide information about the spin density distributions on the radical and about ion pairing, solvation, and restricted internal rotation. Because the spectrum is very sensitive to the environment of the radical ion, comparative measurements of the same species in different media can yield information about medium effects (145). For example, the ESR spectrum of methyl viologen radical cation shows a rich hyperfine structure due to the interactions of the unpaired electron with the paramagnetic nuclei in the molecule (^{1}H, ^{14}N). A very similar spectrum is seen for this species incorporated in the polymer Nafion, which indicates that the radical ion is free to tumble in the polymer; free tumbling is needed to average out dipole–dipole interactions and to give hyperfine structure. However, in a polymer in which the cation radical is in the backbone, no hyperfine structure is found, as expected for the very restricted mobility of this species (146). ESR has also been widely used to measure electron-transfer rates between the radical ion and the parent compound, by noting concentration effects on line widths. Electrogenerated radicals that are too unstable to observe directly by ESR can often be trapped with a suitable *spin trap* (e.g., phenyltertbutylnitrone), to yield a stable radical species that can be studied over a longer time period (147, 148).

(a)   (b)
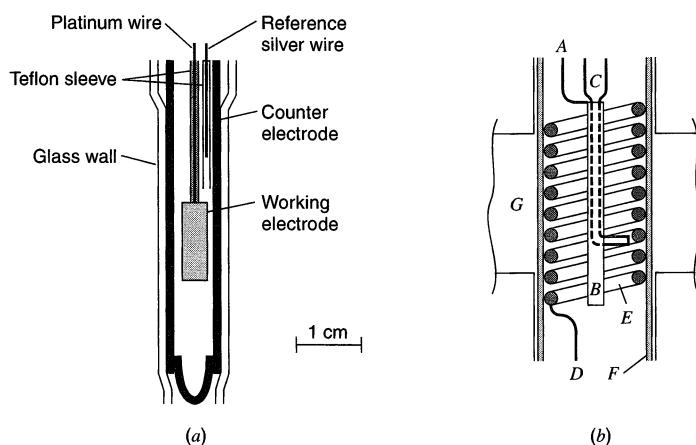
Figure 17.4.2 Cells for simultaneous electrochemical-ESR experiments. (*a*) Flat cell with platinum working and tungsten auxiliary electrodes for use in a rectangular cavity. [Reprinted with permission from I. B. Goldberg and A. J. Bard, *J. Phys. Chem.*, **75**, 3281 (1971). Copyright 1971, American Chemical Society.] (*b*) Cell with a helical gold working electrode (*E*) that forms the center conductor of a coaxial cylindrical microwave cavity (*G*). *A*, auxiliary electrode lead; *B*, central platinum auxiliary electrode; *C*, Luggin capillary for reference electrode; *D*, working electrode lead; *F*, quartz tube. [Reprinted with permission from R. D. Allendoerfer, G. A. Martinchek, and S. Bruckenstein, *Anal. Chem.*, **47**, 890 (1975). Copyright 1975, American Chemical Society.]

17.4.2 Nuclear Magnetic Resonance

Although nuclear magnetic resonance (NMR) has been used to analyze products of bulk electrolysis, there are few references to investigations of the electrode/electrolyte interface. The problem is largely the relatively low sensitivity of NMR. The detection limit for a single observation is about 10^{18} protons, with 1–2 orders-of-magnitude higher sensitivities by signal averaging of many scans. The sensitivities for detection of other nuclei, like ^{13}C, are much lower. If solids with typical coverages by adsorbates are to be examined by NMR, several m^2 of surface must be examined. Nevertheless, by using finely divided powders, NMR has been applied to surface studies, including those of catalysts (149, 150).

In the electrochemical studies reported so far, NMR has been applied as an *ex situ* technique, where a powdered metal is used as an electrode in an electrochemical cell and then the metal powder is transferred, usually with electrolyte, to a NMR sample tube for observation (151–154). For example, the formation of surface CO from methanol on Pt was studied (153). High-surface-area Pt (24 m^2/g) was placed in a Pt boat that served as the working electrode, and a solution of 0.1 M ^{13}C-enriched methanol in 0.5 M sulfuric acid was used as the electrolyte. The electrode was held at the desired potential, then a 0.2 g sample of the Pt was removed, mixed with glass beads, and placed in a glass NMR sample tube. The ^{13}C spectrum showed the presence of about 10^{19} spins in the form of CO. So far only special purpose NMR instruments have been used in such studies.

▶ 17.5 QUARTZ CRYSTAL MICROBALANCE

17.5.1 Introduction and Principles

In many electrochemical experiments, mass changes occur as material is either deposited on or lost from the electrode. It is of interest to monitor these changes simultaneously with the electrochemical response, and the *quartz crystal microbalance* (QCM) is the usual means of doing so. The basic principles and applications of the QCM to electrochemical problems have been reviewed (155–157). The operation is based on the piezoelectric properties of a slice of quartz crystal, which cause it to deform when an electric field is applied to it (Figure 17.5.1). This piezoelectric effect is also important in scanning probe microscopy (Chapter 16), which is based on piezoelectric elements (usually of barium titanate) that produce small displacements of an electrode. The bare quartz crystal has a particular mechanical resonant mode depending upon its size and thickness, and it oscillates at a frequency, f_0, when a sinusoidal electrical signal of this frequency is applied to the gold contacts. Typical quartz crystals used in QCM experiments have a 1-inch diameter and $f_0 = 5$ MHz. The frequency of oscillation is sensitive to mass changes on the crystal surface as expressed by the *Sauerbrey equation*:

$$\Delta f = -2f_0^2 mn/(\rho\mu)^{1/2} = -C_f m \tag{17.5.1}$$

where Δf is the frequency change caused by addition of a mass per unit area, m, to the crystal surface, n is the harmonic number of the oscillation (e.g., $n = 1$ for 5 MHz with a 5 MHz crystal), μ is the shear modulus of quartz (2.947×10^{11} g cm^{-1}s^{-2}), and ρ is the density of quartz (2.648 g/cm^3). The constants are usually lumped together to yield a single constant, the sensitivity factor, C_f, which has the value of 56.6 Hz cm^2/μg for a 5 MHz crystal in air. However, the behavior depends on the medium in which the crystal is operating, because the medium couples to (or "loads") the crystal surface and affects the shear mode. Thus, f_0 and C_f values in liquids are lower than those in air or vacuum (158);
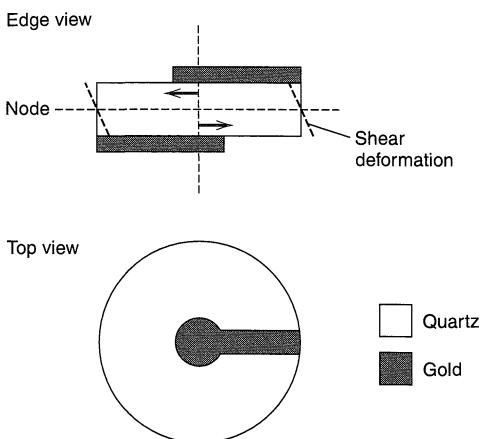
Edge view

Top view

Figure 17.5.1 Schematic edge and top views of a QCM crystal with deposited gold electrodes. The acoustic wave and the deformation (shear) of the crystal under application of an electric field across the crystal is shown in the edge view. A typical 5-MHz crystal would have a 1-inch diameter, with disk-shaped contacts of 0.5-in. and 0.25-in. diameter on either side. The active area of the crystal is defined by the applied electric field and is thus limited by the smaller electrode.

for usual aqueous solutions, C_f is about 42 Hz cm^2/μg for a 5 MHz crystal. The frequency of oscillation is also a function of temperature. Although a crystal can be cut with a particular orientation that shows a small inherent temperature coefficient (e.g., an "AT cut" with about 5 Hz/K for a 5 MHz crystal), the density and viscosity of a solution in which the crystal is operating affect the frequency, and these are functions of temperature, yielding overall effective temperature coefficients of 15–50 Hz/K (155). In studies where small mass changes are monitored over a long time period, it is usually important to thermostat the system.

17.5.2 Electrochemical Apparatus

A schematic diagram of the apparatus for QCM in an electrochemical experiment is given in Figure 17.5.2. The quartz crystal is frequently clamped in an appropriate O-ring joint to expose only one of the contacts to the solution as suggested in Figure 17.5.2.

This contact (usually Au or Pt) is also the working electrode for electrochemistry and is thus part of both the potentiostat and oscillator circuits. The crystal is driven by a broadband oscillator circuit that tracks the resonant frequency of the crystal, measured with a commercial frequency counter, during electrochemically-induced mass changes on the electrode surface. A typical calibration experiment might involve the electrodeposition of Cu or Pb on the electrode, which produces a decrease in frequency. For example, if
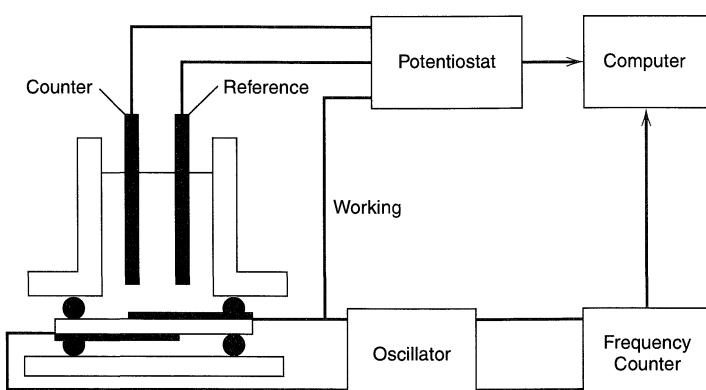
Figure 17.5.2 Schematic diagram of cell and apparatus for electrochemical QCM studies.

the Au electrode area is 0.3 cm^2, and a monolayer of Pb (mass about 0.1 μg) is deposited on it, the observed frequency change, taking $C_f = 42$ Hz cm^2/μg, will be about 14 Hz.

Although the direct application of the QCM to mass changes on electrodes during electrochemical experiments appears straightforward, in fact viscoelastic effects and the nature of the deposit often come into play in these measurements (155–157). Equation 17.5.1 is derived with the assumption that the deposited material is rigid (i.e., with a large shear modulus like a metal) and in a very thin film on the surface (at the shear wave antinode) of the crystal. For thicker deposits, especially of materials like polymer films that can undergo viscoelastic shear, the situation is more complicated. One approach to representing the situation is in terms of an equivalent circuit for the quartz crystal along with any loading attributable to solution or deposit (Figure 17.5.3) (159). These loadings can be taken into account in relating frequency changes to mass changes. One approach is to measure, in addition to Δf, the admittance of the QCM and utilize equations relating the elements of the equivalent circuit to physical parameters of the deposit. However, this procedure greatly complicates the measurements, particularly when one desires to measure changes as functions of time (e.g., during a potential sweep), and is rarely carried out in practice.

Typically the frequency can be measured to 1 Hz, with even higher resolution available with signal averaging techniques, so that fractional monolayer sensitivities are possible. As is evident from (17.5.1), the sensitivity increases with the square of f_0 and linearly with n. Thus by working with crystals of higher f_0 (e.g., 10 MHz), or at higher harmonics, higher sensitivities are obtained. However, 10 MHz and higher crystals are quite thin and fragile, and higher harmonics involve lower signal levels and require more complex circuitry, so operation with a 5 MHz crystal at the fundamental mode is the common practice.

17.5.3 Applications

The QCM has been used in many types of electrochemical studies involving mass changes on electrodes, including the underpotential deposition of metals, adsorption/desorption of surfactants, and changes in polymer films during redox processes. In a typical experiment Δf is monitored during a potential step or sweep. As an example of a QCM study, we con-
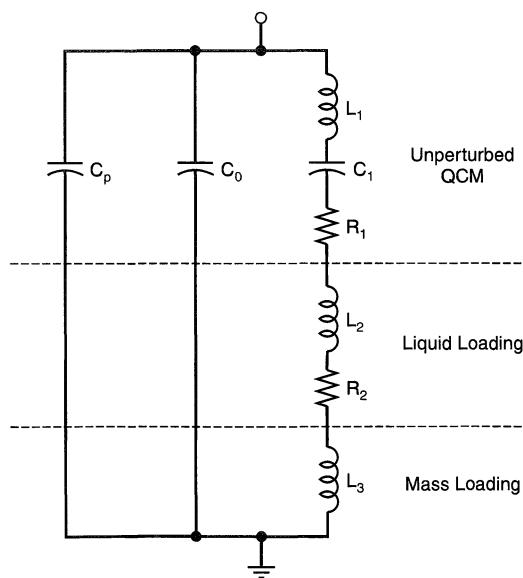
Figure 17.5.3 Equivalent circuit for a quartz crystal under mass and liquid loading. The circuit elements of the unperturbed crystal are L_1, C_1, R_1, and C_0. Liquid- and mass-loading adds additional elements L_2, R_2, and L_3. C_p represents any parasitic capacitance of the test fixture. [Reprinted with permission from S. J. Martin, V. E. Granstaff, and G. C. Frye, *Anal. Chem.*, **63**, 2272 (1991). Copyright 1991, American Chemical Society.]
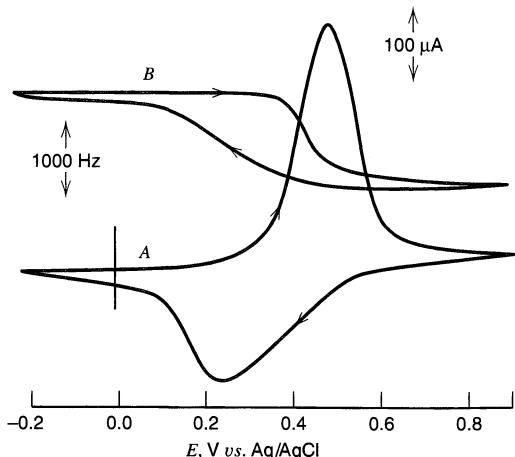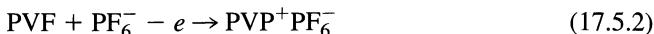
Figure 17.5.4 (*A*) Cyclic voltammogram and (*B*) frequency change of QCM during scan of a poly(vinylferrocene) film on a gold electrode in 0.1 *M* KPF$_6$ at 10 mV/s. Note that anodic currents are positive and potential becomes more positive to the right. [Reprinted with permission from P. T. Varineau and D. A. Buttry, *J. Phys. Chem.*, **91**, 1292 (1987). Copyright 1987, American Chemical Society.]

sider the mass changes that occur on oxidation of a film of the polymer polyvinylferrocene (PVF) on an electrode (Figure 17.5.4). As discussed in Chapter 14, polymer films can be deposited on electrodes by different means. In the experiment described here, the film was deposited by oxidation of a solution of PVF in CH$_2$Cl$_2$ containing tetra-*n*-butylammonium tetrafluoroborate (TBA$^+$BF$_4^-$) to form an insoluble film of PVP$^+$BF$_4^-$ on the Au electrode on the QCM. The solution was then replaced by an aqueous solution of 0.1 *M* KPF$_6$ and the potential cycled between the oxidized and reduced states of PVF.

$$PVF + PF_6^- - e \rightarrow PVP^+PF_6^- \tag{17.5.2}$$

Consider the scan shown in curve *A* beginning at -0.2 V *vs.* Ag/AgCl, where the film is fully reduced. Upon oxidation, the QCM frequency decreases (*curve B*), signaling the increase in mass because of incorporation of PF$_6^-$ into the film. Upon scan reversal, reduction of the film occurs, and the frequency increases back to the original value. The mass changes were correlated with the charge passed during the redox processes to show that the redox process did not cause solvent or electrolyte incorporation into the film (160).

Another example of the use of the QCM to monitor a process involving a film on an electrode involves the study of fullerene (e.g., C$_{60}$) films. These are produced by dropping a solution of C$_{60}$ in benzene on an electrode surface and allowing the solvent to evaporate. A thin film of C$_{60}$ crystals remains on the electrode surface when it is immersed in a solvent like acetonitrile. During a sweep to negative potentials, the C$_{60}$ is reduced in successive one-electron steps. The fate of the reduced forms, like C$_{60}^{-}$, depends upon the nature of the cation in the supporting electrolyte. With large tetra-alkylammonium salts the C$_{60}$ anion precipitates, so the film adds mass, while with K$^+$ the anion dissolves and the film loses weight. QCM is a very convenient way to monitor such processes (133,161).

▶ 17.6 X-RAY METHODS

Because the wavelength of X-rays with energies of about 12 keV is 1 Å (comparable to atomic spacings), the interaction of this radiation with matter can provide high-resolution structural information on the atomic scale, just as in X-ray crystallography of single crystals and powders. However, in studying surfaces, there are relatively few atoms to interact with the X-rays, so signals are much weaker than in studies of bulk materials. Moreover, with *in situ* studies of an electrode in a solvent like water, the X-ray intensity is diminished through scattering by the solvent molecules. For example, 12 keV X-rays only penetrate a

few millimeters through a water layer. These factors imply that studies of the electrode/solution interface require very intense X-ray sources. It has been only recently that such high-intensity X-ray radiation has become available at particle accelerator (synchrotron) facilities, and most research involving X-ray characterization in electrochemistry has employed synchrotron light sources. These sources are 8 to 10 orders of magnitude brighter than laboratory (rotating anode) sources and have the additional advantage of a broad featureless spectrum without the sharp spikes associated with conventional sources. Several reviews of this area are available (162–168). Broadly, these studies can be divided into methods concerning either the absorption or the diffraction of the X-ray beam.

17.6.1 X-Ray Absorption Spectroscopy

As described in Section 17.3.1, X-rays interact with atoms by ejecting core electrons. The absorption of X-rays follows the same general expression as for absorption of lower-energy radiation, that is,

$$I = I_0 \exp(-\mu x) \qquad (17.6.1)$$

where I and I_0 are the intensities of transmitted and incident radiation, respectively, x is the distance, and μ is the linear absorption coefficient, which is a function of energy, **E**. Thus the absorption spectrum is a plot of μ [or $\ln(I/I_0)$ at a fixed x] vs. **E** (in keV). The spectrum is characterized by an *absorption edge*, which is the energy that is just needed to eject (or photoionize) a particular core electron, usually a 1s electron (K edge) or $2p_{3/2}$ electron (L_3 edge). The K-edge absorption spectra for iron and several iron oxides are shown in Figure 17.6.1. The spectrum (at 7.112 keV) is usually divided into two regions.
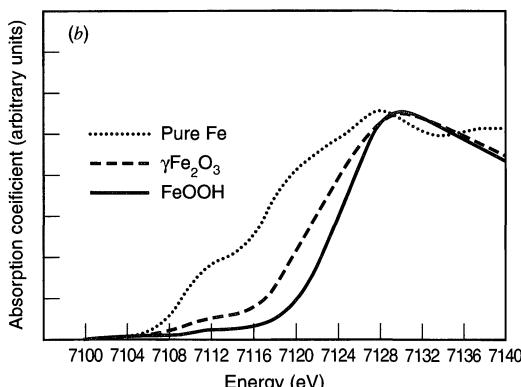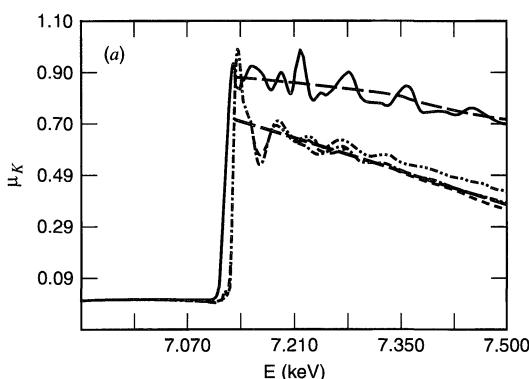
Figure 17.6.1 (a) Fe K-edge spectra of pure Fe (———), γ-Fe_2O_3 (- - - -), Fe_3O_4 (- · - · ·); γ-FeOOH (- · ·· · ·). (b) Near-edge spectra for Fe, γ-Fe_2O_3, and γ-FeOOH. The ordinate in both cases is the absorption coefficient due only to the K shell (i.e., background subtracted). [From G. G. Long and J. Kruger, in "Techniques for Characterization of Electrodes and Electrochemical Processes," R. Varma and J. R. Selman, Eds., Wiley, New York, 1991, with permission.]

Examination of the region within about 10–40 eV of the absorption edge is termed *X-ray absorption near-edge structure* (XANES) [or *near-edge absorption fine structure* (NEXAFS)]. This region (Figure 17.6.1*b*) contains features due to core-electron transitions to unoccupied orbitals in the atom and is sensitive to the oxidation state and ligand environment of the atom. The oscillations observed about 50 keV above the absorption edge (Figure 17.6.1*a*) make up the *extended X-ray absorption fine structure* (EXAFS), which can be interpreted in terms of interference between the ejected electron waves with waves that are backscattered by the neighboring atoms. The EXAFS spectrum can be related to the distance and arrangement of atoms neighboring those responsible for the absorption edge in the sample (i.e. the atoms neighboring Fe in the samples used for Figure 17.6.1*a*).

Electrochemical cells for x-ray absorption spectroscopy (XAS) must be designed to minimize absorption losses in the cell windows and electrolyte. Thus, cell windows are typically thin films of polyethylene or polyimide, and only thin layers of solution (~10 μm) are used. The sample itself must be sufficiently thin (e.g., a metal film no thicker than a few microns on a transparent substrate) that appreciable transmission is observed (165).

17.6.2 X-Ray Diffraction Techniques

X-ray diffraction (XRD) experiments involve scattering of a monochromatic X-ray beam from the surface of a single-crystal electrode and measurement of surface reflectivity or determination of the diffraction pattern. Again, the cell design must minimize absorption of the X-rays in the cell window and minimize the path length of the X-rays through the electrolyte (Figure 17.6.2). In diffraction measurements, one uses a small angle (a *grazing angle*) between the X-ray beam and the sample surface. As in X-ray crystallography, diffraction patterns result from interference of beams scattered from surface atoms in accord with Bragg's law. These patterns provide information about surface structure and about processes that alter surface structure, such as reconstruction of a single-crystal electrode or the UPD of a metal monolayer.

The application of X-ray methods to electrochemical studies is still in its infancy. The need for synchrotron radiation, rather sophisticated cells, and elaborate data interpretation has limited the use of these techniques. However, the atomic-level structural information that these methods provide is rivaled only, perhaps, by the scanning probe methods (Chapter 16) and suggests that wider application of X-ray methods is in the offing.
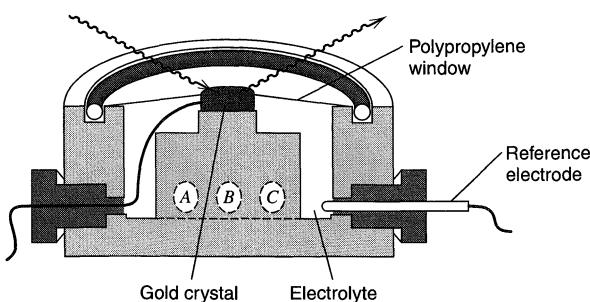
Figure 17.6.2 Cell design for X-ray diffraction experiments with a single-crystal gold electrode. A thin layer of solution is held between the polypropylene window and the electrode. The window is held in place by an O-ring that clamps it to the Kel-F cell body. *A* and *C* are electrolyte ports and *B* is the counter electrode. [Reprinted from J. McBreen, in "Physical Electrochemistry," I. Rubinstein, Ed., Marcel Dekker, New York, 1995, Chap. 8, by courtesy of Marcel Dekker, Inc.]

17.7 REFERENCES

1. H. D. Abruña, Ed., "Electrochemical Interfaces: Modern Techniques for In-Situ Interface Characterization," VCH, New York, 1991.

2. A. T. Hubbard, Ed., "The Handbook of Surface Imaging and Visualization," CRC, Boca Raton, FL, 1995.

3. R. J. Gale, Ed., "Spectroelectrochemistry," Plenum, New York, 1988.

4. C. Gutierrez and C. Melendres, Eds., "Spectroscopic and Diffraction Techniques in Interfacial Electrochemistry," Kluwer, Amsterdam, 1990.

5. R. Varma and J. R. Selman, Eds., "Techniques for Characterization of Electrodes and Electrochemical Processes," Wiley, New York, 1991.

6. N. Winograd and T. Kuwana, *Electroanal. Chem.*, **7**, 1 (1974).

7. W. R. Heineman, F. M. Hawkridge, and H. N. Blount, *Electroanal. Chem.*, **13**, 1 (1984).

8. W. N. Hansen, *Adv. Electrochem. Electrochem. Engr.*, **9**, 1 (1973).

9. T. Kuwana and W. R. Heineman, *Accts. Chem. Res.*, **9**, 241 (1976).

10. W. R. Heineman, *Anal. Chem.*, **50**, 390A (1978).

11. T. P. DeAngelis, R. W. Hurst, A. M. Yacynych, H. B. Mark, Jr., W. R. Heineman, and J. S. Mattson, *Anal. Chem.*, **49**, 1395 (1977).

12. R Cieslinski and N. R. Armstrong, *Anal. Chem.*, **51**, 565 (1979).

13. R. W. Murray, W. R. Heineman, and G. W. O'Dom, *Anal. Chem.*, **39**, 1666 (1967).

14. T. Gueshi, K. Tokuda, and H. Matsuda, *J. Electroanal. Chem.*, **89**, 247 (1978).

15. M. Petek, T. E. Neal, and R. W. Murray, *Anal. Chem.*, **43**, 1069 (1971).

16. J. Salbeck, *Anal. Chem.*, **65**, 2169 (1993).

17. M. K. Hanafey, R. L. Scott, T. H. Ridgway, and C. N. Reilley, *Anal. Chem.*, **50**, 116 (1978).

18. W. R. Heineman, B. J. Norris, and J. F. Goelz, *Anal. Chem.*, **47**, 79 (1975).

19. D. F. Rohrbach, E. Deutsch, and W. R. Heineman in "Characterization of Solutes in Nonaqueous Solvents," G. Mamantov, Ed., Plenum, New York, 1978.

20. W. R. Heineman, T. Kuwana, and C. R. Hartzell, *Biochem. Biophys. Res. Commun.*, **50**, 892 (1973).

21. See, for example, the biannual reviews in *Anal. Chem.* on Dynamic Electrochemistry, e.g., (a) J. L. Anderson, E. F. Bowden, and P. G. Pickup, *ibid.*, **68**, 379R (1996); (b) J. L. Anderson. L. A. Coury, Jr., and J. Leddy, *ibid.*, **70**, 519R (1998).

22. (a) J. F. Tyson and T. S. West, *Talanta*, **27**, 335 (1980); (b) C.-C. Jan, B. K. Lavine, and R. L. McCreery, *Anal. Chem.*, **57**, 752 (1985).

23. Z. Wang, M. Zhao, and D. A. Scherson, *Anal. Chem.*, **66**, 4560 (1994).

24. D. Halliday and R. Resnick, "Physics," 3rd ed., Wiley, New York, 1978.

25. F. A. Jenkins and H. E. White, "Fundamentals of Optics," 4th ed., McGraw-Hill, New York, 1976.

26. J. D. E. McIntyre, *Adv. Electrochem. Electrochem. Engr.*, **9**, 61 (1973).

27. R. H. Muller, *Adv. Electrochem. Electrochem. Engr.*, **9**, 167 (1973).

28. B. D. Cahan, J. Horkans, and E. Yeager, *Symp. Faraday Soc.*, **4**, 36 (1970).

29. M. A. Barrett and R. Parsons, *ibid.*, p. 72.

30. J. D. E. McIntyre and D. M. Kolb, *ibid.*, p. 99.

31. A. Bewick and A. M. Tuxford, *ibid.*, p. 114.

32. W. J. Plieth, *ibid.*, p. 137.

33. D. M. Kolb and J. D. E. McIntyre, *Surf. Sci.*, **28**, 321 (1971).

34. T. Takamura, K. Takamura, and E. Yeager, *Symp. Faraday Soc.*, **4**, 91 (1970).

35. J. Kruger, *Adv. Electrochem. Electrochem. Engr.*, **9**, 227 (1973).

36. M. Stedman, *Symp. Faraday Soc.*, **4**, 64 (1970).

37. J. O'M. Bockris, M. Genshaw, and V. Brusic, *Symp. Faraday Soc.*, **4**, 177 (1970).

38. S. Gottesfeld, Y.-T., Kim, and A. Redondo in "Physical Electrochemistry," I. Rubinstein, Ed., Marcel Dekker, New York, 1995, Chap. 9.

39. R. H. Muller in "Techniques of Characterization of Electrodes and Electrochemical Processes," R. Varma and J. R. Selman, Eds., Wiley, New York, 1991, Chap. 2.

40. S. Gottesfeld, *Electroanal. Chem.*, **15**, 143 (1989).

41. C. J. Dell'Oca and P. J. Fleming, *J. Electrochem. Soc.*, **123**, 1487 (1976).

42. J. Kruger and J. P. Calvert, *J. Electrochem. Soc.*, **114**, 43 (1967).

43. J. Rishpon, A. Redondo, C. Derouin, and S. Gottesfeld, *J. Electroanal. Chem.,* **294**, 73 (1990).

44. Y.-T. Kim, R. W. Collins, K. Vedam, and D. L. Allara, *J. Electrochem. Soc.*, **138**, 3226 (1991).

45. W. N. Hansen, T. Kuwana, and R. A. Osteryoung, *Anal. Chem.*, **38**, 1810 (1966).

46. N. Winograd and T. Kuwana, *J. Electroanal. Chem.*, **23**, 333 (1969).

47. N. Winograd and T. Kuwana, *J. Am. Chem. Soc.*, **93**, 4343 (1971).

48. W. N. Hansen, *Symp. Faraday Soc.*, **4**, 27 (1970).

49. H. B. Mark and E. N. Randall. *Symp. Faraday Soc.*, **4**, 157 (1970).

50. D. G. Hanken, C. E. Jordan, B. L. Frey, and R. M. Corn, *Electroanal. Chem.*, **20**, 141 (1998).

51. D. M. Kolb in R. J. Gale, Ed., *op. cit.*, Chap. 4.

52. J. D. Rudnicki, F. R. McLarnon, and E. J. Cairns in R. Varma and J. R. Selman, Eds., *op. cit.*, Chap. 3.

53. R. M. Corn and D. A. Higgins, *Chem. Rev.*, **94**, 107 (1994).

54. G. L. Richmond in H. D. Abruña, Ed., *op. cit.*, Chap. 6.

55. G. L. Richmond, *Electroanal. Chem.*, **17**, 87 (1991).

56. D. G. Campbell, M. L. Lynch, and R. M. Corn, *Langmuir*, **6**, 1656 (1990).

57. S. M. Stole, D. D. Popenoe, and M. D. Porter in H. D. Abruña, Ed., *op. cit.*, p. 339.

58. J. Benziger in A. T. Hubbard, Ed., *op. cit.*, p. 265.

59. B. Beden and C. Lamy in R. J. Gale, Ed., *op. cit.*, p. 189.

60. J. K. Foley, C Korzeniewski, J. L. Daschbach, and S. Pons, *Electroanal. Chem.*, **14**, 309 (1986).

61. M. Osawa, *Bull. Chem. Soc. Jpn.*, **70**, 2861 (1997).

62. S. Pons and A. Bewick, *Langmuir*, **1**, 141 (1985).

63. X. D. Zhu, H. Suhr, and Y. R. Shen, *Phys. Rev. B*, **35**, 3047 (1987).

64. A. Tadjeddine and A. Peremans in "Spectroscopy for Surface Science," R. J. H. Clark and R. E. Hester, Eds., Wiley, Chichester, 1998, Chap. 4.

65. S. Baldelli, N. Markovic, P. Ross, Y. R. Shen, and G. Somorjai, *J. Phys. Chem.*, **103**, 8920 (1999).

66. W. H. Flygare, "Molecular Structure and Dynamics," Prentice-Hall, Englewood Cliffs, NJ, 1978, Chap. 8.

67. H. A. Szmanski, Ed., "Raman Spectroscopy," Plenum, New York, 1970.

68. J. E. Pemberton in A. T. Hubbard, Ed., *op. cit.*, p. 647.

69. J.E. Pemberton in H. D. Abruña, Ed., *op. cit.*, p. 193.

70. R. L. Birke, T. Lu, and J. R. Lombardi in R. J. Gale, Ed., *op. cit.*, p. 211.

71. D. L. Jeanmaire and R. P. Van Duyne, *J. Am. Chem. Soc.*, **98**, 4029 (1976).

72. M. R. Suchanski and R. P. Van Duyne, *J. Am. Chem. Soc.*, **98**, 250 (1976).

73. D. L. Jeanmaire, M. R. Suchanski, and R. P. Van Duyne, *J. Am. Chem. Soc.*, **97**, 1699 (1975).

74. R. P. Van Duyne, M. R. Suchanski, J. M. Lakovits, A. R. Siedle, K. D. Parks, and T. M. Cotton, *J. Am. Chem. Soc.*, **101**, 2832 (1979).

75. D. L. Jeanmaire and R. P. Van Duyne, *J. Electroanal. Chem.*, **66**, 235 (1975).

76. (a) A. Campion, J. K. Brown, and V. M. Grizzle, *Surf. Sci.*, **115**, L153 (1982); (b) C. Shannon and A. Campion, *J. Phys. Chem.*, **92**, 1385 (1988).

77. M. Fleischmann, P. J. Hendra, and A. J. McQuillan, *J. Chem. Soc., Chem. Commun.*, **1973**, 80.

78. M. G. Albrecht and J. A. Creighton, *J. Am. Chem. Soc.*, **99**, 5215 (1977).

79. D. L. Jeanmaire and R. P. Van Duyne, *J. Electroanal. Chem.*, **84**, 1 (1977).

80. R. L. Garrell in A. T. Hubbard, *op. cit.*, p. 785.

81. A. Campion in "Vibrational Spectroscopy of Molecules at Surfaces," J. T. Yates and T. E. Madey, Eds., Plenum, New York, 1987, p. 345.

82. S. Efrima, *Mod. Asp. Electrochem.*, **16**, 253 (1985).

83. S. Farquharson, M. J. Weaver, P. A. Lay, R. H. Magnuson, and H. Taube, *J. Am. Chem. Soc.*, **105**, 3350 (1983).

84. S. Zou, C. T. Williams, E. K.-Y. Chen, and M. J. Weaver, *J. Am. Chem. Soc.*, **120**, 3811 (1998).

85. S. Nie and S. R. Emory, *Science*, **275**, 1102 (1997).

86. P. N. Ross and F. T. Wagner, *Adv. Electrochem. Electrochem. Engr.*, **13**, 69 (1985).

87. D. M. Kolb, *Z. Phys. Chem.*, **154**, 179 (1987).

88. M. Grasserbauer and H. W. Werner, Eds., "Analysis of Microelectronic Materials and Devices," Wiley, New York, 1991.

89. A. J. Bard, "Integrated Chemical Systems," Wiley, New York, 1994, pp. 100–108.

90. A. T. Hubbard, E. Y. Cao, and D. A. Stern in "Physical Electrochemistry," I. Rubinstein, Ed., Marcel Dekker, New York, 1995, Chap. 10.

91. T. A. Carlson, "Photoelectron and Auger Spectroscopy," Plenum, New York, 1975.

92. A. W. Czanderna, Ed., "Methods of Surface Analysis," Elsevier, Amsterdam, 1975.

93. C. A. Evans, Jr., *Anal. Chem.*, **47**, 818A, 855A (1975).

94. D. A. Shirley, Ed., "Electron Spectroscopy," North Holland, Amsterdam, 1972.

95. S. H. Hercules and D. M. Hercules in P. F. Kane and G. B. Larrabee, Eds., "Characterization of Solid Surfaces," Plenum, New York, 1974, Chap. 13.

96. B. G. Baker, *Mod. Asp. Electrochem.*, **10**, 93 (1975).

97. D. Briggs and M. P. Seah, Eds., "Practical Surface Analysis: Auger and X-ray Photoelectron Spectroscopy," Wiley, New York, 1990.

98. K. S. Kim, N. Winograd, and R. E. Davis, *J. Am. Chem. Soc.*, **93**, 6296 (1971).

99. C. M. Elliott and R. W. Murray, *Anal. Chem.*, **48**, 1247 (1976).

100. J. S. Hammond and N. Winograd, *J. Electroanal. Chem.*, **80**, 123 (1977).

101. J. S. Hammond and N. Winograd. *J. Electrochem. Soc.*, **124**, 826 (1977).

102. C. C. Chang in P. F. Kane and G. B. Larrabee, Eds., "Characterization of Solid Surfaces," Plenum, New York, 1974, Chap. 20.

103. J. W. Mayer and J. M. Poate in "Thin Films–Interdiffusion and Reactions," J. M. Poate, K. N. Tu, and J. W. Mayer, Eds., Wiley-Interscience, New York, 1978, Chap. 6.

104. S. H. Kulpa and R. P. Frankenthal, *J. Electrochem. Soc.*, **124**, 1588 (1977).

105. C. C. Chang, B. Schwartz, and S. P. Murarka, *J. Electrochem. Soc.*, **124**, 922 (1977).

106. J. L. Kahl and L. R. Faulkner, unpublished results.

107. H. Tachikawa and L. R. Faulkner, *J. Am. Chem. Soc.*, **100**, 4379 (1978).

108. F.-R. Fan and L. R. Faulkner, *J. Am. Chem. Soc.*, **101**, 4779 (1979).

109. J. M. Green and L. R. Faulkner, *J. Am. Chem. Soc.*, **105**, 2950 (1983).

110. G. A. Somorjai and H. H. Farrell, *Adv. Chem. Phys.*, **20**, 215 (1971).

111. J. B. Pendry, "Low Energy Electron Diffraction," Academic, New York, 1974.

112. P. A. Thiel in A. T. Hubbard, Ed., *op. cit.*, p. 355.

113. R. M. Ishikawa and A. T. Hubbard, *J. Electroanal. Chem.*, **69**, 317 (1976).

114. W. E. O'Grady, M. Y. C. Woo, P. L. Hagans, and E. Yeager, *J. Vac. Sci. Technol.*, **14**, 365 (1977).

115. P. N. Ross, Jr., *J. Electroanal. Chem.*, **76**, 139 (1977).

116. E. Yeager, W. E. O'Grady, M. Y. C. Woo, and P. Hagans, *J. Electrochem. Soc.*, **125**, 348 (1978).

117. P. N. Ross, Jr., *J. Electrochem. Soc.*, **126**, 67, 78 (1979).

118. D. G. Frank in A. T. Hubbard, Ed., *op. cit.*, p. 289.

119. L. L. Kesmodel in A. T. Hubbard, Ed., *op. cit.*, p. 223.

120. S. Bruckenstein and R. Rao Gadde, *J. Am. Chem. Soc.*, **93**, 793 (1971).

121. B. Bittins-Cattaneo, E. Cattaneo, P. Königshoven, and W. Vielstich, *Electroanal. Chem.*, **17**, 181 (1991).

122. O. Olter and J. Heitbaum, *Ber. Bunsenges. Phys. Chem.*, **88**, 2 (1984).

123. T. Iwasita, W. Vielstich, and E. Santos, *J. Electroanal. Chem.*, **229**, 367 (1987).

124. K. J. Volk, R. A. Yost, and A. Brajter-Toth, *Anal. Chem.*, **61**, 1709 (1989).

125. G. Hambitzer and J. Heitbaum, *Anal. Chem.*, **58** 1067 (1986).

126. W. Lu, X. Xu, and R. B. Cole, *Anal. Chem.*, **69**, 2478 (1997).

127. G. J. Van Berkel, F. Zhou, and J. T. Aronson, *Int. J. Mass Spectrom. Ion Processes*, **162**, 55 (1997).

128. J. A. McHugh in A. W. Czanderna, Ed., *op. cit.*

129. J. A. Gardella, Jr. in "The Handbook of Surface Imaging and Visualization," A. T. Hubbard, Ed., CRC, Boca Raton, FL, 1995, p. 705.

130. V. R. Deline, W. Katz, C. A. Evans, Jr., and P. Williams, *Appl. Phys. Lett.*, **38**, 832 (1978).

131. C. C. Chang, N. Winograd, and B. J. Garrison, *Surf. Sci.*, **202**, 309 (1988).

132. S. Wilhelm, W. Vielstich, H. W. Buschmann, and T. Iwasita, *J. Electroanal. Chem.*, **229**, 377 (1987).

133. F. Zhou, S.-L. Yau, C. Jehoulet, D. A. Laude, Jr., Z. Guan, and A. J. Bard, *J. Phys. Chem.*, **96**, 4160 (1992).

134. T. M. McKinney, *Electroanal. Chem.*, **10**, 97 (1977).

135. I. B. Goldberg and A. J. Bard in "Magnetic Resonance in Chemistry and Biology," J. N. Herak and K. J. Adamic, Eds., Marcel Dekker, New York, 1975, Chap. 10.

136. B. Kastening, *Progr. Polarogr.*, **3**, 195 (1972); *Chem. Ing. Tech.*, **42**, 190 (1970).

137. R. N. Adams, *J. Electroanal. Chem.*, **8**, 151 (1964).

138. A. M. Waller and R. G., Compton, *Compr. Chem. Kinet.*, **29**, 297 (1989).

139. J. E. Wertz and J. R. Bolton, "Electron Spin Resonance: Elementary Theory and Practical Applications," McGraw-Hill, New York, 1986.

140. R. S. Alger, "Electron Paramagnetic Resonance: Techniques and Applications," Interscience, New York, 1968.

141. N. M. Atherton, "Electron Spin Resonance: Theory and Applications," Halsted, New York, 1973.

142. I. B. Goldberg and A. J. Bard, *J. Phys. Chem.*, **75**, 3281 (1971); **78**, 290 (1974).

143. R. D. Allendoerfer, G. A. Martinchek, and S. Bruckenstein, *Anal. Chem.*, **47**, 890 (1975).

144. R. N. Bagchi, A. M. Bond, and F. Scholz, *Electroanal.*, **1**, 1 (1989).

145. A. J. Bard, "Integrated Chemical Systems," *op. cit.*, pp. 114–120.

146. J. G. Gaudiello, P. K. Ghosh, and A. J. Bard, *J. Am. Chem. Soc.*, **107**, 3027 (1985).

147. E. Janzen, *Accts. Chem. Res.*, **4**, 31 (1971).

148. A. J. Bard, J. C. Gilbert, and R. D. Goodin, *J. Am. Chem. Soc.*, **96**, 620 (1974).

149. J. F. Haw in A. T. Hubbard, Ed., *op. cit.*, p. 525.

150. A. T. Bell and A. Pines, Eds., "NMR Techniques in Catalysis," Marcel Dekker, New York, 1994.

151. K. W. H. Chan and A. Wieckowski, *J. Electrochem. Soc.*, **137**, 367 (1990).

152. M. S. Yahnke, B. M. Rush, J. A. Reimer, and E. J. Cairns, *J. Am. Chem. Soc.*, **118**, 12250 (1996).

153. J. B. Day, P.-A. Vuissoz, E. Oldfield, A. Wieckowski, and J.-P. Ansermet, *J. Am. Chem. Soc.*, **118**, 13046 (1996).

154. Y. Y. Tong, C. Belrose, A. Wieckowski, and E. Oldfield, *J. Am. Chem. Soc.*, **119**, 11709 (1997).

155. D. A. Buttry in H. D. Abruña, Ed., *op. cit.*, Chap. 10.

156. D. A. Buttry, *Electroanal. Chem.*, **17**, 1 (1991).

157. D. A. Buttry and M. D. Ward, *Chem. Rev.*, **92**, 1355 (1992).

158. K. K. Kanazawa and J. G. Gordon, *Anal. Chem.*, **57**, 1770 (1985).

159. S. J. Martin, V. E. Granstaff, and G. C. Frye, *Anal. Chem.*, **63**, 2272 (1991).

160. P. T. Varineau and D. A. Buttry, *J. Phys. Chem.*, **91**, 1292 (1987).

161. W. Koh, D. Dubois, W. Kutner, M. T. Jones, and K. M. Kadish, *J. Phys. Chem.*, **96**, 4163 (1992).

162. H. D. Abruña, *Mod. Asp. Electrochem.*, **20**, 265 (1989).

163. G. G. Long and J. Kruger in R. Varma and J. R. Selman, Eds., *op. cit.*, Chap. 4.

164. J. McBreen in "Physical Electrochemistry," I. Rubinstein, Ed., Marcel Dekker, New York, 1995, Chap. 8.

165. H. D. Abruña in H. D. Abruña, Ed., *op. cit.*, Chap. 1.

166. M. F. Toney and O. R. Melroy, *ibid.*, Chap. 2.

167. J. H. White, *ibid.*, Chap. 3.

168. H. D. Abruña in A. T. Hubbard, Ed., *op. cit.*, Chap. 64.

▷ 17.8 PROBLEMS

17.1 The absorbance values at 710 nm in Figure 17.1.4 are 0.040, 0.072, 0.111, 0.179, 0.279, 0.411, 0.633, 0.695, 0.719, and 0.725 for curves *a* to *j*. Calculate the ratio of concentrations of the Co(II) complex and Co(I) complex for the potentials corresponding to curves *a* to *j*. Plot E *vs.* the logarithm of the ratio, and from the plot verify n and find $E^{0'}$.

17.2 Given $D = 6.2 \times 10^{-6}$ cm^2/s for *o*-tolidine and its oxidation product, calculate the molar absorptivity, ε, for the product from the slope of the absorbance plot in Figure 17.1.3. Calculate the effective area of the minigrid.

17.3 Calculate absorbance-time curves for a gold film OTE at which a reduction product is produced with $\varepsilon_R = 10^2$, 10^3, and 10^4 M^{-1} cm^{-1}. Let $D_O = 1 \times 10^{-5}$ cm^2/s, and $C_O^* = 1$ mM. Draw graphs for times ranging from 1 to 100 ms. Comment on the magnitudes of the absorbances and their experimental implications.

17.4 Calculate the extinction coefficient, k, corresponding to a 10^{-3} M solution of a compound with $\varepsilon = 10^4$ M^{-1} cm^{-1}.

17.5 From data in Figure 17.1.9, calculate the values of n and k for gold at 2.0, 2.4, 2.8, 3.2, 3.6, and 4.0 eV. Plot them versus the wavelengths corresponding to these photon energies. Can you explain gold's color on the basis of your plots?

17.6 An absorbing species R is monitored in an IRS experiment featuring a forward step in which species O is reduced to R at the diffusion-controlled rate, and a reversal step in which R is converted back to O, also under diffusion control. Show that the normalized absorbance is given by

$$\mathcal{A}(t \le \tau)/\mathcal{A}(\tau) = 1 - \exp(a^2 t)\, \mathrm{erfc}(at^{1/2})$$
$$\mathcal{A}(t > \tau)/\mathcal{A}(\tau) = \exp[a^2(t - \tau)]\, \mathrm{erfc}[a(t - \tau)^{1/2}]$$

where τ is the forward step width and $a = D_R^{1/2}/\delta$. Assume that τ is large enough that (17.1.14) applies. For simplicity, you may assume $D_O = D_R = D$. How many parameters are needed to fit the transient? Plot points for about 10 values of t/τ in the range $0 \le t/\tau \le 2$.

17.7 Calculate the value of δ for an IRS system involving an aqueous solution ($n_3 = 1.34$) in contact with a platinum film on glass ($n_1 = 1.55$). The angle of incidence θ_1 is 75°, and the wavelength of incident light is 400 nm. What values of δ would apply at 600 and 800 nm? Suppose the angle of incidence is increased to 80°. What value of δ would apply at 600 nm?

17.8 Derive equations describing the Raman intensity as a function of time for the forward and reversal phases of the experiment of Figure 17.2.10. Prove that the linear relations observed in the plots of Figure 17.2.10*b* are expected. Could any information be obtained from the actual magnitude of the slopes? How could such transients be used for mechanistic diagnosis? Note that this problem can be approached in a manner similar to that employed in the derivation of (17.1.2).

17.9 Suppose the XPS bands in Figure 17.3.8 were excited by the Al K_α line at 1486.6 eV. What were the kinetic energies of the photoelectrons? What kinetic energies would be measured for excitation by the Mg K_α line at 1253.6 eV?

17.10 Why is it necessary to normalize the carbon responses in Figure 17.3.12?

18

PHOTOELECTROCHEMISTRY AND ELECTROGENERATED CHEMILUMINESCENCE
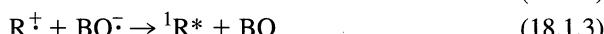
In this chapter, we will examine experiments in which photons actually participate in the electrode processes of interest.

18.1 ELECTROGENERATED CHEMILUMINESCENCE

Electrochemistry is very well-suited to studies of the solution chemistry of radical ions, because one can readily generate these reactive species by oxidizing or reducing stable precursors, such as aromatic amines, nitrites, nitro compounds, or polycyclic hydrocarbons. A particularly striking facet of radical-ion chemistry is the chemiluminescence that arises from some of the homogeneous electron-transfer reactions. Even though this light almost always comes from reactions in solution, it is usually studied by experiments involving electrolytic production of the participants; hence it is called *electrogenerated chemiluminescence* (or *electrochemiluminescence*, ECL). The topic has been extensively studied and thoroughly reviewed (1–5). Here we will simply outline the basic chemical and experimental aspects. The interested reader can pursue details in the reviews.

18.1.1 Chemical Fundamentals

Typical reactions producing ECL are the following ones involving radical ions of rubrene (R), N,N,N',N'-tetramethyl-p-phenylenediamine (TMPD), and p-benzoquinone (BQ):

$$R^{-} + R^{+} \rightarrow {}^{1}R* + R \tag{18.1.1}$$

$$R^{-} + TMPD^{+} \rightarrow {}^{1}R* + TMPD \tag{18.1.2}$$

$$R^{+} + BQ^{-} \rightarrow {}^{1}R* + BQ \tag{18.1.3}$$

The emission in all cases is the yellow fluorescence of rubrene, which arises from the first excited singlet, ${}^{1}R*$:

$$ {}^{1}R* \rightarrow R + h\nu \tag{18.1.4}$$

These reactions are typically carried out in acetonitrile or DMF.

The formation of an excited state as a result of electron transfer involves a kinetic manifestation of the Franck–Condon principle (2–4). The reactions are very energetic (typically 2–4 eV) and very fast (perhaps on the time scale of molecular vibration for the

actual transfer). Since it is difficult for the molecular frames to accept such a large amount of released energy in a mechanical form (e.g., vibrationally) on so short a time scale, there is a significant probability that an excited product will be produced, with consequently smaller vibrational excitation.

Research in this area addresses the fundamental aspects of energy disposition in fast, very exergonic reactions (3, 4), and it serves as a test for theories of electron transfer. By employing ECL-active species as labels on biological molecules, ECL has found application in commercial instruments for immunoassays and DNA analysis. The principles of these methods are outlined in Section 18.1.4.

The free energy released in a redox process producing ground-state products, e.g.

$$R^{\ddagger} + R^{\bar{\cdot}} \rightarrow 2R \qquad (18.1.5)$$

is essentially the energy available for exciting a product.[1] This number is readily computed from reversible standard potentials for ion/precursor couples, and it can be compared with excited state energies obtained via spectroscopy. Excited states lower than the available energy are accessible and may be populated in the reaction. Higher states are energetically inaccessible.

Figure 18.1.1 is a diagram of the energetics of reactions (18.1.1)–(18.1.3). Since all excited states of BQ and TMPD are inaccessible, only the rubrene singlet ($^1R^*$) and triplet ($^3R^*$) species can be produced. In addition, we see that (18.1.2) and (18.1.3) are *energy-deficient* in that the ultimate emitter $^1R^*$ is not accessible to the electron-transfer process. Thus, the reactions written in (18.1.2) and (18.1.3) must be overall processes involving more complex mechanisms. In contrast, (18.1.1) is *energy-sufficient*, in that the emitting state is marginally accessible, hence direct production of $^1R^*$ is possible. Such a path is usually called the S (for singlet) *route*.
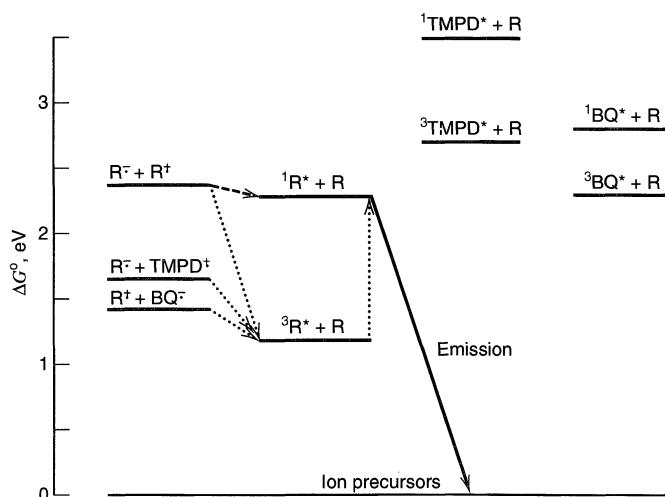
Figure 18.1.1   Energetics for chemiluminescent reactions of rubrene radical ions. All energies measured with respect to ground-state neutral species. Dashed arrow shows S route. Dotted arrows show T route. Promotion from $^3R^* + R$ to $^1R^* + R$ requires another rubrene triplet. [From L. R. Faulkner, *Meth. Enzymol.*, **57**, 494 (1978), with permission from Academic Press, Inc.]

---

[1]Actually, the energy available for exciting a product is the standard internal energy change, ΔE^0. Because the reaction is in a condensed phase, $\Delta E^0 \approx \Delta H^0$, which is $\Delta G^0 + T\Delta S^0$. Since, $T\Delta S^0$ for this kind of reaction is typically only about 0.1 eV, $\Delta E^0 \approx \Delta G^0$.

To rationalize the production of emitters in energy-deficient cases, one usually invokes a mechanism involving triplet intermediates, for example,

$$R^{\bar{\cdot}} + TMPD^{\bar{\cdot}+} \rightarrow {}^3R* + TMPD \tag{18.1.6}$$

$$^3R* + {}^3R* \rightarrow {}^1R* + R \tag{18.1.7}$$

The second step is called *triplet-triplet annihilation*, and it allows the energy from two electron transfers to be pooled into the production of a singlet. There is much evidence favoring the operation of this mechanism, which is usually called the T (for triplet) *route*. Note that it may operate in energy-sufficient systems, as well as energy-deficient ones.

The energetics of the ECL reaction can also be helpful in understanding the formation of the excited state by using Marcus theory (see Section 3.6.2) (6). The relative rates of reactions can be gauged from their free energies, ΔG^0. For modest ΔG^0 values, the rate generally increases as ΔG^0 becomes more negative. However, for large negative ΔG^0 values, the rate becomes slower (the Marcus "inverted region"). In ECL reactions, as shown in Figure 18.1.1, the ΔG^0 for reactants producing ground state species is large, while that producing an excited state is smaller. Thus, an energetic electron-transfer reaction can actually favor excited state formation over the ground state route. Indeed, ECL was the first experimental evidence of the existence of an inverted region in electron-transfer reactions.

Hundreds of ECL reactions have been reported, and many are spectroscopically simple enough to be understood in these terms. Others offer emission bands due to *excimers* [excited dimers such as $(DMA)_2^*$, where DMA is 9,10-dimethylanthracene], exciplexes [excited-state complexes, such as $(TPTA^{\bar{\cdot}+}BP^{\bar{\cdot}})$, where TPTA is tri-*p*-tolylamine and BP is benzophenone], or simply decay products of the radical ions. More complicated mechanisms are obviously needed to describe such situations. Many studies involve radical ions of aromatic compounds, but others have dealt with metal complexes such as $Ru(bpy)_3^{2+}$ [bpy = 2,2′-bipyridine], superoxide, solvated electrons, and classical chemiluminescent reagents, such as lucigenin (1–5).

The primary experimental goals of ECL experiments are to define the nature of the emitting state, the mechanism by which it is produced, and the efficiency of excited-state production. ECL is also useful for chemical analysis.

18.1.2 Apparatus and Reactant Generation (2)

ECL experiments focused on radical ion annihilation are carried out in fairly conventional electrochemical apparatus, but procedures must be modified to allow the electrogeneration of two reactants, rather than one, as is more commonly true. In addition, one must pay scrupulous attention to the purity of the solvent/supporting electrolyte system. Water and oxygen are particularly harmful to these experiments. Thus, apparatus is constructed to allow transfer of solvent and degassing on a high-vacuum line or in an inert-atmosphere box. Other constraints may be imposed by optical equipment used to monitor the light.

Most experiments have been carried out by generating the reactants sequentially at a single electrode. For example, one might start with a solution of rubrene and TMPD in DMF. A platinum working electrode stepped to -1.6 V *vs.* SCE produces $R^{\bar{\cdot}}$ in the diffusion layer. After a forward generation time, t_f, which could be 10 μs to 10 s, the potential is changed to perhaps $+0.35$ V to produce $TMPD^{\bar{\cdot}+}$, which diffuses outward. Since $R^{\bar{\cdot}}$ is oxidized at this potential, its surface concentration drops effectively to zero, and $R^{\bar{\cdot}}$ in the bulk begins to diffuse back toward the electrode. Thus $TMPD^{\bar{\cdot}+}$ and $R^{\bar{\cdot}}$ move together and react. If the reaction rate constant is very large, their concentration profiles do not overlap, and the reaction occurs in the plane where they meet, as shown in Figure 18.1.2. As the experiment proceeds, the $R^{\bar{\cdot}}$ gradually is used up, and the reaction plane moves

(a)

(b)
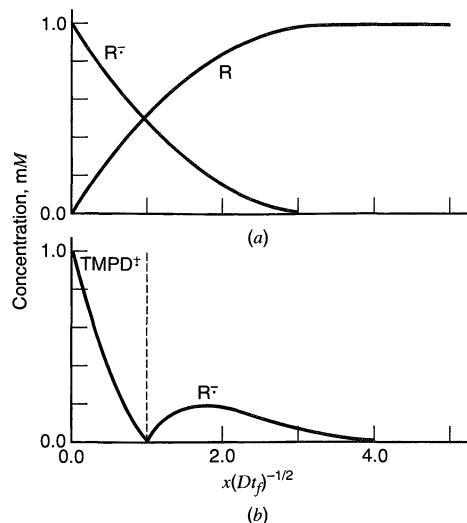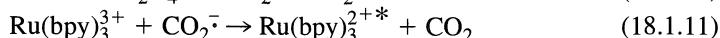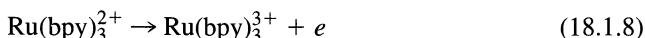
Figure 18.1.2 Concentration profiles near an electrode during an ECL step experiment. Data apply to 1 mM R and 1 mM TMPD. (a) Profiles of R and R$^-$ at the end of the forward step. (b) Concentrations of TMPD$^+$ and R$^-$ during the second step. Reaction boundary is shown by the dotted line. Curves apply for a time 0.4 t_f into the second step, where t_f is the forward step width. For this illustration all diffusion coefficients are taken as equal.

farther from the electrode. The light appears as a pulse that decays with time because of the depletion of R$^-$. Experiments like these may be carried out in a double- or triple-step format to produce one pulse of light; or a train of alternating steps can be used to produce a sequence of light pulses.

Other useful approaches to annihilation ECL involve the generation of the reactants at two different electrodes in close proximity. For example, an RRDE (Chapter 9) can be employed, with one reactant, such as R$^-$, generated at the disk and the other, R$^+$, generated at the ring. As discussed in more detail in the first edition,[2] these are swept together by diffusion and convection, resulting in reaction and a ring of light on the inner edge of the ring electrode (2, 7, 8). Other experiments employ dual-working-electrode systems (9, 10) with thin-layer geometry, interdigitated electrodes, or flow streams to move the reactants together.

Not all ECL reactions require the cycling of the electrode potential to produce the oxidized and reduced forms. By addition of certain species, called *coreactants*, it is possible to generate ECL in a single potential step (11, 12). These systems also permit ECL to be observed in aqueous solutions, where the potential limits are too narrow to allow convenient electrolytic generation of both the oxidized and reduced ECL precursors for annihilation ECL. Consider, for example, an aqueous solution of Ru(bpy)$_3^{2+}$. This species is oxidized at a Pt electrode to form Ru(bpy)$_3^{3+}$ at about $+1$ V *vs.* SCE. To form the excited state species Ru(bpy)$_3^{2+*}$, with an energy of 2.04 eV above the ground state, one needs a reductant produced at a potential more negative than about -1.2 V. This potential is not easily attainable at a Pt electrode in aqueous solution without the evolution of copious amounts of hydrogen. However, in certain ECE reactions (see Chapter 12) one can generate a strong reductant by *oxidizing* a species. For example, the oxidation of oxalate (the coreactant) actually produces a strong *reducing* agent, CO$_2^-$, which can then react with Ru(bpy)$_3^{3+}$ to produce the excited state. The reaction sequence is:

$$\text{Ru(bpy)}_3^{2+} \rightarrow \text{Ru(bpy)}_3^{3+} + e \tag{18.1.8}$$

$$\text{C}_2\text{O}_4^{2-} \rightarrow \text{C}_2\text{O}_4^- + e \tag{18.1.9}$$

$$\text{C}_2\text{O}_4^- \rightarrow \text{CO}_2 + \text{CO}_2^- \tag{18.1.10}$$

$$\text{Ru(bpy)}_3^{3+} + \text{CO}_2^- \rightarrow \text{Ru(bpy)}_3^{2+*} + \text{CO}_2 \tag{18.1.11}$$
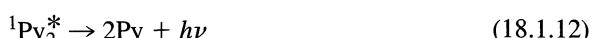
[2]First edition, pp. 624–626.

where $CO_2^{-\cdot}$ appears because the oxidized oxalate decomposes with the formation of very strong bonds in CO_2. Thus, in a mixture of $Ru(bpy)_3^{2+}$ and $C_2O_4^{2-}$, light is generated in a single, oxidizing potential step. A number of other coreactants, like tertiary amines, will also undergo a similar reaction sequence with the $Ru(bpy)_3^{2+}$ system. These have been employed in analytical applications as discussed briefly in Section 18.1.4.

Many ECL investigations involve special optical procedures, such as calibrating the spectral response of a detection system or measuring the absolute total emission rate of an ECL process. These techniques are beyond our purview; discussions of them are available in the review literature (2).

18.1.3 Kinds of Experiments

The most obvious ECL experiments involve recording spectra of the emitted light, which are essential for identification of emitting species. In some cases, ECL produces emission from states that may play only a small role in the fluorescence of the electrolyzed solution. Figure 18.1.3 offers an example (8). The fluorescence of a solution of pyrene (Py) and TMPD excited at 350 nm shows a sharp band at 400 nm, ascribed to $^1Py^*$, and a minor shoulder at 450 nm, due in part to the excimer $^1Py_2^*$, which emits in the dissociative process:

$$^1Py_2^* \rightarrow 2Py + h\nu \tag{18.1.12}$$

In contrast, the ECL from the reaction between $Py^{-\cdot}$ and $TMPD^{+\cdot}$, produced by electrolysis at an RRDE, where Py is reduced at the ring and TMPD is oxidized at the disk, shows predominant emission from the excimer. Thus, the chemiluminescent system has a specific path for relatively efficient production of the excimer. It is believed to be the triplet-triplet annihilation involving $^3Py^*$.

Another useful experiment for deciphering the basic chemistry of ECL can be illustrated by the data in Figure 18.1.4, which shows light intensity from the TMPD/Py system versus disk potential (8). In the upper frame $Py^{-\cdot}$ was generated at the ring, and one sees that light results from the oxidation (at the disk) of TMPD to either $TMPD^{+\cdot}$ (first wave)
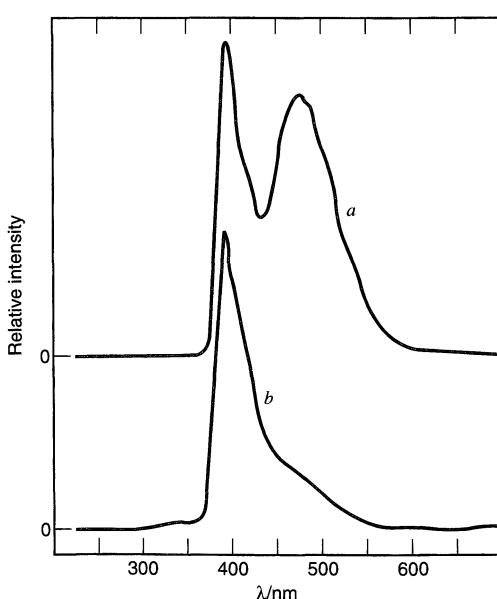
Figure 18.1.3 *Curve a:* Chemiluminescence from the reaction between $Py^{-\cdot}$ and $TMPD^{+\cdot}$ in DMF. Electrogeneration of ions was carried out at an RRDE in a solution of 1 mM TMPD and 5 mM Py. *Curve b:* Fluorescence spectrum of the same solution under excitation at 350 nm. [Original data from J. T. Maloy and A. J. Bard, *J. Am. Chem. Soc.*, **93**, 5968 (1971). Copyright 1975, American Chemical Society. Figure from L. R. Faulkner, *Int. Rev. Sci.: Phys. Chem. Ser. Two*, **9**, 213 (1975). Reproduced with permission of the American Chemical Society.]
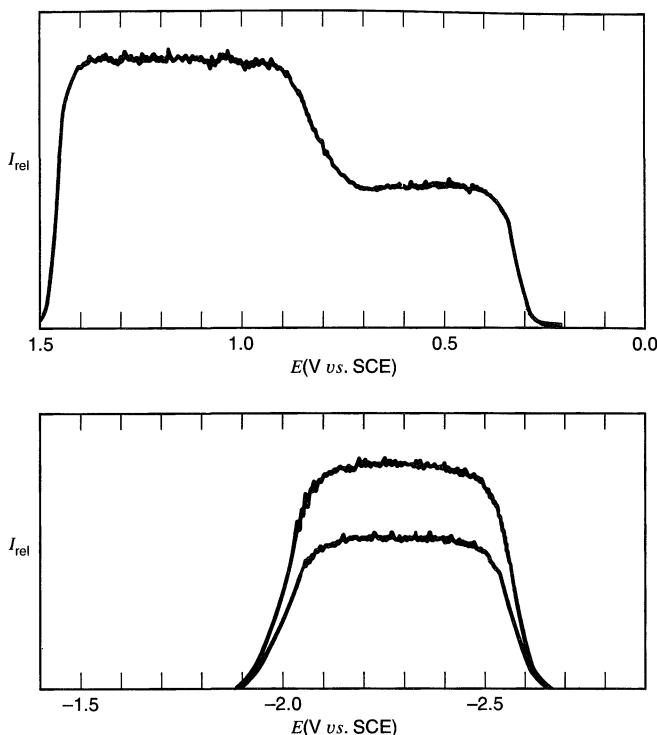
Figure 18.1.4 Steady-state ECL behavior versus disk potential in the pyrene-TMPD system. *Top*: Py⁻̇ generated at ring (emission detected at 393 nm). *Bottom*: TMPD⁺̇ generated at ring [emission detected at 393 nm (*upper curve*) and 470 nm (*lower curve*)]. [Reprinted with permission from J. T. Maloy and A. J. Bard, *J. Am. Chem. Soc.*, **93**, 5968 (1971). Copyright 1971, American Chemical Society.]

or $TMPD^{2+}$ (second wave). Oxidation products generated at very positive potentials (perhaps Py^{+} or its decay products) quench the ECL. Interpretation of the lower frame is left as Problem 18.3.

The mechanism of light production is always of interest, and many experiments have been devised to probe it. One approach is based on shapes of single pulses of light produced in a step sequence like that described above (2–4). The basic idea is to find the dependence of light intensity on the rate of redox reaction between the oxidant and reductant. For example, the S route calls for a linear dependence, whereas the T route generally would yield a relationship of higher order. The diffusion-kinetic problem for step generation of ECL has been solved (13), and the time decay of the redox reaction rate can be calculated for a given system. It can then be compared with the observed intensity transient. Data (14) for the reaction between the energy-sufficient reaction between the cation radical of thianthrene (TH) and the anion radical of 2,5-diphenyl-1,3,4-oxadiazole (PPD) are shown in Figure 18.1.5. These results show that the observed intensity follows the *square* of the reaction rate, even through a rather complex potential program, and this fact alone has some useful things to say about the mechanism of light production. The reason for the dip is part of Problem 18.4.

By using an ultramicroelectrode as the generator in annihilation experiments, it is possible to bring the time scale of the measurements into the microsecond regime. In reported experiments (15), a continuous symmetric square wave with step times down to
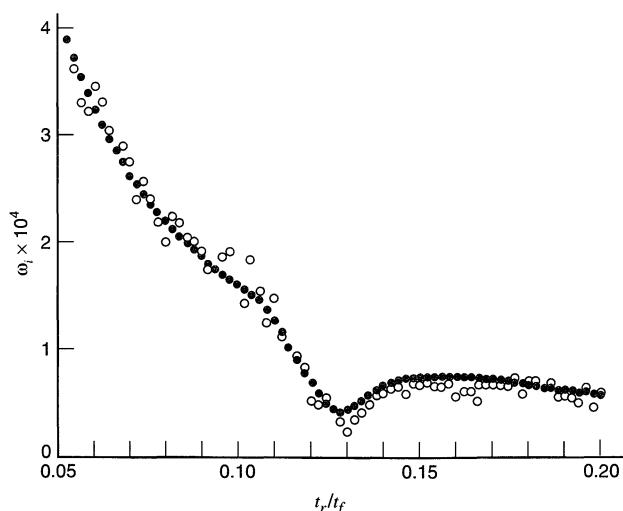
Figure 18.1.5 Light intensity (open circles) and square of redox reaction rate (filled circles) versus time t_r measured into the second step of a transient experiment. Forward step width, t_f, was 500 ms. The ECL process involved TH$\overset{+}{\cdot}$ and PPD$\overline{\cdot}$. See Problem 18.4 for a discussion of the dip. [Reprinted with permission from P. R. Michael and L. R. Faulkner, *J. Am. Chem. Soc.*, **99**, 7754 (1977). Copyright 1977, American Chemical Society.]

5 μs was applied to electrodes with radii of 1 to 5 μm in a solution of radical precursors of about 0.2 mM. The emission was measured with a single photon counting apparatus. By comparing the shape of the relative intensity *vs.* time to theoretical behavior obtained by digital simulation, it was possible to find the rate constant for the ion-annihilation reaction. These short-time steps (or high square-wave frequencies) are not useful with larger electrodes, because the current during the step is dominated by double-layer charging and the electrode potential does not follow the applied potential step waveform (see Sections 5.9.1 and 15.6.1). Under these conditions, the emission intensity is small because the faradaic current is small. From such measurements with UMEs, the ion-annihilation rate constants for DPA and Ru(bpy)$_3^{2+}$ were found to be at the diffusion-controlled level, 2×10^{10} $M^{-1}s^{-1}$ in MeCN solutions. In a later experiment (16), the DPA solution concentration was decreased to 15 μM and the temporal resolution to the nanosecond regime. In this case, a 500 μs pulse was used to generate DPA$\overset{+}{\cdot}$ followed by a 50 μs cathodic pulse to generate DPA$\overline{\cdot}$. Emission during the cathodic pulse was observed with a single photon counting apparatus. When the output was observed with nanosecond resolution (i.e., bin size of 5 ns), individual annihilation reaction events could be observed.

Still other experiments are designed to intercept intermediates, such as triplets or singlet oxygen. Results for such a case are given in Figure 18.1.6, which arose from a study of the energy-deficient reaction between the cation radical of 10-methylphenothiazine (10-MP) and the anion radical of fluoranthene (FA) (17). The system is believed to produce light by the annihilation of ^{3}FA*. Addition of anthracene (An) could be accomplished without disturbing the electrochemistry needed to produce the reactants, but it transformed the emission spectrum from that of ^{1}FA* to that of ^{1}An*. Apparently, this result was caused by the energy transfer:

$$An + {}^3FA^* \rightarrow FA + {}^3An^* \qquad (18.1.13)$$

followed by annihilation of ^{3}An*.

Sometimes magnetic fields enhance ECL intensities, and studies along this line have been used for mechanistic diagnosis (2). The effects seem to arise from field-dependent rate constants for certain reactions involving triplets; hence they are associated with the T route.
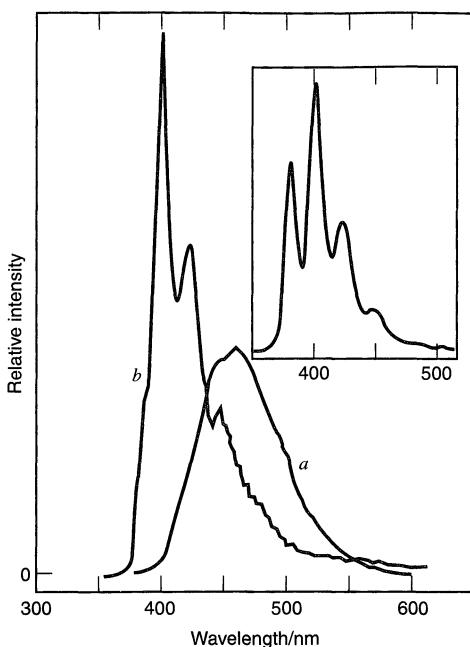
Figure 18.1.6 *Curve a*: Chemiluminescence from FA^{-} and 10-MP^{+} in DMF. Reactants were generated from solutions containing 1 mM FA and 10-MP. *Curve b*: Spectrum upon addition of anthracene. Inset shows fluorescence from anthracene at 10 μM in DMF. Shortest wavelength peak is not seen in ECL because of self-absorption. [Original data from D. J. Freed and L. R. Faulkner, *J. Am. Chem. Soc.*, **93**, 2097 (1971). Copyright 1971, American Chemical Society. Figure from L. R. Faulkner, *Int. Rev. Sci.: Phys. Chem. Ser. Two.*, **9**, 213 (1975). Reproduced with permission of the American Chemical Society.]

In its classic form, ECL is regarded as a solution-phase process, on the basis of both direct evidence (Problem 18.4) and the expectation that metal electrodes quench excited states (18, 19). The band structure of semiconductor electrodes sometimes removes the latter difficulty (see Section 18.2), and emission from excited states produced directly in *heterogeneous* charge transfer at semiconductors can occur (20–22). More recently, even surface films, such as monolayer assemblies and polymer-modified electrodes (Chapter 14), have been reported to produce ECL. For example, a Langmuir–Blodgett monolayer of a long chain hydrocarbon with an attached Ru(bpy)$_3^{2+}$ group or a similar self-assembled monolayer will show ECL emission on oxidation in the presence of a coreactant (23, 24). In fact, monolayers at the air-water interface that contain ECL-active groups will emit when contacted by touching the horizontal film with an ultramicroelectrode tip from the air side. In this experiment, the counter and reference electrodes and the coreactant are all contained in the aqueous medium in the Langmuir trough (25). Polymer films on electrodes, such as poly(vinyl-DPA) (26), a polymerized film of tris(4-vinyl-4'-methyl-2,2'-bipyridyl)Ru(II) (27), or Ru(bpy)$_3^{2+}$ in Nafion (28), will also produce ECL. ECL processes that produce light in polymer layers in the absence of solvent (electroluminescent polymers) are of interest in connection with possible display applications (29, 30).
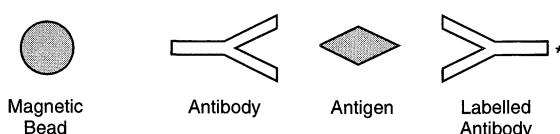
18.1.4 Analytical Applications of ECL

Because the light intensity is usually proportional to the concentration of the emitting species, ECL can be used in analysis (31). In such applications, the system of interest is introduced into a suitable electrochemical cell, and light emission is excited electrochemically, with the emission intensity (and sometimes the emission spectrum) being measured. The ECL technique is very sensitive, since very low light levels can be measured (e.g., by single photon counting methods). In a sense, ECL is similar to a photoexcitation (e.g., fluorescence) method; however, it has the advantage that a light source is not used, so that scattered light and interferences from emission by luminescent impurities are not prob-

lems. ECL is often more convenient than other chemiluminescent methods, since the electrochemical excitation allows temporal and spatial control. ECL can be carried out to analyze either the emitting species (which often serves as a label on a molecule of interest) or a coreactant.
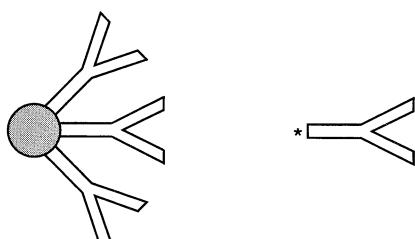
The most frequently used ECL-active label is $Ru(bpy)_3^{2+}$, because its ECL can be generated in aqueous solutions with a suitable coreactant (for example, oxalate for oxidations and peroxydisulfate for reductions) and because the emission is intense and fairly stable. The emission intensity is proportional to concentration over a very wide range (e.g., 10^{-7} to 10^{-13} M) (32). By attachment of a suitable group to the bipyridine moieties, $Ru(bpy)_3^{2+}$ can be linked to biologically interesting molecules, such as antibodies or DNA, where it serves as a label for analysis in an analogous manner to radioactive or fluorescent labels (33). Commercial instruments are available for ECL assays of antibodies, antigens, and DNA (34–36). These are currently based on the use of magnetic bead technology.

The principles of a typical sandwich assay of an antigen are outlined in Figure 18.1.7. The surfaces of commercially available magnetic beads are modified by attaching an antibody to a particular antigen of interest (e.g., prostate specific antigen, PSA). These beads, the sample of interest, and $Ru(bpy)_3^{2+}$-labeled antibodies are mixed. If antigen is present, as shown in Figure 18.1.7, the labeled antibody becomes attached to the magnetic bead, because the antigen behaves as a bridge to form a "sandwich" structure. If no antigen is present, the labeled antibody does not attach to the bead. The magnetic beads are then flushed into an ECL cell, where they are captured on the working electrode by applying a magnetic field (Figure 18.1.8). The beads are washed, and a solution of the appropriate composition containing a coreactant (usually tri-n-propylamine, TPrA) is pumped into the cell. Upon application of a sweep or step to positive potentials, oxidation of $Ru(bpy)_3^{2+}$ and coreactant occur with emission of light from the bead-bound $Ru(bpy)_3^{2+}$, which is de-

(a) Sample with no antigen (labelled antibody not attached to bead)

(b) Sample with antigen (labelled antibody attaches to bead)
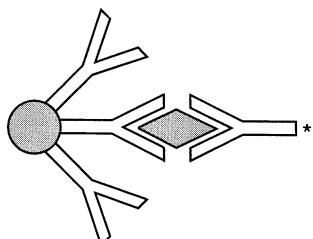
Figure 18.1.7 Representation of ECL-based immunoassay.
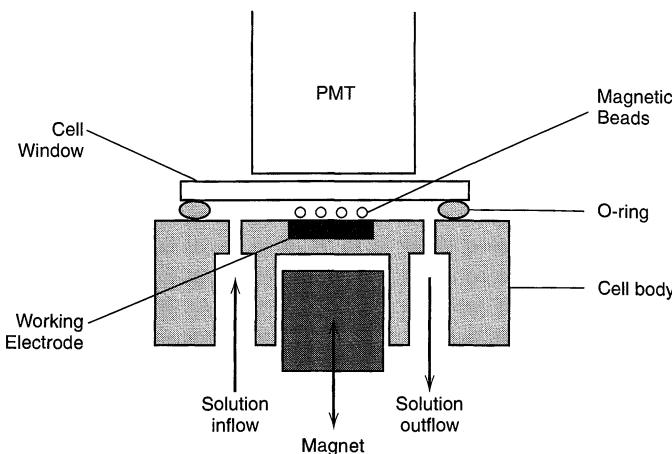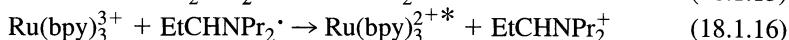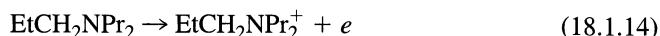
Figure 18.1.8 Flow cell used in a commercial instrument for ECL-based immunoassay employing magnetic beads (33–35).

tected with the photomultiplier. The proposed chemistry (37, 38) in the $Ru(bpy)_3^{2+}$/TPrA system follows that with oxalate as a coreactant, that is, (18.1.8)–(18.1.11):

$$EtCH_2NPr_2 \rightarrow EtCH_2NPr_2^+ + e \qquad (18.1.14)$$

$$EtCH_2NPr_2^+ \rightarrow EtCHNPr_2\cdot + H^+ \qquad (18.1.15)$$

$$Ru(bpy)_3^{3+} + EtCHNPr_2\cdot \rightarrow Ru(bpy)_3^{2+*} + EtCHNPr_2^+ \qquad (18.1.16)$$

Following the measurement, the beads are washed from the cell, which is then cleaned and made ready for the next sample. Automated instruments for clinical diagnostics, capable of handling multiple samples without operator intervention, are available.

ECL has also been used in detector cells in chromatography. These again involve the ECL of $Ru(bpy)_3^{2+}$, where detected species, such as amines, NADH, and amino acids, behave as the coreactant. In one method, *post-column ECL detection*, a solution of $Ru(bpy)_3^{2+}$ is steadily injected into the solution stream containing separated species coming from the HPLC column. The mixed stream flows into an electrolytic cell where the ECL reaction occurs and emission is measured (39). Detection of separated species at the picomole level is possible by this technique. Alternatively the $Ru(bpy)_3^{2+}$ can be immobilized in a film of Nafion on the working electrode (28), and the ECL signal results when the solution from the HPLC column contains a species that can act as a coreactant and produce emission by reaction with immobilized $Ru(bpy)_3^{3+}$ in the detector cell (40). Observation of ECL with flowing streams can also provide information about the hydrodynamics in the detector cell (41).

▶ 18.2 PHOTOELECTROCHEMISTRY AT SEMICONDUCTORS

18.2.1 Introduction

In photoelectrochemical experiments, irradiation of an electrode with light that is absorbed by the electrode material causes the production of a current (a *photocurrent*). The dependence of the photocurrent on wavelength, electrode potential, and solution composition provides information about the nature of the photoprocess, its energetics, and its kinetics. Photocurrents at electrodes can also arise because of photolytic processes occurring in the solution near the electrode surface; these are discussed in Section 18.3. Photoelectrochemical studies are frequently carried out to obtain a better understanding of the nature of the electrode–solution interface. However, because the production of a

photocurrent can represent the conversion of light energy to electrical and chemical energy, such processes are also investigated for their potential practical applications. Since most of the studied photoelectrochemical reactions occur at semiconductor electrodes, we will review briefly the nature of semiconductors and their interfaces with solutions. Consideration of semiconductor electrodes also helps in gaining a microscopic understanding of electron-transfer processes at solid–solution interfaces. A number of detailed reviews of this area have appeared (42–49).

18.2.2 Semiconductor Electrodes

The electronic properties of solids are usually described in terms of the *band model*, which involves the behavior of electrons moving in the combined field of atomic nuclei and other electrons in an array (44, 50–53). Consider the formation of a crystalline solid (e.g., Si, TiO_2). As isolated atoms, which are characterized by filled and vacant orbitals, are assembled into a lattice containing $\sim 5 \times 10^{22}$ atoms/cm^3, new molecular orbitals form. These orbitals are so closely spaced that they fall in essentially continuous bands; the filled bonding orbitals form the *valence band* and the vacant antibonding orbitals form the *conduction band* (Figure 18.2.1). In general, these bands are separated by a *forbidden region* or *band gap* of energy E_g, usually given in units of electron volts. The electrical and optical properties of the solid are strongly influenced by the size of the band gap.

When the gap is very small ($E_g \ll \&T$), or when the conduction and valence bands actually overlap, the material is a good conductor of electricity (e.g., Cu, Ag). Under these circumstances, there exist filled and vacant electronic energy levels at virtually the same energy, so that an electron can move from one level to another with only a small energy of activation. This feature provides electrical mobility for electrons in the solid and allows them to respond to an electric field. In contrast, electrons in a completely full band, with no empty levels nearby in energy, have no means for redistributing themselves spatially in response to a field, so they cannot support electrical conduction.

For larger values of E_g (e.g., for Si, where $E_g = 1.1$ eV), the valence band (VB) is almost filled and the conduction band (CB) almost vacant. Conduction becomes possible because of thermal excitation of electrons from the VB into the CB (Figure 18.2.2). This process produces electrons in the CB, which have electrical mobility because they can
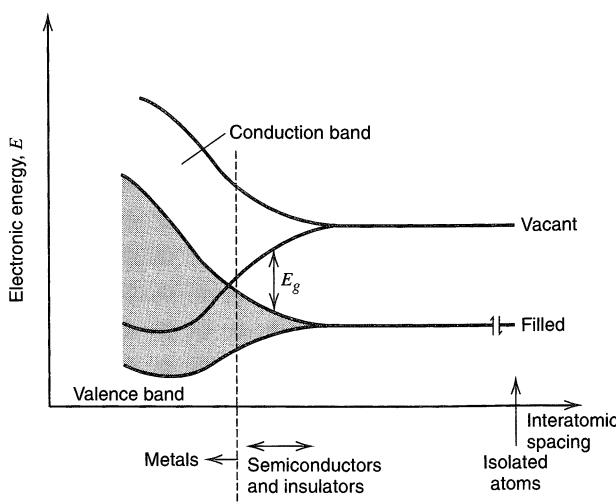
Figure 18.2.1 Formation of bands in solids (at left) by assembly of isolated atoms (characterized by orbitals at far right) into a lattice.
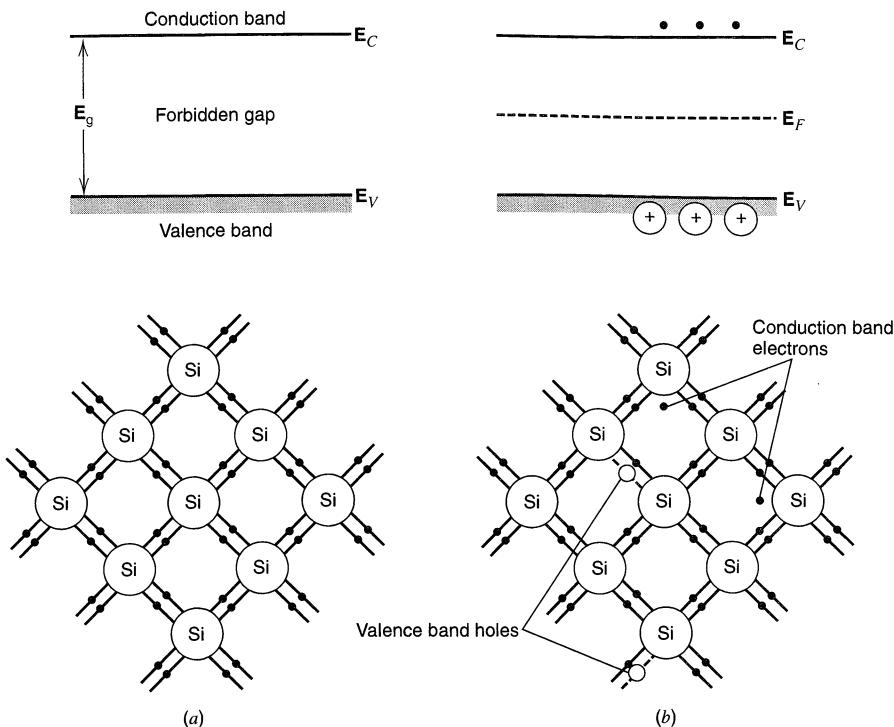
Figure 18.2.2 Energy bands and two-dimensional representation of an intrinsic semiconductor lattice. (*a*) At absolute zero (or $E_g \gg \ell T$), assuming a perfect lattice; no holes or electrons exist. (*b*) At a temperature where some lattice bonds are broken, yielding electrons in the conduction band and holes in the valence band. E_F represents the Fermi level in this intrinsic semiconductor.

transfer freely among vacant levels in the CB, and leaves behind "holes" in the VB that have mobility because VB electrons can rearrange themselves to shift the spatial location and energy of the vacancy. Such a material is called an *intrinsic semiconductor*. The *charge carriers*, electrons and holes, exist in a dynamic equilibrium. They are created by dissociation and eliminated by recombination; and their *densities*, n_i for CB electrons and p_i for VB holes, adhere to an equilibrium constant of the form $n_i p_i = $ (constant) exp $(-E_g/\ell T)$. In an intrinsic semiconductor, the electron and hole densities are equal and are given approximately by the expression (44)

$$n_i = p_i \approx 2.5 \times 10^{19} \exp\left(\frac{-E_g}{2\ell T}\right) \text{cm}^{-3} \text{ (near 25°C)} \qquad (18.2.1)$$

For example, for silicon, $n_i = p_i \approx 1.4 \times 10^{10} \text{ cm}^{-3}$. The mobile carriers move in the semiconductor in a manner analogous to the movement of ions in solution; however the mobilities of these species, u_n and u_p, are orders of magnitude larger than for ions in solution. For example, for silicon, $u_n = 1350 \text{ cm}^2 \text{ V}^{-1}\text{s}^{-1}$ and $u_p = 480 \text{ cm}^2 \text{ V}^{-1}\text{s}^{-1}$.

For materials with $E_g > 1.5$ eV, so few carriers are produced by thermal excitation at room temperature that in the pure state such solids are electrical insulators (e.g., GaP and TiO$_2$, with E_g equal to 2.2 and 3.0 eV, respectively).

Electrons in the CB and holes in the VB can also be introduced by the substitution of acceptor and donor atoms (called *dopants*) into the semiconductor lattice to produce *extrinsic* materials. Thus an arsenic atom (a Group V element) behaves as an electron donor when sub-

stituted into crystalline silicon (a Group IV element) and introduces an energy level at E_D, just below the bottom of the CB (within ~0.05 eV). At room temperature, most of the donor atoms are ionized, each one yielding a CB electron and leaving behind an isolated positive site at the donor atom (Figure 18.2.3a). If the amount of dopant is about 1 ppm, the donor density, N_D, is ~5×10^{16} cm^{-3}, and this will essentially be the CB electron density n. The hole density p is much smaller and is given by the electron-hole equilibrium relationship,

$$p = \frac{n_i^2}{N_D} \tag{18.2.2}$$

Thus, for this example of As-doped Si, $p \approx 4000$ cm^{-3} at 25°C. In such a material, most of the electrical conductivity can be clearly attributed to the CB electrons, which are the *majority carriers*. The holes, which make only a small contribution to the conductivity, are called the *minority carriers*. A material doped with donor atoms is called an *n-type semiconductor*.[3]

If an acceptor atom (e.g., gallium, a Group III element) is substituted into the silicon, an energy level is introduced at E_A, just above the top of the VB (Figure 18.2.3b). In this case, electrons are thermally excited from the VB into these acceptor sites, leaving mobile holes in the VB and isolated, negatively charged acceptor sites. Thus, the acceptor density, N_A, is essentially the same as the hole density, p, and the CB electron density, n, is given by

$$n = \frac{n_i^2}{N_A} \tag{18.2.3}$$
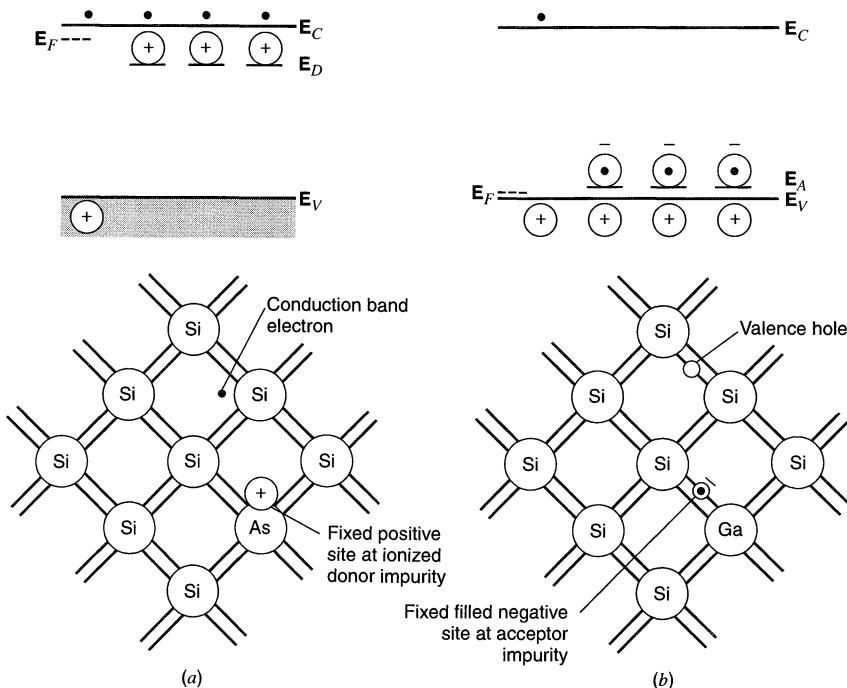
Figure 18.2.3 Energy bands and two-dimensional representation of extrinsic semiconductor lattices. (a) *n*-type. (b) *p*-type.

---

[3]Delocalized electrons and holes can also be introduced by atomic vacancies in the lattice. For example, *n*-type conductivity in the intrinsic insulator TiO_2 can be produced by oxygen vacancies in the lattice.

For example, with $N_A = 5 \times 10^{16}$ atoms of acceptor/cm^3 in Si, $n \approx 4000$ cm^{-3}. In this case, the holes are the majority carriers, the electrons are the minority carriers, and the material is called a *p-type semiconductor*.

An important concept in the description of semiconductor electrodes is that of the *Fermi level*, $\mathbf{E_F}$, which is defined as the energy where the probability is 1/2 that a level is occupied by an electron (i.e., where it is equally probable that the level is occupied or vacant; see also Section 3.6.3). For an intrinsic semiconductor at room temperature, $\mathbf{E_F}$ lies essentially midway between the CB and VB within the forbidden gap region. In contrast to metals, where both occupied and vacant states are present at energies near $\mathbf{E_F}$, neither electrons nor unfilled levels exist near $\mathbf{E_F}$ for an intrinsic semiconductor. For a doped material, the location of $\mathbf{E_F}$ depends on the doping level, N_A or N_D. For moderately or heavily doped *n*-type solids ($N_D > 10^{17}$ cm^{-3}), $\mathbf{E_F}$ lies slightly below the CB edge (Figure 18.2.3a). Similarly, for moderately or heavily doped *p*-type materials, $\mathbf{E_F}$ lies just above the VB edge (Figure 18.2.3b).

It is convenient to identify $\mathbf{E_F}$ in a more thermodynamic way, so that electronic properties of the semiconductor can be correlated with those of solutions. This is easily accomplished, since the Fermi level of a phase α, $\mathbf{E_F^\alpha}$, can be identified as the electrochemical potential (Sections 2.2.4 and 2.2.5) of an electron in α, μ_e^α (42, 43):

$$\mathbf{E_F^\alpha} = \bar{\mu}_e^\alpha = \mu_e^\alpha - e\phi^\alpha \text{ (in eV)} \tag{18.2.4}$$

The absolute value of $\mathbf{E_F}$ depends on the choice made for the reference state. Frequently this is taken as zero for a free electron in a vacuum, and $\mathbf{E_F}$ levels in metals and semiconductors can be determined from measurements of work functions or electron affinities (Figure 18.2.4). Since an electron is at a lower energy in almost all materials than in vacuum, $\mathbf{E_F}$ values are usually negative (e.g., about -5.1 eV for Au or -4.8 eV for intrinsic Si).

Let us now consider the formation of the semiconductor/solution interface. The Fermi level in the solution phase, can be identified as $\bar{\mu}_e^s$ by (18.2.4) and is calculated in terms of E^0 values by the procedures described in Section 2.2. For most electrochemical purposes, it is convenient to refer E^0 values to the NHE (or other reference electrodes), but in this case it is more instructive to estimate them with respect to the vacuum level. This can be accomplished, as discussed in Section 2.2.5, by theoretical and experimental means with relaxation of thermodynamic rigor, so that one obtains an energy level value for the NHE at about -4.5 ± 0.1 eV on the absolute scale (45) (Figure 18.2.5a). Consider the formation of the junction between an *n*-type semiconductor and a solution containing a redox couple O/R, as shown in Figure 18.2.5. When the semiconductor and the solution are brought into contact, if electrostatic equilibrium is attained, $\bar{\mu}_e$ in both phases must become equal (or equivalently the Fermi levels must become equal), and this can occur by
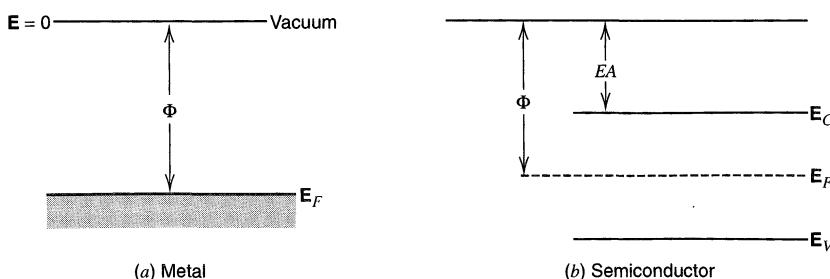
Figure 18.2.4 Relationships between energy levels, Φ (work function), and *EA* (electron affinity) for (a) a metal; (b) a semiconductor.
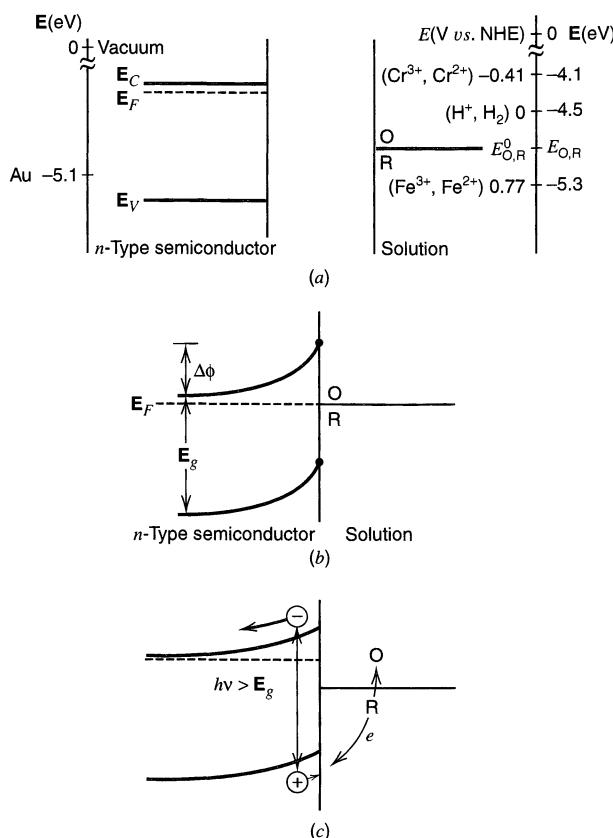
Figure 18.2.5 The formation of a junction between an n-type semiconductor and a solution containing a redox couple O/R. (a) Before contact in the dark. Typical values for energy levels shown referenced to NHE (E^0) and to vacuum (**E**). (b) After contact in the dark and electrostatic equilibration. (c) Junction under irradiation. [From A. J. Bard, *J. Photochem.*, **10**, 59 (1979), with permission. Adapted to show current best values for the absolute scale.]

charge transfer between the phases. In the case illustrated in Figure 18.2.5, where $\mathbf{E}_F$ of the semiconductor lies above that in solution, electrons will flow from the semiconductor (which becomes positively charged) to the solution phase (which becomes negatively charged).[4] The excess charge in the semiconductor does not reside at the surface, as it would in a metal, but instead is distributed in a *space-charge region*. This charge distribution is analogous to that found in the diffuse double layer that forms in solution (see Section 13.3). The resulting electric field in the space-charge region affects the local energy (electrochemical potential) of electrons. Thus, the band energies in this region are different than those in the bulk (field free) semiconductor. Since almost all of the potential drop between the bulk semiconductor and the solution is across the space-charge region, rather than at the semiconductor–solution interface, the position of the band at the interface does not change. The positive charge in the space-region causes the band energies to become more negative with increasing distance into the semiconductor, and then remain to flat in the field-free bulk (see Figure 18.2.5b). This effect is called *band bending*. In this case, when the semiconductor charge is positive with respect to the solution, the bands are bent upward (with respect to the energy level in the bulk semiconductor). An excess electron

---

[4]Although this description is frequently given of the semiconductor–solution junction, in fact, such reversible behavior of a semiconductor electrode is rarely found, especially for aqueous solutions. This lack of equilibration can be ascribed to corrosion of the semiconductor, to surface film (e.g., oxide) formation, or to inherently slow electron transfer across the interface. Under such conditions, the behavior of the semiconductor electrode approaches ideal polarizability (see Section 1.2).

in the space-charge region would therefore move toward the bulk semiconductor in the direction consistent with the existing electric field. An excess hole in the space-charge region would move toward the interface. The potential at which no excess charge exists in the semiconductor is clearly the potential of zero charge, E_z. Since there is no electric field and no space-charge region under these conditions, the bands are not bent. For this reason this electrode potential is called the *flat-band potential*, E_{fb}.[5]

Derivations for the relationships between the excess charge in the semiconductor and the potential, the potential distribution in the space-charge region, and the differential capacitance all follow closely those for the diffuse double layer in solution (44, 50) (see Section 13.3). Thus for an intrinsic semiconductor the relationship between the space-charge density, σ^{SC}, and the potential of the surface with respect to the bulk of the semiconductor, $\Delta\phi$, is given by (13.3.20), with the following replacements: σ^M by σ^{SC}, ϕ_0 by $\Delta\phi$, and n^0 by n_i, with $z = 1$, and ε now referring to the dielectric constant of the semiconductor. Similarly the space-charge capacitance, C_{SC}, is given by (13.3.21) with analogous replacements. For an *n*-type extrinsic semiconductor, C_{SC} is

$$C_{SC} = \frac{(2kTn_i\varepsilon\varepsilon_0)^{1/2} e}{2kT} \left\{ \frac{|-\lambda e^{-Y} + \lambda^{-1}e^{Y} + (\lambda - \lambda^{-1})|}{[\lambda(e^{-Y} - 1) + \lambda^{-1}(e^{Y} - 1) + (\lambda - \lambda^{-1})Y]^{1/2}} \right\}$$ (18.2.5)

where $Y = e\Delta\phi/kT$ and $\lambda = n_i/N_D$.

A particular case of interest for the semiconductor–liquid interface is that shown in Figure 18.2.5*b*, where the surface layer of the *n*-type semiconductor becomes partially emptied of majority carriers (electrons), so that a *depletion layer* forms and the bands are bent upward. Under these conditions several simplifications to (18.2.5) can be made. Since this is an *n*-type material, $\lambda^{-1} >> \lambda$. Under depletion-layer conditions, with $\Delta\phi$ negative so that electrons are repelled from the surface, $\lambda e^{-Y} << \lambda^{-1}$ and (18.2.5) becomes

$$C_{SC} = \left(\frac{e^2\varepsilon\varepsilon_0 N_D}{2kT} \right)^{1/2} \left(-\frac{e\Delta\phi}{kT} - 1 \right)^{-1/2}$$ (18.2.6)

Rearrangement yields a very useful relationship (first derived for the metal/semiconductor junction) called the *Mott–Schottky equation* (54, 55):

$$\frac{1}{C_{SC}^2} = \left(\frac{2}{\varepsilon\varepsilon_0 N_D} \right) \left(-\Delta\phi - \frac{kT}{e} \right)$$ (18.2.7)

which at 298 K (N_D in cm^{-3}, $\Delta\phi$ in V, C_{SC} in μF cm^{-2}) becomes

$$\boxed{\frac{1}{C_{SC}^2} = \left[\frac{1.41 \times 10^{20}}{\varepsilon N_D} \right] [-\Delta\phi - 0.0257]}$$ (18.2.8)

Since $-\Delta\phi = E - E_{fb}$, a plot of $1/C_{SC}^2$ vs. E should be linear. The potential where the line intersects the potential axis yields the value of E_{fb}, and the slope can be used to obtain the doping level N_D. While such *Mott–Schottky plots* have been useful in characterizing the semiconductor–solution interface, they must be used with caution, because perturbing effects, such as those attributable to surface states[6] can cause

---

[5]For the ideally polarized semicondutor electrode, a space-charge region in the semiconductor forms when a potential is applied across the semiconductor–solution interface so that the electrode potential is displaced from E_{fb}.

[6]*Surface states* are energy levels arising from orbitals localized on atoms of the lattice near a surface. It is easy to see, for example, that silicon atoms in a surface plane cannot be surrounded with the tetrahedral symmetry found in the bulk solid. Thus, the electronic properties of these atoms differ. Often surface states have energies in the band gap and have a big effect on the electronic properties of any junction made with the surface.

deviations from the predicted behavior (56). One should verify that the parameters obtained from such plots are independent of the frequency employed in the capacitance measurements.

18.2.3 Current-Potential Curves at Semiconductor Electrodes

Electron-transfer processes at the semiconductor/electrolyte interface are strongly affected by the density of available carriers (electrons and holes) in the semiconductor at the interface. The observed i-E behavior differs from that at metals and carbon (Chapter 3), where there is always a large density of carriers in the conductor. In the dark, electron-transfer processes involving species in solution with energy levels in the band gap of the semiconductor (Figure 18.2.5b) are usually dominated by the majority carrier. Thus, moderately doped n-type materials can carry out reductions, but not oxidations. That is, there are electrons available in the conduction band to transfer to an oxidized solution species, but few holes to accept an electron from a reduced species. The current for a reduction of species O at an n-type semiconductor is given by

$$i = nFAk_f' n_{SC} C_O(x = 0) \qquad (18.2.9)$$

where n_{SC} (cm^{-3}) is the concentration of electrons at the interface and k_f' (cm^4 s^{-1}) is the heterogeneous rate constant. Note that the units of k_f' differ from that used with a metal electrode, where the carrier density in the metal is high and is included in k_f (cm s^{-1}; equation 3.6.29). Similarly, p-type materials with excess holes allow oxidations, but not reductions. The current for an oxidation of species R at a p-type semiconductor is given by

$$i = nFAk_b' p_{SC} C_R(x = 0) \qquad (18.2.10)$$

where k_b' is the heterogeneous rate constant for oxidation, and p_{SC} (cm^{-3}) is the concentration of holes at the surface.

In these equations, both the rate constant (k_f' or k_b') and the carrier concentration at the interface (n_{SC} or p_{SC}) can be affected by the applied potential. The variation in k_f' or k_b' with potential drop across the Helmholtz layer at the semiconductor–solution interface, $\Delta\phi'$, follows expressions like (3.3.9) and (3.3.10), with $(E - E^{0'})$ replaced by $\Delta\phi'$. The surface concentrations of the carriers are given by

$$n_{SC} = N_D \exp[-F(E - E_{fb})/RT] \qquad (18.2.11)$$
$$p_{SC} = N_A \exp[F(E - E_{fb})/RT] \qquad (18.2.12)$$

where $(E - E_{fb})$ represents the amount of band-bending, $-\Delta\phi$.

For an n-type semiconductor at all potentials positive of E_{fb}, $n_{SC} < N_D$, while for a p-type semiconductor at potentials negative of E_{fb}, $p_{SC} < N_A$. When a potential is applied between the semiconductor and the solution under these conditions of depletion, most of any change in the applied potential will drop in the semiconductor space-charge region, rather than across the Helmholtz layer. This effect can be understood in another way by comparing the capacitance of the space-charge region, C_{SC}, given in (18.2.6) with the capacitance of the Helmholtz and diffuse layers, C_d (13.3.29), and noting that generally $C_{SC} \ll C_d$. In tracing a current-potential curve with a semiconductor electrode, it is the variation of n_{SC} or p_{SC}, rather than that of k_f' or k_b', that governs the observed behavior in the depletion region. This means that the slope of a curve of ln (i) $vs.$ E will be RT/F, or in terms of a similar Tafel plot at a metal electrode, $\alpha \approx 1$ (see equation 3.4.15).

When the potential is made more negative than E_{fb} with an n-type material, electrons collect at the semiconductor surface to form an *accumulation layer*. Under these conditions, the semiconductor is said to become *degenerate* and behaves more like a metal. In
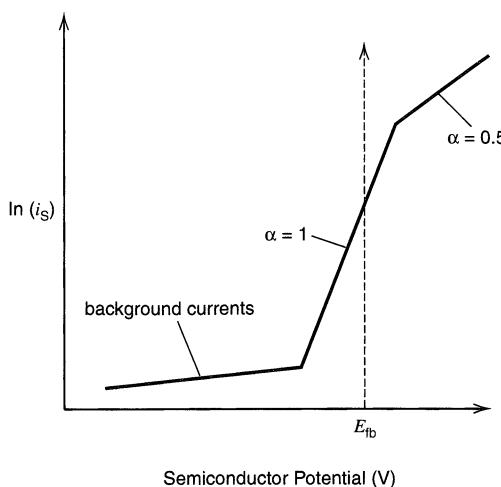
Figure 18.2.6 Schematic representation of the variation of electron-transfer rate, i_S, and transfer coefficient, α, with electrode potential for an ideal semiconductor electrode. The current i_S is equivalent to that defined in (18.2.9) or (18.2.10). At sufficiently extreme potentials (not shown) mass transfer would lead to a limiting current on the right side of the diagram. [Reprinted with permission from B. R. Horrocks, M. V. Mirkin, and A. J. Bard, *J. Phys. Chem.*, **98**, 9106 (1994). Copyright 1994, American Chemical Society.]

this potential region, changes in potential no longer affect n_{SC} significantly, but mainly show up as changes in ϕ' and primarily affect k_f' or k_b', so that $\alpha \approx 1/2$.[7] Similarly, *p*-type materials become degenerate at potentials positive of E_{fb}, where they begin showing metallic electrode behavior.

A schematic representation of the ideal electron-transfer rate and transfer coefficient as functions of potential for a semiconductor electrode is shown in Figure 18.2.6. Although there have been numerous studies with semiconductor electrodes, such ideal behavior is rarely seen (45, 47, 49, 57–59). Difficulties in such measurements include the presence of processes in parallel with the electron-transfer reaction involving dissolved reactant at the semiconductor surface, such as corrosion of the semiconductor material, effects of the resistance of the electrode material, and charge-transfer reactions that occur via surface states.

18.2.4 Photoeffects at Semiconductor Electrodes

Let us return to the situation of the *n*-type semiconductor in contact with the solution containing couple O/R, illustrated in Figure 18.2.5. As described in Section 18.2.2, a space-charge region typically 50 to 2000 Å wide (depending on the doping level and $\Delta\phi$) forms in the semiconductor at the interface. The direction of the electric field is such that any excess holes created in the space-charge region would move toward the surface and any excess electrons would move toward the bulk semiconductor. When the interface is irradiated with light of energy greater than the band gap, $\mathbf{E_g}$, photons are absorbed and electron-hole pairs are created (Figure 18.2.5c). Some of these, especially those formed beyond the space-charge region, recombine with the evolution of heat. However, the space-charge field promotes the separation of electrons and holes. The holes, delivered to the surface at an effective potential corresponding to the valence band edge, cause the oxidation of R to O, while the electrons move from the semiconductor electrode into the external circuit. Thus irradiation of an *n*-type semiconductor electrode promotes photo-oxidations (or causes a *photoanodic current*). This is illustrated in the *i–E* curves in Figure 18.2.7*a*.

---

[7]Semiconductors (notably SnO_2) can be so heavily doped that the carrier density approaches that of a conductor like carbon. These semiconductors are degenerate even at the flat-band potential and show metal-like behavior.
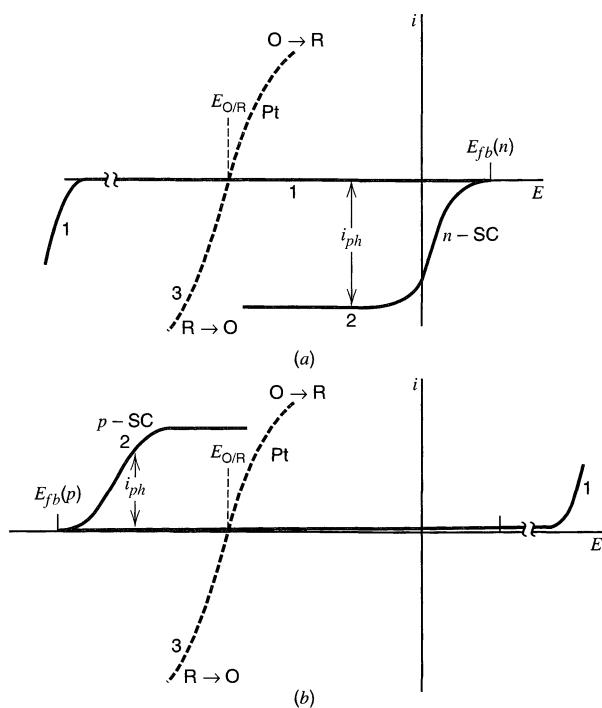
Figure 18.2.7 Current-potential curves for a solution containing couple O/R. (*a*) *n*-type semiconductor in the dark (*curve 1*) and under irradiation (*curve 2*). (*b*) *p*-type semiconductor in the dark (*curve 1*) and under irradiation (*curve 2*). For both (*a*) and (*b*), *curve 3* is the *i-E* curve at a platinum electrode.

In the dark (curve 1), essentially no current flows when the potential of the semiconductor electrode is made more and more positive, because, as discussed in the preceding section, there are few holes in the semiconductor to accept electrons from the reduced form of a redox couple located at potentials within the gap.[8]

Under irradiation (curve 2), a photoanodic current, i_{ph}, flows as long as the potential of the electrode is more positive than E_{fb}, so that electron/hole pair separation can occur. Thus the onset of the photocurrent is near E_{fb} (unless surface recombination processes[9] move the onset potential toward more positive values). The photo-oxidation of R to O occurs at less positive applied potentials than those required to carry out this process at an inert metal electrode (curve 3). This is possible because the light energy helps to drive the oxidation process; hence such processes are frequently called *photoassisted* electrode reactions.

The behavior of a *p*-type semiconductor with a couple having a redox potential in the gap region (see Figure 18.2.8) is analogous to that of the *n*-type material. Here the field in the space-charge region moves electrons toward the surface and holes toward the bulk material. Thus, upon irradiation of *p*-type material, a *photocathodic current* flows and photoreductions are facilitated by the light. Typical *i-E* curves under these conditions are shown in Figure 18.2.7*b*.

Photoeffects are generally not observed at *n*-type materials for redox couples located at potentials negative of E_{fb}. In this case, the bands are bent downwards, the majority carrier tends to accumulate near the surface (i.e., an accumulation layer forms), and the semiconductor behavior approaches that of an inert metal electrode. Similarly, a (hole) accumulation layer forms in a *p*-type material for couples located positive of E_{fb}.

---

[8]At very positive potentials, a "dark" anodic current can flow from breakdown phenomena.

[9]*Recombination* is the annihilation of an electron and a hole. It is often promoted by surface states at interfaces.
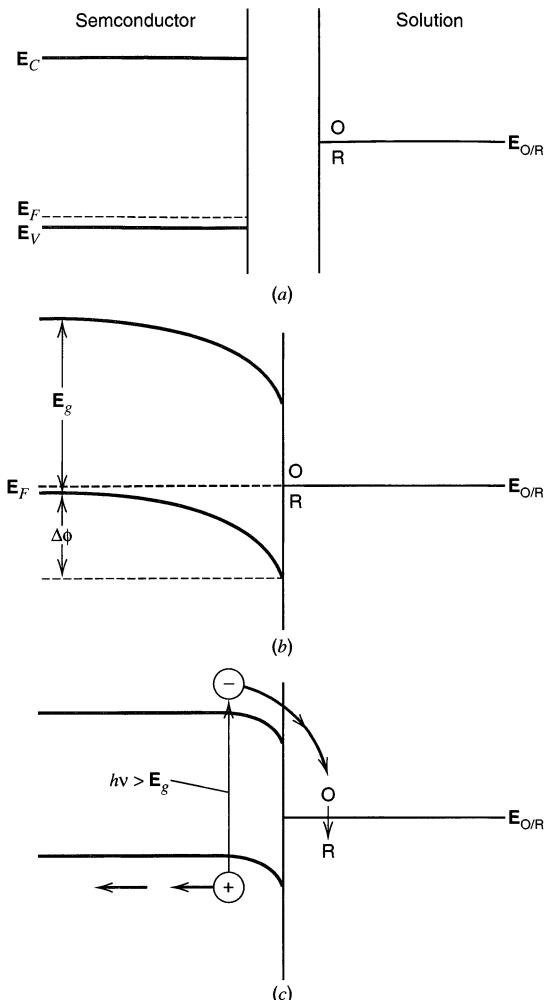
Figure 18.2.8 Formation of the junction between a p-type semiconductor and a solution containing a redox couple O/R. (a) Before contact in the dark. (b) After contact in the dark and electrostatic equilibration. (c) Junction under irradiation.

Photoelectrochemical cells usually consist of a semiconductor electrode and a suitable counter electrode. Such cells, often investigated because of their possible use in the conversion of radiant energy to electrical or chemical energy, will be discussed briefly here. Three types of photoelectrochemical cells can be devised (60). In *photovoltaic cells*, (Figure 18.2.9a,b), the reaction that occurs at the counter electrode is simply the reverse of the photoassisted process at the semiconductor. Ideally, the cell operates to convert light to electricity, but with no net change in the solution composition or the electrode materials. The operating characteristics of such a cell can be deduced from i-E curves such as those in Figure 18.2.7. In *photoelectrosynthetic* cells (Figure 18.2.9c,d), the reaction at the counter electrode differs from that at the semiconductor (so that a separator might be necessary in the cell to keep the products apart). In these systems, the net cell reaction is driven by light in the nonspontaneous direction ($\Delta G > 0$), so that radiant energy is stored as chemical energy. With an n-type semiconductor, for example, the necessary condition for driving the reaction in such a cell is that the potential of couple O/R lies above the valence band edge, while that of O'/R' lies below E_{fb}. If this condition does not exist, it is still possible to drive the reaction in the desired direction by applying an external bias to the cell. *Photocatalytic* cells (Figure 18.2.9e,f) are similar to these, except that the relative lo-
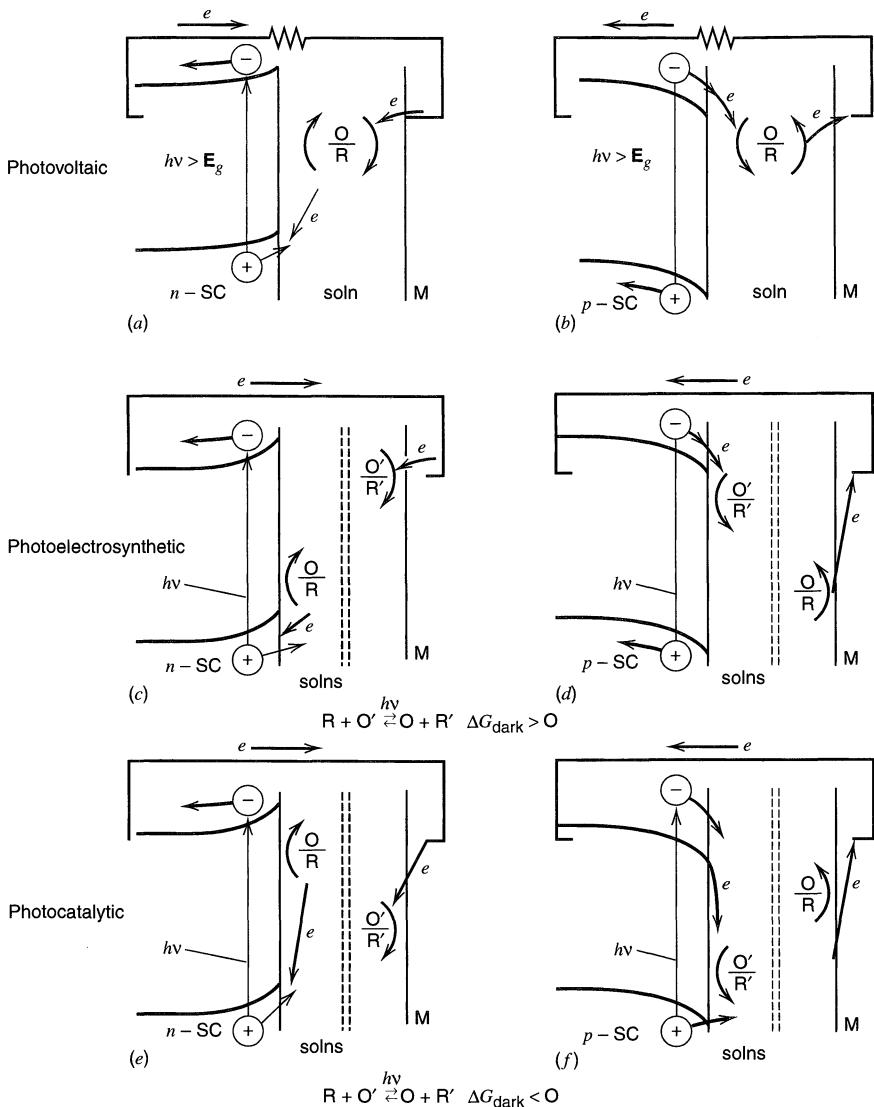
Figure 18.2.9 Different types of photoelectrochemical cells. Examples of each type are:

> **Photovoltaic cells:** (*a*) *n*-type semiconductor, for example, *n*-TiO$_2$/NaOH,O$_2$/Pt (61, 62) or *n*-CdSe/Se$_2^-$,Se$_2^{2-}$/Pt (63–65). (*b*) *p*-type semiconductor, for example, *p*-MoS$_2$/Fe^{3+}, Fe^{2+}/Pt (66).
>
> **Photoelectrosynthetic cells:** (*c*) *n*-type, for example, *n*-SrTiO$_3$/H$_2$O/Pt (H$_2$O → H$_2$ + 1/2O$_2$) (67–69). (*d*) *p*-type, for example, *p*-GaP/CO$_2$ (pH = 6.8)/C (reduction of CO$_2$) (70).
>
> **Photocatalytic cells:** (*e*) *n*-type, for example, *n*-TiO$_2$/CH$_3$COOH/Pt (CH$_3$COOH → C$_2$H$_6$ + CO$_2$ + H$_2$) (71). (*f*) *p*-type, for example, *p*-GaP/DME, AlCl$_3$, N$_2$/Al (reduction of N$_2$ by Al) (72).

cations of the potentials of the O/R and O'/R' couples are changed. In this case the reaction is driven in the spontaneous direction ($\Delta G < 0$) (which normally would be very slow in the dark), with the light energy being used to overcome the energy of activation of the process. Several examples of such processes are listed in the caption of Figure 18.2.9. While some of these are interesting, the efficiencies of many of the processes carried out in photoelectrosynthetic and photocatalytic cells are often rather low.

The light employed to carry out a photoassisted reaction at a semiconductor electrode must have a photon energy greater than that of the band gap E_g, since light of lower energy is not absorbed by the semiconductor. Thus a plot of photocurrent versus the wavelength of irradiating light can be employed to determine E_g. For example, for n-TiO_2 (rutile), only light of photon energy above 3.0 eV is useful. Since more than 95% of the total energy in the solar spectrum at the earth's surface lies below this value, sunlight is not utilized very effectively by TiO_2.

An approach to better utilization of longer wavelength light (and also to interesting experiments in their own right) involves *dye sensitization* of a semiconductor (73, 74). The principles are illustrated in Figure 18.2.10. Assume a thin layer of dye, D, is coated on the semiconductor. When the dye is excited (step 1), it injects an electron into the semiconductor band (step 2), becoming oxidized in the process to D^+. In the absence of a suitable couple in solution, this photoprocess would cease when all of D is consumed. If a species R exists in solution that is capable of reducing D^+, then electron transfer from R to D^+ can occur, regenerating D (step 3). Thus, dye sensitization allows longer-wavelength light to be employed in photoelectrochemistry, but the hole generated by the light is at a less positive potential than the one produced in the valence band of the semiconductor without dye sensitization. An analogous situation arises for a dye whose energy levels bracket the valence band edge; in this case hole injection into the semiconductor takes place. The depiction of the energy-level diagram for this case and a description of the processes involved is left as an exercise for the reader (Problem 18.7).

Photoeffects are also observed at metal electrodes, although the resulting photocurrents are much smaller. For example, the irradiation of a metal electrode can cause the photoejection of an electron into the solvent. If this electron is scavenged by some reactant in solution, a net cathodic photocurrent results (76, 77) (see Section 18.3 and Problem 8.10). These electron *photoejection* studies are of interest, because they can provide information about the nature of an electron at the instant of injection into a medium, as well as the energetics and kinetics of its relaxation to equilibrium solvation. Excitation of dyes adsorbed on metals can also lead to photocurrents, but they are usually much smaller than the photocurrents obtainable at semiconductor electrodes under comparable conditions (74). This low efficiency of net conversion of photons to external photocurrent is attributed to the ability of a metal to act as a quencher of excited states at or very near the surface by either electron or energy transfer (18, 19).
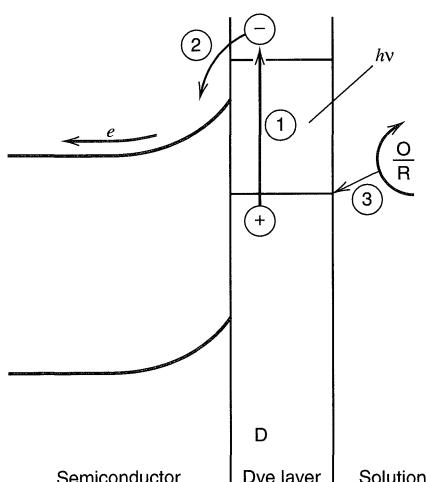
Figure 18.2.10 Dye sensitization of a photoprocess at a semiconductor electrode. For example, n-ZnO/rose bengal/I^-/Pt (75).

18.2.5 Surface Photocatalytic Processes at Semiconductor Particles

The principles that govern electrochemistry at semiconductor electrodes can also be applied to redox processes in particle systems. In this case, one considers the rates of the oxidation and reduction half-reactions that occur on the particle, usually in terms of the current, as a function of particle potential. One can use current-potential curves to estimate the nature and rates of heterogeneous reactions on surfaces. This approach applies not only to semiconductor particles, but also to metal particles that behave as catalysts and to surfaces undergoing corrosion.

Let us consider first a heterogeneous catalytic reaction that occurs on a metal particle. Many thermodynamically favorable reactions of reducing agents (such as the reaction of methyl viologen cation radical (MV^{+}) or Cr^{2+} with protons to produce hydrogen) are slow in homogeneous solution, because the mechanisms are complex. For example, H_2 evolution requires two electrons, but the reactants are one-electron reductants; moreover, the one-electron intermediate from proton reduction (a hydrogen atom) is produced only at very negative potentials. However, in the presence of a Pt particle the overall process can occur, with the particle acting as an electrode (and electron reservoir) at which both anodic and cathodic half reactions take place (Figure 18.2.11a). The efficacy of the particle for this catalysis, as expressed by the rate of the reaction, can be obtained by consideration of the current-potential curves for both half reactions (Figure 18.2.11b) (78, 79). The cathodic current, i_c, represents the rate of proton reduction at the particle surface

(a)

(b)

(c)
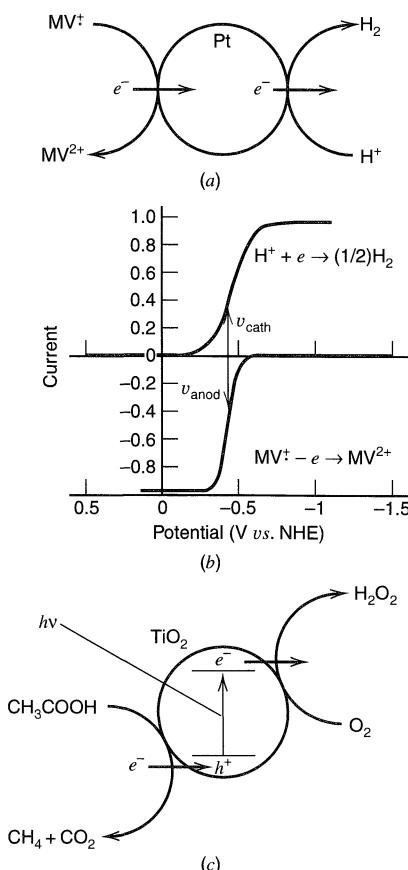
Figure 18.2.11   (a) Schematic representation of the two half-reactions occurring at a Pt particle that catalyzes the overall reaction $MV^{+} + H^{+} \rightarrow MV^{2+} + (1/2)H_2$. ($b$) Current-potential curves for the two half reactions. Arrows show predicted currents and the mixed potential where $v_{cath} = v_{anod}$ (or $i_c = i_a$). (c) Half-reactions occurring during irradiation of a TiO_2 particle in an oxygen-saturated acetic acid solution.

while the anodic current, i_a, represents the oxidation of the reducing agent, such as $MV^{+\cdot}$. At steady state, the rates of both of these reactions must be equal, so the particle should establish a potential (sometimes called a *mixed potential*) where $i_c = -i_a$.[10]

When this principle is applied to irradiated semiconductor particles, the rate of the photoreaction is balanced by that of a dark reaction. For example, consider a TiO_2 particle immersed in a solution containing acetic acid and oxygen and irradiated with UV light having an energy greater than the band gap of TiO_2. The particle behaves as a short-circuited version of the cell shown in Figure 18.2.9 (57), and at its surface, the oxidation of acetic acid by photogenerated holes (to CO_2 and CH_4) is balanced by the reduction of oxygen (Figure 18.2.11*c*). In a more chemical view, one can describe the photoexcitation process as a ligand-to-metal transition, such that the photogenerated hole is manifested as oxidized hydroxide ion at the surface of TiO_2 to produce hydroxyl radical (which in turn reacts with acetic acid), while the electron reduces a Ti(IV) center to Ti(III), (which then reacts with oxygen). The generation of hydroxyl radicals at the surface of irradiated TiO_2 has been established by electron spin resonance and spin trapping techniques (80).

Electrochemical methods can be used to characterize photoprocesses in slurries of semiconductor particles. Irradiation of semiconductor particles suspended in solution either generates dissolved species that can be detected at an electrode or produces excess charge in the particles that can be collected at an electrode. Consider a suspension of TiO_2 in an electrochemical cell (81, 82). Irradiation of the particles in a deaerated solution in the presence of an irreversible electron donor (such as acetic acid or EDTA) will result in the photogenerated holes reacting with the donor, leaving the electrons trapped at the surface of the particle. These are then collected at an electrode held at an appropriate potential, resulting in an anodic photocurrent during irradiation. Alternatively, irradiation in the presence of an irreversible electron acceptor, such as oxygen, can produce cathodic photocurrents. If the experiment with the irreversible donor is carried out also in the presence of a species (a *mediator*) that can be reversibly reduced at the semiconductor particles, such as methyl viologen dication (MV^{2+}) or Fe^{3+}, then greatly enhanced photocurrents are measured. In this case, the photoprocess produces reduced forms (MV^+ or Fe^{2+}), which are then oxidized at an electrode held at a potential where the required anodic process can occur (83). The large enhancement of the current comes about because the mediator is much more mobile than the particles and establishes better communication with the electrode.

While it might seem surprising that rather large (μm-scale) particles can be characterized as slurries in solution by electrochemical techniques, there have been many papers concerned with the dark electrochemistry of suspended solids. For example, voltammetric studies of suspensions of AgBr are possible (84). In addition, there have been numerous studies of solid particles mounted on electrode surfaces (85).

Electrodes can be prepared with films of semiconductor particles. A straightforward approach involves suitable chemical treatment of a substrate metal, e.g., chemical or anodic oxidation of Ti to form a film of TiO_2, which is made up of many small crystals, called *grains*. An alternative is to spread a film of semiconductor particles on an electrode surface. Films of nm-size semiconductor particles (*nanocrystalline films*) have been of special interest. Such small particles (variously called *quantum particles*, *Q-particles*, or *quantum dots*), have properties that differ from those of larger (μm) dimension (86, 87).

---

[10]This same principle applies to corrosion reactions at interfaces, where the rate of the corrosion reaction (the oxidation of metal) is balanced by the rate of a reduction reaction occurring at a neighboring site on the metal surface. Consider, for example the corrosion of metallic iron. Here the oxidation of Fe to Fe_2O_3 occurs at one site and is balanced by the reduction of O_2 or protons at another.

The band structure and general properties of large particles are essentially the same as those of bulk material (e.g., a large single crystal). However, when the particle dimensions start to approach molecular dimensions, the properties tend towards those of the molecules, with band gaps increasing as the particle size decreases. Moreover, such particles have very large surface area/volume ratios, and electrodes formed from such preparations tend to have a high porosity and large roughness factors. Suspensions of particles can be prepared by a variety of techniques used in colloid formation. For example, TiO_2 nanocrystals can be formed by hydrolysis of $TiCl_4$ or alkoxides of Ti(IV) (88–90). Electrodes prepared by coating ITO/glass with such nanocrystalline films have been of interest in dye-sensitized photoelectrochemical cells and other devices (89, 90).

18.3 ELECTROCHEMICAL DETECTION OF PHOTOLYTIC AND RADIOLYTIC PRODUCTS

18.3.1 Photoemission of Electrons (77, 91–95)

A metal surface exposed to light generally will eject electrons that travel 20 to 100 Å into the electrolyte and then become solvated. These electrons are reactive and produce some interesting chemistry if *scavengers* are available to interact with them. In the absence of such species, the electrons return to the electrode by diffusion, and no net loss of charge is detected. If a scavenger exists, for example N_2O in water, some react and fail to return, and therefore the faradaic charge transfer can be detected:

$$e_{aq} + N_2O + H_2O \rightarrow N_2 + OH^- + OH\cdot \tag{18.3.1}$$

In fact the OH· diffuses to the electrode and, depending on the potential, may withdraw additional charge.

Since the time for recollection of the electrons is 100 ns to 1 ms, this method is well-suited to the study of fast reactions that may not be readily examined by purely electrochemical methods. Usually the stimulus is a pulsed (10–20 ns) laser. Since the quantum yield for photoemission is low, an intense source is needed ($\sim$10–100 kW/cm^2).

The detection method resembles that of the coulostatic technique (Section 8.7), in that one observes the potential shift caused by charge ejection and the resulting relaxation back to the original state. Figure 8.9.2 offers some typical data for the N_2O system, and Problem 8.10 deals with its interpretation.

This technique is especially useful in examining the electrochemistry of free radicals having lifetimes that are too short to study by purely electrochemical techniques like those described in Chapter 12. A number of radicals, such as $CH_3\cdot$, $CH_2OH\cdot$, phenyl radicals, and inorganic ion radicals in water have been investigated (96). A good example is H·, whose chemistry bears on electrolytic hydrogen evolution. This species can be generated cleanly in acidic solutions by photoemission, and its chemistry can be studied without complication from other steps in the hydrogen evolution reaction. Problem 8.11 concerns this case. The technique has also been applied to radicals in nonaqueous solvents like MeCN and DMF. Here a precursor species, RX, is used, where R· is the desired radical (e.g., $PhCH_2\cdot$) and X is Cl or Br. The reactions that occur upon electron emission from the electrode (Hg or Au) are shown in Figure 18.3.1. Addition of an electron to RX causes dissociation to R· and X^-, producing a thin layer of R· near the electrode surface. The potential of the electrode is held at a fixed value during the experiment. If this value is more positive than the potential for reduction of R· to R^-, $E^{0'}_{R/R-}$, the injected charge represents those electrons scavenged by RX. If the value is more negative than $E^{0'}_{R/R-}$, additional charge is passed for this reduction. Thus $E^{0'}_{R/R-}$ can be found from a plot of photoinjected
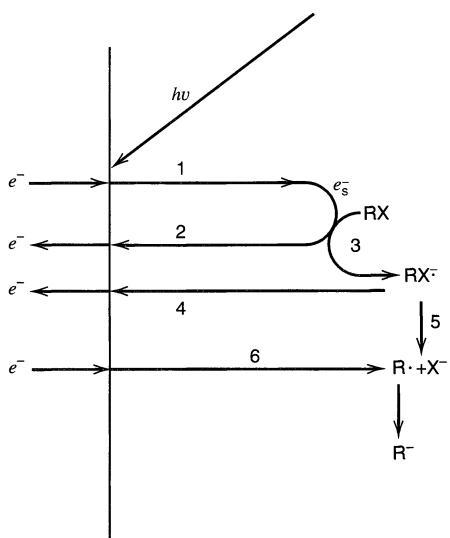
Figure 18.3.1   Reactions that occur after photoejection of solvated electrons. Photoejection (*1*) gives solvated electrons that can either return to the electrode (*2*) or react with RX (*3*), forming RX⁻. This species can return to the electrode and be oxidized (*4*) or dissociate to form R· (*5*). At sufficiently negative potentials, R· is reduced at the electrode (*6*). The net current observed is the sum of all electron-transfer processes.

charge, $Q(E)$, against E (Figure 18.3.2) (96). Alternative methods of representing the experimental data, to take account of the dependence of photoemission of electrons on potential, yield plots resembling conventional voltammograms (96).

18.3.2   Monitoring Products of Pulse Radiolysis (97)

The system shown in Figure 18.3.3 provides another approach to the electrochemical study of species produced by reactive electrons. Excitation is carried out by a pulsed (~20 ns) beam of high-energy electrons. Their passage through the cell creates solvated electrons, radicals, and ions, whose distribution can often be controlled by known
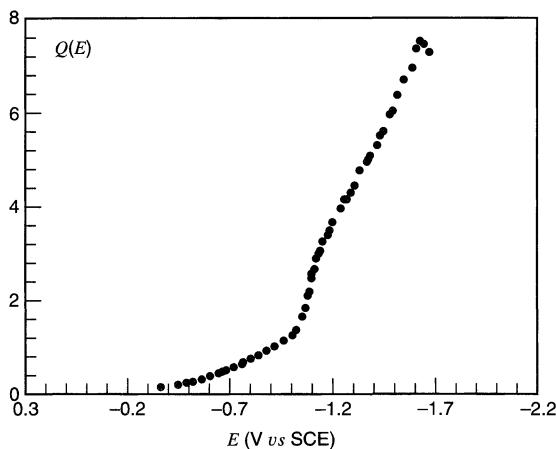
Figure 18.3.2   Normalized charge *vs.* potential for photoemission of electrons from a gold electrode into a solution of 52 m*M* diphenylmethylchloride in DMF containing 0.1 *M* TEAP. The increase in charge at about −1 V *vs.* SCE represents reduction of the diphenylmethyl radical and yields a half-wave potential for the reaction Ph₂CH· + e → Ph₂CH⁻ of −1.05 V *vs.* SCE. [Reprinted with permission from P. Hapiot, V. V. Konovalov, and J.-M. Savéant, *J. Am. Chem. Soc.*, **117**, 1428 (1995). Copyright 1995, American Chemical Society.]
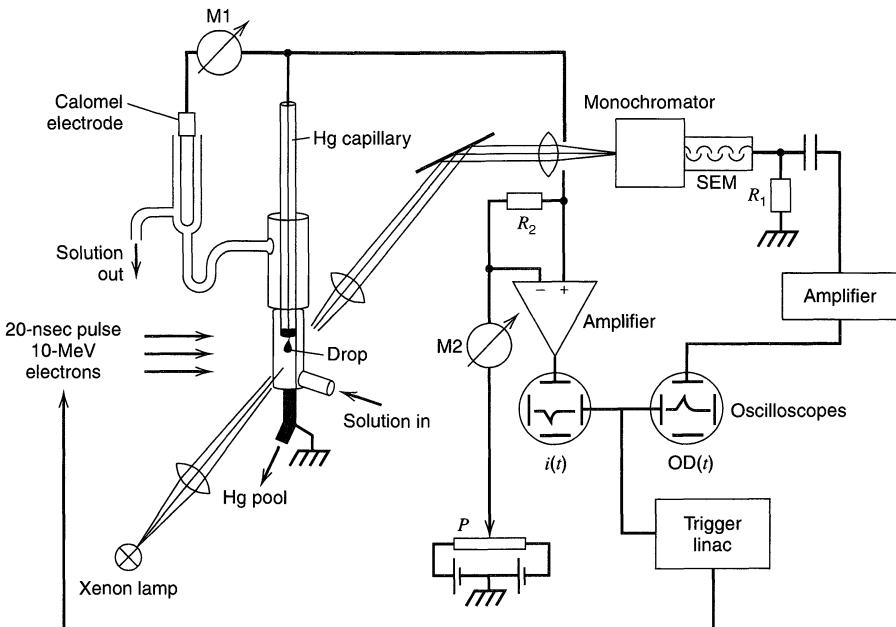
Figure 18.3.3 Apparatus for electrochemical and optical monitoring of pulse radiolysis at an HMDE. [From A. Henglein, *Electroanal. Chem.*, **9**, 163 (1976), by courtesy of Marcel Dekker, Inc.]

chemistry. Significant concentrations of these species are produced, and they can be detected faradaically.

If the radiolytic species of interest has a fairly long lifetime, then a potentiostatic experiment will yield a Cottrell-like response after the pulse, because the faradaic current is controlled by diffusion, or possibly in part by the electrode kinetics. Data for this case are shown in Figure 18.3.4. The radiolytically generated radical of ascorbic acid decays on a millisecond time scale. Current transients following separate radiolytic pulses were recorded for different potentials, and samples were taken at a fixed delay time to produce the sampled-current voltammogram displayed in Figure 18.3.4.

If the radicals are short-lived, the current transients are controlled by their homogeneous decay, as well as by diffusion and heterogeneous kinetics. This complication must be taken into account if the current-time curves are to be interpreted.

18.3.3 Electrochemistry of Photolytic Products (1, 95, 98)

Similar in concept to the approaches described above is the use of electrochemistry to monitor the products of flash photolysis. The apparatus resembles that of Figure 18.3.3, except that the excitation beam comprises photons from a pulsed discharge. Flashlamps dissipating perhaps 100 to 500 J of energy and producing a light pulse 10 to 30 μs wide (98–100), high-intensity (1000 W) Hg/Xe lamps (101), or lasers can be used. The current-time curves are controlled by reactant decay, diffusion, and heterogeneous charge transfer exactly as described above. At very short times, the current transient can have substantial contributions from photoemission of electrons from the electrode. An interesting application of this approach concerns the intermediates formed in the photolysis of ferrioxalate (102, 103).

As with the techniques described in Sections 18.3.1 and 18.3.2, photolytic methods are useful in the study of unstable intermediates, such as radicals. Again a suitable precur-
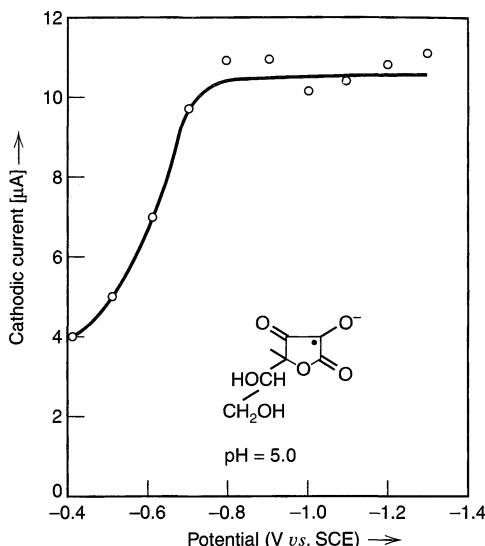
Figure 18.3.4 Sampled-current voltammogram for the ascorbic acid radical at 15 μs after the radiolytic pulse. [From A. Henglein, *Electroanal. Chem.*, **9**, 163 (1976), by courtesy of Marcel Dekker, Inc.]
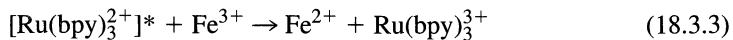
sor molecule, such as a ketone, RC(O)R, that will decompose to the desired radical upon photoexcitation, is employed (101, 104):

$$RC(O)R + h\nu \rightarrow 2\,R\cdot + CO \tag{18.3.2}$$

A chopped incident light beam irradiates a gold minigrid electrode, producing radicals in the vicinity of the electrode. The photocurrent for the oxidation or reduction of R· can be measured with a lock-in amplifier as a function of potential. For example, the voltammogram for the diphenylmethyl radical generated by photolysis of 1,1,3,3-tetraphenylacetone in MeCN (0.1 M TBAP) yielded a half-wave potential of -1.14 V *vs.* SCE for reduction (101).

18.3.4 Photogalvanic Cells (105)

It is possible to drive many homogeneous redox systems in a nonspontaneous direction by using light energy. For example, the complex $Ru(bpy)_3^{2+}$, where bpy is 2,2'-bipyridine, can absorb light to produce an excited state that is a fairly good reductant. Thus one observes the reaction:

$$[Ru(bpy)_3^{2+}]^* + Fe^{3+} \rightarrow Fe^{2+} + Ru(bpy)_3^{3+} \tag{18.3.3}$$

In general, the products Fe^{2+} and $Ru(bpy)_3^{3+}$ can be expected to react to give back the starting materials:

$$Ru(bpy)_3^{3+} + Fe^{2+} \rightarrow Fe^{3+} + Ru(bpy)_3^{2+} \tag{18.3.4}$$

hence the net effect is a quenching of the excited complex by a reversible electron-transfer mechanism. The light energy is thermalized.

On the other hand, (18.3.4) is not very fast (106). Thus, one can build up appreciable concentrations of $Ru(bpy)_3^{3+}$ and Fe^{2+} in the system. By inserting electrodes into the solution, one can effect reaction (18.3.4) faradaically by reducing the complex at one electrode and oxidizing ferrous iron at the other. Usually one electrode is chosen to be reversible only toward one of the half-reactions, in order to enforce specific behavior at each electrode. Since the energy of (18.3.4) is available in the external circuit, these de-

vices, called *photogalvanic cells*, have been of interest for solar energy conversion. A number of specific chemical systems have been studied. Obviously the efficiency of conversion depends strongly on the degree to which the kinetics can be optimized (105, 107–109).

▶ 18.4 REFERENCES
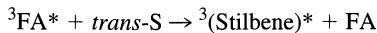
1. T. Kuwana, *Electroanal. Chem.*, **1**, 197 (1966).

2. L. R. Faulkner and A. J. Bard, *Electroanal. Chem.*, **10**, 1 (1977).

3. L. R. Faulkner, *Meth. Enzymol.*, **57**, 494 (1978).

4. L. R. Faulkner and R. S. Glass in "Chemical and Biological Generation of Excited States," W. Adam and G. Cilento, Eds., Academic, New York, 1982, pp. 191–227.

5. A. W. Knight and G. M. Greenway, *Analyst*, **119**, 879 (1994).

6. R. A. Marcus, *J. Chem. Phys.*, **43**, 2654 (1965).

7. J. T. Maloy in "Computers in Chemistry and Instrumentation," Vol. 2, "Electrochemistry," J. S. Mattson, H. B. Mark, Jr., and H. C. MacDonald, Jr., Marcel Dekker, New York, 1972, Chap. 9.

8. J. T. Maloy and A. J. Bard. *J. Am. Chem. Soc.*, **93**, 5968 (1971).

9. G. H. Brilmyer and A. J. Bard, *J. Electrochem. Soc.*, **127**, 104 (1980).

10. J. E. Bartelt, S. M. Drew, and R. M. Wightman, *J. Electrochem. Soc.*, **139**, 70 (1992).

11. M. Chang, T. Saji, and A. J. Bard, *J. Am. Chem. Soc.*, **99**, 5399 (1977).

12. I. Rubinstein and A. J. Bard, *J. Am. Chem. Soc.*, **103**, 512 (1981).

13. L. R. Faulkner, *J. Electrochem. Soc.*, **124**, 1725 (1977).

14. P. R. Michael and L. R. Faulkner, *J. Am. Chem. Soc.*, **99**, 7754 (1977).

15. M. M. Collinson, R. M. Wightman, and P. Pastore, *J. Phys. Chem.*, **98**, 11942 (1994).

16. M. M. Collinson and R. M. Wightman, *Science*, **268**, 1883 (1995).

17. D. J. Freed and L. R. Faulkner, *J. Am. Chem. Soc.*, **93**, 2097 (1971).

18. E. A. Chandross and R. E. Visco, *J. Phys. Chem.*, **72**, 378 (1968).

19. H. Kuhn, *J. Chem. Phys.*, **53**, 101 (1970).

20. M. Gleria and R. Memming, *Z. Phys. Chem.*, **101**, 171 (1976).

21. L. S. R. Yeh and A. J. Bard, *Chem. Phys. Lett.*, **44**, 339 (1976).

22. J. D. Luttmer and A. J. Bard, *J. Electrochem. Soc.*, **125**, 1423 (1978).

23. X. Zhang and A. J. Bard, *J. Phys. Chem.*, **92**, 5566 (1988).

24. Y. S. Obeng and A. J. Bard, *Langmuir*, **7**, 195 (1991).

25. C. J. Miller, P. McCord, and A. J. Bard, *Langmuir*, **7**, 2781 (1991).

26. F.-R. F. Fan, A. Mau, and A. J. Bard, *Chem. Phys. Lett.*, **116**, 400 (1985).

27. H. D. Abruña and A. J. Bard, *J. Am. Chem. Soc.*, **104**, 2641 (1982).

28. I. Rubinstein and A. J. Bard, *J. Am. Chem. Soc.*, **102**, 6641 (1980).

29. K. M. Maness, R. H. Terrill, T. J. Meyer, R. W. Murray, and R. M. Wightman, *J. Am. Chem. Soc.*, **118**, 10609 (1996).

30. Q Pei, Y. Yang, G. Yu, C. Zhang, and A. J. Heeger, *J. Am. Chem. Soc.*, **118**, 3922 (1996).

31. S. A. Cruser and A. J. Bard, *Anal. Lett.*, **1**, 11 (1967).

32. D. Ege, W. G. Becker, and A. J. Bard, *Anal. Chem.*, **56**, 2413 (1984).

33. A. J. Bard and G. M. Whitesides, U. S. Patent 5,221,605 (June 22, 1993).

34. H. Yang, J. K. Leland, D. Yost, R. J. Massey, *Bio/Technol.*, **12**, 193 (1994).

35. G. F. Blackburn, H. P. Shah, J. H. Kenten, J. Leland, R. A. Kamin, J. Link, J. Peterman, M. J. Powell, A. Shah, D. B. Talley, S. K. Tyagi, E. Wilkins, T.-G. Wu, and R. J. Massey, *Clin. Chem.*, **37**, 1534 (1991).

36. N. R. Hoyle, *J. Biolumin. Chemilumin.*, **9**, 289 (1994).

37. J. B. Noffsinger and N. D. Danielson, *Anal. Chem.*, **59**, 865 (1987).

38. J. Leland and M. J. Powell, *J. Electrochem. Soc.*, **137**, 3127 (1990).

39. J. A. Holeman and N. D. Danielson, *J. Chromatogr.*, **679**, 277 (1994).

40. T. M. Downey and T. A. Nieman, *Anal. Chem.*, **64**, 261 (1992).

41. L. L. Shultz, J. S. Stoyanoff, and T. A. Nieman, *Anal. Chem.*, **68**, 349 (1996).

42. H. Gerischer, *Adv. Electrochem. Electrochem. Engr.*, **1**, 139 (1961).

43. H. Gerischer, in "Physical Chemistry—An Advanced Treatise," Vol. IXA, H. Eyring, D. Henderson, and W. Jost, Eds., Academic Press, New York, 1970, p. 463.

44. V. A. Myamlin and Yu. V. Pleskov, "Electrochemistry of Semiconductors," Plenum, New York, 1967.

45. A. J. Nozik and R. Memming, *J. Phys. Chem.*, **100**, 13061 (1996).

46. Yu. V. Pleskov and Yu. Ya. Gurevich, "Semiconductor Photoelectrochemistry," Consultants Bureau, New York, 1986.

47. N. S. Lewis, *Accts. Chem. Res.*, **23**, 176 (1990).

48. N. S. Lewis, *Annu. Rev. Phys. Chem.*, **42**, 543 (1991).

49. C. A. Koval and J. N. Howard, *Chem. Rev.*, **92**, 411 (1992).

50. A. Many, Y. Goldstein, and N. B. Grover, "Semiconductor Surfaces," North Holland, Amsterdam, 1965.

51. A. K. Jonscher, "Principles of Semiconductor Device Operation," Wiley, New York, 1960.

52. D. Madelung in "Physical Chemistry—An Advanced Treatise," Vol. X, W. Jost, Ed., Academic Press, New York, 1970, Chap. 6.

53. G. Ertl and H. Gerischer, *ibid.*, Chap. 7.

54. W. Schottky, *Z. Phys.*, **113**, 367 (1939); **118**, 539 (1942).

55. N. F. Mott, *Proc. Roy. Soc. (London)*, **A171**, 27 (1939).

56. E. C. Dutoit, F. Cardon, and W. P. Gomes, *Ber. Bunsenges. Phys. Chem.*, **80**, 1285 (1976).

57. D. Meissner and R. Memming, *Electrochim. Acta*, **37**, 799 (1992).

58. B. R. Horrocks, M. V. Mirkin and A. J. Bard, *J. Phys. Chem.*, **98**, 9106 (1994).

59. A. M. Fajardo and N. S. Lewis, *Science*, **274**, 969 (1996).

60. A. J. Bard, *J. Photochem.*, **10**, 59 (1979).

61. A. Fujishima and K. Honda, *Bull. Chem. Soc. Jpn.*, **44**, 1148 (1971); *Nature*, **238**, 37 (1972).

62. D. Laser and A. J. Bard, *J. Electrochem. Soc.*, **123**, 1027 (1976).

63. B. Miller and A. Heller, *Nature*, **262**, 680 (1976).

64. G. Hodes, D. Cahen, and J. Manassen, *Nature*, **260**, 312 (1976).

65. M. S. Wrighton, A. B. Bocarsly, J. M. Bolts, A. B. Elllis, and K. D. Legg in "Semiconductor Liquid-Junction Solar Cells," A Heller, Ed., Electrochem. Soc., Princeton, NJ, Proc. Vol. 77-3, 1977, p. 138.

66. H. Tributsch, *Ber. Bunsenges. Phys. Chem.*, **81**, 361 (1977).

67. M. S. Wrighton, A. B. Ellis, P. T. Wolczanski, D. L. Morse, H. B. Abrahamson, and D. S. Ginley, *J. Am. Chem. Soc.*, **98**, 2774 (1976).

68. J. G. Mavroides, J. A. Kafalas, and D. F. Kolesar, *Appl. Phys. Lett.*, **28**, 241 (1976).

69. T. Watanabe, A. Fujishima, and K. Honda, *Bull. Chem. Soc. Jpn.*, **49**, 355 (1976).

70. M. Halman, *Nature*, **275**, 115 (1978).

71. B. Kraeutler and A. J. Bard, *J. Am. Chem. Soc.*, **99**, 7729 (1977).

72. C. R. Dickson and A. J. Nozik, *J. Am. Chem. Soc.*, **100**, 8007 (1978).

73. H. Gerischer and F. Willig, "Topics in Current Chemistry," Springer Verlag, Berlin, Vol. 61, 1976, p. 31.

74. H. Gerischer, *J. Electrochem. Soc.*, **125**, 218C (1978).

75. H. Tsubomura, M. Matsumura, Y. Nomura, and T. Amamiya, *Nature*, **261**, 402 (1976).

76. G. A. Kenney and D. C. Walker, *Electroanal. Chem.*, **5**, 1 (1971).

77. G. C. Barker, *Ber. Bunsenges. Phys. Chem.*, **75**, 728 (1971).

78. M. Spiro. *J. Chem. Soc., Faraday Trans. 1*, **75**, 1507 (1979).

79. D. S. Miller, A. J. Bard, G. McLendon, and J. Ferguson, *J. Am. Chem. Soc.*, **103**, 5336 (1981).

80. C. D. Jaeger and A. J. Bard, *J. Phys. Chem.*, **83**, 3146 (1979).

81. W. W. Dunn, Y. Aikawa, and A. J. Bard, *J. Am. Chem. Soc.*, **103**, 3456 (1981).

82. M. D. Ward and A. J. Bard, *J. Phys. Chem.*, **86**, 3599 (1982).

83. M. D. Ward, J. R. White, and A. J. Bard, *J. Am. Chem. Soc.*, **105**, 27 (1983).

84. I. M. Kolthoff and J. T. Stock, *Analyst*, **80**, 860 (1955).

85. F. Scholz and B. Meyer, *Chem. Soc. Rev.*, **1994**, 341; *Electroanal. Chem.*, **20**, 1 (1998).

86. A. Henglein, *Chem. Rev.*, **89**, 1861 (1989).

87. M. L. Steigerwald and L. Brus, *Accts. Chem. Res.*, **23**, 183 (1990).

88. N. Vlachopoulos, P. Liska, J. Augustynski, and M. Grätzel, *J. Am. Chem. Soc.*, **110**, 1216 (1988).

89. B. O'Regan and M. Grätzel, *Nature*, **353**, 737 (1991).

90. T. Gerfin, M. Grätzel, and L. Walder, *Prog. Inorg. Chem.*, **44**, 345 (1997).

91. G. C. Barker, D. McKeown, M. J. Williams, G. Bottura, and V. Concialini, *Faraday Discuss. Chem. Soc.*, **56**, 41 (1974).

92. Yu. V. Pleskov, Z. A. Rotenberg, V. V. Eletsky, and V. I. Lakomov, *Faraday Discuss. Chem. Soc.*, **56**, 52 (1974).

93. A. Brodsky and Yu. V. Pleskov, in "Progress in Surface Sciences," Vol. 2, Part 1, S. G. Davidson, Ed., Pergamon, Oxford, 1972.

94. Yu. V. Pleskov and Z. A. Rotenberg, *Adv. Electrochem. Electrochem. Engr.*, **11**, 1 (1978).

95. A. B. Bocarsly, H. Tachikawa and L. R. Faulkner in "Laboratory Techniques in Electroanalytical Chemistry," 2nd ed., P. T. Kissinger and W. R. Heineman, Eds., Marcel Dekker, New York, 1996, Chap. 28.

96. P. Hapiot, V. V. Konovalov, and J.-M. Savéant, *J. Am. Chem. Soc.*, **117**, 1428 (1995).

97. A. Henglein, *Electroanal. Chem.*, **9** 163 (1976).

98. S. P. Perone and H. D. Drew in "Analytical Photochemistry and Photochemical Analysis: Solids, Solutions, and Polymers," J. Fitzgerald, Ed., Marcel Dekker, New York, 1971, Chap. 7.

99. S. P. Perone and J. R. Birk, *Anal. Chem.*, **38**, 1589 (1966).

100. G. L. Kirschner and S. P. Perone, *Anal. Chem.*, **44**, 443 (1972).

101. D. D. M. Wayner, D. J. McPhee and D. Griller, *J. Am. Chem. Soc.*, **110**, 132 (1988).

102. R. A. Jamieson and S. P. Perone, *J. Phys. Chem.*, **76**, 830 (1972).

103. J. I. H. Patterson and S. P. Perone, *J. Phys. Chem.*, **77**, 2437 (1973).

104. B. A. Sim, P. H. Milne, D. Griller, and D. D. M. Wayner, *J. Am. Chem. Soc.*, **112**, 6635 (1990).

105. M. D. Archer, *J. Appl. Electrochem.*, **5**, 17 (1975).

106. C. T. Lin and N. Sutin, *J. Phys. Chem.*, **80**, 97 (1976).

107. W. J. Albery and M. D. Archer, *Electrochim. Acta*, **21**, 1155 (1976).

108. W. J. Albery and M. D. Archer, *J. Electrochem. Soc.*, **124**, 688 (1977).

109. W. J. Albery and M. D. Archer, *J. Electroanal. Chem.*, **86**, 1, 19 (1978).
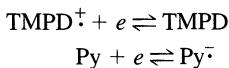
▶ 18.5 PROBLEMS

18.1 It is possible to measure the efficiency of triplet production in some redox processes by using *trans*-stilbene as an interceptor. For example, the fluoranthene triplet undergoes the reaction:

$$^3FA^* + trans\text{-}S \rightarrow {}^3(Stilbene)^* + FA$$
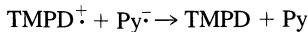
then the stilbene triplet decays to *cis* and *trans* ground-state forms with a known partition ratio. Devise a bulk electrolysis experiment to measure the efficiency of triplet formation (triplets per redox event) in the reaction between $10\text{-}MP^{+\cdot}$ and $FA^{-\cdot}$. Derive an equation relating the measured quantities to this efficiency. Why is bulk electrolysis needed?

18.2 From the half-wave potentials in Figure 18.1.4, the values of $E^{0'}$ for the electrode reactions:

$$TMPD^{+\cdot} + e \rightleftharpoons TMPD$$
$$Py + e \rightleftharpoons Py^{-\cdot}$$

can be estimated. What are they? Estimate the free energy released in the reaction

$$TMPD^{+\cdot} + Py^{-\cdot} \rightarrow TMPD + Py$$

From the fluorescence spectrum in Figure 18.1.3, estimate the energy of $^1Py^*$ relative to Py. Comment on the probability of forming $^1Py^*$ in the reaction between $TMPD^{+\cdot}$ and $Py^{-\cdot}$, and account for the light.

18.3 Interpret the lower frame of Figure 18.1.4.

18.4 The transient in Figure 18.1.5 was generated by a more complex waveform than usually applies. The first step generated PPD^{-} for 500 ms, then the second step produced TH^{+}. However, for the period $0.10 \leq t_r /t_f \leq 0.12$, the potential was stepped to 0.0 V, where TH^{+} is reduced heterogeneously, then electrogeneration of TH^{+} was resumed. The fact that the dip in light output lagged the application of the pulse to 0.0 V was cited as evidence that the light-producing reaction took place in solution at some distance from the electrode. Argue this point. Can you estimate the distance of the reaction zone from the surface?

18.5 The properties of a semiconductor photovoltaic cell can be deduced (neglecting the effect of internal resistance) from i-E curves such as those in Figure 18.2.7a. Assume that couple O/R is Fe(CN)$_6^{3-}$ (0.1 M)/Fe(CN)$_6^{4-}$ (0.1 M), that $E_{fb} = -0.20$ V $vs.$ SCE, and that the limiting photocurrent is governed by the light flux, 6.2×10^{15} photons/s, which is completely absorbed and converted to separated electron-hole pairs. For a cell comprising the n-type semiconductor and a platinum electrode in the electrolyte, what are the maximum open-circuit voltage and the short-circuit current under illumination? Sketch the expected output current $vs.$ output voltage for this cell. What is the maximum output power for the cell?

18.6 An expression frequently used for the "thickness of the space-charge region," L_1, is (42–44)

$$L_1 = \left(\frac{2\varepsilon\varepsilon_0}{eN_D} \Delta\phi \right)^{1/2} \approx \left(1.1 \times 10^6 \frac{\Delta\phi}{N_D}\varepsilon \right)^{1/2} \text{ cm}$$

(with N_D in cm^{-3} and $\Delta\phi$ in V). Sketch the variation of L_1 with $\Delta\phi$ for several values of N_D for a semiconductor with $\varepsilon = 10$. For efficient utilization of light, most of the radiation should be absorbed within the space-charge region. The absorption of light follows a Beer's law relationship with an absorption coefficient, α (cm^{-1}); hence a "penetration depth" of $\sim 1/\alpha$ can be estimated. If $\alpha = 10^5$ cm^{-1} and a band-bending of 0.5 V is to be used, what is the recommended doping level, N_D? Why would much lower doping in a semiconductor photoelectrochemical cell be undesirable?

18.7 Consider the dye sensitization of a semiconductor electrode with the energy level situation depicted in Figure 18.5.1. Explain how this system operates under illumination.

18.8 The Mott-Schottky plots in Figure 18.5.2 for n- and p-type InP in 1 M KCl, 0.01 M HCl were reported by Van Wezemael, et al. Estimate the flat-band potentials and doping levels of the two semiconductors. How does the difference in E_{fb} for n- and p-type InP compare to $\mathbf{E}_g$ for this material (1.3 eV)?
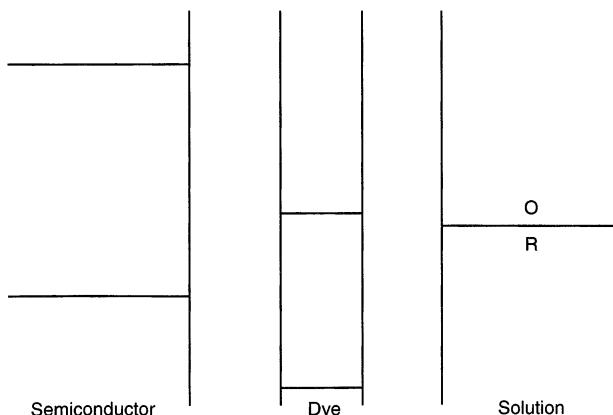
Semiconductor   Dye   Solution   **Figure 18.5.1**
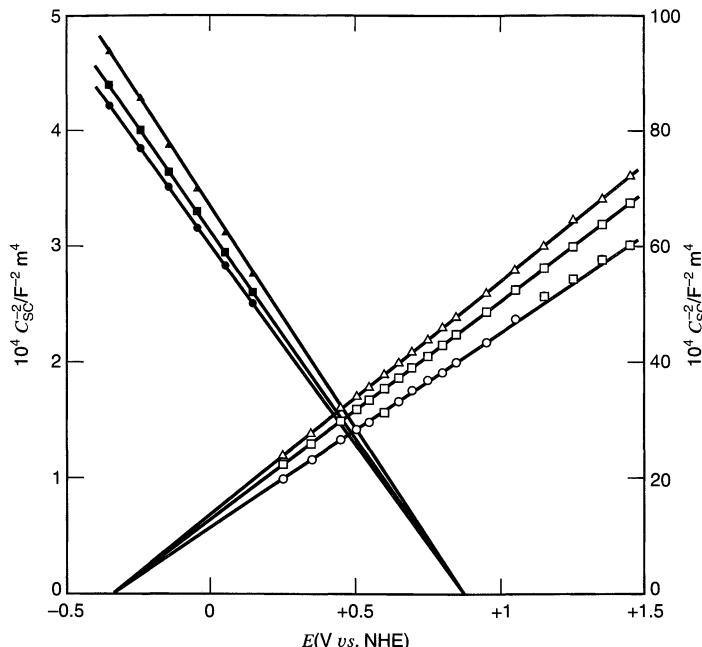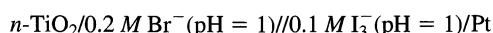
Figure 18.5.2 Mott-Schottky plots for n- and p-type InP, (111) face. Electrolyte composition: 1 M KCl + 0.01 M HCl, n-type: (○) 200 Hz, (□) 2500 Hz, (△) 20,000 Hz; p-type: (●) 200 Hz, (■) 2500 Hz, (▲) 20,000 Hz. The vertical axis to the left applies to p-type, the one to the right to n-type. [From A. M. Van Wezemael, W. H. Laftere, F. Cardon, and W. P. Gomes, *J. Electroanal. Chem.*, **87**, 105 (1978), with permission.]

18.9   The following cell is proposed as a photoelectrochemical storage battery:

$$n\text{-TiO}_2/0.2\ M\ \text{Br}^-(\text{pH} = 1)//0.1\ M\ \text{I}_3^-(\text{pH} = 1)/\text{Pt}$$

The E_{fb} for n-TiO$_2$ under these conditions is -0.30 V vs. SCE. Under irradiation, a photo-oxidation producing Br$_2$ occurs at TiO$_2$. (a) Write the half-cell reactions that occur at both electrodes during irradiation. What is the maximum open-circuit voltage under illumination (assume no liquid junction potential)? (b) During the "photo-charge cycle" Br$_2$ and I$^-$ accumulate in the cell. If half of the I$_3^-$ is converted during charging and a platinum electrode is used in the Br$_2$/Br$^-$ cell for dark discharge, what is the cell voltage of the charged cell? Write the half reactions that take place during dark discharge.

A

MATHEMATICAL METHODS

An understanding of many electrochemical phenomena depends strongly on an ability to solve certain differential equations, so it is worthwhile to summarize some of the important mathematical tools. This appendix is meant only as a review or an introduction. It is not a mathematically rigorous exposition. If more complete information is desired, the references should be consulted. Nevertheless, the level of the presentation will enable the reader to solve the accompanying problems and to follow the derivations in the text.

▷ A.1 SOLVING DIFFERENTIAL EQUATIONS BY THE LAPLACE TRANSFORM TECHNIQUE

A.1.1 Partial Differential Equations

Our main encounter with partial differential equations (PDEs) arises in the treatment of diffusion near the surface of an electrode at which a heterogeneous reaction is under way. Solute concentrations are therefore functions both of time t and of distance x from the electrode. The concentration $C(x, t)$ ordinarily will obey some form of Fick's diffusional laws (Section 4.4), such as

$$\frac{\partial C(x, t)}{\partial t} = D \frac{\partial^2 C(x, t)}{\partial x^2} \tag{A.1.1}$$

where D is the diffusion coefficient of the substance at hand. This equation is a *linear* PDE, because it contains only first or zeroth powers of $C(x, t)$ and its derivatives. The *order* of the equation is that of the highest derivative; hence the example above is of the second order.

Much of the difficulty in solving partial differential equations derives from the fact that the PDE does not fix even the functional form of its solution. Indeed, there usually are many functional solutions to a given PDE; for example, the equation:

$$\frac{\partial z}{\partial x} - \frac{\partial z}{\partial y} = 0 \tag{A.1.2}$$

is satisfied by any of the following relations:

$$z = A\, e^{(x+y)} \tag{A.1.3}$$
$$z = A \sin(x + y) \tag{A.1.4}$$
$$z = A(x + y) \tag{A.1.5}$$

This feature contrasts with the properties of *ordinary differential equations* (ODEs), which contain only derivatives of functions of a single variable. Usually the form of the solution to an ODE is dictated by the ODE itself. Thus, the linear, first-order ODE describing unimolecular decay:

$$\frac{dC(t)}{dt} = -kC(t) \tag{A.1.6}$$

has the single general solution:

$$C(t) = (\text{constant}) \, e^{-kt} \tag{A.1.7}$$

The boundary condition applied to a specific problem serves only to supply the constant.

The solution to a PDE usually depends on the boundary conditions for its form as well as for the evaluation of constants; and the same PDE solved under different boundary conditions will often yield different functional relations.

A.1.2 Introduction to the Laplace Transformation (1–3)

The Laplace transformation is of great value in solving certain kinds of differential equations—especially those encountered in electrochemistry—because it enables a conversion of the problem into a domain where simpler mathematical manipulation is possible. A familiar analogy is the use of logarithms to solve complex multiplication problems. One begins with a transformation of the operands into their images, the logarithms. In the transform domain, the problem is solved by addition. Thus, one attains the transform of the desired result, and inverse transformation yields the result itself. In a similar manner, Laplace transformation of an ODE yields an expression that can be manipulated algebraically to provide the transform of the ODEs solution. Inverse transformation then completes the solution. By similar means, PDEs can be transformed into ODEs, which are then solved conventionally or by further application of transform techniques. This method is extremely convenient, but it is restricted almost entirely to linear differential equations.

The Laplace transform in t of the function $F(t)$ is symbolized by $L\{F(t)\}, f(s)$, or $\overline{F}(s)$, and is defined by

$$\boxed{L\{F(t)\} \equiv \int_0^\infty e^{-st} F(t) \, dt} \tag{A.1.8}$$

The existence of the transform is conditional. It requires (a) that $F(t)$ be bounded at all *interior* points on the interval $0 \le t < \infty$; (b) that it have a finite number of discontinuities; and (c) that it be of "exponential order." This last condition means that $e^{-\alpha t}|F(t)|$ must be bounded for some constant α as $t \to \infty$; thus, it requires the function's magnitude to rise more slowly than some exponential $e^{\alpha t}$ as t becomes very large. It is plain that e^{-2t} is of exponential order, whereas e^{t^2} is not. The first condition clearly rules out $(t - 1)^{-1}$ as having a transform, but it says nothing about $t^{-1/2}$ or t^{-1}. It turns out that $F(t)$ may possess an infinite discontinuity at $t = 0$ if $|t^n F(t)|$ is bounded there for some positive value of n less than unity. Thus, $t^{-1/2}$ does have a Laplace transform, but t^{-1} does not. In practical applications, conditions (a) and (c) do occasionally offer obstacles, but (b) rarely does.

Many transforms are obtained directly from the integral of definition, but others are more conveniently extracted from indirect approaches. Table A.1.1 gives a short list of some commonly encountered functions and their transforms. More extensive tables can be found in the references (1, 2, 4, 5).

TABLE A.1.1   Laplace Transforms of Common Functions (1)

$F(t)$	$f(s)$
A(constant)	A/s
e^{-at}	$1/(s + a)$
$\sin at$	$a/(s^2 + a^2)$
$\cos at$	$s/(s^2 + a^2)$
$\sinh at$	$a/(s^2 - a^2)$
$\cosh at$	$s/(s^2 - a^2)$
t	$1/s^2$
$t^{(n-1)}/(n - 1)!$	$1/s^n$
$(\pi t)^{-1/2}$	$1/s^{1/2}$
$2(t/\pi)^{1/2}$	$1/s^{3/2}$
$\dfrac{x}{2(\pi k t^3)^{1/2}} [\exp(-x^2/4kt)]$	$e^{-\beta x}$, where $\beta = (s/k)^{1/2}$
$\left(\dfrac{k}{\pi t}\right)^{1/2} [\exp(-x^2/4kt)]$	$e^{-\beta x}/\beta$
$\mathrm{erfc}[x/2(kt)^{1/2}]$	$e^{-\beta x}/s$
$2\left(\dfrac{kt}{\pi}\right)^{1/2} \exp(-x^2/4kt) - x\,\mathrm{erfc}[x/2(kt)^{1/2}]$	$e^{-\beta x}/s\beta$
$\exp(a^2 t)\,\mathrm{erfc}(at^{1/2})$	$\dfrac{1}{s^{1/2}(s^{1/2} + a)}$

A.1.3   Fundamental Properties of the Transform (1–3)

The Laplace transformation is linear in that

$$L\{aF(t) + bG(t)\} = af(s) + bg(s) \tag{A.1.9}$$

where a and b are constants. This property follows directly from the definition and the basic properties of integral calculus.

   The value of the transformation for solving differential equations issues from its conversion of derivatives with respect to the transformation variable into algebraic expressions in s. For example,

$$L\left\{\frac{dF(t)}{dt}\right\} = L\{F'(t)\} = sf(s) - F(0) \tag{A.1.10}$$

A proof rests upon integration by parts:

$$L\left\{\frac{dF(t)}{dt}\right\} = \int_0^\infty e^{-st} \frac{dF(t)}{dt}\, dt \tag{A.1.11}$$

$$= [e^{-st}F(t)]_0^\infty + s\int_0^\infty e^{-st}F(t)dt \tag{A.1.12}$$

$$= -F(0) + sf(s) \tag{A.1.13}$$

One can show similarly that

$$L\{F''\} = s^2 f(s) - sF(0) - F'(0) \tag{A.1.14}$$

and generally that

$$\boxed{L\{F^{(n)}\} = s^n f(s) - s^{n-1}F(0) - s^{n-2}F'(0) - \cdots - F^{(n-1)}(0)} \tag{A.1.15}$$

The transformation is oblivious to differential operators other than those involving t:

$$L\left\{\frac{\partial F(x, t)}{\partial x}\right\} = \frac{\partial f(x, s)}{\partial x} \tag{A.1.16}$$

because variables other than t are regarded as constants for purposes of conversion.

Other useful properties involve the transforms of integrals and the effect of multiplication by an exponential:

$$L\left\{\int_0^t F(x)dx\right\} = \frac{1}{s}f(s) \tag{A.1.17}$$

$$L\{e^{at}F(t)\} = f(s - a) \tag{A.1.18}$$

For example,

$$L\{\sin bt\} = \frac{b}{s^2 + b^2} \tag{A.1.19}$$

$$L\{e^{at} \sin bt\} = \frac{b}{(s - a)^2 + b^2} \tag{A.1.20}$$

When inversion of the transform cannot be carried out from tabulated functions, one can sometimes obtain it from the *convolution integral:*

$$L^{-1}\{f(s)g(s)\} = F(t)*G(t)$$

$$= \int_0^t F(t - \tau)G(\tau)d\tau \tag{A.1.21}$$

Note that $F(t)*G(t)$ merely symbolizes the convolution integral. It does not imply a multiplication.

A.1.4 Solving Ordinary Differential Equations by Laplace Transformation

As an example, let us determine the time-dependent position of a mass on a spring, relative to its equilibrium position, after release from an initial displacement A. This is, of course, the linear harmonic oscillator problem. Let $y(t)$ be the displacement and k be the spring's force constant. The force on the mass is then

$$m\frac{d^2y}{dt^2} = -ky \tag{A.1.22}$$

with $y'(0) = 0$. Under transformation, we have

$$s^2\bar{y} - sy(0) - y'(0) = -\frac{k}{m}\bar{y} \tag{A.1.23}$$

$$s^2\bar{y} - As = -\frac{k}{m}\bar{y} \tag{A.1.24}$$

$$\bar{y} = \frac{As}{s^2 + k/m} \tag{A.1.25}$$

The inverse transform then gives the solution:

$$L^{-1}\{\bar{y}\} = y(t) = A\cos\left(\frac{k}{m}\right)^{1/2}t \tag{A.1.26}$$

As a second example, let us find $i(t)$ resulting from closure of the switch in the circuit of Figure A.1.1. If we assume the initial charge on C to be zero, the sum of voltage drops across the circuit elements is

$$E = iR + \frac{1}{C} \int_0^t i(\tau) \, d\tau + L \frac{di}{dt} \tag{A.1.27}$$

Proceeding to the solution as before, we find

$$\frac{E}{s} = \bar{i}R + \frac{1}{sC} \bar{i} + Ls\bar{i} \tag{A.1.28}$$

$$\bar{i} = \frac{E/L}{s^2 + Rs/L + 1/LC} \tag{A.1.29}$$

This has the form of

$$L\{A \, e^{-at} \sin bt\} = \frac{Ab}{(s + a)^2 + b^2} \tag{A.1.30}$$

and algebraic comparison of (A.1.29) and (A.1.30) identifies a as $R/2L$ and b^2 as $(1/LC - R^2/4L^2)$. The constant A is therefore E/Lb, and the solution is

$$i = \frac{E}{Lb} e^{-at} \sin bt \tag{A.1.31}$$

Several times in our study we will need to solve equations of the following form:

$$\frac{d^2C(x)}{dx^2} - a^2C(x) = -b \tag{A.1.32}$$

Transformation and further manipulation yields

$$s^2\overline{C}(s) - sC(0) - C'(0) - a^2\overline{C}(s) = -b/s \tag{A.1.33}$$

$$\overline{C}(s) = \frac{-b + s^2C(0) + sC'(0)}{s(s - a)(s + a)} \tag{A.1.34}$$

It is inconvenient to invert this expression without first segmenting it into *partial fractions*; hence we will suspend our consideration of this solution while we summarize the technique.

The expression to be expanded must first be factored as far as possible into real linear and real quadratic factors; for example,

$$\frac{s + 3}{(s - 1)^2(s - 2)(s - 3)(s^2 + 2s + 2)} \tag{A.1.35}$$
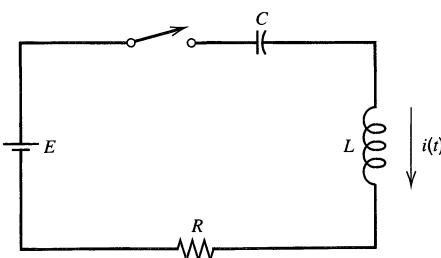
Figure A.1.1

A series-sum representation of the expression is then written according to the following rules (6):

1. If the linear factor $as + b$ occurs n times as a factor in the denominator, there corresponds to this factor a sum of n partial fractions:

$$\frac{A_1}{as + b} + \frac{A_2}{(as + b)^2} + \cdots + \frac{A_n}{(as + b)^n} \qquad \text{(A.1.36)}$$

where the A_i are constants and $A_n \neq 0$.

2. If a quadratic factor $as^2 + bs + c$ occurs n times as a factor in the denominator, there corresponds to this factor a sum of n partial fractions:

$$\frac{A_1 s + B_1}{as^2 + bs + c} + \frac{A_2 s + B_2}{(as^2 + bs + c)^2} + \cdots + \frac{A_n s + B_n}{(as^2 + bs + c)^n} \qquad \text{(A.1.37)}$$

where the A's and B's are constants and $A_n s + B_n$ is not identically zero. Thus, the example above expands to

$$\frac{s + 3}{(s - 1)^2(s - 2)(s - 3)(s^2 + 2s + 2)} = \frac{A}{s - 1} + \frac{B}{(s - 1)^2} + \frac{C}{s - 2}$$

$$+ \frac{D}{s - 3} + \frac{Es + F}{s^2 + 2s + 2} \qquad \text{(A.1.38)}$$

Ordinarily there are two ways to evaluate the constants. One can either multiply by the denominator on the left-hand side, expand both sides into polynomials, and equate coefficients of like powers of s; or one can substitute values for s and solve simultaneous equations.

Returning now to our suspended problem, we find that we can factor the right side of (A.1.34) and then expand it as follows.

$$\overline{C}(s) = \frac{-b + s^2 C(0) + s C'(0)}{s(s - a)(s + a)} \qquad \text{(A.1.39)}$$

$$= \frac{A'}{s + a} + \frac{B'}{s - a} + \frac{D'}{s} \qquad \text{(A.1.40)}$$

By multiplying the last equation by s and then setting $s = 0$, one easily determines the constant D' to be b/a^2. Evaluation of A' and B' must await definition of the boundary conditions $C(0)$ and $C'(0)$, but we nevertheless can invert the transform to a general result:

$$C(x) = \frac{b}{a^2} + A' e^{-ax} + B' e^{ax} \qquad \text{(A.1.41)}$$

We will come back to this equation in Section A.1.6.

A.1.5 Solutions of Simultaneous Linear Ordinary Differential Equations

To illustrate the usefulness of transform methods for solving simultaneous linear ODEs, we consider the following kinetic scheme.

$$A \xrightarrow{k_1} B + C$$

$$B \xrightarrow{k_2} D \qquad \text{(A.1.42)}$$

$$C + (Z) \xrightarrow{k'_3} D$$

where k_3' is a pseudo-first-order rate constant. Our goal is to determine the time profiles of the concentrations of A, B, C, and D. Suppose at $t = 0$, $[A] = A*$, and $[B] = [C] = [D] = 0$. The ODEs describing the system are written straightforwardly:

$$\frac{d[A]}{dt} = -k_1[A] \tag{A.1.43}$$

$$\frac{d[B]}{dt} = k_1[A] - k_2[B] \tag{A.1.44}$$

$$\frac{d[C]}{dt} = k_1[A] - k_3'[C] \tag{A.1.45}$$

$$\frac{d[D]}{dt} = k_2[B] + k_3'[C] \tag{A.1.46}$$

Denoting $L\{[A]\} = a$, *etc.*, we can write the following simultaneous *algebraic* equations:

$$sa - A* = -k_1a \tag{A.1.47}$$
$$sb = k_1a - k_2b \tag{A.1.48}$$
$$sc = k_1a - k_3'c \tag{A.1.49}$$
$$sd = k_2b + k_3'c \tag{A.1.50}$$

These relations obviously can be solved easily for a, b, c, and d, which can in turn be inverted to the desired concentrations.

A.1.6 Solutions of Partial Differential Equations (1, 2)

We have already anticipated above our continuing need for solving the diffusion equation:

$$\frac{\partial C(x, t)}{\partial t} = D\frac{\partial^2 C(x, t)}{\partial x^2} \tag{A.1.51}$$

in a variety of circumstances with differing boundary conditions. The solution requires an *initial condition* ($t = 0$), and two *boundary conditions* in x. Typically one takes $C(x, 0) = C*$ for the initial state, and one uses the *semi-infinite limit*:

$$\lim_{x \to \infty} C(x, t) = C* \tag{A.1.52}$$

as one x condition. Thus, only one additional boundary condition is required to define a problem completely. Normally, this third boundary condition is defined by the particular experimental situation being treated. Even without the third condition, a partial solution can be obtained, and it is instructive for us to carry it through.

Transforming the PDE on the variable t, we obtain

$$s\overline{C}(x, s) - C* = D\frac{d^2\overline{C}(x, s)}{dx^2} \tag{A.1.53}$$

$$\frac{d^2\overline{C}(x, s)}{dx^2} - \frac{s}{D}\overline{C}(x, s) = -\frac{C*}{D} \tag{A.1.54}$$

In considering ODEs above, we were able to solve this equation, and we can immediately write from (A.1.41)[1]

$$\overline{C}(x, s) = \frac{C^*}{s} + A'(s) \exp[-(s/D)^{1/2}x] + B'(s) \exp[(s/D)^{1/2}x] \qquad \text{(A.1.55)}$$

The semi-infinite limit can be transformed to

$$\lim_{x \to \infty} \overline{C}(x, s) = \frac{C^*}{s} \qquad \text{(A.1.56)}$$

hence, $B'(s)$ must be zero for the conditions at hand. Therefore,

$$\boxed{\overline{C}(x, s) = \frac{C^*}{s} + A'(s) \exp[-(s/D)^{1/2}x]} \qquad \text{(A.1.57)}$$

and

$$C(x, t) = C^* + L^{-1}\{A'(s) \exp[-(s/D)^{1/2}x]\} \qquad \text{(A.1.58)}$$

Final evaluation of $\overline{C}(x, s)$ and $C(x, t)$ depends on the third boundary condition.

A.1.7 The Zero-Shift Theorem (1)

In electrochemical experiments, one often encounters abrupt changes in boundary conditions. Simple step techniques are the most obvious examples. Theoretical treatments of these experiments are often simplified by application of the *unit step function*, $S_\kappa(t)$, which rises from zero to unity at $t = \kappa$. More precisely,

$$S_\kappa(t) = 0 \qquad t \le \kappa \qquad \text{(A.1.59)}$$
$$S_\kappa(t) = 1 \qquad t > \kappa \qquad \text{(A.1.60)}$$

It can be regarded as a mathematical "switch" that is "closed" at time $t = \kappa$, and it allows compact expression of complex boundary conditions. For example, consider a potential that is held at E_1 until $t = \kappa$, then is changed abruptly to E_2. The whole sequence can be written

$$E(t) = E_1 + S_\kappa(t)(E_2 - E_1) \qquad \text{(A.1.61)}$$

Similarly, the potential program representing a linear scan following a period of constant potential could be expressed as

$$E(t) = E_1 + S_\kappa(t)v(t - \kappa) \qquad \text{(A.1.62)}$$

Once the boundary conditions are written out, they must usually be transformed. The *zero-shift theorem* provides the necessary basis. It is summarized by

$$\boxed{L\{S_\kappa(t)F(t - \kappa)\} = e^{-\kappa s}f(s)} \qquad \text{(A.1.63)}$$

The proof rests on the definition:

$$L\{S_\kappa(t)F(t - \kappa)\} \equiv \int_0^\infty e^{-ts}S_\kappa(t)F(t - \kappa)\,dt = \int_\kappa^\infty e^{-ts}F(t - \kappa)\,dt \qquad \text{(A.1.64)}$$

---

[1]In equation A.1.55, the "constant" A' is shown as a function of s to highlight that possibility, which is actually encountered in Section 5.2 and elsewhere. It is necessary only that A' be constant with respect to the variable on which the ODE is based, which is x in (A.1.54). In the derivation leading up to (A.1.41), A' was not allowed to be function of s, because s was the transform variable corresponding to x. In the present case, s is the transform variable corresponding to t; hence A' can be a function of s.
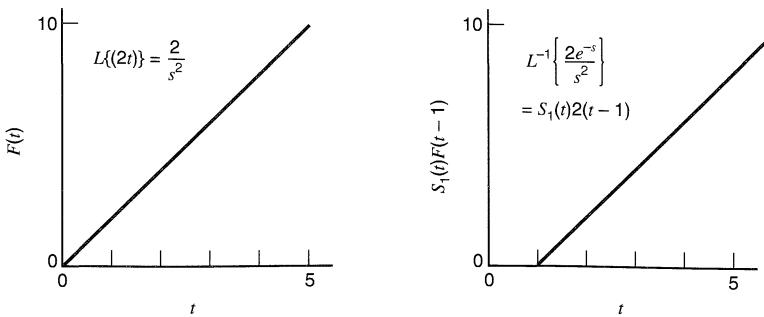
Figure A.1.2 Effect of the zero-shift theorem on $F(t) = 2t$.

Defining $\theta = t - \kappa$ and rearranging, we obtain the desired result:

$$\int_{\kappa}^{\infty} e^{-ts}F(t - \kappa)\,dt = e^{-\kappa s}\int_{0}^{\infty} e^{-\theta s}F(\theta)\,d\theta = e^{-\kappa s}f(s) \tag{A.1.65}$$

Equation A.1.63 is called the zero-shift theorem because it shows that multiplication by $e^{-\kappa s}$ in transform space corresponds to a shift in the real time axis by an amount κ. This effect is shown in Figure A.1.2 for the simple function $F(t) = 2t$.

A.2 TAYLOR EXPANSIONS

It is often useful to expand a function into a series when direct use of the function is impractical because of complexity or when a linear approximation is sought (2, 7). In general, a particular point is chosen as a central location, and the expansion is developed as a representation of the function in the neighborhood of that point. Truncated series can be expected to give accurate descriptions near the central value and less accurate representations at more remote points.

A.2.1 Expansion for a Function of Several Variables

A function of three variables, $f(x, y, z)$, can be expanded about the point (x_0, y_0, z_0) by the *Taylor formula:*

$$f(x, y, x) = f(x_0, y_0, z_0) + \sum_{j=1}^{\infty} \frac{1}{j!}\left[\left(\delta x \frac{\partial}{\partial x} + \delta y \frac{\partial}{\partial y} + \delta z \frac{\partial}{\partial z}\right)^{j} f(x, y, z)\right]_{(x_0, y_0, z_0)} \tag{A.2.1}$$

where $\delta x = x - x_0$, $\delta y = y - y_0$, and $\delta z = z - z_0$. The expression in parentheses is a differential operator that is raised to the jth power. The various powers of $\partial/\partial x$, $\partial/\partial y$ and $\partial/\partial z$ are symbols for repeated differentiation. After the operator acts on $f(x, y, z)$, the limits are taken for (x_0, y_0, z_0).

As an example, consider the expansion of the current-overpotential equation (3.4.10):

$$g[C_O(0, t), C_R(0, t), \eta] = i/i_0 = \frac{C_O(0, t)}{C_O^*}e^{-\alpha f\eta} - \frac{C_R(0, t)}{C_R^*}e^{(1-\alpha)f\eta} \tag{A.2.2}$$

The central point is chosen at $(C_O^*, C_R^*, 0)$, where $g = 0$. If only the terms for $j = 1$ are kept then we have

$$\frac{i}{i_0} = \left[\delta C_O(0, t) \frac{\partial}{\partial C_O(0, t)} + \delta C_R(0, t) \frac{\partial}{\partial C_R(0, t)} + \delta\eta \frac{\partial}{\partial \eta}\right] g\left[C_O(0, t), C_R(0, t), \eta\right]$$

$$\text{(derivatives evaluated at } C_O^*, C_R^*, \eta = 0) \tag{A.2.3}$$

Substituting for the derivatives and evaluating at the central point, one obtains

$$\frac{i}{i_0} = \frac{\delta C_O(0, t)}{C_O^*} - \frac{\delta C_R(0, t)}{C_R^*} - f\delta\eta \tag{A.2.4}$$

or

$$i = i_0\left[\frac{C_O(0, t)}{C_O^*} - \frac{C_R(0, t)}{C_R^*} - f\eta\right] \tag{A.2.5}$$

which is equivalent to (3.4.30). By truncating the series at $j = 1$, we have derived a simple linear approximation to the more complex relation, (3.4.10). It is valid for small excursions from the central point. For larger values of $\delta C_O(0, t)$, $\delta C_R(0, t)$, and $\delta\eta$, additional terms of the expansion would have to be included. The complete series is readily derived, but it is left as an exercise for the reader.

A.2.2 Expansion of a Function of a Single Variable

If the function of interest has only a single independent variable, the Taylor formula is a simplified version of (A.2.1):

$$f(x) = f(x_0) + \sum_{j=1}^{\infty} \frac{1}{j!} (x - x_0)^j \left[\frac{\partial^j}{\partial x^j} f(x)\right]_{x=x_0} \tag{A.2.6}$$

In this case, the expansion is made about the point $x = x_0$.

A.2.3 Maclaurin Series

When a Taylor expansion of $f(x)$ is carried out about $x = 0$, it is called a *Maclaurin series*. The general formula is

$$f(x) = f(0) + \sum_{j=1}^{\infty} \frac{1}{j!} x^j \left[\frac{\partial^j}{\partial x^j} f(x)\right]_{x=0} \tag{A.2.7}$$

▶▶ A.3 THE ERROR FUNCTION AND THE GAUSSIAN DISTRIBUTION

In treating diffusion problems, one frequently encounters the integrated normal error curve, that is, the *error function* (2, 7):

$$\text{erf}(x) \equiv \frac{2}{\pi^{1/2}} \int_0^x e^{-y^2} \, dy \tag{A.3.1}$$

This relation approaches a unit limit as x becomes very large; hence, its *complement*, which also arises often, is straightforwardly defined as

$$\text{erfc}(x) \equiv 1 - \text{erf}(x) \tag{A.3.2}$$

Both functions are illustrated graphically in Figure A.3.1. A few values of each function are given in Table C.5. Note that erf(x) rises steeply and essentially reaches its limit for any x greater than 2.

Evaluations are made by series representations (8, 9). The Maclaurin expansion is

$$\text{erf}(x) = \frac{2}{\pi^{1/2}}\left(x - \frac{x^3}{3} + \frac{x^5}{5 \cdot 2!} - \frac{x^7}{7 \cdot 3!} + \frac{x^9}{9 \cdot 4!} - \cdots\right) \tag{A.3.3}$$

which is convenient for $0 \leq x \leq 2$. For values of x less than 0.1, one can take the linear approximation from the first term:

$$\text{erf}(x) \approx \frac{2x}{\pi^{1/2}} \qquad (x < 0.1) \tag{A.3.4}$$

Large arguments ($x > 2$) are better evaluated from

$$\text{erf}(x) = 1 - \frac{e^{-x^2}}{\pi^{1/2}x}\left[1 - \frac{1}{2x^2} + \frac{1 \cdot 3}{(2x^2)^2} - \frac{1 \cdot 3 \cdot 5}{(2x^2)^3} + \cdots\right] \tag{A.3.5}$$

The derivative of erf(x) can be evaluated by the Leibnitz rule as described in the next section.

The argument of the error function integral is related to the *gaussian distribution*, also frequently called the *normal error distribution*, which is given by

$$f(y) = \frac{1}{(2\pi)^{1/2}\sigma}\exp\left[-\frac{(y - \bar{y})^2}{2\sigma^2}\right] \tag{A.3.6}$$

This is the familiar bell-shaped error curve having a maximum at the *mean value*, $\bar{y}$, and a width described by the *standard distribution*, σ. The integral of the gaussian distribution over all values of the argument is unity. Because the function is symmetrical, the integral from the mean value over all values on either side is 0.5.

By comparison of (A.3.1) and (A.3.6), one can see that the error function is twice the integral to the defined argument, x, of the positive side of a gaussian having a mean value of zero and a standard deviation of $1/\sqrt{2}$. In fact, any gaussian can be expressed in that way by transforming its argument to $x = (y - \bar{y})/(\sqrt{2}\sigma)$ and recognizing the effect of the transformation on the standard deviation of the function. Thus, erf($1/\sqrt{2}$) = erf(0.707) = 0.68, consistent with the well-known fact that a gaussian distribution has 68% of its area between limits of one standard deviation on either side of the mean.
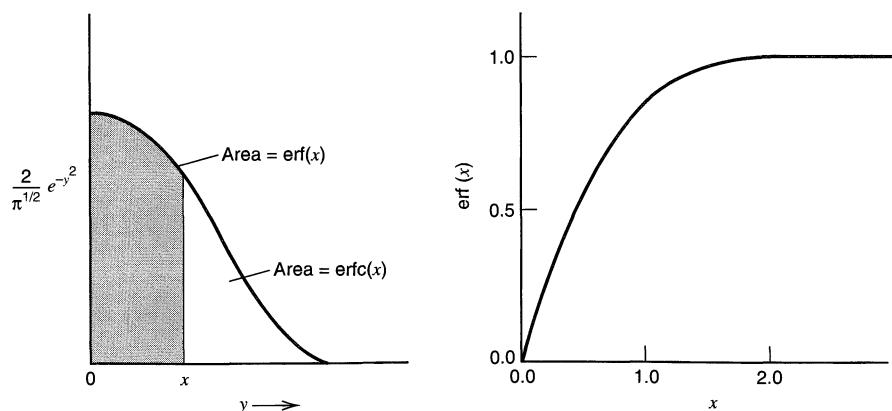
Figure A.3.1 Definition and behavior of erf(x) and erfc(x).

▶ A.4 LEIBNITZ RULE

The Leibnitz rule (7) furnishes a basis for differentiating a definite integral with respect to a parameter:

$$\frac{d}{d\alpha} \int_{u_1(\alpha)}^{u_2(\alpha)} f(x, \alpha) \, dx = f[u_2(\alpha), \alpha]\frac{du_2}{d\alpha} - f[u_1(\alpha), \alpha]\frac{du_1}{d\alpha} + \int_{u_1(\alpha)}^{u_2(\alpha)} \frac{\partial f(x, \alpha)}{\partial \alpha} \, dx \quad \text{(A.4.1)}$$

For example,

$$\frac{d}{dx} \operatorname{erf}(x) = \frac{2}{\pi^{1/2}} \frac{d}{dx} \int_0^x e^{-y^2} \, dy = \frac{2}{\pi^{1/2}} e^{-x^2} \quad \text{(A.4.2)}$$

▶ A.5 COMPLEX NOTATION

In many problems involving vector-like variables, such as ac circuit analysis (Chapter 10), it is useful to represent physical quantities as complex functions (10), so that two dimensions are available. A *complex number* is written as $z = x + jy$, where $j = \sqrt{-1}$, and x and y are called the *real* and *imaginary components*. One can think of z as a point in the *complex plane* representing all possible combinations of x and y, or it could be a vector in a Cartesian coordinate system, as shown in Figure A.5.1a. The component x is plotted along the *real axis*, and y is plotted versus the *imaginary axis*. Two complex numbers $z_1 = x_1 + jy_1$ and $z_2 = x_2 + jy_2$ are equal only if $x_1 = x_2$ and $y_1 = y_2$.

Functions of a complex variable can also be defined, and they are always separable into real and imaginary parts. That is, the function $w(z)$ can always be written for $z = x + jy$ as

$$w(z) = u(x, y) + jv(x, y) \quad \text{(A.5.1)}$$

where $u(x, y)$ and $v(x, y)$ are wholly real. For example, one might have

$$w(z) = x^2 + y^2 - 2jxy \quad \text{(A.5.2)}$$

where the *real part* of $w(z)$, that is, $\text{Re}[w(z)]$, is $u(x, y) = x^2 + y^2$ and the *imaginary part*, $\text{Im}[w(z)]$, is $-2xy$. Two functions $w_1(z) = u_1(x, y) + jv_1(x, y)$ and $w_2(z) = u_2(x, y) + jv_2(x, y)$ are equal only if $u_1(x, y) = u_2(x, y)$ and $v_1(x, y) = v_2(x, y)$.
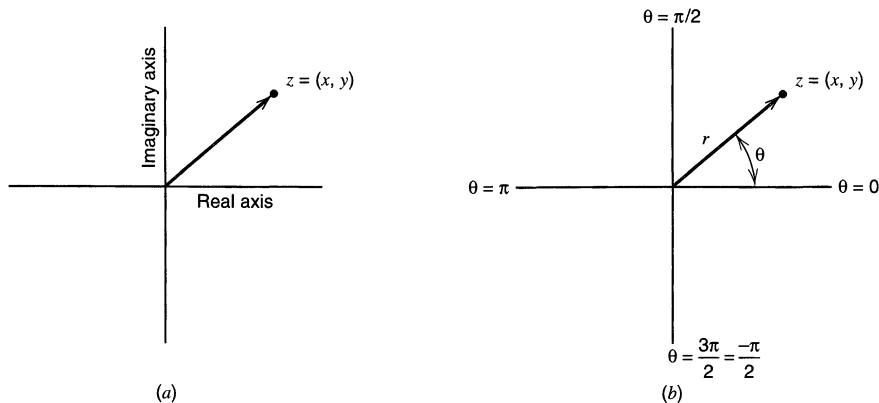
Figure A.5 1 Points in the complex plane. (*a*) Cartesian system. (*b*) Polar system.

A valuable alternative notation for a complex number is to specify its position in polar coordinates, as shown in Figure A.5.1*b*. The length of the vector is

$$r = (x^2 + y^2)^{1/2} \tag{A.5.3}$$

and the phase angle θ is

$$\theta = \tan^{-1}\left(\frac{y}{x}\right) \tag{A.5.4}$$

An important function relates directly to this notation. We *define* the complex exponential as

$$\exp(z) = e^x(\cos y + j \sin y) \tag{A.5.5}$$

Thus,

$$e^z = e^x e^{jy} \tag{A.5.6}$$

where

$$\boxed{\exp(jy) = \cos y + j \sin y} \tag{A.5.7}$$

Note that e^{jy} always has a magnitude of unity, so that all values of the function lie on the circle of unit radius about the origin, as shown in Figure A.5.2, and y is the phase angle of the vector. Very often in science, sine and cosine terms are carried through derivations in terms of functions like (A.5.7).

The exponential function gives us a convenient way to express a complex number z in its polar form; that is,

$$z = x + jy = re^{j\theta} \tag{A.5.8}$$

Often the polar notation is the more useful form for applications, and functions may be written in terms of r and θ, instead of x and y.

Finally, we note that any function of a complex variable $w = u + jv$ can always be converted into a wholly real function by multiplying it by its *complex conjugate* $w^* = u - jv$:

$$ww^* = u^2 + v^2 \tag{A.5.9}$$

This feature is very useful in algebraic manipulation, for example, in removing imaginary components from denominators in fractions.
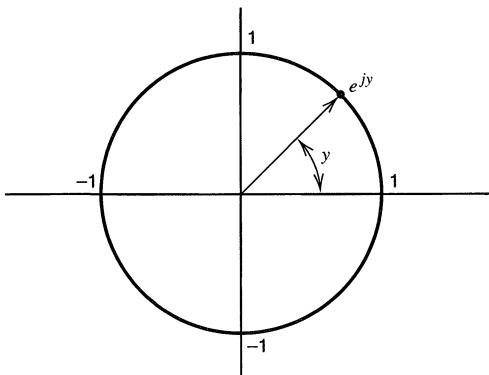
Figure A.5.2   Locus of values of exp(jy) in a polar coordinate system with y as the angle and the magnitude of the function as the radius. The result is a circle at unit radius. Vector shows one value of the function.

▷▷ A.6 FOURIER SERIES AND FOURIER TRANSFORMATION

Any periodic waveform, such as the square wave in Figure A.6.1a, can be represented as a superposition of sinusoidal components (11–14) comprising a *fundamental frequency* $f_0 = 1/T_0$, where T_0 is the period of the waveform, plus the *harmonics* of f_0. That is,

$$y(t) = \frac{a_0}{2} + \sum_{n=1}^{\infty} [a_n \cos(2\pi n f_0 t) + b_n \sin(2\pi n f_0 t)] \tag{A.6.1}$$

or, alternatively,

$$y(t) = A_0 + \sum_{n=1}^{\infty} A_n \sin(2\pi n f_0 t + \phi_n) \tag{A.6.2}$$

where A_n is the *amplitude* of the component with frequency $n f_0$, and ϕ_n is its *phase angle*. The term A_0 is the *dc level*. This series is called a *Fourier series*, and the signal is a *Fourier synthesis* of the components. A few such components of the square wave are shown in Figure A.6.1b, and one can see how their sum begins to approximate the square wave.

The existence of the Fourier series makes it possible to represent a signal either in the *time domain*, as signal level *vs.* time, or in the *frequency domain*, as the set of amplitudes and phase angles of the component sinusoids. Sometimes it is useful to dissect a time-domain signal into its components or to synthesize the time-domain signal from its components. Section 10.8 provides excellent illustrations of both cases. Our concern here is with the mechanism of interdomain conversions.

The *Fourier integral* (11–14) creates a frequency-domain function $H(f)$ from the time-domain relation $h(t)$:

$$H(f) = \int_{-\infty}^{\infty} h(t) e^{-j2\pi ft} \, dt \tag{A.6.3}$$

This operation is called *Fourier transformation*, and $H(f)$ is the *Fourier transform* of $h(t)$. *Inverse transformation* by the integral:

$$h(t) = \int_{-\infty}^{\infty} H(f) e^{j2\pi ft} \, df \tag{A.6.4}$$

allows generation of the time-domain function, given $H(f)$.

(a)

Signal level

(b)
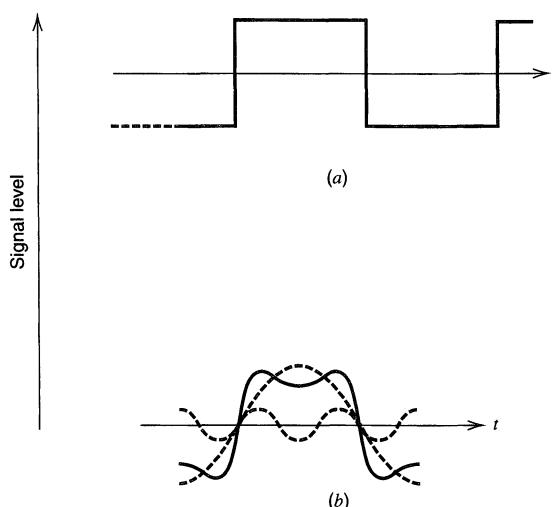
Figure A.6.1 (a) A square wave. (b) Two components (dashed) of the square wave, $\cos(2\pi f_0 t)$ and $-(1/3)\cos(6\pi f_0 t)$, and their sum (solid).

In most applications of interest to us, we must deal with waveforms that have been digitized (sampled) at a constant rate. For example, we might represent the current through a cell as a list of data points taken at evenly spaced times. Then a numeric algorithm, based on the integral (A.6.3), would be used to generate the frequency-domain information, which would be a list of amplitudes and phase angles. The input to the algorithm is one period, T_0, of the waveform represented as n points (often a power of 2, e.g. 128, 256, 512, . . .). The output is a list of the amplitudes and phase angles for $n/2$ frequencies comprising the dc level, $1/T_0$, $1/2T_0$, . . . , $1/[(n/2) - 1]T_0$. The algorithm would probably be based on the *fast Fourier transform* (FFT) technique (12–14), and it might be implemented either in software in a computer or in a peripheral hardware device.

The FFT algorithms also have provision for inversion. One supplies amplitudes and phase angles for $n/2$ components at the frequencies given above, and the output is n evenly spaced time-domain points comprising one period.

The Fourier transformation has many properties that can be applied usefully to signal processing. A simple illustration is noise reduction, or smoothing. Suppose one has a signal in which the information is at a few low frequencies, but there is noise at high frequencies. Transformation of signal yields the frequency spectrum, which one alters by setting the amplitudes of high-frequency components to zero. Inverse transformation then yields smoothed time-domain data. Other operations allow integration and differentiation, correlations between two signals, or correlation of a signal with itself. Their details are beyond our scope, but they are covered thoroughly in specialized sources (12–16).

▶ A.7 REFERENCES

1. R. V. Churchill, "Operational Mathematics," 3rd ed., McGraw-Hill, New York, 1972.

2. G. Doetsch, "Laplace Transformation," Dover, New York, 1953.

3. H. Margenau and G. M. Murphy, "The Mathematics of Physics and Chemistry," 2nd ed., Van Nostrand, New York, 1956.

4. A. Erdelyi, W. Magnus, F. Oberhettinger, and F. Tricomi, "Tables of Integral Transforms," McGraw-Hill, New York, 1954.

5. G. E. Roberts and H. Kaufman, "Table of Laplace Transforms," Saunders, Philadelpia, 1966.

6. T. S. Peterson, "Calculus," Harper, New York, 1960.

7. W. Kaplan, "Advanced Calculus," 3rd ed., Addison-Wesley, Reading, MA, 1992.

8. F. S. Acton, "Numerical Methods That Work," Mathematical Association of America, Washington, 1990, Chap. 1.

9. M. Abramowitz and I. A. Stegun, Eds., "Handbook of Mathematical Functions," Dover, New York, 1977.

10. J. W. Brown and R. V. Churchill, "Complex Variables and Applications," 6th ed., McGraw-Hill, New York, 1996.

11. J. W. Brown and R. V. Churchill, "Fourier Series and Boundary Value Problems," 5th ed., McGraw-Hill, New York, 1993.

12. R. N. Bracewell, "The Fourier Transform and its Applications," 2nd ed., McGraw-Hill, New York, 1986.

13. E. O. Brigham, "The Fast Fourier Transform," Prentice-Hall, Englewood Cliffs, NJ, 1974.

14. P. R. Griffiths, Ed., "Transform Techniques in Chemistry," Plenum, New York, 1978.

15. G. Horlick and G. M. Hieftje in "Contemporary Topics in Analytical Chemistry," Vol. 3, D. M. Hercules, G. M. Hieftje, and L. R. Snyder, Eds., Plenum, New York, 1978, Chap. 4.

16. J. W. Hayes, D. E. Glover, D. E. Smith, and M. W. Overton, *Anal. Chem.*, **45**, 277 (1973).

▶ A.8 PROBLEMS

A.1 Show from the definition that

$$L\{\sin at\} = a/(a^2 + s^2)$$
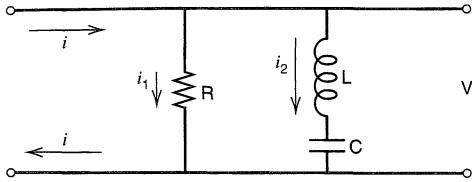
Figure A.8.1

A.2 Derive (A.1.17).

A.3 Find $L\{\sin at\}$ using (A.1.14).

A.4 Use convolution to find the inverse transform of $1/[s^{1/2}(s - 1)]$.

A.5 Use the Laplace transform method to solve for Y in the following cases, where the primes denote differentiation by t:

(a) $Y'' + Y' = 0$ with $Y(0) = 5$, $Y'(0) = -1$.

(b) $Y = 2\cos(t) - 2\int_0^t Y(\tau) \sin(t - \tau) \, d\tau$.

(c) $Y''' - Y'' - Y' + Y = \cos(t)$ with $Y(0) = Y'(0) = 0$, $Y''(0) = 1$.

A.6 After $t = 0$, a constant current, i, is supplied to the network in Figure A.8.1. Before then $i = 0$ and $V = 0$. Find $V(t)$ for $t > 0$. Different combinations of R, L, and C will provide markedly different responses. Why?

A.7 Obtain a Taylor expansion of $\exp(ax)$ about $ax = 1$. Obtain the Maclaurin series. What approximations could be made for $\exp(ax)$ near $ax = 1$ and $ax = 0$?

A.8 Derive (A.3.3).

B

DIGITAL SIMULATIONS OF ELECTROCHEMICAL PROBLEMS

We have seen that the rate of an electrochemical process is affected by the rates at which reactants can be supplied to the electrode and products can be dispersed from it. Often the overall process is governed completely by the rates of mass transport and homogeneous chemical reaction. One can usually write the set of coupled differential equations describing the transformations and movements of material, but often they can be solved in closed form with difficulty or not at all. Numerical methods are frequently applied to the solution of such equations (1).

Most commonly situations of this kind are attacked by variants of the *method of finite differences*. A numerical model of the electrochemical system is set up within a computer, and the model is allowed to evolve by a set of algebraic laws derived from the differential equations. In effect, one carries out a *simulation* of the experiment, and one can extract from it numeric representations of current functions, concentration profiles, potential transients, and so on.

We will outline the basic features of simulation here, because the method has been so useful in solving complex electrochemical problems involving complicated kinetic schemes, nonuniform current distributions at the working electrode, or spectroscopic-electrochemical interactions. Explicit simulation is a numerical approach to the solution of partial differential equations, but it is conceptually simpler than other numerical techniques. In addition, it is valuable in developing an intuitive grasp of the important processes in an electrochemical system. Several reviews have covered this topic, and they are recommended to the reader interested in more detail than we present below (1–8).

▶ B.1 SETTING UP THE MODEL

B.1.1 The Discrete Model

By resorting to a simulation, we are admitting our inability to handle the calculus for an electrochemical system described by complex continuous functions. So, we move backward one stage in sophistication and consider the electrolyte solution in terms of small, discrete volume elements.[1] Throughout any element, the concentrations of all substances are

---

[1]One could address the problem at the molecular level by treating diffusion as a random walk process. Although this computational approach is possible, it is very slow compared to the finite difference method described here. However, it might be useful when one is considering exceedingly small volumes containing a small number of molecules.

regarded as uniform, but they vary from element to element. In many instances, we wish to study electrochemical experiments featuring linear diffusion to a planar electrode of area A. If edge diffusion is prevented, then even in the real system the concentration of any substance is constant over any plane parallel to the electrode. The concentration can vary only normal to its surface.

Thus, we construct a model featuring a sequence of volume elements extending away from the interface as shown in Figure B.1.1. The electrode surface is usually envisioned as being in the center of the first box, and each box j is taken to characterize the solution at a distance $x = (j - 1)\Delta x$ from the interface.[2] If species A, B, ... are present, their concentrations are $C_A(j)$, $C_B(j)$, ... What we have created, then, is a discrete model of the solution, comprising arrays of concentrations whose properties approximate those of the continuous system. Since we can choose the size of Δx, it is said to be a *model variable*. The smaller we set Δx, the more elements will be needed in the arrays and the more refined our model will be.

It is also clear that if C_A at distance x_1 differs from that at a nearby distance x_2, diffusion will tend to equalize the concentrations. In addition, homogeneous reactions such as A + B → C might occur. Thus, the arrays $[C_A(j)]$, $[C_B(j)]$, ... can represent the chemical system only for a limited period. There are laws of diffusion and reaction by which the concentrations interact with each other so that they are transformed into different arrays describing the system at a later time.

This approach implies that time is broken into segments, too. Let one of the segments have a duration Δt. To model the system's evolution, we cast the reaction and mass transport laws into algebraic relations that describe the changes that these processes would bring about over one interval Δt. We start by applying the relations to a set of concentration arrays characterizing the initial condition of the system. This first application transforms the arrays to a different set that can be viewed as a picture of the system at time Δt. Applying the laws again on the new arrays yields a picture for $t = 2\Delta t$, and so on. The kth *iteration* of the laws of transformation therefore yields the model for $t = k\Delta t$.[3] The time evolution of the continuous system is approximated by that of the model, and the discrepancy between the two grows smaller as Δt, a second model variable, is reduced.

B.1.2 Diffusion

The most common interactions between array elements are defined by Fick's laws of diffusion (see Section 4.4). The first law is

$$J(x, t) = -D \frac{\partial C(x, t)}{\partial x} \tag{B.1.1}$$
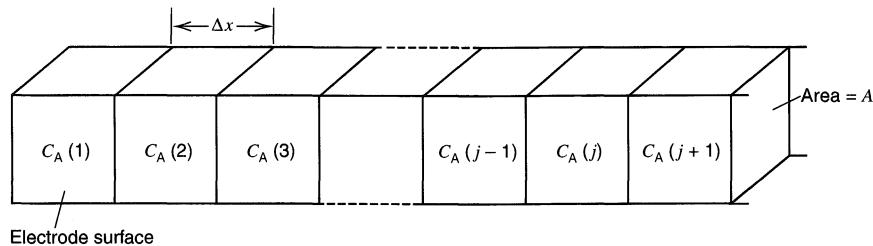
Figure B.1.1 Discrete model of the solution adjacent to an electrode.

[2]The electrode could also be placed at the left edge of first box, where a special concentration at the electrode surface, $C_A(0)$ is assumed. In this case, $x = (j - 1 + 0.5)\Delta x = (j - 0.5)\Delta x$.

[3]For some purposes, such as calculation of the current that flows during a given interval, it is more accurate to take time as midway through the interation, so that $t = (k - 0.5)\Delta t$. This distinction becomes less significant as k increases.

but the definition of a derivative allows (B.1.1) to be recast as

$$J(x, t) = \lim_{\Delta x \to 0} -D \frac{[C(x + \Delta x, t) - C(x, t)]}{\Delta x} \tag{B.1.2}$$

The essence of the finite difference method is the assertion that Δx in a practical discrete model (a finite difference) can be made small enough that one can take

$$J(x, t) = -D \frac{[C(x + \Delta x, t) - C(x, t)]}{\Delta x} \tag{B.1.3}$$

or

$$J(x, t) = -\frac{D}{\Delta x} [C(x + \Delta x/2, t) - C(x - \Delta x/2, t)] \tag{B.1.4}$$

Now consider the second law:

$$-\frac{\partial C(x, t)}{\partial t} = \frac{\partial J(x, t)}{\partial x} \tag{B.1.5}$$

In finite difference form, it is

$$-\frac{C(x, t + \Delta t) - C(x, t)}{\Delta t} = \frac{J(x + \Delta x/2, t) - J(x - \Delta x/2, t)}{\Delta x} \tag{B.1.6}$$

Using (B.1.4) to substitute for the fluxes, one finds

$$C(x, t + \Delta t) = C(x, t) + \frac{D\Delta t}{\Delta x^2} [C(x + \Delta x, t) - 2C(x, t) + C(x - \Delta x, t)] \tag{B.1.7}$$

If one refers equation B.1.7 back to the model in Figure B.1.1, it is easy to see that this relation allows one to calculate the concentration in any box at $t + \Delta t$ from the concentrations in that box and its immediate neighbors at time t. In the jargon of the simulation, the meaning of (B.1.7) is that for any box j, the concentration resulting from iteration $k + 1$ is calculated from the concentrations produced in boxes $j - 1, j$, and $j + 1$ in iteration k. Thus,

$$C(j, k + 1) = C(j, k) + \frac{D\Delta t}{\Delta x^2} [C(j + 1, k) - 2C(j, k) + C(j - 1, k)] \tag{B.1.8}$$

Because the new concentration, $C(j, k + 1)$ is calculated using only the old concentrations in iteration k, this is called an *explicit simulation*.

Equation B.1.8 is the general law defining diffusion effects on any species in any box, except the first box. In the first box, the electrode boundary condition creates special circumstances that we will treat in Section B.4.

These ideas are probably best consolidated by considering just how one might model a step experiment. The first stages are shown in Figure B.1.2. Initially the solution is uniform; hence every box has a concentration $C_A(j, 0) = C_A^*$. If B is initially absent, $C_B(j, 0) = 0$. Suppose the step magnitude is large enough that the surface concentration of A is zero. Then in the first iteration, all of the A in the first box is converted to B. Diffusion does not occur, because the concentrations for $k = 0$ are uniform. Thus, $C_A(1, 1) = 0$ and $C_B(1, 1) = C_A^*$, but for $j > 1$, $C_A(j, 1) = C_A^*$ and $C_B(j, 1) = 0$. In the second iteration, diffusion will alter the concentration in box 2, because fluxes of both A and B will cross the boundary between boxes 1 and 2. In order to maintain the interfacial condition that $C_A(1, k) = 0$ (for $k > 0$), the incoming flux of A must be converted into B. This yields the current for the second iteration. Continuing the process will generate the concentration profiles and the current as functions of time.
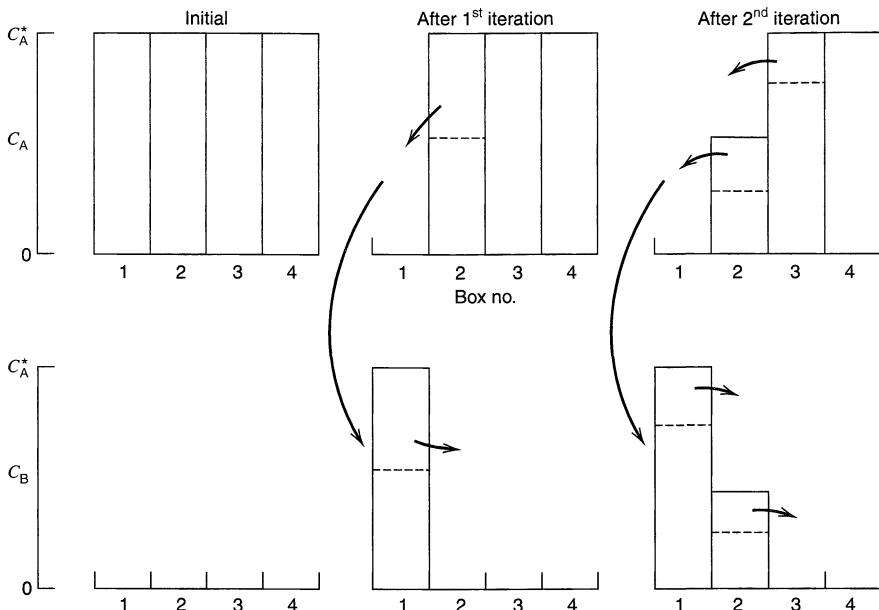
Figure B.1.2 Developing concentration profiles for a system undergoing the electrode reaction A + $ne \rightarrow$ B. Arrows show mass flow.

B.1.3 Dimensionless Parameters

If one wanted results for several starting concentrations, C_A^*, an equal number of simulations would be needed. Consider, though, the effects of dividing (B.1.8) by C_A^*. If $f(j, k) = C(j, k)/C_A^*$, then

$$f(j, k + 1) = f(j, k) + \mathbf{D}_M[f(j + 1, k) - 2f(j, k) + f(j - 1, k)] \qquad \text{(B.1.9)}$$

The constant $\mathbf{D}_M = D\Delta t/\Delta x^2$ is called the *model diffusion coefficient*. More will be said about it later. The f's, which are called *fractional concentrations*, are examples of *dimensionless parameters*.

Now suppose we simulate the step experiment again, but in place of concentrations we substitute f_A's and f_B's. Equation B.1.9 describes the way in which these parameters are altered by diffusion, and the boundary condition is simply $f_A(1, k) = 0$ $(k > 0)$. Initially, $f_A = 1$ and $f_B = 0$ everywhere. Carrying out the simulation is straightforward, and one obtains the time evolution of the fractional concentration profiles. The difference in using the dimensionless parameters is that these profiles from a *single simulation* describe the characteristics of the experiment for *every possible value of* C_A^*. To obtain the dimensioned profiles for a specific starting concentration, one need only multiply the f's by that value of C_A^*.

As an example of the usefulness of dimensionless parameters in the compact display of theoretical results, consider the homogeneous reaction A $\rightarrow$ B with rate constant k. The familiar solution for the concentration of A at any time, t, is $C_A = C_A^* \exp(-kt)$, where C_A^* is the concentration at $t = 0$. Since the real variables are C_A and t, one might first think of making a graphical display of the results by plotting C_A *vs.* t for different values of C_A^* and k. This involves a family of $m \times n$ curves, where m is the number of values of C_A^*, and n is the number of k values for each C_A^* (Figure B.1.3a). If one recognizes that the combination kt is a dimensionless parameter that always accounts wholly for the effects

1. $C_A^* = 2.5$ mM, $k = 0.2$ s^{-1}
2. $C_A^* = 1.0$ mM, $k = 0.2$ s^{-1}
3. $C_A^* = 2.5$ mM, $k = 1$ s^{-1}
4. $C_A^* = 1.0$ mM, $k = 1$ s^{-1}

1. $C_A^* = 2.5$ mM
2. $C_A^* = 1.0$ mM
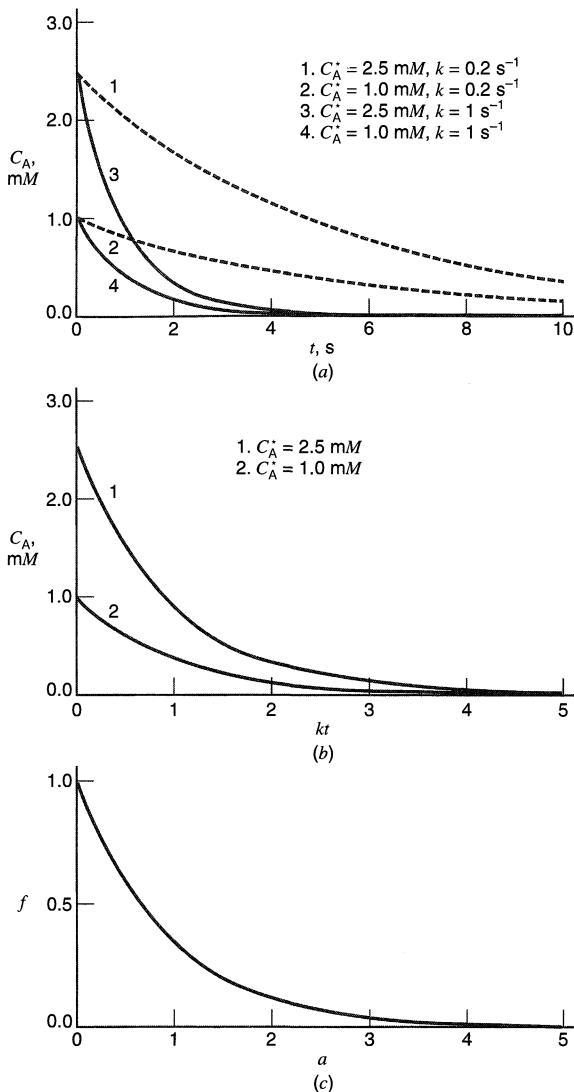
Figure B.1.3 Curves describing exponential decays.

of k and t in this problem, then one could plot C_A vs. kt and represent the same informa-tion as before in m curves for different C_A^* values, as shown in Figure B.1.3b. If one fur-ther realizes that C_A/C_A^* is also a useful dimensionless parameter, then the equation can be written $f_A = \exp(-a)$, where $f_A = C_A/C_A^*$ and $a = kt$. Hence, a plot of f_A vs. a shows all of the desired information in a single curve (Figure B.1.3c), which is the essential shape function of the system. It is an example of a *working curve.*

Solving differential equations in terms of dimensionless parameters generally does yield solutions that characterize whole families of specific experimental situations. This is a magnificent asset, especially where numerical solutions are required; consequently, the use of dimensionless variables has become standard practice.

A confusing aspect of these parameters is their tendency to combine the effects of more than one observable, so that one can have difficulty in mentally separating the ef-fects of a single observable individually. For example, the abscissa of Figure B.1.3c deals with changes in k, or in t, or in both. It is easier to understand the working curve by think-

ing in terms of a given experiment, which normally involves holding some variables constant. For example, one might study the reaction A → B by looking at the decay of A continuously with time. A given experiment would involve constant C_A^* and k values; hence the working curve can be regarded as a scaled decay function of concentration C_A vs. time t. We might even call f the *dimensionless concentration* and a the *dimensionless time*. Alternatively, we might study A → B by measuring C_A at a fixed elapsed time t. In that experimental context, the working curve in Figure B.1.3c would be seen as a plot of the concentration of A remaining (relative to the initial concentration) at the sampling time t versus a scaled rate constant. For that purpose, a could be called a *dimensionless rate constant*. Thus, the interpretation we apply to a working curve depends on the specific experiment at hand.

Dimensionless parameters are normally created by dividing the variables of interest by one or more variables that describe some *characteristic feature* of the system. For example, fractional concentrations describe concentrations relative to a characteristic concentration C_A^*. The parameter a can be understood similarly by recognizing that $1/k$ is the average lifetime of A (see Problem 3.8). Thus a is the ratio of the observation time to the lifetime of species A. Understood in this way, a is more than a numerical value; it is a guide to the design and interpretation of experiments. This capacity for expressing relationships between observables and characteristic features is a powerful aspect of dimensionless parameters, and with practice it can aid one's intuition in very useful ways. (See, for example, Section 12.3.1.)

B.1.4 Time

Time, t, measured into the simulation is $k\Delta t$, where k is the iteration number. Since Δt is a model variable, it is our choice, and in choosing its value we are making the equivalent statement that some known characteristic time t_k (which might be a step width, a scanning time, or some similar characteristic experimental duration) will be broken into ℓ iterations in our model. Thus,

$$\Delta t = t_k/\ell \tag{B.1.10}$$

Either ℓ or Δt can be selected arbitrarily as the model variable, though it usually is more convenient to work in terms of ℓ. Thus, we might carry out simulations of a step experiment with duration t_k by breaking t_k into 100, 1000, or 10,000 iterations at will. All of the simulations will yield equivalent results within their individual abilities to approximate events, but the larger the value of ℓ, the higher the quality of the simulation. On the other hand, a larger ℓ requires more computations, so a compromise is chosen. In simple explicit simulations, ℓ is typically 100 to 1000 iterations per t_k.

Note also that time is easily expressed in dimensionless terms as the ratio t/t_k. Thus,

$$\boxed{\frac{t}{t_k} = \frac{k}{\ell}} \tag{B.1.11}$$

B.1.5 Distance

The center of box j is at a distance $(j-1)\Delta x$ from the electrode surface. As we have already noted, Δx is also our choice; therefore we can determine the fineness of the model in spatial terms. However, there is a limit to the smallness of Δx. It turns out that $\mathbf{D_M}$ the model diffusion coefficient, cannot exceed 0.5 for an explicit simulation. Otherwise the finite difference calculation will not be stable. The reason is that Δx and Δt are not independent. In our treatment of diffusion, we implicitly assumed that within a period Δt, material

could diffuse only between neighboring boxes. If we try to set Δx too small for a given Δt, this assumption becomes inadequate, and the simulation diverges from reality. For example, consider the flux between boxes $j = 1$ and $j = 2$ in Figure B.1.2 for $k = 2$, when $f_A(1) = 0$ and $f_A(2) = 1$. If $\mathbf{D_M} = 0.5$, than half of the material in box $j = 2$ will move into box $j = 1$, resulting in $f_A(1) = 0.5$ and $f_A(2) = 0.5$. If $\mathbf{D_M} > 0.5$, the result of the computation will place more A in box $j = 1$ than in box $j = 2$, which is physically unreasonable.

Note also that, given Δt, $\mathbf{D_M}$ is an equivalent model variable to Δx. Instead of specifying Δx, it usually is more convenient to specify the dimensionless $\mathbf{D_M}$. Then,

$$\Delta x = \left(\frac{D\Delta t}{\mathbf{D_M}}\right)^{1/2} \tag{B.1.12}$$

The larger we choose $\mathbf{D_M}$, the smaller is Δx and the better is the model; hence $\mathbf{D_M}$ is usually set at a high constant value such as 0.45. Substituting for Δt, one obtains

$$\boxed{\Delta x = \left(\frac{Dt_k}{\mathbf{D_M}\ell}\right)^{1/2}} \tag{B.1.13}$$

and it becomes clear that ℓ is really the determinant of both temporal and spatial resolution for any simulation.

The distance of the center of box j from the electrode can now be written

$$x(j) = (j - 1)\left(\frac{Dt_k}{\mathbf{D_M}\ell}\right)^{1/2} \tag{B.1.14}$$

The convenient dimensionless distance is obtained by placing the real system variables on the left and the model variables on the right:

$$\boxed{\chi(j) = \frac{x(j)}{(Dt_k)^{1/2}} = \frac{j - 1}{(\mathbf{D_M}\ell)^{1/2}}} \tag{B.1.15}$$

The expression $(j - 1)/(\mathbf{D_M}\ell)^{1/2}$ allows one to calculate $\chi(j)$ easily from the simulation parameters, and the expression $x(j)/(Dt_k)^{1/2}$ allows one to correlate the properties of box j with the properties of the experimental solution segment situated at a real distance x from a physical electrode. Note that $\chi(j)$ is the ratio of actual distance to the diffusion length $(Dt_k)^{1/2}$ for the characteristic time t_k.

Recalling the step simulation considered above, we see that the most efficient way to use the calculation is to report the concentration profiles as functions of f_A and f_B vs. χ for various values of t/t_k. These curves would then fully characterize every possible electrochemical experiment satisfying the initial conditions and the boundary conditions. Given specific values of C_A^*, t_k, and D, it is a simple matter to convert the curves into functions of C_A and C_B vs. x for various values of t.

B.1.6 Current

In general, there is a flux of electroactive species across the boundary between boxes 1 and 2. For species A in iteration $k + 1$, it is

$$-J_A^{1,2}(k + 1) = DC_A^* \frac{[f_A(2, k) - f_A(1, k)]}{\Delta x} \tag{B.1.16}$$

In the absence of other processes, this flux will effect a concentration change in box 1. However, there is in every experiment a boundary condition that dictates the circum-

stances at the electrode surface, and it must be maintained. Consider the example we have taken above, where $f_A(1, k) = 0$ at all $k > 0$. Since the surface concentration of A is zero, a flux of A will always move toward the electrode across the boundary between boxes 1 and 2. Maintenance of the surface condition demands that the arriving molecules be eliminated, but the only way to eliminate them is to convert them electrochemically to B. For iteration $k + 1$, then, the current is defined by $J_A^{1,2}(k + 1)$. We can write it as

$$i(k + 1) = \frac{nFADC_A^* f_A(2, k)}{\Delta x} \tag{B.1.17}$$

Substituting for Δx yields

$$i(k + 1) = \frac{nFAD^{1/2}C_A^* f_A(2, k)(\mathbf{D_M}\ell)^{1/2}}{t_k^{1/2}} \tag{B.1.18}$$

We can obtain a dimensionless current, $Z(k)$, by following the standard recipe: Rearrange (B.1.18) so that experimental variables are on the left and model variables are on the right:

$$Z(k + 1) = \frac{i(k + 1)t_k^{1/2}}{nFAD^{1/2}C_A^*} = (\mathbf{D_M}\ell)^{1/2} f_A(2, k) = \left(\frac{\ell}{\mathbf{D_M}}\right)^{1/2} \mathbf{D_M} f_A(2, k) \tag{B.1.19}$$

The product of the last two quantities on the right, $\mathbf{D_M} f_A(2, k)$, is the fractional concentration that would exist in box 1 after iteration $k + 1$ if it were not eliminated by electrolysis. This definition of Z relates the actual current to the Cottrell current expected at time t_k (see Problem B.1).

The current for the first iteration[4] is calculated differently because there is no flux. Instead, the current flows because we first establish the surface condition by eliminating A from box 1 at that time. The number of moles electrolyzed in the Δt interval is $\Delta x A C_A^*$; hence the current is

$$i(1) = \frac{nFAC_A^* \Delta x}{\Delta t} = \frac{nFAC_A^* D^{1/2}\ell}{t_k^{1/2} \mathbf{D_M}^{1/2}} \tag{B.1.20}$$

Thus,

$$Z(1) = (\ell/\mathbf{D_M})^{1/2} \tag{B.1.21}$$

To what time should we assign $Z(k)$? Since our current calculation really involves dividing the integral charge passed during an iteration by the duration of the iteration, it is appropriate to assign the current to the midpoint, rather than to the end, of the iteration. Thus, we say that the dimensionless current $Z(k)$ flowed at $t/t_k = (k - 0.5)/\ell$.

B.1.7 Thickness of the Diffusion Layer

In doing these calculations, one needs to know how many boxes are needed in the simulation. A rule of thumb provides a safe answer: Any experiment that has proceeded for time t will alter the solution from its bulk character for a distance no larger than about $6(Dt)^{1/2}$. Thus,

$$j_{max} \approx \frac{6(Dt)^{1/2}}{\Delta x} + 1 \tag{B.1.22}$$

---

[4]Because the early computations in a finite difference approach are inaccurate, a computation of the current for the first iteration is usually not of importance. Recall that in the Cottrell experiment, $i \to \infty$ as $t \to 0$.

and

$$j_{\max} \approx 6(\mathbf{D}_M k)^{1/2} + 1 \tag{B.1.23}$$

Since $\mathbf{D}_M \leq 0.5$, one never needs to make calculations for more than $4.2k^{1/2}$ boxes during iteration k.

B.1.8 Diffusion Coefficients

Note that the parameter $\mathbf{D}_M$ exists in diffusion expressions for each species. Each $\mathbf{D}_M$ contains the diffusion coefficient for the pertinent species, but since Δx and Δt are constants and since $D_A \neq D_B \neq D_C \ldots$, the $\mathbf{D}_M$'s cannot all be equal. We should write them as $\mathbf{D}_{M,A}$, $\mathbf{D}_{M,B}$, $\ldots$ This obviously complicates the model, therefore, one frequently makes the assumption that all diffusion coefficients are equal. Then a single value of $\mathbf{D}_M$ suffices.

When this procedure is not satisfactory, one must take explicit account of the differences in D values by using different $\mathbf{D}_M$ values for each species. We have already seen that one of these parameters is equivalent to a model variable, and hence it can be chosen at will. The others then are determined by the fact that

$$\mathbf{D}_{M,i}/\mathbf{D}_{M,A} = D_i/D_A \tag{B.1.24}$$

This procedure ensures that the model will behave diffusively as the real system does.[5]

▶ B.2 AN EXAMPLE

Figure B.2.1 is a FORTRAN listing of an actual simulation. The treated problem is the Cottrell experiment, which was solved analytically in Section 5.2.1. An electroreactant A is uniformly distributed initially, but a potential step is applied at $t = 0$ to force the surface concentration of A to zero by converting it faradaically to species B.

The program starts by setting up arrays to represent the fractional concentrations of A and B in each box. There are "old" and "new" arrays for each species that are related by rules discussed later. In addition, an array for the current-time curve is declared, and the model variables ℓ, $\mathbf{D}_{M,A}$, and $\mathbf{D}_{M,B}$ are fixed. Since ℓ is only 100, this simulation has relatively low resolution. At most, 42 boxes will represent the diffusion layer. The concentration arrays are initialized to reflect the uniform starting concentration of A and the absence of B.

Upon beginning the first iteration, the new concentration arrays are calculated from the old according to the laws of diffusion. The boundary conditions require that species A be zero in the first box; hence FANEW(1) is then reset to zero and FBNEW(1) is incremented by an equal amount to reflect the faradaic conversion. The current $Z(k)$ is calculated from the amount of A converted. These operations conclude the chemical activity for the iteration.

If $k \neq 50$, the new arrays are reassigned to the old ones in preparation for the next iteration, then k is incremented and the chemical processes are applied again. When $k = 50$ the concentration profiles are typed out. The distance parameter, $\chi(j)$, is calculated and printed, along with the fractional concentrations in each box.

When $k = \ell$, the program exits the iteration loop and prints the current-time curve. The parameter T is the value of t/t_k associated with a given $Z(k)$, and ZCOTT is the di-

---

[5]The model also assumes that diffusion coefficients are not functions of x. Although the simulations could be altered to accommodate spatial variations in diffusion coefficients, they are rarely important.

```
C       SET UP ARRAYS AND MODEL VARIABLES

        DIMENSION FAOLD(100),FBOLD(100),FANEW(100),FBNEW(100),Z(100)
        L=100
        DMA=0.45
        DMB=DMA

C       INITIAL CONDITIONS

        TYPE "START"
        DO 10 J=1,100
        FAOLD(J)=1
        FANEW(J)=1
        FBOLD(J)=0
        FBNEW(J)=0
     10 CONTINUE
        K=0

C       START OF ITERATION LOOP

   1000 K=K+1

C       DIFFUSION BEYOND THE FIRST BOX

        JMAX=4.2*SQRT(FLOAT(K))
        DO 20 J=2,JMAX
        FANEW(J)=FAOLD(J)+DMA*(FAOLD(J-1)-2*FAOLD(J)+FAOLD(J+1))
        FBNEW(J)=FBOLD(J)+DMA*(FBOLD(J-1)-2*FBOLD(J)+FBOLD(J+1))
     20 CONTINUE

C       DIFFUSION INTO THE FIRST BOX

        FANEW(1)=FAOLD(1)+DMA*(FAOLD(2)-FAOLD(1))
        FBNEW(1)=FBOLD(1)+DMB*(FBOLD(2)-FBOLD(1))

C       FARADAIC CONVERSION AND CURRENT FLOW

        Z(K)=SQRT(L/DMA)*FANEW(1)
        FBNEW(1)=FBNEW(1)+FANEW(1)
        FANEW(1)=0

C       TYPE OUT CONCENTRATION ARRAYS FOR K=50

        IF(K.NE.50) GO TO 100
        TYPE
        TYPE
        DO 30 J=1,JMAX
        X=(J-1)/SQRT(DMA*L)
        TYPE X,FANEW(J),FBNEW(J)
     30 CONTINUE
        TYPE
        TYPE

C       SET UP OLD ARRAYS FOR NEXT ITERATION

    100 DO 40 J=1,JMAX
        FAOLD(J)=FANEW(J)
        FBOLD(J)=FBNEW(J)
     40 CONTINUE

C       RETURN FOR NEXT ITERATION IF K<L

        IF(K.LT.L) GO TO 1000

C       TYPE OUT CURRENT--TIME CURVE

        TYPE
        TYPE
        DO 50 K=1,L
        T=(K-0.5)/L
        ZCOTT=1/SQRT(3.141592*T)
        R=Z(K)/ZCOTT
        TYPE T,Z(K),ZCOTT,R
     50 CONTINUE
        END
```

Figure B.2.1 A simulation program for the Cottrell experiment.

mensionless current calculated from the Cottrell equation, (5.2.11). It is an exact solution to this problem, and is easily shown by rearrangement of (5.2.11) to be

$$Z_{Cott} = \left[\pi^{1/2} \left(\frac{t}{t_k} \right)^{1/2} \right]^{-1} \tag{B.2.1}$$

The ratio $R = Z/Z_{Cott}$ is an index of the simulation's quality. Figure B.2.2 is a display of this ratio as a function of time through the simulation. The numbers by the points are the corresponding values of k. Ideally, R is exactly unity always. Figure B.2.2 shows that large errors occur in the first few iterations, as one must expect from the coarse nature of the model at that stage. However, by the tenth iteration, the error is only a few percent, and it falls steadily. For $t/t_k = 0.1995$, there is an error of only 0.2%. Better results would have been obtained with a larger value for ℓ.

Figure B.2.3 displays the concentration profiles for $t/t_k = 0.5$. The points are from the simulation, and the curves are the analytical results from equation 5.2.13 and its complement. The agreement is clearly quite good.

Note that the sum of fractional concentrations for A and B is unity in each box. This rule always holds when $\mathbf{D}_{M,A} = \mathbf{D}_{M,B}$ (see equation 5.4.28); and it is useful for diagnosing programming errors leading to losses or gains of material. One of the problems with simulations is that errors are difficult to detect, so it is important to use every possible safeguard.
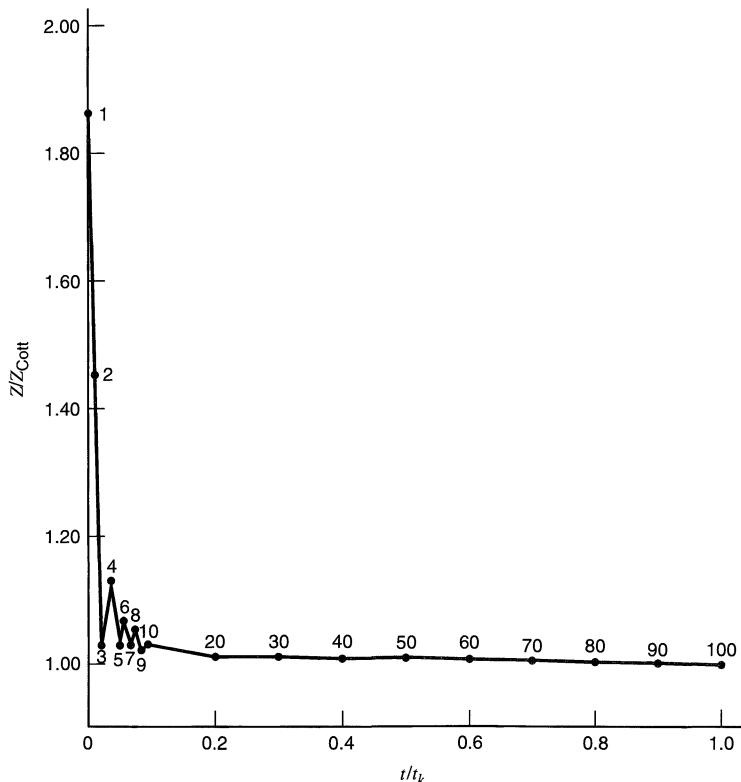
Figure B.2.2 Results of the simulation in Figure B.2.1 for $\ell = 100$ and $\mathbf{D}_M = 0.45$. Simulated current parameter, Z, divided by analytical solution. Numbers by points are iteration numbers.
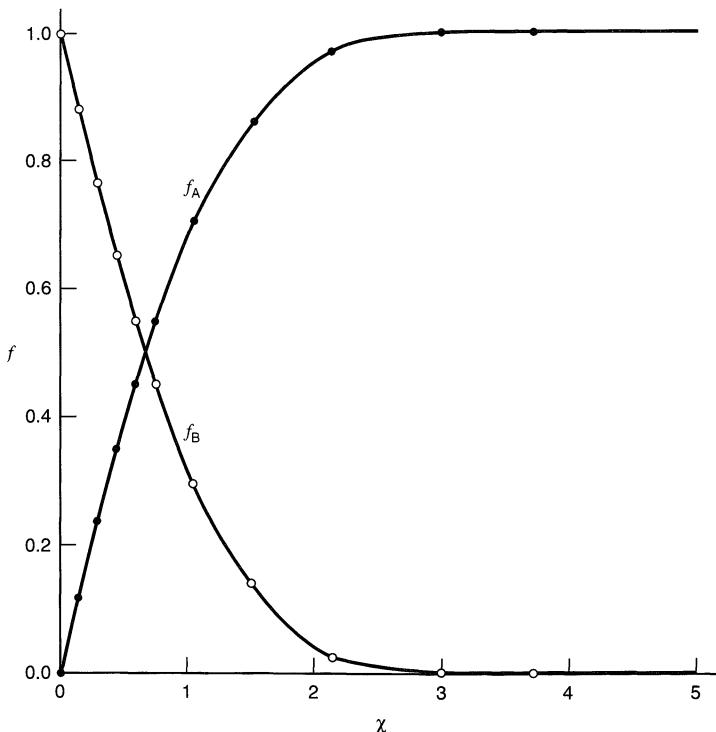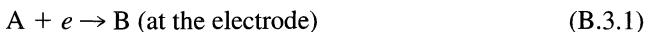
Figure B.2.3 Concentration profiles from the simulation program in Figure B.2.1 for $\ell = 100$, $D_M = 0.45$, and $t/t_k = 0.5$. Points are simulated; curves are analytical.

▷ B.3 INCORPORATING HOMOGENEOUS KINETICS

If the only homogeneous dynamics of concern were the diffusion processes, simulation would find much less use than it does. Its utility is especially appreciated when the electrochemical process is coupled to one or more homogeneous chemical reactions. Then, the differential equations describing the system can easily become too difficult for an analytical solution.

B.3.1 Unimolecular Reactions

Consider the system in which an electrode reaction is followed by a unimolecular conversion:

$$A + e \rightarrow B \text{ (at the electrode)} \tag{B.3.1}$$

$$B \xrightarrow{k_1} C \text{ (in solution)} \tag{B.3.2}$$

The differential equations describing B and C must account for both diffusion and reaction (see Chapter 12). For example,

$$\frac{\partial C_B(x, t)}{\partial t} = D_B \frac{\partial^2 C_B(x, t)}{\partial x^2} - k_1 C_B(x, t) \tag{B.3.3}$$

The first term on the right is Fick's second law, and we have seen that its finite difference representation is given by (B.1.6). Thus, we can immediately write the finite difference analog to (B.3.3) as
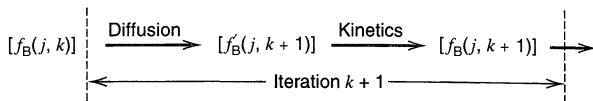
$$C_B(x, t + \Delta t) = C_B(x, t) + D_{M,B}[C_B(x + \Delta x, t) - 2C_B(x, t)$$
$$+ C_B(x - \Delta x, t)] - k_1 \Delta t \cdot C_B(x, t) \tag{B.3.4}$$

Dividing by C_A^* and introducing the notation of the simulation, we obtain

$$f_B(j, k + 1) = f_B(j, k) + \mathbf{D}_{M,B}[f_B(j + 1, k) - 2f_B(j, k) + f_B(j - 1, k)] - \frac{k_1 t_k}{\ell} f_B(j, k)$$

(B.3.5)

Equation B.3.5 allows a one-step accounting of diffusion and kinetic effects for the B array during iteration $k + 1$.

In practice, the simultaneous calculation of diffusion and kinetic manifestations is not usually made. Instead, one ordinarily calculates the effects of diffusion first, without considering the reaction. Then one allows the reaction to modify the concentration arrays that were created just beforehand by the diffusion equations. We could diagram the operation as follows:

$$[f_B(j, k)] \xrightarrow{\text{Diffusion}} [f_B'(j, k+1)] \xrightarrow{\text{Kinetics}} [f_B(j, k+1)] \longrightarrow$$
$$\longleftarrow \text{Iteration } k+1 \longrightarrow$$

Thus,

$$f_B'(j, k + 1) = f_B(j, k) + \mathbf{D}_{M,B}[f_B(j + 1, k) - 2f_B(j, k) + f_B(j - 1, k)] \quad \text{(B.3.6)}$$

and

$$\boxed{f_B(j, k + 1) = f_B'(j, k + 1) - \frac{k_1 t_k}{\ell} f_B(j, k)} \qquad \text{(B.3.7)}$$
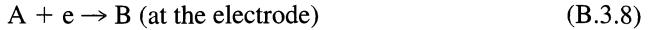
Of course, it makes no difference in the final results whether the calculation is carried out in a single equation, (B.3.5), or in two steps, (B.3.6) and (B.3.7). There are, however, two practical advantages to the stepwise calculation:

1. Since kinetic effects appear separately from diffusion in the computer program, it is easier to make programming changes to account for different mechanistic details.

2. Equation B.3.5 can easily produce negative values of $f_B(j, k + 1)$ if kinetic effects are very important. Sometimes it is difficult to predict this behavior, and it is hard to apportion the available mass when it does happen. Mass allocation is more straightforward in the sequential approach, because the total destruction of a reactant can happen only in a kinetic step.

Equation B.3.7 shows that the dimensionless kinetic parameter is $k_1 t_k$. Since it must be given a numeric value for any particular simulation, the results of that simulation are valid for all those experiments, but only those experiments, for which the product of t_k and k_1 is equal to the predetermined value. Following the argument of Section B.1.3, we see that this dimensionless parameter is the ratio of the characteristic time t_k to the lifetime of B, which is $1/k_1$. In general, the effects of the unimolecular decay of B will hardly be felt in the experiment if $k_1 t_k$ is much less than unity, and they will be completely manifested for $k_1 t_k$ much greater than unity. The finite difference method is based on an approximation of true derivatives, and hence one can expect (B.3.7) to supply an accurate accounting of the kinetic effect only when $k_1 t_k / \ell$ is not too large. Otherwise, the extent of decay per unit of time resolution is excessive. The upper limit of the most useful modeling range is therefore $k_1 t_k \approx \ell/10$. The lower limit is reached when the kinetic perturbation no longer registers an experimentally significant impact.

B.3.2 Bimolecular Reactions

Now consider a bimolecular complication to an electrode process:

$$A + e \rightarrow B \text{ (at the electrode)} \tag{B.3.8}$$

$$B + B \xrightarrow{k_2} C \text{ (in solution)} \tag{B.3.9}$$

For B, we have

$$\frac{\partial C_B(x, t)}{\partial t} = D_B \frac{\partial^2 C_B(x, t)}{\partial x^2} - k_2 C_B(x, t)^2 \tag{B.3.10}$$

Transforming this to the notation of the simulation exactly as above, we obtain the analogue to (B.3.5):

$$f_B(j, k + 1) = f_B(j, k) + D_{M,B}[f_B(j + 1, k) - 2f_B(j, k) + f_B(j - 1, k)] - \frac{k_2 t_k C_A^*}{\ell}[f_B(j, k)]^2 \tag{B.3.11}$$

Again, it is useful to handle diffusion and homogeneous reaction sequentially, so we split (B.3.11) into two parts. The diffusion effects are registered by (B.3.6) and the changes in concentration due to reaction are given by

$$\boxed{f_B(j, k + 1) = f'_B(j, k + 1) - \frac{k_2 t_k C_A^*}{\ell}[f_B(j, k)]^2} \tag{B.3.12}$$

The dimensionless parameter pertaining to the second-order process is $k_2 t_k C_A^*$. Its value must be fixed for a given simulation, and several successive simulations must be carried out to show the effects of variations in $k_2 t_k C_A^*$. For reasons equivalent to those outlined above, the most useful modeling range for $k_2 t_k C_A^*$ is the interval below $\ell/10$.

▶ B.4 BOUNDARY CONDITIONS FOR VARIOUS TECHNIQUES

So far, we have considered only a step to a potential where the electroreactant is brought to the electrode at the mass-transfer-limited rate. We use a particularly simple boundary condition in that case: $C_A(0, t) = f_A(1, k) = 0$. In the example of Figure B.2.1, this boundary condition is enforced in the section headed "Faradaic Conversion and Current Flow." Other situations demand other conditions, and we outline some of them here.

B.4.1 Potential Steps in a Nernstian System

Suppose the electrode reaction

$$A + ne \rightleftharpoons B \tag{B.4.1}$$

is nernstian, so that the equation:

$$E = E^{0'} + \frac{RT}{nF} \ln \frac{C_A(0, t)}{C_B(0, t)} \tag{B.4.2}$$

always applies. In terms of fractional concentrations,

$$E = E^{0'} + \frac{RT}{nF} \ln \frac{f_A(1, k)}{f_B(1, k)} \tag{B.4.3}$$

which can be rearranged to give a dimensionless potential parameter:

$$\mathbf{E}_{norm} = \frac{(E - E^{0'})nF}{RT} = \ln \frac{f_A(1, k)}{f_B(1, k)} \tag{B.4.4}$$

or

$$\boxed{\frac{f_A(1, k)}{f_B(1, k)} = \exp(\mathbf{E}_{norm})} \tag{B.4.5}$$

To simulate, for example, an experiment in which the initial system is a uniform solution of A and a step is made to potential E, one would set up the initial conditions just as we have done before; then the ratio of $f_A(1, k)$ and $f_B(1, k)$ would be maintained at the value dictated through (B.4.5) by a value of $\mathbf{E}_{norm}$ corresponding to the step potential E. This value of $\mathbf{E}_{norm}$ is therefore a model variable, and a separate simulation would have to be carried out for each desired value of E. Note that the normalized potential $\mathbf{E}_{norm}$ is simply the value of the potential E expressed as the energy difference between nFE and $nFE^{0'}$ in units of $\mathcal{K}T$.

Maintaining condition (B.4.5) usually will cause a diffusive flux across the boundary between boxes 1 and 2. This flux alters the ratio $f_A(1)/f_B(1)$ after the diffusive step in the simulation; therefore, the ratio must be reestablished by converting species A into B or vice versa. The amount converted gives rise to a current that is calculated as the dimensionless parameter $Z(k)$ by the methods discussed in Section B.1.6.

B.4.2 Accounting for Heterogeneous Kinetics

For an electrode reaction:

$$A + e \underset{k_b}{\overset{k_f}{\rightleftharpoons}} B \tag{B.4.6}$$

where

$$k_f = k^0 e^{-\alpha f(E - E^{0'})} \tag{B.4.7}$$
$$k_b = k^0 e^{(1-\alpha)f(E - E^{0'})} \tag{B.4.8}$$

the current is always given by

$$\frac{i}{nFA} = k_f C_A(0, t) - k_b C_B(0, t) \tag{B.4.9}$$

In terms of simulation variables, we obtain

$$\frac{it_k^{1/2}}{nFAD_A^{1/2}C_A^*} = Z(k + 1) = \left(\frac{k_f t_k^{1/2}}{D_A^{1/2}}\right)f_A(1, k) - \left(\frac{k_b t_k^{1/2}}{D_A^{1/2}}\right)f_B(1, k) \tag{B.4.10}$$

where the clusters $(k_f t_k^{1/2}/D_A^{1/2})$ and $(k_b t_k^{1/2}/D_A^{1/2})$ are dimensionless rate constants. The dimensionless current can be calculated for any iteration from (B.4.10) if those parameters are specified.

To see how to make the specification, let us recast (B.4.7)and (B.4.8)into the appropriate forms:

$$\frac{k_f t_k^{1/2}}{D_A^{1/2}} = \left(\frac{k^0 t_k^{1/2}}{D_A^{1/2}}\right) \exp(-\alpha \mathbf{E}_{norm}) \tag{B.4.11}$$

$$\frac{k_b t_k^{1/2}}{D_A^{1/2}} = \left(\frac{k^0 t_k^{1/2}}{D_A^{1/2}}\right) \exp[(1 - \alpha)\mathbf{E}_{norm}] \tag{B.4.12}$$

where $\mathbf{E}_{norm} = F(E - E^{0'})/RT$. Now we see that both rate constants can be calculated from $\mathbf{E}_{norm}$ when two dimensionless model variables are supplied, *viz.* the *transfer coefficient*, α, which is dimensionless in itself, and a *dimensionless standard rate constant*, $k^0 t_k^{1/2}/D_A^{1/2}$. The normalized potential $\mathbf{E}_{norm}$ is used as in Section B.4.1 for potential step experiments.

In a simulation, the fractional concentrations in box 1 are obtained by considering diffusion into or out of box 2 as well as the change in box 1 caused by passage of current.

$$f_A(1, k + 1) = f_A(1, k) + \mathbf{D}_{M,A}[f_A(2, k) - f_A(1, k)] - Z(k)\left(\frac{\mathbf{D}_{M,A}}{\ell}\right)^{1/2} \qquad (\text{B.4.13})$$

$$f_B(1, k + 1) = f_B(1, k) + \mathbf{D}_{M,B}[f_B(2, k) - f_B(1, k)] + Z(k)\left(\frac{\mathbf{D}_{M,A}}{\ell}\right)^{1/2} \qquad (\text{B.4.14})$$

For iteration $k + 1$, the current parameter $Z(k + 1)$ is first calculated from (B.4.10), which implies that an amount of species A equivalent to $(k_f t_k^{1/2}/D_A^{1/2})f_A(1)$ is converted to B, while a quantity of species B equivalent to $(k_b t_k^{1/2}/D_A^{1/2})f_B(1)$ is converted to A. Then the fractional concentrations in box 1 for iteration $k + 1$ can be calculated from (B.4.13) and (B.4.14).

B.4.3 Potential Sweeps

If we want to apply the program

$$E = E_i + vt \qquad (\text{B.4.15})$$

to the system expressed in (B.4.6), then we have

$$\mathbf{E}_{norm} = \frac{F(E_i - E^{0'})}{RT} + \frac{Fvt}{RT} \qquad (\text{B.4.16})$$

The first term is a normalized initial potential $\mathbf{E}_{i,norm}$, which would have to be specified as a model variable to the simulation. The second term describes the effects of the sweep, and its value will change as the simulation evolves; that is, the second term is a function of the iteration number k. The specific function is obtained by substitution from (B.1.11):

$$\mathbf{E}_{norm} = \mathbf{E}_{i,norm} + \frac{Fvt_k}{RT} \cdot \frac{k}{\ell} \qquad (\text{B.4.17})$$

We have yet to define the known time t_k corresponding to ℓ iterations. Several choices could be made, but probably the most convenient one is to let t_k be the time required to scan from E_i to the final potential, E_f. Then $t_k = (E_i - E_f)/v$, and

$$\boxed{\mathbf{E}_{norm} = \mathbf{E}_{i,norm} + \frac{(E_i - E_f)}{(RT/F)} \cdot \frac{k}{\ell} = \mathbf{E}_{i,norm} + (\mathbf{E}_{i,norm} - \mathbf{E}_{f,norm})\frac{k}{\ell}} \qquad (\text{B.4.18})$$

At the end of each iteration, the value of $\mathbf{E}_{norm}$ is calculated from (B.4.18) and then used in (B.4.11) and (B.4.12) to find the dimensionless rate constants for determination of $Z(k + 1)$ in (B.4.10). Calculation of concentrations for the first box then proceeds from (B.4.13) and (B.4.14), as in the potential step experiment.

Sweep experiments are often simulated to study the effects of coupled homogeneous kinetics, which are added into the model as described in Section B.3.

B.4.4 Controlled Current

For the electrode reaction (B.4.1), the application of controlled current is equivalent to exercising control over the gradient in the concentration of A at the electrode surface, since

$$\frac{i}{nFA} = -J_A(0, t) = D_A\left(\frac{\partial C_A(x, t)}{\partial x}\right)_{x=0} \tag{B.4.19}$$

To convert this expression to the finite difference notation relevant to the simulation, we make the assumption that the concentration profile is linear from the center of box 1 (the electrode surface) to the center of box 2. Then,

$$\frac{i}{nFA} = D_A C_A^* \frac{[f_A(2, k) - f_A(1, k)]}{\Delta x} \tag{B.4.20}$$

Controlling the current in a real experiment is therefore equivalent to controlling the difference in fractional concentrations between boxes 1 and 2 in the model.

Now we rearrange (B.4.20) to obtain the usual current parameter:

$$Z = \frac{it_k^{1/2}}{nFAD_A^{1/2}C_A^*} = \frac{D_A^{1/2}t_k^{1/2}}{\Delta x}[f_A(2, k) - f_A(1, k)] \tag{B.4.21}$$

Substituting from (B.1.13) gives

$$Z = (\mathbf{D}_{M,A}\ell)^{1/2}[f_A(2, k) - f_A(1, k)] \tag{B.4.22}$$

If the current has a constant magnitude, it is most convenient in this treatment to define the known time, t_k, as the transition time given by the Sand equation (8.2.14) for species A. Thus, $\ell^{1/2}$ iterations correspond to

$$\tau^{1/2} = t_k^{1/2} = \frac{nFAD_A^{1/2}C_A^*\pi^{1/2}}{2i} \tag{B.4.23}$$

and the current parameter is

$$Z = \frac{\pi^{1/2}}{2} = (\mathbf{D}_{M,A}\ell)^{1/2}[f_A(2, k) - f_A(1, k)] \tag{B.4.24}$$

In carrying out an actual simulation, one must hold the difference in fractional concentration between the first two boxes at a constant value. With $t_k = \tau$, the required difference is given from (B.4.24) as

$$\boxed{f_A(2, k) - f_A(1, k) = \frac{\pi^{1/2}}{2(\mathbf{D}_{M,A}\ell)^{1/2}}} \tag{B.4.25}$$

In each iteration, one allows diffusion to occur; then the value of $f_A(1)$ is adjusted downward so that (B.4.25) is maintained. Since this adjustment corresponds to a faradaic conversion, $f_B(1)$ must be adjusted upward by an equal amount. These steps give the final values, $f_A(1, k)$ and $f_B(1, k)$, for iteration k.

If the system is the uncomplicated case of (B.4.1), the transition time, which is found when $f_A(1, k) = 0$, will be reached ideally in the ℓth iteration. Deviations from this result will occur when complications, such as homogeneous kinetics, are introduced into the electrode process.

The potential-time curve for a reversible system can be obtained by reporting the value of $\mathbf{E}_{norm}$ calculated with equation B.4.4 at each iteration. Equivalent data for a qua-

sireversible system would require the specification of heterogeneous rate parameters in a fashion like that outlined in Section B.4.2.

▸ B.5 SIMULATIONS IN CONVECTIVE SYSTEMS

Convective effects, such as those that occur with the rotating disk and rotating ring-disk electrodes (RDE and RRDE) can also be simulated (4, 5, 9). In this case, the flow of solution is taken into account by movement of the contents of the boxes from one location in solution to another. For example, near the surface of the RDE, the solution flow normal to the disk is given by (9.3.9); that is,

$$-\frac{dy}{dt} = -v_y = 0.51\ \omega^{3/2}\nu^{-1/2}y^2 \tag{B.5.1}$$

The solution of this equation for movement of a solution element from y_1 to y_2 during the time increment Δt is

$$\frac{1}{y_2} - \frac{1}{y_1} = 0.51\ \omega^{3/2}\nu^{-1/2}\ \Delta t \tag{B.5.2}$$

If the distances y_2 and y_1 are measured from the electrode surface, and if we now let Δy play the role earlier held by Δx, then as in (B.1.14),

$$y_1 = (j-1)\Delta y = (j-1)\left(\frac{Dt_k}{D_M\ell}\right)^{1/2} \tag{B.5.3}$$

The position y_2, where this solution element will reside at the end of the time increment is $(j'-1)\Delta y$, with j' representing the position in terms of box number. It can be obtained from the equation

$$\left[\frac{1}{(j'-1)\Delta y}\right] - \left[\frac{1}{(j-1)\Delta y}\right] = 0.51\ \omega^{3/2}\nu^{-1/2}\ \Delta t \tag{B.5.4}$$

or

$$\boxed{j - 1 = \frac{(j'-1)}{1 - (j'-1)V_N}} \tag{B.5.5}$$

where V_N is a dimensionless constant,

$$V_N = 0.51\omega^{3/2}\nu^{-1/2}\Delta y\Delta t = D_M^{-1/2}\ell^{-3/2} \tag{B.5.6}$$

In this expression, Δy is $(Dt_k/D_M\ell)^{1/2}$ and

$$\Delta t = \frac{t_k}{\ell} = \frac{(0.51)^{-2/3}\omega^{-1}\nu^{1/3}D^{-1/3}}{\ell} \tag{B.5.7}$$

where t_k is defined in terms of convenient time parameters for the RDE.

Thus the contents (i.e., concentrations, C_A, C_B, ...) of each box at the end of a time period are replaced by those at locations calculated with (B.5.5); this procedure results in a new array representing the effect of convection normal to the electrode. In practice, better accuracy is obtained at smaller ℓ if (B.5.5) is modified slightly (9):

$$\boxed{j - 1 = \frac{(j'-1)}{1 - [1.11(j'-1)V_N]}} \tag{B.5.8}$$

Diffusion normal to the electrode is also taken into account by the procedures described in Section B.1.2.

For the RRDE, convection in the radial (r) direction is treated in a similar manner. In this case, volume elements or boxes are also constructed in the radial direction, measured from the center of the electrode and indexed by r_i, so that

$$r = r_i \Delta r \tag{B.5.9}$$

where Δr is defined in terms of the dimensions of the electrodes. In this case, each solution element is indexed by two simulation distance parameters, j and r_i. The application of the equation for solution velocity in the radial direction, (9.3.10), ultimately yields (9)

$$\boxed{r_i = r'_i \exp[-1.03(j')\mathbf{V_N}]} \tag{B.5.10}$$

where r_i is the radial position of a volume element that will be in position r', j' at the end of Δt. Radial diffusion is taken into account in the usual manner. Results of such two-dimensional simulations were described in Section 9.5.

Again, an especially valuable aspect to these simulations is the straightforward incorporation of kinetic effects, as described in Section B.3. This allows rather complicated problems, such as those involving dimerizations of the disk-generated species, to be solved for the RDE and RRDE (see Section 12.4) (10–12). Similar simulations have been carried out for the rotating double-ring system (13–15). The simulation approach discussed here involves the assumption that the solution flow profiles follow the analytical solutions. Simulation of the solution flow itself, for example, to a rotating disk, is also possible (16). This technique might be especially valuable in electrochemical systems involving more complicated solution flow situations. Simulation of the hydrodynamics occurring at the expanding spherical surface of the DME has also been described (17).

B.6 MISCELLANEOUS DIGITAL SIMULATIONS

B.6.1 Electrical Migration and Diffuse Double-Layer Effects

The flux of a species A arising from an electric field $\mathscr{E} = \partial\phi/\partial x$ is [see (4 .1.11)]

$$J_A(x, t) = -\left(\frac{F}{RT}\right)z_A D_A C_A(x, t)\mathscr{E}(x) \tag{B.6.1}$$

Transfer of a species from box to box is treated in a manner similar to that used for diffusion, except that the change in concentration in this case depends on the field. The calculation of the field distribution is based on the usual electrostatic considerations (18), using, for example, the Poisson equation, (13.3.5):

$$\frac{d^2\phi}{dx^2} = \frac{d\mathscr{E}(x)}{dx} = \frac{-\rho(x)}{\varepsilon\varepsilon_0} \tag{B.6.2}$$

By such a procedure, Feldberg (19) treated the relaxation of the diffuse double layer following a coulostatic injection of charge. When a charge density σ^M is injected into the electrode, assumed to be initially at E_z, the field at any time is given by the Gauss law:

$$\mathscr{E}(x) = \left(\frac{-1}{\varepsilon\varepsilon_0}\right)\left[\sigma^M + F\int_0^x \sum_{i=1}^n z_i C_i(x)\, dx\right] \tag{B.6.3}$$

where i indexes the different species. At the instant of charge injection, before any ionic movement occurs, electroneutrality exists at all points in the solution, so that

$$\sum_{i=1}^{n} z_i C_i(x) = 0 \qquad \text{(for all } x) \tag{B.6.4}$$

and the field is constant, given by

$$\mathscr{E}(x) = \frac{-\sigma^M}{\varepsilon\varepsilon_0} \qquad \text{(for all } x) \tag{B.6.5}$$

This initial field induces a flux of ions that can be calculated by use of the finite difference form of (B.6.1), as well as the diffusional flux, calculated in the usual manner. At any time, the potential $\phi(x)$ can be calculated by integration of the field; thus ϕ_2 is given by

$$\phi_2 - \phi_\infty = \int_\infty^{x_2} \mathscr{E}(x)\, dx \tag{B.6.6}$$

Eventually the system relaxes to the distribution and ϕ_2 value obtained by the GCS approach (Section 13.3). A similar simulation approach was taken to calculate the charge and potential distributions in the space-charge region that forms inside the electrode at a semiconductor electrode/electrolyte interface (20) (See Section 18.2). Migrational effects in voltammetry can be taken into account in a similar way by using the full Nernst–Planck equation to treat mass transfer (21).

B.6.2 Thin-Layer Cells and Resistive Effects

In the treatment of thin-layer cells (see Section 11.7), two additional effects must be considered. First, the distance between the electrode and the cell wall is small, so the total number of simulation boxes taken, n_L, must represent the cell thickness. Moreover, the counter electrode is usually placed outside the thin-layer portion and an appreciable resistive drop occurs between each segment of the working electrode and the counter electrode. This effect is taken into account by dividing the working electrode into n_M segments, each at a different potential with respect to the reference electrode, and each with a different current density. An iterative procedure is used to determine the potential and current distribution at any given time in the manner of other two-dimensional simulations described below (22). The resistive effects in thin-layer cells can be significant in determining the electrochemical response and are important in the interpretation of behavior in thin-layer (e.g. electrochemical-ESR) cells and at thin-film electrodes (23).

B.6.3 Two-Dimensional Simulations

The simulation methodology discussed so far has concerned one-dimensional mass transfer, that is, linear diffusion. One can extend this same approach to problems where two-dimensional (2D) effects are important, such as in consideration of microelectrode arrays (24) and scanning electrochemical microscopy (25). A 2D space grid is used and different boundary conditions apply to different parts of the surface, such as the generator and collector electrodes and insulating portions. Difficulties in treating the complex geometry in 2D problems can be addressed by using *conformal mapping,* in which one defines new space coordinates, related by algebraic transformations to the original rectilinear or spherical coordinates (26, 27). The large increase in the number of boxes that must be considered, with an attendant increase in computation time, usually necessitates the use of more efficient methods, such as those discussed in the next section.

B.6.4 Advanced Simulation Methods

The explicit finite difference simulation methods described here are quite straightforward and have been employed for a variety of electrochemical problems. Nevertheless, there are cases when the computation times required for accurate solutions become excessive, and more efficient numerical methods are appropriate. This is generally the case when very rapid coupled homogeneous reactions occur. As discussed in Section B.3, when k_1 is large, the reaction layer thickness $(D/k_1)^{1/2}$ may be small compared to the box thickness Δx. The requirement for accurate simulation can be given as $(D/k_1)^{1/2} \gg \Delta x$ or, from (B.1.13), $(1/k_1) \gg (t_k/\ell)$. In other words, the box size must be sufficiently small that the simulation treats the reaction layer near the electrode surface with good accuracy, and if the reaction is rapid, this layer is very thin.

Several approaches have been suggested for the more demanding problems, and they are described in detailed reviews (1, 7, 8). One can abandon the model of boxes with equal widths and use space elements of variable dimensions (8, 28, 29). An *exponentially expanding grid* is frequently used, where the width of a box, $\Delta x(j)$ depends on j:

$$\Delta x(j) = \Delta x \exp[\beta(j - 1)] \tag{B.6.7}$$

Frequently, β is taken as 0.5. When $\beta \to 0$, a uniform grid results. The effect of the expanding grid can be taken into account by writing (B.1.7) as (29)

$$f(j, k + 1) = f(j, k) + \mathbf{D}_{j,M}''[f(j + 1, k) - f(j, k)] - \mathbf{D}_{j,M}'[f(j, k) - f(j - 1, k)] \tag{B.6.8}$$

where

$$\mathbf{D}_{j,M}'' = \mathbf{D}_M \exp[2\beta(3/4 - j)] \tag{B.6.9}$$
$$\mathbf{D}_{j,M}' = \mathbf{D}_M \exp[2\beta(5/4 - j)] \tag{B.6.10}$$

and $\mathbf{D}_M$ is the dimensionless model diffusion coefficient defined earlier. Thus, thin boxes are used near the electrode, where the fast reactions are occurring, and the elements become wider farther out into the solution. Expanding grids are also very useful in 2D problems.

Another approach involves using *implicit methods* (28, 30, 31) for obtaining $f(j, k + 1)$ [e.g., the *Crank–Nicolson* (32), the *fully implicit finite difference* (FIFD) (33), and the *alternating-direction implicit* (ADI) (34) methods] rather than the explicit solution in (B.1.9). In implicit methods, the equations for calculation of new concentrations depend upon knowledge of the new (rather than the old) concentrations. There are a number of examples of the use of such implicit methods in electrochemical problems, such as in cyclic voltammetry (35) and SECM (36).

More advanced numerical procedures, such as the *orthogonal collocation* technique, which has been applied to heat transfer problems and involves solutions of simultaneous differential equations, have also been used (37, 38). These methods can result in appreciable savings of computer time, but require more mathematical sophistication and more difficult computer programming. Their use will probably only be justified when the computation times required for the accurate solution of an electrochemical problem by the simpler methods become unacceptable. The growing use of spreadsheet programs and mathematical applications for personal computers, such as PDEase (Macsyma, Inc., Arlington, MA), will also probably impact computations in electrochemistry. There is also an increasing number of simulation programs tailored specifically for electrochemical problems (e.g., DigiSim, CVSIM, ELSIM, EASI)(1).

▶ B.7 REFERENCES

1. B. Speiser, *Electroanal. Chem.*, **19**, 1 (1996).

2. S. W. Feldberg, *Electroanal. Chem.*, **3**, 199 (1969).

3. S. W. Feldberg in "Computers in Chemistry and Instrumentation," Vol. 2, "Electrochemistry," J. S. Mattson, H. B. Mark, Jr., and H. C. Mac-Donald, Jr., Eds., Marcel Dekker, New York, 1972, Chap. 7.

4. K. B. Prater, *ibid.*, Chap. 8.

5. J. T. Maloy, *ibid.*, Chap. 9.

6. J. T. Maloy in "Laboratory Techniques in Electroanalytical Chemistry," P. T. Kissinger and W. R. Heineman, Eds., 2nd ed., Marcel Dekker, New York, 1996, Chap. 20.

7. M. Rudolph in "Physical Electrochemistry," I. Rubinstein, Ed., Marcel Dekker, New York, 1995, Chap. 3.

8. D. Britz, "Digital Simulation in Electrochemistry," Springer-Verlag, Berlin, 1988.

9. K. B. Prater and A. J. Bard, *J. Electrochem. Soc.*, **117**, 207 (1970).

10. K. B. Prater and A. J. Bard, *J. Electrochem. Soc.*, **117**, 335, 1517 (1970).

11. V. J. Puglisi and A. J. Bard, *J. Electrochem. Soc.*, **119**, 833 (1972).

12. L. S. R. Yeh and A. J. Bard, *J. Electrochem. Soc.*, **124**, 189 (1977).

13. J. Margarit and M. Levy, *J. Electroanal. Chem.*, **49**, 369 (1974).

14. J. Margarit, G. Dabosi, and M. Levy, *Bull. Soc. Chim. France*, **1975**, 1509.

15. J. Margarit and D. Schuhmann, *J. Electroanal. Chem.*, **80**, 273 (1977).

16. S. Clarenbach and E. W. Grabner, *Ber. Bunsenges. Phys. Chem.*, **80**, 115 (1976).

17. I. Ruzic and S. W. Feldberg, *J. Electroanal. Chem.*, **63**, 1 (1975).

18. K. J. Binns and P. J. Lawrenson, "Analysis and Computation of Electric and Magnetic Field Problems," Macmillan, New York, 1963.

19. S. W. Feldberg, *J. Phys. Chem.*, **74**, 87 (1970).

20. D. Laser and A. J. Bard, *J. Electrochem. Soc.*, **123**, 1828, 1837 (1976).

21. J. D. Norton, W. E. Benson, H. S. White, B. D. Pendley, and H. D. Abruña, *Anal. Chem.*, **63**, 1909 (1991).

22. I. B. Goldberg and A. J. Bard, *J. Electroanal. Chem.*, **38**, 313 (1972).

23. I. B. Goldberg, A. J. Bard, and S. W. Feldberg, *J. Phys. Chem.*, **76**, 2250 (1972).

24. A. J. Bard, J. A. Crayston, G. P. Kittlesen, T. V. Shea, and Mark S. Wrighton, *Anal. Chem.*, **58**, 2321 (1986).

25. J. Kwak and A. J. Bard, *Anal. Chem.*, **61**, 1221 (1989).

26. J. Newman, *J. Electrochem. Soc.*, **113**, 501 (1966).

27. A. C. Michael, R. M. Wightman, and C. Amatore, *J. Electroanal. Chem.*, **267**, 33 (1989).

28. T. Joslin and D. Pletcher, *J. Electroanal. Chem.*, **49**, 171 (1974).

29. S. W. Feldberg, *J. Electroanal. Chem.*, **127**, 1 (1981).

30. N. Winograd, *J. Electroanal. Chem.*, **43**, 1 (1973).

31. T. B. Brumleve and R. P. Buck, *J. Electroanal. Chem.*, **90**, 1 (1978).

32. G. D. Smith, "Numerical Solutions of Partial Differential Equations," Oxford University Press, Oxford, 1969.

33. P. Laasonen, *Acta Math.*, **81**, 309 (1949).

34. D. W. Peaceman and H. H. Rachford, *J. Soc. Ind., Appl. Math.*, **3**, 28 (1955).

35. M. Rudolph, D. P. Reddy, and S. W. Feldberg, *Anal. Chem.*, **66**, 586A (1994).

36. P. R. Unwin and A. J. Bard, *J. Phys. Chem.*, **95**, 7814 (1991).

37. L. F. Whiting and P. W. Carr, *J. Electroanal. Chem.*, **81**, 1 (1977).

38. S. Pons, *Electroanal. Chem.*, **13**, 115 (1984).
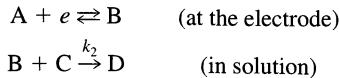
▶ B.8 PROBLEMS

B.1 Show that $Z(t)$ is proportional to the ratio of the current at time t to the Cottrell current at time t_k. What is the proportionality factor?

B.2 Using a spreadsheet, set up a simulation of the Cottrell experiment and work through the first 10 iterations. Use $\ell = 50$ and $\mathbf{D}_M = 0.40$. Calculate $Z(k)$ for each iteration and compare it to $Z_{Cott}(k)$. Calculate the χ values corresponding to the first 12 boxes, and plot the concentration profiles f_A and

f_B vs. χ for $t/t_k = 0.2$. Derive the functions describing f_A and f_B vs. χ and t/t_k from (5.2.13), and draw the analytical curves on your graphs of concentration profiles. Comment on the agreement between your model and the known solution.
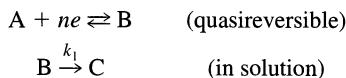
B.3 Suppose one desired a simulation of chronocoulometry. Derive a dimensionless charge parameter analogous to $Z(k)$. In carrying out a simulation, to what time should the charge parameter calculated for iteration k be assigned?

B.4 Consider the following mechanism:

$$A + e \rightleftarrows B \qquad \text{(at the electrode)}$$

$$B + C \overset{k_2}{\rightarrow} D \qquad \text{(in solution)}$$

Derive the diffusion-kinetic equations analogous to (B.3.11) and (B.3.12) and identify the dimensionless kinetic parameter involving k_2.

B.5 Using a computer, carry out simulations of cyclic voltammetry for a quasireversible system. Let $\ell = 50$ and $D_M = 0.45$. Take $\alpha = 0.5$ and let the diffusion coefficients of the oxidized and reduced forms be equal. Cast your dimensionless intrinsic rate parameter in terms of the function ψ defined in (6.5.5), and carry out calculations for $\psi = 20$, 1, and 0.1. Compare the peak splittings in your simulated voltammograms with the values in Table 6.5.2.

B.6 To the simulation program devised for Problem B.5, add a provision for first-order homogeneous decay of the reduction product B, that is,

$$A + ne \rightleftarrows B \qquad \text{(quasireversible)}$$

$$B \overset{k_1}{\rightarrow} C \qquad \text{(in solution)}$$

Run a simulation for $\psi = 20$ and $k_1 t_k = 1$. Compare the results with those predicted by R. S. Nicholson and I. Shain, *Anal. Chem.*, **36**, 706 (1964).

C

REFERENCE TABLES

TABLE C.1   Selected Standard Electrode Potentials in Aqueous Solutions at 25°C in V *vs*. NHE[a]

Reaction	Potential, V
$Ag^+ + e \rightleftarrows Ag$	0.7991
$AgBr + e \rightleftarrows Ag + Br^-$	0.0711
$AgCl + e \rightleftarrows Ag + Cl^-$	0.2223
$AgI + e \rightleftarrows Ag + I^-$	−0.1522
$Ag_2O + H_2O + 2e \rightleftarrows 2Ag + 2OH^-$	0.342
$Al^{3+} + 3e \rightleftarrows Al$	−1.676
$Au^+ + e \rightleftarrows Au$	1.83
$Au^{3+} + 2e \rightleftarrows Au^+$	1.36
p-benzoquinone $+ 2H^+ + 2e \rightleftarrows$ hydroquinone	0.6992
$Br_2(aq) + 2e \rightleftarrows 2Br^-$	1.0874
$Ca^{2+} + 2e \rightleftarrows Ca$	−2.84
$Cd^{2+} + 2e \rightleftarrows Cd$	−0.4025
$Cd^{2+} + 2e \rightleftarrows Cd(Hg)$	−0.3515
$Ce^{4+} + e \rightleftarrows Ce^{3+}$	1.72
$Cl_2(g) + 2e \rightleftarrows 2Cl^-$	1.3583
$HClO + H^+ + e \rightleftarrows \frac{1}{2}Cl_2 + H_2O$	1.630
$Co^{2+} + 2e \rightleftarrows Co$	−0.277
$Co^{3+} + e \rightleftarrows Co^{2+}$	1.92
$Cr^{2+} + 2e \rightleftarrows Cr$	−0.90
$Cr^{3+} + e \rightleftarrows Cr^{2+}$	−0.424
$Cr_2O_7^{2-} + 14H^+ + 6e \rightleftarrows 2Cr^{3+} + 7H_2O$	1.36
$Cu^+ + e \rightleftarrows Cu$	0.520
$Cu^{2+} + 2CN^- + e \rightleftarrows Cu(CN)_2^-$	1.12
$Cu^{2+} + e \rightleftarrows Cu^+$	0.159
$Cu^{2+} + 2e \rightleftarrows Cu$	0.340
$Cu^{2+} + 2e \rightleftarrows Cu(Hg)$	0.345
$Eu^{3+} + e \rightleftarrows Eu^{2+}$	−0.35
$1/2F_2 + H^+ + e \rightleftarrows HF$	3.053
$Fe^{2+} + 2e \rightleftarrows Fe$	−0.44
$Fe^{3+} + e \rightleftarrows Fe^{2+}$	0.771
$Fe(CN)_6^{3-} + e \rightleftarrows Fe(CN)_6^{4-}$	0.3610

(continued)

TABLE C.1 (*continued*)

Reaction	Potential, V
$2H^+ + 2e \rightleftarrows H_2$	0.0000
$2H_2O + 2e \rightleftarrows H_2 + 2OH^-$	-0.828
$H_2O_2 + 2H^+ + 2e \rightleftarrows 2H_2O$	1.763
$2Hg^{2+} + 2e \rightleftarrows Hg_2^{2+}$	0.9110
$Hg_2^{2+} + 2e \rightleftarrows 2Hg$	0.7960
$Hg_2Cl_2 + 2e \rightleftarrows 2Hg + 2Cl^-$	0.26816
$Hg_2Cl_2 + 2e \rightleftarrows 2Hg + 2Cl^-$ (sat'd. KCl)	0.2415
$HgO + H_2O + 2e \rightleftarrows Hg + 2OH^-$	0.0977
$Hg_2SO_4 + 2e \rightleftarrows 2Hg + SO_4^{2-}$	0.613
$I_2 + 2e \rightleftarrows 2I^-$	0.5355
$I_3^- + 2e \rightleftarrows 3I^-$	0.536
$K^+ + e \rightleftarrows K$	-2.925
$Li^+ + e \rightleftarrows Li$	-3.045
$Mg^{2+} + 2e \rightleftarrows Mg$	-2.356
$Mn^{2+} + 2e \rightleftarrows Mn$	-1.18
$Mn^{3+} + e \rightleftarrows Mn^{2+}$	1.5
$MnO_2 + 4H^+ + 2e \rightleftarrows Mn^{2+} + 2H_2O$	1.23
$MnO_4^- + 8H^+ + 5e \rightleftarrows Mn^{2+} + 4H_2O$	1.51
$Na^+ + e \rightleftarrows Na$	-2.714
$Ni^{2+} + 2e \rightleftarrows Ni$	-0.257
$Ni(OH)_2 + 2e \rightleftarrows Ni + 2OH^-$	-0.72
$O_2 + 2H^+ + 2e \rightleftarrows H_2O_2$	0.695
$O_2 + 4H^+ + 4e \rightleftarrows 2H_2O$	1.229
$O_2 + 2H_2O + 4e \rightleftarrows 4OH^-$	0.401
$O_3 + 2H^+ + 2e \rightleftarrows O_2 + H_2O$	2.075
$Pb^{2+} + 2e \rightleftarrows Pb$	-0.1251
$Pb^{2+} + 2e \rightleftarrows Pb(Hg)$	-0.1205
$PbO_2 + 4H^+ + 2e \rightleftarrows Pb^{2+} + 2H_2O$	1.468
$PbO_2 + SO_4^{2-} + 4H^+ + 2e \rightleftarrows PbSO_4 + 2H_2O$	1.698
$PbSO_4 + 2e \rightleftarrows Pb + SO_4^{2-}$	-0.3505
$Pd^{2+} + 2e \rightleftarrows Pd$	0.915
$Pt^{2+} + 2e \rightleftarrows Pt$	1.188
$PtCl_4^{2-} + 2e \rightleftarrows Pt + 4Cl^-$	0.758
$PtCl_6^{2-} + 2e \rightleftarrows PtCl_4^{2-} + 2Cl^-$	0.726
$Ru(NH_3)_6^{3+} + e \rightleftarrows Ru(NH_3)_6^{2+}$	0.10
$S + 2e \rightleftarrows S^{2-}$	-0.447
$Sn^{2+} + 2e \rightleftarrows Sn$	-0.1375
$Sn^{4+} + 2e \rightleftarrows Sn^{2+}$	0.15
$Tl^+ + e \rightleftarrows Tl$	-0.3363
$Tl^+ + e \rightleftarrows Tl(Hg)$	-0.3338
$Tl^{3+} + 2e \rightleftarrows Tl^+$	1.25
$U^{3+} + 3e \rightleftarrows U$	-1.66
$U^{4+} + e \rightleftarrows U^{3+}$	-0.52
$UO_2^+ + 4H^+ + e \rightleftarrows U^{4+} + 2H_2O$	0.273
$UO_2^{2+} + e \rightleftarrows UO_2^+$	0.163

TABLE C.1 (*continued*)

Reaction	Potential, V
$V^{2+} + 2e \rightleftarrows V$	-1.13
$V^{3+} + e \rightleftarrows V^{2+}$	-0.255
$VO^{2+} + 2H^+ + e \rightleftarrows V^{3+} + H_2O$	0.337
$VO_2^+ + 2H^+ + e \rightleftarrows VO^{2+} + H_2O$	1.00
$Zn^{2+} + 2e \rightleftarrows Zn$	-0.7626
$ZnO_2^{2-} + 2H_2O + 2e \rightleftarrows Zn + 4OH^-$	-1.285
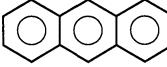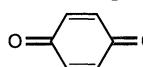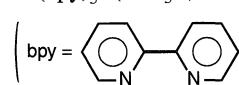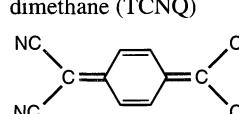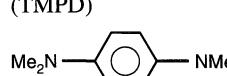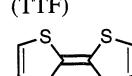
[a] The data in this table are mainly taken from A. J. Bard, J. Jordan, and R. Parsons, Eds., "Standard Potentials in Aqueous Solutions," Marcel Dekker, New York, 1985 (prepared under the auspices of the Electrochemistry and Electroanalytical Chemistry Commissions of IUPAC). Other sources of standard potentials and thermodynamic data include: (1) A. J. Bard and H. Lund, Eds., "The Encyclopedia of the Electrochemistry of the Elements," Marcel Dekker, New York, 1973–1986. (2) G. Milazzo and S. Caroli, "Tables of Standard Electrode Potentials," Wiley-Interscience, New York, 1977. The data here are referred to the NHE based on a 1-atm standard state for H_2. See the footnote in Section 2.1.5 concerning the recent change in standard state.

Table C.2   Selected Formal Potentials in Aqueous Solution at 25°C in V *vs.* NHE[a]

Reaction	Conditions	Potential, V
$Cu(II) + e \rightleftarrows Cu$	$1\ M\ NH_3 + 1\ M\ NH_4^+$	0.01
	$1\ M\ KBr$	0.52
$Ce(IV) + e \rightleftarrows Ce(III)$	$1\ M\ HNO_3$	1.61
	$1\ M\ HCl$	1.28
	$1\ M\ HClO_4$	1.70
	$1\ M\ H_2SO_4$	1.44
$Fe(III) + e \rightleftarrows Fe(II)$	$1\ M\ HCl$	0.70
	$10\ M\ HCl$	0.53
	$1\ M\ HClO_4$	0.735
	$1\ M\ H_2SO_4$	0.68
	$2\ M\ H_3PO_4$	0.46
$Fe(CN)_6^{3-} + e \rightleftarrows Fe(CN)_6^{4-}$	$0.1\ M\ HCl$	0.56
	$1\ M\ HCl$	0.71
	$1\ M\ HClO_4$	0.72
$Sn(IV) + 2e \rightleftarrows Sn(II)$	$1\ M\ HCl$	0.14
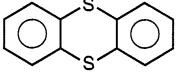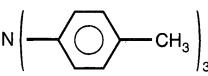
[a] The data in this table are taken mainly from G. Charlot, "Oxidation-Reduction Potentials," Pergamon, London, 1958. Additional values are found in J. J. Lingane, "Electroanalytical Chemistry," Interscience, New York, 1958, and L. Meites, Ed., "Handbook of Analytical Chemistry," McGraw-Hill, New York, 1963.

TABLE C.3 Estimated Standard Potentials in Aprotic Solvents, in V *vs.* aq SCE[a,b]

Substance	Reaction	Conditions[c]	Potential, V
Anthracene (An)	$An + e \rightleftarrows An^{-\cdot}$	DMF, 0.1 M TBAI	-1.92
	$An^{-\cdot} + e \rightleftarrows An^{2-}$	DMF, 0.1 M TBAI	-2.5
	$An^{+\cdot} + e \rightleftarrows An$	MeCN, 0.1 M TBAP	$+1.3$
Azobenzene (AB)	$AB + e \rightleftarrows AB^{-\cdot}$	DMF, 0.1 M TBAP	-1.36
Ph—N=N—Ph	$AB^{-\cdot} + e \rightleftarrows AB^{2-}$	DMF, 0.1 M TBAP	-2.0
	$AB + e \rightleftarrows AB^{-\cdot}$	MeCN, 0.1 M TEAP	-1.40
	$AB + e \rightleftarrows AB^{-\cdot}$	PC, 0.1 M TBAP	-1.40
Benzophenone (BP)	$BP + e \rightleftarrows BP^{-\cdot}$	MeCN, 0.1 M TBAP	-1.88
	$BP + e \rightleftarrows BP^{-\cdot}$	THF, 0.1 M TBAP	-2.06
PhCPh	$BP + e \rightleftarrows BP^{-\cdot}$	NH_3, 0.1 M KI	-1.23^d
	$BP^{-\cdot} + e \rightleftarrows BP^{2-}$	NH_3, 0.1 M KI	-1.76^d
1,4 Benzoquinone (BQ)	$BQ + e \rightleftarrows BQ^{-\cdot}$	MeCN, 0.1 M TEAP	-0.54
	$BQ^{-\cdot} + e \rightleftarrows BQ^{2-}$	MeCN, 0.1 M TEAP	-1.4
Ferrocene (Cp$_2$Fe)	$Cp_2Fe^+ + e \rightleftarrows Cp_2Fe$	MeCN, 0.2 M LiClO$_4$	$+0.31$
Nitrobenzene (NB)	$NB + e \rightleftarrows NB^{-\cdot}$	MeCN, 0.1 M TEAP	-1.15
Ph—NO$_2$	$NB + e \rightleftarrows NB^{-\cdot}$	DMF, 0.1 M NaClO$_4$	-1.01
	$NB + e \rightleftarrows NB^{-\cdot}$	NH_3, 0.1 M KI	-0.42^d
	$NB^{-\cdot} + e \rightleftarrows NB^{2-}$	NH_3, 0.1 M KI	-1.241^d
Oxygen	$O_2 + e \rightleftarrows O_2^{-\cdot}$	DMF, 0.2 M TBAP	-0.87
	$O_2 + e \rightleftarrows O_2^{-\cdot}$	MeCN, 0.2 M TBAP	-0.82
	$O_2 + e \rightleftarrows O_2^{-\cdot}$	DMSO, 0.1 M TBAP	-0.73
Ru(bpy)$_3^{n+}$(RuL$_3^{n+}$)	$RuL_3^{3+} + e \rightleftarrows RuL_3^{2+}$	MeCN, 0.1 M TBABF$_4$	$+1.32$
	$RuL_3^{2+} + e \rightleftarrows RuL_3^{+}$	MeCN, 0.1 M TBABF$_4$	-1.30
$\left(bpy = \right.$	$RuL_3^{+} + e \rightleftarrows RuL_3^{0}$	MeCN, 0.1 M TBABF$_4$	-1.49
	$RuL_3^{0} + e \rightleftarrows RuL_3^{-}$	MeCN, 0.1 M TBABF$_4$	-1.73
Tetracyanoquino-dimethane (TCNQ)	$TCNQ + e \rightleftarrows TCNQ^{-\cdot}$	MeCN, 0.1 M LiClO$_4$	$+0.13$
	$TCNQ^{-\cdot} + e \rightleftarrows TCNQ^{2-}$	MeCN, 0.1 M LiClO$_4$	-0.29
*N,N,N′,N′-*Tetramethyl-*p*-phenylenediamine (TMPD)	$TMPD^{+\cdot} + e \rightleftarrows TMPD$	DMF, 0.1 M TBAP	$+0.21$
Tetrathiafulvalene (TTF)	$TTF^{+\cdot} + e \rightleftarrows TTF$	MeCN, 0.1 M TEAP	$+0.30$
	$TTF^{2+} + e \rightleftarrows TTF^{+\cdot}$	MeCN, 0.1 M TEAP	$+0.66$

(*continued*)

TABLE C.3 Estimated Standard Potentials in Aprotic Solvents, in V *vs.* aq SCE^{a,b}

Substance	Reaction	Conditions^c	Potential, V
Thianthrene (TH)	$TH^{+\cdot} + e \rightleftarrows TH$	MeCN, 0.1 M TBABF$_4$	+1.23
	$TH^{2+} + e \rightleftarrows TH^{+\cdot}$	MeCN, 0.1 M TBABF$_4$	+1.74
	$TH^{+\cdot} + e \rightleftarrows TH$	SO$_2$, 0.1 M TBAP	+0.30^e
	$TH^{2+} + e \rightleftarrows TH^{+\cdot}$	SO$_2$, 0.1 M TBAP	+0.88^e
Tri-N-p-tolylamine (TPTA)	$TPTA^{+\cdot} + e \rightleftarrows TPTA$	THF, 0.2 M TBAP	+0.98

^{a}See footnote in Table C.1.

^{b}Problems arise in reporting potentials in nonaqueous solvents. The practice of using an aqueous SCE as a reference electrode introduces an unknown and sometimes irreproducible liquid junction potential. Sometimes reference electrodes made up in the solvent of interest (e.g., Ag/AgClO$_4$) or QREs are employed. Results here are reported *vs.* an aqueous SCE unless noted otherwise. While there has not yet been an adopted convention for reporting potentials in nonaqueous solvents, a frequent practice is to reference these to the potential of a particular reversible couple in the same solvent. This couple (sometimes called the "reference redox system") is usually chosen on the basis of the extrathermodynamic assumption that the redox potential of this system is only slightly affected by the solvent system. Suggested reference redox systems include ferrocene/ferrocenium, Rb/Rb$^+$, Fe(bpy)$_3^{2+}$/Fe(bpy)$_3^{2+}$ (bpy = 2,2'-bipyridine), and aromatic hydrocarbon/radical cation. For further information concerning these problems, the following references can be consulted: (1) O. Popovych, *Crit. Rev. Anal. Chem.*, **1**, 73 (1970); (2) D. Bauer and M. Breant, *Electroanal. Chem.*, **8**, 282 (1975); (3) A. J. Parker, *Electrochim. Acta*, **21**, 671 (1976).

^{c}See Standard Abbreviations.

^{d}*vs.* Ag/Ag$^+$ (0.01 M) in NH$_3$ at $-50°C$.

^{e}*vs.* Ag/AgNO$_3$ (sat'd) in SO$_2$ at $-40°C$.

TABLE C.4   Selected Diffusion Coefficients at or near 25°C

Substance	Medium	$T/°C$	$10^5 D/cm^2 s^{-1}$	Ref.
$Fe(CN)_6^{3-}$	aq. 0.1 M KCl	25	0.76	1
$Fe(CN)_6^{3-}$	aq. 1.0 M KCl	25	0.76	1
$Fe(CN)_6^{4-}$	aq. 0.1 M KCl	25	0.65	1
$Fe(CN)_6^{4-}$	aq. 1.0 M KCl	25	0.63	1
Cd^{2+}	aq. 0.1 M KCl	25	0.70	2
Cd	Hg	25	1.5	8
$Ru(NH_3)_6^{3+}$	aq. 0.1 M NaTFA	RT	0.67	3
$Ru(NH_3)_6^{3+}$	aq. 0.09 M phosphate	RT	0.53	4
Ferrocene	MeCN, 0.5 M TBABF$_4$	RT	1.7	5
Ferrocene	MeCN, 0.6 M TEAP	RT	2.0	3
Ferrocene	MeCN, 0.1 M TEAP	RT	2.4	6
Stilbene	DMF, 0.5 M TBAI	RT	0.80	7

Abbreviations:
TFA, trifluoroacetate; TBA, tetra-n-butylammonium; TEA, tetraethylammonium; P, perchlorate; RT, room temperature (exact temperature not specified).

References:

1. M. von Stackelberg, M. Pilgram, and W. Toome, *Z. Elektrochem.*, **57**, 342 (1953).
2. D. J. Macero and C. L. Rulfs, *J. Electroanal. Chem.*, **7**, 328 (1964).
3. D. O. Wipf, E. W. Kristensen, M. R. Deakin, and R. M. Wightman, *Anal. Chem.*, **60**, 306 (1988).
4. R. M. Wightman and D. O. Wipf, *Electroanal. Chem.*, **15**, 267 (1989).
5. M. V. Mirkin, T. C. Richards, and A. J. Bard, *J. Phys. Chem.*, **97**, 7672 (1993).
6. A. M. Bond, T. L. E. Henderson, D. R. Mann, T. F. Mann, W. Thormann, and C. G. Zoski, *Anal. Chem.*, **60**, 1878 (1988).
7. H. Kojima and A. J. Bard, *J. Electroanal. Chem.*, **63**, 117 (1975).
8. I. M. Kolthoff and J. J. Lingane, "Polarography," 2nd ed., Interscience, New York, 1952, p. 201.

TABLE C.5   Values of the Error Function and Its Complement[a]

x	erf(x)	erfc(x)	x	erf(x)	erfc(x)
0.00	0	1	1.10	0.8802	0.1198
0.05	0.0564	0.9436	1.20	0.9103	0.0897
0.10	0.1125	0.8875	1.40	0.9523	0.0477
0.20	0.2227	0.7773	1.60	0.9764	0.0236
0.30	0.3286	0.6714	1.80	0.9891	0.0109
0.40	0.4284	0.5716	2.00	0.9953	0.0047
0.50	0.5205	0.4795	2.20	0.9981	0.0019
0.60	0.6039	0.3961	2.40	0.9993	0.0007
0.70	0.6778	0.3222	2.60	0.9998	0.0002
0.80	0.7421	0.2579	2.80	0.9999	0.0001
0.90	0.7969	0.2031	3.00	1.0000	0.0000
1.00	0.8427	0.1573	∞	1	0

[a] For $x < 0.05$, erf(x) $\approx 2x/\pi^{1/2} = 1.1284x$.

INDEX